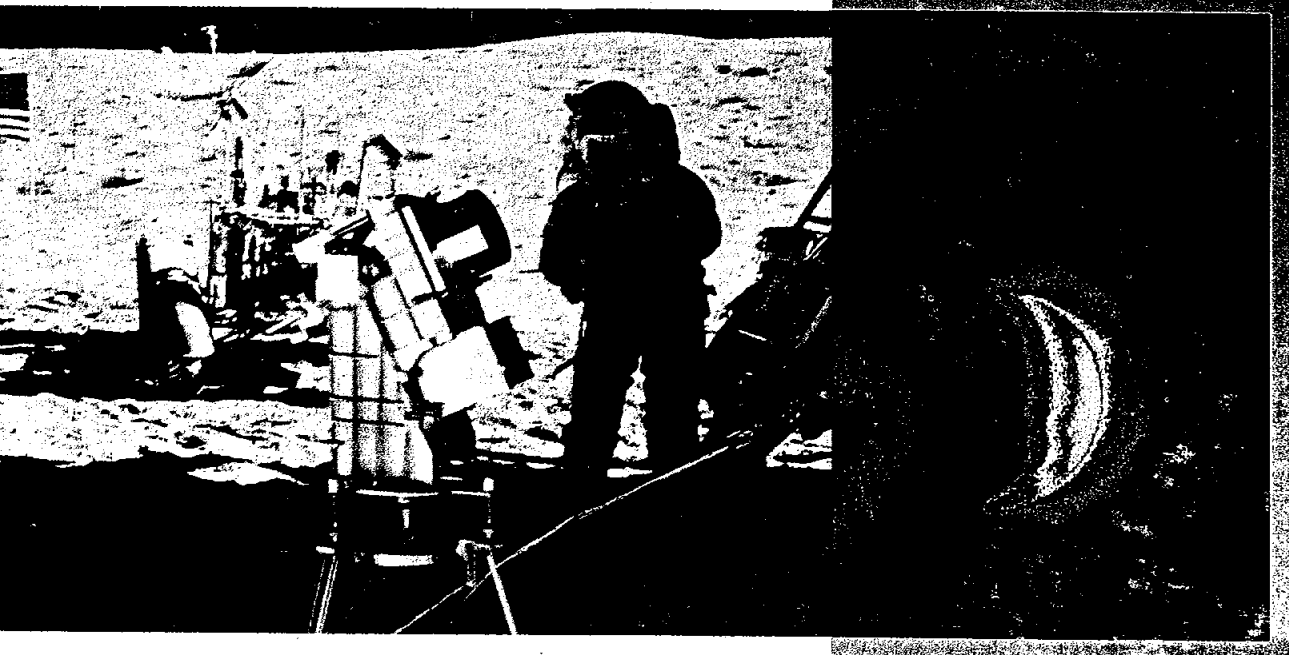
NASA SP-315

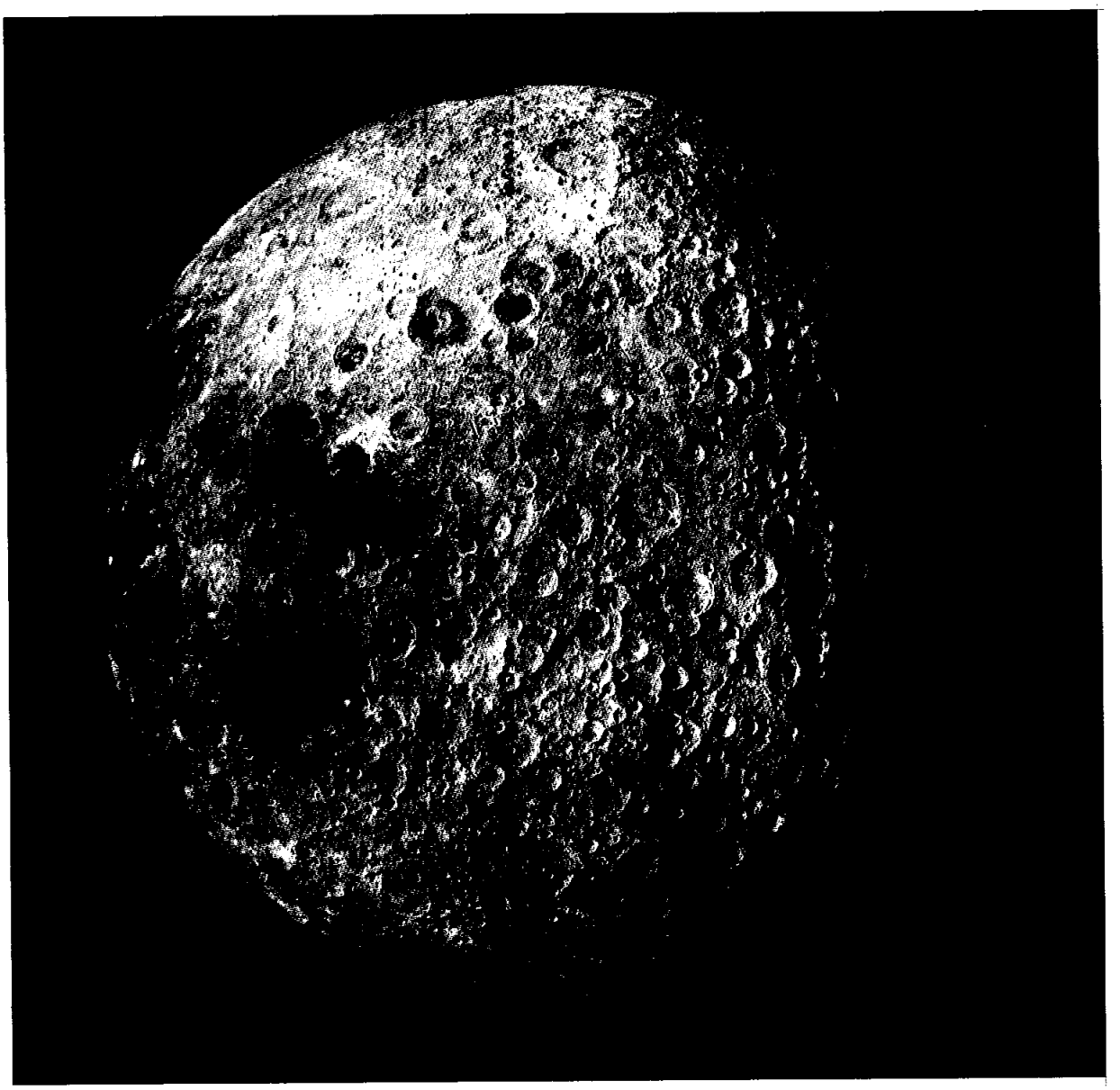
APOLLO 16

Preliminary Science Report



NATIONAL AERONAUTICS
AND SPACE ADMINISTRATION

APOLLO 16 PRELIMINARY SCIENCE REPORT



The Moon, as photographed by the Apollo 16 astronauts on their way back to the Earth. The darker areas show: Mare Crisium, near the horizon at the upper left; Mare Marginis, right and below Mare Crisium; and Mare Smythii, below Mare Marginis. The far-side highlands are also visible.

NASA SP-315

APOLLO 16

Preliminary Science Report

PREPARED BY

NASA MANNED SPACECRAFT CENTER



Scientific and Technical Information Office 1972

NATIONAL AERONAUTICS AND SPACE ADMINISTRATION

Washington, D.C.

EDITORIAL BOARD

The material submitted for the "Apollo 16 Preliminary Science Report" was reviewed by a NASA Editorial Review Board consisting of the following members: Robin Brett and Anthony W. England (Cochairmen), Jack E. Calkins, Robert L. Giesecke, David N. Holman, Robert M. Mercer, Michael J. Murphy, and Scott H. Simpkinson.

Cover Photographs: Clockwise from upper right: (1) Earthrise over the lunar horizon as the command and service module orbits the Moon, as seen from the lunar module. (2) Rock sample 68416 inset in a cross-polarized photomicrograph of thin section from the sample. Sample 68416 is a crystalline rock chipped from a boulder on the rim of a small crater in the ejecta from South Ray Crater. (3) Shadow Rock with Smoky Mountain in the right background. The sampling scoop leaning against the rock is approximately 1 m long. (4) Color-enhanced ultraviolet photograph of the geocorona, the halo of low-density hydrogen around the Earth. The photograph was taken from the lunar surface with the far UV camera/spectrograph. (5) Tripod-mounted far UV camera/spectrograph in the shadow of the lunar module, with the lunar roving vehicle and the U.S. flag in the background.

For sale by the Superintendent of Documents,
U.S. Government Printing Office, Washington, D.C. 20402
Price $10.25, Stock Number 3300-00481

Foreword

Ever since Galileo's telescope made the rugged lunar surface more clearly visible (in 1610), men have strived to learn more about the origin and history of the Earth's big natural satellite, and never has so much progress been made as in the last few years. The fifth manned lunar landing was in a highlands area, quite different from the sites visited previously, and the discoveries there now seem certain to result in significant improvements in the hypotheses of lunar scientists.

Much of the Moon's surface is similar to the Descartes Highlands that the Apollo 16 astronauts examined. From this highly productive mission, more photographs were obtained than on any previous Apollo flight, a greater amount of time was spent outside the lunar module, a greater weight of scientific equipment landed on the Moon, and a record weight of scientific samples was brought back to laboratories on Earth. The network of automatic scientific stations at work on the Moon was extended into a new area and has since detected a moonquake caused by the largest meteoroid impact that has yet been recorded. Additional experiments on the surface and in flight also were successfully performed on this mission for the enlightenment of students of natural phenomena. The Apollo 16 astronauts observed, and scientists studying material they collected have subsequently deduced, that this landing site differed surprisingly from earlier expectations.

Future generations consequently may benefit from better concepts of the operation of the solar system and events throughout the physical universe than have hitherto been possible. This volume is but one of a series of NASA Special Publications being issued promptly to document potentially significant discoveries in the course of the Apollo Program, thereby possibly increasing their usefulness to scientists grappling with problems that have long perplexed mankind.

Dr. James C. Fletcher
Administrator
National Aeronautics and Space Administration

November 10, 1972

Contents

	Page
INTRODUCTION *A. J. Calio*	xiii
1. APOLLO 16 SITE SELECTION *N. W. Hinners*	1-1
2. MISSION DESCRIPTION *Richard R. Baldwin*	2-1
APPENDIX. TOPOGRAPHIC MAPPING OF THE APOLLO 16 LANDING SITE *Robert O. Hill and Merritt J. Bender*	2-11
3. SUMMARY OF SCIENTIFIC RESULTS *Anthony W. England*	3-1
4. PHOTOGRAPHIC SUMMARY *John W. Dietrich and Uel S. Clanton*	4-1
5. CREW OBSERVATIONS *John W. Young, Thomas K. Mattingly, and Charles M. Duke*	5-1
6. PRELIMINARY GEOLOGIC INVESTIGATION OF THE APOLLO 16 LANDING SITE *W. R. Muehlberger, R. M. Batson, E. L. Boudette, C. M. Duke, R. E. Eggleton, D. P. Elston, A. W. England, V. L. Freeman, M. H. Hait, T. A. Hall, J. W. Head, C. A. Hodges, H. E. Holt, E. D. Jackson, J. A. Jordan, K. B. Larson, D. J. Milton, V. S. Reed, J. J. Rennilson, G. G. Schaber, J. P. Schafer, L. T. Silver, D. Stuart-Alexander, R. L. Sutton, G. A. Swann, R. L. Tyner, G. E. Ulrich, H. G. Wilshire, E. W. Wolfe, and J. W. Young*	6-1
7. PRELIMINARY EXAMINATION OF LUNAR SAMPLES	7-1
PART A. A PETROGRAPHIC AND CHEMICAL DESCRIPTION OF SAMPLES FROM THE LUNAR HIGHLANDS *The Lunar Sample Preliminary Examination Team*	7-1
PART B. APOLLO 16 SPECIAL SAMPLES *Friedrich Hörz, W. D. Carrier, III, J. W. Young, C. M. Duke, J. S. Nagle, and R. Fryxell*	7-24
PART C. CAUSE OF SECONDARY MAGNETIZATION IN LUNAR SAMPLES *G. W. Pearce and D. W. Strangway*	7-55
8. SOIL MECHANICS *James K. Mitchell, W. David Carrier, III, William N. Houston, Ronald F. Scott, Leslie G. Bromwell, H. Turan Durgunoglu, H. John Hovland, Donald D. Treadwell, and Nicholas C. Costes*	8-1

9. PASSIVE SEISMIC EXPERIMENT 9-1
Gary V. Latham, Maurice Ewing, Frank Press, George Sutton, James Dorman, Yosio Nakamura, Nafi Toksoz, David Lammlein, and Fred Duennebier

10. ACTIVE SEISMIC EXPERIMENT 10-1
Robert L. Kovach, Joel S. Watkins, and Pradeep Talwani

11. LUNAR SURFACE MAGNETOMETER EXPERIMENT 11-1
P. Dyal, C. W. Parkin, D. S. Colburn, and G. Schubert

12. LUNAR PORTABLE MAGNETOMETER EXPERIMENT 12-1
P. Dyal, C. W. Parkin, C. P. Sonett, R. L. DuBois, and G. Simmons

13. FAR UV CAMERA/SPECTROGRAPH 13-1
George R. Carruthers and Thornton Page

14. SOLAR WIND COMPOSITION EXPERIMENT 14-1
J. Geiss, F. Buehler, H. Cerutti, P. Eberhardt, and Ch. Filleux

15. COSMIC RAY EXPERIMENT 15-1

PART A. COMPOSITION AND ENERGY SPECTRA OF SOLAR COSMIC RAY NUCLEI 15-2
R. L. Fleischer and H. R. Hart, Jr.

PART B. COMPOSITION OF INTERPLANETARY PARTICLES FROM 0.1 TO 150 MeV/NUCLEON 15-11
P. B. Price, D. Braddy, D. O'Sullivan, and J. D. Sullivan

PART C. SOLAR COSMIC RAY, SOLAR WIND, SOLAR FLARE, AND NEUTRON ALBEDO MEASUREMENTS 15-19
D. Burnett, C. Hohenberg, M. Maurette, M. Monnin, R. Walker, and D. Wollum

16. GEGENSCHEIN-MOULTON REGION PHOTOGRAPHY FROM LUNAR ORBIT 16-1
L. Dunkelman, C. L. Wolff, and R. D. Mercer

17. UV PHOTOGRAPHY OF THE EARTH AND MOON 17-1
Tobias Owen

18. GAMMA RAY SPECTROMETER EXPERIMENT 18-1
James R. Arnold, Albert E. Metzger, Laurence E. Peterson, Robert C. Reedy, and J. I. Trombka

19. X-RAY FLUORESCENCE EXPERIMENT 19-1
I. Adler, J. Trombka, J. Gerard, P. Lowman, R. Schmadebeck, H. Blodget, E. Eller, L. Yin, R. Lamothe, G. Osswald, P. Gorenstein, P. Bjorkholm, H. Gursky, B. Harris, L. Golub, and F. R. Harnden, Jr.

20. ALPHA-PARTICLE SPECTROMETER EXPERIMENT 20-1
Paul Gorenstein and Paul Bjorkholm

CONTENTS

21. LUNAR ORBITAL MASS SPECTROMETER EXPERIMENT 21-1
R. R. Hodges, J. H. Hoffman, and D. E. Evans

22. SUBSATELLITE MEASUREMENTS OF PLASMA AND ENERGETIC PARTICLES 22-1
K. A. Anderson, L. M. Chase, R. P. Lin, J. E. McCoy, and R. E. McGuire

23. THE PARTICLES AND FIELDS SUBSATELLITE MAGNETOMETER EXPERIMENT 23-1
P. J. Coleman, Jr., B. R. Lichtenstein, C. T. Russell, G. Schubert, and L. R. Sharp

24. S-BAND TRANSPONDER EXPERIMENT 24-1
W. L. Sjogren, P. M. Muller, and W. R. Wollenhaupt

25. BISTATIC-RADAR INVESTIGATION 25-1
H. T. Howard and G. L. Tyler

26. APOLLO WINDOW METEOROID EXPERIMENT 26-1
Burton G. Cour-Palais, Milton L. Brown, and David S. McKay

27. BIOMEDICAL EXPERIMENTS 27-1

PART A. BIOSTACK EXPERIMENT 27-1
Horst Bücker, G. Horneck, E. Reinholz, W. Scheuermann, W. Rüther, E. H. Graul, H. Planel, J. P. Soleilhavoup, P. Cüer, R. Kaiser, J. P. Massué, R. Pfohl, R. Schmitt, W. Enge, K. P. Bartholomä, R. Beaujean, K. Fukui, O. C. Allkofer, W. Heinrich, H. François, G. Portal, H. Kühn, H. Wollenhaupt, and G. H. Bowman

PART B. MICROBIAL RESPONSE TO SPACE ENVIRONMENT 27-11
G. R. Taylor, C. E. Chassay, W. L. Ellis, B. G. Foster, P. A. Volz, J. Spizizen, H. Bücker, R. T. Wrenn, R. C. Simmonds, R. A. Long, M. B. Parson, E. V. Benton, J. V. Bailey, B. C. Wooley, and A. M. Heimpel

PART C. VISUAL LIGHT FLASH PHENOMENON 27-17
Richard E. Benson and Lawrence S. Pinsky

28. OBSERVATIONS AND IMPRESSIONS FROM LUNAR ORBIT 28-1
T. K. Mattingly, Farouk El-Baz, and Richard A. Laidley

29. PHOTOGEOLOGY 29-1

PART A. RELATIVE AGES OF SOME NEAR-SIDE AND FAR-SIDE TERRA PLAINS BASED ON APOLLO 16 METRIC PHOTOGRAPHY 29-3
Laurence Soderblom and Joseph M. Boyce

PART B. CAYLEY FORMATION INTERPRETED AS BASIN EJECTA 29-7
R. E. Eggleton and G. G. Schaber

PART C. SMALL-SCALE ANALOGS OF THE CAYLEY FORMATION AND DESCARTES MOUNTAINS IN IMPACT-ASSOCIATED DEPOSITS 29-16
James W. Head

PART D. DESCARTES HIGHLANDS: POSSIBLE ANALOGS AROUND THE ORIENTALE BASIN 29-20
Carroll Ann Hodges

PART E. ORIENTALE BASIN DEPOSITS (RICCIOLI AREA) IN APOLLO 16 EARTHSHINE PHOTOGRAPHY 29-24
D. D. Lloyd and J. W. Head

PART F. REINTERPRETATIONS OF THE NORTHERN NECTARIS BASIN 29-27
Don E. Wilhelms

PART G. STRUCTURAL ASPECTS OF IMBRIUM SCULPTURE 29-31
David H. Scott

PART H. DISCOVERY OF TWO LUNAR FEATURES 29-33
Farouk El-Baz

PART I. ARTIFICIAL LUNAR IMPACT CRATERS: FOUR NEW IDENTIFICATIONS 29-39
Ewen A. Whitaker

PART J. RANGER AND OTHER IMPACT CRATERS PHOTOGRAPHED BY APOLLO 16 29-45
H. J. Moore

PART K. LUNAR SECONDARY CRATERS 29-51
Verne R. Oberbeck, Robert H. Morrison, and John Wedekind

PART L. CRATER MORPHOMETRY 29-56
Richard J. Pike

PART M. KING CRATER AND ITS ENVIRONS 29-62
Farouk El-Baz

PART N. EJECTA BLANKETS OF LARGE CRATERS EXEMPLIFIED BY KING CRATER 29-70
Keith A. Howard

PART O. SELECTED VOLCANIC AND SURFICIAL FEATURES 29-78
R. A. Young, W. J. Brennan, and R. W. Wolfe

PART P. LUNAR VOLCANISM: MARE RIDGES AND SINUOUS RILLES 29-79
Richard A. Young

PART Q. PLANIMETRIC SHAPES OF LUNAR RILLES 29-80
Verne R. Oberbeck, Michio Aoyagi, Ronald Greeley, and Michael Lovas

PART R. LUNAR VOLCANISM: FRACTURE PATTERNS AND RILLES IN MARGINAL PREMARE CRATERS 29-89
Richard A. Young

PART S. MARE RIDGES AND ARCHES IN SOUTHERN OCEANUS PROCELLARUM 29-90
George W. Colton, Keith A. Howard, and Henry J. Moore

CONTENTS

PART T. THE ALHAZEN TO ABUL WAFA SWIRL BELT: AN EXTENSIVE FIELD OF LIGHT-COLORED, SINUOUS MARKINGS 29-93
Farouk El-Baz

PART U. LOW-RELIEF FEATURES IN TERRAIN OF THE DESCARTES REGION AND OTHER AREAS: NEAR-TERMINATOR PHOTOGRAPHY 29-97
J. W. Head and D. D. Lloyd

PART V. COLOR CONTRASTS IN MARE NUBIUM AND THE SOUTHERN OCEANUS PROCELLARUM 29-104
Ewen A. Whitaker

PART W. APOLLO 16 LANDING SITE: SUMMARY OF EARTH-BASED REMOTE SENSING DATA 29-105
S. H. Zisk, Harold Masursky, D. J. Milton, G. G. Schaber, R. W. Shorthill, and T. W. Thompson

PART X. CALIBRATION OF RADAR DATA FROM APOLLO 16 RESULTS 29-110
S. H. Zisk and H. J. Moore

PART Y. PHYSICAL AND GEOLOGICAL ASPECTS OF HEILIGENSCHEIN MEASUREMENTS 29-113
Robert L. Wildey

30. PHOTOGRAMMETRY AND ALTIMETRY 30-1

PART A. APOLLO 16 LASER ALTIMETER 30-1
W. R. Wollenhaupt and W. L. Sjogren

PART B. PHOTOGRAMMETRY USING APOLLO 16 ORBITAL PHOTOGRAPHY 30-5
Sherman S. C. Wu, Francis J. Schafer, Raymond Jordan, and Gary M. Nakata

PART C. FREQUENCY DISTRIBUTIONS OF LUNAR SLOPES 30-10
Sherman S. C. Wu and H. J. Moore

31. ASTRONOMICAL PHOTOGRAPHY 31-1

PART A. GUM NEBULA, GALACTIC CLUSTER, AND ZODIACAL LIGHT PHOTOGRAPHY 31-1
R. D. Mercer, L. Dunkelman, and Thomas K. Mattingly

PART B. SOLAR CORONA PHOTOGRAPHY 31-3
R. M. Mac Queen, C. L. Ross, and Thomas K. Mattingly

APPENDIX A—Glossary A-1

APPENDIX B—Abbreviations and Acronyms B-1

APPENDIX C—Units and Unit-Conversion Factors C-1

Introduction

". . . there is nothing so far removed
from us to be beyond our reach or so hidden
that we cannot discover it."

René Descartes

In most difficult endeavors, experience engenders both confidence and skill. The manned exploration of the Moon is no exception. The reaching of those parts of the Moon that contain both the oldest and most intriguing rocks had to await acquisition of such experience. The character of the relatively smooth expanses of the lunar maria was established by the samples and results of experiments from the Apollo 11, 12, and 15 missions. The exploration of the older lunar terra began with the Apollo 14 and 15 missions. The Apollo 15 orbital-science results and the detailed study of soils from the Luna 20, Apollo 11, and Apollo 14 sites demonstrated that the terra materials in the Fra Mauro and Hadley regions do not exemplify most of the lunar terra. Geochemical studies indicate that the typical terra must be underlain by rocks richer in aluminum and poorer in the radioactive elements uranium, thorium, and potassium than the samples from the Hadley and Fra Mauro sites.

The characterization of the aluminum-rich highlands, which make up more than four-fifths of the lunar surface, became the major objective of the last two Apollo missions as soon as the Apollo 15 results were understood. The ultimate origin of the aluminum- or plagioclase-rich terra rocks is a secret that may be buried under a thick debris that was produced by an intense bombardment of the lunar surface before the formation of the mare surfaces. It was thought that the accessibility of the primitive rocks was complicated further by younger igneous rocks that intruded and covered the early aluminum-rich crust in many parts of the terra. The investigation of such igneous rocks, along with a search for samples of the primitive aluminum-rich crust, was the prime objective of the Apollo 16 mission. The three men who flew this mission took part in more than 18 months of intensive training in science. They again demonstrated that sophisticated observations about one's surroundings are possible in a totally foreign environment. Astronauts Young and Duke returned approximately 95 kg of rock samples and more than 1700 photographs from their 20 hr of extravehicular activity on the lunar surface. The first study of these rocks and pictures already shows that the terra regions of the lunar surface must be much more complex than the earlier visited mare regions. It is very unlikely that these regions could have been characterized meaningfully by a single soil or rock sample.

The complement of both orbital and surface experiments carried on this mission essentially was identical to that carried on the Apollo 15 mission; the main difference was the addition of the lunar portable magnetometer, the ultraviolet camera, and the cosmic-ray experiment, along with the substitution of the active seismic experiment for the suprathermal ion detector experiment in the Apollo lunar surface experiments package. The Apollo 16 orbital experiment results confirm the regional compositional variations of the lunar surface that were surmised from the first flight of these experiments on the Apollo 15 mission. The measurement of the natural gamma-ray activity of the lunar surface again reveals a surprising asymmetrical distribution of potassium-, uranium-, and thorium-rich rocks on the lunar surface. Rocks with 10 to

20 times the mean gamma-ray activity of the surface are very common in the western portion of the Moon and are virtually absent from the far-side and eastern-limb regions. The origin of this large-scale asymmetry is a first-order characteristic that must be understood before the early evolution of the Moon becomes clear. The complementary measurement of characteristic fluorescent X-radiation attributable to aluminum, magnesium, and silicon has shown that the near-side terra is as rich in aluminum as most of the far-side terra. Seismic refraction profiles determined from a series of rocket-launched explosive charges confirm that the regolith in the Descartes highland region is, indeed, much thicker than that found over the mare surfaces. The fact that the local magnetic-field intensity is surprisingly high and variable in direction suggests that some strongly magnetized rocks must underlie the regolith.

The successful deployment of the fourth passive seismometer resulted in a seismometer network that was an integral part of the Apollo science program from its inception. The objective of this network is to record the velocity of sound for a variety of paths through the lunar interior. Acoustic events with energy sufficient to transmit waves of several hundred kilometers are extremely rare on the Moon. Thus, the occurrence of such an event less than 3 weeks after the completion of this network is incredible scientific luck. The May 13, 1972, event conclusively confirmed the existence of a major seismic discontinuity at 60 to 65 km below the lunar surface. The origin of this discontinuity also plays a significant role in understanding the early history of the Moon.

While on the lunar surface, Astronauts Young and Duke were puzzled by the absence of clear-cut igneous characteristics in most of the rocks they examined. Their observations and deductions indicated that the abundant rock specimens found at this site consisted of mechanical mixtures of preexisting rocks. The preliminary description of these rocks given in this report confirms their observations. Neither the photographic documentation nor the samples themselves provide support for the hypothesis that the landing site was underlain by a type of volcanic rock peculiar to the highlands. Even though the explanation of the landforms that resulted in the choice of this site is not in hand, it is already obvious that the Descartes region is a much more typical terra site than was originally expected by many investigators. The diverse collection of Descartes specimens may, in fact, be interpretable in terms of a subregolith, crustal model that probably applies to a large fraction of the lunar terra. The aluminum, potassium, and thorium contents found for the Descartes soil are in excellent agreement with the concentrations inferred from the X-ray and gamma-ray spectra recorded for this region. Thus, the results of experiments and the textural and chemical characteristics of the rock all agree in one respect; that is, they indicate that the earliest outer portion of the Moon must consist of a thick, feldspar-rich crust. Whether this crust formed in a single, moonwide, cataclysmic event that may coincide with the formation of the Moon or evolved over a period of hundreds of millions of years is not known. Indeed, this may be the major question to be answered in unraveling the earliest epochs of lunar history.

Not all the activities of Astronauts Young and Duke had to do with the investigation of the Moon itself. Their temporary lunar base provided an opportunity to perform several astronomical experiments that could not be done within the magnetic and particle environment surrounding the Earth. The pictures taken by the ultraviolet camera will allow astronomers to compare the universe seen in visible light with that seen in ultraviolet light. The ultraviolet pictures and spectra of the environment of the Earth already have revealed upper atmospheric species and patterns that were not observed previously.

In the euphoria that follows the successful completion of a difficult endeavor, one is tempted to make historical value judgments. In this vein, we are confident that the new understanding summarized in this report is only the broad outline of a much more substantial and permanent scientific edifice that is yet to come. We also recognize that the accelerated pace of learning experienced by most scientists associated with the Apollo Program has left most of us without adequate reference points from which we can gage the importance of our own achievements. Following the example of previous explorers and scientists, we accept as our first duty the documentation and preservation of the observations made in our mission so that future generations can evaluate these efforts with objectivity and facility.

A. J. CALIO
NASA Manned Spacecraft Center

1. Apollo 16 Site Selection

N. W. Hinners[a]

INTRODUCTION

The Apollo 16 mission had two prime sampling objectives, the Cayley Formation and the Descartes Formation. Although both units had been hypothesized to be volcanic in site selection discussions, impact breccias predominate among returned samples. This result raises questions concerning the site selection process and the fundamentals of photogeology. Recognizing that many of the basic premission interpretations of the geology of the Apollo 11, 12, 14, and 15 sites have been correct, the job at hand is to improve the photogeologic technique, for this technique remains the prime method for extrapolation of Apollo findings to the entire Moon and to the planets.

The rationale that led to the selection of Descartes as the Apollo 16 site is briefly reviewed in this paper. A discussion of pertinent studies that took place after site selection but prior to the mission is also provided. The last section is devoted to lessons learned and to implications for future lunar or planetary site selection activities.

DESCARTES SITE SELECTION RATIONALE

The Apollo 16 landing site, Descartes, was selected after the Apollo 11, 12, and 14 missions, but before the Apollo 15 mission to Hadley-Apennine. The Apollo 11 and 12 flights had returned material which conclusively demonstrated that the mare fill is dominantly basalt of lava-flow origin and that the maria are actually very old, although they appear very young. The isotopic age information, when used in conjunction with data on crater densities and morphologies on many mare surfaces, suggested that mare lava generation might have been limited to the period between roughly 3 and 3.7 billion years ago. The Apollo 14 mission established that the Fra Mauro Formation is ejecta from the Imbrium Basin and that the Imbrium impact, one of the youngest basin-forming events, occurred about 3.9 billion years ago. Model ages of lunar soils from all sites indicate that the Moon originated about 4.5 billion years ago. The composition of Apollo 12 putative Copernicus ray material and of Fra Mauro samples indicated extensive premare igneous differentiation that created high-alumina basalts of relatively high radioactivity. Additionally, exotic fragments at all sites indicated that large regions of the highlands might be anorthositic.

The foregoing factors led to a consensus that the prime objective of both Apollo 16 and 17 should be direct sampling of highlands material that would be compositionally different from Fra Mauro and mare fill, and that would provide detail on lunar evolution before the Imbrium impact, 3.9 billion years ago. A second high-priority objective was to sample the youngest widespread lunar volcanics to determine whether the lunar heat engine really stopped 3 billion years ago.

The Apollo 16 site selection discussions commenced by considering many candidate sites. After the scientific attributes and the engineering and operational constraints were considered, two high-priority highland candidate sites remained: Alphonsus and Descartes, both multiple-objective sites in terms of photogeologic units. The crater wall of Alphonsus was argued to be made of pre-Imbrium highlands material, and the dark halo craters on the crater floor were thought to consist of relatively young postmare volcanic material, possibly originating at significantly great depth within the lunar interior. The third sampling objective at Alphonsus was the crater filling itself, represented as a type of upland basin fill, and at one time referred to as Cayley Formation.

Two prime sampling objectives were delineated for the Descartes site; the upland basin fill, or Cayley Formation, and the hilly and furrowed unit now known as the Descartes Formation. Crater densities and stratigraphic relationships indicate that in some

[a]National Aeronautics and Space Administration, Washington, D.C.

regions these formations are slightly older than the Imbrium impact, and in other regions, including the Apollo 16 site, slightly younger. An early (1962) interpretation by Eggleton and Marshall (ref. 1-1) of the origin of the Cayley and Descartes Formations was that they might be of impact origin and related to the Imbrium impact. However, in most subsequent, and especially in the recent, astrogeologic literature (refs. 1-2 to 1-7) and in all site selection discussions for which a record exists (Group for Lunar Exploration Planning (GLEP), GLEP Site Selection Subgroups, Ad Hoc Site Selection Committees, and the Apollo Site Selection Board), both the Cayley and Descartes Formations are overwhelmingly interpreted as volcanic units. More specifically, the Cayley Formation has been argued to have a lower iron and higher silica content than mare basalts because of its higher albedo and more hummocky terrain, the latter a result of higher viscosity. The prime reason for arguing the basalt-flow origin of the Cayley Formation is the characteristic location as a relatively flat fill in crater interiors and other topographic lows. The Descartes Formation, of higher albedo than Cayley, was thought to represent a more silicous, higher viscosity extrusive. It was further argued by H. Masursky before the Site Selection Board that the Apollo 16 site is located on the highest topographic region of the frontside highlands, indicating that the Descartes volcanics represent remobilized highlands, and that analysis of these volcanics would shed light on the basic process of highland formation.

There was no clear consensus among the scientists involved in the site selection as to the better site. Those favoring Descartes argued that the Alphonsus crater wall might be mantled by Cayley volcanics and that the Alphonsus floor fill is not typical Cayley. On the other hand, Alphonsus protagonists felt that relatively young highland volcanics at Descartes was not significant when contrasted with more primitive highlands. When pro and con arguments were presented before the Apollo Site Selection Board, there were no compelling discriminators. Two factors led the Board to recommend Descartes. First, the Apollo 14 samples (not yet thoroughly analyzed) and the samples to come from the Apollo 15 mission to Hadley-Apennine might yield pre-Imbrian highland material similar to that sought at Alphonsus. If not, the opportunity would exist to go to Alphonsus on Apollo 17. Second, the Cayley and Descartes Formations cover about 11 percent of the lunar near side; and, thus, regardless of the details of their origin, these formations must represent significant lunar units that should be sampled.

POSTSELECTION STUDIES

Site selection discussions were based on the most recent photointerpretations available. Because of the large number of candidate landing sites and limitations of manpower, the site photogeologic maps and interpretations have usually been of a preliminary nature. It is only after the site has been selected that detailed mapping commences.

The 1:250,000, 1:100,000, and 1:50,000 scale maps of the Descartes region, prepared for the mission by Milton and Hodges (ref. 1-2), and Elston et al. (refs. 1-5 and 1-6), are dominated by volcanic interpretations for both the Cayley and Descartes Formations. The emphasis is so strong that aspects of the morphology, which might argue against a volcanic interpretation (i.e., the paucity of ridges and flow front scarps), were interpreted as suggesting "... that the Cayley may consist of ash-flow deposits rather than lava beds." However, evidence that these interpretations might be incorrect was provided by Oberbeck (ref. 1-8), who found that the apparent regolith thickness was less than one would predict (based upon the number of craters assumed to be of impact origin) and that the craters appeared more subdued than expected. Oberbeck's preferred interpretation was that a deep regolith that has been mantled by a deposit indurated after deposition underlies the area. However, he suggested that the mantling deposit might be a welded-ash from the volcanic terrain (Descartes Mountains) south of the site. Support for this interpretation can be found in a study by Head and Goetz (ref. 1-9) who use Orbiter photography, Apollo 12 multispectral photography, Earth-based spectrophotometry, and thermal infrared and radar data in concluding that there has been Copernican-age volcanism in the Descartes Mountains.

RETROSPECT AND LESSONS LEARNED

The discovery of a large preponderance of apparent impact breccias at the Apollo 16 site must be treated with caution; it would be foolhardy to immediately postulate an impact origin for all lunar

units labeled Cayley or Descartes. First, it is not certain that the Descartes Formation was adequately sampled. Second, it has long been recognized that the Cayley is not everywhere morphologically identical (e.g., Wilhelms, ref. 1-4). Further evidence for the inhomogeneity of the Cayley comes from the Apollo 16 orbital X-ray spectrometer results, which indicate that the Apollo 16 materials are significantly compositionally different from what is called Cayley in the crater Ptolemaeus (Adler et al., ref. 1-10). Interestingly, the X-ray results are consistent with an interpretation of the Ptolemaeus Cayley as material intermediate in composition between low-alumina mare basalts and the high-alumina terra. Just as interesting and somewhat ironic are the X-ray data, confirmed by analysis of returned samples, that indicate the Apollo 16 site is representative of large regions of the type of highlands thought to exist in the wall of Alphonsus.

The surprising findings at the Apollo 16 landing site have forced a re-evaluation of the process of photogeology and site selection. The following are lessons that have been learned and that should be considered in any future work.

(1) Care must be taken to separate observation (basically, what is shown in maps) from interpretation. Photointerpretation is not foolproof. Trask and McCauley (ref. 1-7) note that, regarding the Descartes materials, "photogeologic interpretation alone cannot rule out the possibility that all the hilly and gently undulating terrain belongs to one or more of the hummocky ejecta blankets surrounding the large circular basins."

(2) The art of lunar (and planetary) photogeology could benefit by using the method of multiple working hypotheses.

(3) When lacking other definitive data, it is reasonable to select a site in an extensive morphologic unit previously unsampled. Although what was found on the Apollo 16 mission was not expected, the samples are nevertheless just as, or possibly more, valuable. Those who predicted a volcanic terrane did so for good reason; thus, the observations that led to the supposition of volcanism must be explained. It is probable that we will now decipher many previously unknown characteristics of large impacts and ejecta mechanics. This information is essential to the future extrapolation of Apollo results when using photogeologic techniques.

(4) It is highly desirable that detailed site mapping be done prior to site selection and that alternate interpretations be examined thoroughly. Identical interpretations of similar morphologic units at great distances from each other should be examined thoroughly and treated with caution.

(5) Compositional data acquired from orbit (and, in the case of the Moon, from Earth-based observations) can be an invaluable aid in site selection. These data enable discrimination among morphologically similar-looking units that may not be genetically related.

REFERENCES

1-1. Eggleton, R. E.; and Marshall, C. H.: Notes on the Apenninian Series and Pre-Imbrian Stratigraphy in the Vicinity of Mare Humorum and Mare Nubium. Astrogeologic Studies Semiannual Progress Report, Feb. 26, 1961, to Aug. 24, 1961. U.S. Geol. Survey Open-File Rept., 1962, pp. 132-137.

1-2. Milton, D. J.; and Hodges, C. A.: Geologic Maps of the Descartes Region of the Moon: Apollo 16 Pre-Mission Map. U.S. Geol. Survey Misc. Geol. Inv. Map I-748, 1972.

1-3. Wilhelms, D. E.; and McCauley, J. F.: Geologic Map of the Near Side of the Moon. U.S. Geol. Survey Misc. Geol. Inv. Map I-703, 1971.

1-4. Wilhelms, D. E.: Summary of Lunar Stratigraphy – Telescopic Observations. U.S. Geol. Survey Professional Paper 559-F, 1970.

1-5. Elston, D. P.; Boudette, E. L.; and Schafer, J. P.: Geology of the Apollo 16 Landing Site Area. U.S. Geol. Survey Open-File Rept., 1972.

1-6. Elston, D. P.; Boudette, E. L.; and Schafer, J. P.: Geologic Map of the Apollo 16 (Descartes) Region. U.S. Geol. Survey Open-File Rept., 1972.

1-7. Trask, N. J; and McCauley, J. F.: Differentiation and Volcanism in the Lunar Highlands: Photogeologic Evidence and Apollo 16 Implications. Earth and Planetary Science Letters, Vol. 14. 1972, pp. 201-206.

1-8. Oberbeck, V. R.: Implications of Regolith Thickness in the Apollo 16 Landing Site. NASA TM X-62089, 1971.

1-9. Head, J. W., III; and Goetz, A. F. H.: Descartes Region: Evidence for Copernican-Age Volcanism. J. Geophys. Res. Vol. 77, 1972, pp. 1368-1374.

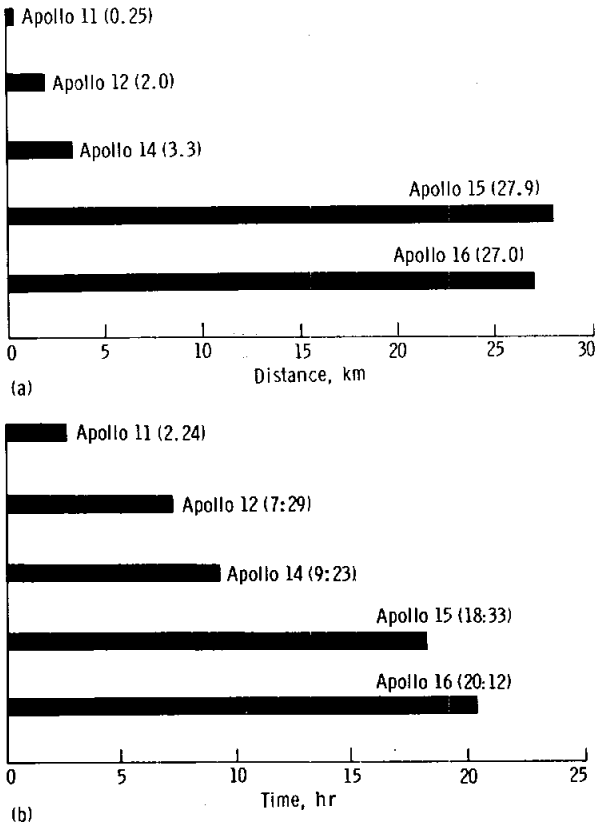
1-10. Adler, I.; Trombka, J.; Gerard, J.; Lowman, P., Schmadebeck, R.; Blodget, H.; Eller, E.; Yin, L.; Lamothe, R.; Osswald, G.; Gorenstein, P.; Bjorkholm, P.; Gursky, H.; and Harris, B.: Apollo 16 Geochemical X-ray Fluorescence Experiment: Preliminary Report, X-641-72-198,, preprint, NASA Goddard Space Flight Center, 1972.

2. Mission Description

Richard R. Baldwin[a]

The successful Apollo 16 manned lunar-landing mission was the second in a series of three J-type missions planned for the Apollo Program. These missions are characterized by a larger scientific payload, increased hardware capability, and a battery-powered lunar roving vehicle (Rover). These additions resulted in benefits to the Apollo 16 mission, such as a mission of 11.1 days, a stay on the lunar surface of 71 hr, a lunar-surface traverse distance of approximately 27 km, and a scientific instrument module (SIM) containing equipment for orbital experiments and photographic tasks. Crewmen were on the lunar surface for 20.2 hr and collected approximately 96 kg of samples. Figure 2-1 compares the science payload weight delivered to the lunar surface, extravehicular activity (EVA) duration, lunar-surface distance traversed, and weight of lunar samples returned to Earth for Apollo 11, 12, 14, 15, and 16.

The landing site for Apollo 16 is in the lunar highlands north of the crater Descartes shown in figure 2-2. High-resolution photography of the lunar surface, obtained on Apollo 14, played an important part in the selection of this site. The use of this photography to develop topographic maps and a three-dimensional model for planning and simulation of traverse activities is discussed in the appendix to this section.



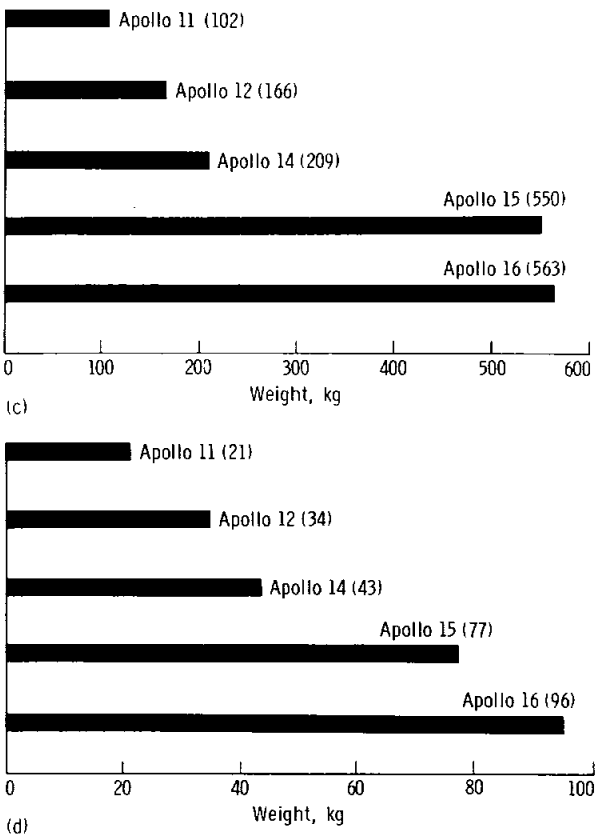


FIGURE 2-1.–Comparison of Apollo missions. (a) Traverse distance. (b) Time outside the LM. (c) Weight of experiment equipment landed on the lunar surface. (d) Weight of lunar samples returned.

[a]NASA Manned Spacecraft Center.

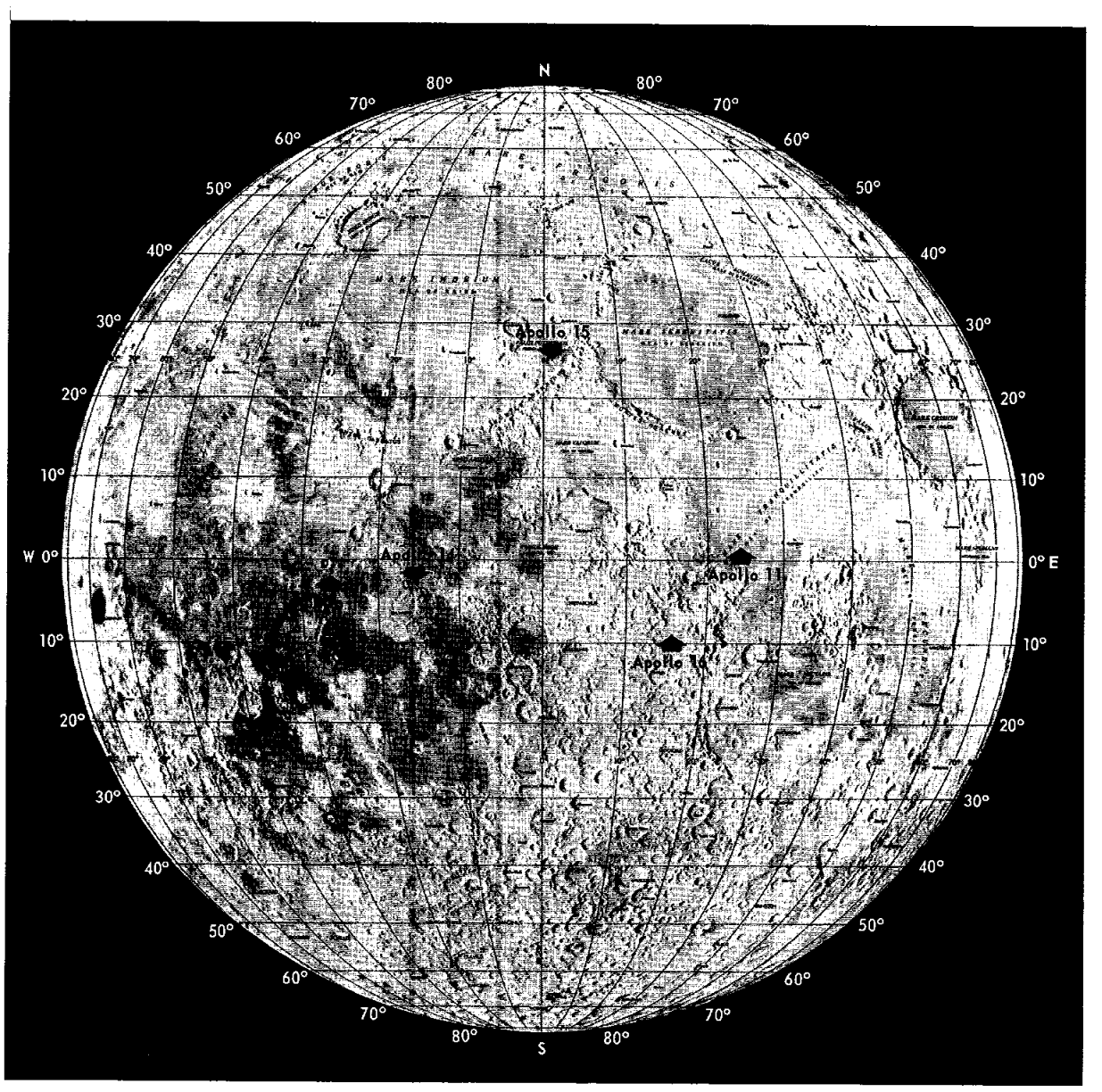


FIGURE 2-2.--Landing site of Apollo lunar-landing missions. Apollo 11 landed in Mare Tranquillitatis on July 20, 1969; Apollo 12 in Oceanus Procellarum on November 19, 1969; Apollo 14 in the Fra Mauro highlands on January 31, 1971; Apollo 15 in the Hadley-Apennines region on July 30, 1971; and Apollo 16 in the Descartes region on April 21, 1972.

The primary scientific objectives of the mission were to geologically survey and sample surface features in a preselected area of the Descartes region, to emplace and activate surface experiments, and to conduct inflight experiments and photographic tasks from lunar orbit. To satisfy these objectives, 10 lunar-surface experiments, 12 lunar-orbital experiments, service module orbital photographic tasks, and command module photographic tasks were conducted. Specific experiments and photographic tasks were as follows.

1. Lunar-surface activities
   a. Emplaced experiments
      (1) Apollo lunar-surface experiments package (ALSEP)

(a) Heat flow
(b) Passive seismic
(c) Active seismic
(d) Lunar-surface magnetometer
(2) Solar-wind composition
(3) Far UV camera/spectrograph
(4) Portable magnetometer
(5) Cosmic ray detector

b. Sampling
(1) Lunar geological investigation
(a) Soil and rock samples
(b) Core-tube samples
(c) Special samples
(d) Drill-core samples
(2) Soil-mechanics experiment
(a) Penetrometer measurements
(b) Trench excavation

2. Lunar-orbital activities
a. Orbital experiments
(1) Gamma-ray spectrometer
(2) X-ray fluorescence
(3) Alpha-particle spectrometer
(4) Mass spectrometer
(5) Bistatic radar
(6) S-band transponder
(7) Subsatellite
(a) Particle shadows/boundary layer
(b) Magnetometer
(c) S-band transponder
(8) Apollo window meteoroid
b. Photographic and support tasks
(1) Ultraviolet photography of Earth and Moon
(2) Photography of gegenschein from lunar orbit
(3) Service module orbital photographic tasks
(4) Command module photographic tasks
(5) Visual observations from lunar orbit

3. Biomedical experiments
a. Microbial response in space environment (microbial ecology evaluation device (MEED))
b. Biostack (study of biologic effects of individual heavy nuclei of galactic cosmic radiation)
c. Apollo light flash moving emulsion detector (ALFMED)

MISSION OPERATIONAL DESCRIPTION

The space vehicle (manned by John W. Young, commander; Charles M. Duke, lunar module (LM) pilot; and Thomas K. Mattingly, command module pilot) was launched on schedule from NASA Kennedy Space Center, Florida, at 11:54:00 a.m. c.s.t. (17:54:00 G.m.t.) on April 16, 1972. The combined command and service module (CSM), LM, and SIVB booster stage were inserted 11 min 56 sec later into an Earth parking orbit of 90 by 95 n. mi.

The CSM was separated from the SIVB stage at 20:58:20 G.m.t. on April 16. Shortly after separation, CSM/LM docking and extraction from the SIVB was accomplished. The SIVB stage was then fired to impact the lunar surface 118 n. mi. west of the Apollo 12 site. Impact occurred on April 19 at 21:02:02 G.m.t. Because of an SIVB transponder failure, the SIVB impacted the lunar surface 74 n. mi. north-northeast of the Apollo 12 site (approximately 153 n. mi. from the preplanned target point). The impact was recorded by the passive seismic experiments deployed during the Apollo 12, 14, and 15 missions.

Only midcourse correction (MCC) 2 was required during translunar coast to reduce the closest approach to the Moon to 71.4 n. mi. The correction, a 12.5-ft/sec velocity change, occurred at 00:33:01 G.m.t. on April 18. During translunar coast, a significant CSM navigation problem developed. A false indication caused the loss of inertial reference. However, a software program was provided to inhibit the computer from responding to such indications during critical operations.

The SIM door was jettisoned at 15:57:00 G.m.t. on April 19. Lunar-orbit insertion, executed at 20:22:28 G.m.t. on April 19, placed the spacecraft into a lunar orbit of 170 by 58 n. mi. Two revolutions later, the orbit was lowered to 58 by 11 n. mi. After 18 hr in this low orbit, the scheduled CSM 60-n. mi. circular-orbit maneuver and subsequent LM descent were delayed approximately 5-3/4 hr because of a propulsion system problem in the CSM.

The commander and lunar module pilot entered the LM at 15:24:00 G.m.t. on April 20 to prepare for descent to the lunar surface. During activation of the LM systems, the S-band steerable antenna was found to be inoperative in the yaw plane; the omnidirectional antennas were therefore used for most of the

remaining lunar operations. Also, a pressure-regulation problem in the LM reaction control system was discovered; however, the condition had no significant effect on the mission.

LUNAR-SURFACE ACTIVITIES

The LM descent proceeded normally, and the spacecraft landed approximately 230 m northwest of the planned landing site at 2:23:36 G.m.t. on April 21. The best estimate of lunar-surface position is 8°59′34″ S latitude and 15°30′47″ E longitude, referenced to the Lunar Topographic Photomap of Descartes, First Edition, January 1972 (published by the U.S. Army Topographic Command). The Apollo 16 landing site, in relation to those for Apollo 11, 12, 14, and 15, is shown in figure 2-1. The lunar-surface activity was rescheduled because of the delayed landing, and the surface stay began with an 8-hr rest period.

The first lunar-surface EVA began at 16:47:38 G.m.t. on April 21; the commander stepped onto the lunar surface at 16:58:00 G.m.t. Television coverage of the EVA was delayed 1 hr by the loss of the LM steerable antenna. The quality of the television image was excellent when the high-gain antenna on the Rover was available. The U.S. flag was deployed and ALSEP preparation began approximately 1-1/2 hr after the start of the first EVA. The relative location of ALSEP experiments is shown in figure 2-3. At 1 hr 45 min after the start of the first EVA, the cosmic ray experiment was activated. The ALSEP radioisotope thermoelectric generator (RTG) was deployed, the central station erected, and the antenna alined. The passive seismic experiment was deployed as planned and deployment of the lunar-surface magnetometer was successful. After drilling the first heat-probe hole and emplacing the probe for the heat-flow experiment, the cable connecting the heat-flow electronics package to the central station was inadvertently pulled loose from the connector on the central station when one of the astronauts caught his foot in the loose cable. While the astronaut wears a pressure suit, his sense of feel is greatly degraded. The connection has been strengthened on this experiment for the Apollo 17 mission and should not fail even under an excessive force. The separation of the cable from the central station did, however, render the experiment useless. Drilling of the second planned heat-probe hole for the experiment was therefore eliminated. The third planned drill operation was performed and the 2.6-m drill core stem was retrieved from the hole. The active seismic experiment (ASE)

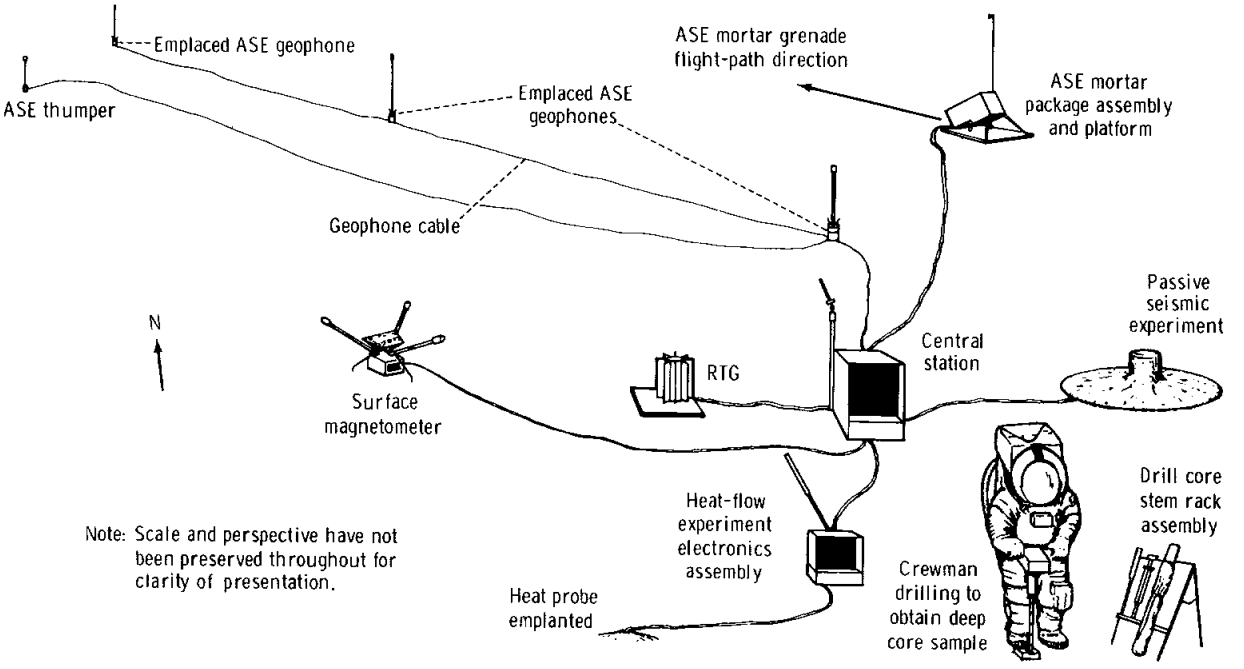


FIGURE 2-3.–Deployment of the Apollo 16 ALSEP, showing the relative locations of the central station, RTG, and the four experiments.

was deployed during the fourth hour of the first EVA. All 19 thumpers (explosive charges to provide known seismic stimuli) were successfully fired by the commander.

Deployment of the ASE mortar package was successful, although only three of the four legs for the package could be emplaced. On May 23, 1972, the mortar package sequentially launched, upon command from Earth, three of four explosive grenades which detonated upon impact and provided additional artificial seismic sources for the experiment. After firing the third grenade, the pitch-angle sensor on the mortar package went off scale in a high direction. Consequently, the pitch position of the mortar package is uncertain and firing of the fourth grenade has been deferred.

The far UV camera/spectrograph was deployed in the shadow of the LM by the commander and repointed by him at 10 other times: three during the first EVA, four during the second EVA, and three during the third EVA. The film was retrieved and stowed in the LM at the end of the third EVA.

At Flag Crater, the first geological sampling site, the crew explored the crater, collected samples, and made observations of the ray material from South Ray Crater. The second sampling site was Spook Crater where, in addition to collecting samples, the crew photographed distant targets using the Hasselblad electric data camera equipped with the 500-mm lens and obtained magnetic field measurements with the lunar portable magnetometer. Near the end of the first EVA (6 hr 15 min), the solar-wind-composition experiment foil was deployed.

During the last part of the first EVA, the cosmic ray detector was moved from its location on the LM descent stage and placed in the shadow of the LM because the experiment had experienced, or was experiencing, excessively high temperatures.

During the second EVA, the planned traverse was made to the south to reach the Cinco Crater area of Stone Mountain. At this site, station 4, geologic investigations were continued and soil-mechanics penetrometer readings were made. At station 5, midway down the slope of Stone Mountain, samples were collected and another magnetometer reading was made. Near the base of the mountain at station 6, samples were taken from numerous boulders in the vicinity. Station 7, also at the mountain base, was eliminated and the time was apportioned to the other stops. Two samples of the topmost lunar-surface layer were collected on special adhesive plates. The chemistry of these samples will be compared to that of the underlying soil. A core sample was collected and sealed in a vacuum container to provide a pristine sample for future analyses. Because the remaining time was insufficient for all the planned activities at the LM (station 10), digging of the soil-mechanics trench was deleted. Soil-mechanics penetrometer readings were made.

As a result of the delayed lunar landing, the time for the third EVA was reduced to 5 hr. Activities at stations 11 and 12 on the southeast rim of North Ray Crater included far-field polarimetric photography, 500-mm photography of the opposite wall, and sampling. Because of time limitations, near-field polarimetric photography was not performed. Samples were obtained in the vicinity of House Rock, which is the largest boulder that has been closely observed and sampled on the lunar surface. Samples were collected and a magnetometer measurement was made at station 13 at the base of Smoky Mountain. Two samples were placed in special padded bags to reduce abrasion of the sample surfaces. Because stations 15, 16, and 17 were deleted from the abridged time line, two magnetometer measurements were made near the final parking place of the Rover, 50 m east of the LM. For one of these measurements, a lunar rock sample was placed on top of the magnetometer sensor head in order to obtain data on the residual magnetism of undisturbed lunar samples. Near the end of the third EVA, the cosmic ray detector experiment, the solar-wind-composition foil, and the rock used in the residual magnetism measurement were retrieved for return to Earth.

Lift-off of the LM ascent stage occurred at 1:25:48 G.m.t. on April 24. Lift-off and ascent coverage by the ground-commanded television mounted on the Rover was excellent. The ascent stage was inserted into a 40.2- by 7.9-n. mi. orbit. At insertion, the range between the two spacecraft was too small, and a small burn by the LM was initiated at 1:36:18 G.m.t. to give the proper separation for the planned rendezvous. The LM burn of 3.1 sec was executed on time at 2:20:53 G.m.t. with a nominal velocity change of 78 ft/sec and a resultant orbit for rendezvous of 64.2 by 40.1 n. mi. The CSM and LM were docked at 3:35:23 G.m.t. The LM ascent stage, jettisoned at 20:54:12 G.m.t., had been targeted to impact near the Apollo 16 site; however, this impact

was not possible because of a loss of attitude control. The estimated orbital life of the LM ascent stage is about 1 yr.

INFLIGHT EXPERIMENTS AND PHOTOGRAPHIC TASKS

Inflight experiments and photographic tasks were performed in Earth orbit and lunar orbit and during translunar coast and transearth coast. Camera equipment needed to satisfy requirements of the UV photography of the Earth and Moon, of gegenschein from lunar orbit, and of the command module photographic tasks was stowed in the command module. Additional science equipment was housed in the SIM bay. This equipment (fig. 2-4) included the gamma-ray spectrometer, X-ray fluorescence spectrometer, alpha-particle spectrometer, mass spectrometer, subsatellite, panoramic camera, mapping camera, and laser altimeter. Existing S-band and VHF communications systems were used for the bistatic radar and S-band transponder experiments. Operational periods for these experiments and tasks are shown in figure 2-5; the groundtrack envelope of the orbiting spacecraft is shown in figure 2-6.

Inflight science activities were begun when the SIM door was jettisoned at 15:57:00 G.m.t. on April 19 and terminated about 5 hr before splashdown. During this 191-hr interval, the following tasks were accomplished for areas overflown: photography of most of the lunar area in sunlight; geochemical mapping of the lunar surface; determination of the geometric shape of the Moon; a visual geological survey of various lunar regions in sunlight; investigation of lunar-atmosphere composition; and astronomical surveys for gamma-ray and X-ray galactic sources, as well as detailed observations of two known galactic X-ray sources.

Gamma-ray data were obtained for 55 hr during transearth coast and 121 hr in lunar orbit. Of the 121 hr of data collected in lunar orbit, 50 hr of data were prime data (extended boom and closed mapping-camera cover), 32 hr of data were degraded (open mapping-camera cover), and 39 hr of data were dominated by radiation from the plutonium-fuel capsule in the RTG mounted on the LM. During SIM experiment operations, the gamma-ray spectrometer boom mechanism stalled and would not fully retract for three of five retractions. The boom mechanism always retracted to within the envelope for safe firing of the service propulsion engine.

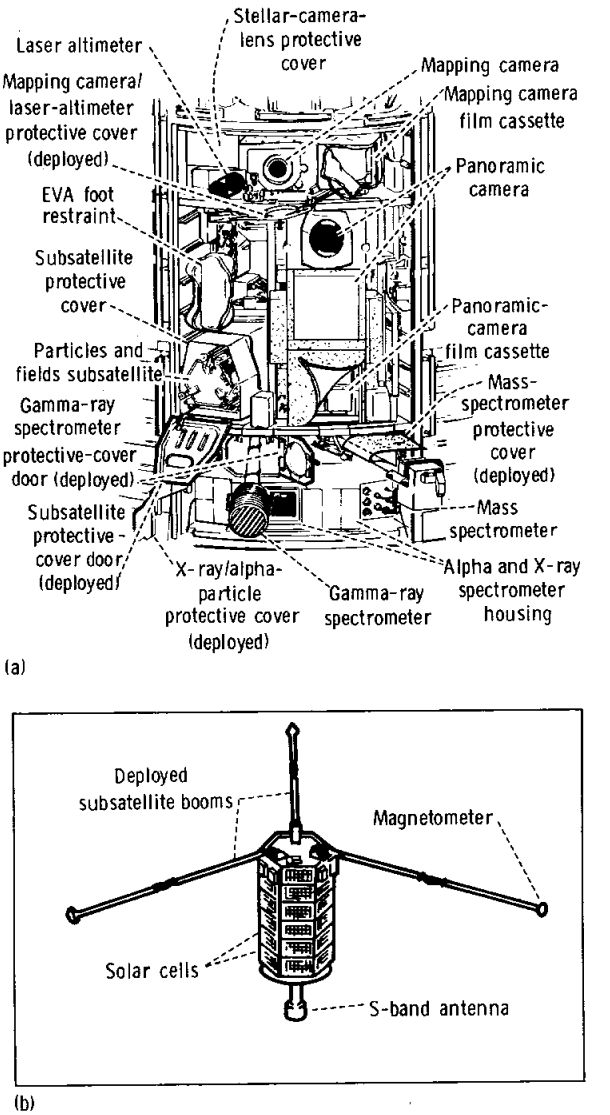


FIGURE 2-4.–Scientific equipment, including orbital experiment instruments and photographic equipment, located in the SIM of the service module. (a) Drawing of the SIM bay. (b) Deployed subsatellite configuration.

The X-ray fluorescence data were collected for a total of 122 hr, 26 hr during transearth coast and 96 hr in lunar orbit (64 hr of prime data and 32 hr with the LM attached to the CSM).

Alpha-particle data were collected for a total of 177 hr, 55 hr during transearth coast (background data) and 122 hr in lunar orbit (81 hr of prime data and 41 hr with the LM attached to the CSM).

Mass spectrometer data were collected for a total of 94 hr in lunar orbit, all of which were prime data. Approximately 76 hr of data were obtained with the CSM flying with the experiment opening forward, and about 18 hr of data were obtained with the CSM flying with the experiment opening rearward. During SIM experiment operations, the mass spectrometer boom mechanism stalled and would not fully retract. The mechanism always retracted to within the envelope for safe firing of the service propulsion engine except for the retraction before transearth injection. At that time, the mechanism stalled two-thirds extended (approximately 5 m) and would neither extend nor retract. The boom mechanism and experiment were jettisoned before the transearth injection maneuver; consequently, no data were collected during transearth coast.

During lunar orbit, bistatic radar data were acquired during one dual-frequency and four VHF passes. The S-band signals were received by the 64-m diameter antenna at Goldstone, California, and VHF signals were received by the 46-m diameter antenna at Stanford University, California. Dual S-band/VHF bistatic radar observations were conducted during lunar revolution 40. Although the S-band signals were strong, the VHF signals were weak throughout the pass.

The quality of the S-band transponder data is excellent, and many new lunar features can be resolved. The amplitudes are not as large as those recorded during the Apollo 15 mission, because the trajectory path was not over any mascon areas.

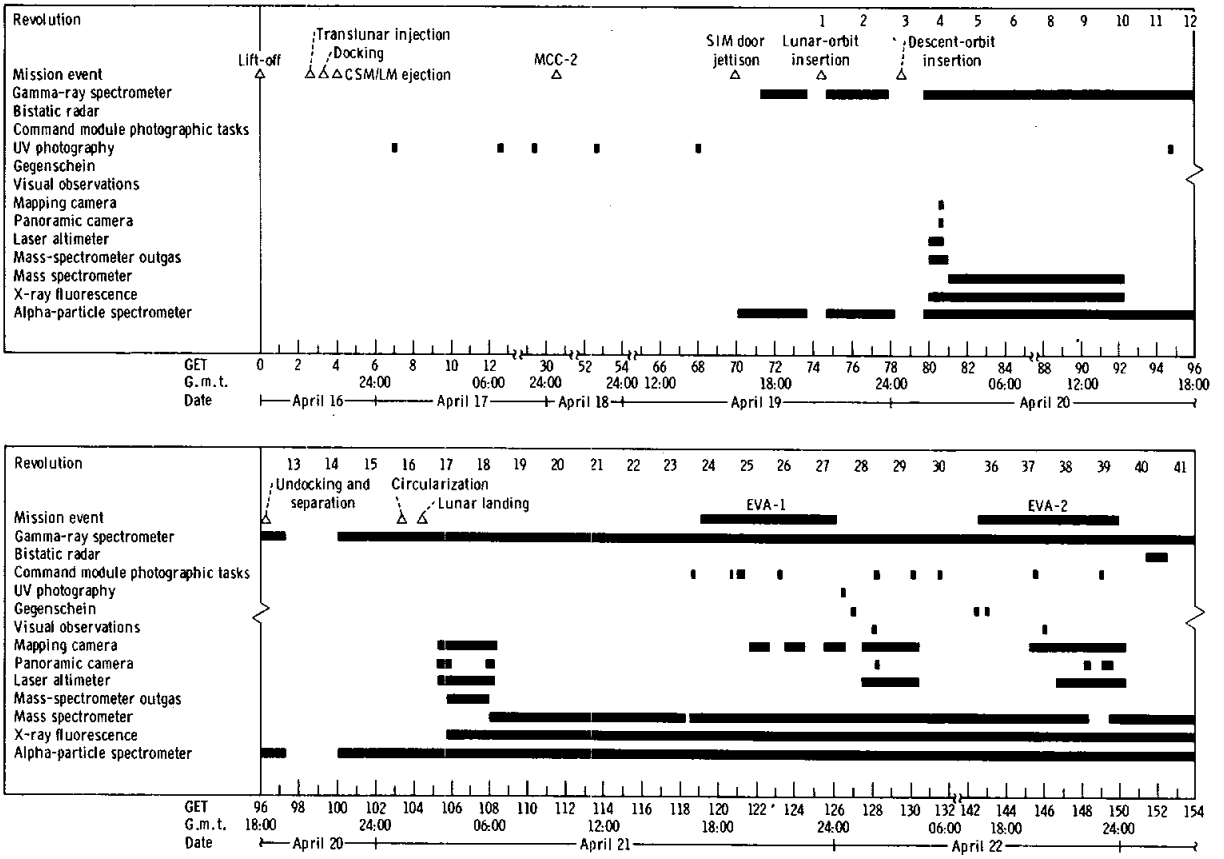


FIGURE 2-5.–Major mission events and data-collection periods correlated to G.m.t. and ground elapsed time (GET).

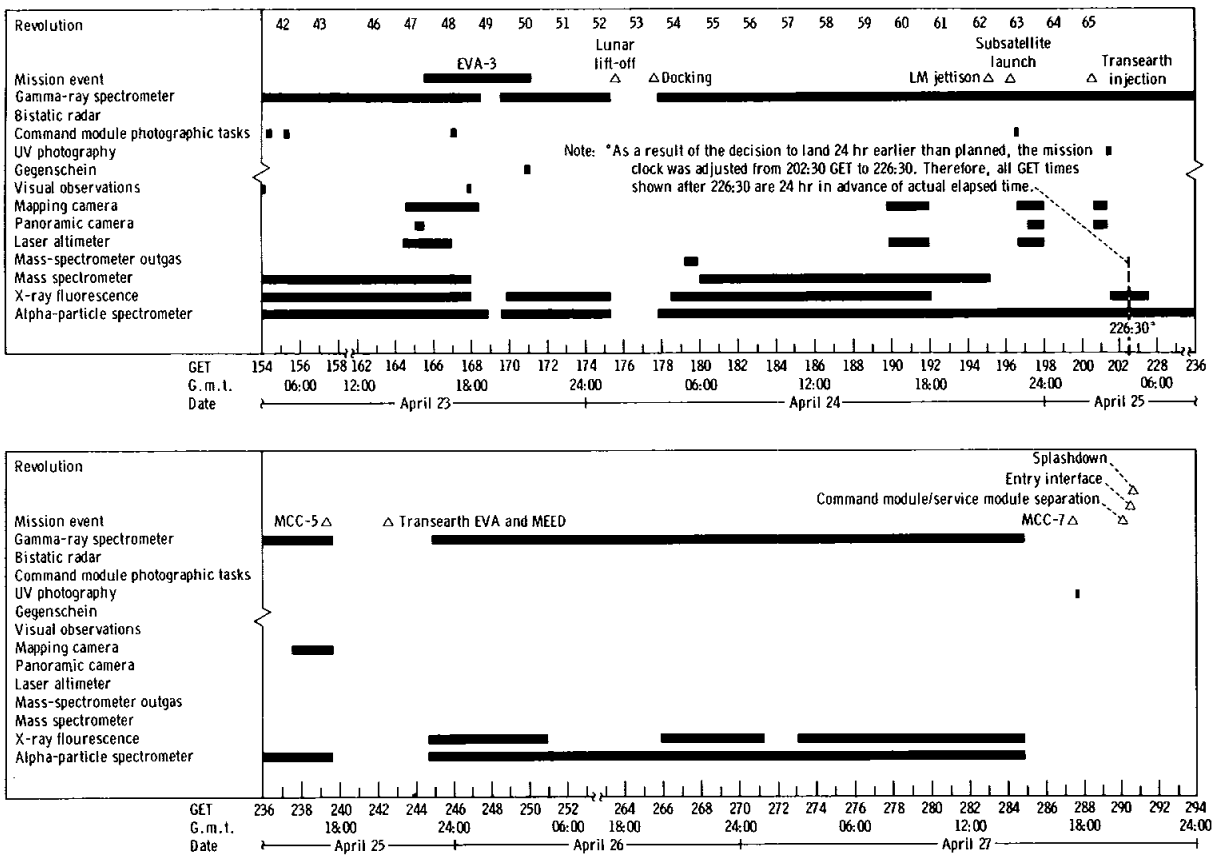


FIGURE 2-5.–Concluded.

At 22:07:00 G.m.t. on April 24, the subsatellite was launched. The subsatellite was the host carrier for an S-band transponder experiment, a particle shadows/boundary layer experiment, and a magnetometer experiment, which were to be conducted for a 1-yr period. The short lifetime of the subsatellite (425 revolutions before it impacted the Moon on May 29) resulted from a decision not to perform the required orbit change before jettisoning the subsatellite. The maneuver was not performed to avoid firing the main engine any more than absolutely necessary due to the degraded backup thrust vector control of the main engine.

The Apollo window meteoroid experiment was a passive experiment and required no crew activities. The command module window has been retrieved.

Panoramic-camera photography was obtained during portions of eight revolutions and after transearth injection, including one sequence over the landing site with the camera axis inclined 10° forward. The initial sequence of the camera was terminated after only four frames, because of a spacecraft undervoltage indication. Subsequent operation of the panoramic camera was nominal with the exception of the automatic exposure sensor, which displayed consistently low values of illumination. The resulting overexposure (one to two stops in regions away from the terminator) was substantially compensated during the development of the panoramic film.

Vertical mapping-camera photography was obtained during 13 revolutions and after transearth injection. Oblique photography was obtained during five revolutions. Operational anomalies occurred in the mapping-camera deployment mechanism. The first mapping-camera extension was normal, but the retraction required more time than was expected. The

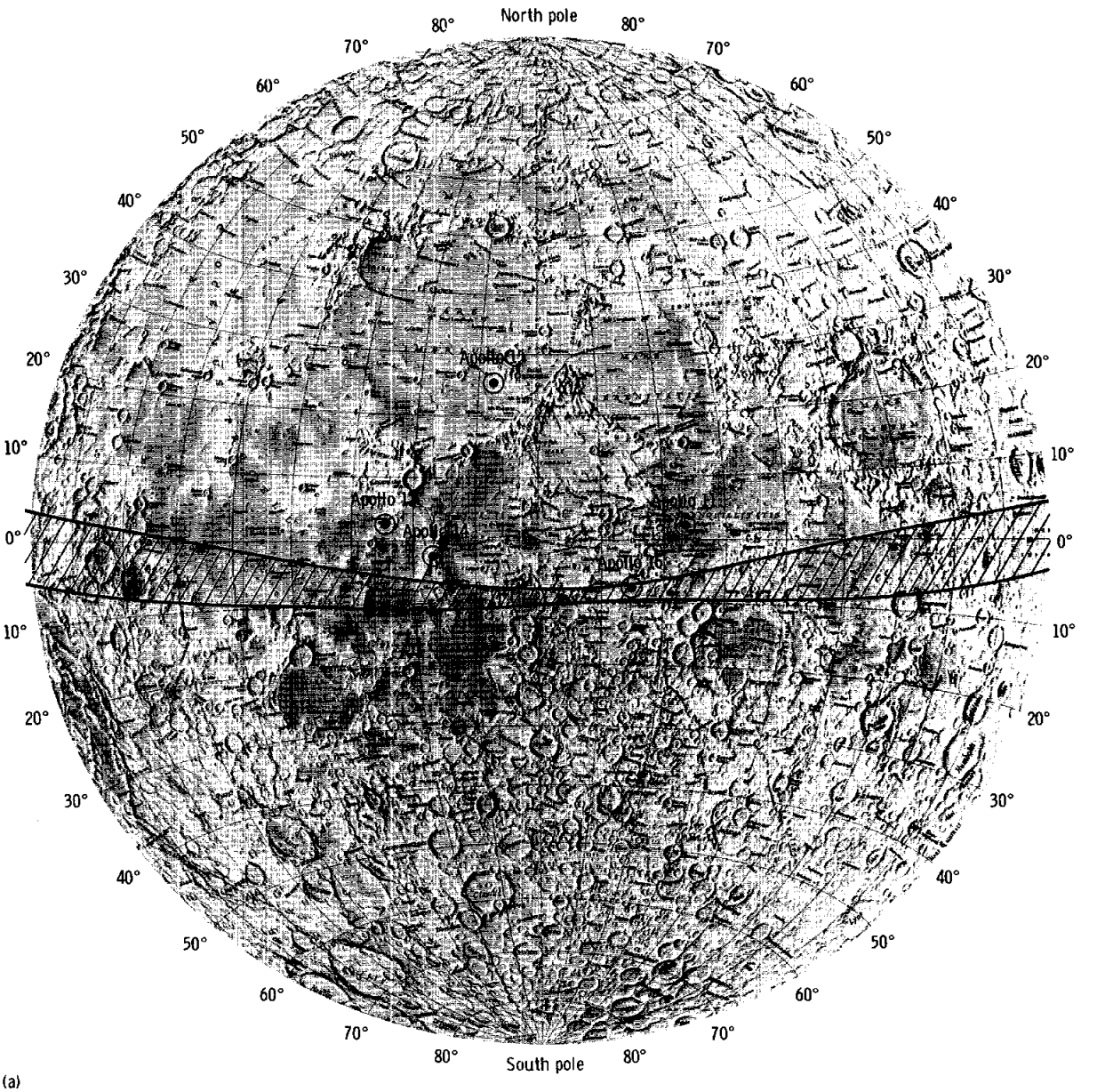


FIGURE 2-6.–Lunar-surface groundtrack envelope of the Apollo 16 orbiting spacecraft for revolutions 1 to 65. Areas of additional data coverage outside the envelope are determined by the fields of view of experiment instruments and photographic cameras. (a) Near side.

second and third extensions and retractions required about 3 min, but both the fourth and fifth retractions were normal at 1 min 18 sec.

The laser altimeter performed normally during the first operating period of 41 min during lunar revolutions 3 and 4. Evidence of laser degradation began to appear early in the second operating period. During the last scheduled operating period (revolution 63), laser output degraded to the point that no further altitude data were obtained.

Ultraviolet photographs of the Earth and Moon were taken during translunar coast, lunar orbit, and transearth coast as planned, using the 70-mm camera configured with a UV lens and filter. The panes of

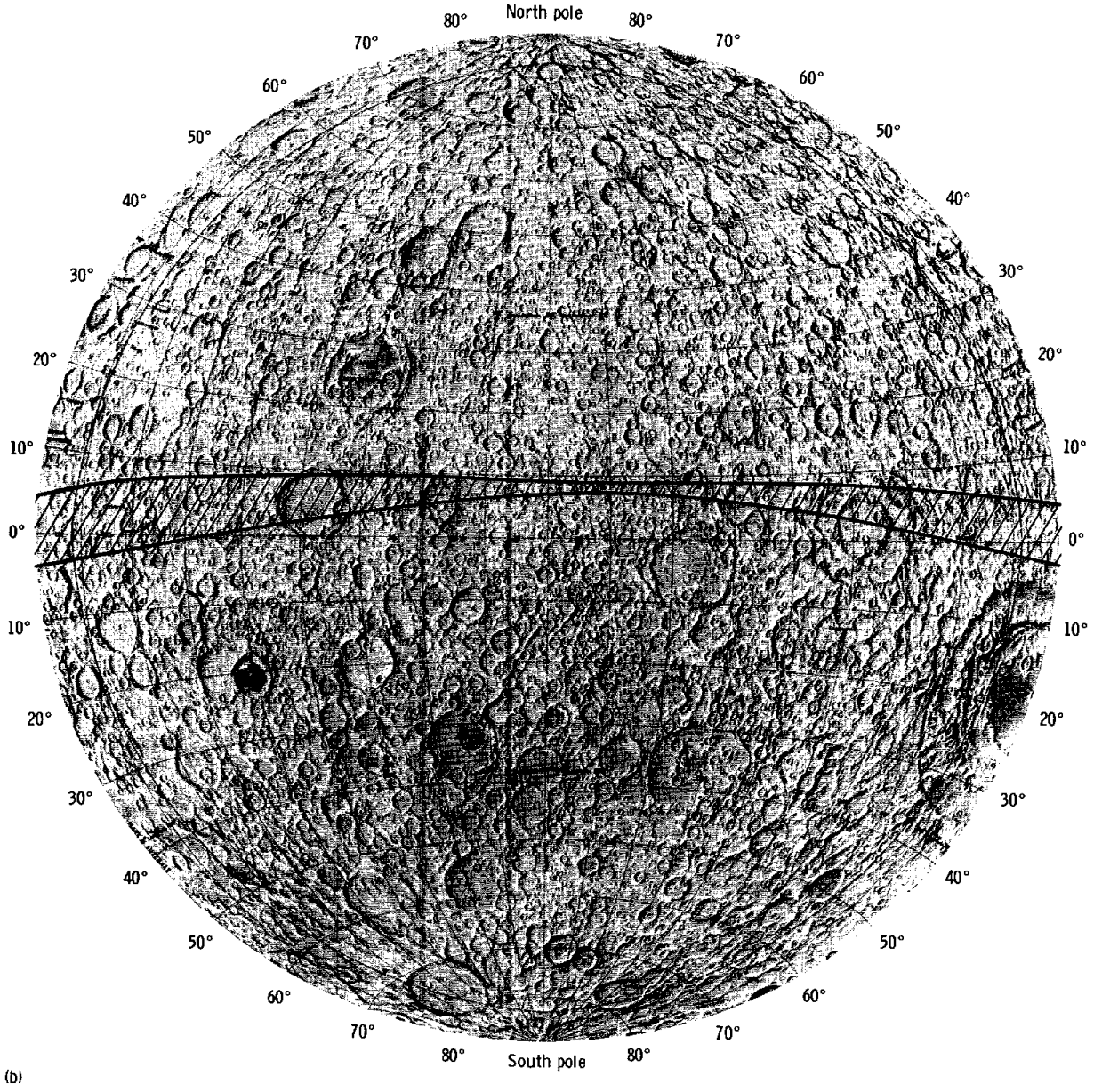


FIGURE 2-6.–Concluded. (b) Far side.

command module window 5, selected for the experiment, were replaced with panes that transmit a higher fraction of incident UV radiation.

The experiment to determine microbial response in space environment was successfully conducted during the transearth EVA. The experiment was exposed for 10 min. After completion of the experiment, difficulty was experienced in latching the experiment cover.

The biostack experiment was a passive experiment and did not require any crew activities. The experiment was recovered after mission completion.

APPENDIX

TOPOGRAPHIC MAPPING OF THE APOLLO 16 LANDING SITE

By Robert O. Hill[a] and Merritt J. Bender[a]

The lack of Lunar Orbiter stereoscopic photography from which the basic positional and topographic information could be derived presented some problems on the premission science planning for the Apollo 16 landing site in the lunar highlands north of Descartes Crater. In an attempt to obtain adequate high-resolution stereoscopic photography of the Descartes area, several passes during the Apollo 14 mission had been planned to photograph the area with the 18-in. lunar terrain camera (LTC). On the first photographic pass, the LTC malfunctioned before the prime target area was reached, and the camera was not usable for the rest of the mission. The alternate plan for obtaining high-resolution photography was to use a Hasselblad camera with a 500-mm lens. Because of the narrow field of view (approximately 6° across the field) of the camera, a technique for obtaining convergent photography was employed (fig. 2-7).

Three separate photographic passes were made over the site using this convergent technique. The timing interval between exposures on these passes was 5 sec. In addition, a pass of vertical photography was obtained using the 80-mm Hasselblad (with a field of view of 38° across the field and fitted with a reseau) and 60-percent forward overlap. This camera was bracket-mounted and triggered by a 20-sec intervalometer. The normal Apollo landmark tracking procedure was also used to establish the position of a crater in the immediate area of the potential landing site and the position of a second landmark 125 km east of the first landmark. Using these two landmarks for scale and orientation, in conjunction with the spacecraft ephemeris and attitude data, an analytical triangulation was performed with 12 of the 80-mm Hasselblad photographs.

The two tracked landmarks, along with an array of points in a standard five-square-point pattern, were identified, marked, and transferred using a multiscale point transfer instrument. The photographic coordinates of the points were measured on a monoscopic comparator. In addition to the control points and pass points, the reseau points contained in a glass plate near the focal plane of the Hasselblad and imaged on each frame of photography by scene light were also measured. The reseaus were used to define the origin of the photographic coordinate system and to remove film distortions incurred primarily because of the lack of a film-flattening device in the camera.

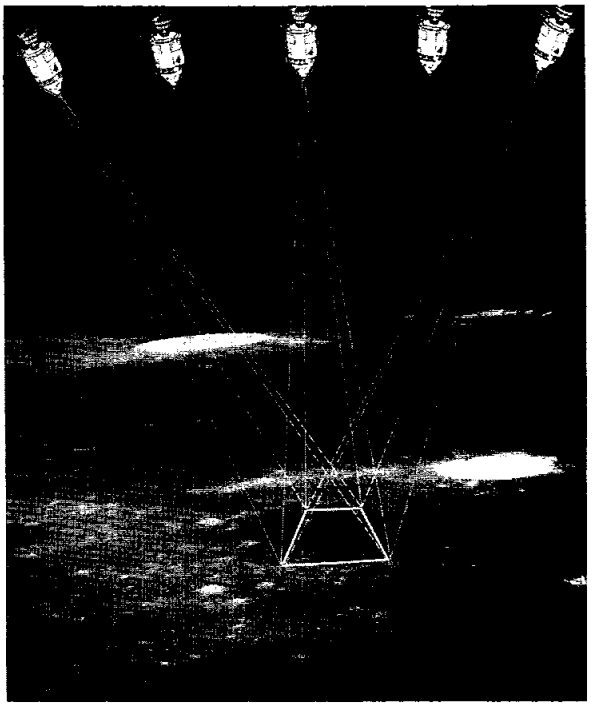


FIGURE 2-7.–Technique used for obtaining convergent photography.

The data reduction of the photocoordinates was processed in the Lunar Orbiter Strip Analytical Triangulation Program, which was run on a computer at the Manned Spacecraft Center (MSC). Initial estimates for the orientation parameters for each exposure station were derived from spacecraft position and attitude data. The two ground control points, established by optical tracking from the command module on separate passes, are also completely dependent on spacecraft trajectory and attitude data. Thus, because of uncertainties in spacecraft position, certain incompatibilities existed between the photographic pass and the landmark tracking pass. The decision was made to hold to the landmarks and to allow the exposure stations to

[a]NASA Manned Spacecraft Center.

adjust. Using these techniques, the adjustment converged satisfactorily to provide a control network to support subsequent map compilation.

This network of points was used to orient a model of the 80-mm photography on the AS-11-A1 analytical stereoplotter. Coordinates were read from the model for points identifiable on the 500-mm photography, and the 500-mm convergent model was then set to this control. The convergent angle for the pair selected for compilation was approximately 38°. The absolute orientation computation on the AS-11-A1 resulted in a model with mean Y-parallax at 11 control points of 22 μm. Radial distortion was compensated in the AS-11-A1 according to the distortion model established through preflight calibration of the camera using stellar photography and stellar reduction software. Corrections were also employed for lunar curvature.

One of the major uses of the topographic compilation was to generate a three-dimensional model for the lunar landing simulator. Therefore, it was more important to portray the general landforms and to describe the shapes of individual features than to meet some preestablished accuracy criteria for contour data. The contour or form line interval was pushed to an absolute minimum, resulting in a 1:15,000-scale compilation with a vertical interval of 10 m. Crater overlays, outlining features too shallow to be described with the 10-m interval, were also constructed at the same scale.

The compilation manuscript and crater overlay were shipped to the U.S. Army Topographic Command (TOPOCOM) in Washington, D.C., where the simulator relief model was cut at a scale of 1:2000. An independent triangulation and compilation of the site area was also done by TOPOCOM. The MSC and TOPOCOM map compilations were compared, and, in areas where disagreements were evident, a check was made on the stereo instrument to attempt to resolve the differences. In addition to the simulator relief model at 1:2000 scale, a plastic relief model at 1:12,500 scale was published for the immediate site area.

The TOPOCOM published a 1:25,000-scale map of the Apollo 16 landing site area. The graticule plotted on the map represented the Apollo coordinate system, because the absolute values for longitude, latitude, and radius were established by orbital positions derived from Apollo tracking data. These data were processed in the Apollo orbit determination programs, using the same libration and gravity models as were used for the operational Apollo data. Thus, the position and radius for features on the map, including the landing site and landmarks (easily identifiable craters), were used directly for providing coordinates for trajectory targeting, for determining offsets from landmarks to the landing site, for deriving terrain profiles along the approach path, and for deriving other topographic and positional data in direct support of the mission.

The Apollo 16 spacecraft landed approximately 250 m from the selected target point (fig. 2-8). The surface activity progressed remarkably well, considering the quality of the premission photography, and relatively few topographic surprises were encountered. The success of the mission again demonstrated (as with Apollo 14) the value of "nonmetric" photography in the photogrammetric process, especially when supported by information such as orbitally derived positions for the exposure stations, accompanied by approximate orientation data. Instruments used to process these data have proved valuable in giving the Apollo Program flexibility to visit locations whose scientific merit became more evident as the program progressed.

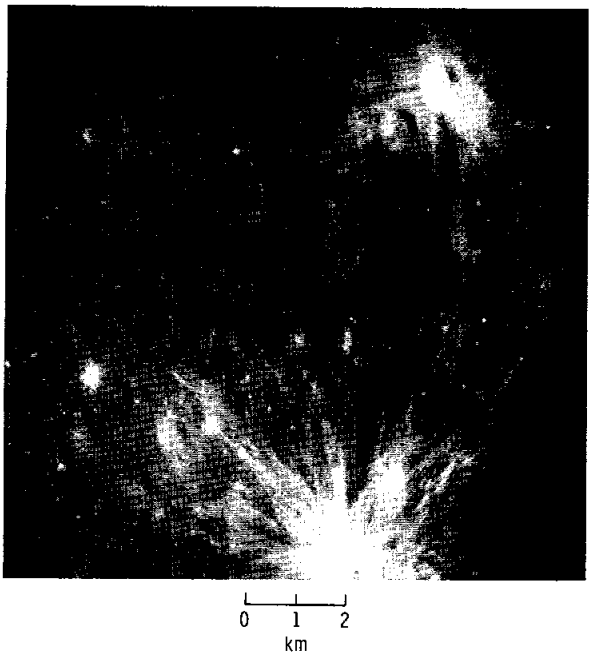


FIGURE 2-8.–Photograph taken with the 500-mm Hasselblad camera showing the Apollo 16 Descartes landing site.

3. Summary of Scientific Results

Anthony W. England[a]

The exploration of the Descartes region by the Apollo 16 crewmen provides the best look at lunar highlands. As a result, many theories concerning lunar geologic structure and processes will be improved greatly. Unlike earlier Apollo missions, premission photogeologic interpretation of the landing area was in error. Far from diminishing the mission, however, discovery of the unexpected enhanced the scientific impact. The surprise at Descartes was the state of the rocks, not their composition. That is, breccias rather than volcanics were dominant. The compositions are near those of anorthositic gabbro and gabbroic anorthosite. This composition is consistent with the hypothesis that highlands are an early differentiate of a primitive lunar mantle. Aluminum-to-silicon (Al/Si) and magnesium-to-silicon (Mg/Si) ratios, as determined by the orbiting X-ray fluorescence experiment, indicate that the Descartes area differs compositionally from previous Apollo sites and that its chemical characteristics are representative of large regions of the lunar highlands. Thus, lessons learned at Descartes will support new generalizations potentially applicable to much of the lunar surface.

Although the dramatic phase of the Apollo 16 mission ended with the splashdown, the scientific adventure will continue for many years. This report presents the first fruits of the mission; and, inevitably, a number of its conclusions will be short lived. Few disciplines are as dynamic as the lunar sciences.

GEOLOGY EXPERIMENT

The two morphologically distinct units at the Apollo 16 site are the highland plains-forming unit, called the Cayley Formation, and the ridges and mountains of the Descartes highlands. The Cayley Formation was sampled extensively at nine stations spread over 7 km in a north-south direction. The goal was to construct a vertical section and lateral variation of the Cayley Formation based on samples from the rims of various-sized craters. Before the mission, the Cayley Formation was thought to be a sequence of lava flows interbedded with ancient regoliths. Instead, the Cayley Formation is composed dominantly of four types of heterogeneous fragmental rocks or breccias. Although the relative proportions of the four breccias varied over the traverse area, no basic differences in the rock assemblages were seen. Based on the sample distribution and Apollo 16 panoramic camera photographs of South Ray and Baby Ray Craters, the only stratification exhibited by the Cayley Formation is a crude, horizontal layering of alternating light and dark breccia units.

The Cayley Formation appears to be a thick (at least 200 m, possibly more than 300 m), crudely stratified debris unit, the components of which are derived from plutonic anorthosites and feldspathic gabbros and from metamorphic rocks of similar composition. The Cayley Formation has an elemental composition similar to that observed over large regions of the lunar highlands by the orbital X-ray experiments of the Apollo 15 and 16 missions (ref. 3-1 and sec. 19 of this report). The observed textures and structures of the breccias resemble those of impact breccias. The observed textures and structures of the breccias do not resemble those of volcanic rocks, nor do the plutonic or metamorphic source rocks of the breccias have the textures or compositions of terrestrial or previously sampled lunar volcanic rock.

Stations 4 and 5 on the northern flank of Stone Mountain were selected as sampling locales for the Descartes highlands. However, the documented samples and the soils collected on Stone Mountain are indistinguishable from those collected on the Cayley Plains. This similarity may be caused by a heavy mantle of ejecta from South Ray Crater. If so, the cores taken at station 4 and the rake samples collected from the inner slopes of small craters at stations 4 and 5 may contain unique Descartes highland material. However, the upper layers of the Descartes highlands may be lithologically identical to the bulk of the Cayley Formation.

[a]NASA Manned Spacecraft Center; now with U.S. Geological Survey.

Although caution dictates that a volcanic origin for the Cayley Formation not be eliminated as a possibility, all the evidence of the preliminary analysis argues against it. Several alternate hypotheses are suggested by the geology team and by various authors of the photogeologic sections contained in this report. The dominant theme is deposition of debris from combinations of the ejecta from the Imbrium and Nectaris Basins.

PRELIMINARY SAMPLE ANALYSIS

A preliminary characterization of the rocks and soils returned from the Apollo 16 site has substantiated most of the widely held inferences that the lunar terra is commonly underlain by plagioclase-rich or anorthositic rocks. The texturally complex rocks exhibit cataclastic textures with intergrowths of shock-induced glass, of devitrified glass, or of relict preexisting clasts that indicate a multistage history. In contrast to the complexity of the fabric, the chemical characteristics of the rocks and soils were comparatively simple. The dominant chemical feature is the high abundance of aluminum and calcium. In a number of rocks, the absolute and relative abundances of these elements approach those of pure calcic plagioclase. Each Apollo 16 rock falls into one of three groups, based on its alumina (Al_2O_3) content. Rocks in the first group are nearly pure plagioclase and can be called cataclastic anorthosites. The second group, characterized by Al_2O_3 contents of between 26 and 29 percent, consists of several breccias, two crystalline rocks, and all soil samples. The third group, all metamorphosed igneous rocks, has Al_2O_3 contents below 26 percent. Many samples in this third group are similar chemically to the basalts that are rich in potassium, rare-Earth elements, and phosphorus (KREEP) found at the Apollo 12, 14, and 15 sites. With a few qualifications, the chemistry of the Apollo 16 rocks can be accounted for by a rather simple geologic model consisting of a large igneous complex that is variably enriched in plagioclase and is intruded by a trace-element-rich liquid after its formation.

In addition to normal rock and soil samples, many special samples were collected. A few of the investigations based on these samples will be the study of small-scale stratigraphy in the regolith; the study of the interaction of solar wind and cosmic rays with the lunar surface; and the study of special processes such as erosion by micrometeorites, mobility of volatile elements, and darkening with time of freshly exposed lunar soil. Essentially all planned special samples were collected.

Lunar samples exhibit two components of remanent magnetism: (1) a "hard" component that can be erased only at temperatures near the Curie point of the sample and (2) a "soft" component, most of which can be lost by degaussing in a weak magnetic field. The implication of the hard component is that the sample cooled from a temperature above 850° C in the presence of a strong magnetic field. This hypothesis places stringent requirements on the early history of the Moon. Either the Moon once generated an internal field, or the Moon was once located near a strong external field. The soft component might reflect the lunar magnetic environment from the time the rock cooled to the present. An alternate hypothesis was that the soft component was largely an artifact of handling by the astronauts and of traveling in magnetically dirty spacecraft. The results of several tests, one involving a controlled sample sent on the Apollo 16 mission, indicate that much of the soft remanent magnetism in lunar samples was acquired from magnetic fields within the spacecraft.

SOIL MECHANICS EXPERIMENT

The mechanical properties of lunar regolith are governed by the distribution of grain sizes, by the angularity of the grains, and by packing density or porosity. The distribution of grain sizes for the soil samples from Descartes lies near the coarse boundary of a composite distribution composed of soils from all previous sites. Statistical analysis of bootprint depths indicates that the near-surface porosities at the Apollo 16 landing site were slightly higher than the average of those of the four previous missions, 45 percent compared with 43.3 percent. The average porosity on crater rims was 46.1 percent. The resistance to penetration measured with the self-recording penetrometer is highly variable on both regional and local (points as close as 1 m) scales. As a result, no general conclusion is possible concerning whether the soil on slopes is weaker or stronger than that on flat areas. However, the pattern of resistance as a function of depth correlates well with the stratigraphy observed in X-radiographs of the core tubes, and stratigraphic profiles of the lunar surface have been determined for the first time. The density and density

distribution in the 2.6-m core at Descartes differed significantly from those in the deep core taken at Hadley. The Apollo 16 densities were lower (by approximately 0.2 g/cm^3). The densities increased smoothly with depth. The density of the Apollo 15 deep core varied erratically with depth. The soils at the two locations must have experienced distinctly different histories.

PASSIVE SEISMIC EXPERIMENT

The activation of the Apollo 16 passive seismometer resulted in a four-station seismic network on the near side of the Moon. Because of a fortuitous impedance match between the Apollo 16 seismometer, the local regolith, and the underlying lunar crust, the seismic station at Descartes is an order of magnitude more sensitive than stations on the maria (Apollo 12 and 15) and five times more sensitive than the station at the Fra Mauro site (Apollo 14). The Apollo 16 seismometer is detecting moonquakes at the rate of 10 000/yr. One quake was the result of the largest meteoroid impact yet recorded. The event occurred 145 km north of the Apollo 14 station. The resulting seismic waves were well recorded at all four stations of the seismic network. Analysis of this single event has greatly improved the concept of the structure beneath the lunar crust. Measured seismic velocities are close to those expected for gabbroic anorthosites, which predominate in the highlands of the Descartes site. Analysis of data from the lunar orbiting X-ray fluorescence experiment suggests that this rock type is representative of the lunar highlands on a global scale. The combination of velocity information with laboratory data from returned samples suggests the following conclusions.

(1) The lunar crust in the highlands is approximately 60 km thick.

(2) The lunar crust in the highlands consists primarily of gabbroic and anorthositic material.

(3) The maria were formed by the excavation of the initial crust by meteoroid impacts and subsequent flooding by basaltic material.

(4) From seismic evidence, the basalt layer in the southeastern portion of Oceanus Procellarum may be 25 km thick, which is comparable to the thickness inferred for mascon maria.

The seismic velocities below the crust and to the maximum depth that was investigated (approximately 120 km) are roughly equivalent to velocities observed in the upper mantle of the Earth.

Although the Moon is seismically active, the total energy released is many orders of magnitude below that of the Earth. All seismic sources of internal origin are, apparently, discrete and are located below the lunar crust. Twenty-two source locations have been identified. In the five source regions in which focal depths have been determined, all quakes occurred in the range from 800 to 1000 km. The occurrence of these quakes correlates with maximum lunar tides. Either they represent a release of tidal energy or the tides trigger the release of internally generated stresses.

A new model for the meteoroid flux that is consistent with the seismically observed frequency of meteoroid impacts is proposed. This new flux estimate is from one to three orders of magnitude lower than models derived from photographic measurements of luminous trails striking the atmosphere of the Earth.

ACTIVE SEISMIC EXPERIMENT

The objective of the Apollo 16 active seismic experiment was to determine the local structure of the regolith and of the shallow lunar crust. The near-surface, compressional-wave velocity at the Descartes site was 114 m/sec; this value can be compared to 104, 108, and 92 m/sec at the Apollo 12, 14, and 15 sites, respectively. A refracting horizon at 12.2 m may be the base of the regolith. The velocity below this depth was 250 m/sec. A crustal velocity of 250 m/sec is comparable to the 299-m/sec velocity observed in the Fra Mauro breccias and is incompatible with the velocity of 800 m/sec or more expected for competent lava flows. This finding, along with the prevalence of breccias in the returned samples, argues that the Cayley Formation is composed of low-velocity brecciated material and impact-derived debris. Preliminary analysis indicates that this brecciated zone is more than 70 m thick.

LUNAR SURFACE MAGNETOMETER EXPERIMENT

The activation of the Apollo 16 lunar surface magnetometer resulted in a network of three active magnetic observatories on the lunar surface. The objective of this network is to observe the global response of the Moon to variations in the magnetic field carried

by the solar wind. Variations in the solar wind magnetic field generate eddy currents within the Moon. These currents create a magnetic field that suppresses the change in the total field observed on the surface of the Moon, and the character of this suppression can be related to the electrical conductivity of the lunar interior. Because this electrical conductivity is dominantly a function of temperature, these temporal studies of the magnetic field can be used to infer temperature distributions for the lunar interior. For the model of a peridotite Moon, preliminary analysis indicated a temperature profile that rises sharply to 850° to 1050° K at a depth of approximately 90 km, then increases gradually to 1200° to 1500° K at approximately 1000 km, and may be above 1500° K at greater depths. Greater detail as well as a comparison of the response of the Moon under maria (Apollo 12), under the edge of a large basin (Apollo 15), and under highlands (Apollo 16) should be possible as more data are received.

LUNAR PORTABLE MAGNETOMETER

The lunar portable magnetometer was used at four sites along the traverse route. These measurements and the magnetic measurement by the lunar surface magnetometer yield a total of five spatial measurements at Descartes. The remanent magnetic field was the largest yet observed on the Moon. Its strength was 180 gammas near Spook Crater, 125 gammas on Stone Mountain, and 313 gammas at station 13 near North Ray Crater. Not only were the field strengths higher at Descartes than at other Apollo sites, the gradients were significantly greater: 370 gammas/km maximum observed at Descartes compared to less than 133 gammas/km (resolution limit of the lunar surface magnetometer) at the Apollo 12 and 15 sites and a measured 54 gammas/km at the Apollo 14 site.

FAR UV CAMERA/SPECTROGRAPH EXPERIMENT

The far UV camera/spectrograph was operated from the lunar surface for the first time on Apollo 16. The instrument was sensitive to light in the 50- to 160-nm range and "blind" to ordinary visible light. The experiment was completely successful in that the experiment team obtained 178 photographic frames of far UV data on the airglow and polar auroral zones of the Earth and the geocorona; on over 550 stars, nebulae, or galaxies; and on the nearest external galaxy, the Large Magellanic Cloud. The detailed analysis will take many months. However, the lack of quantitative results in time for this preliminary report cannot dull the accomplishment of emplacement of the first lunar astronomical observatory.

SOLAR WIND COMPOSITION EXPERIMENT

The solar wind composition experiment was designed to measure with high precision the abundances and isotopic compositions of noble gases in the solar wind. It has been demonstrated that both elemental abundances and isotopic ratios varied with time. The Apollo 16 experiment hardware is composed of aluminum and platinum foils that were exposed on the lunar surface for periods of several hours to trap various components of the solar wind. The relative elemental and isotopic abundances of helium and neon measured for the Apollo 12, 14, 15, and 16 exposure times are quite similar and differ from those obtained during the Apollo 11 mission. Particularly noteworthy is the absence of any indication of electromagnetic separation effects that might have been expected at Descartes because of the relatively strong local magnetic field.

COSMIC RAY EXPERIMENT

The relative abundances and energy spectra of heavy solar and cosmic rays convey a wealth of information about the Sun and other galactic particle sources and about the acceleration and propagation of the particles. In particular, the lowest energy range from a few million electron volts per nuclear mass unit (MeV/nucleon) down to 1 keV/nucleon (a solar wind energy) is largely unexplored. The cosmic ray experiment contained a variety of detectors designed to examine this energy range. The precise nature of the experiment is dependent on the radiation environment during the mission. If the Sun were relatively quiescent, the objective was to determine whether the low-energy nuclei are primarily solar or galactic in origin. If the Sun were active, the objective was to study the composition of solar cosmic rays and the solar acceleration processes. Because a solar flare occurred during the mission, the latter objective was served.

A preliminary analysis indicates that the spectrum for iron-group cosmic rays is given by an $(\text{energy})^{-3}$ relation in the energy range from 30 MeV/nucleon

down to 0.04 MeV/nucleon and flattens to (energy)$^{-1}$ from 0.04 to 0.01 MeV/nucleon. The higher energy relation is identical to previous results for the 0.16- to 100-MeV/nucleon range. A striking aspect is the relative enrichment of iron at the lower energies during a solar flare. This enrichment is estimated to be a factor of approximately 450 greater than the photospheric value. Although the precise value of the enhancement might be in question, the data do strongly suggest that the heavier particles are appreciably more abundant in the solar flares than in the surface of the Sun. At higher energies, however, the abundances were normal for galactic cosmic rays.

Mica and feldspar were included as detectors in addition to Lexan and glass. By comparing the sensitivities of the natural materials against those of the Lexan, a calibration will be established applicable to studies of particle tracks in lunar samples.

GEGENSCHEIN EXPERIMENT

Gegenschein is the phenomenon of sky brightness in the antisolar region as viewed from the Earth. A possible mechanism for this brightness might be backscatter of light by particles lingering in the Moulton region, a libration point of the Earth-Sun system. The objective of the experiment was to use fast film and long exposures in lunar orbit to map the luminance of the gegenschein. If it were a result of particles in the Moulton region, the gegenschein would be displaced 15° from the antisolar point as viewed from the Moon. Preliminary analysis indicates that the gegenschein as viewed from the Moon appears at the antisolar point and, thus, argues against the Moulton region as a source.

GAMMA RAY SPECTROMETER EXPERIMENT

The gamma ray spectrometer is one of the three instruments in a geochemical remote-sensing package flown for the second and last time on Apollo 16. The spectrometer is sensitive primarily to gamma rays produced by natural radioactivity in the lunar soil. The secondary emissions induced by galactic cosmic rays constitute a second source. The experiment team's initial conclusions, based upon the natural rather than the induced radiation, are as follows.

(1) In agreement with the Apollo 15 results, the western maria are generally more radioactive than other regions of the Moon.

(2) Detailed structure exists within the high-radioactivity regions. The high observed in the Fra Mauro area is at approximately the same level as those seen around Aristarchus and south of Archimedes on the Apollo 15 mission. Those levels are comparable to that observed in the soil returned on the Apollo 14 mission.

(3) Radioactivity is lower and more variable in the eastern maria.

(4) The lunar highlands are regions of low radioactivity. The Descartes area appears to have undergone some admixing of radioactive material.

A second objective of the experiment was to map the anisotropies in the galactic cosmic ray fluxes by using the spacecraft as an occulting disk. Although the analysis has just begun, a preliminary look at the data indicates that discrete, celestial gamma ray sources were, in fact, detected.

X-RAY FLUORESCENCE EXPERIMENT

The X-ray spectrometer was the second of the three geochemical remote sensors flown on the Apollo 16 mission. By analyzing the characteristic secondary X-ray emissions produced by solar X-rays impinging on the lunar surface, maps of the Al/Si and Mg/Si ratios can be constructed for the sunlit portions of the Moon. Preliminary conclusions reaffirmed the validity of the Apollo 15 result and extended the interpretation over new areas. Most important, and the objective of all the orbiting geochemical sensors, is the ability to compare the compositions of returned lunar samples to those of remote areas of the Moon. The Al_2O_3 concentration in the Descartes soil inferred from the X-ray measurements (26 to 27 percent) was confirmed by the preliminary analysis of the returned soil (26.5 percent). Descartes soils appear to be similar to those of the eastern limb and the far-side highlands. Remotely sensed Al/Si and Mg/Si ratios for Descartes are 0.67 ± 0.11 and 0.19 ± 0.05 and those of the eastern limb and the far-side highlands are approximately 0.60 to 0.71 and 0.16 to 0.21, respectively. Generally, the highlands are high in aluminum and low in magne-

sium, whereas the reverse is true for the maria. However, there are exceptions, such as Ptolemaeus, where both magnesium and aluminum are high. The emerging picture of the lunar highlands is one of an ancient lunar crust composed of materials with a composition varying between anorthositic gabbro and gabbroic anorthosite.

During transearth coast, the Apollo 16 X-ray spectrometer was used to observe the temporal behavior of two pulsating X-ray stars, Scorpius (Sco X-1) and Cygnus (Cyg X-1). Sco X-1 may be characterized by quiet periods and by periods of up to a day in length in which 10- to 30-percent changes in X-ray intensity occur in a few minutes. These changes in intensity are concurrent but not necessarily simultaneous with changes in optical and radio intensity. Cyg X-1 can double in intensity within a day or so. The increase occurs in all three energy ranges, 1 to 3 keV, 3 keV, and 7 keV. The time variability of the two sources does not appear to be similar at time scales of several seconds to 2 hr.

ALPHA PARTICLE SPECTROMETER EXPERIMENT

The third of the remote geochemical sensors, the alpha particle spectrometer, is sensitive to radioactive radon gas emanating from the lunar surface. Because radon itself is a product of the decay of uranium and thorium, mapping the concentration of radon gas is tantamount to mapping regions of high radioactivity. This capability is especially significant where the radioactivity lies below the lunar surface yet might be detected by its escape through fissures. Results from a still incomplete analysis of Apollo 15 data indicate that the region including Aristarchus, Schröter's Valley, and Cobra Head is an area of relatively high radon emanation. Because of the limited spatial resolution of the technique, only general source regions can be designated. Another area that has been identified is the broad region from west of Mare Crisium to the Van de Graaff-Orlov area. A real-time analysis of Apollo 16 data indicates a strong high centered on Mare Fecunditatis.

MASS SPECTROMETER EXPERIMENT

The objectives of the lunar orbital mass spectrometer carried on both the Apollo 15 and 16 missions were to detect a lunar atmosphere and to search for active lunar volcanism. The instrument covered the mass range from 12 to 67 amu and was sensitive to partial pressures as low as 1×10^{-14} torr. Unfortunately, contamination from the spacecraft tends to mask the lower concentrations of the atmospheric gases. However, shortly after the plane change and rendezvous of the Apollo 16 command and service module (CSM) and lunar module (LM), the contamination levels as recorded by the mass spectrometer were the lowest yet observed in lunar orbit. During this period, data were obtained on the partial pressure of neon-20. A preliminary analysis indicates that, at the orbital altitude of 100 km, the concentration of neon-20 is $8.3\ (\pm 5) \times 10^3$ atoms/cm^3. Because 100 km is 4 scale heights above the lunar surface at night, the nighttime surface concentration would be $4.5\ (\pm 3) \times 10^5$ atoms/cm^3. This value is approximately a factor of 3 less than previous estimates.

SUBSATELLITE MEASUREMENTS OF PLASMA AND ENERGETIC PARTICLES

Along with a magnetometer and an S-band tracking function, plasma and energetic particle detectors were carried on the subsatellite launched into lunar orbit by the Apollo 16 CSM. These detectors were included to observe the various plasmas in which the Moon moves, to study the interaction of the Moon with the solar wind plasma, and to observe certain features of the structure and dynamics of the magnetosphere of the Earth. The detectors were sensitive to electrons in the 0.5- to 15- and 20- to 300-keV ranges and to protons in the 40-keV to 2-MeV range.

A first look at the data indicates that the sensors experienced passage of a hydromagnetic shock wave in the solar wind. The magnetometer recorded a sharp discontinuity at the time of electron onset, and, 10 min later, Earth-based magnetometers observed a similar disturbance. This magnitude corresponds to a shock-propagation velocity that is greater than 400 km/sec. The rise times for the proton and electron increases yield profiles for the region of shock discontinuity. The inferred thickness of this region is approximately 4000 km. Solar wind electrons maintained abnormally high temperatures for 12 hr following the shock.

At the time of the Apollo 16 subsatellite launch, the Moon was just entering the geomagnetic tail. During the time the Moon was in the magnetotail, the subsatellite returned 22 orbits of data on the high-latitude magnetotail and nine orbits of data on the plasma sheet. From these data, the fluxes and the energy spectra were constructed. A continuing feature of the plasma sheet is a large flux of energetic protons. Plasma-sheet protons greater than 40 keV often have flux an order of magnitude greater than electrons of the same energy. This difference is in contrast to the high-latitude magnetotail, in which the electron and proton fluxes are approximately the same.

S-BAND TRANSPONDER EXPERIMENT

S-band transponder tracking of the LM-CSM and of the Apollo subsatellites is used to map the lunar gravitational field. The degree of correlation between the gravity map and physiographic features such as craters or mountains is used to infer density contrasts or to detect buried structures.

Unlike spacecraft on previous Apollo missions, the Apollo 16 LM-CSM did not traverse any known completely visible mascons. However, several features do appear in the new gravity profiles. An extensive gravity that does not correlate well with the surface feature was found in the area of the Riphaeus Mountains. The mountains may be associated with a much larger subsurface structure. The Nubium and Fra Mauro areas are gravity lows; and the Descartes area, although essentially a gravity high, is flanked on the east by a definite negative anomaly. Although the detailed analysis continues, several generalizations may be made.

(1) All unfilled craters are negative anomalies.

(2) All filled "craters" and circular seas with diameters greater than approximately 200 km are positive anomalies, or mascons. The smallest is Grimaldi at 150 km; an exception is the unique Sinus Iridum.

(3) Filled craters less than 200 km in diameter are negative anomalies; an example is Ptolemaeus.

(4) Part of the central highlands appears as a positive anomaly.

(5) Mountain ranges observed so far have positive anomalies (Marius, Apennines); whether isostatic equilibrium has been achieved is undetermined.

(6) Gravitational anomalies associated with the ring structure of Orientale are verified independently; the suggestion of ring structure for some of the other mascons is consistent with the additional data.

(7) There are definable features not correlated with obvious surface features of geologic blocks, and these features presumably represent subsurface characteristics.

BISTATIC RADAR EXPERIMENT

The bistatic radar experiment uses CSM S-band and very-high-frequency (VHF) transmissions to probe the electromagnetic and structural properties of the lunar surface. Radio signals from the CSM are reflected by an approximately 10-km-diameter area of the Moon and recorded by radiotelescopes on the Earth. As the CSM orbits, the reflecting spot scans the lunar disk. The characteristics of that reflecting area can be interpreted in terms of dielectric properties, block sizes, and slopes.

Initial conclusions are that the oblique geometry scattering properties of the lunar surface are wavelength dependent in the decimeter to meter range. At a given wavelength, the scattering law is highly dependent on local topography. Furthermore, there are systematic differences in the average scattering properties of mare and highland units. Generally, reflections off maria at the S-band wavelength are uniform and consistent with a lunar surface dielectric constant of 3.1 ± 0.1. The VHF reflection is not as easily interpreted. Evidently, the maria are not simple half-space reflectors at VHF wavelengths. Both the Apennines and the central highlands show a reduction in the dielectric constant from 3.1 for S-band to 2.8 for VHF. Typical root-mean-square slopes for the highlands are 5° to 7° for both S-band and VHF wavelengths, whereas, for the maria, the data are consistent with 2° to 4° slopes at S-band but only to 1° or 2° at VHF wavelengths.

ADDITIONAL EXPERIMENTS

A continuation of an experiment flown on the Apollo 15 mission, the ultraviolet photography of the Earth and Moon, was to allow comparison of ultraviolet and color photographs under equivalent circumstances. The results will be applied to telescopic observations of the planets. A 70-mm camera was

used with four filters having passbands between 255 and 400 nm. A survey of the returned images of the Moon shows little of the loss of detail at the shorter wavelengths observed in telescopic ultraviolet photographs of Mars. The photographs of the Earth show the expected diminution of detail with shorter wavelengths caused by the increased opacity of the atmosphere of the Earth at ultraviolet wavelengths.

The Apollo command module heat shield windows are studied to obtain information about the flux of meteoroids with masses of 1×10^{-7} g down to the detection limit of 1×10^{-11} g for optical studies or of meteoroids of much lower masses for anticipated electron microscope studies. The resulting estimate of mass flux is in good agreement with Surveyor III data and with models generated from near-Earth studies.

Three biomedical experiments were flown on the Apollo 16 mission. These were the biostack, an experiment to study the biological effects of galactic cosmic radiation; the Apollo light flash moving emulsion detector, to study the subjective observation of faint light flashes seen by nearly all Apollo crewmen while in space; and the microbial ecology evaluation device, to study the response of various microbes to a space environment. All three experiments were executed successfully. Although a few qualitative results are included in this report, the detailed analyses have just begun.

An impressive array of cameras was flown in the Apollo 16 CSM. These ranged from the highly sophisticated 24-in. panoramic camera and the 3-in. mapping camera with its laser altimeter and star-field recorder to the 16-, 35-, and 70-mm cameras used for astronomical photography, earthshine lunar photography, and solar corona photography and to support crew observations of lunar features. The more than two dozen sections in this report resulting from this Apollo 16 photography are ample testimony of its value. These sections, as well as summaries of Earth-based radar and infrared studies, are included as valid products of the Apollo 16 effort.

REFERENCE

3-1. Adler, I.; Trombka, J.; Gerard, J.; Schmadebeck, R.; et al.: X-Ray Fluorescence Experiment. Sec. 17 of Apollo 15 Preliminary Science Report. NASA SP-289, 1972.

4. Photographic Summary

John W. Dietrich[a] *and Uel S. Clanton*[a]

The photographic objectives of the Apollo 16 mission were to provide precisely oriented mapping-camera photographs and high-resolution panoramic-camera photographs of the lunar surface, to support a wide variety of scientific and operational experiments, and to document operational tasks on the surface and in flight. These photographic tasks were integrated with other mission objectives to achieve a maximum return of data from the mission.

The variety of photographic equipment, the latitude and unique morphological setting of the Descartes landing site, and the planned 147.8-hr stay in lunar orbit enhanced the potential photographic data return from the Apollo 16 mission. A far-ultraviolet (UV) camera/spectrograph introduced on this mission provided a capability to acquire imagery and spectroscopy in the far-UV range. The remaining photographic equipment inventory for the Apollo 16 mission resembles that of the preceding Apollo 15 mission. Panoramic- and mapping-camera systems mounted in the scientific instrument module (SIM) bay of the service module provide each of the J-series missions (Apollo 15 to 17) an orbital photographic capability that was not available on any earlier manned or unmanned mission to the Moon.

The orbital inclination required for a landing at the Descartes site carried the spacecraft 9° north and south of the equator. A plane change that would have carried the command and service module (CSM) approximately 13.5° north and south of the equator during the last day of the mission was canceled because of a real-time modification of the Apollo 16 mission. Moon rotation during the scheduled 6-day lunar-orbit phase of CSM operations would have exceeded 75°; the terminators shifted approximately 65° during the abbreviated mission. Terminator advance during the mission provided the opportunity for observing and photographing targets under a wide range of lighting conditions and also expanded the total surface area lighted for observation during a single mission.

More photographs were returned by the Apollo 16 mission than by any preceding mission. A total of 1587 images were exposed in the 61-cm-focal-length panoramic camera. Of these, more than 1415 are high-resolution photographs from lunar orbit. The remainder were exposed near the beginning of transearth coast (TEC). Each panoramic-camera image is 11.4 cm wide and 114.8 cm long; assuming the nominal spacecraft altitude of 110 km, each image exposed from orbit covers a 21- by 330-km area on the lunar surface. The 7.6-cm-focal-length mapping camera exposed 2514 11.4-cm-square frames that contain lunar-surface imagery. Another 927 frames were exposed while the camera operated over unlighted lunar surface in support of the laser-altimeter experiment. A companion 35-mm frame from the stellar camera permits precise reconstruction of the camera-system orientation at the time of each mapping-camera exposure. Approximately 440 photographs with lunar imagery were exposed between transearth injection (TEI) and the TEC extravehicular activity (EVA).

The Apollo 16 crew also returned approximately 2860 frames of 70-mm photography, 58 frames exposed in the 35-mm camera, and 21 magazines of exposed 16-mm film. Of these, some 1800 frames of 70-mm photography and eight magazines of 16-mm film were exposed in the lunar module (LM) or on the lunar surface. At the time this report was submitted, all photography had been screened and the locations of most of the lunar-surface imagery had been identified. Index preparation was at an advanced stage, and the lunar-surface footprints of orbital photographs were being plotted on lunar charts for index map printing.

[a]NASA Manned Spacecraft Center.

TRANSLUNAR PHOTOGRAPHY

Photographic activity began during the first revolution of Earth orbit when crew-option targets (including the Houston, Texas, area) were photographed with the Hasselblad electric (EL) 70-mm camera. After the translunar injection (TLI) burn, the crew documented the transposition and docking maneuvers with the Hasselblad EL camera and the 16-mm data acquisition camera (DAC) as the world watched real-time television (TV) pictures of the operation. Approximately 4 hr after lift-off, extraction of the LM from the SIVB stage was photographed by the DAC and the Hasselblad camera. Crew-option photographs of the receding Earth were taken before, during, and after the transposition, docking, and ejection maneuvers.

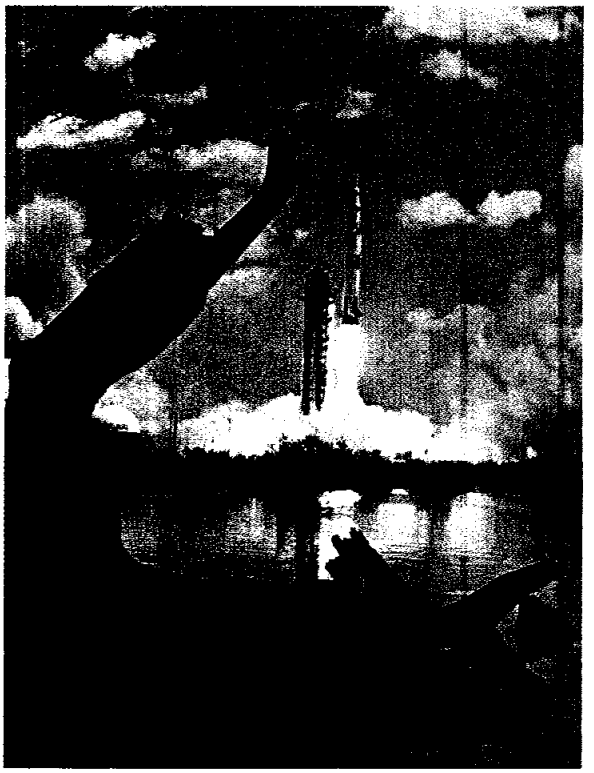


FIGURE 4-1.–The Apollo 16 launch vehicle lifts off from pad A, launch complex 39, Kennedy Space Center, Florida (S-72-35347).

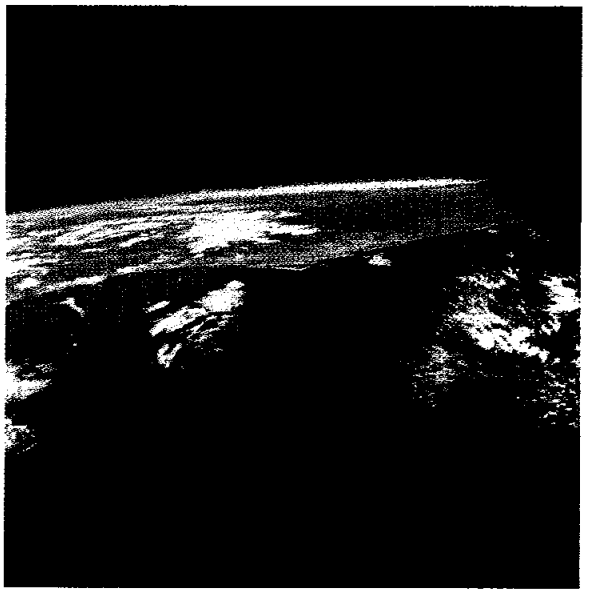


FIGURE 4-2.–View eastward across the Pacific waters to Southern Baja California Peninsula as Apollo 16 approaches the coast of North America on the first revolution in Earth orbit (AS16-118-18859).

Lift-off of the Apollo 16 spacecraft is shown in figure 4-1. Figures 4-2 and 4-3 are photographs taken in Earth orbit. Typical TLC views are shown in figures 4-4 to 4-6, and figures 4-7 to 4-10 are photographs made from either the LM or the CSM following the LOI burn.

Photographic activity was at a low level through most of the translunar-coast (TLC) phase of the Apollo 16 mission. Four sets of UV photographs of the Earth and one set of the Moon were exposed at scheduled times during TLC. Each set consists of a color photograph and four frames recorded on special spectroscopic film sensitive to the shorter wavelengths; one frame was taken through each of four filters that pass energy in different bands of the UV spectrum. A special lens that transmits UV wavelengths was used on the camera. The target was photographed through a special command module (CM) window that is transparent to UV radiation; the window was covered with a shade or a UV filter when not in use.

One Hasselblad magazine of high-speed, black-and-white film was exposed while the electrophoresis experiment was being performed after the first rest period. Jettisoning of the SIM-bay door



FIGURE 4-3.–View eastward from Earth orbit across the coastal plain of Texas and Louisiana. The thin band of blue that separates Earth from the blackness of outer space along the gently curved horizon (upper right corner) graphically illustrates the limited nature of the Earth atmosphere. Coastal features from Freeport, Texas (right margin), to the Atchafalaya Bay south of Morgan City, Louisiana, are readily identified. Interstate Highway 10 extends from near the center of the bottom margin to Houston, near the center of the frame. Dense forests in northeast Texas, central Louisiana, and Mississippi make up the dark-green area that dominates the upper left quarter of the frame. The Mississippi River flood plain crosses the forest as an irregular, light-colored band that roughly parallels the top margin (AS16-118-18860).



FIGURE 4-4.–This spectacular view of North America was photographed approximately 1 hr 50 min after the TLI burn. The solid white area at the upper left is the north polar icecap and snow-covered terrain in Canada. A pronounced spiral cloud pattern covers the upper Ohio Valley, the eastern Great Lakes, and New England. The western Great Lakes are free of clouds, but western Lake Superior, northern Lake Michigan, and western Lake Huron are ice covered. Snow in the Sierra Nevada, the Cascade Range, the Rocky Mountains, and other mountain ranges combines with some clouds to conceal terrain at places in western Canada and in the northwestern United States. The Yucatan Peninsula and many of the islands bordering the Caribbean Sea are clearly visible, but most of Central and South America is obscured by clouds (AS16-118-18879).

approximately 4.5 hr before lunar orbit insertion (LOI) was documented by DAC photography. Before the protective door was removed, the SIM camera systems required little attention; the mapping and panoramic cameras were cycled once to reduce the chances of film set. After SIM-bay-door jettison, the housekeeping requirements increased because the SIM camera temperatures had to be maintained within operational limits.

Following a nominal LOI burn, the Apollo 16 crew transmitted visual impressions of features observed during revolutions 1 and 2. Selected crew-option targets were photographed with the

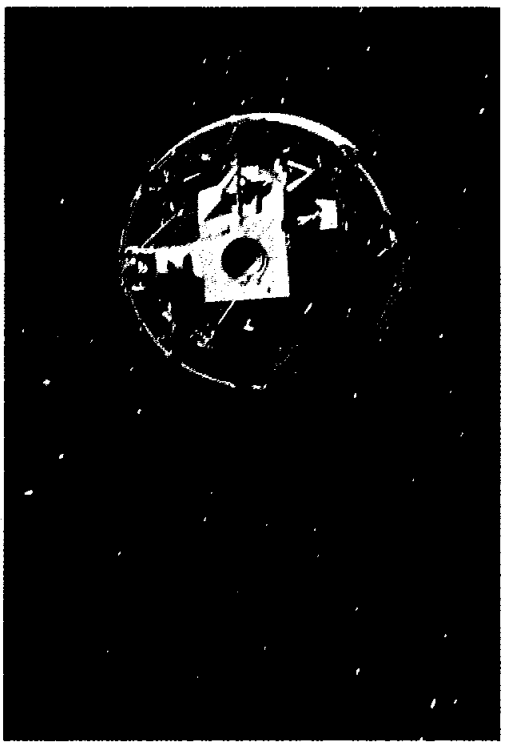


FIGURE 4-5.–The LM before extraction from the SIVB stage. The CSM separated from the SIVB stage approximately 30 min after the TLI burn. This photograph was taken after the vehicle turned to permit examination of the LM before docking. Abundant particles released from the vehicles during separation shine against the blackness of space. The top hatch, used for docking, is clearly visible in this photograph; but the docking target is partly in shadow (AS16-118-18875).



FIGURE 4-6.–The SIVB stage after LM ejection. On command from the Mission Control Center in Houston, the spent SIVB maneuvered away from the hard-docked CSM and LM. The SIVB continued along the modified trajectory to impact on the lunar surface. Part of the LM, including three of the four thrusters in a reaction control system thruster quad, can be seen along the bottom edge of the frame (AS16-118-18881).

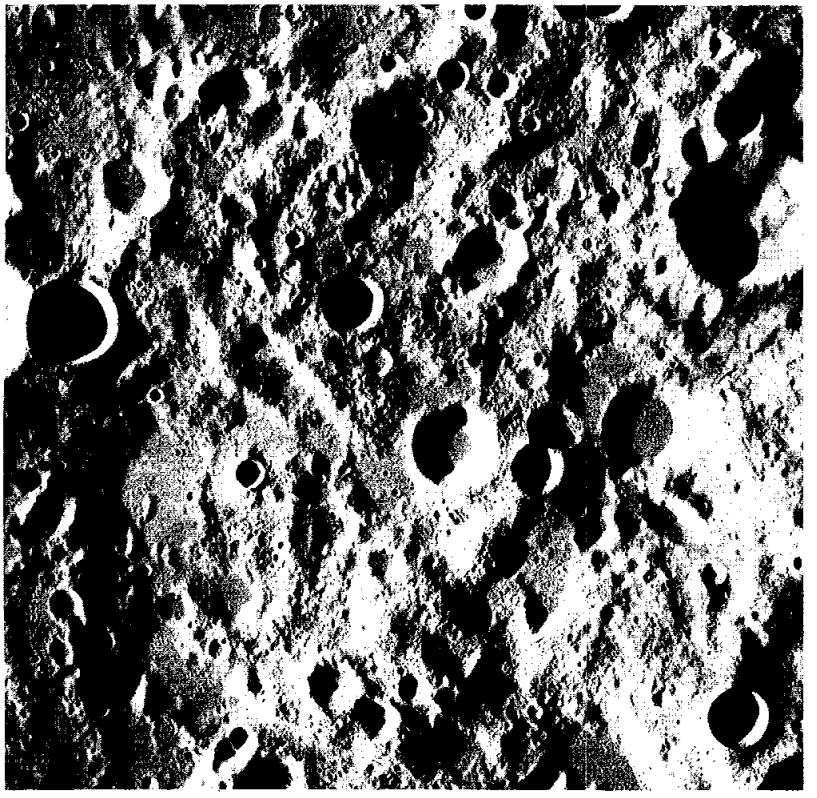


FIGURE 4-7.–Rugged far-side terrain exhibits a wide dynamic range from black shadows to bright, Sun-facing slopes when illuminated by a low Sun. This mapping-camera frame, centered between the Craters Zhukovsky and Stein near latitude 8.6° N, longitude 175.9° W, was exposed before the first rest period in lunar orbit. The sunset terminator crossed this area before the next scheduled period of camera operation. North is at the top of the frame, which is alined within 10° of the selenographic grid (Apollo 16 mapping-camera frame 0011).

Hasselblad EL camera. Mapping- and panoramic-camera operation was scheduled for approximately 8 min near the end of revolution 3 and the beginning of revolution 4 to photograph terrain that would be crossed by the sunset terminator during the first rest period in lunar orbit. Twenty-six frames were exposed with the mapping camera; however, only four frames were exposed with the panoramic camera before it had to be switched to the standby mode because of an electrical anomaly. During revolution 11, the sunrise terminator was in the vicinity of the Descartes landing area. By using the CSM Hasselblad EL camera, the crew obtained low-Sun-angle photographs of the landing site. Undocking occurred on revolution 12.

After separation, the LM Hasselblad data camera (DC) photographed the CSM during stationkeeping and captured a prelanding earthrise sequence that included both the Earth and the distant CSM. On the last scheduled low-altitude pass over the landing site, the DAC (mounted on the CSM sextant) documented the tracking of a landmark near the landing target.

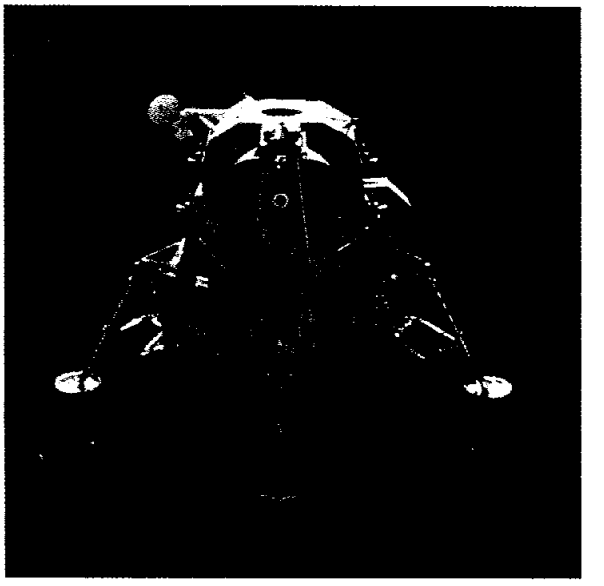


FIGURE 4-8.–The LM prepared for lunar landing. After separation from the CSM, the LM maneuvered to permit inspection by the CMP. Both LM hatches, the round docking hatch in the top surface and the square hatch at the top of the ladder, are clearly visible in this Hasselblad photograph (AS16-118-18897).

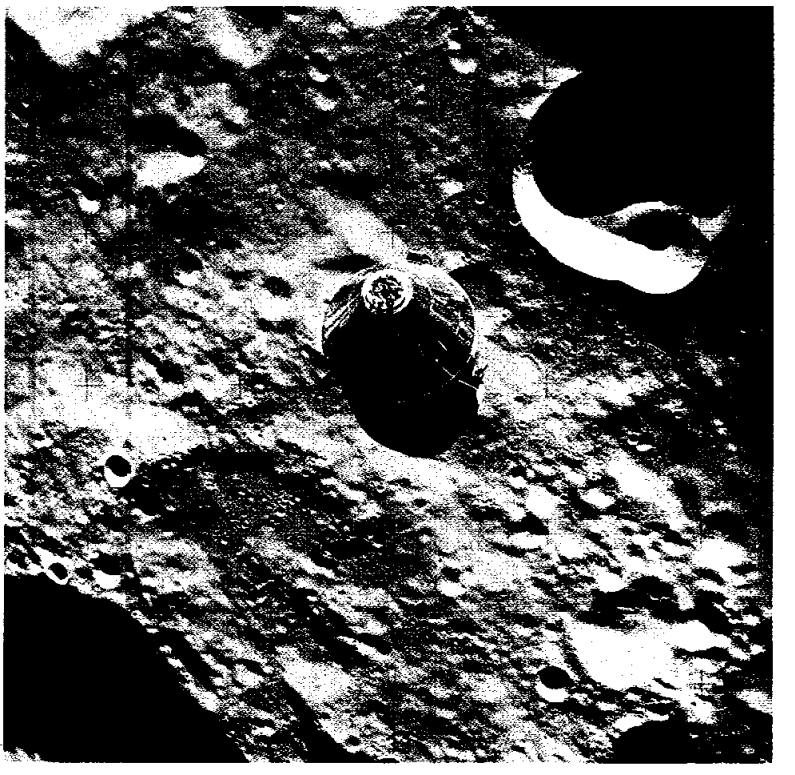


FIGURE 4-9.–The CSM at close range above far-side terrain. In this 60-mm Hasselblad DC photograph, the CSM is above the far-side terrain near latitude 8° N, longitude 172° E. The double crater at the upper right corner of the frame is unnamed. The northwest rim of Valier Crater is at the lower left corner. North is to the right in this near-vertical view (AS16-113-18294).

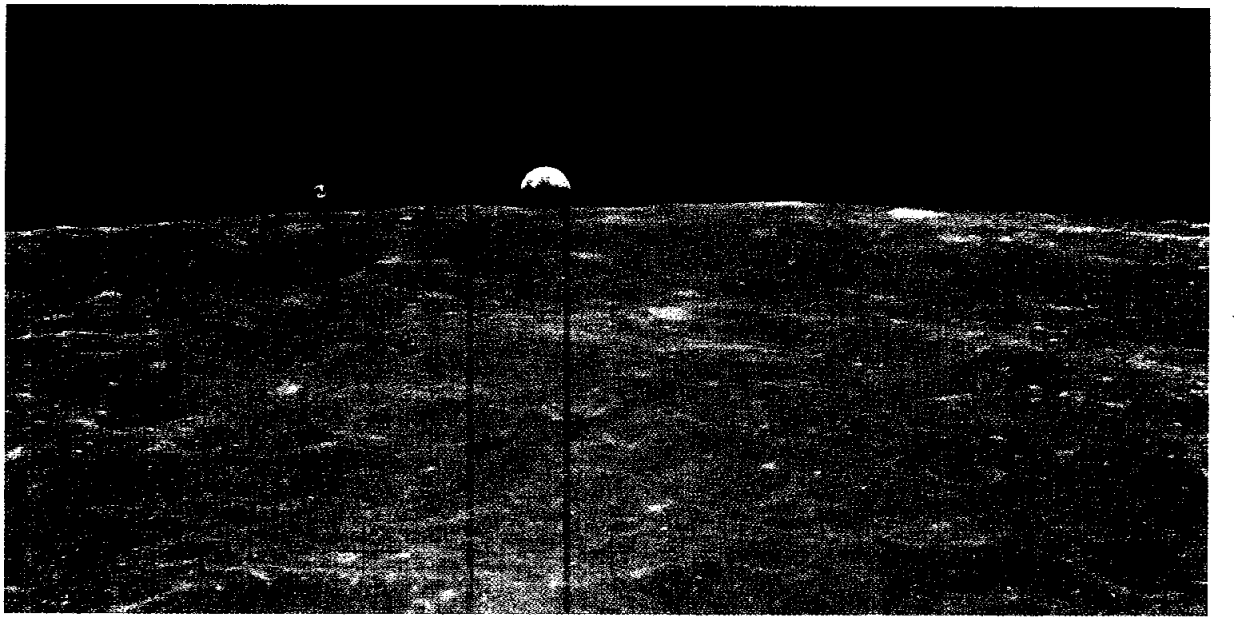


FIGURE 4-10.–Earthrise. In this 60-mm Hasselblad DC photograph from the LM, the CSM is to the left of the Earth. This photograph was taken during the hold period before landing (AS16-113-18288).

LUNAR MODULE/LUNAR-SURFACE PHOTOGRAPHY

The crew used an enlarged inventory of photographic equipment (table 4-I) to document the LM-descent, surface-operations, and LM-ascent phases of the mission and to support scientific experiments on the surface. The new far-UV camera/spectrograph gave the Apollo 16 crew the capability of recording UV radiation from distant sources that the atmosphere blocks from Earth-based observatories and that is below the threshold of detectability with the short time exposures feasible in a moving spacecraft.

The fifth lunar landing was unique in the manned exploration of the Moon. The Apollo 16 mission has been the only opportunity to explore and sample the major geomorphic unit of the Moon, the lunar highlands. The 71 hr 14 min stay time of the LM on the lunar surface accommodated three EVA periods for a total of 40.5 man-hr of lunar-surface activity. The commander (CDR) and the LM pilot (LMP) took 1800 photographs, collected 95 kg of material, and completed three traverses covering 21.7 km. Throughout the stay at the Descartes site, a TV camera mounted on the lunar roving vehicle (LRV) provided real-time viewing of most of the crew's activity on the lunar surface. The crew was required to aline the high-gain antenna at each station to establish contact with the Mission Control Center; but, once alined, the camera could be controlled remotely from Earth. These TV transmissions enabled observers to evaluate the operational capabilities of the crew, to observe the Apollo lunar-surface experiments package (ALSEP) deployment and the collection of samples, and to select samples of special scientific interest to be returned to Earth.

Approximately 4 hr into the first EVA period (EVA-1), with ALSEP deployment completed, the crew drove west to station 1 near Flag and Plum

TABLE 4-I.–Photographic Equipment Used in LM and on Lunar Surface

Camera	*Features*	*Film size and type*	*Remarks*
Hasselblad DC, 2	Electric; 60-mm-focal-length lens; reseau plate	70-mm; SO-168 Ektachrome EF color-reversal film exposed and developed at ASA 160; 3401 Plus-XX black-and-white film, aerial exposure index (AEI) 64	Handheld within the LM; bracket-mounted on the remote control unit for EVA photography; used for photography through the LM window and for documentation of surface activities, sample sites, and experiment installation
Hasselblad DC	Electric; 500-mm lens; reseau plate	70-mm; 3401 Plus-XX black-and-white film, AEI 64	Handheld; used to photograph distant objects from selected points during the three EVA periods
DAC	Electric; 10-mm lens	16-mm; SO-368 Ektachrome MS color-reversal film, ASA 64	Mounted in the LM right-hand window to record low-altitude views of the landing site one revolution before landing, to record the LMP view of the lunar scene during descent and ascent, and to document maneuvers with the CSM
Lunar DAC	Electric; 10-mm lens; battery pack and handle	16-mm; SO-368 Ektachrome MS color-reversal film, ASA 64	Handheld or mounted on the LRV to document lunar-surface operations
Far-UV camera/ spectrograph	3-in. Schmidt electronographic camera; external batteries with connecting cable, tripod mount, leveling/pointing mechanism, external controls	NTB-3 electronographic film	Deployed and leveled on tripod in LM shadow, with cable-connected batteries in the Sun. Point camera with elevation and azimuth adjustments for each target. Activate automatic exposure sequencer. Changes in EVA times because of delay in landing forced the recalculation of all pointing values

Craters for geologic sampling. The stop at station 2 near Buster and Spook Craters confirmed the findings at station 1; both stations had the same rock types. The scientists had expected volcanic rocks, but the crew found mostly impact breccias.

Back at the LM, the CDR put the LRV through a series of "Gran Prix" maneuvers, which were photographed by the LMP to document the performance characteristics of the vehicle. After closeout, the crew returned to the LM to eat, sleep, and prepare for the second EVA period (EVA-2). Representative EVA-1 photographs are shown in figures 4-11 to 4-21. The far-UV camera/spectrograph is shown in figure 4-22, and figure 4-23 is a color enhancement of a far-UV photograph.

The second EVA period began with a drive to Stone Mountain on a modified traverse. Station 7 had been eliminated from the original traverse to provide more time at station 10. The first stop, at station 4, was high on the side of Stone Mountain. The angular blocks photographed at this location appeared to be ejecta from South Ray Crater. In addition to acquiring the usual 60-mm photography at station 4, the LMP used the Hasselblad camera with the 500-mm telephotographic lens to record details of South Ray and Baby Ray Craters and of the North Ray Crater-Smoky Mountain area.

The crew retraced the LRV tracks down Stone Mountain and located station 5 on the rim of a 15-m-diameter crater. Photographs indicate that this area contains the smallest amount of ejecta from South Ray Crater of any station visited during EVA-2. The crew turned west to find a fresh, blocky crater for station 6. A 10-m-diameter secondary crater was selected, sampled, and photographed.

Station 8 was located on the east side of Wreck Crater in a boulder field. The plan at station 8 was to photograph a boulder and surrounding area and to collect material from the boulder, from around the boulder, and then from under the boulder. Unfortunately, the first three boulders picked by the crew were too deeply embedded to be rolled over. These collections, together with the documenting photography, however, provided examples of glass, breccias, igneous rocks, and soils that are valuable in the investigation of the petrology of the area. The crew drove north and located a small boulder near station 9. At this location, their efforts were successful; a boulder was moved and the photography and sample sequence completed. The crew stopped near the ALSEP site, station 10, on the route back to the LM for additional photography, samples, cores, and penetrometer measurements. Figures 4-24 to 4-27 are photographs taken during EVA-2.

The third EVA period (EVA-3) was modified extensively from the mission plan, both for time and number of stops to be made. The crew drove first to the eastern edge of North Ray Crater, station 11. The usual 60-mm photography at station 11 was complemented with a series of panoramas, using polarizing filters, and with additional telephotography, using the Hasselblad camera with the 500-mm lens to photograph Smoky Mountain. Samples from North Ray Crater and House Rock were found to be impact breccias and not volcanic rocks as anticipated. Closeup photography documented the clastic texture of the breccia boulders. Station 13 provided additional samples, including samples from the shadowed area under Shadow Rock. Material from the shadowed area provided soil and rock samples that had been shaded for millions of years. From station 13, the crew returned to the LM area (station 10) to collect additional samples, to complete activation of the ALSEP, and to package the samples for return to Earth.

The LRV was parked near the LM with the high-gain antenna alined and with the TV camera on and remotely controlled from Earth. From this location, live coverage during final closeout and during the lift-off of the ascent stage from the lunar surface was provided by TV. The LM-window-mounted DAC photographed the receding lunar surface and provided detailed photographic coverage of terrain west of the landing point as the LM headed toward rendezvous with the CSM. Figures 4-28 to 4-36 are representative EVA-3 photographs.

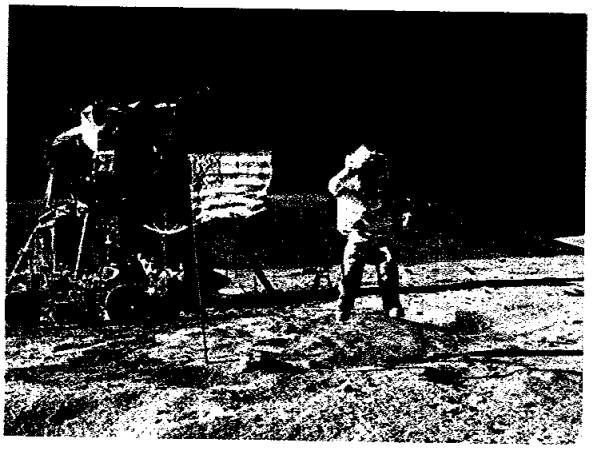


FIGURE 4-11.–With a salute and a leap into space, the CDR honors the flag and the people of the United States of America. Stone Mountain, 5 km in the distance and approximately 500 m higher than the landing site, forms the skyline behind the astronaut. The LRV is parked near the LM. The far-UV camera/spectrograph sits on a tripod partially shaded by the shadow of the LM. Note the astronaut's position and shadow and compare with figure 4-12 (AS16-113-18339).

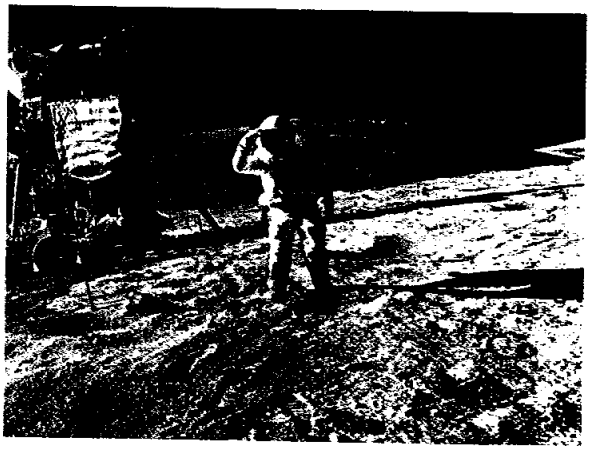


FIGURE 4-12.–The LMP honors the flag, the Nation, and the American people in this salute to the Stars and Stripes. Note especially the astronaut's position and shadow and compare with figure 4-11 (AS16-113-18341).

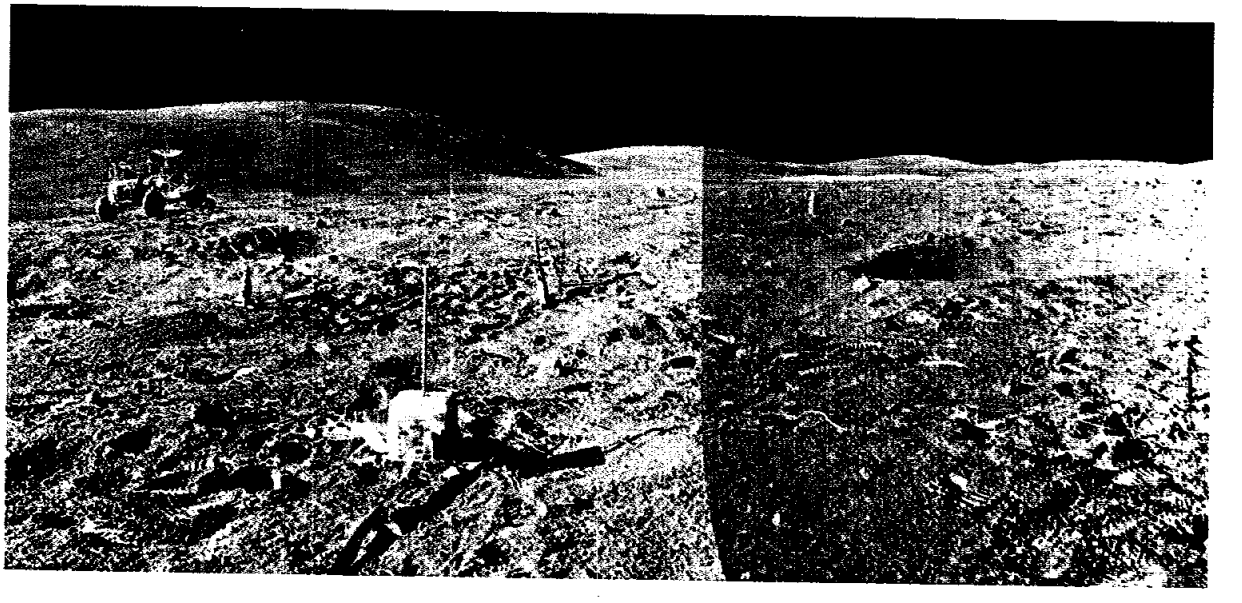


FIGURE 4-13.–Stone Mountain, approximately 5 km in the distance, forms the skyline behind the LRV in this view from the ALSEP site. The white object in the foreground is part of the heat-flow experiment (HFE); the universal handling tool, which is used to level the package, sticks up from the top of the package. The heat-flow probe in the bore stem at the right margin of the photograph is connected by cable to the HFE electronics package. The golden tape in the immediate foreground connects the HFE to the ALSEP central station. To the left rear of the electronics package is the lunar-surface drill; the drill rack with core and bore stems is just behind the electronics package. In the distance to the right rear of the drill rack is the treadle and core stem extractor. The horizontal splash of white above the extractor is South Ray Crater, approximately 6 km in the distance (AS16-113-18366, 18367, 18368).



FIGURE 4-14.–The gold-and-white object in the foreground is the lunar-surface magnetometer. The CDR works with the thumper, to provide energy to activate the geophones of the active seismic experiment. The large, golden, rectangular object is the ALSEP central station; the long, white antenna extending from the central station telemeters data to Earth from each of the experiments. The dark, cylindrical object in front of the central station is the radioisotope thermoelectric generator, which provides electrical power for the experiments. Objects to the right of the central station include the passive seismic experiment and the mortar box assembly (MBA), another part of the active seismic experiment. The golden tape at the upper right extends to the HFE (AS16-113-18373).

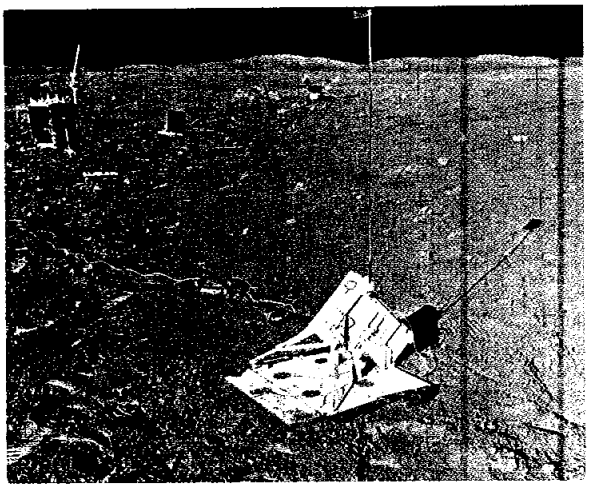


FIGURE 4-15.–The MBA (in the foreground) is part of the active seismic experiment. The MBA contains four grenades that are designed to be fired remotely by ground control. The grenades, which explode on contact with the lunar surface, provide a calibrated seismic-signal source to the geophone line. The geophone line, which extends some 94 m out from the central station, can be seen in the upper center and upper right in this photograph. (Energy from the explosions is used to produce a seismogram, a record of energy propagation through the crust of the Moon. Seismograms provide scientists with information about the internal structure of the Moon.) The golden, rectangular object at the upper left is the ALSEP central station; the gray, finned object is the radioisotope thermoelectric generator; the three-armed, white-and-gold object is the lunar-surface magnetometer (AS16-113-18379).

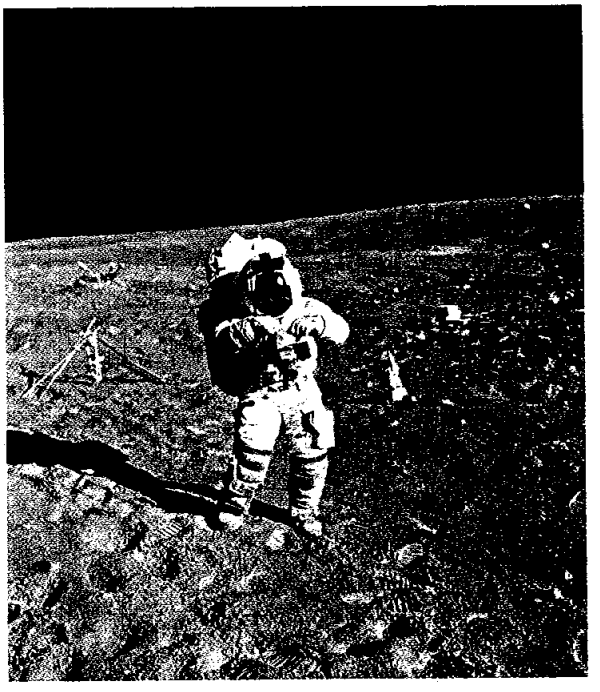


FIGURE 4-16.–The CDR bags a sample of the Moon at the ALSEP station during EVA-1. Components of the ALSEP cover the surface immediately behind the CDR. The lunar-surface drill appears behind the CDR's left elbow. The square box behind the drill is part of the HFE. The dark object in the background is the radioisotope thermoelectric generator. To the astronaut's right is the drill rack with bore stems. The three-sensor lunar-surface magnetometer is in the background beyond the drill rack (AS16-114-18388).



FIGURE 4-17.–This partial panorama at station 1 shows the beauty and stark bleakness of the lunar surface. With antenna pointed toward Earth, the LRV beams a TV picture to vicarious explorers around the world. To the left, the LMP stands near the rim of Plum Crater. The Hasselblad camera and documented sample bags hang from the remote control unit on his chest. The sample collection bag hangs from the primary life support system on his back. The scoop is stuck into the lunar surface near his left hand. The reflection of the CDR, the photographer for this panorama, can be seen in the LMP's visor. To the right, the "second" astronaut is the LMP after he has moved during the photographic sequence. The apparent change in shadow direction is an illusion caused by flat reproduction of the curved panoramic sequence. Stone Mountain, some 500 m high and 5 km in the distance, forms the skyline to the right (AS16-114-18422, 18423, 18425, 18427).

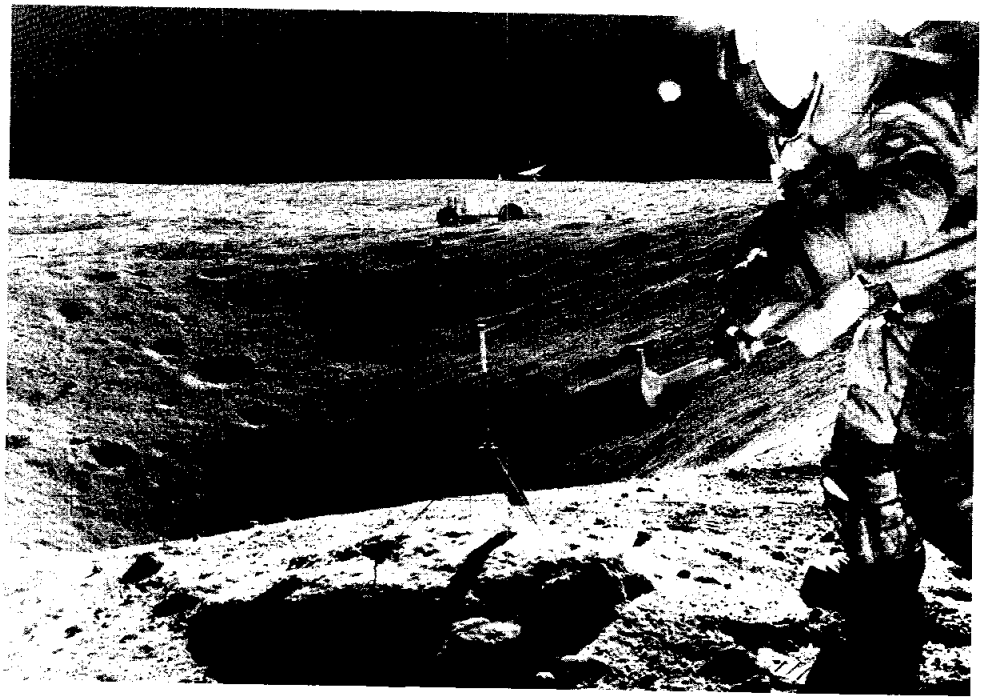


FIGURE 4-18.–The CDR, with hammer in hand, prepares to sample a boulder on the rim of Plum Crater at station 1 during EVA-1. Plum Crater has an unusual morphology; there is a bench or break in the slope along the inner wall of the crater. Smaller craters give a pock-marked appearance to the inner slopes. The gnomon marks the area to be sampled. The Hasselblad camera is partially visible above the CDR's left hand. Sample bags, which are hanging from the camera bracket, appear just below his left hand. Above the gnomon is the LRV. The flash of light in front of the visor is a light reflection on the camera lens (AS16-109-17804).

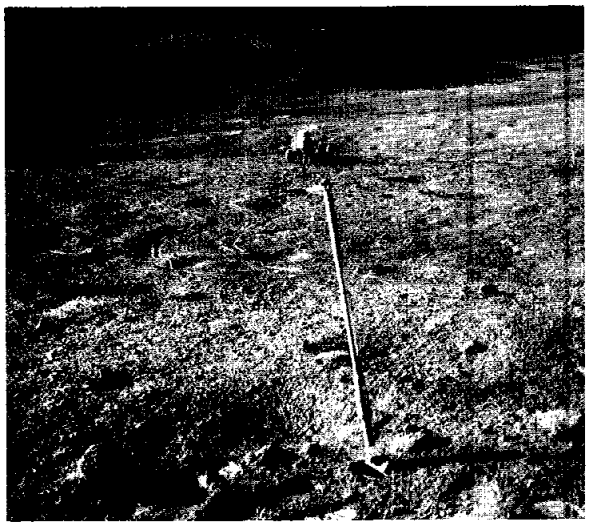


FIGURE 4-19.–The LMP has collected two samples in the immediate foreground near the scoop. This photograph, which was taken to document the location of the samples, catches the CDR (at the LRV) deeply involved with the portable magnetometer experiment. The tripod-sensor assembly is at the right margin of the photograph. The large crater in front of the LRV is Spook Crater, which is approximately 100 m in diameter. Stone Mountain, 500 m high and 5 km in the distance, forms the skyline. Boot tracks and LRV tracks cross in the foreground (AS16-109-17841).



FIGURE 4-20.–The CDR, with Hasselblad camera and documented sample bags hanging from the remote control unit on his chest, folds up a sample bag with his left hand. The LRV is partially visible above the astronaut's left shoulder. The large crater along the right margin of the photograph is Plum Crater. The horizontal splash of white just below the skyline is South Ray Crater and associated ejecta. The gnomon with color chart, marking the locations from which samples have been collected, sits in the foreground (AS16-109-17797).

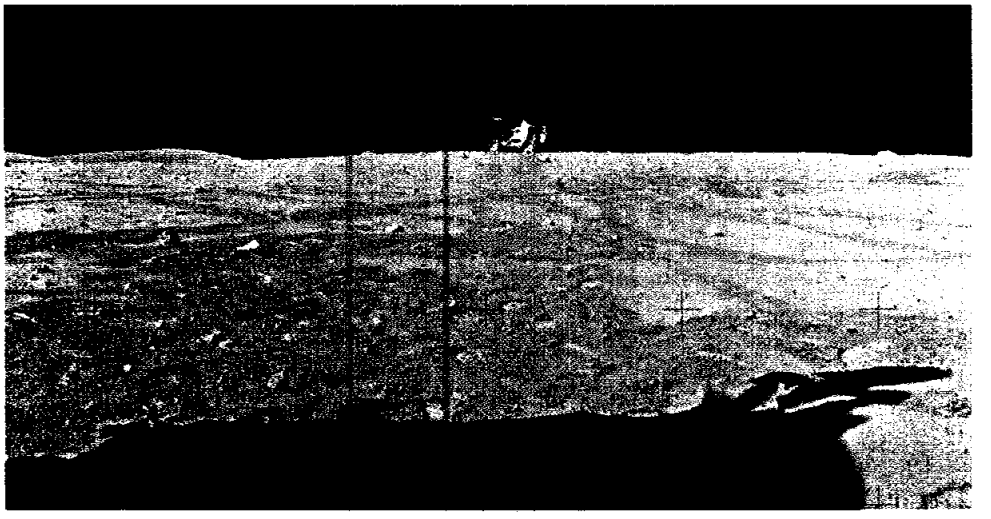


FIGURE 4-21.–The CDR races through a series of Gran Prix maneuvers to demonstrate the performance of the LRV. The vehicle cannot be fully tested on Earth for operational constraints because of the great differences in the environment of the Earth and the Moon. Motion pictures and photographs help to define the performance characteristics of the vehicle in the lunar environment. The bands of dark gray are LRV tracks; bootprints clutter the foreground (AS16-115-18559).



FIGURE 4-22.–The gold-colored far-UV camera/spectrograph stands in the shadow of the LM. The far-UV camera/spectrograph is a miniature observatory that acquires imagery and spectroscopy in the far-UV range. The astronauts must initially deploy the equipment and then periodically retarget the camera/spectrograph during their stay on the lunar surface. At the end of EVA-3, the CDR removed the film cassette from the top of the camera for return to Earth. Behind the far-UV camera/spectrograph is the LRV; to the left is the American flag. The LMP carries a boulder to the footpad by the ladder. During the EVA-3 closeout, this sample was bagged for return to Earth (AS16-114-18439).

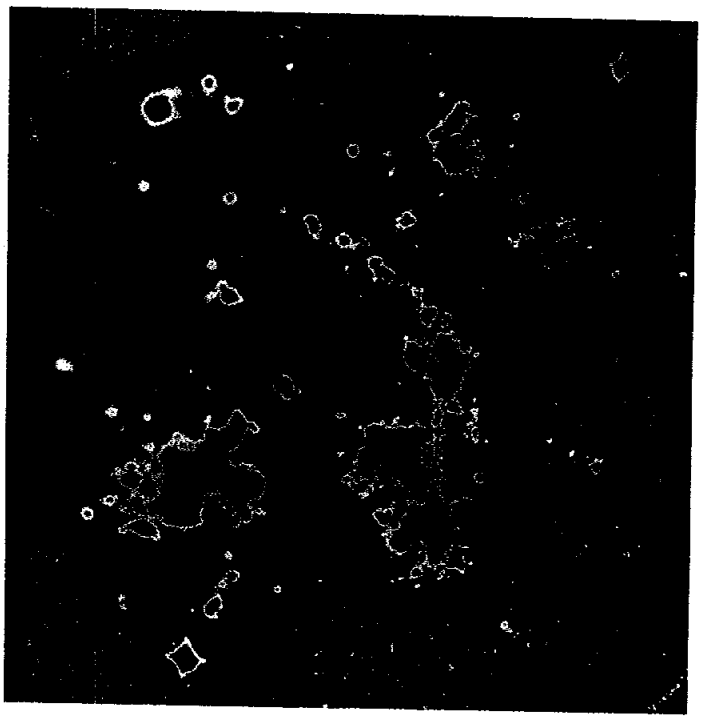


FIGURE 4-23.–Color-enhanced far-UV photograph of the Magellanic Cloud. Ultraviolet radiation from specific astronomical targets was recorded on special spectroscopic black-and-white film in the far-UV camera/spectrograph. This photograph of the Magellanic Cloud, the nearest neighboring galaxy to the Milky Way, has been color enhanced to facilitate interpretation. Areas of similar intensity, recorded as a narrow range of gray tones on the black-and-white image of the UV-sensitive film, are reproduced as a color. In this photograph, blue areas indicate UV radiation levels below the threshold of detectability. Several other levels of UV intensity are indicated by different colors, such as red (faint UV), yellow (stronger UV radiation), and orange (most intense UV radiation within this field of view) (S-72-39660).

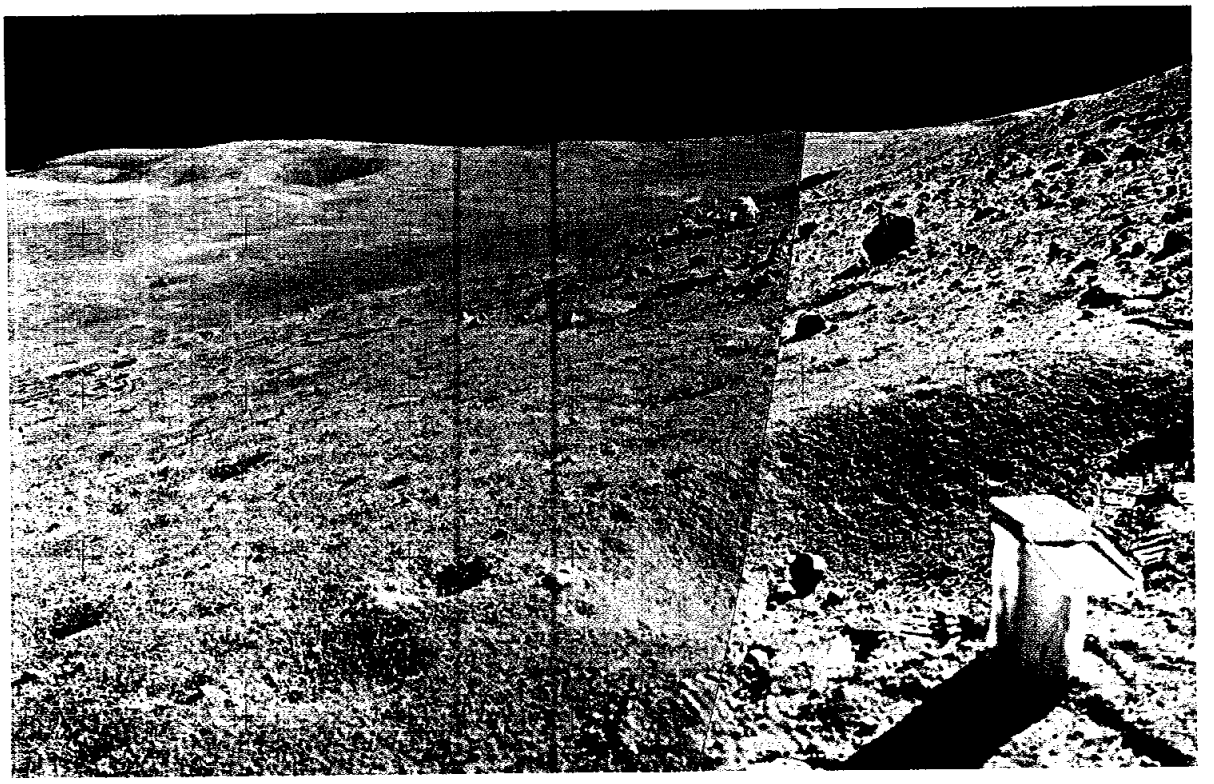


FIGURE 4-24.–At station 4 during EVA-2, the astronauts parked the LRV in a crater to keep it from sliding down the slope of Stone Mountain. A distinct band of boulders crosses this slope. Above the LRV, boulders are numerous; below the LRV, the frequency of boulders is much less. The boulders are ejecta from South Ray Crater, a 600-m-diameter crater that is approximately 4 km to the west of the location shown. The white object in the foreground is a sample collection bag. This container is used to collect large samples and to carry documented sample bags (AS16-107-17472, 17473).



FIGURE 4-25.–The LMP works near the LRV at station 4 high on the side of Stone Mountain. The high-gain antenna appears above the astronaut's head. The golden TV camera, the white low-gain antenna, the dark-gray motion picture camera, and the rectangular map package complete the array of equipment on the front of the vehicle. The gray, cylindrical object near the motion picture camera is a penetrometer. The tool carrier with tongs, handtool extension, and rake are attached to the rear of the vehicle. The golden tape on the right rear of the vehicle is a power cable for the lunar portable magnetometer. The gnomon with color chart, a device to aid in sample documentation, is in the center foreground (AS16-107-17446).

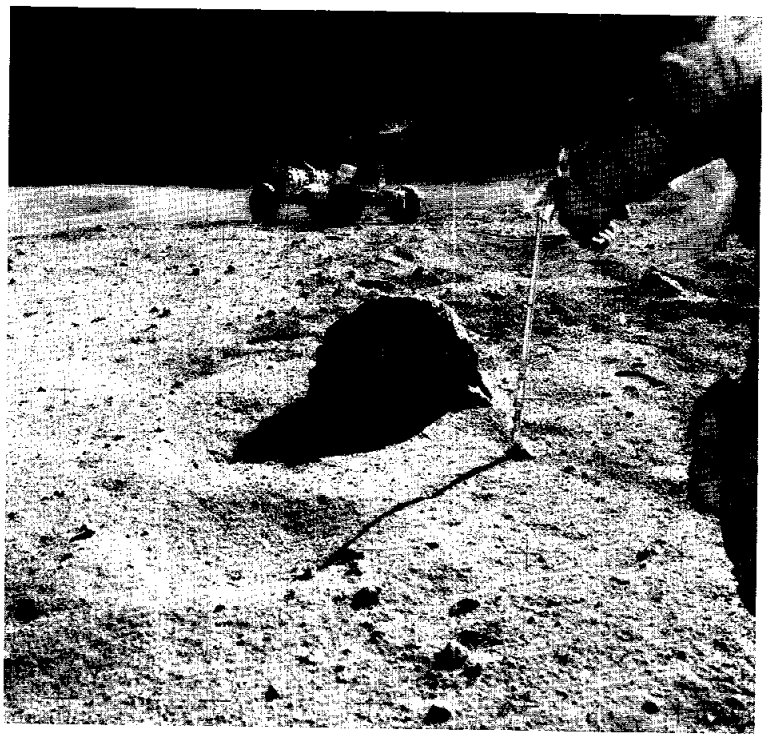


FIGURE 4-26.–Much of the activity at station 9 occurred near the boulder shown in this photograph. This boulder is a breccia, a rock made up of fragments of other rocks. At least three different types of rock fragments or clasts can be identified in this boulder. The scoop marks an area near which soil has been collected. The CDR can be seen in the right margin of the photograph. The cuff checklist is on his left arm; sample bags and the Hasselblad camera hang from the remote control unit. The knee pocket produces the rectangular outline. The LRV stands on the near horizon (AS16-108-17741).

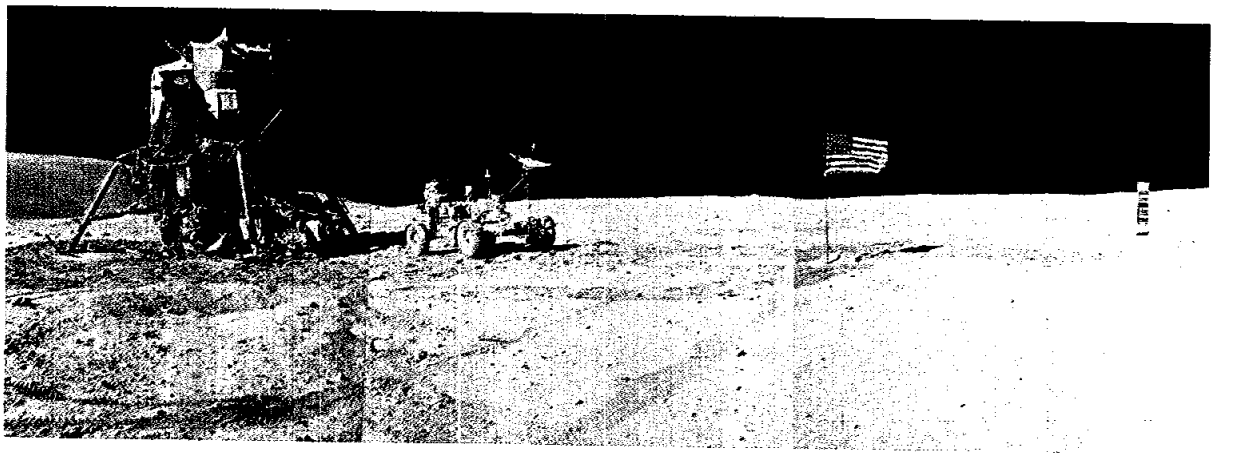


FIGURE 4-27.–The landing area is shown in this partial panorama that was taken by the CDR during EVA-2. Stone Mountain, approximately 5 km in the distance, forms the skyline behind the LM. Below the "United States" sign on the LM is the modularized equipment stowage assembly pallet, a storage area for experiments and tools. A white insulation blanket protects the area from excessive heating and cooling. To the left is a white area with gold-colored insulation draping to the surface. This is the quad III payload area, a storage area for the far-UV camera/spectrograph, the lunar portable magnetometer, and handtools. The probes sticking up from the two landing pads are designed to detect LM touchdown on the Moon and then to crush and bend out of the way during the completion of the landing maneuver. The LRV is parked to the right of the LM. To the right of the American flag is the solar wind composition experiment, which provides data on the elemental and isotopic composition of the solar wind. The dark areas on the surface are boot and vehicle tracks (AS16-107-17435, 17438, 17440).

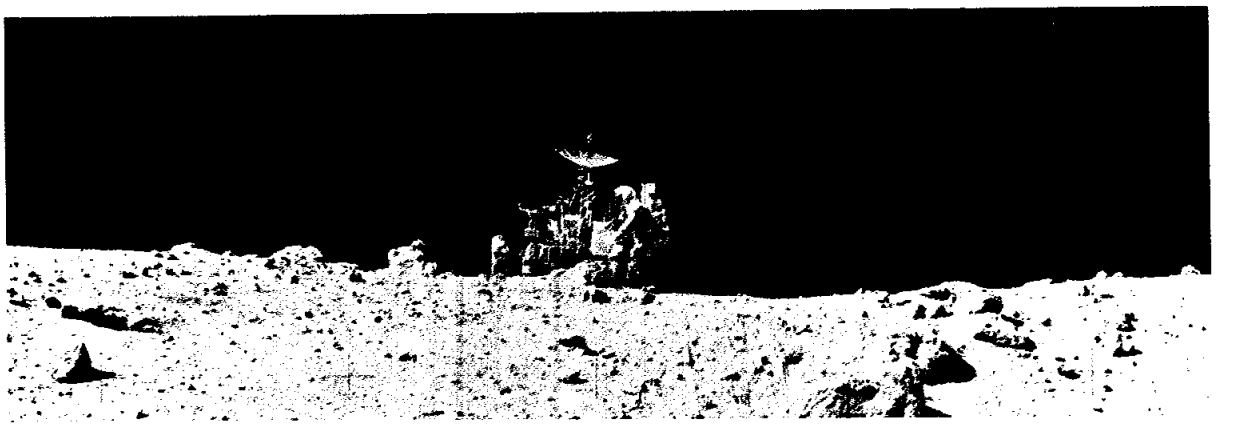


FIGURE 4-28.–The LMP removes the 500-mm Hasselblad camera from the LRV during the stop at station 11. This camera was used to obtain telephotographs of North Ray Crater and Smoky Mountain. The LRV is parked on the rim of North Ray Crater; boulders in the foreground and on the horizon are ejecta from this crater (AS16-116-18607).



FIGURE 4-29.–Station 11 is characterized by an abundance of white breccia boulders. An aphanitic, black rock was collected from the fillet area near the tongs. The CDR carries the rake and sample bags in his left hand. Smoky Mountain forms the skyline; the large boulder in the background is House Rock (AS16-106-17336).



FIGURE 4-30.–The tongs are used to measure the distance between the camera and the boulder for this closeup photograph. The depth of field is approximately 4 cm at this lens setting. This photograph illustrates the fragmental texture of most of the rocks found during the Apollo 16 mission (AS16-106-17328).



FIGURE 4-31.–The LMP inspects House Rock at station 11 before sampling the area. This rock is composed of crushed rock fragments set in a fine-grained matrix. In the area by the astronaut's hands, bands of black glass that have been injected into the boulder can be seen. The intense brecciation and injection suggest a complex history for this boulder. A sample bag is held in the LMP's right hand; the cuff checklist on his left arm indicates the tasks to be performed at each station (AS16-116-18649).

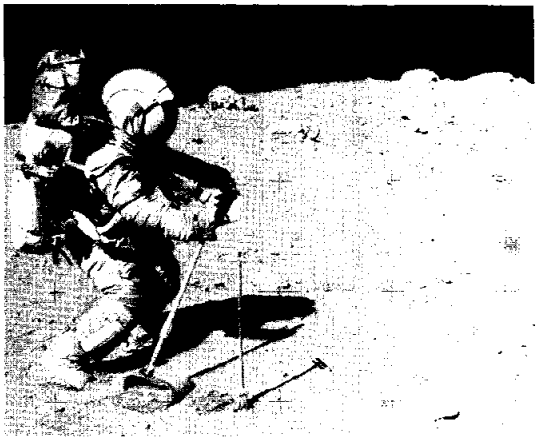


FIGURE 4-32.–The CDR rakes with his right hand and holds a sample bag in his left hand. The tongs mark the area to be sampled. Because of mobility permitted by the suit, raking is a one-arm operation. The rake is used to collect a comprehensive sample, a selective collection of rocks ranging in size from 1 to 3 cm in diameter. These walnut-sized fragments along with the sand-sized material present a more complete history of the area than do isolated rock samples. The LRV sits over the rise in this view at station 11. Note the boulder on the skyline behind the LRV (AS16-106-17340).



FIGURE 4-33.–The stop at station 13 was to collect a series of samples from a permanently shadowed area. Shadow Rock, a 4-m-diameter boulder to the right in the photograph, was the location of the sampling. Permanently shadowed areas act as cold-traps, or areas where volatile and semivolatile components collect. Studies of samples from these permanently shadowed areas permit scientists to identify volatile components that are present in the lunar environment. The CDR works at the front of the LRV, adjusting the high-gain antenna. The high-gain antenna must be pointed at the Earth before ground control can receive TV. The hill above the LRV is the rim of North Ray Crater; to the right of Shadow Rock on the skyline is Smoky Mountain, approximately 1 km in the distance (AS16-106-17390, 17392, 17393).

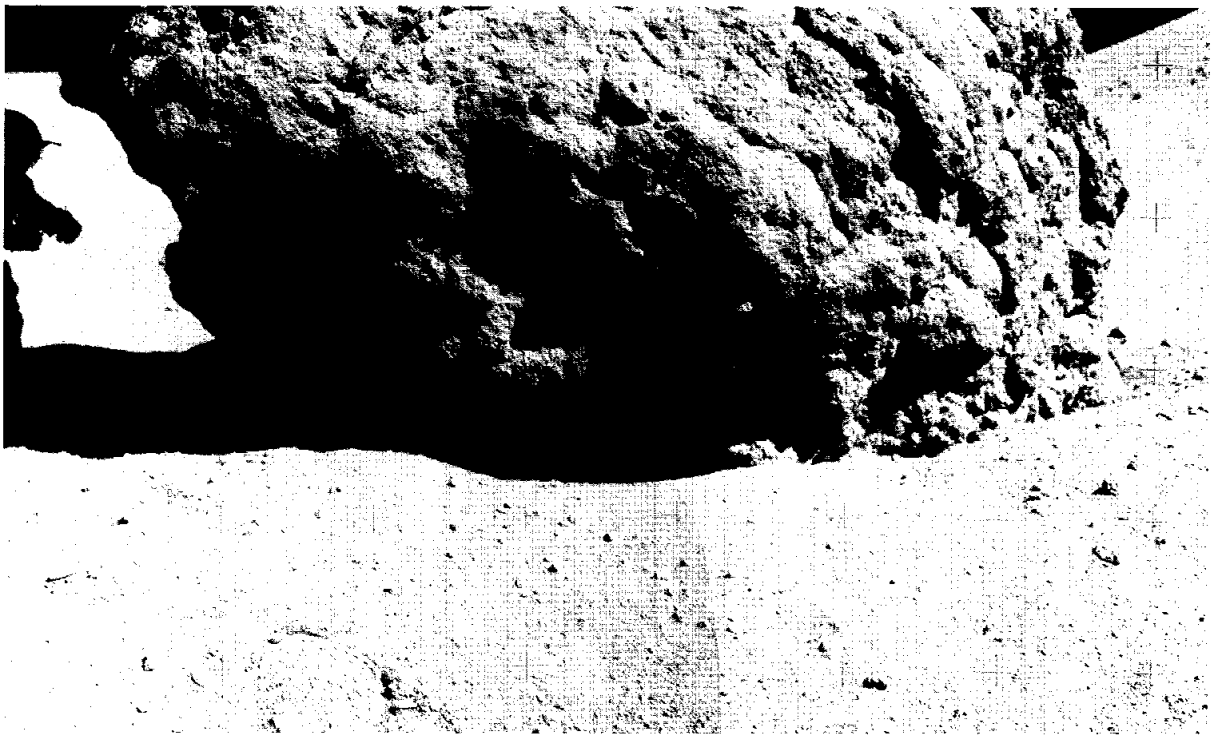


FIGURE 4-34.–The CDR prepares to sample material from the permanently shadowed area under the overhang at Shadow Rock. Close observation of the photographs indicates that Shadow Rock is a multirock breccia, a rock made up of other rock fragments that have been recombined to form a new rock. The holes or vesicles in the rock are much more elongated than previously observed; they appear to be more like vesicle pipes produced by venting gas. The rock also shows the presence of lineations, lines, or bands along the upper and right margin of the boulder. These bands may be caused by differences in lithology or may represent zones where the rock has been fractured and faulted (AS16-106-17413, 17415).

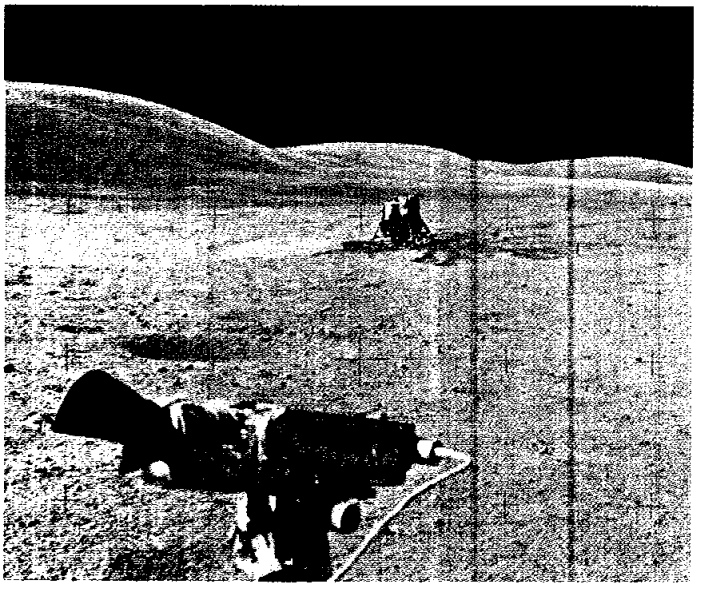


FIGURE 4-35.–This photograph was taken by the LMP from the LRV as the astronauts drove toward the LM near the end of the third EVA period. The dark areas around the LM are vehicle and boot tracks, which reflect the intense activity associated with the vehicle, ALSEP deployment, and sample collection. The ALSEP station can be seen along the right margin of the photograph. The white area just above the ALSEP station is composed of South Ray and Baby Ray Craters approximately 6 km in the distance. The light color is from the blanket of material that was ejected from the craters when they were formed. Just to the left of the LM is a crater that is approximately 25 m in diameter. The CDR flew the LM over this crater just before landing. Stone Mountain forms the skyline along the upper left in the photograph. The golden object in the foreground is the TV camera that provided the Earth with real-time coverage of the mission (AS16-117-18799).



FIGURE 4-36.–The CDR prepares to take samples at station 10 near the end of EVA-3. The gnomon minus the central staff marks the area to be sampled. Sample bags are held in the CDR's left hand, the cuff-card checklist is on his left arm, and the Hasselblad camera is mounted on the remote control unit on his chest. The sample collection bag, which is attached to the primary life support system, is seen behind the CDR's left arm. The LRV, with only a partial right rear fender, stands in the background. Light penetrates the woven wire tires. The tool carrier, handtools, the penetrometer, and the magnetometer extend upward from the rear of the vehicle. The low-gain antenna, the map packet, and the motion picture camera occupy the center of the vehicle. The disk of the high-gain antenna and the TV camera protrude from the front of the vehicle (AS16-117-18825).

COMMAND AND SERVICE MODULE ORBITAL PHOTOGRAPHY

During the period of separate operation of the LM and the CSM, the CM pilot (CMP) completed photographic assignments covering a wide range of targets and requiring the use of various combinations of cameras, lenses, and films (table 4-II) or operation of the complex SIM camera systems (table 4-III). The dominant CMP photographic task, measured in terms of both time and budgeted film, was lunar-surface photography. Other tasks included the documenting of operations with the LM and the photographing of Earth and deep-space targets in support of specific scientific experiments.

TABLE 4-II.–Photographic Equipment Used in Command Module

Camera	*Features*	*Film size and type*	*Remarks*
Hasselblad EL	Electric; interchangeable lenses of 80-, 105-, and 250-mm focal length. The 105-mm lens will transmit UV wavelengths	70-mm; SO-368 Ektachrome MS color-reversal film, ASA 64; 3414 high-definition aerial film, AEI 6; 2485 black-and-white film, ASA 6000; IIa-O spectroscopic film (UV sensitive)	Used with 80-mm lens and color film to document operations and maneuvers involving more than one vehicle. Used with appropriate lens-film combinations to photograph preselected orbital-science lunar targets, different types of terrain at the lunar terminator, astronomical phenomena, views of the Moon after TEI, Earth from various distances, and special UV spectral photographs of Earth and Moon
Nikon	Mechanically operated; through-the-lens viewing and metering; 55-mm lens	35-mm; 2485 black-and-white film, ASA 6000	Used for dim-light photography of astronomical phenomena and photography of lunar-surface targets illuminated by earthshine
DAC	Electric; interchangeable lenses of 10-, 18-, and 75-mm focal length; variable frame rates of 1, 6, 12, and 24 frames/sec	16-mm; SO-368 Ektachrome MS color-reversal film, ASA 64; SO-368 Ektachrome EF color-reversal film, exposed and developed at ASA 1000; 2485 black-and-white film, ASA 6000; AEI 16 black-and-white film	Bracket-mounted in CSM rendezvous window to document maneuvers with the LM and CM entry; handheld to document nearby objects such as SIM door after jettison and to photograph general targets inside and outside the CSM; bracket-mounted on sextant to document landmark tracking

TABLE 4-III.–Photographic Equipment in the Scientific Instrument Module

Camera	*Features*	*Film size and type*	*Remarks*
Mapping	Electric; controls in CSM; 7.6-cm-focal-length lens; 74° by 74° field of view; a square array of 121 reseau crosses, eight fiducial marks, and the camera serial number recorded on each frame, with auxiliary data of time, altitude, shutter speed, and forward-motion control setting	457.2 m of 127-mm film type 3400	The 11.4- by 11.4-cm frames with 78-percent forward overlap provide photographs of mapping quality. Data recorded on the film and telemetered to Earth will permit reconstruction of lunar-surface geometry with an accuracy not available with earlier systems.
Stellar	Part of mapping-camera subsystem; 7.6-cm lens; viewing angle at 96° to mapping-camera view; a square array of 25 reseau crosses, four edge fiducial marks, and the lens serial number recorded on each frame with binary-coded time and altitude	155.4 m of 35-mm film type 3401	A 3.2-cm circular image with 2.4-cm flats records the star field at a fixed point in space relative to the mapping-camera axis. Reduction of the stellar data permits accurate determination of camera orientation for each mapping-camera frame.
Panoramic	Electric; controls in CSM; 61-cm lens; 10° 46′ by 108° field of view; fiducial marks printed along both edges; IRIG B time code printed along forward edge; data block includes frame number, time, mission data, velocity/height, and camera-pointing altitude	1981.2 m of 127-mm film type EK 3414	The 11.4- by 114.8-cm images are tilted alternately forward and backward 12.5° in stereo mode. Consecutive frames of similar tilt have 10-percent overlap; stereopairs, 100-percent overlap. Panoramic photographs provide high-resolution stereoscopic coverage of a strip approximately 330 km wide, centered on the groundtrack.

After the LM was cleared to remain on the lunar surface, the CMP turned to a heavy schedule of solo tasks. Revolutions 17 and 18 were used almost exclusively for photographic tasks. A 3-hr operating period for the mapping camera and two 30-min periods of panoramic-camera operation provided terminator-to-terminator coverage by both camera systems. Hasselblad targets that had slipped from earlier revolutions were photographed during these revolutions, and the CMP provided a running commentary on visual observations between and during the periods of camera operation.

The first full day of solo operations covered revolutions 23 to 30. Mapping-camera operations totaled approximately 6 hr on five successive revolutions (25 to 29) to provide vertical and oblique coverage of the lighted lunar surface and to provide stellar orientation for the laser altimeter during one pass across the unlit lunar surface. Panoramic-camera operation was limited to a 14-frame burst over the landing site on revolution 28. The CSM Hasselblad EL camera, used on most of the revolutions, photographed one orbital-science target and several targets of opportunity. Terminator photography scheduled in the Davy Rille area on revolution 23 was bypassed because the feature was still on the dark side of the terminator. As the terminator advanced, parts of the rille were photographed on each of the two following revolutions; two additional terminator targets were covered during this operating day. Highland terrain near the Descartes landing site was photographed on revolution 27 with the special lens, film, and filters specified for the UV photography experiment. Astronomical dim-light targets and

photography of the lunar surface illuminated by earthshine occupied the Nikon camera on three revolutions. During revolution 31, the CMP entered a rest period that lasted until revolution 35.

The second full day of solo operations included approximately 7 hr of mapping-camera operation that provided 429 frames of lunar-surface imagery on three successive revolutions (37 to 39). Operation during the intervening dark-side passes provided stellar-camera attitude data to support laser-altimeter data analysis. During 32 min of panoramic-camera operation on two revolutions, 284 frames were exposed. The Hasselblad camera was used to photograph two orbital-science photographic targets and two sets of terminator images. Visual descriptions accompanied taking of the photographs. During revolution 41, more than one-half magazine of DAC film was exposed at slow frame rate while the deployed mass spectrometer boom was monitored. Gegenschein, solar-corona, and Gum Nebula photographs were taken with the Nikon 35-mm camera during the dark-side portions of three revolutions. The CMP entered a rest period during revolution 43.

The fourth rest period in lunar orbit ended during CSM revolution 46. Flight-plan changes read up to the CMP consumed much of the communication periods on several subsequent revolutions. After scheduled terminator photography and an orbital-science visual description on revolution 47 were canceled, the CMP requested assignment of two periods on several subsequent revolutions. After scheduled terminator photography and an orbital-science visual description on revolution 47 were canceled, the CMP requested assignment of two DAC magazines for photographing the scene passing the CM window on the following light-side pass.

The mapping camera was turned on in the far-side darkness of revolution 46 to begin a 3.5-hr operation period that yielded 196 frames of lunar imagery from light-side passes on revolutions 47 and 48. Starting near the far-side terminator, the panoramic camera operated for 32 min on revolution 47; close to the near-side terminator, the CMP briefly described extensive benches around positive features near the Riphaeus Mountains. On revolution 48, a solar-corona sequence was exposed and a large water bubble that had formed in the onboard gas separator was photographed. The requested DAC magazines recorded the lunar scene visible out the CM window throughout most of the light-side pass of revolution 48.

From the plane-change 1 burn shortly after acquisition of signal on revolution 49 to LM lift-off on revolution 52, operational tasks and flight-plan modifications occupied most of the CMP's time. Gegenschein photography near the end of revolution 49 and sextant-mounted DAC documentation of landmark tracking during revolution 51 were accomplished as scheduled. An area near the Riphaeus Mountains, where the CMP had described low benches around most positive features, was photographed during revolution 50 as a target of opportunity. Figures 4-37 to 4-50 are representative photographs from the orbiting CSM.

The remotely controlled, LRV-mounted TV camera permitted earthbound viewers to watch the LM lift-off from the lunar surface during CSM revolution 52. A special photographic and visual survey of the LM followed the revolution 53 rendezvous because flying debris seen during lift-off suggested to some observers a possible failure of the LM insulation.

Sample and equipment transfer, LM shutdown tasks, and extensive flight-plan changes occupied the remainder of the working day after the successful docking. As the crew rested during revolutions 53 to 59, the planning teams reevaluated priorities and modified experiment schedules in terms of the shortened mission and the decision to drop the plane-change 2 maneuver. The final wakeup in lunar orbit began a day of extensive updates to the flight plan.

Mapping-camera operations totaled 2 hr 20 min of revolutions 59 and 60. To document possible anomalies in the rates of cover movement or camera extension, the mapping camera was started a few seconds before opening the cover and was stopped after cover closing was completed. Detailed analysis of positions relative to the image of the gamma-ray boom in frames near the ends of the sequence will document the regularity of movement.

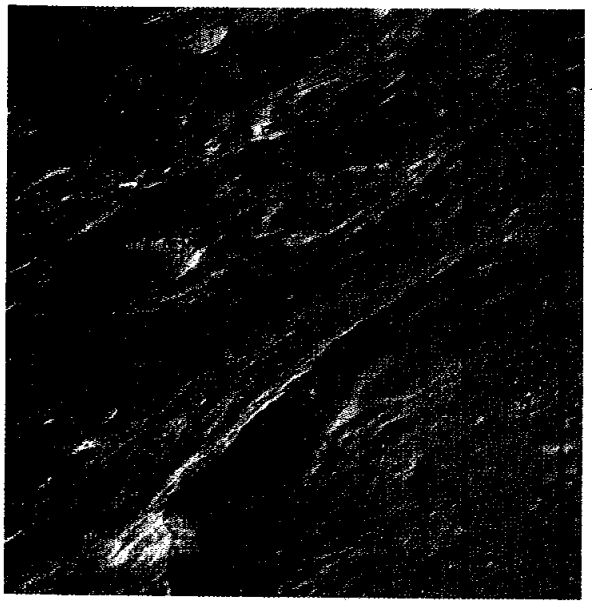


FIGURE 4-37.–West wall of the far-side Crater Lobachevsky. The CMP described a black flow associated with a small crater in the wall of a large far-side crater. This oblique telephotograph northwestward across terrain in and northwest of Lobachevsky, an 80-km-diameter crater centered near latitude 9° N, longitude 113° E, shows a 2.5-km-diameter crater near the top of the west wall of the large crater. A tongue of low-albedo material extends approximately 2 km down the steep wall of Lobachevsky from the low point on the rim of the small crater (AS16-121-19407).



FIGURE 4-38.–Alpetragius Crater. Shadows are rare in this high-Sun, oblique view southward across Alpetragius. This 35-km-diameter neighbor of the Crater Alphonsus has a conspicuous, dome-like central peak larger than 10 km in diameter. The southwest rim of Alphonsus cuts the lower left corner of the frame (AS16-119-19057).

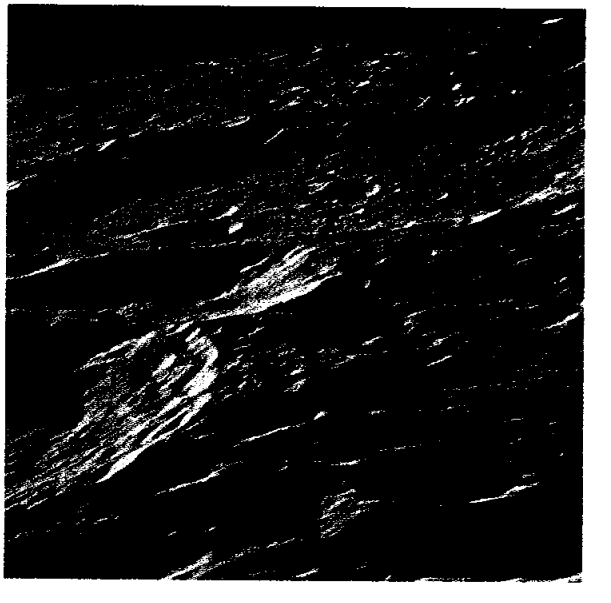


FIGURE 4-39.–Highland terrain illuminated by a low Sun. Anderson, the large crater that extends across the frame, is centered near latitude 16° N, longitude 171° E, in terrain that is typical of the far-side highlands. Sun elevations in this oblique view toward the northwest range from approximately 6° at the lower right corner of the frame to 12° at the far rim of Anderson. The high proportion of shadow in highland terrain demonstrates the abundance of slopes exceeding the Sun elevations (AS16-118-18905).

Jettison of the LM on revolution 62 was documented by DAC photographs. Operating periods of 1 hr for the mapping camera and 35 min for the panoramic camera during revolution 63 completed the SIM-bay camera orbital photography; a long strip of 250-mm Hasselblad photographs documented terrain south of the SIM camera coverage from Vogel Crater to the near-side terminator. Preparations for the TEI burn occupied revolution 64, the last in lunar orbit. Figures 4-51 and 4-52 are views of the LM ascent stage after lunar lift-off.

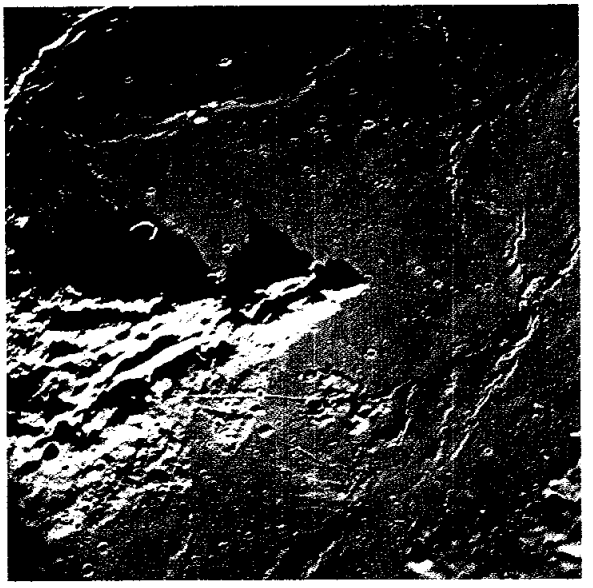


FIGURE 4-40.–Typical mare terrain illuminated by a high Sun. The smooth surface of the Sea of Clouds approximately 20 km west of the Crater Lassell C is pocked by craters as large as 6 km in diameter. A conspicuous 3-km-diameter crater and scattered craters less than 200 m across exhibit bright halos when illuminated by a Sun 35° to 40° above the eastern horizon. The craters without halos appear almost as sharp as the bright-halo craters; Sun-facing crater walls commonly are brighter than adjacent rim deposits. Most craters have low, narrow rims that merge imperceptibly with the adjacent mare materials. An anomalously dark 3-km-diameter crater in the lower right quarter of the frame has no detectable halo, either light or dark. The Sun-facing wall is approximately as dark as the adjacent mare materials; the rim does not merge with the surrounding mare because of a sharp change in slope along its outer margin (AS16-119-19071). (Compare with fig. 4-42 (AS16-120-19223).)

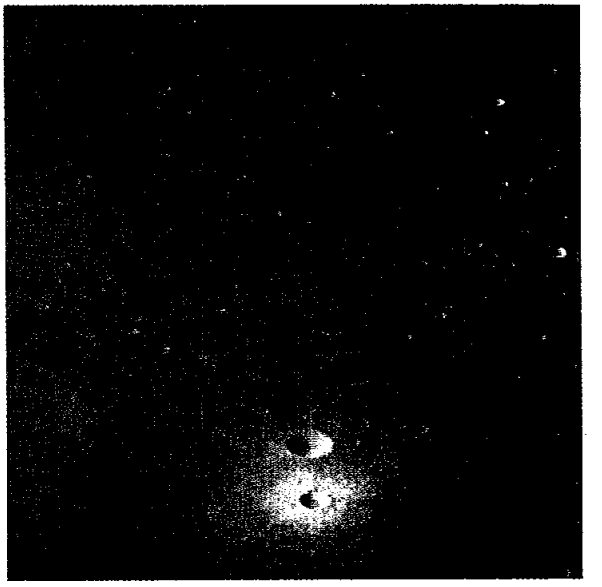


FIGURE 4-41.–Mixed mare and highland terrain illuminated by a low Sun. In this oblique view westward across the mare-flooded Crater Letronne, Sun elevations range from approximately 6° at the lower right corner to 0° near the upper left corner. This low illumination shows the ropy features mapped as mare ridges to be superimposed on gentle swells generally 5 to 10 km wide; yet, except within craters, shadows are rare on the mare materials. By comparison, large areas of the highland materials are shadowed at elevations as great as 6° in the lower half of the photograph. Approximately half the rim of the 110-km-diameter Crater Letronne is exposed. The crater is centered near latitude 10° S, longitude 42.5° W (AS16-122-19553).

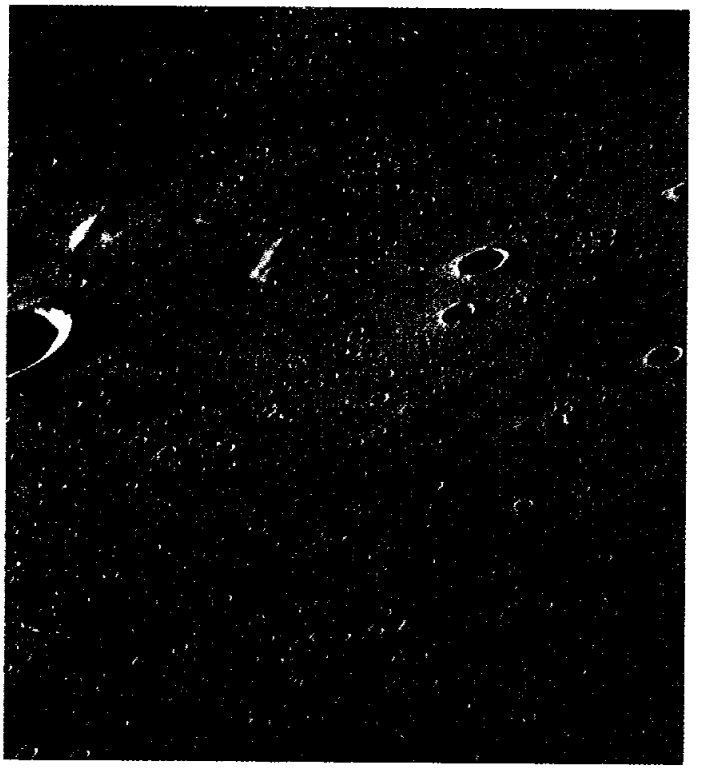


FIGURE 4-42.–Mare terrain illuminated by a low Sun. The Sea of Rains west of the Crater Lassell C is illuminated by an extremely low Sun. Sun elevation ranges from 3° to 4° along the left margin of the frame and from 1° to 2° along the right margin. (Compare the upper right quarter of this figure with the lower right quarter of fig. 4-41 (AS16-119-19071). Four prominent craters permit correlation of the two figures.) The low Sun enhances the detectability of faint slopes. Numerous linear patterns similar to features that have been described as flow fronts or faint mare ridges cross the surface that appeared smooth under the higher Sun. The crater population appears to have increased because the faint depressions that were inconspicuous at higher Sun now are marked by hard shadows. The prominent bright halo of the 3-km-diameter crater has faded. Although not conspicuous, the dark 3-km-diameter crater retains its anomalously dark Sun-facing inner wall and the break in slope at the outer margin of the rim which set it apart at higher Sun (AS16-120-19223).



FIGURE 4-43.–Southeastern Alphonsus Crater. The dark-halo crater and the rilles near the bottom of the frame are in the southeastern quarter of the floor of Alphonsus. Grooves or irregular valleys, like the conspicuous feature extending upward from the base of the wall near the dark-halo crater, are the dominant crater wall structures in the eastern half of Alphonsus. These features are radial to the Imbrium Basin and are part of that family of widespread structures called Imbrium sculpture. Terraces, which are more typical of the walls of large craters, predominate on the northern wall of Arzachel Crater at the extreme top of the frame (AS16-119-19050).

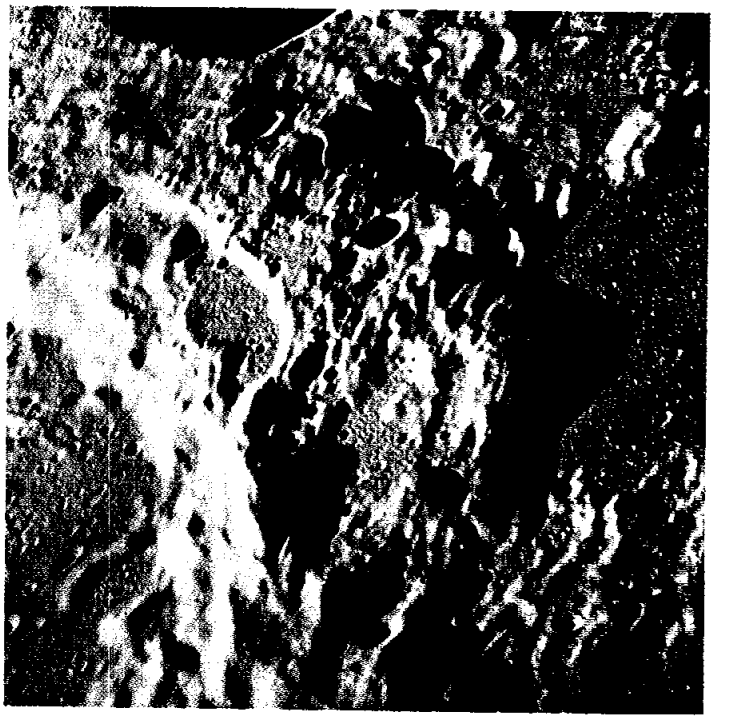


FIGURE 4-44.—Oblique view southeastward along the southwestern rim of the Crater Alphonsus. Smooth terrain at the right side of the frame is the eastern Sea of Clouds. Deep shadows at the top of the photograph are in the Crater Alpetragius. The dark-halo-crater area on the western floor of Alphonsus, considered as a candidate site during the selection of the landing sites for the Apollo 16 and 17 missions, is at the lower left corner of the photograph. The albedo contrast between the normal Alphonsus floor and dark-halo material is not striking at this viewing angle and low Sun elevation. The dark-halo material is approximately 100 km south of the ground-track as this photograph was exposed. Note the large pockets of flat terrain similar to the Alphonsus floor that are perched at intermediate levels up the terraced western wall of Alphonsus (AS16-120-19222).

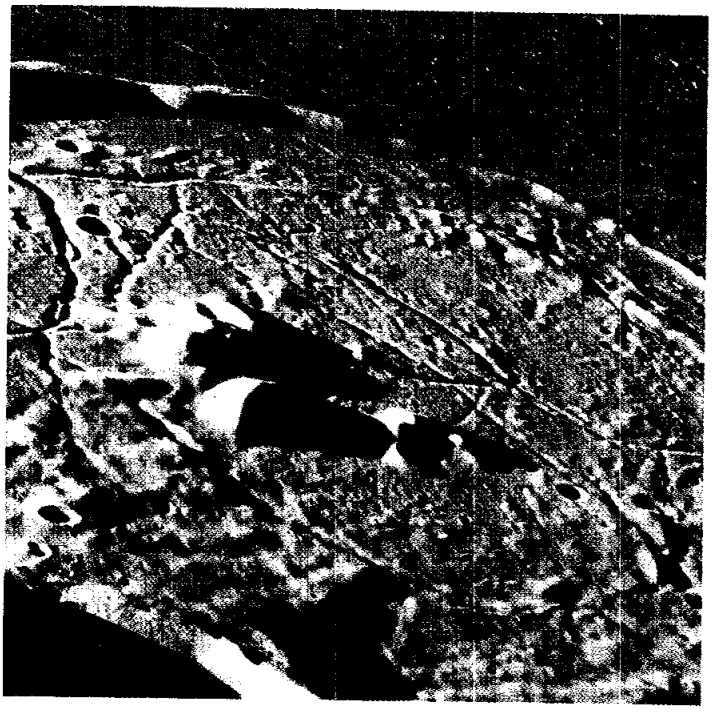


FIGURE 4-45.—Gassendi Crater. Low Sun illumination enhances the contrast between the rough and cracked surface on the floor of Gassendi and the smoother surface of the Sea of Moisture beyond the low crater rim at the top of the frame. The high northern rim of Gassendi is at the lower right corner of this oblique view southward across the 110-km-diameter crater. Gassendi was one of three candidate sites for the Apollo 17 lunar landing mission; sampling and study of the central peak complex would have been the scientific objective of the proposed mission. The shadow at the lower left corner of the frame conceals the floor of the Crater Gassendi A (AS16-120-19295).

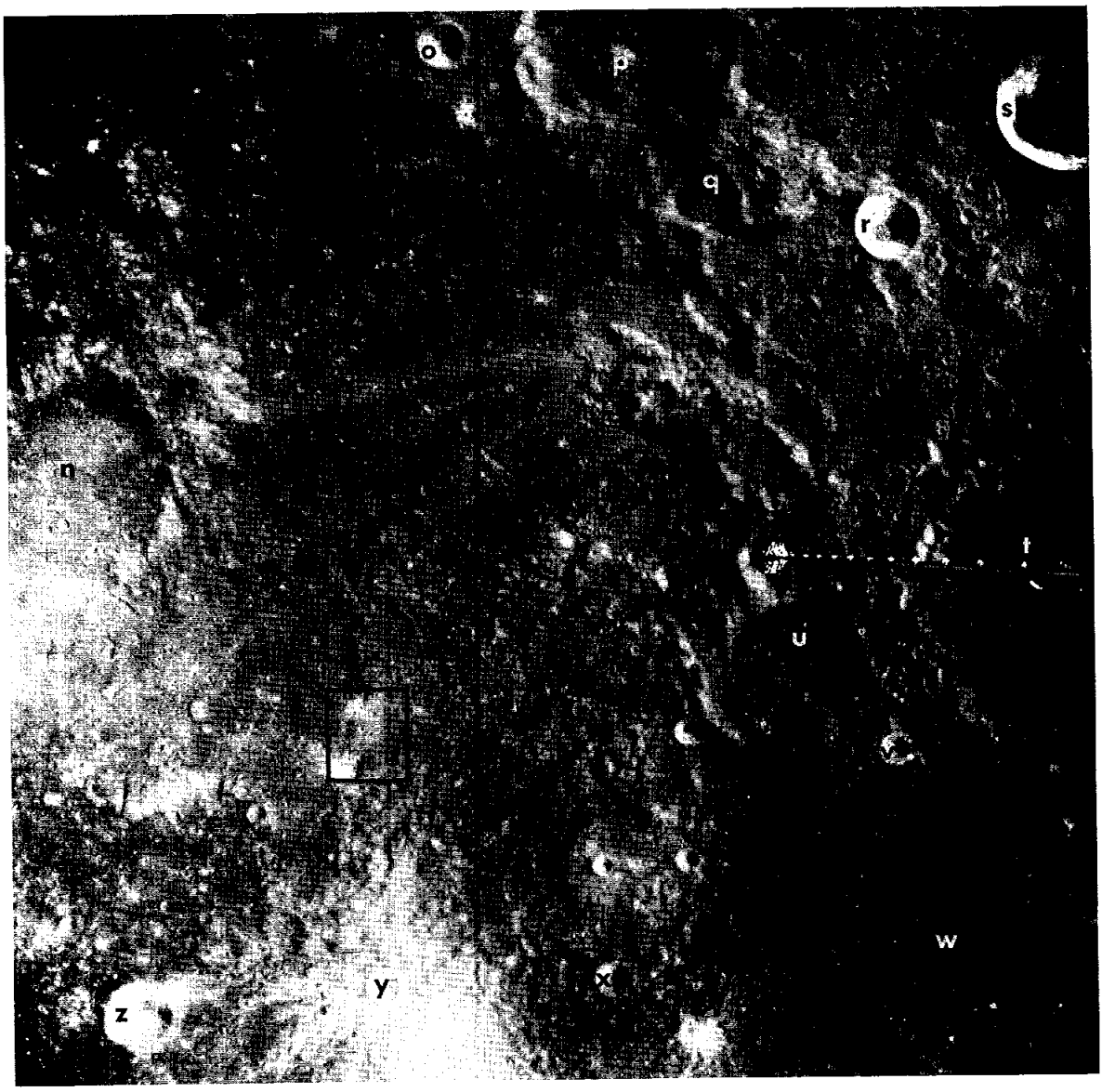


FIGURE 4-46.–The Apollo 16 landing site and surrounding terrain is illuminated by a moderately high Sun in this mapping-camera frame exposed on CSM revolution 47. North is at the top of the frame, which is alined within 5° of the selenographic grid. Sun elevation ranges through 6° across the 180- by 180-km surface area, from 49° along the east side to 43° along the west. The Apollo 16 landing site is within the rectangular outline, which indicates the area of figure 4-47. The mass spectrometer boom, mounted behind the mapping camera in the SIM bay, extends into the field of view from the east side of the frame. Selected craters are identified by the letters n to z. The 11-km-diameter Crater Alfraganus C (r) near the northeast corner is one of several sharp craters with minor accumulations of floor materials. Others include Taylor D (o), Zöllner E (v), Dollond (z), Dollond E (y), and Dollond M (x). Other craters have smooth to slightly degraded walls and abundant filling that forms floors ranging from textured to smooth. Examples are Alfraganus (s), Zöllner D (u), Taylor E (q), and Kant B (w). The three named craters larger than 30 km in diameter, Taylor (p), Zöllner (t), and Dollond B (n), are highly degraded. Dollond B (n) has a flat, filled floor; the other two have sparse floor deposits. The north rim of Descartes Crater is approximately 20 km south of Dollond E (y), just outside the south boundary of the photographed area (Apollo 16 mapping-camera frame 2179).

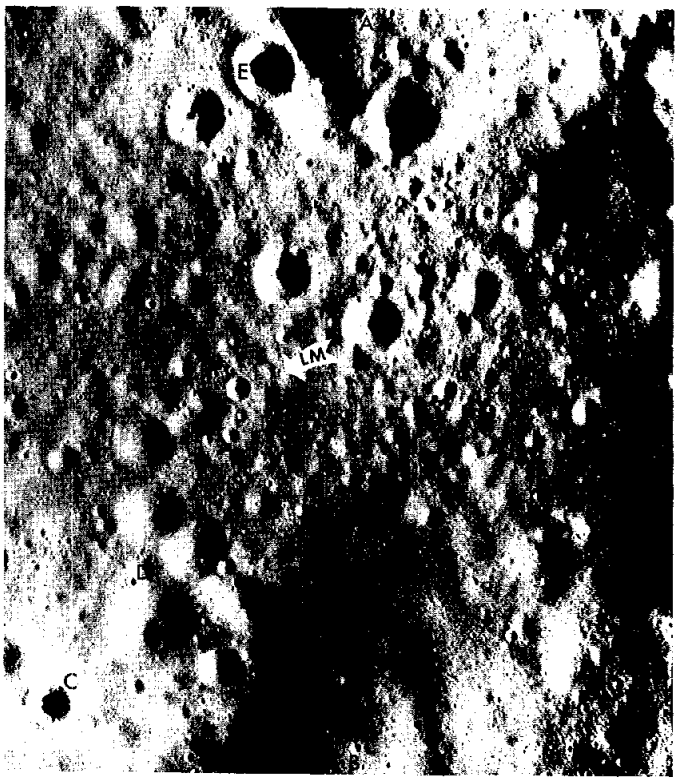


FIGURE 4-47.–Position of the landed LM is shown on this panoramic-camera image of the landing site. The Sun was only 17° above the eastern horizon when this frame was exposed; western slopes on Smoky (A) and Stone (B) Mountains are shadowed. Rays extending outward from South Ray (C) and Baby Ray (D) Craters are sharp but not conspicuous; the rays of North Ray Crater (E) are hardly detectable in this low-Sun illumination (part of Apollo 16 pan-camera frame 4563).

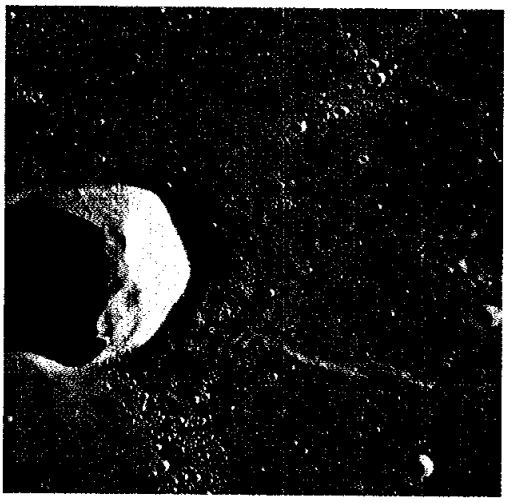


FIGURE 4-48.–Herigonius Crater. The 16-km polygonal crater Herigonius is centered near latitude 13.5° S, longitude 34.0° W, near the southern margin of the Ocean of Storms. Part of the irregular crater floor and the extensive ejecta blanket west of the crater can be seen with greater clarity in this photograph than in any available before the Apollo 16 mission (AS16-119-19156).



FIGURE 4-49.–Telephotographic view southward across the Sea of Clouds to the Mercator Scarp. Bullialdus, a 60-km-diameter crater centered near latitude 21° S, longitude 22° W, and the two smaller craters, Bullialdus A and B, dominate the foreground. Ejecta deposits associated with the three craters are extensive (AS16-119-19094).

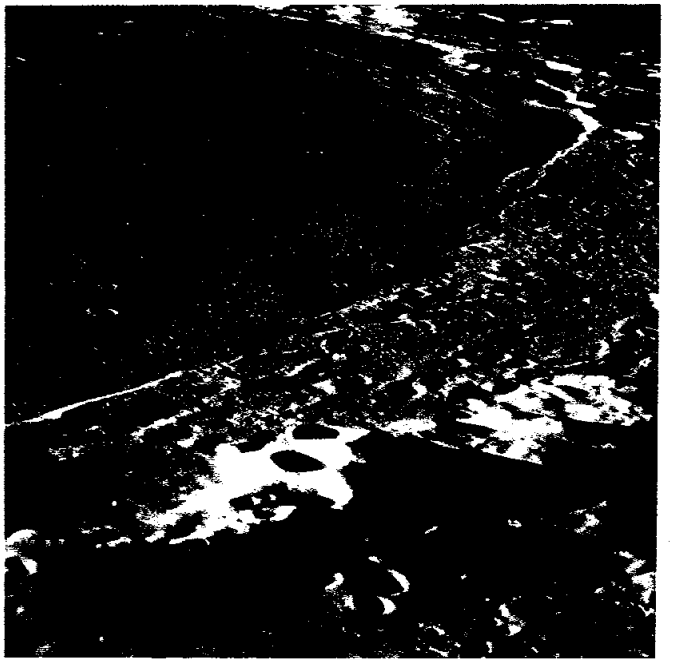


FIGURE 4-50.–Oblique view southward along the western margin of the Sea of Moisture. The sharp contact between smooth mare deposits and rougher highland materials has been mapped as Mersenius Rille Number III. Note that the mare deposits stand higher than the highland block near the center of the photograph, whereas the highlands stand higher along both sides of the frame (AS16-120-19323).



FIGURE 4-51.–The LM ascent stage approaches rendezvous above rugged highland terrain east of the Foaming Sea. The LM conceals terrain near latitude 1° S, longitude 70° E, in this view westward across heavily cratered highlands between Smyth's Sea and the Sea of Fertility. High Sun illumination enhances the albedo difference. At the horizon, smooth mare deposits in the northeastern Sea of Fertility are broken by ridges and craters northwest of the Crater Langrenus (AS16-122-19530).

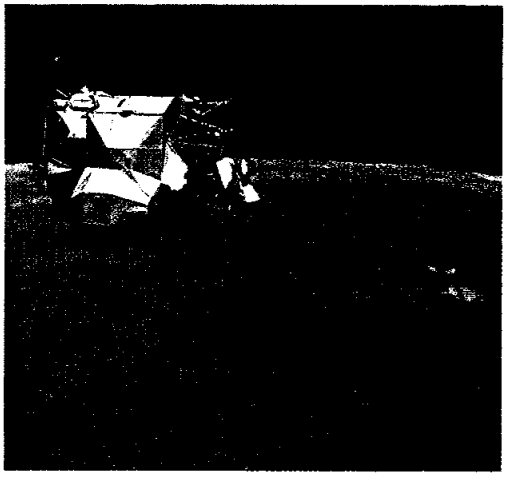


FIGURE 4-52.–The LM ascent stage over the Sea of Fertility. Before docking, the LM ascent stage maneuvered to permit complete inspection by the CMP. The distinctive Craters Messier and Messier A are near the right edge of this view westward across the Sea of Fertility. Extensive ray systems, bright crater walls, and bright halos stand out sharply because of the high Sun angle. Highlands separating the Seas of Tranquility and Nectar to the west of the Sea of Fertility form the irregular horizon beyond the LM (AS16-122-19536).

TRANSEARTH PHOTOGRAPHY

As the CSM came around the Moon headed toward the Earth, the crew photographed earthrise (fig. 4-53), the first TEC earthrise sequence documented by an Apollo crew. Hasselblad photographs of the lunar surface (figs. 4-54 to 4-57) were exposed over an extended period as the Moon receded. Many frames have provided significant supplementary coverage; some provided the best coverage of far-side areas north of the equator that have been obtained. The mapping camera exposed 442 frames during 2.5 hr of operation. After TEI, the panoramic camera exposed 171 frames (fig. 4-58) before the film was exhausted. This sequence could provide basic data for evaluating the use of similar camera systems in a whole-Moon photographic survey when lunar exploration is revived. An hour after TEI, a sequence of UV photographs of the Moon ended the Moon phase of the UV photography experiment. Approximately 3 hr into TEC, the crew shared views of the receding Moon (fig. 4-59) with the Earth by way of television. A 9-hr rest period began 3.8 hr after the TEI burn.



FIGURE 4-53.–Crescent Earth rises as the Apollo 16 crew heads home. This frame is from the first earthrise sequence photographed after TEI by an Apollo crew. The large crater in the lower left quarter of the frame is Chang Heng, a 35-km-diameter crater centered near latitude 18.5° N, longitude 111.5° E (AS16-122-19563).

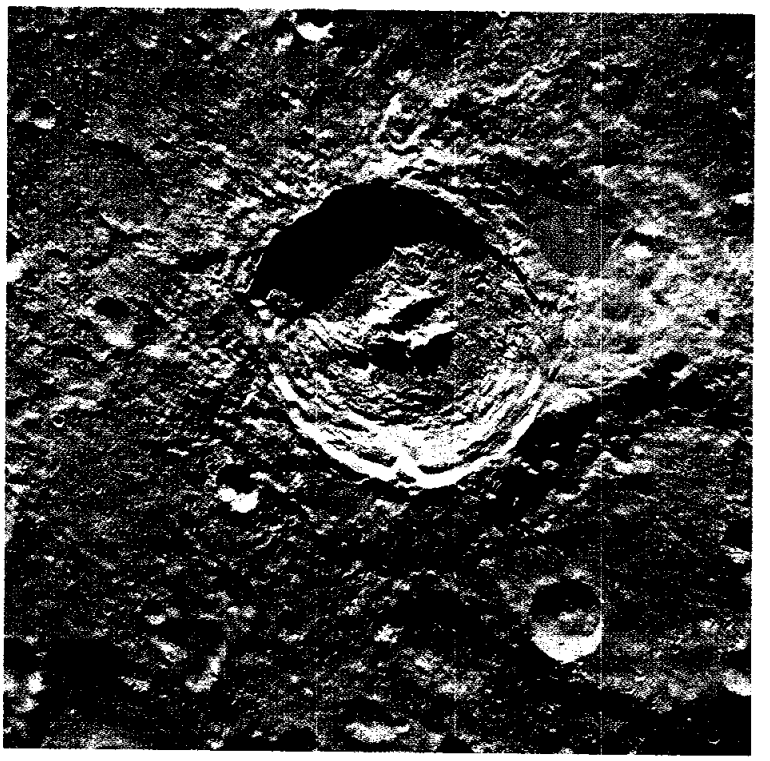


FIGURE 4-54.--Post-TEI view of King Crater near latitude 5.5° N, longitude 120.5° E. King has an unusual central peak. The crater was the subject of visual observations and photography on more than one revolution during the Apollo 16 mission. Oblique views from orbit show specific features in and near the crater in greater detail. See also figures 4-55 (AS16-120-19268) and 4-56 (AS16-120-19273). North is to the right in this near-vertical view (AS16-122-19580).

After the initial period of high activity, photographic tasks were minimal throughout TEC. Following completion of the first rest period, the mapping camera was operated with the cover closed until the film supply was exhausted. The CMP recovered film cassettes from the mapping-camera system and from the panoramic camera during a 1-hr EVA period approximately 18 hr after the TEI burn (fig. 4-60). Television and DAC photography documented the activity outside the depressurized spacecraft. Sequences of still and DAC photography during the second day of TEC documented experiments supporting the Skylab Program. The final sequence of UV photographs of Earth was exposed during the third day of TEC, approximately 3 hr before splashdown. Reentry, documented by the window-mounted DAC, closed this successful photographic mission. Splashdown is shown in figure 4-61.

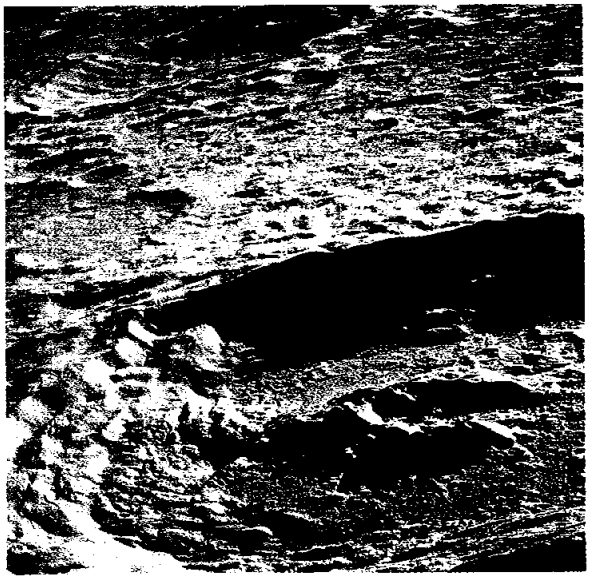


FIGURE 4-55.–Oblique view southwestward across King Crater. The wishbone-shaped central peak and the terraced southern wall are clearly visible in this 250-mm Hasselblad photograph. The crater near the upper left corner of this frame is Abul Wáfa, which is centered near latitude 1.5° N, longitude 116.5° E (AS16-120-19268).

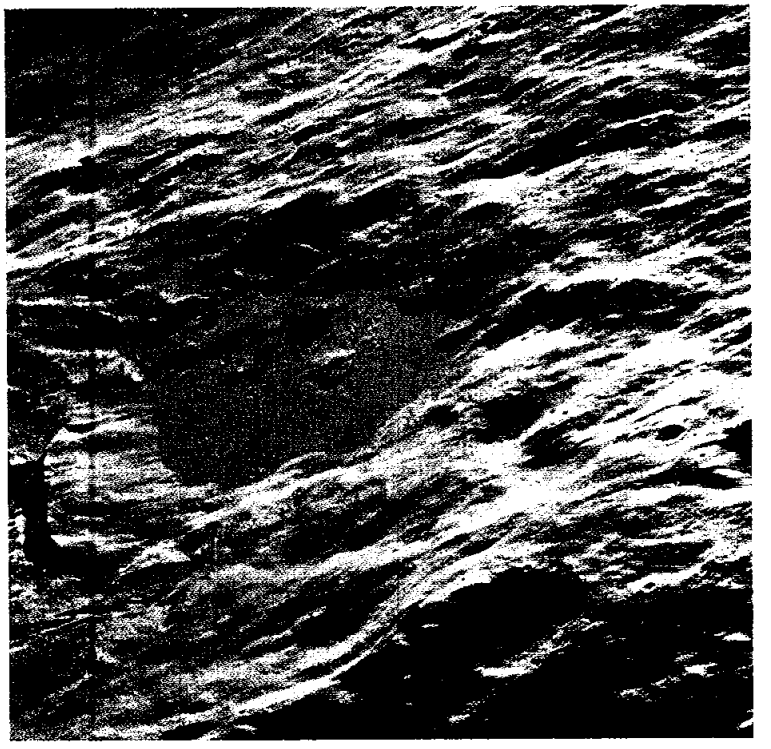


FIGURE 4-56.–Partly filled crater north of King. The smooth, flat filling resembles mare material except that it is lighter in color. Note the numerous small "ponds" with similar filling materials that are perched at various levels above the floor in rim deposits of the crater. Similar ponds have been described near Tycho and Copernicus Craters. The north rim of King Crater extends into the left side of this oblique view westward (AS16-120-19273).



FIGURE 4-57.–Post-TEI view northwestward across far-side terrain. The irregular, shallow crater with a flat floor to the left of frame center is the 70-km-diameter Crater Artamonov located near latitude 26° N, longitude 104° E. A straight chain of craters trends northwest farther than 170 km, with minor interruptions, from near the lower edge to the center of the frame. At the upper left corner of the frame, the crater with the smooth, dark floor is the 95-km-diameter Crater Lomonosov (AS16-122-19575).

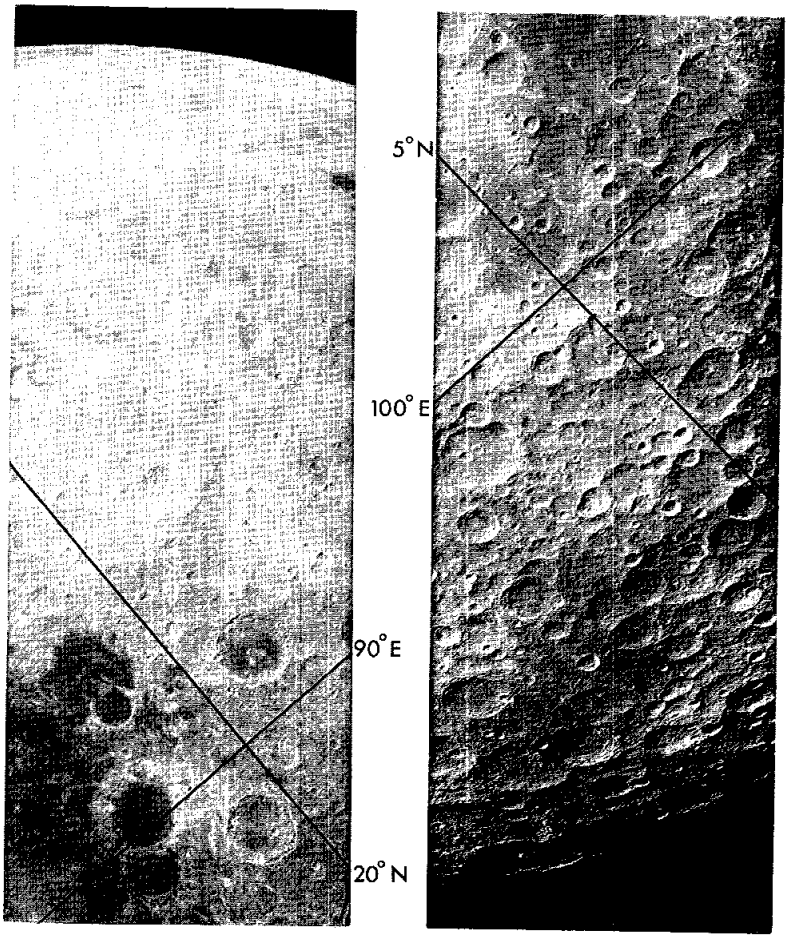


FIGURE 4-58.–Panoramic-camera frame exposed after TEI. The frame is centered near latitude 13° N, longitude 93° E, and spans the lunar disk with its long axis oriented northwest-southeast. The frame has been cut in half; the northwest half is on the left side of this figure, the southeast half is on the right. Approximate selenographic coordinates are indicated on each half of the figure. Near the southeastern limb, an extremely low Sun illuminates the crater Tsiolkovsky, which is centered near latitude 20° S, longitude 129° E. The Crater Hercules, centered near latitude 47° N, longitude 39° E, is illuminated by a high Sun near the northwest limb. The large area of mare material near the northwestern limb is in the Lake of Dreams northeast of the Sea of Serenity (Apollo 16 pan-camera frame 5586).



FIGURE 4-59.–Post-TEI view of the Moon. This Hasselblad EL photograph was exposed after the TEC trajectory had carried the CSM high above a point near the lunar equator at approximately 55° E longitude. Near-full-Moon illumination accentuates the difference in albedo and permits detailed examination of the extensive ray patterns associated with craters that are near or beyond the eastern limb when the Moon is viewed from the Earth (AS16-121-19451).



FIGURE 4-60.–Transearth coast extravehicular activity. The CMP left the depressurized CM during the TEC to recover film from the SIM camera systems. The CMP is assisted by the LMP, who is standing in the open CM hatch. This view is a frame from DAC motion pictures of the EVA (S-72-37001).

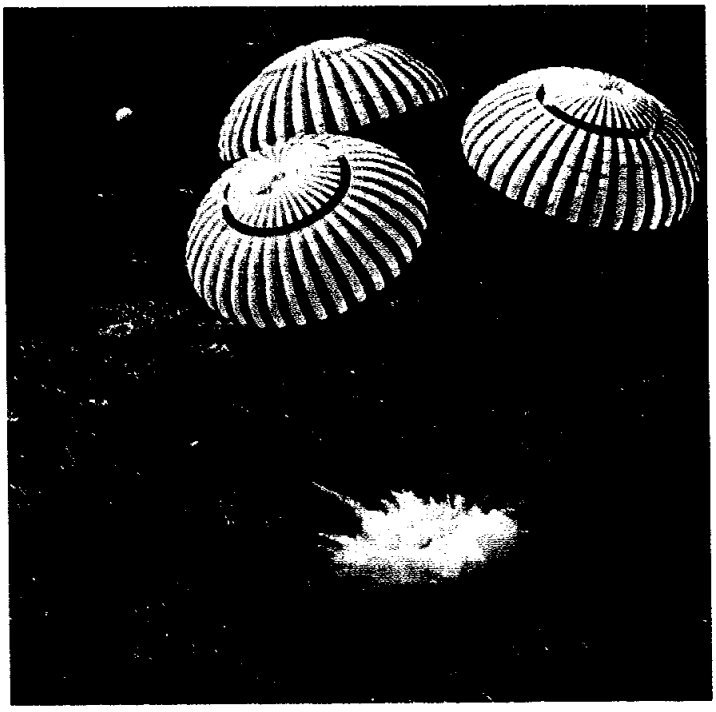


FIGURE 4-61.–Apollo 16 splashdown. The CM entered the central Pacific Ocean approximately 215 miles southeast of Christmas Island to successfully conclude the Apollo 16 mission 265 hr 51 min after launch. Television cameras on board the U.S.S. Ticonderoga and its helicopters transmitted real-time coverage of the landing to the world by way of communication satellites (S-72-36293).

5. Crew Observations

John W. Young,[a] Thomas K. Mattingly,[a] and Charles M. Duke[a]

The Apollo 16 expedition to the Descartes region was the second of the series of advanced manned lunar missions designed to enhance the scientific exploration of the Moon both from lunar orbit and on the surface. Although these advanced missions are very demanding, previous experience with the mechanical aspects of Apollo missions permitted us to devote 40 percent of our training time to the study of experiment objectives and operations. During this training period, a stimulating and fruitful relationship grew between the scientific investigators and the crew; by the time of the mission, we were confident that we could perform our share of the exploration. The great breadth of instruction they gave us was rewarded by a reasonably adequate documentation of both the expected and unexpected found at Descartes.

A close coordination between experimenter and crew aids in building and revising a viable flight plan. Because of hardware requirements and limited discretionary time available on an Apollo mission, the crew is committed to follow a preplanned, extremely complex, and relatively inflexible sequence of operations outlined in this flight plan. The peculiar requirements of each experiment must be considered in developing the flight plan, and, because of the interdependence of each element, real-time changes become difficult and sometimes even hazardous. Hardware failures during our mission prompted many real-time revisions to the flight plan. The cooperative efforts of the experimenter and the operations teams, and our long association with both, resulted in the achievement of nearly all scientific objectives.

A key to a successful mission is close coordination among the experimenters, the hardware manufacturers, the operations teams, and the crew. To be most effective, this communication must begin with experiment definition and continue through postflight data reduction.

[a]NASA Manned Spacecraft Center.

LUNAR ORBIT AND LUNAR LANDING

Because of the problem with the command and service module (CSM) engine, we remained for three revolutions in low lunar orbit with an 8-n. mi. perilune centered on the landing site. As we had anticipated, the landing site was easily recognized. Most prominent were the bright rays from South Ray Crater. By using these as keys, we quickly identified Stone Mountain, North Ray Crater, Gator Crater, Palmetto Crater, and the inverted V of craters Stubby, Wreck, Trap, Cove, Eden Valley, and Spook. The right leg of the V points to the landing site. We were surprised at the amplitude of the undulations in the Cayley Plains. "Plains" is definitely a misnomer.

During lunar module (LM) descent, at approximately 20 000 ft, the commander (CDR) could lean forward and see South Ray Crater and its distinctive ray pattern. By 11 000 ft, the entire landing site was visible. At approximately 6000 ft, the lunar module pilot (LMP) remarked on the absence of boulders along the planned traverse route to North Ray Crater. The LM computer was guiding the spacecraft north and west of the intended landing spot, so we manually corrected our descent. As we approached touchdown, we saw that the landing area had a few blocks as large as 1 m in diameter. At 200 ft, we became increasingly aware of the hummocky local terrain. The LM exhaust plume began blowing dust at 80 ft. However, blocks and small craters remained visible all the way to touchdown. The good visibility may have been due in part to our having descended from 150 ft to 30 ft over a 16-m crater. At 30 ft, we translated forward to a level area and landed. We could not detect slopes during the descent, except in those regions such as crater rims where shadows were cast. A survey after landing revealed that although we had landed in a level area, a touchdown 25 m in any direction would have placed the LM on local slopes of from 6° to 10°.

The LM landed in a subdued old crater, approximately 75 m in diameter. In general, the landing area is saturated with these old craters so that the few young sharp-rimmed craters provide a notable con-

trast to the pervasiveness of the old craters. In the immediate vicinity of the LM, a few 1- to 2-m craters have glass-coated bottoms. This glass is cracked and wrinkled so that it looks like dried mud. A low percentage of the surface is covered by subrounded to subangular blocks. To the north, the Turtle Mountain ridge shields the traverse route of the third period of extravehicular activity (EVA-3). To the south, except between the many 5- to 10-m ridges, we could see the EVA-2 traverse route as far as station 4. The surface sloped to the south an estimated 100 m, where a gentle rise marked the beginning of Stone Mountain.

SURFACE EXPERIMENT DEPLOYMENT

The Apollo lunar surface experiments package (ALSEP) was deployed approximately 100 m west-southwest of the LM in a similarly blocky, cratered, and hummocky terrain. There is a small boulder between the passive seismic experiment and the central station, and another approximately 2 m south of the lunar surface magnetometer. No significant problems were encountered with the hardware during the ALSEP deployment. Unfortunately, the cable to the heat flow experiment had looped, became snagged on a boot, and tore free from the central station. This rendered the experiment useless.

Aiming the far UV camera/spectrograph was more difficult than we had anticipated. Because of high friction in the azimuth adjustment, the camera often needed re-leveling after a new target was selected. Because of this friction, the uneven and sloping surface, and the occasional camera moves to keep the camera in the LM shadow, we used more EVA time than we had anticipated.

The cosmic ray experiment is deployed by pulling a lanyard. During deployment, this lanyard broke. Because we had never seen the experiment deployed, we could not tell whether the lanyard broke at the end of its normal travel or at an intermediate point. The experiment used in training was not functional and the flight hardware could not be cycled. We believe that, in training, the crew should operate a functional replica of every experiment. By the beginning of EVA-2, the temperature labels indicated that the experiment was reaching its upper temperature limit. The experiment was removed from the LM and was placed on the -Y footpad so that it faced away from the Sun.

Because of improvements to the lunar surface drill, the LMP had little difficulty in drilling or extracting the deep core. Very little soil was lost during capping of the core stems.

LUNAR TRAVERSE GEOLOGY

Premission Photography

The premission topographic and geologic maps of the Descartes site were based on 20-m-resolution photographs from the Apollo 14 mission. Although these maps are excellent considering the limited resolution of the source photographs, several interpretations are misleading. The maps do not show the true hummocky character of the plains but do depict many north-south trending, 10- to 15-m scarps that are in fact not found. In addition, the small crater distribution, the block distribution around North Ray and South Ray Craters, the local slopes on Stone Mountain and on the North Ray Crater rim, and the subdued craters that saturate the Cayley Plains were surprises that could have been avoided if high-resolution photography had been available. Because the Cayley Plains are so uniformly gray and featureless, except near sharp-rimmed craters and on bright rays, it is possible that several craters even larger than the resolution limit are not plotted on the topographic map. We observed a few such craters between stations 8 and 10 and along the route from the LM to station 11.

EVA-1 and EVA-2

During the first two EVA periods, we noticed that the abundance of blocks is essentially the same along the east-west line from the LM to Flag Crater, except in the lighter albedo rays where blocks are larger and more numerous. To the south, Survey Ridge has a 10- to 25-percent cover of subangular blocks, some as large as 2 m. The dominant size is 25 to 35 cm. The southwest slope of Survey Ridge appears to be saturated with secondary craters; the source is undoubtedly South Ray Crater. From station 4 on Stone Mountain, a major ray can be traced from Survey Ridge into South Ray Crater. However, the albedo contrast between ray- and non-ray-covered surface is subtle and cannot be detected at close range.

Both South Ray and Baby Ray Craters are clearly visible from Stone Mountain. The stark bright rays from Baby Ray lie on top of rays from South Ray. South Ray has both white and black rays. Within a white ray, white boulders are dominant; within a black ray, such as the one north from South Ray, black boulders are dominant. All rays from South Ray Crater appear to extend over the rim and into the crater. The block concentration increases significantly near the South Ray rim; it would have been very difficult or perhaps even impossible to drive to the rim. The blocks are typically subangular and angular, although approximately 10 percent of those near the LM in the ray from South Ray are rounded. These rounded rocks are more friable and may have simply eroded rapidly, or they may have had a different source.

The slope at the base of Stone Mountain is a gentle 6° to 10°. Those surfaces of the mountain that face northeast, away from South Ray Crater, are noticeably less block covered than the west-facing slopes. Nothing in the apparent color or albedo of the soil on Stone Mountain distinguishes it from that on the Cayley Plains. Although we had noted lineations on Stone Mountain from the LM, these were not detected at close range. We could not identify any rocks on Stone Mountain that were different from those on the Cayley Plains. However, if distinctly different material were returned, it will likely be in the rake samples from the inside slopes of two 15-m craters. The slopes facing the northeast were selected to maximize the chance of sampling true Descartes material rather than South Ray ejecta. One rake sample was collected from a crater at station 4; from the asymmetric distribution of nearby blocks, this crater was clearly caused by ejecta from South Ray Crater. The second crater from which we took a rake sample is more subdued than the first, but we believe it too is a secondary. For the most part, the rake samples appear to contain friable clods of soil.

EVA-3

There were gradual changes in block distribution as we traversed from the LM to North Ray Crater. North of Palmetto, there are very few blocks, the crater rims are rounded, and the craters are generally subdued. The blocks and cobbles are rounded and partially buried in the regolith. The impression is one of a very old and relatively undisturbed surface. From orbit, the command module pilot (CMP) had the impression that this area north of Palmetto is distinctly different and, in fact, represents a mappable unit.

We observed and photographed two shallow, 100-m-diameter, rimless depressions that may well have been endogenic. North of Palmetto is a gentle slope leading to a broad valley. After crossing the valley, we began the climb toward the rim of North Ray Crater. The route was free of obstructions so that the Rover easily reached the rim crest.

The inner slope of North Ray Crater is gentle for the first 50 m. Beyond that, it steepens so rapidly that the bottom of the crater cannot be seen. We collected rocks and soil along the southeast rim. Many rocks are well rounded, nearly buried in the soil, and characteristically white and shocked. Farther east on the rim near House Rock, the blocks are subrounded, are not buried in the soil, and show little filleting. House Rock itself is a huge breccia (estimated to be 10 m high by 20 m long) that contains both black and white clasts, some as large as 2 m. The rock is complex, with no obvious organization; it is shocked and fractured and has glass veins through it. One face shows what we thought was either a shatter cone or spall zone.

Those inner walls of North Ray that we could see are covered by boulders as large as 5 m. As at South Ray Crater, blocky rays extend up the inner walls, across the rim, and radially outward (in this case, as far as the top of Smoky Mountain). These rays are also both black and white.

Sample Description

The overwhelming majority of sampled rocks are breccias. In hand specimens, there appear to be two types: one with black clasts in a white matrix and the other with white clasts in a black matrix. A few of the breccias contain veinlets of glass. All breccias show some stage of shock metamorphism. A few contain recognizable crystals of a gray-white feldspar.

Several soil samples were collected at each station. With few exceptions, the soils appear to be identical. The exceptions are from those areas like station 1 where a white soil appeared under 5 cm of the typical gray surface material. Nearly all surfaces are loosely compacted so that our boots compressed the soil 3 to 4 cm and raking was easy. On areas of the rim of North Ray Crater, the soil is definitely firmer. Our

bootprints were only 2 cm deep, and the rake was nearly useless.

The permanently shadowed soil sample was collected from under a ledge on a boulder approximately 1 km from the North Ray rim. The boulder, Shadow Rock, appears to be of the same material as House Rock.

ASCENT

The ascent was smooth and without problems from lift-off to lunar orbit insertion. We had a little time to observe the Cayley Plains west of the landing site. These plains are ridged, hummocky, and generally appear identical to the area at the landing site.

ORBITAL OBSERVATIONS

Visual observations of the lunar surface from orbit received a great deal of attention throughout the training and execution of this mission. Specific details and impressions are recorded in section 28.

One of the most intriguing orbital observations was made at approximately 123:07 GET (3:01 c.s.t., April 21, 1972). The CMP was watching the stars rise over the approaching sunrise horizon while he was waiting to execute one of the zodiacal light photographic sequences. While in a totally darkened cockpit, he noticed a bright flash that appeared to the south of the ground track and several degrees below the horizon. This flash was of very short duration and did not remain long enough to permit recording a geographical position.

Several times during lunar orbit, the CMP could see small particles that were apparently in orbit with the spacecraft. These sightings were not related directly to the periodic effluent dumps from the spacecraft. The best time to view these objects was the period between the time the spacecraft crossed the lunar surface terminator and the time of spacecraft sunrise or sunset.

Although he did not view lunar sunsets because of the revisions to the flight plan, the CMP observed several sunrises. The horizon could be discerned approximately 17 min before sunrise and gradually increased in definition as the sky took on a radiance near the ecliptic. The actual sunrise was very abrupt with an apparent step function increase in intensity as the disk of the Sun came into view. The CMP looked for, but failed to see, any asymmetry in the solar corona or evidence of streamers or prominences.

Earthshine provided a rather well-illuminated lunar surface during the early portions of the mission. The lunar surface appeared much like a snow-covered scene on the Earth when illuminated by a full Moon, but the lunar surface was considerably brighter. As the mission progressed and the effective reflective area of the Earth decreased, the lunar detail quickly faded. The attempt to photograph the lunar surface in earthshine was postponed because of the delay in LM landing. This technique ought to provide some very useful data about the western areas that Apollo spacecraft have not and will not see in sunlight. However, these photographs ought to have been taken when the Earth provided the maximum reflective area.

In an attempt to resolve the question of the colors of the Moon, we were provided with a wheel with color chips for comparison. We were to hold the color chip and compare it with the lunar surface. There were two difficulties. First, we could not agree on the color chip that was closest in color. We did agree that none really matched. The second problem was the impossibility of viewing the color chip and the lunar surface under the same lighting conditions. The CMP saw very obvious tonal differences on the lunar surface, especially in the western maria, but could not quantitatively describe them. The color impressions of an area of far-side highlands changed as the Sun angle changed.

Craters on lunar photographs often appear as hills; a similar problem exists in viewing the Moon through a spacecraft window. This reversal occurs almost always over the more nondescript areas of the far side.

The Moon is exceptionally bright, almost painful to the eyes. After the first 2 days in lunar orbit, the CMP's eyes were fatigued; however, after the third day, they seemed to have adjusted enough to make visual observations comfortably. Looking through the sextant and the telescope at the surface presented a similar problem. The CMP could actually feel the heat coming through the optics.

There is very little on the lunar surface to act as a scale for determining the size of objects. Because the Moon is so heavily cratered at all scales, it looks very similar from 15-km (8 n. mi.) and 111-km (60 n. mi.) distances. The difference is really in the types of

features that can be detected at different ranges. For instance, the small-scale lineations, which are typical of all of the Moon except for the mare surfaces, cannot be seen by the unaided eye at 111 km (60 n. mi.), but they begin to appear at approximately 46 to 55.5 km (25 to 30 n. mi.).

The hardware for the low-light-level astronomical photography includes three filters. The filters were also used for visual observation of lunar features from orbit. The first was a polarizing filter that showed only a slight change in lunar brightness as the filter was rotated 90°. There were no selective changes in feature brightness or in image enhancement. The other two filters are blue (420 to 510 nm) and red (610 to 700 nm) and are used in the photography of areas that had been shown as color anomalies in Earth-based telescopic observations. Again, no visual differences were noted.

GENERAL OBSERVATIONS

One characteristic that has been mentioned jokingly on previous flights is that loose objects seem to collect eventually in the LM/CSM tunnel area. This phenomenon was evident throughout the flight. Also, we noticed that there was a preferential resting place for a tool which was tethered to a handhold. Invariably, we would find the tool with the strap nearly taut, oriented towards the tunnel and away from the handhold. The phenomenon was independent of the attitude of the spacecraft. In an attempt to evaluate the contributing effect of cabin gas circulation, a set of hoses was placed in the tunnel adjacent to the hatch with the exhaust hose open and the intake hose alternately capped and uncapped. This action seemed to have no effect on the phenomenon. No attempt was made to evaluate a time dependency. However, we did note that the tunnel area was almost always cooler than the rest of the spacecraft cabin.

A particularly puzzling phenomenon occurred when the CSM initially docked with the LM. As the CSM closed to approximately 10 ft, we could hear the sound of the CSM attitude control jets impinging on the light skin of the LM, even though the two vehicles were undocked. After docking, the sound was the same except for an increase in volume.

Previous Apollo crews have reported seeing water dump particles approaching the spacecraft. Therefore, special attention was directed toward observation of this phenomenon. We never saw any indication of curved trajectories, except when a particle would rebound off the surface of the LM or off another particle that had previously bounced off the LM. Several times during the mission, we had the opportunity to look down-Sun after a water dump. Although there was never a visible cloud, there was an obvious increased luminance in the direction of the antisolar point.

Observation of liquids in the absence of acceleration is a fascinating pastime. One experiment that had been suggested was to try to project one sphere of water into another. Water was shot from the drinking gun at a 2.54-cm (1 in.) sphere that had formed on the food preparation panel. The projectile appeared to hit the target with a minimum of deformation, followed almost immediately by a discharge of water from the opposite side of the target. The target bubble vibrated slightly but remained stable in position and, apparently, in volume. It was impossible to discern whether the projectile had passed through the target or had displaced some portion. One major difficulty in conducting this experiment is in trying to release a bubble with essentially no relative velocity. In fact, it is very difficult to release even a solid object without imparting some motion.

Mass measurement in an unaccelerated environment is another challenging problem in space flight. We attempted to make a rough measure of mass by recording accelerations induced by a known force. The scheme was to use a spring to accelerate a mass across a grid while we photographed the translation with a sequence camera. This technique had been evaluated on an air table with encouraging results. The major source of error seemed to be the difficulty in obtaining repeatable initial conditions. In flight, the experiment was dynamically evaluated but not photographed because of poor lighting conditions. Qualitatively, the mass could be smoothly accelerated with little or no rotation. That is, we obtained relatively stable and repeatable initial conditions.

The Apollo light flash moving emulsion detector was to be worn by the CMP. However, by the time the experiment was to be conducted, the CMP had not seen any light flashes and the LMP had consistently observed them. Therefore, the LMP wore the detector. The CDR saw a few flashes, although not with the frequency experienced by the LMP. Throughout the mission, the CMP looked for, but never saw, a light flash, even though he tried various

locations and orientations. The LMP did not notice any demonstrable frequency variation associated with his location within the spacecraft. The LMP also saw the flashes while he was in the LM on the lunar surface. The only related physical difference among crewmen was a qualitative judgment that the CMP had relatively poor night vision.

One salient impression we have of our journey was the variety of lunar terranes and geologic structures. We suspect that there is a general lack of appreciation for the complexity of lunar processes and probably of lunar geologic history. We believe that lunar studies will prove fascinating and rewarding for many years and through many programs.

6. Preliminary Geologic Investigation of The Apollo 16 Landing Site

W. R. Muehlberger,[a†] R. M. Batson,[b] E. L. Boudette,[b] C. M. Duke,[c] R. E. Eggleton,[b] D. P. Elston,[b] A. W. England,[c] V. L. Freeman,[b] M. H. Hait,[b] T. A. Hall,[b] J. W. Head,[d] C. A. Hodges,[b] H. E. Holt,[b] E. D. Jackson,[b] J. A. Jordan,[b] K. B. Larson,[b] D. J. Milton,[b] V. S. Reed,[b] J. J. Rennilson,[e] G. G. Schaber,[b] J. P. Schafer,[b] L. T. Silver,[e] D. Stuart-Alexander,[b] R. L. Sutton,[b] G. A. Swann,[b] R. L. Tyner,[b] G. E. Ulrich,[b] H. G. Wilshire,[b] E. W. Wolfe,[b] and J. W. Young[c]

SUMMARY OF RESULTS

The Apollo 16 landing site in the lunar central highlands encompassed terra plains and adjacent mountainous areas of hilly and furrowed terra. These morphologic units, representing important terrane types in the lunar highlands, had been interpreted as volcanic on most premission geologic maps. However, it became apparent during the mission that there are indeed few or no volcanic rocks or landforms at the site but rather that the area is underlain by a wide variety of impact-generated breccias.

During the three extravehicular activity (EVA) traverses of the mission, 95 kg of rocks and soils were collected, 1774 surface photographs were taken, and a traverse length of 20.3 km was covered. These data and the observations and geologic descriptions of the astronauts provide a wealth of basic data for analysis and synthesis.

Ray materials derived from North Ray and South Ray Craters are the two most apparent sources of surface debris on the Cayley Plains. Ejecta from South Ray Crater also appear to mantle much of the surface of Stone Mountain in the vicinity of stations 4 and 5, so that it is still uncertain whether Descartes materials were, in fact, sampled. Size distribution studies of fragments on the lunar surface suggest that the ejecta units of these two craters differ in character. Rock fragments are much less abundant in the North Ray ejecta blanket, which suggests that the North Ray impact may have excavated more friable material, that the length of time since the cratering event has been sufficient for subsequent impacts to destroy the smaller blocks, or both. South Ray ejecta, as mapped, include bright and dark areas, but the only surface differences observed are that the brightest areas have larger block sizes and a greater abundance of blocks. The mapped interray areas have no lunar surface characteristics that distinguish them from adjacent South Ray ejecta. Both ray and interray areas show a progressive northward decrease in total rock abundance and in relative abundance of the coarser sizes.

The regolith present on the ejecta blanket of North Ray Crater is only a few centimeters thick. Where ejecta blankets or ray deposits are not identifiable, the regolith is 10 to 15 m thick. The surface of the regolith is medium gray, but high-albedo soils are present at depths of 1 to 2 cm in most of the traverse area.

The Cayley Plains in the region of the lunar module (LM) and the Apollo lunar surface experiments package (ALSEP) are smooth but broadly undulating with a maximum relief of several meters. Two percent of the surface is covered by 2- to 20-cm fragments. Subdued craters between 150 and 240 m in diameter are present together with many smaller, more youthful craters, including abundant 0.5- to 2.0-m secondaries and some primary craters as large as 30 m in diameter.

Station 1 is near the rim of Plum Crater, a 30-m-diameter crater on the rim of the 300-m-diameter Flag Crater. Flag Crater is approximately 50 m deep and probably penetrates through the regolith

[a]The University of Texas at Austin.

[b]U.S. Geological Survey.

[c]NASA Manned Spacecraft Center.

[d]Bellcomm, Incorporated.

[e]California Institute of Technology.

†Principal Investigator.

into the underlying bedrock. The crater is subdued and no rocky exposures are visible in its walls or floor. The eastern part of the station 1 area appears to be crossed by a very faint ray from South Ray Crater, but rock fragments larger than approximately 10 cm cover less than 1 percent of the surface. A number of slightly buried, angular rocks in the photographs are interpreted to be ejecta from South Ray Crater. Because of the depth of penetration by Flag Crater and the relative scarcity of South Ray ejecta, samples from station 1 have the highest probability of being material representative of the upper units of the subjacent Cayley Formation.

Station 2 is located just north of Spook Crater (400 m in diameter) on the south rim of Buster Crater (90 m in diameter). The area is crossed by a faint ray that is apparently derived from South Ray Crater. Fragments, most of which are 5 to 10 cm, cover 2 to 3 percent of the surface. Scattered craters as large as 2 m in diameter are generally subdued, but a few small fresh ones have sharp rims and associated ejecta. Spook Crater is symmetrical with a slightly raised rim. No rock exposures occur in the walls and no deposits of ejecta were seen. In contrast, the floor and part of the walls of Buster Crater are covered by blocky debris with angular rocks as large as 5 m across.

Stone Mountain is a westward projection of the Descartes highlands into the southeastern part of the landing area. The mountain rises approximately 540 m above the Cayley Plains and is domical in form. Major though subtle step and bench topography parallels the slope of Stone Mountain. Stations 4 and 5 were located on Stone Mountain; station 6 was on the Cayley Plains near the foot of its lowest bench. Approximately 2 percent of the traverse area is sprinkled with blocks 10 cm and smaller. Blocks range from well rounded to angular but most are of intermediate shape. Local concentrations of blocks are found especially on the east sides and rims of craters facing away from South Ray Crater. It is presumed that these blocks were contributed largely from South Ray Crater and that an appreciable fines fraction accompanied them. The majority of craters on Stone Mountain range from 50 m down to the limit of resolution. The crater density is approximately that seen in the adjacent Cayley Plain, but craters larger than 100 m are more abundant in the Cayley Plain than on Stone Mountain.

The lunar surface in the vicinity of stations 8 and 9 is gently undulating with a northeasterly slope of a few degrees. Between 1 and 3 percent of the surface is covered by fragments 1 cm and larger. The largest blocks (1 to 2 m) are few and scattered. The blocks increase in size and abundance between stations 8 and 9 but decrease again at station 9, where blocks are somewhat less abundant than at station 8. There are many subdued craters as large as 3 m in diameter in this area. Most have slightly raised, rounded rims. Several craters at station 8 have concentrations of blocks on the northeast rims, and a few of these are somewhat elongate in a northeast-southwest direction, suggesting that they are South Ray secondaries.

At stations 11 and 13, a large young crater was investigated along its rim crest, walls, and continuous ejecta blanket and was extensively photographed and sampled. North Ray Crater, 900 to 950 m in diameter, is on a 50-m-high ridge at the western edge of Smoky Mountain near the eastern boundary of the Cayley Formation in this area. The geologic importance of North Ray Crater lies in its youth and in the depth of penetration (160 to 200 m) into materials underlying the Cayley Plains. The abundance of blocks on the rim of North Ray Crater was less than had been anticipated, although the size of some of the blocks makes them the largest investigated on the Moon so far. The distribution of craters superposed on North Ray Crater is apparently random and the density is very low. Few craters larger than 25 m are observed, and very few are recognized in the surface photographs. The random distribution and low density presumably reflect the relative youth of the crater and, for the smaller craters, probably result from a thin regolith over a hard subunit.

The total returned net sample weight is approximately 95.33 kg. Of the total sample weight, almost 75 percent consists of rock fragments larger than 1 cm in diameter, nearly 20 percent consists of soil or residue fines, and the remainder consists of core and drive tube samples. The Apollo 16 rocks may be divided into three broad groups: (1) fine- to coarse-grained, mostly homogeneous crystalline rocks; (2) rocks composed substantially of glass; and (3) fragmental rocks (breccias). The proportion of fragmental rocks in the returned samples exceeds 75 percent. Twenty-five rocks are classified as crystalline rocks. Of these, seven appear to be igneous rocks. Although all the igneous rocks have been shattered and deformed to some extent, the predeformation textures

are substantially intact. The two largest samples returned are coarse-grained, nonvesicular rocks composed largely of plagioclase. These rocks resemble Apollo 15 anorthosite sample 15415 but are probably more severely shock deformed. Three are fine-grained, highly feldspathic rocks with crystal-lined vugs. Eighteen crystalline rocks appear to be metaclastic rocks with generally small proportions of lithic debris. These are hard, angular rocks characterized by fine-grained sugary textures. Five samples largely composed of glass were returned. Two of these are glass spheres, one hollow and one solid. The remaining three glass samples are irregular, coarse, vitric agglutinates with numerous small lithic inclusions. The fragmental rocks have been divided into five main groups on the basis of proportions of light and dark clasts and matrix color. All five groups are varieties of impact-generated breccias; none appear to be of volcanic origin. The majority of the rocks are polymictic breccias, but a substantial minority are monomictic. Two types of clasts are clearly dominant: (1) dark, aphanitic to finely crystalline metaclastic rocks and (2) white, partly crushed to powdered feldspathic rocks. Less common clast types include light-gray or white rocks with granoblastic textures, a variety of gabbroic to anorthositic rocks with medium to coarse grain size, and rare feldspar-poor basaltic rocks. Matrices of the light- and medium-gray-matrix breccias are, for the most part, friable and not visibly altered by subsequent thermal events, whereas those of dark-matrix breccias are coherent and annealed or fused.

The rock distribution suggests that the section underlying the Cayley Plains is stratified, with an upper unit of medium-gray breccia and lower units composed mainly of light- and dark-matrix breccias. The areal extent of the supposed upper unit is not known but presumably extends at least between stations 1 and 6; considering the relative scarcity of the medium-gray breccias, the unit is probably not more than a few meters thick. Evidence derived from the photographs, astronaut descriptions, and samples collected at station 11 suggests that light-matrix breccias overlie dark-matrix breccias, whereas the color of ejecta on the rims of South Ray and Baby Ray Craters suggests that dark-matrix breccias overlie light-matrix breccias in the vicinity of those craters. Such a stratigraphic sequence in the South Ray area is consistent with the dominance of dark-matrix breccias described and photographed in South Ray ejecta between the LM site and station 8.

The Cayley Formation at the Apollo 16 site is a thick (at least 200 and possibly more than 300 m), crudely stratified debris unit, the components of which are derived from plutonic anorthosites and feldspathic gabbros and from metamorphic rocks of similar composition. The Formation has an elemental composition similar to that observed over large regions of the lunar highlands by the orbital X-ray experiments of the Apollo 15 and 16 missions. The observed textures and structures of the breccias resemble those of impact breccias. They do not resemble those of volcanic rocks nor do the plutonic or metamorphic source rocks of the breccias have the textures or compositions of terrestrial or nearly all previously sampled lunar volcanic rocks.

The nature of the materials comprising the Descartes highlands remains, at this time, unknown. Available sample data indicate that the Descartes highlands differ from the adjacent Cayley Formation more in physiographic expression than in actual lithologic character. Whether it is a stratified unit, as suggested by several subtle topographic benches, has not been established.

The character of the Cayley Formation emerging from the Apollo 16 site studies supports consideration of an impact-related origin. The sources of the debris that might be considered include (1) ejecta from the Imbrium Basin (ref. 6-1), (2) ejecta from the Nectaris Basin, or (3) some combination of ejecta from various local and more distant sources accumulated over an extended time interval. Each possibility has a very different historical implication. Isotopic age studies on samples of the various breccia types and their included clasts should permit a test of these possibilities.

The incomplete characterization of the Descartes materials on Stone Mountain makes extended geological speculation premature. Materials of the same morphological unit partially fill the crater Descartes to the south. These steep-sloped, relatively uncratered, high-albedo uplands have been interpreted as relatively youthful, volcanic constructional features. If work in progress confirms that the Descartes Mountains are composed of breccias similar in lithology and composition to materials of the Cayley Formation, the postulated volcanic origin will require reassessment. Additional petrologic information, soil analyses, and possibly age studies of the returned samples are necessary to conduct such an evaluation.

INTRODUCTION

The lunar module, Orion, landed at the western edge of the Descartes Mountains approximately 50 km west of the Kant Plateau, part of the highest topographic surface on the near side of the Moon (fig. 6-1). The Apollo 16 mission accomplished the first landing in the central lunar highlands, and the crew successfully explored and sampled a kind of terrane never before visited on the lunar surface. The landing site was selected as an area characteristic of both terra plains and rugged hilly and furrowed terra. The consensus of premission photogeologic interpretation was that both units were of probable volcanic origin. However, it became apparent during the mission that there are indeed few or no volcanic rocks or landforms at the landing site but rather that the area is underlain by a wide variety of impact-generated breccias.

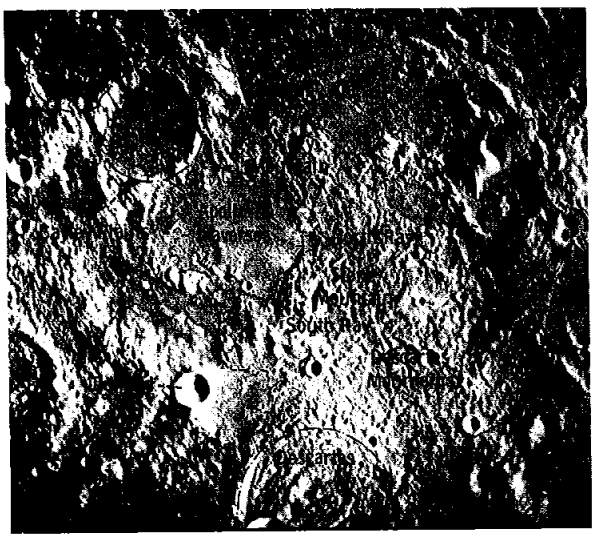


FIGURE 6-1.–Regional physiography of the Apollo 16 landing site (Apollo 16 metric camera frames 439 and 440).

The Apollo 16 mission is the only manned landing accomplished or planned in the central lunar highlands. The geologic diversity and significance of the site; the extended traverse capability provided by three EVA periods and by the lunar roving vehicle (LRV); the real-time television coverage of the site and of crew activities; the large suite of returned samples and surface photographs; and, especially, the fine performance of the crew contributed to a very successful mission. A summary of lunar surface photographic activities is given in appendix A of this section. The Apollo 16 mission has proved to be exceedingly important from the standpoint of understanding the evolution of the terra and in providing data that ultimately may be extrapolated over wide areas of the lunar surface.

PREMISSION GEOLOGIC STUDIES

The central highlands region surrounding the Apollo 16 landing site represents a major geologic province that has long attracted attention because of its distinctive densely cratered appearance and its unique position between dark maria (fig. 6-2). Three main geologic units have been recognized in the area: the Cayley Formation, materials of the Descartes highlands, and materials of the Kant Plateau. The first two units form clearly distinct terranes with some transitional facies; the last unit shares some morphologic characteristics with the first two. At the beginning of the lunar mapping program, these units were interpreted as facies of the Imbrium ejecta blanket (ref. 6-1) but later were considered as probable volcanic deposits (refs. 6-2 to 6-10). Imbrium sculpture is not pronounced or is absent on the three units, and Imbrian trends were expressed as basement control on the topography of overlying units. The relative abundance of craters 300 m to 2 km in diameter on the Cayley Formation suggests that the Formation is older than the maria. Therefore, the maximum inferred age of the deposits was Imbrian. Most photogeologic maps show the three units as emplaced in approximately the same span of time so that locally determined age relations between them may not be valid over wide areas. If these interpretations are correct, then the Cayley Formation and Descartes and Kant materials were deposited during the relatively narrow time interval between the Imbrium event and the filling of the mare basins with basalt. However, Milton (ref. 6-2) suggested that Descartes materials in an area approximately 50 km south of the landing site might be as young as Copernican. More recently, Head and Goetz (ref. 6-11) presented multispectral data of this area that support a Copernican age assignment.

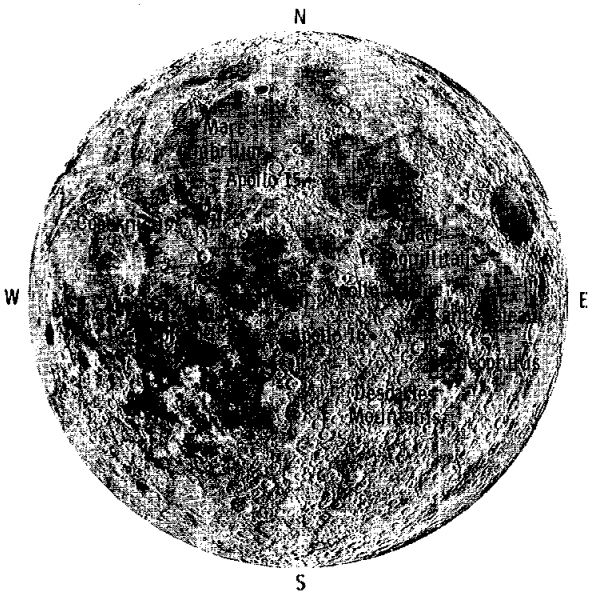


FIGURE 6-2.–Near side of the Moon showing relation of the Descartes area to the surrounding maria.

Terra plains-forming units, of which the Cayley Formation is an example, cover approximately 7 percent of the near side of the Moon and occupy more area than any other identifiable unit except mare material. Characteristically, the Cayley Formation forms low-relief plains of light albedo that lie in the floors of older depressions (fig. 6-1). Small craters (300 m to 2 km in diameter) are abundant on most of its surface; positive landforms such as ridges and domes like those on the maria are generally absent. Near the landing site, the Formation is divided into smooth and irregular subunits (refs. 6-5 and 6-6), but only the less representative irregular unit was within the planned traverse area. Impact and volcanic origins have been the main interpretations advanced for the Cayley Formation. Eggleton and Marshall (ref. 6-1) showed a zone of "continuously hummocky Apenninian material" (interpreted as Imbrium ejecta) extending from the rim of Mare Imbrium to about the distance of the crater Fra Mauro. Farther out, and concentric to Mare Imbrium, they identified a smooth facies with an easily recognizable outer limit, crossing the northwest corner of the Theophilus quadrangle some 80 km northwest of the Apollo 16 site. Still farther out, they concluded that "isolated hummocky patches of probably Apenninian material may be exposed over much of the intervening area." However, Milton (ref. 6-12) separated a "plains-forming unit" (subsequently called Cayley Formation) from the Fra Mauro Formation and believed that he saw evidence of its superposition on Fra Mauro deposits. A volcanic origin was tentatively suggested. He also specifically rejected Eggleton and Marshall's idea that what is now called Descartes material is Imbrium ejecta and considered it another volcanic unit. This interpretation was subsequently preferred by Wilhelms (ref. 6-13), Trask and McCauley (ref. 6-10), and Elston et al. (refs. 6-5 to 6-7). Most workers, however, have reserved the possibility that some of the terra plains consist of deeply churned fragmental debris derived by mass wasting and ballistic transport from nearby topographic highs.

Materials of the Descartes highlands form hilly and mountainous regions that are topographically higher than the Cayley Formation (fig. 6-1). The Descartes unit is one of the better examples of a type of material that occurs in several places in the lunar terrae as patches of rugged terrain not obviously related to craters or multi-ring basins. Based on low-resolution (1 to 2 km) telescopic photographs, the unit was interpreted by Eggleton and Marshall (ref. 6-1) to be an isolated outlier of Imbrium ejecta. Their analysis depended on the morphologic similarity between the Descartes highlands and the hummocky deposits nearer to the Imbrium Basin. Milton (ref. 6-2) noted that the unit forms a deposit of considerable thickness, perhaps about a kilometer, and that its relief is largely intrinsic. Both Milton (ref. 6-2) and Trask and McCauley (ref. 6-10) interpreted positive landforms in the Descartes highlands to be volcanic, although the latter pointed out morphologic similarities to one of the depositional facies of the Orientale blanket. The broad domes, generally 2 to 8 km across, were thought to be analogous to terrestrial shield volcanoes. Some domes appear to have funnel-shaped summit craters with convex interior slopes rather than the concave-upward interior slopes characteristic of most lunar craters. Milton (ref. 6-3) suggested that these features are a form of caldera produced by slumping into a void caused by withdrawal of material at depth. He further suggested that as individual domes broaden, they coalesce into plateaus cut by irregular furrows. Some of these furrows were thought to be areas between constructional features, but most were interpreted to be either grabens or sites of fissure eruptions.

The Kant Plateau occupies much of the central region of the Theophilus quadrangle (ref. 6-2, fig. 6-1). Materials of the Plateau were not believed to underlie the Apollo 16 site, but exotic blocks derived from the Plateau might be present in the traverse area. Materials of the Kant Plateau were interpreted by Milton (ref. 6-2) to be volcanic, although he noted a lack of distinctive volcanic landforms.

The Fra Mauro Formation and the similar Nectaris Basin ejecta (the Janssen Formation) were shown in cross section as underlying both the Cayley Formation and the Descartes Mountains in the Apollo 16 landing area (ref. 6-4). In another cross section (refs. 6-5 and 6-6), the surface of a highly cratered pre-Imbrian hill, approximately 25 km southwest of the landing site, was projected beneath the Cayley Formation to where it lay less than 1 km below the surface at the landing site.

Ray materials from North Ray and South Ray Craters, both situated on the Cayley Formation, were mapped as mantling a considerable part of the traverse area, both within the plains and within the adjacent highlands (refs. 6-4 to 6-6). Impact craters of Imbrian to late-Copernican age are scattered throughout the region. In addition, rimless to low-rimmed, irregular depressions of unknown origin were noted and mapped. Topographic benches were mapped on the flanks of Stone Mountain. In the walls of several craters, albedo bands and ledges suggested lithologic layering. Lineaments in photomap units locally constituted as many as four intersecting sets (refs. 6-5 and 6-6).

GEOLOGIC OBJECTIVES

The geologic objectives of the Apollo 16 mission were to understand better the nature and development of the highland area near the Descartes Mountains and to study processes that have modified highland surfaces. The objectives were to be met through the study of geologic features documented both on the surface and from orbit and through subsequent analysis of the returned samples.

The three traverses were designed to investigate two distinct highland morphologic units, the upland plains mapped as Cayley Formation and the mountainous Descartes highlands. Specifically, the study of the Cayley Formation was planned to yield the lateral variation of the stratigraphic section between North Ray and South Ray Craters (fig. 6-3), the petrology of the Formation throughout the area, and the characteristics of the upland plains regolith. The prime Cayley sampling areas were located at Flag and Spook Craters and the ALSEP, where crater dimensions suggested that the unit might be sampled to depths of approximately 60 m. Deeper parts of the Cayley Formation were expected to have been excavated by the larger North Ray and South Ray impacts and exposed near the rim of North Ray Crater (stations 11, 12, and 13) and in the ray deposits of South Ray Crater.

Stations 4, 5, and 6 on the flank of Stone Mountain were the principal sampling sites for Descartes highland materials (fig. 6-3). These stations were located on benches recognizable on the topographic map. An additional station (14) was planned on the lower slopes of Smoky Mountain to compare the two mountain units.

Several special procedures were used with the objectives of (1) supporting studies of the surface character of the regolith, the optical properties of the lunar surface, the unabraded surfaces of lunar rocks, boulder erosion and filleting, the adsorption in shaded areas of mobile elements, cosmic ray tracks in large boulders, and chemical homogeneity throughout single units, and (2) supporting future studies on uncontaminated lunar soil. (See part B of sec. 7 of this report.)

PHYSICAL DESCRIPTIONS

The Site and Traverse Routes

The Apollo 16 landing-site area included a portion of the Cayley Plain and two areas of mountainous terrain to the south and north. The Plain is a heavily cratered surface that slopes to the south-southwest. The presence of craters and their rim deposits gives the appearance of hummocks and swales with intervening relatively flat areas of limited extent. The Stone Mountain area to the south is terraced.

The LM landed approximately 210 m north and 60 m west of the nominal landing site (fig. 6-4) in a large swale that is relatively flat and that may be the floor of a very subdued old crater. The maximum local relief is several meters. Stations 1 and 2 (fig. 6-4) were traversed at their nominal locations. Both stations were located on rim material of a moderately

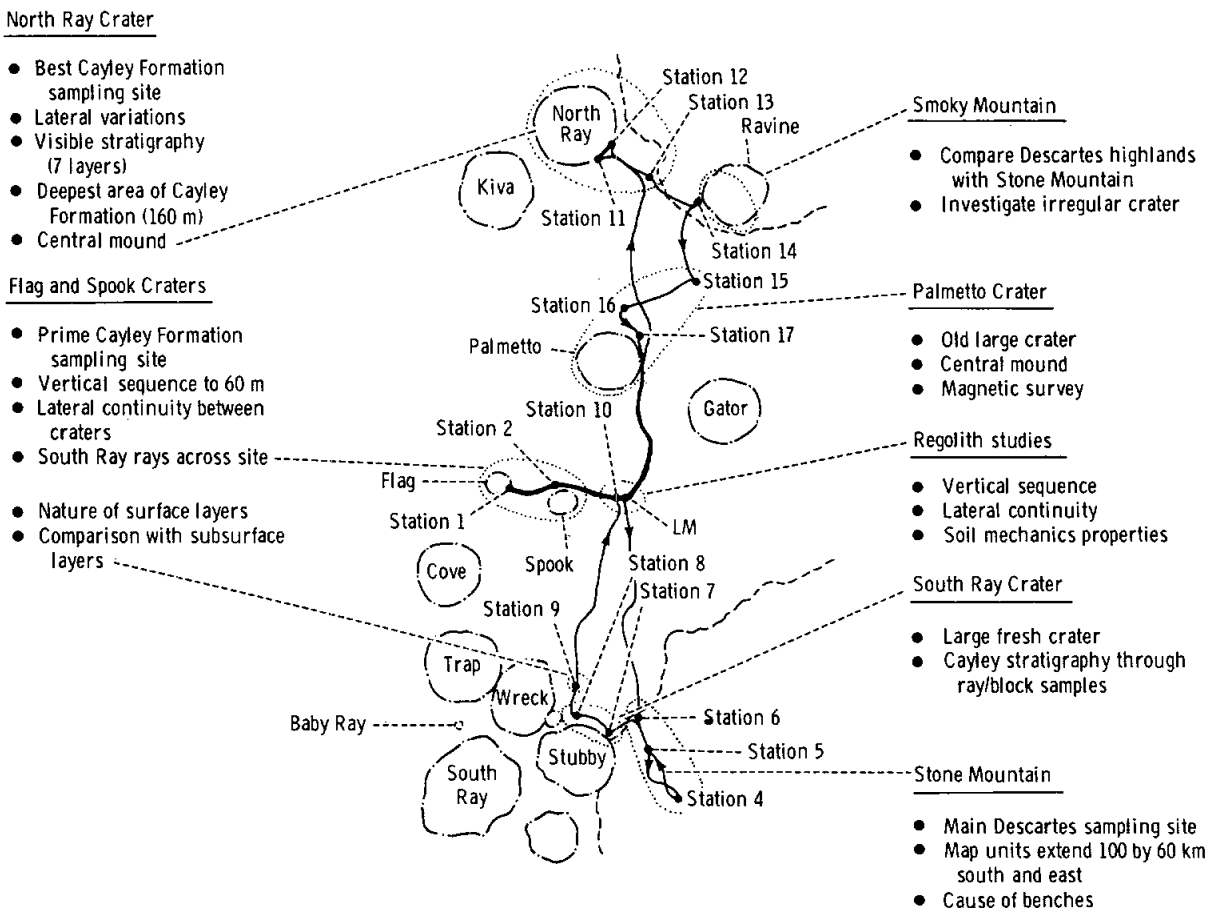


FIGURE 6-3.–Preplanned traverses and geologic objectives.

large crater adjacent to a younger small crater. Station 2 was more blocky because of the relative freshness of Buster Crater.

During EVA-2, the nominal traverse required a climb of approximately 200 m up the slope of Stone Mountain. Station 4, the highest point reached on the mountain, was located short of the nominal station and approximately 75 m lower on the slope. The station was on a steep slope that is more blocky than expected because of the presence of ray material from South Ray Crater. Station 5 was lower on the slope and approximately 0.5 km north of station 4. The station was on a gently sloping bench near a 15-m crater in an area sparsely covered with blocks. Station 6 was located on the edge of the Cayley Plain at the base of Stone Mountain. A subdued 10-m crater and several small craters are present in the station 6 area, and small blocks are fairly common. Nominal station 7 was bypassed, and station 8 was located somewhat north of nominal in a rocky area considered part of a ray from South Ray Crater. Station 9 was positioned somewhat to the east of its nominal location in an area with less South Ray ejecta.

The third EVA was shortened and station tasks were concentrated principally on areas near North Ray Crater (fig. 6-4). Station 11, an elongate area on the southeast rim of North Ray Crater, was blocky with a few exceedingly large blocks. Station 13 was located on the ejecta blanket of North Ray Crater at a distance approximately equal to three-fourths of the diameter of North Ray Crater to the southeast of station 11. The station 13 area had few blocks projecting above its gently south-sloping surface.



FIGURE 6-4.–Traverse map (Apollo 16 pan camera frame 4618).

Surficial Deposits

Ray deposits.—Ray materials derived from North Ray and South Ray Craters are the two most apparent sources of surface debris on the Cayley Plains. Ejecta from South Ray Crater also appear to mantle much of the surface of Stone Mountain in the vicinity of stations 4 and 5. The wide extent of the rays greatly increases the possibility that ray material rather than local bedrock was sampled at many of the traverse stations. It is therefore important to attempt to distinguish ray material and, if possible, to differentiate between North Ray and South Ray ejecta.

On orbital photographs, rays from South Ray Crater can be observed to extend at least 9 to 10 km from their source into areas west and southeast of North Ray Crater, overlapping older North Ray rays (fig. 6-5). This suggests that South Ray ejecta probably occur in at least small quantities on the rim of North Ray Crater itself, on the surface or mixed into North Ray ejecta. Most of the interray areas within 3 to 4 km of South Ray Crater were not separately outlined at the scale of map compilation (1:12,500). Radially outward, interray areas are more extensive, until only a few strong rays are recognizable at distances of 6 km or more. The traverses included the area of this transition.

The mapped ejecta of North Ray Crater extend shorter distances outward (less than 3 km south into the traverse area) than do those of South Ray Crater and are less streaked with strong rays. This apparent difference in distribution presumably is mainly the result of the greater age of North Ray Crater and the greater amount of "weathering" of the ejecta. One may guess from orbital and surface photographs that North Ray Crater is more than twice as old as South Ray Crater and that North Ray ejecta have undergone more than twice as much modification. Because North Ray Crater is larger than South Ray Crater, its ejecta blanket should originally have been at least as extensive as that of South Ray Crater. Recognizable amounts of North Ray ejecta probably were deposited on Stone Mountain, though now obscured by downslope mass wasting and by covering by South Ray ejecta.

Rays from Baby Ray Crater are draped across those of South Ray Crater. Other, still smaller, younger craters are scattered across the map area. Of these, only the ejecta of WC Crater are shown on the map.

Discrimination of ray material from South Ray and North Ray Craters on the lunar surface is a difficult task. Rocks exposed on the lunar surface tend to become more rounded, more deeply buried, and more filleted with age. Because of the relative youth of South Ray Crater, these characteristics are, in some cases, helpful in distinguishing South Ray from North Ray ejecta. Boulders in the vicinity of South Ray Crater and on its mappable rays are more angular than those in the vicinity of North Ray Crater and on North Ray ejecta (shape terminology from ref. 6-14). A preliminary study of the Apollo 16 samples, however, shows that the surfaces of many are eroded, whether they were collected from South Ray or North Ray ejecta. Chips from South Ray boulders are also eroded on the exposed surfaces. Angularity appears to be consistently preserved only on the largest rocks from South Ray Crater. Small rocks, even those from South Ray ejecta, are probably sufficiently eroded so that angularity alone is not a unique identification of the source of any single small sample. The amount of apparent erosion is, of course, also dependent on friability, structure, and other rock characteristics. Angularity as a means of identifying South Ray from North Ray ejecta is probably useful in individual cases only for boulder-sized blocks of similar tensile strengths.

To characterize the ray materials further, therefore, it proved necessary to investigate the size distribution of fragments along the Apollo 16 traverse routes. Frequency and size of fragments were measured in 324 surface photographs with the aid of a perspective grid. The smallest size class, 2 to 5 cm, was measured within 6 m of the camera. Larger fragments, in classes increasing by a 5-cm increment (e.g., 5 to 10, 10 to 15, 15 to 20), were measured to 10 m from the camera. Size and frequency data were converted to percentage of surface area covered by fragments of each size class (fig. 6-6). For simplicity, fragments larger than 15 cm have been grouped in a single class.

Most fragments range from 2 to 40 cm, but a few larger fragments (as large as 90 cm in diameter) were measured. Larger blocks are present locally but were too far from the camera to be included in the measurements. The most abundant fragments are in the 2- to 5-cm class, which typically makes up 25 to 90 percent of the area covered by fragments in a photograph. Fragments in the 5- to 10-cm size class



FIGURE 6-5.–Map of ejecta distribution in the Descartes landing site area. Derived from second-generation film positives of Apollo 14 orbital photographs AS14-69-9520 and 9522 (500 mm), using stereographic analytic plotter.

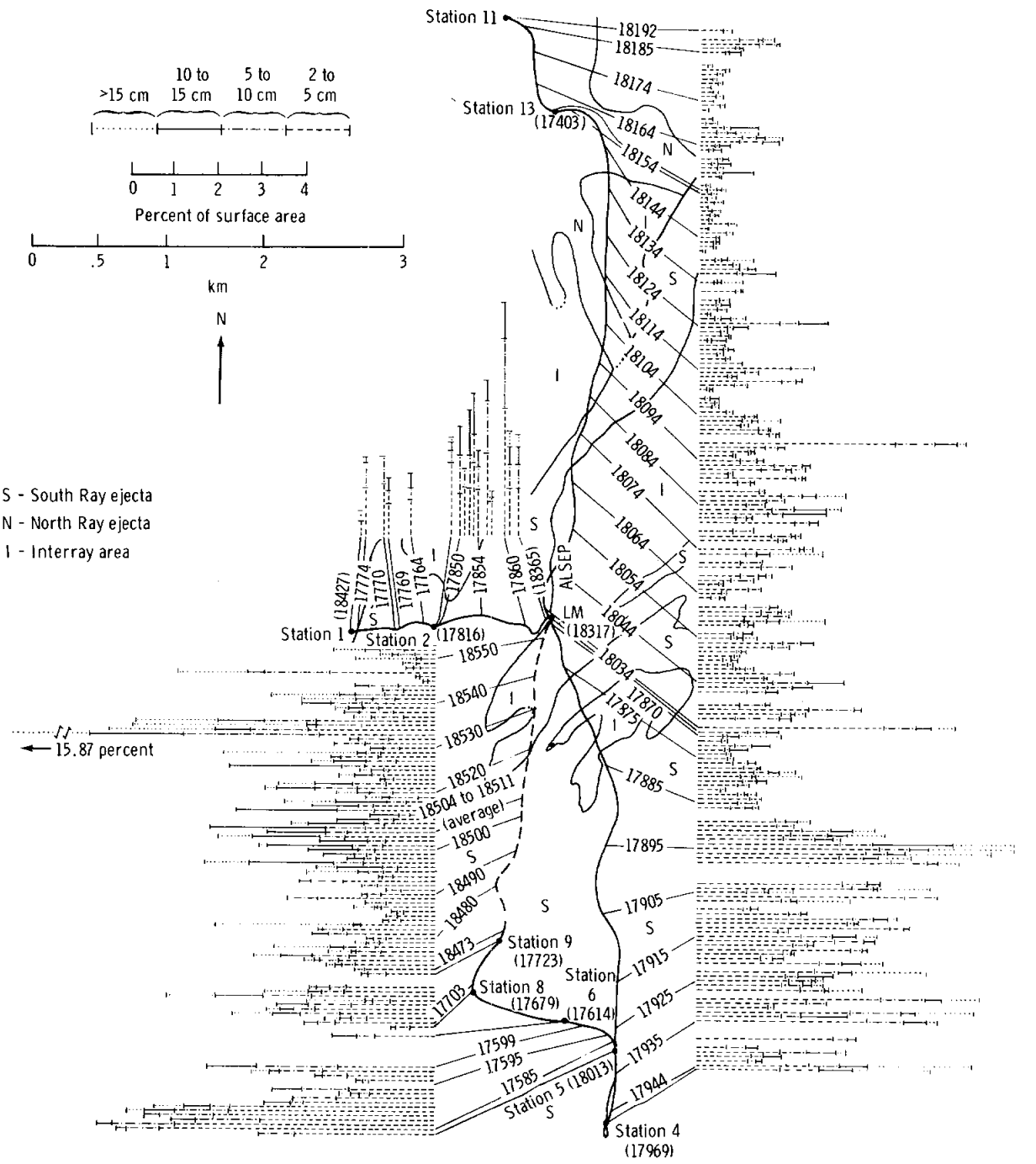


FIGURE 6-6.–Size distribution of fragments larger than 2 cm as determined from lunar surface photographs. Each line represents a size distribution determination from a single photograph. The length of each line is proportional to the surface area covered by fragments as shown by the bar scale. Five-digit numbers identify photographs; leaders tie them to their approximate positions along the traverse path.

are second in abundance. In general, the frequency of 2- to 5-cm fragments and of larger fragments varies with the total fragment abundance.

The abundance of fragments larger than 2 cm in diameter increases progressively from north to south over the entire traverse area. Typically, fragments on the ejecta blanket of North Ray Crater cover considerably less than 1 percent of the surface area, whereas abundances as high as 7 percent are common south of the LM area in rays from South Ray Crater. Abundances increase locally in the vicinity of fresh craters (e.g., approximately 200 m north of station 13) and in some of the bright rays from South Ray Crater. The most extreme abundance (nearly 16 percent) was measured in photograph AS16-115-18533, taken approximately 600 m south of the LM. This area is near WC Crater, which may have excavated fragments from beneath the South Ray ejecta.

Ejecta from South Ray Crater are characterized by a relative abundance (generally 2 to 7 percent surface cover) of angular fragments that are commonly perched on the surface. Fragments are generally less than 0.5 m in diameter and most are 2 to 10 cm. Large, worn boulders like those in the North Ray ejecta blanket are absent; the angular nature of the larger blocks emphasizes the relative youth of South Ray ejecta. In addition, the surface is pocked by abundant small craters approximately 2 m or less in diameter. In relatively dark areas of South Ray ejecta (fig. 6-7), fragments ordinarily cover 4 percent or less of the surface (fig. 6-6). Most areas with a higher percentage of fragments occur in bright ray patches. Figure 6-8 is a photograph taken on Survey Ridge, a bright northeast-trending ray patch approximately 1500 m north of station 5. Approximately 7 percent of the surface at this location is covered by fragments, and the larger sizes are more abundant than in the area shown in figure 6-7.

The edge of the continuous ejecta blanket from North Ray Crater was crossed approximately 400 m south of station 13. The surface of the ejecta blanket (fig. 6-9) is characterized by the extreme paucity (less than 1 percent surface cover) of rock fragments and by the scarcity of small secondary craters. Widely scattered, worn-looking, partly buried blocks, many several meters in diameter, dot the surface. These larger blocks seem especially characteristic of the North Ray blanket and presumably were ejected from North Ray Crater; their eroded character demonstrates that the North Ray event preceded the South Ray event. The generally fine grain size of the surface materials also suggests that North Ray ejecta are older than South Ray materials, that much of the North Ray blanket may have been derived from relatively friable materials, or both.

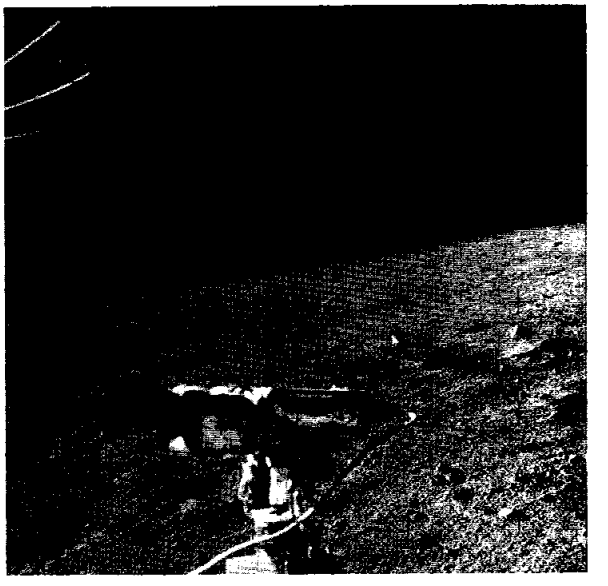


FIGURE 6-7.–South Ray Crater ejecta near station 5. No bright ray deposits are visible in the immediate area. Fragments cover almost 3 percent of the surface ("driving" photograph AS16-110-17925).

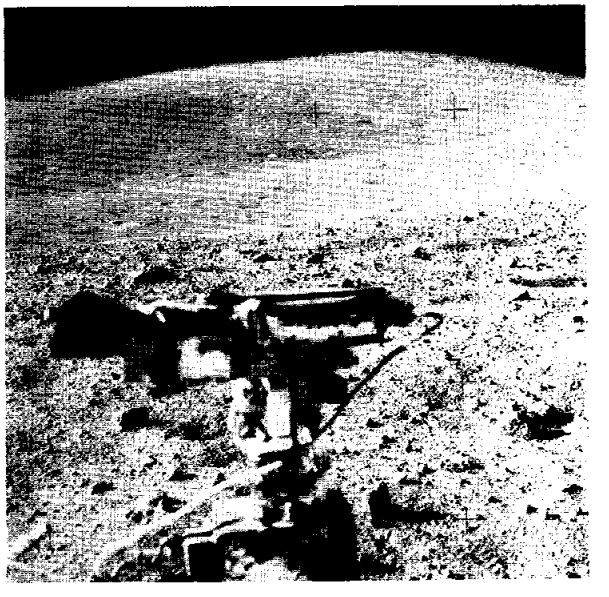


FIGURE 6-8.–South Ray Crater ejecta in bright ray area on Survey Ridge approximately 1500 m north of station 5. Fragments cover 7 percent of the surface ("driving" photograph AS16-110-17895).

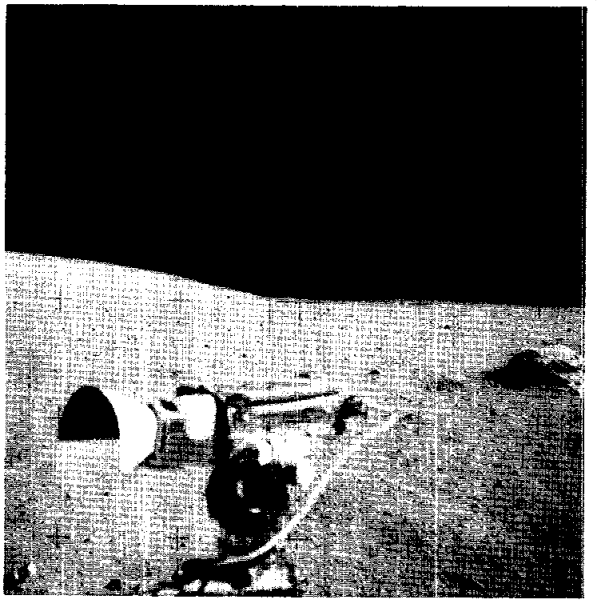


FIGURE 6-9.–Typical North Ray Crater ejecta blanket surface. Fragments cover 0.2 percent of the surface. The large block to the right is approximately 2 m in diameter ("driving" photograph AS16-111-18146).

Interray areas not mapped as North Ray or South Ray ejecta are shown at several localities in figure 6-5. In size distribution, frequency, and shape of fragments and in occurrence of small craters, these areas resemble adjacent areas not mapped as South Ray ejecta.

In summary, ejecta from North Ray and South Ray Craters have been distinguished and mapped on orbital photographs (fig. 6-5). Size distribution studies of fragments on the lunar surface suggest that the two ejecta units differ in character. Rock fragments are much less abundant in the North Ray ejecta blanket, which suggests that the North Ray impact may have excavated more friable material, that the length of time since the cratering event has been sufficient for subsequent impacts to destroy the smaller blocks, or both. Large blocks are considerably more rounded in the North Ray blanket, which also suggests that the debris is older than that of South Ray Crater. South Ray ejecta, as mapped (fig. 6-5), include both dark and bright areas. The size and frequency data show that the brightest surfaces, such as that of Survey Ridge, are characterized by a greater abundance of fragments and a relative increase of fragments in the coarser sizes. Generally, areas mapped as interray areas on orbital photographs are indistinguishable from nearby South Ray ejecta in the surface photographs or in the size distribution data from nearby South Ray ejecta. It seems likely that South Ray ejecta lightly cover the mapped interray areas. Both ray and interray areas show a progressive northward decrease in total rock abundance and in relative abundance of the coarser sizes. Size and abundance of fragments are inversely related to distance from South Ray Crater. Distribution of fines (less than 2 cm) from North Ray and South Ray Craters has not been determined from the surface photographs. The core samples may serve to identify fine-grained ejecta units.

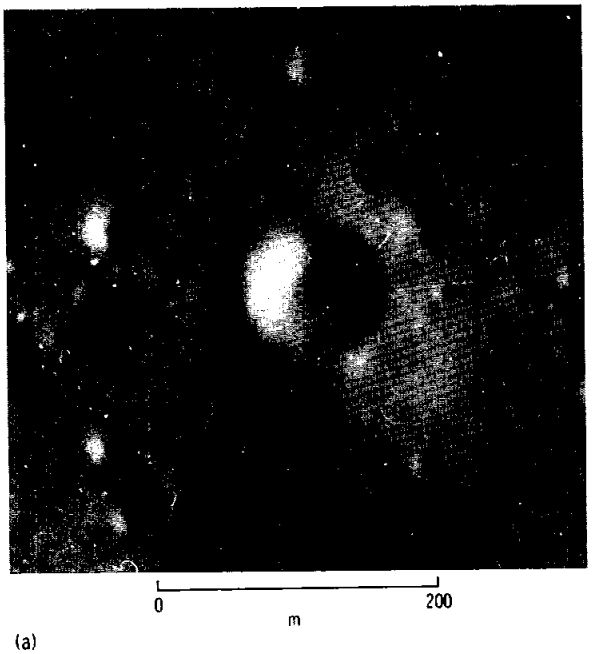
Regolith.–The lunar regolith is defined as a layer of fragmental debris of relatively low cohesion that overlies a more coherent substratum (ref. 6-15). At the Apollo mare sites, the regolith averages 3 to 6 m thick and was derived primarily from underlying basaltic units. Analysis of nonmare areas has been difficult because of the lack of high-resolution photographs and the apparent modification of craters by downslope movement in rolling terrain.

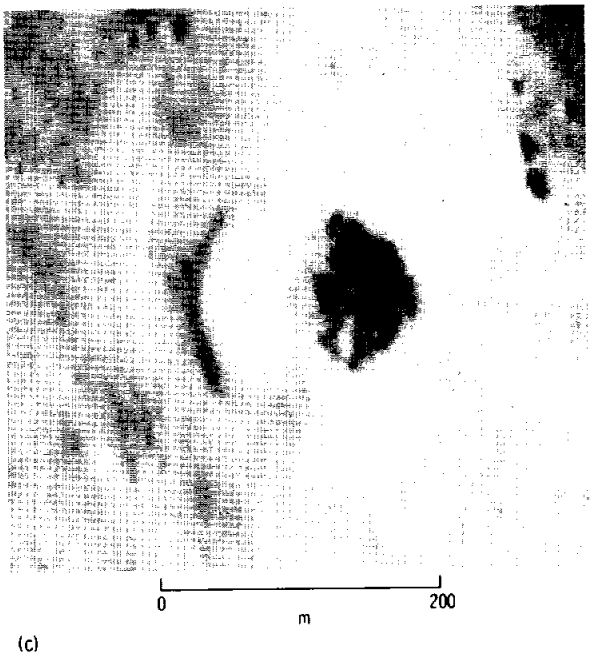
The regolith formed on the "hard" ejecta blanket of North Ray Crater is only a few centimeters thick as was demonstrated by astronaut activities (rake sampling, footprints, LRV tracks). The scarcity of blocks on the ejecta blanket is notable (fig. 6-6) and may be the result of (1) the crater event ejecting fine-grained, disaggregated material that filled the interstices of the blocky ejecta blanket and added a very thin surface mantle, and (2) micrometeorite erosion of the surface rocks, which, judging from the boulders remaining, were generally friable. The "hardness" of the underlying ejecta blanket indicates that it is either continuous, overturned layers of coherent material or, more probably, contiguous blocks the interstices of which are filled with finer debris.

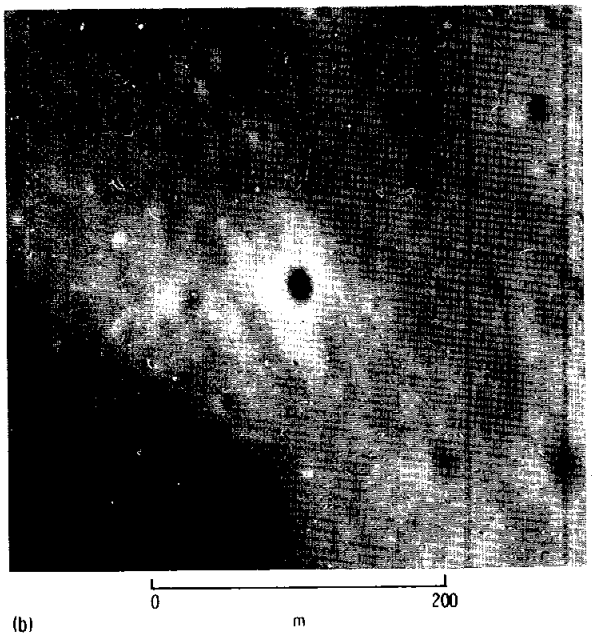
Soil breccias are rare at this site compared to previous Apollo sites, probably because most of the Apollo 16 stations were deliberately located on ejecta blankets of fresh craters where the regolith would be thin so that the underlying bedrock units could be best sampled. The part of an ejecta blanket that is composed of earlier regolith should contain soil breccias. Because of the relative ease of fracturing, however, these older soil breccia fragments should be small in size and may be concentrated in rake samples rather than in larger documented samples.

Where ejecta blankets or ray deposits are not identifiable, the average thickness of regolith in this area should be many meters. The following discussion is concerned with the identification of average regolith thickness in the landing-site area as deduced from crater shapes.

The Apollo 16 high-resolution panoramic camera photographs show that fresh craters in the 40- to 60-m-diameter range commonly are characterized by flat, blocky floors or terraces (figs. 6-10(a) and







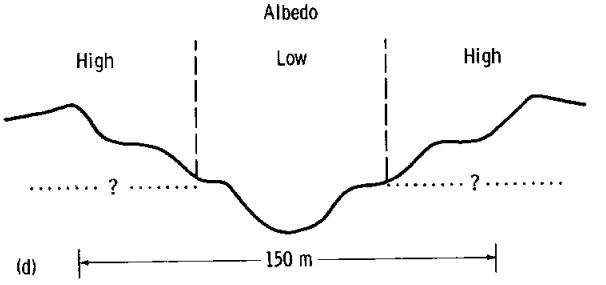
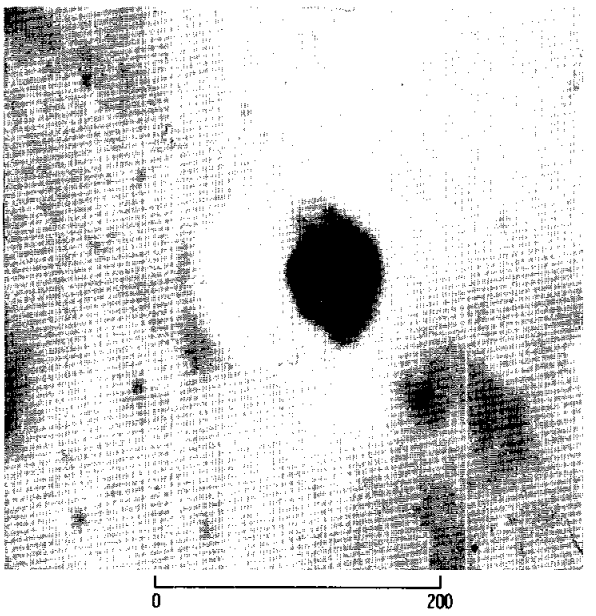
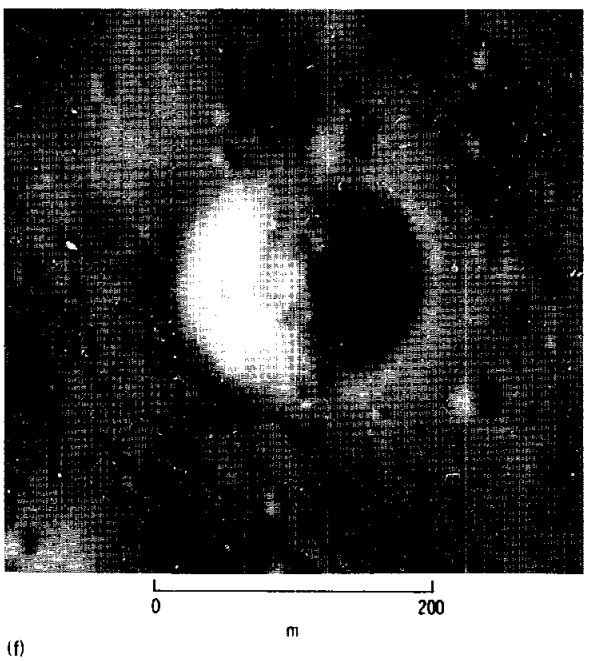


FIGURE 6-10.–Typical crater shapes at the Apollo 16 landing site. All illustrations are at the same scale. (a) Flat bottomed – Sunset Crater. (b) Concentric – terraced unnamed crater 1.3 km northeast of Haystack Crater. (c) Multiple terrace – fresh Baby Ray Crater. (d) Schematic profile through Baby Ray Crater. (e) Multiple terrace eroded – Haystack Crater. (f) Multiple terrace eroded – unnamed crater 2.8 km northeast of Haystack Crater. Refer to figure 6-4 for locations.

6-10(b)). Flat-floored craters take the form of a truncated cone and some of the floors are hummocky, suggesting the presence of blocks (ref. 6-16).



(e)



(f)

FIGURE 6-10.–Concluded.

These craters are approximately 50 to 200 m in diameter, the smaller ones having the sharper rims and more hummocky floors. The Apollo 16 crew visited only one crater that, from orbital photographs, appears to be flat bottomed (station 2, Buster Crater). The floor and part of the wall of Buster Crater are covered with angular to subangular blocks that may be derived from the substrate. This suggests that at least a local source for angular blocky material exists within approximately 10 to 15 m of the surface at this station. Terraces in craters in this size range commonly are about halfway between the floor and the rim. There are no obvious albedo changes that might be attributed to compositional differences.

A number of sharp-rimmed craters between 125 and 175 m in diameter have at least one, and locally several, concentric rings or terraces. Figure 6-10(c) illustrates Baby Ray Crater (approximately 150 m in diameter), which is the sharpest crater of this size in the region, postdating even the formation of South Ray Crater. Baby Ray is a sharp-rimmed blocky crater with apparently two terraces nested within the rim (fig. 6-10(d)). A small, sharp 25-m crater centered in the floor of Baby Ray Crater is surrounded by lower albedo deposits to the base of the first scarp, approximately 25 to 30 m from the crater center. The second terrace has a higher albedo and ranges from 10 to 20 m in width. A number of similar size craters with more subdued rims and less distinct remnants of multiple terraces appear to be more eroded versions of Baby Ray Crater (e.g., Haystack Crater, fig. 6-10(e), and the crater approximately 2.8 km northeast of Haystack Crater, fig. 6-10(f)). The topographic and albedo variations in Baby Ray Crater suggest that there may be as many as three layers within the upper 20 m of material at this site. This apparent layering may be the result of successive penetration of South Ray ejecta, local regolith, and underlying bedrock. Other examples showing that blocky ejecta blankets over regolith apparently provide layers of sufficiently different physical properties to produce terraces and concentric craters occur near the rims of craters almost 1 km in diameter such as those on Kiva, Palmetto, and Gator Craters.

Crater morphology thus suggests that the thickness of the regolith over the landing site is approximately 10 to 15 m (depth to blocky substrate). Active seismic data in the ALSEP area (sec. 10 of this

report) indicate a thickness of approximately 12 m, which is in good agreement with estimates based on crater shapes.

Station Descriptions

The LM/ALSEP station.–The LM/ALSEP station was located in five general areas (LM, ALSEP, station 10, station 10′, and the LRV parking site) ranging from approximately 70 m east to 140 m southwest of the LM (figs. 6-11 to 6-13). All five areas lie within distinct ray material ejected from South Ray Crater (fig. 6-5).

The Cayley Plains in the LM/ALSEP region are smooth but broadly undulating with a maximum relief of several meters. Approximately 2 percent of the surface is covered by 2- to 20-cm fragments, and a relatively large number of blocks as large as 0.5 m are present (fig. 6-14). The largest boulder in the LM/ALSEP sample area is several meters across. The rocks are fairly uniformly distributed, appear to be buried less than one-fourth of their height, and are poorly filleted; indeed, some appear not to be buried or filleted at all. The poorly filleted rocks are thought to represent ejecta from South Ray Crater. However, the fillet is well developed on a large rock approximately 33 m north of the ALSEP central station; this boulder may have been ejected from North Ray Crater.

The LM was situated on the western wall of a very subdued crater approximately 160 m in diameter and was 10 m west of a moderately subdued crater approximately 30 m in diameter. There are six additional very subdued craters between 150 and 240 m in diameter within a radius of 450 m from the LM (fig. 6-15). The ALSEP was situated in an intercrater area at a slightly higher elevation than that of the LM. Stations 10 and 10′ were on the western rim crest of the 160-m-diameter crater in which the LM rested.

Smaller, more youthful craters are common in the LM/ALSEP area and range from abundant 0.5- to 2-m secondaries (probably from South Ray Crater) to less frequent primary craters as large as 30 m in diameter.

Samples[1] collected in the LM/ALSEP area include coarse- and fine-grained crystalline rocks; glass; light-matrix, dark-clast breccias; and dark-matrix, light-clast breccias. Four of the five documented crystalline rocks collected at the LM/ALSEP station were from the LM and the LRV parking site areas and may be ejecta from the 30-m crater just east of the LM (fig. 6-13). Rocks sampled at the ALSEP site (fig. 6-16) include glass and white-matrix breccias. Station 10 and 10′ (figs. 6-17 and 6-18) samples were restricted to fine-grained crystalline rocks and light- and dark-matrix breccias.

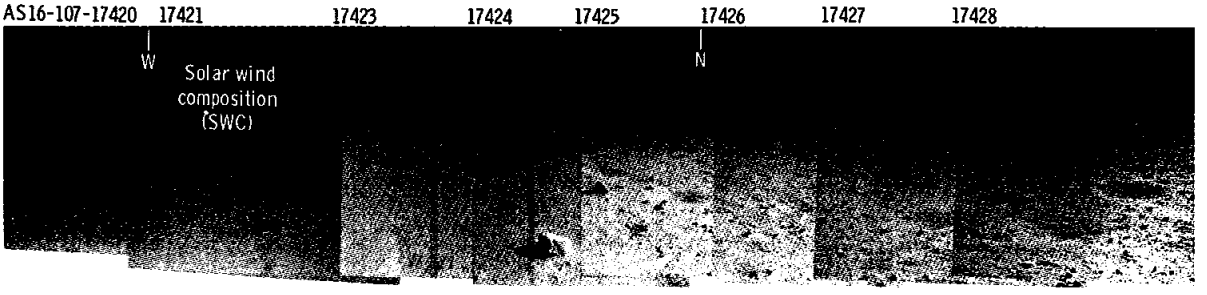


FIGURE 6-11.–Panoramic view taken north of the LM.

Many samples in the LM/ALSEP area are at least partly glass coated. Rocks range from very angular to subrounded. In general, the fine-grained chalky and crystalline rocks are smaller (6- to 12-cm range) than most breccia fragments and represent approximately 5 percent of the rocks observed.

Documentation photographs of the samples collected at the LM/ALSEP station show that the great majority of the rocks were either perched or partly buried. It is therefore assumed that most LM/ALSEP samples represent South Ray material. However, the deep core, rake, and double core samples taken at the LM/ALSEP station may contain material more representative both of North Ray Crater ejecta and of the Cayley Plain beneath the LM/ALSEP station site.

[1]Rake fragments are not included in these summaries.

The soil in the LM/ALSEP area is generally medium gray, but scattered areas of high-albedo soil are present near the ALSEP area. White soils are more abundant to the west and underlie a thin, darker layer. The soil in the LM/ALSEP area generally is moderately to very firm except in the vicinity of the ALSEP where it is exceptionally loose and powdery. This may be explained by the fact that the LM, station 10, and station 10′ are situated on the wall and rim crest of the 160-m subdued LM site crater while the ALSEP was placed on a more level intercrater area (fig. 6-15). The intercrater regions associated with very subdued 200- to 300-m craters typically have a less compact soil than the walls and rim crests of such craters (ref. 6-17).

Station 1.–Station 1 was approximately 1400 m west of the LM near the rim of Plum Crater, a 30-m-diameter crater on the rim of the 300-m-diameter Flag Crater (figs. 6-19 to 6-21). Flag Crater is approximately 50 m deep and probably penetrates through the regolith into the underlying bedrock. The crater is subdued, with only a slightly raised rim, and no rocky exposures are visible in its walls or floor.

The eastern part of the station 1 area appears to be crossed by a very faint ray from South Ray Crater (fig. 6-5), but rock fragments are less abundant than at station 2 or at the LM area (figs. 6-14, 6-22, and 6-23). Lineaments such as those in the station 2 and LM areas that are visible from orbital photographs and that are radial to South Ray Crater are absent at station 1. These observations suggest that South Ray ejecta, if present, is thin. Small, subdued craters as large as 10 m in diameter are common in the area.

Rocks larger than approximately 10 cm cover less than 1 percent of the surface. A number of rocks in the photographs appear to be angular to subangular and are only slightly buried; these are interpreted to be ejecta from South Ray Crater. A number of the

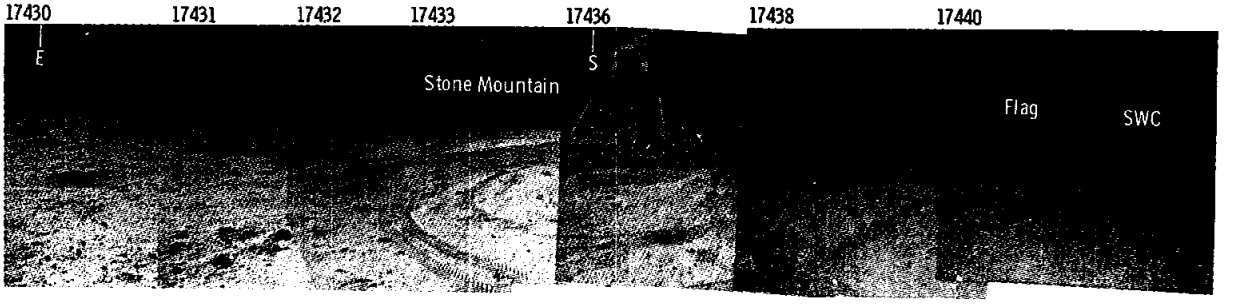


FIGURE 6-11.–Concluded.

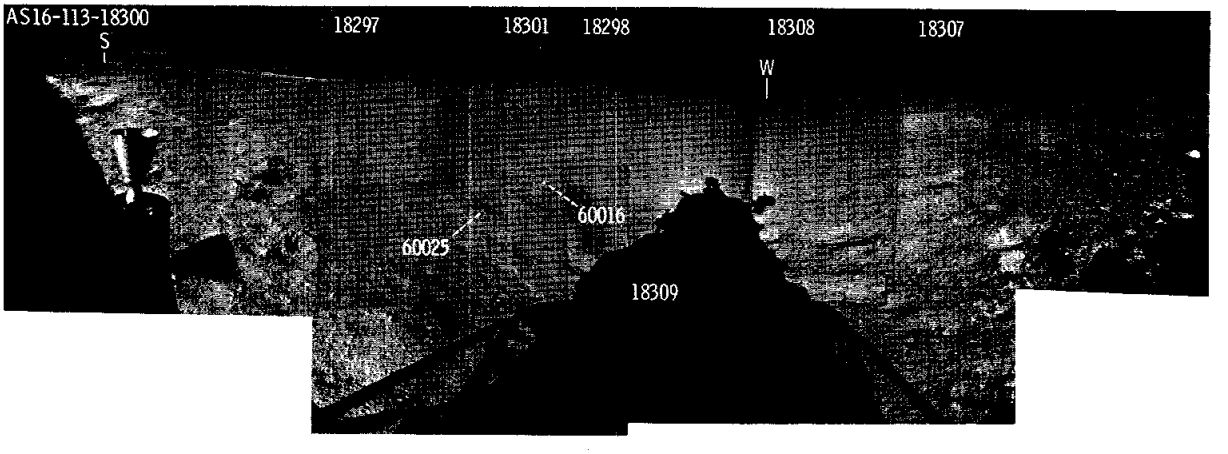
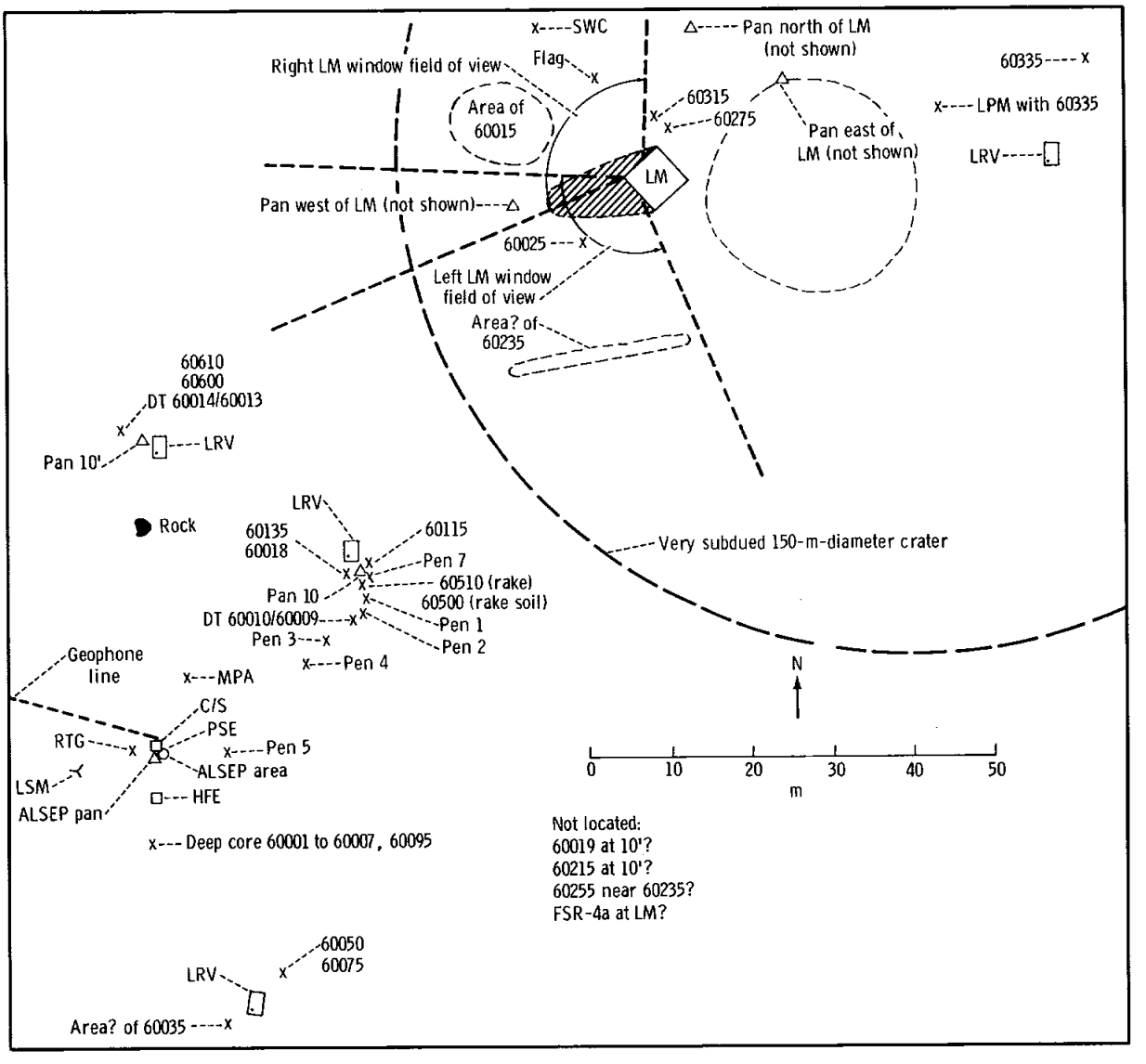


FIGURE 6-12.–Partial panorama taken from the LM windows.



Explanation

	Crater rim	C/S	Central station
	Boulder	PSE	Passive seismic experiment
x 67012	Sample number	LSM	Lunar surface magnetometer
DT	Drive tube	HFE	Heat flow experiment
△ P pan	Partial panorama	RTG	Radioisotopic thermoelectric generator
△	Panorama	MPA	Mortar package assembly
	LRV; dot shows television camera	LPM	Lunar portable magnetometer
x Pen 5	Penetrometer reading	SWC	Solar wind composition
FSR	Football-size rock		

FIGURE 6-13.–Planimetric map of the LM/ALSEP area.

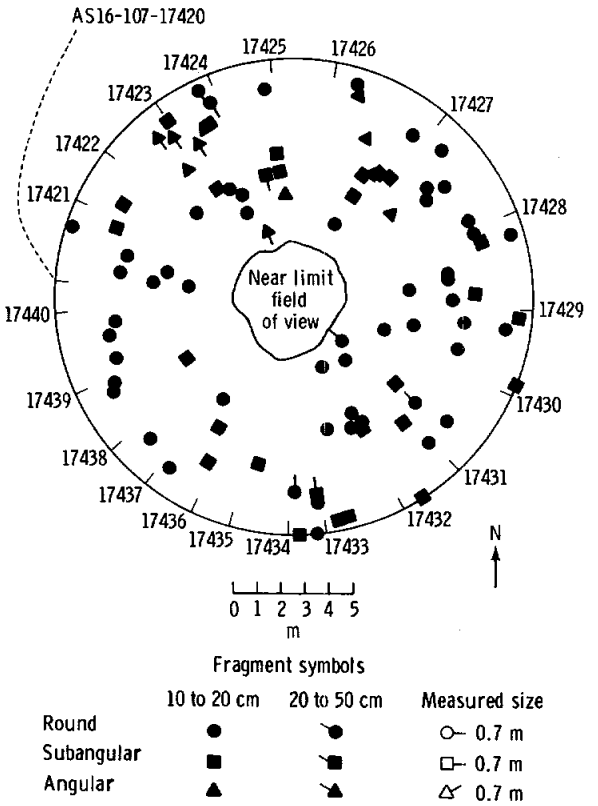


FIGURE 6-14.–Rock distribution within 10 m of the panorama north of the LM.

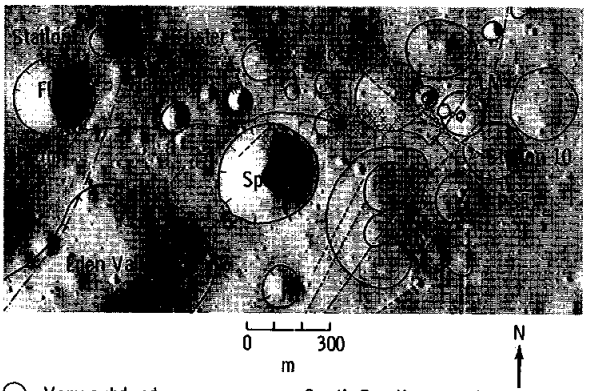


FIGURE 6-15.–The LM/ALSEP area showing moderately fresh to very subdued craters that may have influenced the distribution of samples collected (part of Apollo 16 pan camera frame 4618).

returned samples, however, appear rounded and eroded; these were probably ejected from older craters in the area. Both angular and eroded samples were collected (figs. 6-24 and 6-25).

The documented samples collected at station 1 include fine- and coarse-grained crystalline rocks; glass; light-matrix, dark-clast breccias; dark-matrix, light-clast breccias; and breccias containing nearly equal proportions of light and dark clasts in a medium-gray matrix. Sample 61295, a medium-gray-matrix breccia, was collected from a 1-m rounded and filleted boulder (fig. 6-26). Because of the large size of the boulder and its proximity to the rim, Flag Crater is the most likely source. The boulder may be representative of the local bedrock.

At two places on the rim of Plum Crater, the astronauts noted white regolith beneath a top layer of gray material 1 to 2 cm thick. At one of these places, the light material lay beneath the gray on the fillet of the large boulder (fig. 6-27). This suggests that the fillet was formed by either of two mechanisms: (1) deposition of light material followed by postfillet deposition of a thin, dark layer; or (2) deposition of light material followed by a period of time during which the upper part of the light material was darkened.

A distinct but smooth and somewhat subdued bench occurs in Plum Crater approximately 3 m below the surface. No outcrop is visible, but the bench is sufficiently distinct that it probably represents a change in cohesion of the materials in the walls of the crater. It may reflect the contact between Flag ejecta and raised bedrock in the eroded rim of Flag Crater.

Because of the depth of penetration by Flag Crater and the relative scarcity of South Ray ejecta, samples from station 1 have the highest probability of being material representative of the upper units of the subjacent bedrock of the Cayley Plains. However, some South Ray material is present, and the contribution of ray material from older large craters such as North Ray and Palmetto cannot presently be assessed.

Station 2.–Station 2 was located approximately 550 m west of the LM just north of Spook Crater, which is approximately 400 m in diameter, and on the southern rim of Buster Crater, which is approximately 90 m in diameter (figs. 6-28 and 6-29).

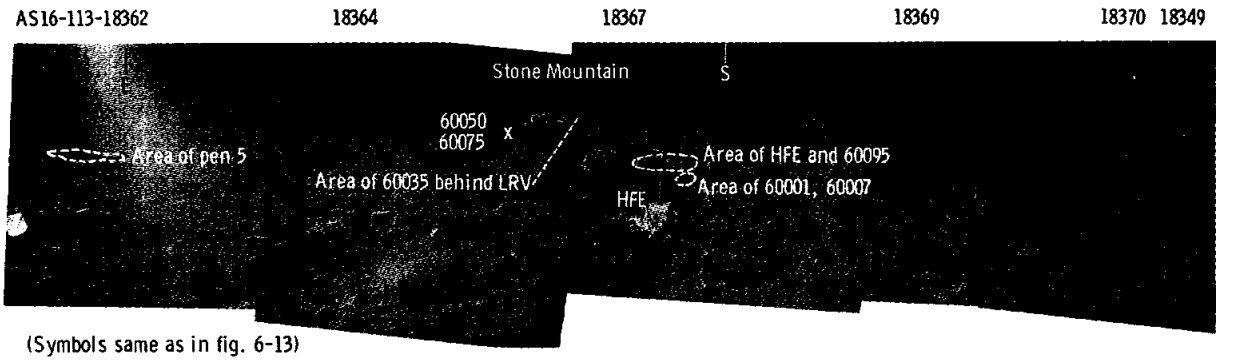


FIGURE 6-16.–Panoramic view taken near the central station of the ALSEP.

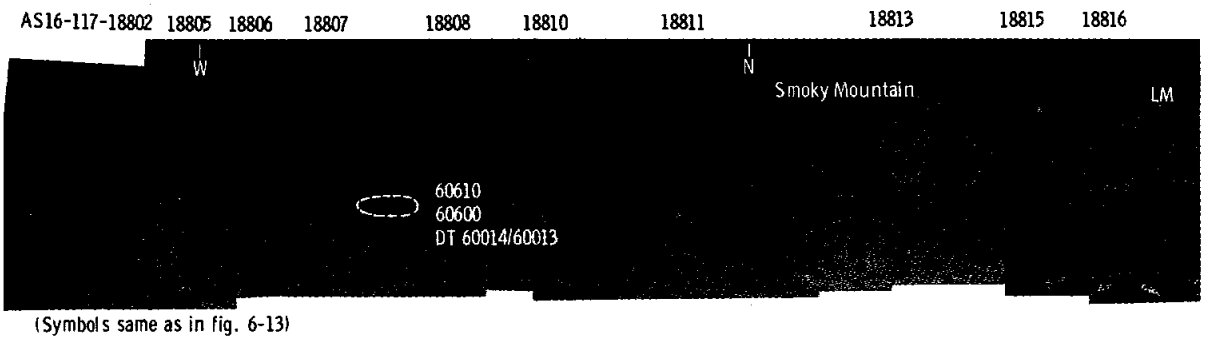


FIGURE 6-17.–Panoramic view taken at station 10.

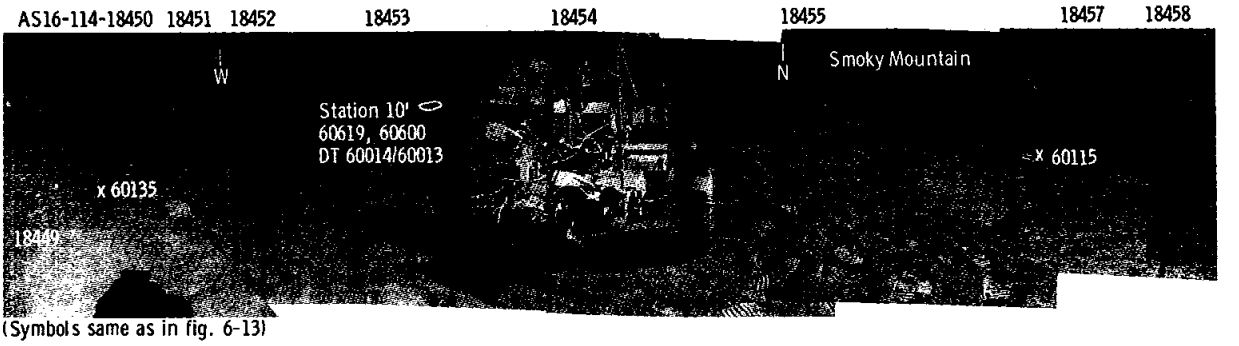


FIGURE 6-18.–Panoramic view taken at station 10'.

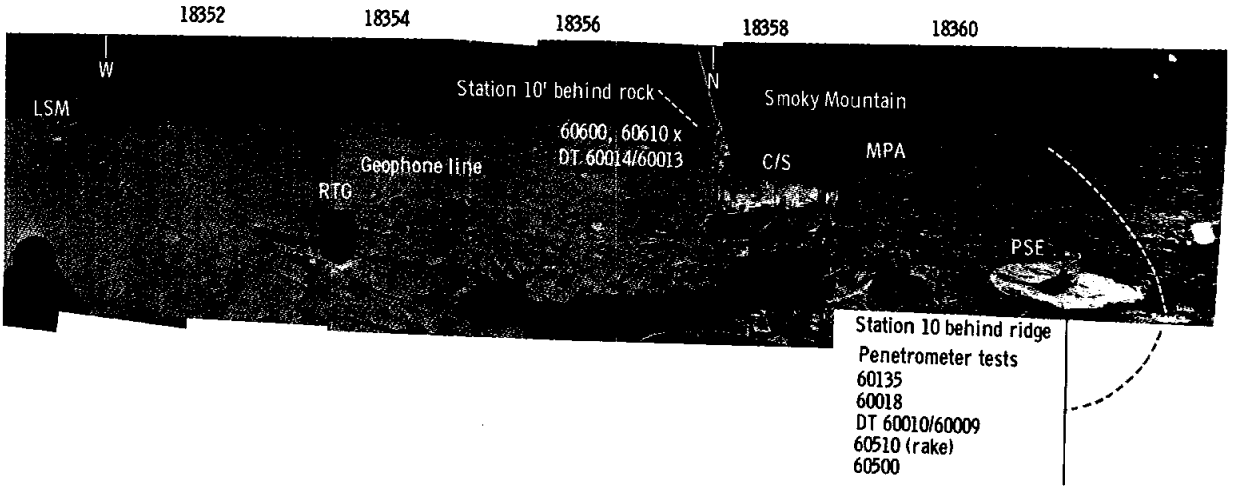


FIGURE 6-16.–Concluded.

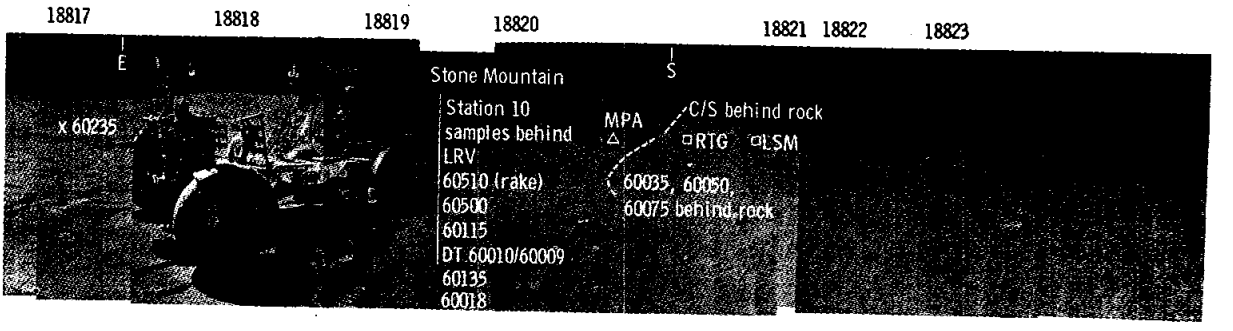


FIGURE 6-17.–Concluded.

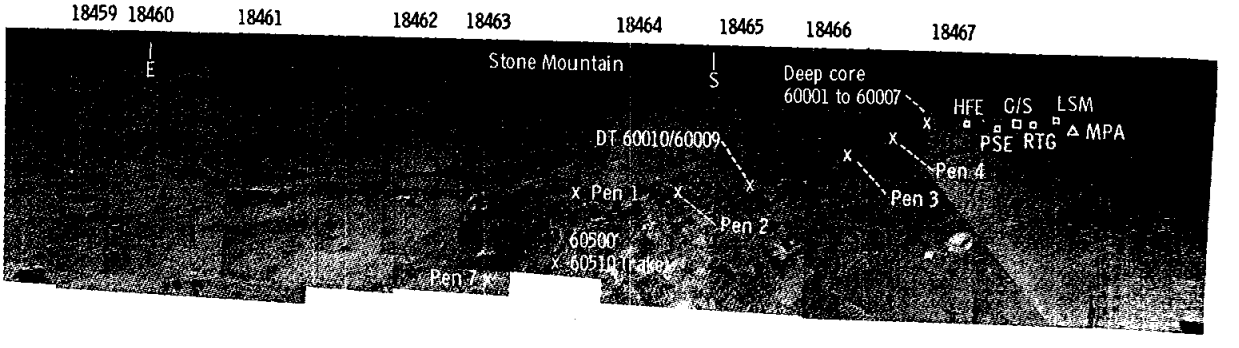


FIGURE 6-18.–Concluded.

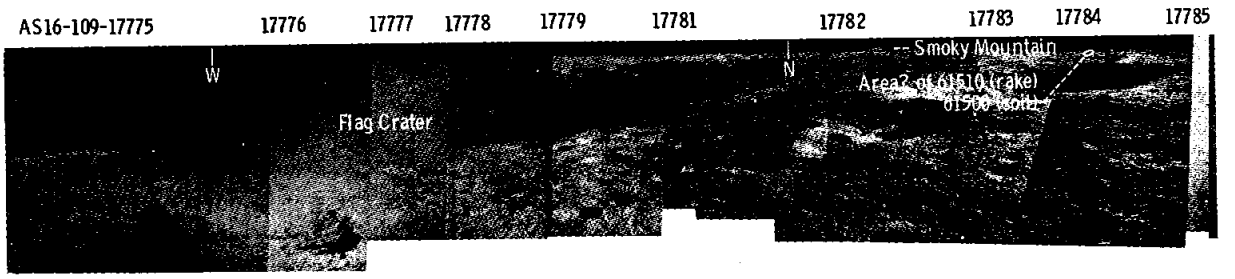


FIGURE 6-19.–Panoramic view taken northeast of station 1.

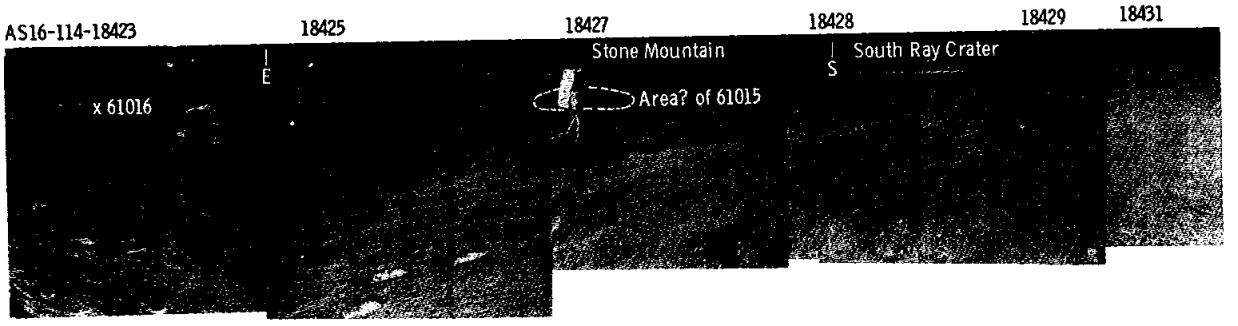


FIGURE 6-20.–Panoramic view taken southwest of station 1.

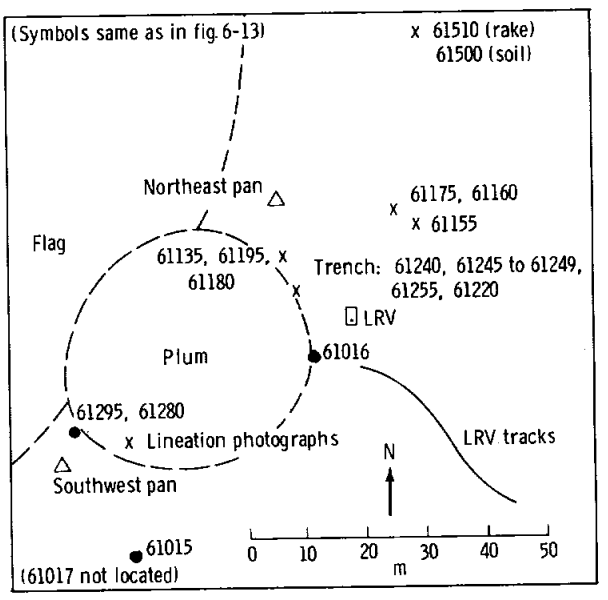
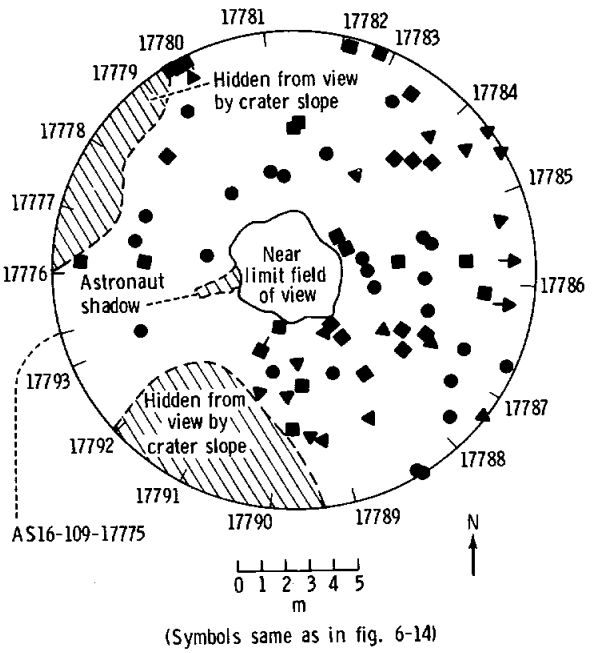


FIGURE 6-21.–Planimetric map of station 1.



(Symbols same as in fig. 6-14)

FIGURE 6-22.–Rock distribution within 10 m of the station 1 northeast panorama.

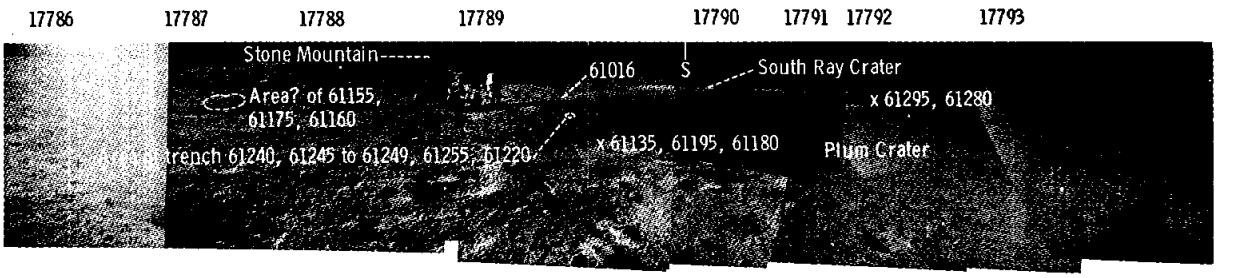


FIGURE 6-19.–Concluded.

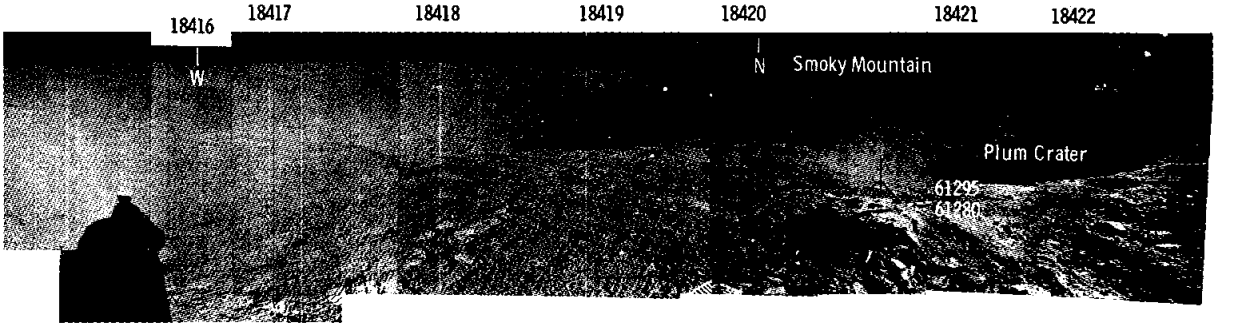
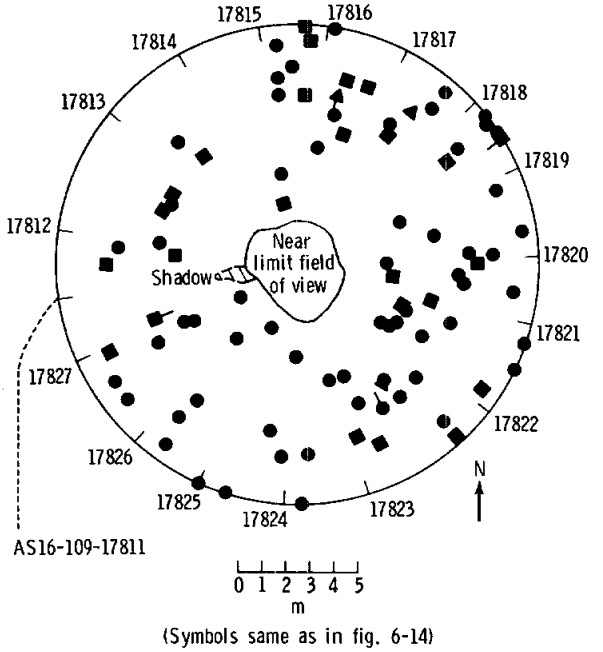


FIGURE 6-20.–Concluded.



(Symbols same as in fig. 6-14)

FIGURE 6-23.–Rock distribution within 10 m of the station 2 panorama.

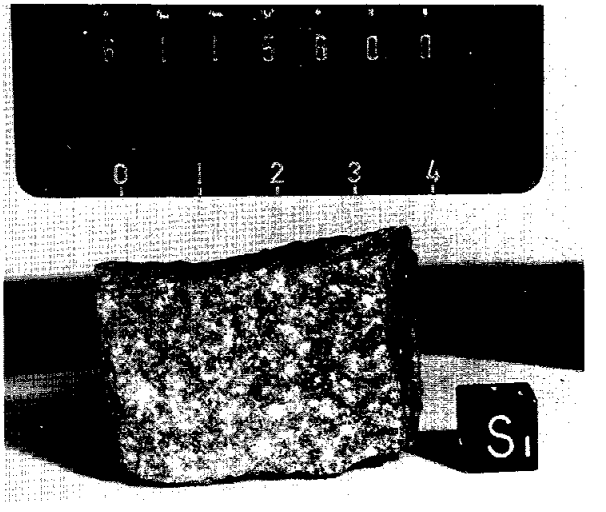


FIGURE 6-24.–Sample 61156, an angular rock (S-72-38391).

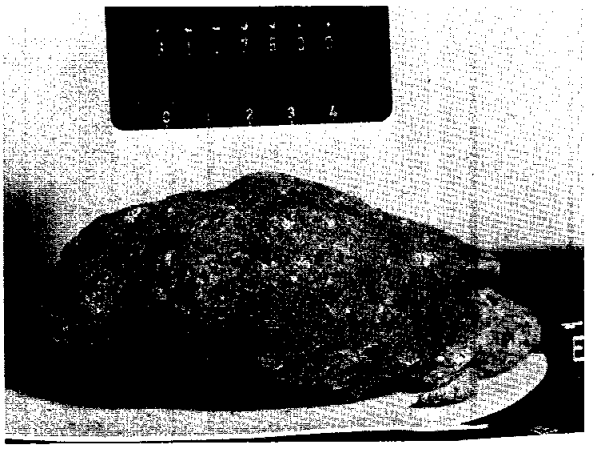


FIGURE 6-25.–Sample 61175, an eroded rock (S-72-39285).

The area is crossed by a faint ray of light albedo material that is apparently derived from South Ray Crater. Subdued, grooved lineaments radial to South Ray Crater also cross the area (fig. 6-15). Fragments as large as 0.5 m but mostly 5 to 10 cm are scattered more or less evenly around the station area and cover 2 to 3 percent of the surface (fig. 6-23). Most fragments are angular and are perched on the surface or buried only slightly. Fillets are not abundant; the overall impression is that the fragment population is fairly young. The faint ray, the lineaments, and the apparent freshness of the fragment population suggest that the area is blanketed by South Ray Crater ejecta.

Rock types as represented by surface textures of the fragments appear to include both friable and coherent rocks. The hand-sample-size rocks collected at station 2 include fine-grained crystalline rocks and light-matrix breccias.

The soil is medium gray except for an underlying light-colored material where the LRV was parked. The compaction and granularity are typical of most of the lunar soil elsewhere in the area. Small craters as large as 2 m in diameter are distributed fairly uniformly; they are generally subdued but a few, small, fresh ones have sharp rims with identifiable ejecta.

Spook Crater is symmetrical with a slightly raised rim but is otherwise subdued, with no apparent rock exposures in the walls and no visible deposits of ejecta. Buster Crater is approximately 100 m north of Spook Crater and is superposed on its outer rim. The rim of Buster Crater is fairly sharp and Buster ejecta



FIGURE 6-26.–Large, filleted boulder showing location of sample 61295 (AS16-114-18412).

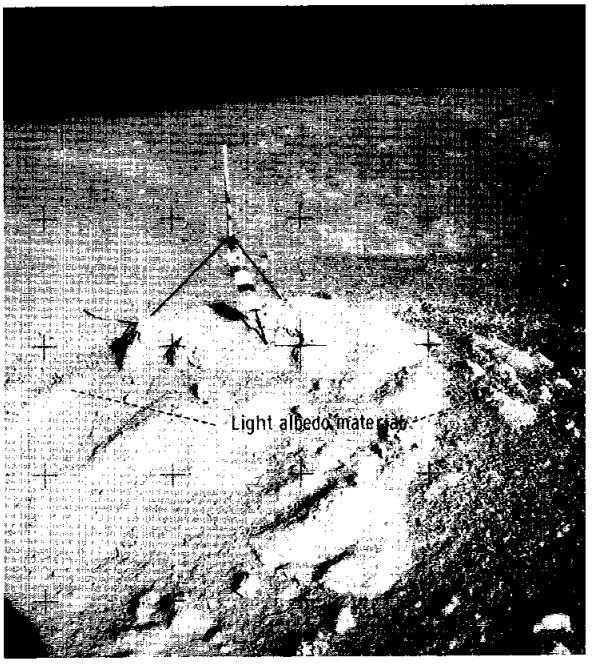


FIGURE 6-27.–Large, filleted boulder showing white regolith kicked by astronauts (AS16-109-17802).

are barely visible in the panoramic photographs (fig. 6-28). The floor and part of the walls of Buster Crater are covered by blocky debris that the crew reported trends northeast across the floor of the crater. The rocks are as wide as 5 m and are angular in shape. There is a suggestion of northeast-trending planar structures within the blocks (fig. 6-30) and a parallel organization of the blocks. Both structures appear to have a northward dip.

Buster Crater appears too young to be a secondary from any primary crater in the region, with the possible exception of South Ray Crater. Its relatively large size, compared to South Ray Crater secondaries, and its long distance from South Ray Crater make a secondary origin for Buster Crater unlikely. It is therefore interpreted to be a primary crater.

The distribution of blocks in Buster Crater suggests that it either penetrated a large block in the regolith in the eastern part of the crater or that it penetrated bedrock (fig. 6-31). If it is bedrock, the northward dip of the structures in the blocks may be related to expected radial dips in the flanks of Spook Crater. The bench in the blocky part of the wall of Buster Crater may represent a strength change between regolith and bedrock. Small, shallow, irregular gouges in the crater wall were probably formed as a result of impact uplift of blocks to small heights (fig. 6-30). Samples collected near the rim of Buster Crater may be either South Ray or Buster ejecta or both.

Stations 4, 5, and 6.–Stone Mountain (fig. 6-32) is a westward projection of the Descartes highlands into the southeastern part of the landing area. The mountain rises approximately 540 m above the Cayley Plains and is domical in form. Major though subtle step and bench topography parallels the slope of Stone Mountain, and a north-northwesterly trending crease interrupts its domical form. The Apollo 16 panoramic photographs show linear features trending parallel to the major crease.

Albedo contrasts appeared to coincide with the benches in premission studies. Such contrasts were not corroborated in the oblique photographs from surface operations, probably because of the low angle of incidence of the Sun combined with low contrast. The regolith is loosely packed and is characterized by the "tree bark" texture seen in many other areas studied on the Moon. This texture is commonly enhanced out of proportion to its real scale (fig. 6-32(a)). In places, a shadow reinforcement effect is seen as closely spaced lines on oblique photographs (fig. 6-32(b)).

The largest craters on Stone Mountain include Crown (100 m in diameter) and two unnamed craters. One of the unnamed craters, 2.3 km to the east of Crown Crater, is 80 m in diameter and the other, 1.3 km to the south-southeast, is 140 m in diameter (fig. 6-4). The majority of craters, however, range from 50 m down to the limit of resolution. The crater density on Stone Mountain is qualitatively the same as that seen in the adjacent Cayley Plain, but craters larger than 100 m are more abundant in the Cayley Plain than on Stone Mountain (fig. 6-4). Furthermore, no resolvable primary craters on Stone Mountain appear to be younger than South Ray and Baby Ray Craters. Crown is a relatively youthful crater, but the remainder, in all size populations, are notably degraded.

As much as 2.3 percent of the traverse area (and of the adjacent area photographed in detail) is sprinkled with blocks in the 10- to 100-cm size range (table 6-I, figs. 6-33 and 6-34) and with smaller blocks down to the limit of resolution (4 cm). The crew observed that blocks in the less-than-30-cm size range are the most abundant. Their observation is confirmed by block counts made from the station panoramic surface photographs (figs. 6-35 and 6-36). The plots of differential distribution of blocks (fig. 6-35) and cumulative size frequency (fig. 6-37) indicate that blocks in the less-than-10-cm size range are the most abundant at stations 5, 6, and probably 4; however, anomalous distribution is indicated for station 4 that is probably attributable to a relatively heavy concentration of ray material there. The number of blocks at all stations is inversely proportional to size (fig. 6-35). At station 5, the blocks appear to be distributed bimodally into 5- to 10-cm and 10- to 30-cm ranges. Blocks range from well rounded to angular, but most are of intermediate shape (fig. 6-36). Block angularity (shape) and size, estimated from surface panoramic photographs, when considered on a direct-count basis, have an apparent spatial relationship to the stations that are disposed more or less radially to Stone Mountain (table 6-I, fig. 6-36). Local concentrations of blocks are found especially on the east sides and rims of craters facing away from South Ray Crater (fig. 6-34). It is presumed that these blocks were contributed largely from South Ray Crater and that an appreciable fines fraction accompanied them.

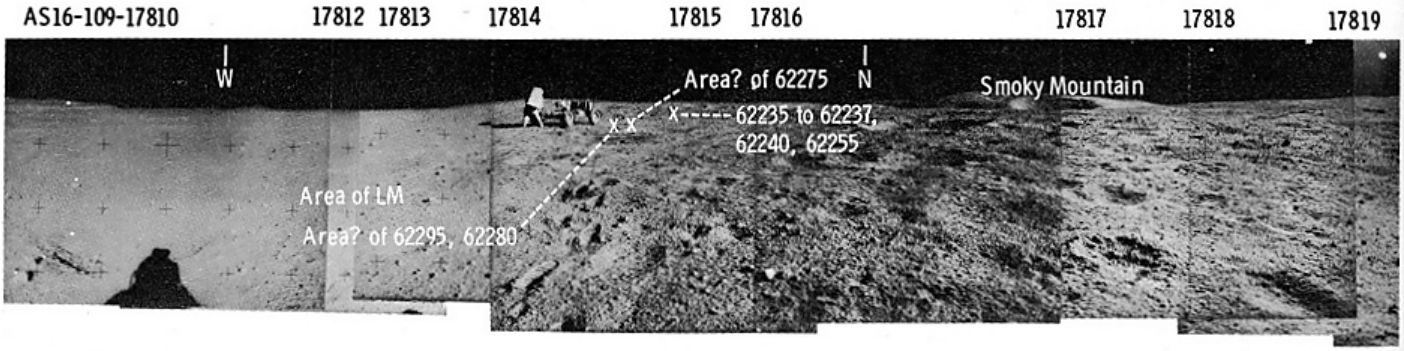


FIGURE 6-28.–Panoramic view taken at station 2.

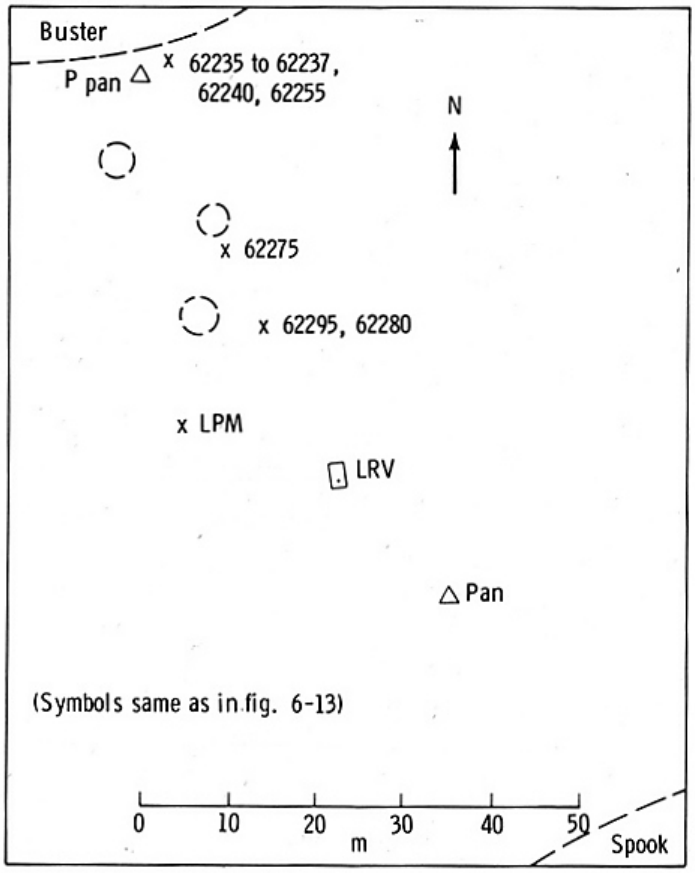


FIGURE 6-29.–Planimetric map of station 2.



FIGURE 6-30.–Partial panorama of Buster Crater at station 2 (AS16-109-17828 to 17836).

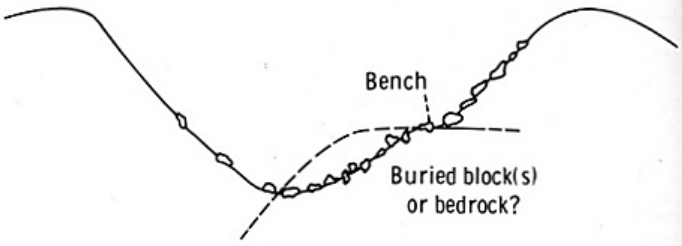


FIGURE 6-31.–Diagrammatic section across Buster Crater at station 2.

The blocks can be divided into light and dark varieties, some of which appear to be breccias. Blocks range from angular to well rounded, with or without fillets (figs. 6-38 and 6-39). A few blocks are notably rhombic and contain well-defined fractures. A few blocks are perched. Generally, the well-rounded rocks are filleted, and the incidence of fillets increases from station 4 toward station 6. The fillets are not recognizably asymmetrical.

The thickness of the regolith on Stone Mountain, based on crater shapes, is similar to that on the Cayley Plains. The surface of the regolith is relatively smooth and undulating. The upper portion of the regolith here is probably appreciably diluted by South Ray Crater material.

Station 4 marked the highest point reached on Stone Mountain, and samples were collected from two separate localities (fig. 6-33). The LRV was parked between two subdued, shallow craters approximately 15 m across. The predominant rock type in the area is apparently breccia, and clasts are readily visible in some of the blocks photographed; the samples collected confirm this interpretation. Within

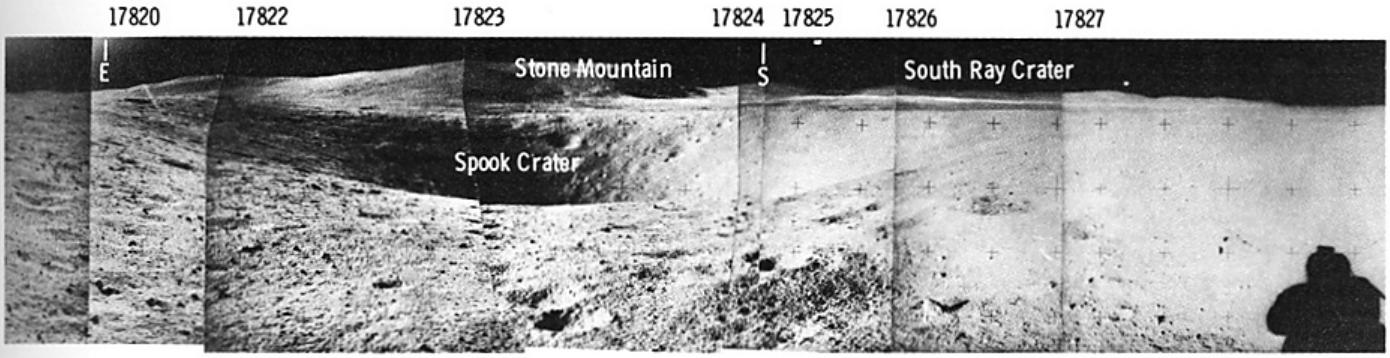


FIGURE 6-28.–Concluded.

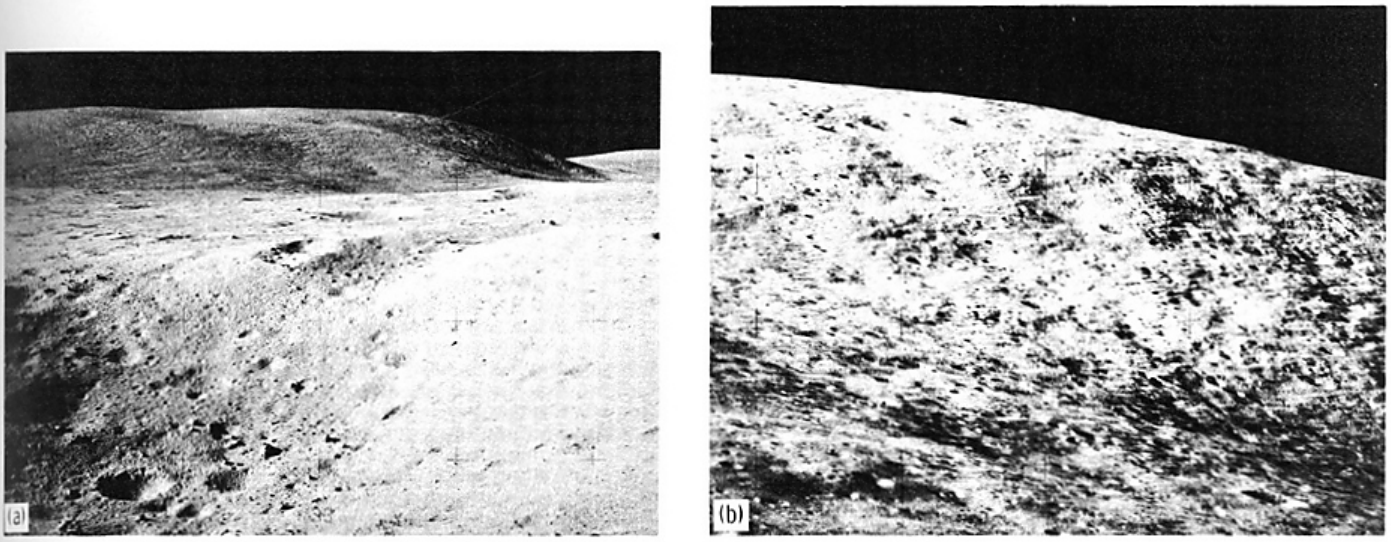


FIGURE 6-32.–Stone Mountain. (a) Profile showing "tree bark" texture (AS16-113-18325). (b) Crest of Stone Mountain showing closely spaced lines of shadows (AS16-112-18217).

the doublet crater, rocks are much less numerous on the southwest wall, which was shielded from South Ray Crater ejecta. The regolith surface is gray, but white material similar to that in the Cayley Plain regolith at station 1 occurs near the rim of the crater at a depth of about a centimeter. A trench in the floor of the crater, however, exposed no white soil or evidence of layering. Four penetrometer measurements and a drive tube indicated that the material was unconsolidated to depths of at least 75 cm, but at one location (penetrometer 3), progressive resistance suggested that more indurated regolith was reached or that a buried rock was approached. The angular, perched appearance of the blocks near the LRV suggests derivation from South Ray Crater. Preliminary examination of the rocks indicates that light-matrix, dark-clast and dark-matrix, light-clast breccias are predominant, with some fine-grained rocks.

The second sampling site was at a 20-m crater to the southwest. Angular blocks are concentrated on the northeast wall and rim of the crater, apparently continuous with a well-defined strip of blocks to the northeast. The remainder of the crater rim is relatively block free. Soil and rake samples consisting mainly of friable, poorly consolidated clods were collected from the west rim. No white soil or evidence of layering was found beneath the surface at this location. The blocks on the northeast wall of the crater are apparently breccias with large white clasts in dark matrices and are probably ejecta from South Ray Crater. The strongly asymmetric distribution of these blocks within the crater, the lack of recognizable ejecta elsewhere around the crater, and the relatively large size of the crater suggest that it probably is not of secondary origin but was formed before South Ray Crater and was subsequently mantled by ray materials. The indurated regolith

TABLE 6-I.–Block Density and Shape Distribution in the Size Ranges of 10 to 20, 20 to 50, and 50 to 100 cm at Stations 4, 5, and 6

Parameter	Size range, cm				Shape			
	10 to 20 (0.0176)[a]	20 to 50 (0.0962)[a]	50 to 100 (0.4420)[a]	Total	Angular	Intermediate	Rounded	Total
Station 4								
No. of blocks	122	32	1	155	40	71	44	155
Area, m^2	2.1472	3.0784	.4420	5.6676				
Percent of surface area	.75	1.08	.15	2.0	25.8	45.8	28.4	100
Area seen, m^2				282.67				
Blocks/m^2 X 100	43.2	11.3	.3					
Station 5								
No. of blocks	189	21	1	211	30	113	68	211
Area, m^2	3.3264	2.0202	.4420	5.7886				
Percent of surface area	1.34	.81	.17	2.3	14.2	53.6	32.2	100
Area seen, m^2				246.87				
Blocks/m^2 X 100	76.6	8.5	.4					
Station 6								
No. of blocks	104	8	1	113	12	71	30	113
Area, m^2	1.8304	.7696	.4420	3.0420				
Percent of surface area	.66	.27	.16	1.1	10.6	62.8	26.6	100
Area seen, m^2				275.87				
Blocks/m^2 X 100	37.7	2.9	.4					

[a]Mean circumferential area in square meters.

samples from the block-free rim of the crater may thus have been partly derived from underlying Descartes materials and reworked by local impacts; however, cursory sample examination shows no obvious differences between these rocks and larger samples collected near the LRV.

Station 5, downslope and approximately 0.5 km from station 4, was on a topographic bench that was approximately 50 m wide and that sloped north approximately 5°; the LRV was parked near the rim of a 20-m crater (figs. 6-40 and 6-41).

Large angular blocks are scattered sparsely around the crater, but 10- to 15-cm cobbles and smaller fragments are abundant (fig. 6-42). Block shapes are mainly subangular to subrounded, but some cobbles and small fragments are well rounded and a few very angular, platy fragments are also present. Fillets occur around some rounded cobbles; some rocks are partly buried, others perched. Among the samples collected at station 5 are fine-grained crystalline rocks; light-matrix, dark-clast breccias; a single dark-matrix, light-clast breccia; and a glass sample. All but two of the rocks from station 5 have significant glass rinds, and vesicular glass forms a major component of some samples. Such glass is thought to be impact melt, and these samples probably were ejected from South Ray Crater. Soil samples are characteristically gray, although lighter soils were present beneath a gray surface at one locality. Blocks are asymmetrically distributed within the crater. There are very few blocks on the southwest wall, which apparently was shielded from South Ray ejecta. The gray soil samples from steep parts of this wall may include regolith derived from underlying Descartes materials, but the fragments are apparently similar to the larger samples.

Station 6 was near the base of Stone Mountain on the Cayley Plain (figs. 6-43 and 6-44). The surface is scarred by numerous small shallow craters, with only a few as large as 10 m. Angular blocks as large as 0.5 m are scattered throughout the area, but rocks and cobbles of 5 to 15 cm are most common (fig. 6-45). The rock distribution within the subdued 10-m crater at the LRV is apparently asymmetric; in the crater at station 5, rocks are very sparse on the southwest wall. The rocks described and photographed exhibit a wide variety of shapes and sizes, ranging from angular to

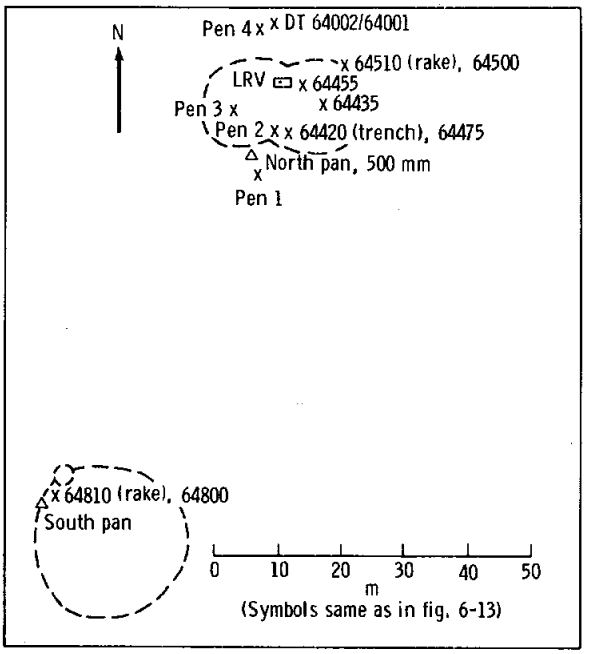


FIGURE 6-33.–Planimetric map of station 4.

rounded and from pebble size to as large as 0.5 m. Angular, glass-coated blocks are strewn over much of the surface. White clasts are common in many of these rocks, suggesting that breccias are predominant. Fillets are moderately developed around some rocks, and several rocks appear to be partly buried whereas others are clearly perched. A unique white "splotch" of indurated soil was collected from the southwest wall of the crater, but the regolith elsewhere was apparently gray throughout. The large, angular blocks in this vicinity are probably ejecta from South Ray Crater. Medium-gray-matrix breccias closely resemble those collected at station 1.

The apparent prevalence of ray materials from South Ray Crater at stations 4 and 5 and the similarities of the samples to those collected elsewhere within the ejecta of South Ray and North Ray Craters suggest that the specimens from Stone Mountain may represent only the Cayley Formation and that underlying Descartes bedrock may not have been sampled. Alternatively, both plains and highlands may be accumulations of similar breccias.

Stations 8 and 9.–Station 8 was located near two 15- to 20-m craters (figs. 6-46 and 6-47) on a bright ray from South Ray Crater approximately 2.8 km south-southwest of the LM. Station 9 was just south of a 50-m crater (figs. 6-48 and 6-49) northeast of station 8 in an area of lower albedo. The surface in the station 8 and 9 area is gently undulating with a northeasterly slope of a few degrees. The regolith is moderately firm away from small crater rims. The depth of penetration of the bootprints and LRV tracks is generally 2 cm or less. The soil is medium gray throughout, with no noticeable light layer under the surface.

Between 1 and 3 percent of the surface at station 8 is covered by fragments 1 cm and larger. The largest blocks (1 to 2 m) are few and scattered (fig. 6-50). The blocks increase in size and abundance between stations 8 and 9 but decrease again at station 9 (fig. 6-6). In the station 9 area, the abundance of blocks is somewhat less than at station 8 (fig. 6-51).

Four meter-size boulders were sampled in the station 8 and 9 area. Samples from two boulders at station 8 are dark-matrix breccias, and samples from a third boulder are fine-grained crystalline rocks (fig. 6-52). The meter-size boulder at station 9 is a dark-matrix, light-clast breccia. A chip collected from the bottom of this boulder is a coarse-grained crystalline rock (fig. 6-53). A small fragment collected from the surface at station 8 is a light-matrix breccia with dark clasts.

The dark breccias, which comprise approximately 75 percent of the blocks at both stations 8 and 9, are generally rounded, although some subrounded to subangular blocks are present. Most are partly buried, although they range from perched to nearly completely buried. A few blocks have poorly developed fillets on all sides. Well-developed fillets can be seen on the uphill side of blocks lying on the inside walls of larger craters. The light-colored crystalline rocks in the station 8 and 9 area are generally subrounded, with a number of rounded smaller fragments. Most rocks are partly buried although several appear to be perched on the surface. Fillets are generally absent to poorly developed.

There is an abundance of subdued craters as large as 3 m in diameter in this region. Most have slightly raised, rounded rims. Several of the craters at station 8 have concentrations of blocks on the northeast rims, and a few of these are somewhat elongate in a northeast-southwest direction (fig. 6-54). A 15-m crater southeast of the panorama site at station 8 has a concentration of blocks that begins in the center and continues out of the crater in a northeast direction for at least one crater diameter (fig. 6-55). The same pattern occurs in a slightly larger crater to

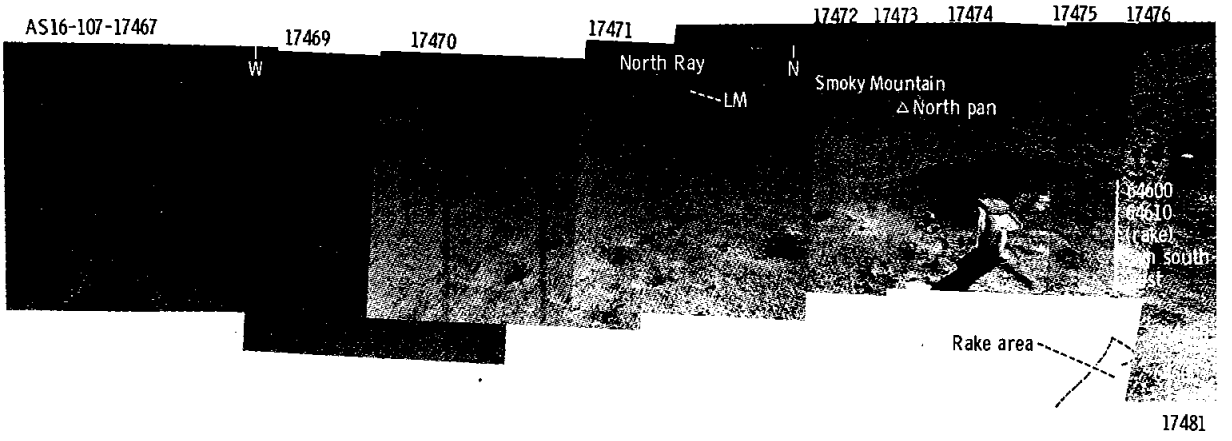


FIGURE 6-34.—Panoramic view taken south of station 4.

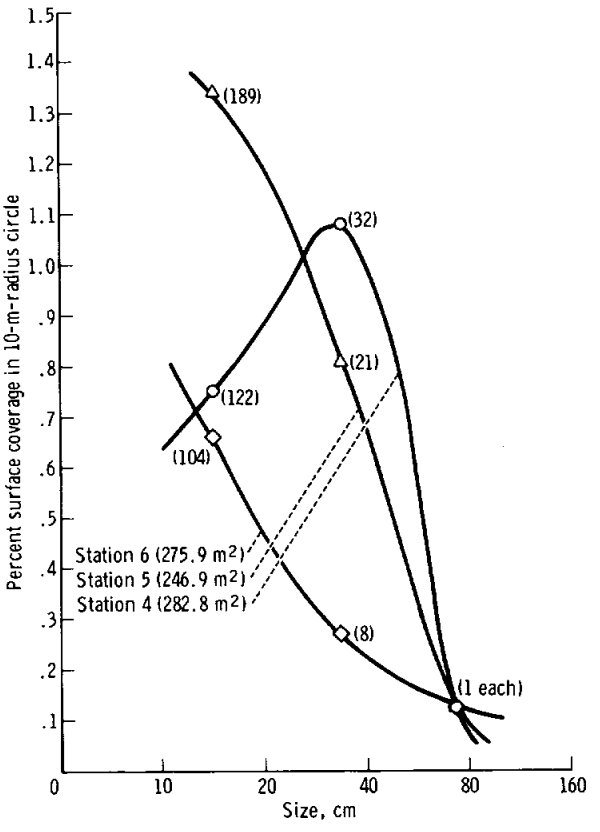


FIGURE 6-35.—Differential distribution of blocks in the size ranges of 10 to 20, 20 to 50, and 50 to 100 cm at stations 4, 5, and 6. Numbers near symbols show number of blocks counted in size range; numbers on curves show actual areas within 10-m-radius circles counted.

the north. Because of their large size and subdued rims as compared to the fresh block trains, both craters appear to predate overlying South Ray ejecta.

The general appearance and distribution of blocks and secondary craters at both stations strongly suggest that most of the surface material is ejecta from South Ray Crater. However, there is evidence for both younger and older material in the region. A few small, very fresh craters can be seen that may be secondaries from the Baby Ray event, and several small, angular fragments (both light and dark) that may have been derived from Baby Ray Crater are perched on the surface. A few very well-rounded and well-filleted blocks are probably older than South Ray Crater. Therefore, it seems probable that the drive tube at station 9 penetrated the South Ray ejecta and sampled older regolith below.

Stations 11 and 13.—For the first time in lunar exploration, a large young crater was investigated along its rim crest, walls, and continuous ejecta blanket and was extensively photographed and sampled. North Ray Crater, 900 to 950 m across, lies on a 50-m-high ridge at the western edge of Smoky Mountain near the eastern boundary of the Cayley Formation in this area (fig. 6-56). The geologic importance of North Ray Crater lies in its youth and in the depth of penetration (160 to 200 m) into materials underlying the Cayley Plains.

The abundance of blocks on the rim of North Ray Crater was less than had been anticipated, although the size of some of the blocks makes them the largest

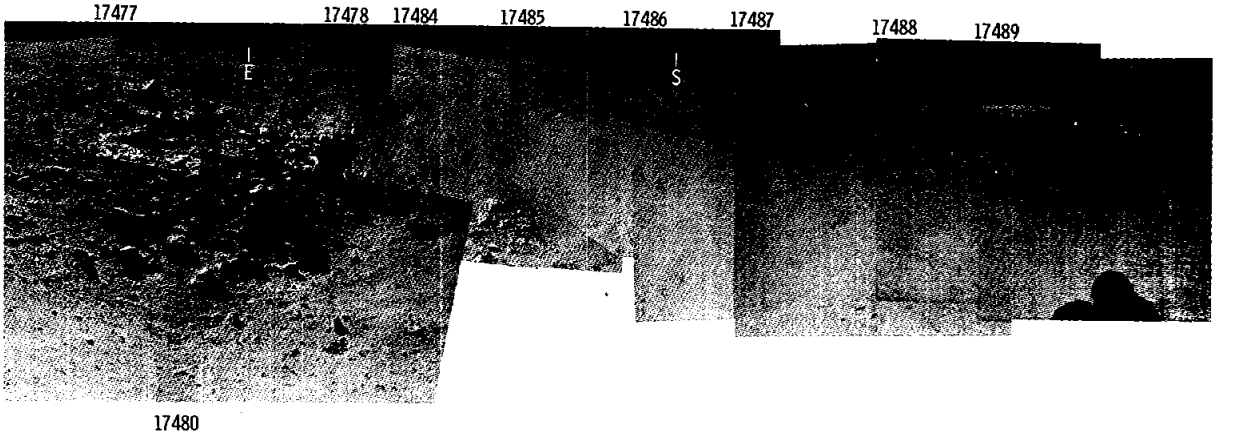


FIGURE 6-34.—Concluded.

investigated so far on the Moon. The blocks are as large as 12 m high by 25 m long (fig. 6-57) and are coarse breccias of two general types. Dark-matrix breccias have pronounced jointing and angular edges (figs. 6-57 and 6-58); light-matrix boulders are distinctly more rounded, more poorly jointed, and deeply filleted (fig. 6-59). Boulders larger than several meters are rare and stand out in far-field views because of the very small population of boulders one to several meters in size. Blocks smaller than 1 m are relatively abundant with notable increases around fresh craters 25 m in diameter and larger. A sharp increase in boulder density (1 meter and less in diameter) occurs at the rim crest and continues down the crater walls as illustrated in figure 6-60.

The distribution of craters superposed on the North Ray Crater rim is random and the density is very low (fig. 6-61). Few craters larger than 25 m are observed and very few are recognized in the surface photographs even in the several-meter class. The random distribution and low density presumably reflect the relative youth of the crater. The paucity of smaller craters, however, may reflect both the youthfulness of the crater and a thin regolith over a coherent subsurface unit. This suggests that hypervelocity impacts have sufficient energy to form a crater in the resistant substrate and that secondary impacts would not.

Samples collected on North Ray Crater rim (figs. 6-62 to 6-65) and outlying ejecta (figs. 6-66 to 6-68) consist of a variety of breccias, some of which are glass coated and glass veined, and a few crystalline rocks. Surface photographs permit separation of most rocks in the near field into light and dark rocks, some having recognizable fragmental textures. Most of the light rocks are breccias with light matrices, and the dark rocks are breccias with dark matrices. Other types include light-gray crystalline rocks and glass-coated and glass-veined rocks. The glass coating covers 80 to 100 percent of some rocks and doubtless obscures the real character of some rocks seen in the surface photographs. The relative proportions of

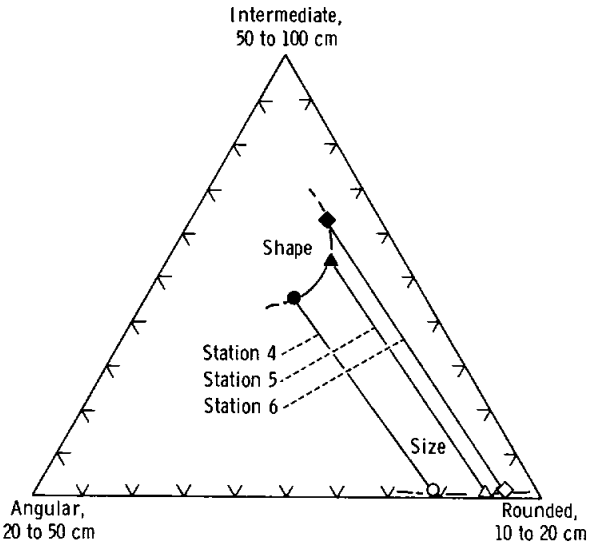


FIGURE 6-36.—Variation diagram showing block angularity (solid symbols) and size (open symbols) for stations 4, 5, and 6 on Stone Mountain.

dark- and light-colored rocks, as determined from the photographic panoramas at stations 11 and 13, are shown in figure 6-69. The conclusions that can be made from the more than 800 blocks counted are

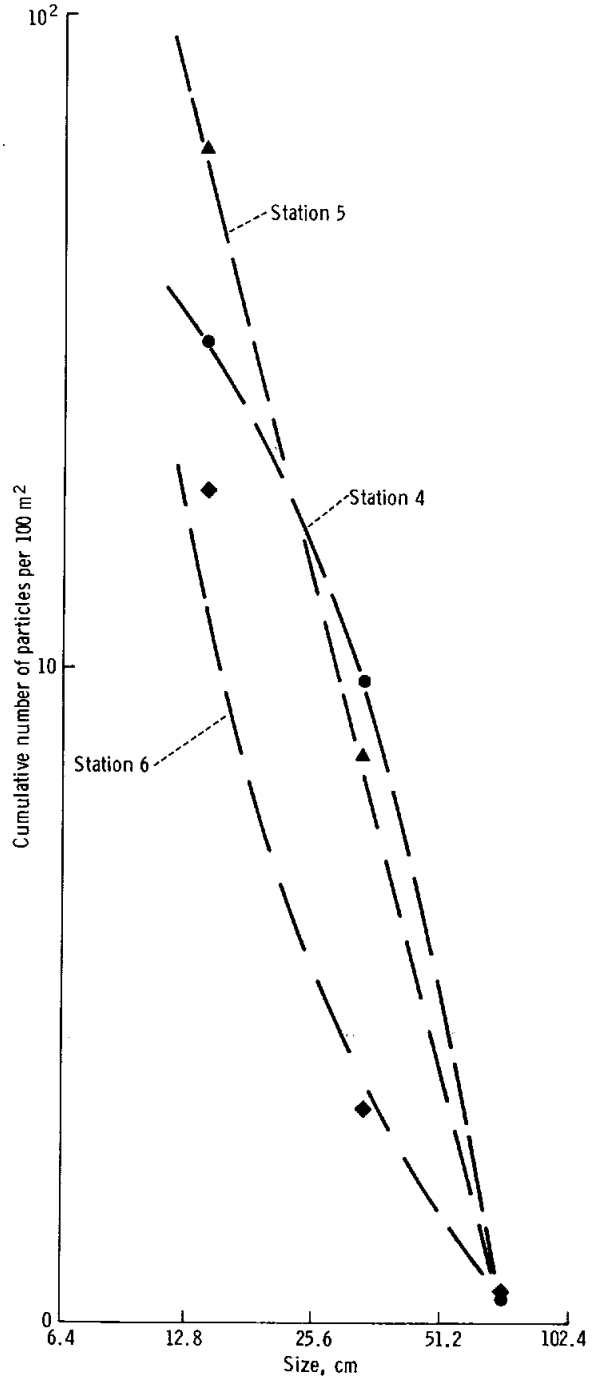


FIGURE 6-37.–Cumulative size frequency distribution of rock fragments coarser than 10 cm at stations 4, 5, and 6.

(1) that light-colored rocks (mostly white-matrix breccias) are strongly predominant everywhere on the rim and ejecta blanket of North Ray Crater and (2) that the percentage of dark rocks (dark-matrix breccias and glass-coated rocks) increases from 8 to 10 percent in the western part of the southeast rim to 28 percent eastward toward House Rock. The dark rocks make up approximately 18 percent in the Shadow Rock area.

Four localities were sampled, described, and photographed on the rim and ejecta of North Ray Crater. The locations and rock types collected are illustrated in figure 6-70, omitting the rake and soil samples for which Lunar Receiving Laboratory (LRL) photographs were not available. Areas near the white breccia boulders and at a location between there and House Rock (200 m to the northeast) have a high proportion of light-matrix breccias. Figures 6-59 and 6-71 show the typical textures of these boulders. In the House Rock area (fig. 6-57) and at Shadow Rock (fig. 6-58), dark-matrix breccias are relatively more abundant. These are typically hard and have angular shapes and vesicular textures as shown in figure 6-72.

At the boulder sampled adjacent to House Rock, the crew observed, photographed, and sampled the largest impact spall zone seen thus far on any lunar rock. The feature was described as a shatter cone, and in the photographs (AS16-106-17345 and 17346, AS16-116-18647 to 18649, and AS16-116-18653), it appears to be a percussion cone surrounded by a roughly circular spall zone with a diameter of approximately 40 to 45 cm (figs. 6-57 and 6-73). The energy required to produce this size crater was calculated by H. J. Moore[2] to be on the order of 1 to 2 X 10^{12} ergs, depending on the depth/diameter ratio, which is unknown. In any case, the energy calculated permits either primary or secondary origin for the impact feature.

The geometry of the photographs taken of the soil sample area beneath the overhang of Shadow Rock (the "permanently shadowed sample") is inadequate to determine whether the deep niche sampled is still shadowed in the late afternoon Sun. It seems likely that the sample area is exposed to direct sunlight for part of each lunar day.

The soils traversed in the vicinity of North Ray Crater are mostly firm, light-colored, and apparently very thin. The bootprints and LRV tracks form

[2]Oral communication.

depressions of a centimeter or less almost everywhere except at three areas: (1) near the white breccia boulders (fig. 6-59) where the crew reported sinking 15 cm (6 in.) into fillets developed around the boulders; (2) near the LRV where 2- to 3-cm-deep tracks are observed; and (3) in the vicinity of Shadow Rock 0.7 km southeast of the rim crest, where the LRV tracks are 2 to 3 cm deep within approximately 100 m of the station and bootprints as deep as 4 to 5 cm may be observed.

The occurrence of overhangs and poorly developed fillets around House Rock (fig. 6-57) and Shadow Rock (fig. 6-58) probably indicates that these dark-matrix breccias are more resistant to erosion than the white-matrix breccias. Concentric ridges of fines around the overhanging edges are evidence for the slow "wearing down" of these rocks. In contrast, the white breccia boulders (fig. 6-59) are surrounded by deep fillets, which can be attributed to the friability of these rocks. A different type of fillet is illustrated by the concentration of fines on the uphill sides of boulders prominent on the walls of North Ray Crater (fig. 6-60). These occur most notably on uphill sides of well-rounded boulders and are remarkably sparse on more angular rocks, regardless of size. This evidence points to a partial contribution from the boulders to their own fillets, although active downslope movement must be the contributing cause of uphill fillets.

The upper part of the regolith on the rim of North Ray Crater is a darker gray tone than the underlying material. The distribution of the darker soil provides one of the most convincing examples of mass wasting yet documented on the Moon: dark tongues of gray material on the north crater wall are perched at the angle of repose and apparently have moved downslope as debris slides during comparatively recent times (fig. 6-60). These tongues are concave upward, draping over the crater rim, and locally show breakaway scarps where they have moved as relatively coherent slabs.

The geology of the materials exposed in the walls of North Ray Crater, at this early stage of investigation, is interpreted to be a grossly layered sequence of breccias exposed only in the east wall and largely obscured elsewhere by recently active debris slides (figs. 6-60 and 6-61). Beneath 20 to 30 m of rim-flap debris, the "upper layer," which is approximately 70 m thick, is predominantly white-matrix breccias with some mixed dark rocks. The more coherent materials form discontinuous rows or benches, indicating sublayering at 5 to 10 m intervals. The absence of blocks on the west wall and the heavy concentration on the east wall and in the ejecta extending up Smoky Mountain are suggestive of a steeply dipping discontinuity between the east and west sides of the crater that separates two major units. These asymmetrical relations also can be explained as lenticular variations in induration within the same rock unit. A low-angle impact by the projectile that formed North Ray Crater is not likely because it would not explain the asymmetry of large-rock distribution in the crater walls nor the radial symmetry of the main ejecta blanket on the crater rim.

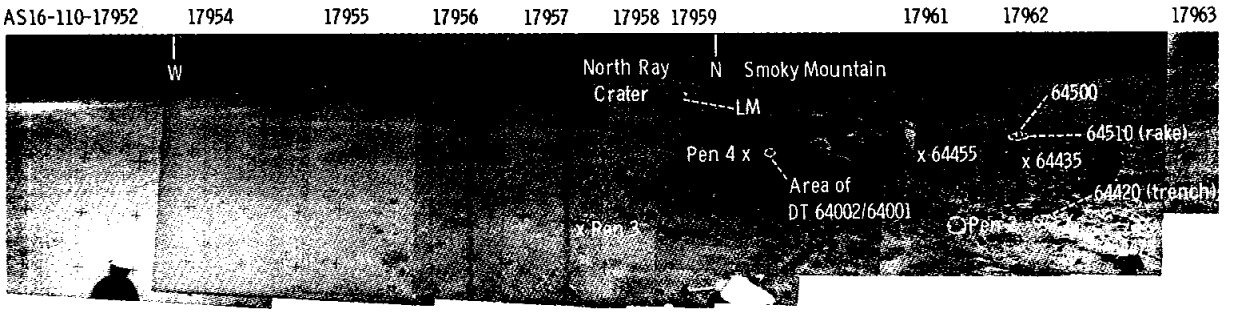
The next underlying unit is a light-colored slope of possibly unconsolidated material approximately 100 m thick. The rugged floor mound is a dark, rubbly material that may be represented by House and Shadow Rocks, which were sampled on the ejecta blanket. The large size (25 m) and the angularity of House Rock reflect the strength, or coherence, and the wide spacing of joints of the rock mass from which it was derived. In terrestrial analogs such as Meteor Crater, Arizona, the largest blocks on the crater rim reflect the more coherent and thicker-bedded rock units penetrated, regardless of depth. Therefore, because House Rock is similar both in size and appearance to the coarse, dark rubble forming the crater floor and because it and Shadow Rock are very similar in composition but represent the least abundant rock type on North Ray Crater rim, they are interpreted as coming from a stratigraphic horizon exposed in the deepest part of the crater.

The principal results of the North Ray Crater rim traverse are as follows.

(1) Extensive sampling of the rim and of a small area on the ejecta blanket

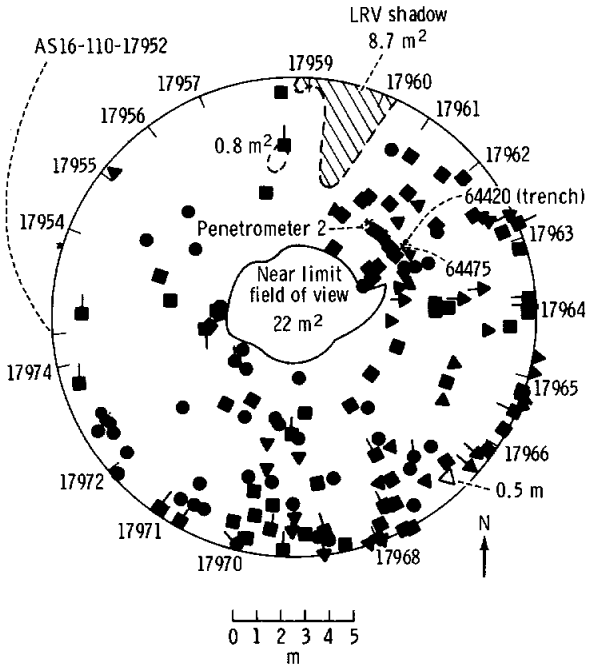
(2) Extensive photographic documentation of the samples collected, of the fragmental textures in large rocks on the surface and those exposed in the crater wall, and of optical properties of materials exposed on the crater walls

(3) Determination of terrain characteristics on the crater from astronaut observations and photography, including the general thinness of the regolith, the remarkably low density of large blocks that were expected to cover a large part of the rim, the unburied or perched nature of many blocks and fragments on all scales, and the general lack of smaller craters.



(Symbols same as in fig. 6-13)

FIGURE 6-38.–Panoramic view taken north of station 4.



(Symbols same as in fig. 6-14)

FIGURE 6-39.–Rock distribution within 10 m of the station 4 north panorama.

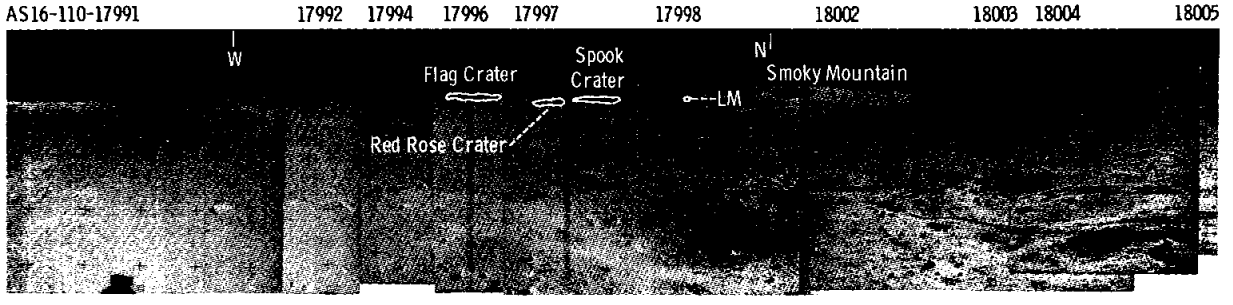


FIGURE 6-40.–Panoramic view taken at station 5.

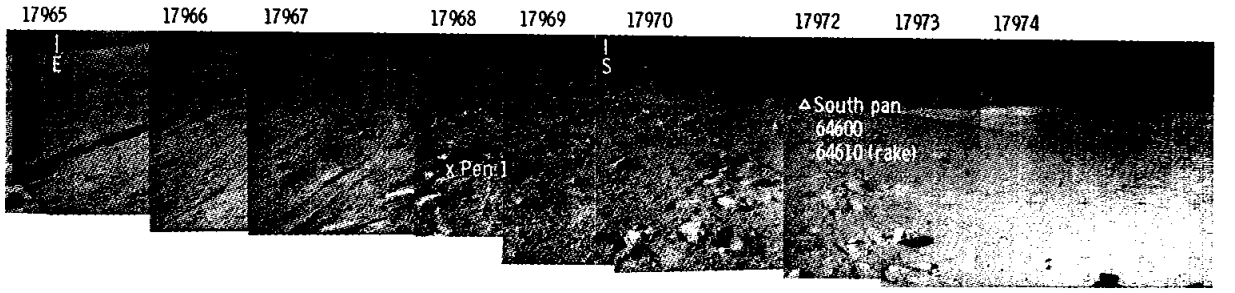


FIGURE 6-38.–Concluded.

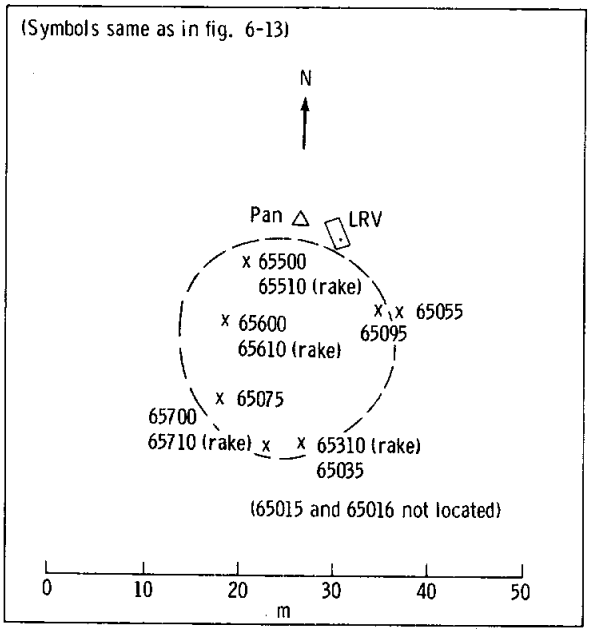


FIGURE 6-41.–Planimetric map of station 5.

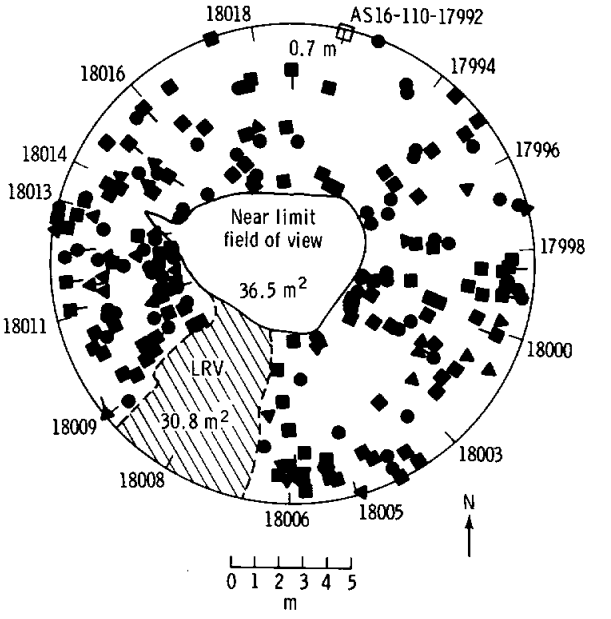


FIGURE 6-42.–Rock distribution within 10 m of the station 5 panorama.

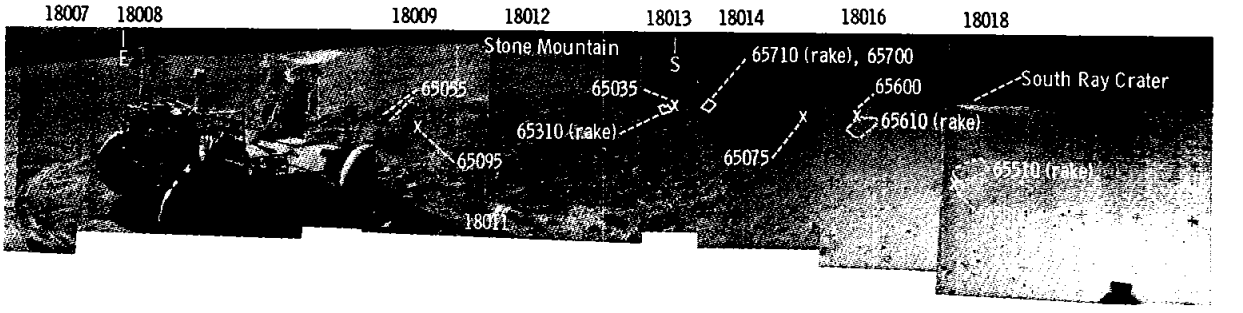


FIGURE 6-40.–Concluded.

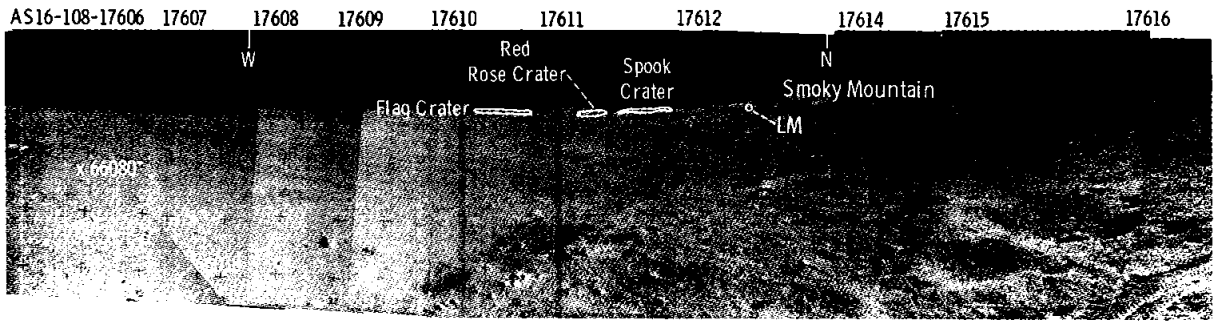


FIGURE 6-43.–Panoramic view taken at station 6.

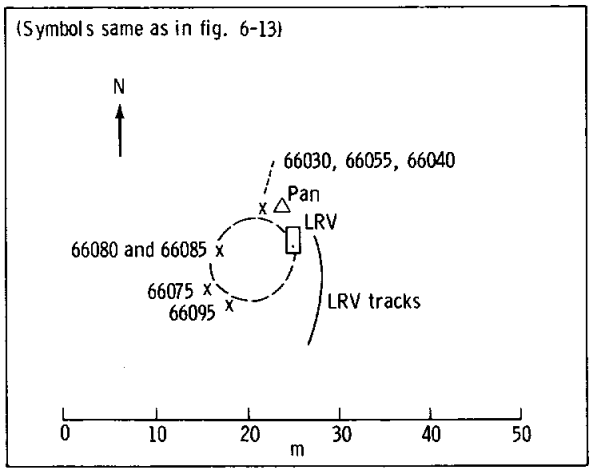


FIGURE 6-44.–Planimetric map of station 6.

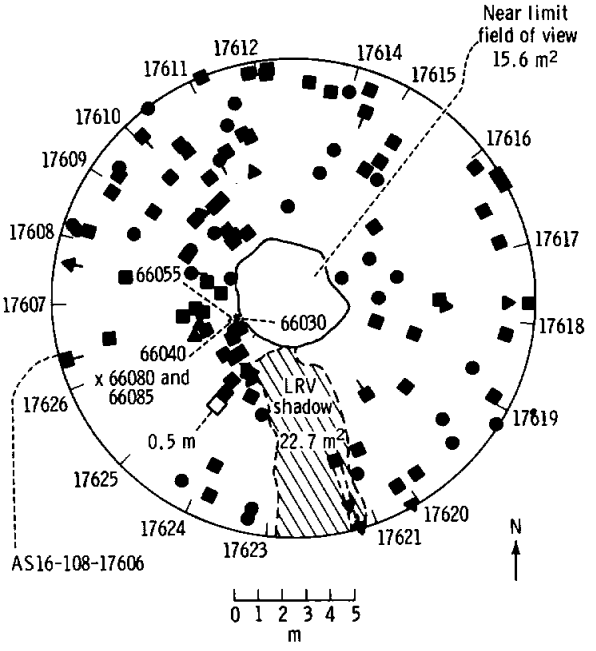


FIGURE 6-45.–Rock distribution within 10 m of the station 6 panorama.

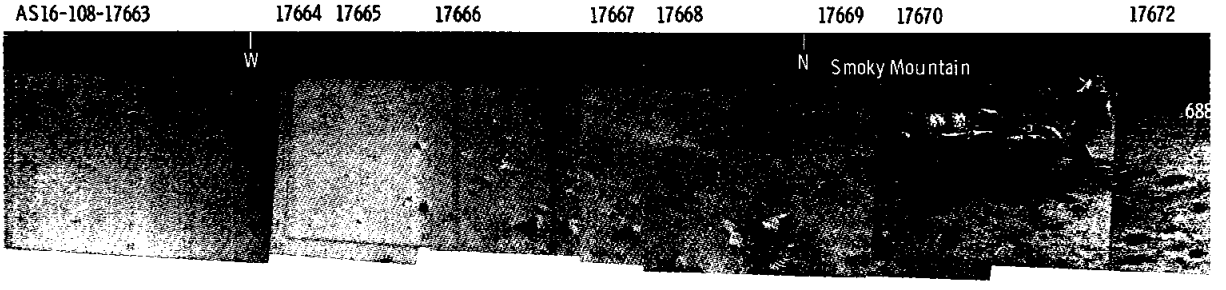


FIGURE 6-46.–Panoramic view taken at station 8.

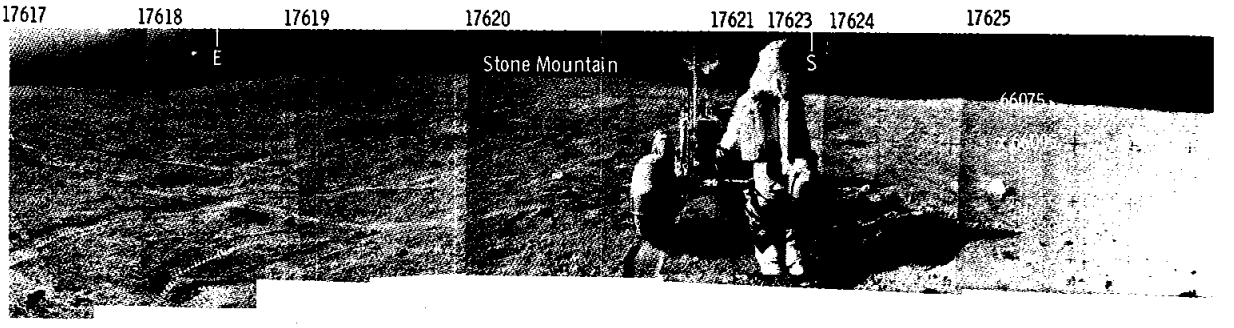


FIGURE 6-43.–Concluded.

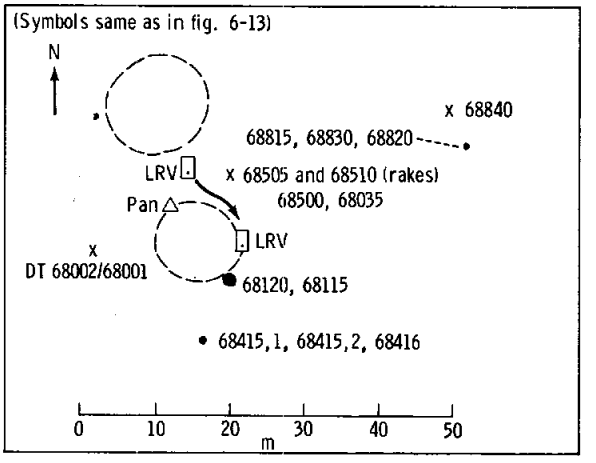


FIGURE 6-47.–Planimetric map of station 8.

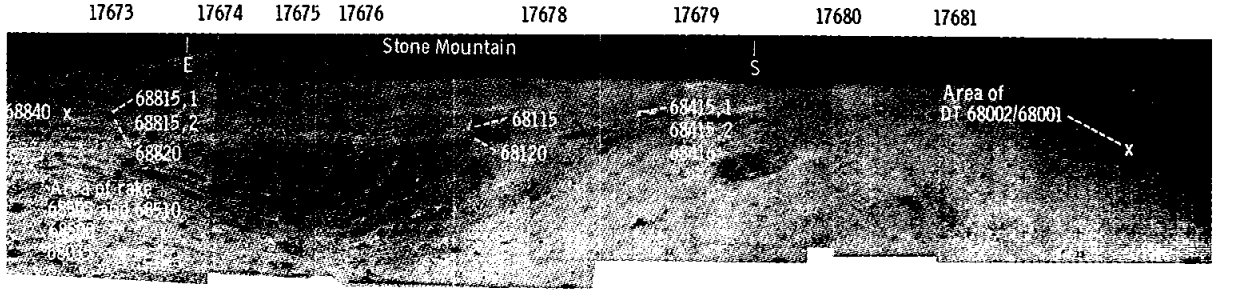


FIGURE 6-46.–Concluded.

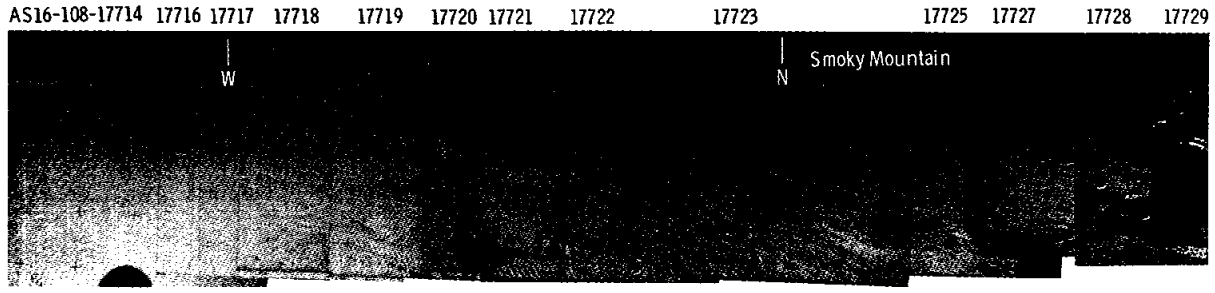


FIGURE 6-48.–Panoramic view taken at station 9.

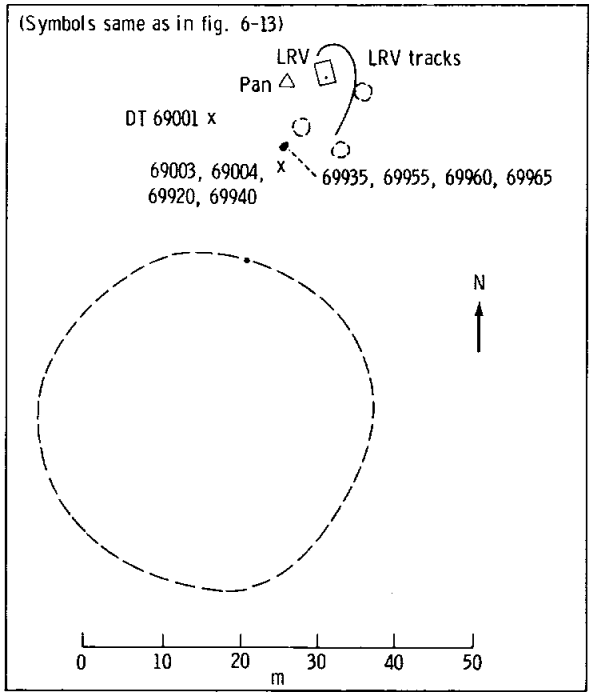


FIGURE 6-49.–Planimetric map of station 9.

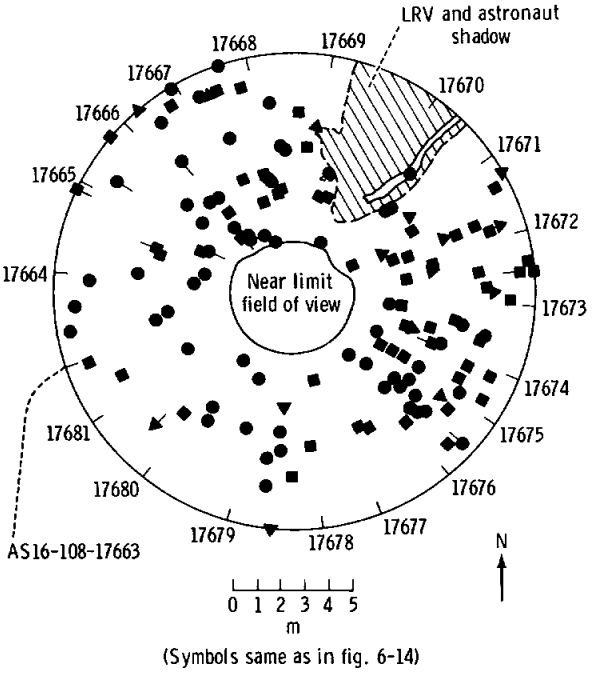


FIGURE 6-50.–Rock distribution within 10 m of the station 8 panorama.

Samples

Sample summary.–The total returned net sample weight is 95.33 kg (≈210 lb). The EVA-1 net weight was 29.84 kg (≈66 lb); EVA-2, 30.16 kg (≈66 lb); and EVA-3, 35.33 kg (≈78 lb). These figures are based on the inventory list from the Curator of the LRL, dated June 30, 1972. They do not include the minor amounts of sample lost by attrition during processing. Of the total sample weight, almost 75 percent consists of rock fragments larger than 1 cm in diameter, nearly 20 percent is soil or residue fines, and the remainder consists of core and drive tube samples.

The 111 rock samples larger than 25 g are listed in table 6-II, which shows the container number, station, EVA on which collected, weight, and classification used in this report. Rake fragments are identified but not classified. Those rock samples for which the lunar orientation at the time of collection is known are listed in table 6-III. Orientations were determined

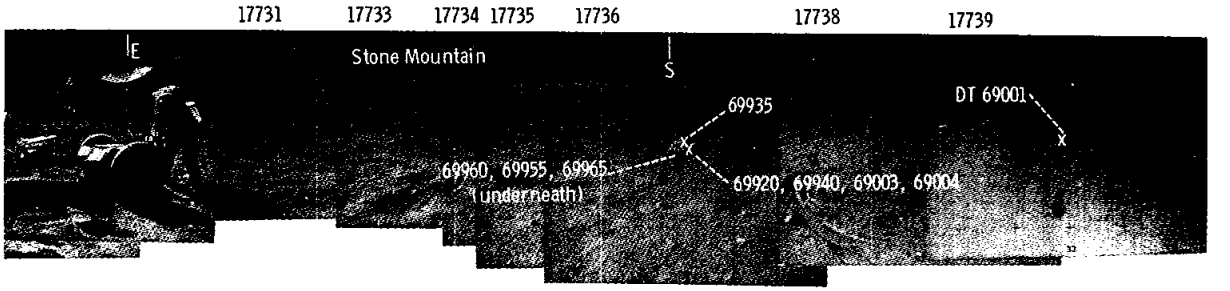
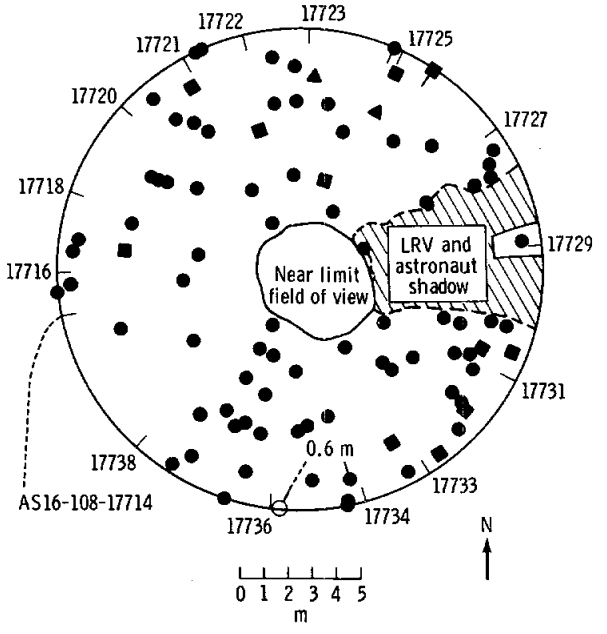


FIGURE 6-48.–Concluded.



(Symbols same as in fig. 6-14)

FIGURE 6-51.–Rock distribution within 10 m of the station 9 panorama.

in the laboratory by comparing presample photographs taken on the lunar surface with the same samples lighted by a collimated source. The table lists 45 oriented rocks as well as 52 other rocks that have not been oriented because of small size, breakage, lack of lunar surface photographs, or lack of time. No attempt was made to orient rake fragments. The comparisons between oriented samples in the laboratory and photographs taken on the lunar surface are shown in appendix B of this section. The figures are in order of the ascending sample number.

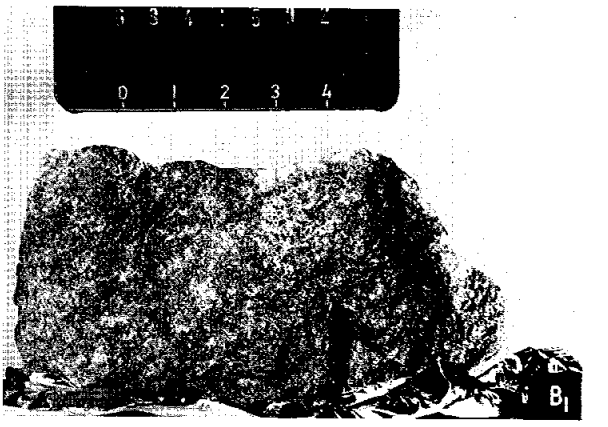


FIGURE 6-52.–Fine grained, crystalline, igneous rock (sample 68415,2) from a 0.5-m boulder at station 8 (S-72-39590).

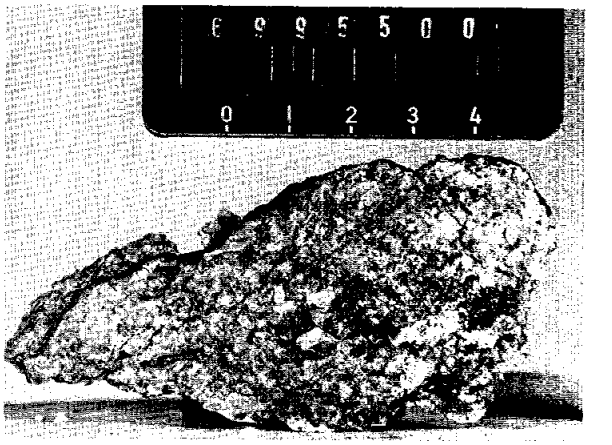


FIGURE 6-53.–Coarse-grained, crystalline, igneous rock (sample 69955) from a 0.5-m boulder at station 9 (S-72-40124).

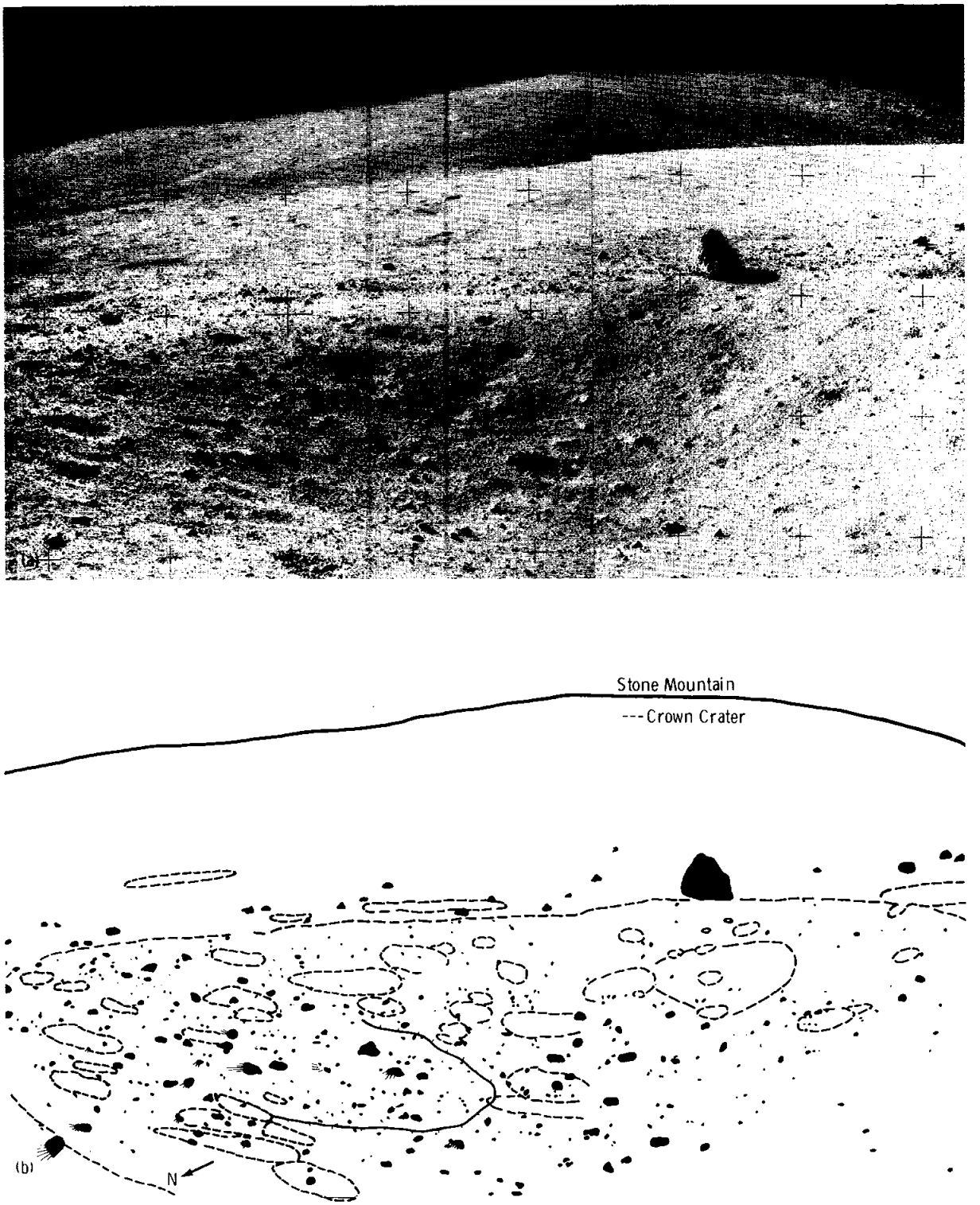


FIGURE 6-54.–Block concentration at station 8. (a) South Ray block distribution in a 15-m crater (AS16-108-17674 and 17676). (b) Sketch map.

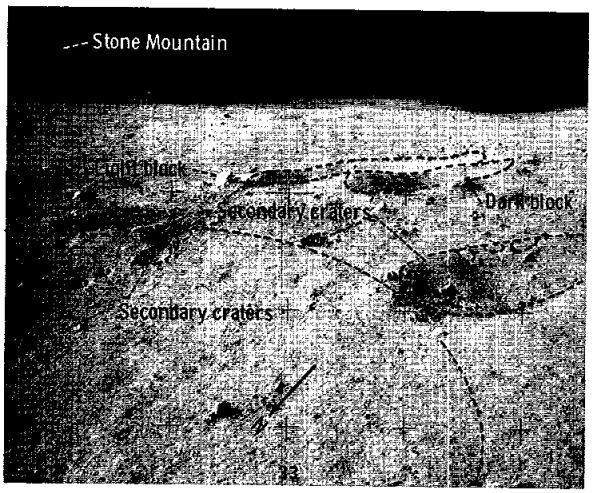


FIGURE 6-55.–Light-colored igneous and dark-colored breccia rocks in the vicinity of station 8 (AS16-108-17678).

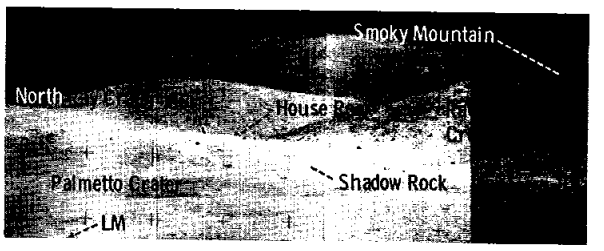


FIGURE 6-56.–A 500-mm partial panorama looking north from station 4 (AS16-112-18270 to 18276).

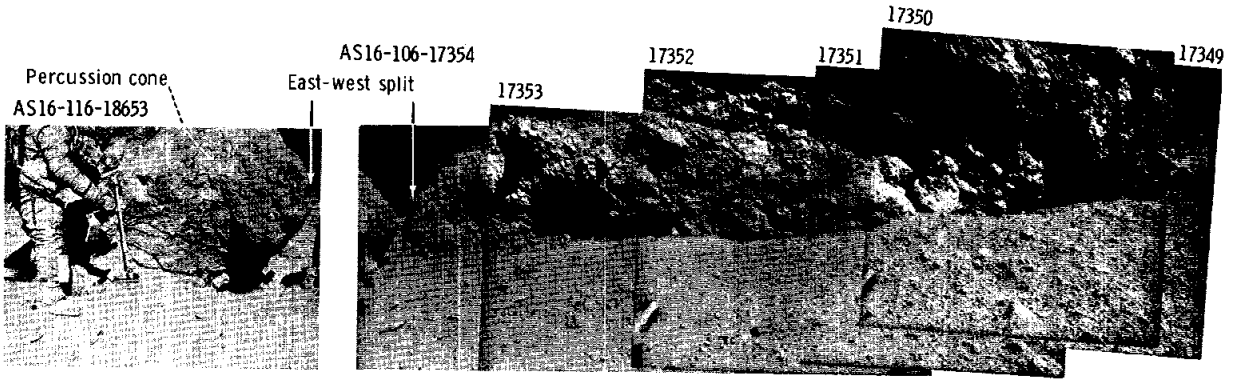


FIGURE 6-57.–Partial panorama of House Rock (right) and South Boulder (left), east exposure, showing typical dark-matrix breccia textures. Note lack of fillets at base and angular, jointed faces (AS16-116-18653 (left) and AS16-106-17349 to 17354 (right)).

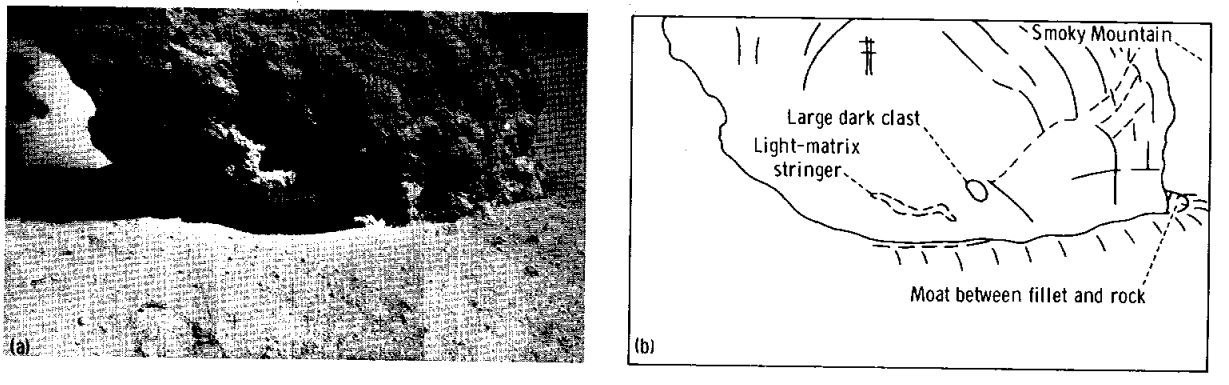


FIGURE 6-58.–Shadow Rock at station 13. (a) Partial panorama of south face, approximately 5 m wide, showing steep to overhanging boulder sides and rough surface texture of typical dark-matrix breccias (AS16-106-17413 to 17416). (b) Sketch of fracture patterns, clast and matrix features, and rock/soil interface.

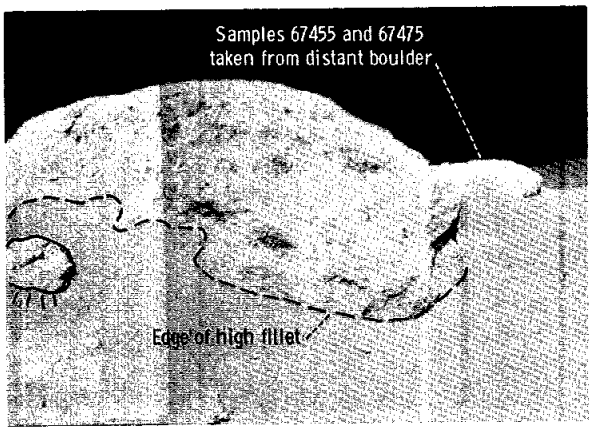
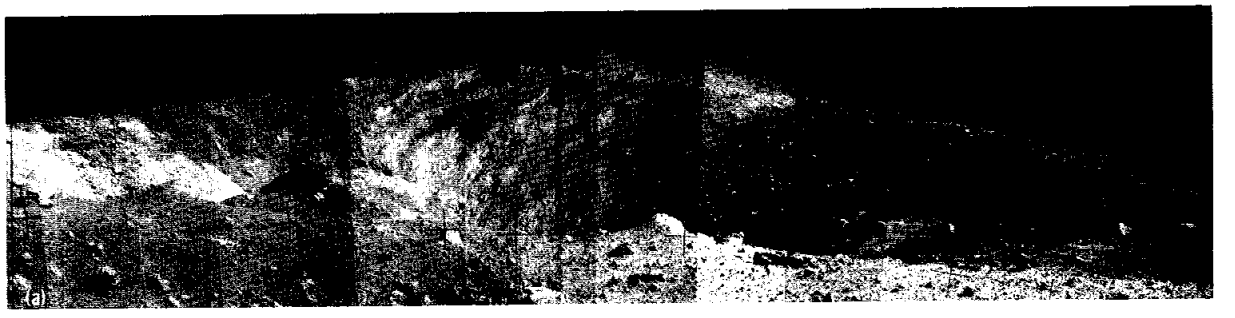
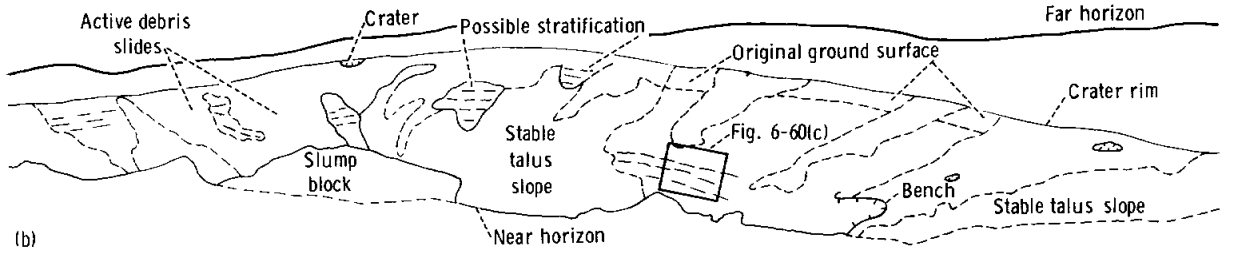


FIGURE 6-59.–White breccia boulders showing typical dark-clast population, rounded, unjointed surfaces, and well-developed fillet (AS16-106-17325 and 17326).

These sample lists and documentation photographs update information previously published in the Apollo 16 preliminary sample documentation report (ref. 6-18).

Sample classification.–Early in the first EVA, the crew recognized the dominance of breccias in the regolith of the Descartes area. Subsequent activities demonstrated the abundance of breccias throughout the area traversed, and the proportion of fragmental rocks among the returned samples (table 6-IV) exceeds 75 percent. Indeed, special effort was made to find crystalline rocks, and the proportion in the returned samples probably exceeds the true proportion at the Descartes site. The crew further recognized two main types of breccia: (1) fragmental rocks with dark clasts in a friable white matrix, and





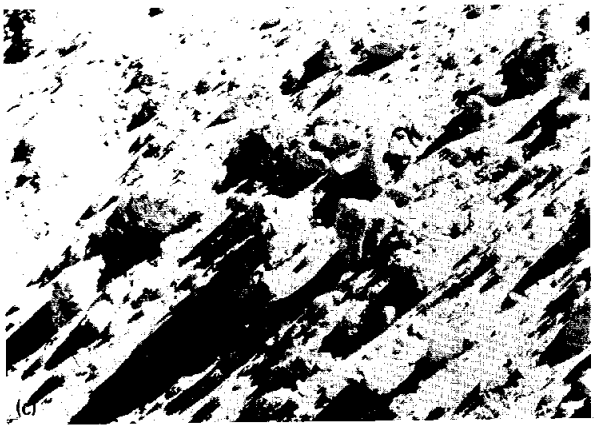


FIGURE 6-60.–North Ray Crater wall partial panorama and telephotographic detail seen from 25 m inside the southeast rim. (a) Left polarization panorama (AS16-106-17251 to 17262). (b) Sketch map showing possible stratification, products of mass wasting, and location of figure 6-60(c). (c) Telephotograph of light-matrix breccia blocks in area shown in figure 6-60(b) (AS16-105-17172; purposely underexposed to illustrate details in shadow).

(2) fragmental rocks with white clasts in a very coherent dark matrix. These observations form the basis of the preliminary classification.

The Apollo 16 rocks may be divided into three broad groups (fig. 6-74): (1) fine- to coarse-grained, mostly homogeneous crystalline rocks; (2) rocks composed substantially of glass; and (3) fragmental rocks (breccias). The crystalline rock and breccia groups have been subdivided on the basis of megascopic properties described in the following paragraphs. In table 6-IV, samples examined as of June 15, 1972, are classified into one of eight categories. Two groups (C_1 and C_2) represent subdivisions of the crystalline rocks, one group (G) consists of glass, and five groups (B_1 to B_5) represent subdivisions of the breccias.

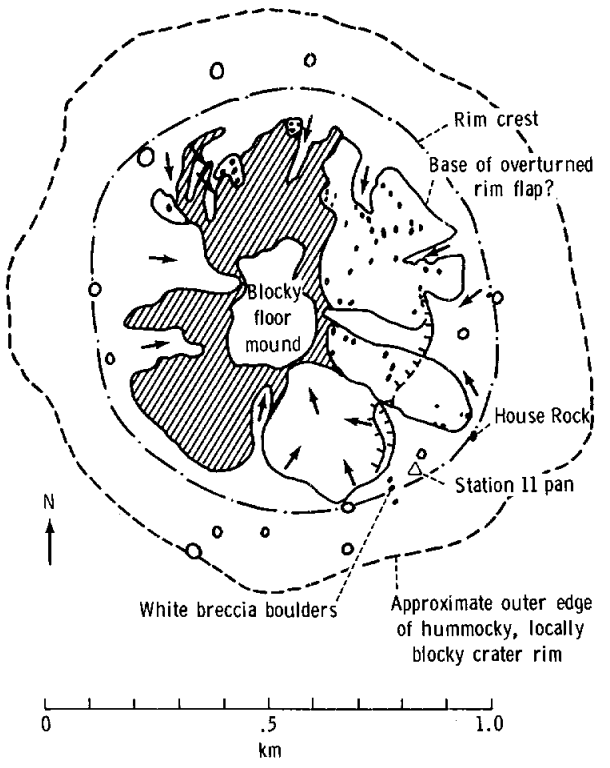


FIGURE 6-61.–Geologic map of North Ray Crater.

Twenty-five rocks are classified as crystalline rocks. Of these, seven (group C_1) appear to be igneous rocks. Although all the igneous rocks have been shattered and deformed to some extent, the predeformation textures are substantially intact. The two largest samples returned (60015 and 61016) and a small one (69955) are, as recognized by the crew, coarse-grained, nonvesicular rocks composed largely of plagioclase. These resemble Apollo 15 anorthosite sample 15415 but are probably more severely shock deformed. Three of the remaining four igneous rocks (68415,1, 68415,2, and 68416) were taken from a single boulder and are fine-grained, highly feldspathic rocks with crystal-lined vugs; the rocks are texturally inhomogeneous and contain large (to 1 cm), irregular inclusions of plagioclase. The seventh igneous rock (67956) is a small piece of medium-grained gabbroic rock containing approximately 25 percent mafic silicates. A very small proportion of the rake samples, as yet unnumbered, also are igneous rocks: one rock from the LM site is similar to sample 68415, and one rock from station 1 is coarse-grained anorthosite. The rake samples also contain igneous rocks not seen in the larger documented samples. Among these are a few basaltic rocks with ophitic textures, brown pyroxenes, low plagioclase contents, and comparatively abundant ilmenite.

Eighteen crystalline rocks (group C_2) appear to be metaclastic rocks with generally small proportions of lithic debris. These are hard, angular rocks characterized by fine-grained, sugary textures, some with megascopically recognizable poikiloblastic texture. The rocks are typically inequigranular with variable, but usually small, proportions of irregular mineral fragments, mostly plagioclase. One sample, 65055, appears to be transitional between the C_1 and C_2 groups; it closely resembles sample 68415 in texture in its vuggy parts but elsewhere has a sugary, granoblastic texture with relict irregular plagioclase and mafic mineral grains. A substantial proportion of the rocks in some rake samples is metaclastic; these probably are concentrated in the raked fragments because of their toughness and resistance to breakdown compared to many breccia matrices.

Five samples largely composed of glass were returned. Two of these are glass spheres, one hollow and one solid. The remaining three samples are irregular, coarse, vitric agglutinates with numerous

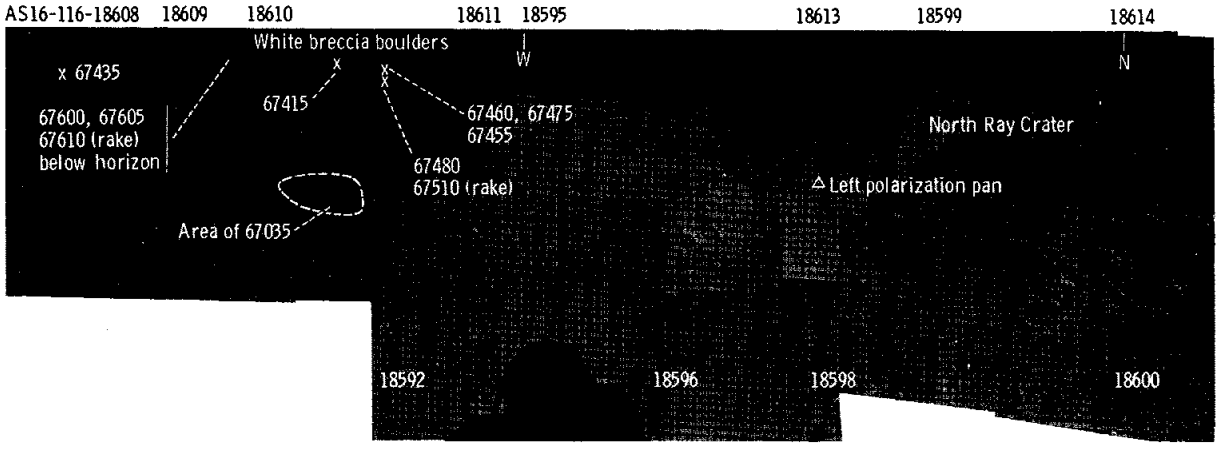
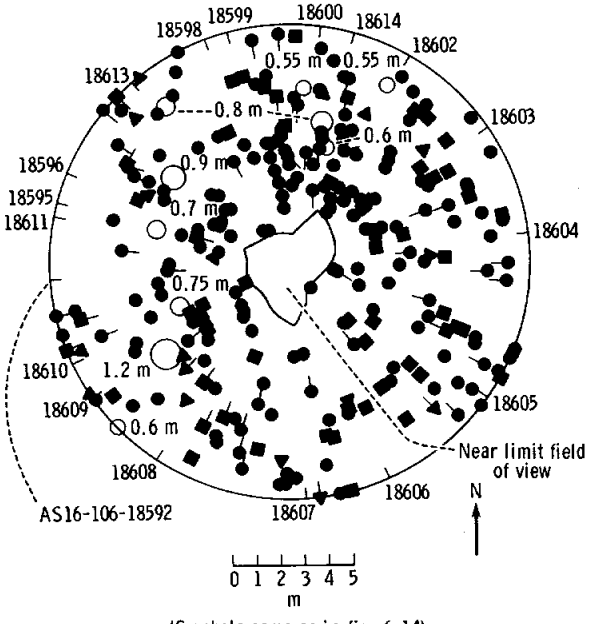


FIGURE 6-62.–Panoramic view taken at station 11.



(Symbols same as in fig. 6-14)

FIGURE 6-63.–Rock distribution within 10 m of the station 11 panorama.

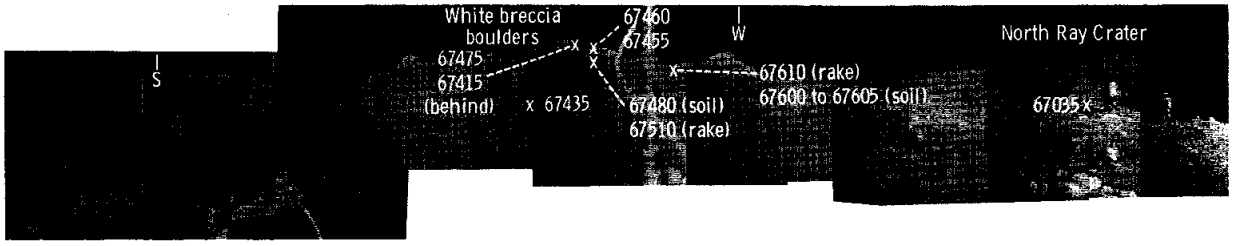


FIGURE 6-64.–Panoramic television view taken at the LRV parked south of station 11 panorama.

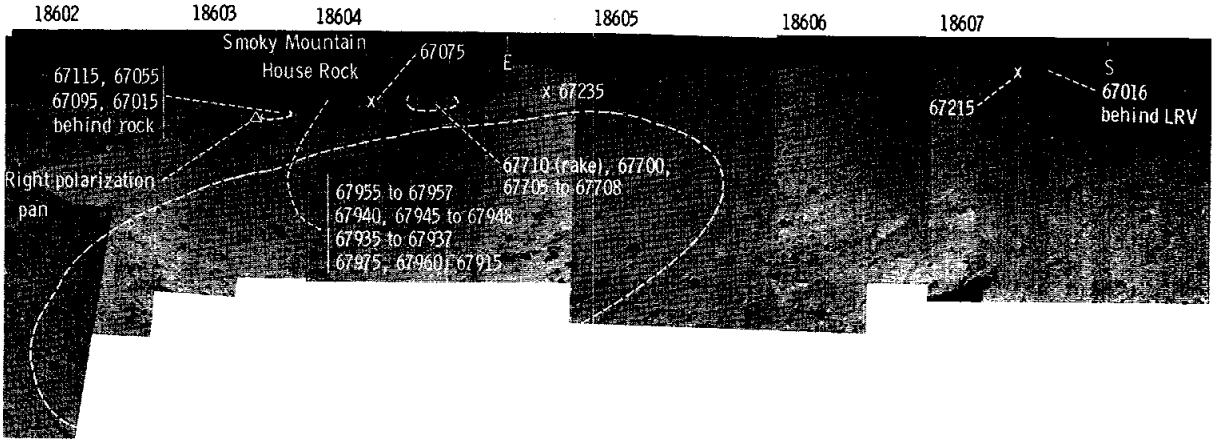


FIGURE 6-62.–Concluded.

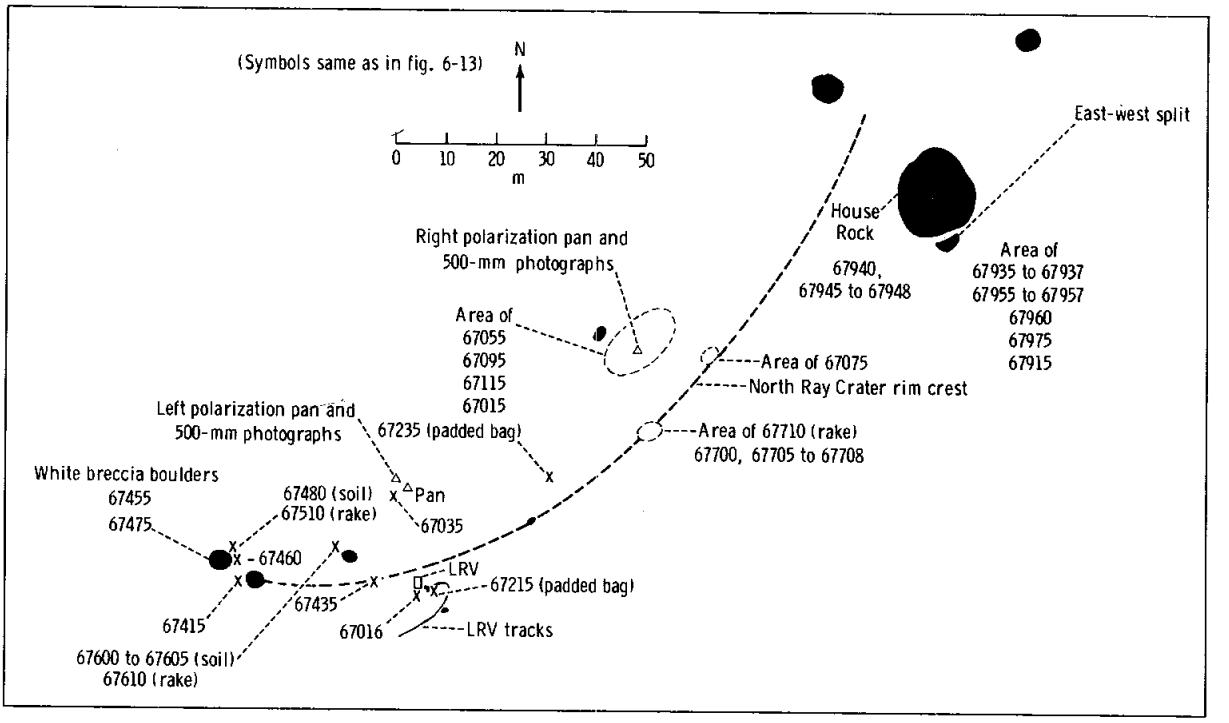


FIGURE 6-65.–Planimetric map of station 11.

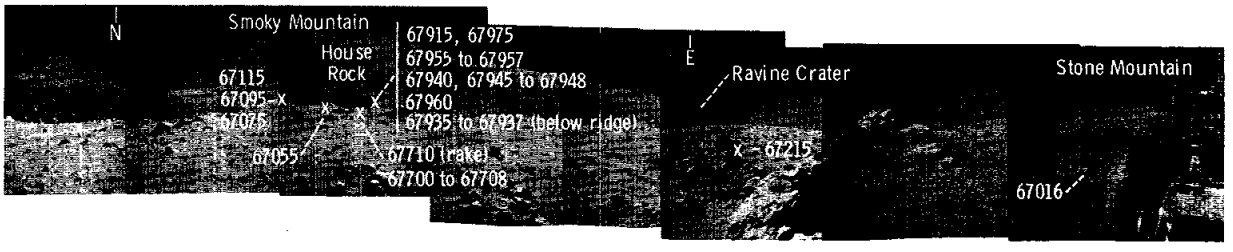


FIGURE 6-64.–Concluded.

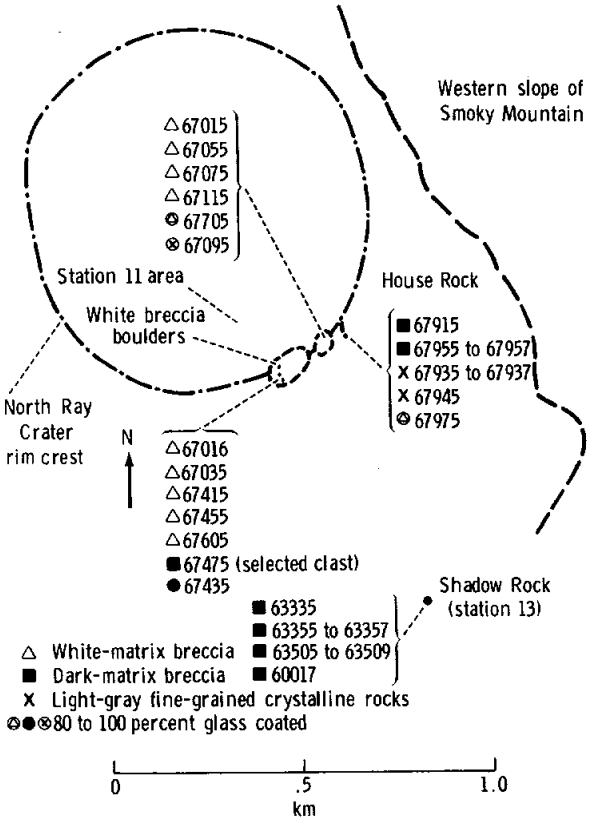


FIGURE 6-70.–Distribution of rock types on the North Ray Crater continuous ejecta blanket (excluding rake and soil samples).



FIGURE 6-71.–Typical white-matrix breccia, sample 67015, showing variety of dark-clast sizes and shapes (S-72-37216).

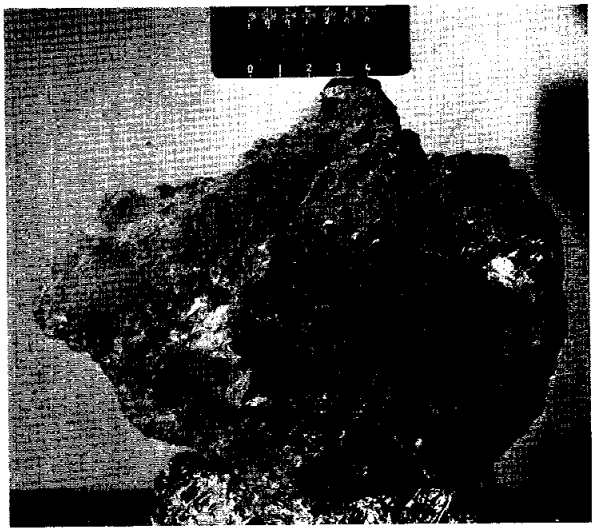


FIGURE 6-72.–Typical dark-matrix breccia, sample 60017, from House Rock and Shadow Rock with white irregular clasts and vesicular texture (S-72-36943).

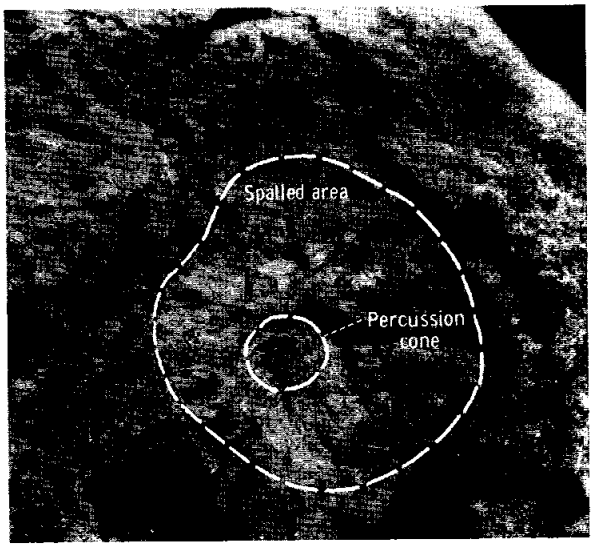


FIGURE 6-73.–Percussion cone surrounded by a circular spall zone on South Boulder (AS16-106-17345).

rocks in this category range from 2 to 4307 g (ref. 6-18). The abundance of clasts in these rocks is generally much higher than in B_1 rocks (fig. 6-75), and a substantial number of the rocks contain both light and dark clasts (fig. 6-76). Mineral fragments

larger than 1 mm are common and, as in B_1 rocks, are mainly plagioclase. Most of the rocks are polymictic breccias but some contain only a single kind of clast; in contrast to B_1 breccias, comminution of the clasts in these breccias cannot give rise to the matrix materials. Group B_2 breccias are typically friable, and the matrices appear to be unmetamorphosed fragmental debris.

Group B_3 rocks are intermediate types having more or less equal proportions of light and dark clasts and medium-gray matrices. These are subdivided into two groups, B_{3a} and B_{3b}, mainly on the basis of coherence.

The four rocks in the B_{3a} group range from 1.4 to 2.8 g (ref. 6-18). These rocks have very low clast abundances. They closely resemble typical soil breccias returned by other Apollo missions: they are very soft and friable, have a brownish cast due to an abundance of matrix glass, and contain fragmental glass and glass beads. Small pieces of similar rocks are present in most of the rake samples. Some of these rocks also are grooved and display poorly developed slickensides probably formed during weak lithification of soil. Some consist of clusters of clods loosely cemented by glass. Both these features are common in soil breccias returned by previous Apollo missions.

The six rocks in the B_{3b} group range from 4 to 510 g (ref. 6-18), although sample 61295 was broken from a large boulder. The abundance of clasts is moderate (fig. 6-75), and all six rocks contain both light and dark clasts (fig. 6-76). Mineral fragments larger than 1 mm are not as abundant as in B_1 and B_2 rocks. All these rocks are polymictic breccias and contain a notably wider range of lithologies as clasts than any other type of breccia. Although these rocks contain fragmental glass like the B_{3a} samples, they are much more coherent (though still not apparently annealed) and lack the other features typical of soil breccias described previously.

Group B_4 rocks are fragmental rocks containing light lithic clasts in excess of dark ones and having dark matrices. The 33 rocks in this category range from 1.3 to 2559 g (ref. 6-18). The abundance of clasts ranges from low to high (fig. 6-75), and most contain only light clasts with few or no dark clasts (fig. 6-76). It should be emphasized, however, that dark clasts in a dark matrix are quite difficult to discern, and the relative proportions of such clasts may be changed with more detailed study. Mineral fragments larger than 1 mm, though still widespread, are considerably less abundant than in B_1 to B_3 breccias. Most of these rocks are monomictic breccias or have a narrow range of clast types. The intergranular coherence of these rocks is high, and most appear to have finely annealed matrices.

Group B_5 rocks are fragmental rocks containing dark lithic clasts in equal or greater proportion than light lithic clasts and having dark matrices. The three rocks in this category range from 65 to 1789 g (ref. 6-18). The clast abundance is high (fig. 6-75), and all three rocks contain both light and dark clasts (fig. 6-76); the dark clasts differ only slightly from the matrix. Mineral fragments larger than 1 mm are present but sparse in all three breccias. These rocks are polymictic breccias, but the range of lithologies among light and dark clasts is not great. The intergranular coherence of the breccias is high, and the matrices appear finely annealed. Gas cavities are spectacularly developed in the matrices of the two larger rocks.

Field petrology and areal distribution of samples.—The field distribution of documented samples classified according to the scheme described in the preceding paragraphs is shown in figures 6-77 and 6-78. Only samples larger than 50 g are plotted because smaller fragments are more likely to have been transported long distances and breakdown of the breccias yields small samples not representative of the source rocks. Two stations, the LM/ALSEP site and station 11, were much more thoroughly sampled than other stations. Of the eight categories of rocks described in the preceding section, only two – B_3 and B_5 type breccias – were not found at these two stations. This suggests that more thorough sampling at other stations would likely have expanded the range of rock types found there.

The stations can be divided into four main groups. The members of each of these groups have similar settings: (1) the LM/ALSEP site, stations 8 and 9, and probably station 2, which were located on the Cayley Plains and covered by South Ray ejecta; (2) stations 4 and 5, which were located on Stone Mountain and also covered by South Ray ejecta; (3) stations 11 and 13, which were located on the continuous ejecta blanket of North Ray Crater; and (4) stations 1 and 6, which were located on the Cayley Plains in areas lacking extensive blocky ray material.

TABLE 6-II.–Apollo 16 Rock Samples Larger Than 25 g (Including Rake Fragments)

Sample no.	*Documentation bag no. (a)*	*Station (b)*	*EVA*	*Weight, g (c)*	*Classification (d)*
60015 (FSR-3)[e]	SCB-5	10/LM	1	5 574.0	C_1
60016 (FSR-12)	SCB-7	LM	3	4 307.0	B_2
60017 (FSR-9)	SCB-7	13	3	2 102.0	B_4
60018 (FSR-10)	SCB-7	10	3	1 501.0	B_4
60019 (FSR-11)	SCB-4	10′	3	1 887.0	B_4
60025 (FSR-4)	SCB-3	LM	2	1 836.0	B_1
60035	351	ALSEP	1	1 052.0	B_1
60055	355	ALSEP	1	34.5	B_1
60075	373	ALSEP	1	183.8	B_2
60095	4	ALSEP	1	46.6	G
60115	381	10	2	132.5	B_4
60135	430	10	3	137.7	C_2
60215	13	10′	3	385.8	B_2
60235	15	LM	3	70.1	C_2
60255	17	LM	3	871.0	B_4
60275	18	LM	3	255.2	B_4
60315	20	LM	3	787.7	C_2
60335	331	LRV parking site	3	317.8	C_2
60615	347	10′	3	33.0	Rake
60619	347	10′	3	28.0	Rake
60625	347	10′	3	117.0	Rake
60636	347	10′	3	35.6	Rake
60639	347	10′	3	175.1	Rake
60645	347	10′	3	33.5	Rake
60665	347	10′	3	90.1	Rake
61015 (FSR-1)	SRC-1	1	1	1 803.0	B_2
61016 (FSR-2)	BSLSS bag	1	1	11 729.0	C_1
61135	362	1	1	245.1	B_2
61155	371	1	1	47.6	B_4
61156	371	1	1	58.5	C_2
61175	364	1	1	542.7	B_3
61195	2	1	1	587.9	G
61295	353	1	1	187.0	B_3
61536	372	1	1	86.0	Rake
61546	372	1	1	110.7	Rake
62235	5	2	1	319.6	C_2
62236	5	2	1	57.3	B_1
62237	5	2	1	62.3	B_1
62255	7	2	1	1 192.0	B_2
62275	9	2	1	443.0	B_1
62295	10	2	1	250.8	C_2
63335	428	13	3	65.4	B_5
63355	429	13	3	68.2	B_4
63538	345	13	3	35.1	Rake
63549	345	13	3	26.6	Rake
63585	345	13	3	32.6	Rake
64435	394	4	2	1 079.0	B_4
64455	397	4	2	56.7	C_2
64475	398	4	2	1 032.0	B_2
64476	398	4	2	125.1	B_2
64535	395	4	2	256.6	Rake
64536	395	4	2	177.5	Rake
64537	395	4	2	124.3	Rake

TABLE 6-II.–Apollo 16 Rock Samples Larger Than 25 g (Including Rake Fragments) – Continued

Sample no.	*Documentation bag no. (a)*	*Station (b)*	*EVA*	*Weight, g (c)*	*Classification (d)*
64538	395	4	2	30.0	Rake
65015 (FSR-5)	SCB-3	5	2	1 802.0	C_2
65035	404	5	2	446.1	B_2
65055	337	5	2	500.8	C_2
65056	337	5	2	64.8	B_4
65075	403	5	2	107.9	B_2
65095	336	5	2	560.1	B_2
65315	405	5	2	300.4	B_2 (rake)
65325	405	5	2	67.9	Rake
65326	405	5	2	36.4	Rake
65515	332	5	2	50.2	Rake
65715	334	5	2	31.4	Rake
65757	334	5	2	26.2	Rake
65786	334	5	2	83.0	Rake
66035	407	6	2	211.4	B_3
66055	408	6	2	1 306.0	B_2
66075	409	6	2	347.1	B_3
66095	410	6	2	1 185.0	C_2
67015 (FSR-7)	SCB-7	11	3	1 194.0	B_2
67016 (FSR-8b)	BSLSS bag	11	3	4 262.0	B_2
67035	382	11	3	245.2	B_2
67055	383	11	3	221.9	B_2
67075	384	11	3	219.2	B_1
67095	385	11	3	339.8	G
67115	386	11	3	240.0	B_2
67210	PSCB-1	11	3	276.9	Special sample
67230	PSCB-2	11	3	938.3	Special sample
67415	387	11	3	174.9	B_1
67435	415	11	3	353.5	B_4
67455	416	11	3	942.2	B_2
67475	418	11	3	175.1	B_4
67515	420	11	3	60.8	Rake
67549	420	11	3	43.1	Rake
67556	420	11	3	82.1	Rake
67559	420	11	3	32.9	Rake
67605	422	11	3	44.5	B_2 (rake soil)
67627	421	11	3	79.6	Rake
67628	421	11	3	49.7	Rake
67629	421	11	3	32.8	Rake
67647	421	11	3	47.7	Rake
67718	423	11	3	41.0	Rake
67729	423	11	3	73.2	Rake
67915 (FSR-8)	SCB-4	11	3	2 559.0	B_4
67935	389	11	3	108.9	C_2
67936	389	11	3	61.8	C_2
67937	389	11	3	59.7	C_2
67955	425	11	3	162.6	B_1
67975	392	11	3	446.6	B_2
68115	340	8	2	1 190.0	B_5
68415	[f]341, 342	8	2	371.2	C_1
68416	341	8	2	178.4	C_1
68515	411	8	2	236.1	Rake
68516	411	8	2	34.0	Rake
68518	411	8	2	29.8	Rake

TABLE 6-II.–Apollo 16 Rock Samples Larger Than 25 g (Including Rake Fragments) – Concluded

Sample no.	*Documentation bag no. (a)*	*Station (b)*	*EVA*	*Weight, g (c)*	*Classification (d)*
68525	411	8	2	39.0	Rake
68815 (FSR-6)	SRC-2	8	2	1 826.0	B_5
69935	378	9	2	127.6	B_4
69955	380	9	2	75.9	C_1

[a]SCB, sample collection bag; SRC, sample return container; BSLSS, buddy secondary life support system; PSCB, padded sample collection bag.

[b]For station maps, refer to station descriptions.

[c]Weight given to the nearest 0.1 g based on the inventory listing from the Curator of the LRL dated June 30, 1972.

[d]Classification by H. G. Wilshire and E. D. Jackson.

[e]FSR, football size rock.

[f]Two fragments in different bags.

Although the proportions of rock types vary from station to station and in part depend on thoroughness of sampling, there are no distinctive differences in rock populations between the first two station groups. Figure 6-5 shows an extensive cover of all the station areas of groups 1 and 2 by blocky ray material from South Ray Crater. It is therefore likely that all these samples represent Cayley materials derived from South Ray Crater. Hence, if materials from Stone Mountain differ from those excavated by South Ray Crater, they were not sampled. Lithologies represented include all major types except B_3 breccias, but breccias with light clasts in a dark matrix (B_4) and those with dark clasts in a light matrix (B_2) are clearly dominant. Clasts resembling the lighter gray metaclastic rocks (C_2) occur in some breccias, and a breccia source for all of them is not unlikely. A sample of igneous rock (coarse-grained anorthosite) was collected from a dark-matrix breccia boulder at station 9, so that at least some of the igneous rocks originally occurred as clasts in breccias.

Group 3 stations, on North Ray Crater ejecta, yielded samples that do not appear to differ in any significant respect from those of groups 1 and 2. This is important because North Ray Crater excavated material from a low ridge rather than from smooth, plains-forming material more typical of the Cayley Plains and excavated by South Ray Crater. The dominant rock types are again B_2 and B_4 type breccias. There is a much higher proportion of B_4 breccias in samples collected at the northeastern part of station 11 near House Rock, itself a large boulder of dark-matrix breccia. These are presumed to be derived from lower in the section than the abundant B_2 breccias observed and collected at the southwestern end of the traverse area. Small, dark-matrix breccias are concentrated in the rake sample at station 13, and, although these are classified as B_4 breccias, they generally have adhering films of white clastic material and are probably clasts derived by the breakup of B_2 breccias.

Group 4 stations, which occupy interray areas on the Cayley Plains, also yielded B_2 and B_4 breccias as well as the usual small proportion of crystalline rocks. These stations, however, are the only sources of B_{3b} breccias. These rocks, characterized by a wide range of clast types, may therefore represent the uppermost materials of the Cayley Plains, which are mantled by North Ray and South Ray Crater ejecta elsewhere in the traverse area.

The rock distribution suggests that the section underlying the Cayley Plains at the Apollo 16 site is stratified, with an upper unit of B_{3b} breccia and lower units composed mainly of B_2 and B_4 breccias. The areal extent of the supposed upper unit is not known but presumably extends at least between stations 1 and 6; considering the relative scarcity of B_{3b} breccias, the unit is probably not more than a few meters thick. Evidence derived from panoramic photographs and astronaut descriptions at station 11 suggests that B_2 breccias overlie B_4 breccias, whereas the color of the ejecta on the rims of South Ray and Baby Ray Craters suggests that B_4 breccias overlie B_2 breccias in the vicinity of those craters. Such a

TABLE 6-III.–Lunar Orientation of Apollo 16 Rock Samples

(a) Samples for which the orientation at the time of sampling has been established by correlation with lunar surface photographs

Sample no.	*Lunar top (a)*	*Lunar north (a)*	*Sample no.*	*Lunar top (a)*	*Lunar north (a)*
60016	T	E	62275	B	W
60018	S	T	62295	B	W
60019	B	S/W	64435	S/E	T
60025	N	B/W	64475	B	E
60035	B	N/W	64476	T	W/N
60115	S/B	S/E	65035	B	E
60215	N	W	65055	W/S	B
60255	S	T	65095	T	E
60275	B	N/E	66035	B	N
60315	T	E/N	66055	W/B	S
60335	S	T/W	66075	T	W
61015	T	S	66095	B	S
61016	T	E	67016	B	W
61135	N	E/B	67055	S/T	S/E
61155	T	S	67435	B	S/E
61156	S	E/B	67915	B/E	B[b]
61175	T	W	[c]68035	B/S	E
61195	T	E	68115	E	N
61295	B/W	W/T	68415,1	S/T	T/E
62235	W/B	W/N	68415,2	S/T	T/E
62236	S	E/T	68416	E	N
62237	S	E	68815	S/T/E	S
62255	T	S/E			

[a]Directions are those of the identification cube used in orthogonal and stereoscopic photography (LRL mug shots): north, south, east, west, top, and bottom.

[b]Not exposed.

[c]Orientation obtained from LRL photographs compared with surface photographs; sample not lighted using collimated light.

(b) Samples deleted from orientation attempt

Sample no.	*Reason*	*Sample no.*	*Reason*
60015	Lack of surface photographs	67015	Breakage
60017	Lack of surface photographs	67025	Small size
60055 to 60059	Small size	67035	Breakage
60075	Breakage	67075	Breakage
60095	Small size	67095	Unsuccessful attempt
60135	Lack of time	67115	Breakage
60235	Lack of time	67215	Padded bag sample
61157 and 61158	Small size	67235	Padded bag sample
63335	Breakage; lack of surface photographs	67415	Breakage
63355	Breakage; lack of surface photographs	67455	Breakage
63505 to 63509	Small size	67475	Lack of surface photographs
64455	Small size	67935 to 67937	Small size; breakage; lack of surface photographs
64477 and 64478	Small size		
65015 and 65016	Lack of surface photographs	67955 to 67957	Small size; breakage; lack of surface photographs
65056	Breakage		
65075	Breakage	67975	Lack of surface photographs
65315	Lack of surface photographs	69935	Small size
66036 and 66037	Small size	69955	Small size
66085 and 66086	Small size		

TABLE 6-IV.—Classification of Samples

Crystalline			*Breccia*[d]					
					Medium-gray matrix			
Igneous[a] *(C_1)*	*Metaclastic*[b] *(C_2)*	*Glass*[c] *(G)*	*Light-matrix light-clast (B_1)*	*Light-matrix dark-clast (B_2)*	*Friable (B_{3a})*	*Coherent (B_{3b})*	*Dark-matrix light-clast (B_4)*	*Dark-matrix dark-clast (B_5)*
60015	60135	60095	60025	60016	[e]62247	61175	60017	63335
61016	60235	61195	60035	60075	[e]62248	61295	60018	68115
67956	60315	65016	[e]60055	60215	[e]62249	66035	60019	68815
68415,1	60335	67095	[e]60056	61015	63507	66036	60115	
68415,2	61156	[e]67486	[e]60057	61135		66037	60255	
68416	62235		[e]60058	[e]61157		66075	60275	
69955	62295		61226	[e]61158			61155	
	64455		62236	62255			61225	
	65015		62237	[e]64425			[e]62245	
	65055		[e]62246	64475			63355	
	65905		62275	64476			63505	
	65906		67075	65035			63506	
	66095		67415	65075			63508	
	67025		67705	65095			63509	
	67935		67948	65315			63515	
	67936		67955	[e]65907			64435	
	67937			66055			64477	
	67945			[e]66085			64478	
				[e]66086			65056	
				67015			67435	
				67016			67475	
				67035			[e]67485	
				67055			[e]67487	
				67115			[e]67488	
				67455			[e]67489	
				[e]67605			67915	
				67975			67946	
				68035			67947	
							67957	
							[e]68505	
							69935	
							69945	
							69965	

[a]All medium- and coarse-grained rocks in this group are somewhat deformed cataclastically but comparatively large parts of their original textures remain intact.

[b]Includes breccias with matrices annealed to coarser-than-aphanitic grain size.

[c]Sample predominantly composed of glass.

[d]"Breccia" includes fine breccia (clast size 1 to 5 mm) and microbreccia (clast size <1 mm).

[e]Tentative classification based on examination of LRL photographs or cursory examination of the sample.

stratigraphic sequence in the South Ray area is consistent with the dominance of dark-matrix (B_4) breccias described and photographed in South Ray ejecta between the LM site and station 8. The nature of the materials of the Descartes highlands remains, at this time, unknown.

Optical Properties

The first detailed study of the fine-scale optical properties of highland materials from lunar surface photographs makes use of polarimetric data obtained with a polarizing filter on a 70-mm camera at two panoramic stations on North Ray Crater rim. In addition, the use of a Hasselblad camera with a 500-mm lens gave detailed photographs of South Ray Crater, which, photometrically, is the brightest lunar area ever measured. Down-Sun photographs of most of the documented samples and of the geologic terrane at each traverse station permit analysis of the photometric properties of the materials throughout the area.

The Descartes landing area showed the greatest variation in phase-function normal albedos of any lunar landing area. Premission estimates were of 13 to 15 percent normal albedos based on photoelectric telescopic measurements that integrated several 10-km^2-sized areas over the Descartes region. Photometric measurements of the fine-grained regolith in the lunar surface photographs range from 14 to 24 percent phase-function normal albedo. Rock measurements vary from 18 to 51 percent, and the bright ray materials from South Ray Crater measured 55 percent phase-function normal albedo. This extreme range of albedos is the result of the high resolution of the surface photography; telescopic integration results in an average albedo over a large area. The

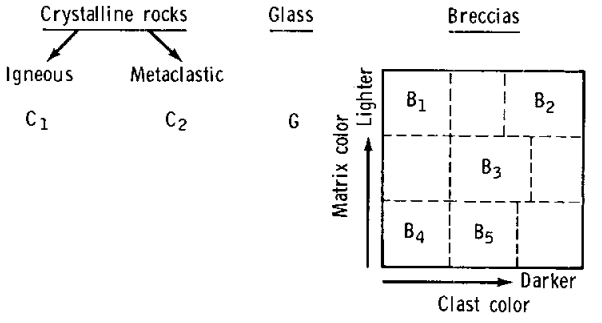


FIGURE 6-74.–Classification scheme for Apollo 16 rocks.

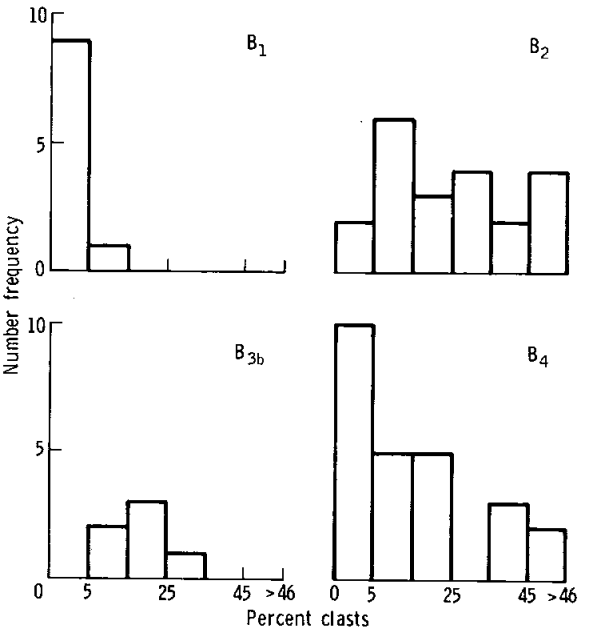


FIGURE 6-75.–Frequency distribution of clasts larger than 1 mm in breccia groups B_1, B_2, B_{3b}, and B_4.

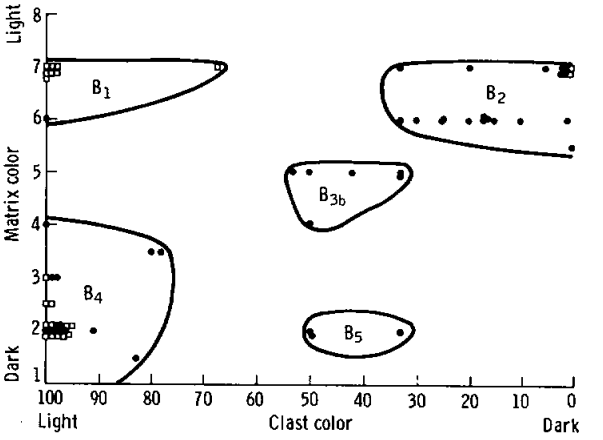


FIGURE 6-76.–Classification of breccias. Only samples for which clast proportions were available as of June 15, 1972, are plotted. The matrix color is estimated from the Munsell gray scale and modified to fit the seven-figure gray scale used in orthogonal photographs of the rocks. The clast-color scale represents the proportions of clasts lighter and darker than the breccia matrix.

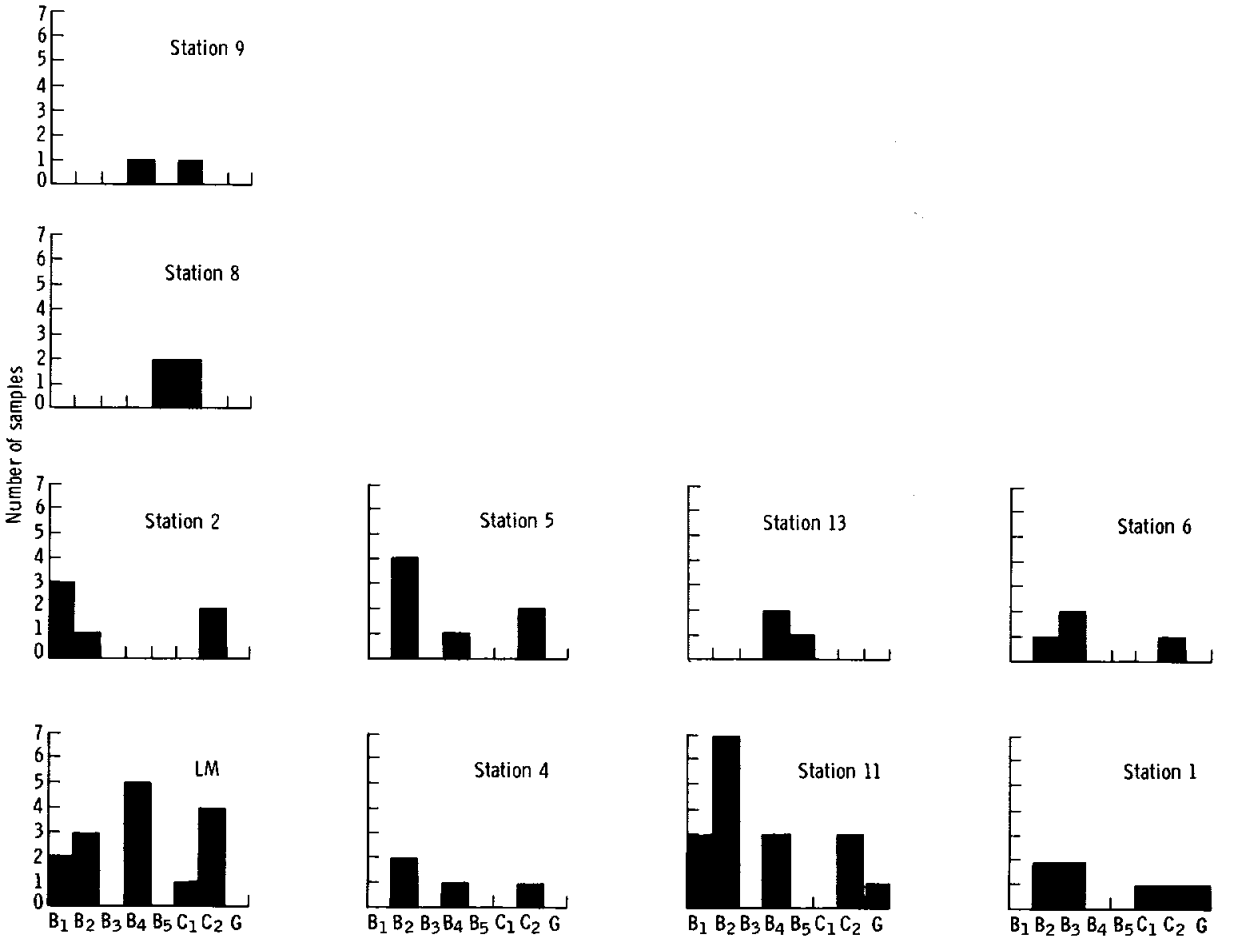


FIGURE 6-77.–Number of rock types greater than 50 g collected at stations.

highest telescopically measured normal albedo on the Moon is 24 percent and occurs in the crater Aristarchus (ref. 6-19). The highest phase-function albedo measured before the Apollo 16 mission was 31 percent and occurred near Cone Crater at the Apollo 14 landing site.

Originally measured telescopically (ref. 6-20) and later refined in the mare areas by measurements of high-resolution Surveyor and Apollo photographs (refs. 6-21 and 6-22, respectively), the lunar photometric function was tested for highland variations in the Apollo 16 landing area. Photographs taken down-Sun, which include astronaut shadows, allow the measurement of surface reflectance from approximately 30° phase angle to near zero phase angle. Microdensitometer scans were made across photographs AS16-106-17386 (station 13), AS16-108-17702 (station 8), and AS16-108-17628 (station 6). The film-density luminances were calculated and plotted relative to phase angle (fig. 6-79). Slight differences in the slopes of the curves occur near zero phase angle, indicating small variations in the backscattering nature of lunar materials. The Apollo 16 photographs do not show as sharp a backscatter peak as the telescopic data, again caused by higher resolution of the surface photography. The similarity of the lunar photometric function on the highland and mare surfaces is remarkable considering the different composition of bedrock. Apparently, the comminution of lunar material by repetitive cratering produces the unique backscatter lunar photometric function and composition controls the albedo.

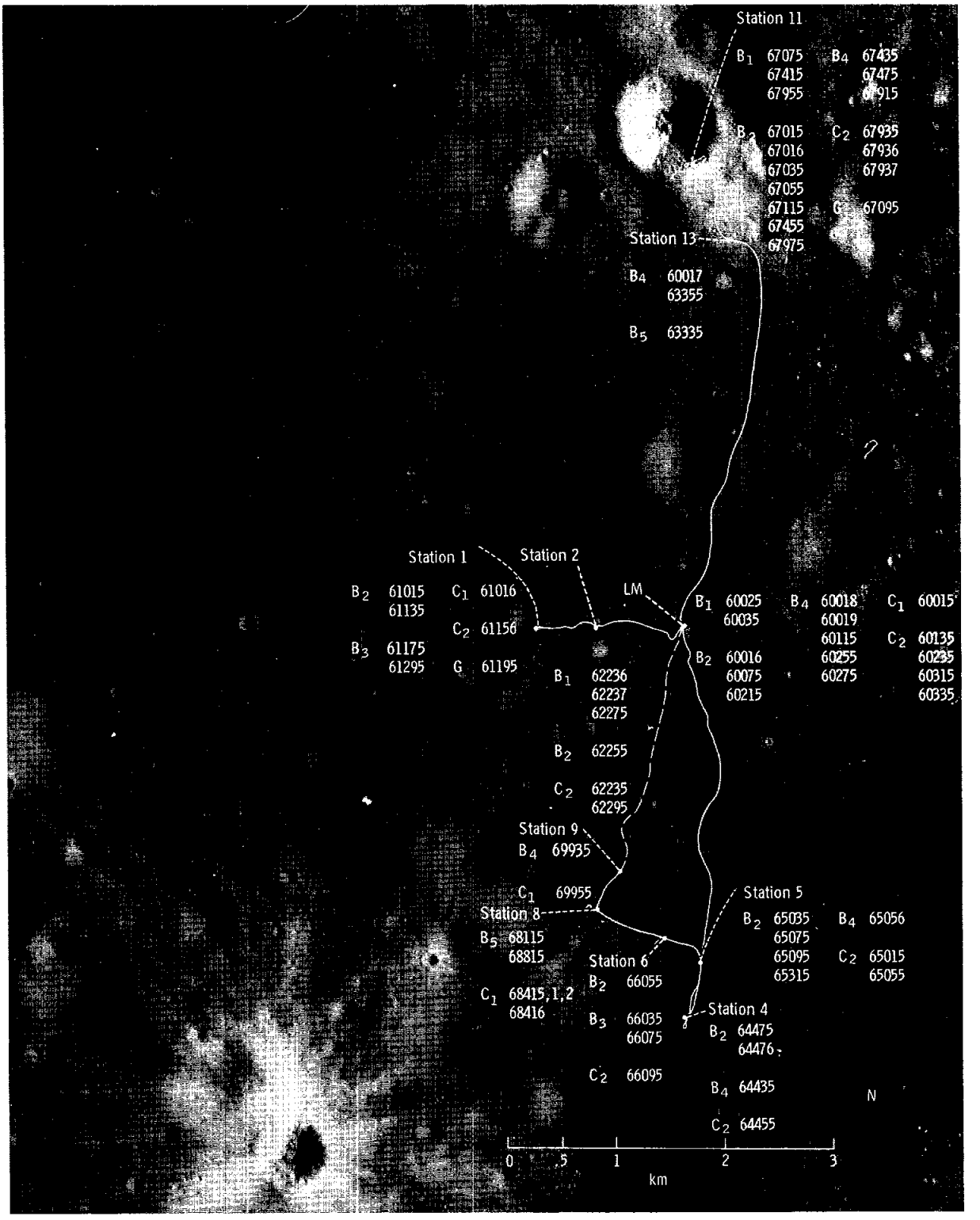


FIGURE 6-78.–Areal distribution of rock types and samples greater than 50 g.

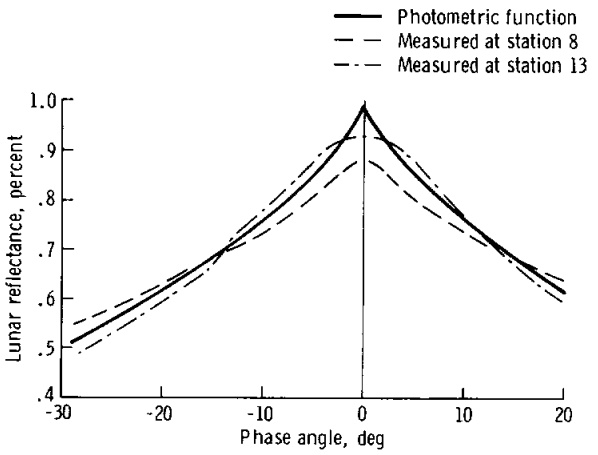


FIGURE 6-79.–Comparison of telescopically measured lunar photometric function with measured luminances from photographs AS16-106-17386 (station 13) and AS16-108-17702 (station 8).

A second-generation direct-duplicate negative of Apollo 16 pan camera frame 4618 was used for the generation of the preliminary Apollo 16 phase-function normal albedo map. Surface photographs used in determining the albedos were primarily second-generation master-positive stock from the Hasselblad 70-mm cameras. In addition, a few 500-mm-lens photographs were used to confirm the high albedo measurements at South Ray Crater.

All surface photographs containing surface areas close to zero phase angle were densitometered using a 1-mm aperture. The geometry was established for each photograph through reference to horizon control points and precalculated geometrical computer listings. The average phase angle for the best photographs was 3° to 4°. The previously used functional behavior between the phase angle and the amount of reflected radiant flux was assumed for all surface photometry. Photometric control was obtained from the photometric chart and gnomon photographed on the lunar surface and from film sensitometry data. The photometric chart was instrumental in verifying the f-stop and shutter speed at which the surface photographs were taken. The gnomon and chart were disabled at station 6, and subsequent photometric measurements were based on film sensitometry data.

The panoramic photographs were digitized and stored on a 200-BPI magnetic tape. The scanning aperture size at the negative plane was 0.05 by 0.05 mm, and the microdensitometer was adjusted to give continuous readings. The preflight gray scale was also densitometered.

The digital tape was converted to the proper VICAR format at 800 BPI and processed in the same manner as used for Apollo 15 tapes. The panoramic frame was divided into four sectors and the station locations determined in line and sample coordinates. Albedo values for the stations as obtained from surface photographs were used as controls in producing the albedo map shown in figure 6-80.

There are two important qualifications to the preliminary albedo map. The first is that the usual phase or lunar photometric function was assumed for the Apollo 16 site. Preliminary surface measurements indicate that this is probably valid (fig. 6-79). The second qualification is that variations of the albedo values due to topography were not computationally removed. Thus, comparisons of albedo values are reliable only between areas with the same slope.

Many areas having an albedo greater than 45 percent are shown in figure 6-80. These areas are brighter than any found at previous Apollo sites. The 500-mm-lens photographs resulted in geometrically corrected albedos of 50 to 55 percent for South Ray Crater. Exposure values from the automatic exposure control on the orbital panoramic camera are consistent with these high albedos.

On the Apollo 16 mission, a polarizing filter attached to the lunar surface Hasselblad camera permitted measurement of the degree of polarization and the orientation of the plane of maximum polarization of light reflected from the lunar surface. Three photographs are needed, one each with the polarizing filter at the 0°, 45°, and 90° positions. This was accomplished by taking overlapping photographs at one filter position through a 120° sector across North Ray Crater from station 11. The filter was rotated to the second position and the sector rephotographed. This was repeated a third time in the final filter position. Differences in image intensity of the same image element or object in the three photographs are a function of the amount and orientation of the linear polarized component of the reflected light from that object. From the returned photographs, three sets of polarization frames were selected for computer processing. These sets were frames AS16-106-17239, 17259, and 17266 and frames AS16-106-17241, 17257, and 17268 from the southwestern panoramic position at station 11 and

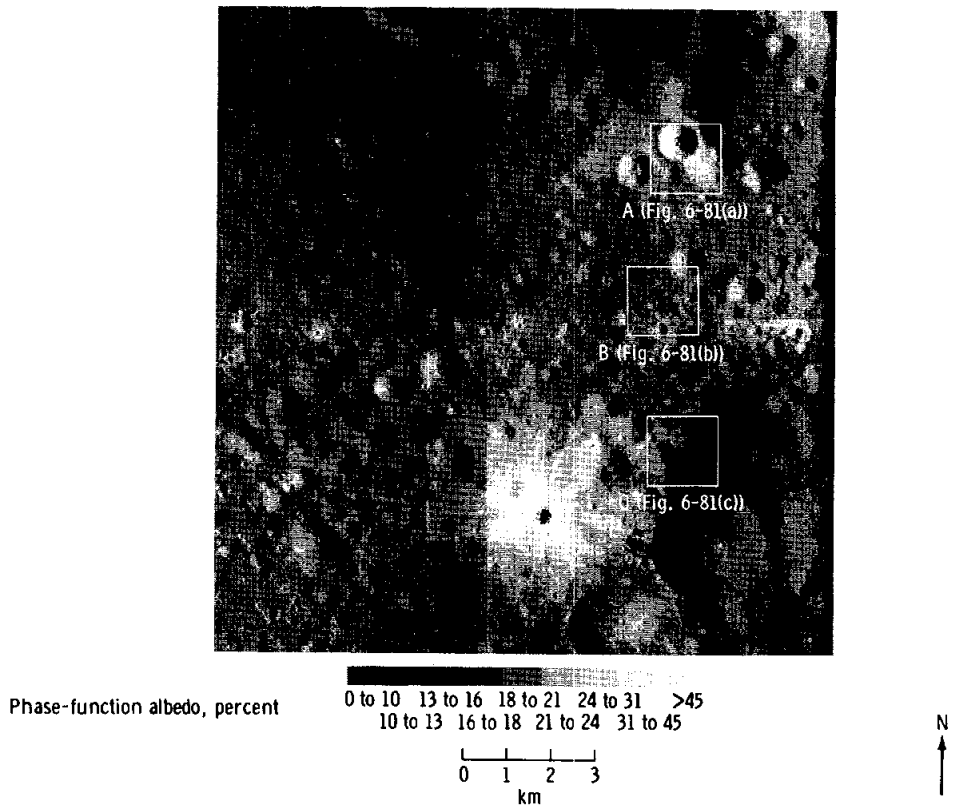


FIGURE 6-80.–Composite of four computer-generated sectors of the Apollo 16 site based on Apollo 16 pan camera frame 4618. The phase-function normal albedos are shown in nine shades of gray. A gray scale with the appropriate albedo ranges is included for interpretation. The three scribed areas denoted A, B, and C are the sections of the map enlarged 5 times in the computer and shown in figure 6-81. No albedo corrections were made for topography.

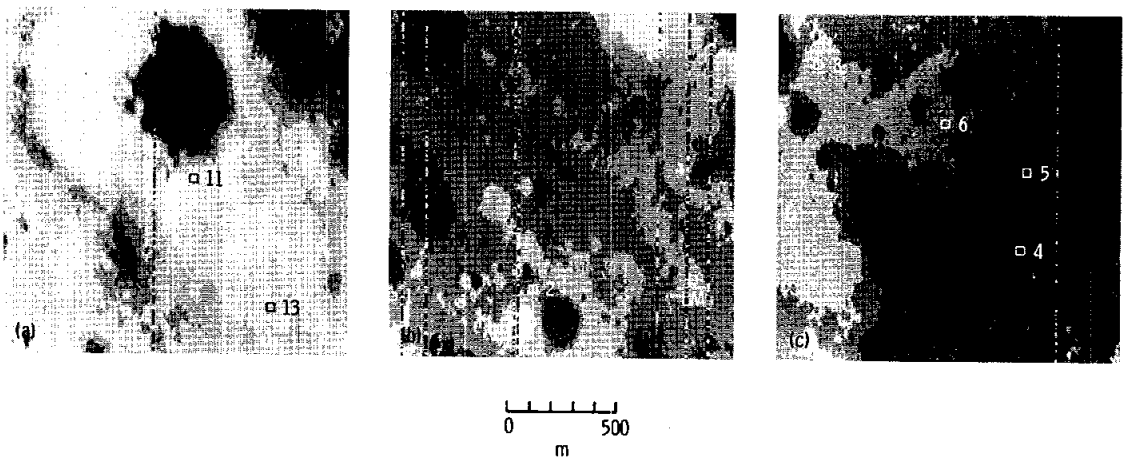


FIGURE 6-81.–Computer-generated enlargements of areas A, B, and C outlined in figure 6-80. The station locations are identified by number beside the scribed areas. The gray shades depict the same ranges as given in figure 6-80. The lines on the photographs are line dropouts during microdensitometry. (a) Area A. (b) Area B. (c) Area C.

frames AS16-106-17283, 17296, and 17310 from the northeastern panoramic position at station 11. The data for computer reduction were taken from second-generation master positives. The sets of photographs were digitized, as were the preflight and postflight gray-scale wedges.

The first step in computer reduction involved building a histogram of the digital data over each photograph. The digitized values for the sky and shadow areas from photograph to photograph were forced to agree to ensure the validity of comparisons between photographs. The data were also verified as lying on the linear portion of the sensitivity of the film.

The frames were filtered using a 3- by 3-pixel matrix to smooth the data. The first frame (horizontal polarization) became the prime photograph against which the remaining two were registered. Camera displacements between frames were sufficiently large to yield stereopairs from frames within a given set. Registration of stereopairs to pixel resolution is extremely difficult and requires lengthy computer processing. To reduce expensive computer time, a special set of positive transparency enlargements of the digitized photographs was made. The frames were then registered using visual techniques, and displacement coordinates were determined for 70 to 80 points in each frame. These point displacements were used to compute a linear interpolation of the displacement coordinates. This interpolation factor was then applied to each photograph element. The registrations, while still imperfect, were within 5 pixels in the far field.

The three registered frames were used to compute the degree of polarization and the angle of its maximum. (These equations can be found in ref. 6-23.) Following this calculation, a nine-gray-step conversion table was generated to illustrate areas of equivalent polarization in the three sets. One of the sets taken at high phase angle is shown in figure 6-82. Relatively good agreement exists between polarization values on overlapping areas of the photograph sets.

Each lunar material has a characteristic polarimetric function. A comparison of the polarimetric functions of returned samples with those of rocks in inaccessible areas or of remote objects permits some correlation and classification of materials at a distance. In the area of North Ray Crater, for instance, such a study shows three polarimetrically

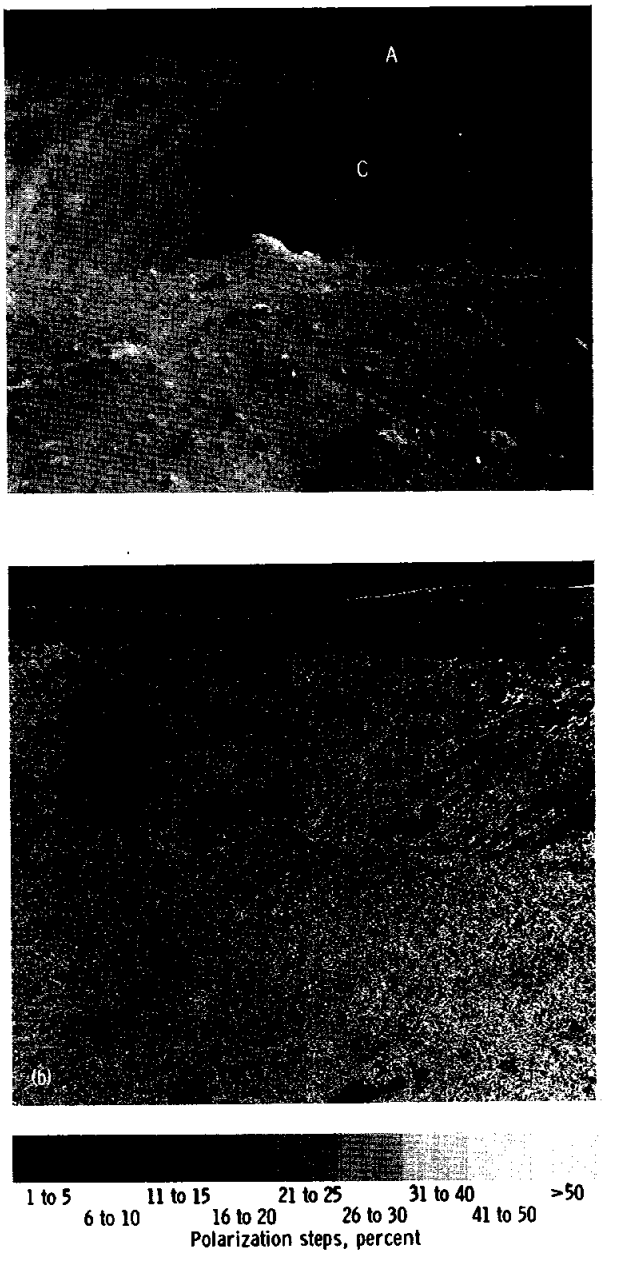


FIGURE 6-82.–Polarimetry results of north wall and southeast rim (near field) of North Ray Crater. (a) One frame (AS16-106-17239) from the left polarization panorama. Filter orientation is horizontal. This frame was the basis for registering the two additional filter positions. (b) Computer printout of polarization data from the scene in figure 6-82(a). Degree of polarization is divided into nine percentage ranges. The gray scale indicates the percent of polarization from 0 to more than 50 percent. The apparent mean of the scene polarization is 10 to 11 percent with a maximum of approximately 30 percent on a few rocks.

distinct materials: (1) a region of regolith that covers Smoky Mountain (area A, fig. 6-82(a)) and drapes over the northwest rim of the crater (area B, fig. 6-82(a)), (2) a crater rim deposit (area C, fig. 6-82(a)), and (3) a region on the west wall of the crater characterized by high albedo and by a unique polarimetric function. It was found that individual rock fragments varying in width from 25 cm in the foreground to 10 m on the northwest rim have low degrees of polarization. All rock fragments around North Ray Crater show less than one-half of the polarization measured on the Apollo 11 and 12 crystalline rocks and one-half to two-thirds of the polarization measured on Apollo 14 samples from the Fra Mauro region.

The albedo measurements of lunar materials at the various stations of the three EVA traverses can be arranged into three groups. The albedos of stations 1, 2, and the LM area ranged from 15 to 18 percent. The albedos of stations 4, 5, 6, and 8 were higher, ranging from 17 to 20 percent. North Ray Crater stations 11 and 13 have albedos ranging from 20 to 24 percent. The albedo variations seemed to be superimposed on a regional albedo of approximately 15 percent, with ray ejecta from South Ray Crater raising the albedos of the southern traverse stations and with North Ray ejecta increasing the albedos of stations 11 and 13. The landing site area is apparently underlain by light material that is being mixed with darker regolith by cratering mechanics. Proximity to relatively recent sources of lighter materials influences the local albedo.

The rock surfaces around North Ray Crater apparently contain little crystalline material that can polarize reflected light. The polarimetric properties of these rocks suggest that they are much more highly shocked than the Fra Mauro breccias from Cone Crater. No areas, layers, or blocks of intermediate to strong polarization were observed such as would be expected for relatively unshocked basaltic crystalline rock. All measurements of rock blocks at North Ray Crater are consistent with the polarimetric properties of highly brecciated and shocked material.

PRELIMINARY GEOLOGIC INTERPRETATION OF THE SITE

The enormous yield of Apollo 16 photographs, samples, and crew observations permits a tentative evaluation of the local geology in the landing site area. Early synthesis of the data demonstrates the geologic complexity of the site and emphasizes the importance of the diverse types of data provided by manned exploration of the Moon. The Apollo 16 investigations clearly require modifications of prevailing geological models for the nature and evolution of the Cayley Formation in this area and elsewhere in the lunar highlands.

The Cayley Formation probably has been sampled to a depth of approximately 200 m at North Ray Crater; to shallower depths at stations 1, 2, and 6; and, intermittently, over a distance of approximately 10 km between North Ray and South Ray Craters. Sampling of South Ray ejecta from some of its conspicuous rays may have provided both light and dark materials (fig. 6-83) from as deep as 150 m, although most are from shallower depths. The difference in the rim elevations of the two major craters suggests that a vertical range of more than 300 m may have been sampled (fig. 6-84).

Heterogeneous fragmental rocks (breccias) are the dominant lithology of the Cayley Formation. Although several distinctly different types are present, light- and dark-matrix breccias dominate the surface debris that was sampled and photographed. Significant variations in proportions of breccia types appear in the ejecta of each major sampled crater, but there do not appear to be any differences between the rock assemblages from North Ray and South Ray Craters. The sample distribution data and the new photography of South Ray and Baby Ray Craters (figs. 6-85 and 6-86) suggest a possible crude horizontal stratification, with alternating lighter and darker breccia units. These data support interpretations made in the premission photogeologic mapping. The Apollo 16 rocks closely resemble those collected on the Apollo 15 mission from the Apennine Front. They do not show the characteristic multiple brecciation and metamorphism of the Apollo 14 samples.

Bulk compositions of Cayley soils obtained by the Lunar Sample Preliminary Examination Team show a surprising uniformity throughout the traverse area. Rock compositions show a slightly larger range but still have a remarkably small range of variation. Both soil and rocks are roughly equivalent in composition to terrestrial anorthosites and feldspar-rich gabbros. This indicates that the textural and albedo differences in the several breccia types probably reflect variations in their history rather than in their source materials.

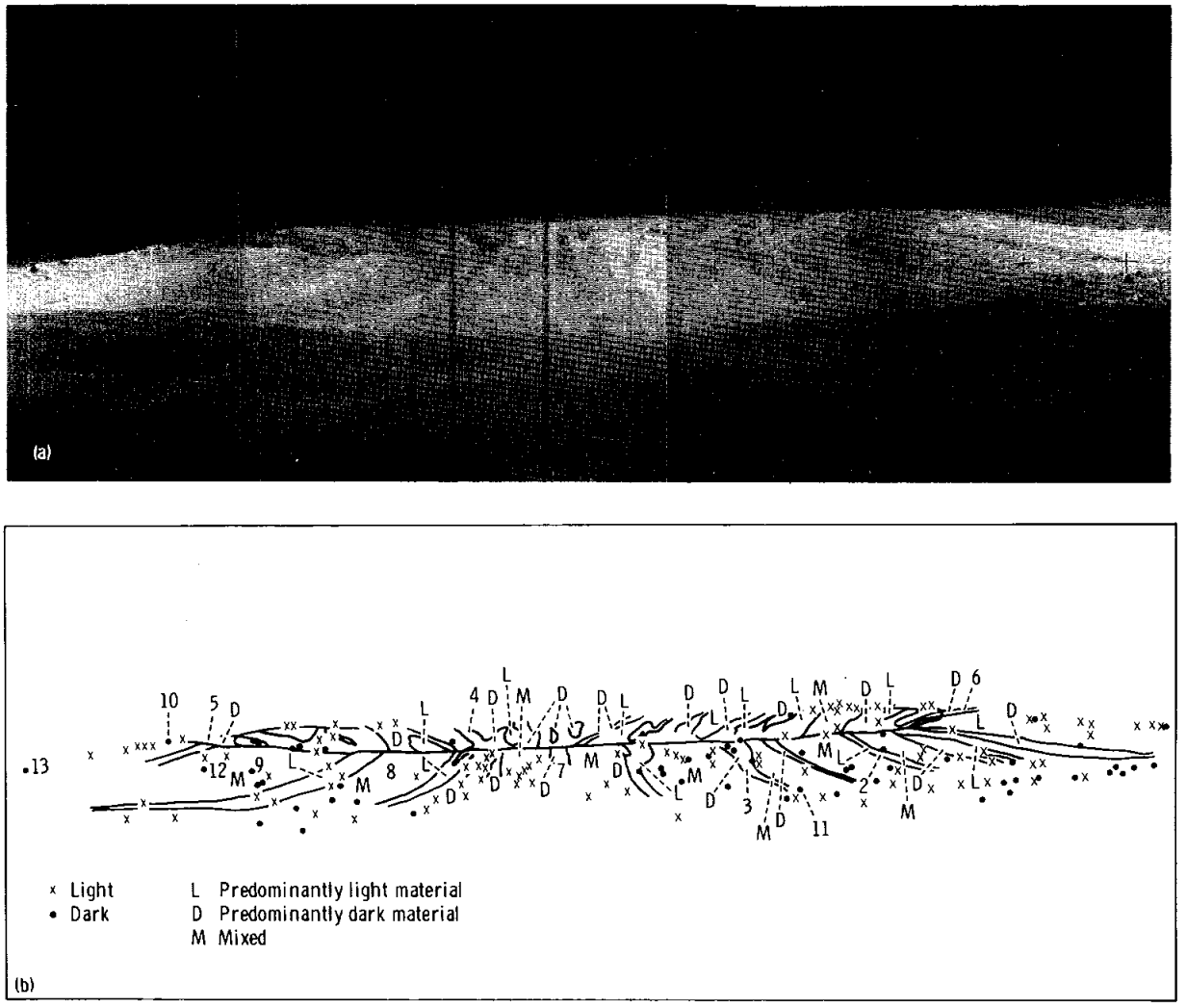


FIGURE 6-83.–South Ray Crater telephotographic view and interpretation as seen from Stone Mountain (station 4). (a) Partial panorama (AS16-112-18246, 18247, and 18256). (b) Distribution of light and dark ray patterns and individual blocks. Numbers correspond to features in map view (fig. 6-85(b)).

Some individual crystalline rock fragments were recovered along with the more abundant breccias. They fall into two apparent groups: igneous and metamorphic. The igneous rocks range from anorthosites to feldspar-rich gabbros and include minor amounts of fine-grained, highly feldspathic, vuggy igneous rocks. The metamorphic rocks are recrystallized fragmental rocks of a similar highly feldspathic composition. Clasts of these various types are observed in the breccias, and it is possible that all the crystalline rocks collected are simply clasts liberated from their breccia matrix. The general compositional range of the crystalline rocks is compatible with such an interpretation. However, the presence of some igneous rocks, either intrusive or extrusive, within the Cayley Formation at this site cannot be precluded at this time.

In summary, the Cayley Formation at the Apollo 16 site appears to be a thick (at least 200 and possibly more than 300 m), crudely stratified debris unit, the components of which are derived from plutonic anorthosites and feldspathic gabbros and from metamorphic rocks of similar composition. The Formation has an elemental composition similar to

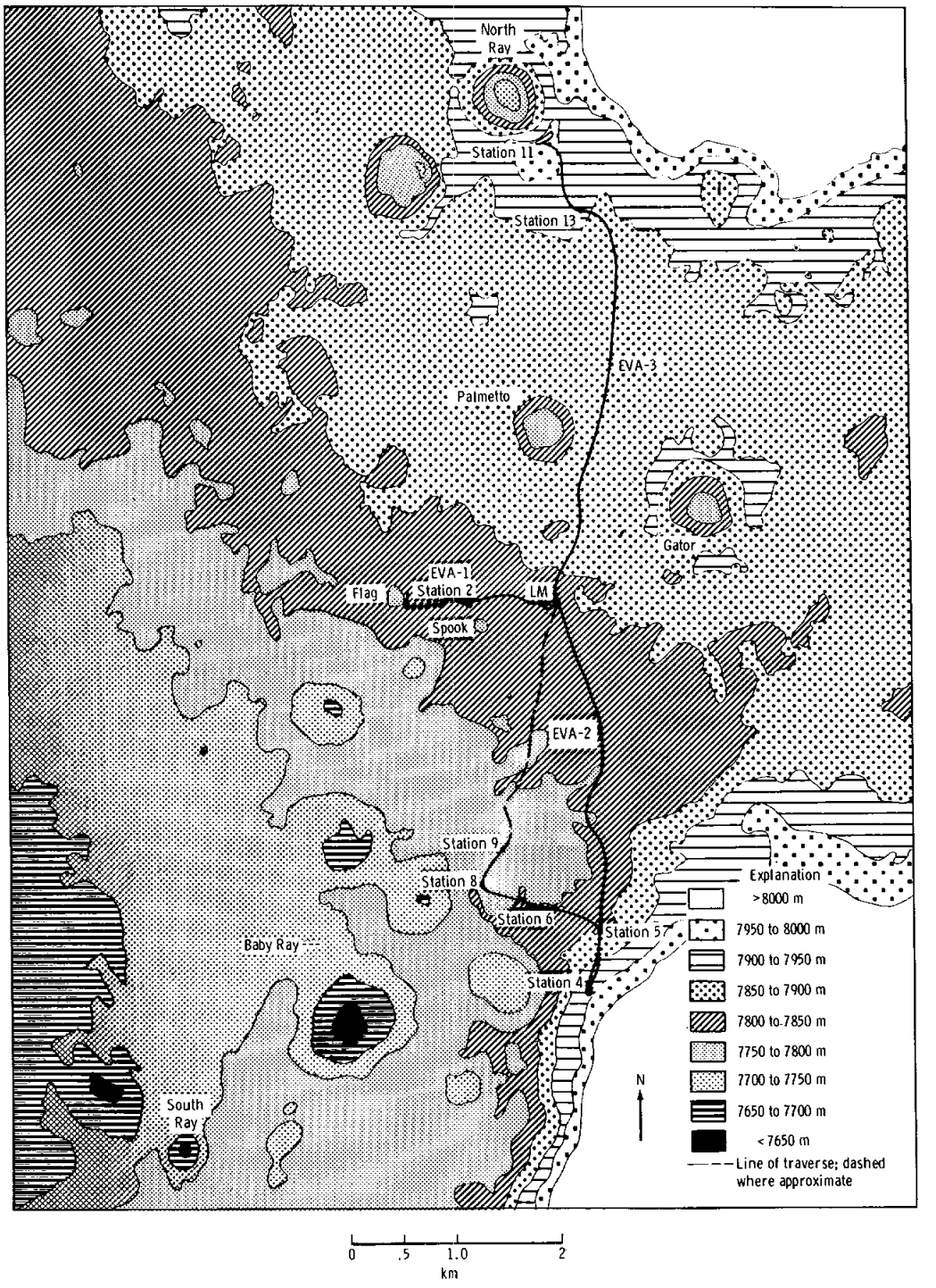


FIGURE 6-84.–Hypsographic map of the Descartes site, showing relative elevations to which craters penetrate. Adapted from premission topographic map compiled by Topographic Command, U.S. Army, by smoothing the index contours. The depth of South Ray Crater has been modified to reflect new data from the Apollo 16 panoramic photographs, from which profiles were derived by the U.S. Geological Survey.

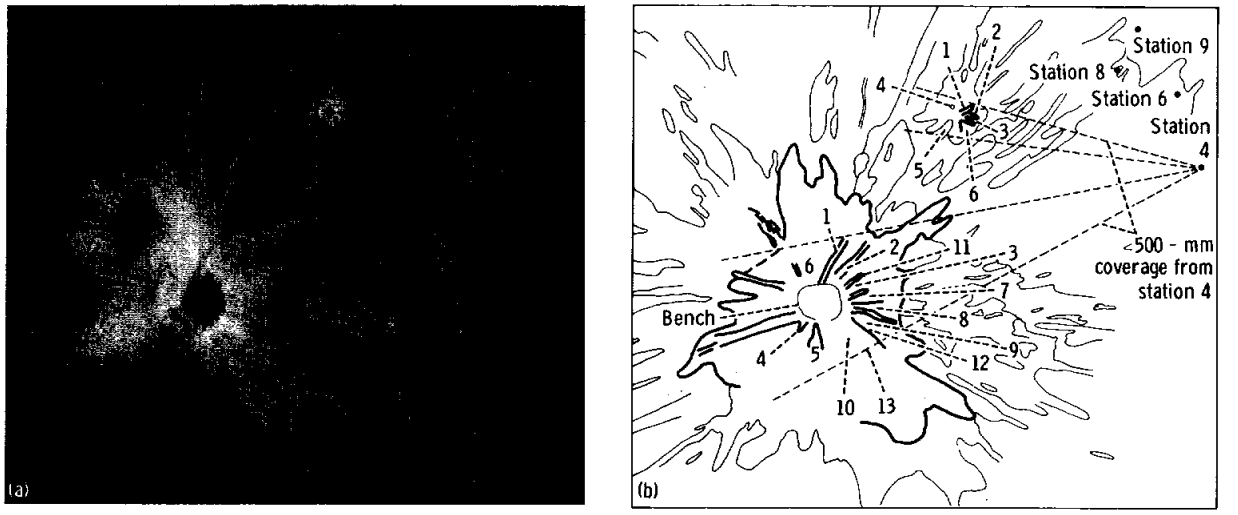


FIGURE 6-85.–South Ray and Baby Ray Craters. (a) Ray map (Apollo 16 pan camera frame 4618). (b) Sketch map; numbers correspond to features on figures 6-83(b) and 6-86(b).

that observed over large regions of the lunar highlands by the orbital X-ray experiments of the Apollo 15 and 16 missions (ref. 6-24). The observed textures and structures of the breccias resemble those of impact breccias. They do not resemble those of volcanic rocks nor do the plutonic or metamorphic source rocks of the breccias have the textures or compositions of terrestrial or previously sampled lunar volcanic rocks.

Whether the Cayley materials sampled are representative of the Cayley Formation elsewhere is at present unknown. The local relief in the traverse area is greater than in the Cayley Plains to the west. This roughness may be an edge effect of the Cayley basin against the Descartes Mountains or an intrinsic difference between the sampled Cayley Plains and the main area of plains. Detailed topographic maps (as yet unavailable) and photogeologic interpretation of the region will contribute data toward resolving this problem.

The materials of the Descartes highlands were the sampling objectives at stations 4 and 5 on Stone Mountain. The traverse route in this area is heavily mantled by angular, blocky debris, apparently ejected

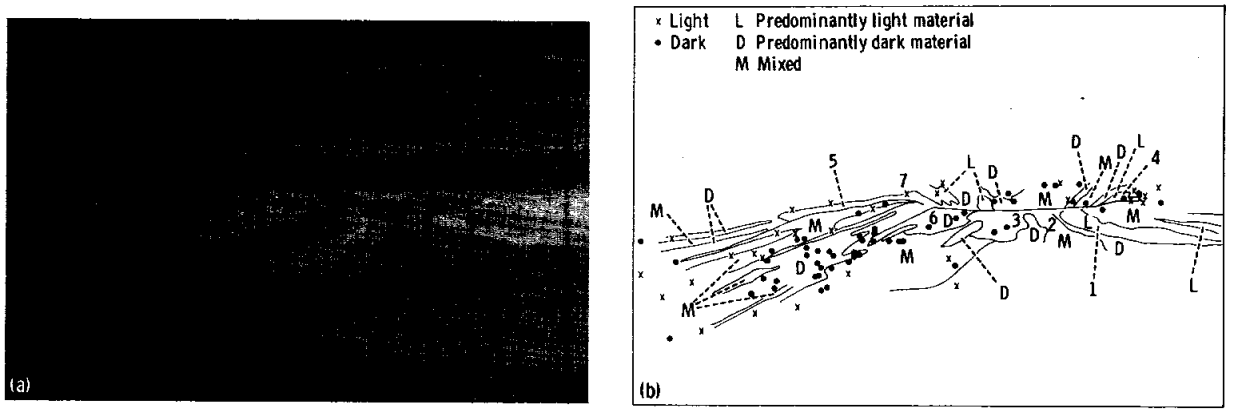


FIGURE 6-86.–Baby Ray Crater telephotographic view and interpretation as seen from Stone Mountain (station 4). (a) Partial panorama (AS16-112-18253 and 18254). (b) Distribution of light and dark ray patterns and individual blocks. Numbers correspond to features in map view (fig. 6-85(b)).

from South Ray Crater. The regolith under this blocky material is relatively fine grained with few coarse fragments. The crew observed no craters that penetrated to bedrock or that exposed coarse blocks of underlying materials.

Most of the rock samples, particularly at station 4, probably represent South Ray ejecta. At station 5, the crew sought and collected a number of more rounded fragments that did not appear to be ray associated. The rock types found at station 5 are generally similar to those found in Cayley localities. Some samples were collected from shielded crater-wall locations and probably include some Descartes materials, but none have yet been uniquely identified as such.

A number of soil samples were taken at the surface and in drive tubes at stations 4 and 5. Although variable dilution by South Ray fines is expected, these samples may be dominantly Descartes materials. Bulk comparisons of some of these soils with soils from Cayley terranes show marked compositional similarities. These observations add support to the indirect evidence from the rock collections that the Descartes materials may be lithologically similar to the Cayley Formation.

In summary, the precise nature of the Descartes highlands materials has not yet been established. Available evidence indicates that the Descartes highlands differ from the adjacent Cayley Formation more in physiographic expression than in actual lithologic character. Whether it is a stratified unit as suggested by several subtle topographic benches has not been established.

The stratigraphic and structural relations between the Cayley and Descartes units have not been directly established at this preliminary stage of the surface geology investigation. The contact between them was mapped from premission photography primarily as the break in slope at the base of Stone Mountain. No observations were made during the mission that would locate the contact more precisely. Detailed comparisons of soils and rocks from stations 5 and 6, which lie on opposite sides of the apparent contact, may ultimately provide some critical information. The asymmetrical distribution of lighter and darker breccias noted on the rim of North Ray Crater and the apparent contrast in albedo of its interior surficial debris raise the possibility that the North Ray impact may have penetrated a significant geologic contact. Whether this albedo contrast relates to a formational boundary cannot at present be demonstrated.

Premission geologic interpretations of the Apollo 16 landing site emphasized a probable volcanic origin for both the Cayley Formation and the materials of the Descartes highlands. The apparent nonvolcanic aspects of the many rocks sampled and photographed, combined with the absence of recognizable volcanic features at any scale in the region examined by the astronauts, do not support these interpretations.

The character of the Cayley Formation emerging from the Apollo 16 site studies supports consideration of an impact-related origin. The sources of the debris that might be considered include (1) ejecta from the Imbrium Basin (ref. 6-1), (2) ejecta from the Nectaris Basin, or (3) some combination of ejecta from various local and more distant sources accumulated over an extended time interval.

Derivation from the distant Imbrium Basin requires special mechanisms and timing. The plains-forming, depression-filling Cayley materials both overlap and extend beyond Imbrium sculpture and the Fra Mauro Formation. An Imbrium source would probably require a late-stage transport and deposition mechanism, perhaps in the form of a fluidized debris cloud generated by the impact. (See also part B of sec. 29 of this report.)

The Cayley surface at the Apollo 16 site has been interpreted from superposed crater frequency as slightly younger than the Fra Mauro surface at the Apollo 14 site.[3] If the interval in implied ages is significant, the stratigraphic relations strain the plausibility of an Imbrium origin. The sum of available stratigraphic and crater-frequency data does not favor derivation of the Cayley Formation during the development of the Nectaris Basin in pre-Imbrian time. However, Nectaris ejecta may be part of the breccia sequence beneath the Cayley surfaces in this area. Other impact mechanisms require more and smaller depositional events, probably integrated over long periods of time. Mass wasting has been suggested as a debris contributor, but it is not a satisfactory means of forming the plains of broad extent and considerable thickness present at the Apollo 16 site. There remains, of course, the remote possibility that unfamiliar explosive volcanic processes have produced widespread crustal fragmentation and breccia

[3] R. Greeley, written communication, 1971.

accumulation on the lunar surface or that postdepositional devolatilization of the basin-derived blankets has been responsible for emplacement of most of the terra plains. No obvious test for such a process suggests itself in the present data.

Each of the several possibilities has a very different implied time position in lunar history. Isotopic age studies on samples of the various breccia types and their included clasts may provide important additional constraints on these possibilities. (Papers in this report related to the origin of the Cayley and Descartes types of materials include parts A, C, D, F, U, and X of sec. 29.)

The incomplete characterization of the Descartes materials on Stone Mountain makes extended geological speculation premature. Materials in the same morphological unit partially fill the Descartes Crater to the south. These steep-sloped, relatively uncratered, high-albedo uplands have been interpreted as rather youthful, volcanic constructional features. If work in progress confirms that the Descartes Mountains comprise breccias similar in lithology and composition to materials of the Cayley Formation, the postulated volcanic origin will require reassessment. Additional petrologic information, soil analyses, and age studies of the returned samples are necessary to conduct such an evaluation.

APPENDIX A

SURFACE PHOTOGRAPHIC SUMMARY

A total of 1774 photographs was taken on the lunar surface with Hasselblad electric data cameras (refs. 6-18 and 6-21). Most of these photographs were taken according to procedures designed for geologic documentation. The number of photographs taken and the rate at which they were taken are given in table 6-V. A comparison of station times with the number of samples collected and the number of 70-mm photographs taken is shown in figure 6-87. This comparison illustrates the resulting allotment of effort to sampling and photography at each of the traverse stations and also the relative return from the major geologic entities of the Cayley Plains, Stone Mountain, and North Ray Crater.

The following photographic procedures were used.

(1) Sample documentation photographs were taken to show the in situ character of a returned sample or of a feature that could not be returned. Documentation of samples included a single photograph for photometric study taken down-Sun of the sample in place and a cross-Sun stereoscopic pair. After the sample was collected, a photograph was taken of the sample area from near the same place as the stereoscopic photographs to establish which of the samples visible in the presampling photograph was actually collected. A final photograph was taken of the sample area and of the LRV to establish the locality of the sample within the station area. Where time was short or footing awkward, one or more of these photographs were eliminated. A few stereoscopic pairs of interesting features impractical to collect were taken from distances of approximately 0.76 m.

(2) A special polarization survey was taken from the rim of North Ray Crater in an attempt to gather lithologic information about distant materials. This panoramic series of photographs was taken three times with a polarizing filter in three orientations 45° apart. The survey was repeated from a second vantage point, providing stereoscopic coverage of the area together with the polarization information.

(3) Panoramas were taken at each station to permit precise location of the station by resection and to illustrate and supplement geologic descriptions by the crew. A complete panorama consists of 15 or more photographs covering 360°. Partial panoramas were taken of features such as House Rock (fig. 6-57). The overlap zones between photographs in panoramas can be viewed stereoscopically because the aiming direction of the camera was changed and the lens position was shifted slightly each time. This provides a stereoscopic baseline a few centimeters long, which is useful for study of topography within 50 to 100 m of the camera.

(4) Photographs were taken with a 500-mm-focal-length camera to permit study of features inaccessible to the crew. Although a few photographs were degraded by camera motion, even those photographs have more resolution than the 60-mm pictures and contain information not otherwise available. The 500-mm photographs are also being used for precise measurement of spot elevations in the traverse area. The measurement requires that discrete points in the traverse be positively identified in panoramas taken from distant stations. This is rarely possible in the lower resolution photographs taken with the 60-mm-focal-length cameras but frequently possible in photographs taken with the 500-mm lens. For example, in

TABLE 6-V.–Apollo 16 Film Usage

Station	Type of photograph							Magazine	Rate (a)
	Sample documentation	Polarization	Panorama	500-mm lens	En route	Other	Blank or fogged		
[b]EVA-1									
LM			18			13		113	
ALSEP			22			17		113	
ALSEP	6							114	23
ALSEP						1		109	
ALSEP to 1					28			109	19
1	16		19					109	68
1	27		18					114	
2	12		26					109	
2						1		114	191
2				50				112	
2 to LM					14			109	16
LM						2		109	
LM			3			5	2	114	
EVA-1 total	61	0	106	50	42	39	2		44
[c]EVA-2									
LM			21			3		107	
LM	3					1		110	
LM to 4					77			110	20
4				35				112	
4	26		23					107	116
4	5		23					110	
4 to 5					16			110	42
5	13		28				1	110	76
5	18					2		107	
5 to 6					21			108	66
6	7		21					108	112
6	15							107	
6 to 8					29			108	51
8	21		19					108	63
8	31							107	
8 to 9					11			108	34
9	4		26			1		108	
9	23					3		107	104
9						2		115	
9 to 10					[d]81			115	39
10	4						1	115	60
10	5		19					114	
LM						4		115	
LM						3		114	
EVA-2 total	175	0	180	35	235	19	2		91

TABLE 6-V.–Apollo 16 Film Usage – Concluded

Station	Type of photograph							Magazine	Rate (a)
	Sample documentation	Polarization	Panorama	500-mm lens	En route	Other	Blank or fogged		
[e]EVA-3									
LM				63			1	105	
LM			29					116	
LM to 11					159			111	34
11				118				105	
11	46		23					116	215
11	29	79	10					106	
11 to 13					29			106	45
13	5		27					106	
13	9					2		116	99
13			4			1		117	
13 to 10′					9			116	
13 to 10′					[f]70			117	19
10′	4		23					117	
10′	27							116	108
LM	4					13		116	
LM	11					16		117	
EVA-3 total	135	79	116	181	267	32	1		168
Apollo 16 totals	371	79	402	266	544	90	5		94

[a]Rates are given in photographs per hour at stations and photographs per kilometer between stations. Totals are given in photographs per hour.

[b]The total for EVA-1 was 300 frames.

[c]The total for EVA-2 was 646 frames.

[d]Includes five frames in "LRV turnaround panorama."

[e]The total for EVA-3 was 811 frames.

500-mm photographs taken from station 4, House Rock (the most distant point on the traverse from station 4) is clearly visible (fig. 6-56).

(5) The lunar module pilot (LMP) took photographs at regular intervals while the LRV was in motion. These photographs are being used to reconstruct the traverse and to measure block distributions over wide areas. Twice during these "en route" sequences, the commander (CDR) drove the LRV in a tight circle while the LMP took photographs, resulting in what has been termed an "LRV turnaround" panorama.

In addition to photographs taken for geologic documentation, several photographs were taken to illustrate ALSEP deployment and other subjects not related to geology. These are listed under "other" in table 6-V. A few blank frames or frames fogged when magazines were changed were assigned numbers and are therefore shown in table 6-V, even though the information content is minimal.

APPENDIX B

LUNAR SURFACE ORIENTATIONS OF APOLLO 16 ROCK SAMPLES

The lunar surface orientations of some of the Apollo 16 rock samples at the time of their collection (table 6-III) are shown in this appendix (figs. 6-88 to

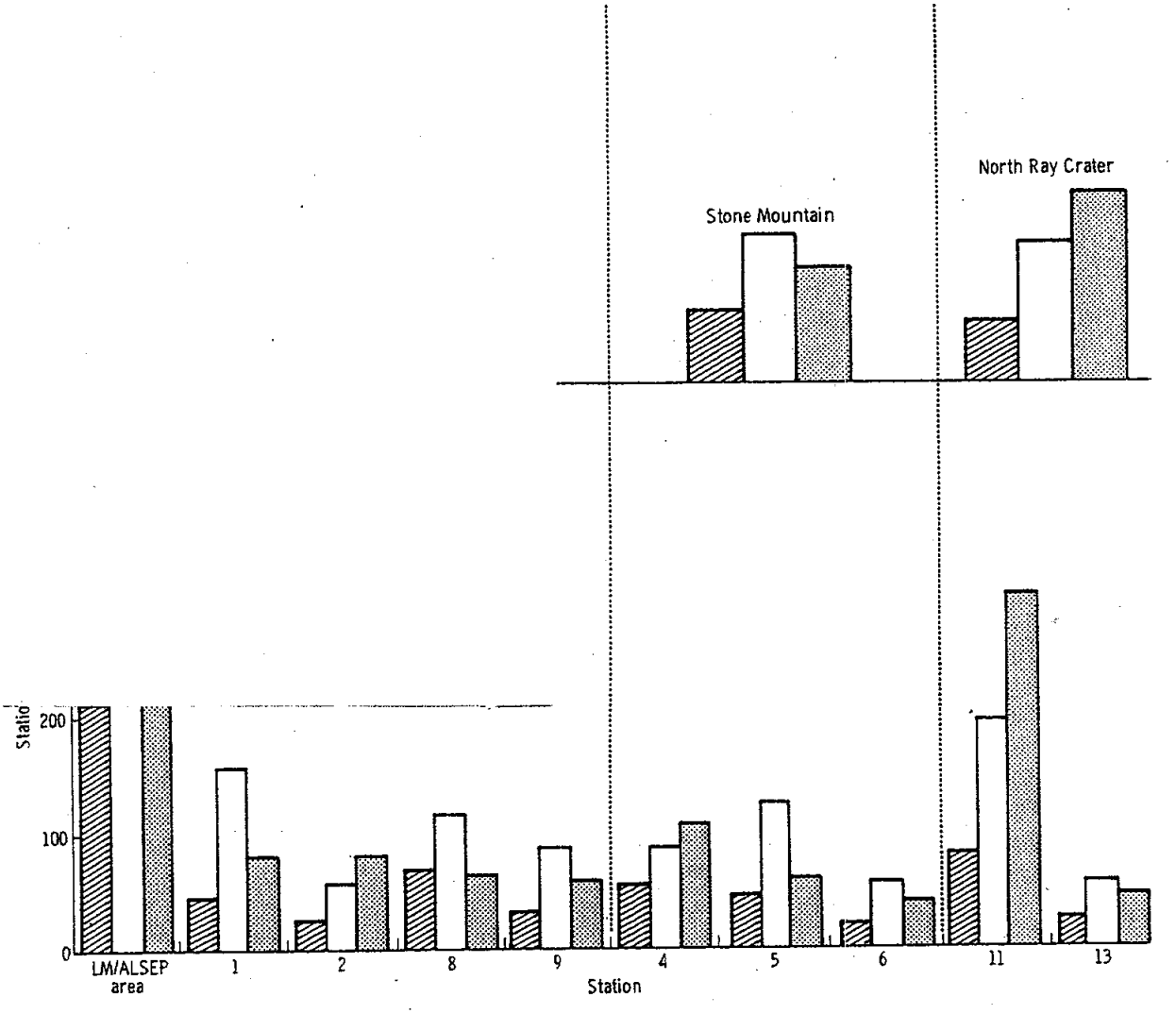


FIGURE 6-87.–Comparison of station times, number of samples collected, and number of 70-mm photographs taken. The number of samples collected is shown 10 times the actual value for clarity.

6-128). These orientations were determined by correlating lunar photographs of samples before collection with shapes and shadow characteristics of the same samples in the LRL when they are illuminated obliquely by nearly collimated light. The light source in the LRL portrays the Sun. It is important to emphasize that the orientations shown are those at the time of collection and do not necessarily apply to the entire history of the exposure of the sample on the lunar surface. Tumbling and turning of some rock fragments on the lunar surface has already been well documented.

The small lettered cube included in each laboratory orientation photograph is not meant to indicate the lunar attitude of samples but is designed to tie the lunar perspective orientations to documentary views of the same samples in orthogonal and stereoscopic photographs (mug shots) taken in the LRL using the same orientation cube.

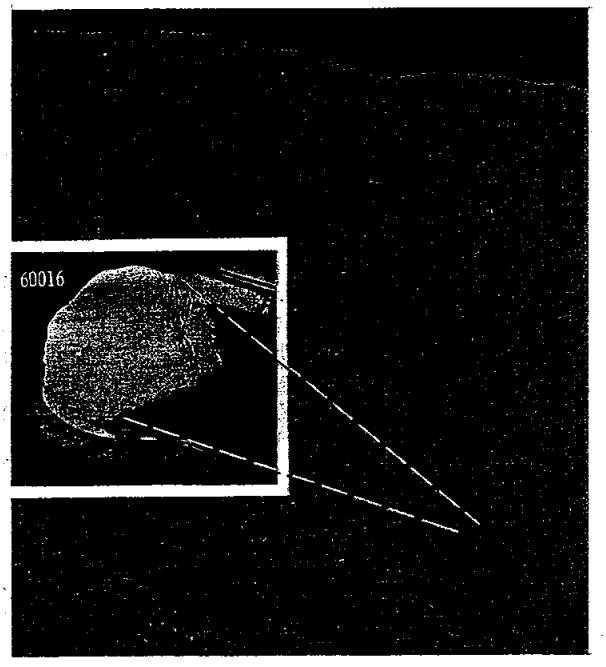


FIGURE 6-88.–Sample 60016 showing approximate lunar orientation reconstructed in the LRL compared to an enlarged part of photograph AS16-113-18298 taken from the LM window before EVA-1, looking southeast (inset photograph, S-72-44510).

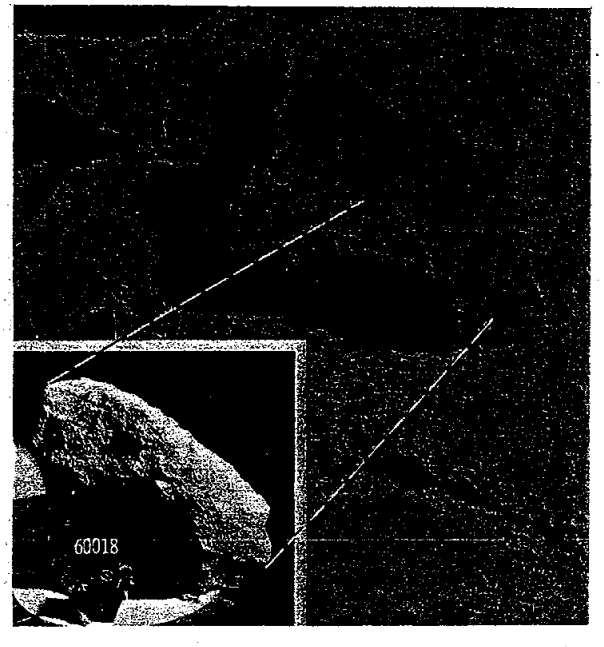


FIGURE 6-89.–Sample 60018 showing approximate lunar orientation reconstructed in the LRL compared to an enlarged part of EVA photograph AS16-116-18689 taken cross-Sun, looking north (inset photograph, S-72-41840).

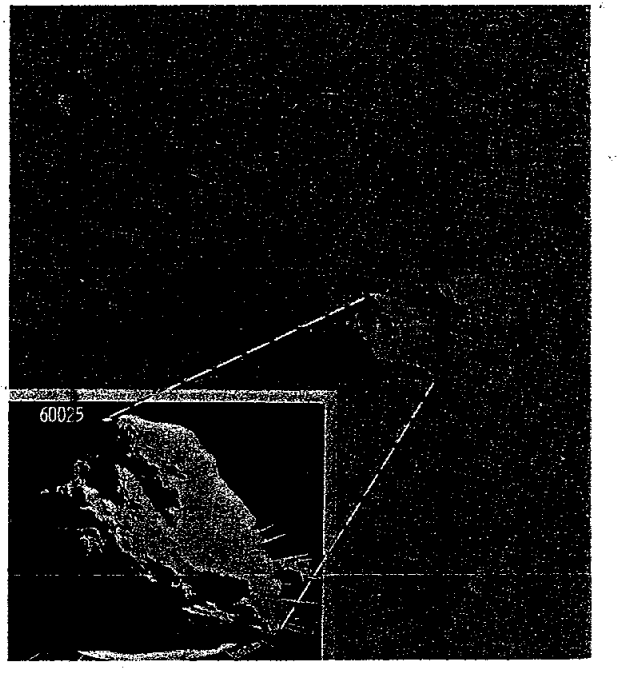


FIGURE 6-91.–Sample 60025 showing approximate lunar orientation reconstructed in the LRL compared to an enlarged part of EVA photograph AS16-110-17866 taken cross-Sun, looking north (inset photograph, S-72-44019).

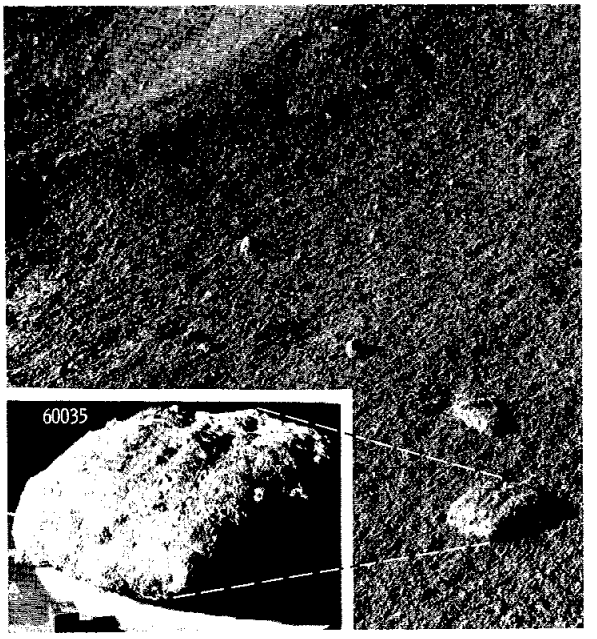


FIGURE 6-92.–Sample 60035 showing approximate lunar orientation reconstructed in the LRL compared to an enlarged part of EVA photograph AS16-114-18384 taken cross-Sun, looking south (inset photograph, S-72-41610).

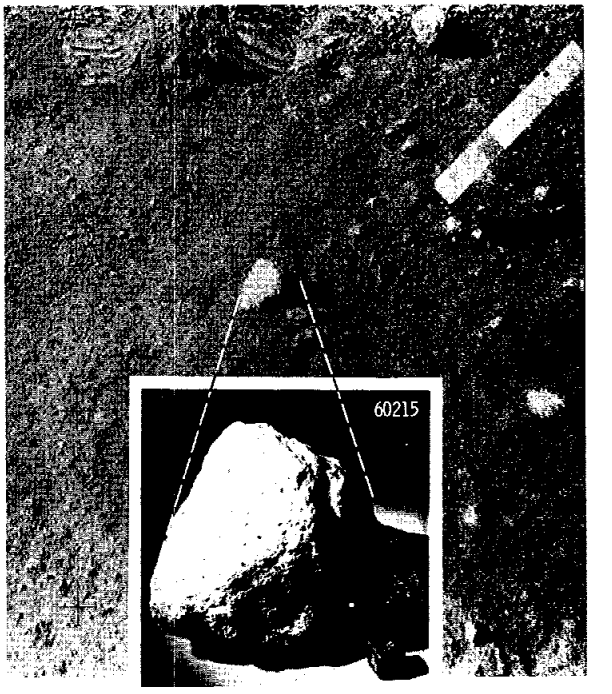


FIGURE 6-94.–Sample 60215 showing approximate lunar orientation reconstructed in the LRL compared to an enlarged part of EVA photograph AS16-116-18705 taken cross-Sun, looking south (inset photograph, S-72-42836).

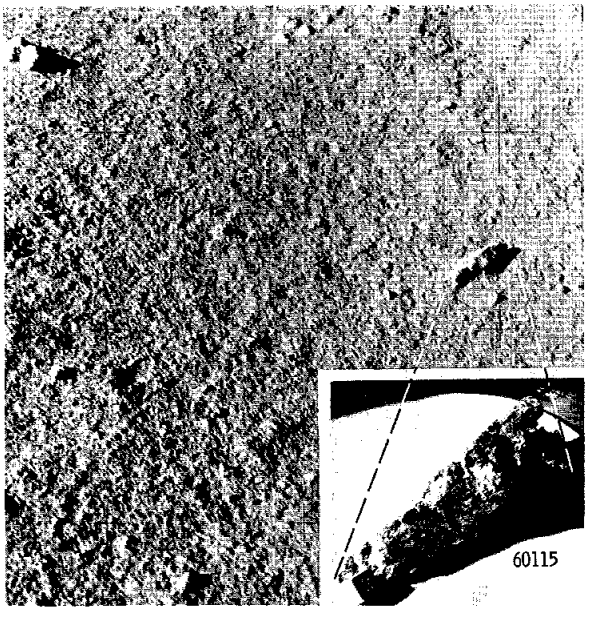


FIGURE 6-93.–Sample 60115 showing approximate lunar orientation reconstructed in the LRL compared to an enlarged part of EVA photograph AS16-114-18446 taken cross-Sun, looking south (inset photograph, S-72-42559).

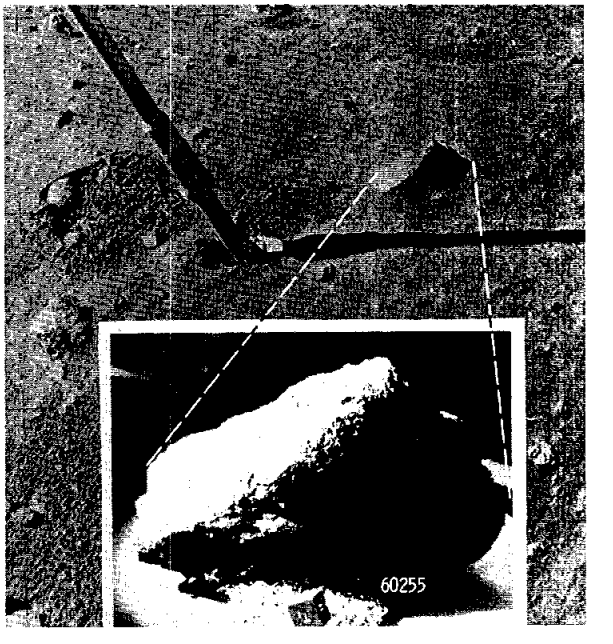


FIGURE 6-95.–Sample 60255 showing approximate lunar orientation reconstructed in the LRL compared to EVA photograph AS16-117-18832 taken cross-Sun, looking south (inset photograph, S-72-42837).



FIGURE 6-96.–Sample 60275 showing approximate lunar orientation reconstructed in the LRL compared to EVA photograph AS16-117-18833 taken cross-Sun, looking south (inset photograph, S-72-43115).

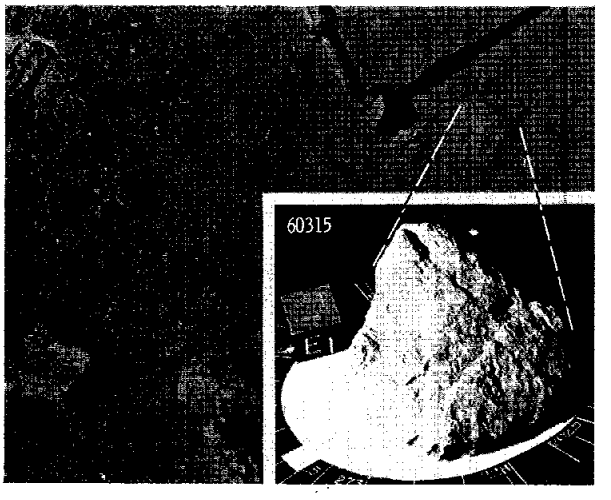


FIGURE 6-97.–Sample 60315 showing approximate lunar orientation reconstructed in the LRL compared to an enlarged part of EVA photograph AS16-117-18836 taken oblique-to-Sun, looking southwest (inset photograph, S-72-41842).

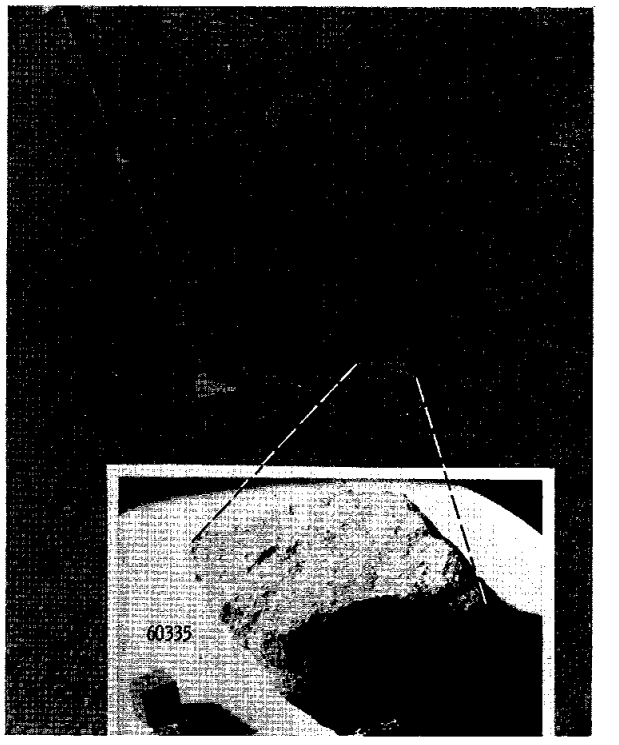


FIGURE 6-98.–Sample 60335 showing approximate lunar orientation reconstructed in the LRL compared to an enlarged part of EVA photograph AS16-116-18712 taken cross-Sun, looking south (inset photograph, S-72-41335).

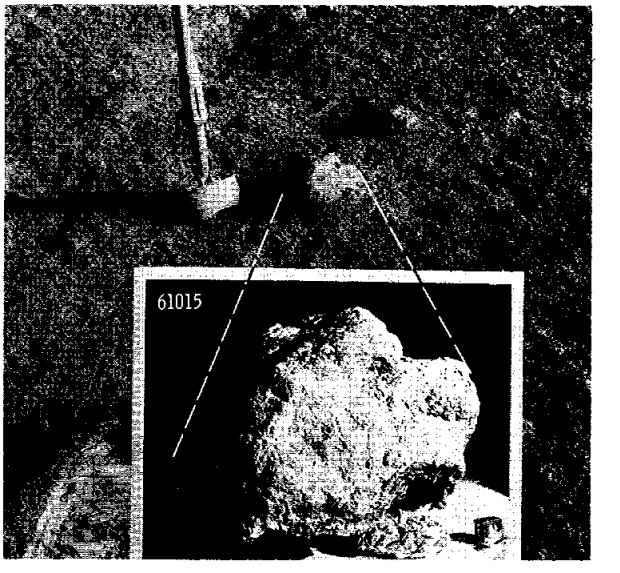


FIGURE 6-99.–Sample 61015 showing approximate lunar orientation reconstructed in the LRL compared to an enlarged part of EVA photograph AS16-109-17808 taken cross-Sun, looking north (inset photograph, S-72-41058).

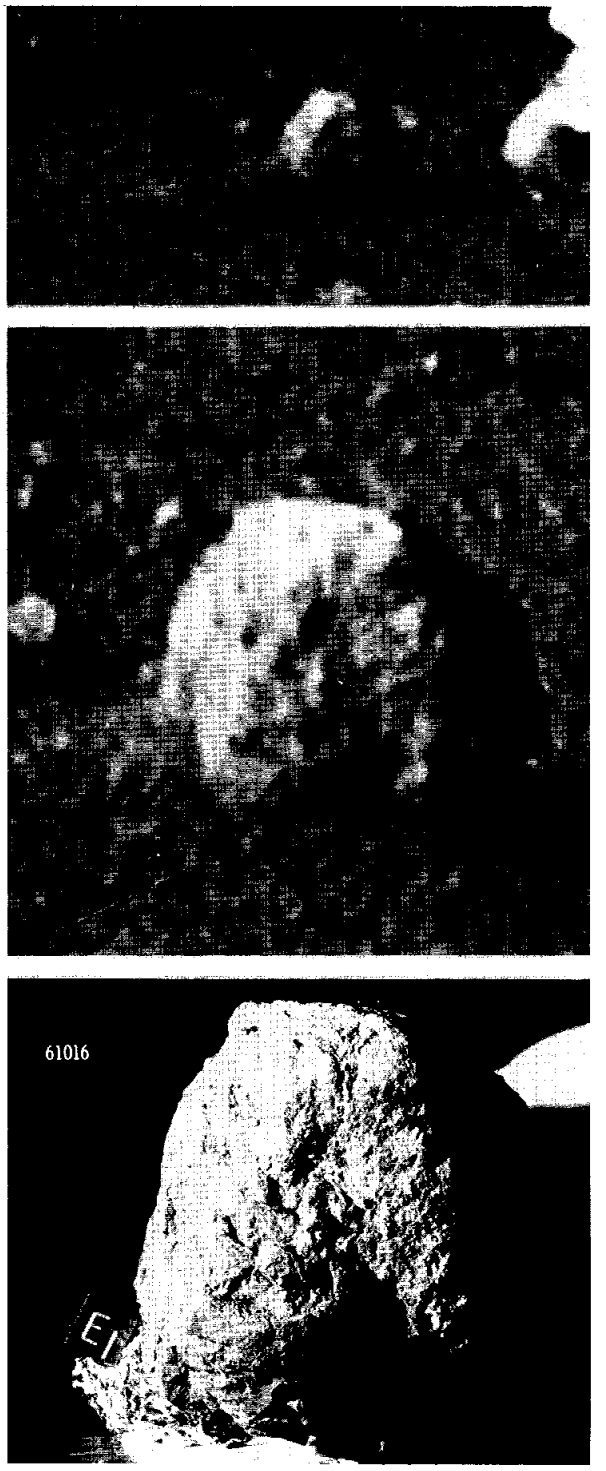


FIGURE 6-100.–Sample 61016 showing approximate lunar orientation reconstructed in the LRL compared to an EVA television picture looking south from the LRV (bottom photograph, S-72-41841).

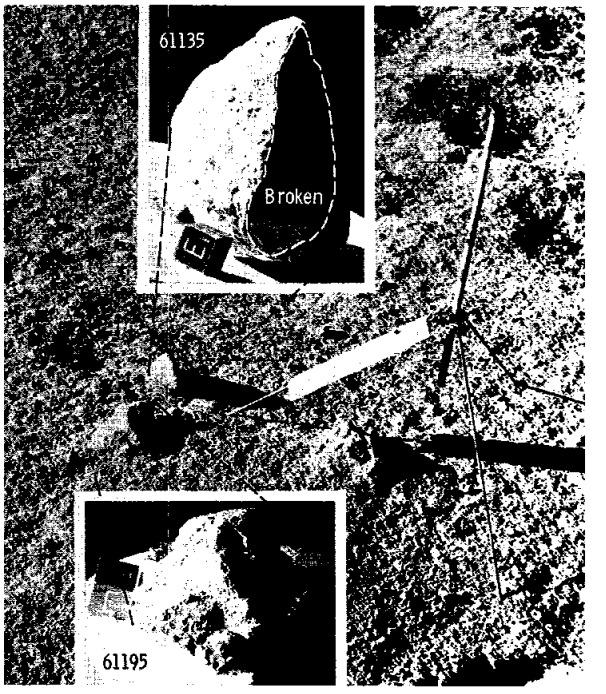


FIGURE 6-101.–Samples 61135 and 61195 showing approximate lunar orientations reconstructed in the LRL compared to an enlarged part of EVA photograph AS16-114-18405 taken cross-Sun, looking south (inset photographs, S-72-41609 and 43315, respectively).

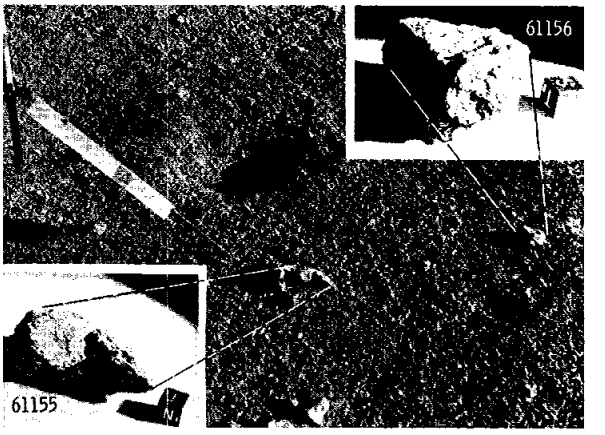


FIGURE 6-102.–Samples 61155 and 61156 showing approximate lunar orientations reconstructed in the LRL compared to an enlarged part of EVA photograph AS16-114-18397 taken cross-Sun, looking north (inset photographs, S-72-41613 and 41544, respectively).

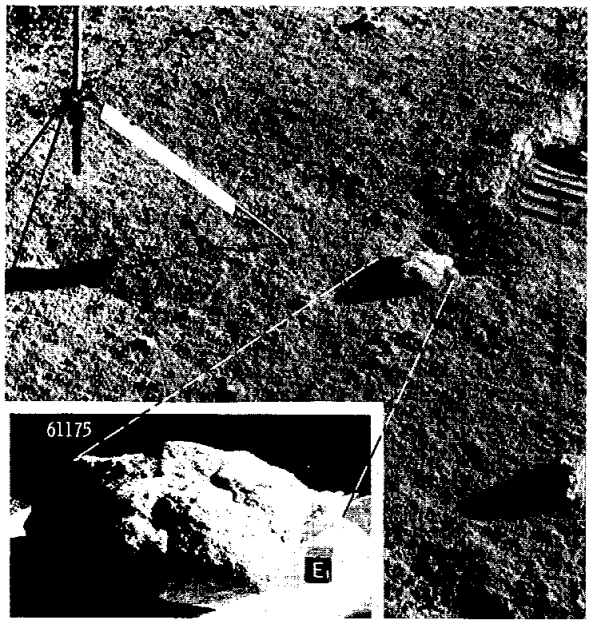


FIGURE 6-103.–Sample 61175 showing approximate lunar orientation reconstructed in the LRL compared to an enlarged part of EVA photograph AS16-114-18400 taken cross-Sun, looking north (inset photograph, S-72-40965).

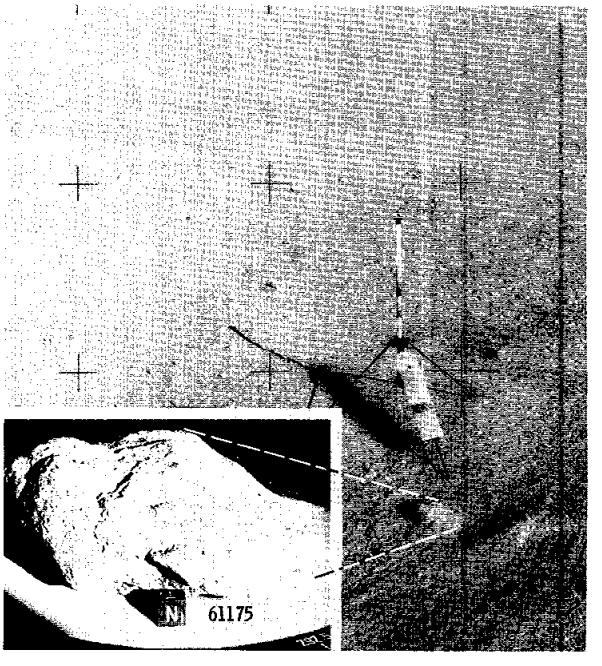


FIGURE 6-104.–Sample 61175 showing approximate lunar orientation reconstructed in the LRL compared to EVA photograph AS16-109-17798 taken down-Sun, looking west (inset photograph, S-72-40966).

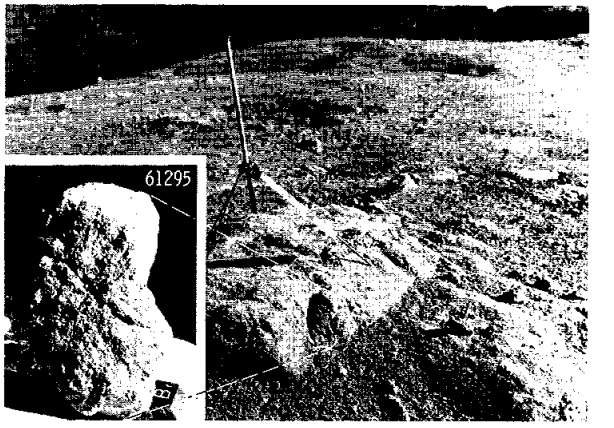


FIGURE 6-105.–Sample 61295 showing approximate lunar orientation reconstructed in the LRL compared to an enlarged part of EVA photograph AS16-114-18412 taken cross-Sun, looking north (inset photograph, S-72-40967).

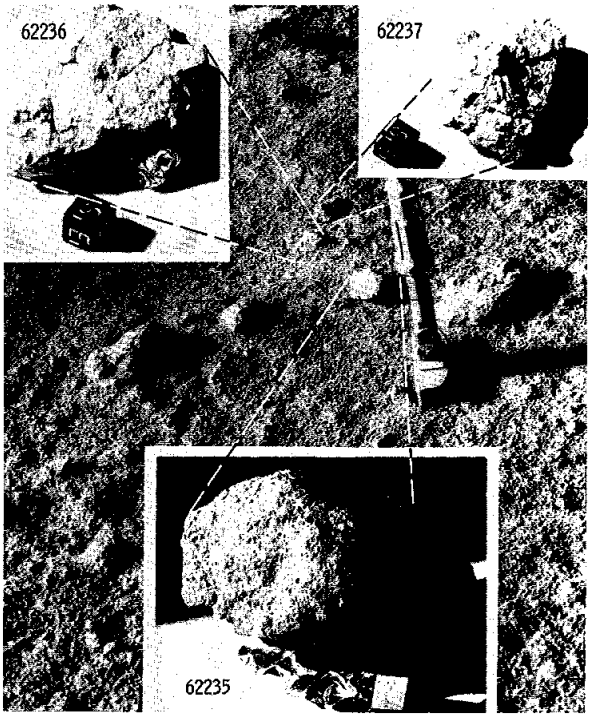


FIGURE 6-106.–Samples 62235, 62236, and 62237 showing approximate lunar orientations reconstructed in the LRL compared to an enlarged part of EVA photograph AS16-109-17838 taken cross-Sun, looking south (inset photographs, S-72-41424, 41837, and 41838, respectively).

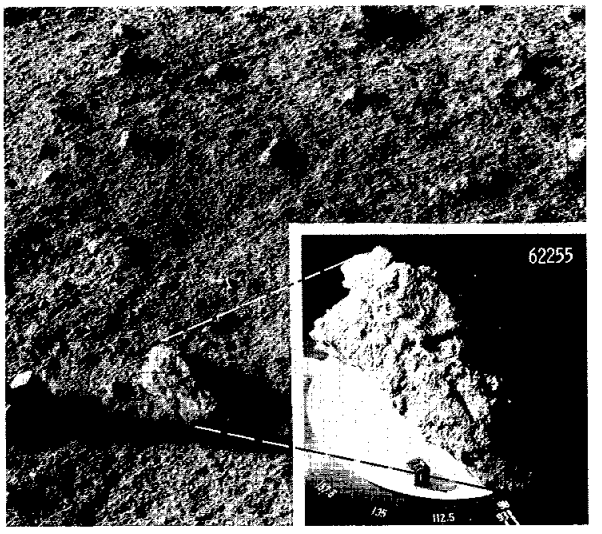


FIGURE 6-107.–Sample 62255 showing approximate lunar orientation reconstructed in the LRL compared to an enlarged part of EVA photograph AS16-109-17844 taken cross-Sun, looking south (inset photograph, S-72-41834).

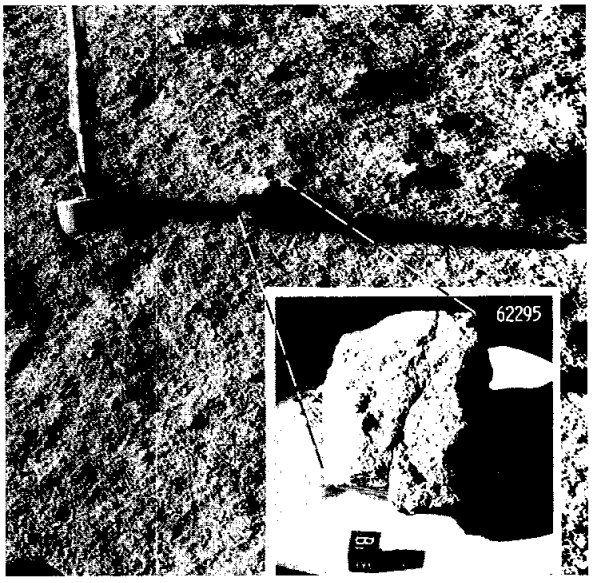


FIGURE 6-109.–Sample 62295 showing approximate lunar orientation reconstructed in the LRL compared to an enlarged part of EVA photograph AS16-109-17848 taken cross-Sun, looking south (inset photograph, S-72-42563).

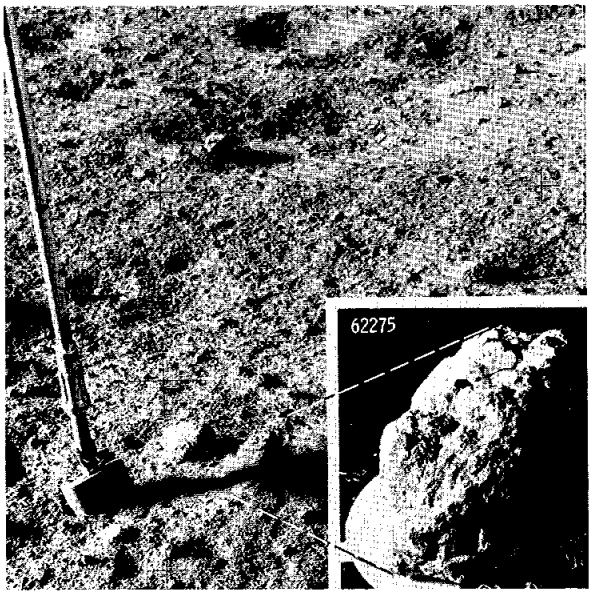


FIGURE 6-108.–Sample 62275 showing approximate lunar orientation reconstructed in the LRL compared to an enlarged part of EVA photograph AS16-109-17846 taken cross-Sun, looking south. The sample is fragile and minor breakage has occurred, thus making shadow details impossible to duplicate accurately in the laboratory (inset photograph, S-72-41426).

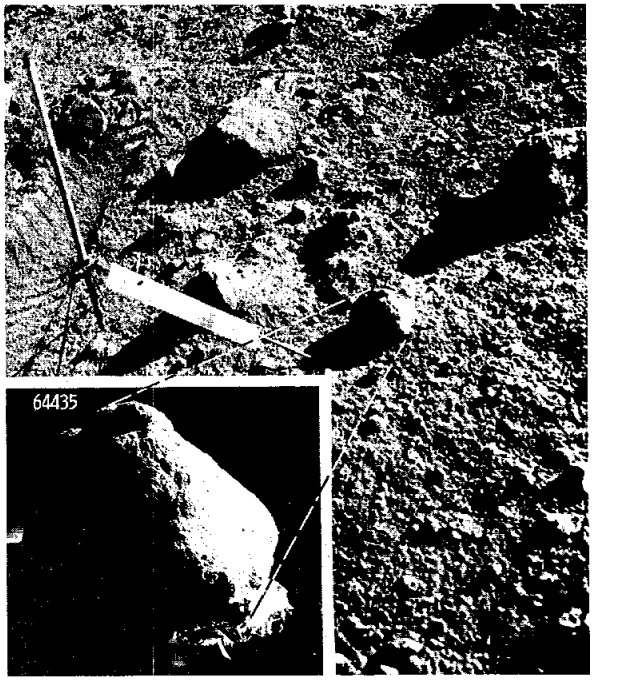


FIGURE 6-110.–Sample 64435 showing approximate lunar orientation reconstructed in the LRL compared to EVA photograph AS16-107-17444 taken oblique-to-Sun, looking northeast (inset photograph, S-72-41423).

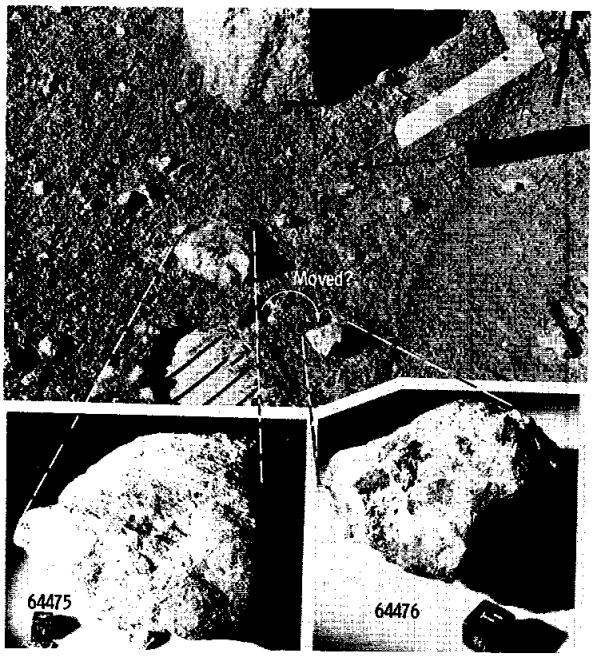


FIGURE 6-111.–Samples 64475 and 64476 showing approximate lunar orientations reconstructed in the LRL compared to EVA photograph AS16-107-17452 taken cross-Sun, looking south. Sample 64476 appears to have been moved before the lunar photograph (inset photographs, S-72-43117 and 43118, respectively).

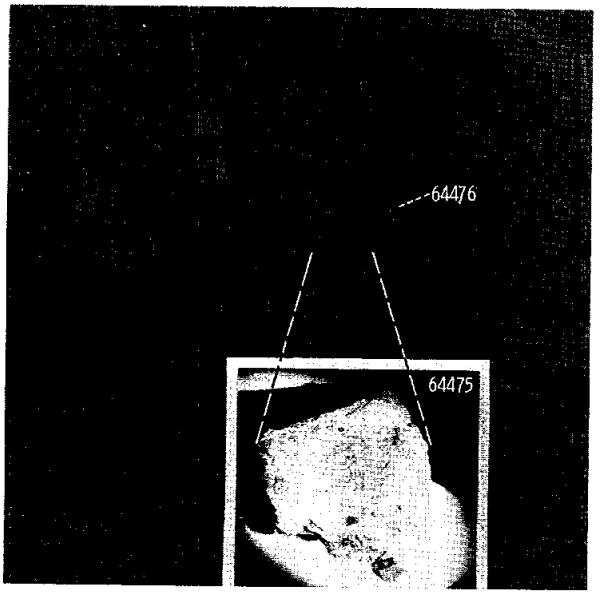


FIGURE 6-112.–Sample 64475 showing approximate lunar orientation reconstructed in the LRL compared to an enlarged part of EVA photograph AS16-107-17453 taken oblique-to-Sun, looking northwest (inset photograph, S-72-43116).

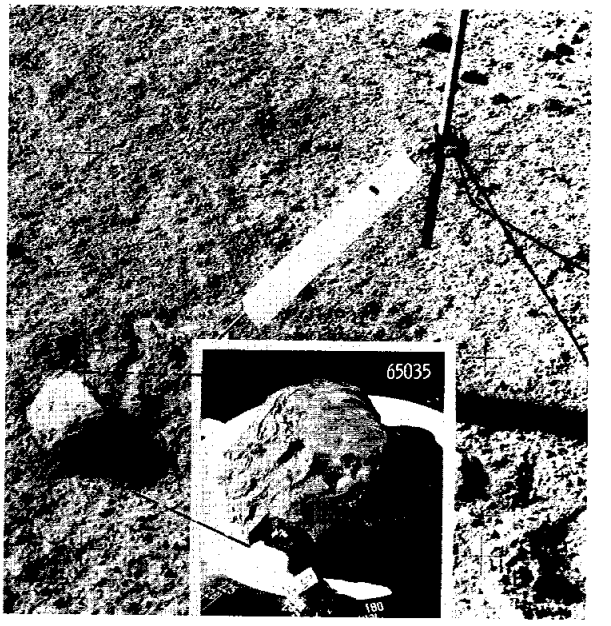


FIGURE 6-113.–Sample 65035 showing approximate lunar orientation reconstructed in the LRL compared to an enlarged part of EVA photograph AS16-110-18023 taken cross-Sun, looking south (inset photograph, S-72-43313).

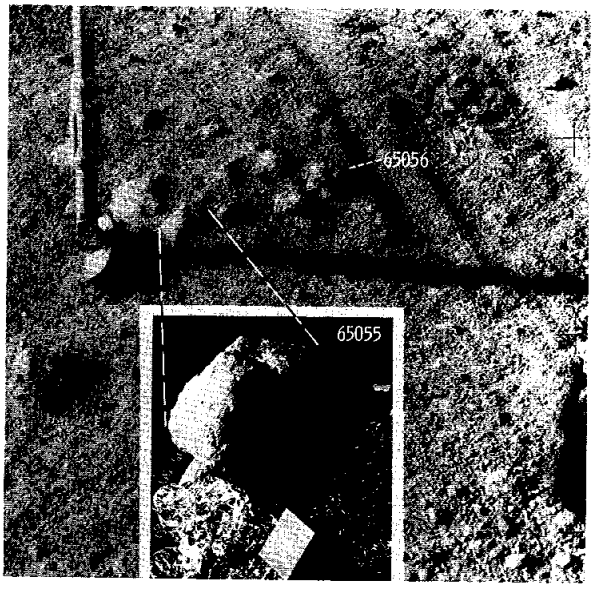


FIGURE 6-114.–Sample 65055 showing approximate lunar orientation reconstructed in the LRL compared to an enlarged part of EVA photograph AS16-110-18029 taken cross-Sun, looking south. Sample 65056 is in the same group of fragments photographed but was not oriented in the laboratory because of breakage (inset photograph, S-72-43314).

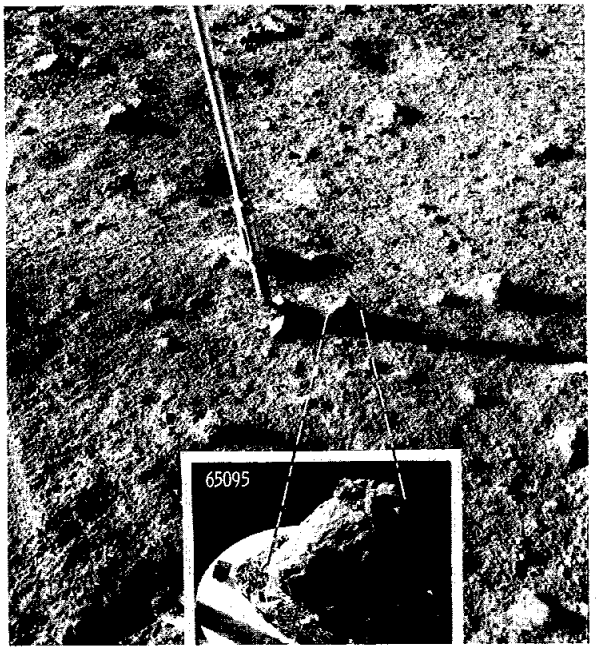


FIGURE 6-115.–Sample 65095 showing tentative lunar orientation reconstructed in the LRL compared to EVA photograph AS16-110-18027 taken cross-Sun, looking south.

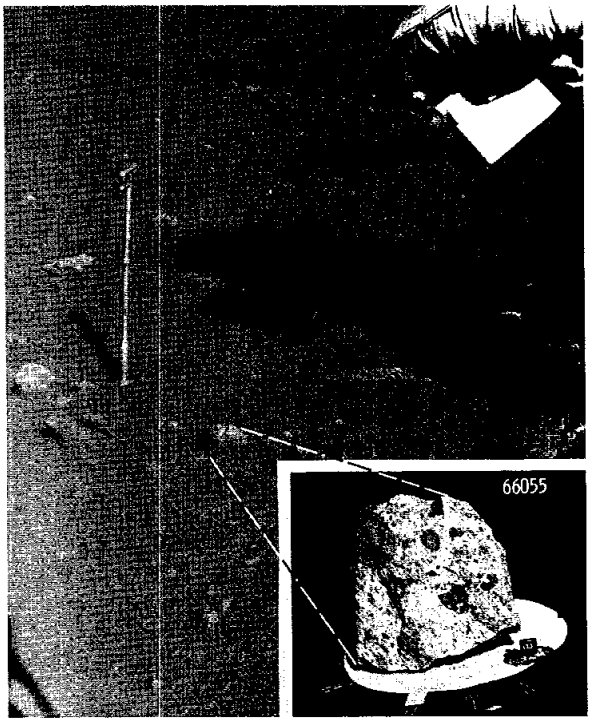


FIGURE 6-117.–Sample 66055 showing approximate lunar orientation reconstructed in the LRL compared to EVA photograph AS16-108-17627 taken oblique-to-Sun, looking northwest (inset photograph, S-72-42562).

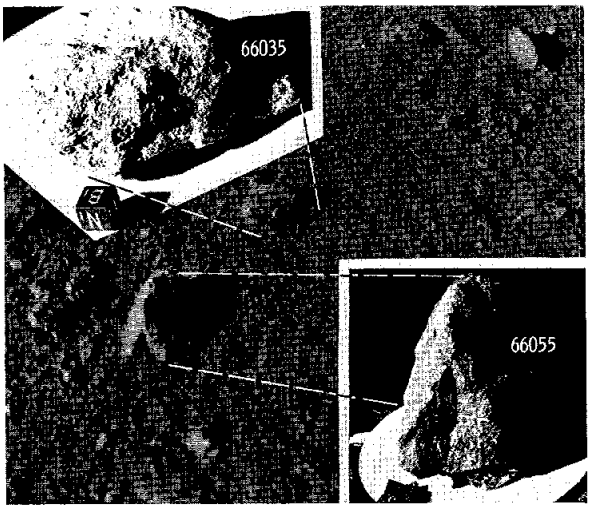


FIGURE 6-116.–Samples 66035 and 66055 showing approximate lunar orientations reconstructed in the LRL compared to an enlarged part of EVA photograph AS16-107-17512 taken oblique-to-Sun, looking southwest (inset photographs, S-72-41427 and 42560, respectively).

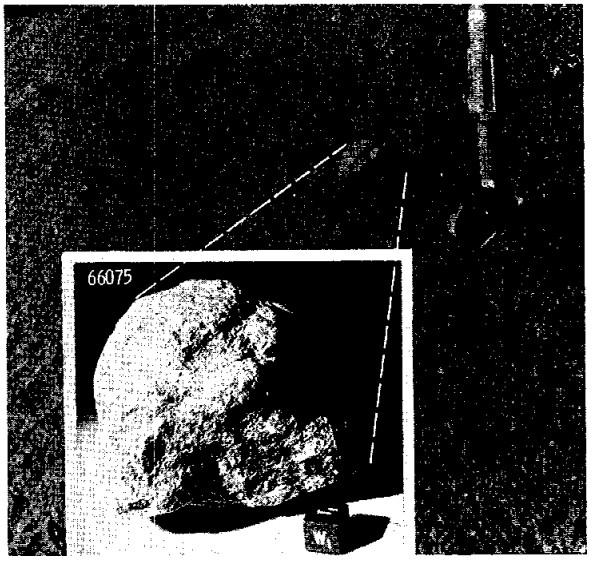


FIGURE 6-118.–Sample 66075 showing approximate lunar orientation reconstructed in the LRL compared to an enlarged part of EVA photograph AS16-107-17521 taken cross-Sun, looking south (inset photograph, S-72-40571).

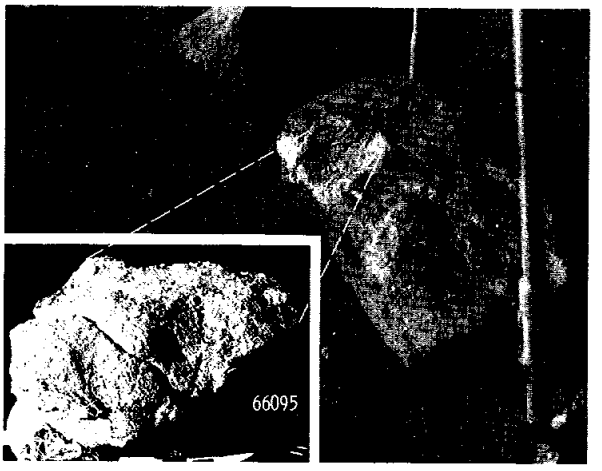


FIGURE 6-119.–Sample 66095 (broken into two pieces) showing approximate lunar orientation reconstructed in the LRL compared to an enlarged part of EVA photograph AS16-108-17632 taken cross-Sun, looking south. No photograph was taken before chipping the sample from the boulder. The reconstruction of orientation was done by matching the shapes of the sample and the boulder scar (inset photograph, S-72-41433).

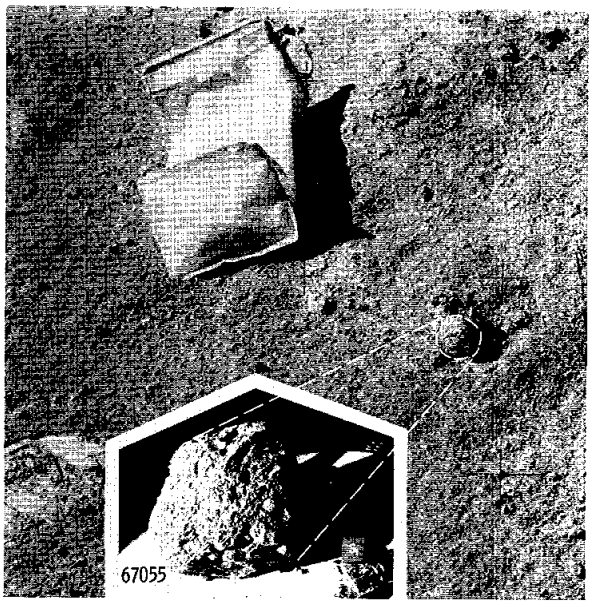


FIGURE 6-121.–Sample 67055 showing approximate lunar orientation reconstructed in the LRL compared to an enlarged part of EVA photograph AS16-116-18617 taken cross-Sun, looking south. The sample is friable and minor breakage has occurred, thus making shadow details impossible to duplicate accurately in the laboratory (inset photograph, S-72-44550).

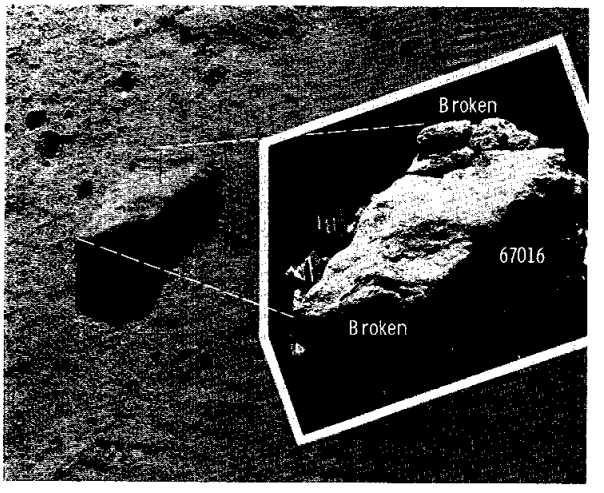


FIGURE 6-120.–Sample 67016 showing approximate lunar orientation reconstructed in the LRL compared to an enlarged part of EVA photograph AS16-116-18659 taken up-Sun, looking east. The sample was partly broken during transport, probably because the large rock 61016 (the "muley" rock) was on top of it in the bag (inset photograph, S-72-44509).

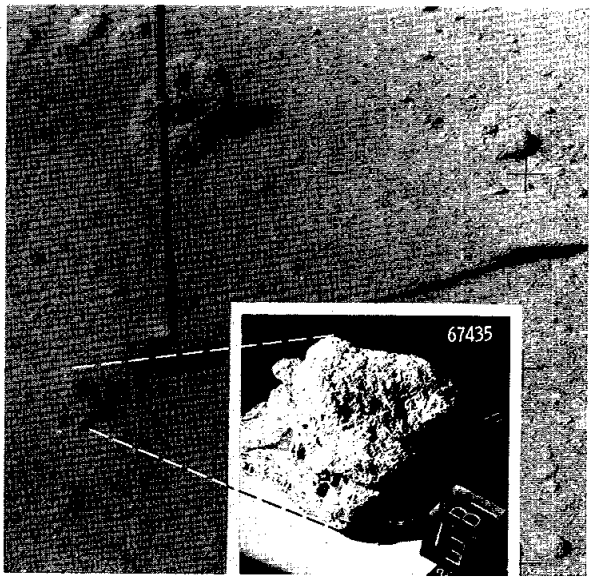


FIGURE 6-122.–Sample 67435 showing approximate lunar orientation reconstructed in the LRL compared to an enlarged part of EVA photograph AS16-106-17320 taken oblique-to-Sun, looking southwest (inset photograph, S-72-44507).

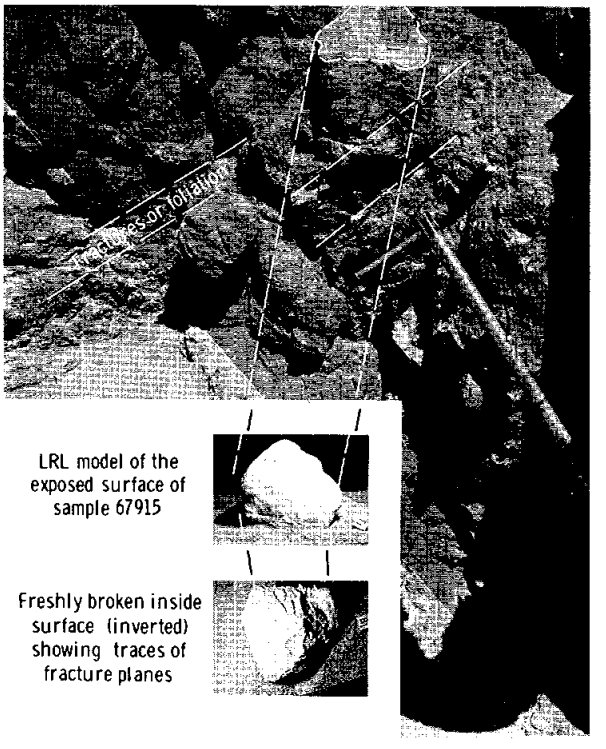


FIGURE 6-123.–Sample 67915 showing approximate lunar orientation reconstructed using an LRL model to depict the fragment broken from the larger boulder. The sample scar is shown in EVA photograph AS16-116-18652 taken oblique-to-Sun, looking northwest. Reconstruction was aided by noting the direction of pervasive shear, or foliation, in the large boulder as well as on the freshly broken surface of the sample.

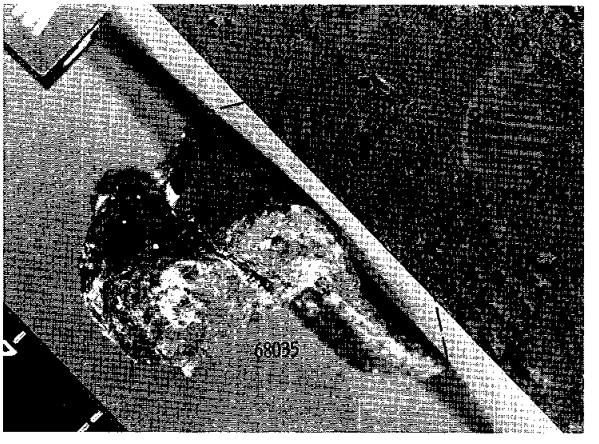


FIGURE 6-124.–Sample 68035 showing approximate lunar orientation by comparing the LRL orthogonal west view to EVA photograph AS16-107-17534 taken cross-Sun, looking north (inset photograph, S-72-40513).

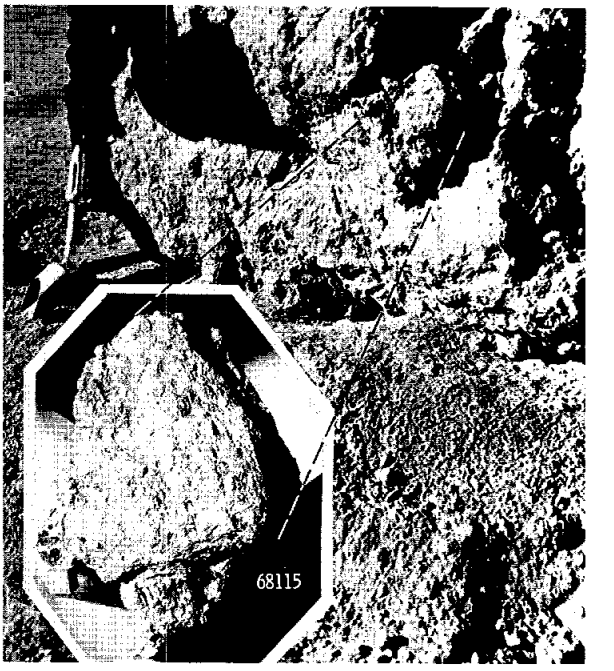


FIGURE 6-125.–Sample 68115 showing approximate lunar orientation reconstructed in the LRL compared to EVA photograph AS16-107-17544 taken cross-Sun, looking south (inset photograph, S-72-41056).



FIGURE 6-126.–Sample 68415 broken in two parts (68415,1 and 68415,2) showing approximate lunar orientation reconstructed in the LRL compared to an enlarged part of EVA photograph AS16-107-17549 taken cross-Sun, looking south. Sample 68416 was broken from the top of the same boulder (inset photographs, S-72-41545 and 42600).

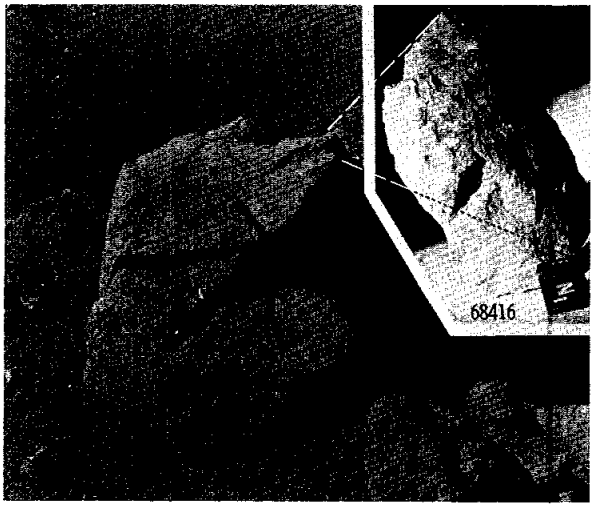


FIGURE 6-127.–Sample 68416 showing approximate lunar orientation reconstructed in the LRL compared to an enlarged part of EVA photograph AS16-107-17549 taken cross-Sun, looking south. Sample 68415 was broken from the same boulder (inset photograph, S-72-40964).

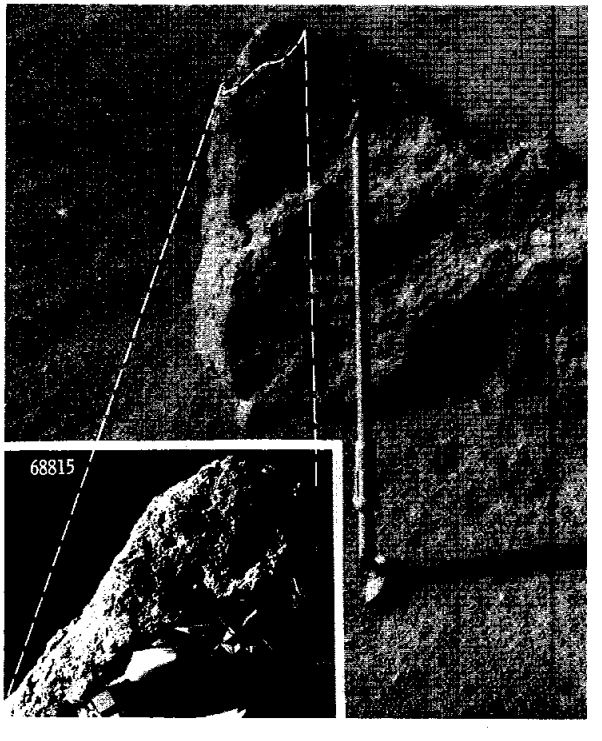


FIGURE 6-128.–Sample 68815 showing approximate lunar orientation reconstructed in the LRL compared to an enlarged part of EVA photograph AS16-108-17699 taken cross-Sun, looking south (inset photograph, S-72-41425).

REFERENCES

6-1. Eggleton, R. E.; and Marshall, C. H.: Notes on the Apenninian Series and Pre-Imbrian Stratigraphy in the Vicinity of Mare Humorum and Mare Nubium. Astrogeologic Studies Semiannual Progress Report, Feb. 26, 1961, to Aug. 24, 1961, U.S. Geol. Survey, Mar. 1962, pp. 132-137.

6-2. Milton, D. J.: Geologic Map of the Theophilus Quadrangle of the Moon. U.S. Geol. Survey Misc. Geol. Inv. Map I-546, 1968.

6-3. Milton, D. J.: Geologic Map of the Descartes Region of the Moon, Apollo 16 Pre-Mission Map. U.S. Geol. Survey Misc. Geol. Inv. Map I-748, sheet 1, 1972.

6-4. Hodges, C. A.: Geologic Map of the Descartes Region of the Moon, Apollo 16 Pre-Mission Map. U.S. Geol. Survey Misc. Geol. Inv. Map I-748, sheet 2, 1972.

6-5. Elston, D. P.; Boudette, E. L.; and Schafer, J. P.: Geology of the Apollo 16 Landing Site Area. U.S. Geol. Survey Open File Rept., 1972. (Available from Center of Astrogeology, Flagstaff, Ariz.)

6-6. Elston, D. P.; Boudette, E. L.; and Schafer, J. P.: Geologic Map of the Apollo 16 (Descartes) Region. U.S. Geol. Survey Open File Rept., 1972. (Available from Center of Astrogeology, Flagstaff, Ariz.)

6-7. Elston, D. P.; Boudette, E. L.; Schafer, J. P.; Muehlberger, W. R.; and Sevier, J. R.: Apollo 16 Field Trips. Geotimes, vol. 17, no. 3, Mar. 1972, pp. 27-30.

6-8. Boudette, E. L.; Schafer, J. P.; and Elston, D. P.: Engineering Geology of the Apollo 16 (Descartes) Traverse Area. U.S. Geol. Survey Open File Rept., 1972. (Available from Center of Astrogeology, Flagstaff, Ariz.)

6-9. Wilhelms, D. E.; and McCauley, J. F.: Geologic Map of the Near Side of the Moon. U.S. Geol. Survey Misc. Geol. Inv. Map I-703, 1971.

6-10. Trask, N. J.; and McCauley, J. F.: Differentiation and Volcanism in the Lunar Highlands: Photogeologic Evidence and Apollo 16 Implications. Earth Planet. Sci. Letters, vol. 14, Mar. 1972, pp. 201-206.

6-11. Head, J. W., III; and Goetz, A. F. H.: Descartes Region: Evidence for Copernican-Age Volcanism. J. Geophys. Res., vol. 77, no. 8, Mar. 10, 1972, pp. 1368-1374.

6-12. Milton, D. J.: Stratigraphy of the Terra Part of the Theophilus Quadrangle. In Part A of Astrogeologic Studies Annual Progress Report, July 1, 1963, to July 1, 1964. U.S. Geol. Survey, Nov. 1964, pp. 17-27.

6-13. Wilhelms, D. E.: Fra Mauro and Cayley Formations in the Mare Vaporum and Julius Caesar Quadrangles. In Part A of Astrogeologic Studies Annual Progress Report, July 1964-July 1965. U.S. Geol. Survey, Nov. 1965, pp. 13-28.

6-14. Pettijohn, F. J.: Sedimentary Rocks. Second ed., Harper and Row Pub., Inc., 1957, p. 59.

6-15. Shoemaker, E. M.; Batson, R. M.; Holt, H. E.; Morris, E. C., et al.: Television Observations from Surveyor 7. In Surveyor 7: A Preliminary Report. NASA SP-173, 1968, pp. 13-81.

6-16. Oberbeck, Verne R.; and Quaide, William L.: Estimated Thickness of a Fragmental Surface Layer of Oceanus Procellarum. J. Geophys. Res., vol. 72, no. 18, Sept. 15, 1967, pp. 4697-4704.

6-17. Schaber, G. G.; and Swann, G. A.: Surface Lineaments at the Apollo 11 and 12 Landing Sites. Proceedings of the Second Lunar Science Conference, vol. 1, A. A. Levinson, ed., MIT Press (Cambridge, Mass.), 1971, pp. 27-38.

6-18. Apollo Lunar Geology Investigation Team: Documentation and Environment of the Apollo 16 Samples: A Preliminary Report. U.S. Geol. Survey Interagency Rept., Astrogeol. 51, May 26, 1972.

6-19. Pohn, Howard A.; and Wildey, Robert L.: A Photoelectric-Photographic Study of the Normal Albedo of the Moon. U.S. Geol. Survey Professional Paper 599-E, 1970.

6-20. Willingham, D.: The Lunar Reflectivity Model for Ranger Block III Analysis. JPL Tech. Rept. 32-664, Nov. 2, 1964.

6-21. Holt, H. E.: Photometry and Polarimetry of the Lunar Regolith as Measured by Surveyor. Radio Sci., vol. 5, no. 2, Feb. 1970, pp. 157-170.

6-22. Holt, H. E.; and Rennilson, J. J.: Photometric and Polarimetric Properties of the Lunar Regolith. Sec. 10, Part B, of the Apollo 12 Preliminary Science Report. NASA SP-235, 1970.

6-23. Budde, W.: Photoelectric Analysis of Polarized Light. Appl. Optics, vol. 1, no. 3, May 1962, pp. 201-205.

6-24. Adler, I.; Trombka, J.; Gerard, J.; Schmadebeck, R.; et al.: X-ray Fluorescence Experiment. Sec. 17 of the Apollo 15 Preliminary Science Report. NASA SP-289, 1972.

7. Preliminary Examination of Lunar Samples

PART A

A PETROGRAPHIC AND CHEMICAL DESCRIPTION OF SAMPLES FROM THE LUNAR HIGHLANDS

The Lunar Sample Preliminary Examination Team[a]

Introduction

More than four-fifths of the surface of the Moon consists of a profoundly cratered, irregular surface designated terra or highlands by analogy with the terrestrial continents. These terra regions have much higher albedos than the physiographically lower and much smoother mare regions. The difference in albedo can now be ascribed to a fundamental difference in the chemical and mineralogical character of these two regions. Lunar samples from landing sites in the mare regions and high-resolution photographs taken from lunar orbit have shown that the lunar maria are underlain by extensive lava flows. Isotopic dating of samples from four mare regions (refs. 7-1 to 7-4) indicate that mare volcanism covered a time span of 600 million years, beginning approximately 3.7 billion years ago. The intensely cratered character of the terra regions is due to both the greater antiquity of these parts of the Moon and the higher flux of incoming objects that hit the Moon during very early lunar history (ref. 7-5). In contrast with the mare region, the origin of the underlying material of the terra is not easily inferred from physiographic criteria. The surface manifestations of early plutonic or extrusive igneous activity – if indeed they ever existed – were erased from the terra regions by the intense early bombardment of the lunar surface. Some portions of the highlands may be exceptions to this generalization; in particular, large craters such as Ptolemaeus, Hipparchus, Albategnius, and Alphonsus. The regions bounded by these craters are much smoother than the typical densely cratered highlands. These regions are generally assumed to be physiographic lows that have, in some way, been filled by younger material. The nature of the material and the mechanism by which it was introduced into the basins are not well understood. On the basis of rather detailed studies of the physiographic and albedo characteristics of the basin material, it has been suggested (ref. 7-6) that the filling of the highland basins was a result of volcanic processes similar to those which filled the large mare basins. Some highland basin areas also contain hilly, hummocky regions that bear no relation to large crater rims or crater ejecta. These regions have been interpreted as extrusive igneous features formed by viscous, silicic, igneous liquids (ref. 7-6).

The elucidation of the origin of both the filled basins and the hilly volcanic regions was the major objective of the Apollo 16 mission. Both types of landforms are remarkably common in the eastern equatorial portion of the near-side southern highlands (fig. 7-1). Basin-filling deposits (designated Cayley Formation in the U.S. Geological Survey (USGS) stratigraphic nomenclature, refs. 7-7 and 7-8) and irregular, hilly topography (designated Descartes Formation in the USGS stratigraphic nomenclature, refs. 7-7 and 7-8) occur there in close proximity.

Analysis of high-resolution photographs obtained during the Apollo 14 mission showed that a relatively smooth region 60 km north of the old crater, Descartes, could provide a landing point with access to both landform types. In addition, two very young bright-rayed craters were relatively accessible from this landing point. The age and mode of formation of these craters are of great interest, but much more

[a]The team composition is listed in "Acknowledgments" at the end of this section.



FIGURE 7-1.–Metric camera photograph of the region around the Apollo 16 landing site, which is designated by a white cross on the figure (9° S 16° E). The inset shows the approximate location of this region on the near side of the Moon. The hummocky landforms that dominate the central portion of the southern part of the region are designated Descartes Formation. The smooth regions that dominate the northern part of the region are typical Cayley Formation. This area receives its name from the very old crater, Descartes, which is seen in the lower portion of the photograph.

important is the fact that the ejecta from these craters provides samples from material well below the regolith or gardened surface.

The Apollo 16 lunar module (LM) landed successfully within less than 100 m of the planned landing point. Three traverses that extended over a region approximately 9 km long and 2 km wide were made. Rock and soil samples were collected from 10 different stations within these regions. These samples include several specimens from rocks that are several tens of meters in size. At five of the sampling stations, rocks that are unambiguous ejecta from nearby craters were obtained. These ejecta blocks and associated soil were sampled in particular detail to obtain samples that allow a more detailed study of the interaction of the lunar surface with both solar and galactic particles (part B of this section).

This section summarizes the chemical, petrographic, and textural characteristics of a representative suite of the Apollo 16 rock and soil specimens. Data on rocks that weigh more than 25 g and those collected with the lunar raking tool are summarized in tables 7-I and 7-II, respectively. At the present time, no clear-cut correlation of any of the observed characteristics with the position of the rocks in the site has been observed. This generalization is based on a detailed examination of only a portion of the returned samples.

Most of the Apollo 16 rocks are texturally complex in the sense that their macroscopic and microscopic textures are the result of two or more events in the history of a given specimen. Cataclastic, highly crushed rocks are common in addition to complex intergrowths of shock-produced glass, devitrified glass, and preexisting clasts. Other rocks seem to be the product of simple thermal recrystallization with textures resembling those found near large igneous intrusions. The understanding of the textural characteristics of most samples cannot be based on terrestrial analogs or counterparts because such counterparts cannot be found on Earth.

TABLE 7-I.–Apollo 16 Rocks That Weigh More Than 25 g[a]

Sample number (b)	*Rock type (c)*	*Weight, g*
60015	II	5 574
60016	I	4 307
60017 (station 13)	IV	2 102
60018	IV	1 501
60019	I	1 887
60025	II	1 836
60035	II	1 053
60055	II	35.5
60075	II	184
60095	Glass	46.6
60115	?	133
60135	II	138
60215	II	386
60235	III	70.1
60255	I?	871
60275	IV	255
60315	III	788
60335	III	318

TABLE 7-I.–Apollo 16 Rocks That Weight More Than 25 g[a] – Concluded

Sample number (b)	*Rock type* (c)	*Weight, g*
60615 R	III	33.0
60619 R	III	28.0
60625 R	III	117
60636 R	III	35.6
60639 R	I	175
60645 R	IV	33
60665 R	Glass	90.1
61015	IV	1 803
61016	II	11 729
61135	I	245
61155	IV	47.6
61156	III	58.5
61175	I	543
61195	II	588
61295	I	187
61536 R	I	86.0
61546 R	Glass	111
62235	III	320
62236	II	57.3
62237	II	62.4
62255	II	1 192
62275	II	443
62295	III	251
63335	IV?	65.4
63355	I?	68.2
63538 R	III	35.1
63549 R	III	26.6
63585 R	I	32.6
64435	IV	1 079
64455	II	56.7
64475	IV	1 032
64476	IV	125
64535 R	IV	257
64536 R	IV	177
64537 R	IV	124
64538 R	IV	30.0
65015	III	1 802
65035	II	446
65055	III	501
65056	Glass	64.8
65075	II	108
65095	II	560
65315	II	300
65325 R	II	67.9
65326 R	II	36.4
65515 R	Clod	50.2
65715 R	I	31.4
65757 R	IV	26.2
65786 R	I	83.0
66035	I	211
66055	IV	1 306
66075	I	347
66095	III	1 185
67015	I	1 194
67016	I	4 262
67035	II	245
67055	IV	222
67075	II	219
67095	II	340
67115	II	240
67215	Padded bag	–
67235	Padded bag	–
67415	II	175
67435	IV	354
67455	II	942
67475	IV	175
67515 R	II	60.8
67549 R	IV	43
67556 R	IV	82
67559 R	III	32.9
67065	I	44.5
67627 R	Glass	79.6
67268 R	Glass	49.7
67629 R	Glass	32.8
67647 R	I	47.7
67718 R	IV	41.0
67729 R	Glass	73.2
67915	IV	2 559
67935	IV	109
67936	IV	61.8
67937	IV	59.7
67955	II	163
67975	Glass	447
68115	IV	1 190
68415	III	371
68416	III	178
68515 R	IV	236
68516 R	IV	34.0
68518 R	IV	29.8
68525 R	III	39.0
68815	IV	1 826
69935	IV	128
69955	II	75.9

[a]This inventory includes a total of 111 samples, including 36 rake samples.

[b]R = rake sample.

[c]Numerals assigned to rock types correspond with those discussed in text.

TABLE 7-II.–Samples Obtained With the Rake

Station	Sample number	Rock type (a)						Total
		I	II	III	IV	Glass	Other	
1	61515	16	2	3	–	12	–	33
4	64535	2	1	13	14	–	–	30
4	64815	8	1	4	–	–	–	13
5	65515	–	1	–	–	3	35 soil clods	39
5	65715	25	2	4	5	5	–	41
5	65925	3	–	–	–	–	–	3
5	65325	6	7	4	–	4	1 glass coated	22
8	68515	–	–	6	6	–	1 glass coated	13
LM site	60615	3	3	9	10	10	–	35
LM site	60515	1	5	3	–	2	–	11
11	67515	2	19	3	3	5	–	32
11	67615	15	3	9	–	5	–	32
11	67715	13	0	9	7	3	–	32
13	63525	9	–	19	–	11	–	39
	Total	103	44	86	45	60	37	375

[a]Numerals assigned to rock types correspond with those discussed in text.

Chemical Characteristics

Unlike the textural characteristics, the chemical characteristics of the Apollo 16 rocks are relatively simple and straightforward. The dominant chemical feature is the high abundance of aluminum and calcium. In a number of rocks, the absolute and relative abundances of these elements approach those of pure calcic plagioclase to a very good first approximation. The aluminum (Al) content of these rocks is directly correlated with the plagioclase abundance. Except for silicon (Si), most of the rock-forming elements are either strongly concentrated in or excluded from plagioclase. Thus, the abundance of virtually all elements except silicon is strongly correlated with the aluminum oxide (Al_2O_3) content in the Apollo 16 rocks. The concentrations of all the major elements and several trace elements for 12 rock samples and 11 soil samples are summarized in tables 7-III and 7-IV, respectively. The correlation with the Al_2O_3 abundance for calcium oxide (CaO), magnesium oxide (MgO), iron oxide (FeO), titanium dioxide (TiO_2), and potassium oxide (K_2O) is illustrated in figure 7-2. These data show that three distinct groups of rocks can be defined from the Al_2O_3 content alone. The first of these groups approaches pure plagioclase in composition. In this section, they are designated as cataclastic anorthosites. The second group, which consists of several complex breccias, one crystalline rock, and all soil samples, has Al_2O_3 contents between 26 and 29 percent. The third group has less than 26 percent Al_2O_3 and consists of rocks that are of metamorphosed igneous origin. The rocks can be subdivided into one group that has approximately 18 percent Al_2O_3, with bulk compositions similar to those of the potassium, rare-Earth elements, and phosphorus (KREEP) basalts found at the Apollo 12, 14, and 15 sites and a second more aluminum-rich group that has no well-defined counterpart at other sites. The KREEP basalt type (i.e., samples 62235 and 60315) is the only rock composition from the Apollo 16 site that has major elemental abundances corresponding to those of liquids known to have been produced by partial melting of the lunar or terrestrial interior.

The rather narrow range of soil compositions found at this site is remarkable when compared to soils from other sites. In spite of the small range of compositions, all elements (with the possible exception of strontium (Sr) and nickel (Ni)) in the soils form well-defined correlations with each other. The simplicity of these correlations suggests that two end members or components prevail in the soils found at

TABLE 7-III.–X-Ray Fluorescence Analyses of Apollo 16 Rocks

(a) Crystalline rocks

Component or element	Location, rock type, and sample number					
	LM site, crystalline (III), 60315,3	*Station 2, crystalline (III), 62235,4*	*LM site, crystalline (III), 60335,1*	*Station 1, crystalline (III), 61156,2*	*Station 6, crystalline (III), 66095,5*	*Station 8, crystalline (III), 68415,6*
	Abundance, percent					
SiO_2	45.61	47.04	46.19	44.65	44.47	45.40
TiO_2	1.27	1.21	.58	.64	.71	.32
Al_2O_3	17.18	18.69	25.27	22.94	23.55	28.63
FeO	10.53	9.45	4.51	7.75	7.16	4.25
MnO	.12	.11	.07	.12	.08	.06
MgO	13.15	10.14	8.14	9.60	8.75	4.38
CaO	10.41	11.52	14.43	13.34	13.69	16.39
Na_2O	.56	.48	.52	.39	.42	.41
K_2O	.35	.34	.23	.11	.15	.06
P_2O_5	.45	.41	.19	.22	.24	.07
S	.14	.11	.07	.12	.12	.04
Total	99.77	99.50	100.20	99.88	99.34	100.01
	Abundance, ppm					
Sr	156	165	162	153	159	185
Rb	9.8	9.3	6.4	2.5	3.9	2.1
Y	142	193	62	64	72	23
Th	7.2	10.5	3.2	3.8	2.7	2.2
Zr	640	851	281	293	322	98
Nb	37	49	16	17	18	5.6
Ni	191	248	77	184	258	49
Cr	1460	1370	900	960	1010	710

this site: a feldspar-rich material, perhaps similar to sample 67075, and the more ferromagnesium-rich KREEP basalt. Both the relatively low TiO_2 abundance and the high yttrium (Y)/Ti and niobium (Nb)/Ti ratios of the high-alumina metaigneous rocks suggest that this compositional category is relatively rare in the soil. The nickel content of the soils varies by more than a factor of 3. If the nickel abundance is an indicator of a meteoritic component and thus, in turn, a measure of the maturity of the soil, the data obtained suggest that some soils are probably associated with deep ejecta from young craters that have been less gardened than a typical soil from this region. The abundance concentrations of Nb, Y, zirconium (Zr), and Ti are clearly correlated with each other in both rock and soil samples. Data for these elements are illustrated in figure 7-3. The correlation of these elements within the soil samples is particularly good. The four complex breccia samples that have Al_2O_3 contents similar to the soils have much more variable TiO_2, K_2O, Y, and Nb concentrations than the soils, indicating that the breccias are derived from a more heterogeneous milieu.

Several additional generalizations and comparisons with other lunar materials may be inferred from the Sr, Zr, Y, Nb, and thorium (Th) contents determined for the rocks from this site. Both mare and nonmare basaltic rocks are characterized by relatively high abundances of large quadrivalent and trivalent ions (e.g., Th, the lanthanide elements, and Zr) relative to divalent ions (e.g., europium (Eu^{++}) and Sr^{++}). This characteristic is best illustrated by the commonly observed low abundance of Eu, relative to samarium (Sm) and gadolinium (Gd). The inverse of this

TABLE 7-III.–X-Ray Fluorescence Analyses of Apollo 16 Rocks – Concluded

(b) Breccias and cataclastic rocks

Component or element	Location, rock type, and sample number					
	Station 1, breccia matrix (I), 61295,5	Station 8, breccia matrix (IV), 68815,9	Station 11, crushed anorthosite (II), 67955,8	Station 13, breccia clast (II, IV), 63335,1	Station 1, crushed anorthosite (II), 61016,3	Station 11, crushed anorthosite (II), 67075,4
	Abundance, percent					
SiO_2	45.19	45.10	45.01	45.20	44.15	44.80
TiO_2	.56	.49	.27	.42	.20	.09
Al_2O_3	28.29	27.15	27.68	30.86	33.19	31.54
FeO	4.52	4.75	3.84	3.23	1.40	3.41
MnO	.06	.06	.05	.04	.02	.06
MgO	4.72	5.88	7.69	2.81	2.51	2.42
CaO	16.16	15.45	15.54	17.25	18.30	18.09
Na_2O	.45	.42	.40	.57	.34	.26
K_2O	.09	.14	.05	.05	.02	.01
P_2O_5	.10	.18	.03	.03	.05	.00
S	.06	.06	.01	.03	.01	.01
Total	100.20	99.68	100.57	100.49	100.19	100.69
	Abundance, ppm					
Sr	187	175	170	225	179	144
Rb	2.3	3.4	.6	1.2	.7	.8
Y	33	61	16	11	11	2.5
Th	1.0	3.7	1.9	1.4	1.7	N.D.[a]
Zr	143	266	59	41	48	2.7
Nb	8.6	16	4.0	3.1	2.4	N.D.
Ni	114	206	108	26	39	N.D.
Cr	570	690	750	340	200	420

[a]N.D. = not detected.

characteristic is observed in pure plagioclase and plagioclase-enriched materials returned from the lunar surface. The ubiquitous fractionation of these groups of elements on the lunar surface indicates that the separation of plagioclase from igneous liquids is common in igneous processes on the Moon. The relatively high and relatively constant Sr content of most of the Apollo 16 samples and the highly variable and frequently low Zr, Y, Nb, and Th contents suggest that these samples have been involved in processes in which they have become enriched in plagioclase. The Y, Zr, Th, Nb, and Sr contents of samples 60315 and 62235 are distinctly different from all other samples, which suggests that these rocks are depleted in divalent elements relative to trivalent (i.e., similar to other lunar basaltic rocks) and quadrivalent elements. The relative abundances are, in fact, similar to those observed for KREEP basalts. The similarity of trace element characteristics of these two rocks, with those of primary magmas, supports the conclusion that they represent a relatively undifferentiated magmatic rock. The concentrations of Y, Zr, Th, Nb, and Sr in samples 61156, 66095, and 60335 are intermediate between those found for rocks that are clearly enriched in plagioclase; for example, sample 60016 and the aforementioned basaltic rocks. Neither the trace element concentrations nor the major element compositions of these rocks exclude the possibility that they are derived from an undifferentiated hyperaluminous parent magma. This possibility is particularly interesting because it suggests that rocks representing the parent liquids for anorthosites may occur at this site. With the aforementioned exception, the chemistry of

TABLE 7-IV.–X-Ray Fluorescence Analyses of Apollo 16 Soils

Component or element	*Location, soil type, and sample number*										
	LM site, rake soil, 60600,2	*Station 1, subsurface white soil, 61220,2*	*Station 1, upper-gray soil, 61241,2*	*Station 1, crater rim, 61501,1*	*Station 4, trench bottom, 64421,1*	*Station 5, rake soil, 65701,2*	*Station 6, gray soil, 66041,1*	*Station 6, white soil, 66081,2*	*Station 11, fillet reference soil, 67480,2*	*Station 11, crater rim rake soil, 67600,1*	*Station 8, fillet reference soil, 68841,2*
	Abundance, percent (by weight)										
SiO_2	45.35	45.35	45.32	44.66	44.88	45.03	45.07	45.38	44.95	45.28	45.08
TiO_2	.60	.49	.57	.56	.55	.64	.64	.67	.41	.42	.59
Al_2O_3	26.75	28.25	27.15	26.50	27.60	26.47	26.39	26.22	29.01	28.93	26.49
FeO	5.49	4.55	5.33	5.31	5.03	5.87	6.08	5.85	4.66	4.09	5.65
MnO	.07	.06	.07	.07	.06	.08	.08	.08	.06	.06	.07
MgO	6.27	5.02	5.75	6.08	5.35	6.02	6.14	6.39	4.20	4.75	6.27
CaO	15.46	16.21	15.69	15.33	15.81	15.29	15.29	15.28	16.54	16.40	15.30
Na_2O	.38	.42	.55	.41	.39	.41	.38	.39	.42	.44	.41
K_2O	.11	.09	.10	.11	.10	.12	.12	.13	.06	.07	.11
P_2O_5	.13	.10	.13	.11	.13	.13	.15	.13	.13	.06	.12
S	.07	.06	.07	.08	.07	.09	.09	.09	.03	.04	.08
Total	100.68	100.60	100.73	99.22	99.97	100.15	100.43	100.61	100.47	100.54	100.17
	Abundance, ppm										
Sr	173	182	175	167	172	173	167	170	188	194	169
Rb	2.9	2.4	2.7	3.0	2.9	2.9	3.0	3.1	1.4	1.3	3.1
Y	43	31	37	40	42	48	44	48	22	22	46
Th	1.9	2.6	1.2	2.2	2.8	1.9	2.6	3.2	N.D.[a]	1.6	2.4
Zr	186	131	162	177	183	207	197	205	86	89	201
Nb	12	7.6	9.8	11	11	13	12	13	5.4	5.4	13
Ni	293	109	220	256	316	356	362	342	176	111	296
Cr	770	590	720	760	710	820	820	830	520	540	780

[a]N.D. = not detected.

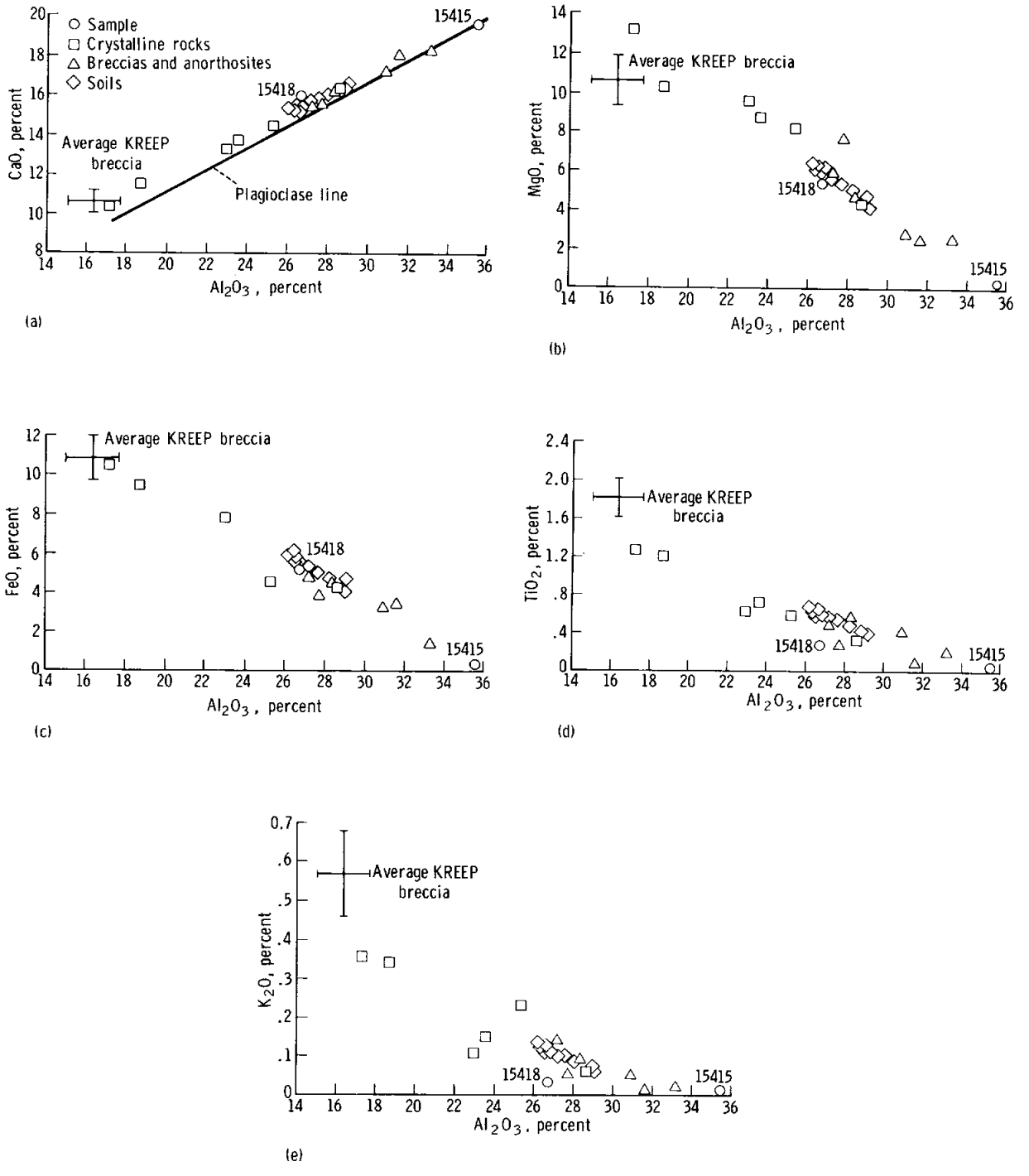


FIGURE 7-2.–Correlation of CaO, FeO, MgO, TiO_2 and K_2O concentrations with Al_2O_3 in Apollo 16 samples. (All percentages are by weight.) Data for samples 15418 and 15415 are from reference 7-9, and data for average KREEP breccias are from reference 7-10. (a) Al_2O_3/CaO correlation. (b) Al_2O_3/FeO correlation. (c) Al_2O_3/MgO correlation. (d) Al_2O_3/TiO_2 correlation. (e) Al_2O_3/K_2O correlation.

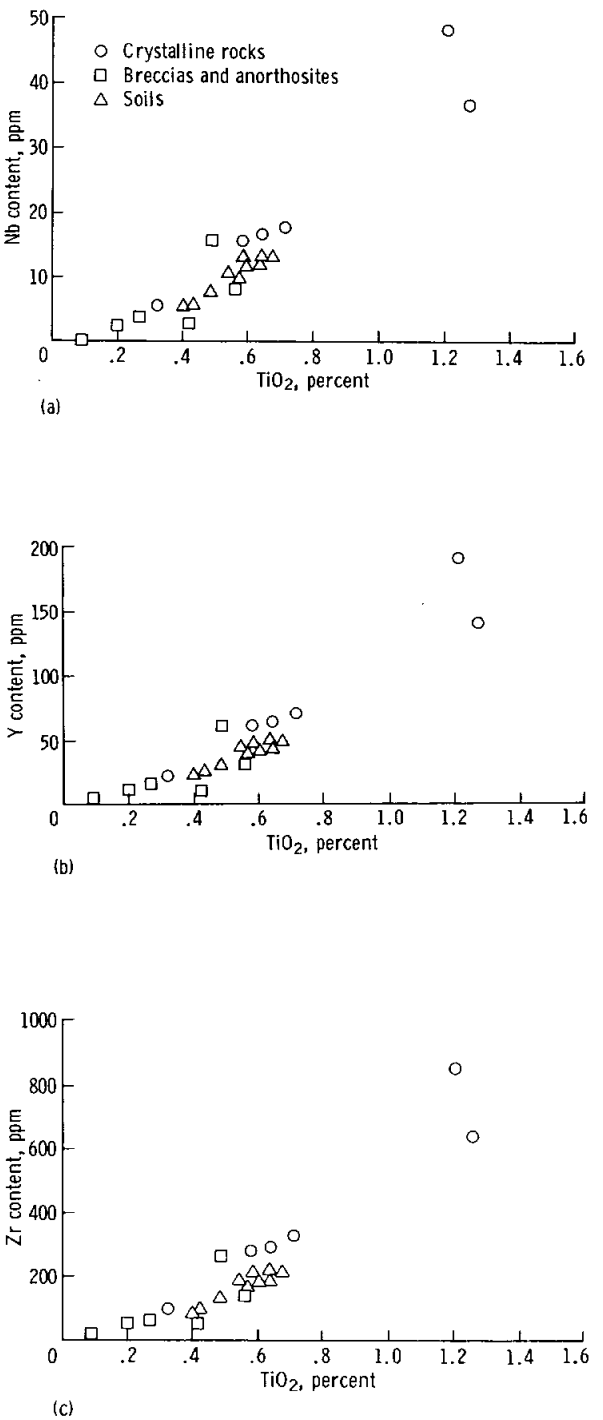


FIGURE 7-3.–Correlation of Nb, Y, and Zr concentrations with TiO_2 in Apollo 16 samples. Note the nearly identical patterns of data points on these three graphs. (a) TiO_2/Nb correlation. (b) TiO_2/Y correlation. (c) TiO_2/Zr correlation.

the Apollo 16 rocks can be accounted for by a rather simple geologic model that consists of a large igneous complex variably enriched in plagioclase and intruded by a trace-element-rich liquid after its formation.

The abundance of potassium (K), uranium (U), Th, and short-lived radioactive elements has been determined for 43 rock and soil samples (table 7-V). These data show that the Th/U ratio of highland materials, like that of most mare samples, is similar to that of chondrites. The K/U ratios of all except two samples from this site fall within the range of 1000 to 2000. These data are compared with K and U contents of rocks from previous landing sites in figure 7-4. Even though the abundance of potassium in the rocks and soils from the Apollo 16 highland site is relatively low, the samples have similar K/U ratios to those of the KREEP basalts and distinctly lower K/U ratios than those of most mare basalts. These data are

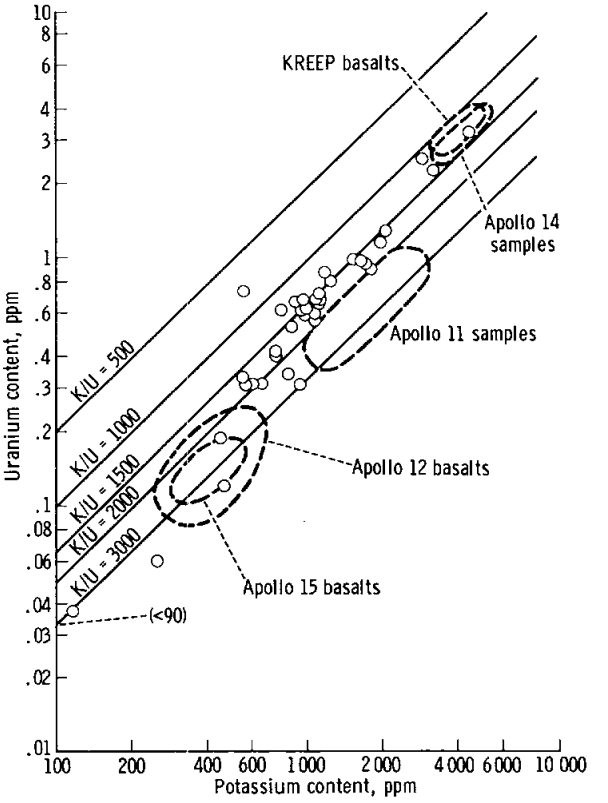


FIGURE 7-4.–The K/U ratios for Apollo 16 samples as compared to the general range of samples from previous missions. (Data supplied by the NASA Manned Spacecraft Center, Oak Ridge National Laboratory, and Battelle Pacific Northwestern Laboratory.)

TABLE 7-V.–Gamma Ray Analyses of Apollo 16 Lunar Samples

Sample no.	Weight, g	Th, ppm	U, ppm	K, percent (by weight)	^{26}Al, dpm/kg	^{22}Na, dpm/kg
60017,0	2102.0	0.80 ± 0.20	0.20 ± 0.04	0.050 ± 0.015	–	–
60135,0	137.6	.29 ± .04	.08 ± .03	.015 ± .003	159 ± 16	41 ± 6
60255,0	862.6	2.4 ± .2	.63 ± .12	.110 ± .002	120 ± 6	39 ± 3
60275,0	255.2	2.99 ± .18	.88 ± .03	.115 ± .002	129 ± 8	48 ± 6
60315,0	787.7	8.56 ± .90	2.34 ± .24	.318 ± .030	92 ± 9	47 ± 6
60335,0	311.0	2.75 ± .10	.92 ± .04	.174 ± .008	140 ± 8	43 ± 8
61195,0	587.9	1.1 ± .1	.31 ± .03	.057 ± .006	34 ± 7	35 ± 8
62235,0	317.7	9.4 ± .6	2.57 ± .06	.284 ± .004	137 ± 8	50 ± 7
62295,0	250.8	2.8 ± .3	.74 ± .07	.055 ± .010	95 ± 10	60 ± 12
63355,1	43.55	4.85 ± .18	1.31 ± .06	.202 ± .005	98 ± 6	48 ± 4
64435,0	1059.6	.10 ± .03	.03 ± .01	.010 ± .003	–	–
64476,0	125.14	1.19 ± .08	.31 ± .03	.066 ± .002	132 ± 11	48 ± 5
65015,0	1802.2	10.0 ± 2.0	3.0 ± .7	.40 ± .09	–	–
65055,0	500.9	1.18 ± .07	.311 ± .019	.060 ± .004	109 ± 6	31 ± 4
66075,0	347.1	2.05 ± .11	.55 ± .03	.083 ± .005	149 ± 8	39 ± 5
67055,0	221.4	3.69 ± .37	.98 ± .10	.162 ± .016	137 ± 15	56 ± 8
67055,0	221.4	3.6 ± .3	.99 ± .08	.16 ± .02	116 ± 8	43 ± 3
67095,0	339.8	3.89 ± .21	1.18 ± .06	.195 ± .010	89 ± 5	58 ± 8
67115,9	187.48	.43 ± .07	.121 ± .011	.0463 ± .0014	62 ± 6	29 ± 3
67475,0	174.1	.67 ± .08	.19 ± .02	.045 ± .007	126 ± 9	38 ± 3
68415,1	202.5	1.22 ± .10	.35 ± .03	.093 ± .008	159 ± 15	47 ± 5
68416,0	175.4	1.24 ± .13	.34 ± .04	.083 ± .008	160 ± 15	41 ± 4
68815,2	34.49	2.74 ± .14	.81 ± .03	.122 ± .003	150 ± 30	56 ± 11
69935,0	127.57	2.52 ± .15	.62 ± .06	.079 ± .008	153 ± 15	41 ± 7
69955,0	75.77	.14 ± .02	.038 ± .006	<.009	76 ± 7	35 ± 5
60501,2	116.72	2.2 ± .3	.61 ± .03	.098 ± .005	107 ± 8	42 ± 5
60501,2	116.72	2.44 ± .06	.60 ± .02	.106 ± .005	110 ± 5	38 ± 2
61241,28	106.55	1.98 ± .09	.51 ± .02	.085 ± .004	183 ± 7	62 ± 2
62281,0	107.9	2.10 ± .17	.62 ± .03	.093 ± .004	225 ± 13	63 ± 9
63501,3	100.13	1.53 ± .15	.41 ± .04	.0728 ± .008	220 ± 20	55 ± 8
63501,4	100.05	1.76 ± .15	.41 ± .03	.074 ± .003	142 ± 7	57 ± 2
64421,3	100.0	2.0 ± .4	.62 ± .04	.093 ± .005	111 ± 10	39 ± 6
64801,1	126.53	2.23 ± .22	.60 ± .06	.106 ± .011	105 ± 11	50 ± 5
66041,4	108.44	2.40 ± .06	.70 ± .04	.103 ± .005	151 ± 8	40 ± 3
66041,4	108.44	2.5 ± .4	.66 ± .04	.096 ± .006	161 ± 11	51 ± 7
66041,28	100.00	2.2 ± .3	.74 ± .03	.102 ± .005	159 ± 10	54 ± 6
66081,25	100.03	2.3 ± .4	.70 ± .03	.110 ± .006	102 ± 7	44 ± 5
67481,1	100.03	1.12 ± .09	.323 ± .019	.055 ± .003	168 ± 10	60 ± 8
67941,1	50.71	1.89 ± .19	.55 ± .06	.106 ± .011	158 ± 20	27 ± 5
68121,1	99.99	2.63 ± .08	.63 ± .03	.095 ± .004	112 ± 4	41 ± 2
68501,2	100.03	2.28 ± .23	.58 ± .06	.0965 ± .010	84 ± 9	38 ± 5
68501,3	100.03	2.59 ± .10	.64 ± .03	.092 ± .003	96 ± 3	36 ± 2
69921,1	46.96	2.47 ± .10	.67 ± .03	.087 ± .003	305 ± 10	86 ± 3

in accord with the suggestion that the older and shallower parts of the Moon have lower K/U ratios than the deeper interior, which presumably produced the mare basalts.

The carbon contents of 12 soil and rock samples are given in figure 7-5 with data from previous Apollo landing sites. The soil samples from the Apollo 16 regolith have carbon contents similar to those of most lunar soils. In contrast, the rock samples have carbon contents no more than one-half those of most mare basalts. This difference may be the result of a very low carbon content of highland crustal materials or a result of extensive degassing of all samples during their formation. The latter explanation is unlikely for the cataclastic anorthosites that show only minimal evidence of thermal metamorphism. Therefore, it is concluded that many of the highland rocks are derived from a source rock that has a distinctly lower carbon content than that of most mare basalts. These additional data on the carbon regime of the lunar surface further support the hypothesis that the bulk of the carbon found on the lunar surface originates from the solar wind.

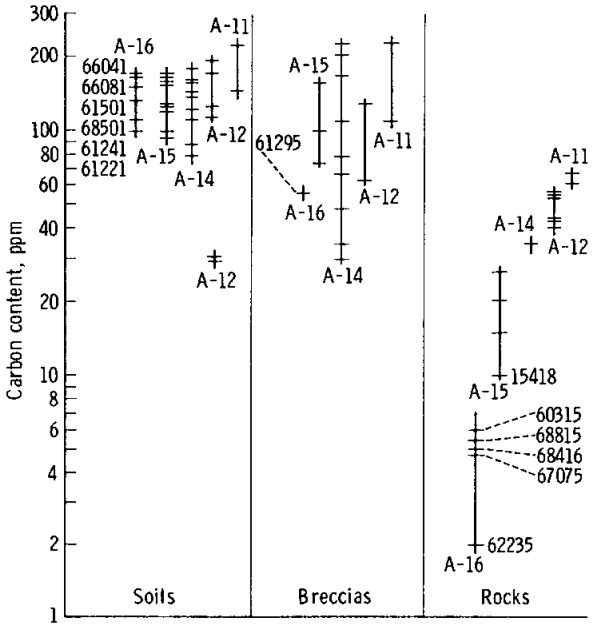


FIGURE 7-5.–Comparison of the total carbon abundances for the Apollo 16 sample types with those of previous Apollo missions. (Previous total carbon abundance data are from references 7-9 and 7-11 to 7-13.)

Textural and Mineralogic Description

Both visual and microscopic examinations show that the coherent rocks from the Apollo 16 site are highly variable in character and complex in origin. The diversity of textures clearly must be understood before more general inferences on the origin of these rocks can be drawn. At the outset, it was noted that none of the rocks have the hallmarks of lavas or hypabyssal rocks that were so evident in the Apollo 11, 12, and 15 mare basalts. To date, petrographic studies of Apollo 16 rocks have uncovered only two specimens that can be unambiguously categorized as holocrystalline igneous rocks. The scarcity of such rocks at this site is well illustrated by the astronauts' descriptions while they were on the surface. The lunar module pilot commented while he was driving to station 1 during the first extravehicular activity period, "I haven't seen any [rock] that I'm convinced is not a breccia." In this preliminary examination, all rock samples, including several hundred fragments collected with the lunar raking tool, have been examined after the surfaces were cleaned to remove dust coatings. The first preliminary classification of these rocks is based on visual and low-power binocular microscopic examinations of the rock surfaces for all rocks. In addition, petrographic thin sections of 35 specimens were studied by using conventional petrographic methods. The following four broadly defined rock types can be identified from this examination.

(1) Cataclastic anorthosites (type II)

(2) Partially molten breccias (type IV)

(3) Igneous and high-grade metamorphic rocks (type III)

(4) Polymict breccias (type I)

The characteristics of these rock types are described in the following paragraphs.

Cataclastic anorthosites (type II).–The type II rocks consist of white, generally friable, highly brecciated, anorthositic rocks. Degrees of coherency in this group vary from those samples that (during transit and handling) have broken into tens of fragments (fig. 7-6(a)) to those that have remained as single fragments (fig. 7-6(b)). Under the binocular microscope, the type II samples appear to consist of 70 percent or more plagioclase in the form of clear, gray, or white grains. (Generally, all three types occur in each specimen). A few light yellow to honey brown to light green minerals occur in textures that

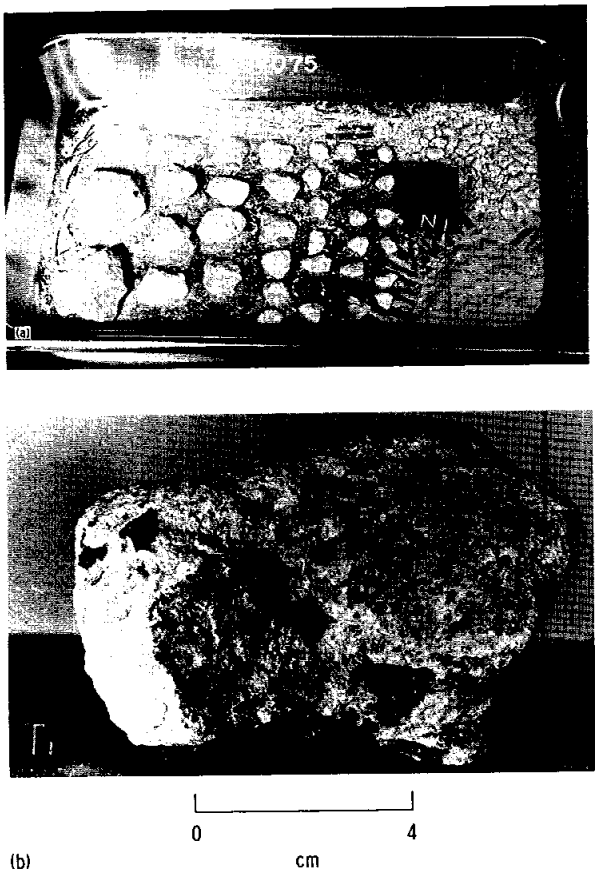


FIGURE 7-6.–Typical examples of type II rocks. (a) Sample 67075 shows the extremely friable nature of this material, which was collected as a single rock on the lunar surface. The cube is 1 cm on the edge (S-72-37541). (b) Sample 65315 is a more coherent but still friable rock of crushed plagioclase. Note the preserved glass-lined impact pits on the weathered surface. A few remnants of a black glass coating remain (S-72-39416).

suggest that these rocks are cataclastically deformed anorthositic fragments. Thin-section observations confirm a very high plagioclase content and highly crushed or annealed textures. The following question needs to be answered for this category. Are all these rocks cataclastically deformed fragments or are some detrital in origin? Most of these rocks have partial, dark gray, vesicular, glass coatings; in some cases, the rocks appear to have been totally glass coated but have lost much of the coating through micrometeorite erosion. (Rocks typical of this category are listed in table 7-I.) Reasons for the differing degrees of coherency and relationships of different types of plagioclase grains should be studied. These may be associated with differing degrees of shock and may be geographically distributed in a meaningful way. A first impression suggests that the most friable and least coherent white rocks were collected at the rim of North Ray Crater.

The extremely crushed nature of the plagioclase in thin section is illustrated in figures 7-7(a) and 7-7(b). In figure 7-7(a), the crushed material of the darker area appears to have behaved as a fluid and to have

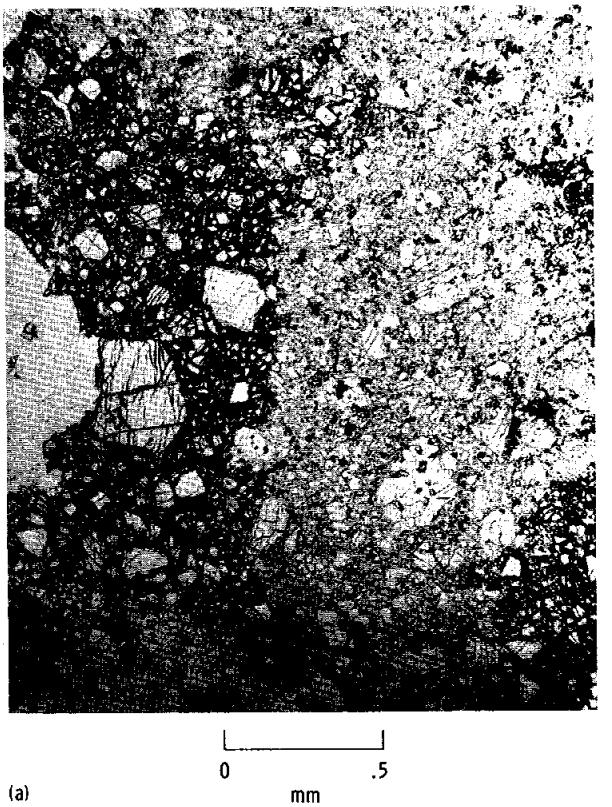
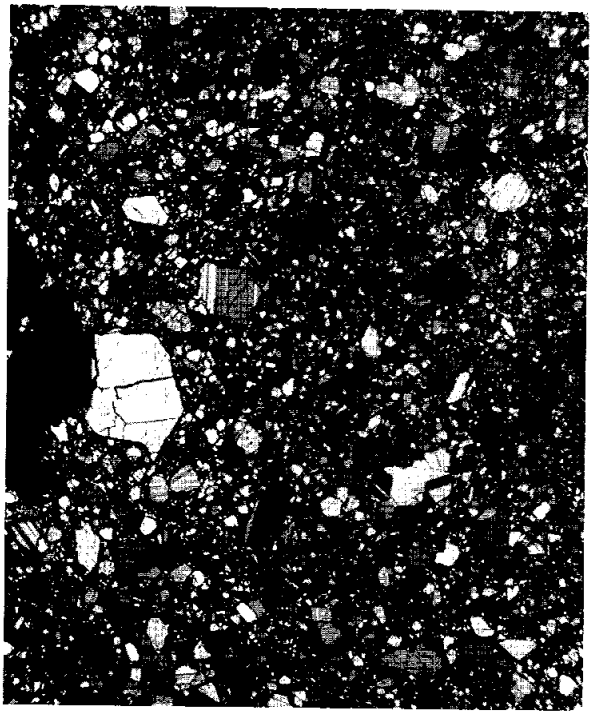


FIGURE 7-7.–Thin sections of crushed anorthosites. (a) Plane light view of sample 67075, showing flow of gray crushed material between two lighter zones of crushed material (S-72-43657). (b) Crossed polars view of same area, showing the recognizable clasts to be primarily plagioclase (S-72-43678). (c) Crossed polars view, showing the annealed texture of some grains. Note the typical 120° triple junctions, which are clearly displayed in the upper right. (d) Plane light view of same area, showing the small percentage of mafic silicates that stand out in higher relief. (e) Patch of diabasic to subophitic intergrowth of plagioclase needles and pyroxene (upper right) with a small projection of similar finer grained material at the lower end. Similar fine-grained material occurs around the margin and in the fractures of the large crushed plagioclase grain that makes up the remainder of the photomicrograph (S-72-45701).



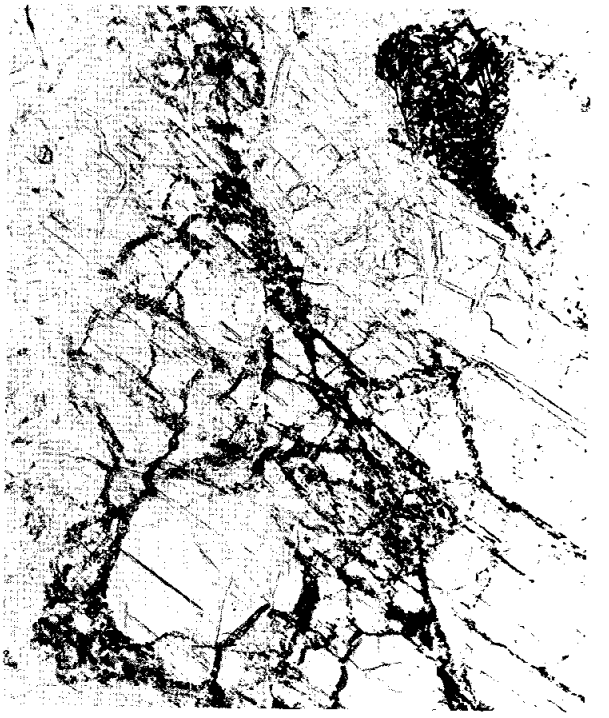
(b) 0 .5 mm



(d) 0 .5 mm



(c) 0 .5 mm



(e) 0 .2 mm

squeezed between the two lighter areas. The somewhat annealed nature of the crushed plagioclase is seen in figure 7-7(c); some of the grains meet at triple junctions. The small percentage of mafic silicates is shown in figure 7-7(d). Indications of partial melting are present in this rock type. Small patches of diabasic to subophitic textures occur interstitially to some plagioclase grains. Small veinlets of finer grain size occur sporadically as offshoots from these patches. Similar veins often occur along parts of the margins of plagioclase grains or as veins in them (fig. 7-7(e)). Apparently, the white, clear, and gray areas seen under the binocular microscope represent partly crushed plagioclase, diaplectic glass, and partially melted zones, respectively. Some specimens of this rock type contain a somewhat higher percentage of mafic silicates but are still in the range of anorthositic rocks (greater than 70 percent plagioclase). For example, samples 67955, 64435, and 60025 have at least 10 percent olivine as subhedral grains, both as small inclusions in plagioclase and as larger grains in pyroxene that is interstitial to plagioclase. These rocks are highly crushed, but thin sections display a few areas in which the original texture is preserved. The samples are probably troctolitic anorthosites.

Some special problems are posed by these cataclastic rocks. There is evidence that they retain relicts of a much coarser grained fabric. The relicts suggest that, although the grains are intensely crushed, the rocks were not necessarily highly stirred and may retain discernible preshock textures. The relicts are generally most clearly evident in plagioclase but may be seen also in mafic minerals. For instance, in sample 60025, the orthopyroxene is generally much coarser than olivine and is of a size comparable to the largest plagioclase relicts. The olivine grains can be arranged in a series in which progressive polygonalization and rotation of small blocks are seen. The series suggests that the original average grain size of olivine is at least as large as the largest mildly polygonalized grains and is probably comparable to that of orthopyroxene. Such grain sizes and shapes are a clue to the preshock nature of the rocks that may be parts of the original lunar crust.

In sample 67955, a clearly discernible relict cumulus texture is evident in the form of extensive orthopyroxene oikocrysts that enclose ovoid olivine and plagioclase. Early ovoidal olivine, without an orthopyroxene mantle, is enclosed in plagioclase. The whole specimen (as judged from a view of the thin section under low magnification) appears to have a lamination that may be relict layering which, like the relicts of coarse-grained texture, indicates that this rock and probably others were not necessarily highly stirred when they were shocked.

Partially molten breccias (type IV).–The type IV rocks consist of a rather complex series of breccias that contain white and gray material. In some cases, the white material appears to be matrix that contains gray clasts; in other cases, the gray material appears to be matrix that contains white clasts (fig. 7-8). In many instances, these two cases occur in the same rock. The dark material is aphanitic and, under the binocular microscope, is suggestive of devitrified glass. Thin sections confirm this observation but also show varying amounts of mineral debris and small fine-grained gray clasts included in the devitrified glass that contains abundant flow texture. In some areas, the gray material consists of many rounded to angular fragments of plagioclase in a finer grained matrix, which contains many needles of plagioclase in a random arrangement as though they were crystallized from a melt (fig. 7-9). Possibly this material was partially melted and contained inclusions of plagioclase. The rather ragged edge of the large white

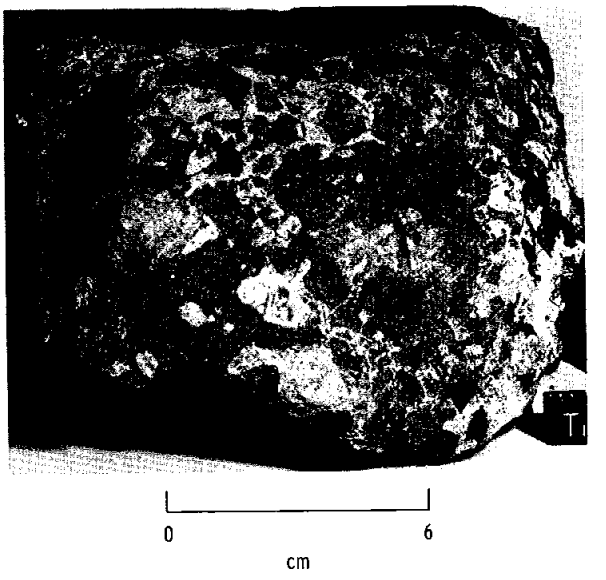


FIGURE 7-8.–Complex gray and white breccia. Sample 61015 shows the complex arrangements that in some areas show white clasts in a gray matrix but in others show gray clasts in a white matrix (S-72-37758).

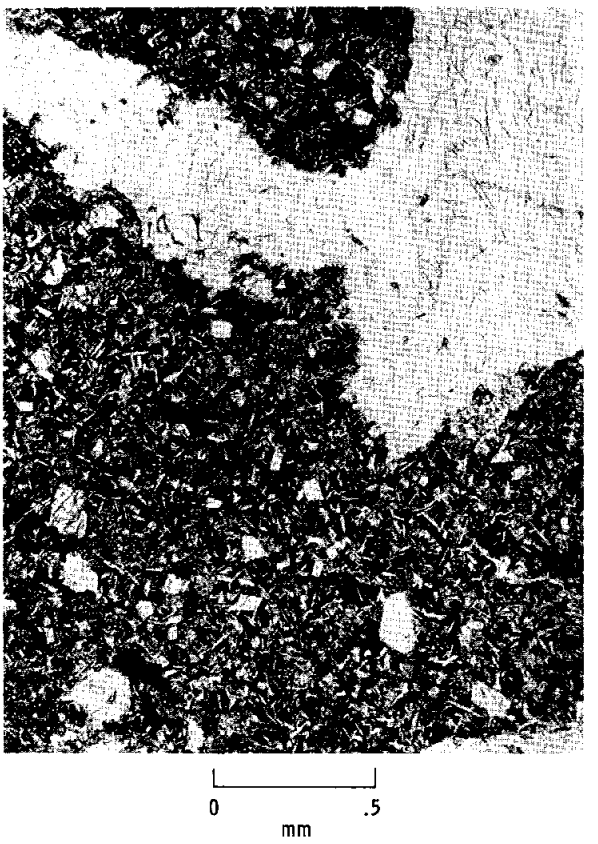


FIGURE 7-9.–Complex gray and white breccia. Sample 61015, plane light view of white vein through gray area. Plagioclase occurs in gray material as both small needles and larger rounded to angular fragments (S-72-45703).

plagioclase area in contact with the small needle-bearing matrix, the small islands of plagioclase that seem to have been wedged off the lower edge of the plagioclase arm (fig. 7-9, upper left), and the small dikelike embayment on the upper edge of the arm all lead to the conclusion that the gray material was, at one time, in large part, melted. The composition of the material is similar to that of anorthositic rocks (table 7-III). The white area is anorthositic material in various stages of brecciation or recrystallization. Proportions of white and gray material vary considerably from one specimen to another. For example, samples 68815 and 60017 consist primarily of the dark material but show a few small spots of white (fig. 7-10). These two rocks also contain long wormlike tubular vesicles. In sample 68815, there is a higher proportion of white material that occurs for the most part as distinct clasts in the dark matrix, but other portions of this same rock have larger white areas in which a few gray fragments occur. A frothy vesiculated zone also occurs on one side of this rock. In sample 61015 (figs. 7-8 and 7-9), the dark material generally appears to be the matrix; yet on one side of the rock, the white material forms several distinct veins through the dark areas. Clearly, these rocks form a heterogeneous set of gray and white partially melted rocks that are found throughout the landing site. (Other rocks of this type are listed in table 7-I.) These rocks may be part of a series in which varying degrees of melting and assimilation of clasts and fine debris have occurred. The white clasts may be granulated to the point where they behaved mechanically as a fluid and were squeezed into the partially melted matrix as veins and blebs that may, in turn, have picked up a few fragments of the dark material (fig. 7-11(a)). Some of the white clasts have not been significantly deformed and contain textures that probably reflect a previous environment. One of these clasts in sample 67435 contains subhedral olivine and pink spinel in a poikilitic plagioclase matrix (figs. 7-11(b) and 7-11(c)). Many of the olivines in the Apollo 16 rocks have unusually low interference colors and are difficult to distinguish from orthopyroxene.

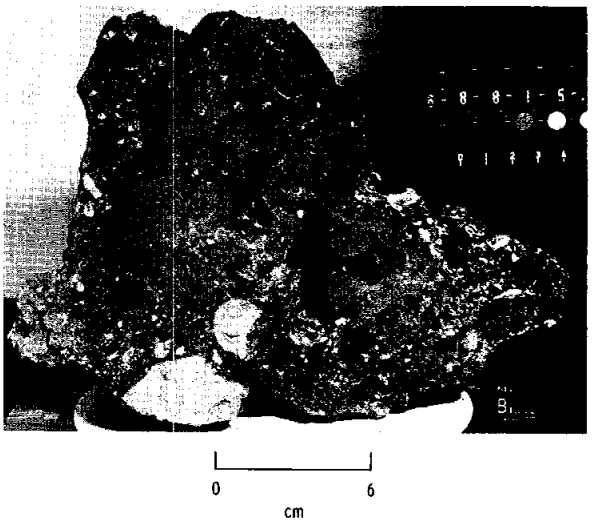


FIGURE 7-10.–Sample 68815 shows the predominantly gray version of the complex gray and white breccia. Note the striking tubular vesicles that indicate the once fluid nature of this rock. Smaller vesicles are concentrated along the margins of tubes (S-72-37155).

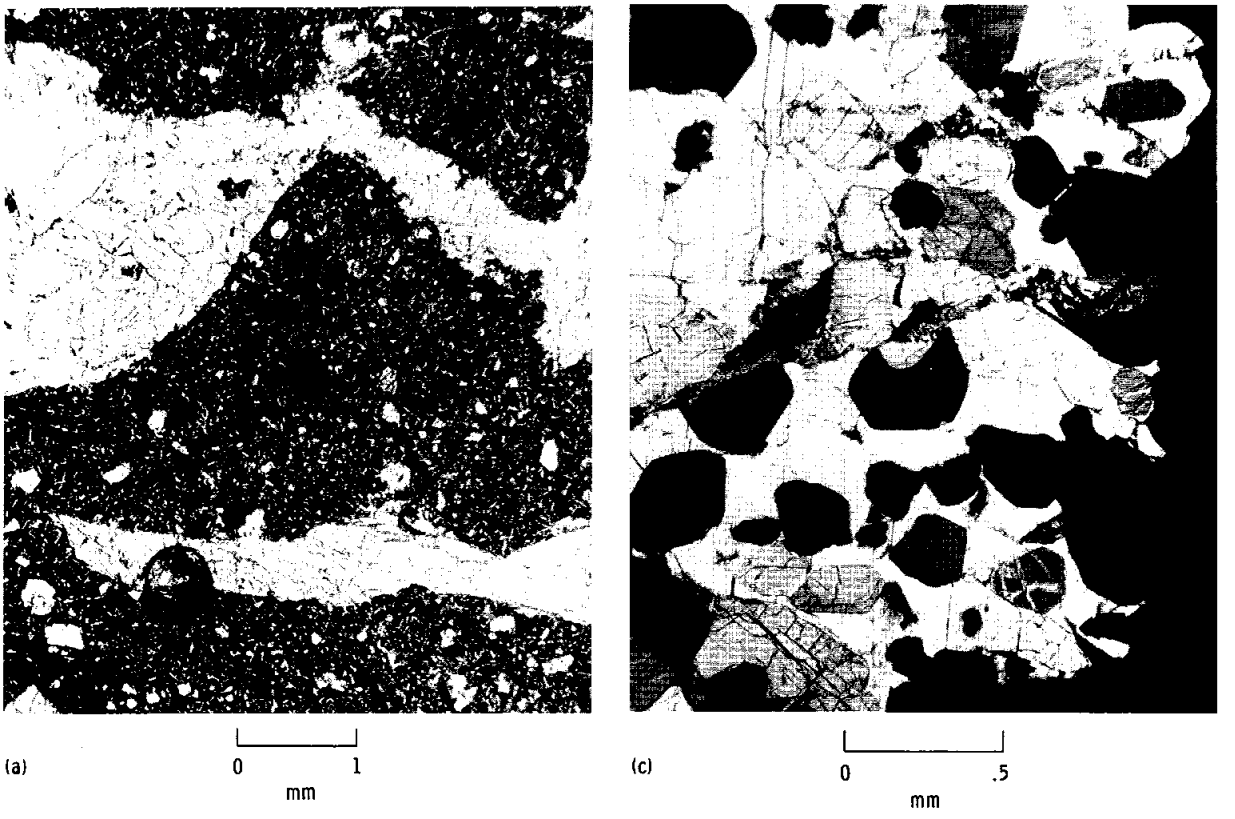


FIGURE 7-11.–Complex gray and white breccia. (a) View of larger area of sample 61015, showing veinlike nature of white crushed plagioclase (S-72-45698). (b) Sample 67435, plane light view of plagioclase (very light gray), subhedral olivine (light gray), and spinel (gray) (S-72-43658). (c) Crossed polars view to illustrate isotropic nature of spinel and poikilitic nature of plagioclase (S-72-43655).

Igneous and high-grade metamorphic rocks (type III).–The type III rocks include a variety of homogeneous, coherent, crystalline rocks. Among these rocks, the greatest variation in chemical composition of the Apollo 16 rocks occurs. Again, there is a general predominance of plagioclase which seems to be present in quantities that normally range upward from approximately 70 percent, although in some instances the percentage of mafic minerals is significantly greater. In two of the rake samples, 67667 and 64815, the percentage approaches that of an ultramafic rock. Grain size is generally on the order of a millimeter or less. In some rocks (such as samples 68415, 68416, and 65015) (fig. 7-12), the plagioclase is euhedral, but in others (such as samples 61156 and

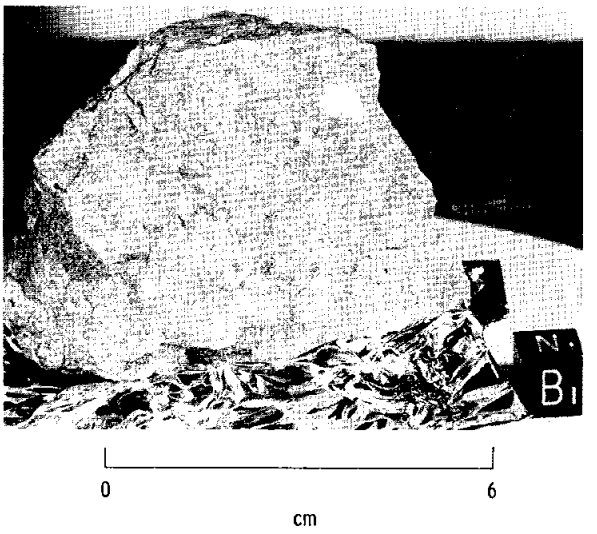


FIGURE 7-12.–Example of one of the two major textural features of the angular, gray, tough, crystalline rocks. Sample 68416, plagioclase laths of approximately 1-mm grain size make up more than 70 percent of this rock, but large plagioclase phenocrysts highlighted by the bright reflections from cleavage surfaces occur sporadically (S-72-37533).

65095), it is anhedral. Light green or yellow to honey brown mafic materials are seen in most of this group under the binocular microscope. Thin sections of this type indicate two major subgroups. One subgroup contains euhedral plagioclase laths of various sizes plus pyroxenes and perhaps olivine in a texture clearly indicative of crystallization from a melt. The plagioclase occurs both as well-developed laths in a diabasic texture complete with large phenocrysts (fig. 7-13(a)) and as skeletal crystals that formed during rapid cooling (fig. 7-13(b)). The other subgroup has large poikilitic pyroxene grains that include plagioclase and other mafic minerals (figs. 7-14, 7-15(a), and 7-15(b)). The poikilitic grains are made up of numerous individual irregularly shaped areas of pyroxene (fig. 7-15(c)). The texture is indicative of recrystallization as in a metamorphic hornfels.

An interesting observation on sample 66095 of the second subgroup is the alteration of numerous areas in which original phases have taken on a rusty appearance. In many instances, the rust penetrates as a stain into the zone around these phases. The rustlike material also forms a very thin crust along some fracture surfaces. The optical properties in polished thin sections are those of goethite. Although some of this alteration appears to have occurred on the lunar surface, it remains to be determined how much might have resulted from exposure to the atmospheres of the spacecraft and Earth during the return trip.

Polymict breccias (type I).–The type I rocks consist of white to very light gray, moderately friable, clastic matrix polymict breccias in which matrix material of less than a few tenths of a millimeter grain size predominates (fig. 7-16). This matrix appears to be a more crushed equivalent of the clast materials and is essentially free of glass. Clasts in these breccias are generally on the order of a few millimeters in size, although rarely there may be clasts a few centimeters across. The clasts range from very white and plagioclase rich through various shades of gray to medium dark gray and aphanitic. The lighter clasts may contain as much as 20 or 30 percent mafic minerals, and they range from anorthositic to gabbroic, noritic, or troctolitic in composition. The darker clasts may be devitrified glass and rarely contain small white spots. Distribution of various clast types appears to vary from sample to sample.

This category is typified by samples 60016, 60019, 61135, 61175, 61295, 66035, and 66075. Similar specimens include samples 63355, 67015, 67016, and 67115, which are lighter in color, more coherent, and contain predominantly aphanitic dark gray clasts of a larger size than in the previously mentioned samples. Yet, other specimens such as samples 65786, 65925, and 61525 display a slightly darker color and are somewhat more coherent than the typical type. However, the matrix and the variety of small clasts appear to be similar in all subgroups. It may be significant that the lighter colored subgroup occurs in the northern part of the landing site at stations 11 and 13, and the more typical examples occur farther south.

Thin sections of this type (fig. 7-17) show the matrix to consist entirely of crushed mineral fragments (fig. 7-17(a)) with essentially no glass present even down to a very fine scale (fig. 7-17(b)). Although there is a variety of clast types, the predominant one is plagioclase as one would predict from the chemical analysis of sample 61295 (table 7-III). The plagioclase clasts exist as large ragged single crystals, annealed aggregates, finely crushed material, and some maskelynite (fig. 7-17(c)). The various gray aphanitic clasts seen under the binocular microscope apparently consist of finely crushed plagioclase aggregates or devitrified glass. Finally,

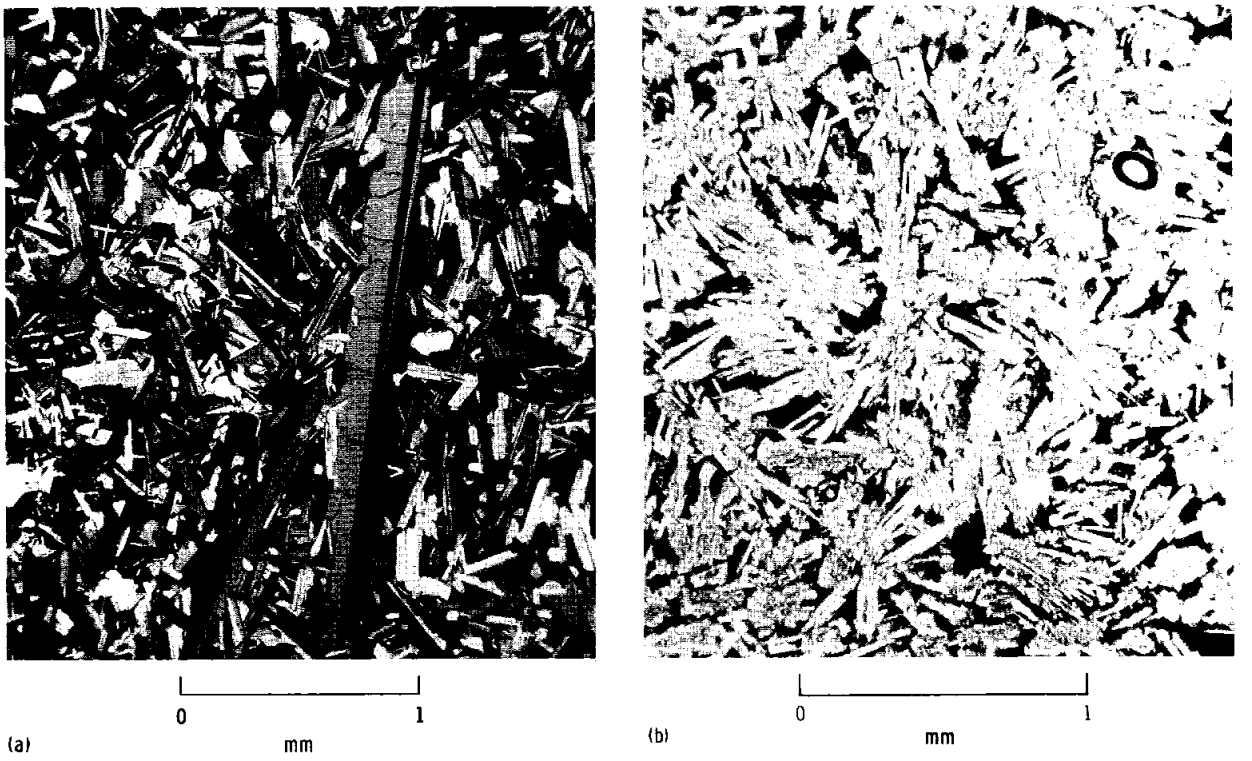


FIGURE 7-13.–Igneous crystalline rocks. (a) Sample 68416, crossed polars view, showing euhedral plagioclase laths both as phenocrysts and in a diabasic matrix that also contains approximately 20 percent pyroxene as smaller, irregularly shaped grains between the laths (S-72-43652). (b) Sample 62295, plane light view, showing skeletal plagioclase laths, some in a radiating pattern, with interstitial diabasic plagioclase and orthopyroxene that formed from a trapped interstitial melt. Higher relief mineral intergrown with large plagioclase grains is orthopyroxene.

there are a few clasts containing poikilitic pyroxene and some consisting of glass.

The clast population of these rocks is, at the present level of examination, similar to the other rock types found at this site. Except for the near absence of glass, the characteristics of these rocks, including the moderately high carbon content of one analyzed example of this type, suggest that these rocks are indurated equivalents of the local regolith. The variability of TiO_2 and K_2O contents, in contrast to the smooth trends exhibited by the present surface soils (fig. 7-2), suggests that these rocks are derived from a more heterogeneous source than the present regolith.

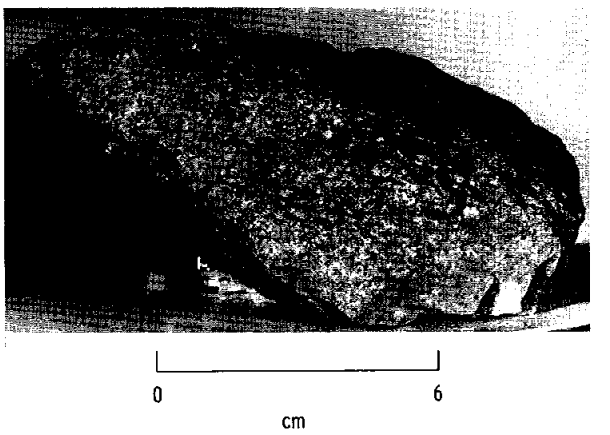
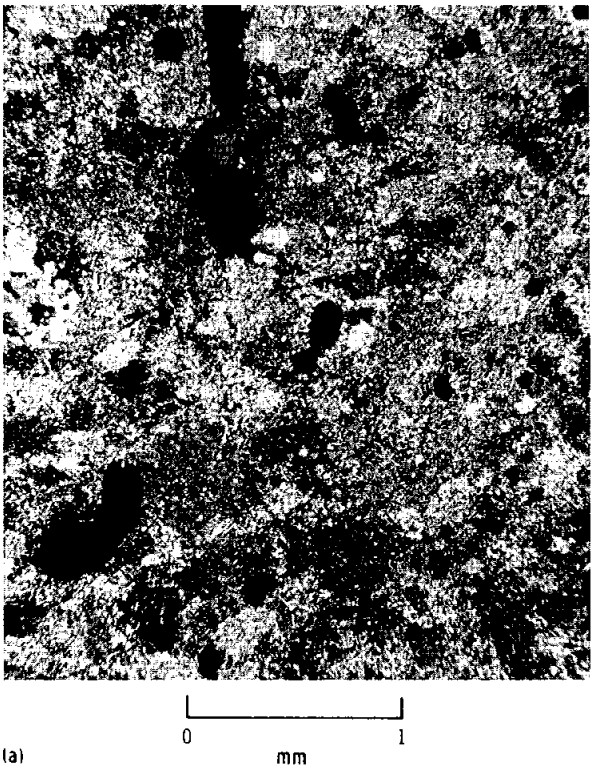
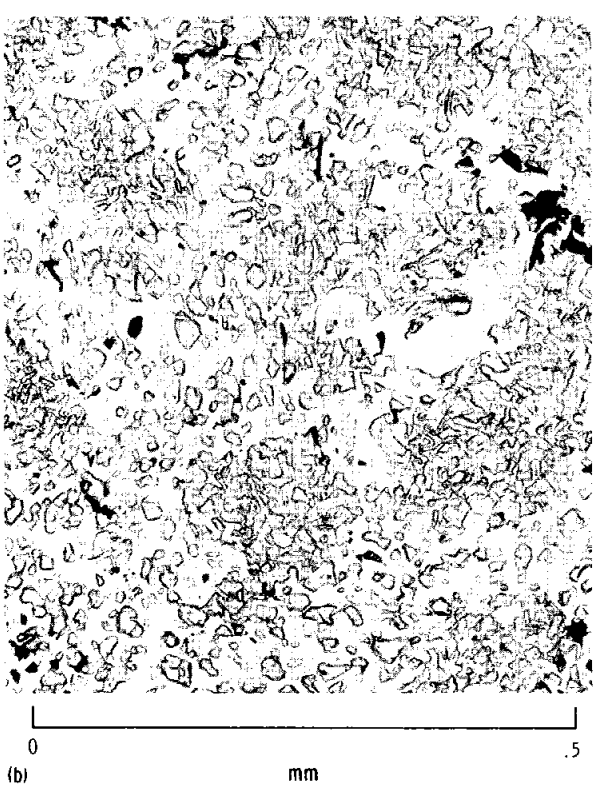


FIGURE 7-14.–Example of the second of two major textural features of the angular, gray, tough, crystalline rocks (fig. 7-12). Sample 60315, the lath-shaped white areas (distinct from round, white, impact pits) are poikilitic orthopyroxenes in a recrystallized texture (S-72-37189).





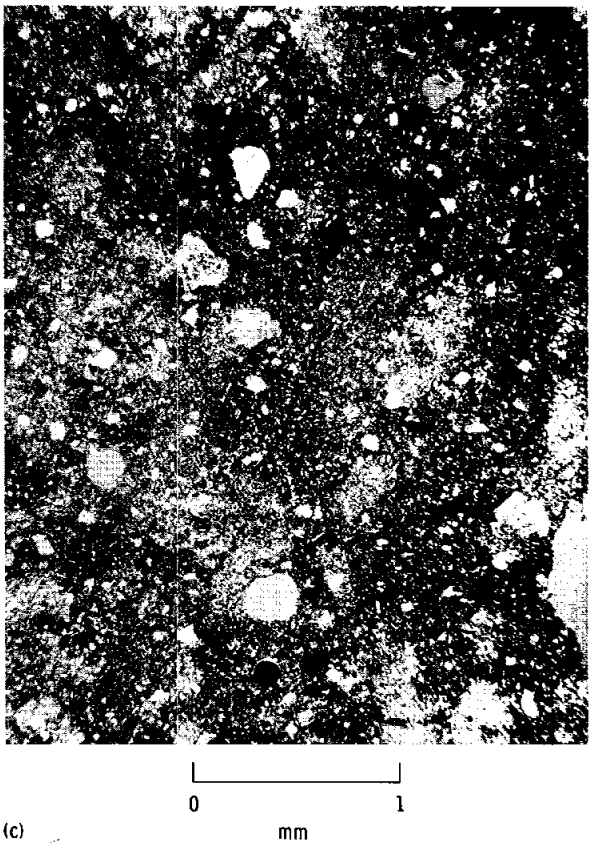


FIGURE 7-15.–Poikilitic crystalline rocks. (a) Sample 61156, crossed polars view, showing irregularly shaped poikilitic patches of pyroxene accented by the different shades of gray. Each of the patches contains numerous individual grains. (b) Plane light view of highly magnified area of one poikilitic crystal. (c) Sample 62235, crossed polars view of poikilitic patches of pyroxene (S-72-45689).

The opaque mineral content of most type II and IV rocks is generally low compared to rocks from other landing sites, being generally less than 1 percent and ranging to less than 0.01 percent. The cataclastic anorthosites contain the lowest opaque mineral content of the four rock types; sample 65315 contains no more than approximately 0.001 percent opaque minerals. The poikilitic rocks of type III contain the highest ilmenite contents; it is consistently present in amounts greater than approximately 2 percent. Rock 63335 contains even greater amounts. The high ilmenite content is a reflection of the relatively high Ti content of this group. The following minerals were

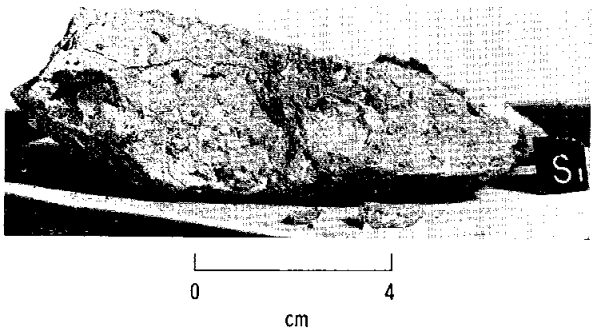
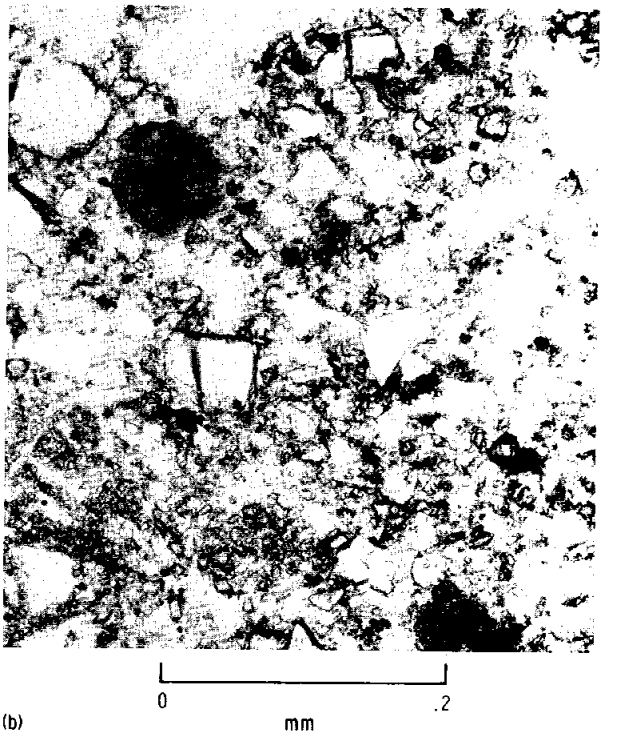


FIGURE 7-16.–Typical type I rock, sample 61295, showing gray and white clasts in a friable, light gray matrix that is predominant over clasts. Note the fracture that trends subparallel to the top surface. Such fractures are common in this rock type (S-72-38962).





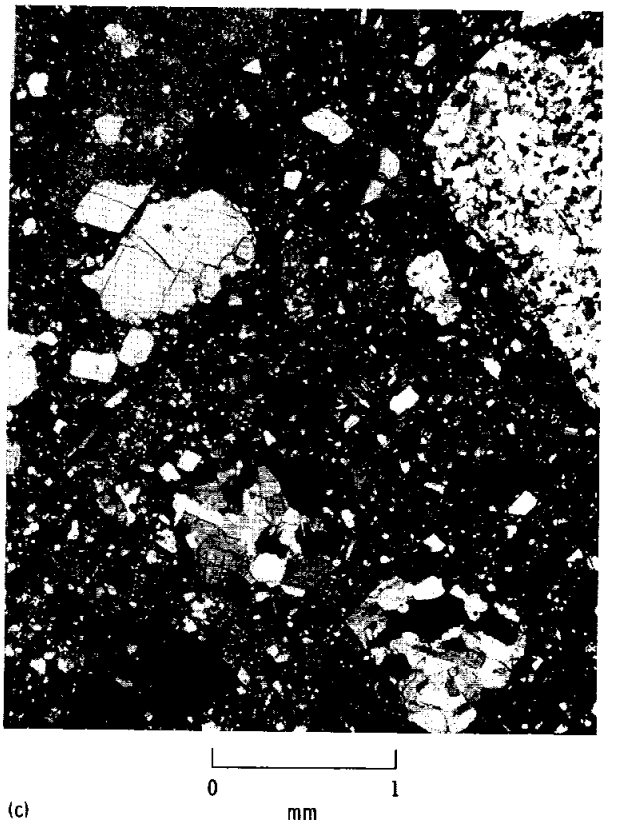


FIGURE 7-17.–Thin section of rock 61295 (plane light). (a) Angular clasts of a wide variety of mineral and lithic fragments in a gradation of sizes down to resolution (S-72-45706). (b) High-resolution view of matrix, showing that clastic mineral fragments make up the matrix even on the scale of a few micrometers. (c) Crossed polars view of clasts, showing the variety of plagioclase assemblages: finely crushed in upper right, annealed in lower center, large ragged single crystal in upper left (S-72-43967).

identified: metallic iron, troilite, ilmenite, ulvöspinel, (Zr?) armalcolite, schreibersite, spinel, and chrome spinel.

Unlike most rocks from previous missions, metal and troilite commonly predominate over opaque oxide minerals; generally, the metal and troilite contents do not appear to be exceptionally high for lunar breccias. In no rock examined is the metallic iron content greater than approximately 1 percent. Ilmenite is commonly the dominant oxide mineral. The shape and the size of ilmenite grains appear to be useful indexes for determining degree of crystallinity of breccias.

In addition to the previously listed four rock types, there are several forms of glass, including two glass spheres, samples 60095 and 65016; sample 65016 is hollow. Other predominantly glass samples are listed in table 7-I and are generally vesicular agglutinates.

In addition, both type IV and type II rocks are commonly coated with a dark gray glass. Types I and III do not show such coatings. A thin section of this glass coating shows a high degree of devitrification, much of which appears to be plagioclase, but the fine-grained nature of the crystals makes it difficult to be certain of the nature of all the crystals. No chemical analysis was made of this glass coating, but it may well be similar to the anorthositic rocks of types II and IV and may represent the nearly totally melted equivalent of the gray areas in these rocks.

Description of Petrography

The textural characteristics suggest that types II and IV may not be clearly distinguishable. These rocks may form a continuous series that ranges from crushed anorthositic rocks with little or no partial melting to those with a high degree of melting and crushing. The similarities in mineralogy, clast types, chemical composition, and textural gradations all support such a continuous series. Some rocks are nearly all white crushed anorthosite, and others are nearly all gray partially melted anorthositic material; the entire range of white and gray mixtures between these extremes can be observed. Many of these rocks seem to be cataclastically crushed, preserving relict textures of the original rocks, but others seem to be more highly brecciated and melted, leaving only a few clasts with a clue to the texture of the original rocks. Nevertheless, the clasts are similar to the relict cataclastic textures in their anorthositic affinities, both mineralogically and texturally. Moreover, the textures of the type II and IV rocks suggest that these rocks are distinct from all other lunar breccias. No evidence exists that the rocks are mechanically produced mixtures of preexisting rocks. They are monomict rather than polymict breccias in the sense that these terms were used by Wahl (ref. 7-14) to describe meteorites. The rocks exhibit peculiar melting textures, perhaps related to macroscopic or submacroscopic heterogeneities. The molten parts, whether they are the major portions of the type IV rocks or small molten portions within the type II rocks, are generally more rich in iron and magnesium than the surrounding or enclosed material. It has been suggested that the heterogeneous occurrence of mixtures with lower melting temperatures determined whether particular parts of a rock underwent melting. Thus, the early melting patches in some rocks may, in fact, represent late crystallizing interstitial liquids in a coarse-grained anorthositic cumulate.

From these descriptions of the rocks, it seems quite clear that rock types II and IV originated from a relatively coarse-grained igneous complex consisting predominantly of anorthosite (some of which is troctolitic as indicated by the early euhedral crystallization of olivine in some rocks and clasts) that has been directly transformed to the observed rocks by impact or cataclysmic metamorphism. The rare ultramafic rocks among the rake samples may be related to this complex either as small layers or sparse fragments from a greater depth. Although the original source area for these particular rocks is uncertain, it does not appear to be in the upper few tens of meters beneath the landing site, based on the photographs of North Ray Crater, which contains breccia boulders, the ejecta from North Ray and South Ray Craters, and the interpretation of the active seismic experiment data. Nevertheless, the widespread distribution of the rock type II and IV series over both the mountains and plains areas and the similar widespread conformity of soil composition which has gabbroic anorthosite chemistry and represents the homogenization and reworking of many layers of material in the upper few hundred meters of the entire area suggest that the entire area is underlain at some depth by an anorthositic complex.

The origin of at least some of the type III rocks (in particular, those with KREEP basalt chemistry) may be unrelated to the anorthosites. The igneous

rocks 68416 and 68415 are two chips (separated by 20 to 30 cm) from a large boulder. Even though these specimens are clearly from a single rock, they are appreciably different in grain size. This rock may represent a portion of a pool of impact molten material rather than an unshocked part of the underlying anorthosite. In this case, these two rocks are genetically the extreme end members of the type II and IV series.

When the classification of the Apollo 16 rock specimens is reviewed in terms of their petrogenesis, the following three major types emerge.

(1) A series of cataclastically and cataclysmically modified anorthositic rocks, probably derived from an anorthositic complex that contained from 70 to 90 percent plagioclase

(2) Igneous rocks, at least some of which underwent thermal metamorphism

(3) Polymict breccias that are mechanical mixtures of the preexisting rock types

None of the returned samples are in accord with the preflight hypotheses concerning the origin of landform units in this region. The rocks that apparently underlie the regolith of the plains region are in no sense volcanic. No evidence for lava flows or pyroclastic rocks was observed. The only possible rocks that could correspond to the Descartes volcanic unit presumed to underlie the hilly region to the north and southeast of the landing site are the high-alumina igneous rocks (e.g., samples 66095 and 61156) or the KREEP basalts which have metamorphic textures. The absence of sharp compositional gradients over the surface argues against the latter possibility. The more detailed study of soils and rake samples from stations 5 and 6 should clarify this conjecture.

Soil Characteristics

The >1-mm fractions of 32 soil samples were examined surficially. Thin sections of the <1-mm fraction of nine of these soil samples were further investigated. The fragments observed in these studies can be grouped into glass-coated particles (agglutinates), mineral or lithic fragments that largely correspond to the previously discussed rock types, and a variety of vitric fragments. Lithic fragments include the breccias previously described and the cataclastic anorthosites. Discrete mineral fragments of plagioclase, clinopyroxene, orthopyroxene, and olivine are relatively common. Trace quantities of pink spinel and potassium feldspar are also found. The prevailing glass type is colorless with a relatively high refractive index. Brown or colored glasses are much rarer at this site than they were at other Apollo landing sites. The relative abundances of glassy and crystalline fragments are given for nine soil samples in table 7-VI. The abundance of glass varies rather markedly.

The median grain size of most soil samples ranges from 76 to 112 μm. However, the two samples from North Ray Crater (67480 and 67600) and one whitish soil from station 1 (61220) are much coarser; the median grain size ranges from 250 to 300 μm.

It is noteworthy that the three coarser soils all have relatively low abundances of agglutinates as well as relatively low nickel contents. The concurrence of these three parameters suggests that these soils have been subject to gardening for a much shorter time than the typical soil. The occurrence of an immature soil in the bottom of the trench at station 1 (sample 61220) suggests that remnants of relatively young rays from North Ray Crater may be overlain by mature soils ejected from small shallow craters. If this interpretation of the North Ray Crater soils is accepted, it is clearly distinguishable from soil interpreted as South Ray Crater ejecta, which contains dark brown to black vesicular glass droplets and dark gray breccias.

Core samples collected during the mission are summarized by Hörz et al. (part B of this section). Of particular note are the three sets of cores taken within 100 m of each other in the LM-Apollo lunar surface experiments package area. The X-radiographs of these returned cores indicate that some correlations are possible between cores, thus enabling the most detailed reconstruction of lunar soil strata to date. The nature of the Descartes material may be recoverable from the core that was taken at station 4. Because of the ubiquitous covering of South Ray Crater ejecta on Stone Mountain, the sampling of Descartes material on the surface is difficult. The X-radiographs of station 4 core tubes indicate a distinct change in grain size, abundance of rock fragments, and rock types at a depth of approximately 51 cm. It is possible that the underlying 20 cm of soil may contain evidence of any differences in chemical or mineralogical components in the Descartes material.

TABLE 7-VI.–Comparison of the 62.5 to 125 μm Fractions

[Numbers are given in percentages]

Component	Sample number								
	61220	*64421*	*66041*	*66081*	*68820*	*68841*	*69940*	*67480*	*67600*
Agglutinates	8	54	39	53.4	52	80	64	24	20
Colorless glass fragments	23	3	3.8	9.8	2	2	4	–	3
Colorless glass droplets	2	1	–	1.7	1	–	–	–	2
Brown glass fragments	–	–	–	2.9	–	2	6	3	1
Brown glass droplets	–	1	–	1.7	Trace	–	–	1	Trace
Orthopyroxene	–	–	–	2.9	2	–	1	4	–
Clinopyroxene	8	1	2.8	–	–	3	1	5	3
Plagioclase	35	15	16.1	9.2	15	7	7	22	22
Metaigneous breccia	12	17	21.9	7.5	21	6	7	15	21
Vitric breccia	10	7	15.2	9.8	1	Trace	7	24	22
Anorthosite	–	–	–	–	6	–	2	1	5
Basalt	1	1	–	.6	–	Trace	1	–	1
Olivine	1	–	–	–	–	–	–	–	–
Ilmenite	–	–	.9	–	–	–	–	–	–
Potassium feldspar (?)	–	–	–	.6	–	–	–	–	–
Total no. of grains	100	100	105	174	100	100	100	100	100

Summary

The preliminary characterization of the rocks and soils returned from the Apollo 16 site has substantiated most of the widely held inferences that the lunar terra is commonly underlain by plagioclase-rich or anorthositic rocks. The first examination of the rock samples has confirmed the suspicion voiced by the astronauts during their traverses; that is, that the volcanic rocks which had been hypothesized to underlie the regolith in the Apollo 16 region were largely nonexistent. In their place, anorthositic rocks that are thoroughly modified by crushing and partial melting were found. The textural and chemical variations in these rocks provide some evidence for the existence of anorthositic complexes that have differentiated on a scale of tens to hundreds of meters.

The occurrence of deep-seated or plutonic rocks in place of volcanic or pyroclastic materials at this site suggests that the widespread occurrence of volcanic or pyroclastic materials in terra regions, which was inferred by physiographic evidence, may be incorrect.

The following several additional and more specific conclusions derived from this preliminary examination should be noted.

(1) The combination of the data from the Descartes region with data from the orbital X-ray fluorescence experiment indicates that some far-side highland regions are underlain by materials which consist of more than 80 percent plagioclase.

(2) The soil or upper regolith between North Ray and South Ray Craters has not been completely homogenized since the time of formation of these craters.

(3) Based on the chemistry of the soil, it is inferred that potassium-, uranium-, and thorium-rich rocks similar to those that prevail at the Fra Mauro site are relatively abundant (10 to 20 percent) in the Descartes region.

(4) The potassium-to-uranium ratio of the lunar crust is similar to that of the KREEP basalts.

(5) The carbon content of the premare lunar crust is even lower than that of the mare volcanic rocks.

Acknowledgments

The membership of the Lunar Sample Preliminary Examination Team is as follows: Members of the steering group are P. W. Gast, NASA Manned Spacecraft Center (MSC); W. C. Phinney, MSC; M. B. Duke, MSC; E. D. Jackson, USGS; N. J. Hubbard, MSC; P. Butler, MSC; and R. B. Laughon, MSC. Members of the mineralogy and petrology group are S. O. Agrell, University of Cambridge, England; M. N. Bass, Lunar Science Institute (LSI); R. Brett, MSC; W. D. Carrier, MSC; U. S. Clanton, MSC; A. L. Eaton, Brown & Root-Northrop (BRN); J. Head, Bellcomm, Inc.; G. H. Heiken, MSC; F. Hörz, MSC; G. E. Lofgren, MSC; D. S. McKay, MSC; D. A. Morrison, MSC; W. R. Muehlberger, USGS; J. S. Nagle, BRN; A. M. Reid, MSC; W. I. Ridley, LSI; C. Simonds, LSI; D. Stuart-Alexander, USGS; J. L. Warner, MSC; R. J. Williams, MSC; and H. Wilshire, USGS. Members of the chemical analysis group are B. M. Bansal, Lockheed Electronics Company (LEC); J. A. Brannon, LEC; A. M. Landry, LEC; J. M. Rhodes, LEC; K. V. Rodgers, LEC; and J. E. Wainwright, LEC. Members of the low level counting group are L. Bennett, MSC; R. S. Clark, MSC; J. E. Keith, MSC; G. D. O'Kelley, Oak Ridge National Laboratory; R. W. Perkins, Battelle Pacific Northwestern Laboratory (BPNL); W. R. Portenier, BRN; L. A. Rancitelli, BPNL; M. K. Robbins, BRN; and E. Schonfeld, MSC. Members of the carbon analysis group are E. K. Gibson, MSC; C. F. Lewis, Arizona State University (ASU); C. B. Moore, ASU; and D. R. Moore, BRN.

PART B

APOLLO 16 SPECIAL SAMPLES

Friedrich Hörz,[a] W. D. Carrier III,[a] J. W. Young,[a]
C. M. Duke,[a] J. S. Nagle,[b] and R. Fryxell[c]

Introduction

The interaction of the space environment with the lunar surface is the subject of a variety of investigations. Such investigations are concerned with the particle track record of solar and galactic radiation, the chemical characteristics of the solar wind, radioactive isotopes produced by solar flares and cosmic radiation, noble gases, micrometeoroids, and selective volatilization and ionization of specific elements. A quantitative understanding of these processes will contribute to knowledge of the solar system. It also is required to determine the character and dynamics of lunar surface processes such as the erosion of rocks, the mechanisms of regolith transport, the turnover rate of the regolith, the obliteration of impact craters, the migration of volatile and semivolatile species, and the influx of meteoritic materials. Collectively, these studies will also have important implications for remote sensing, not only of the lunar surface but other planetary bodies as well.

Although the investigation of Apollo 11, 12, 14, and 15 materials yielded valuable information about some general trends, it became increasingly mandatory for a more quantitative understanding of these processes that specific samples be obtained or some samples be collected in a very specific fashion (or both). A successful attempt was made during the Apollo 16 mission to return a variety of such materials.

The purpose of this section is to give documentary background information about these special samples. Although most of the samples were collected for the purpose of investigating rather specific problems, most returned materials will serve multiple purposes. Where appropriate, the main rationale for collecting a specific sample is outlined; in general, these materials will be particularly suitable for the purposes indicated.

[a]NASA Manned Spacecraft Center.
[b]Brown and Root-Northrop.
[c]Washington State University.

Pristine Surface Materials

Most of the previously mentioned investigations are specifically concerned with the properties of the uppermost lunar surface (i.e., materials from a depth of less than 1 mm). Thus, an effort was made to collect regolith materials from various extremely shallow depths and to return rock samples, the surfaces of which were carefully protected to ensure their pristine character.

Regolith materials.—Two special contact soil sampling devices (CSSD's) were used to collect the uppermost regolith layer at station 9. The CSSD is essentially an aluminum box into which a collector plate is inserted (fig. 7-18(a)). The collector plates are draped with nylon fabrics; one fabric has properties similar to Beta cloth and the draped plate is floating freely in the container. Therefore, no load other than its own weight is applied during sampling. Thus (ideally), the CSSD collects a layer of approximately 100 μm. The fabric on the other plate is a velvetlike nylon fabric, and the plate is spring loaded. A force of 4.5 N (1 lb) is applied during sampling, and a layer approximately 0.5 mm thick is recovered (fig. 7-18(b)). Samples 69003 (Beta cloth) and 69004 (velvet) were collected approximately 2.5 km from the landing site. This distance is considered safe to rule out possible effects of the lunar module (LM) descent engine blast. Furthermore, the actual sampling area was behind a boulder facing away from the LM. Thus, because of distance and ballistic shielding of the boulder, LM descent engine effects can probably be excluded. The CSSD's were carefully sealed before and after deployment, and great care was taken by the crew not to contaminate the samples with local regolith.

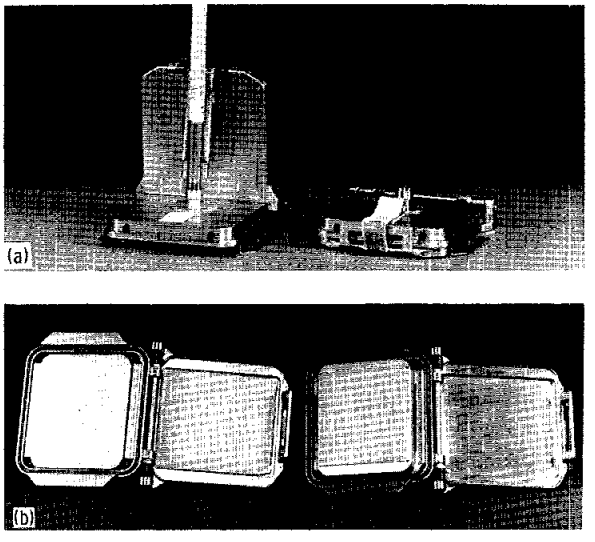


FIGURE 7-18.—Contact soil sampling device (S-72-43792). (a) The CSSD in deployed position. The sampler is essentially an aluminum box (12 by 10 by 2.5 cm) into which an aluminum collector plate is inserted. (b) The collector plates are draped with nylon fabrics; one has properties similar to Beta cloth (left). The plate on the other sampler (right) is draped with a velvetlike nylon fabric.

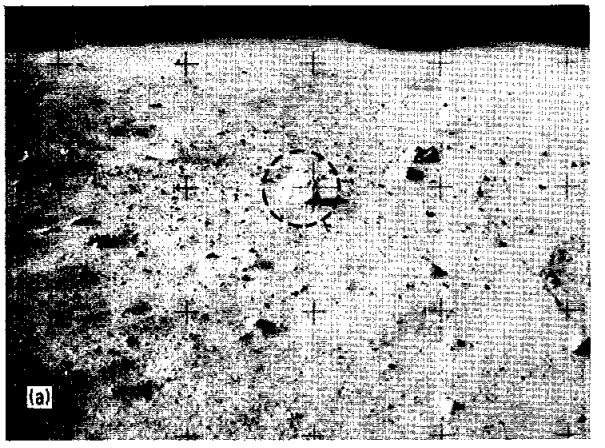
Next to the two CSSD's, two other regolith samples were taken, which incorporated successively deeper soil materials. The skim sample (69920) was retrieved by carefully skimming across the regolith surface with the regular scoop. It is estimated that the maximum penetration was 5 mm. The fourth sample was a regular scoop sample (69940), and it had an estimated penetration of 3 cm (fig. 7-19). A drive tube taken in the vicinity provides material from an even greater depth (estimated penetration, 27 cm).

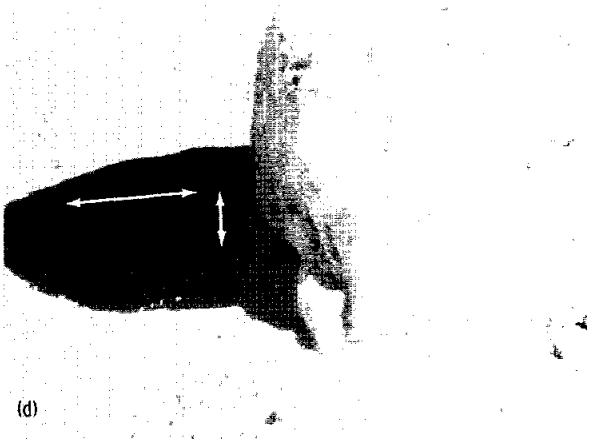
After collection of these materials, the boulder was turned over and a soil sample (69960) was taken from underneath the boulder. This soil was shielded from the space environment since the time the boulder was deposited; therefore, it may be valuable material to compare exposed and shielded soils.

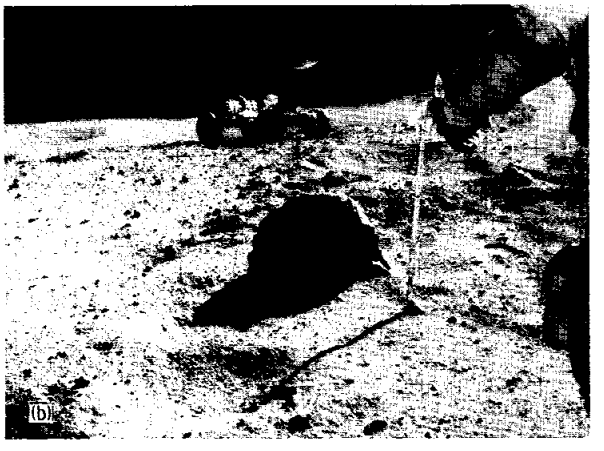
The CSSD's arrived at the Lunar Receiving Laboratory (LRL) in apparently nominal condition, although the outside was heavily dust coated (S-72-39186). Because the CSSD's require special processing, they have not been opened to date. No information is available as to the amount and type of material collected.

Rock surfaces.—To avoid abrasion and other factors resulting in a possible degradation of rock surfaces, two padded bags (fig. 7-20) were used for samples 67215 and 67235, taken at station 11. (For surface documentation, see sec. 6 of this report.)

Because of the scarcity of crystalline rocks (which would have made more ideal samples) at the rim of North Ray Crater, the crew had to select breccias. In addition, the Velcro strap tightening mechanism failed. When the samples arrived in the LRL, it was obvious that the two bags were well protected by soil-filled documented sample bags around the padded bags within the larger sample collection bag (SCB). Sample 67215 seems to be a moderately tough breccia (fig. 7-21(a)); it appears that sample 67235 is a hard recrystallized breccia (fig. 7-21(b)).







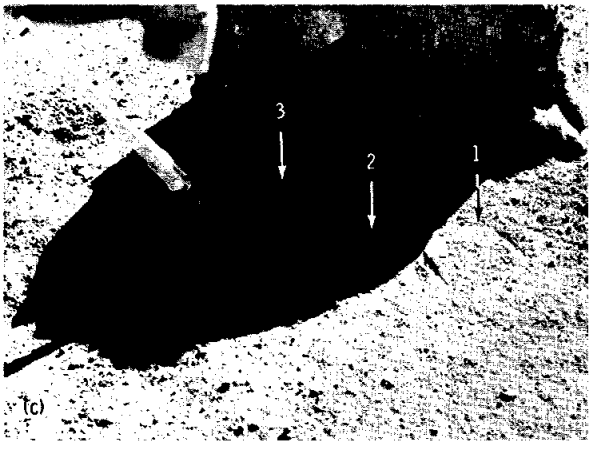


FIGURE 7-19.–Lunar surface documentation of soil surface samples (S-72-43806). (a) Station 9 boulder field related to South Ray Crater; view approximately to the south. Circle indicates sampling area. (b) Locator photograph of sampling area; view approximately to the northeast. (c) After Beta cloth sample (1), velvet cloth sample (2), and skim sample (3) were taken; before scoop sample was taken. (d) After scoop sample. (Documentation of the shielded soil is shown in NASA photograph S-72-43802.)

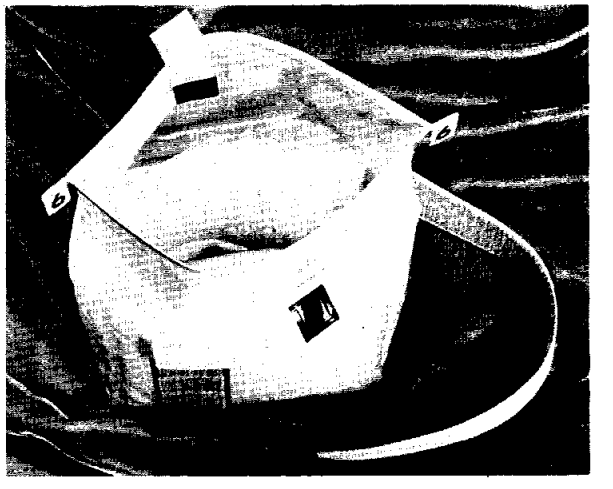


FIGURE 7-20.–Padded bag used to preserve pristine nature of rock surfaces. The bag is double walled with knitted Teflon between the walls to provide padding. The inner wall of the bag, which is in contact with the rock, has a knobby relief to keep the cross sectional area of contact at a minimum and to decrease relative motion, which is further restricted by tightening a circumferential Velcro strap (S-72-43790).



FIGURE 7-21.–Padded bag samples during cursory inspection. (Only the top was opened; the rocks were left untouched.) (a) Sample 67215 (bag 1) appears to be a moderately tough, polymictic breccia, and considerable dust has accumulated on the inner walls of the bag and on the bottom. (b) Sample 67235 (bag 2) is a hard breccia, probably of the recrystallized dark matrix type. Some soil was present on the bag walls, although considerably less than in padded bag 1. Both rocks are dust covered, which prevents a more detailed description at present. The rocks await special processing.

Fillet Samples

Although the combination of a variety of special investigations (particle tracks, gamma ray spectroscopy of short-lived isotopes, noble gases, micrometeorite craters) may eventually lead to a quantitative understanding of lunar erosion processes, another approach would be to sample fillets banked against a boulder and compare the fillet soil with a rock chip from the parent boulder. Furthermore, such fillet samples may yield some information about the transportation mechanisms and transportation rates of regolith materials. Fillet samples were collected from stations 1, 8, and 11.

A boulder on the south rim of Plum Crater (station 1) possessed a well-developed fillet (61280, fig. 7-22). The boulder chip taken is a moderately friable breccia (61295) and is shown in figure 7-23.[1] It is not established at present whether the boulder is related to the Plum, Flag, or South Ray cratering event.

Station 8 was located in a boulder-strewn field related to the South Ray cratering event (fig. 7-24). Boulder A consisted of a highly recrystallized breccia (68115, fig. 7-25). Hardly any fillet had developed around the boulder (68120); thus, the erosion of hard rocks could be studied.

A group of white boulders at station 11 attracted the attention of the crew. Although a fillet sample was not necessarily planned, the variety of materials collected (67455, 67475, 67460) satisfies the requirements for such a sample set. (See sec. 6 of this report.) The white boulders have a feldspar-rich, friable breccia matrix and are probably very easily eroded.

[1] All subsequent orientation photographs are arranged in the same orthogonal manner. The main surface exposed to space is in the center of the orthogonal composites. Adjacent views are only approximately orthogonal to each other because the rocks were placed in naturally stable positions during the photographic process. Consequently, some views deviate from strict orthogonality in such an extreme way that they become unsuitable to be incorporated into the figures. Numbers in the lower right insert are NASA photograph numbers.

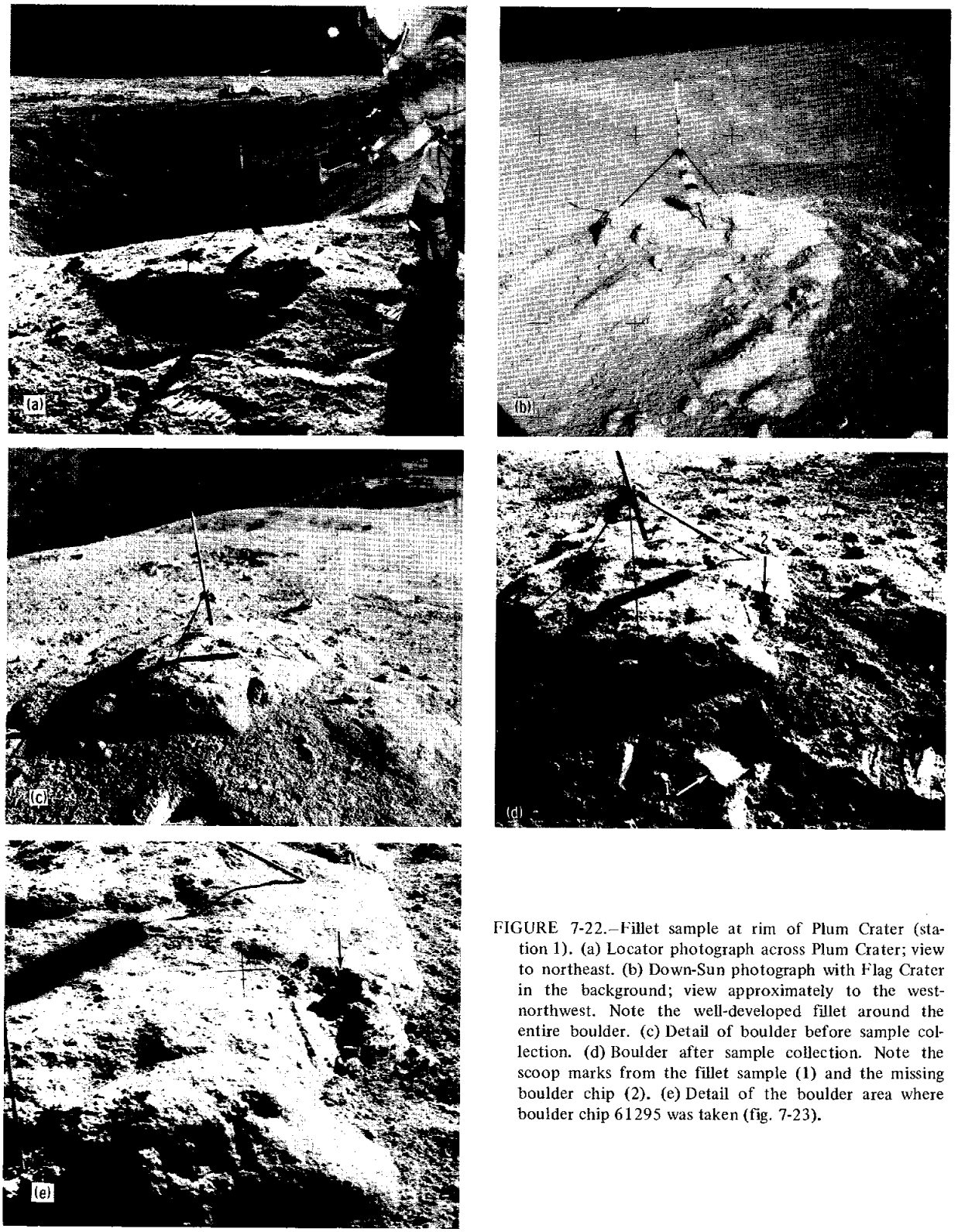


FIGURE 7-22.–Fillet sample at rim of Plum Crater (station 1). (a) Locator photograph across Plum Crater; view to northeast. (b) Down-Sun photograph with Flag Crater in the background; view approximately to the west-northwest. Note the well-developed fillet around the entire boulder. (c) Detail of boulder before sample collection. (d) Boulder after sample collection. Note the scoop marks from the fillet sample (1) and the missing boulder chip (2). (e) Detail of the boulder area where boulder chip 61295 was taken (fig. 7-23).

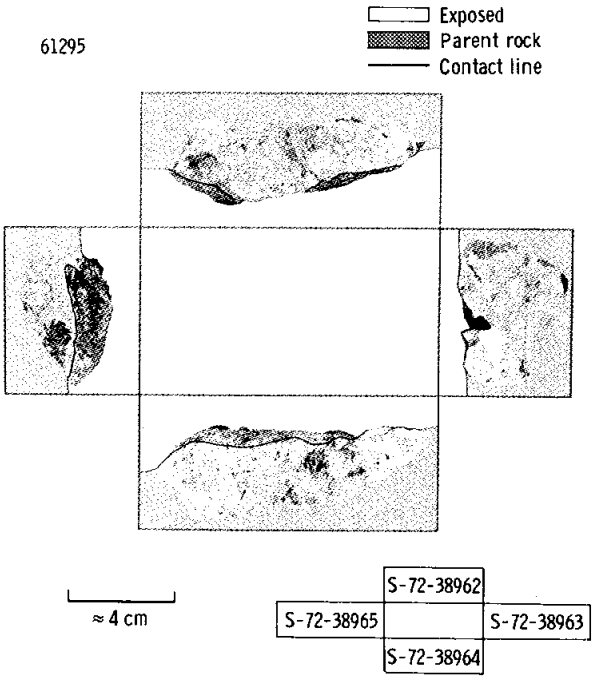
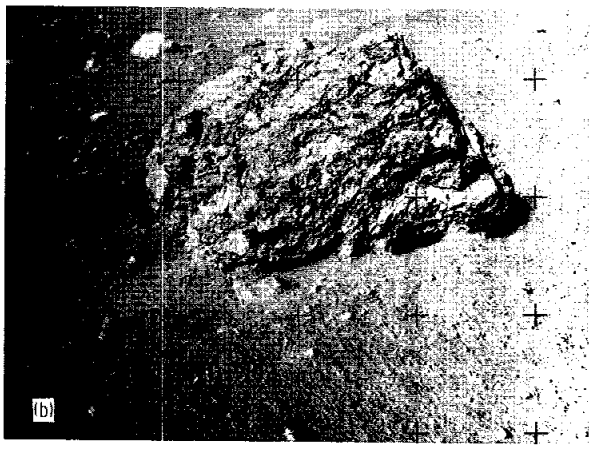
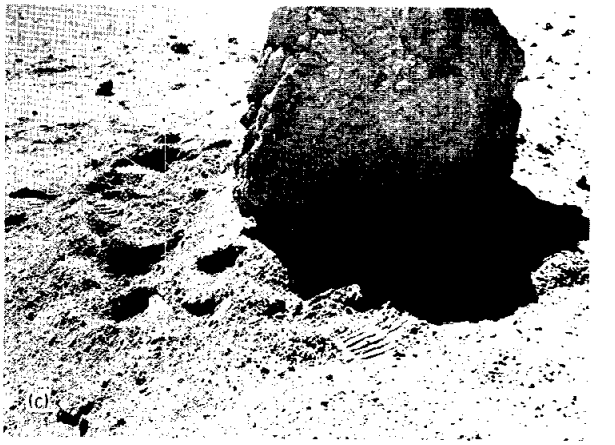


FIGURE 7-23.–Reconstruction of exposed and shielded surfaces (i.e., fresh fracture surfaces) of boulder chip 61295 according to micrometeorite crater distribution. (The surface orientation is presented in sec. 6 of this report.) (S-72-43137)



FIGURE 7-24.–Fillet samples were taken at boulder A at station 8. (a) Overall location of boulder A; view approximately to the south. (b) Closeup of boulder; view approximately to the southwest. Note the breccia nature of the boulder. (c) Closeup of boulder A; view approximately to the east-southeast. (d) Before fillet sample.







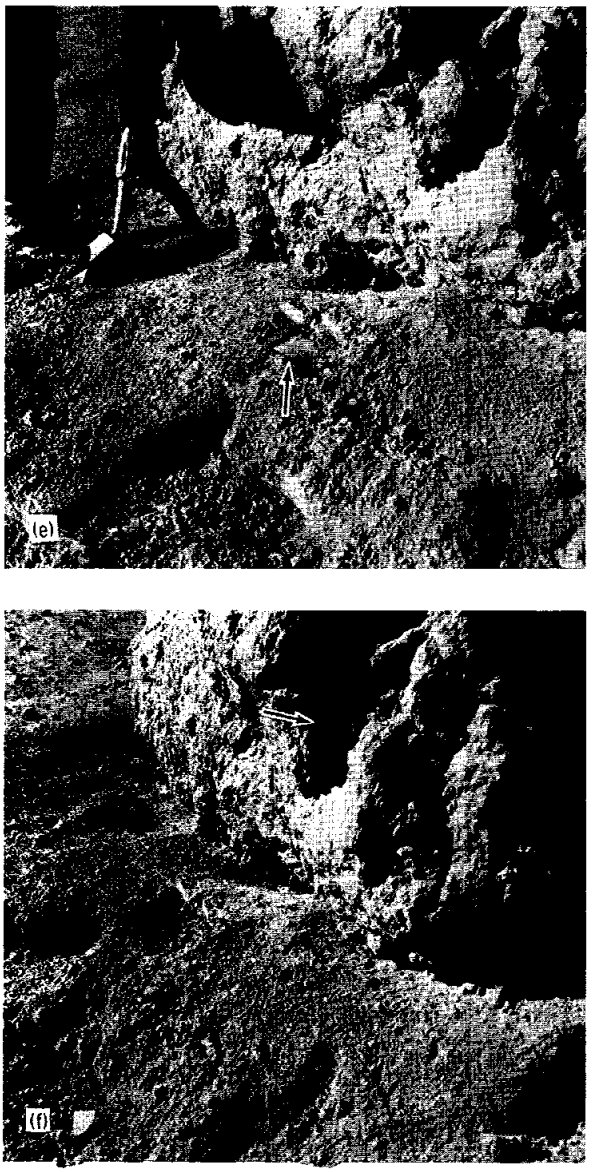


FIGURE 7-24.–Concluded. (e) After fillet sample. (f) After boulder chip 68115 (fig. 7-25).

Dating of Impact Craters

By combining a variety of surface exposure age studies (e.g., particle tracks, gamma ray spectroscopy, noble gases), it is possible to date the age of a cratering event, provided the materials collected can be unambiguously related to the event in question. Two basic approaches are possible. Either a large number of small rocks (with possibly complex surface histories) are investigated, which leads to a statistical best estimate of the impact event, or a few chips taken from large boulders are investigated. The latter case is preferred because it is assumed that large boulders have a less complex tumbling history; therefore, the interpretation of the exposure age measurements is less ambiguous. Consequently, an attempt was made to collect representative chips of meter-sized boulders on the ejecta blankets of the South Ray and North Ray impact craters.

Dating of South Ray Crater.–Several chips were taken at stations 8, 9, and 10 from boulders that, according to field evidence, are part of the South Ray ejecta blanket. If necessary, these chips can be supplemented with a large number of normal hand specimens collected on the surface, which are also interpreted to be associated with the South Ray Crater event. (See sec. 6 of this report.)

At station 8, boulder A, one chip was taken, which is a dense, recrystallized breccia (68115, figs. 7-24 and 7-25). At boulder B, two chips of igneous appearance were taken (68415, 68416; figs. 7-26 to 7-28). Although the parent boulder appears to be a breccia with many genuine clasts, the two chips dislodged from this boulder are rather homogeneous to the unaided eye (figs. 7-27 and 7-28). Surface documentary photographs indicate that the materials collected may be typical of the boulder matrix. At boulder C, the parent boulder is a dense, probably

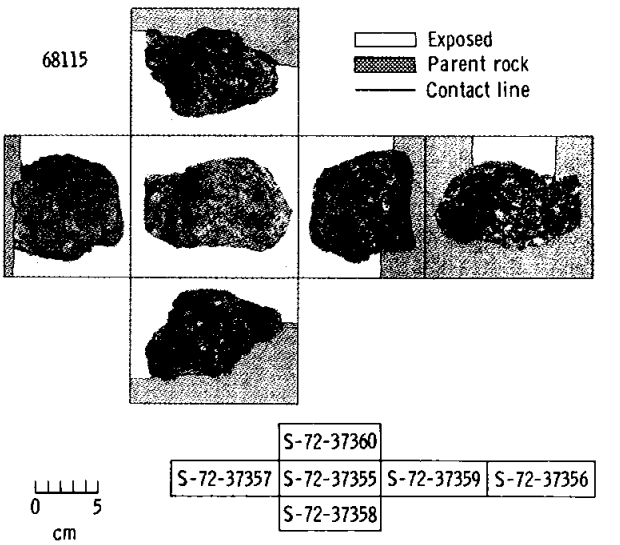


FIGURE 7-25.–Reconstruction of exposed and shielded surfaces of boulder chip 68115. (The surface orientation is presented in sec. 6 of this report.) (S-72-43804)

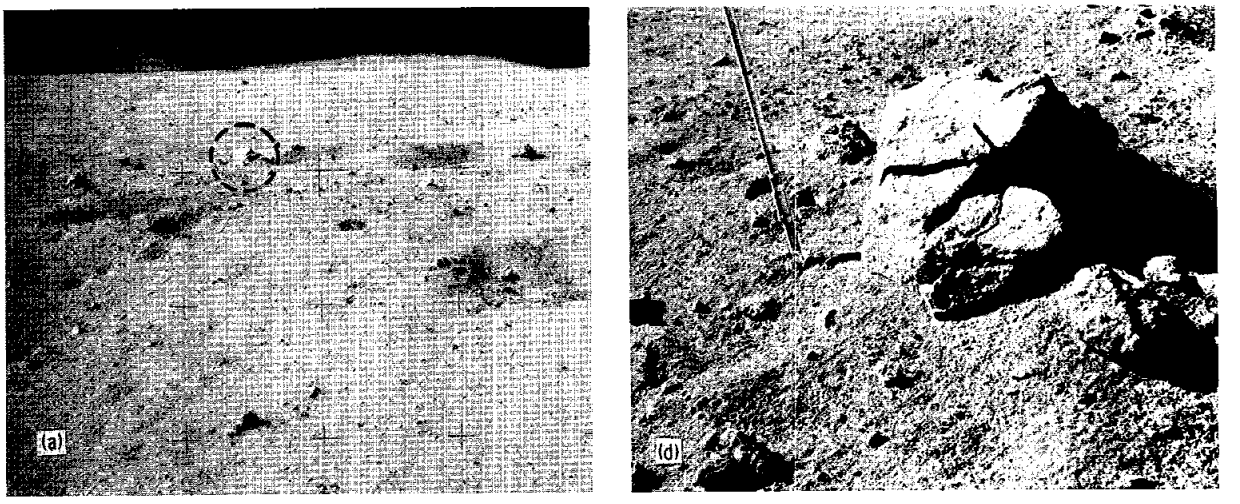


FIGURE 7-26.–Boulder chips were taken from boulder B at station 8 (S-72-43795). (a) General location of boulder field, emanating in a raylike linear fashion from South Ray Crater; view approximately to the south. Circle indicates sampling area. (b) Closeup photograph of boulder B after chips 68415 and 68416 were taken. (See sec. 6 of this report.) (c) Side view of boulder B; view approximately to the west-northwest. (d) Side view of boulder B; view almost due south. Note the breccia nature of boulder B, and compare it with figures 7-27 and 7-28.

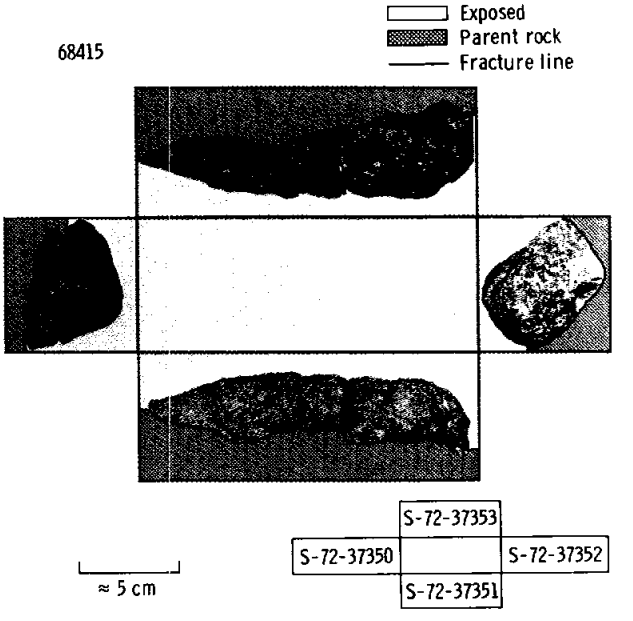


FIGURE 7-27.–Reconstruction of exposed and shielded surfaces of rock 68415. (The surface orientation is presented in sec. 6 of this report.) (S-72-43136)

glass-rich breccia (fig. 7-29). The rock (68815, fig. 7-30) has no igneous texture; in thin section, a multitude of flow structures of the original glass can be seen.

At station 9, two chips were taken from a breccia boulder that is approximately 60 cm in diameter (fig. 7-19). One chip originated from the very top of the

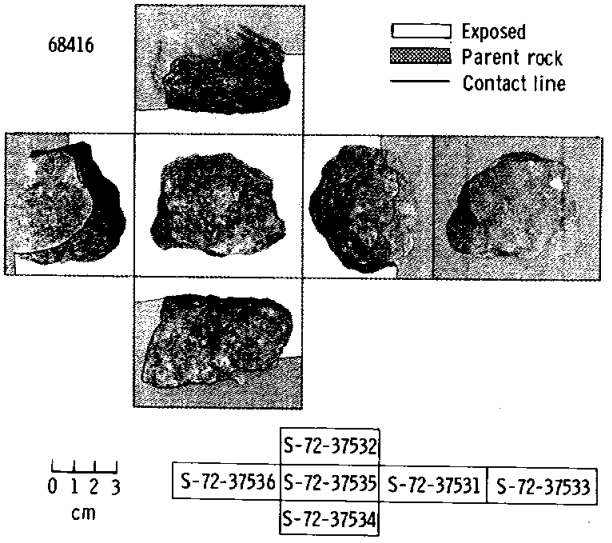


FIGURE 7-28.–Reconstruction of exposed and shielded surfaces of rock 68416. (The surface orientation is presented in sec. 6 of this report.) (S-72-43129)

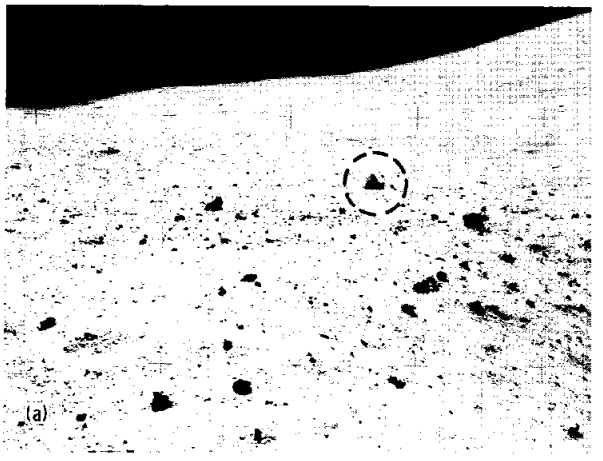
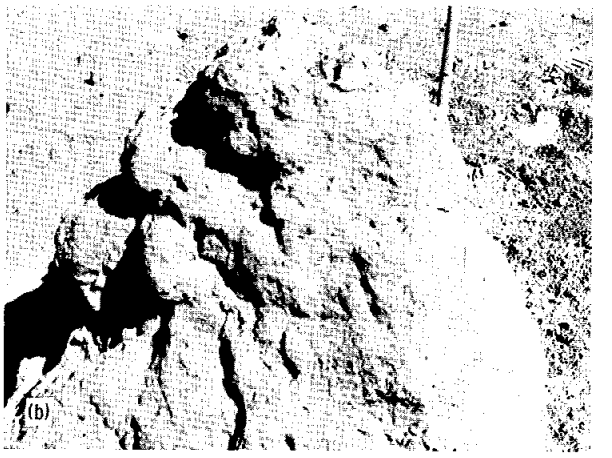
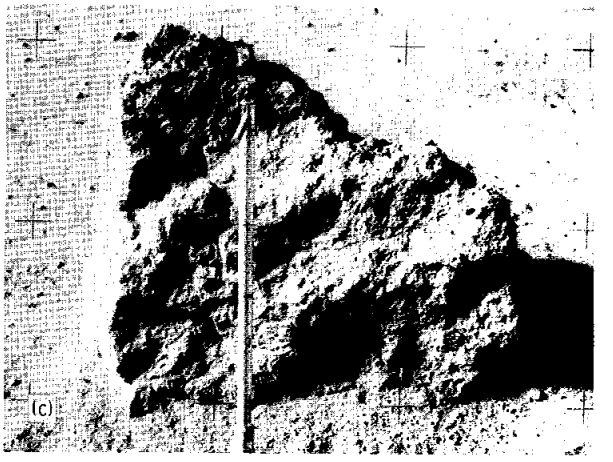


FIGURE 7-29.–A boulder chip was taken from boulder C at station 8 (S-72-43812). (a) General location of boulder C; view to the southeast. Circle indicates sampling area. (b) Closeup photograph of boulder C after sample 68815 was taken from the very top. (See sec. 6 of this report.) (c) Boulder C; view toward the south. (d) Boulder C; view toward the north-northwest.







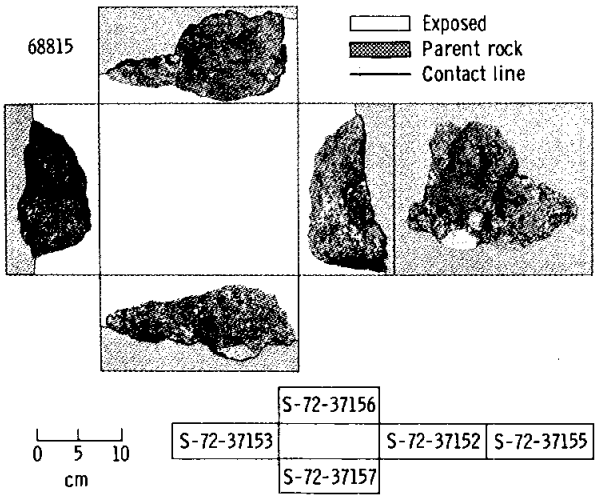


FIGURE 7-30.–Reconstruction of exposed and shielded surfaces of rock 68815. (The surface orientation is presented in sec. 6 of this report.) (S-72-43120)

boulder (69935, fig. 7-31(a)), and the other one was dislodged from the bottom side after the boulder was turned over by the crew (69955, fig. 7-31(b)). Thus, not only a comparison of shielded and exposed materials is possible, but the set of chips may also serve to investigate large-scale gradients of the production of radioactive isotopes of particle tracks caused by very energetic galactic radiation. Therefore, these two chips are particularly valuable in determining the formation age of South Ray Crater.

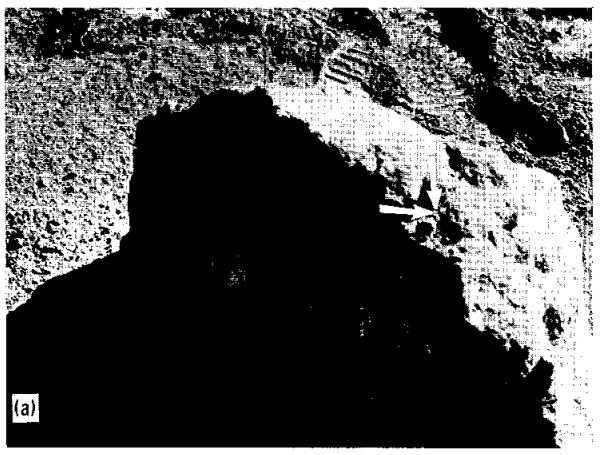


FIGURE 7-31.–Documentation of location of samples 69935 and 69955 (S-72-43789). (a) Chip 69935 was taken from the top of the boulder.

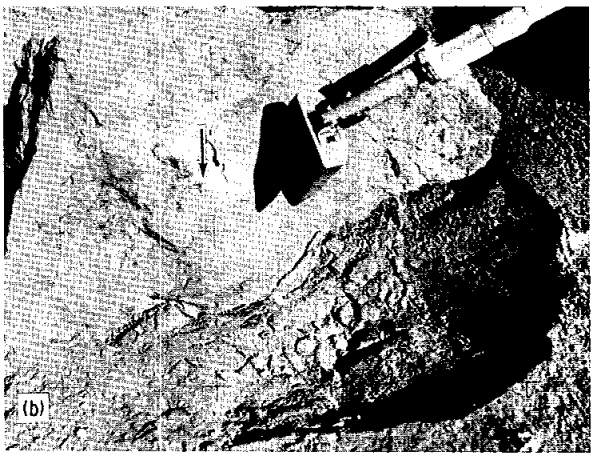


FIGURE 7-31.–Concluded. (b) Bottom of boulder (chip 69955) after the boulder was turned over. (See also fig. 7-19; the overall boulder geometry may be reconstructed from NASA photograph S-72-43793.)

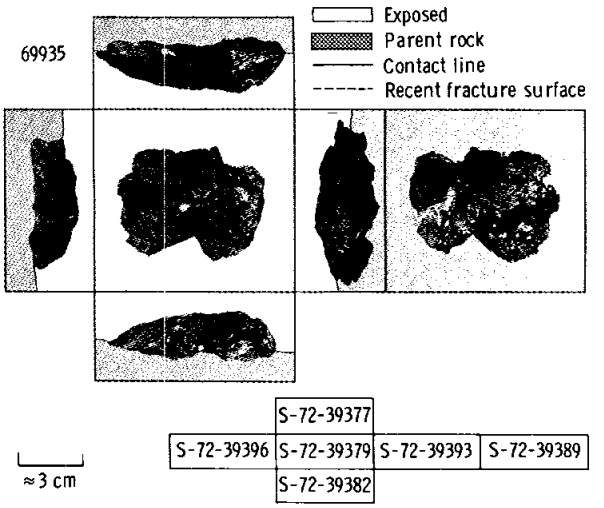


FIGURE 7-32.–Reconstruction of exposed and shielded surfaces of chip 69935. (The surface orientation is given in sec. 6 of this report.) (S-72-43128)

Unfortunately, a straightforward comparison of the two chips may be complicated because the individual chips differ drastically in their lithology. The top chip is a dense breccia, and the bottom chip is an anorthositic clast (figs. 7-32 to 7-34).

At station 10, a dense, tough breccia chip with a variety of clasts (60018) was taken from a breccia boulder approximately 40 cm in diameter in the vicinity of the LM (figs. 7-35 and 7-36). According to the crew, this boulder originated also from the South

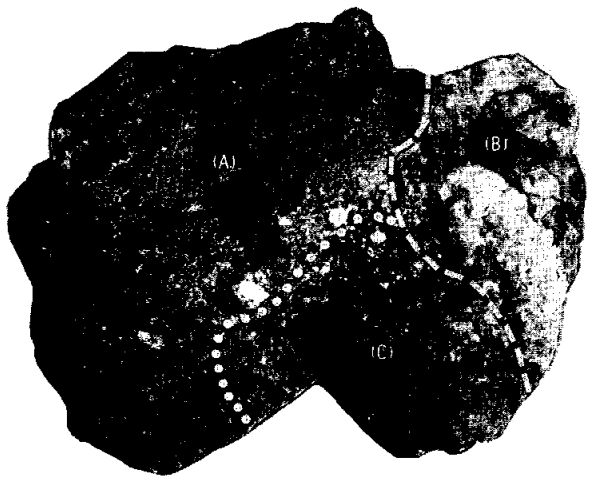


FIGURE 7-33.–Detailed microgeology of the top surface of chip 69935. Note the presence of rejuvenated surfaces (i.e., rocks of different exposure histories). The cratered surface (A) is densely and homogeneously covered with microcraters. The production surface (B) displays only few microcraters and was therefore generated more recently. The freshly broken surface (C) was very likely created by the hammering action of the crew; it is the most recent surface and contains no microcraters (S-72-44431).

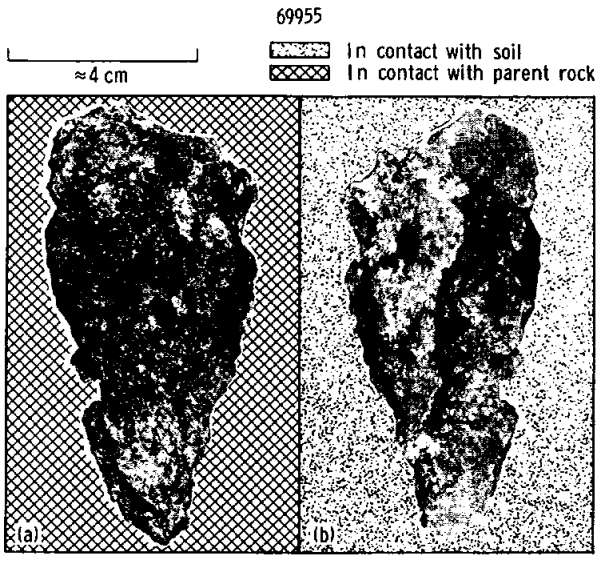


FIGURE 7-34.–Reconstruction of exterior and interior surfaces of chip 69955 (S-72-43130). This reconstruction is based on the presence or absence of a conspicuous soil cover on the exterior sides. However, none of the surfaces display microcraters, indicating that the parent boulder did not tumble and very likely was in the same position since it was ejected by the South Ray cratering event. (a) Interior (S-72-40124). (b) Exterior (S-72-40125).





FIGURE 7-35.–Parent boulder of breccia chip 60018 collected in the LM-ALSEP area (S-72-43788). (a) Boulder before chipping. (b) Boulder after chipping.

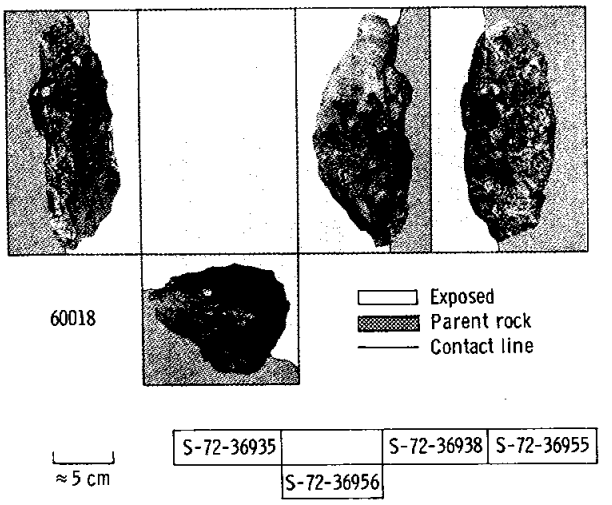


FIGURE 7-36.–Reconstruction of exposed and shielded sides of rock 60018. (The surface orientation is given in sec. 6 of this report.) (S-72-43123)

Ray cratering event, although admittedly with less certainty than the boulders that were sampled at stations 8 and 9.

Dating of North Ray Crater.–As was the case for South Ray Crater, numerous rocks were collected at the rim of North Ray Crater. However, because of the more advanced state of degradation, North Ray Crater is judged to be considerably older than South Ray. As a consequence, most of the hand specimens collected may have complicated surface histories, so that some of the exposure age techniques mentioned previously are not applicable because of saturation and exposure geometry difficulties. Again, the most suitable materials originate from very large boulders.

At station 11 (white boulders), two samples were dislodged from a white breccia boulder approximately 5 m long and 2 m high. (See sec. 6 of this report.) One of the samples (67455) represents the highly friable, feldspar-rich matrix. Because of its friable nature, it broke into several large pieces during transit, and the surface orientation cannot be reconstructed (fig. 7-37). The other sample (67475) is a dense, very fine-grained, isolated clast dislodged from the white boulder (fig. 7-38).

Also at station 11, a boulder approximately 5 by 2 by 2.5 m was next to the even larger House Rock (fig. 7-39). Although three different samples were taken, only one is highly suitable for attempting to date the North Ray cratering event. This chip is part of a very dense, feldspar-rich clast (67915, fig. 7-40). The other two areas sampled (67935, 67955) are within a freshly broken spall zone of an impact crater, the center of which resembles a percussion cone. The depth of the spall zone (i.e., the thickness

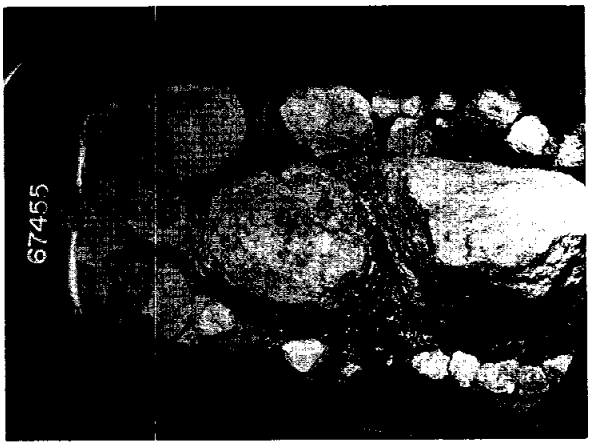


FIGURE 7-37.–Broken pieces of boulder chip 67455. The materials essentially represent the matrix of the white parent boulders. (See sec. 6 of this report.) Note the cube in the bottom of the tray to reconstruct orientation. Because of the highly abraded surfaces and a thick dust cover, no exposed surfaces could be identified with high confidence (S-72-38194).

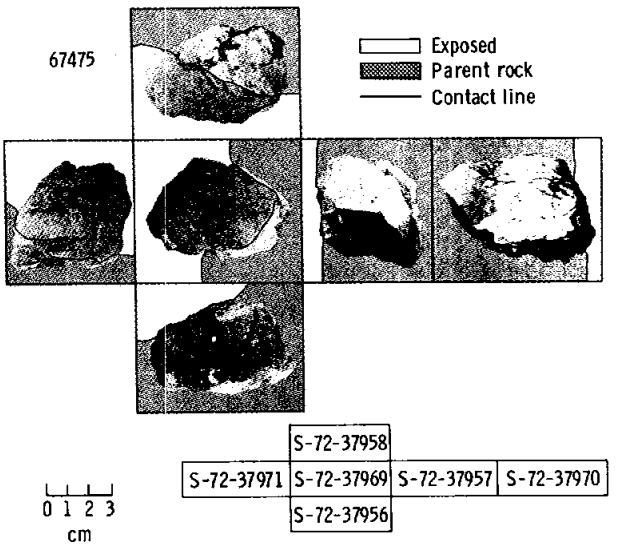


FIGURE 7-38.–Reconstruction of exposed and shielded sides of rock 67475. White areas represent the matrix of the parent boulder adhering to the clast (S-72-43133).

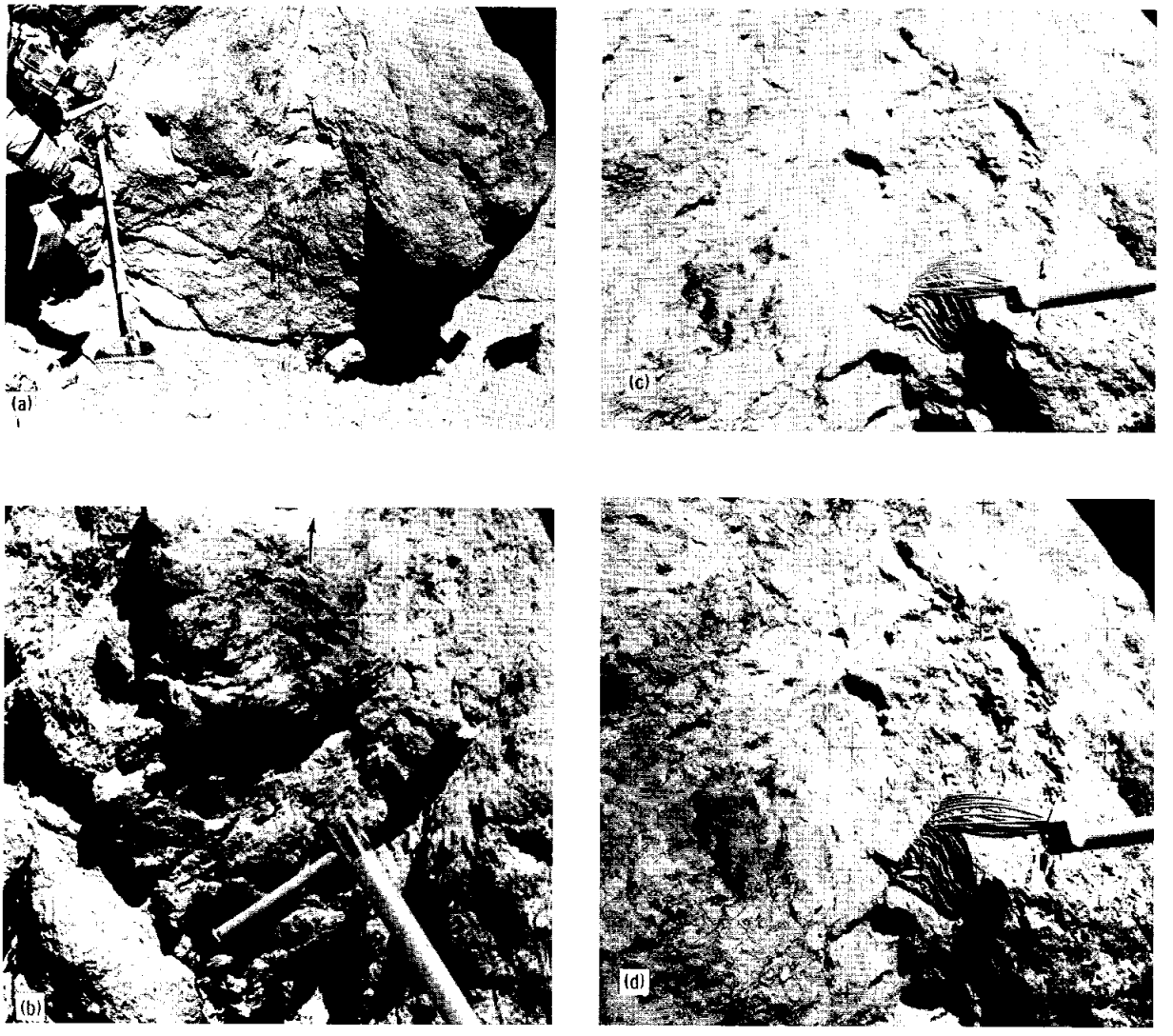


FIGURE 7-39.–Photographic documentation of samples collected on a 5-m boulder next to House Rock (S-72-43806). (a) Overall view of boulder. (b) Closeup view of area where rock 67915 was taken. (c) and (d) Closeup photographs of a recent impact event on a 5-m boulder. Details of the boulder and the impact event become more apparent if the photographs are available for stereoscopic viewing. Within the spall zone of this event, two additional samples (67935 and 67955) were collected. (For detailed sample location, see sec. 6 of this report.)

of the material removed) is approximately 2 to 3 cm. For the latter two samples, the only techniques that may still obtain useful information for the time of emplacement of the parent boulder may be a variety of noble gas studies. However, according to field evidence, there is the distinct possibility that the entire 5-m boulder may have been dislodged from the larger House Rock at an unknown time after the North Ray cratering event. Thus, the total exposure history and especially the geometry of the boulder cannot be established with great confidence.

At station 13 (Shadow Rock), a boulder approximately 6 by 5 by 3 m was encountered at about one crater diameter (approximately 800 m) away from the rim of North Ray Crater (fig. 7-41). Three different areas were chipped. (See sec. 6 of this report.) The samples obtained are all of the dense, dark-matrix, breccia type. All samples should be

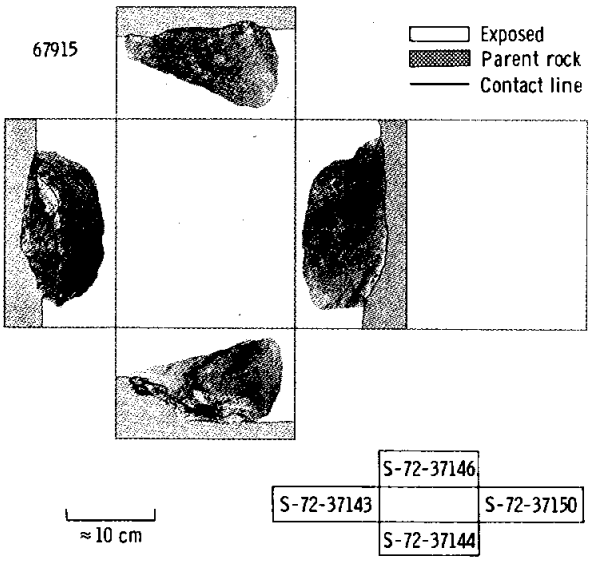


FIGURE 7-40.–Reconstruction of exposed and shielded sides of rock 67915. The exposed surfaces were oriented approximately vertically and were pointed approximately to the east (S-72-43803).

suitable for the crater dating studies, although sample 60017 is probably most suitable because of its large size (fig. 7-42). Because of the time line considerations, photographic documentation was kept at a minimum. Sample 63335 (fig. 7-43) consists of a number of small fragments; a reliable surface orientation of the individual pieces is not easily obtained.

Dating of Buster Crater.–Six rock samples weighing more than 25 g were collected on the rim of Buster Crater, notably samples 62235 (fig. 7-44) and 62295 (fig. 7-45). These samples can be associated with the Buster ejecta blanket with high confidence. On the basis of its diameter and state of preservation, Buster is probably a rather recent event. However, no information is available to establish the relative age compared to South Ray Crater. If the ages should differ significantly, valuable information about erosion and obliteration of 100- to 1000-m craters could be obtained and applied to other lunar terrains.

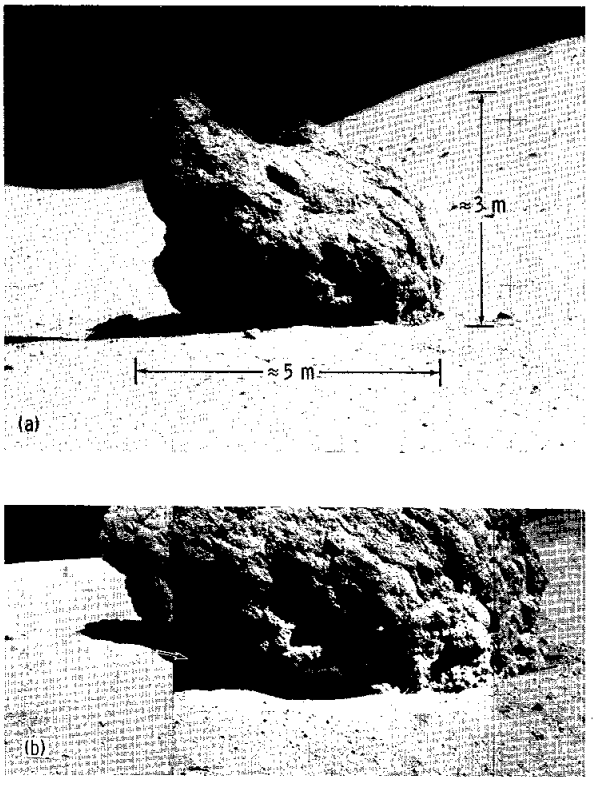


FIGURE 7-41.–General photography of Shadow Rock at station 13. (For general sample location, see sec. 6 of this report.) (a) Overall view of Shadow Rock; view approximately to the north. (b) Overall view of Shadow Rock; view approximately to the northwest. The "gopher hole" where the shadowed soil sample was taken is located at the left side of the boulder. (c) Closeup photograph of the area where samples 60017, 63335, and 63355 were collected. (For detailed sample location, see sec. 6 of this report.)

implantation of rare gases.

CSVC was immediately placed into another vacuum



container. The sample will be stored for an undetermined time under a nitrogen vacuum of approximately 10^{-4} torr. Because the history of this particular sample is known, spacecraft contamination can be excluded because the drive tube sample was collected 2.5 km from the LM and was protected by two vacuum seals. Contamination by the life support systems was minimized by taking samples from depth and placing them immediately into a specially sealed container.

Core Samples

Four double drive tubes and one 2.25-m drill core were taken at stations 4, 8, and 10′ and in the Apollo lunar surface experiments package (ALSEP) area (table 7-VII). A total length of approximately 480 cm of core materials was returned (excluding the CSVC). These cores were X-rayed shortly after they were unpacked; the following preliminary descriptions are based on the resulting X-radiographs.

In addition to providing documentation, X-radiographs have been successfully used on previous missions as a preliminary guide to stratigraphy and dissection. Changes in texture and structure, including grain size and shape, degree of packing, density, bedding types, and contacts, are clearly seen in the films. Particles with a metallic composition are readily detected because of their high X-ray absorption coefficient. By use of stereopairs, components can be located in three dimensions, and selective emphasis of coarse and X-ray opaque particles simplifies some aspects of interpretation. On the other hand, there are several limitations that should be kept in mind when the detailed core logs are read. Particles with a low X-ray absorption such as feldspars tend to be invisible; data on grain size distribution, sorting, and density are ambiguous, and the exact location of components may be uncertain because of parallax distortion. The X-radiographs of four double drive tubes are illustrated in figure 7-47.

Station 4.—The purpose of the double drive tube (64001, 64002), which was taken at station 4 at the highest elevation reached on Stone Mountain, was to recover typical Descartes material. Because of the omnipresence of South Ray ejecta material, however, the original objective may have not been attained. Nevertheless, the X-radiographs indicate a distinct change in grain size and an abundance of rock fragments and rock types at a depth of 51 cm. As a working hypothesis, this change is interpreted as a contact of South Ray ejecta (upper 51 cm) and underlying Descartes (?) material.

The stratigraphy described previously can be closely correlated with the penetrometer resistance taken from a penetrometer section adjacent to the drive tube site. As indicated in figure 7-48, the upper 11 cm of the core contains abundant rock fragments; penetration resistance, as indicated by stress, increases markedly. The next 3.5 cm is distinctly finer grained, and there is a correspondingly small increase in resistance. From 14.5 to 49 cm is a reverse-graded bed with an abundance of rock fragments at the top. Highest resistance in the penetrometer section was encountered in the upper part of the bed, where it appears that repeated pushes were necessary to overcome the resistance of the rocks in the interval. Stress then decreased to 49 cm, in correspondence to a decrease in grain size. From 49 to 51 cm in the drive tube is a thin rock layer; a thin zone of high resistance reflects the layer in the penetrometer. Stress again decreases with grain size to 58 cm, where the increase in soil density on the X-radiograph corresponds to an increase in penetrometer resistance.

Figure 7-47 illustrates seven different units in the drive tube from station 4. Unit 1 is at a depth of 58 to 70 cm and is 12 cm thick. The soil is characterized by angular to subangular opaques, coarser than the overlying layer. The matrix (70 percent of the unit) is relatively dense and contains approximately 2 percent opaque fragments as large as 5 mm in diameter (most 0.5 to 1.0 mm), but with only moderately good sorting. Most fragments are equant but notably angular to subangular, some with an irregular outline.

The framework (30 percent) contains approximately 5 percent semiopaque rock fragments with distinct outlines from 0.3 to 0.8 cm in diameter. Most are approximately 0.5 cm in diameter, with an irregular, equant, subangular outline. Twenty-five percent is composed of semiopaque rock fragments with indistinct mottled outlines as large as 1.0 cm in diameter, but most appear to be in the range of 0.5 cm. Fragments appear to be equant to slightly elongate and irregular in outline.

Unit 2 occurs at a depth of 51 to 58 cm and is 7 cm thick. It is the finest grained section in the core tube. The matrix (approximately 80 percent) is mostly very finely granular, with only 1 percent opaques, similar in appearance to those of unit 1.

TABLE 7-VII.–Preliminary Data on Apollo 16 Core Samples

Station	*LRL sample no.*	*Weight, g*	*Length, cm*	*Bulk density, g/cm³*	*Tube depth (pushed), cm*	*Total depth (pushed and driven), cm*	*Hammer blows, no.*	*Core recovery, percent*	*Return container*
4	[a]64002	584.1	31.7	[b]1.38 to 1.40	32.6 ± .5	[c]65 ± 6	⩾3	103 ± 10	[d]ALSRC 2
	64001	752.3	[e]33.9	1.66					[f]SCB 3
8	68002	583.5	27.4	1.59	17.8 ± .5	68.6 ± .5	~56	91	[d]ALSRC 2
	68001	840.7	[e]34.9	1.80					[f]SCB 3
9	69001	558.4	–	–	20.6 ± .5	[c]27.5 ± 2	8	–	CSVC[d]
10′	60014	570.3	[b]28.4 to 28.8	1.48	28 ± 2	70.5 ± 1	27	90 ± 1	[f]SCB 7
	60013	757.2	[e]34.7	1.63					[f]SCB 7
ALSEP area	[a]60010	635.3	32.3	1.47	17.9 ±.5	[c]71 ± 2	~53	95 ± 3	[d]ALSRC 2
	60009	759.8	[e]33.1	1.72					[d]ALSRC 2
ALSEP area (drill stem)	60007	105.7	22.2	1.46	Deep drill	223 ± 2	–	88 to 100	Core sample bag[f]
	60006	165.6	35.5 ± .5	1.43 ± .02					
	60005	76.1							
	60004	202.7	39.9	1.56					
	60003	215.5	39.9	1.66					
	60002	211.9	42.5	1.75					
	60001 (bit)	30.1							

[a]Crew neglected to insert the keeper.
[b]Corrected for void.
[c]Measured from kinescopes.
[d]In vacuum-sealed ALSRC 2 (i.e., not exposed to spacecraft environment).
[e]The nominal length of the sample in a lower core tube is 34.9 cm; for those tubes in which the actual sample length is less, either some sample fell out, or the keeper compressed the top of the sample. The former is considered the more likely explanation, and the densities have been calculated accordingly. The internal diameter of the core tubes is 4.13 cm.
[f]In open SCB's (i.e., exposed to spacecraft environment).

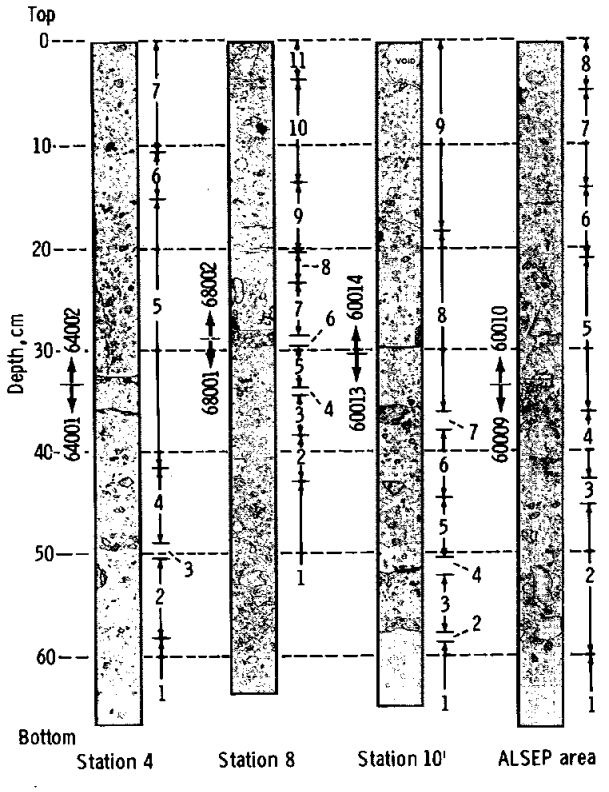


FIGURE 7-47.–Preliminary stratigraphy of the Apollo 16 double drive tubes, based on interpretation of X-radiographs. Depths may not correspond exactly to descriptions in text because of graphical adjustment (S-72-44433).

The framework (20 percent) is equally divided into rock fragments with distinct outlines and rock fragments with indistinct outlines. Ten percent is semiopaque with moderately indistinct outlines shaped as in unit 1, except that most are 0.3 to 0.8 mm in diameter. Ten percent is semiopaque rock fragments with indistinct irregular outlines and diameters as large as 1.1 mm. Most are 0.5 to 1.0 mm in diameter, equant, and scattered in indistinct layers at approximately 53 and 56 cm. At 54 cm is a partially void space surrounding a large elongate rock fragment. The void is interpreted as being created by disturbance of the rock fragment during sampling.

Unit 3 is at a depth of 49 to 51 cm and is 2 cm thick. The unit is characterized by abundant large rock fragments. The matrix occupies only 30 percent of this interval and is indistinctly granular, with 1 percent opaques as large as 0.8 mm in diameter. Most pieces are 0.3 to 0.5 mm in diameter with a fairly even size distribution, good sphericity, and rounding.

The framework (70 percent) is composed of densely packed fragments. Of these, 60 percent is semiopaque with moderately indistinct outlines. In contrast to the upper layers, rock fragments in this unit do not show distinct outlines throughout, but some are distinct and others vague. Rock fragments range from 0.3 to 1.6 cm in diameter, although most are between 0.5 and 1.1 cm and are elongate and irregular. Ten percent is composed of semiopaque fragments with vague outlines (clods) as in unit 2.

Unit 4 occurs at a depth of 42 to 49 cm and is 7 cm thick. It has the same types of components as unit 3, but with 75 percent matrix. Most of the matrix is uniformly fine grained, and 2 percent of the unit is opaque with fragments as large as 1.5 mm in diameter. Sorting and rounding occur as in unit 3.

Included in the scattered rock fragments of the framework (25 percent) are 15 percent semiopaque fragments with distinct outlines, similar to unit 3, except for the absence of elongate rock fragments. Ten percent is semiopaque with a vague outline, similar in appearance to unit 7.

Unit 5 is at a depth of 14.5 to 42 cm and is 27.5 cm thick. The unit is characterized by very abundant, large, varied rock fragments that form a tightly packed framework. The matrix (20 percent) is indistinctly granular, with 2 percent opaque fragments as large as 2.0 mm in diameter. Most are approximately 0.2 to 0.5 mm in diameter and are relatively poorly sorted. Most pieces are equant and well rounded.

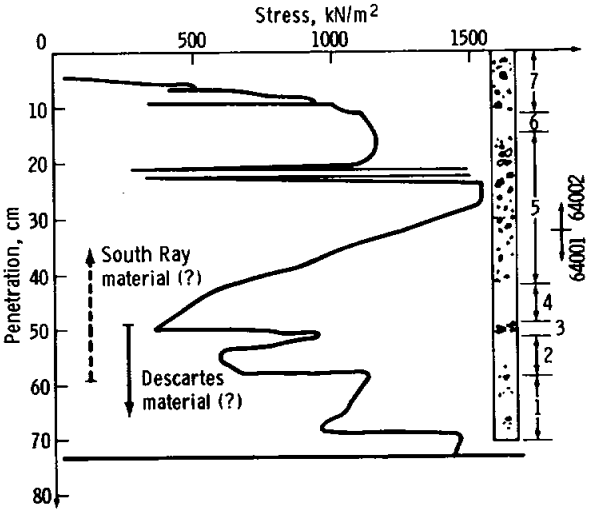


FIGURE 7-48.–Correlation of penetrometer resistance and stratigraphy of double drive tubes 64001 and 64002 (S-72-44428).

Of the framework (80 percent), 20 percent is semiopaque with a distinct outline. Most of these fragments are 0.5 to 1.0 cm in diameter but range up to 1.4 cm. Most fragments are equant, but approximately 5 percent (of the total rock) is distinctly elongate. Margins are straight and subangular. Sixty percent is semiopaque with a vague outline, similar in appearance to unit 7.

Unit 6 occurs at a depth of 11 to 14.5 cm and is 3.5 cm thick. The soil is finer grained than in unit 5, with fewer rock fragments. Seventy percent of the interval is indistinctly granular matrix, with 1 percent opaque fragments as large as 0.8 mm in diameter. Most are 0.3 to 0.8 mm in diameter and are well sorted and rounded.

The framework (30 percent) is semiopaque with a vague outline. The largest rock fragments are 0.8 cm in diameter, in contrast to unit 5. Most fragments are smaller than 0.5 cm and appear to have a more even size distribution than units 5 and 7.

Unit 7 is at a depth from the surface to 11 cm and is characterized by abundant, coarse rock fragments. Forty percent of the interval is finely granular matrix, which includes 2 percent opaque fragments smaller than 1.2 mm in diameter. Most fragments are between 0.5 and 1.0 mm and appear to be of an even size distribution (well sorted). Most are spherical and well rounded.

The remaining 60 percent is distributed among a moderately dense framework, of which 10 percent is semiopaque with sharp outlines. Lengths vary from 0.5 to 1.3 cm, but most are approximately 1.0 cm. The pieces are subangular with noticeably straight edges. Fifty percent is semiopaque with a vague outline. The size ranges from 0.1 to 1.2 cm, most between 0.3 and 0.5 cm. The soil has a clodlike appearance but is probably not made up of clods, which tend to be transparent to X-rays.

Station 8.–The double drive tube (68001, 68002) was taken at station 8 within a field of meter-sized boulders originating from South Ray Crater (fig. 7-49). As indicated in figure 7-49(b), the tubes were driven approximately 2 m from the edge of a 10- to 15-m crater that appears to be approximately 2 m deep. Small craters, less than 0.5 m, are common in the area. Stereopair examination of these photographs also reveals concentric ridges of coarser material, scalloped and lineated radially to the 10- to 15-m crater. This field configuration of the coarse and fine material suggests the presence of ejecta from the 10- to 15-m crater, some of which should be represented in the drive tube section.

Within the core, the upper 13.5 cm is notably coarse grained with diverse rock types. The upper 3 cm is highly fractured, possibly the effect of impact and generation of the small crater from which the sample was taken, or it is possibly an artifact.

Unit 8 is distinctive in that it has no rock fragments and a very low content of X-ray opaque material in the matrix. Beneath the finer grained units 8 and 9 is a bed with very coarse, abundant rock fragments that are notably lumpy, in contrast to the smooth-outlined rock fragments of other coarse-grained units. The coarse-grained unit 7 is underlain by finer grained layers (units 4, 5, and 6) with scattered rock fragments, soil fractures, and nodules. Opaques of the matrix in these beds are notably blocky and angular, in strong contrast to opaques of the other units in which there is a strong component of spherical opaques.

The lowest 22 cm of the core, unit 1 (possibly even more below the core), is very coarse grained and consists of a single graded bed with a great diversity of rock fragment shapes and densities. The top surface of this interval is gently undulating and may represent a buried topographic surface. Unit 1 is the most distinct unit in the core. By bringing together a diversity of larger rock fragments, this event is comparable to an action that may have deposited coarse-grained, lithologically diverse beds in other Apollo 16 core samples.

Figure 7-47 illustrates 11 units in the drive tube from station 8. Unit 1 is at a depth of 42.5 to 64 cm and is at least 21.5 cm thick. It is a coarse-grained unit with diverse rock types. The matrix (40 percent of the unit) is X-radiographically very dense and distinctly granular. Approximately 4 percent of the unit is composed of opaques, which range from the limit of resolution to 3.5 mm in diameter and appear to be very poorly sorted, with equal numbers of each size class. Approximately 80 percent of the matrix is equant; the remaining fragments are elongate and commonly comma shaped. Half the fragments are well rounded, and the others tend to be blocky and angular.

In the framework (60 percent of the unit), 25 percent is semiopaque material composed of rock fragments with distinct outlines 0.3 to 2.6 cm in length, with very poor sorting and many large fragments of more than 1 cm in diameter. These rock

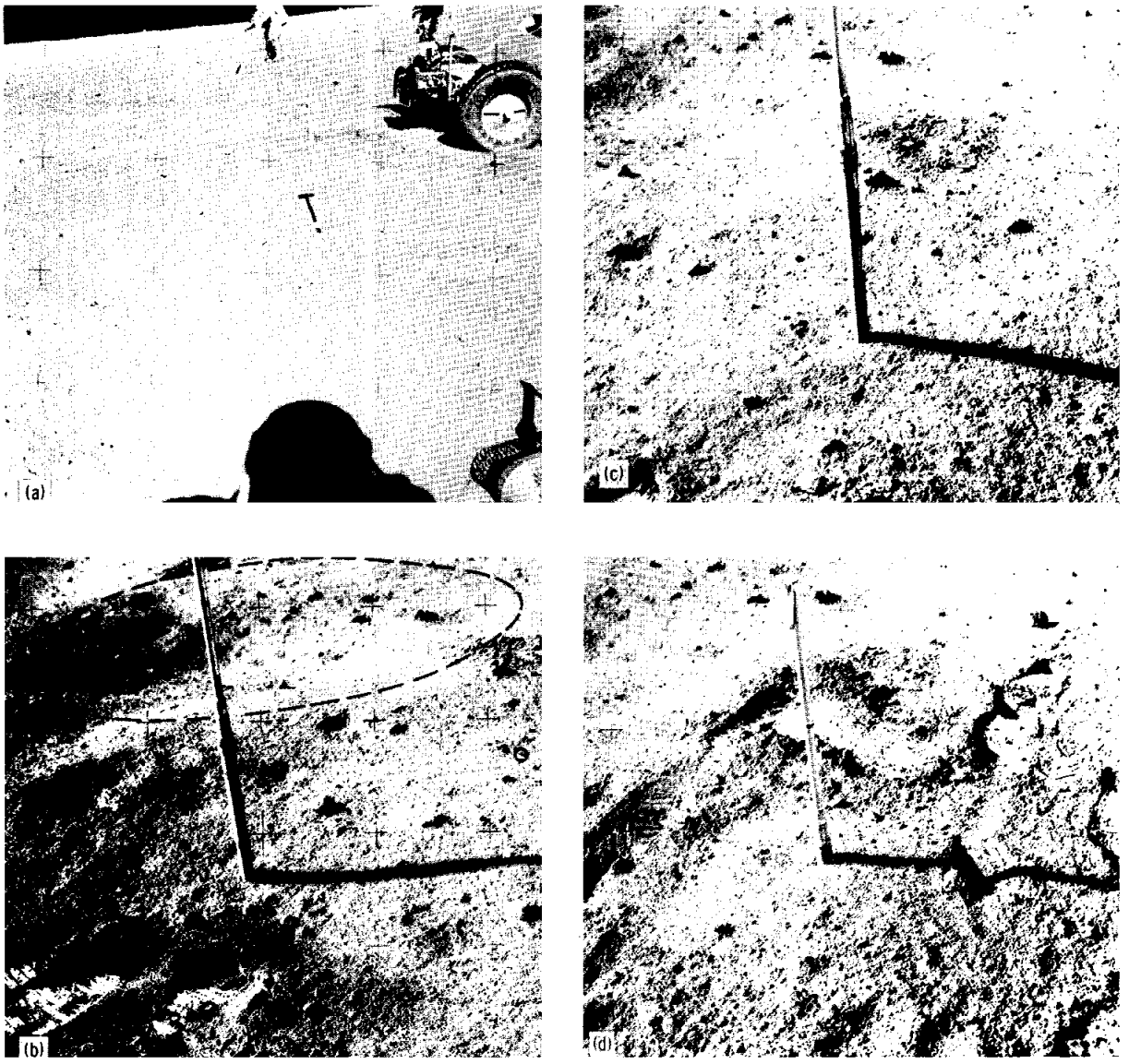


FIGURE 7-49.–Lunar surface photographic documentation of the double drive tube taken at station 8 (S-72-44434). (a) General location. (b) A first attempt to sink the double drive tube failed, and the sample was actually taken where indicated with a solid circle. Note the 10- to 15-m-sized crater in the vicinity of the sample location (dashed circle). (c) Second and successful attempt; drive tube halfway inserted. (d) Second attempt; drive tube completely inserted.

fragments tend to be equant to polygonal to wedge shaped with straight to slightly curved edges and angular to subangular corners. The remaining 35 percent is composed of semiopaque density concentrations with indistinct outlines, probably rock fragments. (Some particles may be soil clods, but clods tend to be more transparent to X-rays.) They are 0.1 to 2.0 cm; most are equant with lumpy outlines tending to rounded edges. Less than 5 percent of these semiopaque fragments is elongate; the elongate particles, however, tend to be ragged in outline with long horizontal axes and may be glass fragments.

Unit 2 occurs at a depth of 38 to 42.5 cm and is 4.5 cm thick. It is a thin bed with well-sorted small rock fragments and spherical opaques. As in unit 1, the matrix (70 percent of unit 2) is notably denser than the overlying unit 3 and has a much higher percentage of rounded spherical opaque fragments than unit 3, which contains mostly blocky angular fragments.

The framework (30 percent of the unit) is composed of semiopaque density concentrations with an indistinct outline. The size range is 0.1 to 0.5 cm, most 0.3 cm. The fragments are well sorted, equant to elongate (1:1.5) with long axes (where present, horizontal), and notably lumpy rounded edges. Lithologic units 1 and 2 form a continuous graded bed with a sharp upper contact marked by a gently undulating surface.

Unit 3 is at a depth of 34.5 to 38 cm and is 3.5 cm thick. The unit is a fine-grained bed with scattered rock fragments, which are blocky angular opaques. The matrix (80 percent) is distinctly less dense than unit 2, although the fragments are finely granular. This bed contains approximately 2 percent opaques as large as 1.5 mm in diameter. The soil is poorly sorted with a median size of approximately 0.7 mm; fragments are all equant and blocky with subangular to angular corners. Rounded and elongate particles are noticeably absent.

The framework (20 percent) is made of 5 percent semiopaque fragments with a distinct outline. Equant, blocky rock fragments are 0.2 to 0.6 cm in diameter; most are approximately 0.2 cm with relatively straight sides and subangular corners. The remaining 15 percent is semiopaque material with vague outlines and diameters of 0.1 to 0.8 cm. Most fragments are approximately 0.3 cm in diameter and are very indistinctly equant and lumpy to rounded.

Unit 4 occurs at a depth of 34 to 34.5 cm and is 0.5 cm thick. This unit is a fractured zone, which is like unit 3 in composition but is penetrated by numerous en echelon crescentic fractures as long as 8 mm and 1 mm across.

Unit 5 is at a depth of 29.5 to 34 cm and is 4.5 cm thick. It is a fine-grained bed with scattered rock fragments, which are blocky angular opaques. The matrix (80 percent) is finely granular with approximately 3 percent opaque material, ranging from the limit of resolution to 2.5 mm in diameter. The fragments are poorly sorted, with the median size approximately 0.8 mm. Fragments are equant to blocky with only approximately 10 percent spherical and 5 percent elongate to comma shaped and irregular. The rest is blocky with subangular to angular corners.

In the framework (20 percent), 10 percent is composed of semiopaque rock fragments with distinct outlines. The diameters range from 0.2 to 0.5 cm. Fragments are equant to elongate, rectangular to wedge shaped, with relatively straight edges and subangular to subrounded corners. The remaining 10 percent is semiopaque with indistinct outlines and diameters from 0.1 to 0.4 cm. Most fragments are approximately 0.3 cm, equant, and lumpy in outline.

Unit 6 occurs at a depth of 28 to 29.5 cm and is 1.5 cm thick. The unit is a fractured zone at the top of the core. The matrix (40 percent) is distinctly less dense than the underlying layers, principally because of void space, but it is also noticeably less finely granular. Approximately 4 percent is opaque material with a diameter of 0.1 to 2.1 mm. Most pieces are 0.6 to 0.8 mm, principally equant to teardrop shaped, with blocky outlines and angular to subangular corners.

The framework (60 percent) is composed of semiopaque density concentrations with irregular outlines. Fragments range from 0.2 to 1.3 cm in diameter and are poorly sorted with equant lumpy outlines. Internal fractures in some of these fragments could be a result of disturbance during sampling and handling.

Unit 7 is at a depth of 23.5 to 28 cm and is 4.5 cm thick. It is a coarse-grained bed with abundant rock fragments. The matrix (30 percent) is distinctly and irregularly granular to finely lumpy. The opaques (3 to 4 percent) range from the limit of resolution to 1.5 mm in diameter. Most are approximately 1.0 mm and tend to be equant and blocky with only a few elongate, comma-shaped particles. Approximately 10 percent of the opaque material shows rounding, and the rest is angular.

In the framework (70 percent), 40 percent is semiopaque rock fragments with distinct outlines and lengths of 0.2 to 2.3 cm. They are poorly sorted, equant to rod shaped, with irregularly lumpy edges and subrounded corners. These lumpy rock fragments contrast strongly with rock fragments of some other intervals, with noticeably straight sides. The large elongate fragment at a depth of 25 cm has a long axis parallel to the tube, is associated with some cracking and void space, and appears to have been rotated to

this configuration during sampling. The remaining 30 percent is semiopaque with indistinct outlines, probably rock fragments. The size ranges from 0.1 to 1.3 cm in diameter, although most pieces are approximately 1.5 mm and are moderately poorly sorted. Most fragments are equant and irregularly lumpy.

Unit 8 occurs at a depth of 20.5 to 23.5 cm and is 3 cm thick. The unit is a fine-grained bed with sparse mottles. The matrix (75 percent) is distinctly finely to very finely granular. Approximately 1 percent is composed of opaques as large as 0.9 mm in diameter. It is moderately well sorted, with most particles approximately 0.5 mm, equigranular, and subangular to subrounded.

The framework (25 percent) is composed of semitransparent density concentrations with indistinct outlines. They are possibly rock fragments 0.1 to 0.9 cm in diameter and are poorly sorted. All sizes are present in equal abundances; most are equant to subequant with lumpy nodular outlines. More appear to be mottles than rock fragments. The contact between units 7 and 8 is abrupt but indistinct.

Unit 9 is at a depth of 13.5 to 20.5 cm and is 7 cm thick. The soil is a fine-grained unit with sparse rock fragments. The matrix (85 percent) is definitely finely granular, with 3 percent made up of opaques as large as 1.5 mm in diameter. Most are between 0.5 to 1.0 mm and are only moderately sorted. Of the opaques, 80 percent is equant, most rounded and spherical, although approximately 10 percent is blocky. The remaining 20 percent of the opaque material is ovoid or rod or comma shaped with well-rounded corners.

In the framework (15 percent), 10 percent is composed of semiopaque rock fragments with distinct outlines, 0.3- to 0.5-cm diameters, ovoid to equant to polyhedral shapes, straight margins, and rounded to subrounded corners. There is a thin layer of these rock fragments at a depth of 16 cm. The remaining 5 percent is semiopaque, probably rock fragments with indistinct outlines and diameters of 0.2 to 0.8 cm. They are poorly sorted with an equal size distribution throughout, an equigranular lumpy to nodular appearance, and rounded to subrounded corners, where visible. A fractured zone marks the contact between units 8 and 9.

Unit 10 occurs at a depth of 3.5 to 13.5 cm and is 10 cm thick. The unit is a coarse-grained bed with diverse rock types. The matrix (50 percent) is distinctly finely granular, with 3 percent opaque material, ranging from the limit of resolution to 1.6 mm in diameter. Most pieces are 0.5 to 1.0 mm and are only moderately well sorted. As in unit 9, nearly all fragments are equant and spherical, with a small but distinct component of blocky, ovoid, rod- or comma-shaped particles.

Within the framework (50 percent), 5 percent is opaque. One large fragment (at an approximate depth of 8 cm) is 1.2 cm in diameter; it is equant with jagged, angular protuberances on all sides. Twenty percent is composed of semiopaque rock fragments with distinct outlines and diameters from 0.1 to 1.3 cm. They are poorly sorted with all sizes equally represented. Rock fragments are mostly elongate to polygonal with some equant particles; a few elongate fragments have smooth edges and angular corners, and the remaining pieces have irregular to lumpy margins and are angular to subangular. The remaining 25 percent is semiopaque with indistinct outlines, and diameters range from 0.1 to 1.2 cm. This segment is moderately poorly sorted as are the fragments with distinct outlines, but these particles have very irregular, subrounded lumpy outlines (where visible).

Unit 11 is at a depth from the surface to 3.5 cm. This fractured interval has abundant rock fragments. The matrix (40 percent) is not very dense, probably because of the void space. The fragments are finely granular, with approximately 4 percent opaque material, ranging from the limit of resolution to 1.5 mm in diameter. Most fragments are 0.5 to 0.7 mm and are moderately poorly sorted. Approximately half are spherical, and half are lumpy and subangular.

The framework is 60 percent of unit 11. One large fragment occupies 30 percent of the unit; it is 2.7 cm in diameter, an equidimensional block, subrhomboidal in outline, with moderately irregular margins and angular corners. The remaining 30 percent is composed of semiopaques with vague outlines and 0.2- to 0.5-cm diameters. The soil is well sorted, mostly equigranular and lumpy, reminiscent of lumps of cotton. The entire interval appears to be somewhat fractured and has much void space. This is probably a sampling artifact, but the core was collected from the center of a small crater, and fracturing could also be a result of the crater.

Station 10′.—Drive tubes 60013 and 60014 were taken at station 10′ in the vicinity of the LM. (See sec. 6 of this report.) In comparison to the other Apollo 16 core samples, the soils are relatively fine

grained. The surface material is relatively coarse grained; 50- to 20-cm-diameter blocks are moderately abundant. Furthermore, the area is unusual in that there are few small craters, even though there are some large (10 to 20 m) craters.

The basal 8 cm of the core section appears to be fine grained in figure 7-47. (However, it may contain an abundance of whitish aggregates as noted by the lunar module pilot on the Moon. If so, the whitish aggregates would not show on the X-radiograph because of the low X-ray absorption.) The basal 8 cm has sparse opaques and a few percent of rock fragments. The rock fragments that are present appear as indistinct mottled clusters. Unit 2 shows a concentration of similar fragments, but with a matrix similar to unit 1, and probably is genetically akin to unit 1.

The next 22.5 cm is relatively coarse grained and relatively thinly laminated and terminates at the top in a very noticeable surface. The intermediate bedded zones are more or less transitional, distinguished on the basis of grain size and type.

Units 3 and 5 are similar in that they contain a dense matrix with a fair scattering of equant, sharp-edged rock fragments. Unit 4 seems to contain a mixture of properties of the lower beds, because the matrix of the basal units and the rock fragments is characteristic of unit 3. Furthermore, opaques in the matrix of unit 4 are bimodal; coarse particles occur as in unit 3, and fines resemble those of unit 1. Unit 6 seems to be similar to unit 5 but is better sorted. Unit 7 exhibits the matrix properties of units 5 and 6 but is distinctly coarser grained.

The uppermost 36 cm is much more massively layered, with a less grainy and less compact matrix. There is a noticeable component of oval, 2- to 4-mm matrix opaques and ragged-edge-appearing semi-opaque density concentrations that probably represent a rock type not found in lower intervals.

Units 1 and 2 may represent fine-grained Cayley Formation. Units 3 to 7 are physically similar and are believed to represent variations on one major event, presumably ejecta from a major nearby crater (possibly North Ray). The upper massive zone differs physically from the lower zones, indicating a different source, and its massiveness suggests less reworking by small-scale cratering events as a result of newness. On the basis of this evidence, it is inferred that this zone resulted from South Ray activity.

Figure 7-47 illustrates the nine units in the drive tube core sample taken at station 10′. Unit 1 occurs at a depth of 59 to 67 cm and is 8 cm thick. The unit is a fine-grained interval with sparse opaques and indistinct mottles. The matrix (95 percent) is X-radiographically dense and medium to finely granular. Approximately 1 percent is composed of opaque material from 0.3 to 1.0 mm in diameter, averaging approximately 0.6 mm, with good sorting. The fragments are consistently equant, somewhat irregular and subrounded to subangular, with only a trace of spherical particles.

The coarse fraction (5 percent) is semitransparent with indistinct outlines and diameters of 0.2 to 1.6 cm, most approximately 0.6 cm. The fragments are equant, fading out over broad areas or in well-rounded curves, which is distinctly different from the lumpy particles that commonly occur in the Apollo 16 core samples.

Unit 2 is at a depth of 58 to 59 cm and is 1 cm thick. The unit is a layer of small rock fragments, and 50 percent of it forms the matrix, which is similar in appearance to unit 1.

The framework (50 percent) is semiopaque rock fragments with distinct outlines and diameters from 0.2 to 0.6 cm and a median diameter of approximately 0.4 to 0.5 cm, indicating good sorting. Rock fragments are equidimensional or polyhedral to slightly elongate with relatively straight margins and subangular to subrounded corners. This lamina may be a micrometeoritically winnowed concentration of coarse particles at the top of unit 1, because matrix and rock types are similar, and opaques and semi-opaques at the top of the interval are alined horizontally.

Unit 3 occurs at a depth of 53 to 58 cm and is 5 cm thick. It is fine grained with a dense matrix, sparse rock fragments, and varied opaques. The matrix (85 percent) is finely, irregularly (not uniformly) granular and moderately dense, with 3 percent opaques, ranging from the limit of resolution to 7 mm. The average size is approximately 1 mm. More than half are equant and angularly lumpy to dendritic, only one-tenth are spherical, and one-third are elongate to rod shaped with smooth edges and rounded corners (not angular).

In the coarse fraction (15 percent), 5 percent is composed of semiopaque rock fragments with distinct outlines and 0.2- to 0.8-cm diameters, moderately to poorly sorted, with a relatively even

distribution throughout the size ranges. These rock fragments are equant to rectangular, with trapezoidal or polyhedral outlines, relatively smooth edges, and angular to subangular corners. The remaining 10 percent is semitransparent, with indistinct outlines and diameters from 0.1 to 0.4 cm, and is moderately well sorted. The average size is approximately 0.3 cm. The overall effect is of elongate particles or clumps of equant lumps disposed into elongate rock fragments.

Unit 4 is at a depth of 50.5 to 53 cm and is 2.5 cm thick. It is a fine-grained unit with a thin matrix and bimodal opaques. The matrix (80 percent) is less dense than underlying layers, is finely granular, with 2 percent opaques ranging from the limit of resolution to 1.8 mm in diameter, and is noticeably bimodal. Most fragments are well sorted and approximately 0.4 mm in diameter; the remaining pieces are 1.3 to 1.8 mm in diameter. The finest grained opaques are equant and rounded to subrounded and blocky; coarser fragments are equant and lumpy to shardlike.

The coarse fraction (20 percent) is semitransparent rock fragments with moderately distinct outlines and 0.2- to 0.5-cm diameters. They are fairly well sorted, equant to polygonal with subrounded to subangular corners; sides are slightly curved to straight, not irregularly rounded or lumpy. Fragments are scattered through the matrix and do not form a framework.

Unit 5 occurs at a depth of 44.5 to 50.5 cm and is 6 cm thick. The unit is a zone with large rock fragments and angular opaques. The matrix (40 percent) is denser than underlying layers and is medium to finely granular; 2 percent is opaque material, ranging from the limit of resolution to 1.7 mm, averaging 0.5 mm, and is moderately to poorly sorted. The shapes of the fragments are as follows: 10 percent spherical; 5 percent shards; and the remainder equant to slightly elongate, blocky to lumpy, with subrounded to subangular corners.

In the framework (60 percent), 20 percent is semiopaque rock fragments with distinct outlines and 0.2- to 2.3-cm diameters. The material is poorly sorted, with all sizes about equally represented. Fragments are blocky and equant, with straight to slightly curved (some possibly conchoidal) edges and angular to subangular corners. The remaining 40 percent is semiopaque to semitransparent, with indistinct outlines. Sizes range from 0.1 to 1.3 cm, with most fragments approximately 0.3 cm in diameter. The pieces are moderately well sorted and have a lumpy to nodular appearance with many elongate particles composed of multiple aggregates.

Unit 6 is at a depth of 38.5 to 44.5 cm and is 6 cm thick. It is a fine-grained interval with abundant granule-sized fragments. The matrix (60 percent) is moderately dense in appearance, with the density noticeably increasing toward the top of the interval, and is medium to finely granular. Approximately 3 percent is opaque material, ranging from the limit of resolution to 1.8 mm; the average grain size is approximately 0.5 mm. The matrix is moderately poorly sorted, with approximately 10 percent spherical fragments, 10 percent angular fragments, and the remaining fragments equant to slightly elongate, and blocky and subangular to lumpy and subrounded.

Within the framework (40 percent), 10 percent is composed of semiopaque rock fragments that are well sorted and have distinct outlines and 0.2- to 0.5-cm diameters, most approximately 0.4 cm. Fragments are polygonal with relatively straight to slightly curved sides and subangular corners. The remaining 30 percent is semitransparent with indistinct outlines and diameters of 0.1 to 0.5 cm, most approximately 0.3 cm. Equant or elongate objects are composed of clumps of equant particles, which results in a lumpy texture.

Unit 7 occurs at a depth of 36.5 to 38.5 cm and is 2 cm thick. It is a concentration of centimeter-sized rock fragments. The matrix (30 percent) is moderately dense and medium to finely granular, with approximately 2 percent opaque material, ranging from the limit of resolution to 1.8 mm. The fragments are generally coarse but are bimodal with one mode approximately 0.3 mm. The other fragments are 1.2 to 1.8 mm, equant to slightly elongate with 50 percent of the particles ovoid to spherical, 25 percent lumpy to equigranular, 15 percent elongate and smooth sided, and 10 percent angular. The matrix of this zone is much denser than the matrix of the overlying unit.

In the framework (70 percent), 50 percent is semiopaque rock fragments with distinct outlines and diameters from 0.2 to 1.0 cm, most approximately 0.7 to 0.8 cm. They are well sorted and blocky to irregular, with straight to slightly curved sides. Some edges look conchoidal and angular to subangular. The remaining 20 percent is semitransparent and well sorted and have indistinct outlines and diameters of

0.1 to 0.4 cm, with a median diameter of approximately 0.2 cm. Fragments appear as equant density concentrations or are arranged into elongate lumps as composites of individual particles.

Unit 8 is at a depth of 18.5 to 38.5 cm and is 20 cm thick. It is a massive fine-grained unit with sparse rock fragments. The matrix (70 percent) is thin (not dense) and finely granular; 3 percent of it is opaque material, ranging from the limit of resolution to 2.2 mm, and is poorly sorted, averaging approximately 0.5 mm. About one-third of the particles are spherical, about one-fourth are elongate to dendritic, and the remaining fragments are blocky to lumpy and tend to be equant with subangular to subrounded corners.

In the framework (30 percent), 10 percent is composed of semiopaque rock fragments with distinct outlines and 0.2- to 1.1-cm diameters. Most are coarse, with the median size approximately 0.8 cm. Rock fragments in this zone differ from other horizons because they are noticeably elongate and irregularly rectangular to wedge shaped with slightly irregular edges and subangular corners. The remaining 20 percent is semiopaque with indistinct outlines and 0.1- to 1.1-cm diameters. The median size in the lower part of the bed is approximately 0.3 cm, gradually increasing to approximately 0.6 cm at the top of the bed. Particles appear as density concentrations, tending to be equant and nodular to lumpy where individual particles coalesce.

Unit 9 occurs at a depth from the surface to 18.5 cm. It is a massive fine-grained unit with sparse equant rock fragments. The matrix (60 percent) is light appearing, not densely granular, medium to finely granular, with 3 percent opaque material ranging from the limit of resolution to 3 mm in diameter. The matrix is characterized by bimodal distribution. The coarser fragments are 2 to 3 mm in diameter and are elongate, dendritic, or shard shaped. The finer fragments, all of which are smaller than 1 mm (most 0.6 mm), tend to be equant with about one-third spherical, one-tenth elongate and dendritic, and the rest blocky to lumpy and equant with subangular corners.

Within the framework (40 percent), 15 percent is semiopaque rock fragments with distinct outlines and 0.1- to 0.9-cm diameters; the median size is approximately 0.5 cm. These rock fragments are equant, most with a lumpy to rounded to irregular outline and only a few with relatively straight margins and subangular corners. Many are concentrated in an indistinct layer at a depth of 12 cm. The remaining 25 percent is semitransparent with indistinct outlines and 0.1- to 0.8-cm diameters, most approximately 0.2 to 0.3 cm, is moderately well sorted, and is composed of density concentrations that give the appearance of compound lumps.

ALSEP area.—The double core tube samples (60009, 60010) were taken on the eastern margin of a 50- to 60-cm, shallow, subdued crater in the ALSEP area, which was approximately 100 m southwest of the LM. Although the core was taken on the rim of a crater, it appears that there is no visible ejecta from the crater and that the surface of the area is covered with relatively fine-grained material, including fines, granule-size fragments, and other rocks, none larger than a few centimeters (fig. 7-50).

The basal unit of the core, 8 cm thick, is noticeably finer grained than any other interval in the section and consists of 80 percent matrix. Within the matrix, opaques (approximately 1 percent) are less abundant than in the rest of the core, and the coarse fraction consists of indistinct mottles. In contrast, unit 2 is extremely coarse grained and has abundant large rock fragments, a greater percentage of opaques (2 percent) than the underlying unit, and anomalous sorting between the coarse rock fragments and the mottles and opaques. Interestingly enough, the matrix of unit 2 (60 percent) is unusually high for a coarse-grained unit, and there is a size gradation of the coarse material that becomes finer grained in the upper units. Unit 3 seems to be largely a repetition of unit 1, with a small percentage of rock fragments. Correspondingly, unit 4 appears to be a fine-grained repetition of unit 2, with a lesser abundance of very coarse material. At the top of unit 4 is the most distinctive stratigraphic break in the section, which consists of a gently rolling, slightly irregular surface, emphasized by the density contrast between the matrix of units 4 and 5.

The matrix of unit 5 and all overlying units is much less densely compacted than that of the underlying beds and contains a higher percentage of opaques, which tend to be finer grained but less well sorted than does the underlying interval. Some of the opaques are relatively large ovoid objects. Units 5 and 6 form a massive bed, graded normally, from coarse at the bottom to fine at the top. Additionally, rock fragments with distinct outlines in X-radiographs are much more abundant at the base of the bed and

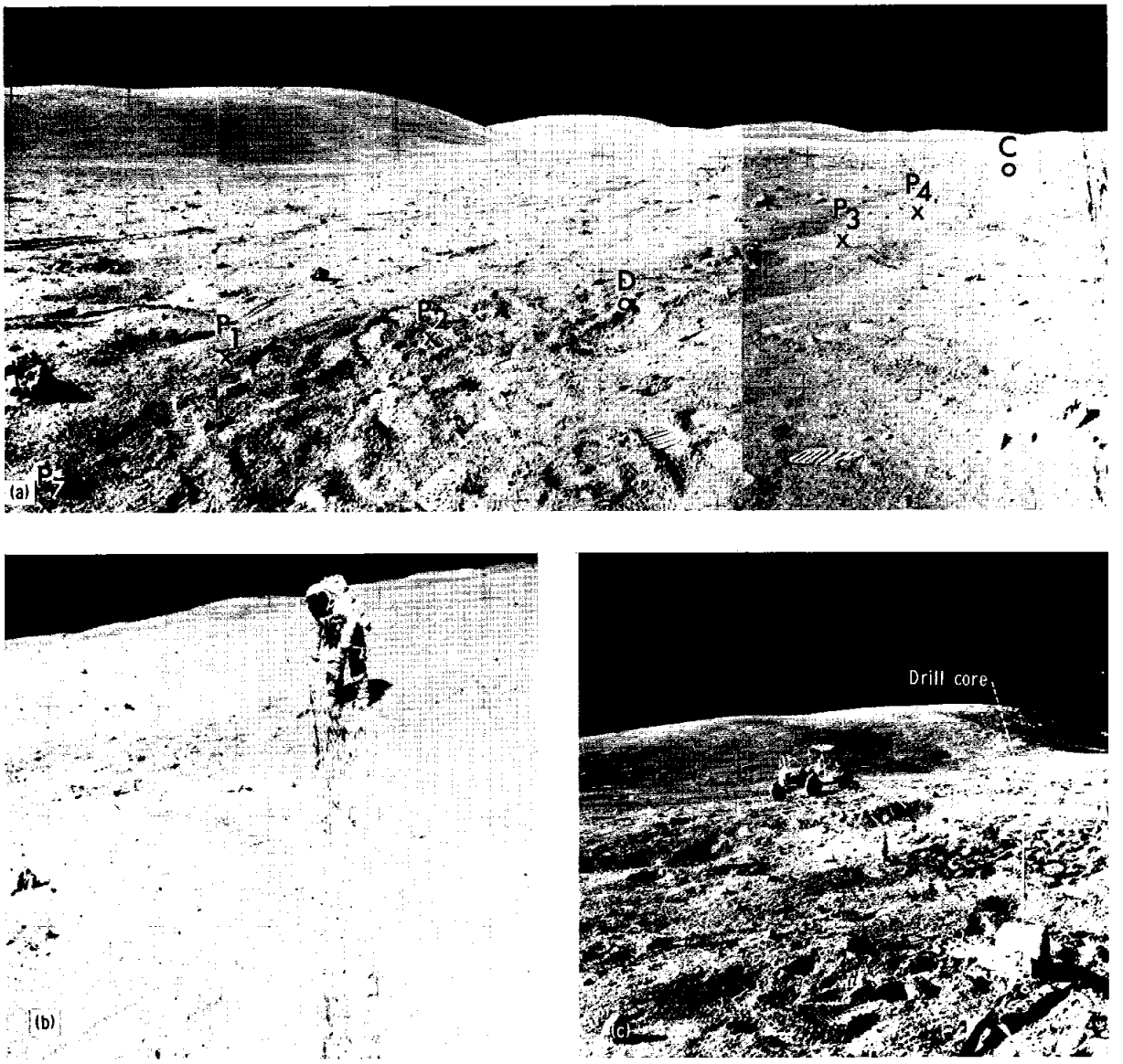


FIGURE 7-50.–Lunar surface photographic documentation of the deep drill core, double drive tubes 60009 and 60010, and penetrometer tests in the ALSEP area (S-72-44435). (a) General location (C, drill core; D, drive tube; P, penetrometer tests). (b) General view of the drive tube location. (c) General view of the drill core location, shown by the circle at the right.

disappear toward the top, where they are replaced by material with indistinct outlines. There is an indistinct density break at the top of units 5 and 6, and unit 7 is similar in nearly all respects to unit 5.

Unit 8, as unit 2, is classified as a pebbly mudstone and has a relatively low percentage of variable, poorly sorted, but coarse rock fragments. This surficial unit penetrates the highest point on the rim of a small crater, and the 5 cm of material probably represents ejecta from the crater.

Figure 7-47 illustrates eight units in the drive tube core sample taken from the ALSEP area. Unit 1 occurs at a depth of 60 to 68 cm and is 8 cm thick. It is a fine-grained unit, sparse in opaques. The matrix (80 percent) is indistinctly granular and is made up of less than 1 percent opaque material, ranging from the

limit of resolution to 1.5 mm in diameter. The soil is poorly sorted, equigranular, and generally subrounded.

In the framework (20 percent), 5 percent is composed of semiopaque rock fragments with distinct outlines and diameters of 0.2 to 0.6 cm. They are blocky, equant, and subangular to angular. The remaining 15 percent is semiopaque density concentrations with indistinct outlines and 0.1- to 0.4-cm diameters. They are moderately well sorted and equidimensional to slightly elongate with lumpy outlines.

Unit 2 is at a depth of 45.5 to 60 cm and is 14.5 cm thick. The unit is a pebbly mudstone with angular opaques. The matrix (60 percent, which is unusually high for an interval with this degree of coarseness) is finely granular, with approximately 2 percent opaque material ranging from the limit of resolution to 2.5 mm. They are moderately well sorted and coarse, with an average grain size of approximately 0.9 mm. Approximately 90 percent of the fragments are equant and spherical to lumpy and subrounded; only approximately 10 percent are elongate, although many elongate fragments are sharply angular.

In the framework (40 percent), 30 percent is composed of semiopaque rock fragments with distinct outlines and 0.1- to 3.3-cm diameters. Most rocks are relatively coarse and range from 0.5 to 1.5 cm in diameter, but show a poor degree of sorting. Most rock fragments are slightly to moderately elongate (1:1.5 to 1:2.5) and polygonal to blocky, with straight to slightly curved edges and angular corners. Distribution of these particles indicates matrix rather than framework support, which is relatively uncommon in Apollo 16 core samples. The remaining 10 percent is semiopaque with indistinct outlines, and diameters range from 0.5 to 0.8 cm, averaging approximately 0.3 cm. The fragments are fairly well sorted and equant with lumpy outlines. Sorting of these particles is comparable to that of the opaques and seems to be very different from that of the distinct rock fragments.

Unit 3 occurs at a depth of 43 to 45.5 cm and is 2.5 cm thick. It is a fine-grained interval with sparse rock fragments. The matrix (75 percent) is very finely granular with 1 percent opaque material, ranging from the limit of resolution to 1.2 mm. The opaques are relatively coarse grained, average approximately 0.8 mm in diameter, are equant, and are spherical to subrounded and blocky. The angular opaque component is notably absent in this thin bed.

The framework (25 percent) is semiopaque with indistinct outlines and 0.1- to 0.8-cm diameters. Most pieces are approximately 0.3 to 0.4 cm and are moderately well sorted. Within the framework, 80 percent of the fragments have a lumpy outline, but the other pieces are notably dendritic to fragmental in appearance with ragged outlines.

Unit 4 is at a depth of 36.5 to 43 cm and is 6.5 cm thick. The unit is a pebbly bed with small rock fragments and dendritic opaques. The matrix (60 percent) is very finely granular and noticeably more dense than the overlying unit, with approximately 3 percent opaque material, ranging from the limit of resolution to 3.5 mm in diameter. The average size is 0.8 to 1.2 mm, and fragments are moderately poorly sorted. About half the opaque fragments are spherical to slightly elongate; the others are lumpy to elongate, many showing a dendritic outline.

Within the framework (40 percent), 15 percent is composed of semiopaque rock fragments with a distinct outline. The size is 0.1 to 1.1 cm, averaging approximately 0.6 cm. The soil is moderately well sorted, especially in the two layers at the top of the interval. Fragments are nearly all elongate and wedge shaped to polygonal, with straight to slightly curved margins and angular to subangular corners. The remaining fragments (25 percent) are semiopaque with vague outlines with 0.1- to 1.3-cm diameters, and most are equidimensional to slightly elongate and distinctly lumpy.

Unit 5 occurs at a depth of 21.5 to 36.5 cm and is 15 cm thick. It is a coarse-grained, loosely compacted zone with fine-grained opaques. The matrix (35 percent) is notably less dense than the underlying or overlying beds. Of this segment, 3 percent is opaque, ranging from the limit of resolution to 1.2 mm in diameter, but is noticeably much finer grained than are the underlying beds. The average size is approximately 0.5 mm. Approximately 30 percent of the opaque material tends to be spherical, about half of the fragments are blocky to lumpy and subangular, and the remaining material is elongate and comma shaped to dendritic.

The framework (65 percent) is similar compositionally to unit 2 but is distinctly more tightly packed and appears to have a framework-supported

texture in notable contrast to the matrix-supported texture of unit 2. Within the framework, 40 percent is composed of semiopaque rock fragments with distinct outlines and 0.1- to 2.4-cm diameters. The average size is approximately 0.7 cm but with poor sorting. Most of the rock fragments are slightly to moderately elongate (1:1.5 to 1:2.5) and blocky to polygonal to wedge shaped, with straight to slightly curved edges and angular corners. The remaining 25 percent of the framework is composed of semiopaque density concentrations with indistinct outlines. The fragments are 0.1 to 0.6 cm in diameter, most approximately 0.3 cm, and are moderately well sorted. Density concentrations appear as nodular fragments with no ragged fragments.

Unit 6 is at a depth of 14.5 to 21.5 cm and is 7 cm thick. The unit is a coarse-grained, dense zone. This interval is gradationally transitional with unit 5, and is separated arbitrarily at the highest occurrence of rock fragments larger than 1 cm. The matrix (35 percent) is finely granular, dense in X-radiographs, and transitional to the underlying unit. Approximately 3 percent is opaque, ranging in size from the limit of resolution to 1.2 mm in diameter, averaging approximately 0.5 mm. The shape distribution is about equal among spherical particles, lumpy to blocky and subangular particles, and elongate to dendritic material.

Within the framework (65 percent), 25 percent is semiopaque with a distinct outline. The size ranges from 0.1 to 0.8 cm in diameter, averaging approximately 0.4 cm. The fragments are moderately well sorted, equant to slightly elongate, with straight to slightly curved outlines. About one-third have irregular scalloped outlines, but all fragments are angular to subangular. The remaining 40 percent of the framework is semiopaque with indistinct outlines and diameters from 0.1 to 0.7 cm, most approximately 0.2 cm. The soil is moderately well sorted and equant or in clumps of equant particles with irregular outlines.

Unit 7 occurs at a depth of 5 to 14.5 cm and is 9.5 cm thick. This loosely compacted zone has a moderate number of rock fragments and abundant opaques. The matrix (50 percent) is loosely compacted, less dense than the underlying bed, and very finely granular. In the matrix, 4 percent is opaque material, ranging from the limit of resolution to 3.5 cm in diameter, and is poorly sorted, with a median diameter of approximately 0.5 mm. One-fourth of the opaque fragments are spherical, about half are equant to slightly elongate and notably lumpy to subangular, and the others are elongate to comma shaped but not dendritic.

In the framework (50 percent), 15 percent is composed of semiopaque rock fragments with distinct outlines and 0.1- to 0.8-cm diameters, most approximately 0.4 to 0.5 cm, and is moderately well sorted. Most rock fragments are equant to only slightly elongate, with a tendency to irregularly jagged, subrounded to subangular outlines with angular sharp corners. The remaining 35 percent is semiopaque with indistinct outlines and diameters of 0.1 to 0.5 cm, most in the 0.2-cm range, and is moderately well sorted. As in unit 8, these particles appear as equant individual particles or lumpy concentrations of particles, fading to nothingness as subrounded particles.

Unit 8 is at a depth from the surface to 5 cm. The unit is a fine-grained interval with scattered rocks. The matrix (70 percent) is very finely granular and thin. Approximately 4 percent of this matrix is opaque material, ranging from the limit of resolution to 2.5 mm, and is moderately well sorted with most particles approximately 0.5 mm in diameter. About one-third are spherical, one-half are equant and lumpy subangular, and the remaining fragments are elongate and comma shaped to notably dendritic.

In the framework (30 percent), 25 percent is composed of rock fragments with distinct outlines and 0.2- to 1.7-cm diameters. The soil is poorly sorted and equant to slightly elongate with straight to slightly curved margins and angular corners, which is noticeably different from the lumpy rocks below. The remaining 5 percent of the fragments are density concentrations with vague outlines and 0.1- to 0.3-cm diameters, but most are approximately 0.2 cm and are well sorted.

ALSEP area, deep drill core.—The deep drill stem (60001 to 60007) was taken approximately 175 m southwest of the LM and 25 m south of the ALSEP site in a generally flat spot in an area of rolling topography with numerous 2- to 6-m craters and relatively loose, uncompacted soil. Two other core samples and soil from seven penetrometer stations were taken within 100 m of the drill stem (fig. 7-50), which enables the most detailed correlation and reconstruction of lunar soil strata to date.

The upper section (60007) and the bit (60001) have been dissected and described; other information

discussed in this section is based on X-radiographs (fig. 7-51). The surficial 15.7 cm of the drill stem is relatively fine grained, contains an abundance of glass, and has been subdivided into four subunits. Of these, the uppermost 2 cm is relatively dark and crumbly and is underlain by a 3.5-cm zone that is high in whitish aggregates. Indistinct massive bedding characterizes the next 10 cm, with a rock concentration at 10.5 cm marking a break in bedding. The massive zone tends to be poorly sorted and contains a coarse fraction dominated by glass fragments, droplets, and feldspar fragments. The lowest 6.4 cm of section 60007 is reverse graded and coarse grained and contains a diversity of rock fragment types. The X-radiographs indicate that the coarse material at the base of section 60007 continues into section 60006 into the regolith for a total of approximately 50 cm. Bedding is thicker and more massive toward the top of this coarse-grained interval, but there are more large semiopaque rock fragments in the thinner beds at the base of the zone. As explained in the next paragraph, section 60005, with 76.1 g of sample, was only one-third full, and section 60006 was partially void. On the basis of density calculations, it is estimated that these two core tubes would contain approximately 50 cm of actual section in an undisturbed condition. The basal sections of the drill stem are fine grained in comparison to the upper sections. The top 11 cm of section 60004 is very fine grained, followed by 25 cm of lumpy coarse material with a few distinct rock fragments. The basal 85 cm of the drill string is fine grained with a rock layer only in the middle of section 60003 at a depth of approximately 135 cm below the lunar surface.

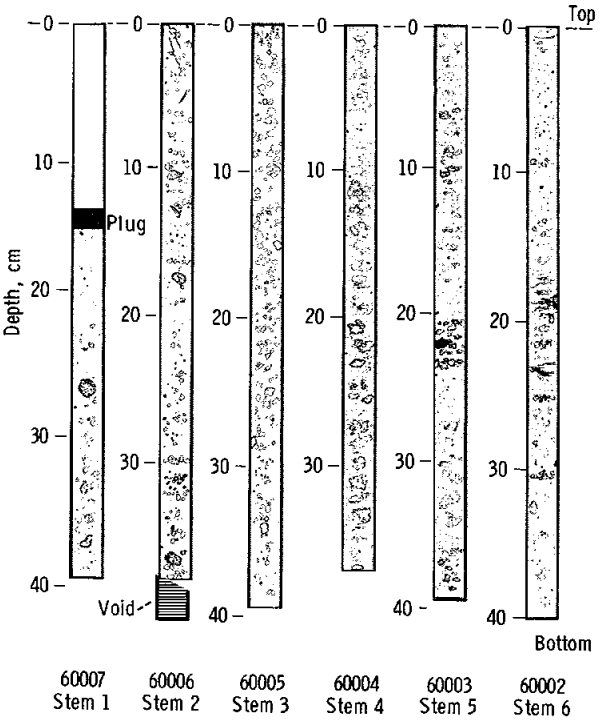


FIGURE 7-51.—Survey of X-radiographs of the Apollo 16 deep drill core. The zero level of each stem is arbitrarily set at the top of the sample surface within each core. Because of parallax distortion, dissection is necessary before absolute depths of individual strata can be given (S-72-44432).

The absolute depth of soil materials from the deep drill core, however, cannot be given with confidence at present, because the core was not filled completely. The drill was separated on the lunar surface into two sections of three stems each, the lower one also containing the drill bit. The X-radiographs indicate that the lower section (60001 to 60004) is completely filled. However, the bottom segment (60005) of the upper section (60005 to 60007) contains only 76 g of material distributed along the entire length of the stem in an obviously highly disturbed condition; the bottom 5 cm of the middle stem (60006) is empty, and the top (60007) is half full.

To date, three hypotheses have been proposed to explain the condition of the deep drill core sample. The first possibility is that the drill core was not completely filled initially, which left a space at the top into which the contents of the upper section could slip sometime later. The second hypothesis is that sampling was complete but material was lost from the bottom of the upper section when the two halves were separated on the lunar surface. Thirdly, there could have been complete sampling, but some material dropped from the base of the core when it was extracted from the lunar surface.

Because the crew noted the loss of only a few grams of material (at the most) during the separation and capping operations, the second hypothesis is unlikely. The third hypothesis is also unlikely, because the heat flow rammer-jammer, which was dropped into the open drill core hole after the drill operations, indicated the hole was clear to within a few centimeters of full depth. Consequently, the first hypothesis is presently considered to be the most likely explanation. Even so, determination of the

original depth of a given sample must await correction for density changes that occurred both during and after drilling.

Comparison of Drive Tubes With Deep Drill Stem Samples

The three cores in the ALSEP area were taken at the apexes of an isosceles triangle. Drive tubes 60013 and 60014 were taken 95 m due north of the drill stem; and drive tubes 60009 and 60010 were taken at the eastern apex of the two 60-m legs of the triangle. Despite irregularities of the lunar surface, it was possible to correlate major units between the cores.

Basal units of all three core sections are fine grained in X-radiographs, with 80 to 95 percent matrix (much higher than in overlying units) and a very low percentage of opaques. What opaques there are tend to be relatively large (average diameter, approximately 0.6 mm) and equant and have a high percentage of spherical particles.

Overlying the basal fines is a coarse-grained interval 55, 59, and approximately 50 cm thick in drive tubes 60009 and 60010, 60013 and 60014, and the drill stem, respectively. In each core, the coarse interval can be further subdivided into a basal thin-bedded portion and an upper massive portion. The basal zone contains an abundance of large semiopaque blocky rock fragments with distinctly straight to conchoidally curved margins and angular to subangular corners; the interval also tends to have a relatively dense matrix with a significant percentage of shardlike opaques. The interval, which is 20 to 25 cm thick, comprises units 2 to 4 in drive tube 60009, units 2 to 7 in drive tube 60013, and units 39 to 44 in drill stem section 60006.

In the drive tubes, the upper units (approximately 35 cm thick) tend to be more massive and have a matrix that tends to be less compacted and less dense appearing. In all core samples, these upper massive units contain finer, more poorly sorted opaques with a distinctive trace percentage of large oval fragments. Additionally, rock fragments in this upper interval show a lumpy to ragged outline, in contrast to mottled or distinctly outlined rock fragments of lower zones.

Relatively fine-grained, poorly sorted surficial soils may or may not be present, depending on the core tube site. Surficial soils are thickest in the drill stem, intermediate in drive tubes 60009 and 60010, and absent in drive tubes 60013 and 60014.

Because major units reflect principal events of the area, it may be hypothesized that the coarse-grained units in the cores represent North Ray and South Ray ejecta. The lower coarse-grained unit is believed to be North Ray ejecta, and the thinner layering is a result of microscale and small-scale meteoritic reworking of the ejecta blanket. The less compact, more massive upper units are assigned to the more recent, and presumably less reworked, South Ray event. Accordingly, the basal fine-grained soil in all cores may represent the regolith before the North Ray cratering event.

Major horizons between the drill stem and drive tubes 60009 and 60010 were further correlated with the aid of soil from the penetrometer sections (fig. 7-52). In each penetration, a hard zone was encountered at approximately 8 to 15 cm below the surface, corresponding to an increase in rock fragments and soil density in the drill stem and the drive tube 60009 and 60010 section. Below the hard zones is a soft finer grained interval with maximum development at penetrometer station 4. The next lower zone is harder to penetrate because it contains more rock fragments and is underlain by a bed which halts penetration, probably an indication of the lowest rock-bearing unit in the core samples.

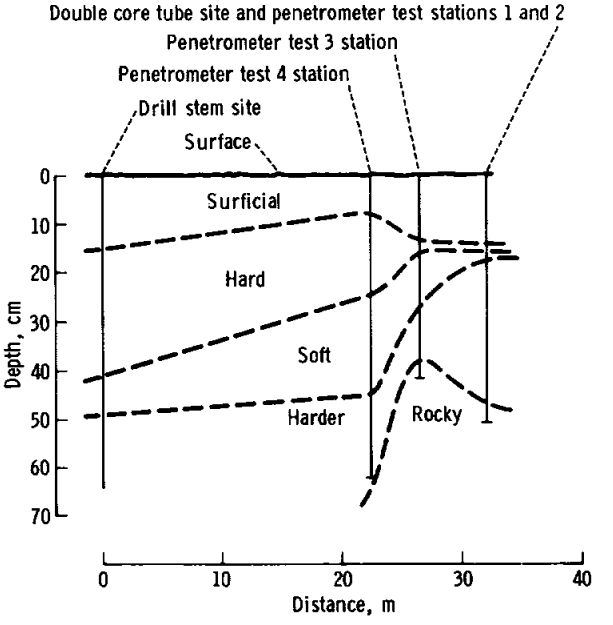


FIGURE 7-52.–Lateral extent of stratigraphic units in the ALSEP area as indicated by the stratigraphy of drive tubes 60009 and 60010, the deep drill core, and penetrometer resistance (S-72-44429).

PART C

CAUSE OF SECONDARY MAGNETIZATION IN LUNAR SAMPLES

G. W. Pearce[a] and D. W. Strangway[b]

Introduction

All lunar samples that have been measured by various investigators (refs. 7-15 to 7-18) carry a natural remanent magnetization (NRM). This NRM is quite variable in its characteristics from sample to sample, although it is generally found to be a combination of two distinct components: a soft component unstable to alternating field demagnetization (AFD), and a hard component stable to AFD. In addition, many samples show a time-dependent effect.

The stable component is considered by most investigators to be of lunar origin. It is stable to AFD to 400 Oe, to temperatures of 750° C, and for times on the order of millions of years (ref. 7-19). This important component of the NRM is carried by single-domain-sized metallic iron grains and grains small enough to have only a few magnetic domains (i.e., grains with diameters from approximately 150 to 1000 Å).[1]

The unstable component can be eliminated by subjecting the sample to AFD in small fields of 20 to 50 Oe. It is much like an isothermal remanent magnetization (IRM) such as that induced by exposing the sample to steady fields of 10 to 50 Oe for a short time (ref. 7-20). Such fields might be produced by a permanent magnet, a coil, or a wire carrying direct current. For example, if the sample should be within a few inches of a wire carrying 10 A or more, such fields would be present. Because the field of a wire decreases linearly with distance from a wire carrying a current, a surge of 100 A would have a strong effect on a sample even a foot or more away. It is probable that there are many times that samples could experience such fields on their journey back from the Moon. This experiment was performed to test this probability.

The time-dependent or viscous remanent magnetization (VRM) is, in its more usual form, a strong magnetization that can be acquired in quite weak fields (a few oersteds) and that decays completely in approximately 8 hr if the sample is stored in a place with no magnetic field. This form of VRM is carried by very small particles (diameters of approximately 150 Å) that are thermally unstable at room temperature (ref. 7-21).

Although all samples have been found to contain a stable component of NRM, the VRM component is found mainly in fragmental rock samples. The soft component has been found in igneous and fragmental samples from the Apollo 12, 14, 15, and 16 missions. The most complete documentation of the soft component is of the Apollo 12 samples: information on eight igneous rocks and one breccia is available.

All three containers used for returning the Apollo 12 samples (the two Apollo lunar sample return containers and the Surveyor bag) contained samples that had a soft component of magnetization. Because there is no one container that does not show the effect, it is difficult to determine the source of the field. It is also difficult to simulate fully the environment that the samples experience between collection on the Moon and delivery to the investigator.

Experiment

On the Apollo 16 mission, a tracer sample was returned to the Moon to be brought back with the Apollo 16 samples. The tracer chosen was a chip from Apollo 12 igneous rock 12002, which had a soft component after its original trip but had no VRM component (fig. 7-53). The chip was demagnetized to 400 Oe, leaving only the stable magnetization. It was then delivered inside the spacecraft in a μ-metal box and unpacked and installed approximately 30 hr

[a]University of Toronto; Lunar Science Institute.

[b]NASA Manned Spacecraft Center.

[1]Gose, W. A.; Pearce, G. W.; Strangway, D. W.; and Larson, E. E.: On the Applicability of Lunar Breccias for Paleomagnetic Interpretations. To be published in The Moon.

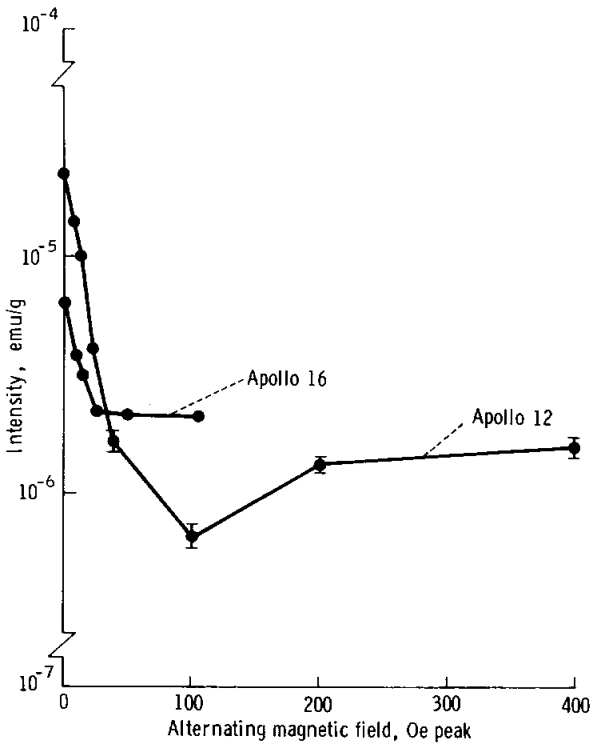


FIGURE 7-53.–Intensity of magnetization of sample 12002,78 as a function of AFD field after the Apollo 12 and 16 missions.

before launch. Because samples normally do not make the outbound trip, it would have been more appropriate to keep the sample in the μ-metal box to protect it from magnetic fields until after lunar landing. However, as this would have been a difficult procedure, the location of the sample in the spacecraft was chosen to be similar on the outbound and inbound trips. During the outbound trip, the chip was in the lunar module ascent stage; during the return trip, it was transferred to the command module with the other lunar samples.

The stowage location was quite similar to that of the Surveyor bag on the Apollo 12 spacecraft. The sample, inside a small Beta cloth bag, was attached to the flap of the interim stowage assembly (ISA), a bag of the type in which samples were returned on the Apollo 14, 15, and 16 missions. At recovery of the Apollo 16 command module, the sample was detached from the ISA and returned to the Manned Spacecraft Center (MSC) in one of the padded crates used for lunar samples. On arrival at MSC, the sample was taken to the magnetic properties laboratory at the Lunar Receiving Laboratory, where the NRM of the sample was measured several times during a period of 4 days. During this time, it was stored in a field-free room. No significant change occurred in the NRM during this storage test. Next, the sample was demagnetized by the AFD technique in steps to 100 Oe (fig. 7-53). It was possible to eliminate the soft, acquired component in the sample in an alternating field of 20 Oe. At this point, the direction and intensity of magnetization were approximately the same as they were in the sample before it left the Earth (fig. 7-54). In figure 7-55, the intensity of the stable component (2×10^{-6} emu/g) has been subtracted from the NRM so that the magnetization added by the Apollo 16 trip can be more easily compared with that of the tests described in the following discussion. The component added by the Apollo 16 trip is very similar in behavior to the original soft component of this rock when it first came back from the Moon. The intensity of the soft component was somewhat less than that found after the first (Apollo 12) trip.

In an attempt to simulate the soft component, a series of IRM's was induced in the sample by using steady fields of 10, 12, 15, 20, and 40 Oe for a period of 1 min each. This magnetization was then cleaned by the AFD technique. These demagnetization curves are compared with the curves of the original Apollo 12 NRM soft component and the Apollo 16 trip-added component in figure 7-55. The IRM curves are

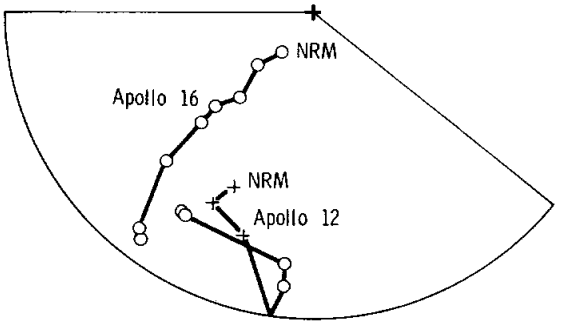


FIGURE 7-54.–Stereographic projection of the direction of magnetization of sample 12002,78 during AFD after the Apollo 12 and 16 missions. Lines connect points representing consecutive degrees of demagnetization. Crosses represent downward-dipping directions and circles upward-dipping directions.

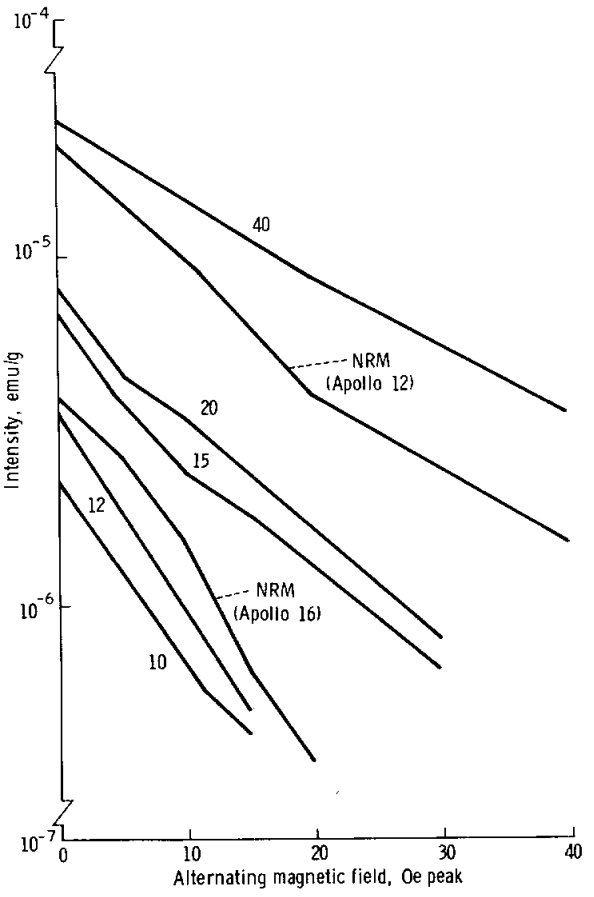


FIGURE 7-55.–Demagnetization curves for sample 12002,78 after return from the Apollo 12 and 16 missions and after exposure to fields of 10, 12, 15, 20, and 40 Oe. Numbers on curves represent magnetizing field intensities in oersteds.

similar to the curve of the trip-added magnetization. Thus, the trip-added magnetization is well simulated by an IRM that is induced by exposure to a steady field of 12 to 15 Oe applied for 1 min, and to simulate the original NRM would require exposure of the sample to 30- to 35-Oe fields.

Conclusions

During the return of lunar samples to Earth, at least some samples are subjected to magnetic fields of some tens of oersteds. These fields are capable of inducing in these samples a magnetization that can easily be removed upon AFD in relatively low fields (50 Oe or less). This magnetization is similar in behavior and intensity to the soft component of magnetization found in many lunar samples; therefore, the soft component is at least in part, if not totally, an artifact of the trip.

Acknowledgments

This experiment was conducted on short notice, and we thank the many people who helped the sample on its way.

REFERENCES

7-1. Papanastassiou, D. A.; and Wasserburg, G. J.: Lunar Chronology and Evolution From Rb-Sr Studies of Apollo 11 and 12 Samples. Earth Planet. Sci. Letters, vol. 11, Aug. 1971, pp. 37-62.

7-2. Wasserburg, G. J.; and Papanastassiou, D. A.: Age of an Apollo 15 Mare Basalt; Lunar Crust and Mantle Evolution. Earth Planet. Sci. Letters, vol. 13, no. 1, Dec. 1971, pp. 97-104.

7-3. Murthy, V. R.; Evensen, N. M.; Jahn, B.; and Coscio, M. R., Jr.: Rubidium-Strontium and Potassium-Argon Age of Lunar Sample 15555. Science, vol. 175, no. 4020, Jan. 28, 1972, pp. 419-420.

7-4. Turner, Grenville: ^{40}Ar-^{39}Ar Ages From the Lunar Maria. Earth Planet. Sci. Letters, vol. 11, Aug. 1971, pp. 169-191.

7-5. Hartmann, William K.: Lunar Cratering Chronology. Icarus, vol. 13, no. 2, Sept. 1970, pp. 299-301.

7-6. Trask, N. J.; and McCauley, J. F.: Differentiation and Volcanism in the Lunar Highlands. Earth Planet. Sci. Letters, vol. 14, Mar. 1972, pp. 201-206.

7-7. Milton, D. J.; and Hodges, C. A.: Geologic Maps of the Descartes Region of the Moon, Apollo 16 Pre-Mission Map. U.S. Geol. Survey Misc. Geol. Inv. Map I-748, sheets 1 and 2, 1972.

7-8. Wilhelms, D. E.; and McCauley, J. F.: Geologic Map of the Near Side of the Moon. U.S. Geol. Survey Misc. Geol. Inv. Map I-703, 1971.

7-9. Apollo 15 Preliminary Examination Team: The Apollo 15 Lunar Samples: A Preliminary Description. Science, vol. 175, no. 4020, Jan. 28, 1972, pp. 363-374.

7-10. Hubbard, N. J.; Rhodes, J. M.; Gast, P. W.; Bansal, B. M.; Wiesmann, H.; and Church, S. E.: Nonmare Basalts: Part II. Proceedings of the Third Lunar Science Conference, vol. 2, Dieter Heymann, ed., MIT Press (Cambridge, Mass.), 1972.

7-11. The Lunar Sample Preliminary Examination Team: Preliminary Examination of Lunar Samples From Apollo 12. Science, vol. 167, no. 3923, Mar. 6, 1970, pp. 1325-1339.

7-12. The Lunar Sample Preliminary Examination Team: Preliminary Examination of Lunar Samples From Apollo 14. Science, vol. 173, no. 3998, Aug. 20, 1971, pp. 681-693.

7-13. Moore, C. B.; Gibson, E. K.; Larimer, J. W.; Lewis, C. F.; and Nichiporuk, W.: Total Carbon and Nitrogen Abundances in Apollo 11 Lunar Samples and Selected Achondrites and Basalts. Proceedings of the Second Lunar Science Conference, vol. 2, A. A. Levinson, ed., Pergamon Press (New York), 1970, pp. 1375-1382.

7-14. Wahl, Walter: The Brecciated Stony Meteorites and Meteorites Containing Foreign Fragments. Geochim. Cosmochim. Acta, vol. 2, 1952, pp. 91-117.

7-15. Strangway, D. W.; Pearce, G. W.; Gose, W. A.; and Timme, R. W.: Remanent Magnetization of Lunar Samples. Earth Planet. Sci. Letters, vol. 13, no. 1, Dec. 1971, pp. 43-52.

7-16. Hargraves, R. B.; and Dorety, N: Magnetic Property Measurements on Several Apollo 14 Rock Samples. Lunar Science-III, Carolyn Watkins, ed. (Rev. abs. of the Third Lunar Science Conference (Houston, Tex.), Jan. 10-13, 1972), pp. 357-359.

7-17. Runcorn, S. K.; Collinson, D. W.; O'Reilly, W.; and Stephenson, A.: Magnetic Properties of Lunar Rocks and Fines. Lunar Science-III, Carolyn Watkins, ed. (Rev. abs. of the Third Lunar Science Conference (Houston, Tex.), Jan. 10-13, 1972), pp. 669-671.

7-18. Nagata, T.; Fisher, R. M.; and Schwerer, F. C.: Lunar Rock Magnetism. The Moon, vol. 4, nos. 1/2, Apr. 1972, pp. 160-186.

7-19. Pearce, G. W.; Strangway, D. W.; and Gose, W. A.: Remanent Magnetization of the Lunar Surface. Proceedings of the Third Lunar Science Conference, vol. 3, David R. Criswell, ed., MIT Press (Cambridge, Mass.), 1972.

7-20. Nagata, Takeshi: Rock Magnetism. Maruzen Co. (Tokyo), 1961.

7-21. Neel, L.: Theorie du Trainage Magnetique des Ferromagnetiques en Grains Fin Avec Application aux Terres Cuites. Ann. Geophysique, vol. 5, 1949, pp. 99-136.

8. Soil Mechanics

James K. Mitchell,[a†] W. David Carrier, III,[b] William N. Houston,[a] Ronald F. Scott,[c] Leslie G. Bromwell,[d] H. Turan Durgunoglu,[a] H. John Hovland,[a] Donald D. Treadwell,[a] and Nicholas C. Costes[e]

INTRODUCTION

The purpose of the soil mechanics experiment is to determine the physical characteristics and mechanical properties of the lunar soil to depths of several decimeters and their variations in lateral directions, on slopes, and between different regions of the Moon. Measurements using a self-recording penetrometer (SRP), in conjunction with observational data and information on soil characteristics obtained from returned samples, have enabled determination of parameters for density profiles, porosity profiles, and strength parameters.

An understanding of lunar-soil properties is important to lunar studies such as (1) formation and compaction of surface layers, (2) characterization of deposits of different composition, (3) slope stability and downslope movement of soil and rock fragments, (4) prediction of seismic velocities, (5) estimation of thermal properties for use in heat-flow studies, (6) characterization of dielectric properties for use in radar-backscatter and electrical-property studies, (7) gas diffusion through the lunar surface, (8) definition of appropriate conditions for later terrestrial-simulation studies, and (9) various types of soil-property-dependent engineering analyses.

The Apollo 16 mission has made it possible to study a lunar highlands area and to compare the properties of the soil on slopes (as exemplified by the soil blanketing the Descartes material on Stone Mountain to the south of the lunar module (LM) landing point) with properties of the soil covering the Cayley Plains in the vicinity of the LM.

Although many of the analyses and results presented in this report are preliminary and more detailed analyses and simulations are planned, it appears that objectives of the experiment have been achieved, as discussed in the following subsections.

SUMMARY OF PREVIOUS RESULTS

The mechanical properties of lunar soil as deduced to date have been summarized by Mitchell et al. (ref. 8-1) who note that the soil behavior is similar to that of terrestrial soils of comparable gradation, even though the two soil types are compositionally dissimilar. Particle-size distribution, bulk density, and particle shape appear to control physical behavior.

A variety of data sources indicates that the soil porosity, density, and strength vary locally and with depth. Densities may be in the range of 1.0 to 2.0 g/cm^3, and values greater than 1.5 g/cm^3 are probable at depths of 10 to 20 cm. Despite these local variations, however, Houston et al. (ref. 8-2) have found that the mean porosity at each of the previous Apollo landing sites was the same (43.3 percent) for the upper few centimeters of soil. The soil on crater rims and on crater and rille slopes was found to have a somewhat higher porosity (an average value of 46 to 47 percent). Apollo 15 results (ref. 8-3) also suggest somewhat lower densities for soil on slopes.

For a given lunar soil, porosity appears to be the most important single variable controlling the strength parameters, with most probable values lying in the range of 0.1 to 1.0 kN/m^2 for cohesion and 30° to 50° for friction angle; the higher values are associated with lower porosities. Data from Lunokhod-1 (ref. 8-4) indicate that strength (and therefore density) increases with depth.

[a]University of California at Berkeley.
[b]NASA Manned Spacecraft Center.
[c]California Institute of Technology.
[d]Massachusetts Institute of Technology.
[e]NASA Marshall Space Flight Center.
[†]Principal Investigator.

METHODS AND THEORY

Data Sources

Soil mechanics data were derived from (1) crew commentary and debriefings, (2) television, (3) lunar-surface photography, (4) performance data and observations of interactions between soil and the lunar roving vehicle (Rover), (5) drive-tube and deep drill samples, (6) sample characteristics as determined by the Lunar Sample Preliminary Examination Team (LSPET), and (7) measurements using the SRP.

The core drive tubes used for Apollo 16 are the same type as those used for Apollo 15. The individual thin-walled tubes are 37.5 cm long and have an inside diameter of 4.13 cm and an outside diameter of 4.38 cm. Tubes can be used singly or in combination (double-core tubes).

The SRP (fig. 8-1), the main quantitative data source for the soil mechanics experiment, was used to obtain data on soil-penetration resistance as a function of depth below ground surface. Maximum possible penetration depth of the SRP is 76 cm, and the maximum recordable penetration force is 215 N. The record of each penetration is inscribed on a recording drum contained in the upper housing assembly. The lunar-surface reference plane rests on the lunar surface during a measurement and serves as a datum for measurement of penetration depth. A 2.54- by 12.7-cm bearing plate and two penetrating cones, each of 30° apex angle and base areas of 1.29 and 3.22 cm^2, were available for attachment to the penetration shaft.

Quantitative Determination of Soil Properties

The results of simulation studies (refs. 8-2 and 8-5 to 8-8) and soil mechanics theories (ref. 8-9) are used as a basis for the deduction of quantitative values of soil properties.

Soil-strength parameters are deduced from the results of the penetration tests in the following way, as shown by Durgunoglu (ref. 8-10). From the results of model tests, it has been found that a failure surface as shown in figure 8-2 represents closely the actual

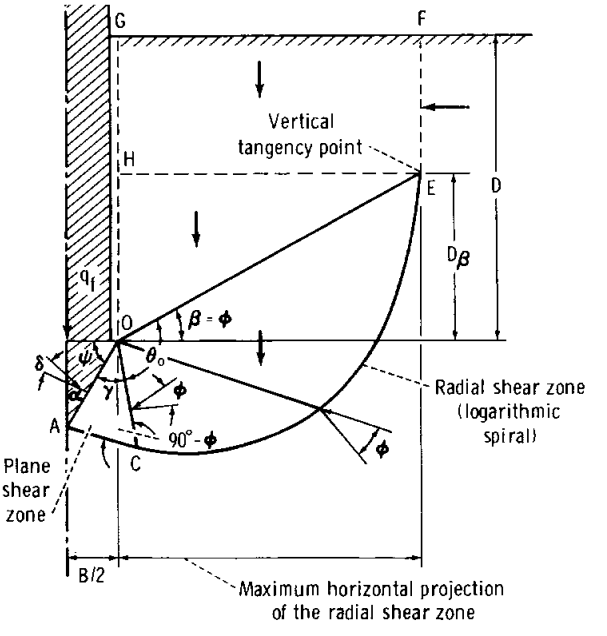


FIGURE 8-2.–Failure mechanism associated with wedge penetration. (Symbols used in this figure are defined in the appendix.)

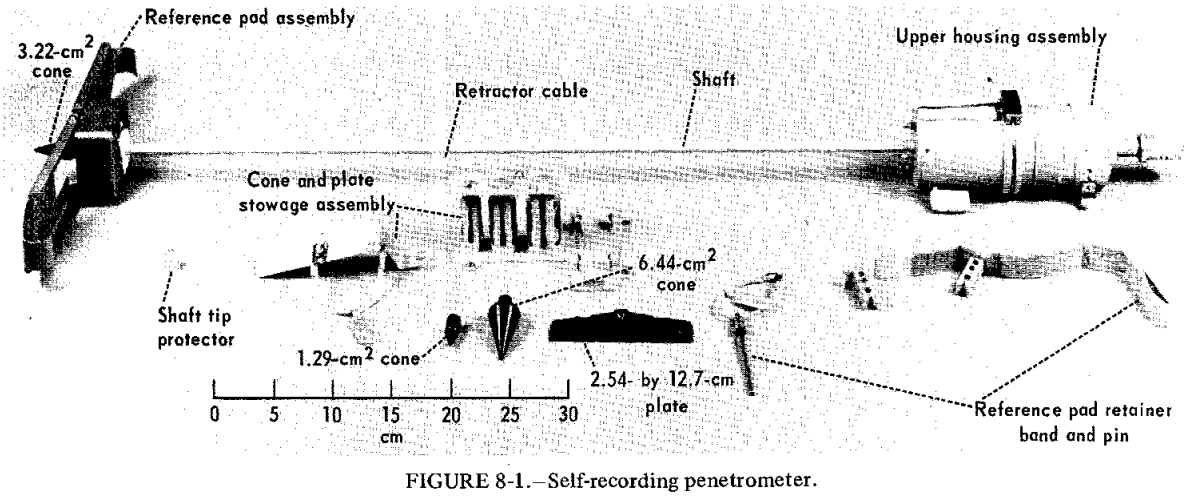


FIGURE 8-1.–Self-recording penetrometer.

failure surface associated with wedge penetration into relatively dense, fine, sandy soils. Equilibrium analysis of the failure zone shown in figure 8-2 leads to

$$q_f = cN_c\xi_c + B\gamma_s N_{\gamma q}\xi_{\gamma q} \qquad (8\text{-}1)$$

where

q_f = ultimate unit tip resistance (force divided by base area)
c = unit cohesion
B = penetrometer base width or diameter
γ_s = unit weight of soil = ρg
ρ = soil density
g = acceleration due to gravity
N_c, $N_{\gamma q}$ = bearing capacity factors = f(D/B, ϕ, α, δ/ϕ)
ξ_c,$\xi_{\gamma q}$ = shape factors
D = depth of penetrometer (wedge) base below ground surface
α = half the wedge apex angle
δ = soil-to-penetrometer friction angle
ϕ = soil friction angle

The value of δ/ϕ has been taken as 0.5, based on the results of friction measurements between a ground-basalt lunar-soil simulant and hard anodized aluminum similar to that used for the SRP cones. Equations for evaluation of the factors N_c and $N_{\gamma q}$ are given in the appendix, and charts for N_c and $N_{\gamma q}$ as a function of ϕ for a range of values of D/B, α, and δ/ϕ are in reference 8-10.

The ultimate penetration resistance of cones is best estimated by using the bearing capacity factors for wedges modified by shape factors. The appropriate equations are

$$\xi_c = 1 + \left(0.2 + \tan^6\phi\right)\frac{B}{L} \text{ for } \phi \geq 25° \qquad (8\text{-}2)$$

$$\xi_{\gamma q} = \left(1.0 - 0.4\,\frac{B}{L}\right) + \frac{1.5}{\frac{B}{D} + \frac{1.5}{\left(0.6 + \tan^6\phi\right)\frac{B}{L}}} \qquad (8\text{-}3)$$

where L is the length of the loaded area and B/L = 1.0 for the SRP cones and 0.20 for the SRP bearing plate.

Infinite combinations of c and ϕ could satisfy equation (8-1) for a given penetration resistance and depth. If penetration resistance values are available for two sizes of cone penetrating the same soil conditions or if the soil deposit is homogeneous and the penetration resistance is known at two depths, then specific values of c and ϕ may be determined by simultaneous solution of two equations of the form of equation (8-1), one for each combination of q_f and D/B values.

RESULTS

General Soil Characteristics at the Descartes Site

Soil cover is present at all points visited in the Descartes landing area. The surface is similar in color (gray and gray-brown) to that at other Apollo sites, although white soil layers were encountered at shallow depths in some areas (e.g., near Flag and Spook Craters and on Stone Mountain). The full lateral extent of this lighter colored (and coarser) material is unknown. Surface textures range from smooth areas almost free of rock fragments through patterned ground to areas heavily populated by larger rocks and fragments.

Substantial variability in soil properties exists from point to point, both regionally and locally. Various quantitative aspects of this variability are discussed in detail subsequently. Figures 8-3, 8-4, and 8-5 provide qualitative indications of local variations in soil properties, as evidenced by differing depths of footprints. The deeper the footprint, the less dense, the weaker, and the more compressible is the soil near the surface. In general, the soil on Stone Mountain (fig. 8-3) was found to be softer and less dense than that in the area including the LM and the Apollo lunar-surface experiments package (ALSEP) (fig. 8-4), which in turn was less strong and less dense than that at station 13, south of the rim of North Ray Crater (fig. 8-5), even though the local variations at any station were significant.

Soil behavior during landing, walking, driving, and sampling was comparable to that observed during the earlier missions. Dust was readily kicked up under foot and by the Rover and tended to adhere to surfaces with which it came in contact. Visibility degradation by blowing dust during the LM descent and landing was less than that of previous missions, probably because of (1) a faster rate of descent and, therefore, a reduced time for erosion and (2) a higher Sun angle, rather than because of any significant difference in soil characteristics.

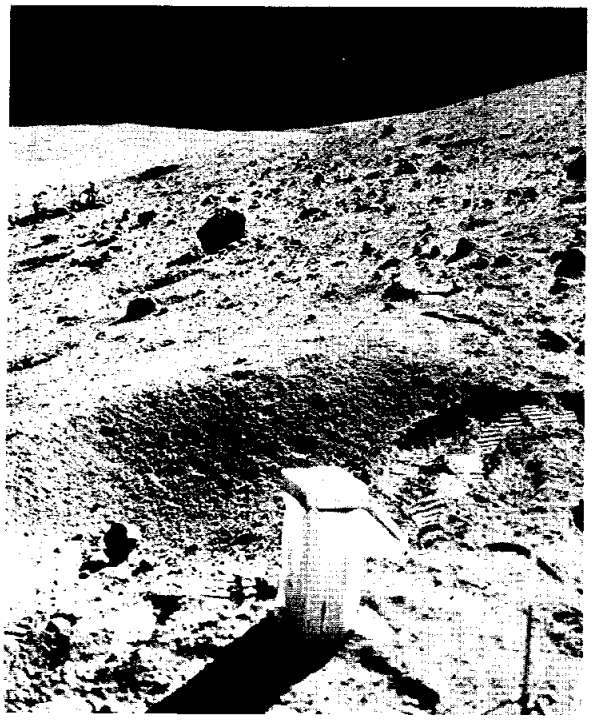


FIGURE 8-3.–Variable soil conditions at station 4 on Stone Mountain (AS16-107-17474).

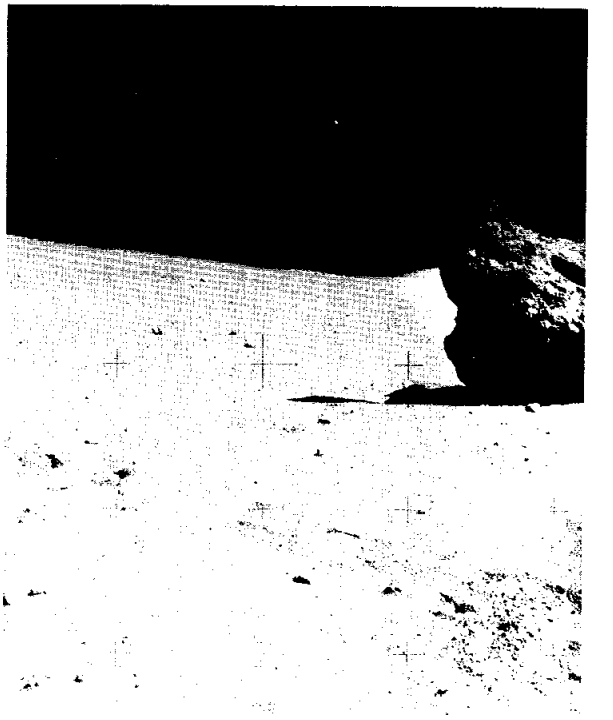


FIGURE 8-5.–Variable soil conditions at station 13 south of North Ray Crater (AS16-106-17392).

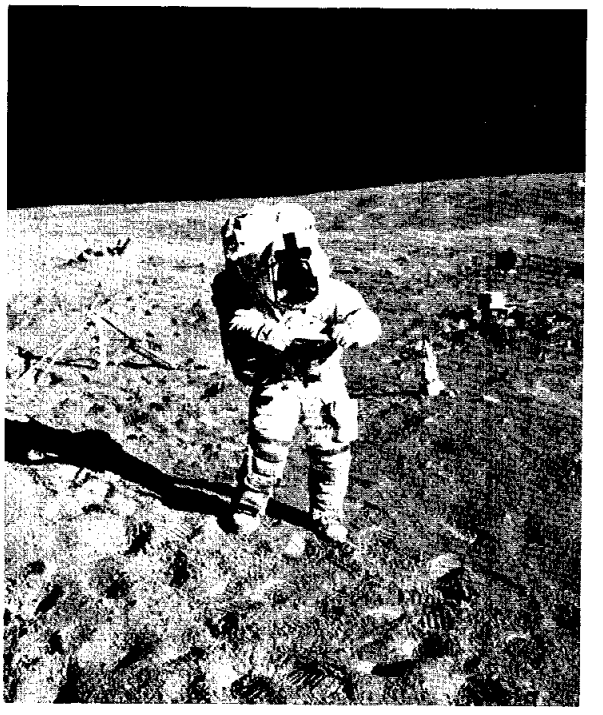


FIGURE 8-4.–Variable soil conditions in the ALSEP area (AS16-114-18387).

Grain-size data have been obtained by the LSPET for samples from several locations. Some of these data curves are shown in figure 8-6 and are compared with a composite distribution for Apollo 11, 12, 14, and 15 samples. The two samples from station 11 (North Ray Crater) are distinctly coarser than the samples from the other stations and coarser than the composite distribution. This may be the result of a significantly lower exposure age, similar to the Apollo 12 double-core-tube coarse-soil layer and the Apollo 14 Cone Crater and trench samples.

The other Apollo 16 samples that have been analyzed to date tend to fall toward the coarser edge of the composite distribution, primarily due to the larger proportion of 10-mm particles which, in many cases, weighed more than the 4-mm and 2-mm fractions. This is probably attributable to an abundance of South Ray Crater rocks that have not yet been worked into the soil matrix. Also shown in figure 8-6 are limited data from Luna 16 (ref. 8-11), which fall within the composite distribution value range.

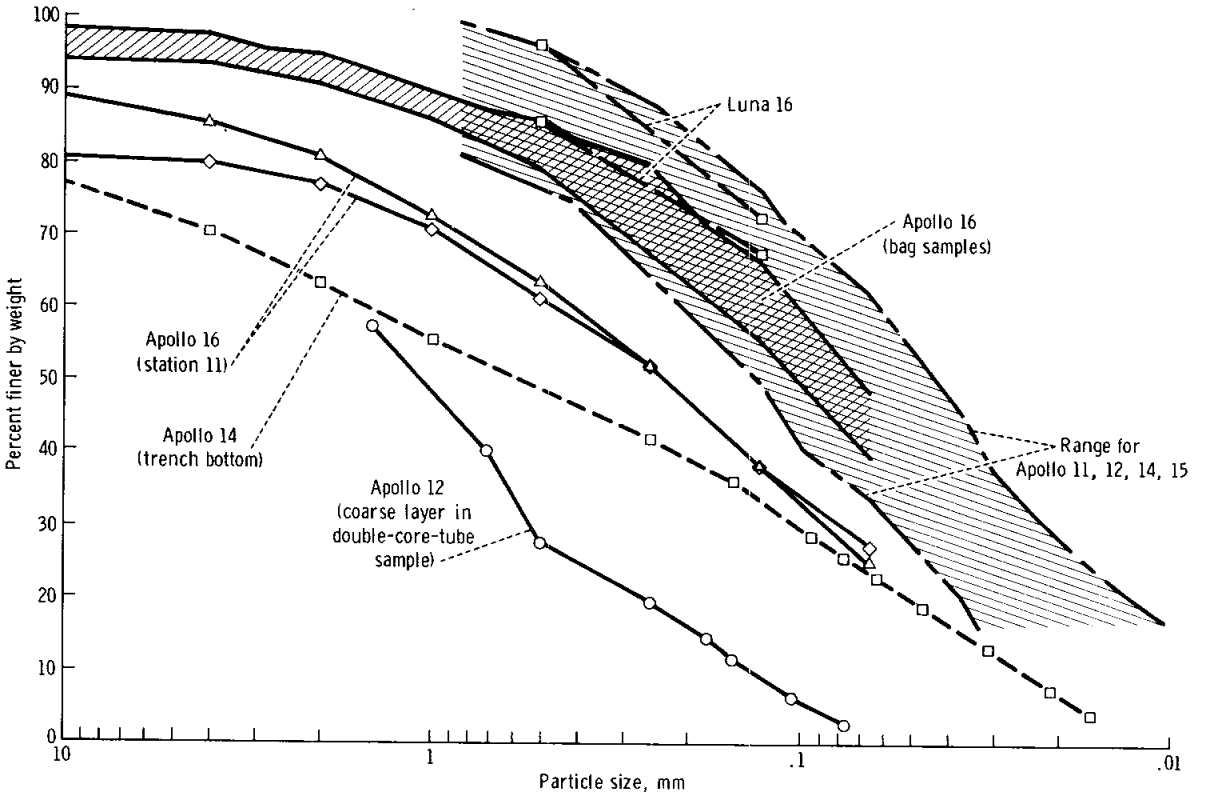


FIGURE 8-6.–Grain-size-distribution curves for several Apollo 16 samples compared with composite distribution for samples from Apollo 11, 12, 14, and 15 missions and from two Luna 16 samples.

Core Samples

Drive tubes.–More than 6 kg of drive-tube samples were obtained in the form of double-core-tube samples from stations 4, 8, 10, and 10′ (fig. 6-4, section 6) and a single-core-tube sample from station 9. The X-radiographs of the as yet unopened tubes indicate that the lunar stratigraphy and soil fabric have been well preserved.

Data on the drive-tube samples are summarized in table 8-I. The core-recovery percentages are comparable to those of the Apollo 15 samples, for which the same type of core tube was used. The double-core-tube data in table 8-I indicate, in all cases, that the soil density in the lower tube is greater than that in the upper tube; that is, density increases with depth. The range of densities (1.40 to 1.80 g/cm^3) is slightly less than that found for the Apollo 15 samples (1.36 to 1.91 g/cm^3).

Drill stems.–The deep core was drilled to a total depth of 2.24 ± 0.03 m in the ALSEP area, located as shown in figure 6-4, section 6. Resistance to drill advance was not great; in fact, the lunar module pilot (LMP) deliberately held up on the drill head to slow the rate of drilling. The first section of core was drilled at a rate of approximately 150 cm/min, whereas subsequent drilling was at a rate of approximately 60 to 75 cm/min.

After the drill stem was withdrawn, the "rammer-jammer" from the heat-flow experiment was dropped into the open hole. It dropped to a depth of about 2.18 m, indicating that the hole had remained open to within approximately 6 cm of the bottom. It is not known whether the hole closed below this depth because of soil failure resulting from insufficient strength in the bottom of the hole, because some sample fell out of the drill stem during withdrawal, or because of side-wall raveling during withdrawal.

TABLE 8-I.–Preliminary Data on Apollo 16 Drive-Tube Samples

Station	Serial no.	Sample no.	Sample weight, g	Sample length, cm (a)	Bulk density, g/cm^3	Tube depth (pushed), cm	Total depth (pushed and driven), cm	No. of hammer blows	Core recovery, percent
4	[b]2043	64002	584.1	31.7	[c]1.38 to 1.40	32.6 ± 0.5	[d]65 ± 6	≫3	103 ± 10
	2038	64001	752.3	[e]33.9	1.66				
8	2029	68002	583.5	27.4	1.59	17.8 ± 0.5	68.6 ± 0.5	~56	91
	2036	68001	840.7	34.9	1.80				
9	2034	69001	558.4	–	–	20.6 ± 0.5	[d]27.5 ± 2	8	–
10	[b]2045	60010	635.3	32.3	1.47	17.9 ± 0.5	[d]71 ± 2	~53	95 ± 3
	2054	60009	759.8	[e]33.1	1.72				
10	2027	60014	570.3	[c]28.8 to 28.4	1.48	28 ± 2	70.5 ± 1	27	90 ± 1
	2032	60013	757.2	[e]34.7	1.63				

[a]Measured from X-radiographs taken by the LSPET.

[b]Crewmen neglected to insert keeper.

[c]Corrected for void.

[d]Measured from kinescopes.

[e]The nominal length of the sample in a lower core tube is 34.9 cm; for those tubes in which the actual sample length is less, either some sample fell out or the keeper compressed the top of the sample. The former is considered to be the more likely explanation, and the densities have been calculated accordingly. The internal diameter of the core tubes is 4.13 cm.

Data for the samples contained in the six drill-stem sections are given in table 8-II. From these data and X-radiographs of the stems, it is known that the top section is half full; the second section is nearly full with a 5-cm-long void at the bottom; the third section is nearly empty, and what little sample it does contain is distributed along its length. The fourth, fifth, sixth, and bit sections are full.

Several hypotheses have been proposed to account for the sample distributions in the different sections. The most plausible explanation at the present time is that the initial core recovery was only about 88 percent because of the low density and high penetration rate near the surface, leaving a void of approximately 1-1/2 sections in the top three sections when the drill stem was separated into two three-section lengths for Earth return. During lunar lift-off, zero-g travel, entry into the Earth atmosphere, splashdown, and transport to and handling in the Lunar Receiving Laboratory, the sample migrated up the sections, finally becoming distributed in various states of compaction over a length of 2-1/2 sections.

TABLE 8-II.–Preliminary Data on Apollo 16 Drill-Stem Sections

Drill-stem serial no.	Sample no.	Sample mass, g	Sample length, cm	Bulk density, g/cm^3	Drill-stem depth, cm
014	60007	105.7	22.2	1.46	
012	60006	165.6	35.5 ± 0.5	1.43 ± 0.02	
024	60005	76.1	–	–	
015	60004	202.7	39.9	1.56	224 ± 3
019	60003	215.5	39.9	1.66	
018	60002	211.9	42.5	1.75	
180 (bit)	60001	30.1			

Penetrometer Test Results

Eleven tests were made using the SRP during the second extravehicular activity period. Four cone-penetration tests were made at station 4 on Stone Mountain; five cone-penetration tests and two plate-load tests were made in the station 10-ALSEP area. The nature of each of these tests is summarized in table 8-III. A planimetric sketch map of station 4 showing the penetrometer test locations is presented in figure 8-7. Similar information for the station 10 area is given in figure 8-8.

Curves representing penetration resistance as a function of depth are plotted in figure 8-9 for cone-penetration tests at station 4, in figure 8-10 for cone-penetration tests at station 10, and in figure 8-11 for plate-load tests at station 10. In each case, the raw data as taken directly from the SRP recording drum are presented. A visual record of all tests except the first cone-penetration test at station 4 and the first plate-load test at station 10 was obtained by the lunar-surface television camera. From a detailed study of the kinescopes, it is clear that the spikes shown on several of the penetration curves, which reflect sudden unloading and reloading, were a direct consequence of the test procedure and not of the soil conditions. These spikes can be ignored in the interpretation of test results. However, where the penetration curves show a simultaneous reduction in stress and an increase in penetration, as in figures 8-9(d), 8-10(c), and 8-10(d), it is a reflection of softer soil layers, as discussed later in more detail.

As shown in figures 8-9, 8-10, and 8-11, an intercept for zero stress on the penetration axis is present in each test. This intercept ranges between 1.9 and 9.0 cm. Careful study of the kinescopes and the test procedures used on the lunar surface indicates that these intercepts most likely resulted from the lunar-reference plane (fig. 8-1) riding up on the penetrometer shaft after initial indexing and positioning. The LMP repositioned the reference plane after each test and before moving to the next test location. As he moved to the next test area, the penetrometer tip was pointed slightly upward. Coupled with movement of the LMP and the sensitive balance between the reference plane and retractor cable, some detectable movement of the reference plane up the shaft occurred. In addition, placing the SRP onto the lunar surface while holding it by the housing could have led to some penetration (because of inertial effects) without recording the accompanying force. Thus, the penetration curves do not reflect soil conditions above the intercept point, but they are correct below it.

TABLE 8-III.–Summary of Penetration Tests Determined From SRP Data

Station	*Test no.*	*SRP index no.*	*Penetrometer tip*	*Location*	*Maximum penetration depth, cm*	*Maximum force to reach maximum depth, N*
4	1	5	3.22-cm^2 cone	Uphill, south of Rover	21.3	215
4	2	6	1.29-cm^2 cone	On bench, south of Rover (near edge of subdued crater)	74	53.5
4	3	7	1.29-cm^2 cone	On bench, southwest of Rover (near edge of subdued crater)	46	215
4	4	8	1.29-cm^2 cone	Downhill, north of Rover (next to double-core tube)	73	199
10	1	10	3.22-cm^2 cone	Near Rover	22	>215
10	2	11	1.29-cm^2 cone	Near Rover (next to double-core tube)	50.5	>215
10	3	12	1.29-cm^2 cone	Southwest of Rover on line to deep drill core	42	>215
10	4	13	1.29-cm^2 cone		62.5	199
10	5	14	1.29-cm^2 cone		70	(a)
10	6	15	2.54- by 12.7-cm plate	Near Rover (next to double-core tube)	9.7	>215
10	7	16	2.54- by 12.7-cm plate	Near Rover	6.3	>215

[a]No data recorded on SRP drum.

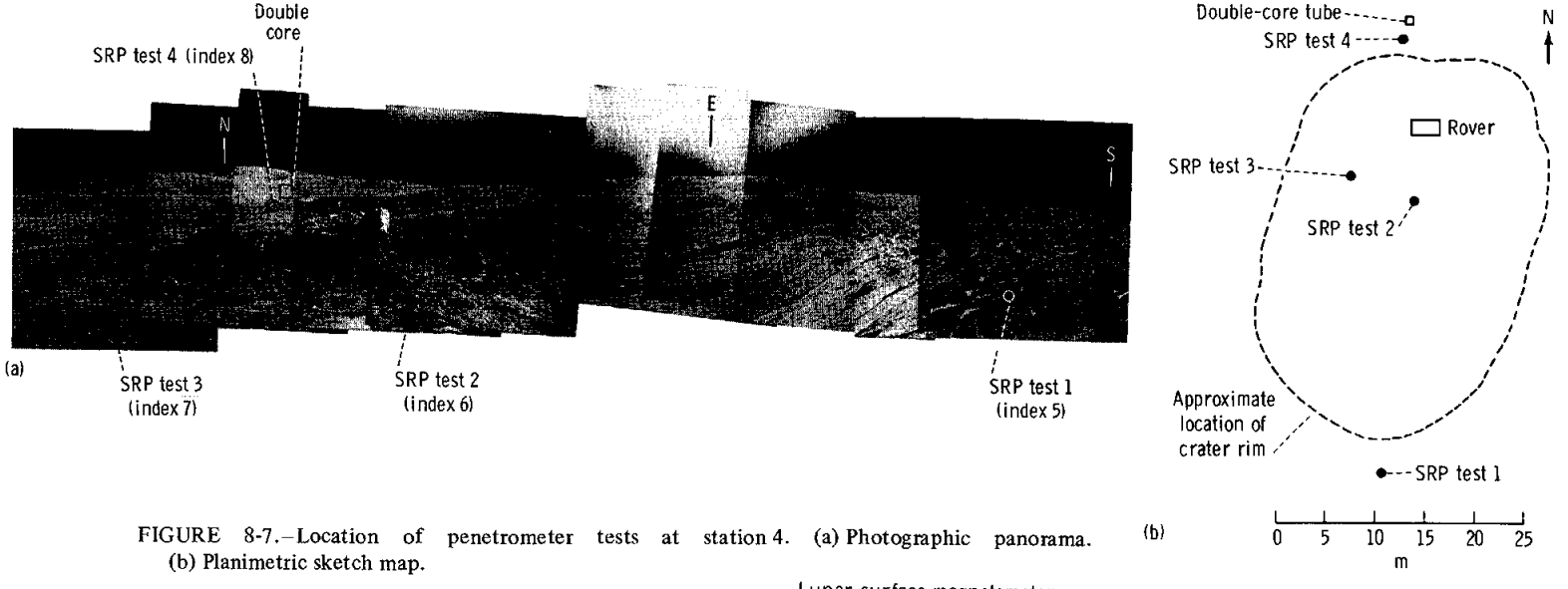


FIGURE 8-7.–Location of penetrometer tests at station 4. (a) Photographic panorama. (b) Planimetric sketch map.

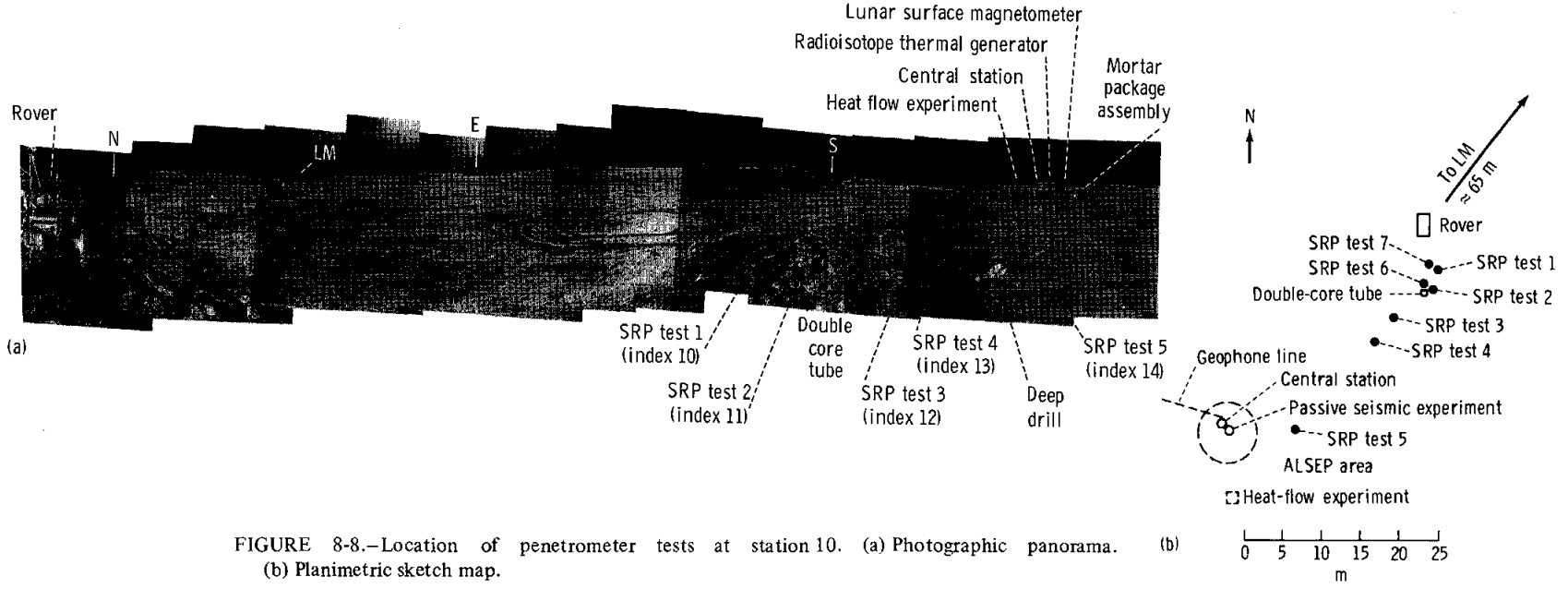


FIGURE 8-8.–Location of penetrometer tests at station 10. (a) Photographic panorama. (b) Planimetric sketch map.

As indicated in table 8-III, data on force as a function of penetration for test 5 at station 10 (index 14) did not record. Analysis of the kinescopes and the performance characteristics of the penetrometer suggests that this probably was because the LMP had placed his left hand around the upper housing assembly in such a manner that the indexing lever was depressed, thus locking the recording drum and preventing inscription of the test data.

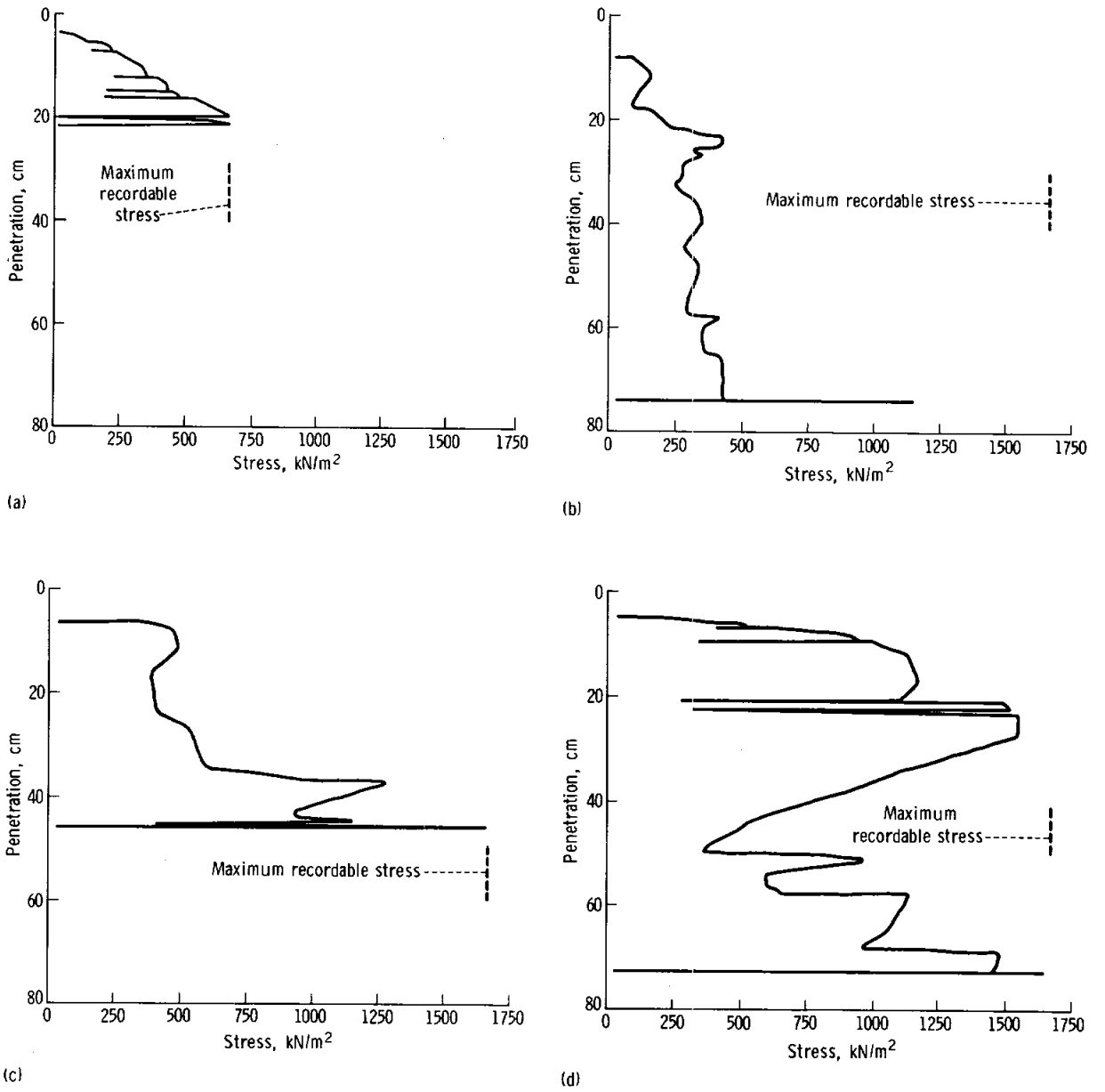


FIGURE 8-9.–Cone-penetrometer-test results for station 4. (a) Test 1, 3.22-cm^2 cone, index 5. (b) Test 2, 1.29-cm^2 cone, index 6. (c) Test 3, 1.29-cm^2 cone, index 7. (d) Test 4, 1.29-cm^2 cone, index 8.

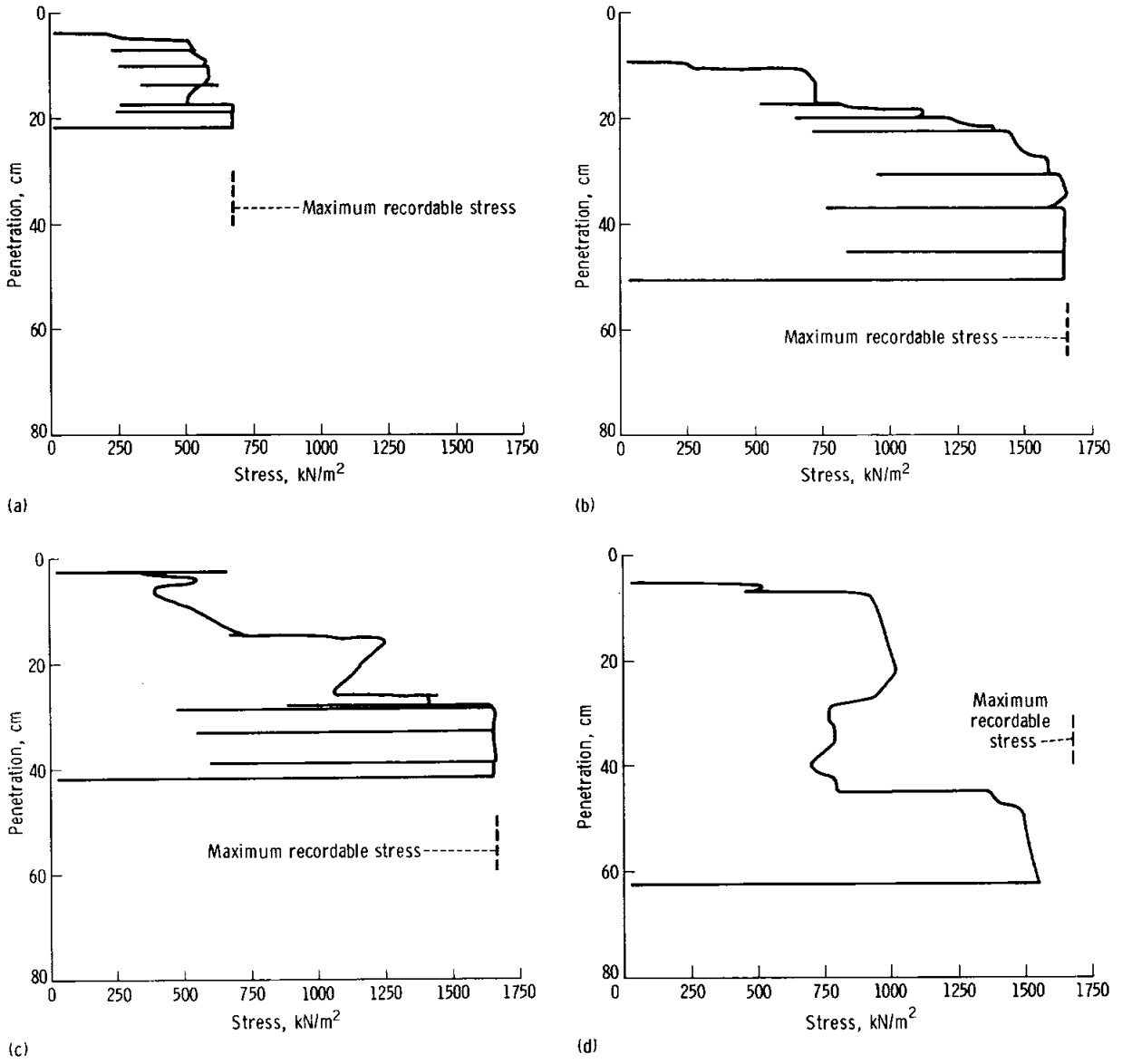


FIGURE 8-10.—Cone-penetrometer-test results for station 10. (a) Test 1, 3.22-cm^2 cone, index 10. (b) Test 2, 1.29-cm^2 cone, index 11. (c) Test 3, 1.29-cm^2 cone, index 12. (d) Test 4, 1.29-cm^2 cone, index 13.

DISCUSSION

Stratigraphy and Variability

The penetration curves in figures 8-9, 8-10, and 8-11 may be used to construct details of the lunar soil to depths of a few decimeters beneath the surface. The rather marked differences among the shapes of the curves are a direct qualitative indication that soil conditions are locally variable. Some characteristics at each test location may be noted.

Station 4 (Stone Mountain).—Penetration test 1 (index 5), made uphill to the south of the Rover, indicates a relatively homogeneous soil to a depth of approximately 20 cm. A smoothed curve fit to the

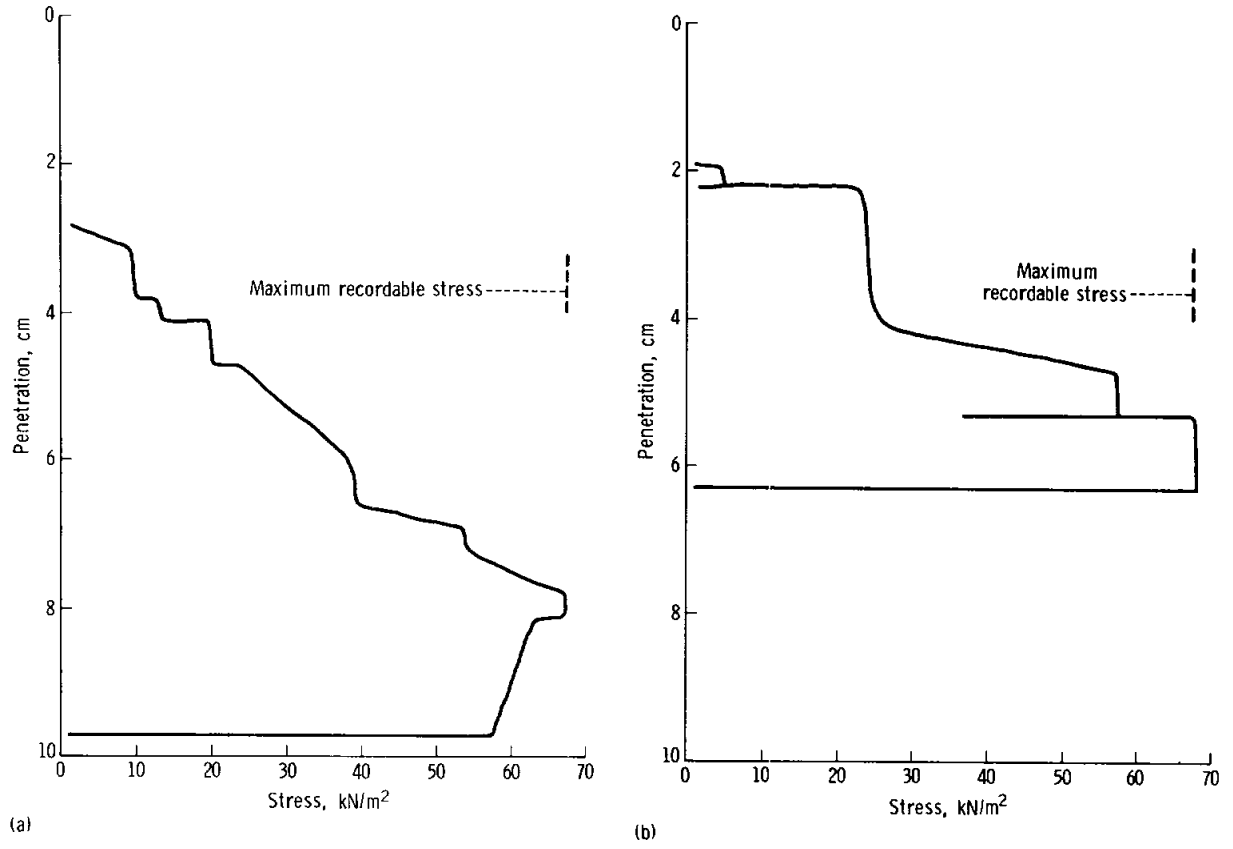


FIGURE 8-11.–Plate-load-test results for station 10. (a) Test 6, 2.54- by 12.7-cm plate, index 15. (b) Test 7, 2.54- by 12.7-cm plate, index 16.

data in figure 8-9(a) is characteristic of that for a dominantly frictional soil with low cohesion.

Penetration test 2, index 6 (fig. 8-9(b)), indicates a much softer soil in the area a few meters south of the Rover. From the photographs (fig. 8-7(a)), the test appears to have been made in an area near the edge of the subdued crater in which the Rover was parked. A layer of higher resistance is indicated at a depth of approximately 24 cm.

From figure 8-9(c), it is evident that a highly resistant layer was encountered at a depth of 45 cm during test 3 (index 7). The soil was stronger, in general, than that observed for test 2. The location for test 3 was southwest of the Rover, also near the rim of the subdued crater.

Test 4 (index 8) was made downhill to the north of the Rover. The penetration curve (fig. 8-9(d)) indicates a very dense and resistant layer extending to a depth of approximately 27 cm. Softer soil was located below this layer to a depth of approximately 50 cm, where firm material was again encountered. To test this interpretation, a simulation test was done on a model soil composed of a soft, weak layer sandwiched between two firm, strong layers. The curve for penetration resistance as a function of depth for this condition is shown in figure 8-12. It is comparable to the curve in figure 8-9(d).

A double-core drive-tube sample was taken at a point near (1 m) the location of penetration test 4. The X-radiograph of the core sample reveals layers that correlate well with the penetration curve in figure 8-9(d). The interpretations made of the soil conditions in the core sample by J. S. Nagle of the LSPET are shown in figure 8-13. Nagle suggests that the coarse-grained layer with abundant rock fragments decreasing with depth is South Ray Crater material and that the Descartes deposit underlies the South Ray layer. This layer is clearly delineated in

figure 8-13 and implies that the Descartes material is at least 45 cm below the surface at the site of test 3, index 7 (fig. 8-9(c)); that the South Ray material is very thin and the Descartes deposit begins at 30 cm at the test 2 site, index 6 (fig. 8-9(b)); and that the Descartes material is at least 21 cm below the surface at the test 1 site, index 5 (fig. 8-9(a)).

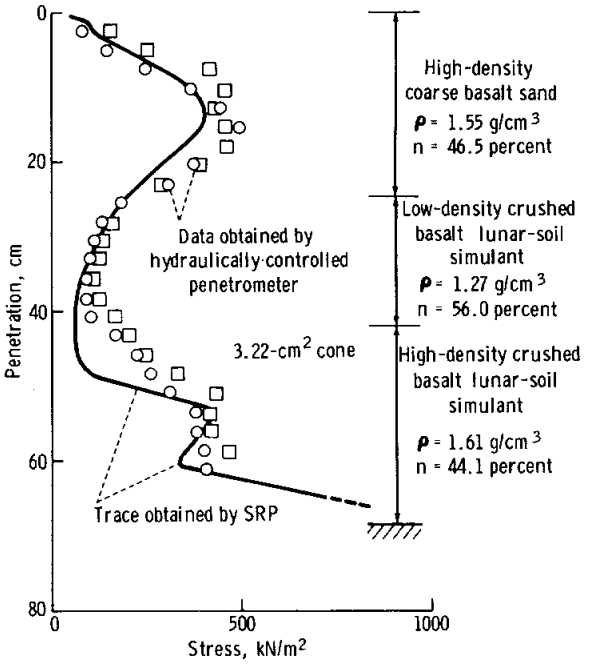


FIGURE 8-12.–Penetration resistance as a function of depth relationship for a soft soil layer sandwiched between two firm layers.

Station 10-ALSEP area.–The penetration tests in this area were located close to the Rover at station 10 and along a line southwest to the ALSEP area (fig. 8-8). The ground surface in this region was generally level and free of large rock fragments.

Tests 1 and 2 (indexes 10 and 11, respectively) were performed with two different sized cones at adjacent locations. Figure 8-10(a) for the 3.22-cm^2 cone shows a soil of high penetration resistance to a depth of approximately 17.5 cm. The penetration resistance increases abruptly at this point, suggesting an even firmer layer, with a resistance to penetration greater than the recording capability of the SRP (215 N) but less than the ability of the astronaut to apply (250 N±), at least to a depth of 22 cm.

With the smaller cone (1.29 cm^2) used for test 2, it was possible to penetrate to a greater depth for a given applied force. The data (fig. 8-10(b)) show the same increase in resistance at a depth of 17.5 cm, below which the recording capacity of the penetrometer was exceeded.

Figure 8-10(c) for test 3 (index 12) again indicates a fairly firm soil overlying a harder layer, encountered here at a depth of 15 cm. The material appears to soften somewhat for the next 10 cm, but then becomes strong at 30 cm, as was true for test 2.

Test 4, index 13 (fig. 8-10(d)), located about midway between the Rover and the deep drill core, indicates a somewhat different stratigraphy, with a softer layer between depths of approximately 28 and 45 cm. The full recording capacity of the penetrometer had not been reached at the maximum penetration depth of 63 cm.

A preliminary stratigraphic profile (fig. 8-14) has been prepared with the cooperation of J. S. Nagle, based on (1) the X-radiographs of the drill-core stem and the station 10 core sample and (2) the penetration curves in figure 8-10. Five layers have been detected with varying thicknesses: surficial, hard, soft, harder, and rocky. This profile is qualitative in nature at this time and more quantitative analyses are planned.

Tests 6 and 7 (indexes 15 and 16, respectively) were plate-load tests (fig. 8-11). Because of the large plate-bearing area compared to the cone-base areas, penetration depths were less than those reached in the other tests. From the kinescopes, it is known that the surface soil at the site of test 7 is quite soft and that the lunar-reference plane penetrated to a depth of 1 or 2 cm. Average curves drawn through the data points in figure 8-11 are characteristic of a soil increasing in strength with depth.

Density and Porosity

Density and porosity values for the soil at different locations are available from analysis of several types of data. Conversion from density to porosity or vice versa requires a knowledge of the specific gravity of soil particles. Because this property has not yet been determined for the Apollo 16 samples, an average value of 3.05 has been assumed, based on the results of one test each on samples from

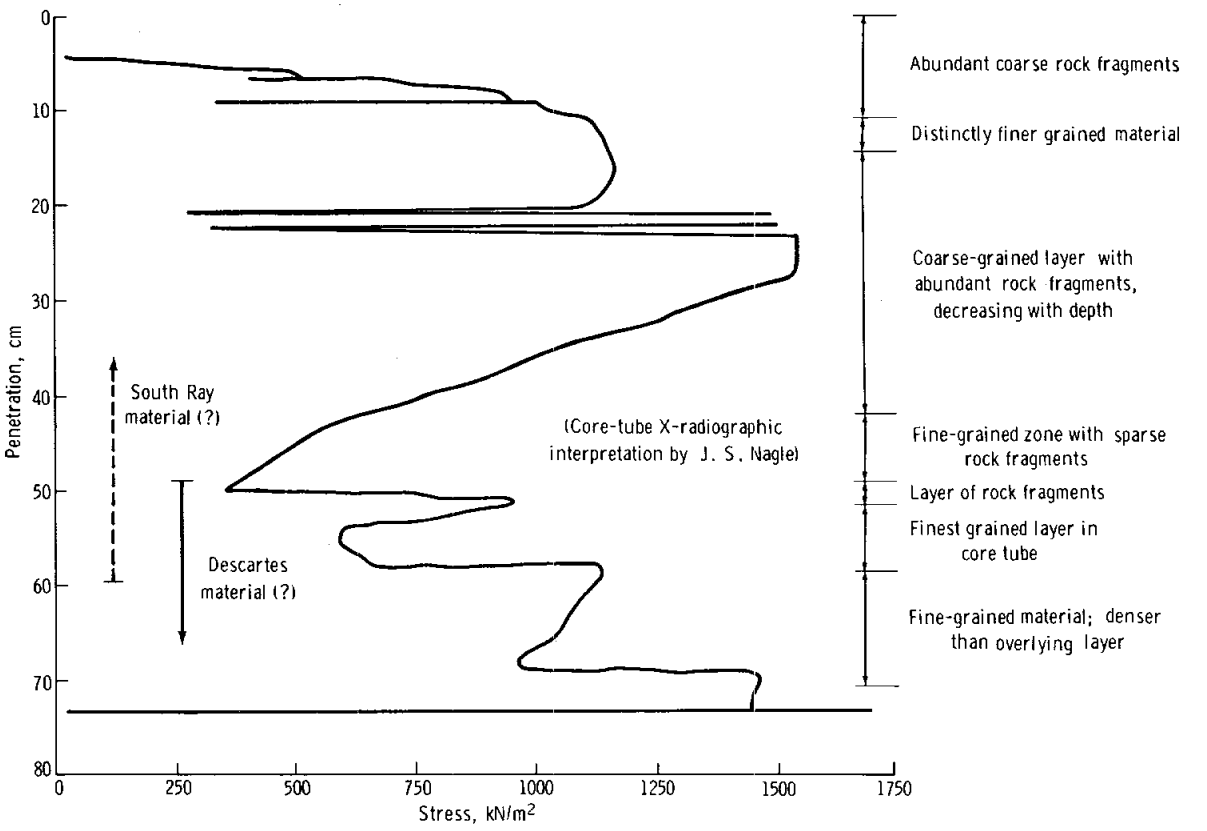


FIGURE 8-13.–Correlation of station 4 double-core-tube stratigraphy with SRP test 4 (index 8).

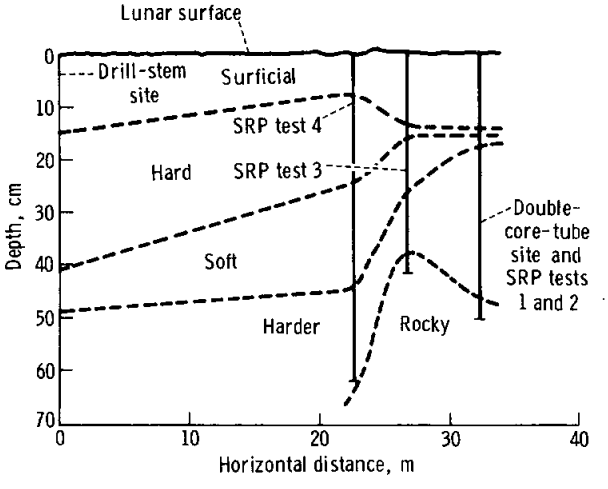


FIGURE 8-14.–Approximate soil profile between station 10 double-core-tube site and deep-drill-stem site in ALSEP area.

the Apollo 11, 12, and 15 missions, and tests on two Apollo 14 samples. Porosity n, density ρ, and specific gravity G_s are related according to

$$\rho = G_s(1 - n)\rho_w \qquad (8\text{-}4)$$

where ρ_w is the density of water.

Drive-tube samples.–Directly measured average densities for the drive-tube samples are presented in table 8-I. Although some correction may be required to give the in situ density because of sampling disturbance (refs. 8-7 and 8-8), these corrections should be small for tubes of the type used on Apollo 16. Density as a function of depth for these samples is shown in figure 8-15, assuming a constant density within each drive tube. Figure 8-16 shows smooth curves that have been fitted to the double-

core-tube density data according to

$$\rho = \rho_0 + k[\ln(z + 1)] \qquad (8\text{-}5)$$

where ρ_0 is the density at the surface (g/cm^3), z is the depth (cm), and k is a densification factor. Such a relationship would be appropriate for densification under self-weight. The curves in figure 8-16 indicate that the surface soil can have a very low density (~0.9 g/cm^3) but the density will increase very rapidly with depth to a depth of 10 cm and then will increase more slowly thereafter. Below 20 cm, the density would generally be expected to be greater than 1.5 g/cm^3. However, these curves describe only a general trend; the actual distributions of density as a function of depth are certainly not monotonic and vary considerably in the lateral direction. This distribution is reflected in the character of the previously described tracings from the SRP.

The number of blows required to hammer the core tubes into the lunar surface generally increased with the density of the soil, as shown in table 8-I. The double core at station 10 required significantly more blows than the double core at station 10′, even though the density of both samples was nearly the same. This is attributable to the higher concentration of rock fragments in the soil at station 10, a difference observed also by the crewmen when they took rake samples at stations 10 and 10′.

Drill-stem samples.—Bulk densities for samples contained in the different sections of the drill stem are given in table 8-II. The initial density in the Apollo 16 drill stem has been reconstructed based on the hypothesis previously described, and the results and densities from the Apollo 15 drill stem are shown in figure 8-17. The Apollo 15 drill-stem-sample densities are significantly higher than those of the Apollo 16 drill stem. Furthermore, the character of the Apollo 15 density distribution is different from that of Apollo 16: the Apollo 15 density variation is erratic, whereas the Apollo 16 sample density generally increases with depth. It is likely that this difference is the result of different modes of deposition; perhaps the soil at the Apollo 16 drill-stem site was deposited in one large event, whereas the Apollo 15 stratigraphy was formed by multiple events.

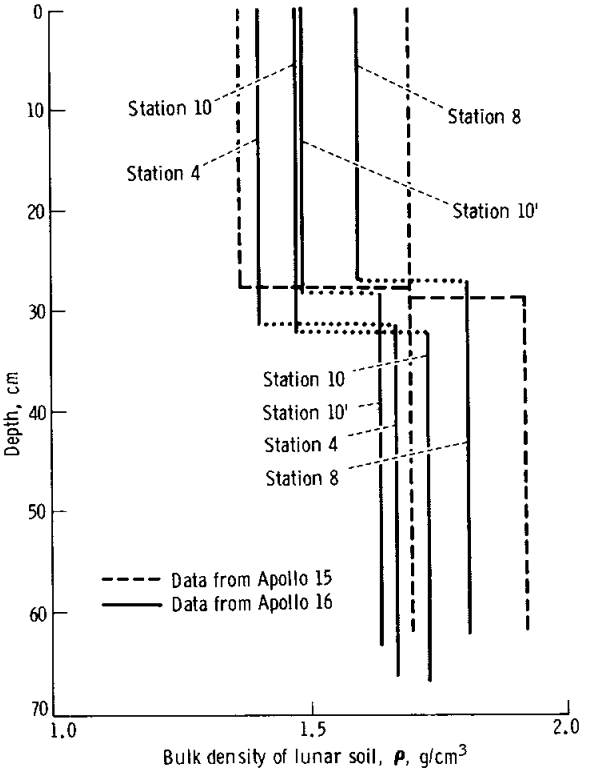


FIGURE 8-15.—Density as a function of depth relationships for drive-tube samples.

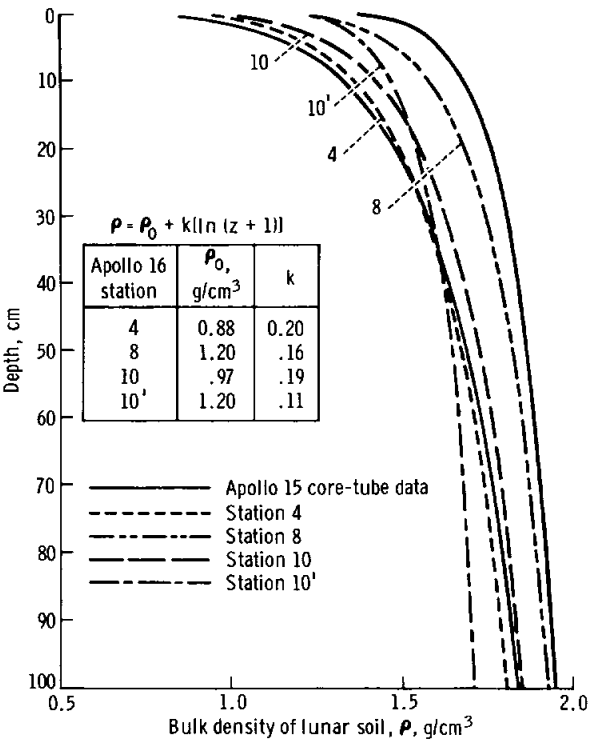


FIGURE 8-16.—Hypothetical relationships for density as a function of depth for homogeneous soil.

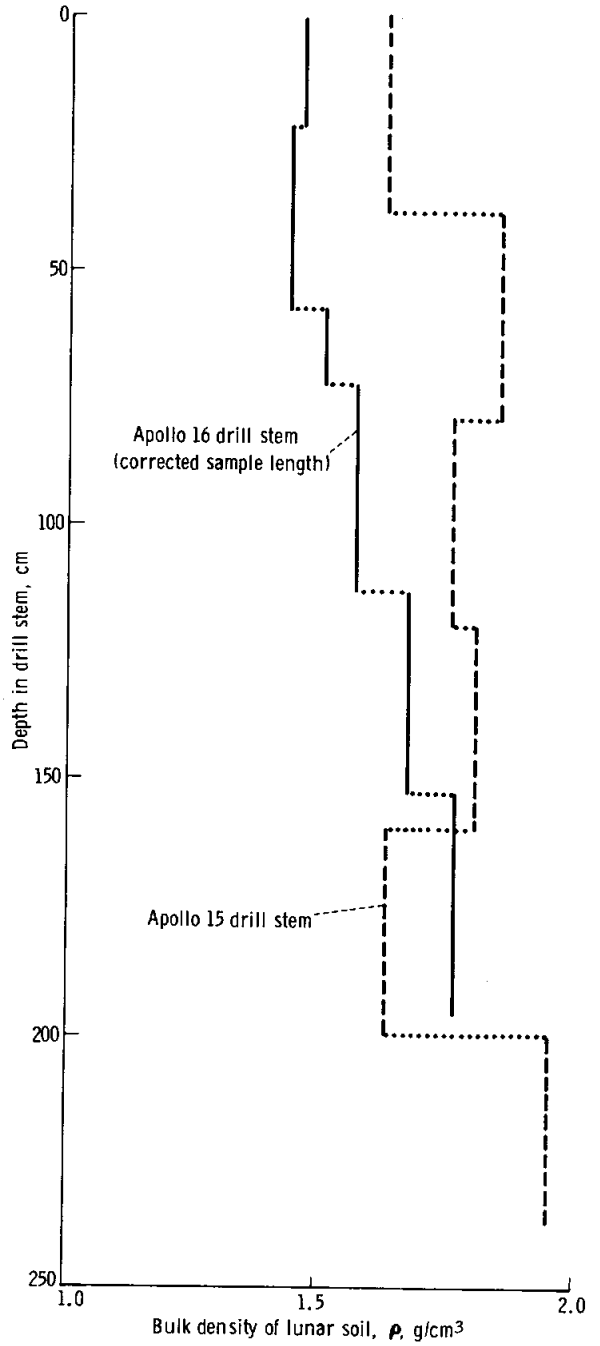


FIGURE 8-17.–Relationships of density as a function of depth for the Apollo 15 and Apollo 16 drill-stem samples.

Penetrometer results.–From simulation studies on soils having properties similar to those on the Moon, a correlation (ref. 8-5) has been developed between porosity and the average slope G_p (measured from the ground surface) of the curve representing cone-penetration resistance as a function of depth. This correlation was developed specifically for a 3.22-cm^2 (base area) cone; its application to results obtained when using cones of a different size or using a bearing plate has not yet been established. However, it has been assumed that, as a first approximation, the same correlation holds for the 1.29-cm^2 cone. A correlation has been developed for the 2.54 X 12.7 cm plate (ref. 8-12). Porosity and density estimates deduced in this way from the penetration curves in figures 8-9, 8-10, and 8-11 are given in table 8-IV.

The values of porosity derived in this way appear to be somewhat low, and the densities seem to be slightly high relative to the values for the core-tube samples. This variance in values could reflect a difference between the characteristics of the soil simulant and those of the actual lunar soil, which means that the correlation curve would be somewhat in error. Analyses on this point thus far are inconclusive. The results do show, however, that the densities at depths greater than a few centimeters are greater at station 10 than at station 4.

Footprint analysis.–Houston et al. (ref. 8-2) have used footprint depths to determine the porosity of the upper few centimeters of the lunar soil and have examined the variation in porosity at and among the Apollo landing sites on a statistical basis. A similar analysis has been applied to the Apollo 16 site. The correlation curve, based on the results of model tests and theoretical analyses (ref. 8-5), is shown in figure 8-18.

A total of 309 different footprints in the Apollo 16 photographs was studied, and the porosity variations were analyzed statistically, giving the results shown in table 8-V. A histogram of the porosity values is shown in figure 8-19. The values determined in this way reflect porosities only to depths of approximately 5 to 10 cm; that is, footprint depth is little affected by soil conditions below these depths.

From the results in table 8-V and figure 8-19 and from the results in reference 8-2, the following conclusions emerge.

(1) The variation of the average porosity of the soil near the surface is slight at the different locations.

TABLE 8-IV.–Porosity and Density Estimates Derived From Curves for Penetration Resistance as a Function of Depth

Station	*Test no.*	*Location*	*Penetrometer tip*	*Gradient of penetration-resistance curve, G_p, $kN/m^2/m$*	*Porosity, n, percent*	*Depth range, cm*	*Density, ρ, g/cm^3*
4	1	Uphill, south of Rover	3.22-cm^2 cone	3370 to 3860	37 to 39	0 to 20	1.86 to 1.92
4	2	On bench, south of Rover	1.29-cm^2 cone	1310 to 2280	41 to 43	0 to 25	1.74 to 1.80
4	3	On bench, southwest of Rover	1.29-cm^2 cone	2000 to 5200	36.5 to 41	0 to 25	1.80 to 1.94
4	4	Downhill, north of Rover	1.29-cm^2 cone	6700 to 10 000	32 to 35	0 to 20	1.98 to 2.07
10	1	Near Rover	3.22-cm^2 cone	[a]6300 to 9850	32 to 34	0 to 8	2.01 to 2.07
10	2	Near Rover	1.29-cm^2 cone	5600	35.5	0 to 25	1.96
10	3	Southwest of Rover on line to deep drill	1.29-cm^2 cone	4800 to 6850	34.5 to 36.5	0 to 25	1.93 to 2.00
10	6	Near Rover	2.54- by 12.7-cm plate		44 to 46	0 to 5	1.65 to 1.71
10	7	Near Rover	2.54- by 12.7-cm plate		42 to 44	0 to 5	1.71 to 1.77

[a]Penetrometer cone may have hit rocks.

TABLE 8-V.–Results of Statistical Analysis of Porosities Deduced From Footprint Depths

Location	*No. of observations*	*Mean porosity, percent*	*Standard deviation*
All data	309	45.1	3.0
All data except crater rims	273	45.0	2.8
Crater rims	36	46.1	4.6
ALSEP area[a]	59	45.2	3.9
LM area[a]	43	43.1	2.3
Station 1[a]	43	44.8	2.8
Station 4[a]	26	44.8	1.3
Stations 4 and 5[a]	35	45.8	2.6
Station 8[a]	20	45.0	2.3
Station 10[a]	15	45.2	2.1
Station 11[a]	12	43.7	1.5

[a]Crater rims excluded.

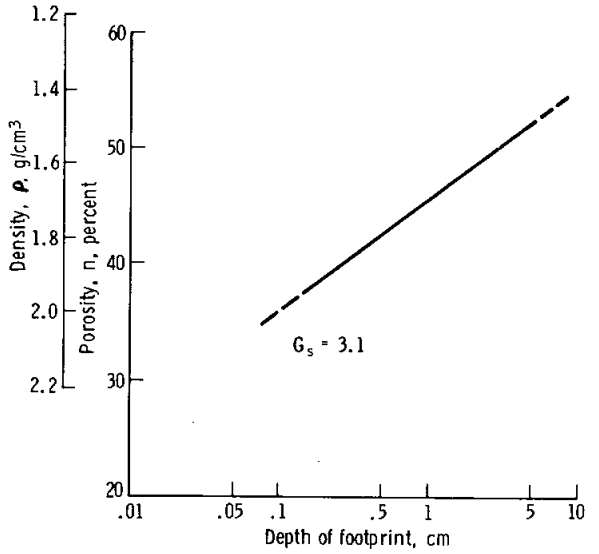


FIGURE 8-18.–Relationship between porosity of the upper few centimeters of lunar soil and footprint depth.

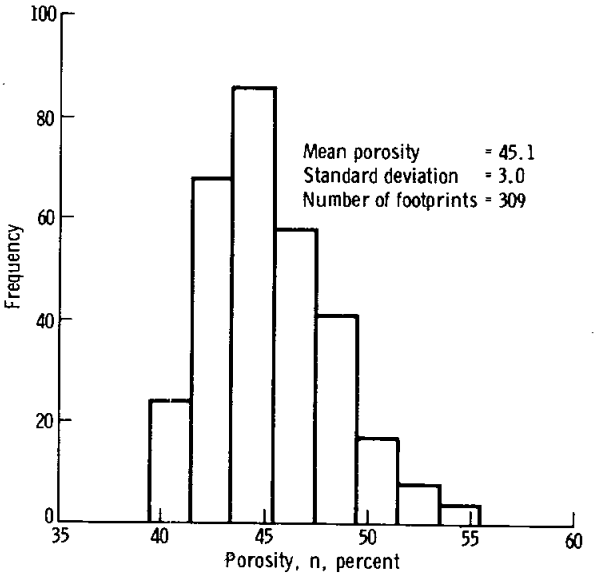


FIGURE 8-19.–Histogram of porosity variations at the Apollo 16 site as deduced from footprint depths.

(2) The average porosity (45.0 percent) of intercrater areas at the Apollo 16 site is slightly greater than that at the four previous Apollo sites (43.3 percent).

(3) The average porosity on crater rims at the Apollo 16 site (46.1 percent) is almost the same as that at the four earlier Apollo sites (46.7 percent).

(4) The standard deviation of porosities for the intercrater areas at the Apollo 16 site is the same as the average standard deviation (2.8 percent) for all previous lunar-landing missions.

(5) The standard deviation of porosities of crater rims is 4.6 percent at the Apollo 16 site as compared with the average of 4.0 percent for all previous sites. Thus, it is concluded that the lunar-soil surface has the same average porosity at all locations, regardless of composition or topography, although significant local (on a meter scale) variations may exist.

Density and porosity comparisons.–The density and porosity values deduced from the several data sources are compared in table 8-VI. From a study of these values, it appears that:

(1) Densities generally increase with depth.

(2) Densities deduced from footprints and penetrometer data are consistently higher and porosities are lower than those derived from core-tube-sample data. Studies of maximum and minimum densities based on simulation studies, tests on two 1-g samples of Apollo 14 soil and on one small sample of Apollo 15 soil, and studies of core-tube densities indicate that the correlations used to obtain densities and porosities from footprints and penetrometer data may give porosities that are too low by as much as 2 to 3 percentage points.

(3) Most probable values of soil porosity in the Descartes region of the Moon are in the range of 40 to 50 percent. Most values of density are likely to be between 1.5 and 1.8 g/cm^3.

Strength Characteristics

The penetration-resistance data in figures 8-9, 8-10, and 8-11 can be analyzed for evaluation of soil-strength characteristics (as indicated by cohesion c and angle of internal friction ϕ) by using the procedures described in the subsection entitled "Methods and Theory." Although the analyses completed to date represent only a preliminary study of the penetration curves, some results have been obtained and preliminary conclusions are possible for a comparison of strength-parameter relationships for the different tests.

Because the penetration-resistance curves indicate that the soil is not homogeneous with depth and because variations in lateral directions are sufficiently great to preclude direct comparison between the

TABLE 8-VI.–Summary of Lunar-Soil Density and Porosity Estimates

Location	*Drive-tube samples*			*Drill-stem samples*			*Penetrometer data*			*Footprint analysis*		
	Density, ρ, g/cm³	*Porosity, n, percent*	*Depth, z, cm (a)*	*Density, ρ, g/cm³*	*Porosity, n, percent*	*Depth, z, cm (a)*	*Density, ρ, g/cm³*	*Porosity, n, percent*	*Depth, z, cm (a)*	*Density, ρ, g/cm³*	*Porosity, n, percent*	*Depth, z, cm (a)*
LM area										1.73	43.1	0 to 10
Station 10	1.47	52	0 to 32				2.04	33	0 to 8	1.67	45.2	0 to 10
(between LM	1.72	43.5	32 to 65				1.97	35.5	0 to 25			
and ALSEP)							1.97	35.5	0 to 25			
							1.68	45	0 to 5			
							1.71	44	0 to 5			
Station 10'	1.48	51.5	0 to 28									
(between LM	1.63	46.5	29 to 63									
and ALSEP)												
ALSEP				1.46	52							
				1.43	53							
				1.56	49	0 to 223						
				1.66	45.5							
				1.75	42.5							
Station 1										1.69	44.8	0 to 10
Station 4	1.39	53.5	0 to 32				1.89	38	0 to 20	1.69	44.8	0 to 10
	1.66	45.5	32 to 66				1.77	42	0 to 25			
							1.87	39	0 to 25			
Station 8	1.59	48	0 to 27							1.68	45.0	0 to 10
Station 11										1.73	43.7	0 to 10

[a]Range for average porosities and densities indicated.

penetration-resistance curves for cones of two sizes (tests 1 and 2 at station 4 and tests 1 and 2 at station 10), a unique solution for c and ϕ is possible only in special cases. One such case is that of test 1 at station 4 (fig. 8-9(a)), which indicates relatively homogeneous soil with depth. For this case, application of equation (8-1) to the penetration resistance at two depths is possible, giving a simultaneous solution for c and ϕ. In most instances, however, results are presented in the form of plots of cohesion as a function of the friction angle required to give the measured penetration resistance for a given penetration depth. A soil-density value of 1.7 g/cm^3 has been assumed for the computations. The results are insensitive to the value assumed.

Station 4.–Strength parameters have been calculated for test 1 (index 5), performed uphill from the Rover, for the depth range of 10 to 20 cm, based on the assumption that the soil is homogeneous between these depths. The values obtained are 0.6 kN/m^2 and 46.5° for the c and ϕ, respectively. These values compare with c = 1.0 kN/m^2 and ϕ = 46° at a depth of 6 cm in the mare region (Hadley Plains) of the Apollo 15 site. Densities (based on cone-penetration-resistance gradient) at the two locations were almost the same: 1.97 g/cm^3 at the Apollo 15 location and 1.89 g/cm^3 at the location of test 1 at station 4. No evidence exists that grain-size distributions were significantly different at the two sites. Thus, the lower cohesion at the Apollo 16 station 4 location may reflect a different chemical and mineralogical composition for the soil at the site of test 1 on Stone Mountain than for the soil on the Hadley Plains.

Combinations of cohesion and friction angle that would account for measured values of penetration resistance for tests 2, 3, and 4 (indexes 6, 7, and 8,

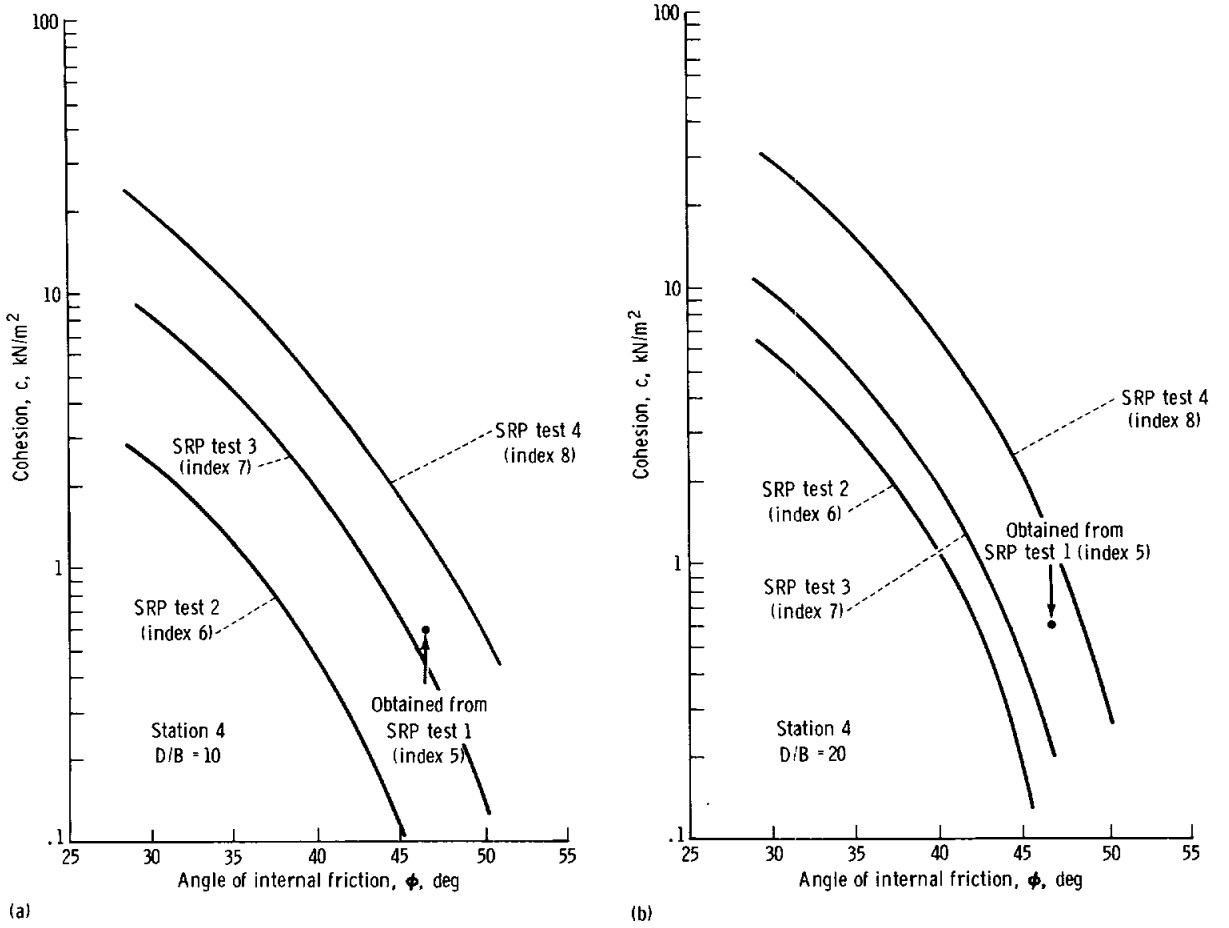


FIGURE 8-20.–Relationships of cohesion as a function of friction angle required to develop measured penetration resistances at station 4. (a) Depth of 12.8 cm. (b) Depth of 25.6 cm.

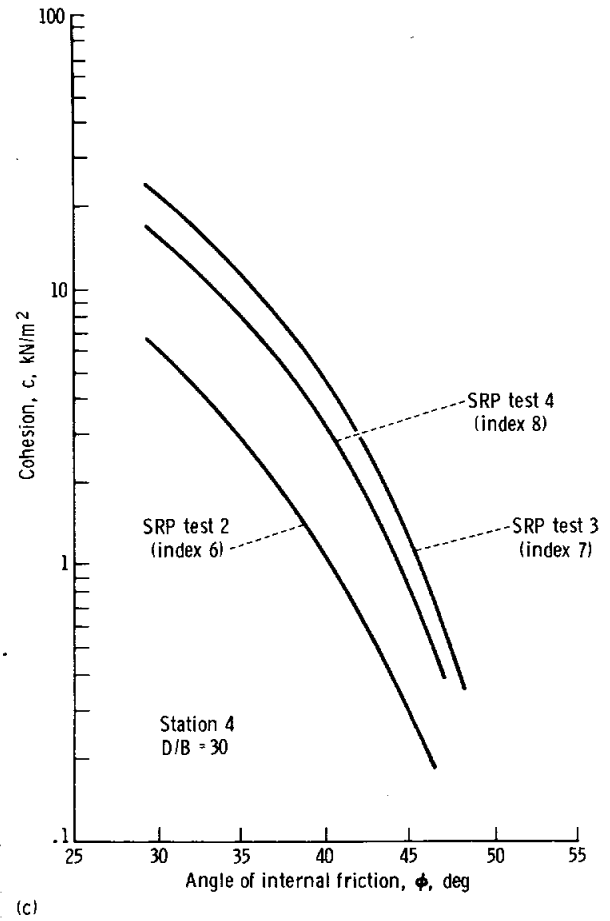


FIGURE 8-20.–Concluded. (c) Depth of 37.4 cm.

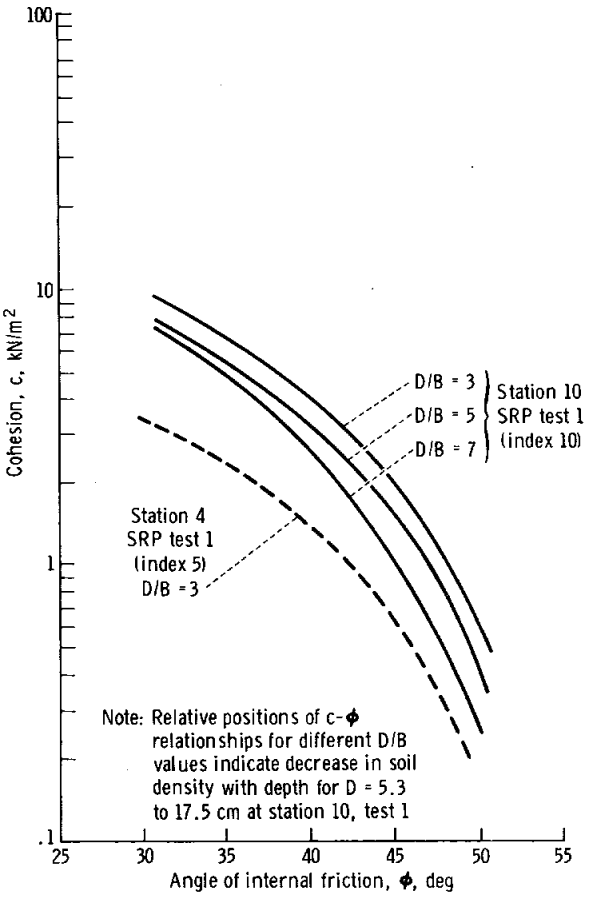


FIGURE 8-21.–Relationships of cohesion as a function of friction angle required to develop measured penetration resistances at station 10, test 1.

respectively) at station 4 are shown in figure 8-20. Relationships are shown for values of the ratio of depth to cone-base diameter (D/B) of 10, 20, and 30. These relationships are for actual depths of 12.8, 25.6, and 37.4 cm, respectively. A point is given on figures 8-20(a) and 8-20(b) to show the strength parameters for test 1 at depths of 10 and 20 cm.

A large difference exists in soil strength within the localized area of station 4. This variability is perhaps expected in view of the irregular sloping topography and relative abundance of large blocks on the surface (fig. 8-7(a)). However, low- and high-strength areas at depth are not readily discernible by observation of the surface or even on the basis of footprints. Thus, any generalizations concerning specific values of soil strength on sloping terrain would appear unwise, and each location should be investigated separately.

Station 10.–Shown in figure 8-21 are the c-ϕ relationships for the station 10 soil at the location of cone-penetration test 1 (index 10) for depths of 5.3 to 17.5 cm. These relationships indicate that soil strength (and probably density) decreases with depth. For a homogeneous soil deposit, a strength increase with depth would be expected.

Comparison between the strength characteristics for test 1 at station 4 and those of test 1 at station 10 (fig. 8-21), both determined by using the 3.22-cm^2 cone, shows that the soil at station 10 is considerably stronger at a depth of 6 cm.

Data from tests 2, 3, and 4 at station 10 (indexes 11, 12, and 13, respectively) indicate that strength varies only slightly between test locations for depths of 12.8 and 25.6 cm (fig. 8-22). Figure 8-10

shows, however, that the soil below a depth of 30 cm at the test 4 location does differ from that at the sites of tests 2 and 3.

The penetration-resistance data for tests 2 and 3 have been analyzed for specific values of c and ϕ (simultaneous solution of equation (8-2)), assuming homogeneous soil conditions between depths of 12.8 and 25.6 cm. Values obtained are given in table 8-VII, where values for test 1 at station 4 are also listed. These comparisons show comparable strengths and densities (based on the gradient of the curve for penetration resistance as a function of depth) for the three locations. An additional value of cohesion is given in table 8-VII, corresponding to that required to prevent collapse of the drill-stem hole at the ALSEP site, which stayed open to a depth of 2.18 m. The method of analysis (ref. 8-3) can be used to determine the cohesion needed to maintain an elastic state of stress in the soil around an open hole. For a Poisson ratio of 0.33, a soil density of 1.8 g/cm^3, and a friction angle of 46.5°, the calculated value of cohesion is 1.3 kN/m^2 at the bottom of a 2.18-m hole. This value of cohesion is at the upper limit of the values presented herein. However, the actual value of cohesion required to prevent collapse of the borehole could be much lower if plastic yielding of the hole occurs, as noted in reference 8-3.

The range in c-ϕ relationships for all tests at station 10 is compared with that at station 4 in figure 8-23. The much greater soil variability at station 4 is evident. Although strength variability appears to be less on plains than on slopes, no general conclusion is possible concerning whether the soil on slopes is weaker or stronger than that on the flat areas.

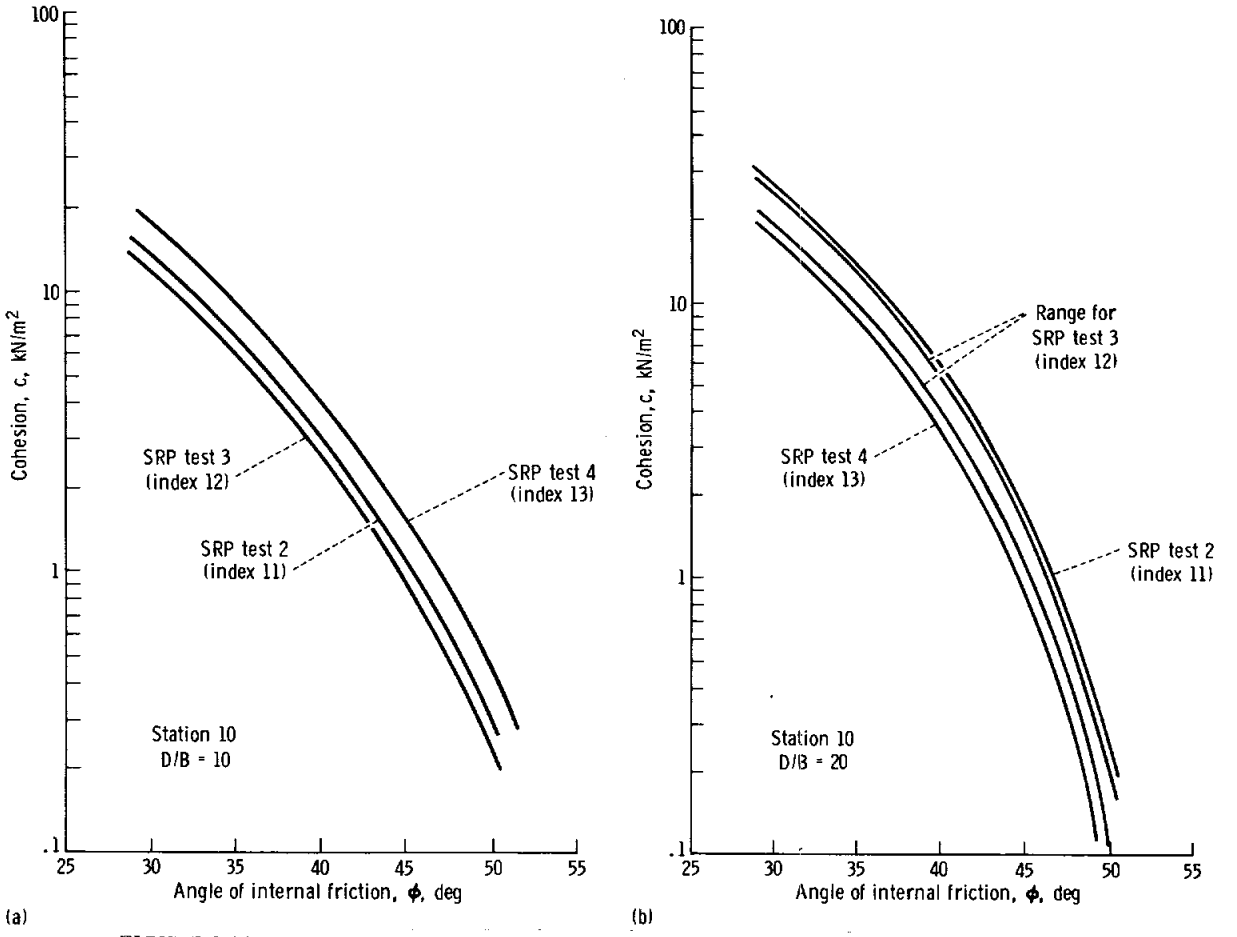


FIGURE 8-22.–Relationships of cohesion as a function of friction angle required to develop measured penetration resistances at station 10, tests 2, 3, and 4. (a) Depth of 12.8 cm. (b) Depth of 25.6 cm.

Preliminary analysis of the plate-load-test data, tests 6 and 7 at station 10 (fig. 8-11), indicates that strength and density are low at the surface but increase rapidly with depth.

TABLE 8-VII.–Strength Parameters at Three Locations

Station	*Test no.*	*Index no.*	*Cohesion, c, kN/m²*	*Friction angle, ϕ, deg*	*Density, ρ, g/cm³*
4	1	5	0.60	46.5	1.89
10	2	11	.37	49.5	1.96
10	3	12	.25 to .60	50 to 47	1.93
ALSEP	–	–	[a]1.3	[b]46.5	[c]1.75

[a]Based on open drill-hole analysis for a depth of 2.18 m.
[b]Assumed.
[c]Drill-stem sample.

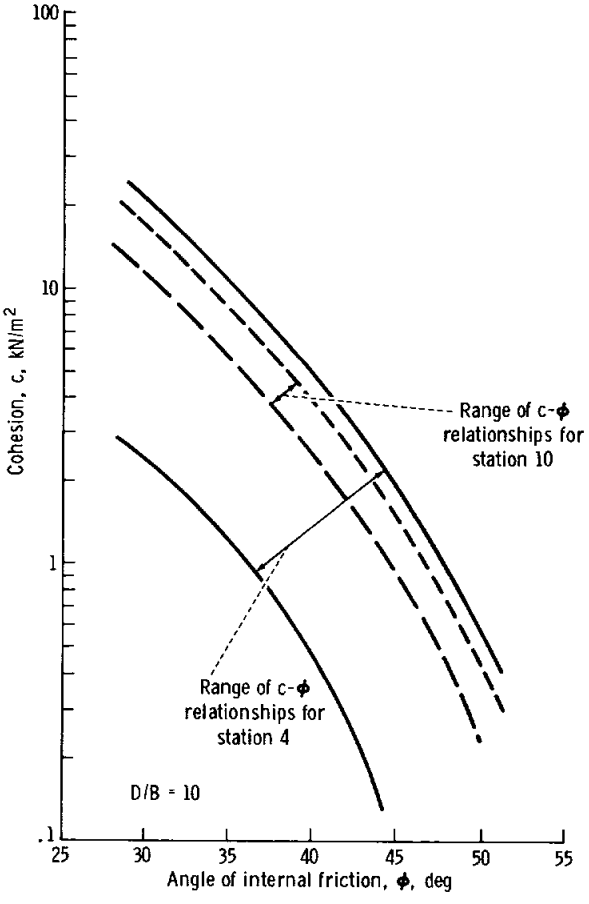


FIGURE 8-23.–Comparison of strength-parameter ranges, stations 4 and 10.

Soil Observations During LM Descent and Landing

During the final stages of descent, the LM crewmen reported the first signs of blowing dust between altitudes of 26 and 16 m above the lunar surface. However, the crewmen also indicated that the surface was clearly distinguishable all the way to touchdown and that no visibility difficulties were caused by the blowing dust. Examination of the descent movie confirms these comments. Indeed, blowing dust during the Apollo 16 landing seems to have caused the least visibility problem of all the Apollo LM landings to date.

As noted previously (ref. 8-3), the appearance of the moving dust sheet, caused by the interaction of the descent engine with the granular lunar surface, is a complex phenomenon. It depends on the small-scale nature of the surface, on the engine thrust, probably on the rate and angle of descent, on the viewer's location, and on the Sun angle. Not enough is yet known about the detailed structure of the lunar-surface material to determine if it varies significantly from site to site, so the effect of this factor cannot be assessed. Because the landing was delayed beyond the planned time, the Sun elevation was higher than on previous missions, and this may have contributed substantially to the improved viewing conditions.

Although detailed evaluation of the descent trajectory has not yet been completed, it is apparent that the vertical descent rate was somewhat higher than that of previous missions. From an altitude of 65 m to contact with the lunar surface, the elapsed time was less than 50 sec. The average descent velocity from an altitude of 65 to 26 m was approximately 1.7 m/sec; from 26 m to contact, the average velocity was approximately 1 m/sec. For the final 30 m of descent, this vertical velocity component was twice as great as that of the Apollo 15 landing, during which the last 18 m of descent were accomplished with a surface visibility of zero.

The actual landing was relatively soft with little or no stroking of the shock absorbers. Penetration of the footpads into the lunar surface was minimal, with the greatest penetration of 8 to 10 cm indicated for the −Y footpad on which the cosmic ray detector was mounted. The bottom panel of the detector was the only panel to which a small quantity of lunar dust adhered. The dust, presumably deposited on the panel during landing, is apparent to a height of

approximately 20 to 25 cm above the base of the pad or 10 to 15 cm above the lunar surface in the postlanding position of the footpad.

In contrast to the Apollo 15 landing, the descent-engine bell of the Apollo 16 LM did not appear to contact the lunar surface; the postlanding clearance was about 20 cm.

Slope Stability

Indications of downslope movement of surficial material can be seen in photographs of North Ray Crater as viewed from station 11. Figures 8-24 and 8-25 (photographs taken using the 60- and 500-mm lenses, respectively) show portions of the North Ray Crater wall. Maximum slope angles may be as great as 55° in rocky areas, although the slopes are probably not steeper than 40° to 45° in areas covered by what appears to be loose soil.

Distinct scarps and depressions where shallow slides have occurred in the upper crater walls are evident in figure 8-24. Other indications of downslope movement, shown in figures 8-24 and 8-25, include small gullies, a low crater density, and soil fillets on the uphill side of many rocks.

Preliminary studies of these features and other evidences of soil movement visible on other photographs, including fillets at the bases of large rocks, are in progress. The following preliminary observations have been made.

(1) If the slope angles are flatter than 45° where downslope movement of soil appears to be taking place, then the strength of the soil near the surface on these slopes must be less than that given by the parameters in table 8-VII.

(2) The steepest slopes in the north wall of North Ray Crater are rocky and may, in fact, be outcrops of a bench-forming rocky layer.

(3) The soil in fillets is probably fine grained and free of coarse particles.

(4) A sorting and segregation process appears to accompany the downslope movement of material. Talus slopes of both soil and coarser material have been identified (AS16-105-17228).

Further study of questions relating to slope stability, downslope movement of soil, and the properties of the soil on slopes is needed before definitive conclusions can be made.

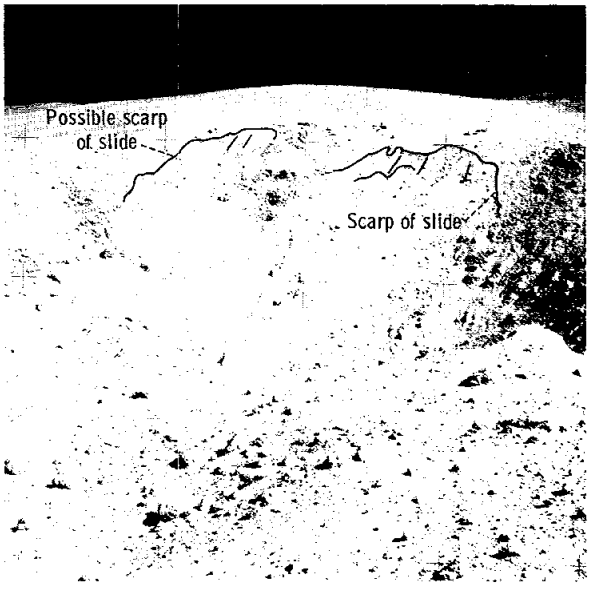


FIGURE 8-24.–View across North Ray Crater to the north showing slide areas near the top of the crater wall (AS16-106-17241).

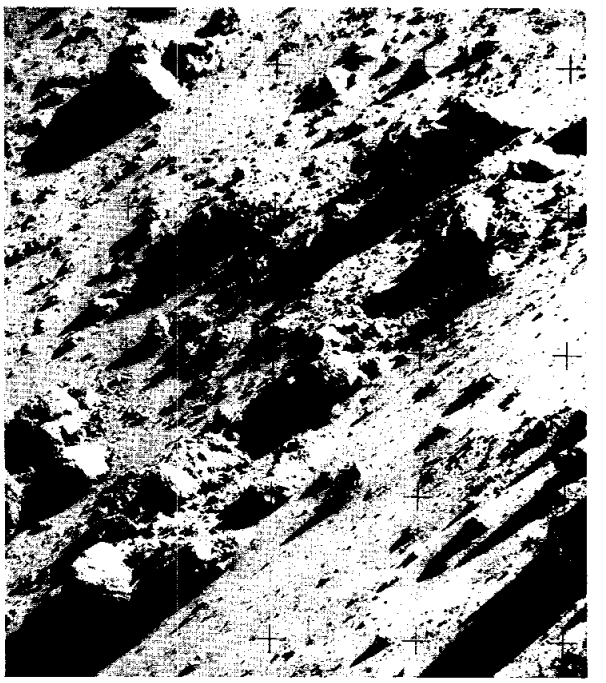


FIGURE 8-25.–A 500-mm photograph of the slope at North Ray Crater (AS16-105-17175).

Drillability of the Lunar Regolith

One probe hole for the heat-flow experiment was drilled to a depth of 2.34 ± 0.05 m in the ALSEP area. For premission drilling simulations, a crushed basalt was used as the drilling medium, leading to predicted rates shown in figure 8-26. The drilling time was 2.3 min, which is less by approximately a factor of 4 than the time obtained from figure 8-26, based on soil conditions at the Apollo 15 drilling site. The Apollo 16 drilling rate corresponded to that predicted for a typical mare plains site.

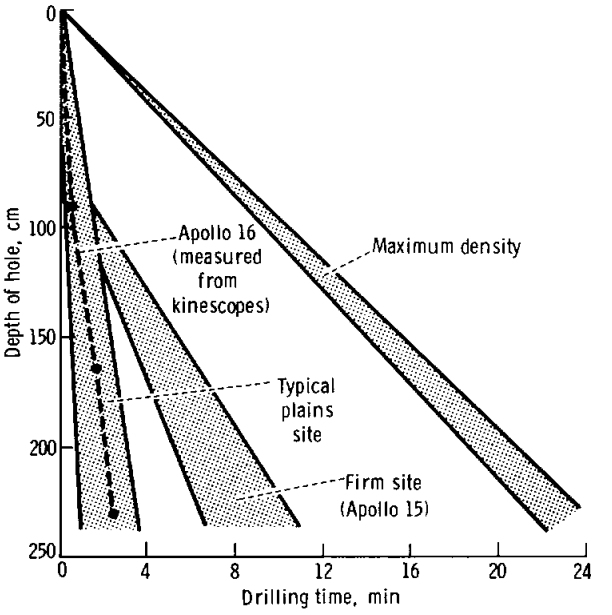


FIGURE 8-26.–Predicted compared to actual drilling time for heat-flow borestem.

Elastic Moduli and Seismic-Wave Velocities

From measurements on terrestrial sands and silts, it is known (ref. 8-13) that shear modulus G and effective confining pressure σ' are related according to

$$G = K(\sigma')^{1/2} \tag{8-6}$$

where K is a constant dependent on porosity. According to elastic theory, the shear-wave velocity v_s and the compression-wave velocity v_p are related to the shear modulus by

$$v_s = \sqrt{\frac{G}{\rho}} \tag{8-7}$$

$$v_p = \sqrt{\frac{\lambda + 2G}{\rho}} \tag{8-8}$$

where

ρ = density of the medium
λ = Lame constant = $2\upsilon G/(1 - 2\upsilon)$
υ = Poisson ratio

The profiles were obtained for the shear- and compression-wave velocities as a function of depth (fig. 8-27) with (1) the aid of the relationships between K, porosity, and shear strain given in reference 8-13; (2) an assumed shear strain of 10^{-4} percent for lunar seismic waves; (3) density profiles as shown in figure 8-16; (4) an at-rest lateral Earth pressure coefficient of 0.5; and (5) an assumed Poisson ratio of 0.28. The predicted low velocities in the upper few meters are consistent with the values measured in the active seismic experiment (ASE) at the Apollo 14 Fra Mauro landing site (ref. 8-14). These low velocities result from the low confining

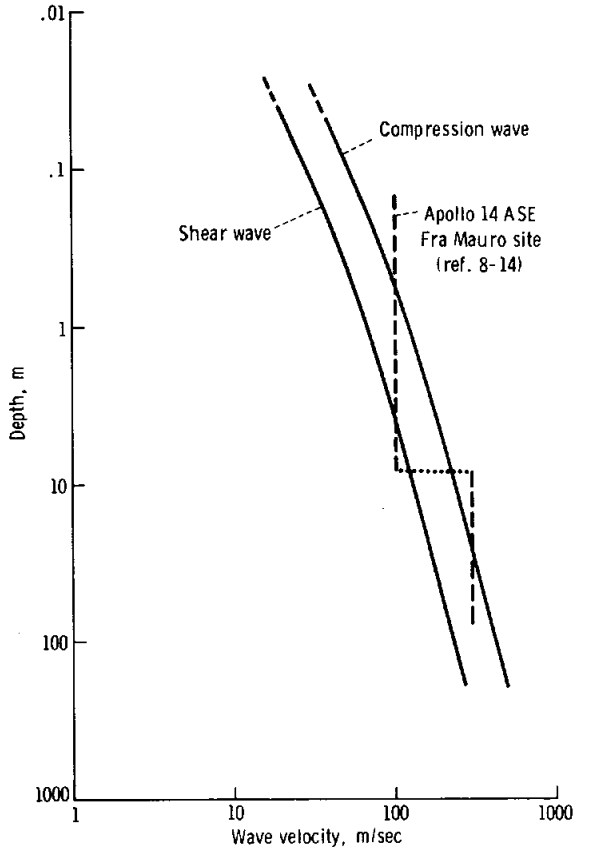


FIGURE 8-27.–Estimated seismic-wave velocities as a function of depth below the lunar surface.

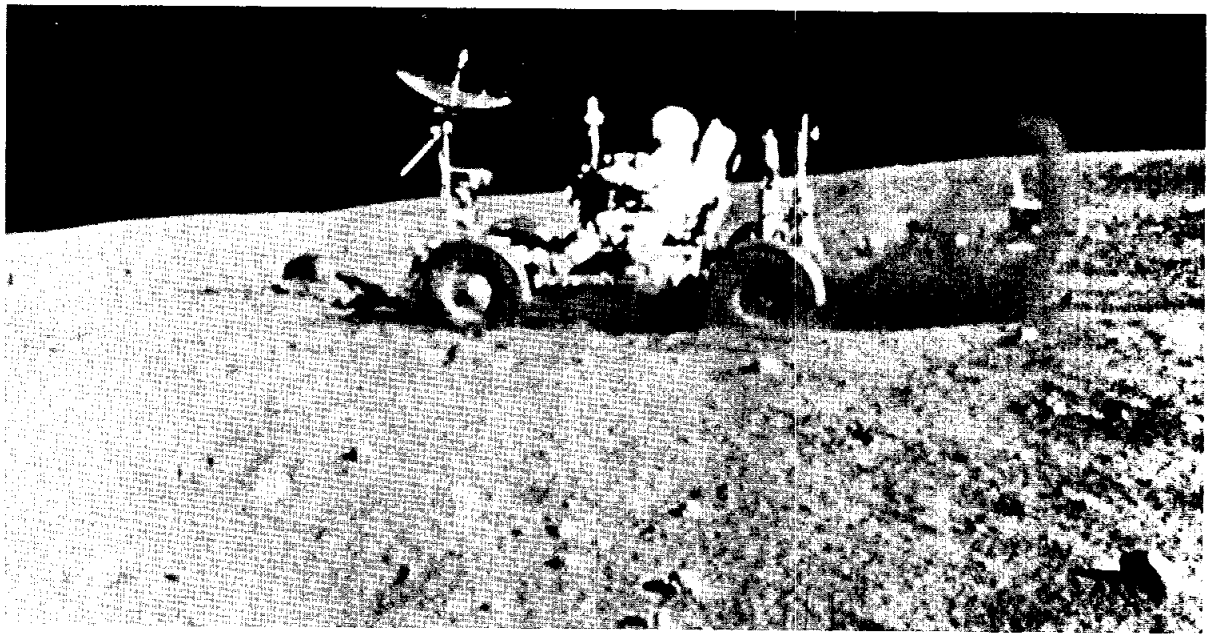


FIGURE 8-28.–Rover during Grand Prix. The "rooster tail" is indicative of a fine-grained, nearly cohesionless surficial soil (AS16-72-1718).

pressure σ' (which is a consequence of the low lunar-gravity field) rather than from unusual soil properties.

Soil and Rover Interaction

No direct quantitative information exists regarding the interaction of the Rover with the lunar surface while the vehicle was in motion. However, some information concerning the interaction of the vehicle with the lunar surface can be extracted from (1) crew descriptions; (2) photographic coverage of the extravehicular activities including 16-mm motion pictures taken with the data acquisition camera during the Grand Prix (fig. 8-28) and during parts of the Rover traverses while the vehicle was in motion; and (3) real-time read-outs from the Rover ampere-hour integrators and limited data from the navigation system components.

On the basis of crew observations and close examination of photographs of Rover tracks obtained throughout the mission, it appears that the vehicle developed excellent flotation and that the interaction between the wheels and the soil did not extend to any appreciable depth below the lunar surface. The observed wheel tracks ranged in depth from almost 0 to approximately 5 cm (at the rims of small fresh craters) with an average depth on the order of 1.25 cm. Further, the Rover wheels appear to have developed excellent traction with the lunar-surface material; in most cases, a sharp imprint of the chevron tread was clearly discernible, indicating that the surficial soil possessed some cohesion and that the amount of wheel slip was minimal.

The steepest slopes were encountered at Stone Mountain and near the edge of the rim of North Ray Crater. It appears that the Rover was operated on slopes ranging to 18°. Figure 8-3 shows such a slope at station 4. Extensive wheel-soil interaction tests performed with prototype Rover wheels on crushed-basalt lunar-soil simulants (refs. 8-15 and 8-16) indicate the maximum slope-climbing capability of the Rover to be within the slope-angle range of 19° to 23°. Further, the crew thought that, in negotiating the slope shown in figure 8-3, the Rover was approaching the limit of its slope-climbing capabilities.

In general, however, maneuvering the vehicle on slopes did not present any serious operational problems. The soil behavior appeared to reflect surficial deformation conditions and not any deep-seated soil movements. The vehicle could be

controlled more easily upslope than downslope. Some control problems were noted while driving downhill, especially at high speeds. (Maximum speed was 17 km/hr.)

Many photographs of Rover tracks were examined for variations in track depth, shape, and texture. Analysis of these tracks indicates that the regional variability in the consistency of the surficial soil throughout the Descartes site is less than that observed at the Hadley-Apennine region (Apollo 15). Accordingly, from a trafficability viewpoint, the surficial soil traversed by the Rover at the Descartes site may be considered relatively uniform on a regional scale. This uniformity does not preclude the significant local variations in soil consistency at depths greater than a few centimeters, as indicated previously from the results of core-tube, penetrometer, and deep drill tests.

Analyses of the average track depth (1.25 cm) by the methods developed by Freitag (ref. 8-17) yield an equivalent cone-penetration-resistance gradient G_p value of about 840 kN/m^2/m for the shallow depths influenced by the soil-wheel interaction. The values of the cone-penetration-resistance gradient presented in table 8-IV are somewhat greater than the derived equivalent value, but they represent soil characteristics to greater depths. Correcting for the gravity difference, the G_p value deduced from the Rover tracks corresponds to a crushed-basalt lunar-soil simulant on Earth having a porosity of approximately 41 percent. This porosity compares favorably with the porosity range (42 to 46 percent) calculated from the results of plate-load tests at station 10 (table 8-IV) and the statistical analysis of footprint depths (table 8-V).

CONCLUSIONS

The physical and mechanical properties of the soil at the Apollo 16 landing site are generally similar to those of the soils encountered at the previous Apollo sites. Data obtained using the self-recording penetrometer have provided a basis for quantitative study of stratigraphy, density, and strength characteristics. These results, in conjunction with crew observations, photography, and soil samples (particularly the core-tube samples), have been used to develop the following preliminary conclusions.

(1) Soil cover appeared to blanket all areas visited or observed at the Descartes landing area.

(2) Soil properties are variable on regional and local (1 m) scales.

(3) Visibility degradation by blowing dust was less during the Apollo 16 LM descent than during previous missions, probably due to a faster descent rate and a higher Sun angle rather than to different soil conditions.

(4) The grain-size distributions of soil samples from the Descartes area are comparable to those of samples from other areas of the Moon, although distributions for most Descartes samples fall toward the coarser edge of a composite distribution.

(5) The drive-tube samples indicate that soil density increases with depth, but the overall range of densities (1.40 to 1.80 g/cm^3) is slightly less than the range (1.36 to 1.91 g/cm^3) found for Apollo 15 core-tube samples.

(6) South Ray Crater material appears to cover the station 4 area to depths of 20 to 50 cm. Descartes Formation material may have been found at greater depths.

(7) Density distributions with depth for the Apollo 16 deep drill-stem samples are distinctly different from those of Apollo 15 and suggest that the modes of soil deposition at the two sites may have been different.

(8) Densities deduced from penetration-test data are slightly greater than but comparable to those obtained from core-tube samples.

(9) Statistical analysis of footprint depths indicates that for the soil near the surface (to depths of approximately 10 cm):

(a) Average porosity does not vary much for the different Apollo sites, although the average value is 45 percent at the Apollo 16 site as compared with 43.3 percent for each of the four previous Apollo sites.

(b) Average porosity on crater rims is somewhat greater (46.1 percent).

(10) At station 4 (Stone Mountain), the values for soil cohesion and friction angle are deduced to be 0.6 kN/m^2 and 46.5°, respectively.

(11) Variations in soil strength are great within short distances at station 4 on Stone Mountain. Because these variations appear to bear little relationship to local slope or surface appearance, generalizations concerning the strength of soils on sloping terrain are not possible.

(12) Less local variation in strength is evident at station 10 on the Cayley Plains than at station 4 on Stone Mountain.

(13) No general conclusion is possible concerning whether the soil on slopes is weaker or stronger than that on flat areas.

(14) Evidence exists for metastable slopes on the inner walls of North Ray Crater.

(15) The relatively low seismic-wave velocities for the upper few meters of the lunar surface measured in the active seismic experiment can be accounted for in terms of the low confining pressure resulting from the low lunar-gravity field.

(16) The Rover performed quite satisfactorily in all maneuvers attempted at the Descartes site. Lunar-soil parameters deduced from observed wheel-soil interactions agree well with those obtained by other methods for shallow depths.

It is expected that information on soil properties obtained thus far will be useful in the future for several types of soil-property-dependent lunar studies.

SUMMARY

The purpose of the soil mechanics experiment is to determine the physical characteristics of the lunar soil to depths of several decimeters and their variations in lateral directions, on slopes, and between different regions of the Moon. Soil mechanics data were derived from television, surface photography, core-tube samples, and measurements using the SRP. Simulation studies and soil mechanics theories have been used to deduce information concerning soil density and strength characteristics and their variations from place to place.

Soil properties are variable on regional and local (1 m) scales in the Descartes area although, in general, the soil grain-size distributions and densities are comparable to those of samples from other areas of the Moon. The overall density range was from about 1.4 to 1.8 g/cm^3. The average porosity of the upper 10 cm of soil at the Descartes site is estimated at 45 percent as compared with 43.3 percent for each of the four previous Apollo sites.

At one location on Stone Mountain, the values for soil cohesion and friction angle are deduced to be 0.6 kN/m^2 and 46.5°, respectively, although variations in strength are great within short distances at this location. These variations bear little relationship to local slope or surface appearance; thus, generalizations concerning the strength of soils on sloping terrain are not possible. No general conclusion is possible concerning whether the soil on slopes is weaker or stronger than that on flat areas, although the soil strength in level areas seems less variable. Some evidence exists for soil instability on the inner walls of North Ray Crater. Based on the known behavior of terrestrial soils of comparable gradation and density to that on the Moon, seismic P-wave velocities on the order of 100 m/sec are to be expected for the upper few meters of the lunar surface, increasing to about 300 m/sec at depths of 50 to 80 meters.

APPENDIX

BEARING CAPACITY FACTORS FOR CONE-PENETRATION RESISTANCE

From the results of model tests (ref. 8-10), it has been found that a failure surface as shown in figure 8-2 represents closely the actual failure surface associated with wedge penetration.

The angle γ, which defines the plane shear zone OAC, depends on the penetrometer-to-soil friction angle δ and soil friction angle ϕ and can be determined from

$$\tan\delta[1 + \sin\phi \sin(2\gamma - \phi)] - \sin\phi\cos(2\gamma - \phi) = 0 \qquad \text{(A-1)}$$

Values of γ determined from equation (A-1) for different values of ϕ and δ/ϕ are presented in reference 8-10. A logarithmic spiral bounds a radial shear zone to a point of vertical tangency at point E, above which the failure surface rises vertically to the ground surface. For large depths of penetration, such as shown in figure 8-2, the angle β, which locates point E, equals ϕ. For shallow penetration depths, the logarithmic spiral breaks out at ground surface before vertical tangency is reached, and the corresponding value of β can be determined iteratively.

Equilibrium analysis of the failure zone shown in figure 8-2 leads to

$$q_f = cN_c\xi_c + B\gamma_s N_{\gamma q}\xi_{\gamma q} \qquad \text{(A-2)}$$

where

q_f = ultimate unit tip resistance
c = unit cohesion
B = penetrometer base width or diameter
γ_s = unit weight of soil
N_c, $N_{\gamma q}$ = bearing capacity factors
ξ_c, $\xi_{\gamma q}$ = shape factors

For wedges, the bearing capacity factors N_c and $N_{\gamma q}$ are given in reference 8-10 as

$$N_c = f_1\left(\frac{D}{B}, \phi, \alpha, \frac{\delta}{\phi}\right) = \frac{1 + \sin\phi \sin(2\gamma - \phi)}{\sin\phi \cos\phi} \exp\left(2\theta_0 \tan\phi\right) - \frac{1}{\tan\phi} + \frac{\cos(2\gamma - \phi)\tan\psi}{\cos\phi} \exp\left(2\theta_0 \tan\phi\right) \qquad \text{(A-3)}$$

$$N_{\gamma q} = f_2\left(\frac{D}{B}, \phi, \alpha, \frac{\delta}{\phi}\right) = \frac{\cos(\psi - \delta)}{\cos\delta} \frac{[1 + \sin\phi \sin(2\gamma - \phi)]}{\cos\phi \cos(\gamma - \phi)} \left[\frac{1}{4} \frac{\cos^2(\gamma - \phi)}{\cos^2\psi \cos^2\phi} \times I_\theta + \frac{3}{4} \frac{\cos(\gamma - \phi)}{\cos\psi \cos\phi} \times \cos^2\beta \exp\left(2\theta_0 \tan\phi\right)\left(m - \frac{2}{3}m'\right) - (1 - \sin\phi) \frac{\cos\psi \cos\phi}{\cos(\gamma - \phi)} (m - m')^2 (m + 2m') + K \frac{\cos\psi \cos\phi}{\cos(\gamma - \phi)} m^3\right] - \frac{\tan\psi}{4} \qquad \text{(A-4)}$$

where

D = depth of penetrometer base below ground surface
ϕ = soil friction angle
$\psi = 90° - \alpha$
α = half the wedge apex angle
δ = soil-to-penetrometer friction angle
γ = the topmost angle of the plane shear zone
$\theta_0 = 180° - (\gamma + \psi) + \beta$
K = lateral Earth-pressure coefficient
m = D/B (relative depth)
$m' = D_\beta/B = 1/2 \sin\beta \cos(\gamma - \phi)/\cos\psi \cos\phi \exp(\theta_0 \tan\phi)$

D_β = vertical position of point E on the failure surface above base level (see fig. 8-2)

and $I_\theta = \frac{1}{1 + 9\tan^2\phi} \{3 \tan\phi [\exp(3\theta_0 \tan\phi) \cos\beta - \cos(\theta_0 - \beta)] + [\exp(3\theta_0 \tan\phi) \sin\beta + \sin(\theta_0 - \beta)]\}$ (A-5)

The bearing capacity factors for cones can be determined by using the bearing capacity factors for wedges modified by the shape factors computed according to equations (8-2) and (8-3).

REFERENCES

8-1. Mitchell, J. K.; Scott, R. F.; Houston, W. N.; Costes, N. C.; et al.: Mechanical Properties of Lunar Soil: Density, Porosity, Cohesion, and Angle of Internal Friction. Proceedings of the Third Lunar Science Conference, vol. 3, David R. Criswell, ed., MIT Press (Cambridge, Mass.), 1972.

8-2. Houston, W. N.; Hovland, H. J.; Mitchell, J. K.; and Namiq, L. I.: Lunar Soil Porosity and Its Variation as Estimated From Footprints and Boulder Tracks. Proceedings of the Third Lunar Science Conference, vol. 3, David R. Criswell, ed., MIT Press (Cambridge, Mass.), 1972.

8-3. Mitchell, J. K.; Bromwell, L. G.; Carrier, W. D., III; Costes, N. C.; et al.: Soil-Mechanics Experiment. Sec. 7 of Apollo 15 Preliminary Science Report. NASA SP-289, 1972.

8-4. Leonovich, A. K.; Gromov, V. V.; Rybakov, A. V.; Petrov, V. K.; et al.: Studies of Lunar Ground Mechanical Properties With the Self-Propelled "Lunokhod-1." Ch. 8 of Peredvizhnaya Laboratoriya na Luna-Lunokhod-1. (Translation by Joint Publ. Res. Service, JPRS 54525, 1971, pp. 120-135.)

8-5. Houston, W. N.; and Namiq, L. I.: Penetration Resistance of Lunar Soils. J. Terramechanics, vol. 8, no. 1, 1971, pp. 59-69.

8-6. Costes, N. C.; Cohron, G. T.; and Moss, D. C.: Cone Penetration Resistance Test – An Approach to Evaluating the In-Place Strength and Packing Characteristics of Lunar Soils. Proceedings of the Second Lunar Science Conference, vol. 3, A. A. Levinson, ed., MIT Press (Cambridge, Mass.), 1971, pp. 1973-1987.

8-7. Houston, W. N.; and Mitchell, J. K.: Lunar Core Tube Sampling. Proceedings of the Second Lunar Science Conference, vol. 3, A. A. Levinson, ed., MIT Press (Cambridge, Mass.), 1971, pp. 1953-1958.

8-8. Carrier, W. D., III; Johnson, S. W.; Werner, R. A.; and Schmidt, R.: Disturbance in Samples Recovered with the Apollo Core Tubes. Proceedings of the Second Lunar Science Conference, vol. 3, A. A. Levinson, ed., MIT Press (Cambridge, Mass.), 1971, pp. 1959-1972.

8-9. Scott, R. F.: Principles of Soil Mechanics. Addison-Wesley (Reading, Mass.), 1963.

8-10. Durgunoglu, H. T.: Static Penetration Resistance of Soils. Ph. D. Dissertation, Univ. of Calif. at Berkeley, 1972.

8-11. Gast, P. W.; Haskin, L. A.; and Wasserburg, G. J.: Introduction. Earth Planet. Sci. Letters, vol. 13, no. 2, Jan. 1972, pp. 223-224.

8-12. Namiq, L. I.: Stress-Deformation Study of a Simulated Lunar Soil. Ph. D. Dissertation, Univ. of Calif. at Berkeley, 1970.

8-13. Seed, H. B.; and Idriss, I. M.: Soil Moduli and Damping Factors for Dynamic Response Analyses. Rept. EERC 70-10, Earthquake Engineering Res. Center, Univ. of Calif. at Berkeley, 1970.

8-14. Kovach, Robert L.; Watkins, Joel S.; and Landers, Tom: Active Seismic Experiment. Sec. 7 of Apollo 14 Preliminary Science Report. NASA SP-272, 1971, pp. 163-174.

8-15. Green, A. J.; and Melzer, K. J.: Performance of the Boeing LRV Wheels in a Lunar Soil Simulant: Effect of Wheel Design and Soil. Tech. Rept. M-71-10, Rept. 1, USAE WES, Vicksburg, Miss., 1971.

8-16. Melzer, K. J.: Performance of the Boeing LRV Wheels in a Lunar Soil Simulant: Effect of Speed, Wheel Load, and Soil. Tech. Rept. M-71-10, Rept. 2, USAE WES, Vicksburg, Miss., 1971.

8-17. Freitag, Dean R.: A Dimensional Analysis of the Performance of Pneumatic Tires on Soft Soils. Tech. Rept. 3-688, USAE WES, Vicksburg, Miss., 1965.

9. Passive Seismic Experiment

Gary V. Latham, [a†] *Maurice Ewing,* [a] *Frank Press,* [b]
George Sutton, [c] *James Dorman,* [a] *Yosio Nakamura,* [d] *Nafi Toksoz,* [b]
David Lammlein, [e] *and Fred Duennebier* [c]

With the successful installation of a geophysical station at the Descartes landing site of the Apollo 16 mission, a four-station lunar seismic network was established. This network spans the near side of the Moon in an approximate equilateral triangle with 1000-km spacing between stations. Continued operation of the Apollo seismic network over a period of several years will provide the data necessary to deduce the gross structure and dynamics of the lunar interior and the present flux of meteoroids in the vicinity of the Earth. This report describes progress toward these objectives at the end of the first 45-day period following activation of the Apollo 16 station.

The Apollo 16 station appears to be the most sensitive of the four lunar seismograph stations. Based on the initial 45-day period of operation, seismic events are recorded at the Apollo 16 station at an average rate of 10 000/yr. Most of these events are moonquakes. This event rate compares with annual rates of 2000/yr at the Apollo 14 station and 700/yr at the Apollo 12 and 15 stations. During the 45-day real-time seismic observation of the Apollo 16 mission, the Mission Control Center was equipped for simultaneous recording of the data from two lunar stations, as in previous missions. The four seismometers of the Apollo 16 station recorded data continuously on four drums, and data from the Apollo 12, 14, or 15 stations were recorded alternately on another four drums, making possible the comparison of the data from the Apollo 16 station with the simultaneous data from one of the three other stations. Comparison of simultaneous data from all four stations can be made by processing the magnetic tapes recorded at the receiving stations of the Manned Space Flight Network. This was done for selected events during the first 45 days after deployment. The signal character and background noise at each station have distinctive characteristics apparently related to the depth and elastic properties of the regolith at each site. To explain these differences, the Apollo 16 station must have the deepest or weakest regolith, or both, according to criteria now applied. This condition also would explain the much higher sensitivity of the Apollo 16 station.

The command module pilot reported seeing a bright flash at 21:03:40 Greenwich mean time (G.m.t.), April 21, 1972, on the lunar far side. If this flash were generated by a meteoroid impact, the mass of the meteoroid must have been less than approximately 10 kg because no seismic signal was detected at that time.

The most important event of the Apollo 16 mission report period for the passive seismic experiment (PSE) was the recording of a large meteoroid impact on May 13, 1972. The impact occurred approximately 145 km north of the Apollo 14 station and was well recorded by all four stations of the Apollo seismic network. The mass of the meteoroid is estimated at approximately 1100 kg, the largest recorded in the 2.5 yr of observation since the installation of the Apollo 12 station. The probability of an impact of this size is estimated to be one every 10 yr for the entire Moon. Data from the impact have greatly improved man's ability to determine the structure beneath the lunar crust.

Significant progress in the measurement of meteoroid flux in near-Earth space and the delineation of active moonquake source regions has been made through this report period. It now appears that moonquakes are concentrated at great depth (800 to 1000 km) and that the apparent disparity between meteoroid flux estimates based on lunar crater counts and those from Earth-based observations can be resolved by seismic measurements in favor of the lower flux indicated by the crater-count method.

[a]The University of Texas at Galveston.

[b]Massachusetts Institute of Technology.

[c]University of Hawaii.

[d]General Dynamics.

[e]Lamont-Doherty Geological Observatory.

[†]Principal Investigator.

INSTRUMENT DESCRIPTION AND PERFORMANCE

A seismometer consists simply of a mass that is free to move in one direction and that is suspended by means of a spring (or a combination of springs and hinges) from a framework. The suspended mass is provided with damping to suppress vibrations at the natural frequency of the system. The framework rests on the lunar surface and moves with the surface. The suspended mass tends to remain fixed in space because of its own inertia, while the frame moves in relation to the mass. The resulting relative motion between the mass and the framework can be recorded and used to calculate original ground motion if the instrument constants are known.

The Apollo seismic stations consist of two main subsystems: the sensor unit and the electronics module. The sensor unit, shown schematically in figure 9-1, contains three matched long-period (LP) seismometers (with resonant periods of 15 sec) alined orthogonally to measure one vertical (Z) and two horizontal (X and Y) components of surface motion. The sensor unit also includes a single-axis short-period (SP) seismometer (with a resonant period of 1 sec) that is sensitive to vertical motion at higher frequencies. The instrument is constructed principally of beryllium and weighs 11.5 kg, including the electronics module and thermal insulation. Without insulation, the sensor unit is 23 cm in diameter and 29 cm high. The total power drain varies between 4.3 and 7.4 W.

Instrument temperature control is provided by a 6-W heater, a proportional controller, and an aluminized Mylar insulation. The insulating shroud is spread over the local surface to reduce temperature variations of the surface material.

The LP seismometer detects vibrations of the lunar surface in the frequency range from 0.004 to 2 Hz. The SP seismometer covers the band from 0.05 to 20 Hz. The LP seismometers can detect ground motions as small as 0.3 nm at maximum sensitivity in the flat-response mode (discussed in a later paragraph); the SP seismometer can detect ground motions of 0.3 nm at 1 Hz.

The LP horizontal-component (LPX and LPY) seismometers are very sensitive to tilt and must be leveled to high accuracy. In the Apollo system, the seismometers are leveled by means of a two-axis, motor-driven gimbal. A third motor adjusts the LP vertical-component (LPZ) seismometer in the vertical direction. Motor operation is controlled by command. Calibration of the complete system is accomplished by applying an accurate increment or step of current to the coil of each of the four seismometers by transmission of a command from the Earth. The current step is equivalent to a known step of ground acceleration.

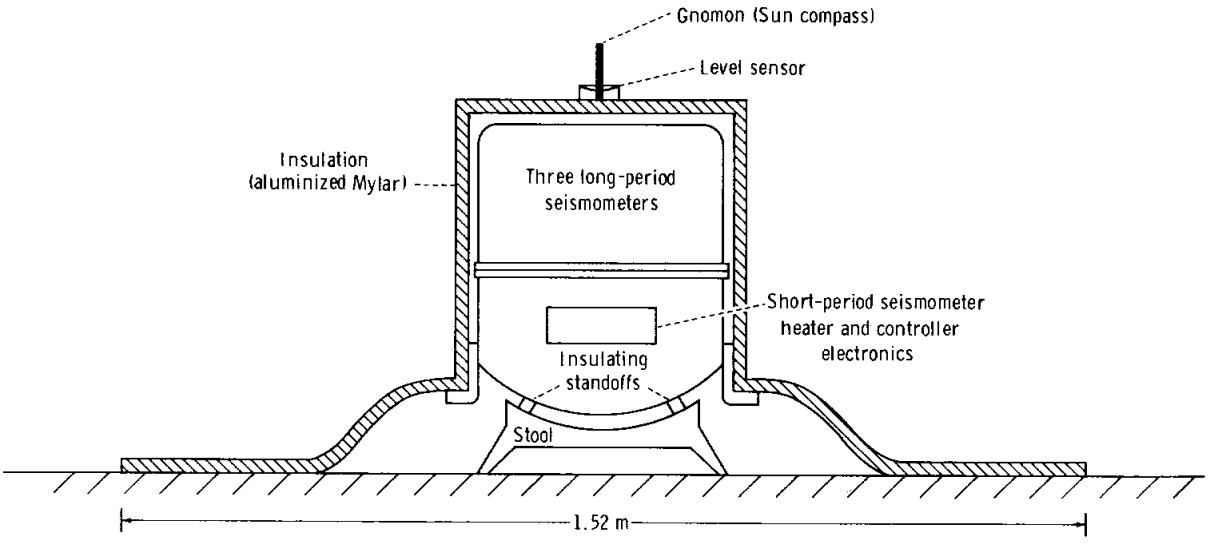


FIGURE 9-1.–Schematic diagram of PSE.

A caging system is provided to secure all critical elements of the instrument against damage during the transport and deployment phases of an Apollo mission. In the present design, a pneumatic system is used in which pressurized bellows expand to clamp fragile parts in place. Uncaging is performed on command by piercing the connecting line by means of a small explosive device.

The seismometer system is controlled from Earth by a set of 15 commands that govern functions such as speed and direction of leveling motors, instrument gain, and instrument calibration. In figure 9-2, the seismometer is shown fully deployed on the lunar surface.

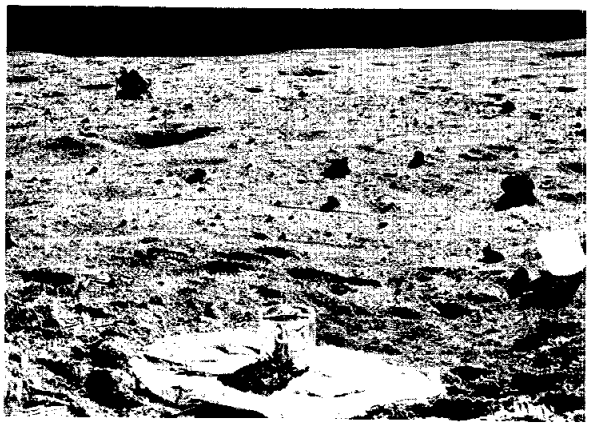


FIGURE 9-2.–Seismometer after deployment on the lunar surface (AS16-113-18360).

Two modes of operation of the LP seismometers are possible: the flat-response mode and the peaked-response mode. In the flat-response mode, the seismometers have natural periods of 15 sec. In the peaked-response mode, the seismometers act as underdamped pendulums with natural periods of 2.2 sec. Maximum sensitivity is increased by a factor of 5.6 in the peaked-response mode, but sensitivity to low-frequency signals is reduced. The response curves for both modes are shown in figure 9-3.

The PSE was deployed without difficulty 3 m southeast of the central station. Since activation, all elements of the PSE have operated as planned, with the exception of the sensor thermal control system and the occurrence of excessive noise from the SPZ seismometer at intervals that appear to correlate with the temperature cycle. The temperature of the PSE exceeded the high-limit indication (142.6° F) approximately 5 days after deployment (near lunar noon) and remained off scale high for approximately 5 days as the local Sun angle decreased. The instrument temperature reading was off scale high for 8 days during the second lunar day. The instrument temperature remained constant at the control set point throughout the lunar night.

As recorded at the previous seismic stations, episodes of seismic disturbances are observed on the LP seismometers throughout the lunar day. These disturbances are most intense near times of terminator passage and are believed to be caused by thermal contraction and expansion of the Mylar thermal shroud that blankets the sensor and the cable connecting the sensor with the central station.

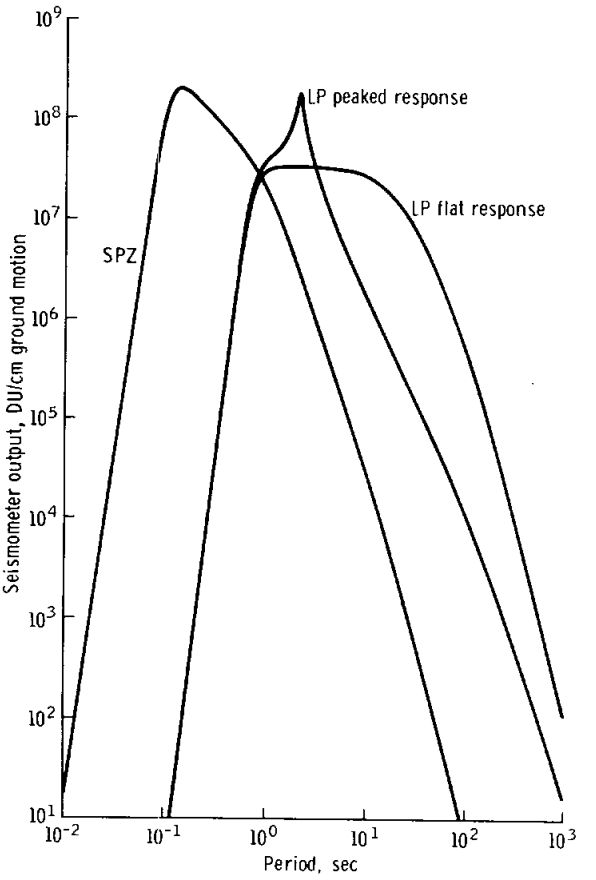


FIGURE 9-3.–Response curves for the LP and SP vertical-component seismometers. The ordinate scale is in digital units (DU)/cm ground displacement amplitude. A DU is the signal variation that corresponds to a change in the least significant bit of the 10-bit data word.

RESULTS AND DISCUSSION

The Apollo 16 PSE is a continuation of observations made during the Apollo 11 to 15 missions (refs. 9-1 to 9-13).

Seismic Signals from the Lunar Rover — Properties of the Surficial Zone

Seismic signals were detected by the SPZ seismometer whenever the lunar roving vehicle (Rover) was in motion along the entire length of its traverse (maximum range = 4.3 km). These signals show two particularly interesting properties that are not explainable as resulting from propagation of seismic waves in a homogeneous medium. First, starting and stopping the Rover produced only gradual buildup and decay (rather than abrupt changes) of the signal intensity. Second, the amplitude of the signals observed at a given range was smaller when the Rover was moving toward the seismometer than when it was moving away from the seismometer by a factor of as much as 3, depending upon range.

These properties are readily explained as resulting from intensive scattering of seismic waves in a layer in which the absorption of seismic energy is extremely low. Using the same formulation as that developed to explain the prolonged character of seismic signals from the lunar impact events (ref. 9-7), the expected variation of the Rover signal amplitude with distance can be calculated for a given set of parameters specifying the degree of scattering and energy dissipation within the near-surface material. A theoretical derivation is given in appendix A to this section. An example of observed amplitude variation with distance is shown in figure 9-4 along with the set of theoretical curves that best fit the data. For the theoretical curves, generation of seismic energy at a constant rate from a moving source of constant velocity and two-dimensional spreading of seismic energy are assumed and the curves are calculated numerically from formulas in appendix A. For a given range between the Rover and the seismic station, larger amplitudes are expected when the Rover is moving away from the seismometer than when it is moving toward the seismometer. This occurs because the major contribution to the observed signal amplitude at a given moment is from the seismic energy generated long before it is detected. The agreement between the theoretical and experimental values is quite good, particularly at large ranges where the scattering process works to average out effects from local irregularities.

The diffusivity ξ and the dissipation factor Q of the lunar surface layer have been calculated from the observed amplitude variations. These quantities are measures of the degrees of scattering and energy loss, respectively. The determined ranges of these quantities are ξ = 0.033 to 0.022 km^2/sec and Q = 1700 to 2300, for a frequency range of 4 to 8 Hz. Assuming

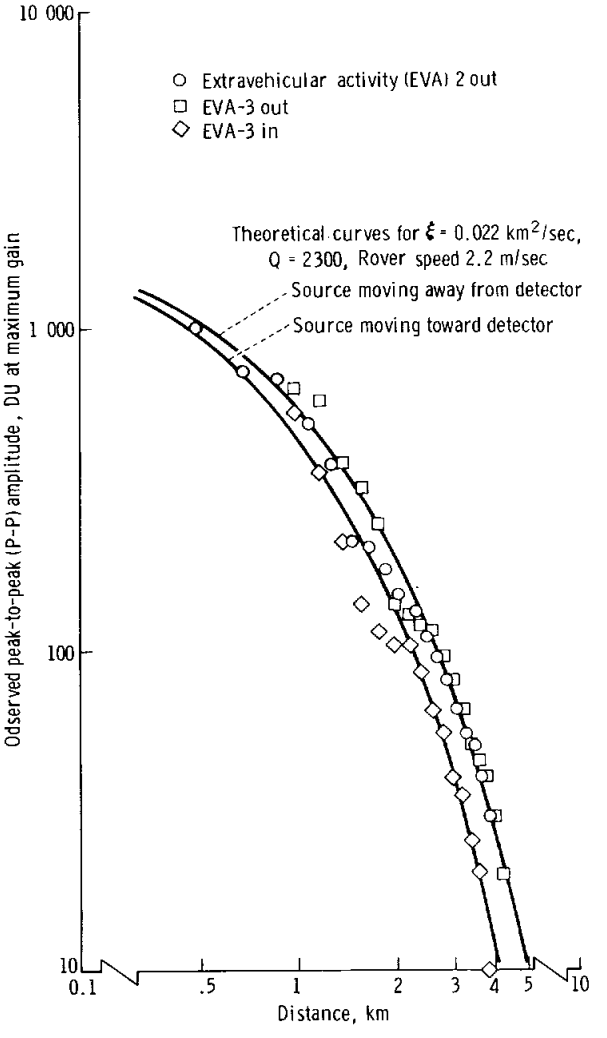


FIGURE 9-4.–Amplitude of seismic signals from the Rover observed by the SPZ seismometer. The data points represent amplitudes measured from a seismogram narrowband filtered at a center frequency of 8.0 Hz. The theoretical curves are calculated from formulas in appendix A.

an average velocity of seismic waves in the lunar surface layer of 55 m/sec, appropriate for surface waves (Rayleigh) of the fundamental mode, the equivalent mean free path μ of seismic waves in the layer can be determined from the diffusivity. The quantity μ can be thought of, in this context, as the mean distance between scattering centers. The determined range of this quantity is from μ = 300 m for signal frequencies of 4 Hz to μ = 200 m for 8-Hz signals.

The decreasing mean free path with increasing frequency means that there are more scattering centers per unit area for higher frequency seismic waves than for lower frequency seismic waves. Because heterogeneities of appropriate dimensions relative to the wavelength of seismic waves act as scattering centers for seismic waves, the expected conclusion is that the degree of heterogeneity increases with decreasing scale size. The heterogeneities considered here are of dimensions on the order of the wavelength of seismic waves considered (i.e., approximately 10 m).

The observed dissipation factor Q given here is not that of the lunar surface material. The loss of seismic energy from the lunar surface layer into deeper layers is also included in the dissipation factor thus determined. The apparent increase of Q with increasing frequency can be accounted for by such an energy loss. Thus, a Q of roughly 2000 is a lower limit to the actual Q of the lunar surface material.

To summarize the previously discussed results, the Rover signals indicate that the lunar surface layer in the Apollo 16 landing area consists of materials having a Q of at least 2000 and containing heterogeneities of dimensions on the order of 10 m in sufficient numbers to produce equivalent mean free paths for seismic waves of from 200 to 300 m.

From the present results, the expected rise times of seismic signals caused by an impulsive source in the distance range of 1 to 4 km can be estimated for the Apollo 16 area. These estimates are shown in figure 9-5. The data are useful in determining distances to such impulsive events as small meteoroid impacts and thermal disturbances at short ranges. Direct measurements of the rise time and frequency of the signal from one of the most distant grenades of the active seismic experiment (ASE) (sec. 10 of this report) are also plotted in figure 9-5. The agreement between these data and the results of the theoretical analysis based on Rover-generated signals supports the validity of the analysis.

Seismic signals generated by the Apollo 15 Rover were very similar to those observed from the Apollo 16 Rover. The Apollo 15 landing area, however, appears to be slightly more heterogeneous than the Apollo 16 landing area. This is indicated by a value for diffusivity obtained from the analysis of the Apollo 15 Rover signals, which is approximately 20 percent lower than the value obtained for the Apollo 16 site. The difference in the heterogeneity of the lunar surface materials at these two landing sites may be a consequence of differing ages for the two areas. If the Apollo 16 site is older than previous sites, a thicker layer of more uniform mechanical properties would be expected to be present at this site as a result

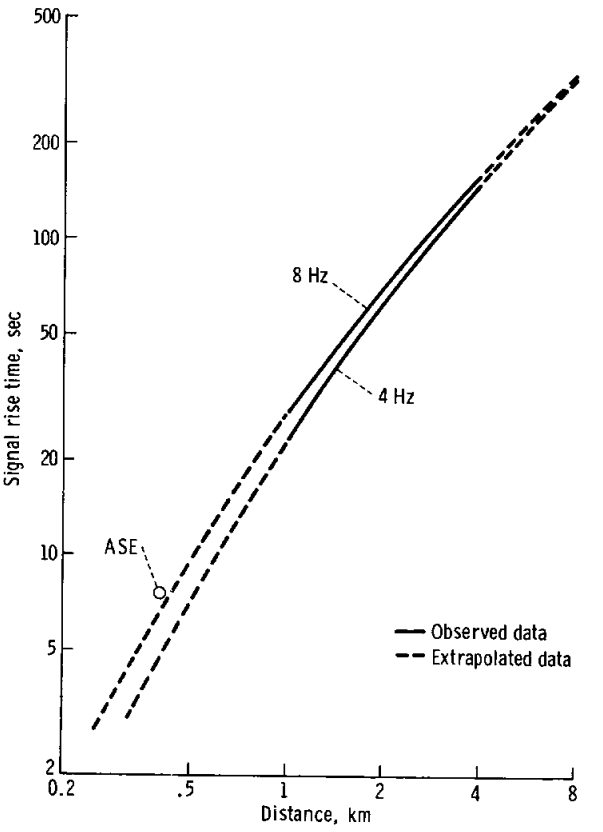


FIGURE 9-5.—Expected rise time of seismic signals from an impulsive source, estimated from the results of Rover signal analysis. The estimates should be valid at least in the distance range of 1 to 4 km. The broken lines indicate extrapolations. A measured value from the ASE at 8 Hz is also indicated.

of more extensive comminution by meteoroid impacts. The relative uniformity in the mechanical state of the rock samples collected in the Apollo 16 area supports this hypothesis.

Short-Period Events

As in previous missions, several hundred rather strong signals were detected by the SPZ seismometer after activation of the PSE. However, these fell mostly into two repetitive waveform types that gradually subsided throughout the first lunar night. Therefore, most of these early events are attributed to venting or circulation of fluids and thermoelastic "popping" within the lunar module (LM) descent stage. The LM-generated seismic activity was also observed at the Apollo 11, 14, and 15 stations. The level of such activity was less at the stations where the LM and the PSE are farther apart. The Apollo 16 PSE is located approximately 95 m from the nearest footpad of the LM.

The variation of both natural and artificial (LM generated) SPZ seismic activity is clearly related to the solar cycle at the Apollo 14 and 15 sites. Comparison with the Apollo 12 site is impossible because of the failure of that SPZ seismometer. The observed SPZ natural seismic activity at the Apollo 14, 15, and 16 sites is shown during complete lunations in figure 9-6. Events that have impulsive beginnings or very small rise times are probably generated by the LM or other equipment left on the Moon and are not included in the data of figure 9-6. The variation of SPZ activity is clearly related to the solar cycle at the Apollo 14 and 15 stations, but the pattern is different at the Apollo 16 station. Daytime activity rates at stations 14 and 15 are 2 to 6 times greater than the nighttime rates. Abrupt increases in activity are observed approximately 30 to 46 hr after sunrise, and abrupt decreases in activity occur approximately 54 hr after sunset. The phase lags noted between sunrise and the initiation of activity, and between sunset and the decrease in activity, most likely reflect the thermal time constant of the sources and variations in local topography. The observation of similar time constants at the Apollo 14 and 15 stations implies that similar source mechanisms are present at both locations. The differing levels of SPZ activity observed at the three stations indicate that the number of natural sources of SPZ seismic activity varies from site to site. Meteoroid impacts alone may be sufficient to account for the observed SPZ activity at the Apollo 16 station. These impacts would explain the apparent lack of correlation with the solar cycle at the Apollo 16 station.

Detailed analysis of events recorded at the Apollo 14 and 15 seismic stations has revealed that many of the events can be grouped into sets, members of each set having nearly identical waveforms. Thirty-five categories of matching SPZ events have been identified in the Apollo 14 station records, and an event of each category is found to occur at a specific phase of the lunar day, some predictable to within a few hours. Events of some categories occur only once per lunar day while others occur more frequently. Matching SPZ events begin to occur approximately 48 hr after sunrise and continue until approximately 7 days after sunset. This correlation with the solar cycle implies that the matching SPZ signals are generated by sources on the lunar surface. Also, the similarity of SPZ activity at the Apollo 14 and 15 stations implies that the SPZ events detected at both stations are generated by the same type of thermal process operating at two locations separated by 1100 km. Probably, this process is operating on a global scale.

The ground-motion amplitudes of these matching SPZ events are small, ranging from 0.2 to 2 nm (2 to 20 Å) (peak to peak). The signal amplitudes of events in any one category do not vary by more than a factor of 2. The frequency content of these signals is variable with broad spectral peaks between 3 and 6 Hz. The signals appear to be dispersed with low frequencies arriving earlier than high frequencies.

The matching property of the SPZ signals detected at the Apollo 14 and 15 stations implies that the source locations remain fixed for periods of many months and rules out the mechanism of random meteoroid impacts. The signal rise times at the Apollo 14 station vary between 20 and 70 sec corresponding to a distance range of 1 to 2 km from the Apollo 14 PSE based on observations of the rise times of SPZ signals generated by the Rover at the Apollo 15 and 16 stations. The exact locations of these sources cannot be determined with present data. Future recording by at least two geophones of the active seismic experiment at the Apollo 14 and 16 stations may yield exact locations of sources in the vicinities of these stations. By contrast to the great variety of natural matching events, LM-generated signals are characterized by rise times of 5 sec or less and have spectral peaks at the resonant frequencies of the LM

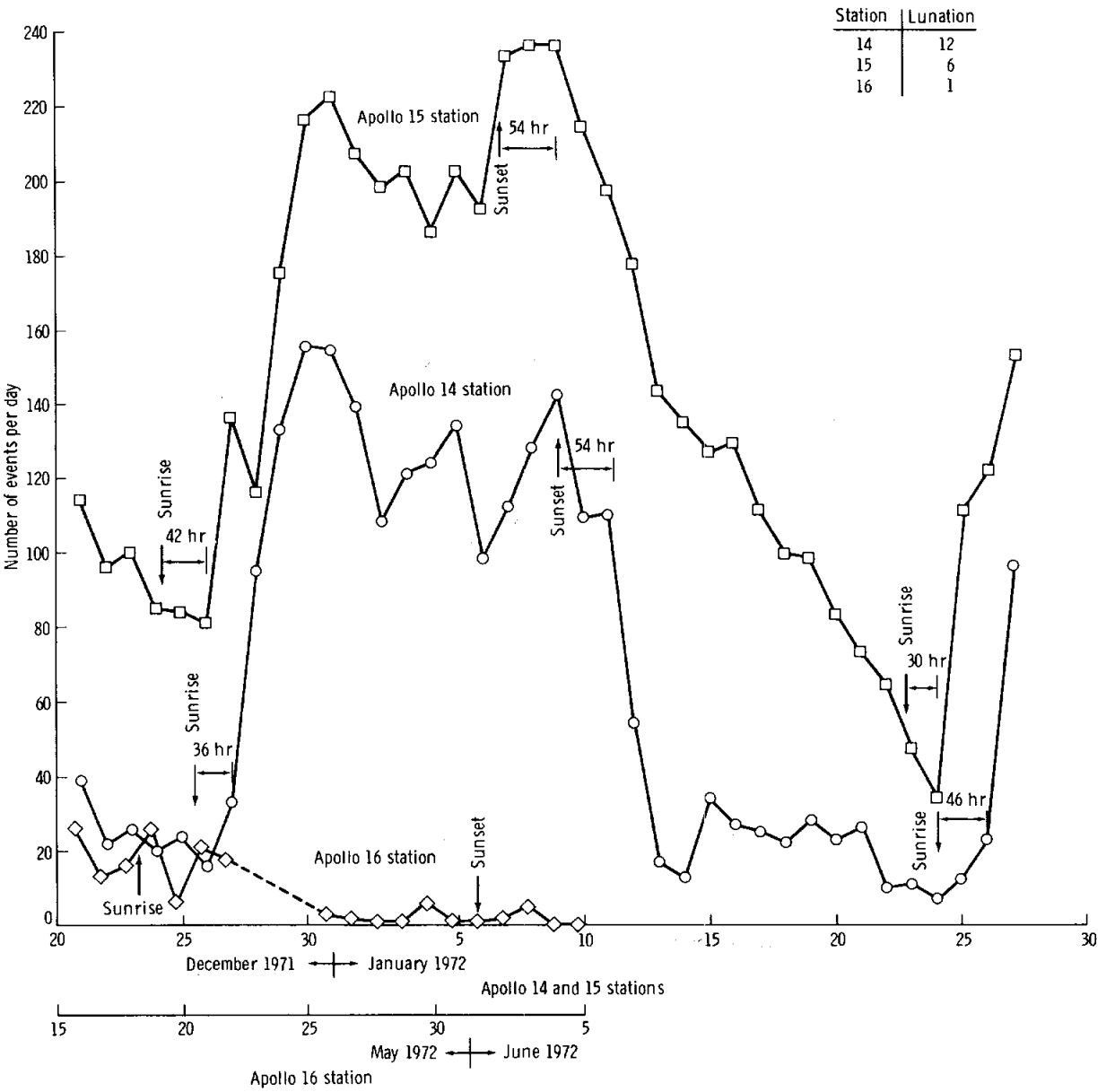


FIGURE 9-6.—Daily number of SPZ events observed as a function of time by the SPZ seismometers at the Apollo 14, 15, and 16 stations. Data are from the 12th, sixth, and first lunations at the Apollo 14, 15, and 16 stations, respectively. Only SPZ signals that show a gradual buildup and decay are included. Signals that have impulsive beginnings or very short rise times are probably generated by the LM or other Apollo lunar surface experiments package instruments and are not included. The variation of SPZ activity is clearly related to the solar cycle at the Apollo 14 and 15 sites. This pattern is not observed at the Apollo 16 site.

that are not observed in the matching signals. It is doubtful that the LM alone could consistently produce the great variety of observed matching signals over the period of a year or more.

The differences in the intensity of SPZ activity at the three stations appear to be related to the number of fresh rock exposures in the vicinity of the Apollo lunar surface experiments package stations. The SPZ

signals are probably generated by movements caused by thermal stresses along preexisting fractures or bedding planes in fresh rock exposures on the lunar surface. The diurnal thermal wave resulting from daytime solar heating and nighttime cooling penetrates the lunar regolith to a depth of approximately 0.5 m and may penetrate fresh and coherent rock exposures to a depth of as much as 5 m. Thermal stresses would result from differential expansion and contraction that are the result of thermal gradients within the larger rocks or rock exposures as the thermal wave advances. The SPZ events may occur when the differential expansion (at sunrise) or contraction (at sunset) between the opposing sides of a large fracture or bedding plane is sufficiently large to cause relative movement (sliding). The great differences in SPZ activity observed at the Apollo 14, 15, and 16 sites result from the varying numbers of fresh rock exposures among the three sites. The large topographic relief present in the Hadley Rille area is favorable for the continued exposure of fresh rock surfaces caused by the steady-state removal of overlying material by meteoroid impacts and slumping of blocks. Fresh exposures of large rocks at the Apollo 14 and 16 sites are provided by only the largest meteoroid impacts. The rarity of such impacts and the greater regolith thicknesses at these two stations decrease the frequency at which fresh rocks are exposed. The higher rate of SPZ activity at the Apollo 14 station as compared to the Apollo 16 station may indicate that the large blocks ejected from Cone Crater near the Apollo 14 station have been exposed more recently or are more competent rocks than those ejected from numerous craters near the Apollo 16 station.

Lunar Structure

The Apollo 16 mission was planned to contribute to the understanding of lunar structure in two major ways: (1) by providing traveltimes to a network of at least three stations from seismic sources (the SIVB and the LM ascent stage impacts) at known times and locations and (2) by expanding the network of seismic stations to improve the capability for locating natural events (moonquakes and meteoroid impacts).

The Apollo 16 SIVB impact point was chosen to verify the lunar velocity structure obtained from data of the previous missions and to extend this structure to greater depth. In addition to this, the Apollo 16 LM impact was to provide a direct comparison of seismic traveltimes and crustal velocities between a highland site (Descartes region) and the maria. Because of operational difficulties, neither of these goals was reached. It was anticipated that the position and time of the impact of the SIVB would be known independently, but the loss of tracking capability eliminated this valuable information. The ascent stage of the Apollo 16 LM did not impact, and the expected independent traveltime data for a highland crust were never obtained.

Nevertheless, valuable data were added to those previously available for seismic studies. The Apollo 16 SIVB impact site, near the Apollo 12 and 14 stations, and the impact time were determined by using the seismic wave traveltimes for the Oceanus Procellarum region determined from previous impacts. The large meteoroid impact that occurred on May 13 in the region of the Apollo 12 and 14 stations was located in a similar manner. In both of these cases, the traveltimes to the distant seismic stations (Apollo 15 and 16 stations) were used to extend the knowledge of the velocity structure into the lunar mantle.

Location of the Apollo 16 SIVB and May 13 meteoroid impact points.—The arrival times read from the seismograms of the Apollo 16 SIVB impact are listed in table 9-I. Only clearly identifiable phases were used for the event locations. Later phases such as shear waves (S) or multiply reflected compressional waves (PP, PPP, etc.) could not be timed as accurately. By using only the first-arrival P-times and envelope amplitude ratios from the Apollo 12 and 14 stations, impact coordinates and impact time were determined. Another determination was made by using two P-wave arrivals and an S-wave time from the Apollo 12 station. For these determinations, the crustal velocity (i.e., traveltime) model from previous studies (refs. 9-9, 9-12, and 9-13) was used. For the average mantle velocity (to a depth of 150 km), various values ranging from 9.2 to 7 km/sec were tried. The P-wave traveltime at the Apollo 15 station, which was confirmed by the large meteoroid impact of May 13, indicated a mantle velocity of approximately 8 km/sec. Relocation of the SIVB event on the basis of three P-wave arrivals gave the most reliable impact coordinates to be 1.3° N 23.8° W and the range time to be 21:02:04 G.m.t. From the consistency of the impact locations found on the basis of three different data sets and the limits of the

TABLE 9-I.– Arrival Times of Seismic Waves at Different Stations

Location	*Arrival time, G.m.t.*	
	P-wave	*S-wave*
Apollo 16 SIVB impact (day 110, 1972)[a]		
Apollo 12 station	21:02:31.6	21:02:54.0 (?)
Apollo 14 station	21:02:47.4	--
Apollo 15 station	21:04:31.0	21:06:18.0 (?)
Meteoroid impact (day 134, 1972)[b]		
Apollo 12 station	08:47:24.6	–
Apollo 14 station	08:47:12.4	–
Apollo 15 station	08:48:54.0	–
Apollo 16 station	08:49:00.8	08:51:00.0 (?)

[a]Calculated impact time: 21:02:04.0 (possible error 4 sec).

[b]Calculated impact time: 08:46:42.5 (possible error 1 sec).

traveltime curves, it can be stated with reasonable confidence that the error in the location does not exceed ±0.7° in latitude and ±0.3° in longitude. The impact time is accurate to approximately 4 sec.

The large meteoroid impact of May 13 gave clearly identifiable P-waves at all four seismic stations. (See table 9-I for arrival times.) The impact coordinates, impact time, and the rms error in impact time can be determined from these four arrival-time data. These parameters were computed for average mantle velocities of 8.0 and 9.2 km/sec. The rms error (0.03 sec as compared to 2.2 sec) favored the 8-km/sec mantle model. The meteoroid impact of May 13 occurred at 08:46:42.5 ± 1.0 sec G.m.t. at 1.1° N 16.9° W. The coordinates are accurate to ±0.2° and thus are better determined than those of the SIVB impact.

The distances and azimuths from the impact sites to the seismic stations are listed in table 9-II. The Apollo 16 SIVB impact site and station locations are shown in figure 9-7.

Velocity models (inversion).–Traveltime data from the previous missions, as well as the Apollo 16 SIVB and the May 13 meteoroid impact data, are shown in figure 9-8. It should be emphasized that the traveltimes to the Apollo 12 and 14 stations from the latest impacts do not provide independent information because the data from these stations were used with existing velocity models to locate the events. Traveltimes to distant stations (Apollo 15 and 16 stations), however, provide additional data about average mantle velocity to a depth of approximately 120 km. The data of previous missions provided information to a depth of approximately 70 km.

Interpretation of the data proceeds in three steps: (1) fitting traveltimes, (2) fitting amplitudes of P-arrivals and angle of incidence (or the ratio of horizontal-to-vertical ground motion), and (3) matching general characteristics of records by computing theoretical seismograms. The traveltimes provide the most direct information. As shown previously (refs. 9-9, 9-12, and 9-13), these include rapidly increasing velocities near the surface, an intermediate crustal zone with a nearly constant velocity, and a discontinuity representing the base of the crust at a depth of approximately 60 km. Two models (one extremely smooth, the other designed to incorporate later phase amplitudes) are given in figure 9-9. The average upper mantle velocity, as can be determined from P-wave traveltimes to the Apollo 15 and 16 stations, is approximately 8 km/sec. The existence or the absence of a very high velocity layer immediately below the crust, as indicated by one data point (a small first arrival of the Apollo 15 SIVB impact recorded at the Apollo 12 station at a distance of 355 km), could neither be confirmed nor denied by the present data. If such a layer does exist, the new traveltime and amplitude data require that its thickness be less than approximately 20 km. Other possibilities might preclude the existence of such a layer altogether. It is possible that a noise pulse preceded the P-wave and was misidentified; or that the refracting crust/mantle interface dips, resulting in a high apparent velocity; or that the particular seismic ray passed through a

TABLE 9-II.– Coordinates, Distances, and Azimuths of Stations and Impacts

Location	Coordinates[a]	Distance and azimuth from Apollo seismic stations			
		12	14	15	16
Apollo 12 station	3.04° S 23.42° W	--	181 km 276°	1188 km 226°	1187 km 276°
Apollo 14 station	3.65° S 17.48° W	181 km 96°	–	1095 km 218°	1007 km 277°
Apollo 15 station	26.08° N 3.66° E	1188 km 40°	1095 km 33°	–	1119 km 342°
Apollo 16 station	8.97° S 15.51° E	1187 km 100°	1007 km 101°	1119 km 160°	–
Apollo 12 LM impact point	3.94° S 21.20° W	73 km 112°	--	–	–
Apollo 13 SIVB impact point	2.75° S 27.86° W	135 km 274°	--	–	--
Apollo 14 SIVB impact point	8.09° S 26.02° W	172 km 207°	–	–	–
Apollo 14 LM impact point	3.42° S 19.67° W	114 km 96°	67 km 276°	–	–
Apollo 15 SIVB impact point	1.51° S 11.81° W	355 km 83°	184 km 69°	–	--
Apollo 15 LM impact point	26.36° N 0.25° E	1130 km 36°	1048 km 29°	93 km 276°	–
Apollo 16 SIVB impact point	1.3 ± 0.7° N 23.8 ± 0.2° W	132 km 355°	243 km 308°	1099 km 231°	--
Day 134, 1972 meteoroid impact point	1.1 ± 0.2° N 16.9 ± 0.2° W	234 km 58°	145 km 7°	967 km 222°	1026 km 286°

[a]Listed coordinates are derived from the Manned Space Flight Network Apollo tracking data. Locations based on these data are referenced to a mean spherical surface and may differ by several kilometers from coordinates referenced to surface features.

high-velocity heterogeneity somewhere along its path. None of these questions can be resolved with the available data.

The velocity models shown by dashed and solid curves in figure 9-9 represent possible structures that fit the traveltimes within the uncertainties of data. The solid curve represents further refinement on the basis of later arrivals, multiply reflected phases, and theoretical seismograms (fig. 9-10) to fit these phases. Whether scattered or converted waves at several distances could consistently bias these methods remains an open question. Thus, the velocity discontinuity shown at approximately 25 km should be regarded as tentative until further observational evidence of its presence can be obtained.

The shear waves recorded at the Apollo 16 station from the May 13 meteoroid impact were most valuable in extending the knowledge of crustal shear velocities into the lunar mantle. Both the traveltime of discrete P- and S-phases and the envelopes of scattered P- and S-waves (discussed in subsection entitled "Seismic Signal Envelope and Wave Transmission in the Moon") show Poisson's ratio for the average upper mantle to be $\sigma = 0.25$, consistent with

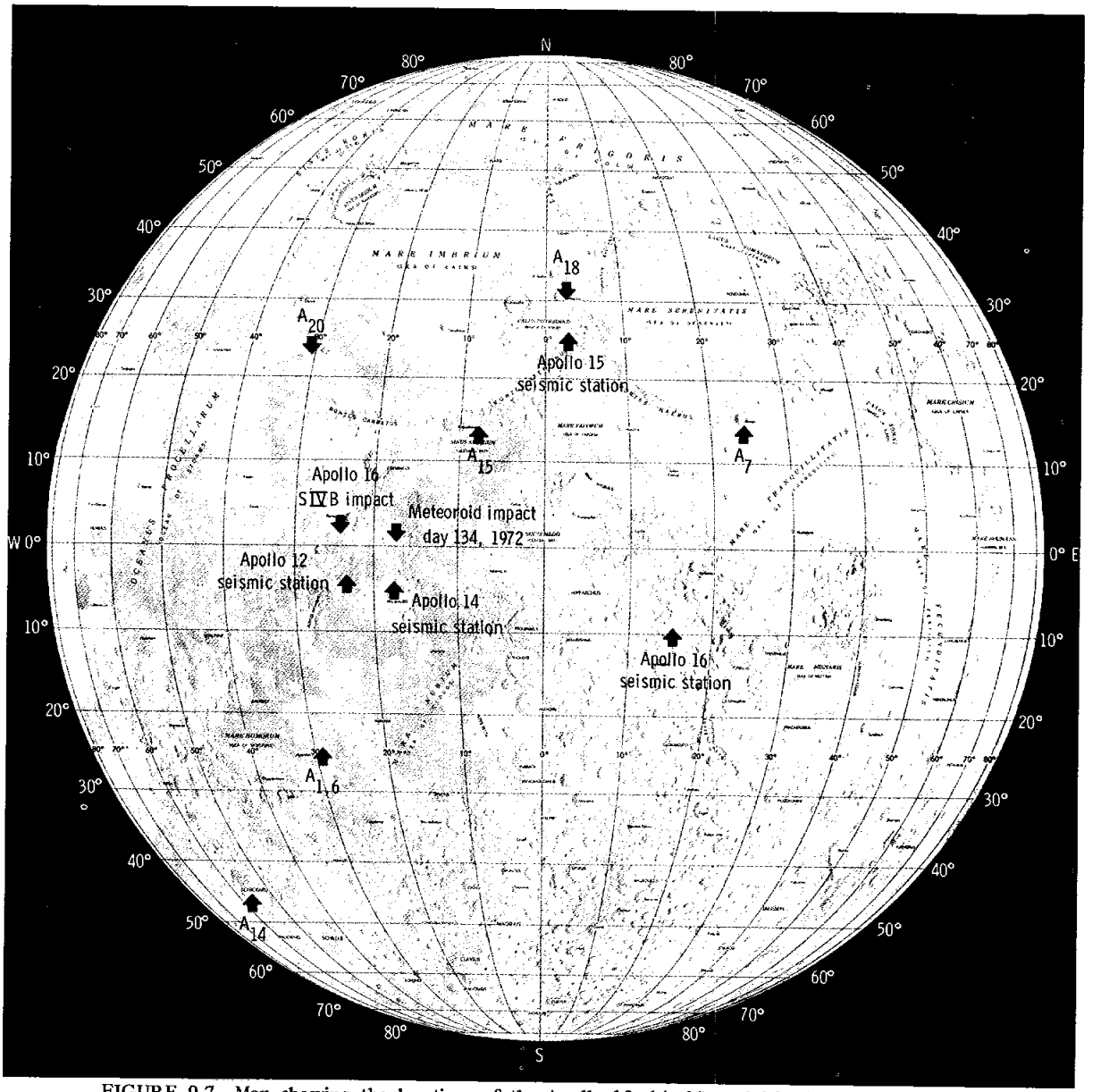
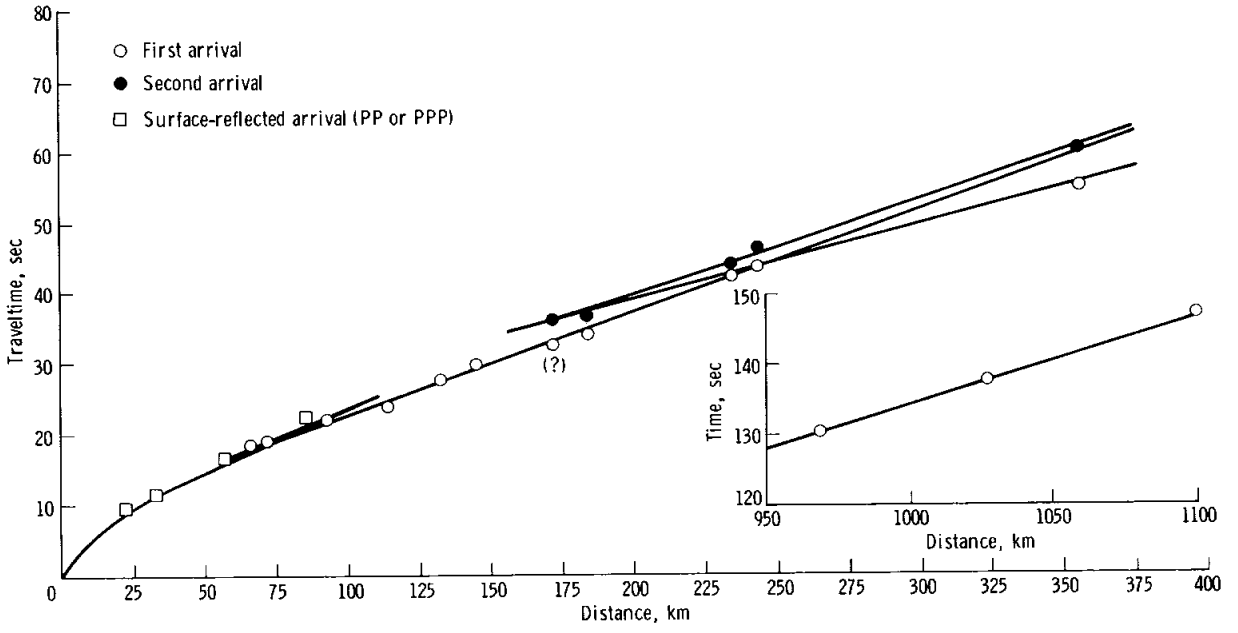


FIGURE 9-7.–Map showing the locations of the Apollo 12, 14, 15, and 16 seismic stations, the category A matching moonquake epicenters, the Apollo 16 SIVB impact point, and the meteoroid impact of May 13, 1972. The epicentral coordinates and depth of the moonquake foci are listed in table 9-III.

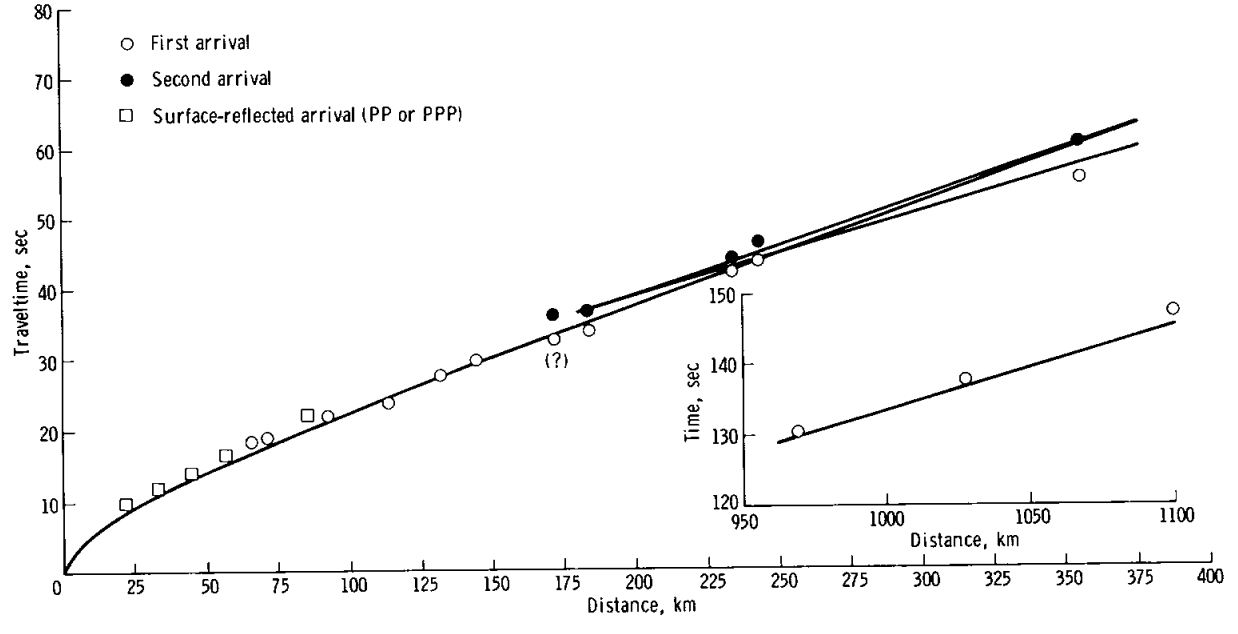
the crustal value and the laboratory value for lunar samples (ref. 9-12).

Nearly constant compressional velocities down to a depth of approximately 150 km can be justified both by comparing P-wave amplitudes at the Apollo 15 and 16 stations with those at the Apollo 12 and 14 stations and on the basis of traveltimes. Amplitude calculations indicate the absence of strong velocity gradients in the mantle down to a depth of approximately 150 km.

Nearly constant model velocity in the upper mantle of the Moon implies that temperature and



(a)



(b)

FIGURE 9-8.–Traveltime observations and theoretical curves recorded as a function of distance for two lunar models. (a) Composite of lunar models 1 and 3 shown in figure 9-9. (b) Lunar model 2. All data are P-wave traveltime observations. Second arrival means large-amplitude wave following the refracted arrival. Surface-reflected arrivals are PP or PPP phases, plotted at one-half or one-third of the source-receiver distance, respectively.

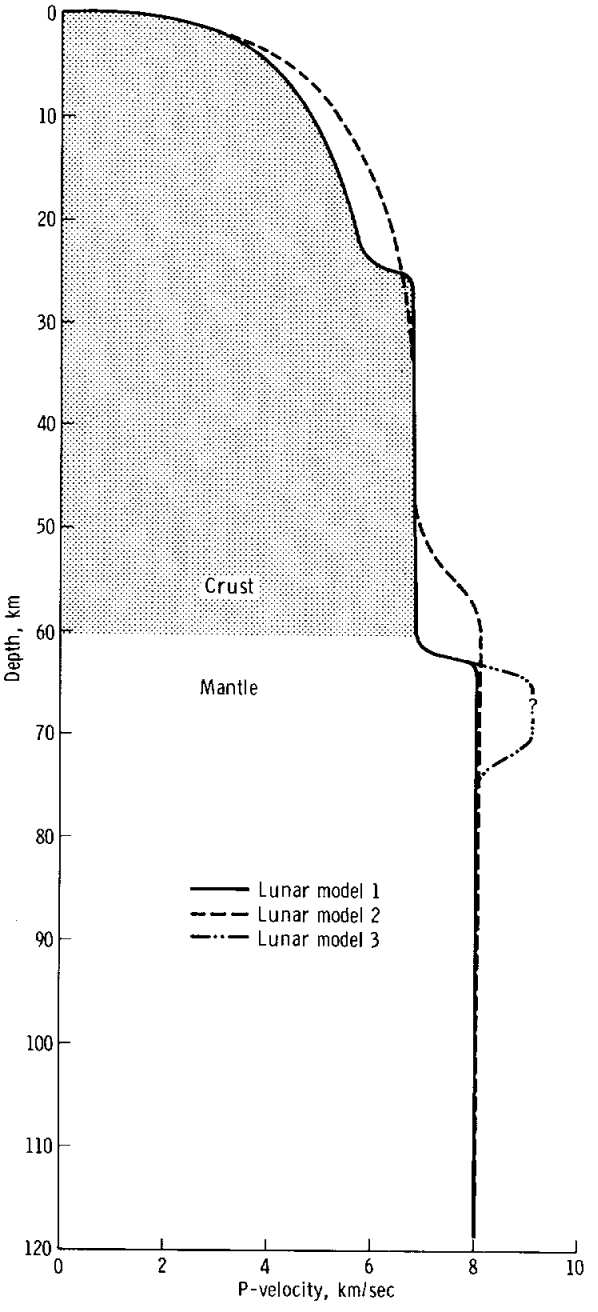


FIGURE 9-9.–Compressional velocity models based on different data subsets. Dashed curve (lunar model 2) fits the traveltimes and first-arrival amplitudes. The solid curve (lunar model 1) fits the data and is further modified on the basis of synthetic seismograms. Based on the unreversed profile, the lunar model 3 curve shows the possible high-velocity layer beneath the crust.

pressure effects on seismic velocities nearly cancel each other. Using temperature and pressure coefficients of velocity for typical laboratory values of terrestrial dunites ($\partial V/\partial T$ = 5 X 10^{-4} km/sec/° K and $\partial V/\partial P$ = 0.02 km/sec/kb (0.2 X 10^{-6} m/sec (N/m^2)) for the depth range of 75 to 175 km, for a constant velocity, a temperature gradient dT/dZ = 2.2° K/km is found. With such a low gradient, the temperature at a depth of 200 km in the Moon would be approximately 500° C (773° K). Until further data are acquired and a more detailed velocity model is obtained for the lunar mantle, more reliable temperature estimates cannot be made. Hopefully, such data

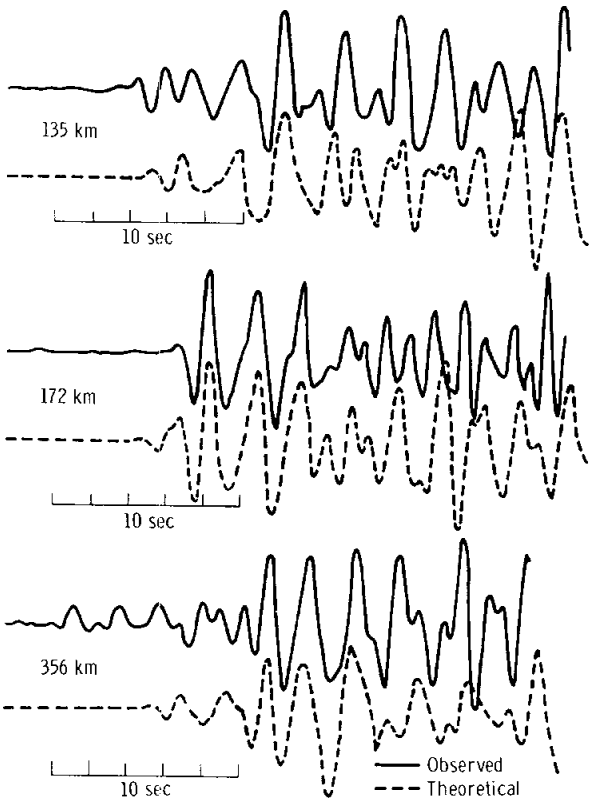


FIGURE 9-10.–Observed (solid line) and synthetic P-wave seismograms for three SIVB impacts recorded at the Apollo 12 station. Seismogram character and relative amplitudes of first and later arrivals change with distance. At 356 km, the first two peaks of the observed seismogram are filtered noise pulses. Theoretical seismograms for Δ = 132 and Δ = 243 km (not shown) also fit the observed records.

will become available as a result of the Apollo 17 SIVB impact.

Physical and petrological implications of the velocity model.–With the new data, compositional implications of the velocity models can be extended into the lunar mantle. Briefly reviewing the previous information about the crust, the following statements can be made.

(1) Velocities increase very rapidly to a depth of approximately 10 km. Very low velocities near the surface correspond to those of the lunar soil and broken rocks representing the regolith. The rapid increase of the velocity can be explained by the pressure effect on dry rocks with macrocracks and microcracks. The velocity models obtained fit the measured velocities of lunar basaltic rocks. Until velocities of more anorthositic lunar samples are measured, a definite statement cannot be made on the exact composition of the upper crustal layer at this site. Furthermore, if there is a velocity discontinuity at 25 km as shown in figure 9-9, it probably represents a change of composition (or phase) at this depth. The data come from Oceanus Procellarum in the region of the Apollo 12 and 14 stations, and the structure refers to this area.

(2) The nearly constant velocities in the crust below approximately 25 km correspond to those of terrestrial anorthosite, gabbro, or gabbroic anorthosite. If this layer is typical old crustal material, it is consistent with the general petrological results obtained from the preliminary examination of Apollo 16 and Luna 20 highland samples and other lunar soils (ref. 9-14).

(3) The average upper mantle velocity (8 km/sec) corresponds to those of terrestrial olivines, pyroxenites, and peridotites and is consistent with petrological inferences made from the analysis of lunar samples (refs. 9-15 to 9-18).

Direct velocity measurements do not penetrate deeper than approximately 125 km. The relatively low Poisson's ratio (σ = 0.25) in the upper mantle, the propagation of short-period S-waves from 800-km-deep moonquakes, and constant attenuation with distance for frequencies of 0.2 to 8.0 Hz indicate that the rigidity and Q of the lunar mantle must be high (at least to the depth of the moonquakes). This precludes extensive melting within the outer half of the Moon.

Seismic Signal Envelope and Wave Transmission in the Moon

Various unusual characteristics of the lunar seismic signals, including the gradual rise and decay of the signal wave train, have been interpreted as resulting from intensive scattering of seismic waves in a heterogeneous but nearly loss-free layer that blankets the entire surface of the Moon (refs. 9-7 and 9-9). Below this surface layer, the lunar material is believed to be sufficiently homogeneous to transmit seismic waves with little scattering. In this structure, seismic waves generated by an impacting object are intensively scattered near the impact point and are observed as a scattered wave train in the near ranges. A part of the scattered energy gradually leaks into the lunar interior where it propagates as a long train of seismic waves, undergoes further scattering when it reenters the lunar surface layer, and is observed as a prolonged wave train at a distant seismic station. Because both compressional and shear waves are transmitted in the lunar interior, separation of the wave train into two components that begin at different times is expected at far ranges. The data obtained from large impacts at far ranges during the Apollo 16 mission not only have confirmed this hypothesis but also have provided information on the physical characteristics of the lunar interior.

Figure 9-11 shows a typical seismic waveform observed at far ranges, reproduced through a narrow bandpass filter. The partial separation of two wave trains, each having a characteristic envelope of a scattered wave train, is easily seen. The scattered P-wave train begins approximately 2 min after impact. The scattered S-wave train arrives after the

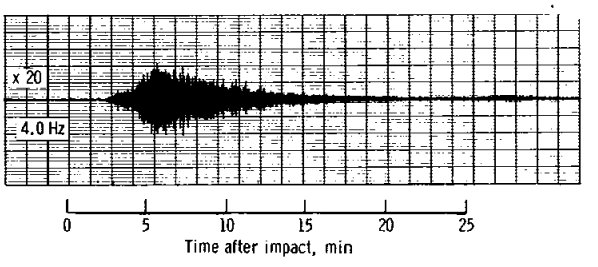


FIGURE 9-11.–Seismic signals for the Apollo 16 SIVB impact observed by the Apollo 15 station SPZ seismometer at a distance of 1100 km. The signal has been narrowband filtered with a center frequency of 4.0 Hz.

P-wave train with maximum amplitude about three times that of the P-wave train. No other arrivals are apparent, at least for seismic waves at this frequency (4 Hz). An efficient reflecting surface in the lunar interior would produce additional wave trains similar to the ones observed at appropriate arrival times. This, however, does not rule out possible existence of a transition zone, which is an effective reflector for lower frequencies. The apparent absence of arrivals corresponding to the reflection of compressional waves and shear waves from the far side of the Moon supports the hypothesis that seismic waves incident from the lunar interior are rediffused rather than reflected by the Moon-wide surface scattering layer.

In figure 9-12, the traveltimes to the peak of the signal envelope, as measured on narrowband filtered seismograms, are plotted against distance.

Three characteristics of these curves are relevant to this discussion: (1) the rise times of seismic signals (time to reach maximum amplitude) increase with distance, but the slopes of the curves decrease markedly at a range of approximately 100 to 150 km, depending upon frequency; (2) signal rise times at far ranges begin to increase sharply as the frequency falls below 1 Hz; and (3) a prominent dip in rise times occurs at all frequencies at a range of approximately 180 km, but it is most pronounced at low frequencies. These characteristics are consistent with the scattering-layer hypothesis described previously.

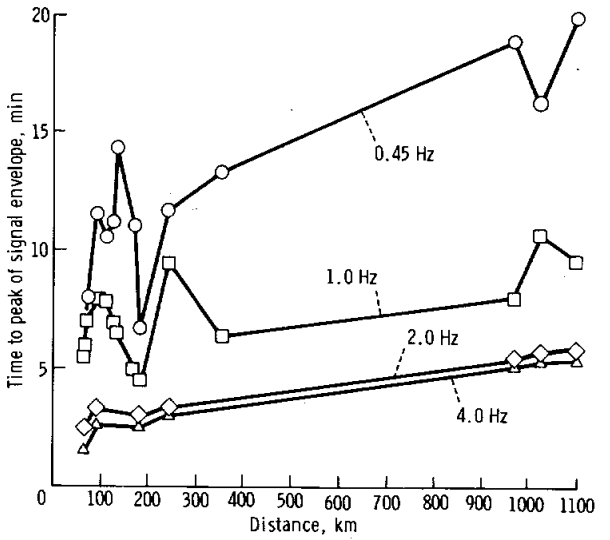


FIGURE 9-12.–Observed time intervals from the times of impact to the peak of the seismic signal envelope for artificial impacts. Data for an accurately located natural impact are included. The time intervals are measured on narrowband filtered seismograms of LPZ (0.45 and 1.0 Hz) and SPZ (2.0 and 4.0 Hz) components.

The propagation of seismic wave energy from an impact in the postulated structure should be considered in greater detail. Seismic energy will radiate outward from the point of impact as body waves (compressional and shear waves, which travel through the lunar interior) and surface waves (which travel along the surface). Surface waves will carry most of the energy initially because they are more efficiently generated by a surface source than are body waves. Surface waves with wavelengths comparable to and shorter than the thickness of the scattering zone are quickly scattered and converted to body waves, which gradually "leak" into the lunar interior. Surface waves of longer wavelengths can propagate to greater ranges. The relative contributions of these three wave types (compressional waves, shear waves, and surface waves) to the maximum amplitude of the detected wave train thus depends on range and the portion of the frequency spectrum considered. According to the present hypothesis, the paths of seismic waves, at ranges of less than 100 to 150 km, are confined primarily to the scattering zone. Thus, scattering will increase with path length, and a pronounced change in signal rise time with distance is to be expected. All three wave types contribute significantly to the peak signal intensity in this distance range. At longer ranges, gradual separation of the wave types as a result of their differing velocities results in the dominance of shear waves at higher frequencies and surface waves at lower frequencies. From the data shown in figure 9-12, it appears that the signal frequency for which surface waves begin to dominate at long ranges is approximately 0.5 Hz, with shear waves dominant at frequencies of 1 Hz and higher. At ranges greater than 100 km, little further scattering of body waves occurs because most of their path is below the scattering zone. Thus, the signal rise times change relatively little beyond this range for frequencies of 1 Hz and higher. However, for lower frequencies (0.5 Hz and lower), in which surface wave energy is dominant, the effect of scattering decreases gradually as wavelength increases. Thus, signal rise times continue to increase markedly with range beyond 150 km at low frequencies. Surface waves (Rayleigh waves of the fundamental mode) have

wavelengths of approximately 1 km at a frequency of 0.5 Hz for the assumed structure. From this, it is concluded that most of the scattering occurs in the upper few hundred meters of the surface layer.

The dip in the rise-time curves at a range of 180 km is caused by focusing of body waves, which contribute to a rapid buildup in signal intensity at this range. Body-wave focusing at a range of 180 km is in accord with theoretical calculations for a model containing a discontinuity at a depth of approximately 60 km (the crust-mantle boundary). Thus, the rise-time data provide independent evidence in support of the model derived in the subsection entitled "Lunar Structure."

The supposition that the lunar interior transmits seismic waves with little scattering implies that, once a seismic wave train leaves the surface scattering layer, its envelope shape is preserved while it propagates through the lunar interior. Shear waves play the major role in determining the high-frequency peak of the signal envelope observed in the far ranges as discussed previously. Therefore, the apparent velocity of the envelope peak along the lunar surface in the far ranges, measurable from figure 9-12, is expected to represent the apparent velocity of shear waves in this range. The velocity thus determined for signals in the frequency range from 2 to 4 Hz is 5.0 km/sec. Correcting for the curvature of the lunar surface, this corresponds to a true shear-wave velocity in the upper mantle of the Moon of 4.7 km/sec. By combining this value with the compressional-wave velocity of 8.1 km/sec, an estimated value of 0.25 can be obtained for the Poisson's ratio of the material in the upper mantle of the Moon. This value is consistent with the presence of low-temperature solids at these depths.

Moonquakes and the Physical State of the Lunar Interior

Observational data.—Hundreds of moonquakes were recorded at the Apollo 16 station during the initial 45-day period of operation. From this sample, it is estimated that approximately 10 000 moonquakes per year will be detected by the Descartes station. By comparison, moonquakes are recorded at the Apollo 14 station at a rate of approximately 2000/yr and at the Apollo 12 and 15 stations at a rate of 700/yr. Thus, it is expected that approximately 700 moonquakes will be recorded simultaneously at all four seismic stations each year. Of these, the signals from fewer than 25 percent (approximately 180) will be large enough to permit detailed analysis of their waveforms. Variations in the rates of moonquake detection among the stations is believed primarily to be a consequence of differences in the local regolith thickness of each site. Corresponding variations in the amplification of ground motion would account for the differences in station sensitivity. That the station sensitivities do vary is confirmed by relative amplitude measurements for seismic signals from the SIVB impacts.

All of the moonquakes are small. With one possible exception, the largest of them have Richter magnitudes of between 1 and 2, and most moonquakes are much smaller than this. The total seismic energy release within the Moon appears to be many orders of magnitude below that of the Earth.

As described in earlier papers (refs. 9-4 to 9-12), signals from moonquakes are distinguished from those of meteoroid impacts primarily by the relative prominence of the shear wave (previously called the H-phase (refs. 9-8 and 9-11)) and by differences in the signal rise times (the time interval between the beginning of a wave train and its peak amplitude). The shear wave is a much more prominent signal in the wave trains from moonquakes than in those from meteoroid impacts, and the rise times of moonquake signals are characteristically much shorter than the rise times of meteoroid impact signals.

With few exceptions, the signals from all moonquakes that are large enough to permit detailed analysis of their waveforms can be grouped into sets, members of each set having waveforms that match one another in detail. Events within each group of matching signals occur at regular intervals, normally once per month, and at specific times during the lunar orbit. In some cases, as many as three or four events of a given matching group will occur during a monthly cycle, but such multiple events occur over a relatively short interval of 5 days or less. The repetitious character of these events strongly supports the hypothesis that they are moonquakes, each group of matching signals corresponding to a zone (focus) within the Moon at which repeating moonquakes originate. The monthly periodicities suggest that they are induced by tidal stresses.

With the aid of the fourth seismic station (Apollo 16 station), 22 categories of matching events have

been identified. Thus, there must be at least 22 zones within the Moon at which the repeating moonquakes (designated A events) originate. A much larger number of active zones, from which the signals are too small to permit detailed analysis of their waveforms, is probable. Thus far, signals from seven of the moonquake foci have been large enough to provide data necessary to compute the source location. The focal depth can be determined in five of these cases. The solutions obtained are listed in table 9-III. The moonquake epicenters (points on the surface immediately above the foci) are plotted in figure 9-7. Seismograms for a moonquake recorded at all four stations are shown in figure 9-13. All of the moonquake foci for which locations are available occur at depths of between 800 and 1000 km.

The influence of tides.—As noted previously, moonquakes from each active zone occur at monthly intervals. Peaks in total moonquake activity, taken as the summation of all events detected at a given station per unit time, occur at intervals of approximately 14 days. This periodicity is shown in figure 9-14, where the data for all moonquakes detected at the Apollo 16 station during the first 45 days of operation have been plotted. The same periodicity is observed over much longer periods of time at the Apollo 12, 14, and 15 stations. In general, peaks in moonquake activity occur near times of apogee and perigee. However, the pattern of moonquake occurrence is not related simply to the monthly changes in Earth-Moon separation (the apogee-perigee cycle) but is complicated by other tidal components arising

TABLE 9-III.– Moonquake Locations

Moonquake category	*Latitude*	*Longitude*	*Depth, km*
A_1	23.3° S	28.3° W	850 (measured)
[a]A_6	23.3° S	28.3° W	850 (measured)
A_7	15.0° N	25.0° E	700 (assumed)
A_{14}	44.8° S	53.4° W	800 (assumed)
A_{15}	14.8° N	7.6° W	Greater than 550 (measured)
A_{18}	30.2° N	2.9° E	800 (measured)
A_{20}	22.3° N	30.2° W	940 (measured)

[a]A_6 focal zone is within approximately 20 km of the A_1 focal zone.

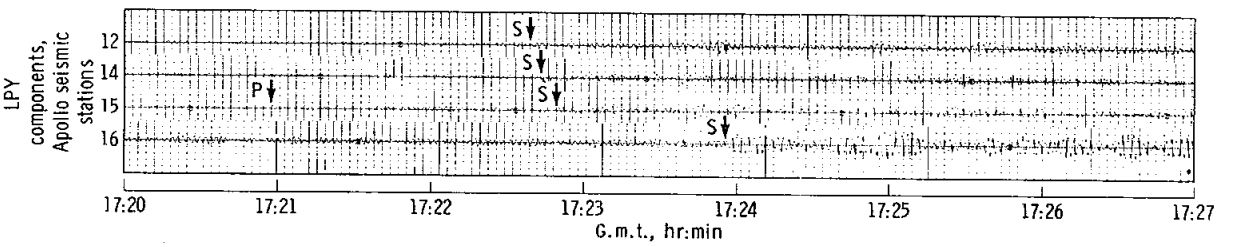


FIGURE 9-13.–Records of a category A_{20} moonquake detected at the Apollo 12, 14, 15, and 16 sites on May 15. The LPY-component seismograms are shown for each station. The most prominent phases are interpreted as the direct compressional wave (P-wave) and the direct shear wave (S-wave) arrivals. A moonquake focus can be uniquely located on the basis of four P- or four S-wave or any combination of four P- and S-wave arrival times at two or more seismic stations. Using the S-wave arrival times at the four stations, the category A_{20} moonquake focus is located at 23.3° N 30.2° W at a depth of 940 km.

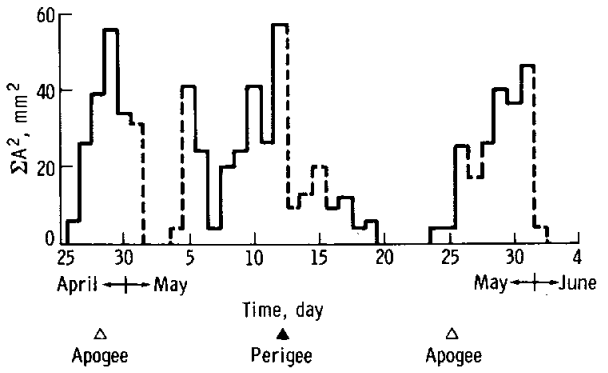


FIGURE 9-14.–Relative moonquake signal energy observed on the LPY component of the Apollo 16 station as a function of time. The A^2 for a moonquake is the square of the amplitude observed on the Y-component seismometer. For each moonquake, amplitude A is the maximum peak-to-peak signal amplitude not exceeded more than 10 percent of the time on seismograms where 0.5 mm is 1 DU. The height of each bar is the sum of A^2 for all events during a 1-day interval. Dashed bars indicate the time periods when the data are incomplete.

from the lunar librations and solar perturbations of the lunar orbit. Further discussion of the tidal influence in moonquake occurrence should be postponed until correlative data are better determined. However, it seems safe to conclude that tidal stresses play a major role in the seismicity of the Moon.

The focal mechanism.–Although the exact nature of moonquake focal mechanisms is presently unknown, some statements can be made. The nearly exact repetition of moonquake signals from a given focal zone over periods of many months requires that the focal zones be small, 10 km in diameter or less, and fixed in location over periods of at least 2 yr. If moonquake foci were separated by as much as 1 wavelength, larger differences would be observed among moonquake signals.

In addition to the monthly periodicities in the times of occurrence of moonquakes apparently related to lunar tides, longer-term variations in the total seismic energy release can also be correlated with tidal variations. Hence, tidal strain must contribute significantly to the total strain energy released as moonquakes. Tidal energy may, in fact, be the dominant source. However, the unipolarity of moonquake signals from a given focal zone implies that the source mechanism is a progressive dislocation and not one that periodically reverses in direction. A progressive source mechanism suggests a secular accumulation of strain energy periodically released by moonquakes. Whether the postulated secular strain component is of thermal or gravitational origin remains to be determined.

Moonquakes appear to be concentrated at great depth. In the few cases for which locations have been determined, the foci occur in a relatively thin zone between 800 and 1000 km deep. Of course, many of the foci not yet located may fall outside this zone.

On Earth, deep quakes are associated with downgoing lithospheric "slabs" subducted to great depths as part of the global convection system. On the Moon, where all evidence appears to preclude the presence of such plate movements, other explanations for deep quakes must be sought. Several possibilities are suggested.

(1) Maximum thermoelastic stresses in a cooling Moon occur at depths of 800 to 1000 km.

(2) Abrupt changes in phase of mantle material are occurring in the active focal zones.

(3) Large, high-density fragments, buried at great depth during the formation of the Moon, presently are "sinking" toward the center of the Moon.

(4) A concentration of fluids leading to a reduction of effective friction or a weakening of the silicate bond may occur at great depth.

(5) Weak convective motions at depth beneath a thick, rigid crust may generate deep moonquakes without the surface manifestations associated with terrestrial plate tectonics.

(6) Radial variations in the rigidity of the lunar material may be such as to concentrate the dissipation of tidal energy at great depth.

Present-day partial melting within the Moon beginning at depths of approximately 1000 km, as suggested by recent thermal models (ref. 9-19), may provide the energy necessary to produce progressive dislocations at great depth or to support weak convective motions.

Just as important as the fact that no young rocks have been found on the Moon, suggesting the absence of the 200-million-year cycle that leads to the emergence and destruction of rock at the surface of the Earth, is the lack of large moonquakes, which implies the absence of plate tectonic activity like that which exists on Earth.

The distribution of moonquake epicenters shows an apparent correlation with the rims of the major mascon basins. The reality of such a correlation,

while it cannot be completely discounted, must be questioned carefully, pending the proposal of a reasonable mechanism by which a narrow feature (such as a mare rim) could show any manifestation at such great depth and only in a narrow range of depths.

Moonquakes and deep structure.–Signals from deep moonquakes provide important data on the physical state of the outer half of the Moon. The locations of moonquake foci are based on a seismic velocity model derived by extrapolation of upper mantle velocities, determined from the LM and SIVB impacts, to great depth. In the two cases (A_1 and A_{20} foci) for which redundant data are available, the validity of this extrapolation can be checked. In both cases, the observed traveltimes agree well with those predicted from the model. Thus, it appears that the compressional wave velocity must remain nearly constant at approximately 8 km/sec to a depth of at least 800 km, and the elasticity of the lunar interior is appropriate for rocks of high rigidity (Poisson's ratio = 0.25). In addition, the presence of high-frequency (1 Hz and higher) shear waves in the moonquake signals is strong support for the conclusion that no zone of partially molten material exists in the outer 800 km traversed by these waves. These points are discussed in greater detail in the subsection entitled "Lunar Structure."

Meteoroid Flux

The positive identification of meteoroid impacts by means of their seismic waveform characteristics and the observation of a population of such events clearly offer the possibility of estimating some parameters of the meteoroid population in near-Earth space. Previously, Earth-based observations have produced estimates of the meteoroid population in terms of the parameters B and γ in the distribution

$$\log N = B + \gamma \log m \qquad (9\text{-}1)$$

where N is the count of particles/km^2/yr that hit the Earth with mass m grams or greater. Notably, Hawkins (ref. 9-20) found $B = 0.73$, $\gamma = -1.0$ for stony meteoroids (masses approximately 300 to 10^{10} g) by compiling visual data on falls and finds, while McCrosky (ref. 9-21) has obtained $B = -1.6$, $\gamma = -0.62$ from photographic measurements of luminous meteoroid trails observed by the Prairie Network. An objective of subsequent work will be to measure B and γ independently by means of lunar seismic data.

McCrosky obtained direct photographic velocity measurements for individual bodies by means of shutter breaks. His analysis is consistent with a preatmospheric average velocity of 25 km/sec for the population. For lunar impacts, this velocity would be equivalent to 22.5 km/sec because of weaker gravitational acceleration near the Moon. It will be shown that, for this impact velocity, the minimum detectable seismic signal is produced by less than 100 g at a distance of 50 km from the seismic station and about 10 kg at the antipodal point of the Moon. The largest signals yet observed were produced by an object falling approximately 233 km from the Apollo 12 station on May 13, shortly after deployment of the Apollo 16 station. At 22.5 km/sec, a mass of approximately 1100 kg would have produced the signal observed at this range. Because only a few of the strongest natural impacts have been located from their seismic signals, other objects of similar size may be represented by weaker signals from greater distances. Thus, the objects observed by use of seismic impact signals appear to be in the lower part of the mass range dominated by stony meteoroids, according to Hawkins (ref. 9-20).

Heretofore, the seismic data available on natural impacts rarely permitted location of the points of individual impacts. The larger natural impact signals observed simultaneously at the Apollo 12, 14, 15, and 16 stations will probably be suitable for finding individual locations, but work of this sort must be deferred until four-station playouts can be made from the digital tapes. The real-time system used during the missions provides for visual recording of data from only two stations at one time. Hence, the best data now available on the meteoroid flux problem are of a statistical nature (i.e., a cumulative count, n (per year)) of events whose signal amplitudes are equal to or greater than A (mm) on the seismic trace. The most reliable data of this sort are 64 events observed during 399 days at the Apollo 12 station, as represented in figure 9-15. In this sample interval, all events with maximum peak-to-peak envelope amplitudes greater than approximately 2.5 mm were examined and classified as either spurious instrumental deflections, moonquakes, or meteoroid impacts on the basis of signal character. Only the latter were included among the 64 events used here. The ranges and masses of individual impacts in this distribution are unknown, but the intercept and slope of the linear distribution, as indicated by the equa-

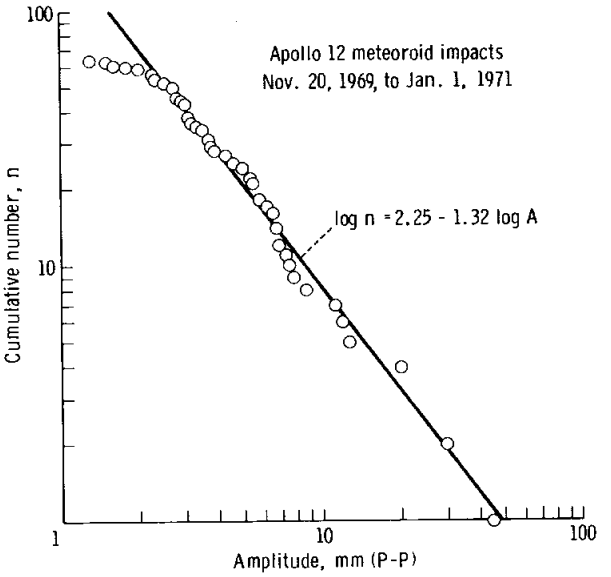


FIGURE 9-15.–Cumulative amplitude distribution for 64 meteoroid impact events. The ordinate of each point represents the number of events observed to have signals of amplitudes equal to or greater than represented by the abscissa of the point. After subtracting instrument downtime, the net interval of observation is 399 days between November 20, 1969, and January 1, 1971. The amplitudes measured are the maximum peak-to-peak amplitudes (mm) of the signal envelope recorded on the LPZ component at the Apollo 12 station, with trace deflection of 0.8 mm/DU. For analysis, the data are represented by the straight line shown. Its equation, after conversion to an annual rate, is $\log n = 2.25 - 1.32 \log A$, A in mm, n in events observed per year.

tion in figure 9-15, are used in evaluating the B and γ values of the meteoroid distribution corresponding to the seismic signals.

To relate seismic amplitude data to meteoroid flux, it is necessary to know the amplitude response of the Moon to an impact of standard size as a function of range. This information is available from the impacts of the SIVB third stage of Apollo booster vehicles as observed at the various stations. The source-receiver distances for the various SIVB impact seismograms are given in table 9-II. The amplitude data measured from these recordings are plotted in figure 9-16. Here, the primary artificial impact amplitude measurements are made on the LPZ component of the Apollo 12 station. Data of other stations, which are more sensitive than the Apollo 12 station because of effects of shallow layering, have been adjusted to represent peak-to-peak envelope amplitudes that would have been recorded by station 12 at the same range. The station corrections are made by comparing the amplitudes of signals from a representative sampling of natural events recorded at two or more stations.

To complete the amplitude plotted against chord range r variation for the entire Moon, the solid curve has been drawn in figure 9-16 on the basis of other data. For ranges less than 135 km at which the Apollo 12 station recorded the Apollo 13 SIVB impact, an amplitude variation as r^{-1} is assumed, because direct surface wave diffusion predominates in the near range as discussed elsewhere in this report. Diffusive spreading of surface waves, which is confined mainly to a surface wave guide approximately 100 m thick, is theoretically characterized by an r^{-1} amplitude variation (ref. 9-7). Distant signals are also interpreted as surface waves scattered locally in the surface wave guide, but the energy reaches the distant locality along deep ray paths through the lunar interior. Therefore, the variation with range of the signal envelope amplitude, represented by the solid segments of figure 9-16, is taken to follow the range variations of body-wave amplitudes calculated from the lunar body-wave velocity model discussed elsewhere. Beyond 356 km, the curve is controlled by a measured SIVB amplitude point at 356 km and another at 1012 km (chord range). No attempt is made to represent the sharp local peaks of the theoretical body-wave amplitude curve because wave guide diffusion is expected to spread the energy when it arrives at the surface.

The straight-line segments in figure 9-16 are represented individually by functions of the form

$$mv^2 = K_i\left(Ar^{\alpha_i}\right)^{2\beta} \qquad (9\text{-}2)$$

In equation (9-2), the quantity mv^2 is taken as 9.2×10^{17} (cgs units) from the kinetic energy of an SIVB impact (ref. 9-7). Subscript i refers to a single line segment, and each K and α is chosen to fit the curve. The product Ar^{α} accounts for variation of amplitude A as $r^{-\alpha}$ over the particular line segment. The exponent 2β permits amplitude scaling or variation of seismic coupling efficiency over a range of natural impact energies. If $2\beta = 2$, signal amplitude varies as the square root of energy, or coupling efficiency is

independent of impact energy. More likely, coupling efficiency increases with impact size, because larger craters penetrate harder material that can sustain larger elastic strains than the loose surface material in which small craters are formed. This condition would imply that $2\beta < 2$. It is possible to evaluate 2β experimentally by the following method.

Appendix B gives a theoretical expression for the cumulative number plotted against the amplitude curve of figure 9-15, which can be written as

$$\log n = D + 2\beta\gamma \log A \qquad (9\text{-}3)$$

Equation (9-3) is directly comparable with the straight-line representation of the lunar seismic data in figure 9-15, whereby the numerical values $D = 2.25$ and $2\beta\gamma = -1.32$ are obtained experimentally from the data.

Because β and γ are not determined separately from the seismic data, it is useful to consider any available constraints on their values. According to McCrosky or Hawkins, $\gamma = -0.62$ or $\gamma = -1.0$ can be adopted, but the wide divergence of these values leaves great uncertainty in completion of the calculations. Also, McCrosky's value leads to $2\beta = 1.32/0.62 = 2.13$, which is improbable from the considerations of seismic energy coupling. Rather, with $2\beta \leqslant 2$, it is expected that $-\gamma \geqslant 1.32/2 = 0.66$.

Gault's (ref. 9-22) summary of data on lunar crater size distributions and the cratering energy-diameter relationship suggests a method of estimating γ without reference to terrestrial meteoroid observations. For the youngest lunar surface examined, the Lunar Orbiter I P-8 site in southeastern Oceanus Procellarum, Gault illustrates a crater distribution where $N \propto d^{-3.7}$ for the range 100 m $< d <$ 1000 m. These craters are a little larger than the largest crater thought to have been formed by impacts observed seismically during the Apollo Program, but the characteristic exponent, -3.7, may apply also to the crater-forming events that have been recorded. If so, this size-frequency variation can be related to the mass-frequency variation of equation (9-1) through an energy or gravity scaling relationship for the cratering process.

Gault points out that energy scaling represented by $1/2\ mv^2 \propto d^3$ is appropriate for very small craters and that $1/2\ mv^2 \propto d^4$ is appropriate for larger craters (gravity scaling) with the transition at a crater diameter of approximately 1 km. He notes that $d^{3.4}$ is sometimes quoted as a compromise. Therefore, for the small cratering events observed seismically, it seems that a scaling law between $m \propto d^{3.0}$ and $m \propto d^{3.4}$ is the best choice. In this, v^2 is removed by assuming an average meteoroid velocity. Combined with the crater frequency law mentioned in the preceding paragraph, these relationships lead to frequency-mass variations of $N \propto m^{-3.7/3.0}$ and $N \propto m^{-3.7/3.4}$, or an acceptable range of $-1.23 \leqslant \gamma \leqslant -1.09$.

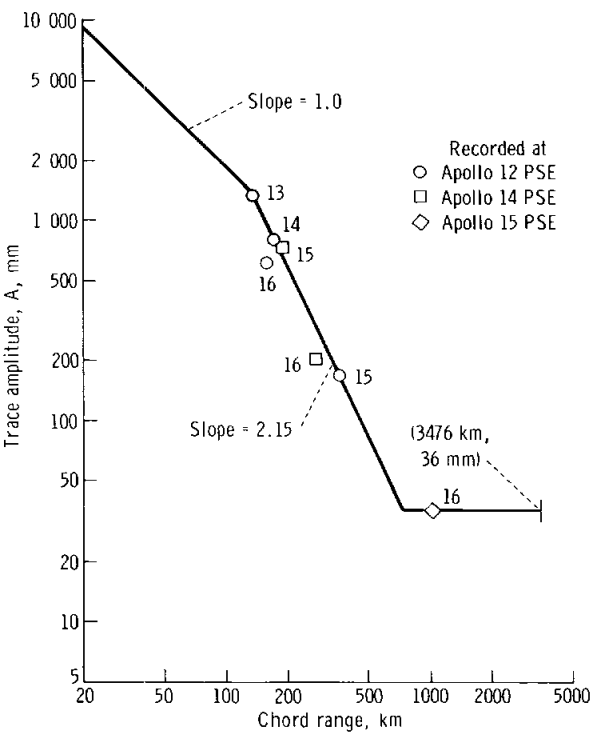


FIGURE 9-16.–Amplitude variation with range for SIVB impacts recorded on the Apollo 12 LPZ component. The open circles represent measurements of the Apollo 12 LPZ component. Other symbols are data derived from recordings at other stations. The number written beside each symbol identifies the mission during which that datum was obtained. All amplitudes except the Apollo 12 LPZ data are scaled for station sensitivity as described in the text. The amplitudes were measured as maximum peak-to-peak deflections of 90 percent of the swings at the time of maximum signal envelope on strip chart oscillograph playouts at a chart speed of 3.75 mm/min. Amplitudes plotted represent a deflection sensitivity of approximately 0.8 mm/DU (exactly 20 X 4 cm/1023 DU). Most records were measured at lower deflection sensitivities and scaled accordingly.

Another constraint on the value of γ may be derived from amplitude scaling considerations. From equation (9-2), the relation between the energies and signal amplitudes of an SIVB impact and an LM impact at the same range is $E_{SIVB}/E_{LM} = (A_{SIVB}/A_{LM})^{2\beta}$. Considering the grazing impact of the LM vehicle, the conversion of LM energy to seismic signal may be even less efficient than implied by this relationship. Therefore, it is possible to substitute the inequality, $E_{SIVB}/E_{LM} \leqslant (A_{SIVB}/A_{LM})^{2\beta}$. Using $E_{SIVB}/E_{LM} = 14$ for the two space vehicles and $A_{SIVB}/A_{LM} = 20$ observed from LM and SIVB impacts (ref. 9-9, fig. 8-16), it is found that $2\beta \geqslant 0.88$, which, combined with the observed $2\beta\gamma = -1.32$, indicates that $\gamma \geqslant -1.50$. This is consistent with the constraint discussed in the preceding paragraph but does not place more stringent limits on the acceptable range of values found there.

Therefore, to calculate the mass flux of meteoroids, data from four sources are accepted: (1) the lunar seismic flux at the Apollo 12 station as shown in figure 9-15 and represented by $\log n = 2.25 - 1.32 \log A/\text{yr}$; (2) the seismic sensitivity of the Moon as represented by response of Apollo 12 station LPZ to SIVB impacts at all ranges, given by the curve of figure 9-16; (3) the average impact velocity of 22.5 km/sec, derived from McCrosky's Earth-based observations of luminous meteoroid trails; and (4) the constraint $-1.23 \leqslant \gamma \leqslant -1.09$ derived from the size distribution of craters in the youngest lunar mare and from a well-established crater diameter scaling relation. All of these except item 3 are derived from measurements on the Moon. The calculation used to obtain the best fitting values of the terrestrial flux intensity parameter B and the size distribution parameter γ is described in the following paragraph.

In appendix B, it is shown that the intercept of the cumulative amplitude curve has the analytic form (eq. (9-18)) and, from figure 9-15, its measured value is $D = 2.25$. The C is evaluated from data of the amplitude fall-off curve (fig. 9-16) according to the expression of equation (9-16). This makes equation (9-18) a relation between B, γ, and v for the given lunar model represented by the fall-off curve. The average meteoroid velocity of 22.5 km/sec is adopted from McCrosky's measurements, and B is evaluated for the two cases listed in table 9-IV. Also from equation (9-13), the lunar flux N_Q is related to the Earth flux N by $N_Q/N = 0.81$, from which the logarithmic intercept for lunar flux B_Q is 0.09 order of magnitude lower than for Earth flux B.

In figure 9-17, McCrosky's and Hawkins' Earth flux models are compared with the lunar flux models represented by cases 1 and 2 of table 9-IV. The two lunar curves correspond to the limits of crater size-frequency variation adopted from Gault's discussion. The difference between these two lunar flux models is very minor compared with their departure from the previously measured Earth flux models. The effect of Earth gravitational attraction as opposed to lunar gravitational attraction accounts for only 0.09 unit on the ordinate; that is, the lunar curves should be raised by 0.09 unit to compare directly with the McCrosky and Hawkins curves.

Thus, the model of flux represents a very great departure from earlier Earth-based measurements. Two explanations are possible: either the flux has decreased markedly in the few years since the Earth-based data were gathered (only approximately 3 yr from the end of McCrosky's observations until the start of the authors' observations), or the flux has remained about the same during this interval and the divergent results are explainable by differences in the methods of measurement. Whereas short-term variations are to be expected if particle orbits cluster into streams, both McCrosky's data and those of the authors span an interval of more than 1 yr (500 days and 399 days, respectively), which should greatly reduce such effects. There seems to be no reason to expect large secular variations on a scale of years.

TABLE 9-IV.– Data Used in Meteoroid Flux Calculations

Case	D	$2\beta\gamma$	γ	2β	C	v, *cm/sec*	B	B_Q	mv^2 *(cgs units)*
1	2.25	-1.32	-1.09	1.211	-9.69	22.5×10^5	-1.81	-1.90	9.2×10^{17}
2	2.25	-1.32	-1.23	1.073	-12.21	22.5×10^5	-1.07	-1.16	9.2×10^{17}

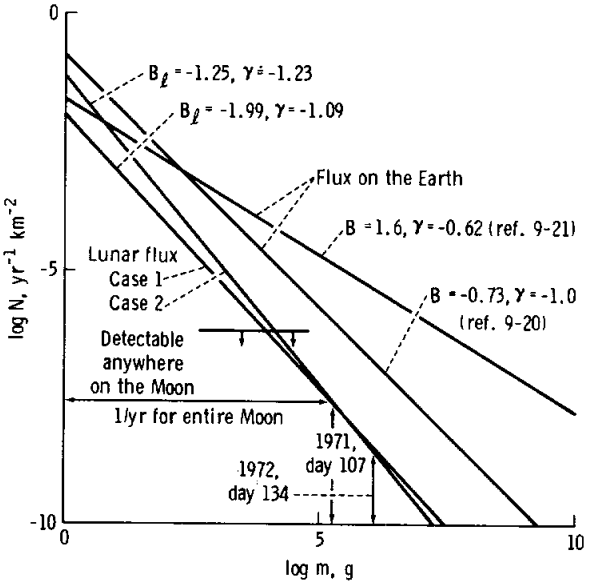


FIGURE 9-17.—Lunar flux curves representing a range of likely values (cases 1 and 2) from lunar data are compared with earlier flux measurements from Earth by Hawkins (ref. 9-20) and McCrosky (ref. 9-21). An impact velocity of 22.5 km/sec is implicit in the lunar curves. For the lunar surface area of 3.794×10^7 km^2, the level of one event per year is represented at −7.58 on the log frequency scale as shown. Mass values of two large events not included in the interval of the data sample are indicated: 1971 day 107 had moonquake waveform characteristics but fits the impact statistics much better than the moonquake statistics; 1972 day 134 had an impact waveform and was the strongest signal ever observed. The smallest mass detectable from any point on the Moon is slightly different for case 1 and 2 because the different values of 2β for these cases imply a difference in seismic coupling for impacts of the same mass.

It is thought that the lunar seismic analysis is weakest on the question of seismic coupling efficiency at various masses or energies. The energy of the calibration impact, an SIVB at 2.56 km/sec, is approximately the same as that of a 180-kg meteoroid at 22.5 km/sec. This seems to be near the upper end of the range of observed natural masses but not outside the range. A scaling relation between impact energy and seismic amplitude (eq. (9-2)) is included in the theory, with parameter 2β determined from the slope $2\beta\gamma$ of the observed cumulative number plotted against the amplitude (fig. 9-15), but it is not possible to check this relation independently by observing the signal generated by an impact of some known lower energy at a known range. It is hoped that this opportunity will be afforded by space vehicle impacts that can be planned before the demise of the seismic stations.

Uncertainties in details of the amplitude fall-off curve of figure 9-16, corresponding to uncertainties in the lunar seismic wave propagation model, probably account for errors no greater than a factor of 0.3 in the value of the parameter C of equation (9-16).

Conversely, it would seem that determining the mass of a meteoroid from its measured velocity and photographic brightness is a difficult problem. It was noted previously that the gentle slope of McCrosky's mass flux curve seems improbable from considerations of impact energy as compared with seismic amplitude scaling. A guess could be made that the luminosity of a meteoroid is proportional to its surface area rather than to its mass, as McCrosky assumed. However, this relationship would flatten the mass flux curve even more. Conversely, a guess could be made that only heavier objects penetrate the denser atmosphere before slowing down much and, therefore, that the surface temperature and brightness of bigger masses would increase out of proportion to mass. This effect, if important, would tend to steepen the mass flux curve and might bring McCrosky's results into better agreement with those of the authors.

A critical examination of both methods is warranted. A network of widely spaced seismograph stations will now permit an approximate location to be determined for many of the larger impacts. This network will permit a more direct measurement of the areal density of detectable impacts, particularly because the minimum detectable mass appears to be constant for ranges beyond approximately 700 km from a station (discussed in the following paragraphs). This result itself can be tested by simultaneous four-station observations.

Some consequences of the measured mass flux and amplitude fall-off function are illustrated in figure 9-18. The curve giving cumulative fraction of events observed within increasing chord distances is calculated by evaluating the definite integral of equation (9-16) in small steps. Ordinates on the curve are the partial value out to a given chord distance divided by the final value obtained for the complete lunar surface. This curve depends on the fall-off curve

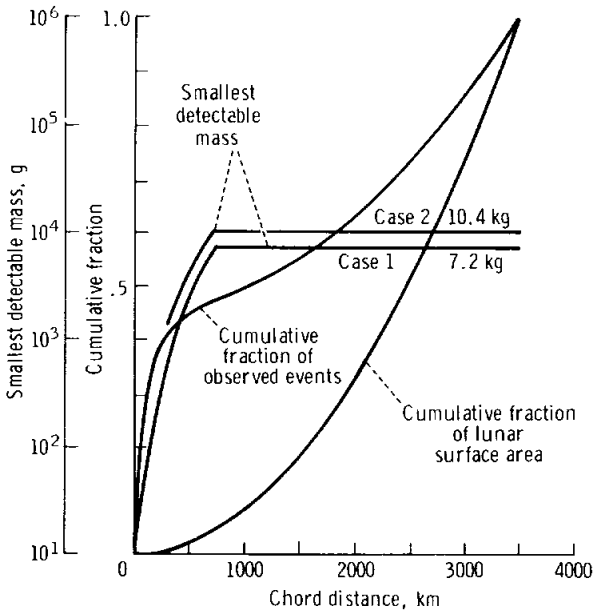


FIGURE 9-18.–Cumulative increase of observed flux is plotted as a function of increasing distance from the seismometer. This curve is the same for cases 1 and 2. Comparison with the cumulative surface area curve shows what fraction of the total surface area receives a given fraction of the total observed flux. The smallest detectable mass (at minimum signal amplitude A = 2.5 mm) is also given as a function of distance. These curves differ for cases 1 and 2 because seismic coupling efficiency differs as indicated by different values of 2β in equation (9-2). The flat portions of these curves correspond to the flat portion of the amplitude fall-off curve in figure 9-16 and to the mass indicated in figure 9-17 as detectable anywhere on the Moon.

but not on the mass flux parameters. The curve giving cumulative fraction of lunar surface area is a parabola. Comparing these two curves shows, for example, that 1 percent of the lunar surface area nearest the station (within a chord range of approximately 340 km) receives approximately 42 percent of the impacts detected seismically, that 50 percent of the detected events occur in approximately 10 percent of the area (chord ranges to approximately 1100 km), and that the nearest hemisphere (50 percent) of the lunar surface receives approximately 72 percent of the detected impacts. Also in figure 9-18 is illustrated the minimum detectable mass (striking at 22.5 km/sec). This is calculated by substituting the minimum detectable signal amplitude (A = 2.5 mm) and other evaluated parameters into equation (9-2). In this, each K_i and α_i is found from the fall-off curve (fig. 9-16) and 2β is found from $2\beta\gamma = -1.32$ (fig. 9-15) and the assumed values of γ. The detectable mass curve is slightly different for the two cases because a different value of 2β implies a different coupling efficiency for impacts. It is thought that there may be significant errors if the minimum detectable mass is calculated by this method for ranges less than 50 km, because the very small masses that are abundant enough to count appreciably in such a small area probably generate signal frequencies above the response spectrum of the seismometers. This does not cause a large error in the other results, however, because the cumulative fraction of events reaches a value of only 15 percent in the first 50 km, but the detectability of masses lower than perhaps 100 g is uncertain on the long-period seismometers.

The lunar flux estimate represented by figure 9-17 has important implications regarding the history of the Moon and the solar system. Wetherill (ref. 9-23) has noted the difficulty of reconciling the high previous measurements of flux with the relatively low present crater density and the great ages of the lunar maria that have been established during the Apollo Program. He refers to flux too high by a factor of 35 by comparison with the mare crater densities quoted by Gault. It is true that the masses observed on the lunar seismograph network fall a little short of the size range that produces craters visible in the Lunar Orbiter photograph. However, if the new mass flux curve is extrapolated to 10^6 kg, approximately 3 or 4 orders of magnitude beyond the authors' data, it can be seen that it indicates an abundance approximately 2 orders of magnitude less than Hawkins' estimate and more than 4 orders of magnitude less than McCrosky's. This would represent a lower present flux rate than the average needed to produce the visible mare craters in 3.5×10^9 yr. This result is acceptable in terms of the concept that the flux has decreased greatly in that time interval as smaller fragments in the solar system are swept up by the planets. It obviates the necessity of a young source of new fragments that could make the present flux abnormally high.

SUMMARY AND CONCLUSIONS

Analysis of seismic data from manmade impacts has established the presence of a lunar crust approximately 60 km thick in the region of the Apollo 12 and 14 stations. The velocity of seismic waves (compressional) is about 7 km/sec throughout the deeper half of the mare crust. Among the major lunar rock types identified thus far, this velocity is close to that expected for only one type – the gabbroic anorthosites that are predominant in the highlands of the Descartes site. Results from the X-ray fluorescence experiment, carried out from lunar orbit, suggest that this rock type is representative of the lunar highlands on a global scale. Thus, combining in situ velocity information with laboratory data from returned lunar samples, the following is the most probable hypothesis that can be put forward at this time.

(1) The primitive lunar crust, which is still preserved in the highlands, is approximately 60 km thick in the Fra Mauro region of the Moon.

(2) The lunar crust consists primarily of gabbroic and anorthositic material.

(3) The maria were formed by the excavation of the initial crust by meteoroid impacts and subsequent flooding by basaltic material.

(4) Seismic evidence suggests that the basalt layer may be 25 km thick in the southeastern portion of Oceanus Procellarum, comparable to the thickness inferred for mascon maria.

Beneath the base of the crust, the velocity of seismic waves increases abruptly to approximately 8 km/sec and remains at, or near, this value to the maximum depth investigated (approximately 120 km). This velocity is close to the average for rocks of the upper mantle of the Earth. Signals from the manmade impacts and deep moonquakes show that the elasticity of the lunar interior is appropriate for rocks of high rigidity (Poisson's ratio $\sigma = 0.25$) and that no widespread zone of melting or partial melting can exist in the outer 800 km of the Moon. If the lunar crust were derived by differentiation, as seems probable, then widespread melting of the outer shell of the Moon early in its history is inferred from the thickness of the lunar crust. The required depth of melting depends on the assumed initial composition of the Moon, but it is likely that at least 50 percent of the Moon was differentiated early in its history.

Moonquakes are recorded at all Apollo seismic stations. Based on the data obtained during the first 45 days of operation of the Apollo 16 station, moonquakes are detected at this station at an average rate of approximately 10 000/yr. This rate compares with annual rates of 700, 2000, and 650 at the Apollo 12, 14, and 15 stations, respectively. The varying rates of detection are believed to be a consequence primarily of differing station sensitivities that appear to be closely correlated with the local structure and the thickness of the weakly cohesive material of the surficial zone at each site. All of the moonquakes are small. With one possible exception, the largest of them have equivalent Richter magnitudes between 1 and 2. The total seismic energy release within the Moon appears to be many orders of magnitude below that of the Earth.

Moonquakes originate at no less than 22 different locations. It is likely that moonquakes originate at numerous other active zones from which the signals are too weak to be analyzed in detail. Moonquakes from a given active focus have essentially identical waveforms at a given recording station. Moonquakes also show a monthly periodicity in their times of occurrence. Peaks in the total number of events detected at a given station occur at approximately 14-day intervals. These cycles strongly suggest that moonquakes are induced by lunar tides. However, the pattern of moonquake occurrence is not related simply to the monthly changes in Earth-Moon separation (the apogee-perigee cycle) but is complicated by the influence of lunar librations and solar perturbations of the lunar orbit. Thus far, signals from seven of the moonquake foci have been large enough to provide data necessary to obtain locations. The focal depths can be determined in five of these cases. All of these occur in the depth range from 800 to 1000 km. Each focal zone must be small (less than 10 km in linear dimension) and fixed in location for periods of at least 2 yr.

In addition to the monthly periodicities in the times of occurrence of moonquakes apparently related to lunar tides, longer-term variations in the total seismic energy release can also be correlated with tidal variations. Hence, tidal strain must contribute significantly to the total strain energy released by moonquakes. Tidal energy may be, in fact, the dominant source. However, it appears that another

source of strain may be present in view of the secular variation and great depth of the moonquake activity. Whether the additional strain component is of thermal or gravitational origin is unknown.

On Earth, deep quakes are associated with lithospheric slabs that sink to great depth in a global convection system. On the Moon, where all evidence appears to preclude the presence of such plate movements, other explanations for deep quakes must be sought. Several possibilities are suggested.

(1) Maximum thermoelastic stresses in a cooling Moon occur at depths of 800 to 1000 km.

(2) Abrupt phase changes of mantle material are occurring in the active focal zones.

(3) Large high-density fragments, buried at great depth during the formation of the Moon are presently "sinking" toward the center of the Moon.

(4) A concentration of fluids at great depth leads to a reduction of effective friction or a weakening of the silicate bond.

(5) Weak convective motions at depth beneath a thick, rigid crust might generate deep moonquakes without the kind of surface manifestations associated with terrestrial plate tectonics.

(6) Radial variations in rigidity of the lunar material may be such as to concentrate the dissipation of tidal energy at great depth.

Present-day partial melting within the Moon beginning at depths of approximately 1000 km, as suggested by recent thermal models (ref. 9-14), might provide the energy for dislocations at great depths or support weak convection.

The absence of cycles of emergence of rock on the surface of the Moon and destruction at depth can be inferred from several observations.

(1) No young rocks have been found on the Moon.

(2) Surface features give no evidence of large horizontal movement such as folded or offset structures.

(3) Large moonquakes are absent.

The distribution of moonquake epicenters (points on the lunar surface directly above the foci) shows an apparent correlation with the rims of the major mascon basins. Although this correlation cannot be completely discounted, its significance must be questioned pending the proposal of a reasonable mechanism by which a narrow surface feature, such as a mare rim, could influence activity at such great depth and in a narrow range of depths only.

Seismic signals detected by the PSE from meteoroid impacts appear to be generated by objects in the mass range 100 g to 1000 kg. The specific flux estimated from the accumulated data varies from 1 order of magnitude lower to as much as 3 orders of magnitude lower than that derived from photographic measurements of the luminous trails of meteoroids striking the atmosphere of the Earth. The mass flux estimate is also lower than the average flux estimated from the distribution of crater sizes on the youngest lunar maria. This estimate is consistent with a hypothesis that the population of small fragments in the solar system decreases with time as they are gathered up by collisions with the planets. The seismic data predict that between 30 and 40 impacts/yr will be detected simultaneously by all stations of the Apollo seismic network and that a meteoroid of mass 7 to 10 kg can be detected by the least sensitive station (Apollo 12 station) from any point on the Moon. The average of acceptable flux estimates derived from seismic measurements is

$$\log N = -1.62 - 1.16 \log m \qquad (9\text{-}4)$$

where N is the cumulative number of meteoroids of mass m (in grams) and greater that strike the Moon per square kilometer per year.

The surface of the Moon is covered by a highly heterogeneous layer in which seismic waves propagate with relatively little damping and are intensively scattered. It is the presence of this layer (the "scattering zone") that accounts for the marked differences between lunar seismic signals and typical terrestrial seismic signals. Most of the heterogeneity effective in scattering seismic waves at the observed frequencies is confined to the upper several hundred meters of the surface layer, although the total thickness of the layer in which significant scattering occurs may be as great as 10 to 20 km. It is probable that the complex structure of the surface layer of the Moon is a consequence primarily of cratering processes.

APPENDIX A

AMPLITUDE OF SCATTERED SURFACE WAVES FROM A MOVING SOURCE

The near-surface layer of the Moon is characterized by (1) a high degree of heterogeneity, resulting in intensive scattering of seismic waves; (2) the nearly complete absence of volatiles, resulting in low absorption of seismic energy; and (3) a rapid increase in velocity with depth, resulting from self-compaction. In such a structure, the transmission of seismic surface-wave energy can be considered as a diffusion process in a two-dimensional space and therefore can be described by the diffusion equation

$$\frac{\partial E}{\partial t} = \frac{\xi}{4}\nabla^2 E - \frac{\omega}{Q}E \qquad (9\text{-}5)$$

where

E = seismic energy density
t = time
$\xi = 2\nu\mu$ = diffusivity
ν = seismic velocity
μ = equivalent mean free path
ω = angular frequency
Q = dissipation factor

A solution of equation (9-5) for an impulsive source of energy E_0 at the origin $r = 0$ of a two-dimensional space at time $t = 0$ is given by

$$E = \frac{E_0}{\pi\xi t}\exp\left[-\frac{r^2}{\xi t} - \frac{\omega t}{Q}\right] \qquad (9\text{-}6)$$

Consider a source that generates seismic energy at the surface at a constant rate of ϵ per unit time while it is moving away from a fixed seismic station at a constant radial velocity c relative to the station. Also choose the origin of time in such a way that the source passes through the seismic station at time $t = 0$. Then, from equation (9-6), the energy density at time t at the seismic station caused by a short burst of energy generated by such a source at a distance $c\tau$ during a time interval $t - \tau$ to $t - \tau + d\tau$ is given by

$$dE = \frac{\epsilon}{\pi\xi(t-\tau)}\exp\left[-\frac{(c\tau)^2}{\xi(t-\tau)} - \frac{\omega(t-\tau)}{Q}\right]d\tau \qquad (9\text{-}7)$$

where $0 \leqslant \tau \leqslant t$. Integrating equation (9-7) over the time inverval $\tau = t_0$ to $\tau = t$, the energy density is obtained at the seismic station at time t caused by the moving source that has started at time t_0 at a distance $r_0 = ct_0$ and has moved to a distance $r = ct$ at time t as

$$E(t) = \int_{r_0/c}^{r/c} \frac{\epsilon}{\pi\xi(t-\tau)}\exp\left[-\frac{(c\tau)^2}{\xi(t-\tau)} - \frac{\omega(t-\tau)}{Q}\right]d\tau \qquad (9\text{-}8)$$

Now let

$$s = \sqrt{\frac{\omega}{\xi Q}}\,r \qquad \text{(normalized distance)}$$

$$z = \sqrt{\frac{\omega}{\xi Q}}\,c(t-\tau)$$

$$u = \sqrt{\frac{Q}{\xi\omega}}\,c \qquad \text{(normalized source velocity)}$$

Then, equation (9-8) becomes

$$E(s) = \frac{\epsilon}{\pi\xi}\,\ell^{25u}\int_{s_0}^{s} z^{-1}\exp\left[-s^2 u z^{-1} - \frac{1+u^2}{u}z\right]dz \qquad (9\text{-}9)$$

where

$$s_0 = \sqrt{\frac{\omega}{\xi Q}}\,r_0 \text{ and } u > 0.$$

Similarly, for a source that has started at a distance r and is moving toward the seismic station

$$E(s) = \frac{\epsilon}{\pi\xi}\,\ell^{25u}\int_{0}^{s_m - s} y^{-1}\exp\left[s^2 u y^{-1} + \frac{1+u^2}{u}y\right]dy \qquad (9\text{-}10)$$

where

$$s_m = \sqrt{\frac{\omega}{\xi Q}}\,r_m,\ y = -z, \text{ and } u < 0.$$

For a given near-surface material, the observed amplitude of seismic signals is proportional to the square root of the energy density given by equation (9-9) or (9-10). Except for a short time after the source starts moving, replacing the lower limit of integration in equation (9-9) by 0 and replacing the upper limit of integration in equation (9-10) by ∞ give approximations of sufficient accuracy.

APPENDIX B

THEORETICAL RELATIONSHIPS BETWEEN SEISMIC FLUX AND MASS FLUX OF METEOROIDS

It is desired to evaluate the parameters B and γ in the equation

$$N = 10^{B} m^{\gamma} \tag{9-11}$$

where m is mass in grams and N is the mass flux on Earth in meteoroids per square kilometer per year of mass m or greater.

It is assumed that a population of seismic signals generated by meteoroid impacts on the Moon has been identified; that the maximum peak-to-peak seismic amplitudes of individual events have been measured at a single seismic station; and that the source-receiver distances of individual events are unknown. The population of seismic data may be represented by the cumulative distribution

$$\log n = D + b \log A \tag{9-12}$$

with $D = 2.25$ and $b = -1.32$ measured experimentally from the data of figure 9-15. Here, n is in events per year observed at the seismic station and A is the amplitude measurement. A point (n, A) on the curve represents the number n of events observed per year that have amplitude A (mm) or greater.

It is also assumed that the variation of maximum signal amplitude for a standard impact source (an SIVB) is known as a function of distance over the Moon. The signal amplitude is represented as $A = A_0(r)$, where r is the chord range (measured as the length of the chord from source to receiver through the Moon). A series of line segments of the form given in equation (9-5) is denoted by $A_0(r)$.

The terrestrial and lunar flux from the same interplanetary population of particles may differ because of the difference in gravitational attraction of the Earth and the Moon. This effect is especially important if the particles are moving in interplanetary space with a velocity that is not large compared to the escape velocity of Earth. This statement would be true of fragments in heliocentric orbits similar to that of Earth. The relative velocity of Earth and Moon caused by the motion of the Moon around the Earth, which is approximately 1 km/sec, is neglected. Then, from conservation of energy, the lunar flux N_ℓ in terms of terrestrial flux N is

$$N_\ell/N = v^2/\left(v^2 - v_\ell^{\,2} + v_e^{\,2}\right) \tag{9-13}$$

where v_ℓ is the lunar escape velocity and v_e is the terrestrial escape velocity. Note here that a particle that strikes the Moon with velocity v has a velocity $(v^2 - v_\ell^{\,2})^{1/2}$ outside the gravitational influence of the Moon, and it would have had an impact velocity $(v^2 - v_\ell^{\,2} + v_e^{\,2})^{1/2}$ if it had struck the Earth instead. With N_ℓ in impacts per square kilometer per year on the surface of the Moon, the total flux per year hitting the Moon is

$$n = \int_0^{2a} N_\ell (2\pi r dr) \tag{9-14}$$

where a is the lunar radius. Note that r is the chord distance from the seismograph station to any point on the surface of the Moon and that the area of a plane circle of radius $2a$ is the same as the surface area of the Moon. To complete the integration in equation (9-14), N_ℓ is expressed in terms of N and v as in equation (9-13), N is substituted for the expression given by equation (9-11), and m in turn is replaced by an expression obtained from equation (9-2). The integral is then

$$n = 2\pi\, 10^{B} v^{2(1-\gamma)} \left(v^2 - v_\ell^{\,2} + v_e^{\,2}\right)^{-1} A^{2\beta\gamma\Sigma_i K_i^{\gamma}} \int_{r_{i-1}}^{r_i} r^{1+2\beta\gamma\alpha_i} dr \tag{9-15}$$

The summation over i includes all the segments of the function $A_0(r)$ that intersect at chord distances r_i. In terms of logarithms, the seismic collector sensitivity C may be defined as

$$C = \log(2\pi) + \log\left[\Sigma_i K_i^{\gamma} \left(2 + 2\beta\gamma\alpha_i\right)^{-1} \left(r_i^{\,2+2\beta\gamma\alpha_i} - r_{i-1}^{\,2+2\beta\gamma\alpha_i}\right)\right] \tag{9-16}$$

so that

$$\log n = C + B + 2(1-\gamma)\log v - \log\left(v^2 - v_\ell^{\,2} + v_e^{\,2}\right) + 2\beta\gamma \log A \tag{9-17}$$

Therefore, by comparison with equation (9-17), the quantity

$$D = C + B + 2(1 - \gamma)\log v - \log\left(v^2 - v_\ell^2 + v_e^2\right) \tag{9-18}$$

is the intercept and $2\beta\gamma$ is the slope of the cumulative amplitude curve (eq. (9-12)) observed at the Apollo 12 station.

REFERENCES

9-1. Latham, Gary V.; Ewing, Maurice; Press, Frank; Sutton, George; et al.: Passive Seismic Experiment. Sec. 6 of Apollo 11 Preliminary Science Report. NASA SP-214, 1969.

9-2. Latham, Gary V.; Ewing, Maurice; Press, Frank; Sutton, George; et al.: Apollo 11 Passive Seismic Experiment. Science, vol. 167, no. 3918, Jan. 30, 1970, pp. 455-467.

9-3. Latham, Gary V.; Ewing, Maurice; Press, Frank; Sutton, George; et al.: Apollo 11 Passive Seismic Experiment. Proceedings of the Apollo 11 Lunar Science Conference, vol. 3, A. A. Levinson, ed., Pergamon Press (New York), 1970, pp. 2309-2320.

9-4. Latham, Gary V.; Ewing, Maurice; Press, Frank; Sutton, George; et al.: Passive Seismic Experiment. Sec. 3 of Apollo 12 Preliminary Science Report. NASA SP-235, 1970.

9-5. Latham, Gary V.; Ewing, Maurice; Press, Frank; Sutton, George; et al.: Seismic Data From Man-Made Impacts on the Moon. Science, vol. 170, no. 3958, Nov. 6, 1970, pp. 620-626.

9-6. Ewing, Maurice; Latham, Gary V.; Press, Frank; Sutton, George; et al.: Seismology of the Moon and Implications of Internal Structure, Origin, and Evolution. Highlights of Astronomy, D. Reidel Pub. Co. (Dordrecht, Holland), 1971.

9-7. Latham, Gary V.; Ewing, Maurice; Press, Frank; Sutton, George; et al.: Passive Seismic Experiment. Sec. 6 of Apollo 14 Preliminary Science Report. NASA SP-272, 1971.

9-8. Latham, Gary V.; Ewing, Maurice; Press, Frank; Sutton, George; et al.: Moonquakes. Science, vol. 174, 1971, pp. 687-692.

9-9. Latham, Gary V.; Ewing, Maurice; Press, Frank; Sutton, George; et al.: Passive Seismic Experiment. Sec. 8 of Apollo 15 Preliminary Science Report. NASA SP-289, 1972.

9-10. Latham, Gary; Ewing, Maurice; Press, Frank; Sutton, George; et al.: Moonquakes and Lunar Tectonism. Proceedings of the Third Lunar Science Conference, vol. 3, David R. Criswell, ed., MIT Press (Cambridge, Mass.), 1972.

9-11. Latham, Gary; Ewing, Maurice; Dorman, James; Lammlein, David; et al.: Moonquakes and Lunar Tectonism. The Moon, vol. 4, no. 3/4, June/July 1972, pp. 373-382.

9-12. Toksoz, M. N.; Press, Frank; Dainty, Anton; Anderson, Ken; et al.: Structure, Composition and Properties of Lunar Crust. Proceedings of the Third Lunar Science Conference, vol. 3, MIT Press (Cambridge, Mass.), 1972.

9-13. Toksoz, M. N.; Press, Frank; Anderson, Ken; Dainty, A.; et al.: Velocity Structure and Properties of the Lunar Crust. The Moon, vol. 4, no. 3/4, June/July 1972, pp. 490-504.

9-14. Reid, Arch M.; Ridley, W. I.; Warner, Jeff; Harmon, R. S.; et al.: Chemistry of Highland and Mare Basalts as Inferred from Glasses in Lunar Soils. Lunar Science – III, Revised Abstracts of the Third Lunar Science Conference, (Houston, Tex., Jan. 10-13, 1972), Carolyn Watkins, ed., Lunar Science Institute Contribution No. 88, Feb. 18, 1972, pp. 640-642.

9-15. Ringwood, A. E.; and Essene, E.: Petrogenesis of Apollo 11 Basalts, Internal Constitution and Origin of the Moon. Proceedings of the Apollo 11 Lunar Science Conference, vol. 1, A. A. Levinson, ed., Pergamon Press (New York), 1970, pp. 769-799.

9-16. Smith, J. V.; Anderson, A. T.; Newton, R. C.; Olsen, E. J.; et al.: Petrologic History of the Moon Inferred From Petrography, Mineralogy and Petrogenesis of Apollo 11 Rocks. Proceedings of the Apollo 11 Lunar Science Conference, vol. 1, A. A. Levinson, ed., Pergamon Press (New York), 1970, pp. 897-925.

9-17. Green, D. H.; Ringwood, A. E.; Hibberson, W. O.; Major, A.; and Kiss, E.: Experimental Petrology and Petrogenesis of Apollo 12 Basalts. Proceedings of the Second Lunar Science Conference, vol. 1, A. A. Levinson, ed., MIT Press (Cambridge, Mass.), 1971, pp. 601-615.

9-18. Biggar, G. M.; O'Hara, M. J.; Peckett, A.; and Humphries, D. J.: Lunar Lavas and the Achondrites: Petrogenesis of Protohypersthene Basalts in the Maria Lava Lakes. Proceedings of the Second Lunar Science Conference, vol. 1, A. A. Levinson, ed., MIT Press (Cambridge, Mass.), 1971, pp. 617-643.

9-19. Toksoz, M. Nafi; Solomon, Sean C.; Minear, John W.; and Johnston, David H.: Thermal Evolution of the Moon. The Moon, vol. 4, no. 1/2, Apr. 1972, pp. 190-213.

9-20. Hawkins, Gerald: Interplanetary Debris Near the Earth. Annual Review of Astronomy and Astrophysics, Leo Goldberg, Armin J. Deutsch, and David Layzer, eds., Annual Reviews, Inc. (Palo Alto, Calif.), 1964.

9-21. McCrosky, R. E.: The Distribution of Large Meteoritic Bodies. Smithsonian Astrophysical Observatory Special Report 280 (Cambridge, Mass.), June 19, 1968.

9-22. Gault, Donald: Saturation and Equilibrium Conditions for Impact Cratering on the Lunar Surface: Criteria and Implications. Radio Science, vol. 5, no. 2, Feb. 1970, pp. 273-291.

9-23. Wetherill, George W.: Of Time and the Moon. Science, vol. 173, no. 3995, July 1971, pp. 383-392.

10. Active Seismic Experiment

Robert L. Kovach,[a†] Joel S. Watkins,[b] and Pradeep Talwani[a]

The purpose of the active seismic experiment (ASE) is to generate and monitor seismic waves to study the lunar near-surface structure. Specifically, how thick is the lunar regolith at the Apollo 16 site? What are the acoustic or seismic properties of the lunar near-surface material? Are there any distinct seismic horizons and do they correlate with our estimates of geological horizons? Is there a characteristic difference in the shallow seismic velocities between the maria and the highlands? Several seismic energy sources are used: an astronaut-activated thumper device, a mortar package that contains rocket-launched grenades, and the impulse produced by the lunar module (LM) ascent.

To date, analysis of some seismic signals recorded by the ASE has provided data concerning the near-surface structure at the Descartes landing site. Two compressional (P-wave) seismic velocities have so far been recognized in the seismic data. The lunar surface material (fig. 10-1) has a seismic wave velocity of 114 m/sec. Underlying this surficial material at a depth of 12.2 m, the lunar rocks have a velocity of 250 m/sec. The 114-m/sec material velocity is assigned to the lunar regolith and agrees closely with the surface velocity measured at the Apollo 12, 14, and 15 landing sites; this agreement indicates that no major regional difference exists in the near-surface acoustical properties of the Moon.

The material underlying the regolith does not indicate that competent lava flows exist in the Cayley Formation at the Apollo 16 site. Instead, this velocity of 250 m/sec is suggestive of brecciated material or impact-derived debris of as yet undetermined thickness. Further analyses of the ASE grenade seismic signals should give more information on the deeper structure at the Apollo 16 landing site.

[a]Stanford University.

[b]University of North Carolina.

†Principal Investigator.

INSTRUMENT DESCRIPTION AND PERFORMANCE

The ASE consists of a thumper and geophones, a mortar package assembly (MPA), electronics within the Apollo lunar surface experiments package (ALSEP) central station, and interconnecting cabling. The components of the ASE are shown in figure 10-2.

The astronaut-activated thumper is a short staff used to detonate small explosive charges – single bridgewire Apollo standard initiators. Twenty-one initiators are mounted perpendicular to the base plate at the lower end of the staff. A pressure switch in the base plate detects the instant of initiation. An arm-fire switch and an initiator-selector switch are located at the upper end of the staff. A cable connects the thumper to the central station to transmit real-time event data. The thumper also stores the three geophones and connecting cables until deployment on the lunar surface.

The three identical geophones are miniature seismometers of the moving coil-magnet type. The coil is the inertial mass suspended by springs in the magnetic field. Above the natural resonant frequency of the geophones (7.5 Hz), the output is proportional to ground velocity. The geophones are deployed at 3-, 48-, and 93-m (10-, 160-, and 310-ft) intervals in a linear array from the central station and are connected to it by cables.

A three-channel amplifier and a logarithmic compressor condition the geophone signals before conversion into a digital format for telemetry to Earth. The low signal-to-noise ratios expected and the lack of knowledge as to the character of the expected waveforms made it desirable to widen the frequency response as much as possible within the constraints of the digital sampling frequency of 500 Hz. Because signal levels were expected to be distributed throughout the system dynamic range, a logarithmic compression scheme was selected to give signal resolution as some constant fraction of signal amplitude. The Apollo 16 system has the properties listed in table 10-I.

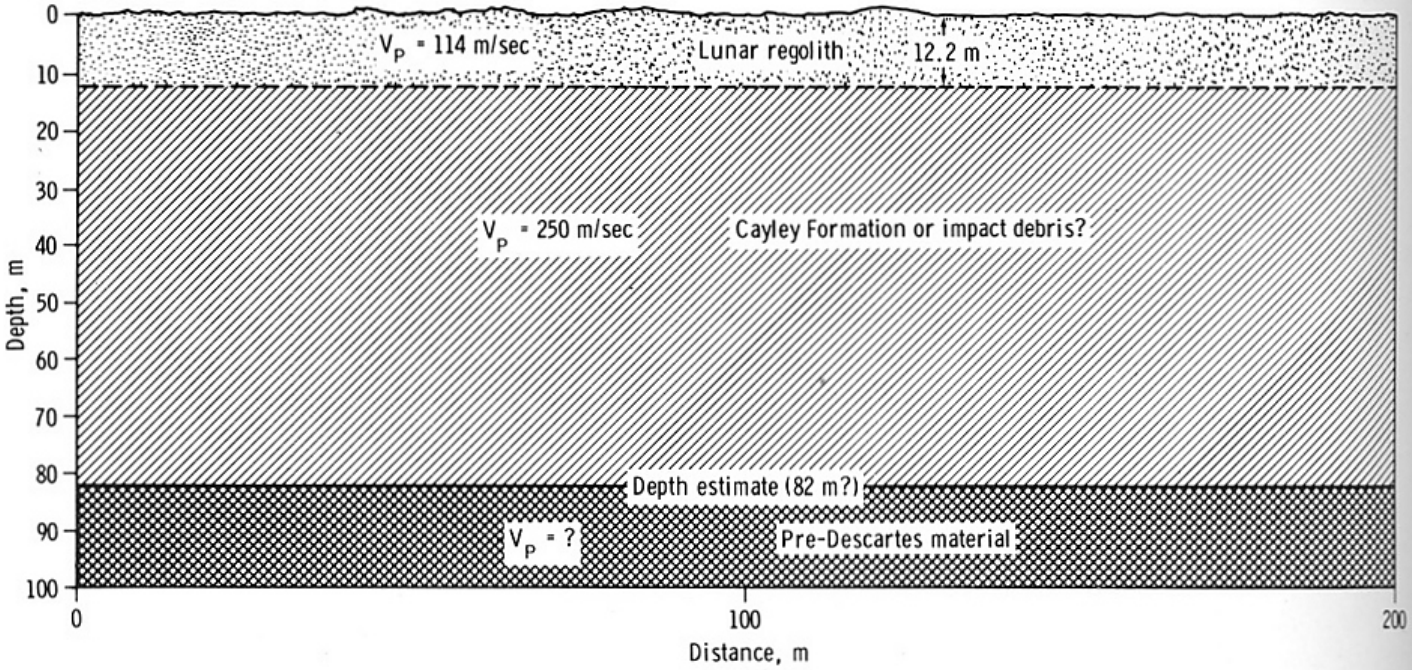


FIGURE 10-1.–Seismic cross section at the Descartes landing site (V_p = seismic wave velocity).

The MPA comprises a mortar box, a grenade-launch-tube assembly, and interconnecting cables. To provide an optimum launch angle for the grenades, the MPA is deployed at an angle approximately 45° to the lunar surface. A two-axis inclinometer provides pitch- and roll-angle (deviation from the 45° nominal and vertical) information on the MPA. The mortar box is rectangular and is made of fiber glass and magnesium; the grenade-launch-tube assembly containing four grenades is mounted in the mortar box.

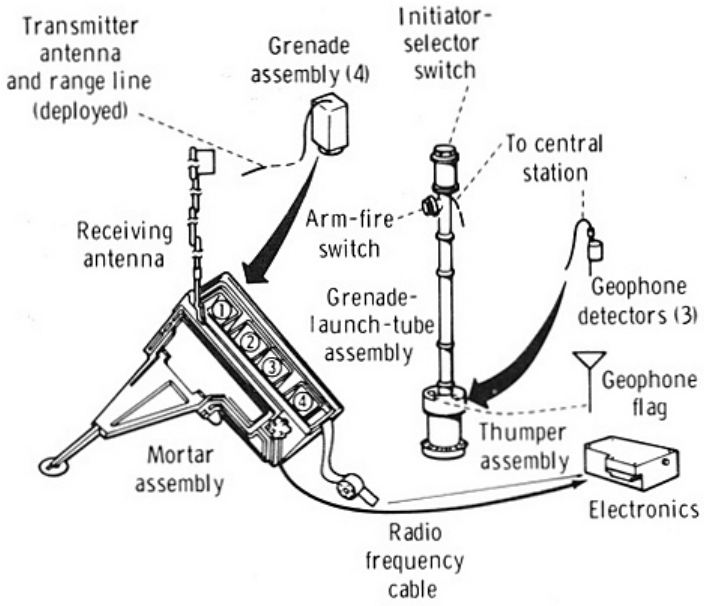


FIGURE 10-2.–Drawing of the ASE.

The forward end of the mortar box is beveled at 45° so that, in the deployed position, the MPA rests upon the 45° bevel. The remainder of the package is supported by two legs that are unfolded and locked into place during deployment. The mortar box is anchored to a pallet assembly in the final deployment. Four 17.8-cm (7-in.) stakes are mounted on the underside of the pallet to provide a stable platform for the grenade launchings.

Each grenade is attached to a range line, which is a thin-stranded cable wound around the outside of the launch tube. Two fine copper wires are looped around each range line. The first loop is spaced so that it will break when the grenade is approximately 0.4 m (16 in.) from the launch tube. A second loop is spaced to break when the range line has deployed an additional 8 m (25 ft) from the first breakwire. Breaking the loops starts and stops a range-gate pulse to establish a time interval for the determination of the initial grenade velocity.

The four grenades are similar but differ in the amount of propellant and high explosive (table 10-II). Each grenade has a square cross section with a thin fiber-glass casing. The casing contains the rocket motor, safe slide plate, high-explosive charge, ignition and detonation devices, thermal battery, and a 30-MHz transmitter. The range line is attached to the transmitter to serve as a half-wave end-feed antenna.

In operation, an arm command from ground

TABLE 10-I.– Apollo 16 ASE Characteristics

Component characteristics	Channel no.		
Geophones:	1	2	3
Generator constant, V/m/sec	255	255	257
Frequency, Hz	7.42	7.44	7.39
Resistance, ohm	6090	6212	6204
Amplifiers:			
Noise level, mV rms at input	.266	.100	.133
Dynamic range, rms signal to rms noise in dB at 10 Hz	84.4	92.4	90
Gain (at 10 Hz) and V_{input} = 2.75 mV peak to peak	698	684	709
Log compressor (compression accuracy for temperature range 288° to 323° K):			
Positive signal error, percent	4.04	3.63	4.83
Negative signal error, percent	2.46	1.87	1.88
System:			
Signal-to-noise ratio (rms signal to rms noise in dB for a 10-nm peak-to-peak signal at 10 Hz)	38.9	37.9	45.0
Minimum discernible signal (based on 0.5-mV zero-to-peak input equal to 1 digital unit at low level)			
Zero to peak at 1 Hz, nm	4	4	4
Zero to peak at 4 Hz, nm	.3	.3	.3
Zero to peak at 10 Hz, nm	.1	.1	.1
Zero to peak at 20 Hz, nm	.05	.05	.05

TABLE 10-II.– Apollo 16 Nominal ASE Grenade Parameters

Parameter	Grenade no.			
	1	2	3	4
Range, m	1 500	900	300	150
Mass, g	1 261	1 024	775	695
High-explosive-charge mass, g	454	272	136	45
Rocket-motor mean peak thrust, N	22 224	11 112	7556	5556
Mean velocity, m/sec	50	38	22	16
Lunar flight time, sec	44	32	19	13
Rocket-motor-propellant mass, g	42	27	15	10
Propellant pellets, no.	2 365	1 520	620	570
Launch angle, deg	45	45	45	45
Rocket-motor thrust duration, msec	6.0	7.5	10.5	8.5

control applies a pulse to charge condensers in the mortar box and the grenade; a fire command discharges the condenser through an initiator, which ignites the rocket motor. When the grenade leaves the tube, a spring-ejected safe slide is removed, activating a microswitch in the grenade.

A thermal battery and the electronics in the grenade make up the firing circuit. The microswitch discharges a condenser across a thermal match to activate the thermal battery, which in turn powers the transmitter and produces a capacitor charge for the detonator. At impact, an omnidirectional impact switch closes, discharging the capacitor into the detonator to ignite the explosive. The explosion terminates radio frequency transmission as an indication of detonation time. The critical parameters

measured are the detonation time, time of flight, initial velocity, and launch angle. Because of the ballistic trajectory followed by the grenades in the lunar vacuum, the necessary data are available to determine grenade range. The mortar mode of operation for the ASE is shown in figure 10-3.

Because some of the geophone parameters might change on the lunar surface, a calibrator circuit is provided to measure these parameters to within 10 percent of the preflight values. The damping resistance across the geophone is altered to underdamp the geophone, and current is introduced into the geophone coil to react with the magnetic field of the geophone, producing a force on the geophone coil. This force moves the coil and, with an underdamped geophone, the signal from the geophone is a logarithmically decaying sinusoidal signal. Analysis of similar calibration pulses transmitted after thumper operations on the Moon demonstrated close agreement of the natural frequency and generator constant of the geophones with measured preflight values.

The ASE system is controlled from Earth by a number of commands that control such functions as switching to high bit rate and firing the grenades from the mortar box assembly. Further technical details of the ASE can be found in references 10-1 and 10-2.

DEPLOYMENT

At the Apollo 16 site, the three geophones are alined on a highly cratered uneven area at a bearing of 287° (clockwise from north) from the ALSEP central station (fig. 6-13, sec. 6). Figure 10-4 shows the commander (CDR) standing at the middle geophone flag during thumper operations.

Minor difficulty was experienced in the deployment of the MPA pallet, and one of the four stakes was not implanted. The MPA was leveled and armed to fire the four grenades on command to distances of 150, 300, 900, and 1500 m in a direction bearing 287° clockwise from north. Figure 10-5 shows the deployed MPA on the lunar surface. A closeup view of the MPA on the special pallet is shown in figure 10-6. Near the end of the third period of extravehicular activity (EVA), the MPA roll sensor was observed to be reading off scale. However, a television panorama taken near the end of the EVA

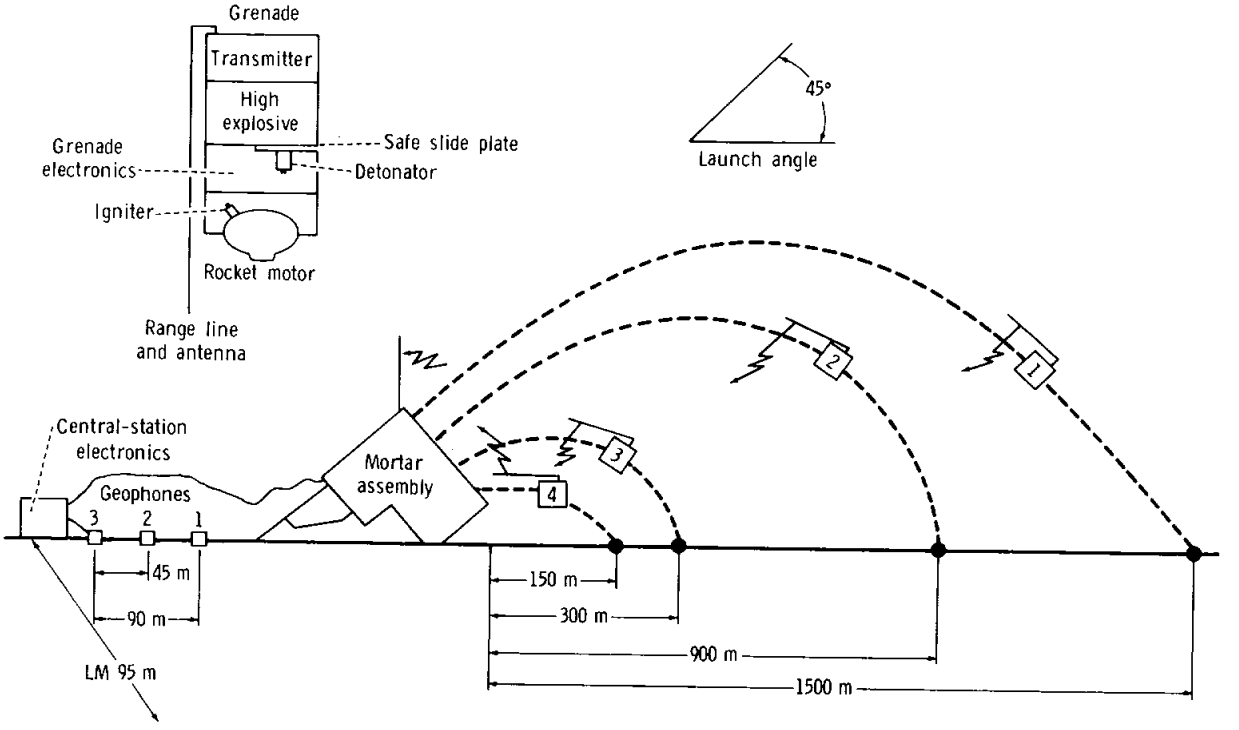


FIGURE 10-3.–Schematic drawing showing the mortar mode of operation for the ASE.

verified that the MPA was properly positioned and alined, suggesting that the roll sensor was inoperative.

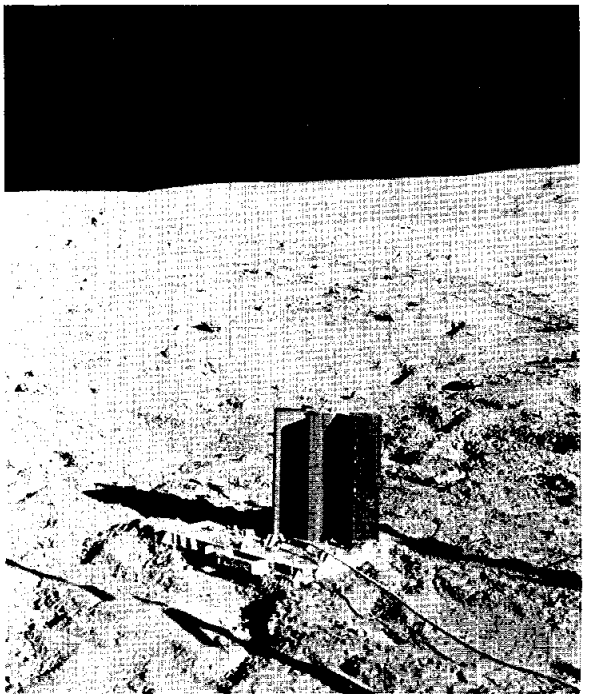


FIGURE 10-4.–The CDR firing the thumper along the geophone line on the lunar surface (AS16-113-18352).

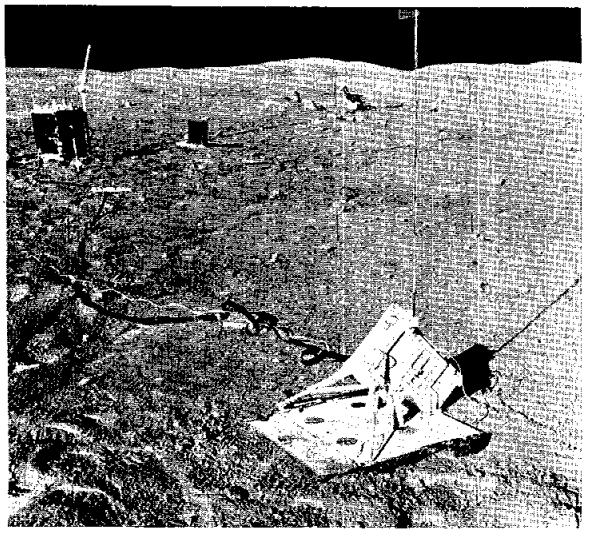


FIGURE 10-5.–Photograph of the deployed mortar assembly on the lunar surface. The MPA is aimed to fire to the right, parallel to the geophone line (AS16-113-18379).

The ALSEP central station was commanded to the high-bit-rate mode at 19:54:30 G.m.t. on April 21, 1972, to record the ASE/thumper mode of operation. Thumping operations began at 20:01:52 G.m.t. at geophone 3 (farthest from the ALSEP central station) and proceeded at 4.75-m (15-ft) intervals (except between positions 11 and 12 and positions 18 and 19, which are at 9.5-m (30-ft) intervals) toward geophone 1 (nearest to the central station). The final thumper shot was fired at 20:16:08 G.m.t., which resulted in a 14-min time line.

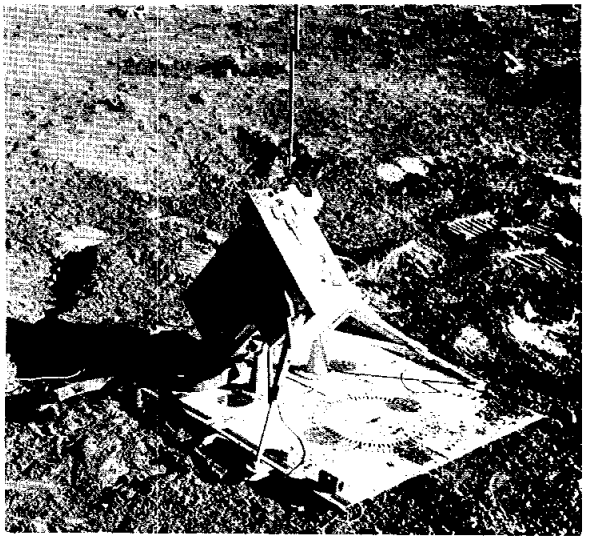


FIGURE 10-6.–Closeup view of the deployed MPA on the lunar surface (AS16-113-18380).

The central station was commanded to normal bit rate at 20:16:32 G.m.t. The thumper was fired at 19 cable positions. Two attempts were needed to fire the thumper at position 2, but this was not due to equipment malfunction. Analysis of the real-time data records shows that the thumper was not armed for the necessary 5 sec prior to firing. Seismic signals were recorded at all three geophones for all 19 thumper firings.

The ALSEP central station was also commanded to high bit rate at 01:06:00 G.m.t. on April 24 to record the impulse produced by the LM ascent. A large seismic signal was recorded by the geophone array. The ALSEP central station is periodically scheduled for the high-bit-rate mode for passive listening to detect seismic signals and to verify experiment operational capability.

On May 23, the ALSEP was commanded to high bit rate between 05:20:00 and 06:44:00 G.m.t. for the ASE/mortar mode of operation. Three of the four high-explosive grenades in the MPA were successfully launched to distances of approximately 900, 150, and 300 m. The decision was made not to launch grenade number 1 (1500 m) because the grenade launch assembly pitch angle sensor went off scale high. This off scale indication made the pitch position of the launch assembly uncertain.

Analyses of the engineering data recorded during the grenade firings indicated that the range line apparently malfunctioned so that initial grenade velocity data were lost. Nevertheless, range data were obtained from knowledge of the initial angle of launch and the time of flight by using the equations

$$T = \frac{2V_I \sin\theta}{g} \qquad R = V_I \cos\theta\, T \qquad (10\text{-}1)$$

where T = time of flight
V_I = computed initial velocity
θ = launch angle
g = lunar gravity
R = range

The validity of this approach was confirmed because of seismic data overlap from the LM ascent.

DESCRIPTION OF RECORDED SEISMIC SIGNALS

Thumper Mode

During thumper operations on the lunar surface, the CDR was instructed to stand still for 10 sec before and 10 sec after each firing. Therefore, 10 sec

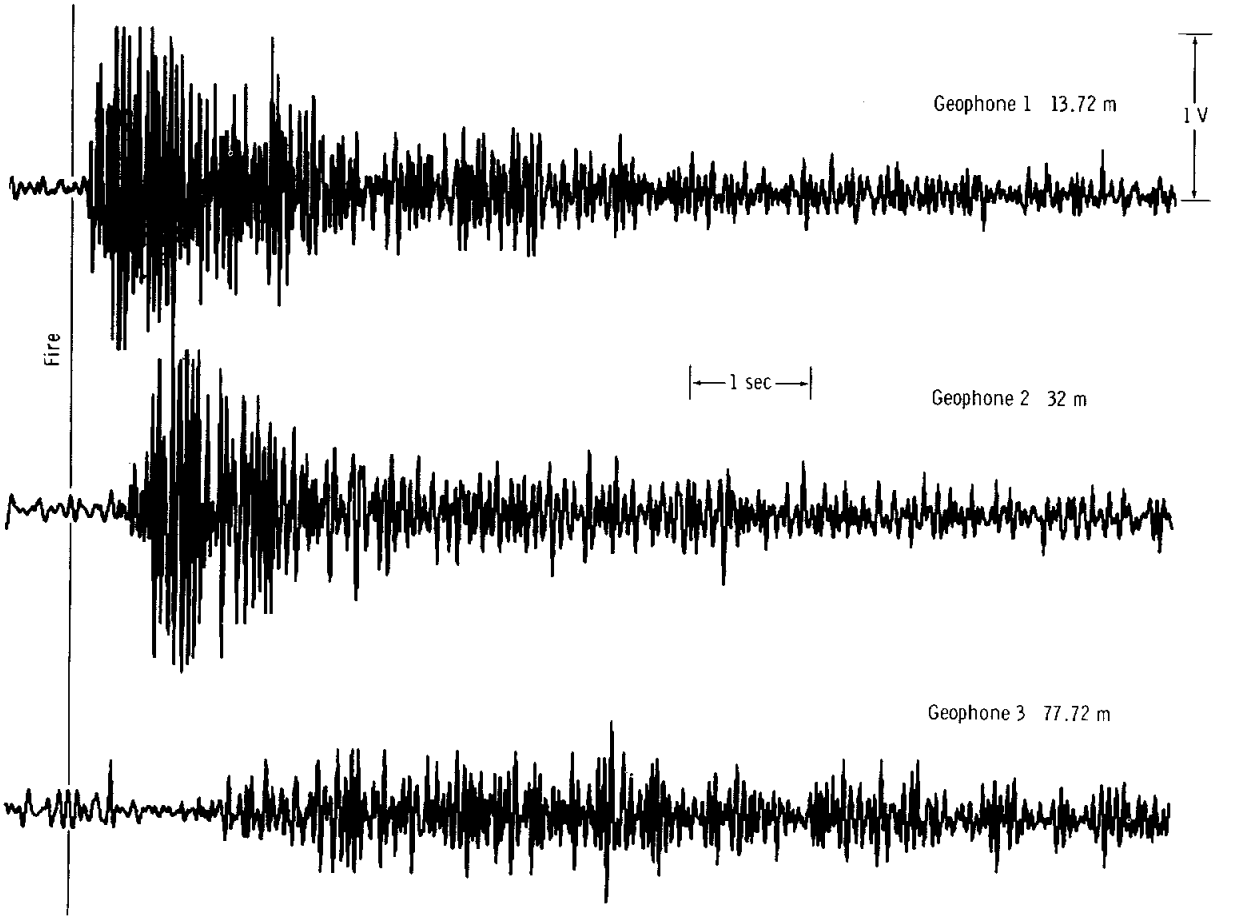


FIGURE 10-7.—Seismic signals produced by thumper firing 17 on the lunar surface.

of seismic data were recorded for each thumper firing. The seismic data recorded for thumper shot 17 are shown in figure 10-7. Examination of these signals reveals that thumper firings within approximately 15 m of a geophone have impulsive beginnings and that the seismic signals have more emergent beginnings with increasing distance. Power spectra for a typical thumper shot are shown in figure 10-8. The spectra are uncorrected for instrument response inasmuch as the ASE has a flat response to input ground velocity over the frequency band from 3 to 100 Hz. The predominant frequency of the thumper signals is 22 Hz.

Figure 10-9 is a record section alined in time to the same instant of firing for thumper shots 2 to 10 as recorded at geophone 2. Little difficulty exists in selecting the onset of the seismic signals to a distance of 41 m; however, at greater distances, uncertainty arises in determining the beginning of the seismic wave arrival because of the more emergent onset. Figure 10-10 is an expanded time scale record section for thumper shots 2 to 9 as recorded at geophone 3. The arrows point to unambiguous onsets of clear first and second arrivals.

Lunar Module Ascent

A signal of particular interest was generated by the thrust of the LM ascent engine. The resulting seismic signal was recorded by the ASE geophone array at distances of 95, 121, and 157 m (fig. 10-11). The arrows point to the measured first and second seismic wave arrivals at the individual geophones. Power spectra of the seismic signals produced by the LM ascent (fig. 10-12) show that most of the signal is concentrated in the frequency band from 5 to 8 Hz. Interpretation of the traveltime curve and related data are given in the subsection entitled "Discussion."

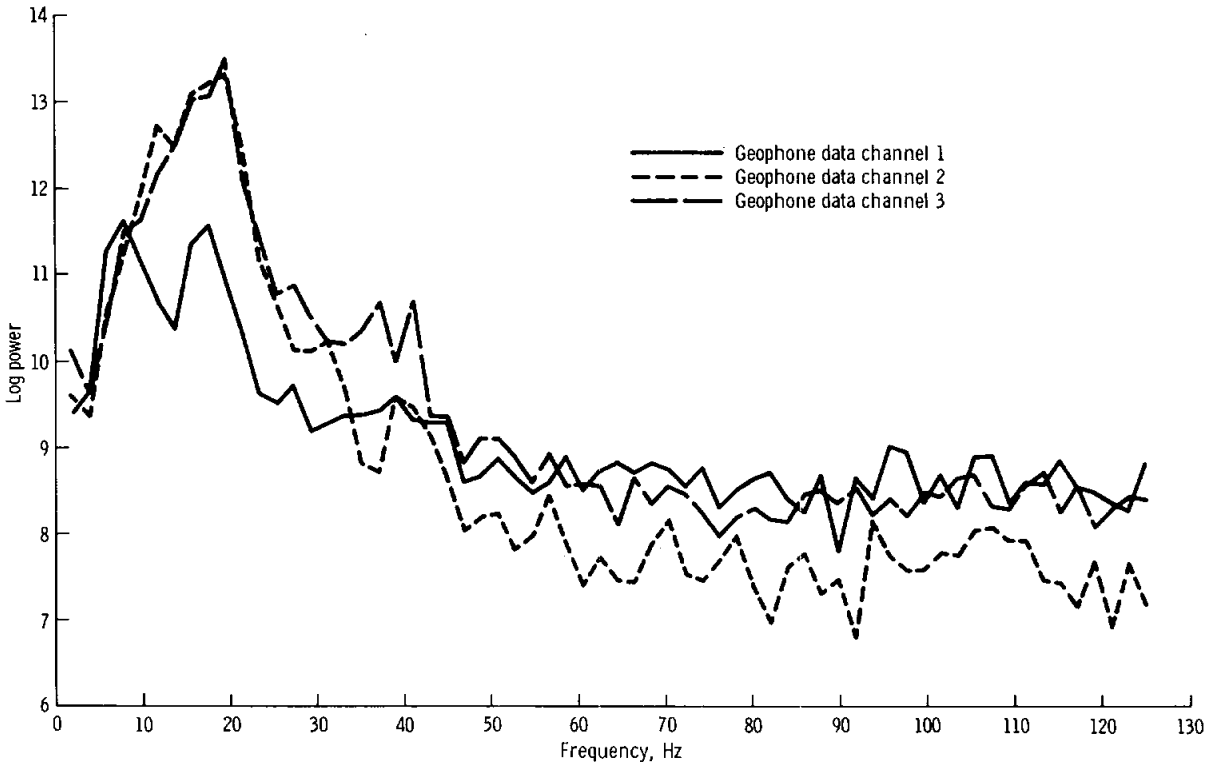


FIGURE 10-8.–Power spectra of seismic signals produced by thumper firing 8.

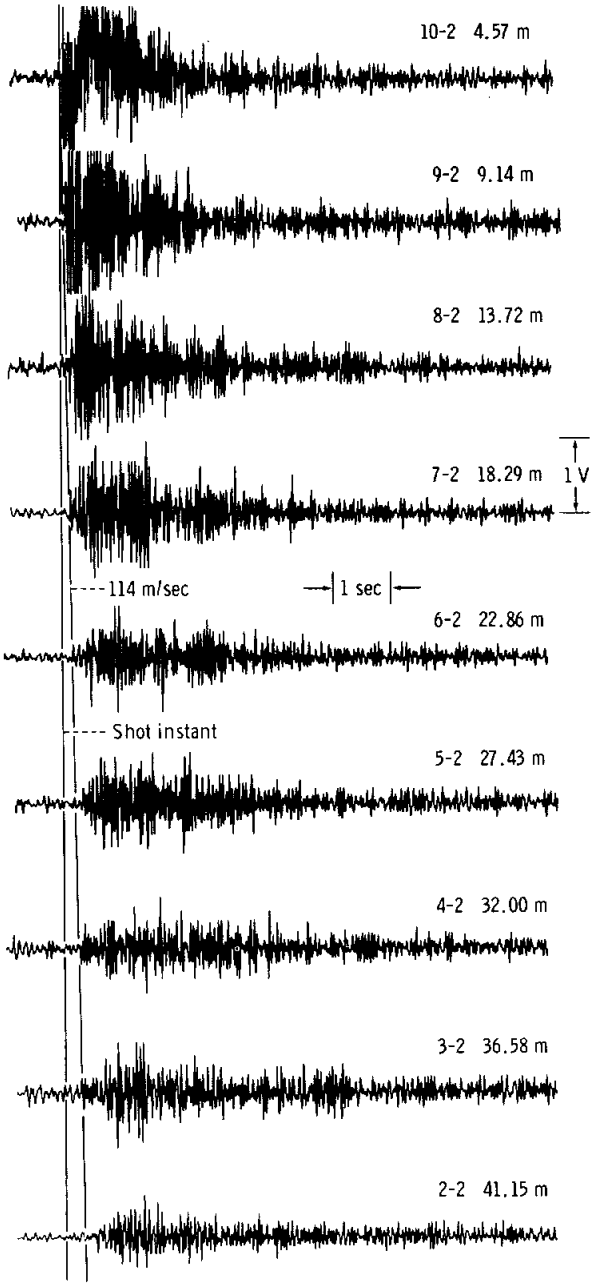


FIGURE 10-9.–Seismic signals produced by thumper firings 2 to 10 as recorded at geophone 2. The traces are alined to the same relative instant of the firing of the thumper. The line marked 114 m/sec is alined to the measured onset of the seismic signal. (The first number in the data identifier is the thumper firing, and the second number is the geophone on which the data were recorded.)

Mortar Firings

The ASE mortar package assembly was located 14 m from geophone 1, pointed to fire parallel to the geophone line and down range toward geophone 3. Firing of grenade 2 was an initial surprise in that the rocket-motor ignition produced a sufficient impulse against the mortar pallet to generate a seismic signal detected by the ASE geophones (fig. 10-13). The seismic signals produced by subsequent grenade launch "thumps" were almost identical in character and form, differing only in overall amplitude. Examination of the power spectra for a grenade launch signal (fig. 10-14) clearly shows the higher frequency content of the signal for the geophone that was closest to the MPA. The signal recorded at geophone 1 (14 m) has a spectral peak at 20 Hz, whereas the signal recorded at geophone 3 (5 m) peaks at approximately 14 Hz.

The seismic signals produced by the detonation of grenade 4 are shown in figure 10-15. This grenade was launched at an angle of 33.67° and had a flight time of 10.785 sec, which resulted in a distance of 48 m from this impact to geophone 3. The seismic records are noisy prior to the onset of the impact signal because the signals produced by the grenade launch itself have not completely decayed to low-level prefiring conditions. Nevertheless, the desired signal can be recognized on the basis of a change in frequency, inasmuch as the power spectra for the impact signals reveal a predominant signal frequency of 10 Hz (fig. 10-16), compared to 15 to 20 Hz for the grenade launch signal. It is expected that narrow band pass and velocity filtering will enhance the desired signals. Furthermore, because the individual grenade launch signals were closely reproducible from launch to launch, a simple noise subtraction procedure can be used. Work is still proceeding on analyses of the grenade 2 (900 m) and 3 (300 m) detonation signals.

DISCUSSION

The traveltime/distance data obtained from the thumper firings are shown in figure 10-17. An example of traveltimes that cannot be precisely determined is shot 10-3, and the range of possible traveltimes is shown by the height of the line. Thumper firings beyond a distance of approximately

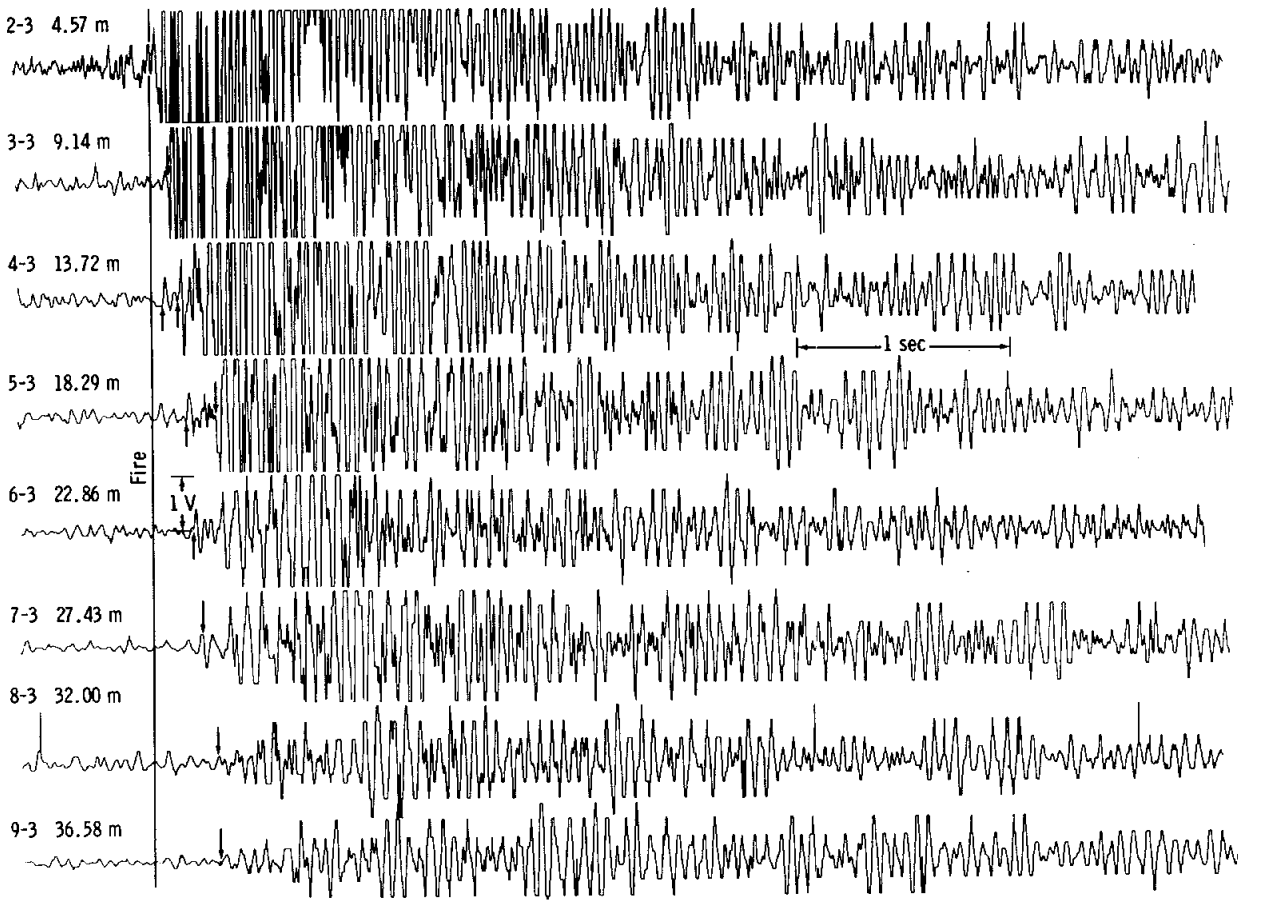


FIGURE 10-10.–Expanded time playouts of seismic signals produced by thumper firings 2 to 9 as recorded at geophone 3. The traces are alined to the same firing instant, and the arrows point to the onset of the seismic signal. (The first number in the data identifier is the thumper firing, and the second number is the geophone on which the data were recorded.)

40 m produced weak seismic arrivals for which it is difficult to determine unambiguously an initial onset.

Only one P-wave velocity is evident in the thumper traveltime data. A direct arrival is observed with a P-wave velocity of 114 m/sec. No detected variation exists in the P-wave velocity across the section sampled, as is evidenced by the uniformity of the velocity across the geophone line. This velocity can be compared to the regolith velocities of 104, 108, and 92 m/sec measured at the Apollo 12, 14, and 15 sites, respectively (refs. 10-3 and 10-4). Even though there is some minor variability from site to site, the fragmental and comminuted layer that covers much of the lunar surface has surprisingly similar seismic or acoustic properties.

Traveltime data from the seismic signals produced by the LM ascent, the grenade 4 detonation, and a grenade launcher thump are shown in figure 10-18. The effective instant of fire for the grenade launches was fixed by "anchoring" the 0.12-sec traveltime (fig. 10-13) for the impulse to the nearest geophone (geophone 1 at 14 m) to agree with thumper firing data at the same distance. This anchoring was necessary because of the finite buildup time for which the impulse of the grenade launch was transmitted to the lunar surface. The data are compared

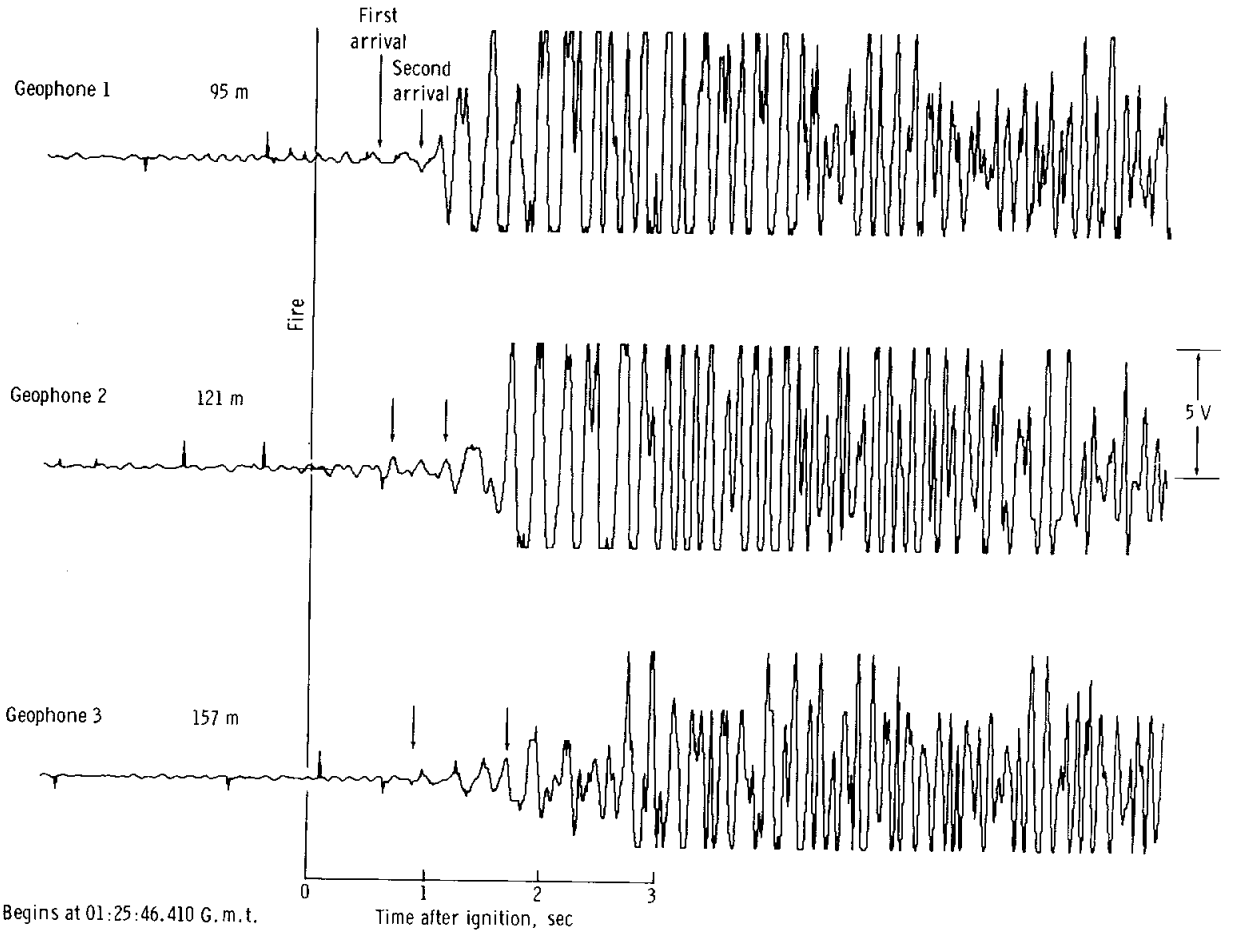


FIGURE 10-11.–Signals recorded by the ASE geophones from the lift-off of the LM ascent stage.

with the extrapolated traveltime/distance curve derived from the thumper firings of the ASE.

A faster arrival having a velocity of 250 m/sec is observed. The depth to the 250-m/sec refracting horizon is 12.2 m. It is proposed that the surface layer, which has a seismic velocity of 114 m/sec, represents the regolith at the Apollo 16 site. Estimates of the regolith thickness at the Apollo 16 site based solely on geological considerations are somewhat ambiguous. Regolith thicknesses are commonly estimated from the total crater population with a higher density of craters implying a greater regolith thickness. If all craters observed on the Cayley Formation are assumed to be impact craters, the indicated mean regolith thickness is 22 m (ref. 10-5). On the other hand, analyses of only concentric craters suggest a regolith thickness of approximately 7 m. Results of the Apollo 16 ASE would thus lend support to the lower estimate.

The underlying material having a seismic velocity of 250 m/sec is certainly not indicative of competent lava flows that typically on Earth have seismic velocities greater than approximately 800 m/sec (ref. 10-6). Field geological investigations have also revealed that the Cayley Formation does not consist of lava flows as had been postulated (ref. 10-7) but rather consists of perhaps interstratified breccias, and no bedrock appears to have been sampled by the Apollo 16 crew (sec. 6). The measured value of 250 m/sec can also be compared to the value of 299 m/sec measured for the underlying Fra Mauro breccias at the Apollo 14 site. Thus, it seems probable

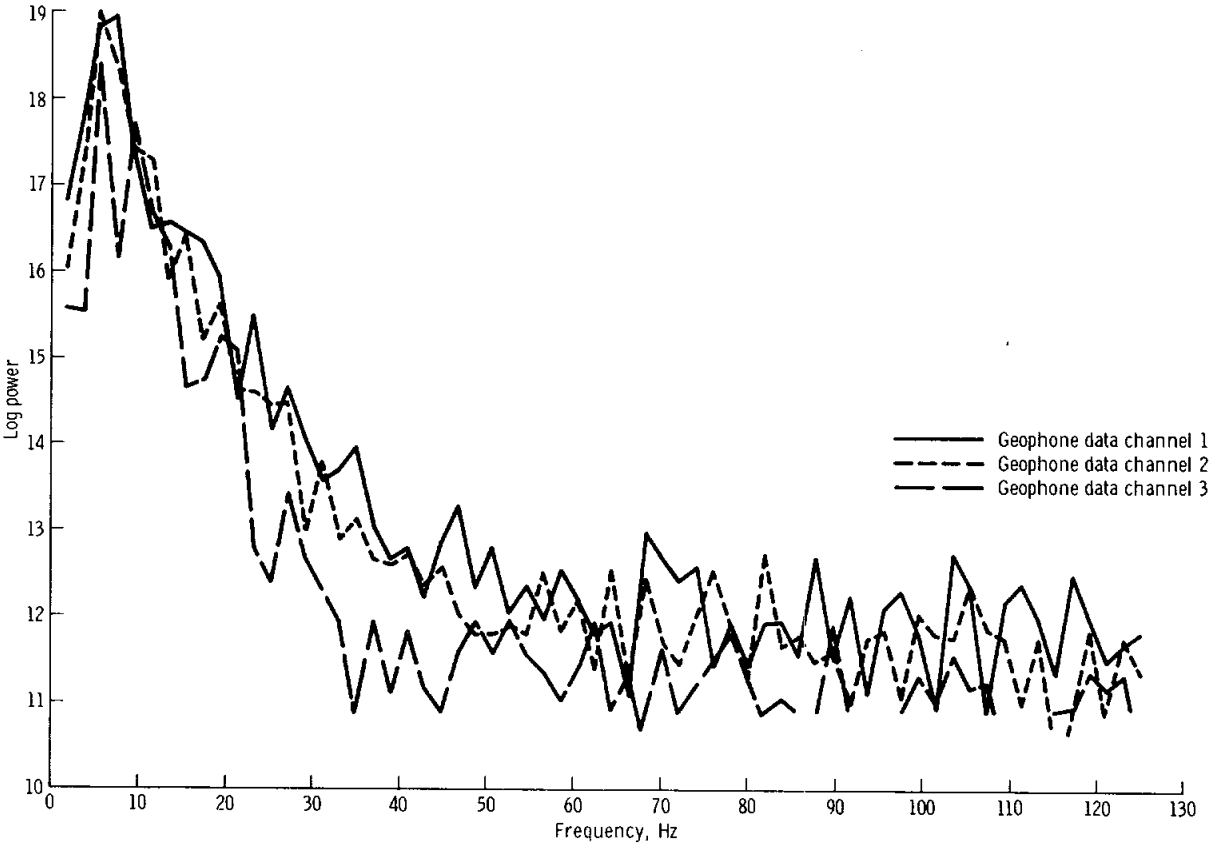


FIGURE 10-12.–Power spectra of seismic signals produced by LM ascent.

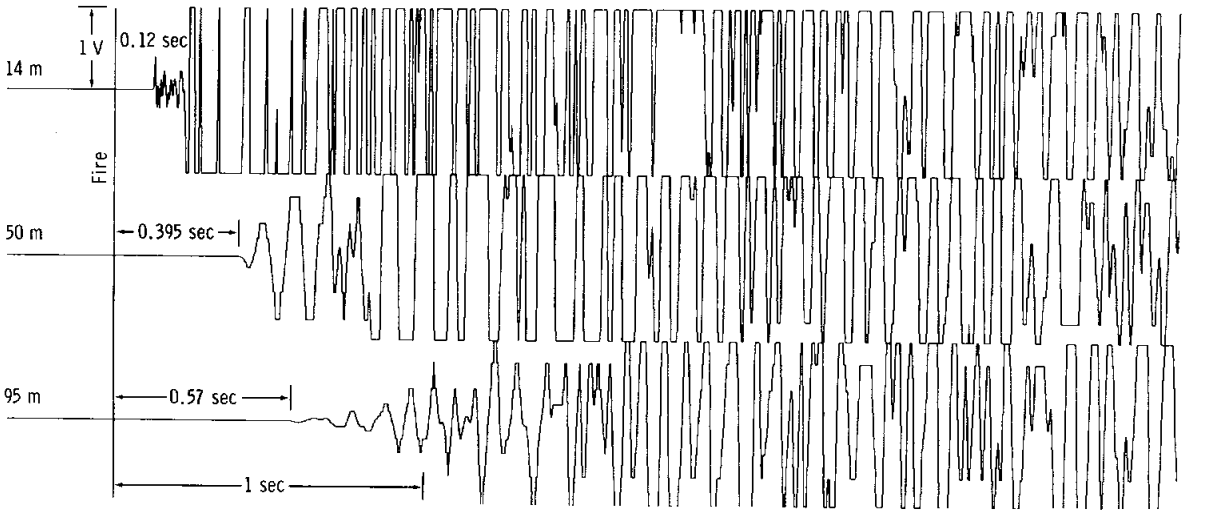


FIGURE 10-13.–Signals recorded by the ASE geophones from the launch of grenade 2.

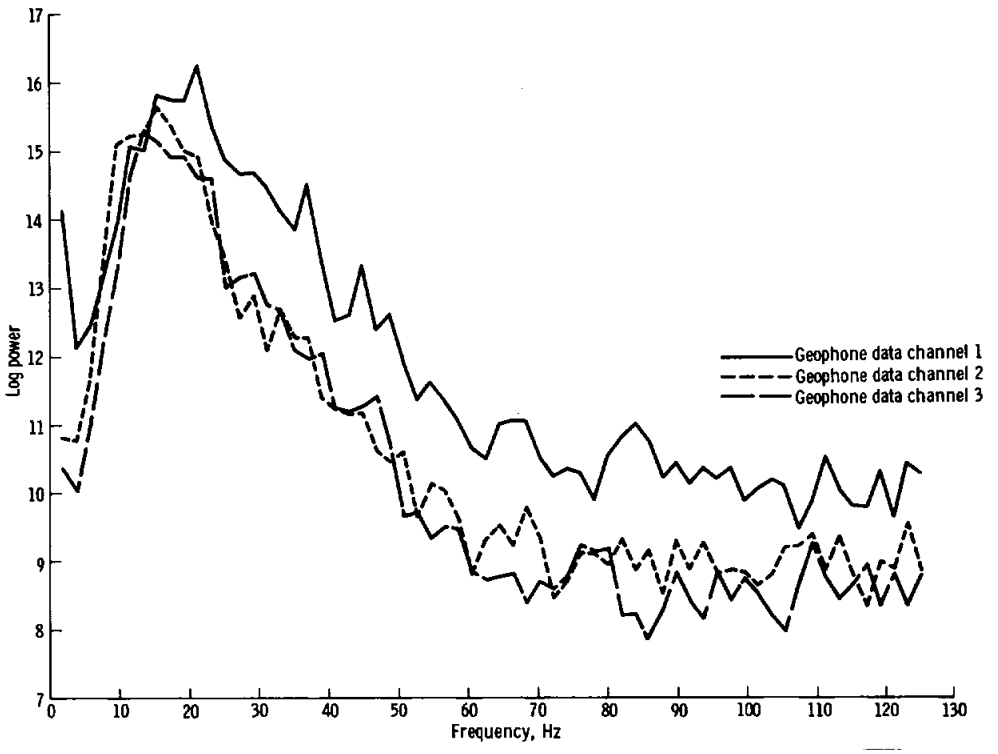


FIGURE 10-14.–Power spectra of seismic signals produced by the launch of grenade 4.

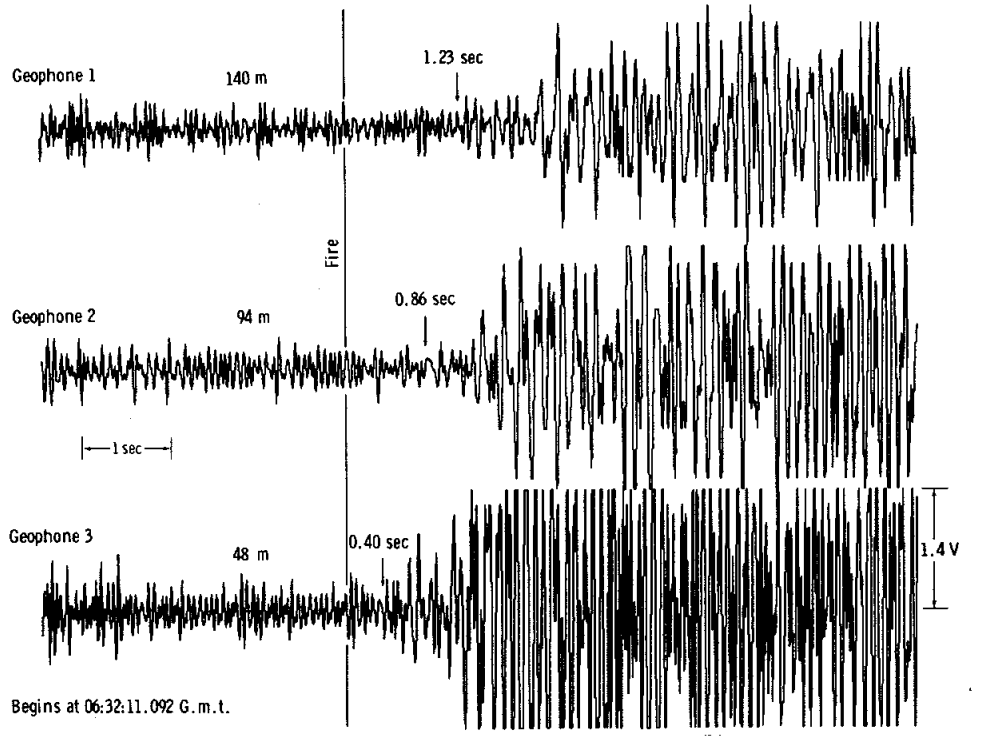


FIGURE 10-15.–Seismic signals produced by the detonation of grenade 4. The detonation time is marked by the vertical line marked fire. The small arrows point to the onset of the seismic signal.

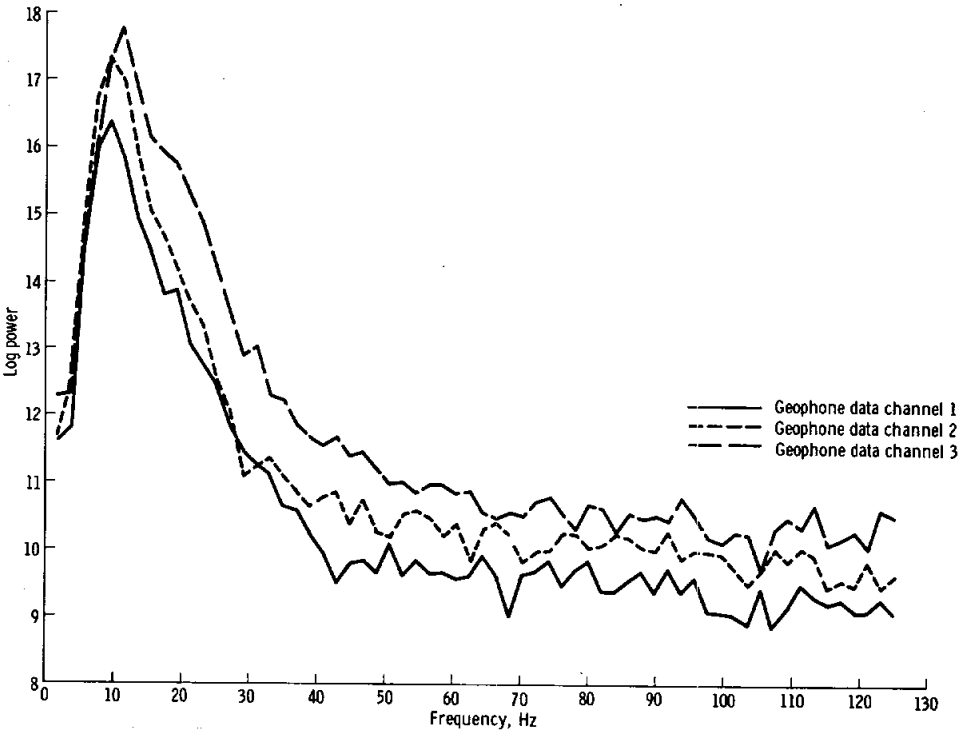


FIGURE 10-16.–Power spectra of the seismic signals produced by the detonation of grenade 4.

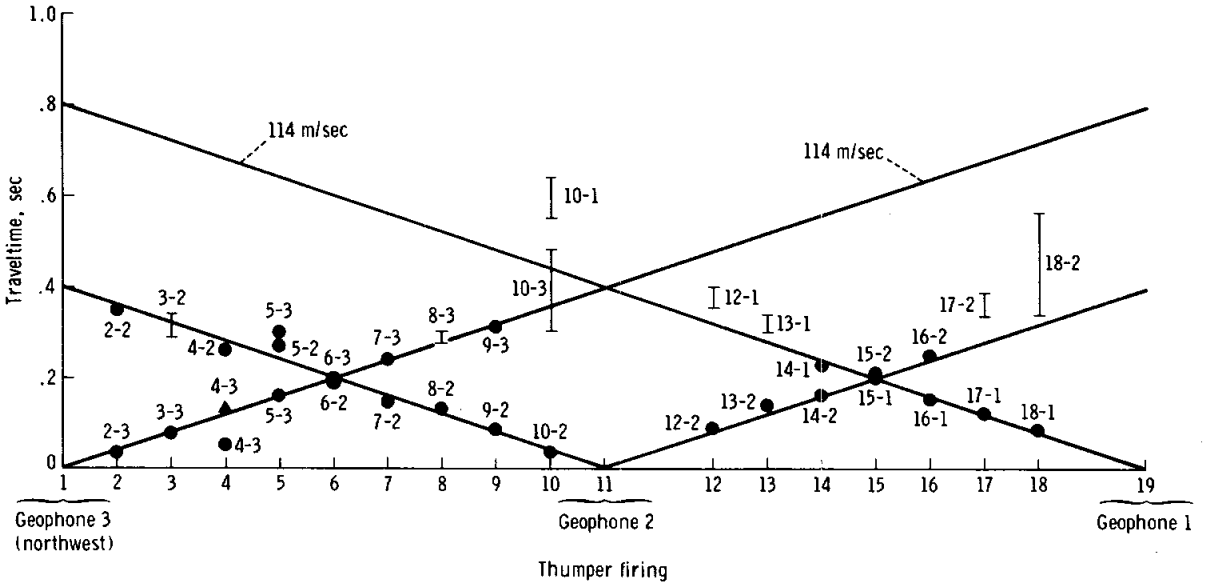


FIGURE 10-17.–Seismic arrivals from the thumper firings plotted on a traveltime/distance graph. The data points are shown as black circles. The distance between thumper shot locations is 4.75 m (except between positions 11 and 12 and positions 18 and 19, which are at 9.5-m intervals). Shot 4-3 has an anomalous early arrival. (The first number in the data identifier is the thumper firing, and the second number is the geophone on which the data were recorded.)

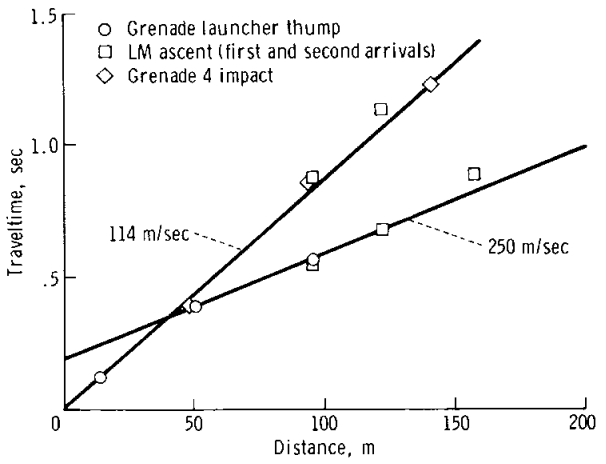


FIGURE 10-18.–Seismic arrivals from the LM ascent, grenade launch, and detonation of grenade 4 compared to extrapolated traveltime/distance data derived from the thumper firings.

that, at the Apollo 16 site, the regolith is underlain by low-velocity brecciated material or impact-derived debris.

If it is assumed that the rocks underlying the probable brecciated material at the Apollo 16 site have a seismic velocity of 1 km/sec, the thickness of the 250 m/sec material is 70 m. This thickness is likely an underestimate based on impact crater models proposed for the lunar highlands (ref. 10-8). It is anticipated that analyses of the complicated seismic signals from the grenade 2 and 3 firings will provide some definitive answers on the intriguing problem of the shallow velocity structure in the lunar highlands and of the severe velocity gradient in the lunar near-surface material (ref. 10-9).

REFERENCES

10-1. McCallister, Bruce D.; Kerr, James; Zimmer, John; Kovach, Robert L.; and Watkins, Joel: A Seismic Refraction System for Lunar Use. IEEE Trans. Geosci. Electron., vol. GE-7, no. 3, July 1969, pp. 164-171.

10-2. McDowell, Jack R.: The Active Seismic Experiment. Bendix Tech. J., vol. 4, no. 2, Summer-Autumn 1971, pp. 40-51.

10-3. Latham, Gary V.; Ewing, Maurice; Press, Frank; Sutton, George; et al.: Passive Seismic Experiment. Sec. 8 of Apollo 15 Preliminary Science Report. NASA SP-289, 1972.

10-4. Kovach, Robert L.; Watkins, Joel S.; and Landers, Tom: Active Seismic Experiment. Sec. 7 of Apollo 14 Preliminary Science Report. NASA SP-272, 1971.

10-5. Oberbeck, V. R.: Implications of Regolith Thickness in Apollo 16 Landing Site. NASA TM X-62089, 1971.

10-6. Watkins, J. S.: Annual Report, Investigation of In Situ Physical Properties of Surface and Subsurface Site Materials by Engineering Geophysical Techniques. NASA Contract T-25091 (G), July 1966.

10-7. Hodges, Carol Ann: Geologic Map of Part of the Descartes Region of the Moon. Apollo 16 Pre-Mission Map, U.S. Geol. Survey Map, 1972.

10-8. Short, Nicholas M.; and Forman, Michael L.: Thickness of Impact Crater Ejecta on the Lunar Surface. Modern Geol., vol. 3, no. 2, 1972, pp. 69-91.

10-9. Kovach, R. L.; and Watkins, J. S.: The Near-Surface Velocity Structure of the Moon. Lunar Science-III, Revised Abstracts of Papers Presented at the Third Lunar Science Conference, Houston, Tex., Jan. 10-13, 1972, Carolyn Watkins, ed., Lunar Science Institute Contribution No. 88, Feb. 18, 1972, pp. 461-462.

11. Lunar Surface Magnetometer Experiment

P. Dyal,[a†] C. W. Parkin,[a] D. S. Colburn,[a] and G. Schubert[b]

INTRODUCTION

The Apollo 16 lunar surface magnetometer (LSM), which was activated at 20:22 G.m.t. on April 21, 1972, completed the network installation of magnetic observatories on the lunar surface and initiated simultaneous measurements of the global response of the Moon to large-scale solar and terrestrial magnetic fields. Analysis of long-term simultaneous measurements by widely separated surface magnetometers will greatly enhance the previous single-instrument studies of lunar internal electrical conductivity and temperature, internal magnetic permeability, and surface remanent magnetic fields.

A continuous electrical conductivity profile of the lunar interior has been calculated by analysis of the decay of eddy-current magnetic fields induced in the Moon by solar field step transients. The conductivity is in turn related to internal temperature, which is calculated for assumed lunar material compositions.

The relative magnetic permeability of the outer layers of the Moon has been calculated from measurements obtained when the Moon was immersed in the geomagnetic tail field. The permeability is related to the amount of permeable material, such as iron, that exists in the outer layers of the Moon.

Fossil remanent magnetic fields have been measured at nine locations on the lunar surface, including the Apollo 16 LSM site in the Descartes highlands area. Remanent fields provide a record of the magnetic field environment that existed at the Moon 3 to 4 billion years ago at the time the crustal material cooled below the Curie temperature. This fossil record indicates the possible existence of an ancient lunar dynamo or a solar or terrestrial field much stronger than exists at present.

THEORY

The external driving magnetic field in the lunar environment can vary considerably with the lunar orbital position. (See fig. 11-1.) Average magnetic field conditions vary from relatively steady fields of magnitude of approximately 9 γ (1 γ = 1 nT) in the geomagnetic tail to mildly turbulent fields averaging ~5 γ in the free-streaming solar plasma region to turbulent fields averaging 8 γ in the magnetosheath. Average solar wind velocity is approximately 400 km/sec in a direction approximately along the Sun-to-Earth line.

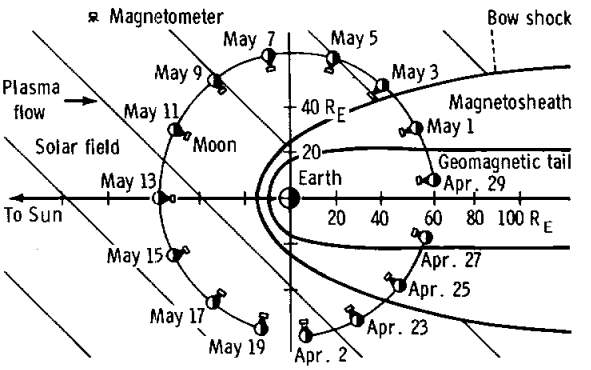


FIGURE 11-1.–Lunar orbit projection onto the solar ecliptic plane, showing the Apollo 16 LSM during the first postdeployment lunation. During a complete revolution around the Earth, the magnetometer passes through the Earth bow shock, the magnetosheath, the geomagnetic tail, and the interplanetary region dominated by solar plasma fields.

Various induced lunar and plasma-interaction fields also exist at the lunar surface; for reference, the sum of these fields is written

$$\mathbf{B}_A = \mathbf{B}_E + \mathbf{B}_S + \mathbf{B}_\mu + \mathbf{B}_P + \mathbf{B}_T + \mathbf{B}_D + \mathbf{B}_F \quad (11\text{-}1)$$

Here $\mathbf{B}_A$ is the total magnetic field measured on the surface by an Apollo LSM; $\mathbf{B}_E$ is the total external (solar or terrestrial) driving magnetic field measured by the Explorer 35 magnetometer and the Apollo 15

[a]NASA Ames Research Center.
[b]University of California at Los Angeles.
†Principal Investigator.

and 16 subsatellite lunar orbiting magnetometers while outside the antisolar lunar cavity; $\mathbf{B}_S$ is the steady remanent field at the surface site; $\mathbf{B}_\mu$ is the global magnetization field induced in permeable lunar material; $\mathbf{B}_P$ is the poloidal field caused by eddy currents induced in the lunar interior by changing external fields; $\mathbf{B}_T$ is the toroidal field corresponding to unipolar electrical currents driven through the Moon by the $\mathbf{V} \times \mathbf{B}_E$ electric fields (where $\mathbf{V}$ is the velocity of the Moon with respect to the solar wind); $\mathbf{B}_D$ is the field associated with the diamagnetic lunar cavity; and $\mathbf{B}_F$ is the total field associated with the hydromagnetic solar wind flow past the Moon. The relative importance of these different fields varies with orbital position; therefore, different magnetic fields and lunar properties can be investigated during selected times of each lunation.

Electrical Conductivity and Temperature

When the Moon is immersed in a free-streaming solar wind and the magnetometer is located on the dark (antisolar) side of the Moon and isolated from solar plasma flow, then $\mathbf{B}_F \rightarrow 0$ and $\mathbf{B}_\mu$ and $\mathbf{B}_T$ can be neglected (ref. 11-1). Equation (11-1) therefore reduces to

$$\mathbf{B}_A = \mathbf{B}_P + \mathbf{B}_E + \mathbf{B}_S \qquad (11\text{-}2)$$

where cavity effects $\mathbf{B}_D$ are neglected to a first approximation for selected measurements made near lunar midnight (ref. 11-2). After $\mathbf{B}_S$ has been calculated from geomagnetic tail data, only the poloidal field $\mathbf{B}_P$ is unknown. Equation (11-2) can then be solved for certain assumed lunar models, and curve fits of data to the solution determine the model-dependent conductivity profile $\sigma(R)$. Furthermore, electrical conductivity is related to temperature, and the lunar interior temperature can be calculated for assumed lunar material compositions.

It is useful to consider the idealized case in which the Moon is represented by a uniformly conducting sphere in a vacuum. This case is solved analytically by Smythe (ref. 11-3). Assume that initially there is no magnetic field but, at a time $t = 0$, an external magnetic field $\Delta\mathbf{B}_E$, which is uniform far from the sphere, is switched on. At this time, a surface current is induced on the sphere, which excludes the applied field completely from the interior (fig. 11-2). The current then diffuses through the sphere and eventually decays to zero strength. Correspondingly, the external field (which was originally excluded) diffuses into the sphere so that, finally, a uniform field occupies all space. If the conductivity of the sphere is large, the eddy currents will be sustained for a long time, and the external field will only slowly diffuse to the interior. At the surface, the tangential component of the field is initially greater than the corresponding external field component, and the radial surface component is initially zero (fig. 11-3). Both components asymptotically approach the values of external field components as the induced currents decay.

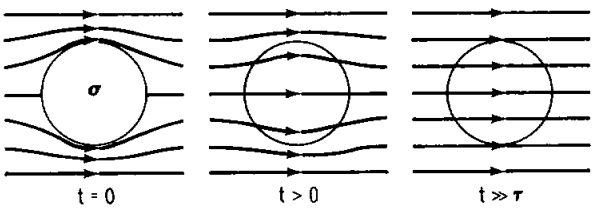


FIGURE 11-2.–Transient magnetic response of a conducting sphere in a magnetic field. At the time of the step transient $t = 0$, eddy currents are generated that exclude field lines to the outer edge of the sphere. At later times, the eddy currents diffuse inward, permitting the field lines to permeate the entire sphere at a time much greater than the time response τ of the conductor.

The response of the Moon, as measured by the Apollo 12 magnetometer on the dark side, is qualitatively similar to the curves shown in figure 11-3. (The response deviates from these curves insofar as the electrical conductivity of the Moon is not homogeneous.) To determine the conductivity profile from the shape of the transient response curves, it is assumed that the dark-side response is that of a sphere in a vacuum. This assumption is justified by the low plasma density on the dark-side surface reported by Snyder et al. (ref. 11-4). Furthermore, it has been found that the lunar response is not a function of position if the magnetometer is more than 400 km inside the optical shadow. Therefore, the effect of currents at the boundary of the lunar cavity (and on the front surface of the Moon) on the shape of the response curves is neglected. It has been shown that the currents in the Moon driven by the solar wind $\mathbf{V} \times \mathbf{B}_E$ field can be neglected (ref. 11-1). The driving field is taken to be spatially uniform, which requires that its scale be much greater than the diameter of the Moon and that the discontinuity be swept past

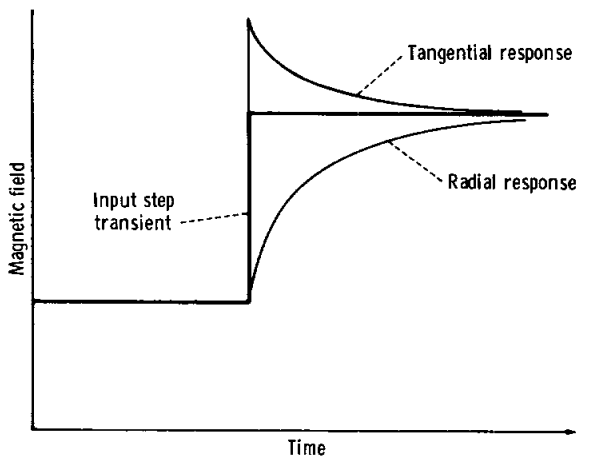


FIGURE 11-3.–Theoretical solutions for the lunar-night vacuum poloidal magnetic field response of a homogeneous conducting sphere to a step function transient in the driving solar wind magnetic field. For a step function change $\Delta \mathbf{B}_E$ in the external driving field (measured by Explorer 35), the total magnetic field at the surface of the Moon $\mathbf{B}_A$ (measured by the Apollo 12, 15, and 16 magnetometers) will be damped in the radial B_{Ax} component and will overshoot in the tangential (B_{Ay} and B_{Az}) components.

the Moon in a time that is short compared with the lunar response time. Both of these conditions are generally fulfilled. Based on these assumptions, it is possible to model the dark-side transient response by that of an inhomogeneous conducting sphere in a vacuum. The solution of the vector diffusion equation for the transient magnetic response of a sphere with radial conductivity distribution $\sigma(R)$ to an arbitrary input $b(t)$ is described in detail in reference 11-5. By assuming the material composition of the lunar interior and using a known conductivity-temperature relationship of that material, an internal radial temperature distribution can be calculated.

Magnetic Permeability and Steady Remanent Fields

When the Moon is passing through a quiet region of the geomagnetic tail, solar wind interaction fields ($\mathbf{B}_T$, $\mathbf{B}_D$, and $\mathbf{B}_F$) and the induced poloidal lunar field $\mathbf{B}_P$ are negligible, and equation (11-1) for the total field at the lunar surface reduces to

$$\mathbf{B}_A = \mathbf{B}_E + \mathbf{B}_\mu + \mathbf{B}_S \qquad (11\text{-}3)$$

The magnetic moment m_μ of the field $\mathbf{B}_\mu$ is proportional to $\mathbf{B}_E$; that is, $m_\mu = K\mathbf{B}_E$. (The proportionality constant K in turn depends on the permeability and the dimensions of the permeable region of the Moon.) The magnetization of the lunar sphere by the Earth magnetic field is shown schematically in figure 11-4.

For the case of a homogeneous permeable lunar shell, equation (11-3) can be written in the following component form (ref. 11-6).

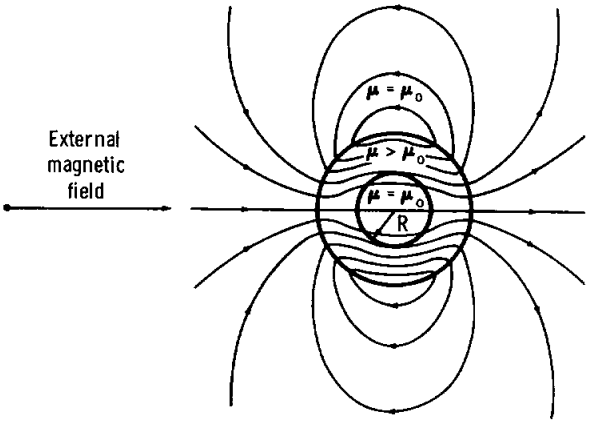
$$B_{Ax} = (1 + 2F)B_{Ex} + B_{Sx} \qquad (11\text{-}4)$$

$$B_{Ay,z} = (1 - F)B_{Ey,z} + B_{Sy,z} \qquad (11\text{-}5)$$

where

$$F = \frac{(2k_m + 1)(k_m - 1)\left[1 - \left(\frac{R}{R_m}\right)^3\right]}{(2k_m + 1)(k_m + 2) - 2\left(\frac{R}{R_m}\right)^3(k_m - 1)^2} \qquad (11\text{-}6)$$

Here k_m is the relative permeability μ/μ_O, R_m is the lunar radius, and R is the radius of the boundary that encloses lunar material with a temperature above the Curie point. The coordinate system origin is at the magnetometer location on the lunar surface with x directed radially outward from the surface, y eastward, and z northward.



Note: For bulk permeability (the case R = 0), $\mu/\mu_0 = 1.01$.

FIGURE 11-4.–Induced magnetization field $\mathbf{B}_\mu$. A global permeable shell of material of permeability $\mu > \mu_O$ placed in the uniform geomagnetic tail tends to concentrate the field lines inside the shell.

Solar Wind Interaction

When the Moon is immersed in free-streaming solar wind and the magnetometer is on the lunar sunlit side, $\mathbf{B}_D \rightarrow 0$ outside the cavity, and the global fields $\mathbf{B}_\mu$ and $\mathbf{B}_T$ can be neglected (ref. 11-2). During times of high solar wind particle density, the interaction term $\mathbf{B}_F$ cannot be neglected; therefore, for daytime magnetometer data, equation (11-1) becomes

$$\mathbf{B}_A = \mathbf{B}_E + \mathbf{B}_S + \mathbf{B}_P + \mathbf{B}_F \qquad (11\text{-}7)$$

At low frequencies ($<3 \times 10^{-4}$ Hz), $\mathbf{B}_P \rightarrow 0$, and the interaction field $\mathbf{B}_F$ can be investigated in terms of measured fields by reference to equation (11-2) in a form rewritten and defined for the low-frequency case as

$$\Delta\mathbf{B} = \mathbf{B}_A - \left(\mathbf{B}_E + \mathbf{B}_S\right) = \mathbf{B}_F \qquad (11\text{-}8)$$

It is found that, during times of high solar wind density, the remanent lunar surface magnetic field is compressed by the solar wind, as determined from simultaneous measurements of the LSM and the solar wind spectrometer (ref. 11-7). This interaction between the solar wind and the local remanent magnetic field is shown schematically in figure 11-5.

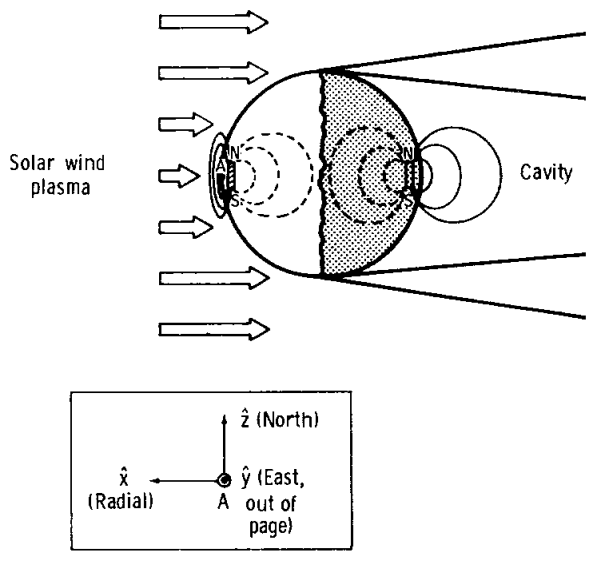


FIGURE 11-5.–Compression of a local remanent magnetic field by a high-density solar wind plasma. The remanent field is unperturbed during lunar night (antisolar side), while on the sunlit side the horizontal components are compressed. The inset shows the coordinate system used.

EXPERIMENTAL TECHNIQUE

For the experimental technique used to measure the magnetic field, the astronauts were required to deploy an LSM that would continuously measure and transmit information by radio to Earth for a period of at least 1 yr. A photograph of the LSM fully deployed and alined at the Descartes landing site is shown in figure 11-6, and the Apollo 16 LSM characteristics are given in table 11-I. (A detailed description of this instrument is provided in reference 11-8.)



FIGURE 11-6.–The Apollo 16 LSM deployed on the Moon in the lunar highlands. Sensors are at the top ends of the booms and approximately 75 cm above the lunar surface.

Fluxgate Sensor

The three orthogonal vector components of the magnetic field are measured by three fluxgate sensors designed and fabricated by the Naval Ordnance Laboratory (refs. 11-9 and 11-10). Each sensor, shown schematically in figure 11-7, consists of a toroidal Permalloy core that is driven to saturation by a sinusoidal current having a frequency of 6000 Hz. The sense winding detects the superposition of the drive-winding magnetic field and the total lunar surface field; as a result, a second harmonic of the driving frequency is generated in the sense winding with a magnitude that is proportional to the strength of the surface field. The phase of the second harmonic signal with respect to the drive signal indicates the direction of the surface field with respect to the sensor axis. This output signal is amplified and synchronously demodulated to drive a

voltage to the analog-to-digital converter and then through the central-station radio to Earth.

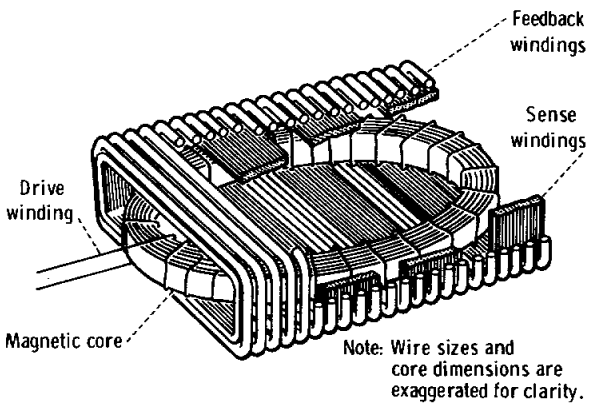


FIGURE 11-7.–Simplified view of the ring core magnetometer sensor developed jointly by the Naval Ordnance Laboratory and NASA Ames Research Center.

TABLE 11-I.–Apollo 16 Magnetometer Characteristics

Parameter	*Value*
Range, γ	0 to ± 200 0 to ± 100 0 to ± 50
Resolution, γ	±0.1
Frequency response	dc to 3 Hz
Angular response	Proportional to cosine of angle between magnetic field vector and sensor axis
Sensor geometry	3 orthogonal sensors at the ends of 100-cm booms; orientation determination to within 1° in lunar coordinates
No. of commands	
Ground	10
Spacecraft	1
Analog zero determination	180° flip of sensor
Internal calibration, percent of full scale	0, ±25, ±50, and ±75
Field bias offset capability, percent of full scale	0, ±25, ±50, and ±75
Modes of operation	Orthogonal field measurements, gradient measurement, internal calibration
Average power, W	
Day	3.5
Night	9.4
Weight, kg	8.9
Size, cm	25 by 28 by 63
Operating temperature, °K	223 to 358

Electronics

The electronic components for the LSM are located in the thermally insulated box. The operation of the electronics is illustrated in figure 11-8. Long-term stability is attained by extensive use of digital circuitry, by internal calibration of the analog portion of the instrument every 18 hr, and by mechanical rotation of each sensor through 180° to determine the sensor zero offset. The analog output of the sensor electronics is internally processed by a low-pass digital filter and a telemetry encoder; the output is transmitted to Earth via the central-station S-band transmitter. A typical internal flip-calibration sequence of the Apollo 16 instrument is shown in figure 11-9.

The LSM has two data samplers: the analog-to-digital converter (26.5 samples/sec) and the central-station telemetry encoder (3.3 samples/sec). The prealias filter following the sensor electronics has attenuations of 3 dB at 1.7 Hz, 64 dB at 26.5 Hz, and 58 dB at the Nyquist frequency (13.2 Hz), with an attenuation rate of 22 dB/octave. The four-pole Bessel digital filter limits the alias error to less than 0.05 percent and has less than 1 percent overshoot for a step function response. This filter has an attenuation of 3 dB at 0.3 Hz and 48 dB at the telemetry-sampling Nyquist frequency (1.6 Hz). The phase response is linear with frequency. The response of the entire LSM measurement system to a step function input is shown in figure 11-10. The digital filter can be bypassed by ground command in order to pass higher frequency information.

Mechanical and Thermal Subsystems

In the exterior mechanical and thermal configuration of the Apollo 16 LSM, the three fluxgate sensors are located at the ends of three 100-cm-long orthogonal booms that separate the sensors from each other by 150 cm and position them 75 cm above the lunar surface (fig. 11-6). Orientation measurements with respect to lunar coordinates are made with two devices. A shadowgraph and bubble level are used by the astronaut to aline the LSM and to measure azimuthal orientation with respect to the Moon-to-Sun line to an accuracy of 0.5°. Gravity-level sensors measure instrument tilt angles to an accuracy of 0.2° every 4.8 sec.

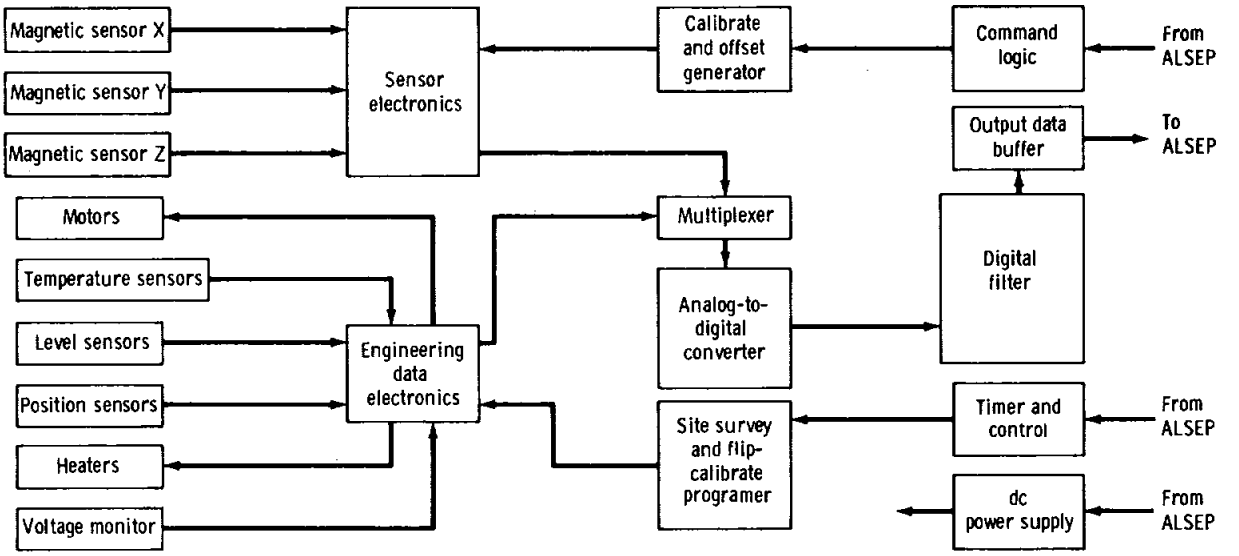


FIGURE 11-8.–Functional block diagram for the LSM electronics.

In addition to the instrument normal mode of operation in which three vector field components are measured, the LSM has a gradiometer mode in which commands are sent to operate three motors, which rotate the sensors such that all simultaneously aline parallel, first to one of the three boom axes, then to each of the other two boom axes in turn. This rotating alinement permits the vector gradient to be calculated in the plane of the sensors and also permits an independent measurement of the magnetic field vector at each sensor position.

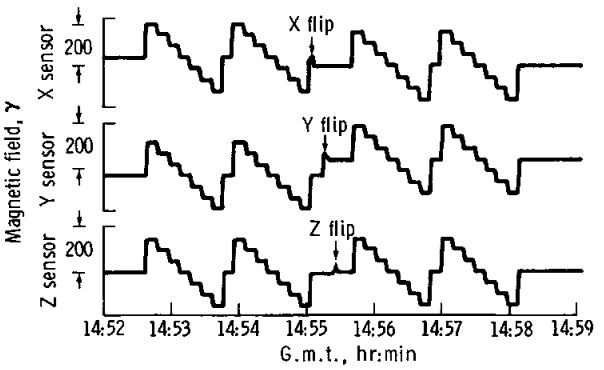


FIGURE 11-9.–Magnetometer data obtained during an internal flip-calibration sequence on April 26, 1972. This sequence is periodically repeated on command and involves internally generated biases in steps of 75, 50, 25, 0, -25, -50, and -75 percent of full scale.

The thermal subsystem is designed to allow the LSM to operate over the complete lunar day-night cycle. Thermal control is accomplished by a combination of insulation, control surfaces, and heaters that operate collectively to keep the electronics between 267° K and 319° K. A plot of the temperature of the X sensor and the electronics for the first postdeployment lunation is shown in figure 11-11.

Data Flow and Mission Operation

The LSM experiment is controlled from the NASA Manned Spacecraft Center (MSC) by commands transmitted to the Apollo lunar surface experiments package (ALSEP) from remote tracking stations. The data are recorded on magnetic tape at the remote sites and are also sent directly to MSC for real-time analysis to establish the proper range, offset, frequency response, thermal control, and operating mode. The one-time gradiometer-mode sequence of commands was successfully executed on April 28.

Explorer 35 Magnetometer

The ambient steady-state and time-dependent magnetic fields in the lunar environment are measured by the Explorer 35 satellite magnetometer. The satellite has an orbital period of 11.5 hr, an apolune of 9390 km, and a perilune of 2570 km (fig. 11-12). The Explorer 35 magnetometer measures three magnetic field vector components every 6.14 sec and has

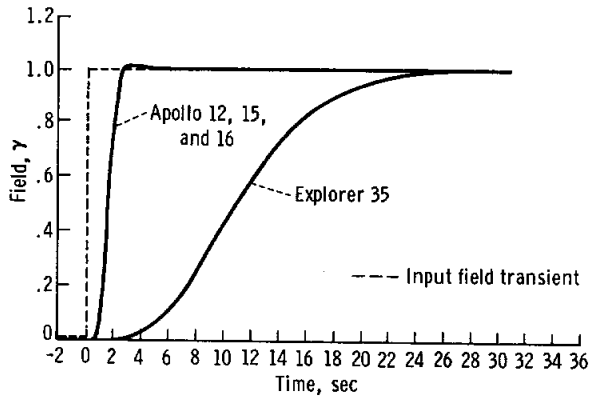


FIGURE 11-10.–Laboratory measurements comparing instrument transient responses of the Apollo 12, 15, and 16 and Explorer 35 magnetometers to a 1.0-γ magnetic step input.

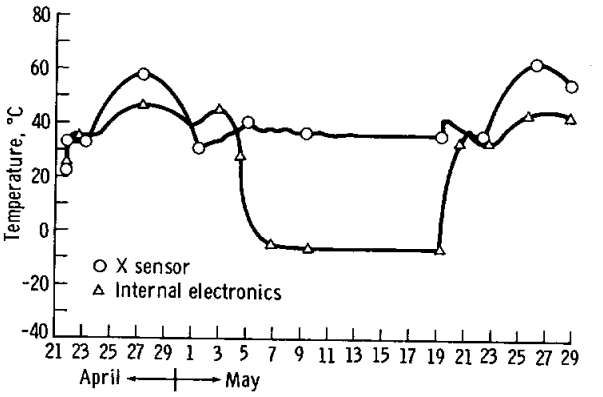


FIGURE 11-11.–Temperature inside one of the fluxgate sensors and inside the electronics box during the first postdeployment lunation of Apollo 16.

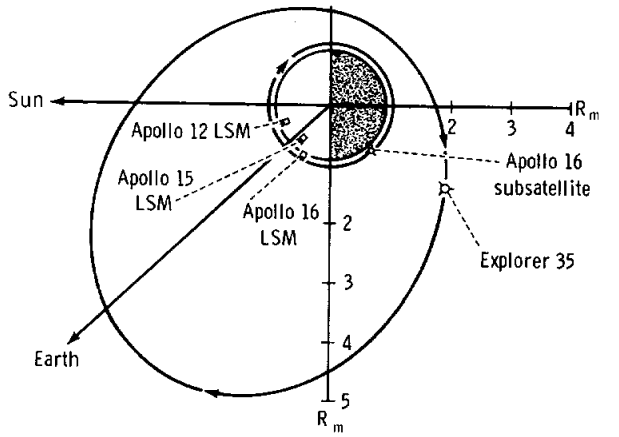


FIGURE 11-12.–The Explorer 35 orbit around the Moon, projected onto the solar ecliptic plane. The period of revolution is 11.5 hr. The Apollo 12, 15, and 16 surface instrument positions and Apollo 16 subsatellite trajectory are shown.

an alias filter with 18 dB attenuation at the Nyquist frequency (0.08 Hz) of the spacecraft data-sampling system. This instrument has a phase shift linear with frequency, and its step-function response is slower than that of the Apollo 12 instrument (fig. 11-10). Further information about the Explorer 35 magnetometer is contained in reference 11-8. Figure 11-12 also shows the orbit of the Apollo 16 particles and fields subsatellite that carries a magnetometer. Additional information on the subsatellite magnetometer is available in section 23 of this report.

RESULTS AND DISCUSSION

Internal Electrical Conductivity Calculations

Electrical conductivity and temperature profiles of the interior of the Moon can be calculated from magnetic transient response measurements made by lunar surface magnetometers on the dark (antisolar) side of the Moon. (A detailed discussion of this calculation is presented in reference 11-5.) The transient-response analytical method is described in the following paragraphs.

A discontinuity in the interplanetary magnetic field that is swept by the Moon induces eddy currents within the Moon. These currents induce a field that tends to oppose the external field, retarding its penetration of the Moon. The currents diffuse and decay in a manner governed by the lunar electrical conductivity distribution. The transient behavior of the induced magnetic field (recorded at the surface by the Apollo lunar surface magnetometers) is related to the conductivity function through the diffusion equation for the induced fields. Hence, the experimental method consists of scanning time-series data from the lunar orbiting Explorer 35 magnetometer (which monitors the solar wind field undisturbed by eddy currents within the Moon) to find interplanetary field discontinuities in the time record of the data from Explorer 35 that have smooth fields before and after the discontinuity. Then the corresponding induced field response recorded at the lunar surface is examined. Finally, a conductivity distribution is sought, which yields this response as a solution of the magnetic field diffusion equation.

From simultaneous radial-component data of a single LSM and the lunar orbiting Explorer 35 magnetometer, a radial electrical conductivity profile can be calculated from the decay characteristics of

the lunar eddy-current field $\mathbf{B}_P$ by a step transient in the solar field. Figure 11-13 shows normalized data from the Apollo 12 and Explorer 35 magnetometers, giving the lunar eddy-current field decay function obtained from radial field components for 11 clean step transient events. In all cases, the Apollo 12 data have been normalized by dividing by the Explorer 35 step magnitude to give the response to an effective unit step driving field.

All these events occurred when the magnetometer was more than 900 km inside the optical shadow; therefore, plasma effects are assumed to be absent, and classical theory of the response of a conducting sphere in a vacuum can be used. The error bars are standard deviations of the measurements.

The theoretical response curves (ref. 11-5) corresponding to a large number of lunar conductivity profiles were compared with the data shown in figure 11-13. It is found that a range of monotonic conductivity profiles, defining the shaded region in figure 11-14, provides fits to the data curve that fall within the error bars. The early response ($t < 20$ sec) is dominated by the finite rise time of the driving function; hence, detailed information on the conductivity at shallow depths is limited. However, it can be calculated that, for the first 90 km into the lunar surface, the average dc electrical conductivity must be very low: less than 10^{-9} mho/m (ref. 11-1).

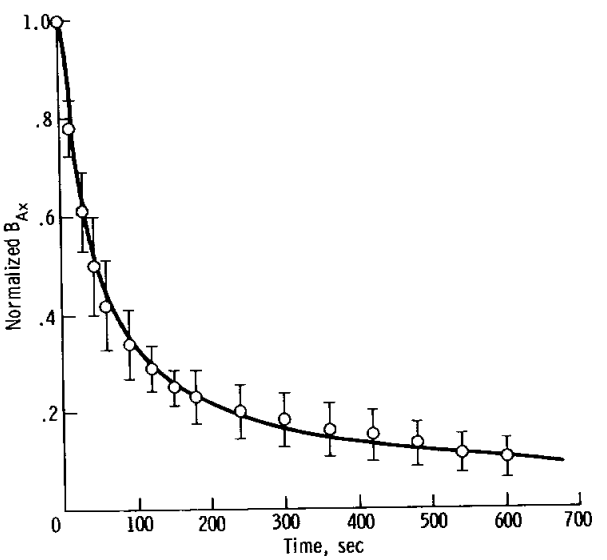


FIGURE 11-13.–Normalized transient response data, showing decay characteristics of the radial component of the total surface field B_{Ax}, after arrival of a step transient that changes the external magnetic field radial component by an amount ΔB_{Ex}, here normalized to a value of 1.

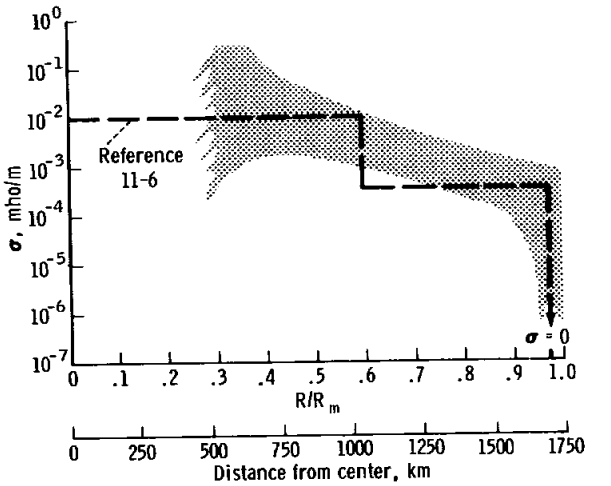


FIGURE 11-14.–Range of electrical conductivity profiles that give radial response time-dependent curves $f(t)$ that fall within the error bars of figure 11-13. A step function input magnetic field, modified by an initial ramp input of 15-sec rise time, is used in the analysis. The information at shallow depths is limited by the uncertainty in the rise time of the interplanetary magnetic field. At large depths, the information is limited by the sensitivity of the LSM.

For intermediate depths, however, the data allow only a rather restricted range of conductivities if the conductivity function is monotonic; hence, the shape of the data curve puts fairly restrictive limits on the conductivity in this region. From depths of approximately 90 km to approximately 1000 km (the region comprising the bulk of the volume of the Moon), the conductivity is seen to rise from approximately $10^{-3.5}$ to 10^{-2} mho/m. For the core region 1000 km into the Moon, there is an inherent limitation on the conductivity information to be gained from the data. (Indeed, a perfectly conducting lunar core with a radius of about 300 km would be undetectable even with large magnitude (approximately 40 γ) inputs.) Conductivities greater than $10^{-1.5}$ mho/m for depths >1000 km are compatible with the transient data.

Internal Temperature Calculations

By assuming the material composition of the lunar interior and by using a known conductivity-temperature relationship of that material, an internal temperature distribution of the Moon can be calculated from its conductivity profile. Figure 11-15 was

obtained by using the expressions for the electrical conductivity as a function of temperature given by England et al. (ref. 11-11) for olivine and peridotite, together with the results shown in figure 11-14 for the lunar conductivity. For the example of a peridotite Moon, a temperature profile that rises sharply to 850° to 1050° K at $R/R_m \sim 0.95$ and then rises gradually to 1200° to 1500° K at $R/R_m = 0.4$ is suggested by the data. At depths greater than $R/R_m = 0.4$, the temperature could be higher than 1500° K.

For description purposes, the Moon can be divided into three conductivity regions, as noted by the lunar three-layer conductivity profile superimposed on figure 11-14. Shown in figure 11-16 are the corresponding three regions, which include a thin outer crust of low conductivity and temperature; an inner shell, comprising the bulk of the lunar volume and of average temperature 900° to 1100° K; and a "core" region of temperature 1100° to 1500° K down to $R/R_m = 0.4$, with possible higher temperatures for $R/R_m < 0.4$.

Internal Magnetic Permeability Calculations

The magnetic permeability of the outer shell of the Moon (where temperatures are below the Curie point) can also be calculated from simultaneous Explorer 35 magnetometer and Apollo LSM data during times when the Moon is magnetized by the steady geomagnetic tail field. Explorer 35 provides a measurement of the steady magnetizing field $\mathbf{B}_E$, whereas the Apollo LSM measures the total field $\mathbf{B}_A = \mathbf{B}_E + \mathbf{B}$ (where the latter term is the magnetization field induced in the Moon). Because $\mathbf{B}_E$ is generally of magnitude less than ~15 γ in the geomagnetic tail, the lunar material is weakly magnetized and hysteresis effects can be neglected to first order. In this case, the linear solutions given by equations (11-4) and (11-5) can be used to determine relative permeability, because the slopes of the equations are related to permeability through equation (11-6).

Figure 11-17(a) shows a plot of radial components of the Apollo 12 LSM field (B_{Ax}) versus the geomagnetic tail field (B_{Ex}) measured by Explorer 35. A least-squares fit and slope calculations determine the factor $F = 0.0030$, which is used to determine the relative magnetic permeability for an assumed inner radius R, as shown in figure 11-4. For the bulk permeability of the Moon (the case $R = 0$),

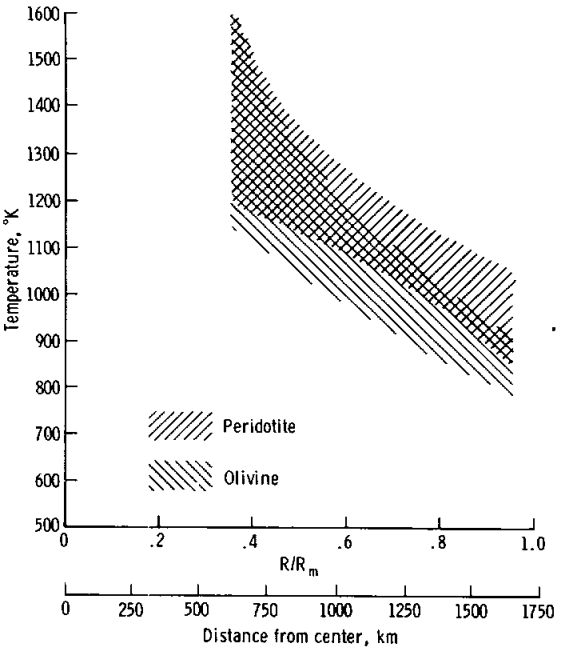
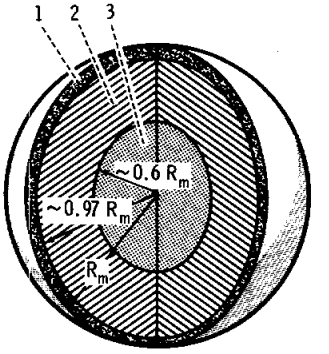


FIGURE 11-15.–Temperature estimates for assumed lunar compositions of peridotite and olivine, calculated from the electrical conductivity profile of figure 11-14.



Region	Electrical conductivity, σ, mho/m	Temperature, °K	
		Olivine	Peridotite
1	$<10^{-9}$	<440	<430
2	$\sim 3.5 \times 10^{-4}$	890	1000
3	$\sim 10^{-2}$	1240	1270

FIGURE 11-16.–Conductivity and temperature contours for a three-layer Moon. Temperature calculations are based on σ as a function of temperature for pure olivine and peridotite (ref. 11-11).

μ/μ_o = 1.01 ± 0.06. For a thinner permeable shell inside the Moon, the permeability is higher, as illustrated in figure 11-17(b). A more accurate calculation of lunar permeability will be determined in the future from network measurements obtained at three locations on the lunar surface. The increased accuracy will make possible a meaningful calculation of the percentage of permeable iron in the outer layer of the lunar sphere.

Remanent Magnetic Field Interaction With the Solar Wind

Steady remanent fields have been measured at nine surface sites during the Apollo 12, 14, 15, and 16 missions. Magnitudes of these steady fields are: Apollo 12, 38 γ; Apollo 14, 103 and 43 γ at two sites separated by 1.1 km; Apollo 15, 6 γ; and Apollo 16, 121, 125, 180, 231, and 313 γ at five sites separated by distances ranging from 0.5 to 7.1 km. All these fields are attributed to remanent magnetization in nearby subsurface materials. The measurements are unexpectedly high, and their presence indicates that, at some time in the past, the Moon either possessed a strong magnetizing field or was immersed in one. A more detailed discussion of these remanent fields is available in reference 11-12 and in section 12 of this document.

Most of the measured steady fields are strong enough to interact with the solar wind plasma, provided the scale sizes of the fields are sufficiently large (ref. 11-13). The Apollo 12 site has an LSM and a solar wind spectrometer operating simultaneously, and data from both instruments have been analyzed

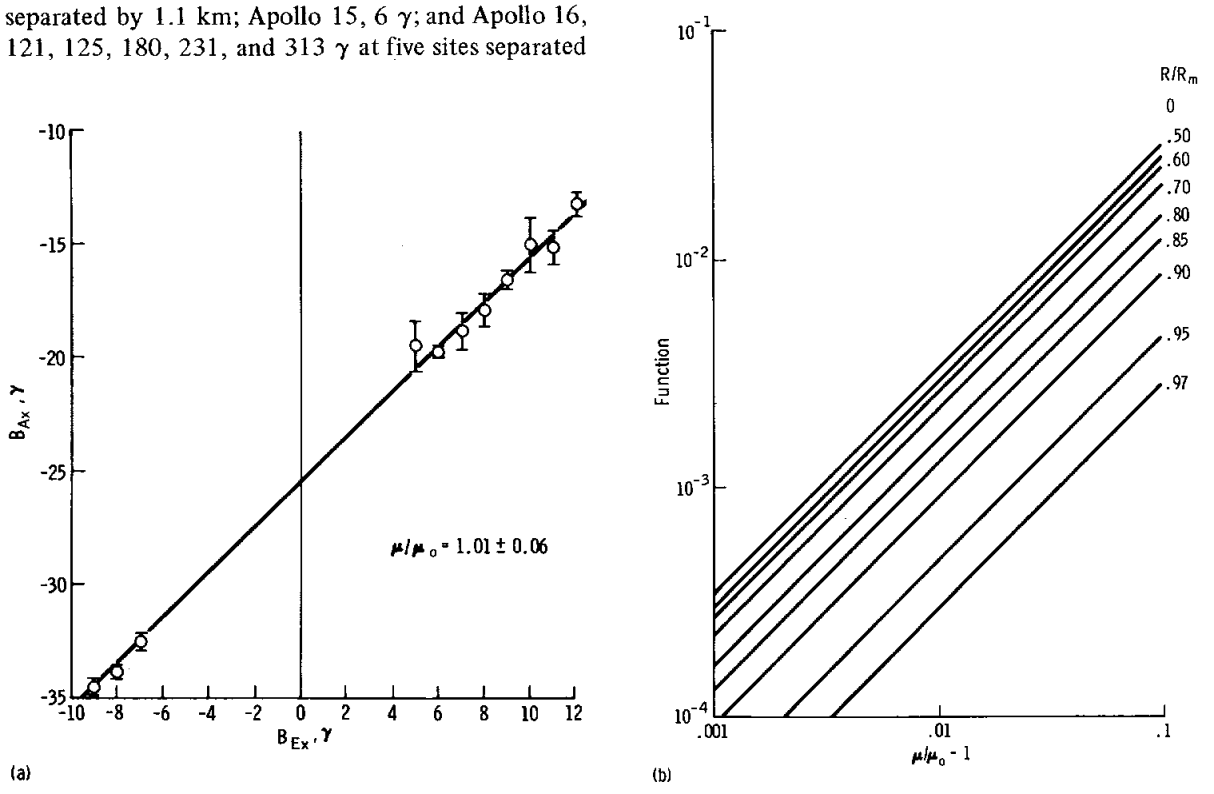


FIGURE 11-17.–Graphical representations of equations (11-4) and (11-6). (a) Radial component of Apollo 12 total surface magnetic field B_{Ax} versus the radial component of external driving field B_{Ex} (eq. (11-4)). Data points consist of measurements in quiet regions of the geomagnetic tail taken during the first four postdeployment lunations. The B_{Ax} intercept of the least-squares best-fit solid line gives the radial component of the Apollo 12 permanent field; the best-fit slope corresponds to a value of 1.01 ± 0.06 for the bulk relative permeability μ/μ_o of the Moon. (b) A graphical representation of equation (11-6), which relates the function to relative magnetic permeability $k_m = \mu/\mu_o$ for various values of R/R_m; R and R_m are internal and external radii, respectively, of a global permeable shell.

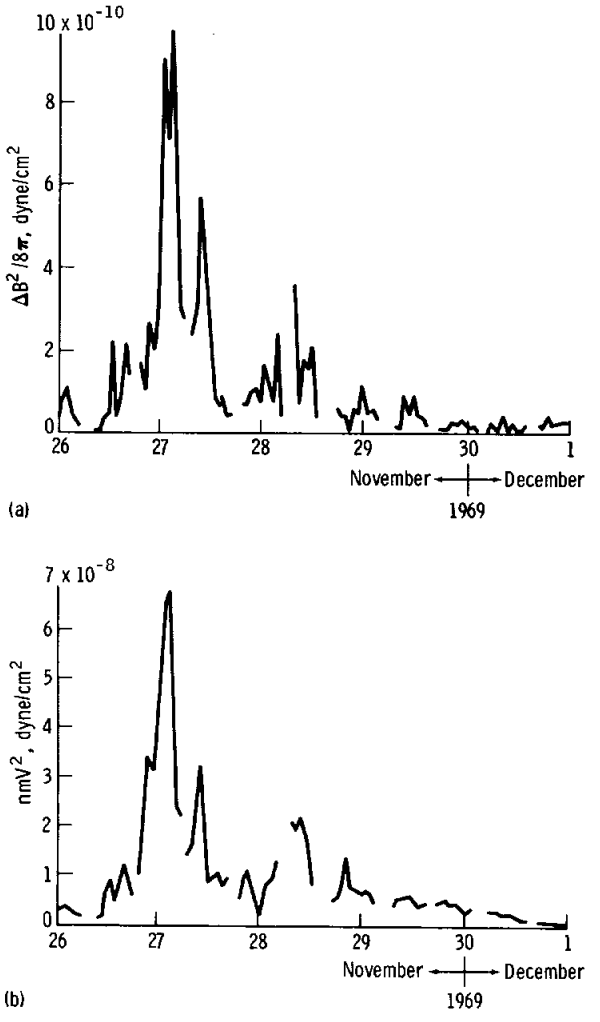


FIGURE 11-18.–Simultaneous plots of the square of (a) horizontal magnetic field difference $\Delta B^2/8\pi = 1/8\pi(\Delta B_x{}^2 + \Delta B_y{}^2 + \Delta B_z{}^2)$ where $\Delta B_i = B_{Ai} - (B_{Ei} + B_{Si})$, and i = x,y,z and (b) solar wind pressure at the Apollo 12 site, showing the correlation between the change in magnetic pressure and dynamic plasma proton pressure.

to investigate the field-plasma interaction (ref. 11-7).[1] Applying the square of equation (11-8), which allows calculation of the magnetic field difference due to the field-plasma interaction, 1-hr averages

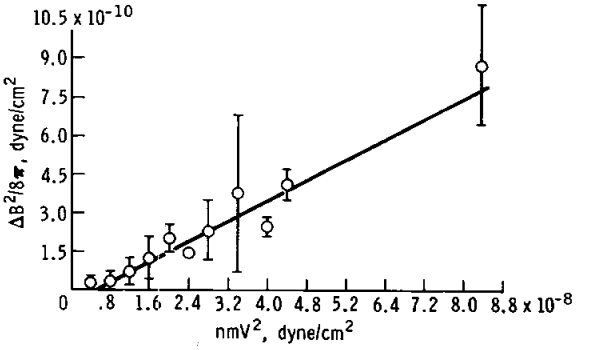


FIGURE 11-19.–Magnetic field pressure difference versus solar wind plasma dynamic pressure at the Apollo 12 site. The ratio of magnetic pressure change to plasma pressure is given by the slope to be ≅0.01. The maximum ratio of dynamic plasma pressure to total magnetic pressure $|\mathbf{B}_{ST}| = |\mathbf{B}_S + \Delta\mathbf{B}|$ is calculated to be $\beta = 5.9$.

of the magnetic pressure change $\Delta B^2/8\pi$ and simultaneous solar wind dynamic pressure nmV^2 are plotted (fig. 11-18). The correlation between the magnetic pressures is emphasized further in figure 11-19, which contains data from two sequential lunations. The correlation suggests that the field change $\Delta\mathbf{B}$ is due to a compression of the local remanent field $\mathbf{B}_S$ by the solar wind. The ratio of plasma dynamic pressure to *total* magnetic pressure is expressed

$$\beta = \frac{nmV^2}{B_{ST}{}^2/8\pi} \qquad (11\text{-}9)$$

where $\mathbf{B}_{ST} = \mathbf{B}_S + \Delta\mathbf{B}$ is the total surface compressed field. During times of maximum plasma pressure as shown in figure 11-18, the value of β is calculated to be 5.9; $\beta \leqslant 1$ would imply that the field had been compressed to the stagnation magnitude required to stand off the solar wind and possibly form a local shock. Compression of the remanent field alone, therefore, does not cause the stagnation condition to be reached during the time period of these data. The Apollo 16 remanent magnetic fields, which exceeded 120 γ at five sites over a 7-km extent, therefore could quite possibly set up a shock during times of high solar wind pressure. Correlation of plasma data with these Apollo 16 remanent magnetic field data will be performed in future studies.

[1] Marcia Neugebauer, Conway W. Snyder, Douglas R. Clay, and B. Goldstein: Solar Wind Observations on the Lunar Surface With the Apollo 12 ALSEP. Submitted to Planetary Space Sci.

Special Events

Data for two special events are illustrated in figures 11-20 to 11-22. All magnetic field components are expressed in their respective local ALSEP surface coordinate systems ($\hat{x},\hat{y},\hat{z}$), which have origins at local deployment sites; each $\hat{x}$ is directed radially outward from the local surface; $\hat{y}$ and $\hat{z}$ are tangent to the surface and directed eastward and northward, respectively.

Apollo 15 magnetic field data for a 30-min interval during the Apollo 15 lunar module (LM) ascent on August 2, 1971, are shown in figure 11-20. The field data show evidence of plasma currents in the LM exhaust gas cloud as the gas passes the magnetometer. Some evidence of a plasma disturbance passing the magnetometer after the Apollo 15 LM impact is shown in figure 11-21. Because the LM impacted approximately 93 km away from the magnetometer, it seems surprising that the effect could travel such a large distance without attenuating

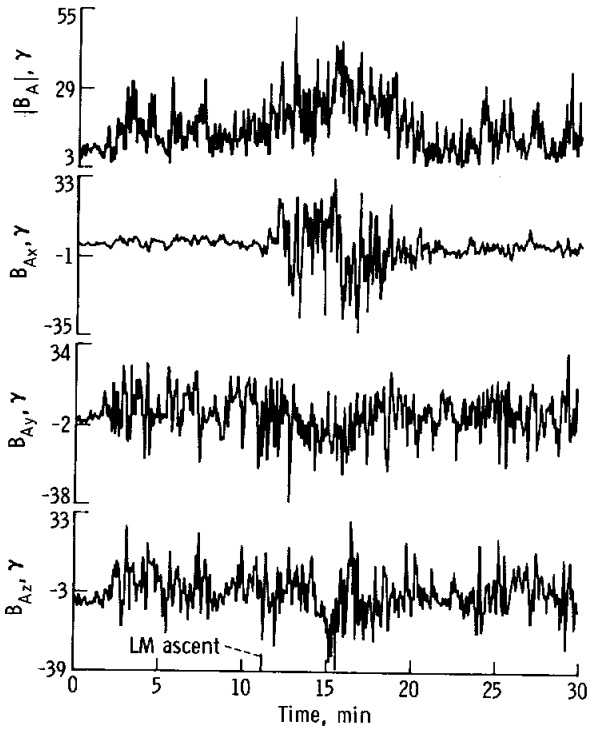


FIGURE 11-20.–Apollo 15 LSM data during lunar module ascent at 17:11 G.m.t. on August 2, 1971. The ALSEP coordinate system is used, with x directed radially outward from the surface, y eastward, and z northward. The exhaust plasma caused an increase in surface field magnitude, most evident in the x (vertical) component.

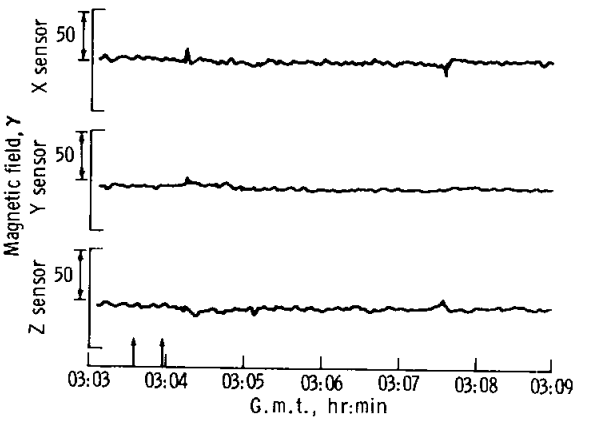


FIGURE 11-21.–Real-time data recordings of Apollo 15 LSM during the time of lunar module impact on August 3 at a position 93 km west-northwest of the magnetometer. The left arrow indicates real time of impact (03:03:35.8 G.m.t.), and the right arrow shows estimated P-wave arrival time at the Apollo 15 passive seismic experiment (ref. 11-14). The signals at 03:03:10 and 03:07:30 G.m.t. possibly show effects of the impact on the local magnetic field. Coordinate axes here refer to the respective sensor boom directions of the instrument and should not be confused with the ALSEP coordinate system used in figures 11-13, 11-17, and 11-20.

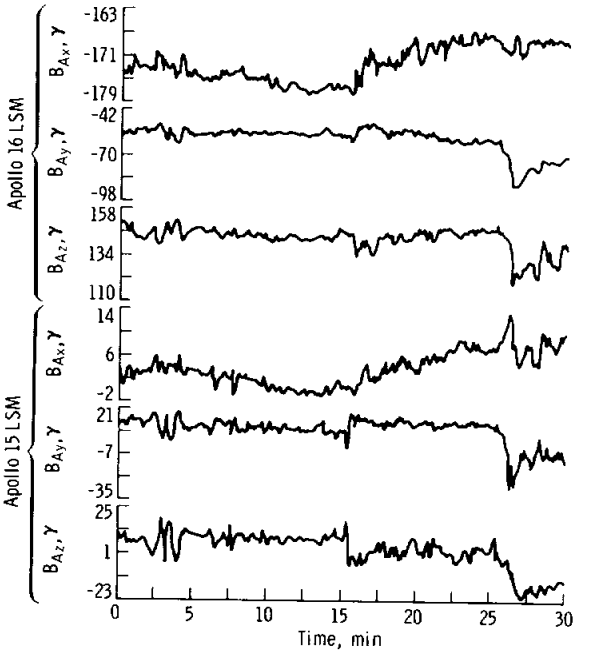


FIGURE 11-22.–Preliminary simultaneous data obtained on April 22, 1972, from Apollo 15 and Apollo 16 lunar surface magnetometers. Start time was 15:30 G.m.t. The top three vector component graphs of Apollo 16 data are shown in the Apollo 16 coordinate system; Apollo 15 components are plotted in the Apollo 15 system.

to magnitudes below instrument resolution. Both the Apollo 15 LM ascent and impact events were also observed by the Apollo 15 suprathermal ion detector experiment (ref. 11-15) and the Apollo 15 passive seismic experiment (ref. 11-14). A preliminary 30-min plot of simultaneously obtained Apollo 15 and 16 magnetometer data is shown in figure 11-22; all components are given in their respective ALSEP coordinate systems. These particular plots show that lunar induced eddy-current fields are of global rather than local extent. Future investigations using simultaneous surface magnetometer data should allow detailed analyses of lunar properties such as azimuthal variations of electrical conductivity and temperature profiles and inhomogeneities in local and global permeable material formations.

SUMMARY

Transient Magnetic Field Response, Internal Electrical Conductivity, and Temperature Implications

The electrical conductivity of the lunar interior has been determined from magnetic step transient measurements made on the lunar dark side. The general aspects of the data fit the classical theory of a conducting sphere in a magnetic field. Radial and tangential magnetic field component measurements indicate a global rather than a local response to these step transients. A continuous conductivity profile, with error limits, has been determined from normalized radial step transient response data. The conductivities, when converted to temperatures for an assumed lunar material of peridotite, suggest the existence of a thin outer layer (perhaps 90 km thick) in which the temperature rises sharply to 850° to 1050° K and then increases gradually to 1200° to 1500° K at a depth of approximately 1000 km. In the deep interior, higher temperatures are compatible with the data.

Relative Magnetic Permeability of the Moon

The whole-Moon relative permeability has been calculated to be $\mu/\mu_o = 1.01 \pm 0.06$ from measurements taken while the Moon was immersed (magnetized) in the geomagnetic tail. If an inner core of radius $R \sim 0.6\ R_m$ is above the Curie temperature (1073° K), the permeability of the outer shell will still lie within the limits listed above.

Remanent Magnetic Field Interaction With the Solar Wind

The remanent magnetic fields measured thus far on the Moon are 38 γ at Apollo 12 in Oceanus Procellarum, 103 and 43 γ at two Apollo 14 Fra Mauro sites separated by 1.1 km, 6 γ at the Apollo 15 Hadley-Apennine site, and 121 to 313 γ at the Apollo 16 Descartes highland site.

Measurements show that the remanent field at the Apollo 12 site is compressed by the solar wind. The 38 γ remanent field is compressed to 54 γ by a solar wind pressure increase of 7×10^{-8} dyne/cm^2. The ratio of plasma dynamic pressure to total magnetic pressure β is 5.9 during the time of maximum field compression. The change in magnetic pressure is directly proportional to the change in plasma dynamic pressure.

REFERENCES

11-1. Dyal, Palmer; and Parkin, Curtis W.: The Apollo 12 Magnetometer Experiment: Internal Lunar Properties From Transient and Steady Magnetic Field Measurements. Proceedings of the Second Lunar Science Conference, vol. 3, A. A. Levinson, ed., MIT Press (Cambridge, Mass.), 1971, pp. 2391-2413.

11-2. Dyal, Palmer; and Parkin, Curtis W.: Electrical Conductivity and Temperature of the Lunar Interior From Magnetic Transient-Response Measurements. J. Geophys. Res., vol. 76, no. 25, Sept. 1, 1971, pp. 5947-5969.

11-3. Smythe, W. R.: Static and Dynamic Electricity. McGraw-Hill Book Co. (New York), 1950.

11-4. Snyder, Conway W.; Clay, Douglas R.; and Neugebauer, Marcia: The Solar-Wind Spectrometer Experiment. Sec. 5 of Apollo 12 Preliminary Science Report. NASA SP-235, 1970.

11-5. Dyal, Palmer; Parkin, Curtis W.; and Cassen, Patrick: Surface Magnetometer Experiments: Internal Lunar Properties and Lunar Field Interactions With the Solar Plasma. Proceedings of the Third Lunar Science Conference, vol. 3, David R. Criswell, ed., MIT Press (Cambridge, Mass.), 1972, pp. 2287-2308.

11-6. Dyal, Palmer; and Parkin, Curtis W.: Lunar Properties From Transient and Steady Magnetic Field Measurements. The Moon, vol. 4, nos. 1 and 2, Apr. 1972, pp. 63-87.

11-7. Dyal, P.; Parkin, C. W.; Snyder, C. W.; and Clay, D. R.: Measurements of Lunar Magnetic Field Interaction With the Solar Wind. Nature, vol. 236, no. 5347, Apr. 21, 1972, pp. 381-385.

11-8. Dyal, Palmer; Parkin, Curtis W.; and Sonett, C. P.: Lunar Surface Magnetometer. IEEE Trans. Geosci. Electron., vol. GE-8, no. 4, Oct. 1970, pp. 203-215.

11-9. Gordon, D. I.; Lundsten, R. H.; and Chiarodo, R. A.: Factors Affecting the Sensitivity of Gamma-Level Ring-Core Magnetometers. IEEE Trans. Magnetics, vol. MAG-1, no. 4, Dec. 1965, pp. 330-337.

11-10. Gordon, Daniel I.; and Brown, Robert E.: Recent Advances in Fluxgate Magnetometers. IEEE Trans. Magnetics, vol. MAG-8, no. 1, Mar. 1972, pp. 76-82.

11-11. England, A. W.; Simmons, G.; and Strangway, D.: Electrical Conductivity of the Moon. J. Geophys. Res., vol. 73, no. 10, May 15, 1968, pp. 3219-3226.

11-12. Dyal, P.; Parkin, C. W.; Sonett, C. P.; DuBois, R. L.; and Simmons, G.: Lunar Portable Magnetometer Experiment. Sec. 13 of Apollo 14 Preliminary Science Report. NASA SP-272, 1971.

11-13. Barnes, A.; Cassen, P.; Mihalov, J. D.; and Eviatar, A.: Permanent Lunar Surface Magnetism and Its Deflection of the Solar Wind. Science, vol. 172, no. 3984, May 14, 1971, pp. 716-718.

11-14. Latham, G. V.; Ewing, M.; Press, F.; Sutton, G.; et al.: Passive Seismic Experiment. Sec. 8 of Apollo 15 Preliminary Science Report. NASA SP-289, 1972.

11-15. Hills, H. K.; Meister, J. C.; Vondrak, R. R.; and Freman, J. W., Jr.: Suprathermal Ion Detector Experiment (Lunar Ionosphere Detector). Sec. 12 of Apollo 15 Preliminary Science Report. NASA SP-289, 1972.

ACKNOWLEDGMENTS

The authors express their appreciation for the efforts of the many persons who contributed to this experiment. In particular, thanks are extended to John Keeler, Fred Bates, Kenneth Lewis, and Marion Legg, whose diligent efforts contributed to the success of this experiment. The authors also wish to thank Dr. C. W. Snyder and Dr. D. R. Clay, Jet Propulsion Laboratory, for the use of Apollo 12 solar wind spectrometer data.

12. Lunar Portable Magnetometer Experiment

P. Dyal,[a†] C. W. Parkin,[a] C. P. Sonett,[a]
R. L. DuBois,[b] and G. Simmons[c]

INTRODUCTION

The purpose of the lunar portable magnetometer (LPM) experiment is to measure the permanent magnetic field at different geological sites on the lunar surface. These measurements can be used to determine the present magnetic and structural properties of the local region and to explain magnetic aspects of the history of the Moon.

Remanent magnetic fields were measured at the landing sites of the Apollo 12, 14, 15, and 16 missions. During the Apollo 16 mission to the lunar highlands, the magnetic field of 313 γ measured in the North Ray area proved to be the highest ever measured on another body of planetary size. Other field measurements obtained by the commander and lunar module pilot at different sites along the three surface traverses varied from 121 to 313 γ. In addition, an in situ magnetic field measurement of lunar rock sample 60335 was made to determine the total remanent magnetization acquired in the native lunar environment of the sample.

The discovery of fossil magnetic fields on the lunar surface has caused modification of existing ideas concerning internal lunar structure and reexamination of theories concerning the origin and early evolution of the Moon. The high magnetic fields measured in the Descartes region should have a strong effect on the accretion of solar wind particles and the reimplantation of outgassed ions into the regolith (ref. 12-1). These will possibly appear as a measurable effect in future angular distribution measurements of the solar wind foil experiment (ref. 12-2) and in lunar sample analyses. The surface fields also provide reference values for extrapolation of subsatellite magnetometer measurements (ref. 12-3) to the lunar surface. Further analysis should yield information on the geological nature and the origin of the lunar remanent field, including the possibility of an ancient lunar dynamo (refs. 12-4 and 12-5), a shock-induced magnetization, or another mechanism to account for the strong magnetization found in lunar surface samples.

[a]NASA Ames Research Center.

[b]Oklahoma University.

[c]Massachusetts Institute of Technology.

[†]Principal Investigator.

THEORY

The magnetic field measured by the LPM is a vector quantity associated with every point in the region, and its space and time variations are described by Maxwell's equations. The total magnetic field measured by the LPM at the Descartes site is primarily the steady remanent field intrinsic to lunar material; secondary fields include external solar fields, time-dependent lunar-induced fields, and fields caused by interaction of the solar wind with the remanent lunar field (ref. 12-6).

By the principle of superposition, the total magnetic field $\mathbf{B}_A$ measured on the lunar surface can be expressed vectorially as

$$\mathbf{B}_A = \mathbf{B}_S + \mathbf{B}_E + \mathbf{B}_\mu + \mathbf{B}_P + \mathbf{B}_T + \mathbf{B}_D + \mathbf{B}_F \qquad (12\text{-}1)$$

where $\mathbf{B}_S$ is the steady remanent field at the surface site; $\mathbf{B}_E$ is the total external (solar or terrestrial) driving magnetic field independently measured by the Explorer 35 magnetometer and the Apollo 15 and 16 subsatellite lunar-orbiting magnetometers while outside the antisolar lunar cavity; $\mathbf{B}_\mu$ is the magnetization field induced in permeable lunar material; $\mathbf{B}_P$ is the poloidal field caused by eddy currents induced in the lunar interior by changing external fields; $\mathbf{B}_T$ is the toroidal field corresponding to unipolar electrical currents driven through the Moon by the $\mathbf{V} \times \mathbf{B}_E$ electric field (where $\mathbf{V}$ is the velocity of the Moon with respect to the solar wind); $\mathbf{B}_D$ is the field

associated with the diamagnetic lunar cavity; and $\mathbf{B}_F$ is the total field associated with the hydromagnetic solar wind flow past the Moon. The fields of equation (12-1) can also be classed as external ($\mathbf{B}_E$), permanent ($\mathbf{B}_S$), induced ($\mathbf{B}_\mu$, $\mathbf{B}_P$, $\mathbf{B}_T$), and solar wind interaction ($\mathbf{B}_D$, $\mathbf{B}_F$).

The Apollo 16 lunar surface magnetometer (LSM), deployed at the Apollo lunar surface experiments package (ALSEP) site, was operating during all LPM measurements. Because the LSM continuously measures three field vectors per second, it monitors all the secondary fields; that is, once $\mathbf{B}_S$ has been determined at the ALSEP site, all remaining fields of equation (12-1) can be determined by vector subtraction. Thereafter, equation (12-1) can be used to calculate the steady remanent field $\mathbf{B}_S$ at each LPM deployment site.

EXPERIMENTAL TECHNIQUE

For the experimental technique, the self-contained LPM shown in figure 12-1 is used to measure the steady magnetic field at different points along the lunar traverse of the astronauts. The LPM field measurements are a vector sum of the steady remanent field from the lunar crust and of the time-varying ambient fields (eq. (12-1)). The ALSEP LSM simultaneously measures the time-varying components of the field; these components are later subtracted from the LPM measurements to give the desired resultant steady field values caused by the magnetized crustal material. The LPM consists of a set of three orthogonal fluxgate sensors mounted on top of a tripod; the sensor-tripod assembly is connected by means of a 15-m ribbon cable to the electronics box, which is mounted on the lunar roving vehicle (Rover). The 15-m cable length was determined from magnetic properties tests of the Rover. The LPM has been calibrated by using magnetic reference instruments directly traceable to the National Bureau of Standards. The pertinent LPM characteristics are listed in table 12-I.

The fluxgate sensor, shown schematically in figure 12-2, is used to measure the vector components of the magnetic field in the magnetometer experiment. Three fluxgate sensors (refs. 12-7 and 12-8) are orthogonally mounted in the sensor block shown in figure 12-1. Each sensor weighs 18 g and uses 15 mW of power during operation. The sensor consists of a flattened toroidal core of Permalloy that is driven

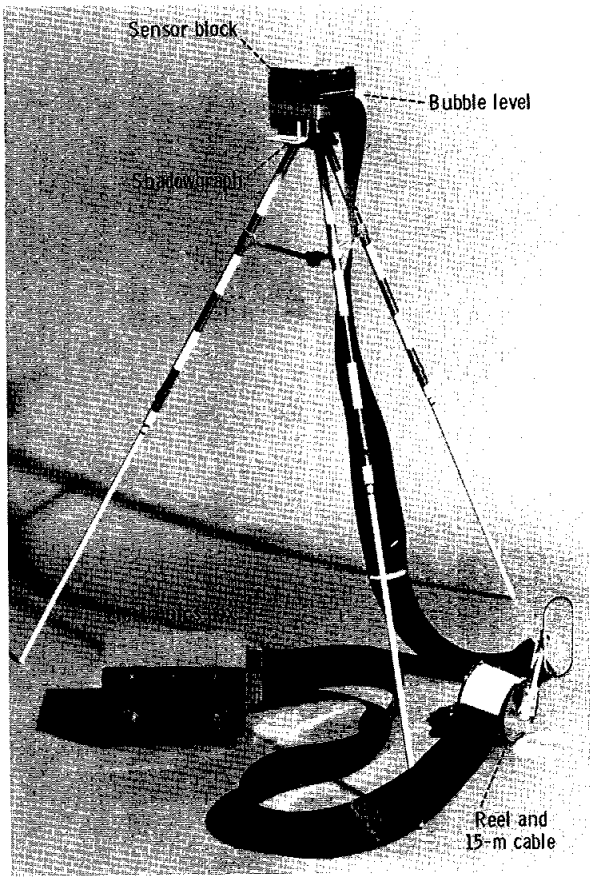


FIGURE 12-1.–The LPM deployed in the laboratory.

TABLE 12-I.–Apollo 16 LPM Characteristics

Parameter	*Value*
Sensor	3 orthogonal fluxgate sensors
Range, γ	-256 to +256
Resolution, γ	±1.0
Frequency response	dc to 0.05 Hz
Battery lifetimes:	
Electronics, hr	8
Display, min	20
Mass, kg	4.6
Size, cm	56 by 15 by 14
Operating temperature, °K	273 to 323

to saturation by a square wave at a frequency f_O = 7250 Hz. This constant-voltage square wave drives the core to saturation during alternate half cycles and modulates the permeability at twice the drive frequency. The voltage induced in the sense windings is equal to the time rate of change of the net flux

contained in the area enclosed by the sense winding. This net flux is the superposition of the flux from the drive winding and the ambient magnetic field. The signal generated in the sense winding at the second harmonic of the drive signal will be amplitude modulated at a magnitude proportional to the ambient magnetic field. The phase of this second harmonic signal with respect to the drive waveform indicates the polarity of the magnetic field. The sensor electronics amplifies and filters the $2f_o$ sense-winding signal and synchronously demodulates it to derive a voltage proportional to the ambient magnetic field. After demodulation, the resulting signal is amplified and used to drive the feedback winding to null out the ambient field within the sensor. Operating at null increases thermal stability by making the circuit independent of core permeability variations with temperature.

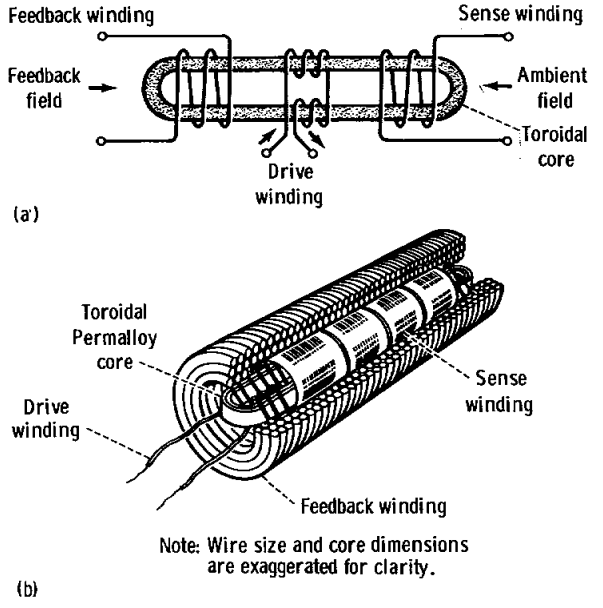


FIGURE 12-2.–The fluxgate sensor used in the LPM to measure each of three components of magnetic field. (a) Functional schematic. (b) Cutaway view of the sensor windings and high-permeability core.

The sensor block, mounted on the top of a tripod, is positioned 75 cm above the lunar surface. The tripod assembly consists of a latching device to hold the sensor block, a bubble level with 1° annular rings, and a shadowgraph with 3° markings used to aline the device along the Moon-to-Sun line.

The magnetometer electronics is self-contained with a set of mercury cells for power and three digital displays for visual read-out of the magnetic field components. A block diagram of the instrument is shown in figure 12-3. The sensors are driven into saturation by a 7.25-kHz square wave, and a 14.5-kHz pulse is used to demodulate the second harmonic signal from the sense windings. The amplifier output

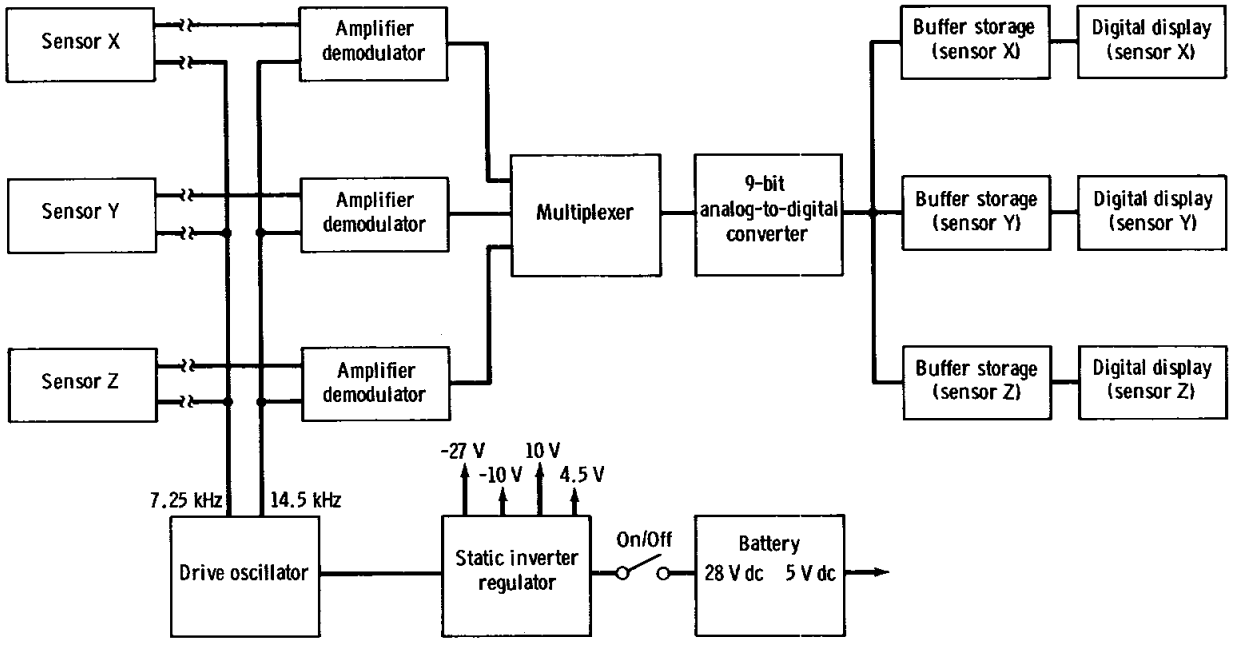


FIGURE 12-3.–Functional block diagram of the LPM electronics.

is synchronously demodulated, producing a direct-current output voltage proportional to the amplitude of the ambient magnetic field. This demodulated output is used to drive the feedback winding of the sensor so that the sensor can be operated at null conditions. The demodulated output from each channel is passed through a low pass filter with a time constant of 20 sec. Upon actuation of the READ switch, this filtered analog signal is converted to a digital 9-bit binary number. The output of the analog-to-digital converter then goes to a storage register for display by the light-emitting diode numeric indicator. Three numeric indicators are used for each axis and read out in octal from 000 to 777 for magnetic field values from −256 to +256 γ.

The astronaut operation is crucial to the execution of this experiment. The following measurement sequence is conducted (fig. 12-4). Leaving the electronics box on the Rover, the astronaut turns the power switch on, reads the digital displays in sequence, and verbally relays the data back to Earth. At the first site only, two sets of additional readings are taken with the sensor block first rotated 180° about a horizontal axis and then rotated 180° about a vertical axis. These additional readings allow determination of a zero offset for each axis.

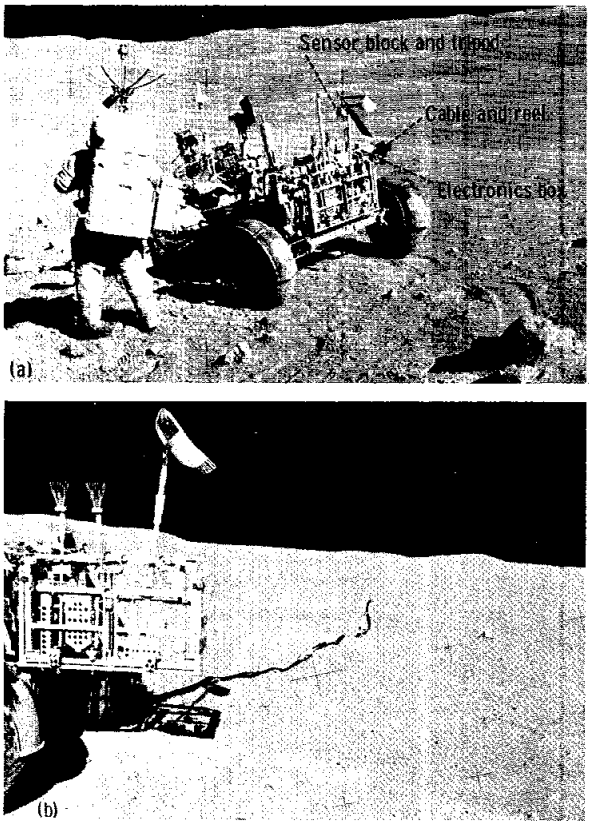


FIGURE 12-4.–The LPM on the lunar surface. (a) Stowed on the Rover. (b) Deployed during a magnetic field measurement.

PRELIMINARY RESULTS

Five LPM measurements were made at four different sites in the Descartes region from April 21 to 23, 1972. During these days, the Moon was submerged in the free-streaming solar wind (fig. 12-5); the solar fields were generally quiet (less than ~5 γ field variations during measurements). The measurement magnitudes and locations are shown in figures 12-6 to 12-9: 180 γ at site 2 near Spook Crater; 125 γ at site 5 on Stone Mountain; 313 γ at site 13 near North Ray Crater; and 121 γ at the final Rover site approximately 180 m east of the lunar module. Maximum separation was 7.1 km between sites 5 and 13.

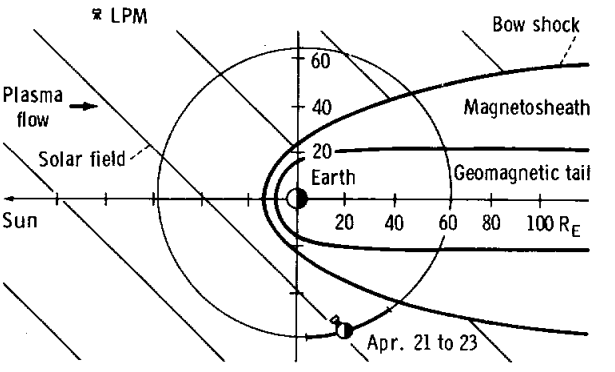


FIGURE 12-5.–The lunar orbit projected onto the solar ecliptic plane. The enhanced segment of the orbit shows the position of the Apollo 16 LPM during measurements on April 21 to 23.

The objective of the LPM measurements was to determine the intrinsic lunar steady magnetic field at various surface locations. The magnetometer actually measured low-frequency (<0.05 Hz) components of the total magnetic field at the surface (defined in eq. (12-1)), which includes the intrinsic lunar remanent field, the external solar field, fields induced in the lunar interior by changing solar fields, and fields caused by solar wind interactions with the lunar remanent field. The last three types of fields were also monitored by the Apollo 16 LSM at the ALSEP

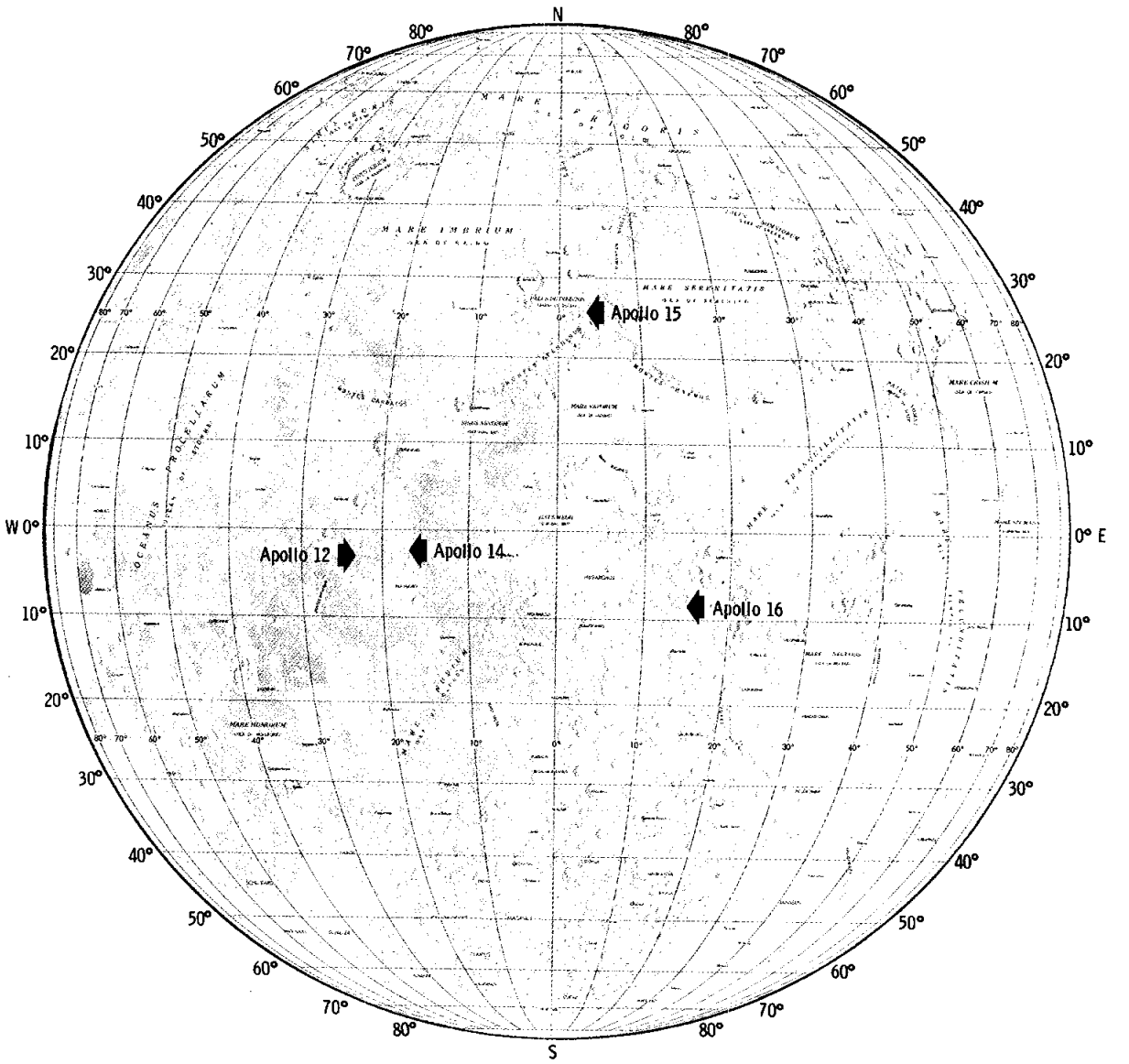


FIGURE 12-6.–Surface magnetic fields measured during four Apollo missions. Vectors represent magnitude and direction of the average of all remanent field measurements made at each landing site.

site; therefore, they can be subtracted vectorially from the LPM readings to calculate the intrinsic lunar remanent field at each LPM surface measurement site.

The calculated surface fields measured by all Apollo surface magnetometers are listed in table 12-II; the Descartes fields are illustrated in figure 12-7. The error limits listed for field components and magnitudes include uncertainties in sensor orientation, instrument temperature measurements, and the compressive effect of the solar wind on the Apollo 16 surface field (ref. 12-6).

Field magnitude gradients vary from a maximum of 370 γ/km between the ALSEP site and final Rover parking site to a minimum of 1.2 γ/km between site 5 and the final Rover parking site. For comparison, gradients had an upper limit (LSM resolution limit) of 133 γ/km at the Apollo 12 and 15 sites and a measured value of 54 γ/km at the Apollo 14 site.

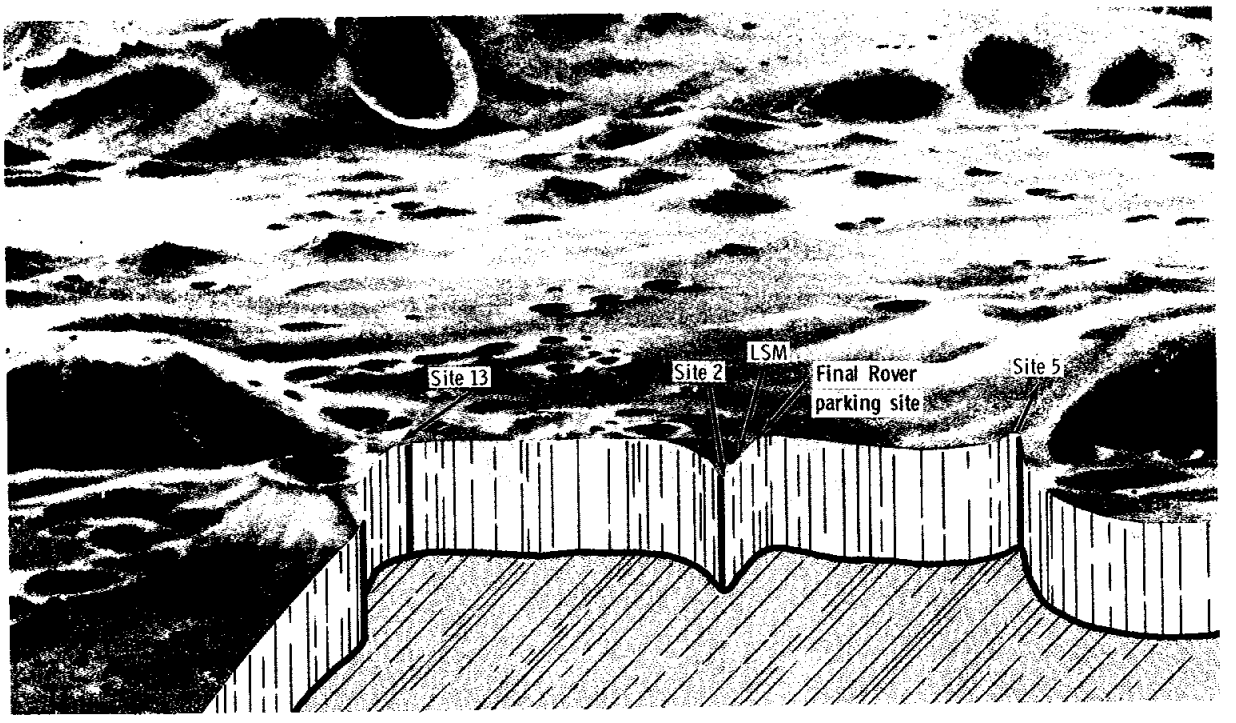


FIGURE 12-7.—Pictorial representation of the magnetic field vectors measured at the Apollo 16 Descartes region.

At the final Rover site, two LPM measurements were made to calculate the magnetic field of a surface rock sample and to determine the total magnetization. The method involved measuring the total (hard plus soft) remanence of a sample on the lunar surface and transporting the sample to Earth to make laboratory measurements of only hard remanence. Subtraction of the two measurements would give a value for the soft remanence of the rock in its native lunar environment. For the rock measurement procedure, an LPM field measurement was made before and after placement of the LPM rock (sample 60335) on the sensor block (fig. 12-10). The two fields were then subtracted, and the difference was corrected for solar and induced lunar fields by using the LSM continuous field data. Components of the net steady magnetic field attributable to the rock alone are calculated to be $B_{up} = -2 \pm 4\ \gamma$, $B_{east} = -2 \pm 4\ \gamma$, and $B_{north} = 2 \pm 4\ \gamma$. Therefore, the rock field is negligible within experimental error, implying that the rock magnetization is below the LPM resolution. The field measurement experiment of the LPM rock (sample 60335) was subsequently repeated in the laboratory using another LPM, which verified that the magnetic field of the rock is below instrument resolution. This fact is consistent with the low total remanence of the sample, measured to be 5.4×10^{-6} emu/g.[1] Thus, no calculation could be made of the native lunar-induced soft remanence of the sample.

DISCUSSION

The remanent magnetic fields measured in the Descartes region are the largest extraterrestrial fields yet measured in situ. These measurements show for the first time that the Descartes highlands have a stronger remanent magnetization than do the mare regions of the previous Apollo landing sites. From the complete set of measurements obtained by the Apollo surface magnetometers (ref. 12-9), the lunar subsatellite magnetometers (ref. 12-10), and the orbiting Explorer 35 magnetometer (ref. 12-11), it is apparent that the Moon is extensively covered with remanent magnetic field sources that show a strong

[1] D. W. Strangway and G. W. Pearce, private communication, May 18, 1972.

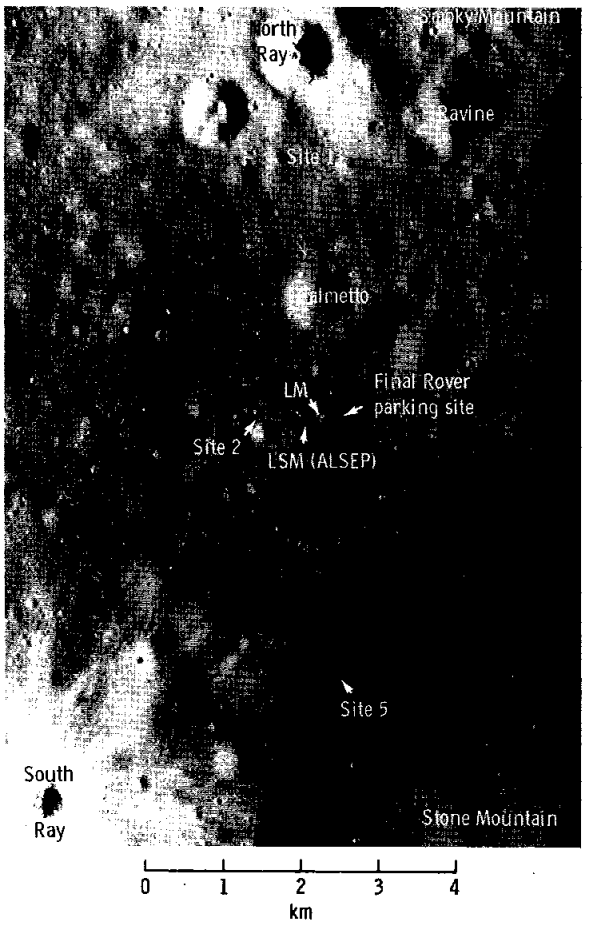


FIGURE 12-8.–The LPM measurement locations during the three extravehicular activity periods.

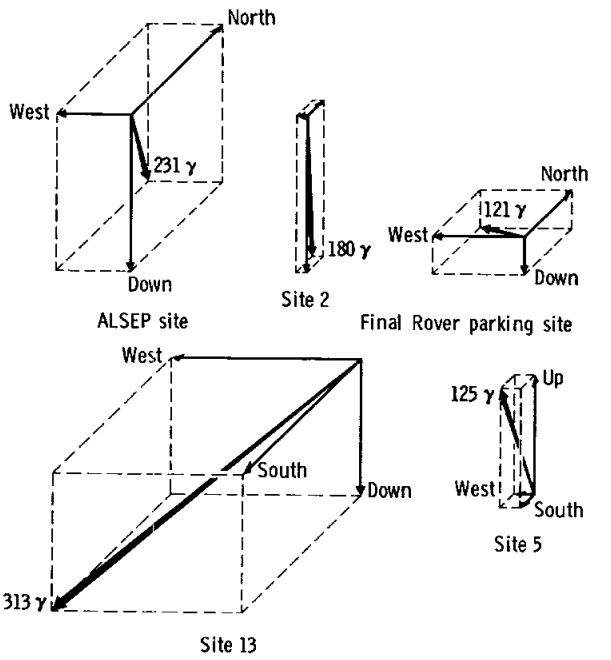


FIGURE 12-9.–The vector fields at each LPM surface measurement site.

regional variation. One elusive but important finding is the negative evidence of a measurable global dipolar field for the Moon.

From lunar sample measurements, it is generally concluded that the lunar remanent field is primarily of thermoremanent origin (refs. 12-12 and 12-13); the lunar crustal material probably became magnetized as the material cooled below the Curie

TABLE 12-II.–Summary of Lunar Surface Magnetic Field Measurements

Site	*Coordinates, deg*	*Field magnitude, γ*	*Magnetic field components, γ*		
			B_{up}	B_{east}	B_{north}
Apollo 16 [a]					
ALSEP site	8.9 S 15.5 E	231	-174	-73	134
Site 2		180	-179	-10	19
Site 5		125	120	-25	-25
Site 13		313	-141	-209	-186
Final Rover parking site		121	-42	-93	66
Apollo 15 ALSEP site	26.1 N 3.7 E	6 ± 4	4 ± 4	1 ± 3	-4 ± 3
Apollo 14 landing site	3.7 S 17.5 W				
Site A		103 ± 5	-93 ± 4	38 ± 5	-24 ± 5
Site C		43 ± 6	-15 ± 4	-36 ± 5	-19 ± 8
Apollo 12 ALSEP site	3.2 S 23.4 W	38 ± 2	-25.8 ± 1.0	11.9 ± 0.9	-25.8 ± 0.4

[a]The error in all components of the Apollo 16 field readings is ±25 γ. These limits will be reduced after further data reduction.



FIGURE 12-10.–Closeup view of the LPM sensor-tripod assembly deployed on the lunar surface during measurements of the magnetic field of a lunar rock sample. The sample has been placed on top of the sensor block by the commander.

temperature in the presence of a strong ambient magnetic field some 3 to 4 billion years ago (ref. 12-14). Sources of this ancient ambient field, which no longer exists on the Moon, include an extinct lunar dynamo, a stronger solar or terrestrial field, and meteorite-shock-induced fields.

REFERENCES

12-1. Manka, R. H.; and Michel, F. C.: Lunar Atmosphere as a Source of Ar-40 and Other Lunar Surface Elements. Science, vol. 169, no. 3942, July 17, 1970, pp. 278-280.

12-2. Geiss, J.; Buehler, F.; Cerutti, H.; and Eberhardt, P.: Solar-Wind Composition Experiment. Sec. 15 of Apollo 15 Preliminary Science Report, NASA SP-289, 1972.

12-3. Coleman, Paul J., Jr.; Schubert, G.; Russell, C. T.; and Sharp, L. R.: The Particles and Fields Subsatellite Magnetometer Experiment. Sec. 22 of Apollo 15 Preliminary Science Report, NASA SP-289, 1972.

12-4. Runcorn, S. K.: Convection in the Moon and the Existence of a Lunar Core. Proc. Roy. Soc. (London), vol. A296, no. 1446, Feb. 7, 1967, pp. 270-284.

12-5. Sonett, C. P.; Colburn, D. S.; and Currie, R. G.: The Intrinsic Magnetic Field of the Moon. J. Geophys. Res., vol ,72, no. 21, Nov. 1, 1967, pp. 5503-5507.

12-6. Dyal, P.; Parkin, C. W.; Snyder, C. W.; and Clay, D. R.: Measurements of Lunar Magnetic Field Interaction with the Solar Wind. Nature, vol. 236, no. 5347, Apr. 21, 1972, pp. 381-385.

12-7. Geyger, W. A.: Nonlinear-Magnetic Control Devices. McGraw-Hill Book Co. (New York), 1964.

12-8. Gordon, D. I.; Lundsten, R. H.; and Chiarodo, R. A.: Factors Affecting the Sensitivity of Gamma-Level Ring-Core Magnetometers. IEEE Trans. Magnetics, vol. MAG-1, no. 4, Dec. 1965, pp. 330-337.

12-9. Dyal, P.; and Parkin, C. W.: Lunar Properties from Transient and Steady Magnetic Field Measurements. The Moon, vol. 4, nos. 1/2, Apr. 1972, pp. 63-87.

12-10. Sonett, C. P.; and Mihalov, J. D.: Lunar Fossil Magnetism and Perturbations of the Solar Wind. J. Geophys. Res., vol. 77, no. 4, Feb. 1, 1972, pp. 588-603.

12-11. Runcorn, S. K.; Collinson, D. W.; O'Reilly, W.; and Stephenson, A.: Magnetic Properties of Lunar Rocks and Fines. Lunar Science – III, Carolyn Watkins, ed. (Rev. abs. of the Third Lunar Science Conference (Houston, Tex.), Jan. 10-13, 1972), pp. 669-671.

12-12. Pearce, G. W.; Strangway, D. W.; and Gose, W. A.: Remanent Magnetization of the Lunar Samples. Lunar Science – III, Carolyn Watkins, ed. (Rev. abs. of the Third Lunar Science Conference (Houston, Tex.), Jan. 10-13, 1972), pp. 599-601.

12-13. Gopalan, K.; Kaushal, S.; Lee-Hu, C.; and Wetherill, G. W.: Rb-Sr and U, Th-Pb Ages of Lunar Materials. Proceedings of the Apollo 11 Lunar Science Conference, vol. 2, A. A. Levinson, ed., Pergamon Press (New York), 1970, pp. 1195-1205.

12-14. Dyal, P.; Parkin, C. W.; Sonett, C. P.; DuBois, R. L.; and Simmons, G.: Lunar Portable Magnetometer Experiment. Sec. 13 of Apollo 14 Preliminary Science Report, NASA SP-272, 1971.

ACKNOWLEDGMENTS

The authors wish to express their appreciation to Drs. D. S. Colburn and B. F. Smith for their help in calibration of the flight instrument and to M. Dix, C. Privette, E. Iufer, and R. Murphy (NASA Ames Research Center) for their efforts in fabrication and testing of the flight instrument. Special thanks are extended to Drs. D. W. Strangway, G. W. Pearce, A. W. England, and W. R. Muehlberger for their direct contribution during real-time operations in making this experiment successful.

13. Far UV Camera/Spectrograph

George R. Carruthers[a†] *and Thornton Page*[a]

In March 1610, Galileo Galilei reported the first use of a telescope to view mountains and maria on the Moon. On April 21, 1972, the Apollo 16 commander pointed a somewhat more complex optical instrument at the Earth from the Moon and obtained several remarkable photographs showing atmospheric rather than surface features. The optical part of the far UV camera (aperture, 7.5 cm) was not much larger than Galileo's telescope. Like his, this instrument was also pointed at other celestial objects that Galileo viewed, including the Milky Way and Jupiter, and the Large Magellanic Cloud (LMC), which is not visible from Italy. More important, the far UV camera/spectrograph recorded light in the invisible band of wavelengths between 50 and 160 nm, approximately one-third the wavelength that can penetrate the atmosphere of the Earth to ground-based telescopes.

As described in more detail in this section, these UV observations from the Moon allow study of the entire atmosphere of the Earth and the geocorona. The photographs show hydrogen and other gases in the solar wind and interplanetary media, and they provide new data on stars, nebulae, and galaxies much farther away. When used as a spectrograph, the instrument distributes the light it receives according to wavelength, and the resulting spectrum shows bright lines or gaps known to be characteristic of various gases, such as hydrogen (H), helium (He), oxygen (O), nitrogen (N), and neon (Ne). If a gas cloud is hot, the atoms are excited and the spectrum shows bright emission lines; if it is cool, the atoms absorb light, leaving gaps or absorption lines.

The far UV camera is blind to ordinary visible light; for that reason, the photographs show very few of the stars mapped by ground-based telescopes. Only the very-high-temperature (blue) stars of spectral classes O, B, and possibly A (temperatures from 50 000° down to 10 000° K) are expected to be recorded. Image blackness or density on the negatives also depends on the brightness of the star, which astronomers measure in an inverted logarithmic scale of magnitudes. A star of 6 magnitudes (mag.) can barely be seen with the unaided eye. An 11-mag. star is 100 times fainter, and a 12-mag. star is 2.5 times fainter yet. The faintest star recorded by the far UV camera is at least 11 mag., which is called the limiting magnitude.

Previous UV studies of stars, nebulae, and galaxies include 2 years of observations from the Orbiting Astronomical Observatory, summarized in references 13-1 and 13-2. Although some of these measurements extend to the Lyman-alpha line of hydrogen at 121.6 nm, most were made at wavelengths longer than 133 nm, and the limiting magnitude was approximately 6 mag. for the scanning spectrometers and approximately 10 mag. for the photometers and the Celescope television pictures. Hence, the far UV camera/spectrograph extended previous stellar research to fainter stars and shorter wavelengths and also obtained quantitative measurements of diffuse background radiation in the far UV wavelengths.

INSTRUMENT DESCRIPTION

Through their visors, astronauts can see no astronomical objects fainter than the Earth, so pointings of the far UV camera/spectrograph were made by setting two graduated circles on an altitude-azimuth telescope mount. At deployment (approximately 17:40 G.m.t. on April 21), three legs were unfolded and locked to form a tripod under a leveled table. The camera/spectrograph was supported between two vertical stanchions on the table, as shown in figure 13-1, so that it could swing vertically from 0° elevation (pointing at the horizon) to 90° (pointing at the zenith). The desired elevation (EL) angle was set by the astronaut on a sector graduated in degrees. The stanchions could be rotated around a vertical axis centered on the leveled table where the azimuth could be read on a circle graduated in degrees. The zero point of this azimuth circle was set by the astronaut sighting down-Sun, a few degrees

[a]Naval Research Laboratory.

†Principal Investigator.



FIGURE 13-1.–Far UV camera deployed in the LM shadow on April 22 (AS16-114-18439).

south of west. Hence, the azimuth (AZ) readings for the far UV camera pointings were 95° larger than conventional AZ readings (measured from lunar north) used in other crew activities near the lunar module (LM).

The camera/spectrograph was designed, fabricated, and calibrated at the Naval Research Laboratory in Washington, D.C., to meet the requirements of the experiment goals and the limitations imposed by other crew activities. The basic component (ref. 13-3) was an f/1.0 Schmidt camera of 7.5-cm aperture (fig. 13-2). Incident light passes through the corrector plate and is focused on a potassium bromide (KBr) photocathode, maintained at -25 000 V. Photoelectrons accelerated by this electrostatic field are focused by an axial magnetic field of approximately 2.39×10^4 A/m (300 Oe) on film coated with a very thin layer of nuclear-track emulsion (Kodak NTB-3) just behind a 32-mm hole in the primary (concave spherical) mirror. Exposures were initiated by the film transport that automatically turned the takeup reel after a specified exposure time. During each exposure, the NTB-3 film was firmly pressed against the thin (7.7-nm) barrier membrane that consists of a thin plastic, coated with aluminum permeable to the 25 000-V electrons but opaque to light.

In order to select different bands of far UV light, the Schmidt camera was provided with two corrector plates, one of lithium fluoride (LiF) and one of calcium fluoride (CaF_2), either of which could be accurately seated by a small motor. To photograph spectra, another motor was provided to turn the Schmidt camera 90° to look at a reflection grating behind a photoengraved grid collimator that admitted light from a 0.25° strip of sky. The motions of film transport, corrector plates, and Schmidt camera were automatically timed by an electronic sequencer, accurate to a fraction of a second.

When the "power on" switch or "reset" switch was pressed by the astronaut, the far UV camera/spectrograph took an automated sequence of exposures in four modes designated as follows.

- ILi: Imagery through an LiF filter-corrector with a pass-band of 105 to 160 nm
- ICa: Imagery through a CaF_2 filter-corrector with a pass-band of 123 to 160 nm
- SLi: Spectra through an LiF filter-corrector with a 3-nm resolution over the pass-band of 105 to 160 nm
- SO: Spectra with no corrector, with a 4-nm resolution over the pass-band of 50 to 160 nm

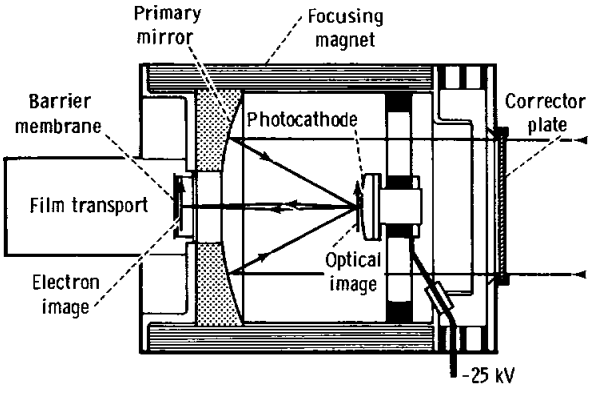


FIGURE 13-2.–Simplified cross section of the electronographic Schmidt camera.

This spectral range was limited by the mirror and grating reflectivity at the low end and by the KBr photocathode sensitivity at the long-wave end. In the imagery modes (ILi and ICa), the camera viewed the sky directly with a field diameter of more than 20° (fig. 13-3) and a resolution of approximately

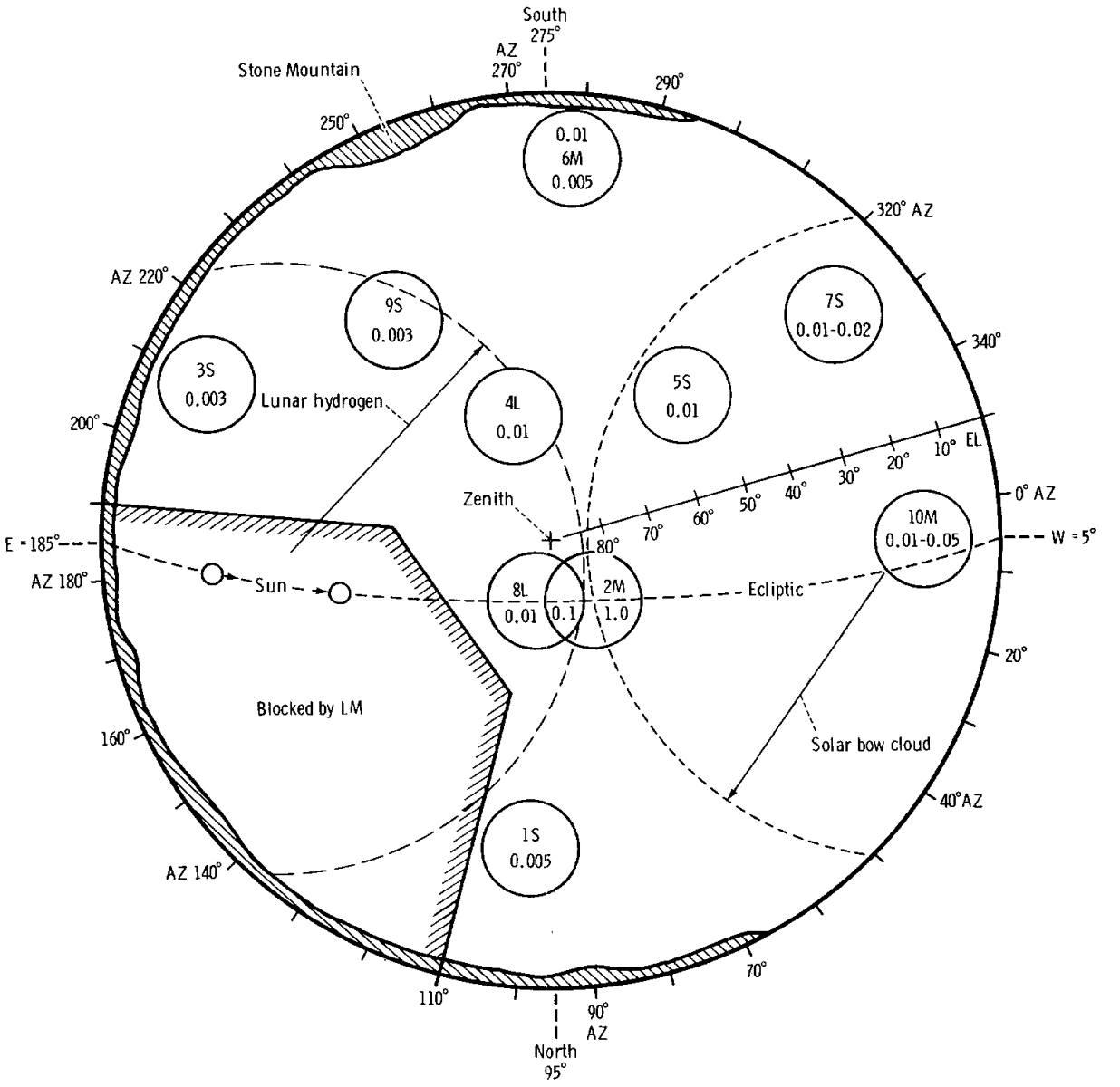


FIGURE 13-3.–Schematic representation of target pointings in the lunar sky from the Descartes site, an outside view of the celestial sphere of the camera. In each 20° circle are given the target number and a rough estimate of background Lyman-alpha surface brightness relative to the inner geocorona on target 2M. In two cases (targets 7S and 10M), there is a marked change across the field, and two ratios are given. The dashed circles show regions of predicted brightness caused by the lunar hydrogen atmosphere and the solar bow cloud.

2 arc-min. For the spectroscopic modes (SLi and SO), spectra were obtained of everything within a 20° X 0.25° strip parallel to the lunar horizon.

The image on the photocathode (fig. 13-2) was transferred to the NTB-3 film behind the primary mirror to give a mirror image of the sky field rotated

10°.5 on the film. Because of the uneven thickness of the barrier membrane, there are streaks in the instrument sensitivity – approximately ±25 percent in electron flux – inclined 50° to the horizontal, upward to the right in the lunar sky. Also, numerous small blank spots were produced by dust on the barrier membrane, and a lenticular area of lower sensitivity appears at the upper right. All these instrument sensitivity deviations, which appear on most of the illustrations in this section, will be removed in the accurate reduction of film density to absolute UV flux. A few scratches on the back of the film, produced by abrasion in the film-transport box (cassette), also affect the photometry and will be removed in the accurate reduction. The illustrations in this section were made from copy negatives and show some dust marks and scratches not on the original flight film.

EXPERIMENT GOALS

Seven scientific goals were established for this experiment, all of which were at least partly achieved.

(1) To determine composition and structure of the Earth upper atmosphere from its spectra

(2) To determine the structure of the geocorona from imagery in Lyman-alpha (121.6-nm) light, and to study day and night airglow and polar aurorae in the longer wavelengths (125 to 160 nm)

(3) To obtain direct evidence of intergalactic hydrogen in distant clusters of galaxies

(4) To obtain spectra and imagery of the solar wind and other gas clouds in the solar system

(5) To detect gases in the lunar atmosphere, including volcanic gases, if any

(6) To obtain spectra and colors of external galaxies in the far UV regions, adding to knowledge of their composition

(7) To obtain spectra and colors of stars and nebulae in the Milky Way

Preliminary results can be reported on four of these goals, most specifically on the first two (figs. 13-4 to 13-10). Less accurate results are available on goals 4 and 6; definite conclusions on goals 3, 5, and 7 must await the detailed analyses of accurate measurements of the densities of the processed flight film.

Numerous target pointings were considered. Because of the 20° field, each pointing would include several significant objects and would help to meet several experiment goals. It was necessary to verify that each target center would be at least 10° above the lunar horizon and would not be occulted by the LM at the scheduled pointing time. To allow for delays in the time line, the EL and AZ settings were computed for all possible pointing times, and six alternate settings were computed in addition to the 11 primary targets. The probable errors in settings were also considered; except for the Earth, which was centered by eye in the sighting tube, these errors were estimated at ±3°. Because the AZ bearing tended to stick, the actual pointing errors were somewhat larger. Table 13-I shows the requested right ascension (RA) and declination (dec) angles compared with the actual values measured on imagery frames.

TABLE 13-I.–Requested and Actual Angles of Right Ascension and Declination

Target	*Requested RA, deg*	*Requested dec, deg*	*Actual RA, deg*	*Actual dec, deg*	*Object*
1S	313	+37	321	+37	Cygnus Loop Nebula (at edge)
2M	318	-15	318	-15	Earth
3S	037	-05	042	-16	NGC 1068 (missed)
4L	357	-41	355	-41	Grus group of galaxies
5S	321	-53	318	-53	Pavo group
6M	081	-70	089	-74	Large Magellanic Cloud
7S	258	-62	261	-59	NGC 6300 group
8L	342	-04	344	-05	Geocorona east of Earth
9S	053	-35	056	-27	Fornax Cluster
10M	275	-23	278	-31	Milky Way center
11S	005	-36	(No film)	(No film)	NGC 134 group (also on target 4L)

To adjust to the extravehicular activity (EVA) time line, pointing times varied from 20 min during crew activities near the LM to 16 or 17 hr during the rest periods between EVA periods. Hence, the targets were designated in advance as S for short pointing times of 20 to 30 min, allowing imagery exposures only; M for medium pointing times of 4 to 5 hr, allowing both imagery and spectroscopic exposures; and L for long pointing times of 16 hr or more, allowing several 200-min spectroscopic exposures. On every target, there is redundancy because of the automatic sequence of repeated exposures. In addition to pure imagery and spectroscopic frames, short combined exposures (designated IS) were obtained during the mode changes when the camera was turned 90° from direct imagery (ILi) to look at the grating and collimator (SLi).

DESCRIPTION OF THE PROCESSED FLIGHT FILM

After each of the 11 pointings, the automatic sequence on the camera, timed by film advance, took the following exposures until the astronaut pressed the "reset" switch for another pointing.

Exposure type	*Exposure time, min*
ILi	1, 3, 10
ICa	.5, 3, 10, 30
SLi	3, 10, 30
SO	.5, 3, 10, 30
SLi	.5, 200
SO	.5, 200

There are 209 exposures on 9.727 m (383 in.) of film, plus 0.467 m (18.4 in.) of step-wedge calibration, both preflight and postflight. The background fog, produced principally by Van Allen belt protons during translunar coast, is less than 0.14 net density. The camera had used the available film at 17:41:00 G.m.t. on April 23, 3 hr 16 min before the end of EVA-3 and 48 hr after camera deployment on EVA-1. The shortage of film was due partly to the extra exposures of the Earth during EVA-1 and EVA-2 and partly to instrument design for a shorter lunar surface stay time.

For proper thermal conditions, the far UV camera had to be in the LM shadow. Because of the 16-hr delay in touchdown and the higher Sun angle, it was necessary to deploy the camera close to the LM (2 m southwest of the down-Sun footpad) during EVA-1 (fig. 13-1) and even closer during EVA-2 and EVA-3. The LM thus occulted a larger region of the eastern sky (fig. 13-3) and eliminated two of the planned targets (NGC[1] 7317 group of galaxies and Abell Clusters 2634 and 2666).

In all, there are 178 usable frames on the exposed film: 85 imagery, 68 spectra, and 25 combined (ILi and SLi) exposures. Of the 85 imagery frames, 13 are heavily overexposed by background Lyman-alpha radiation on the 10-min ILi exposures, and seven are overlapped by adjacent frames because of inadequate film advance. Four of the combined frames are also overlapped. The distribution among the 10 targets is shown in table 13-II. (The regions covered are each 20° circles in the sky.)

EARTH ATMOSPHERE PHOTOGRAPHY

Because the Earth is so bright in the lunar sky, special arrangements were made in advance for the commander to take short ILi exposures by interrupting the normal exposure sequence at specified times. Unfortunately, when these interruptions were made, the film was not advanced properly, so that adjacent frames overlap by approximately 30 percent. Figures 13-4, 13-5, and 13-6 are the 1-, 15-, and 60-sec ILi exposures, respectively (105 to 160 nm). These figures show the airglow of the sunlit atmosphere, the polar auroral zones, and the inner geocorona (ref. 13-4). For all three figures, the original film shows more detail in the polar aurora. The dark limb of the Earth is silhouetted against the far-side geocorona, and the day airglow shows strong limb brightening, evidence that it came from a thin layer of excited air molecules.

Figure 13-7 is a 10-min ICa exposure (125 to 160 nm, excluding the Lyman-alpha line) that records primarily atomic oxygen lines at 130.5 and 135.5 nm and molecular nitrogen bands (table 13-III). The two equatorial airglow bands appear to be symmetrical on

[1]NGC = New General Catalogue of Nebulae and Clusters of Stars by J. L. E. Dreyer, published in 1888.

TABLE 13-II.–Regions Covered by the Far UV Camera/Spectrograph

Target	*Constellation*	*Duration, hr:min*	*Frames*	*Objects*
1S	Cygnus (southeast portion)	00:33.5	3 ILi, 4 ICa, 1 IS	North America nebulae, Loop Nebula, 3 planetary nebulae, 60 stars
2M	Aquarius (with Earth)	04:50	7 ILi,[a] 4 ICa, 8 IS, 5 SLi, 4 SO	Earth aurorae, geocorona, 1 planetary nebula, 55 stars
3S	Cetus-Eridanus	00:38	3 ILi, 4 ICa	3 galaxy groups, 20 stars
4L	Grus-Phoenix-Sculptor	16:55.5	6 ILi, 8 ICa, 4 IS, 10 SLi, 12 SO	3 galaxy groups, 20 stars
5S	Indus-Pavo	00:20	3 ILi, 3 ICa, 2 IS	1 galaxy group, 15 stars
6M	Mensa-Volans	06:03	3 ILi, 4 ICa, 2 IS, 5 SLi, 6 SO	LMC, 4 galaxies, 70 stars
7S	Ara-Pavo	00:22	3 ILi, 3 ICa, 1 IS	N6300 galaxy group, 6 globular clusters, 100 stars
8L	Aquarius-Pisces-Pegasus	15:52	6 ILi, 8 ICa, 4 IS, 10 SLi, 12 SO	Geocorona up-Sun, Pegasus Cluster and 10 galaxies, 32 stars
9S	Fornax-Eridanus	00:20.5	3 ILi, 3 ICa, 1 IS	Fornax Cluster, Eridanus group of galaxies, 29 stars
10M	Sagittarius	01:44	3 ILi, 4 ICa, 2 IS, 3 SLi, 1 SO	Milky Way center, many nebulae and globular clusters, 150 stars, Jupiter

[a]Three of the ILi frames of the Earth have exposures of 1, 5, and 15 sec, and all seven ILi frames are overlapped.

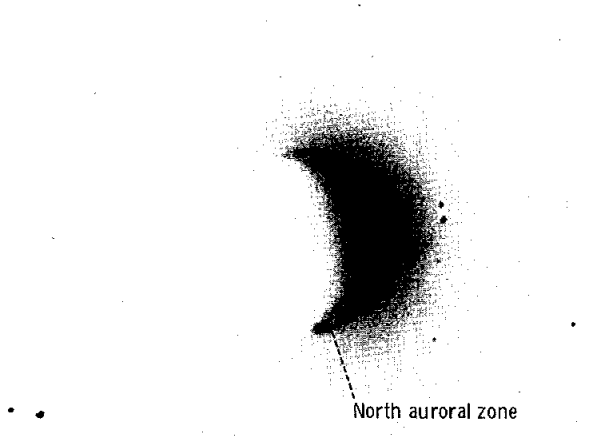


FIGURE 13-4.–Central portion of frame 37, the Earth, target 2M, 1-sec ILi exposure, a positive enlargement showing in particular the day airglow of the sunlit atmosphere. The view is as seen in the lunar sky, the top toward the zenith of Descartes, the Sun to the right. The South Pole of the Earth is at the upper left, the North Pole at the lower right.

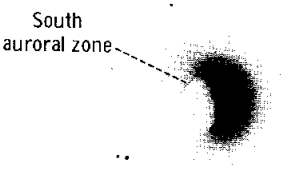


FIGURE 13-5.–Frame 30, the Earth, target 2M, 15-sec ILi exposure, showing in particular the Lyman-alpha inner geocorona. (This negative print, AS16-123-19642, shows the full 20° field, as do all the following photographs, except fig. 13-21.)

TABLE 13-III.–Tentative Spectral Identification

Emission line no.	*Element*	*Energy-state transition*	*Measured wavelength (approximate), nm*	*Laboratory wavelength, nm*
1	He	$2p\ ^1P^o - 1s^2\ ^1S$	58.4	58.43
2	Ne?	$3s(1\text{-}1/2)^o - 2p^6\ ^1S$	74.0	74.37
		$3s^1\ (1/2)^o - 2p^6\ ^1S$		73.59
3	O^+	$2p^4\ ^4P - 2p^3\ ^4S^o$	83.5	83.45 83.33 83.28
4	N_2	$b^1\pi_u - X^1\Sigma_g^+$ (0,0) (0,1)	99.0	98.57 100.86
	O	$3s^1\ ^3D^o - 2p^4\ ^3P$		98.88 99.02 99.08
5	H	$3p\ ^2P^o - 1s\ ^2S$	103.0	102.57
	O	$3d\ ^3D^o - 2p^4\ ^3P$		102.58 102.74 102.82
	N_2	$b^1\pi_u - X^1\Sigma_g^+$ (0,2)		103.26
6	N_2	$b^1\pi_u - X^1\Sigma_g^+$ (0,4)	108.5	108.31
	N^+	$2p^3\ ^3D^o - 2p^2\ ^3P$		108.57 108.46 108.40 108.55 108.46
7	N	$2p^4\ ^4P - 2p^3\ ^4S^o$	113.5	113.50 113.44 113.42
8	O	$3s^1\ ^1D^o - 2p^4\ ^1D$	115.0	115.21
9	H	$2p\ ^2P^o - 1s\ ^2S$	[a]121.6	121.67
10	O	$3s\ ^3S^o - 2p^4\ ^3P$	130.5	130.22 130.49 130.60
11	O	$3s^5\ S^o - 2p^4\ ^3P$	135.5	135.56 135.85
	N_2	$a^1\pi_g - X^1\Sigma_g^+$ (6,2) (3,0)		135.30 135.37
12	N	$3s^2\ ^2P - 2p^3\ ^2D^o$	150.0	149.26 149.47
	N_2	$a^1\pi_g - X^1\Sigma_g^+$ (3,3) (0,1) (4,4)		149.32 150.68 150.81

[a]By comparison with laboratory spectra taken with the instrument during preflight calibrations.

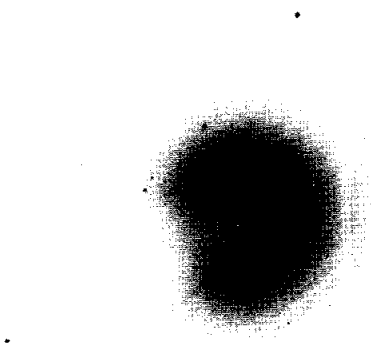


FIGURE 13-6.–Frame 40, the Earth, target 2M, 60-sec ILi exposure, showing in particular the Lyman-alpha geocorona (overlapped by frame 39 on the right). The streaks are caused by the barrier membrane (AS16-123-19652).

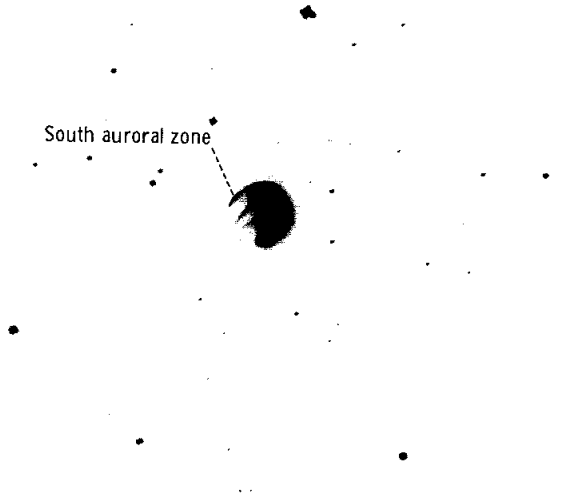


FIGURE 13-7.–Frame 45, the Earth, target 2M, 10-min ICa exposure, showing the overexposed polar aurora and two equatorial airglow belts (AS16-123-19657).

either side of the magnetic-dip equator at the Earth terminator, which was over western Africa at 7° N 17° W (at 18:51:00 G.m.t. on April 21). Farther east, as shown in figure 13-8, the bands appear to cross at 12° N 65° E, near the antisolar point. A general night-side airglow is also visible in figure 13-7 and another ICa exposure not included in this section (30-min ICa exposure).

Figures 13-9 and 13-10 show somewhat overexposed spectra with the slit approximately 34° to the Sun line. Spectra from shorter exposure times show somewhat more detail of the hydrogen Lyman-alpha line, which strengthens sharply at both limbs of the Earth, where the geocorona beyond the Earth adds to that from the near side. The two lines below the Lyman-alpha line are oxygen lines at 130.5 and 135.5 nm, which are limited to the sunlit hemisphere. These and other identified lines are listed in table 13-III. Although the helium line has been detected with broadband photometers on several rocket flights, it is believed that figure 13-10 shows the first astronomical spectrum on which the helium line at 58.4 nm, the ionized oxygen (0^+) line at 83.4 nm, and the Lyman-beta line of hydrogen at 102.6 nm have been identified. (The helium line also

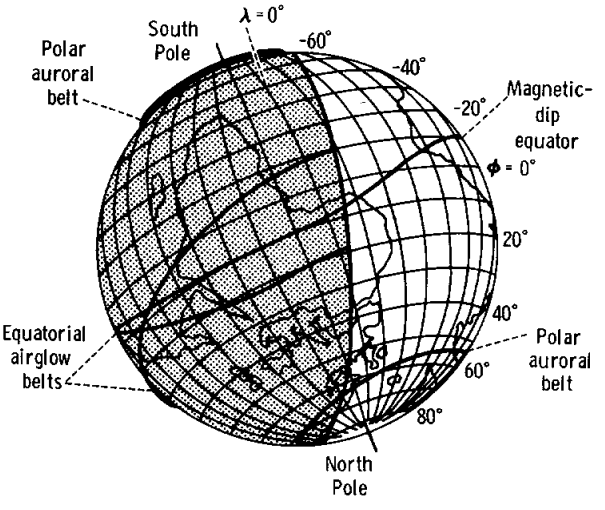


FIGURE 13-8.–Diagram of the Earth as seen from Descartes at 18:51 G.m.t. on April 21, showing polar auroral belts, magnetic-dip equator, and equatorial airglow belts. The South Pole is at the top because the Earth was north of the Descartes zenith.

appears in figure 13-11.) The extent of each line gives some indication of the scale height for each species in the atmosphere and geocorona of the Earth, helium

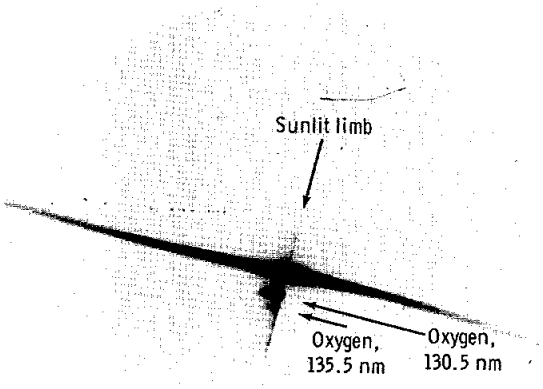


FIGURE 13-9.–Frame 50, the Earth, target 2M, 30-min SLi exposure (AS16-123-19662), showing a strong Lyman-alpha line and a spectrum of sunlit atmosphere (longer wavelengths toward the bottom).

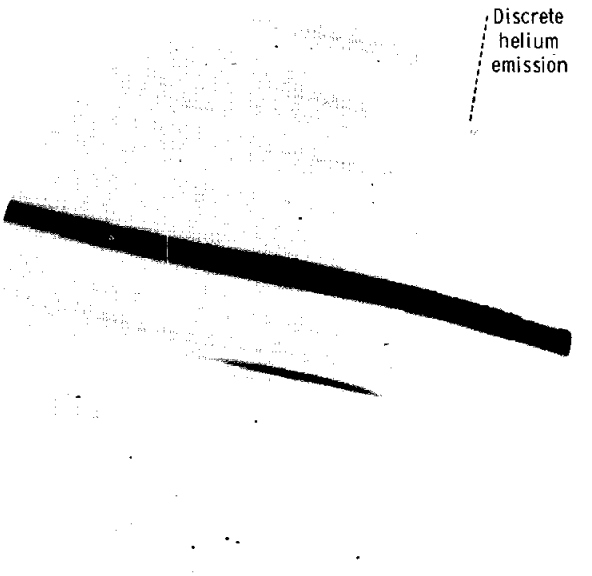


FIGURE 13-11.–Frame 86, Grus-Phoenix-Sculptor, target 4L, 200-min SO exposure, showing an overexposed Lyman-alpha line, numerous ghosts, and helium emission at 58.4 nm from the solar wind and an unidentified discrete source on the right (AS16-123-19698).

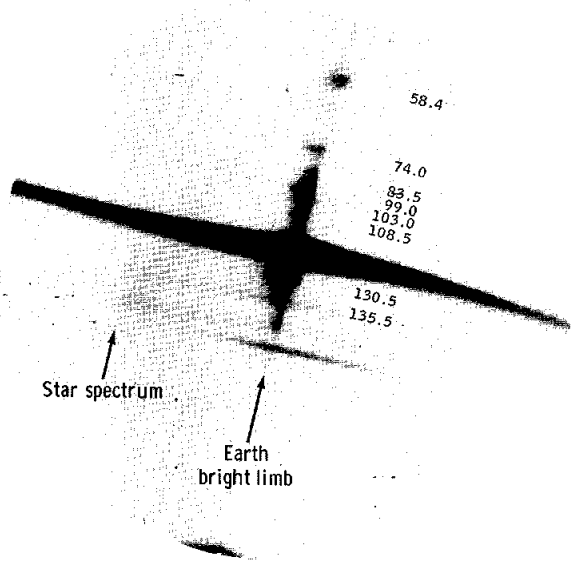


FIGURE 13-10.–Frame 54, the Earth, target 2M, 30-min SO exposure, showing an overexposed Lyman-alpha line and a spectrum of sunlit atmosphere to helium at 58.4 nm near the top. Wavelengths in nanometers of lines identified in table 13-III are listed on the right. The faint star spectrum is 5° to the left (AS16-123-19666).

being intermediate between hydrogen and oxygen as would be expected. Estimated line strengths support the tentative identifications of neon at 74.0 nm and ionized nitrogen (N^+) at 108.5 nm. Another frame (131-min SLi exposure) shows the oxygen lines at 130.5 and 135.5 nm in the night hemisphere, where they are of about equal intensity, supporting the oxygen recombination mechanism of equatorial airglow (refs. 13-5 to 13-8). The geographic distribution of this airglow was first measured by Hicks and Chubb (ref. 13-9) and was most recently discussed by Tinsley et al. (ref. 13-10).

STAR AND DIFFUSE BACKGROUND PHOTOGRAPHY

From visual inspection of copy negatives and photographs such as figures 13-12 to 13-14, several dozen stars have been identified. These are not the faintest star images recorded, but the limiting magnitude for B stars on 1-min ILi or 3-min ICa photographs is at least 9.0 mag. For Be (emission-line) stars in the LMC, the limiting

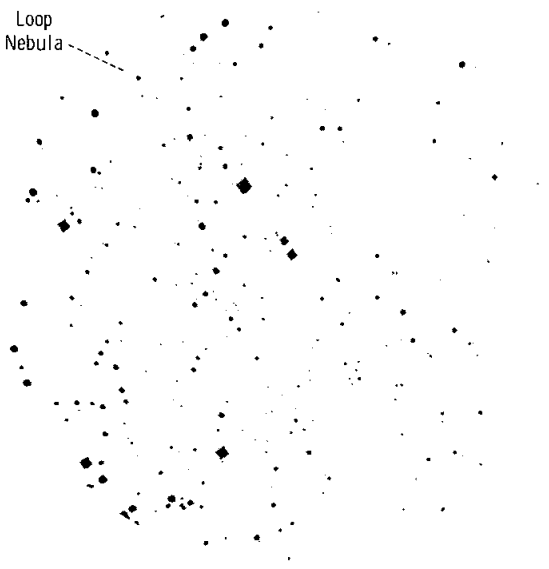


FIGURE 13-12.–Frame 27, Cygnus, target 1S, 10-min ICa exposure, showing a portion of Loop Nebula on the upper left (AS16-123-19639).

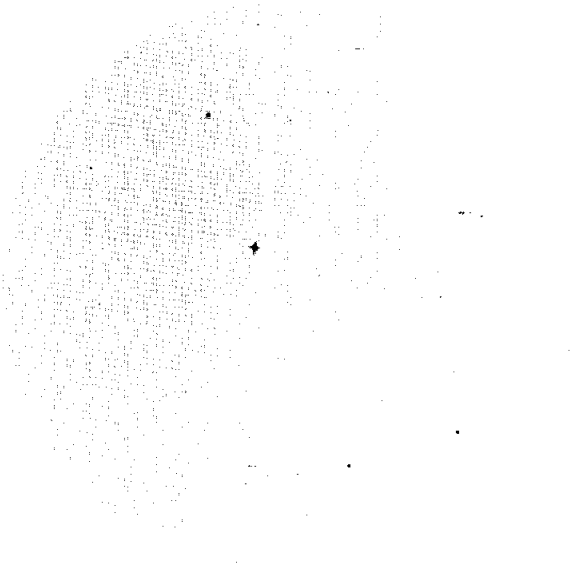


FIGURE 13-13.–Frame 58, Cetus-Eridanus, target 3S, 1-min ILi exposure, showing a low Lyman-alpha background near the eastern horizon of Descartes (AS16-123-19670).

magnitude is at least 11 mag. However, the image of Jupiter (-1.9 mag. at the time the photograph was taken) was too faint to show at its predicted position in figure 13-15, approximately 6° right of center.

The Lyman-alpha background was recorded on twelve 1-min ILi frames that covered approximately 3200 square degrees of the lunar sky with the hemisphere centered on the Descartes zenith at an RA of approximately 22^h40^m, dec -19° as shown in figure 13-3. The background had a maximum strength near the Earth in the geocorona of approximately 3×10^{14} photons/sec-m^2 (30 000 R). In the western third of the sky, the background was only approximately 0.01 of that maximum strength but increased near the western horizon. The background was even fainter at low elevations in the north (target 1S) and the south (target 6M) and was down to approximately 1×10^{12} photons/sec-m^2 (100 R) in the southeast (target 9S) and the east (target 3S), where a small contribution by the lunar hydrogen atmosphere has been predicted (ref. 13-11) with 5×10^{11} photons/sec^2 (50 R) contour shown on the left of figure 13-3. Although the increase near the western and southern horizons is unexpected, the broad area high in the western sky is probably the solar bow cloud, predicted to be at approximately

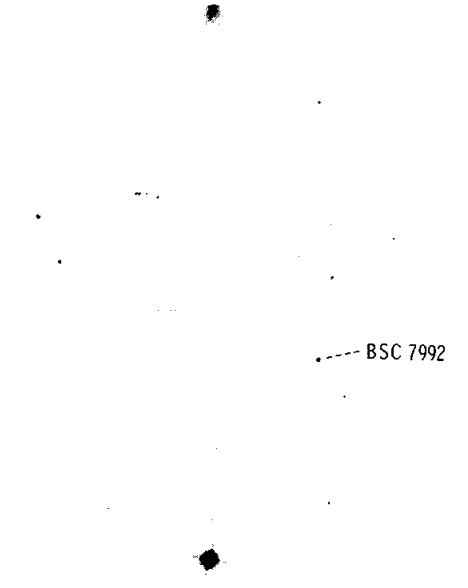


FIGURE 13-14.–Frame 121, Indus-Pavo, target 5S, 3-min ICa exposure (AS16-123-19733), showing Alpha Grus (B5, 1.5 mag.) at the top and Alpha Pavo (B3, 1.9 mag.) near the bottom. The star below the center and slightly to the right is a 6.5-mag. B star (no. 7992 in the Bright Star Catalogue).

RA 18^h20^m, dec -25° on April 22, with 1 X 10^{12} photons/sec-m^2 (100 R) contour shown on the right of figure 13-3.[2]

To measure these background brightnesses quantitatively, each frame of the original flight film has been accurately scanned with a vidicon-type image digitizer (ref. 13-12) that recorded 8-bit digitized film transmittance on magnetic tape (256 gray levels between density 0 and 3) on a 1024 X 1024 raster. The tapes are being analyzed on a large computer at the Manned Spacecraft Center (MSC).

Calibration exposures will provide curves of film response compared to incident flux at several wavelengths between 50 and 160 nm. After corrections for distortion and deviations from mean instrument sensitivity, the computer will read out all star positions for each imagery frame in celestial coordinates (1950 equinox), together with far UV flux from each star in two wavelength bands (105 to 160 nm and 125 to 160 nm), accurate to approximately ±20 percent in absolute values and ±2 percent in relative values. Extended objects and background surface brightnesses will likewise be contoured for each frame. Lyman-alpha background from various sources can then be classified as caused by geocorona, solar bow cloud, solar wind, lunar atmosphere, et cetera.

On spectroscopic frames, 12 emission lines have been identified between 58.4 and 150.8 nm, as shown in table 13-III, mainly in spectra of the Earth atmosphere (figs. 13-9 and 13-10). Several ghosts of the overexposed Lyman-alpha line appear in these spectra. Although more were expected, only five or six spectra of discrete objects (figs. 13-10, 13-11, 13-16, 13-17, and 13-18) have been found to date on these spectral frames. Figure 13-11 appears to show the line of helium at 58.4 nm in the solar wind. The accurate density scans of the original film may reveal fainter spectra of other discrete objects (stars, clusters, galaxies) that happened to fall in the 20° X 0.25° slit. After correction for deviations from mean instrument sensitivity, the MSC computer will provide the flux distribution in each discrete spectrum, the relative intensities of background emission lines, and variations in line intensity with position across the 20° field.

[2]Page, Thornton: Solar Lyman-Alpha Ionization Front. Naval Research Laboratory ESD Memo, Apr. 3, 1970.

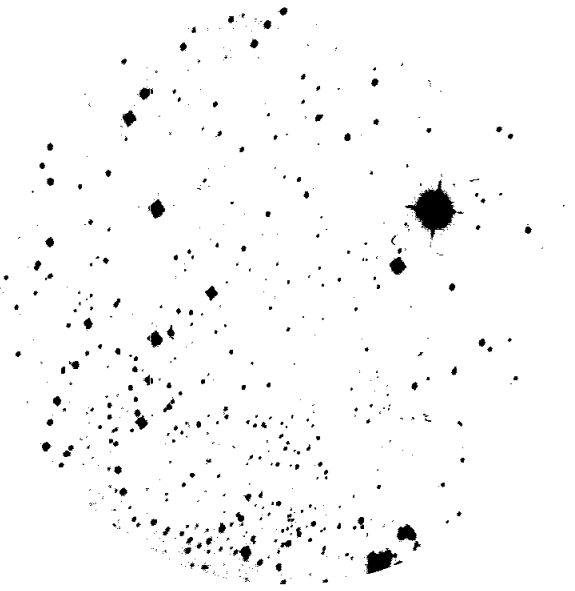


FIGURE 13-15.–Frame 203, Sagittarius, target 10M, 10-min ICa exposure, showing a star field rich in blue stars near σ Sagittarius (B2, 2.1 mag., strongest image). The star to the left and below is φ Sagittarii (B8, 3.2 mag.), whose spectrum appears in figure 13-16. Jupiter is too faint to show at its predicted position, approximately 6° right of center (AS16-123-19815).

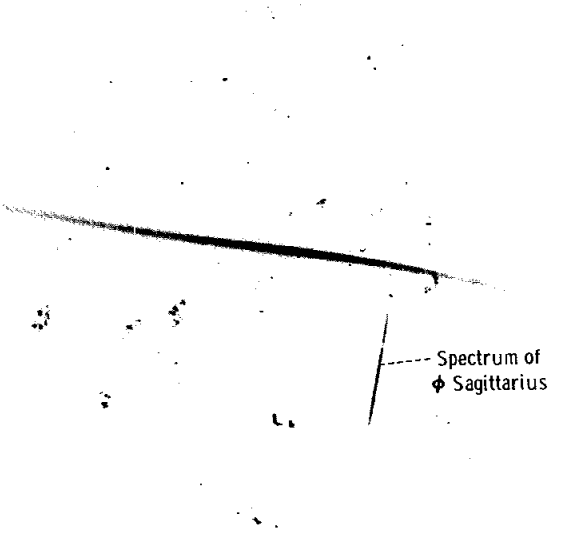


FIGURE 13-16.–Frame 208, Sagittarius, target 10M, 30-min SLi exposure, showing a Lyman-alpha line of medium strength, and the spectrum of φ Sagittarius with very broad Lyman-alpha absorption (to 138.2 nm) and a line at approximately 150 nm (AS16-123-19820).

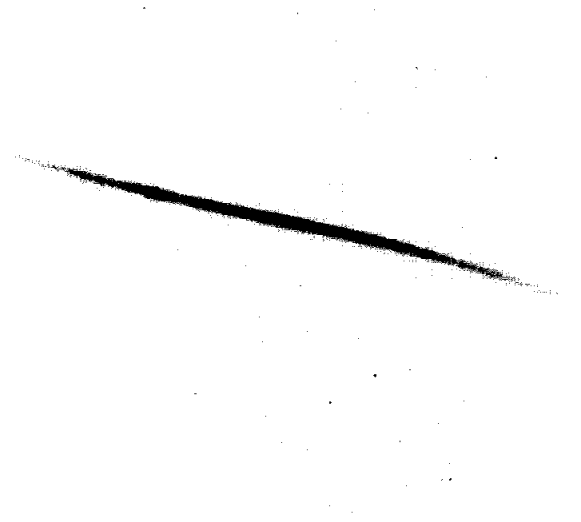


FIGURE 13-17.–Frame 138, Mensa-Volans, target 6M, 30-min SO exposure, showing the Lyman-alpha line and, at left, the spectra of three blue star clusters in the LMC (AS16-123-19750).

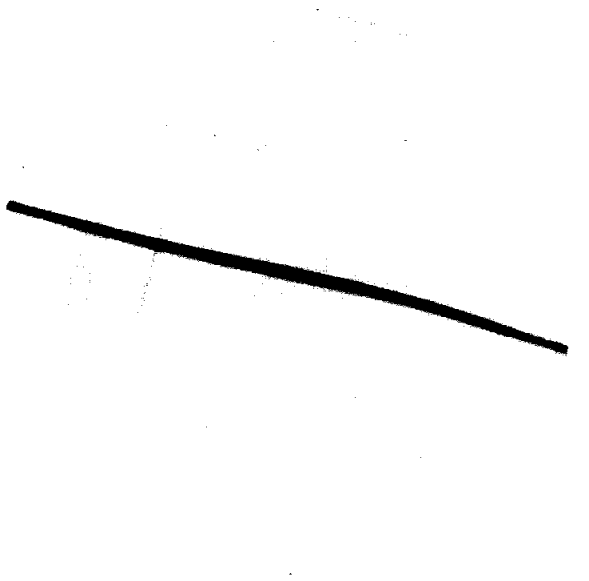


FIGURE 13-18.–Frame 140, Mensa-Volans, target 6M, 200-min SLi exposure, showing an overexposed Lyman-alpha line and ghost lines, at left, and spectra of three or more blue star clusters in the LMC.

LARGE MAGELLANIC CLOUD PHOTOGRAPHY

Figure 13-19 shows the LMC, approximately 70 foreground stars, and foreground Lyman-alpha emission increasing toward the horizon. Hydrogen clouds in the LMC were not expected to show on ILi exposures because the local (near solar-system) hydrogen would absorb Lyman-alpha emission from the LMC, which has a 250-km/sec radial velocity and a Doppler shift of only 0.1 nm. Hence, it is not surprising that figure 13-20 in 125- to 160-nm light (ICa exposure, Lyman-alpha line excluded) reveals a very similar structure with, if anything, more cloudy structures like interstellar gas clouds. Of course, both photographs record only the hot O, B, and A stars. Some small differences may exist in star brightnesses, indicating far UV color differences. For instance, S Doradus, which has a peculiar emission-line spectrum, seems stronger relative to its surroundings in figure 13-19 than in figure 13-20. In both these figures, the top is toward the Descartes zenith, and the direction to the north celestial pole is approximately 95° to the left.

Figure 13-18 (200-min SLi exposure) shows spectra of two or more bright groups of star clusters and nebulae along the lower edge of the LMC, as oriented in figures 13-19 and 13-20. The slit is in position angle of 10°, inclined about 70° to the LMC bar. The right-hand group is near the emission nebula N59 in Henize's list (ref. 13-13) at RA 5^h35^m, dec -67°.4. The left-hand group is near N157 at RA 5^h37^m, dec -69°.1. At a 3-nm resolution, figure 13-18 shows no wide Lyman-alpha absorption line in these cluster spectra, in marked contrast to the spectrum of the B8 star ϕ Sagittarii in figure 13-16. In fact, the LMC cluster spectra show remarkably uniform flux distributions over the full range of far UV sensitivity, 105 to 160 nm in figure 13-18. On the lower resolution 30-min SO exposure in figure 13-17, the spectra extend from approximately 91 to 160 nm without strong absorption lines.

Figure 13-21 illustrates the relation of early-type LMC stars on frame 129 (10-min ICa exposure, on the right) by comparison with a ground-based (Lick Observatory) photograph in photovisual light on the left. North is at the top and east to the left. The LMC star clouds approximately 2° north of the bar are very much more luminous in the far UV wavelengths, and de Vaucouleurs' counterclockwise spiral arm

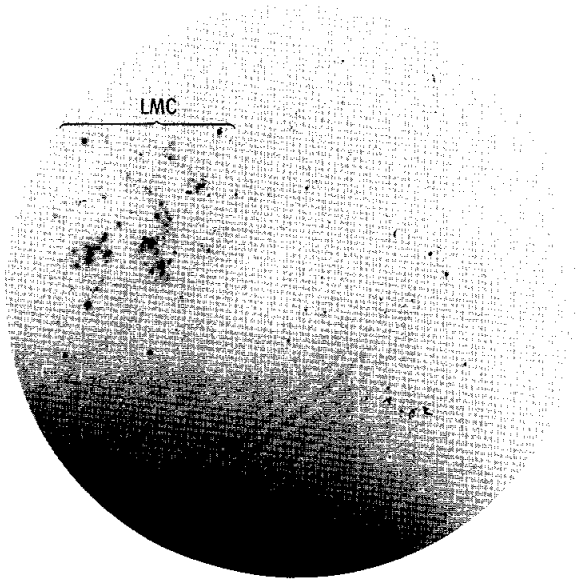


FIGURE 13-19.–Frame 124, Mensa-Volans, target 6M, 1-min ILi exposure, showing the LMC at the upper left and increasing Lyman-alpha background toward the lunar horizon at the bottom (AS16-123-19736).

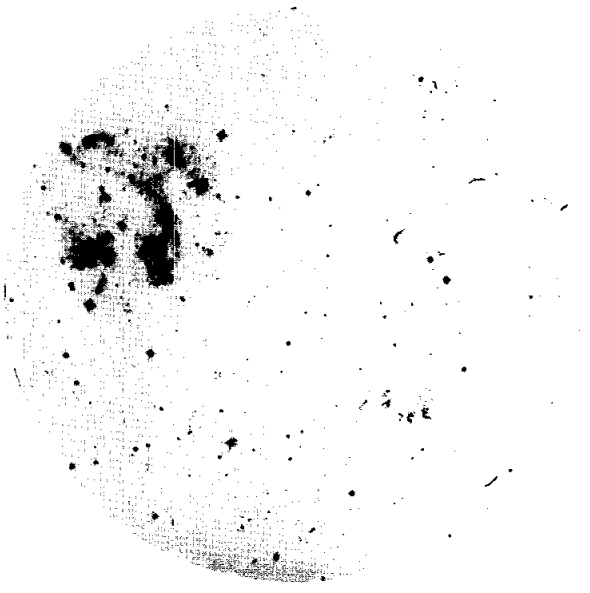


FIGURE 13-20.–Frame 129, Mensa-Volans, target 6M, 10-min ICa exposure, showing the LMC at the upper left (AS16-123-19741).

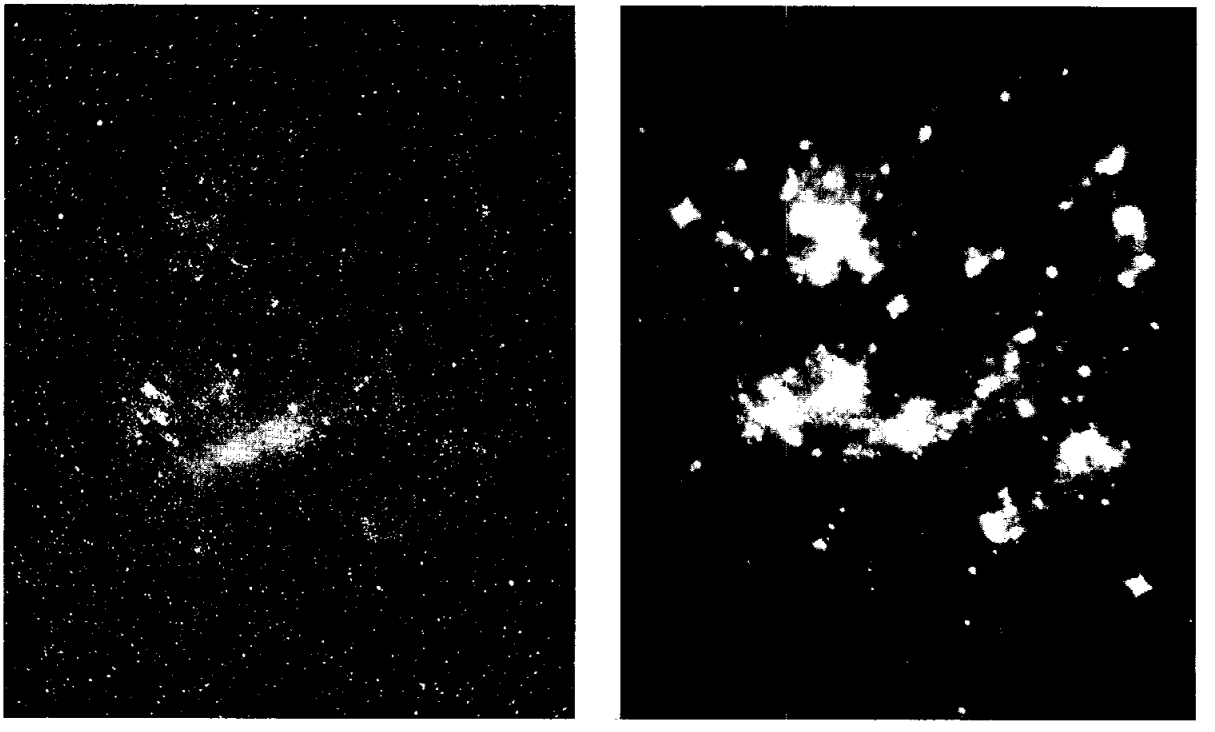


FIGURE 13-21.–The right-hand photograph is a portion of frame 129, enlarged, and the left-hand photograph was taken by Lick Observatory at the same scale. North is at the top, east to the left (rotated 98° clockwise from the Descartes view shown in figures 13-19 and 13-20).

(ref. 13-14) toward the northwest seems to reverse itself down to the star clouds southwest of the bar. The 2-arc-min resolution of the far UV camera gives the impression of emission nebulosity in the six major LMC star clouds (Shapley's constellations) but the evidence, as Karl Henize points out, is just the opposite. The northeastern crescent-shaped constellation centered on N55 in Henize's list (ref. 13-13) (at RA 5^h32^m, dec -66°.4) shows little or no Balmer (atomic hydrogen) emission on ground-based photographs, yet shows very high far UV luminosity in figures 13-19 to 13-21.

SUMMARY OF PRELIMINARY RESULTS

The far UV camera/spectrograph obtained imagery and spectra in the 58- to 160-nm wavelength range in 10 different regions of the sky, each approximately 20° in diameter. The most extensive results to date have come from visual inspection of copy negatives and prints of frames showing the geocorona and the Earth upper atmosphere on both sunlit and dark hemispheres. In addition to day airglow and polar auroral zones, two equatorial airglow belts are shown inclined approximately 15° to the magnetic-dip equator. The geocorona is roughly spherical and extends more than 15 Earth radii up-Sun. Twelve emission lines have been identified in the spectra, including helium at 58.4 nm, ionized oxygen at 83.4 nm, and hydrogen at 102.6 nm, which had not been previously observed. The helium line also appears in spectra of the solar wind and of an unidentified region in the constellation Grus.

Over 550 star images appear on the imagery frames. Quantitative analyses of density scans will yield accurate celestial coordinates and a far UV flux for each such star, some of which are nebulae and galaxies. Parts of the Cygnus Loop and North America nebulae are already identified. The accurate scan analyses will also refine preliminary estimates of Lyman-alpha background showing the solar wind, the solar bow cloud, and probably lunar atmospheric hydrogen.

Far UV imagery of the LMC, the nearest of external galaxies, gives no evidence of Lyman-alpha emission but does provide a very graphic mapping of the hot blue stars, thus allowing the detection of new associations (regions of star formation) in that galaxy.

The identification of diffuse background emissions and the search for faint intergalactic hydrogen emission in clusters of galaxies will require at least 6 months of data analyses on the 178 frames of flight film.

REFERENCES

13-1. Code, Arthur, D.; and Savage, Blair D.: Orbiting Astronomical Observatory: Review of Scientific Results. Science, vol. 177, no. 4045, July 21, 1972, pp. 213-221.

13-2. Davis, Robert J.: The Celescope Catalog of Ultraviolet Observations. The Scientific Results From the Orbiting Astronomical Observatory (OAO-2), Aurthur D. Code, ed. NASA SP-310, 1972, pp. 321-345.

13-3. Carruthers, George R.: Electronic Imaging Devices in Astronomy. Astrophys. and Space Sci., vol. 14, 1971, pp. 332-377.

13-4. Carruthers, George R.; and Page, Thornton: Apollo 16 Far-Ultraviolet Camera/Spectrograph: Earth Observations. Science, vol. 177, no. 4051, Sept. 1, 1972, pp. 788-791.

13-5. Hanson, W. B.: Radiative Recombination of Atomic Oxygen Ions in the Nighttime F Region. J. Geophys. Res., vol. 74, no. 14, July 1, 1969, pp. 3720-3722.

13-6. Hanson, W. B.: A Comparison of the Oxygen Ion-Ion Neutralization and Radiative Recombination Mechanisms for Producing the Ultraviolet Nightglow. J. Geophys. Res., vol. 75, no. 22, Aug. 1, 1970, pp. 4343-4346.

13-7. Knudsen, William C.: Tropical Ultraviolet Nightglow From Oxygen Ion-Ion Neutralization. J. Geophys. Res., vol. 75, no. 19, July 1, 1970, pp. 3862-3866.

13-8. Olson, Ronald E.; Peterson, James R.; and Moseley, John: Oxygen Ion-Ion Neutralization Reaction as Related to Tropical Ultraviolet Nightglow. J. Geophys. Res., vol. 76, no. 10, Apr. 1, 1971, pp. 2516-2519.

13-9. Hicks, G. T.; and Chubb, T. A.: Equatorial Aurora/Airglow in the Far Ultraviolet. J. Geophys. Res., vol. 75, no. 31, Nov. 1, 1970, pp. 6233-6248.

13-10. Tinsley, Brian A.; Christensen, Andrew B.; Gouveira, Hermano: Comparison of OI7774 and Ionosonde Data From Brazil and the Excitation of TROPLES. Trans. Am. Geophys. Union, vol. 53, no. 7, July 1972, p. 730.

13-11. Gott, J. Richard, III; and Potter, A. E., Jr.: Lunar Atomic Hydrogen and Its Possible Detection by Scattered Lyman-α Radiation. Icarus, vol. 13, 1970, pp. 202-206.

13-12. Anon.: Digital Image Data Systems, Short Form Catalog. DICOMED Corp. (Minneapolis, Minn.), Mar. 1972.

13-13. Henize, Karl G.: Catalogues of H-Alpha Emission Stars and Nebulae in Magellanic Clouds. Astrophys. J. Supp. No. 22, vol. II, Sept. 1956, pp. 315-364.

13-14. De Vaucouleurs, G.: Magellanic Clouds and the Galaxy II. The Observatory, vol. 74, 1954, pp. 158-164.

14. Solar Wind Composition Experiment

J. Geiss,[a†] F. Buehler,[a] H. Cerutti,[a] P. Eberhardt,[a] and Ch. Filleux[a]

INTRODUCTION

The solar wind composition (SWC) experiment was designed to measure the abundances and isotopic compositions of noble gases in the solar wind. Instruments flown on unmanned spacecraft have observed the helium/hydrogen (He/H) ratio in the solar wind and have shown that its composition is variable (refs. 14-1 to 14-5). Consequently, the SWC experiment has been conducted on all Apollo missions to date to determine the variability of the relative abundances of isotopes and ions having large differences in their masses and charges. Time variations in the solar wind composition give direct evidence of the changing conditions and processes in the solar wind source region, that is, the corona of the Sun (refs. 14-6 to 14-8). These variations demonstrate that solar wind material is being fractionated with respect to solar surface material, but the degree of fractionation and the physical processes involved are unknown. In particular, whether the longtime average of solar wind abundances is equal to the abundances in the outer convective zone of the Sun is not known; however, this is unlikely. The average He/H ratio derived from a large sample of celestial bodies is 0.1 (ref. 14-9), and this value is generally assumed to correspond to the abundance ratio in the outer convective zone of the Sun. However, the average He/H ratio in the solar wind is only about 0.04 (refs. 14-1 to 14-5), indicating that a systematic depression of the helium abundance relative to hydrogen occurs in the solar wind (refs. 14-10 and 14-8). Thus, to derive abundances for the outer convective zone of the Sun from average solar wind abundances, the comprehension of these fractionation processes is necessary. This comprehension can best be achieved by measuring changes in the abundance of a variety of solar wind ions and relating these measurements to changes of conditions in the solar wind and at the solar surface.

In contrast to many other elements, the abundances of noble gases in the Sun are very poorly known from optical observations; however, a comparison of noble gas abundances in the Sun with those in planetary reservoirs is of particular importance for studying the separation processes occurring at the time of planet formation because the abundances of this group of elements are not affected by geochemical processes. Thus, a comparison of relative abundances of noble gases and their isotopic composition in the major planets or in the atmospheres of the small planets with those in the Sun would give unique information concerning the origin and development of planets. Therefore, precise determinations of elemental and isotopic noble gas abundances in the Sun will attain particular importance when the corresponding abundance data become available for the atmospheres of Venus, Mars, or the major planets.

With the exception of ^{3}He, the abundances of noble gases in the outer convective zone of the Sun cannot have been modified by nuclear reactions; therefore, they should be representative of the abundances in the solar nebula. The ^{3}He has been augmented in the outer convective zone by the burning of deuterium (D) (ref. 14-11); consequently, the solar surface abundance of ^{3}He is essentially the sum of the deuterium and ^{3}He abundances in the solar nebula. On the basis of this argument, the D/H ratio in the solar nebula derived from the ^{3}He abundance in the solar wind (refs. 14-12 and 14-13) was found to be much smaller than that found in sea water or carbonaceous meteorites. The high D/H ratios in the planetary reservoirs can be explained by chemical fractionation during the time of planetary condensation and accretion (ref. 14-12). To gain a quantitative understanding of the deuterium enrichment process, the present ^{3}He abundance in the outer convective zone of the Sun must be determined with the greatest precision.

The Apollo 11, 12, 14, and 15 SWC experiments have determined the relative abundances of helium, neon, and argon in the solar wind and have yielded very accurate data on the isotopic composition of

[a]Physikalisches Institut, University of Bern.

[†]Principal Investigator.

helium and neon (refs. 14-14 to 14-16). Not only elemental abundances but also the isotopic ratio $^3He/^4He$ undergo variations with time. The Apollo 16 SWC experiment is a continuation of the earlier experiments; however, an essential change was introduced in the solar wind particle collection technique. Platinum surfaces were incorporated in the collector foil, and use was made of a layer technique for distinguishing particles of different energies and different directions of arrival. The improvements and the expanded scope of the Apollo 16 experiment, relative to the earlier SWC experiments, can be summarized as follows: elimination of possible residual dust contamination by treating the platinum foil sections with dilute hydrofluoric acid before analysis; increased accuracy of solar wind argon abundance; determination of solar wind albedo; search for helium in the energy range above approximately 40 keV/nucleon; and search for lunar ionospheric neon accelerated by electrical and magnetic field vectors, that is, **E X B** drift.

PRINCIPLE OF THE EXPERIMENT

A metal foil 30 cm wide and approximately 140 cm long was exposed to the solar wind on the lunar surface by the Apollo 16 crewmen on April 21, 1972, at 23:01 G.m.t. The foil was positioned perpendicular to the solar rays in the azimuth direction (fig. 14-1), exposed for 45 hr 5 min, and returned to Earth.

Laboratory calibrations have determined that solar wind ions arriving with an energy of the order of 1 keV/nucleon penetrate approximately 10^{-5} cm into the foil (ref. 14-17), and a large and reproducible fraction is firmly trapped (refs. 14-18 to 14-21). In the laboratory, the returned foil is analyzed for implanted solar wind noble gas atoms. Parts of the foil are melted in ultra-high-vacuum systems, and the noble gas atoms of solar wind origin thus released are analyzed with mass spectrometers for elemental abundance and isotopic composition.

Many details of the principle and procedures of this experiment have been discussed elsewhere (refs. 14-14 to 14-16 and 14-22 to 14-25). Those properties of the capturing foil and the resulting features of the experiment that apply specifically to the Apollo 16 SWC experiment are discussed in this section. The general makeup of the foil is shown in figure 14-2.

The sections labeled 1 are composed of 15-μm aluminum having an oxide layer of 0.7 μm on the back side. The material in these foil sections is similar to the foil material flown on the earlier Apollo flights.

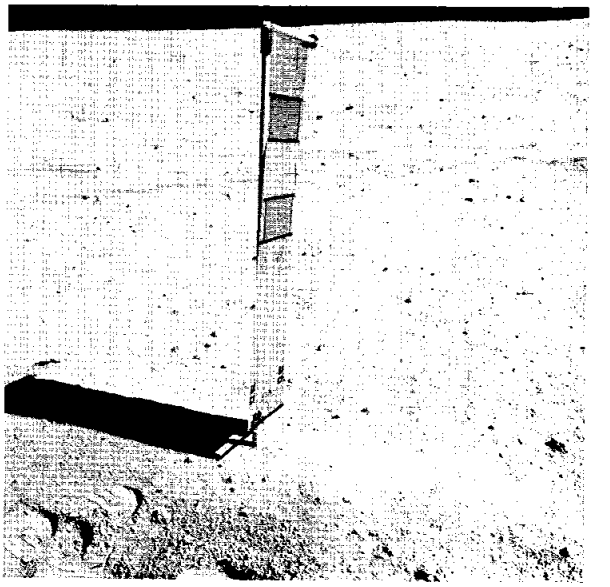


FIGURE 14-1.–Apollo 16 SWC experiment deployed on the lunar surface (AS16-117-18849).

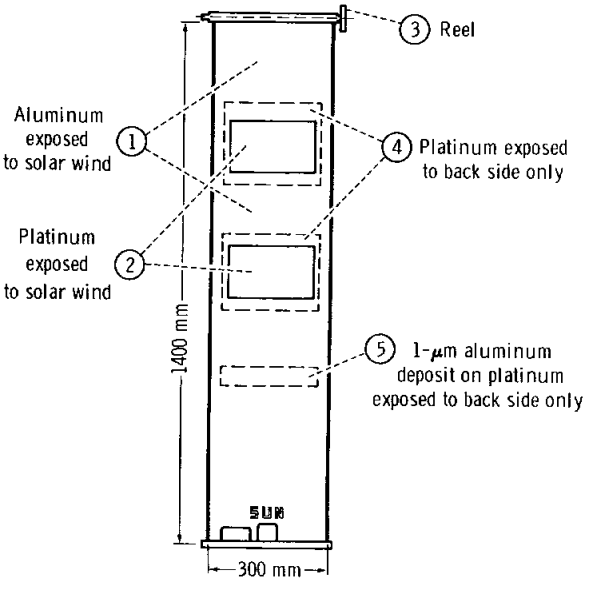


FIGURE 14-2.–Details of exposed foil assembly.

Sections labeled 2 are 5-μm platinum foil areas exposed to the Sun and the shade. Laboratory bombardment experiments (ref. 14-21) demonstrated that only a small percentage of ions implanted in the platinum foil with solar wind energies are removed by washing the foil for several minutes in 2- to 10-percent hydrofluoric acid. However, this treatment removes a high percentage of implanted noble gases from silicates (ref. 14-26) and other constituents of lunar fines material (ref. 14-27); thus, this method will be effective in eliminating any possible interference from residual lunar dust adhering to the foils.

The trapping probabilities of the materials used in the Apollo 16 foil for an average solar wind energy of 750 eV/nucleon are given in table 14-I. The data for aluminum (ref. 14-19), aluminum oxide (ref. 14-20), and olivine (a silicate mineral) (ref. 14-28) are similar; whereas significantly lower trapping probabilities were obtained for platinum. The reason for this observation is that the trapping probability depends primarily on the relation between the mass of impacting ions and the atomic mass of the target material, that is, for a heavy element such as platinum, backscattering is relatively high.

Foil section 3 remained wound around the reel at the top end of the foil. As in the earlier SWC experiments (refs. 14-14 and 14-24), this section will be used to measure the distribution of the angles of arrival of solar wind particles. The mass spectrometer background on masses 3 and 20 has recently been reduced by installing a titanium getter directly at the ion source. This improvement will allow measurements of the arrival directions to be made for ^{4}He, ^{3}He, and ^{20}Ne (neon).

In sections labeled 4, platinum foils were exposed in the antisolar direction. They were shielded from direct impact of solar wind particles on the sunlit side by two layers of 15-μm aluminum. These sections will be used for studying solar wind albedo and in searching for drift-accelerated neon ions originating in the lunar atmosphere.

In section 5, a platinum foil covered by an aluminum deposit 0.98 ± 0.02 μm thick was exposed to the antisolar direction. By using this foil section, a search will be conducted for solar flare helium. After removal of the aluminum deposit, the platinum will retain helium that was implanted with energies above approximately 40 keV/nucleon.

INSTRUMENTATION AND LUNAR SURFACE OPERATION

With the exception of the foil, the experiment hardware was similar to that used on the earlier Apollo missions (ref. 14-23). The experiment consisted of a telescopic aluminum pole approximately 4 cm in diameter and 38 cm in length when collapsed.

TABLE 14-I.–Trapping Probabilities Obtained From Noble Gas Bombardment Experiments on Different Target Materials at an Energy of 750 eV/nucleon

[The reproducibility of these measurements is ±2 to ±3 percent; the absolute errors of the trapping probabilities are ±5 percent or less]

Target material (a)	*Mean atomic mass*	*Trapping probability, percent*		
		^{4}He	^{20}Ne	^{40}Ar
Aluminum	27	89	100	99
Aluminum oxide	20	86	86	92
Olivine	21	90	95	90
Platinum	195	61	71	78

[a]For further details, see reference 14-19 for aluminum, reference 14-20 for aluminum oxide, reference 14-28 for olivine, and reference 14-21 for platinum.

In the stowed position, the foil was enclosed in the tubing and rolled up on a spring-driven reel. The instrument weighed 450 g. When extended on the lunar surface, the pole was approximately 1.5 m long, and a 30- by 130-cm foil area was exposed. Only the foil assembly was recovered at the end of the lunar exposure; it was rolled on the spring-driven reel and returned to Earth. In figure 14-1, the instrument is shown deployed on the lunar surface at the Apollo 16 landing site. The reel handle was color coded to give the exact angular position of the reel and the portion of foil rolled around it. This color code is clearly identifiable in Hasselblad pictures such as the one shown in figure 14-1. Examination of numerous Apollo 16 photographs showed that the foil was standing vertically (within a few degrees) on the lunar surface. After retrieval, the return unit was placed in a special Teflon bag and returned to Earth.

RESULTS FROM THE FIRST FOIL ANALYSES

Thus far, the analyses have been completed for an initial series of five small aluminum pieces from the upper part of the Apollo 16 foil. The results are shown in table 14-II. To prevent possible lunar dust contamination, all foil pieces were cleaned by using ultrasonic treatments and by applying a replicating film technique to both surfaces. As an additional measure of decontamination, the oxide layer was removed from the back side of foil pieces 2-1, 2-3, and 2-5. For comparison, a piece of the Apollo 15 foil was analyzed with the Apollo 16 foil pieces. The results obtained from this piece of Apollo 15 foil agree well with those from previous analyses of the same foil (ref. 14-16).

The measurements on the Apollo 16 flight foil and on several pieces that had been cut from the foil before flight (for noble gas blank measurements) were analyzed. The blank concentrations that had been determined in this manner were subtracted from the noble gas concentrations measured in the pieces of the flight foil, and areal concentrations of the solar wind particles were obtained (table 14-II). The foil blanks for helium and neon were 0.002 and 1.2 percent, respectively, relative to the solar wind particle content. The foil blanks for ^{36}Ar (argon) and ^{38}Ar were approximately 50 percent. Because the foil contains argon of atmospheric composition, which has a very high abundance of ^{40}Ar, the blank corrections for ^{36}Ar and ^{38}Ar can be done with sufficient precision by using ^{40}Ar as a tracer for atmospheric argon.

The results obtained from the five Apollo 16 aluminum foil pieces agree well. The results must be the same, whether or not the oxide layer on the back side of the foil is removed. Measurements on such foil pieces from earlier Apollo flights that were contaminated with lunar dust have shown that removal of the oxide layer reduces the dust contamination by approximately a factor of 3. Therefore, the five Apollo 16 foil pieces investigated thus far do not seem to have been appreciably affected by a residual dust contamination.

The average ^{4}He flux during the Apollo 16 exposure period can be calculated by using the data given in table 14-II. The trapping probabilities of the foil for noble gas ions depend only slightly on energy in the general solar wind velocity region. For helium

TABLE 14-II.—First Results From the Analyses of the Aluminum Foil From the Apollo 16 SWC Experiment

Sample no.	Area, cm^2	^{4}He concentration, 10^{10} atoms/cm^2	$^{4}He/^{3}He$	$^{4}He/^{20}Ne$	$^{20}Ne/^{22}Ne$	$^{22}Ne/^{21}Ne$	$^{20}Ne/^{36}Ar$
Apollo 16:							
[a]2-1	5.02	108	2290	510	14.0	32	29
2-2	4.98	107	2300	490	13.9	27	30
[a]2-3	5.04	101	2280	500	13.5	31	27
2-4	5.17	108	2280	490	13.7	27	31
[a]2-5	10.35	100	2310	490	13.9	35	28
Apollo 15:							
[a]3-9	3.13	140	2370	480	13.8	33	19

[a]Oxide layer on back side of aluminum foil mechanically removed.

TABLE 14-III.–Estimated ^{4}He Flux Averages During the Times of Foil Exposure

[Data for Apollo 11, 12, 14, and 15 are from references 14-24, 14-25, and 14-14 to 14-16]

Mission	Exposure initiation		Exposure duration, hr:min	Average solar wind ^{4}He flux, $10^6 cm^{-2} sec^{-1}$
	Date	G.m.t., hr:min		
Apollo 11	July 21, 1969	03:35	01:17	6.2 ± 1.2
Apollo 12	Nov. 19, 1969	12:35	18:42	8.1 ± 1.0
Apollo 14	Feb. 5, 1971	15:15	21:00	4.2 ± 0.8
Apollo 15	July 31, 1971	19:36	41:08	17.7 ± 2.5
Apollo 16	Apr. 21, 1972	23:01	45:05	12.0 ± 1.8

TABLE 14-IV.–Solar Wind Abundance Ratios Determined From the Foil Exposure Periods of the Apollo Missions

[Data for Apollo 11, 12, 14, and 15 are from references 14-14 to 14-16]

Mission	$^4He/^3He$	$^4He/^{20}Ne$	$^{20}Ne/^{22}Ne$	$^{22}Ne/^{21}Ne$
Apollo 11	1860 ± 140	430 ± 90	13.5 ± 1.0	--
Apollo 12	2450 ± 100	620 ± 70	13.1 ± 0.6	26 ± 12
Apollo 14	2230 ± 140	550 ± 70	13.65 ± 0.50	--
Apollo 15	2310 ± 120	550 ± 50	13.65 ± 0.30	31 ± 4
Apollo 16	2260 ± 100	570 ± 50	13.80 ± 0.40	31 ± 4

with velocities between 280 and 800 km/sec, the trapping probability is 89 ± 5 percent for normal incidence and approximately 22 percent less for an incidence angle of 51°.

The angular distribution and the average angle of incidence on the Apollo 16 foil have not yet been determined. Thus, for the purpose of this report, the average angle of incidence is estimated. The average solar elevation during the foil exposure was 36°. By considering the effects of aberration and corotation, the angle of incidence of the solar wind on the foil is estimated to be 51°. With this assumption, the ^{4}He flux during the Apollo 16 SWC foil exposure can be calculated (table 14-III); it is given with the ^{4}He fluxes previously determined for the Apollo 11, 12, 14, and 15 exposure periods.

From the experimental results given in table 14-I, preliminary values for the relative abundances of ions in the solar wind during the Apollo 16 foil exposure period have been calculated (table 14-IV). Weighted averages of the measured ratios were taken and corrected for differences in trapping probabilities. Thus, the ^{4}He/^{20}Ne ratio was corrected by 14 percent, and the trapping probability for ^{3}He was assumed to be 2 percent lower than the probability determined for ^{4}He (ref. 14-16). The isotopic ratios of neon were not corrected.

The relative abundances of argon in the solar wind obtained thus far are given in table 14-V. The error limits in table 14-V are much larger than the statistical errors (cf. table 14-II) and include estimates of

TABLE 14-V.–Preliminary Results on Argon Abundances in the Solar Wind

Mission	$^{20}Ne/^{36}Ar$
Apollo 14[a]	37^{+10}_{-5}
Apollo 15	20^{+8}_{-5}
Apollo 16	29 ± 6

[a]Data are from reference 14-15.

possible systematic errors. The argon abundances have to be considered as preliminary. The errors in the $^{20}Ne/^{36}Ar$ abundance ratios are expected to be substantially lowered by analyses of larger foil pieces. Furthermore, the etching technique for the platinum should establish independently and clearly that lunar dust contamination is being completely removed by the cleaning procedures applied to the foils.

AIMS OF FURTHER FOIL ANALYSES

The continued analysis of the Apollo 16 foil should bring an increase in the precision of the measurement of relative ion abundances in the solar wind. In particular, the $^{22}Ne/^{21}Ne$ ratio can be obtained with much higher precision by analyzing larger foil areas. A precise argon abundance and the $^{36}Ar/^{38}Ar$ ratio can be obtained by combining results from the aluminum foil and the platinum portions of the foil after washing them with hydrofluoric acid. Detailed analyses of section 3 of the foil, which was wound around the reel during exposure (fig. 14-2), should give the arrival direction of solar wind ions and should allow conclusions to be drawn concerning the local lunar magnetic field.

Section 4 of the foil, which is shielded from the direct impact of solar wind particles, will be used to measure the albedo from the impact of solar wind on the lunar surface and to search for constituents of the lunar ionosphere. The albedo A may be defined as the fraction of incoming ions that are backscattered at an energy above 1 keV. Thus, $A \leqslant 1 - \eta$, if η is the trapping probability. Because of the light mass of helium, its albedo is probably considerably larger than that of the heavier noble gases. For an order-of-magnitude estimate of the helium flux trapped in the back side of the foil, the following simplifying assumptions are made: $A = 1 - \eta$; η is independent of the angle of incidence and is the same for the lunar surface and the foil; and backscattering follows Lambert's law. Then the helium flux f' trapped at the back side of the foil is

$$f' = \frac{1}{2} f \eta (1 - \eta) \sin \theta \qquad (14\text{-}1)$$

where f is the solar wind helium flux and θ is the solar wind elevation angle above the lunar horizon. With $\eta \approx 0.9$ and $\theta \approx 30^\circ$, $f' = 0.02\, f$ is obtained. Concentrations per unit area of this order of magnitude have been observed on the back side of foils from earlier Apollo flights. The acid leaching technique on the shielded platinum foil area should allow quantitative measurement of the albedo effect.

Noble gases released from the Moon into the lunar atmosphere become ionized by solar ultraviolet and solar wind charge exchange after periods of the order of weeks or months. Such ions are then accelerated by the electric field of the solar wind (ref. 14-29), which for a lunar observer is given by

$$\mathbf{E} = -\mathbf{V} \times \mathbf{B} \qquad (14\text{-}2)$$

where $\mathbf{V}$ is the solar wind velocity and $\mathbf{B}$ the strength of the magnetic field in the solar wind. For example, with $\mathbf{V} = 400$ km/sec and $\mathbf{B}_\perp = 5$ gamma, $\mathbf{E} = 2 \times 10^{-3}$ V/m is obtained. Because the interplanetary magnetic field vector normally lies near the ecliptic plane, the lunar ions will be accelerated essentially in the north-south direction. Detailed studies of ion trajectories have been conducted (ref. 14-30). During the Apollo 16 foil exposure time, the direction of the spiral magnetic field was pointing towards the Sun (P. Dyal, private communication, 1972). Thus, the lunar ions were accelerated from north to south. To obtain enough energy to be trapped in the foil, the ions have to come from distances of at least several hundred kilometers. The trajectories are influenced by local magnetic fields. The portable lunar magnetometer recorded that the lunar magnetic field points into the Moon towards the east near the lunar module at station 13, approximately 4 km to the north (sec. 12 of this report). If similar field directions were prevailing farther north, then the lunar ions approaching from the north would be deflected in a manner favorable to collection on the back side of the foil. One of the sources of the lunar atmosphere is the thermal release of trapped solar wind atoms. Most of the helium escapes from the gravitational field before it is ionized; thus, neon should be the lunar ion that is most likely to be identified by this technique. Neutral neon has been observed by the Apollo 16 lunar orbital mass spectrometer experiment in the lunar atmosphere (sec. 21 of this report). A search for helium with energies above 40 keV/nucleon will be conducted on foil section 5. In this energy range, the directions of the particle trajectories are expected to be similar to isotropic because the particle velocities are much larger than the solar wind velocity. Therefore, these particles can be searched for on the back

side of the foil where the competing flux of the solar wind is eliminated. Fluxes of alpha particles in the energy range >40 keV/nucleon in interplanetary space have not been published.

DISCUSSION

The relative elemental and isotopic abundances of helium and neon in the solar wind measured for the Apollo 12, 14, 15, and 16 exposure times are quite similar, in spite of large (factor of 4) variations in the ^{4}He flux. The abundances obtained for Apollo 11 are different. In figure 14-3, ^{3}He/^{4}He is plotted against ^{4}He/^{20}Ne. As shown previously (ref. 14-16), these abundance ratios are correlated with high ^{3}He/^{4}He ratios corresponding to low ^{4}He/^{20}Ne ratios. Just the opposite correlation would be expected if electromagnetic separation effects were operative in the corona (ref. 14-8) or near the Moon (ref. 14-14). Conversely, theoretical considerations (refs. 14-6 and 14-8) on the acceleration of ions in the corona predict larger fluctuations in the ^{4}He abundance than in the ^{3}He

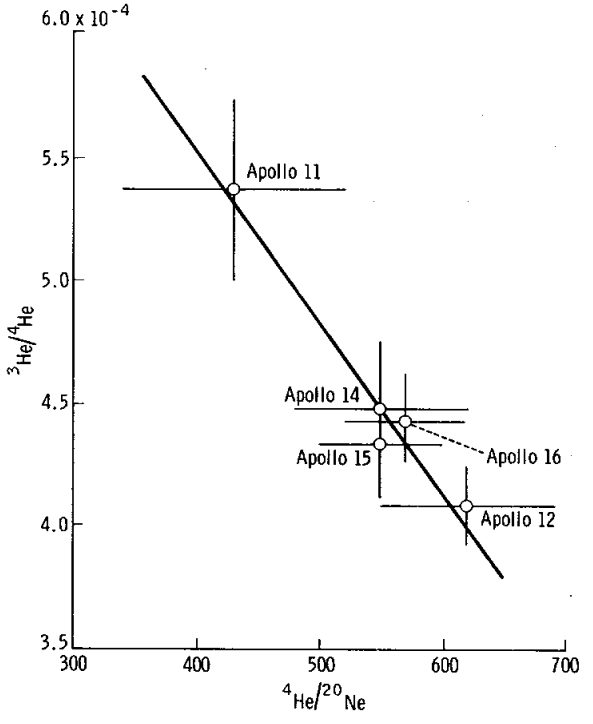


FIGURE 14-3.–Correlation between the ^{3}He/^{4}He and ^{4}He/^{20}Ne solar wind abundance ratios as determined for the five Apollo foil exposure times.

and ^{20}Ne abundances, and, in fact, the ^{3}He/^{20}Ne ratio is the same for the five SWC experiments within the limits of error.

Particularly noteworthy is the absence of any indication of electromagnetic separation effects at the Apollo 16 landing site vicinity where local magnetic fields exist with strengths up to 313 gamma and with an average field of the order of 200 gamma (section 12 of this report). The radii of curvature of ^{3}He^{2+}, ^{4}He^{2+}, and ^{20}Ne^{8+} with energies of 750 eV/nucleon in a field of 200 gamma are 29, 38, and 48 km, respectively. The fact that solar wind ions reach the lunar surface at the Apollo 16 landing site and that there does not appear to be any mass discrimination limits the spatial extent of an organized magnetic field of 200 gamma. The measurement of the arrival directions to be conducted on section 3 of the SWC foil should allow a quantitative estimate of the extent and regularity of the magnetic field in the area east of the Apollo 16 landing site.

Data obtained with the Vela 3A and 3B satellites suggest a dependence of the He/H ratio on solar activity (ref. 14-5). Explorer 34 results have shown an association of high He/H ratios with geomagnetic storms (ref. 14-31). Also, it has been observed that interplanetary shocks are followed by a helium-rich plasma interpreted as the driver gas that produces the shock (refs. 14-7 and 14-32). To gain a better understanding of the dynamic processes underlying these observations, it is important to study the behavior of other ion species. In figure 14-4, the ^{4}He/^{3}He abundance ratio is plotted as a function of the geomagnetic index K_p. Figure 14-4 differs from a similar diagram given in the Apollo 15 Preliminary Science Report (ref. 14-16), inasmuch as in the present section the K_p values correspond to actual exposure periods without introducing any time delays. This fact is in accordance with the observation that helium enhancements in the solar wind often appear during the main phase of a geomagnetic storm (refs. 14-4, 14-33, and 14-7). Included in figure 14-4 is the ^{4}He/^{3}He ratio obtained from a Surveyor III aluminum tube returned from the Moon by the Apollo 12 crewmen. After a correction of 2 percent for the differences in the trapping probabilities of the two helium isotopes, the measured value (ref. 14-34) should represent the average ^{4}He/^{3}He ratio in the solar wind during the exposure period of this material (April 20, 1967, to November 20, 1969). The lower

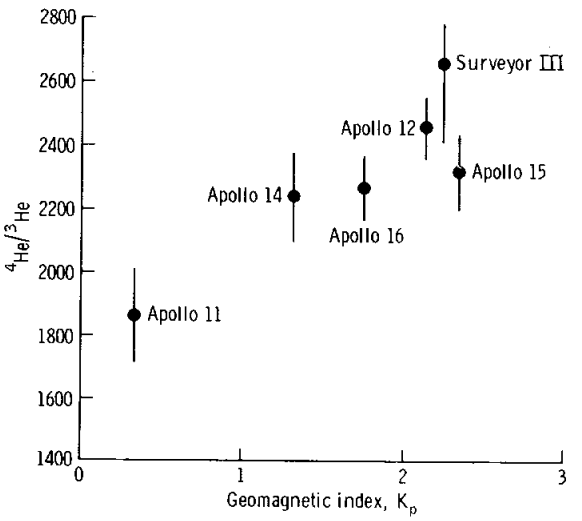


FIGURE 14-4.–Correlation between the solar wind $^4He/^3He$ abundance ratio and the level of disturbance in the solar wind as indicated by the geomagnetic index K_p. The data obtained from the analysis of Surveyor III material are described in reference 14-34.

limit of error in this case includes an estimated possible change of the $^4He/^3He$ ratio as a result of helium diffusion from the aluminum.

A correlation between $^4He/^3He$ ratio and K_p is suggested in figure 14-4. Correlation with K_p is also indicated for the $^{36}Ar/^{20}Ne$ ratio (table 14-V). This latter correlation is to be expected because the charges of the two ions are estimated to be 8 (ref. 14-8); whereas their masses are very different.

The correlation in figure 14-4 rests very strongly on the low $^4He/^3He$ ratio measured during the time of the Apollo 11 extravehicular activity, a period of low K_p. The other exposure periods include times of lower and higher K_p; therefore, it can be assumed that the $^4He/^3He$ variability would be higher if shorter periods were sampled. For example, in the case of the Apollo 16 exposure period, K_p was 0° and 0^+ during the first 12 hr, rising afterwards to reach a maximum value of 4° that lasted 6 hr. On the basis of figure 14-4, it must be assumed that these K_p changes were accompanied by composition changes and that the variability during this exposure period may have been larger than the entire range of measured values given in figure 14-4.

Weighted averages of ion abundances in the solar wind for the five Apollo SWC foil exposure periods are given in table 14-VI. Judging from the K_p values during these exposures, the averages should be fairly representative for the period from the Apollo 11 landing to the Apollo 16 landing (summer 1969 to spring 1972). The errors given are an attempt to estimate the uncertainty of the averages for the indicated period. The errors are based on the variability of the observed abundances obtained from the four long-exposure times. The question is to what extent the averages given in table 14-VI would have to be corrected to obtain values representative for the average solar wind. These corrections should be largest for $^{20}Ne/^{36}Ar$ and $^4He/^{20}Ne$, smaller for $^4He/^3He$, and virtually negligible for the neon isotopic abundances. Measurements of $^{20}Ne/^{36}Ar$ in the

TABLE 14-VI.–Comparison of Weighted Averages of Solar Wind Ion Abundances Obtained From the SWC Experiments With Abundances in Surface-Correlated Gases[a] of Lunar Fines Materials and a Breccia and in the Atmosphere of the Earth

Source	$^4He/^3He$	$^4He/^{20}Ne$	$^{20}Ne/^{22}Ne$	$^{22}Ne/^{21}Ne$	$^{20}Ne/^{36}Ar$
Solar wind (average from SWC experiments)	2350 ± 120	570 ± 70	13.7 ± 0.3	30 ± 4	28 ± 9
Lunar fines 10084	2550 ± 250	96 ± 18	12.65 ± 0.2	31.0 ± 1.2	7 ± 2
Ilmenite from 10084	2720 ± 100	218 ± 8	12.85 ± 0.1	31.1 ± 0.8	27 ± 4
Ilmenite from 12001	2700 ± 80	253 ± 10	12.9 ± 0.1	32.0 ± 0.4	27 ± 5
Ilmenite from breccia 10046	3060 ± 150	231 ± 13	12.65 ± 0.15	31.4 ± 0.4	(b)
Terrestrial atmosphere	7×10^5	.3	9.80 ± 0.08	34.5 ± 1.0	.5

[a]Data for surface-correlated gases in lunar materials are from references 14-27 and 14-35.
[b]Variable.

ilmenites give a ratio of 27. Because this ratio would tend to be lowered by diffusion, an average $^{20}Ne/^{36}Ar$ ratio below 27 in the solar wind seems to be eliminated. Therefore, the average SWC abundances given in table 14-VI are good approximations to the average solar wind abundances.

The average solar wind composition is not necessarily identical with the abundances in the outer convective zone of the Sun. The latter can only be derived accurately after the fractionation processes in the solar wind source region have been sufficiently studied by investigating solar wind abundance variations.

The gases concentrated on the surfaces of the grains of lunar material and in the solar wind differ in their composition (table 14-VI). This difference is probably a result of diffusive losses of gases from the lunar material and perhaps a result of other secondary effects such as saturation or retrapping. The mineral ilmenite ($FeTiO_3$) appears to have preserved the original abundances better than the other constituents in the lunar fines material. However, even in ilmenite, the isotopic ratios of helium and neon are significantly different from the solar wind values. The relative differences for the $^4He/^3He$ and $^{20}Ne/^{22}Ne$ ratios are of the order of $(\Delta M/M)^{1/2}$ where M is the mass of the element and ΔM is the difference in mass of the isotopes. The $^4He/^3He$ ratio in the breccia ilmenite is significantly higher than in the ilmenite separated from the fines material. This observation is an indication of a secular variation in the $^4He/^3He$ ratio (ref. 14-35).

CONCLUDING REMARKS

The isotopic abundance of neon contained in the atmosphere of the Earth is highly fractionated with respect to solar neon. An even stronger fractionation was anticipated long ago (refs. 14-36 and 14-37) on the basis of the apparent element fractionation of noble gases in the atmosphere. On Venus these fractionations might very well be smaller, and, judging from elemental abundances, even less fractionation can be expected for the major planets. If noble gas elemental and isotopic abundances in the different planetary reservoirs are measured in the future, they will have to be discussed in relation to the corresponding solar abundances, which, in turn, have to be derived from precise measurements of abundance averages and variations in the solar wind.

REFERENCES

14-1. Snyder, Conway W.; and Neugebauer, Marcia: Interplanetary Solar-Wind Measurements by Mariner II. Space Res., vol. 4, 1964, pp. 89-113.

14-2. Wolfe, J. H.; Silva, R. W.; McKibbin, D. D.; and Mason, R. H.: The Compositional, Anisotropic, and Nonradial Flow Characteristics of the Solar Wind. J. Geophys. Res., vol. 71, no. 13, July 1966, pp. 3329-3335.

14-3. Hundhausen, A. J.; Asbridge, J. R.; Bame, S. J.; Gilbert, H. E.; and Strong, I. B.: Vela 3 Satellite Observations of Solar Wind Ions: A Preliminary Report. J. Geophys. Res., vol. 72, no. 1, Jan. 1967, pp. 87-100.

14-4. Ogilvie, K. W.; Burlaga, L. F.; and Wilkerson, T. D.: Plasma Observations on Explorer 34. J. Geophys. Res., vol. 73, no. 21, Nov. 1968, pp. 6809-6824.

14-5. Robbins, D. E.; Hundhausen, A. J.; and Bame, S. J.: Helium in the Solar Wind. J. Geophys. Res., vol. 75, no. 7, Mar. 1970, pp. 1178-1187.

14-6. Geiss, J.; Hirt, P.; and Leutwyler, H.: On Acceleration and Motion of Ions in Corona and Solar Wind. Solar Phys., vol. 12, 1970, pp. 458-483.

14-7. Hirshberg, J. A.; Alksne, A.; Colburn, D. S.; Bame, S. J.; and Hundhausen, A. J.: Observation of a Solar Flare Induced Interplanetary Shock and Helium-Enriched Driver Gas. J. Geophys. Res., vol. 75, Jan. 1970, pp. 1-15.

14-8. Geiss, J.: On Elemental and Isotopic Composition of the Solar Wind. Paper presented at the Asilomar Conference on Solar Wind, Mar. 1971.

14-9. Danziger, I. J.: The Cosmic Abundance of Helium. Ann. Rev. Astron. Astrophys., vol. 8, Leo Goldberg, ed., Annual Reviews Inc. (Palo-Alto), 1970, pp. 161-178.

14-10. Hundhausen, A. J.: Composition and Dynamics of the Solar Wind Plasma. Rev. Geophy. Space Phy., vol. 8, no. 4, Nov. 1970, pp. 729-811.

14-11. Ezer, D.; and Cameron, A. G. W.: A Study of Solar Evolution. Can. J. Phys., vol. 43, Aug. 1965, pp. 1497-1517.

14-12. Geiss, J.; and Reeves, H.: Cosmic and Solar System Abundances of Deuterium and Helium-3. Astron. Astrophys., vol. 18, no. 1, Apr. 1972, pp. 126-132.

14-13. Black, D. C.: On the Origins of Trapped Helium, Neon and Argon Isotopic Variations in Meteorites – I. Gas-Rich Meteorites, Lunar Soil and Breccia. Geochim. Cosmochim. Acta, vol. 36, no. 3, Mar. 1972, pp. 347-375.

14-14. Geiss, J.; Eberhardt, P.; Bühler, F.; Meister, J.; and Signer, P.: Apollo 11 and 12 Solar Wind Composition Experiments: Fluxes of He and Ne Isotopes. J. Geophys. Res., vol. 75, no. 31, Nov. 1970, pp. 5972-5979.

14-15. Geiss, J.; Bühler, F.; Cerutti, H.; Eberhardt, P.; and Meister, J.: The Solar-Wind Composition Experiment. Sec. 12 of Apollo 14 Preliminary Science Report. NASA SP-272, 1971.

14-16. Geiss, J.; Bühler, F.; Cerutti, H.; and Eberhardt, P.: Solar-Wind Composition Experiment. Sec. 15 of Apollo 15 Preliminary Science Report. NASA SP-289, 1972.

14-17. Davies, J. A.; Brown, F.; and McCargo, M.: Range of Xe^{133} and Ar^{41} Ions of Kiloelectron Volt Energies in Aluminum. Can. J. Phys., vol. 41, no. 6, June 1963, pp. 829-843.

14-18. Bühler, F.; Geiss, J.; Meister, J.; Eberhardt, P.; et al.: Trapping of the Solar Wind in Solids. Earth Planet. Sci. Lett., vol. 1, 1966, pp. 249-255.

14-19. Meister, J.: Ein Experiment zur Bestimmung der Zusammensetzung und der Isotopenverhältnisse des Sonnenwindes: Einfangverhalten von Aluminium für niederenergetische Edelgasionen. Ph. D. thesis, Univ. of Bern, 1969.

14-20. Filleux, Ch.: Einfangverhalten von Al_2O_3 für niederenergetische Edelgasionen, M. S. Thesis, Univ. of Bern, 1971.

14-21. Stettler, W.: Einfangverhalten von Platin für Edelgasionen mit Sonnenwindenergien. M. S. Thesis, Univ. of Bern, 1972.

14-22. Signer, P.; Eberhardt, P.; and Geiss, J.: Possible Determination of the Solar Wind Composition. J. Geophys. Res., vol. 70, no. 9, May 1965, pp. 2243-2244.

14-23. Geiss, J.; Eberhardt, P.; Signer, P.; Bühler, F.; and Meister, J.: The Solar-Wind Composition Experiment. Sec. 8 of Apollo 11 Preliminary Science Report. NASA SP-214, 1969.

14-24. Bühler, F.; Eberhardt, P.; Geiss, J.; Meister, J.; and Signer, P.: Apollo 11 Solar Wind Composition Experiment: First Results. Science, vol. 166, no. 3912, Dec. 19, 1969, pp. 1502-1503.

14-25. Geiss, J.; Eberhardt, P.; Signer, P.; Bühler, F.; and Meister, J.: The Solar-Wind Composition Experiment. Sec. 8 of Apollo 12 Preliminary Science Report. NASA SP-235, 1970.

14-26. Eberhardt, P.; Geiss, J.; and Grögler, N.: Further Evidence on the Origin of Trapped Gases in the Meteorite Khor Temiki. J. Geophys. Res., vol. 70, no. 17, Sept. 1, 1965, pp. 4375-4378.

14-27. Eberhardt, P.; Geiss, J.; Graf, H.; Grögler, N.; et al.: Trapped Solar Wind Noble Gases, Exposure Age and K/Ar Age in Apollo 11 Lunar Fine Material. Proceedings of the Apollo 11 Lunar Science Conference, Supp. 1, vol. 2, A. A. Levinson, ed., Pergamon Press (New York), 1970, pp. 1037-1070.

14-28. Cerutti, H.: Einfang von niederenergetischen Edelgasionen durch Silikate. M. S. Thesis, Univ. of Bern, 1970.

14-29. Michel, F. C.: Interaction Between the Solar Wind and the Lunar Atmosphere. Planet. Space Sci., vol. 12, no. 11, Nov. 1964, pp. 1075-1091.

14-30. Manka, R. H.; and Michel, F. C.: Lunar Atmosphere as a Source of Argon-40 and Other Lunar Surface Elements. Science, vol. 169, no. 3942, July 17, 1970, pp. 278-280.

14-31. Ogilvie, K. W.; and Wilkerson, T. D.: Helium Abundance in the Solar Wind. Solar Phys., vol. 8, 1969, p. 435.

14-32. Hirshberg, J. A.: Solar Wind Helium Enhancements Following Major Solar Flares. Paper presented at the Asilomar Conference on Solar Wind, Mar. 1971.

14-33. Bame, S. J.; Asbridge, J. R.; Hundhausen, A. J.; and Strong, I. B.: Solar Wind and Magnetosheath Observations during the Jan. 13-14, 1967, Geomagnetic Storm. J. Geophys. Res., vol. 73, no. 17, Sept. 1, 1968, pp. 5761-5767.

14-34. Bühler, F.; Eberhardt, P.; Geiss, J.; and Schwarzmüller, J.: Trapped Solar Wind Helium and Neon in Surveyor 3 Material. Earth Planet. Sci. Lett., vol. 10, no. 3, Feb. 1971, pp. 297-306.

14-35. Eberhardt, P.; Geiss, J.; Graf, H.; Grögler, N.; et al.: Trapped Solar Wind Noble Gases in Apollo 12 Lunar Fines 12001 and Apollo 11 Breccia 10046. Proceedings of the Third Lunar Science Conference, vol. II, Dieter Heymann, ed., MIT Press (Cambridge), 1972, pp. 1821-1856.

14-36. Suess, H. E.: Die Häufigkeit der Edelgase auf der Erde und im Kosmos. J. Geol., vol. 57, 1949, p. 600.

14-37. Geiss, J.: Ueber die Geschichte der Meteorite aus Isotopenmessungen. Chimia (Switzerland), vol. 11, 1957, pp. 349-363.

ACKNOWLEDGMENTS

The authors wish to express their gratitude for the participation of P. Signer, J. Meister, J. Fischer, and W. Stettler in the development and preparation of the experiment. The authors have benefited in their interpretation of the data from discussions with Drs. H. Elliot, N. Grögler, J. A. Hirshberg, P. Wild, and D. T. Young. Hardware construction and foil analyses were supported by the University of Bern and the Swiss National Science Foundation.

15. Cosmic Ray Experiment

INTRODUCTION

The relative abundances and energy spectra of heavy solar and cosmic ray particles convey much information about the Sun and other galactic particle sources and about the acceleration and propagation of the particles. In particular, the lowest energy range, from a few million electron volts per nuclear mass unit (nucleon) to a kiloelectron volt per nucleon (a solar wind energy), is largely unexplored. The cosmic ray experiment contained a variety of detectors designed to examine this energy range.

It is not known whether, in times of solar quiet, the low-energy nuclei are primarily solar or galactic in origin. One objective of this study was to resolve that question by measuring the chemical composition of the particles. Alternatively, if the Sun were active during the mission, it was expected that the flood of solar particles would provide an abundance of detailed compositional information about the Sun and solar acceleration processes. Because a solar flare occurred during the translunar portion of the flight, the latter objective was served.

The cosmic ray experiment equipment consists of a four-panel array of passive particle track detectors to observe cosmic ray and solar wind nuclei and thermal neutrons, and also includes metal foils to trap light solar wind gases. The materials in the panels were chosen for experiments performed by groups at General Electric (GE), the University of California, and Washington University. Preliminary results of the experiments being performed by the GE group are described in part A of this section; the other experiments are described in parts B and C. The experiment equipment is shown mounted on the descent stage of the lunar module (LM) in figure 15-1(a). During the first extravehicular activity (EVA), the equipment was placed on the minus Y footpad of the LM (fig. 15-1(b)).

The detection basis of nearly all of the experiments is that particles passing through solids can form trails of damage, revealable by preferential chemical attack, which allow the particles to be counted and identified. Much of this work is reviewed in references 15-1 to 15-4. An example of an etched track



FIGURE 15-1.—The cosmic ray experiment (a) on the descent stage of the lunar module, of Apollo 16, where originally mounted, and (b) on the LM minus Y footpad (on the left footpad, looking down-Sun), where it was placed during EVA 1. Panel 2 and the bottom of panel 3 were used for the GE experiment; panel 1 (the lowermost panel) and panel 4 (the topmost panel) were used for experiments by the University of California and Washington University, respectively. Solar elevation was 35.8°.

that was identified as a zinc ion is shown in figure 15-2 (ref. 15-5).

The detector array was mounted on the LM before launch and was first exposed to space at the time just after translunar injection when the LM was withdrawn from the service module/LM adapter (the panels that, during launch, enclose the LM with aluminum equivalent to 0.3-cm-thick Lexan polycarbonate plastic). Exposure ended just before the termination of the third EVA on the Moon, at which time the four-panel array was pulled out of its frame and folded into a compact 5- by 18.4- by 30-cm package (fig. 15-3) for return to Earth. Because the folding and stowing of the device ended the period of useful exposure of the detectors, provision was made to distinguish particles detected during the useful period from those that subsequently penetrated the spacecraft and entered the detectors.

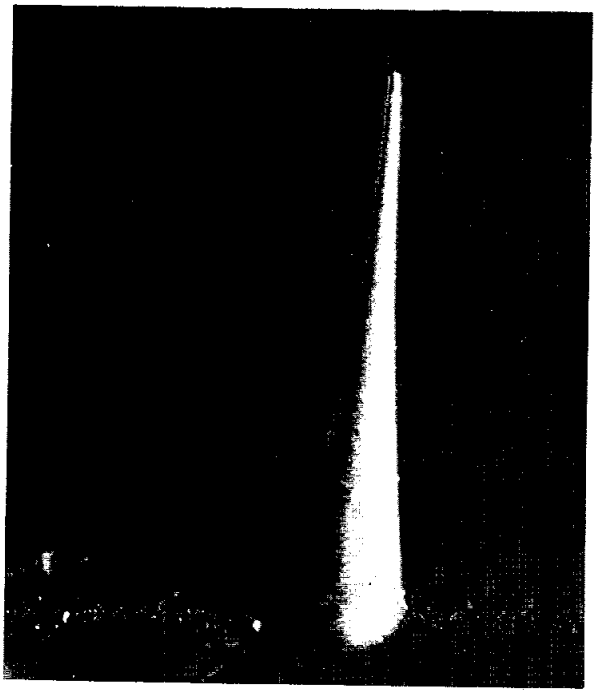


FIGURE 15-2.—Replica of a 0.07-cm etched track in an Apollo space helmet. From the shape, the track can be inferred to have been caused by a zinc ion.

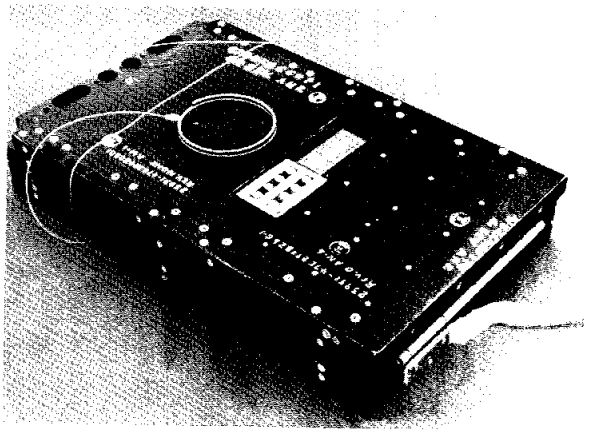


FIGURE 15-3.—Folded detector array. After exposure, the array was folded into the configuration shown to form a convenient package for return to Earth. Temperature labels are visible.

PART A

COMPOSITION AND ENERGY SPECTRA OF SOLAR COSMIC RAY NUCLEI

R. L. Fleischer[a] *and H. R. Hart, Jr.*[a]

The GE experiment consisted of two types of detectors: plastics and glasses located in panel 2 and the lower half of panel 3. In panel 2, the entire exposed detector area of 14.7 by 22.6 cm was composed of 31 sheets of 0.025-cm Lexan polycarbonate plastic 9070-112. In panel 3, 39 sheets of 0.02-cm Eastman Kodacel cellulose triacetate TA-401 with no plasticizer made up the major volume fraction. The lower part of panel 3 contained five types of glass detectors: 2.5- by 1.3- by 0.1-cm GE phosphate-uranium glass 1484 (ref. 15-6), 2.5- by 2.5- by 0.1-cm GE phosphate glass 1457 (ref. 15-7), 2.5- by 2.5- by 0.1-cm Corning alumina-silicate glass 1720, 2.5- by 2.5- by 0.1-cm silicon dioxide (Suprasil 2 silica glass from Amersil, Inc.), and a nearly elliptical tektite slab (Santiago, Philippines, tektite 1, supplied

[a]General Electric Research and Development Center.

by D. Chapman, NASA Ames Research Center) that fit within a 2.5- by 3.8- by 0.1-cm space.

Particles that entered the array after it was folded were recognized, if they crossed from one sheet to another, by means of a 2-mm relative shift of alternate sheets (fig. 15-4). This shift was produced automatically by the folding of the array at the end of EVA 3 just before the array was stowed in the LM. The designed full 2-mm shift occurred in panel 2, and a lesser shift occurred in panel 3.

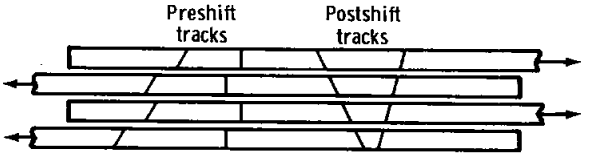


FIGURE 15-4.–Shifting procedure. A 2-mm relative shift of alternate plastic sheets allowed the preshift and postshift tracks to be distinguished. Postshift tracks are interesting only for personnel dosimetry purposes because the tracks represent particles that penetrated the spacecraft before entering the detectors.

Detector temperatures are important because thermal effects can be observed in the plastics and in some of the glasses used in panel 3 after the materials were exposed at temperatures above 328° K. Although tracks are retained to much higher temperatures in all the detectors, the quantitative relation between the ionization rate of the particle and the track etching rate is disturbed. Consequently, for particle identification to be possible, all tracks must have identical thermal histories above 328° K (ideally no exposure above that temperature). To keep temperatures less than 328° K in full sunlight during both translunar flight and the time on the Moon, panels 1, 2, and 3 were covered with a perforated thermal control material, 0.005-cm Teflon backed with thin silver and Inconel coatings (a composite that has a high reflectivity in the visible region of the solar spectrum and a high emissivity at infrared wavelengths). The space-exposed surfaces of the detectors also were coated with a 210-nm aluminum film to avoid ultraviolet (UV) exposure of the plastics, which is known to affect track etching rates (refs. 15-8 and 15-9). Because of the slowing down of cosmic ray nuclei in the silver-backed Teflon, particles of less than 5 to 6 MeV/nucleon are registered in the plastic detectors only through the perforations in the Teflon. There were sixty 0.3-cm-diameter perforations above the Lexan detectors (4.26 cm^2 total area) and 15 above the Kodacel (1.06 cm^2 total). Similarly for the glasses (fig. 15-5), nuclei of less than 10 to 20 MeV/nucleon are registered only beneath the single 0.5-cm-diameter hole that was positioned over the center of each glass plate.

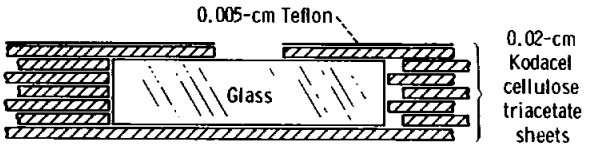


FIGURE 15-5.–Exposure of glass detectors. Glass plates were recessed within the triacetate sheets as sketched. Except for the single 0.5-cm-diameter perforation, the aluminized glass was covered by a 0.005-cm Teflon sheet and a 0.02-cm triacetate sheet. The 0.3-cm-diameter perforations allowed portions of the top Lexan and Kodacel sheets to be directly exposed. The Teflon was backed by a 165 ± 15 nm silver coating covered with an 85 ± 15 nm Inconel layer.

Consequently, for the low-energy nuclei that are of primary interest, the Teflon constitutes a shield, the quantitative effect of which on the observed track density can be calculated. For an isotropic bombardment with φ nuclei/[(area) X (solid angle)], the track density ρ is given by $\int \varphi \cos\theta \, d\Omega$ where θ is the angle of incidence and the integration is over the solid angle Ω permitted by the Teflon shield and the cone angle of the etched tracks. The Teflon is approximated by a straight-edged semi-infinite sheet spaced a distance h from the detector. For this case, the ratio ρ/φ depends only on the track cone angle θ_c and the ratio u of the distance x along the detector under the shield to the spacing h. The result

$$\rho/\varphi = \cos^2\theta_c \cos^{-1}\left(u \tan\theta_c\right) - \left(1 + u^{-2}\right)^{-1/2} \tan^{-1}\left(\left[1 - \left(u \tan\theta_c\right)^2\right]^{1/2} \Big/ \left[\tan\theta_c \left(1 + u^2\right)^{1/2}\right]\right) \quad (15\text{-}1)$$

is plotted in figure 15-6 for various values of θ_c. The figure illustrates how increasing the cone angle decreases the observable track density and increases the abruptness of the transition from maximum to zero track density near the edge of the shield. These same results are useful for computing effective solid angle of detection for particles of all energies in the case of a thick shield such as the Moon was while the experiment was located close to the lunar surface.

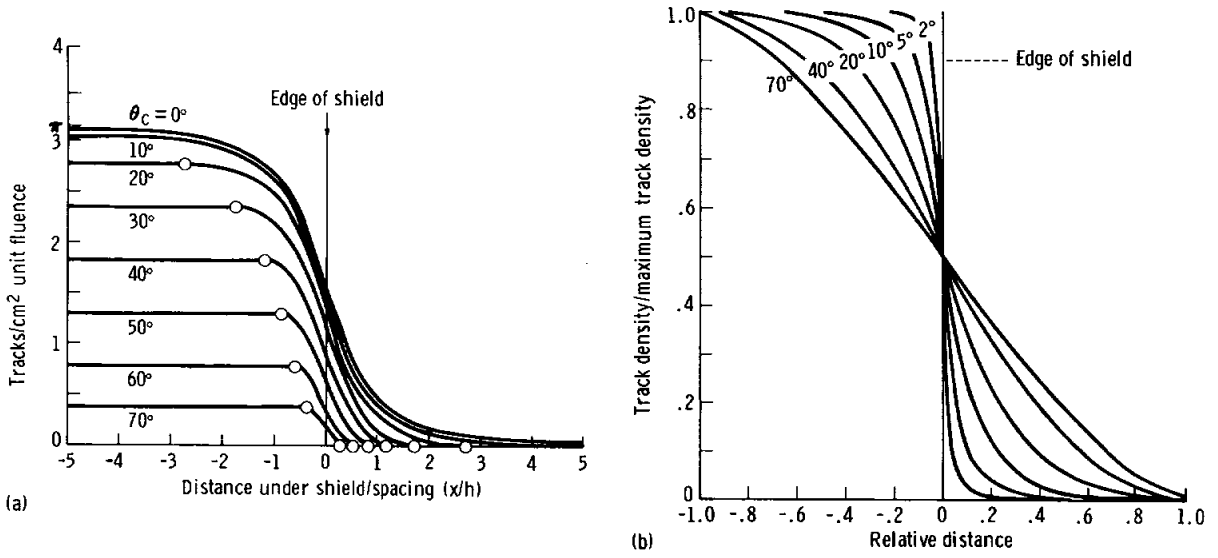


FIGURE 15-6.–Effect of a shield on the etchable tracks per unit fluence as a function of track cone angle. (a) The x is the distance under a parallel, semi-infinite shield a distance h from the detector surface. (b) Normalized data relative to the position where the etched track density goes to zero.

Operation of the Experiment

The experiment was exposed during the mission for nearly 1 week, distributed in time and possible solid angle as listed in table 15-I. The solid angle restrictions listed are merely the shadowing effects of the Moon. The degree of obstruction caused by struts, the scientific equipment bay, and other portions of the spacecraft varies with different positions in the array. For panels 2 and 3, the obstruction is such that the best solid angle factors for $\theta_c < 20°$ are probably those calculated for θ_c = 20°. The LM orientation distribution during lunar orbit prior to landing has been averaged for the appropriate 30.1-hr period. As noted in table 15-I, the last part of the exposure occurred on the LM minus Y footpad with the apparatus leaning against the strut with its face in the down-Sun direction and tilted upward at an angle of 69° to the horizontal, as inferred from a pair of up-Sun and cross-Sun photographs. This shift of the experiment from the LM was a contingency procedure designed to minimize solar heating by exposing to the direct Sun only the multilayer insulation at the back of the experiment.

Although the clean equipment should not have overheated, a deposit of as much as a 10-percent cover of lunar dust or other deposit with similar

TABLE 15-I.–Cosmic Ray Exposure of the Cosmic Ray Experiment

Mission segment	*Time, hr*	*Relative solid angle*	*Tracks per unit flux*		
			$\theta_c = 0°$	$\theta_c = 20°$	$\theta_c = 70°$
En route to Moon	71.4	1.0	3.14	2.76	0.164
In lunar orbit	30.1	0 to [a]1.0	.726	.541	.030
On LM on Moon	20.7	.5	1.57	1.38	.082
On LM footpad (69° to horizontal)	44.9	.64	1.95	1.70	~0
Weighted averages	–	.75	2.19	1.87	.085
Total	167.1	–	–	–	–

[a]Variable with time; 0.5-hr averages used.

optical and infrared properties would have produced excessive heating before the end of EVA 3. Temperature labels designed to sense the approach to the permitted upper limit were located on the outboard face of the frame. Near the end of EVA 1, all these labels were observed by the commander to have been affected, signaling that the polycarbonate temperature had exceeded 318° K; therefore, the contingency procedure was followed at that time. After retrieval, temperature labels within the plastic stacks indicated temperatures of 339° ± 6° K within panel 3 and a part of panel 2, and 350° ± 6° K in another part of panel 2. The temperatures observed in panels 1 to 3 correlate with the dust (or contamination) found on the retrieved panels, the highest temperature (>355° K) occurring in panel 1 and the lowest (<344° K) in panel 3. It is presently not known whether the "dust" cover occurred from rocket exhaust at the time of LM withdrawal from the service module/LM adapter or from ricocheting lunar dust at the time of lunar landing. This is a matter of some consequence because, in the latter case, tracks formed before landing will have had a common thermal history above 328° K.

Solar Flare

During the translunar part of the mission, a medium-size solar flare occurred that contained $\approx 10^8$ protons/cm^2 of energies greater than 5 MeV. Preliminary data, for the flux in various energy intervals, from several satellites are shown in figure 15-7. (The data are from the following satellites: Applied Technology Satellite (ATS), Interplanetary Monitoring Platform (IMP), Pioneer, and Vela.) No extra particles were observed beyond the general steady background at energies greater than 60 MeV. Most of the flare particles arrived before lunar landing; only a few percent greater than 5 MeV arrived after landing, and, even for the slowest particles for which data are available (0.46 to 0.90 MeV), less than 10 percent arrived after landing. If the dust were deposited on the experiment during landing, virtually all the flare tracks recorded will have had the same subsequent thermal history. Even if this were not the case, the highest temperatures to which the detectors were exposed were experienced during the 20.7 hr when the experiment was facing the Sun while on the lunar surface. As a result, most of the thermal effects on solar flare tracks were concentrated in that period and were common to virtually all of the solar particles.

Procedure

Etching and read-out have been performed on Lexan sheets from panel 2 and on glass 1457 from panel 3. For glasses, the final steps in the preflight preparation were annealing (for the tektite and glass 1484, removing preexisting tracks), polishing, etching, inspecting, and coating with an evaporated aluminum reflective coating approximately 210 nm thick. The 210-nm aluminum coating was also present on the top Lexan and Kodacel sheets. After the flight, before the panels were disassembled, the outlines of the 0.5-cm-diameter openings above the glasses and the 0.3-cm-diameter holes above the plastics were scribed into the detector surfaces.

The track etching rates of the detectors can be altered by thermal annealing, the glasses to a lesser extent than the plastics. In figure 15-8, the changes in the track etching rates caused by 1-hr anneals are shown for several glasses. In figure 15-8, V_T is the average track etching rate for californium-252 fission fragments, and V_G is the general etching rate for unirradiated regions. The extreme cases, GE phosphate glass 1457 and Corning glass 1720, are two of the glasses flown on this experiment.

After the panels were disassembled, the glass samples were carefully sectioned by sawing from the underside through most of the thickness and then fracturing the remaining near-upper-surface thickness to avoid the loss of valuable surface material.

One portion of each glass was then etched in room-temperature sodium hydroxide for 1 to 2 min to remove the aluminum coating. The same part was then etched in 50 percent hydrofluoric acid to remove approximately 0.5 μm of glass from each surface to reveal cosmic ray tracks. The etched glasses were scanned at 1000X in an optical microscope, then were replicated (cellulose acetate, gold coated), and scanned at 5000X in a scanning electron microscope (SEM). Parts of the top sheet of Lexan, after removal of the aluminum by a 296° K sodium hydroxide solution, were etched for 3 or 6 hr in 313° K 6.25N sodium hydroxide solution saturated with etch products (ref. 15-10). In one case, a preirradiation with UV was used to accelerate etching attack

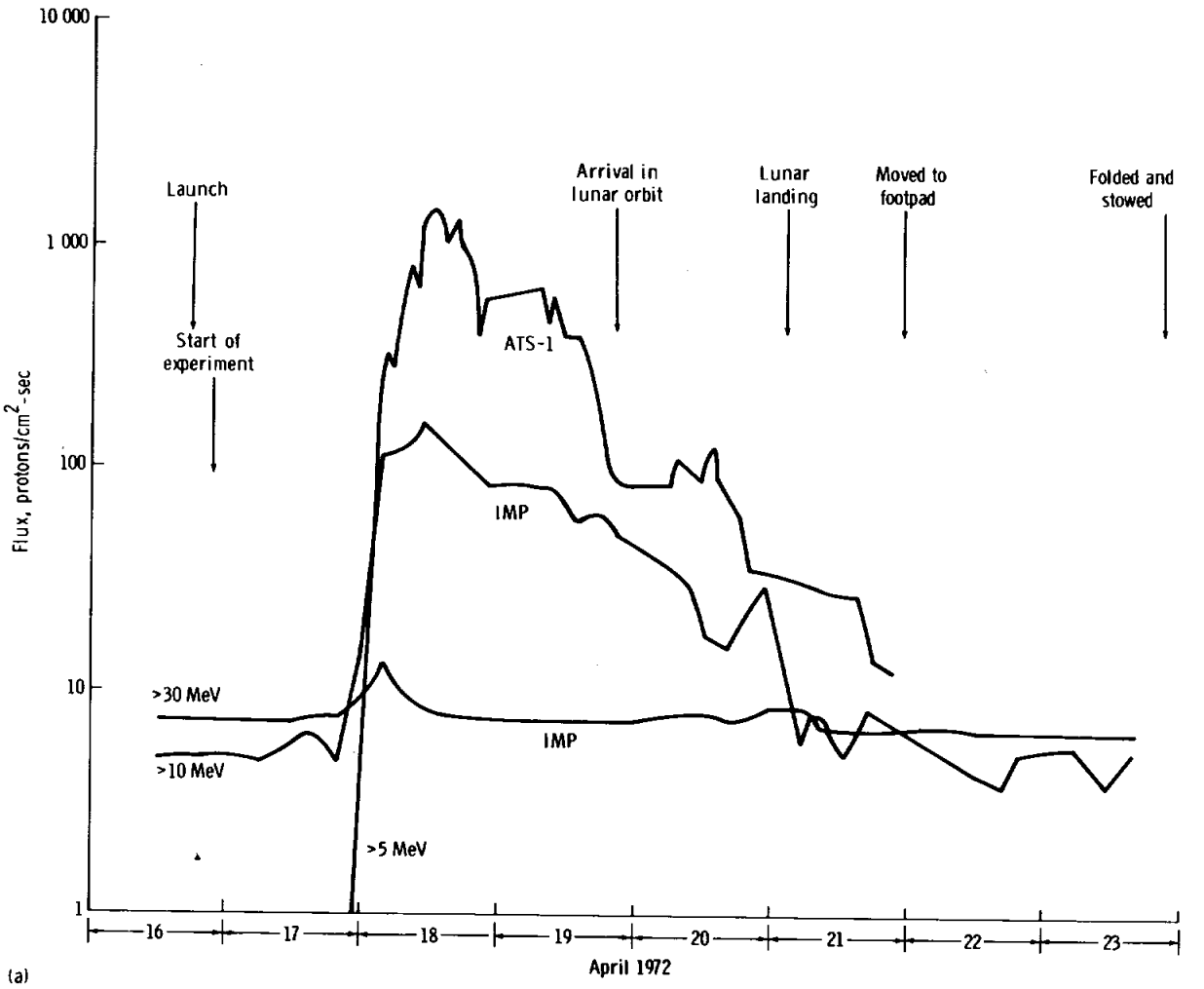


FIGURE 15-7.—Proton flux observed by various satellites during the first week of the Apollo 16 mission. The relevant operations affecting the cosmic ray experiment are noted at the top of each part of the figure. In all cases, the data are preliminary and subject to change. Data courtesy of C. Bostrom (IMP), G. Paulikas (ATS), and S. Singer (Vela). (a) Flux >5, >10, and >30 MeV.

along the tracks (refs. 15-8 and 15-9). Results are given in this subsection for a 6-hr etch of a sheet from the lower left part of panel 2 (hole 2) and a 6-hr etch of a UV-treated sheet from the upper right corner of panel 2 (hole 59). These parts are thought to correspond to the warmest and coolest parts of panel 2, respectively, as judged from the distribution of dust cover and temperature label readings. Sheets 2 to 11 below hole 2 were etched 40 hr under the etching conditions described previously. Solar flare tracks on the exposed surfaces of the phosphate glass and Lexan are shown in figure 15-9. From the optical scans in the central open regions of the different detectors, the track length distributions given in table 15-II were obtained. The differential energy spectrum is derived from these track lengths using range-energy relations (ref. 15-11) for iron nuclei, allowing for the thicknesses of the aluminum layer and the layer etched away and assuming that the aluminum is crossed at 45° incidence.

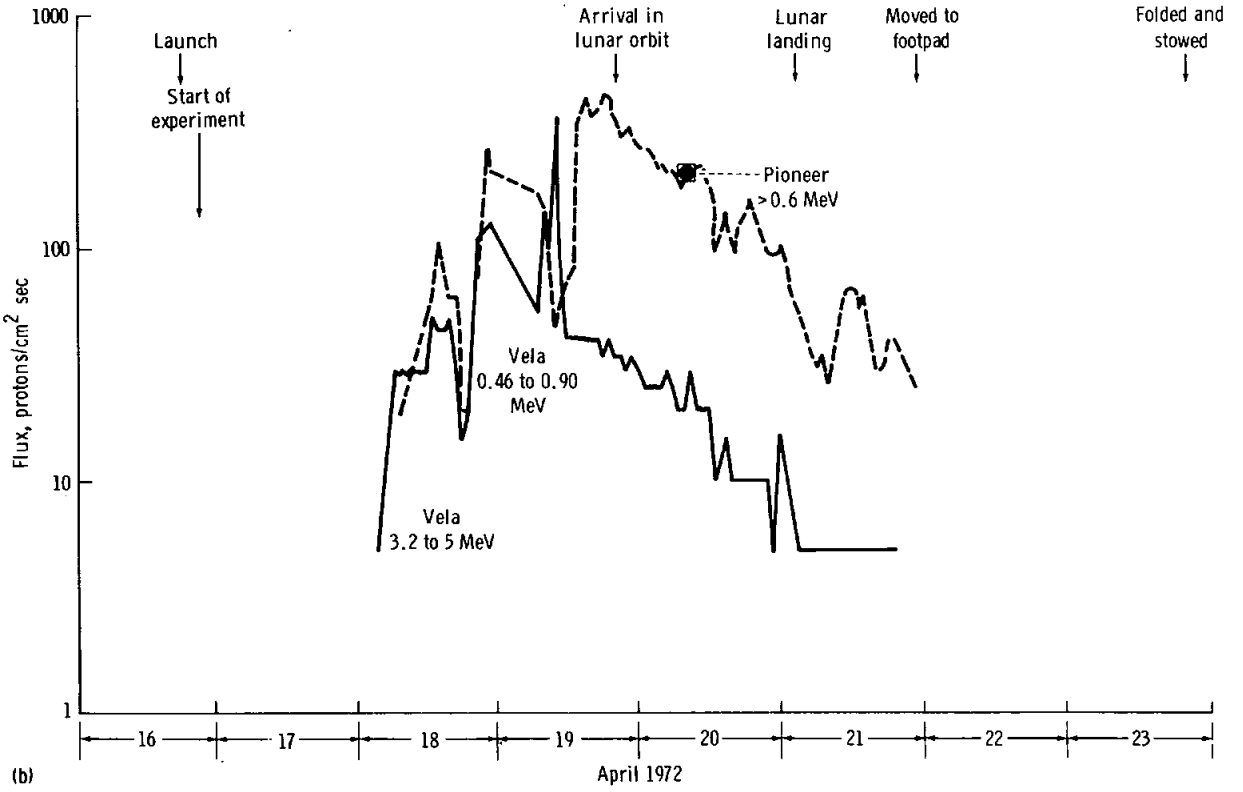


FIGURE 15-7.–Concluded. (b) Flux in the intervals 0.46 to 0.90 MeV and 3.2 to 5.0 MeV.

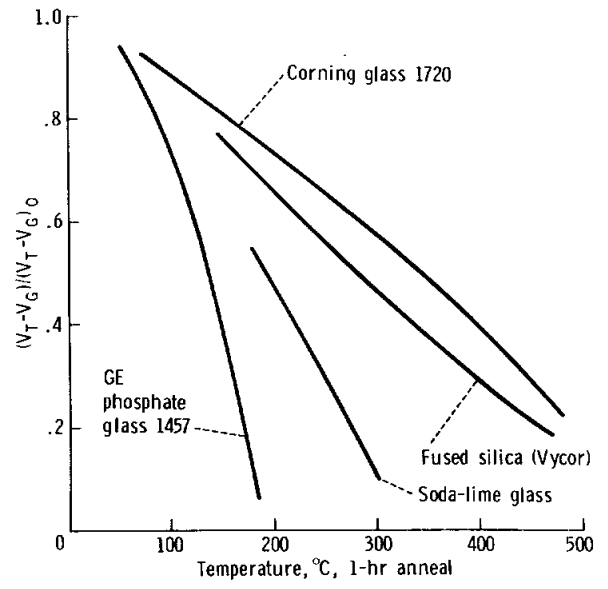


FIGURE 15-8.–Annealing of the track etching rate for californium-252 fission fragments in several glasses. The V_T is the average track etching rate, and V_G is the general etching rate for an unirradiated region. The reference V_T is that obtained after a long time at room temperature.

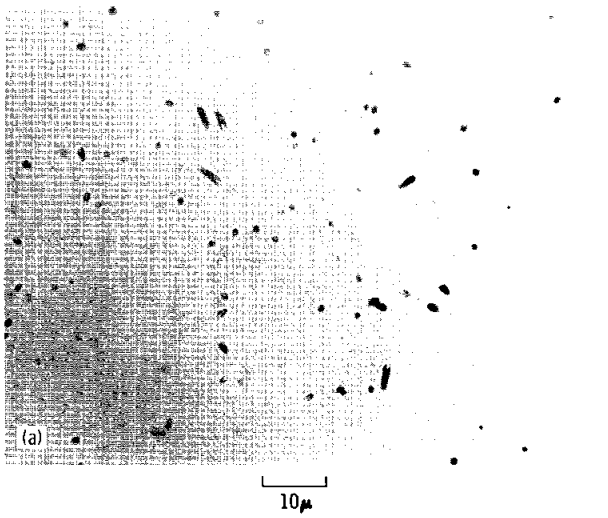
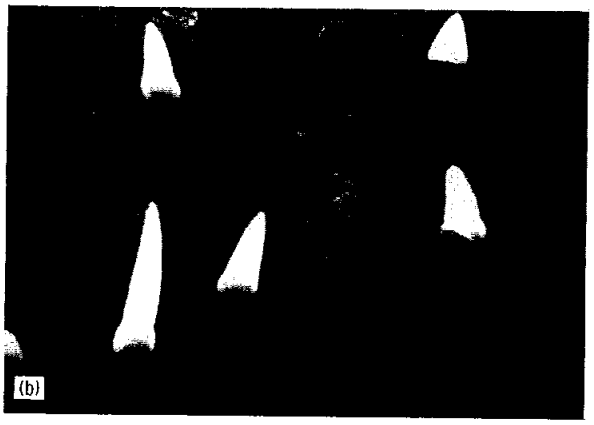
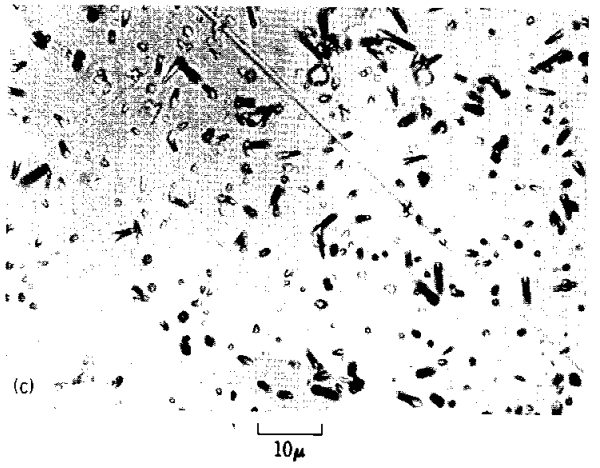


FIGURE 15-9.–Heavy solar cosmic ray tracks in plastic and glass detectors. The surface removal is 5 X 10^{-5} cm for the glass and 10^{-4} cm for the plastic. (a) Glass 1457 viewed optically.





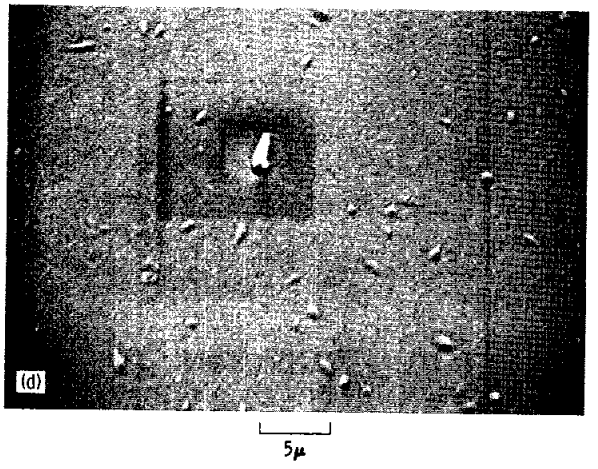


FIGURE 15-9.–Concluded. (b) Glass 1457 viewed in a scanning electron microscope. The SEM replica is cellulose acetate. (c) Lexan polycarbonate hole 4 viewed optically. (d) Lexan polycarbonate viewed in a scanning electron microscope. The SEM replica is silicone rubber.

TABLE 15-II.–Track Length Distributions at Detector Surfaces

(a) Track length

Length, cm	*Number*	*Tracks/cm²*
Phosphate glass 1457		
(0 to 0.5) × 10^{-4}	82	0.92 × 10^{6}
(.5 to 1.0)	26	.29
(1 to 2)	19	.21
(2 to 3)	10	.11
(3 to 6)	10	.11
Lexan (hole 2, 6-hr etch)		
(0.1 to 0.5) × 10^{-4}	108	1.1 × 10^{6}
(.3 to 1)	127	1.3
(.5 to 1)	65	.65
(1 to 2)	~50	1.5
(2 to 3)	51	.52
(3 to 4)	34	.35
(4 to 6)	25	.064
(6 to 8)	20	.034
(8 to 11)	9	.0066
(11 to 14)	9	.0042
(14 to 17)	6	.0028
(17 to 30)	3	.0014
Lexan (hole 59, UV + 6-hr etch)		
(0.5 to 1.5) × 10^{-4}	22	1.34 × 10^{6}
(.5 to 2.0)	79	2.07
(1.5 to 2.5)	8	.49
(2.4 to 4.5)	10	.61
(4.5 to 6.5)	5	.31
(6.5 to 10.5)	3	.18
(10.5 to 18.5)	3	.18

(b) Track density at exterior surface

Phosphate glass 1457	1.8 (±0.1)
Lexan (hole 2, 6-hr etch)	6.10 (±0.35) optical
Lexan (hole 59, UV + 6-hr etch) ..	7.5 (±0.3)

The justification for assuming that all particles are iron in computing the energies derives from the plot given in figure 15-10. For GE phosphate glass 1457, neon ions give tracks having an average cone angle of 30° to 35° over a distance of approximately 15 μm. The SEM photographs of cosmic ray tracks give the cone angle distribution for the >1-μm tracks shown in figure 15-10. This cone angle distribution indicates that the tracks are predominantly from particles much heavier than neon. Separate experiments by the

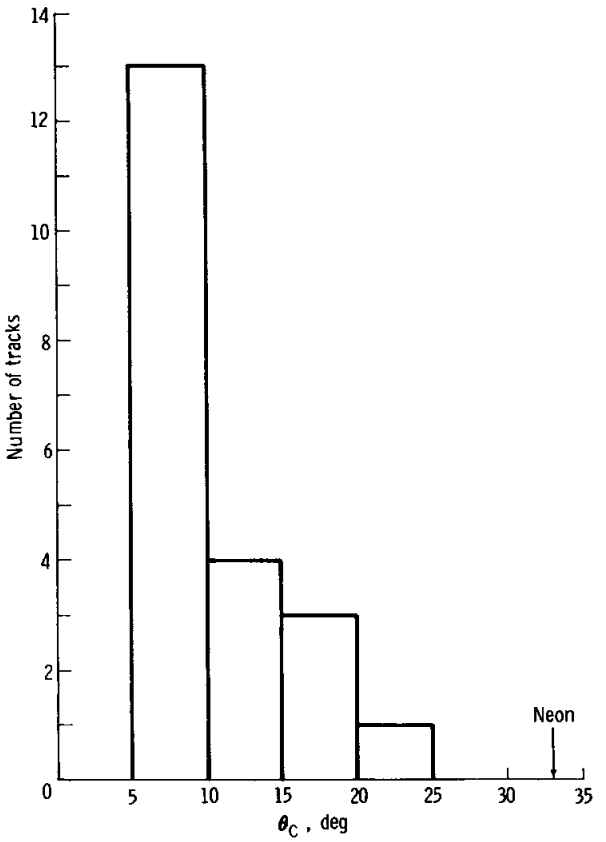


FIGURE 15-10.—Distribution of projected cone angles measured for solar flare tracks in phosphate glass 1457. The angles are obtained from SEM photographs of a cellulose acetate replica after a 12-min etch of the glass in 50 percent hydrofluoric acid.

authors with M. Saltmarsh and A. E. van der Woude of argon-40 and iron-56 beams indicate that the tracks were made by ions heavier than argon and close to iron in atomic number. From known solar abundances (ref. 15-12), it is expected that iron is dominant and that most of the nuclei observed have range-energy relations that are adequately approximated by that of iron. The justification in using iron for the 6-hr etch of hole 2 is that the results there agree with the phosphate glass. For hole 59 (UV treatment before a 6-hr etch), this assumption will be shown to be useful but quantitatively wrong.

Particles stopping at greater depths than were observed at the exposed Lexan surface could be counted on the same surface but beneath the silver-backed Teflon, at the back of the top sheet, and in sheets 2 to 11. These data lead to spectral information at ≈10 MeV/nucleon and above.

One interesting anomaly was the observation beneath the silver-backed Teflon of a high density (≈3000 tracks/cm^2 in the non-UV-irradiated Lexan and ≈10 000 tracks/cm^2 in the UV-irradiated Lexan) of short tracks ranging to ≈10^{-3} cm long with rapidly decreasing numbers of tracks with increasing length. Such tracks were fewer at the opposite side of the Lexan sheet (depth 0.035 to 0.050 cm rather than 0.010 to 0.014 cm). The falloff with depth is too rapid to be consistent with direct effects in the plastic of the appreciable proton irradiation from trapped particles encountered while leaving the vicinity of the Earth. A proton flux of ≈3 X 10^9 protons/cm^2, >3 MeV, and ≈8 X 10^6 protons/cm^2, >30 MeV, is inferred from reference 15-13, extrapolating to greater distances from the Earth on the basis of reference 15-14. The most likely source of the short tracks is the aluminum-Inconel-silver-Teflon composite adjacent to the surface where these short tracks were found. Whether these are reaction products, compound nuclei, or recoil nuclei has not been determined. The cosmic ray flux at 0.010- to 0.014-cm depth was inferred from the abundance of tracks >15 X 10^{-4}-cm length, which appear to form a distinctly separate population.

Energy Spectra

The energy spectra inferred for heavy particles and that derived for protons from the satellite data in figure 15-7 are shown in figure 15-11. The non-UV-irradiated Lexan gives results that are indistinguishable from those of the phosphate glass. Because those tracks have been identified as from iron nuclei or those close to iron in atomic number, the composite curve (the lowest of the three in figure 15-11) applies to the iron group nuclei.

The curve for the UV-irradiated Lexan lies generally above that for the non-UV-irradiated samples; examination of additional samples has shown that this difference is primarily caused by the effect of the UV in lowering the effective threshold for particle track registration (ref. 15-9). The approximate 10-to-1 ratio of differential fluence in the 20- to 60-MeV/nucleon range would be consistent with nuclei down to carbon-12 being revealed in the Lexan, as judged by neon-20 calibration tracks and as is consistent with the solar flare composition observed by Mogro-Campero and Simpson (ref. 15-15). Recalculation of the energy spectrum to include the carbon-nitrogen-oxygen (CNO) group for the UV-

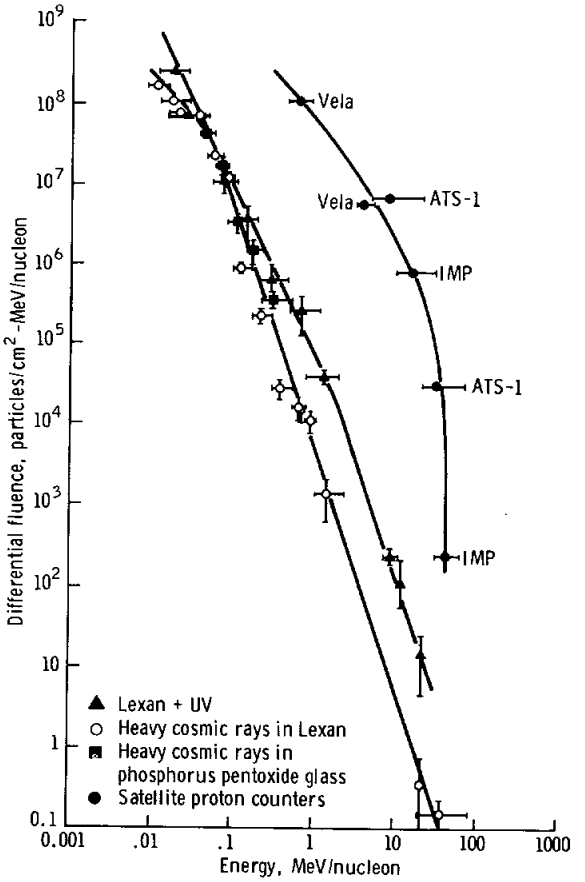


FIGURE 15-11.–Differential energy spectra for heavy cosmic rays during the period April 16 to 23, 1972, compared to the spectrum derived from various satellite proton counters. Fluence is given in protons/cm^2-MeV/nucleon integrated over a 2π solid angle. Proton data are derived from those given in figure 15-7.

irradiated sample would steepen the curve slightly but would not alter its qualitative character significantly.

Discussion

The spectrum for iron group cosmic ray is given by an energy$^{-\gamma}$ $E^{-\gamma}$ relation, where the spectral index γ is 3 (±0.3) from 30 MeV/nucleon down to 0.04 MeV/nucleon and flattens to $\gamma = 1$ (±0.5) from 0.04 to 0.01 MeV/nucleon. The $\gamma = 3$ result is identical to a previous conclusion (ref. 15-16) in the energy range 1 to 100 MeV/nucleon from examination of Surveyor III filter glass and with that of Mogro-Campero and Simpson from their counter telescope in the range 3 to 60 MeV/nucleon (ref. 15-15). The result is also similar to the results of two other studies of the Surveyor glass (refs. 15-17 and 15-18) although the spectrum was not expressed as E^{-3} in those papers.

The proton-to-iron ratios listed in table 15-III were derived from this result. With decreasing energy, the ratio decreases from 15 times the photospheric value at 10 MeV/nucleon to 0.05 times that value at 0.3 MeV/nucleon (ref. 15-19). Although proton data are lacking at the lower energy, the trends in the curves in figure 15-11 suggest that this enrichment in the heavy nuclei continues at least another order of magnitude in energy down to the break in the slope of the iron group curve. The existence of increasing enhancement of iron towards lower energies is in agreement with previous results by Price et al. (ref. 15-18) and Mogro-Campero and Simpson (ref. 15-15) but is quantitatively less at the same energies. The present results, however, extend to much lower energies.

TABLE 15-III.–Ratios[a] of Proton Flux to Iron Flux

Energy, MeV/nucleon	*Proton flux/iron flux*
10	4×10^5
3	6.5×10^4
1	1.2×10^4
.3	1.2×10^3

[a]Abundance ratio in photosphere = 2.5×10^4.

If the UV-irradiated data are recalculated on the assumption that oxygen-16 is the most abundant species present (approximating CNO plus all heavies by using oxygen range-energy curves), ⩾ carbon/⩾ iron ratios can be estimated: 25 (10 MeV/nucleon), 35 (3 MeV/nucleon), 40 (1 MeV/nucleon), 9 (0.3 MeV/nucleon), approximately 2 (0.1 MeV/nucleon), and approximately 1 (0.03 MeV/nucleon). A strong relative enrichment of iron relative to the lighter nuclei is apparent at low energies. These ratios are to be compared with values of 8 found by Mogro-Campero and Simpson (ref. 15-15) near 20 MeV/nucleon and 84 found by Bertsch et al. (ref. 15-20) near 60 MeV/nucleon, both these results being averages for groups of flares. The trend of relative enrichment of iron towards lower energies is again clear.

The relative heavy element enrichment at low energies is associated with the position of the decrease in the magnitude of slope of the energy

spectra, which occurs at progressively higher energies from iron (≈0.04 MeV/nucleon) to "⩾ carbon" (≈1 MeV/nucleon) to hydrogen (≈10 MeV).

Total iron down to ≈0.01 MeV/nucleon is ≈4 X 10^6 particles/cm^2 per 2π solid angle as compared to ≈2.2 X 10^8 protons/cm^2 (as derived from fig. 15-11); these numbers give an enrichment by a factor ≈450 relative to the photospheric value. However, because the proton fluence below 0.3 MeV is unknown, the quantitative meaning of this value is not clear. It does, however, strongly suggest that the heavies in the solar flares are in fact appreciably more abundant than in the surface of the Sun. The preferential enhancement at low energies of the heavier nuclei because of their low charge-to-mass ratio was predicted in 1958 by Korchak and Syrovatskii (ref. 15-21).

Summary

Solid-state track detectors were exposed to the solar flare of April 18, 1972, during the Apollo 16 mission and etched to reveal tracks of cosmic ray nuclei. Iron group nuclei were observed in phosphate glass and desensitized Lexan polycarbonate detectors, and their spectrum was measured down to ≈0.02 MeV/nucleon, nearly two orders of magnitude lower in energy than had previously been observed in such nuclei. The relative enrichment of iron relative to lighter nuclei previously seen at higher energies continues to increase into the new low-energy region. The energy spectrum of particles equal to or greater than carbon is inferred from sensitized Lexan polycarbonate and allows the relative enrichment of iron relative to the medium and heavy nuclei to be estimated down to 0.03 MeV/nucleon.

Acknowledgments

The authors are indebted to C. Bostrum (Johns Hopkins U.), G. Paulikas (Aerospace Corp.), and S. Singer (Los Alamos) for permission to quote their satellite proton results; to W. R. Giard, M. McConnell, and G. E. Nichols (General Electric Research and Development Center) for experimental assistance; and to M. Saltmarsh and A. van der Woude (Oak Ridge National Laboratory) for permission to quote joint work prior to publication.

PART B

COMPOSITION OF INTERPLANETARY PARTICLES AT ENERGIES FROM 0.1 TO 150 MEV/NUCLEON

P. B. Price,[a] D. Braddy,[a] D. O'Sullivan,[ab] and J. D. Sullivan[a]

Introduction

The University of California cosmic ray experiment on Apollo 16 was designed to identify tracks of energetic nuclei with atomic numbers $Z \geqslant 2$ in the energy interval from ≈0.2 to ≈150 MeV/nucleon. Improved techniques allowed the energy interval to be extended to ≈0.1 MeV/nucleon. The goal of the experiment was to determine the composition and origin of interplanetary particles in the little-explored energy interval between solar wind energies (≈10^{-3} MeV/nucleon) and energies accessible to balloon-borne instruments (≈300 MeV/nucleon).

Energy spectra determined during solar quiet times by electronic detectors on satellites have been published (refs. 15-22 to 15-24) for iron group nuclei ($25 \leqslant Z \leqslant 28$) down to energies of ≈150 MeV/nucleon; for neon, magnesium, and silicon down to ≈50 MeV/nucleon; for boron and carbon, nitrogen, and oxygen (CNO) down to ≈40 MeV/nucleon; and for isotopes of hydrogen (H) and helium (He) down to ≈10 MeV/nucleon. The presence of boron, which is largely a spallation product of CNO, suggests that medium-charge galactic cosmic rays are present in interplanetary space down to energies of ≈40 MeV/nucleon. The presence of ^{2}H and ^{3}He, which are

[a]University of California at Berkeley.

[b]On leave from Dublin Institute for Advanced Studies, Dublin, Ireland.

largely spallation products of ^{1}H and ^{4}He, suggests that low-charge galactic cosmic rays are present down to even lower energies (≈10 MeV/nucleon). Nothing has been known before now about the origin (or even the existence) of nuclei at energies less than ≈10 MeV/nucleon present during solar quiet times. For heavy nuclei such as iron, knowledge is limited to greater than ≈150 MeV/nucleon. The limitation has been an experimental one. Electronic detectors on satellites detect only particles with range sufficient to penetrate various windows. Recent improvements in electronic detector design are reducing the minimum accessible energies, but experiment results for quiet times have not yet been published.

At very low energy (≈10^{-3} MeV/nucleon), the Sun continuously emits particles from hydrogen up to at least iron, the solar wind. Light ions of solar origin have occasionally been detected in interplanetary space with suprathermal energies (typically ≈0.01 MeV/nucleon) (ref. 15-25); and tracks of heavy ions ($Z \geqslant 20$) with energies above 0.01 MeV/nucleon have been observed in a glass filter from the Surveyor III camera (refs. 15-26 to 15-28), in an Apollo 12 spacecraft window (ref. 15-28), and in the lunar soils and rocks (refs. 15-29 and 15-30). In all these cases, it is most likely that the ions originated in solar flares.

The Solar Flare of April 18, 1972

A solar particle event occurred on April 18, 1972 (the second day of the Apollo 16 mission). It is not known what activity at the Sun was responsible, but the probable activity was just beyond the west limb, associated with a small X-ray burst and prominence activity about 1800 Greenwich mean time on April 17. The solar particle event had an extremely steep energy spectrum. The proton counting rates are given in figure 15-12. The energy spectrum was so steep that it was possible to study the composition of solar particles and, at the same time, to study preexisting interplanetary particles although not at as low an energy as originally hoped. Previously, the composition of solar particles emitted in only the most intense flares that occur occasionally during an 11-yr cycle had been studied. Rockets, which remain aloft for only approximately 4 min, are reserved for those rare flares of sufficient intensity to provide results of statistical significance. At energies of a few million electron volts per nucleon, flare particles have recently been found to be enriched in heavy nuclei such as iron (refs. 15-28, 15-31, and 15-32). The Apollo 16 experiment made it possible to test whether the composition depends on the strength of the flare as well as on energy.

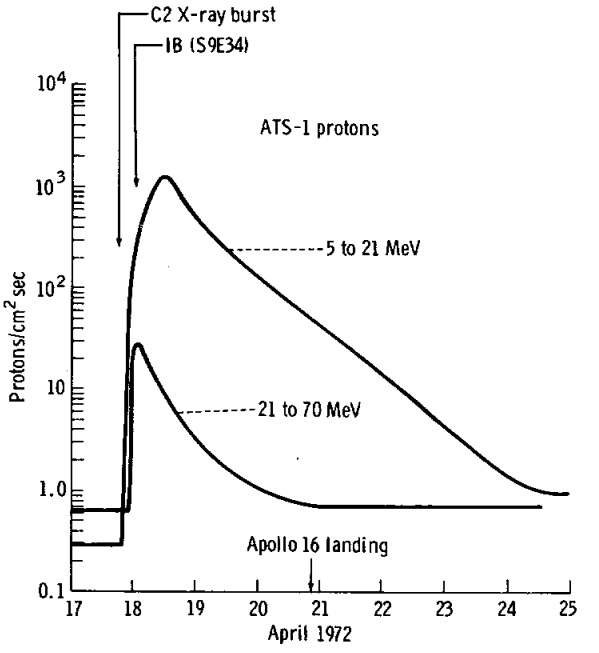


FIGURE 15-12.–Counting rates for protons in two different energy intervals determined on the Applied Technology Satellite (ATS).

Identification of Charged Particles

Dielectric track detectors have the following significant advantages over electronic detectors.

(1) Dielectric track detectors are not restricted in counting rate and can record solar flare particle tracks or galactic particle tracks with equal efficiency. Therefore, the problem of having the most abundant nuclei (hydrogen and helium) monopolize the data storage system does not arise.

(2) With ingenuity, dielectric track detectors can be used to energies much less than 1 MeV/nucleon. No inert window is needed, and the minimum range necessary for an acceptable signal may be as little as 1 μm in special cases.

(3) Dielectric track detectors can be made in virtually any size.

(4) A dielectric track detector can be used with a threshold that discriminates against unwanted particles below some minimum ionization rate.

The sensitivity of certain plastic detectors (Lexan, in particular) is increased by an ultraviolet (UV) irradiation. Coating the top sheet with 100 nm of aluminum is sufficient to eliminate that problem.

The chemical reactivity of tracks may decrease at elevated temperatures such as are reached in full sunlight on the lunar surface. The design of the heat shield is discussed in part A of this section.

The techniques for identifying charged particles by etching dielectric solids have been discussed in a comprehensive review (ref. 15-33), which includes chemical etching reagents for Lexan, cellulose triacetate (CTA), and silica glass. The following paragraphs contain a brief synopsis of the basic technique.

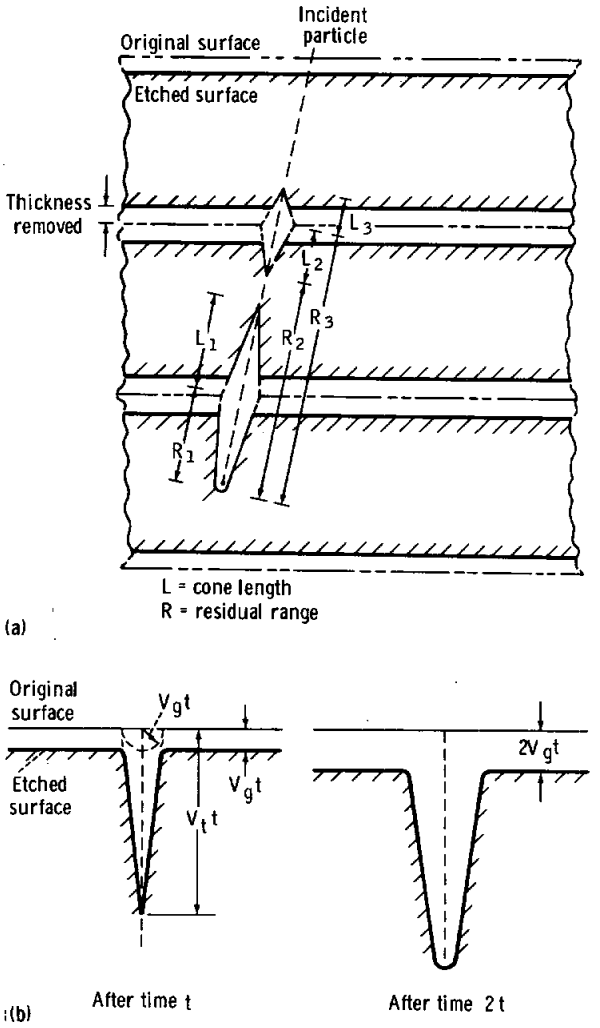


FIGURE 15-13.–Particle identification by etching rate method.

The basic idea (fig. 15-13) is that the rate of dissolution of a dielectric solid in a chemical etching solution is faster along the trajectory of a heavily ionizing particle than elsewhere. The shape of an etched track is roughly conical and is governed by the local ratio of the rate of etching along the track V_t to the general rate of etching V_g, which applies to all surfaces of the solid (including the exposed walls of the track). After the first etch, the length of an etched cone divided by the etching time gives an average value V_t along that part of the trajectory of the particle. If the particle passed completely through one or more sheets of dielectric solid, then several values of V_t will be obtained that fall on a smooth curve of V_t as a function of R, where R is the residual range of the particle at a point halfway along the cone. From appropriate calibrations with heavy ion accelerator beams, together with an ionization equation of the approximate form $J = AZ^{*2}/\beta^2$ and an empirical relationship between J and V_t, it is possible to generate a set of curves showing the response of a detector to slowing ions of differing Z. In this case, A is a constant, Z^* is the effective charge of the ion, and β is the velocity in units of the velocity of light. An example showing an ion that has passed through two plastic sheets and stopped in a third is shown in figure 15-13(a). Only one etching sequence was necessary. In figure 15-13(b), an ion penetrated only part of a detector. To study such low-energy ions, the etching time must be shortened so that the cone can be initially measured; then the detector is re-etched and the final length of the track is measured. The two measurements give V_t and R.

In the case of the etched cones in silica glass, diameter measurements provide additional information that aids in the determination of Z and R even at extremely small ranges.

The University of California experiment consisted of the following four components.

(1) Panel 1 contained 31 sheets of 250-μm Lexan, each 16.5 by 25.4 cm, fastened so that alternate sheets were translated by 2 mm when the astronauts folded the four hinged panels. This feature made possible the rejection of tracks of cosmic rays that passed through the spacecraft on the return trip. The 31 sheets were covered with a sheet of (50 μm) Teflon silvered on the back and with holes 2.5 cm

apart and 0.5 cm in diameter. The holes allowed a fraction of the stack to have a view of space with no covering material. The Teflon sheet was used to minimize absorption of visible sunlight, maximize emission of infrared, and keep the temperature of the underlying sheets below 343° K.

At some time during the mission, panel 1 became covered with a thin, dull, as yet unidentified film. The thermal properties of the film were so impaired that the final temperature exceeded 353° K. This seriously degraded the performance of panel 1, and, at present, an analysis of the panel has not been begun.

(2) One-half of panel 3 was used in the University of California experiment and contained the following detectors.

(a) A stack of sheets of 200-μm CTA, each 16.5 by 11.5 cm, was fastened so that alternate sheets could be translated 2 mm after the last EVA. Actually, the sheets shifted only $\approx$1 mm, which sometimes made difficult the determination of whether a track occurred before or after the stack was folded and brought into the spacecraft. The perforated Teflon sheet covering the CTA stack worked well; the temperature did not exceed 343° K, as judged by temperature indicating labels. Laboratory annealing experiments showed that tracks of argon and silicon ions in CTA sheets held at 343° K for 24 hr were decreased in V_t by only approximately 10 percent. The techniques illustrated in figure 15-13 were used to analyze tracks of particles with $Z \geqslant 3$ at energies from $\approx$0.2 to $\approx$100 MeV/nucleon.

(b) Tabs of Lexan previously irradiated with argon and krypton ions were inserted at three different depths in the CTA stack. After return, the tabs were etched to see if any fading of the tracks had occurred. The etching rate of the argon tracks proved to be the same, within experimental error, as the etching rate of argon tracks in a control piece kept in the laboratory. The krypton tracks etched three times faster than those in a control sample. At present, the only acceptable explanation is that some solar UV leaked into the panel through one of the holes and increased the reactivity of the krypton sample. Fortunately, CTA is extremely insensitive to UV.

(c) One slab of flame-polished silica glass 2.5 by 2.5 cm, aluminized on the bottom, was mounted on the CTA stack and covered with the Teflon heat shield. The center of the silica detector had a view of space through a 0.6-cm-diameter hole in the Teflon. Calibrations with heavy ion beams showed that, to a very good approximation, none of the ions of common elements in the Sun lighter than iron (e.g., silicon) will provide easily visible etched cones in the silica detector. The silica detector is thus extremely useful for determining the energy spectrum of the solar iron nuclei. It is also useful in searching for trans-iron nuclei among solar particles.

(d) A stack of 40 sheets of 6-μm Lexan, each 5 by 5 cm, was mounted on the CTA stack and covered with the Teflon heat shield. Its central portion viewed space through a 0.5-cm-diameter hole. The function of the stack was to determine the energy spectrum of particles of extremely low energy. Each sheet collects tracks of particles coming to rest in a narrow energy interval corresponding to a thickness of 6 μm of plastic. After irradiating each sheet with an intense dose of UV ($\lambda \approx$360 nm), alpha particles leave visible etched cones in the last 1 to 5 μm of their range. The 6-μm stack thus serves as a differential alpha particle detector. Heavier ions leave tracks with nearly parallel walls that are distinctly different from the conical alpha particle tracks.

A more detailed general description of the overall design and deployment of the four panels, including the role of the astronauts, is given in part A of this section.

Results

Because of the passive nature of the detectors, it should be emphasized that the measurements and identification of tracks will extend over at least a 12-month period, in contrast to electronic experiments, which may be completed soon after a mission ends. At present, the results are still being analyzed, but the following conclusions have been reached.

Energy spectrum of particles with $Z \geqslant 6$.–The pair of photographs in figure 15-14(a) compares etch pits in a piece of silica glass irradiated with a beam of 3 MeV/nucleon iron ions in the University of California 224-cm cyclotron and etch pits in the uncovered portion of the silica glass irradiated in the solar flare. The density of tracks in the uncovered portion of the silica glass was 5×10^5 tracks/cm^2, which represents stopping iron nuclei alone. Some of the $\approx 3 \times 10^6$ tracks/cm^2 in the CTA (mainly $Z \geqslant 6$) are shown in figure 15-14(b), and some of the $\approx 2.5 \times 10^6$ tracks/cm^2 in the Lexan from panel 1 are shown in figure 15-14(c). At the top of the stack of 6-μm

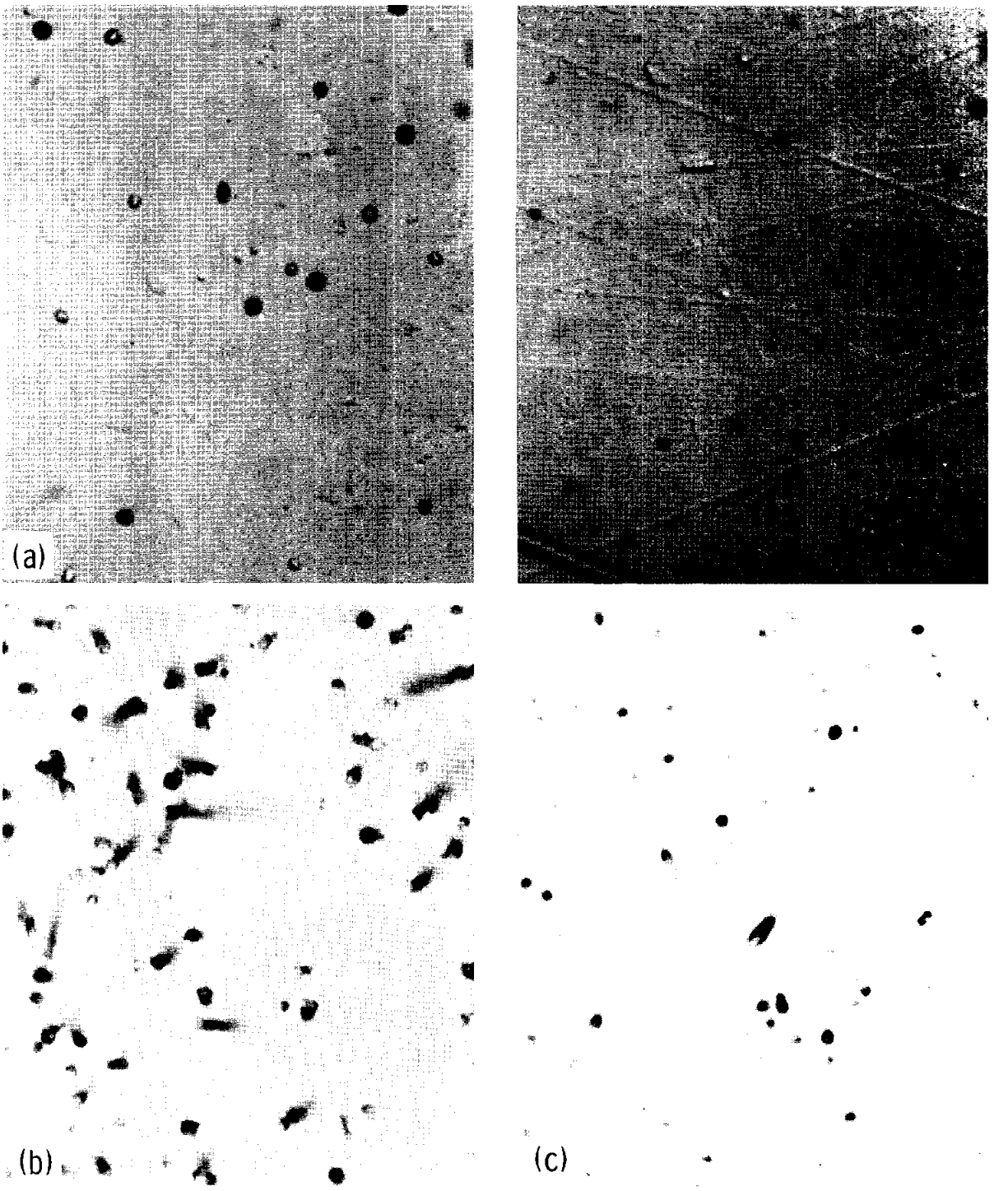


FIGURE 15-14.–Tracks of solar flare particles with $E \approx 0.1$ to ≈ 1 MeV/nucleon. (a) Etch pits of iron nuclei in the silica glass (left) compared with etch pits from iron nuclei produced in an accelerator (right). (b) Etched tracks of nuclei with $Z \geq 6$ in CTA from panel 3. (c) Etch pits of nuclei with $Z \geq 6$ in Lexan from panel 1, which was overheated. Each field of view is 70 by 53 μm.

Lexan sheets, the density of alpha particle tracks was difficult to determine quantitatively amid the background of heavy particle tracks and, at present, only a deeper sheet has been quantitatively studied.

Figure 15-15 shows portions of the energy spectra for four different charge groups: helium, $Z \geqslant 6$ (mainly CNO), $10 \leqslant Z \leqslant 15$, and iron. The helium point at ≈2 MeV/nucleon was determined from tracks of alpha particles that stopped in the part of sheet 3 of the thin Lexan stack that was covered with 50 μm of Teflon. The points for $Z \geqslant 6$ at energies of 0.1 to 1 MeV/nucleon were determined in CTA after a 1-hr etch; the point at 60 MeV/nucleon was obtained from a 30-hr etch. The data for $10 \leqslant Z \leqslant 15$ at low and high energies were obtained from CTA etched for 3 and 30 hr. The low-energy iron point was obtained from measurements in silica glass that was etched 1 hr.

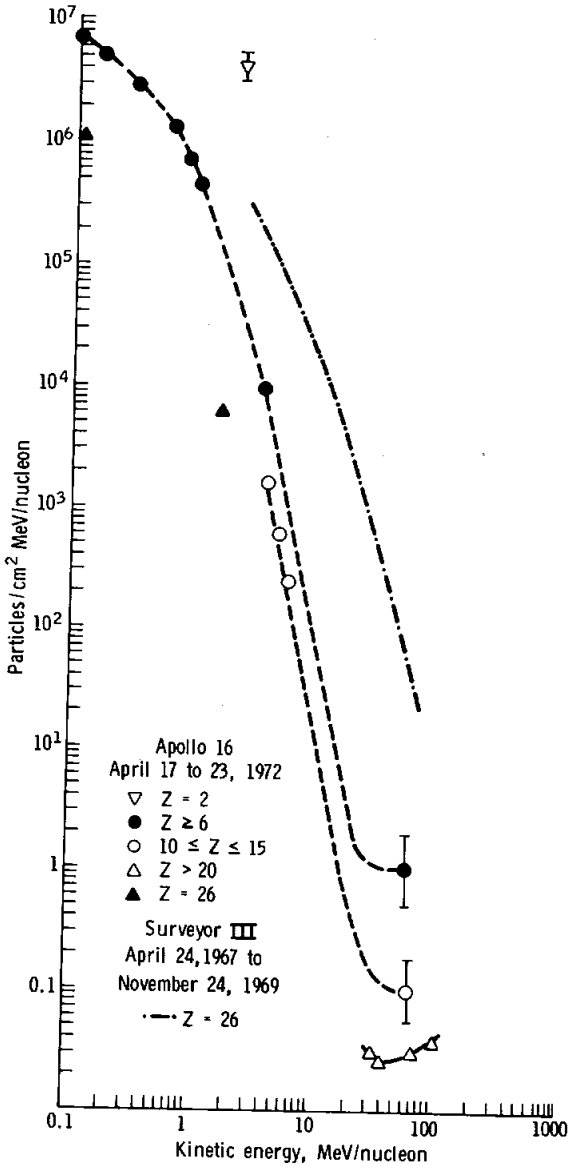


FIGURE 15-15.–Differential energy spectra for various charge groups during the period April 16 to 23, 1972.

One conclusion is that of a steep decrease of flux (by at least seven orders of magnitude) as the energy increases from ≈0.1 to ≈30 MeV/nucleon, followed by a flat portion at higher energies. At its steepest point, the spectrum falls off as $\approx E^{-5}$, where E is energy. With electronic detectors, solar flare energy spectra for protons and alpha particles have previously been observed that range from $\approx E^{-2.5}$ to $\approx E^{-4}$.

The steep portion could be ascribed to a solar contribution and the flatter portion to a galactic contribution that would not be significantly different in the absence of a flare. Compositional evidence supports this contention.

Composition of the solar flare particles.–At present, measurements of individual elements have been made in the CTA only at an energy of ≈4 MeV/nucleon. The limited data obtained from a part of the CTA etched for a time such that nuclei with $2 \leqslant Z \leqslant 14$ could be studied are summarized in table 15-IV. The absence of the secondary nuclei (lithium, beryllium, and boron) strongly supports the contention that the low-energy particles originated in the Sun.

The helium value in table 15-IV was obtained by comparing the helium flux at 2.1 MeV/nucleon in the

TABLE 15-IV.–Relative Abundances of Solar Particles ($E \approx 4$ MeV/nucleon)

Nuclei	*Observed*	*Solar (Cameron)*
Helium	[a]≈3000	2100
Lithium + beryllium + boron	0	≈0
Carbon	11	13.5
Nitrogen	3	2.4
Oxygen	20	24
Neon + magnesium + silicon	4.4	≈3 to ≈7
Iron	[b]6	.9

[a]Determined by comparing the helium flux at 2.1 MeV/nucleon in thin Lexan stack with the curve for $Z \geqslant 6$ in figure 15-15.

[b]Determined from the ratio of track densities in silica glass to track densities in CTA.

stack of the Lexan sheets with the flux of $Z \geq 6$ interpolated from the appropriate curve in figure 15-15.

The iron-to-($Z \geq 6$) ratio was estimated at an energy less than ≈0.5 MeV/nucleon by simply comparing the total track densities in the portions of silica glass and CTA directly under the holes in the Teflon heat shield. From comparisons with the rate of etching of iron tracks in silica bombarded with an iron beam in a cyclotron, it was established that the majority of the tracks in the glass were indeed iron. The result, iron/($Z \geq 6$) ≈ 6 for $E < 0.5$ MeV/nucleon, is uncertain by as much as a factor of 2 because of differences in stopping power of glass and plastic and because of uncertain recording efficiency of iron at large zenith angles in silica and of CNO at large zenith angles in CTA. The iron abundance is recorded in table15-IV.

Until another detector can be flown during a solar quiet time, the composition of the energy spectrum and interplanetary particles in the energy interval ≈0.1 to ≈30 MeV/nucleon cannot be determined.

Composition of the particles with $E > 30$ MeV/nucleon.–A portion of the CTA stack was etched 9 hr, and sheets at four different levels corresponding to mean energies of 34, 40, 75, and 105 MeV/nucleon were scanned for tracks of nuclei with $Z \geq 14$. Definite abundance peaks at silicon and iron, together with peaks at carbon and oxygen obtained in the solar particle identifications, established that the resolution was easily better than ±1 charge unit. Tracks of particles that entered the panel from the back constituted approximately one-third of the total. These tracks were not counted.

The presently available data are summarized in table 15-V. The number of events with $Z \geq 18$, although extremely limited, appears adequate to support the identification of the majority of these nuclei as galactic rather than solar, simply on the basis of the large fraction of secondary nuclei with $17 \leq Z \leq 25$.

Discussion

New capabilities.–With the UV sensitization technique and a stack of 6-μm sheets of Lexan, it is possible for the first time to determine accurate differential energy spectra of alpha particles to energies as low as 0.1 MeV/nucleon and as high as ≈6 MeV/nucleon, the upper value being limited only by the stack depth. When the analysis is complete, it will be possible to determine definitively whether the spectrum rolls over at low energy or monotonically decreases with increasing energy. The identification of the alpha particles is reliable because protons are not recorded and because lithium and heavier nuclei leave tracks with markedly smaller cone angles than those of alpha particles.

Laboratory annealing and etching experiments on CTA have shown that alpha particle tracks are not observable after a 1-hr etch. Assuming no lithium, beryllium, and boron in the solar particles, it is then possible to attribute all observable tracks to nuclei with $Z \geq 6$. Because all nuclei have comparable range-energy relationships over the limited energy interval ≈0.1 to ≈2 MeV/nucleon, it is necessary only to measure range distributions to compute energy distributions for the charge group $Z \geq 6$ in this interval. At higher energies, the tracks are long enough that charges can be identified by the etch/re-etch scheme. One of the major new capabilities in this experiment is the ability to explore the newly accessible interval 0.1 to ≈10 MeV/nucleon.

In this laboratory, studies of the rate of growth of cones with etch time in silica glass have established the feasibility of identifying nuclei heavier than iron. Of the ≈10^5 low-energy solar particles that entered the glass through the hole in the Teflon heat shield,

TABLE 15-V.–Relative Abundances of Heavy Galactic Cosmic Rays

Z	*At ≈40 MeV/nucleon*	*At ≈75 MeV/nucleon*	*At ≈140 MeV/nucleon*
Argon	1	0	2
Calcium	3	3	2
Titanium	1	0	1
Chromium	2	1	0
Iron	3	4	4
Nickel	0	0	1
>30	1	0	0

many are likely to be much heavier than iron. If they have the same composition as the Sun, it should be possible to detect charges to at least $Z = 40$. Several may have already been found that are heavier than iron, but the measurements are still in progress.

Enhancement of heavy nuclei in solar flares.—One of the unexpected results of recent solar flare studies is that at low energies the abundance of heavy elements like iron relative to that of light elements may be enriched by a factor of 10 or more (refs. 15-28, 15-31, and 15-32). At present, it is not clear whether the mechanism is associated with effective charge or ionization potential or some other aspect of atomic physics. It is therefore important to obtain systematic data at various energies and for various flare types. It is particularly important to be able, with the same system, to cover a large charge interval to test the idea of Price et al. (ref. 15-28) of an enhancement that increases with charge. The present system, with a capability of studying particles from helium on up, is ideal.

It is extremely interesting in the present work to find such a large abundance of iron relative to lighter elements at energies of ≈1 MeV/nucleon, as shown in table 15-IV. At energies of tens of million electron volts per nucleon where most of the particles are of galactic origin, no enhancement has been found in this work (fig. 15-15). The relatively high iron flux is thus exclusively associated with the flare particles. As data are accumulated, it will be possible to examine the energy dependence of the enhancement in detail.

Within present statistics, no evidence exists, at energies of ≈2 to 4 MeV/nucleon, for any deviation of the abundances of the elements with $2 \leqslant Z \leqslant 14$ from those expected in the Sun. However, the phosphate glass on Fleischer's panel (part A) shows 1.8×10^6 tracks/cm^2 (private communication) and should record mainly particles with $Z \geqslant 10$; the mica on Walker's panel (part C) shows $\approx 2 \times 10^6$ tracks/cm^2 (private communication) and certainly does not record CNO. These densities are within 50 percent of those in the CTA. All these data together indicate an enhancement of the neon-magnesium-silicon-to-CNO ratio at energies less than 1 MeV/nucleon, which disappears at higher energies.

Comparison of the April 18, 1972, flare spectrum with the Surveyor glass data.—In figure 15-15, the solid curve gives the differential energy spectrum of iron nuclei in interplanetary space integrated over a 2.6-yr interval beginning April 24, 1967 (ref. 15-28). The data were obtained by studying etched tracks as a function of depth in the glass filter within the Surveyor spacecraft camera. Because of the existence of an ≈1-μm coating on the surface and the fact that only those particles at a shallow angle could reach the glass, it was not possible to study energies less than ≈1 MeV/nucleon. If the energy spectrum during that 2.6-yr interval continues to increase steeply with decreasing energy, there would appear to be no inconsistency between it and the present data point at 0.1 MeV/nucleon for a single flare. It should be emphasized that the 1-week interval sampled by the Apollo 16 experiment was atypical in that solar particle events like that on April 18, 1972, are very infrequent.

Comparison of the April 18, 1972, flare spectrum with rocket data on flares.—Lexan detectors on rockets launched from Fort Churchill in Canada have recently been used (ref. 15-34) to study the composition of solar particles in the same energy interval accessible in the present experiment. The energy spectra in the rocket-borne detectors differ in an important way from those in figure 15-15. They go through a maximum at ≈1 to 2 MeV/nucleon and fall to zero at energies less than ≈0.2 MeV/nucleon. The present work shows that a well-defined maximum does not occur in all flares and raises several possible explanations for the maximum (ref. 15-34). Low-energy particles might have been excluded at Fort Churchill by a magnetospheric cutoff or because they had not reached the Earth from the Sun at the times of the rocket flights or even because of energy loss in the atmosphere of the Earth.

Origin of interplanetary charged particles with $E < 30$ MeV/nucleon.—The solar flare interference was an unprecedented opportunity to study a weak solar flare. However, studies of the origin of interplanetary charged particles will depend on future opportunities to use the same detectors to study the quiet-time spectra at energies of 0.1 to 30 MeV/nucleon.

Low-energy galactic cosmic rays.—At an energy of ≈60 MeV/nucleon, the flux of nuclei with $Z \geqslant 6$ shown in figure 15-15 is consistent with the flux at the same energy reported by Comstock et al. (ref. 15-22) during the previous period of minimum solar activity in 1964 and 1965. The level of quiet-time solar activity immediately before the flare of April 16 was only slightly above that in 1964 and 1965, as judged from neutron monitor levels. The flux of nuclei $10 \leqslant Z \leqslant 15$ at ≈65 MeV/nucleon during

Apollo 16 was similar to that reported in 1964 and 1965 at the same energy. No data exist for iron group nuclei at energies comparable to those measured in the present experiment.

The argument that these nuclei originated outside the solar system is based mainly on their composition as reported in table 15-V. At energies greater than 1 MeV/nucleon, the flux of nuclei with $17 \leqslant Z \leqslant 25$ is comparable to the iron flux (ref. 15-35), whereas the abundance of the same elements in the photosphere and in solar flares (ref. 15-34) is less than 15 percent that of iron. It seems inconceivable that these nuclei could actually have originated in the Sun but have passed through the amount of matter necessary to make the observed nuclei with $17 \leqslant Z \leqslant 25$ through nuclear reactions in interplanetary space.

Conclusions

During the Apollo 16 mission, a solar flare produced an enormous amount of low-energy nuclei, many orders of magnitude greater than the level inferred from studies of tracks in the window of the Apollo 12 spacecraft during a time when the Sun was quiet.

The differential energy spectrum of nuclei with $Z \geqslant 6$ falls by seven orders of magnitude over the interval from 0.1 to 20 MeV/nucleon, then remains almost flat up to ≈100 MeV/nucleon. The two parts correspond to contributions from the Sun and from galactic cosmic rays. Any maximum in the spectrum occurs below the lowest energy studied.

At energies much below ≈4 MeV/nucleon, the abundance of heavy elements is enhanced by a large factor relative to lighter elements. At ≈4 MeV/nucleon, the abundances are similar to those in the Sun. At ≳40 MeV/nucleon, the abundances are similar to those in galactic cosmic rays, characterized by the presence of nuclei produced in spallation reactions in interstellar space.

Acknowledgments

The authors thank Joan Steele of the University of California for help in making the measurements. We have had many useful discussions with E. K. Shirk, I. Hutcheon, and E. J. Kobetich of the University of California.

PART C

SOLAR COSMIC RAY, SOLAR WIND, SOLAR FLARE, AND NEUTRON ALBEDO MEASUREMENTS

D. Burnett,[a] *C. Hohenberg,*[b] *M. Maurette,*[c] *M. Monnin,*[d] *R. Walker,*[ab] *and D. Wollum*[a]

Introduction

Panel 4 of the cosmic ray experiment consisted of several detector systems designed to study various aspects of the radiation environment of the Moon. The detectors included mica, feldspar, three varieties of glass, two varieties of plastic, aluminum foil, and aluminum-coated platinum foil. The principal objectives were to study the heavy-element composition of the solar wind; the light-element composition of the solar wind in both interplanetary space and on the Moon; the thermal neutron albedo from the Moon; the radon atmosphere at the landing site; and, in general, all energetic heavy particles with $Z \geqslant 4$, either of solar or galactic origin, from energies from 1 keV/nucleon to tens of million electron volts per nucleon.

Several events occurred during the mission to modify or alter the information gained from panel 4. The most important of these events was an enhancement of particle fluxes, caused by a solar flare

[a]California Institute of Technology.

[b]Washington University, St. Louis, Missouri.

[c]Laboratoire de Spectrometrie Nucleaire et de Spectrometrie de Mass, (C.N.R.S.), Orsay, France.

[d]Laboratoire de Physique-Nucleaire, Universite de Clermont-Ferrand, France.

(described in part A of this section), during the trip to the Moon. The enhancement started approximately 36 hr after launch and diminished over a period of several days. The solar flare produced track densities of $\approx 10^6$ tracks/cm^2 at the surface of all the detectors and has given an unexpected and unprecedented opportunity to study heavy solar particles in the energy region from 10 keV/nucleon to >10 MeV/nucleon.

However, the high track density produced by the solar flare has made difficult the realization of some of the original goals of the experiment package. Measurement of the composition of quiet-Sun low-energy particles is clearly impossible, and measurement of the flux of heavy solar wind particles has been made difficult at best.

Panel 4 also contained a shifting mechanism that activated several experiments, most notably the neutron experiment, on the surface of the Moon. Because of a mistake in the final assembly, the shifting was only partially successful. This circumstance has degraded the information that can be obtained from the neutron experiment and also has made it very difficult to obtain information on the time variation of light solar wind nuclei.

Finally, the temperature rise in the package exceeded design specifications. Although this temperature rise has rendered the analysis of the experiment much more difficult and has limited the amount of hard results that can be presented in this preliminary report, it is felt that the effects of the temperature rise can be taken into account by future work.

General Description of Panel 4 Experiments

Panel 4 as it was returned from the Moon by the Apollo 16 astronauts is shown in figure 15-16. The lower part of the stack, labeled I, consisted of series of alternating layers of 60-μm-thick cellulose triacetate (triafol TN) and polycarbonate plastic (makrofol KG). This detector stack was covered with a 50-μm-thick coating of metallized Teflon to provide thermal protection and could thus be used only to study particles of $\geq$2 MeV/nucleon that were capable of penetrating this thermal shield. The last sheet in the stack consisted of a large TN foil designed to measure alpha particles from thermal neutron capture on an enriched boron-10 target plate found in the rear of part III.

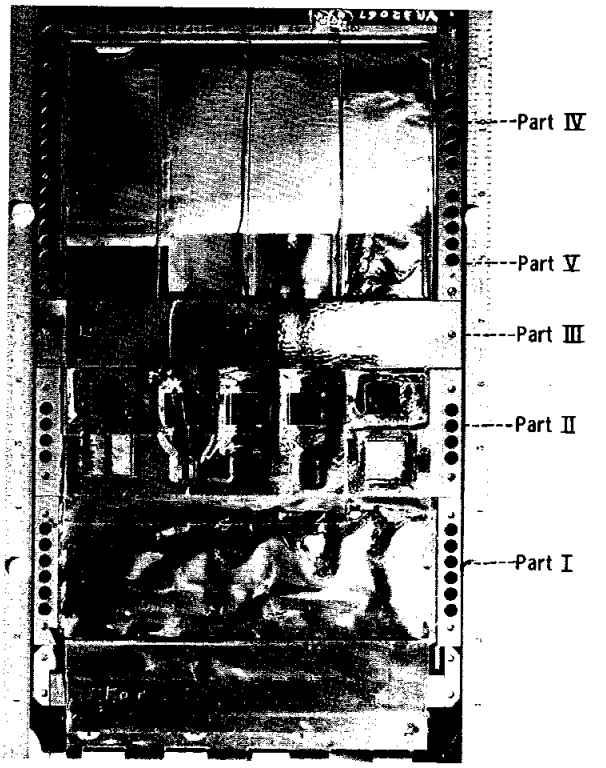


FIGURE 15-16.–Panel 4 as received on return from the Moon. Part labeled I is a stack of plastic detectors. Part II, the mineral assembly plate, contains mica, feldspar, and glass. Parts IV and V (partially visible) contain foils for trapping light solar wind.

Immediately adjacent to the plastic stack was a mineral assembly plate (part II) containing samples of mica, feldspar, soda-lime glass, tektite glass, and fused quartz. The mica detectors, which were included principally for the objective of measuring heavy solar wind ions with $Z \geq 26$, were also to be used to study any heavy particles with energy $\geq$1 keV/nucleon. The other mineral detectors were included to complement the mica and to provide samples that would be more directly comparable with lunar minerals.

Above the mineral assembly plate is an aluminum-coated platinum foil (part IV) that can be seen in figure 15-16 in partially retracted position. This foil was flush against part III during the outbound voyage and was retracted by the astronauts during the first EVA. The purpose of this foil was to measure the light solar wind in the interplanetary region to serve as a calibration for the heavy solar wind ions registered as tracks in the mica detector.

Seen under the partially retracted platinum foil (part IV) is another set of foils mounted in part V. Two of these consisted of aluminum-covered platinum, and one was anodized aluminum. The aluminum foil was provided by J. Geiss of the University of Bern and was the same material used in his more extensive light solar wind experiment (sec. 14 of this report). These part V foils were intended to measure differences in light solar wind flux and composition in time and space.

Two strips of mica (M10 and M11) are located on the left side of part V. During the flight to the Moon, the upper piece of mica (M10) was exposed to space through a 1.9-cm hole in the platinum foil. Half of this hole can be seen at the upper left corner of part IV. If the foil had been fully retracted, the second piece of mica would have been exposed to space starting with the time the astronaut shifted part IV. The purpose of this mica was to assess the importance of radon in producing shallow tracks (through the production of recoil atoms from alpha decay) that could be confused with extremely heavy solar wind ions.

Located in the rear of the panel is the neutron detector experiment. A schematic of this experiment is shown in figure 15-17. During the outbound voyage, a metal plate containing target strips of enriched boron-10 was located in the upper half of the panel behind parts III and IV. This target plate was connected to a wire lanyard, and pulling this lanyard (which moved the target plate down into the bottom part of the panel behind the plastic stack (part I)) activated the experiment. The photograph in figure 15-18, taken after removal of the mineral assembly plate, shows one target strip completely covered with plastic and another that has not moved into the plastic region. The target plate in turn was connected to the platinum foil (part IV), and pulling the lanyard also retracted part IV and exposed part V.

The proposed sequence of events was as follows. When the experiment was originally deployed, the minerals on part III, the plastic detectors (part I), and the aluminum-covered platinum foil (part IV) began registering solar and galactic particles. One piece of mica (M10) mounted on part V was also exposed during this time. Early in the first EVA, the astronaut was supposed to pull a lanyard that would retract part IV and expose part V. The mica (M10) on part V that had been irradiated up to this time would now

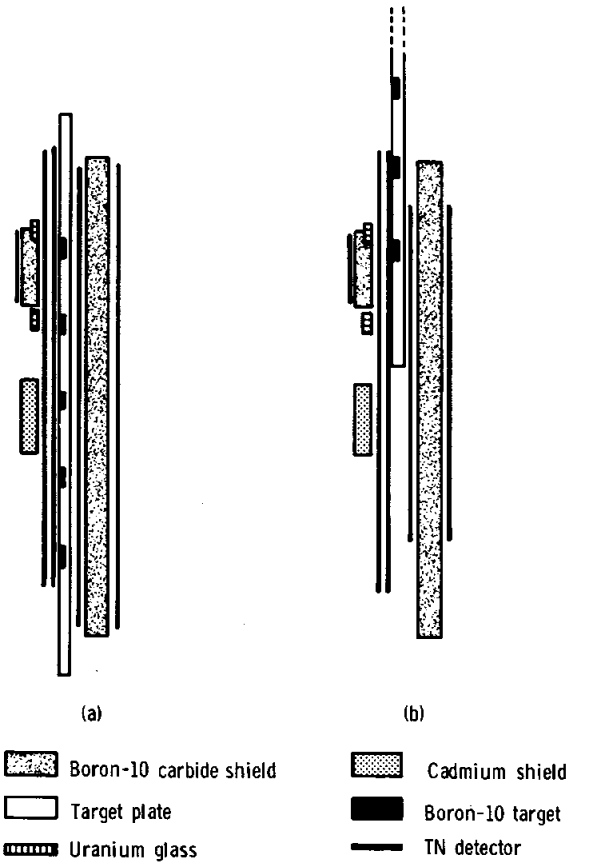


FIGURE 15-17.–Schematic diagrams of the neutron leakage flux experiment in panel 4. The scale in the horizontal direction has been grossly exaggerated to separate the components for easier viewing. (a) The experiment as it was designed. (b) The experiment as it was actually deployed because of the failure to achieve full activation.

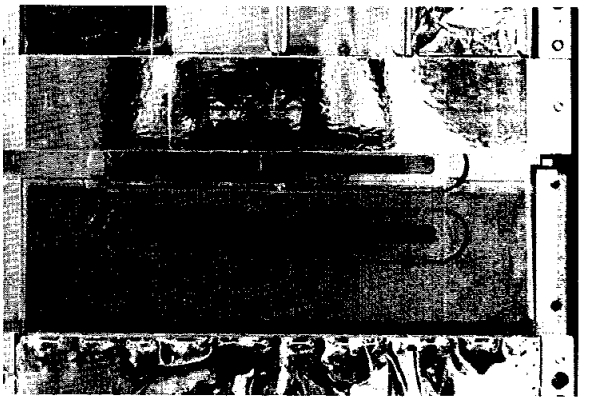


FIGURE 15-18.–Boron-10 target strip. The mineral assembly plate has been removed, and one target strip is visible through the covering sheet of triafol TN detector.

be shut off from low-energy particles by being covered with a tab of platinum foil attached to the lower left edge of part IV. Another piece of mica on part V (M11) would now be uncovered and start to register particle tracks. The lanyard shift would also move a boron-10 target plate into position to measure thermal neutrons. Both the neutron experiment and the plastic stack were deactivated by a final shift in the plastics that occurred automatically when the experiment was folded at the end of the final EVA.

The scheduled sequence of events did not occur completely as planned. When the commander attempted to pull the shifting lanyard that would have retracted part IV, he achieved only a partial shift of 2.5 cm, after which the lanyard broke. Several small screws mounted on the right side of part V were incorrectly installed and projected into the rear region of the panel. In effect, these screws clamped the target plate in position, making it extremely difficult to move. The failure to obtain a complete shift seriously degraded the neutron experiment and reduced the collection area for part V, making difficult the detection of differences in the solar wind at different times in the flight. Also, the mica (M11) on part V was never exposed to the space environment. This latter result was particularly unfortunate because the solar flare was almost over by that time and this mica would not have suffered from the enormous solar flare track background seen in the other micas.

The second unscheduled event was a relocation of the entire package at the end of the first EVA because of an increase in temperature as shown by several color indicators. The entire experiment was placed in the shade, further reducing the time of solar wind registration on the foils of part V. A summary of the exposure histories of the different samples is given in table 15-VI.

The temperature rise in panel 4 was monitored by several color indicators. Readings on the back of parts II and III and on the back of panel 4 indicated that the temperature was $>344^\circ$ K and $<355^\circ$ K.

The effects of temperature on the tracks themselves were monitored in several ways. First, the plastic stack included a set of preirradiated samples of TN and KG that had been exposed to oxygen ions of

TABLE 15-VI.–Exposure Conditions of Various Detectors

Detector	*Size, cm^2*	*Condition and time, hr:min*
Mica (M1 to M5) Quartz Tektite Soda-lime glass Feldspar Lower part of platinum foil Plastic stack	7.7 2.2 0.5 2.7 .58 112 75	LM deployed at 3:04 Experiment set in shade at 125:25 Experiment folded at 140:15 Total space exposure – 167:11 Exposure on Moon – 20:54 in Sun and 44:50 in shade Estimated total Sun exposure – 71:38
Mica (M10) Upper part of platinum foil	3.6 38	LM deployed at 3:04 Mica covered with platinum foil at 120:50 Total space exposure – 117:46 Exposure on Moon – 16:19 in Sun and 00:00 in shade Estimated total Sun exposure – 67:03
Lower part of part V Tab on part IV foil	28 10	Exposed at 120:50 Set in shade at 125:25 Folded at 170:15 Total space exposure – 49:25 Total Sun exposure – 4:35
Mica (M11) Upper part of part V foils		Always covered with 50-μm platinum foil
Neutron experiment		Activated at 120:50 Deactivated at 170:15 Total exposure – 49:25

different energies. This calibration set of plastics was located deep in the plastic stack, next to the TN foil used in the neutron experiment. No difference was observed in the etching of the oxygen tracks in control samples kept in the laboratory and in those returned from the Moon.

However, although no temperature effects were seen in the preirradiated foils, there are clear indications that temperature affected the registration of the tracks produced during flight. For example, in the neutron experiments, the alpha tracks are smaller and harder to recognize than normal alpha tracks registered in vacuum at room temperature.

Experimental Results on Mineral Detectors

The mineral detectors consisted of mica, feldspar (labradorite), soda-lime glass, tektite glass, and fused quartz. The areas and exposure conditions are listed in table 15-VI. The mica was taken from a large sheet of Indian muscovite and was preannealed at 923° K to remove fossil fission and alpha-recoil tracks. As a further step in eliminating stored tracks or potential spurious tracks, the mica was then pre-etched for 4 hr at 298° K in 40-percent hydrogen fluoride (HF). Following this step, it was verified that the surfaces were capable of registering tracks from 1-keV/nucleon heavy ions. The other detectors all consisted of polished surfaces obtained in a sequence of grinding and polishing steps culminating in the use of 0.05-μm aluminum oxide powder. The tektite and feldspar were also annealed, but no pre-etching was done. All samples except the fused quartz had a narrow, vapor-deposited strip of aluminum 100 nm thick across the center of the sample.

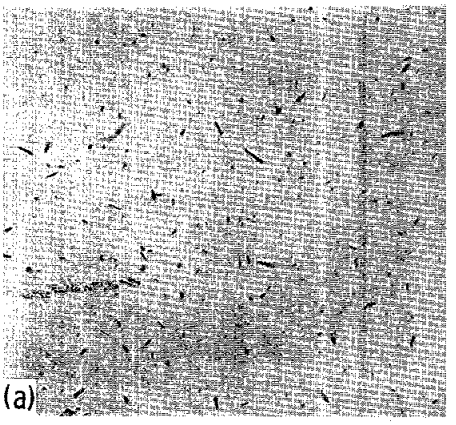
A summary of the track densities observed in the different materials is given in table 15-VII. The differences in track density arise from differences in the registration characteristics of the materials and do not represent inconsistencies in the track data. After photographic documentation, test pieces were removed from the detectors and etched to reveal particle tracks. The appearance of the tracks in mica and in two glass samples is shown in figure 15-19. The appearance of tracks in the feldspar after brief etching is similar to that in the mica and also to that in lunar feldspars etched for similar times.

The mica showed the highest track density and has been the most extensively studied in the work to date. A summary of the integral track length distribution measured by a combination of several techniques is given in table 15-VIII. It must be emphasized that this table does not include data on very shallow pits (or short tracks), the depth of which is in the range $\leqslant$100 nm. The length distribution for tracks in the range from 0.2 to 2 μm was obtained from SEM stereophotographs of a sample that had been etched for 2 hr to produce rather wide pits. A typical example is shown in figure 15-20. The length distribution from 2 to 12 μm was obtained by optical microscopy on a sample etched for 10 min. The length distribution for tracks $\geqslant$12 μm was obtained on a sample etched for 1 hr. Because the total track density did not vary during the etching times used, the data for different samples are directly comparable.

The major motivation for the inclusion of the mica detectors was the study of very shallow pits that should be produced by heavy solar wind ions. This idea was originally stimulated by the observation of alpha-recoil tracks in mica (ref. 15-36). These tracks,

TABLE 15-VII.–Surface Track Densities on Mineral Detectors

Sample	*Density, tracks/cm^2*	*Etching conditions*	*Mode of observation*
Mica (M1 to M5)	$1.8 \pm 0.1 \times 10^6$	10 min to 2 hr, 30° C in 40 percent HF	Optical (OPT) (transmitted light) and scanning electron microscope (SEM)
Feldspar	$6.0 \pm 0.6 \times 10^5$	13 min to 1 hr, boiling sodium hydroxide (6 g sodium hydroxide, 8 g H_2O)	OPT
Soda-lime glass	$5.8 \pm 0.4 \times 10^5$	400 sec in dilute HF, 30° C, maximum pit diameter 3.0 μm	SEM
Tektite	$2.5 \pm 0.3 \times 10^5$	24 min in dilute HF, 30° C, maximum pit diameter 2.0 μm	SEM





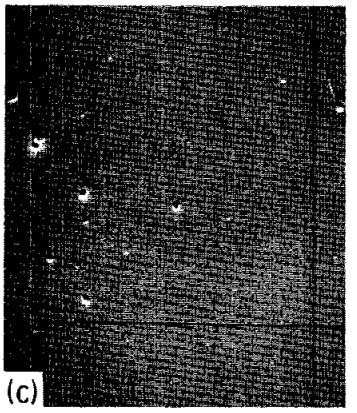


FIGURE 15-19.–Surface track densities in different detectors. Picture (a) was taken in an optical microscope at ≈1000X; (b) and (c) were taken in an SEM at 2000X. A feldspar crystal (not shown) has a similar appearance to picture (a) but has a track density more like picture (b). (a) Mica, 1.8 X 10^6 tracks/cm^2. (b) Soda-lime glass, 6 X 10^5 tracks/cm^2. (c) Tektite glass, 2 X 10^5 tracks/cm^2.

TABLE 15-VIII.–Integral Track Data in Mica

Track length, μm (a)	*Track density, tracks/cm^2*
>0.2	1.8 ± 0.1 X 10^6 (SEM)
>.5	1.8 ± 0.1 X 10^6 (SEM)
>1	1.1 ± 0.15 X 10^6 (SEM)
>2	7.4 ± 0.7 X 10^5 (OPT)
	4.4 ± 0.7 X 10^5 (SEM)
>4	2.6 ± 0.5 X 10^5 (OPT)
>6	5.5 ± 1.5 X 10^4 (OPT)
>8	2.2 ± 0.2 X 10^4 (OPT)
>12	6.3 ± 1 X 10^3 (OPT)
>20	1.4 ± 0.4 X 10^3 (OPT)
>34	2.8 ± 0.5 X 10^2 (OPT)
>50	8.5 ± 3 (OPT)

[a] ≲ 2 percent of total between 0.2 and 0.5 μm.

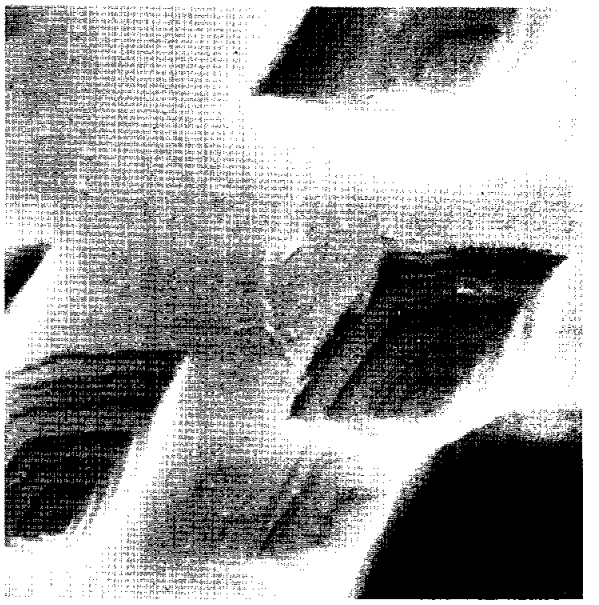


FIGURE 15-20.–An SEM photograph of short tracks in mica. The mica was etched for 2 hr at 30° C in concentrated HF to produce the enlarged pits.

which are produced by recoil nuclei from alpha particle decay of thorium and uranium, have energies similar to heavy solar wind ions. Subsequent, previously unpublished work has established that particles with energies in the range from 0.3 to 3 keV/nucleon produce observable pits in mica down to a charge of $Z = 26$.

It has been further shown that the diameters of the pits so produced vary in a systematic way with

the mass of the bombarding particles. This is illustrated in figures 15-21 and 15-22, which show pits produced by xenon atoms of 1 keV/nucleon and by the recoil atoms from a thorium-228 emanation source. Calibration irradiations with low-energy nickel, krypton, xenon, and lead ions on control pieces of muscovite have been used to establish a scale of mass as a function of diameter for particles with 1-keV/nucleon energy characteristic of the solar wind.

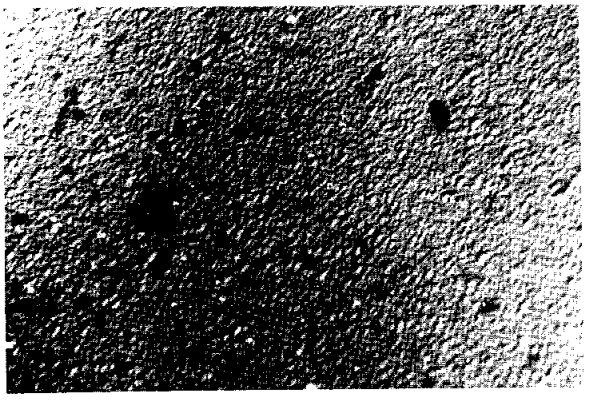


FIGURE 15-21.–Calibration irradiation of mica with 1-keV/nucleon zenon ions. The mica was etched for 2 hr, then silvered. The photograph was taken using a reflected light Nomarski phase contrast system.

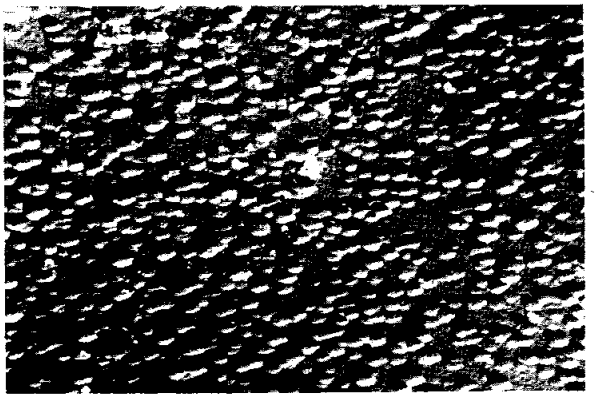


FIGURE 15-22.–Calibration irradiation similar to that in figure 15-21, using recoil atoms from a thorium-228 emanation source.

The best way of observing shallow pits in mica is to use a Nomarski phase contrast reflection system on samples that have surfaces that have been silvered by vacuum evaporation. Pit measurements are not made directly in the microscope but rather on 4- by 5-in. negatives made from high-contrast, high-resolution film. Although copy film has been found to give the best results, most of the measurements reported here were made on Polaroid 55PN film.

A sample of one of the micas, etched for 2 hr at 303° K in 40 percent hydrogen fluoride, using Nomarski phase contrast, is shown in figure 15-23. The principal difficulty in attempting to obtain heavy solar wind data from the Apollo 16 experiment is demonstrated by this figure. There is a large background of deep tracks (bright diamonds) that obscure much of the field of view. Also, there are pits of intermediate depth between the very shallow pits seen on the calibration photographs (figs. 15-21 and 15-22) and the deep pits. Most of the pits, including the very shallow ones, may have been produced in the solar flare and may not be associated with the heavy solar wind.



FIGURE 15-23.–Mica, taken under identical conditions to figures 15-21 and 15-22. The bright diamonds are deep tracks such as seen in figures 15-19(a) and 15-20.

Based on the previous calibration data, a scan was made of the photographs, dividing the shallow flat-bottomed pits into three categories: > xenon, > lead, > thorium. The corresponding densities were 2×10^5, 3.9×10^4, and 4.5×10^3 tracks/cm^2. The numbers are uncertain to at least 30 percent because of the difficulty in correcting for obscured regions. Similar numbers were found for both aluminum-covered and bare mica surfaces.

One sample of feldspar was given a prolonged etching to find the maximum etchable track length for slowing down iron nuclei. The maximum length was >25 μm.

Experimental Results on Plastic Detectors

The plastic stack consisted of a 75-cm^2 area containing 25 60-μm-thick sheets alternating between TN and KG, both manufactured by E. G. Bayer, Inc. One foil of cellulose acetate butyrate (BN) was also included. Adjacent sheets were shifted by 1 cm in the folding operation performed by the astronauts immediately before the storage of the package in the LM. Different batches of TN have been found to vary markedly in track registration properties, particularly when exposed to vacuum; all the sheets were therefore selected from a single roll of material. All calibration and temperature-control runs were made on material from this same roll adjacent to the material included in the flight package.

The first sheet of TN showed a density of 7.5 ± 0.7 X 10^4 tracks/cm^2 of shallow pits less than $\approx$3 μm in length. These pits are similar to those seen in a calibration experiment in which a sample of TN was irradiated with alpha particles in vacuum at 353° K (slightly below the maximum possible temperature indicated by the temperature labels). The alpha particle identification is uncertain, and the short tracks could be recoil nuclei produced by proton and neutron interactions. The density of short pits in succeeding foils of TN are, respectively, 3.1 ± 0.2 X 10^4, 2.2 ± 0.5 X 10^4, and 1.5 ± 0.4 X 10^4 tracks/cm^2.

The first TN sheet also contained a density of 3.9 ± 0.4 X 10^3 tracks >6 μm in length, of which 10 percent penetrated the foil, producing a recognizable track on the back side. The corresponding density of long tracks in the second TN sheet was 3.1 ± 0.5 X 10^2 tracks/cm^2.

Results of the Neutron Albedo Experiment

The neutron experiment was designed to estimate the leakage flux of low-energy (less than 10 eV) neutrons produced as a result of reactions of primary cosmic rays with lunar material. The experiment was based on the capture of neutrons by boron-10 targets producing alpha particles that were detected with a TN track detector. As shown in figure 15-17, a target plate consisting of a series of five boron-10 targets was mounted in the back of part III. Each strip was 5 mm wide and separated by 15 mm. Normally, the target plate should have slid in front of the TN detector (thereby activating the experiment) when the lanyard was pulled to retract the solar wind foil (part IV) in the initial deployment of the package on the lunar surface. The detector was deactivated by a 10-mm offset of the TN, when the panels were folded at the end of the final EVA.

Activation and deactivation were required to separate and eliminate the background from neutrons produced in the spacecraft before and after the lunar surface exposure. In particular, the activation and deactivation shifts were designed to eliminate background from neutrons produced by the radioisotope thermoelectric generator (RTG) on the trip to the Moon. To discriminate against neutrons produced in the LM during the period in which the detector was activated, an absorber made from boron carbide was placed between the neutron detector and the LM. (Control pieces of TN exposed to this boron-10 carbide plate showed track densities caused by the RTG that were 100 times that expected for the lunar neutron capture, showing the importance of the shifting operation.) A similar boron carbide absorber plate was placed between one target strip and the lunar surface to measure directly the contribution from LM-produced neutrons.

Small pieces of uranium glass were included as calibration sources to check possible thermal annealing of the alpha particle tracks. Comparisons of the uranium alpha particle tracks produced before and after the offset of the TN showed a decrease of 20 ± 10 percent in the rate of track production relative to the rate of track production during return of the package from the Moon to the laboratory. This amount of annealing may be important to the extent that it has degraded the appearance and length of the observed tracks, making them less easily identifiable.

The failure of the target plate to deploy completely (fig. 15-17) caused a loss of most of the data that would have been obtained from the neutron detector. It had been intended to have all five boron-10 target strips exposed to the TN detector, one with a cadmium shield between it and the lunar surface to supply spectral information on the neutron leakage flux and one with the small boron-10 carbide shield mentioned previously. However, the partial deployment lowered the bottom target strip (5) to a position beneath the small boron carbide plate and lowered target 4 to a position in line with the top of the TN sheet. The part of the TN that was finally

exposed to target 4 was not intended for data collection and contained glue on the rear side. Although the surface condition of the TN is less than ideal, it is possible to obtain some data from this area. Small uranium metal disks on the boron target plate provided fiducial marks to locate the positions of the boron targets precisely on the TN sheets, but the fiducial marks were lost because the uranium disks were not deployed properly. However, by means of the detailed documentary photography done at the disassembly of the package and a recent neutron exposure (radioautograph) of the reassembled panel, it is believed that the areas on the TN sheets that were exposed to the boron targets are accurately located. In addition, the positions of the uranium glass track distributions in the second large sheet of TN provide a rough check on the amount of shift achieved at the deactivation.

Based on a scan of ≈10 percent of the total area, the observed track density in the area exposed to target 4 is 870 ± 90 tracks/cm^2. However, only approximately one-third of these events are geometrically well-formed tracks. The remaining tracks are relatively short (less than 2 μm) and are more difficult to measure. Background measurements on regions between the target strips and under the shielded target (5) are consistent and give an average density of 700 ± 90 tracks/cm^2. The quoted errors are one standard deviation, but they may not be relevant in assessing the accuracy of the experiment. The ratio of well-formed tracks to total tracks is similar in the background and sample area. The density of long tracks (greater than 6 μm), ascribable to heavy ions, is roughly 10 tracks/cm^2 based on four events. This is consistent with the Apollo 15 measurements made on TN.

The high background is at least an order of magnitude higher than that measured on Apollo 15 TN control sheets and is of unknown origin. The soft spectrum found for the solar flare heavy particle tracks makes it unlikely that the background is of solar flare origin. Similarly, the density appears to be too high to be accounted for by galactic cosmic rays. Possibly, the background is caused by the proximity of the RTG with a subsequent production of alpha tracks by neutron interactions with oxygen-17 and carbon-16 or the production of heavy atom recoil tracks by elastic collisions. Another possibility is the production of tracks during passage through the radiation belts. It is also conceivable that the package was exposed to a high radon background at some time in its history.

Other Measurements

The scheduled measurements of the light solar wind have not been made at present because of difficulties with the appropriate mass spectrometer. However, two additional measurements, both with negative results, have been performed. Immediately after the demounting of the package, both the platinum foil (part IV) and the plastic stack (part I) were taken to the Battelle Memorial Institute, Richland, Washington, and counted in the special low-level counting facility developed by R. Perkins. No counts above background were observed in the counting system, which consisted of two 30-cm-diameter, 20-cm-thick scintillators. Therefore, a limit was set at the 95-percent confidence level of <1 disintegration/min for energetic single photon emitters and $<10^{-1}$ disintegration/min for two photon emitters such as cobalt-60.

A portion of the platinum foil (part IV) ≈1 cm^2 in area was also measured by T. Tombrello and D. Leach of the California Institute of Technology for implanted protons. Using a beam of fluorine ions of variable energy and measuring the gamma yield from the resonant fluorine-proton reaction, a limit was set of less than $\approx 10^{15}$ protons/cm^2 in the energy range 10 to 40 keV. However, a calibration irradiation showed that the platinum foil may not retain implanted protons; therefore, this experiment will be repeated on other materials.

Discussion

Origin of long (>0.5 μm) tracks in minerals: characteristics of the Apollo 16 solar flare event.—The largest tracks (>50 μm) in mica are produced by heavy particles of the heavy-particle group ($20 \leqslant Z \leqslant 28$). As the track length becomes smaller, lighter ions also begin to be included. From previous calibration work (refs. 15-37 and 15-38), it is estimated that the following even Z (i.e., abundant) nuclei would begin to register at different track lengths: argon, 34 μm; sulfur, 14 μm; silicon, 10 μm; and magnesium, 6 μm. Neon is somewhat ambiguous. Although previous work would suggest maximum track lengths of ≈2 μm, a new calibration irradiation with 100-keV/nucleon neon ions on a control mica heat treated in a similar fashion to the cosmic ray experiment mica failed to give any but the shallowest pits.

In figure 15-24, the integral track density as a function of energy has been plotted in two ways. In one set of points, it was assumed that all the tracks were produced by iron ions. In the other, the points have been corrected by taking into account the contribution of lighter elements using the universal abundances as given by Cameron (ref. 15-39). Because recent work (refs. 15-40 and 15-41) has shown that the iron tends to be more abundant in solar flares relative to silicon than given by the Cameron values, the real situation probably lies between these values.

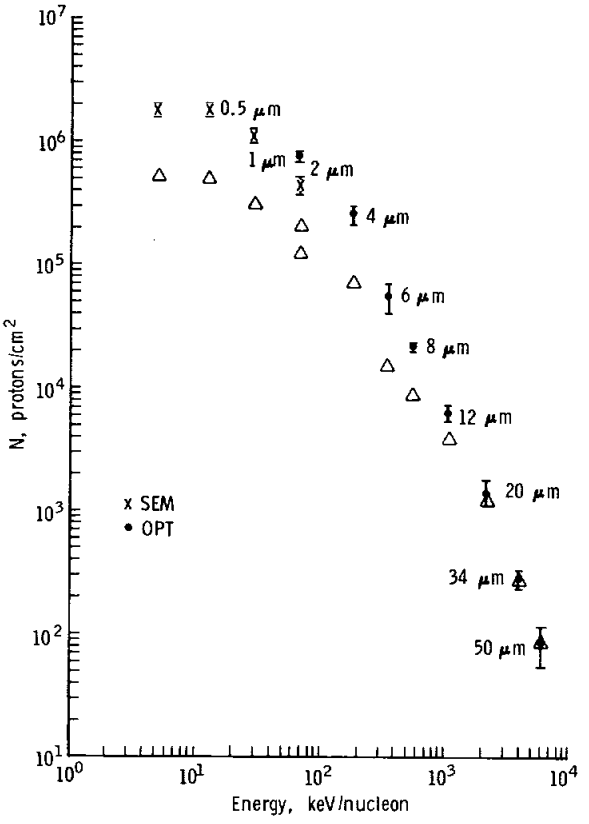


FIGURE 15-24.–Integral track densities as a function of energy in mica. The O and X points assume that all tracks are produced by iron. The Δ points have been corrected for an increasing contribution caused by lighter ions at shorter track lengths.

With either set of assumptions, the same general picture emerges. From ≈200 keV/nucleon to 6 MeV/nucleon, the differential spectrum can be represented by a power law in kinetic energy with

$$\frac{dN}{dE} = 4.2 \times 10^3 E^{-3.2} \text{ particles/cm}^2\text{-ster-MeV/nucleon}$$
(uncorrected)

and

$$\frac{dN}{dE} = 2 \times 10^3 E^{-2.8} \text{ particles/cm}^2\text{-ster-MeV/nucleon}$$
(corrected for light elements)

where E is expressed in million electron volts per nucleon. Below ≈200 keV/nucleon, the spectrum bends over. However, new particles continue to be registered down to an energy of ≈15 keV/nucleon. The bending over of the spectrum is consistent with the limit of $<10^{15}$ protons/cm^2 for 10- to 40-keV implanted protons. If the high-energy proton flare data were extrapolated to low energy with no bending over, then $>10^{16}$ protons/cm^2 would have been expected.

There seems to be a definite break at a track length of 0.5 μm with very few particles in the region of >1 to 15 keV/nucleon. Such a break could be an artifact if the etchable track lengths for low-energy iron ions are less than the actual ranges. However, calibration irradiations of other muscovite samples with 30 and 15 keV/nucleon nickel ions have given etchable ranges in good agreement with the theoretical ranges. A final decision on this point must await calibration irradiations of the mica actually used in flight.

Satellite observations during the mission showed a sudden enhancement in the flux of protons in interplanetary space. The enhancement, which occurred approximately 36 hr after launch and then decayed over a period of several days, was probably associated with a small X-ray burst and prominence activity just beyond the west limb at approximately 1800 Greenwich mean time on April 17, 1972. The flare was soft and rather small, having integrated fluxes of 1.04 X 10^8 tracks/cm^2 at 5 to 31 MeV/nucleon and 1.1 X 10^6 tracks/cm^2 at 21 to 70 MeV/nucleon. The very large track densities seen in the various detectors were probably predominantly caused by this flare. A similar, though somewhat harder, spectrum is observed in the minerals, and the number of iron tracks >5 MeV/nucleon is in reasonable accord with the proton data.

The possibility also exists that some of the tracks may have been produced during passage through the radiation belts where estimated proton fluxes of 3.3 X 10^8 protons/cm^2 > 4 MeV, 4.9 X 10^6 protons/cm^2 > 30 MeV, and 4.3 X 10^6 protons/cm^2 > 50 MeV were encountered. However, in view of the value of ≈10^{-7} given by several authors (refs. 15-42 and 15-43) for the ratio of the carbon-nitrogen-oxygen

group ($E \geqslant 0.3$ MeV/nucleon) to protons, this seems an unlikely source.

The limits on radioactivity measured by Perkins coupled with the measurement of heavy ion tracks in the minerals can be used to set limits on the abundance of specific radio elements in the flare. For example, sodium-22 and cobalt-56 must be present at levels $<10^{-3}$ and 10^{-4} of the total number of atoms from magnesium to iron.

Tracks in plastics.—The plastics in panel 4 were covered with a continuous sheet of 50-μm-thick Teflon instead of with the perforated sheets used in the other panels. Therefore, no low-energy data are available from this stack. However, the other panels in the package contained an abundant amount of plastic with which to study low-energy particles. It is evident also that no internal data on light elements at low energies are available to compare abundances in this part of the preliminary report.

The results on the alpha-sensitive TN are not understood at present. The densities of small pits, similar to those produced by low-energy alpha particles, are too high to be in accord with the heavy-particle data from the mica. Furthermore, the depth dependence is completely different from the behavior of the heavy-particle spectrum. Although previous work (refs. 15-40 and 15-41) has shown that the iron/helium ratio may be energy dependent, the differences are so extreme in this case as to suggest that the small track data refer to a completely different phenomenon.

It is considered possible that the small pits in the top three TN sheets are actually recoil nuclei produced by energetic protons from both the flare and the radiation belts. However, the number of tracks in the first TN sheet appears to be rather high for this explanation, and some helium particles from the radiation belts may be registering directly.

The difference in the density of long tracks (>6 μm) between the first and second TN sheets is compatible with the heavy-particle energy spectrum, and it is possible that these tracks are flare related. However, additional depth measurements are needed to test this point.

Heavy solar wind ions.—The cutoffs that have been used in counting shallow pits correspond roughly to element charge groupings of 50 to 70, 70 to 80, and $\geqslant$90. Taking a nominal solar wind proton flux of 3×10^8 protons/cm^2/sec and the estimated Sun exposure from table 15-VI, abundances relative to protons could be inferred for the charge groups of 2.6×10^{-9}, 5×10^{-10}, and 5.8×10^{-11}, respectively.

These values are similar to those given by the Cameron abundances of 10^{-9}, 3×10^{-10}, and 3×10^{-12} for the same elements. However, the track data on the aluminum-covered part of the mica is essentially identical to that on the bare mica surface. In principle, the aluminum is 100 nm thick and should have stopped all the heavy solar wind particles.

Until additional bombardment experiments on the aluminum-covered surfaces are made, the most likely source of the shallow pits is concluded to be the solar flare event. The solar flare itself could have contained very low-energy, very heavy ions; or, perhaps more likely, the shallow pits could have been produced by subtrack threshold energetic ions that produce occasional small regions of radiation damage capable of nucleating the shallow pits.

One firm conclusion that can be made is that there is no evidence for a large enrichment of very heavy ions in the solar wind.

Neutron albedo at the Apollo 16 site.—The neutron flux is given by the ratio ρ/ϵ where ρ is the measured track density in the TN detector and ϵ is the rate of track production per incident neutron. Coupling the previous values for ϵ, which were based on measurements up to 343° K in vacuum, with recent theoretical calculations of the lunar leakage neutron flux by Lingenfelter, Canfield, and Hampel (submitted to Earth and Planetary Science Letters, June 1972), a density of 400 to 600 tracks/cm^2 is predicted. The chemical composition of Apollo 16 material has been taken into account in this estimate. In contrast, the experimental value is 870 ± 90 minus a large background of 700 ± 90.

The low value of the measured track density relative to the predicted value cannot be taken at this time as indicating disagreement with the theory. The altered nature of the tracks, coupled with the preliminary results of a vacuum heating experiment at 353° K, indicates that the value of ϵ appropriate to the experiment is probably substantially lower than previous estimates.

Additional work is in progress to define ϵ for the actual flight conditions. It is hoped that this determination, coupled with a better understanding of the background problem, will provide a more critical test of the theory of lunar neutron albedo.

Implications for lunar sample studies.—The most significant result of this experiment to date is the

demonstration that heavy ions, capable of registering tracks in lunar-like minerals, continue to increase with decreasing energy down to ≈15 keV/nucleon. One of the intriguing results of lunar sample analysis has been the demonstration by Maurette et al. (ref. 15-44) and subsequently by Price et al. (ref. 15-45) that tiny lunar dust grains less than ≈1 μm size have extremely high track densities in the range 10^{10} to 10^{11} tracks/cm^2. Maurette et al. previously postulated the existence of a large flux of low-energy particles to explain these very high densities. Radiochemical measurements give a value of ≈80 protons/cm^2/sec >10 MeV from solar flares averaged over many solar cycles. If this is taken as the basis of comparison, the present flare represents ≈0.4 percent of a normal yearly dose. To accumulate 10^{10} to 10^{11} tracks would therefore require approximately 10^2 to 10^3 yr exposure. This is compatible with the known solar wind data on the lunar soil and on the estimated depth of the lunar regolith.

However, these calculations should be taken cautiously. Only one flare has been dealt with for this report, and it has a somewhat softer spectrum than solar flares measured over the longer period of time of the nearly 3-yr exposure of the Surveyor III glass filter previously studied (refs. 15-40, 15-46, and 15-47). In particular, in comparing surface track densities with those taken at a depth of ≈5 μm, no evidence was found previously for a large abundance of heavy particles with energies less than ≈0.5 MeV/nucleon in the Surveyor III glass. One major task for the future is to reexamine the Surveyor material to understand the differences with the present results.

The observation of very long iron tracks in feldspar confirms earlier accelerator experiments by Price (private communication). These tracks are much longer than those normally observed in lunar samples that are partially annealed under normal lunar environmental conditions.

At the Apollo 12 conference, Bhandari et al. (ref. 15-48) reported evidence for tracks from extinct superheavy elements. The analysis was based on the separation of fission tracks from cosmic ray tracks on the basis of length. Significantly, it was found that only crystals removed from the soil showed an excess of long tracks that were attributed to the fission of superheavy elements. The lunar soil is an extremely good insulator, and crystals imbedded even a few centimeters into the surface will have only modest temperature fluctuations around a mean of 250° K (refs. 15-49 and 15-50). Thus, cosmic ray tracks will be less annealed than in the case of exposed lunar rocks that reach temperatures of ≈423° K. The long tracks attributed to fission by Bhandari et al. may thus be simply less-annealed, long cosmic ray tracks.

Summary

(1) All mineral detectors exposed on Apollo 16 had high surface track densities (≈10^6 tracks/cm^2) probably produced by a solar flare that occurred during the mission.

(2) The heavy ions followed a power law spectrum with exponent ≈3 down to ≈200 keV/nucleon. Although the spectrum bent over below this energy, a considerable number of particles were present to 15 keV/nucleon. Few particles were evident between 1 and 15 keV.

(3) The abundance of low-energy particle tracks observed in this flare may explain the high track densities observed in lunar dust grains.

(4) Pristine heavy-particle tracks in feldspar give long (>25 μm) tracks. All tracks in lunar feldspars thus appear to be partially annealed. This result also casts doubt on previous claims for fossil tracks from extinct superheavy elements in lunar samples.

(5) Shallow pits similar to those expected from extremely heavy solar wind ions were observed in about the expected number. However, these may be caused by solar flares and not by solar wind. No evidence is found for the enhancement of ions with $Z > 50$ in the solar wind.

(6) Initial results give a low apparent value of neutron albedo relative to theory. However, the results are affected by thermal annealing during flight, and much additional work has to be done to give a critical test of the theory.

(7) The ratio of radioactive atoms to stable atoms in the Apollo 16 flare was such as to give <1 disintegration/min (single-gamma process) and <0.1 disintegration/min (two-gamma process) for 10^8 stopped heavy particles (magnesium-iron).

Acknowledgments

The authors acknowledge the experimental support of P. Swan and S. Sutton of Washington University for the SEM work and of R. Mourior and P. Petor of Laboratoire de Spectrometrie Nucleaire et

de Spectrometrie de Mass for several calibration irradiations. The final package design was arrived at in concert with E. Stockhoff of GE, who was also responsible for its construction and testing. The authors also thank R. Perkins of Battelle Memorial Institute and D. Leach and T. Tombrello of California Institute of Technology for the permission to quote the results given herein. The California Institute of Technology is also gratefully acknowledged.

REFERENCES

15-1. Fleischer, R. L.; Price, P. B.; and Walker, R. M.: Tracks of Charged Particles in Solids. Science, vol. 149, no. 3682, July 23, 1965, pp. 383-393.

15-2. Fleischer, R. L.; Price, P. B.; and Walker, R. M.: Solid-State Track Detectors: Applications to Nuclear Science and Geophysics. Annu. Rev. Nucl. Sci., vol. 15, 1965, pp. 1-28.

15-3. Fleischer, R. L.; Price, P. B.; and Walker, R. M.: Nuclear Tracks in Solids. Sci. Amer., vol. 220, no. 6, June 1969, pp. 30-39.

15-4. Price, P. B.; and Fleischer, R. L.: Identification of Energetic Heavy Nuclei with Solid Dielectric Track Detectors: Applications to Astrophysical and Planetary Studies. Annu. Rev. Nucl. Sci., vol. 21, 1971, pp. 295-334.

15-5. Fleischer, R. L.; Hart, H. R., Jr.; and Giard, W. R.: Particle Track Identification: Application of a New Technique to Apollo Helmets. Science, vol. 170, no. 3963, Dec. 11, 1970, pp. 1189-1191.

15-6. Fleischer, R. L.; Price, P. B.; and Walker, R. M.: Ion Explosion Spike Mechanism for Formation of Charged-Particle Tracks in Solids. J. Appl. Phys., vol. 36, no. 11, Nov. 1965, pp. 3645-3652.

15-7. Fleischer, R. L.; Price, P. B.; and Woods, R. T.: Nuclear-Particle-Track Identification in Inorganic Solids. Phys. Rev., vol. 188, no. 2, Dec. 10, 1969, pp. 563-567.

15-8. Crawford, W. T.; DeSorbo, W.; and Humphrey, J. S., Jr.: Enhancement of Track Etching Rates in Charged Particle-Irradiated Plastics by a Photo-Oxidation Effect. Nature, vol. 220, Dec. 28, 1968, pp. 1313-1314.

15-9. Price, P. B.; and Fleischer, R. L.: Particle Identification by Dielectric Track Detectors. Radiation Effects, vol. 2, 1970, pp. 291-298. Proceedings of the International Topical Conference on Nuclear Track Registration in Insulating Solids and Applications. May 1969, vol. I, D. Isabelle, ed., pp. IV 2-34.

15-10. Peterson, D. D.: Improvement in Particle Track Etching in Lexan Polycarbonate Film. Rev. Sci. Instr., vol. 41, no. 8, Aug. 1970, pp. 1252-1253.

15-11. Northcliffe, L. C.; and Schilling, R. F.: Range and Stopping Power Tables for Heavy Ions, Texas A&M (College Station), 1970; Nuclear Data Tables, vol. 7, 1970, p. 233ff.

15-12. Allen, L. H.: Abundance of the Elements. J. Wiley & Sons (New York), 1961.

15-13. Fillius, R. Walker; and McIlwain, Carl E.: Anomalous Energy Spectrum of Protons in the Earth's Radiation Belt. Phys. Rev. Letters, vol. 12, no. 22, June 1, 1964, pp. 609-612.

15-14. Katz, Ludwig: Electron and Proton Observations. Radiation Trapped in the Earth's Magnetic Field, vol. 5, Billy M. McCormac, ed., Gordon & Breach (New York), 1966, pp. 129-153.

15-15. Mogro-Campero, Antonio; and Simpson, J. A.: Enrichment of Very Heavy Nuclei in the Composition of Solar Accelerated Particles. Astrophys. J. (Letters), vol. 171, no. 1, part 2, Jan. 1, 1972, pp. L5-L9.

15-16. Fleischer, R. L.; Hart, H. R., Jr.; and Comstock, G. M.: Very Heavy Solar Cosmic Rays: Energy Spectrum and Implications for Lunar Erosion. Science, vol. 171, no. 3977, Mar. 26, 1971, pp. 1240-1242.

15-17. Crozaz, G.; and Walker, R. M.: Solar Particle Tracks in Glass from the Surveyor 3 Spacecraft. Science, vol. 171, no. 3977, Mar. 26, 1971, pp. 1237-1239.

15-18. Price, P. B.; Hutcheon, I.; Cowsik, R.; and Barber, D. J.: Enhanced Emission of Iron Nuclei in Solar Flares. Phys. Rev. Letters, vol. 26, no. 15, Apr. 12, 1971, pp. 916-919.

15-19. Unsöld, A.: Abundance of Iron in the Photosphere. Phil. Trans. Roy. Soc. London, vol. A270, no. 1202, July 16, 1971, pp. 23-28.

15-20. Bertsch, D. L.; Fichtel, C. E.; and Reames, D. V.: Nuclear Composition and Energy Spectra in the 1969 April 12 Solar-Particle Event. Astrophys. J., vol. 171, no. 1, part 1, Jan. 1, 1972, pp. 169-177.

15-21. Korchak, A. A.; and Syrovatskii, S. I.: On the Possibility of a Preferential Acceleration of Heavy Elements in Cosmic-Ray Sources. Soviet Phys. Dokl, vol. 3, no. 5, Sept.-Oct. 1958, pp. 983-985.

15-22. Comstock, G. M.; Fan, C. Y.; and Simpson, J. A.: Energy Spectra and Abundances of the Cosmic-Ray Nuclei Helium to Iron from the OGO-I Satellite Experiment. Astrophys. J., vol. 155, no. 2, Feb. 1969, pp. 609-617.

15-23. Hsieh, K. C.; and Simpson, J. A.: The Isotopic Abundances and Energy Spectra of ^{2}H, ^{3}He, and ^{4}He of Cosmic-Ray Origin in the Energy Region ~10-100 MeV Nucleon^{-1}. Astrophys. J. (Letters), vol. 158, no. 1, Oct. 1969, pp. L37-L41.

15-24. Baity, W. H.; Teegarden, B.; Lezniak, J. A.; and Webber, W. R.: Intensities of Low-Energy Cosmic-Ray ^{2}H and ^{3}He Nuclei Measured in 1967-68. Astrophys. J., vol. 164, no. 3, Mar. 15, 1971, pp. 521-527.

15-25. Frank, L. A.: On the Presence of Low-Energy Protons ($5 < E < 50$ kev) in the Interplanetary Medium. J. Geophys. Res., vol. 75, no. 4, Feb. 1, 1970, pp. 707-716.

15-26. Crozaz, G.; and Walker, R. M.: Solar Particle Tracks in Glass from the Surveyor 3 Spacecraft. Science, vol. 171, no. 3977, Mar. 26, 1971, pp. 1237-1239.

15-27. Fleischer, R. L.; Hart, H. R.; and Comstock, G. M.: Very Heavy Solar Cosmic Rays: Energy Spectrum and Implications for Lunar Erosion. Science, vol. 171, no. 3977, Mar. 26, 1971, pp. 1240-1242.

tion of the Earth. This position is the libration point L_1. Similar considerations determine the other points.

In theory, the points L_4 and L_5, which form equilateral triangles with the Sun and Earth, are stable equilibrium points, and the other points are unstable. In practice, the situation is complicated by perturbations caused by other planets and the Moon; thus, the detailed stability of the points remains controversial. However, in the case of the Sun-Jupiter system, the equilateral libration points contain accumulations of objects known as the Trojan asteroids. Furthermore, Earth-based observations of faint clouds at the equilateral points of the Earth-Moon system have been reported; these regions were photographed during the Apollo 16 and Apollo 14 missions. The possibility exists for clouds of particles to persist even at unstable libration points if the loss of particles is sufficiently slow to be compensated by the influx and capture (through collision processes) of interplanetary dust.

An Alternate Explanation of the Gegenschein

An alternate hypothesis to Moulton's explanation is that the gegenschein is a phase effect (preferential backscatter) from sunlight incident on interplanetary dust that is farther out in the solar system. The zodiacal light, a luminous band lying in the ecliptic plane, is caused by scattering of sunlight from micrometeoroids. Because of the scattering properties of small particles, some scientists believe the gegenschein is an intensification of the zodiacal light in the antisolar direction. If this fact is the case, the light perhaps originates between the Earth and the asteroid belt inside the orbit of Jupiter.

Triangulation

Because the orbit of the Moon offsets the Moon from the Sun-Earth line by as much as 384 000 km, observations of the gegenschein from lunar orbit allow triangulation to be used to determine which of these hypotheses is correct. If the light originates at the Moulton point L_1, it should be displaced approximately 15° from the antisolar direction, as seen from the Moon when it is near the quarter phase. If no significant shift in position is observed, the light must come from a much farther distance (fig. 16-2) and can have no significant connection with the Earth.

BACKGROUND EXPERIMENT INFORMATION

This experiment is a conclusive observational test of how much dust at the Moulton point L_1 contributes to the phenomenon of the gegenschein. In addition to the advantage of the geometry afforded by observations of the antisolar and Moulton region from lunar orbit, the optical environment is improved. The gegenschein has a very low brightness; therefore, the experiment photography must be performed from as dark a region as possible. The Apollo 16 spacecraft in low lunar orbit spent approximately 20 min every 2 hr in the darkest region of the universe that man has reached, where both sunlight and earthshine are blocked by the Moon (a region referred to as the "double umbra"). Making observations from lunar orbit also removes the problems associated with the airglow of the Earth.

The earliest experiment on zodiacal light and the gegenschein from a manned spacecraft occurred on the Project Mercury MA-9 flight (ref. 16-2), on which a specially modified, high-speed camera system was used. Similar investigations were conducted during several of the Gemini missions (refs. 16-3 and 16-4) using standard flight camera systems containing higher speed films for their better light-collecting characteristics. A Gemini Program experiment entitled "Dim-Light Photography" (refs. 16-4 to 16-7) provided partial success in similar investigative attempts. Related studies have been performed from rockets, balloons, and unmanned orbiting vehicles under the NASA Goddard Space Flight Center sponsorship.

The gegenschein-Moulton regions experiment was first conducted from lunar orbit during the Apollo 14 mission. The 16-mm data acquisition camera was used with an 18-mm focal-length lens set at f/0.95 and with Kodak 2485, black-and-white, high-speed recording film. A set of 20-sec and 5-sec exposures was made midway between and near the antisolar direction and the Moulton point. The exposures were not long enough, and the film grain on the 16-mm film was fairly large. For this reason, the decision was made that subsequent opportunities for this experiment should employ the 35-mm Nikon camera with

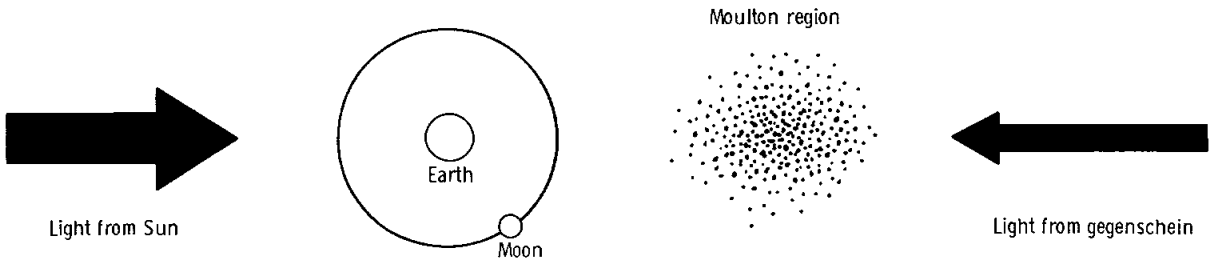


FIGURE 16-2.—The Moulton region.

f/1.2 lens that was just completing flight qualification tests in readiness for the Skylab Program. The data frames also indicated quite clearly that much longer exposure times could be used before image smear from vehicle instabilities would become more important than the gain in flux integration time on the film for such low-brightness objects. Other studies of low-brightness astronomical phenomena on the Apollo 15 mission confirmed these improvements in data quality.

RESULTS

The Nikon f/1.2 camera with extremely fast Kodak 2485 film produced successful results on Apollo 16. In spite of the changes in the flight plan caused by the shortened lunar orbit phase of the mission, critical observations were obtained before transearth injection.

(1) The desired 10 exposures (five 1-min duration and five 3-min duration) were obtained.

(2) The pointings were exactly as planned. For example, on April 25, 1972, they were toward RA 14^h55^m, dec 19° and RA 14^h25^m, dec 19°.

(3) The spacecraft stability during the longer exposures was within the requirement of ±1°. In fact, one of the 3-min exposure frames now being analyzed on the microdensitometer shows a pointing stability better than 0.5°.

(4) The energetic particle radiation of the film during translunar flight caused less than a 0.3 incremental photographic density above chemical fog.

The photographic quality of the data frames is good. The data reduction plan requires careful isodensitometry of all the observational frames including the vignetting calibration.

For this experiment, the two best orbital photographs (AS16-126-19952 and 19954) are 3-min exposures of the antisolar region and Moulton L_1 region. The pointing stability is approximately ±0.5°. Pictures taken in the laboratory of a uniformly illuminated screen were used to correct for the optical transfer function of the lens. More elaborate corrections for lens problems and removal of starlight will be made later.

Each of the pictures was first scanned on the microdensitometer and digitized into about 10^4 separate picture elements, each element representing the emulsion density of a 250- by 250-μm square on the film. Bright stars were then automatically identified in the orbital photographs by noting all picture elements that were more than 20 percent brighter than their immediate neighbors. The brightness of these stars was replaced by the neighborhood average. Noise arising from the grainy nature of film was then averaged away, and rather smooth pictures resulted, showing only astronomical features 1° across or larger. This is quite adequate for preliminary analysis.

Early numerical estimates show that the sky is definitely brighter in the antisolar direction than in the direction of the Moulton region. This fact is true even though the Moulton region is at a lower galactic latitude (-35°) and therefore includes a somewhat brighter galactic background. The galactic light will be removed at a later stage in the analysis when all pictures are available. When the pictures were taken in April, the gegenschein lay so far from the galactic plane that this presents no serious difficulty.

In the meantime, an upper limit can be placed on the brightness of material in the Moulton region. Much less than half of the light seen on Earth as the gegenschein comes from particles lingering in the Moulton region. Further analysis will place a far more stringent limit on the Moulton region brightness and will provide isophotes of the gegenschein without uncertainties introduced by the airglow of the Earth.

REFERENCES

16-1. Danby, J. M. A.: The Three-Body Problem. Fundamentals of Celestial Mechanics, ch. 8, Macmillan Co., 1962, pp. 187-204.

16-2. Anon.: Mercury Project Summary Including the Results of the Fourth Manned Orbital Flight, May 15 and 16, 1963. NASA SP-45, 1963.

16-3. Ney, Edward P.: Night-Sky Phenomena Photographed from Gemini 9. Sky and Telescope, vol. 32, no. 5, Nov. 1966, pp. 276-277.

16-4. Cameron, W. S.; Dunkelman, L.; Gill, J. R.; and Lowman, P. D., Jr.: Man in Space. Introduction to Space Science, ch. 14, second ed., W. N. Hess and G. D. Mead, eds., Gordon and Breach Sci. Pub., 1967, pp. 555-606.

16-5. Dunkelman, L.; and Mercer, R. D.: Dim Light Photography and Visual Observations of Space Phenomena From Manned Spacecraft. NASA TM X-55752, 1966.

16-6. Dunkelman, L.; Gill, J. R.; McDivitt, J. A.; Roach, F. E.; and White, E. H., II: Geo-astronomical Observations. Proceedings of the Manned Space Flight Experiments Symposium, Gemini Missions III and IV (Washington, D.C.), Oct. 18-19, 1965, pp. 1-18.

16-7. Roach, Franklin E.; Dunkelman, Lawrence; Gill, Jocelyn R.; and Mercer, Robert D.: Geoastronomical Observations, Sec. 32 of Gemini Midprogram Conference. NASA SP-121, 1966.

17. UV Photography of the Earth and Moon

Tobias Owen [a†]

The purpose of this experiment was to obtain imagery of the Earth and the Moon at a series of wavelength intervals in the near ultraviolet (UV). Accompanying color photography was scheduled to provide independent identification of the scenes being viewed. In addition to their intrinsic interest, these photographs were to be used to help in the interpretation of the UV appearance of other planets in our solar system, especially Mars and Venus.

Ultraviolet photographs of Mars and Venus obtained from the ground over the last few decades have been the source of considerable controversy. Mars, with a very thin atmosphere, shows a gradual decrease in apparent surface detail as the effective wavelength is diminished (fig. 17-1). Even with the help of closeup views of the planet obtained from the series of Mariner spacecraft, it is not yet clear how much of this loss of detail is caused by a possible haze in the atmosphere of the planet and how much results simply from a lack of surface contrast at short wavelengths (ref. 17-1). In the case of Venus, a planet with a very thick atmosphere, the situation is reversed. Only at wavelengths below approximately 450 nm (4500 Å) do details become readily visible (fig. 17-2). These details consist of shady markings in the cloud cover surrounding the planet. The markings change from day to day and recently have given evidence of high altitude winds corresponding to a rotation period of 4 days, in contrast to the 243-day period of the solid surface of the planet (ref. 17-2).

The Moon has been studied at a variety of wavelengths from the ground and appears to show a decrease in contrast between light and dark areas as shorter wavelengths are approached. Depending on the effect of the translucency of lunar particles, it seems possible that at wavelengths below approximately 300 nm (3000 Å), the lunar ground would exhibit very low contrast, perhaps none at all (ref. 17-3). No UV imagery of the Earth was available before this experiment, but it was anticipated on the

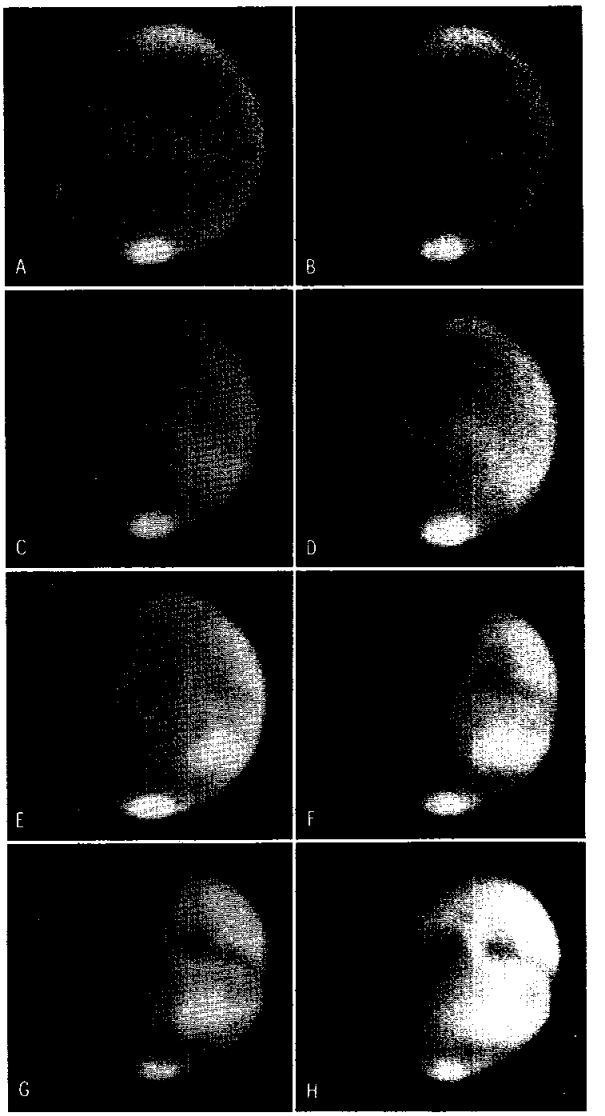


FIGURE 17-1.–Mars photographed at New Mexico State University September 25, 1971, at the following effective wavelengths: (A) 320 nm (3200 Å); (B) 360 nm (3600 Å); (C) 410 nm (4100 Å); (D) 450 nm (4500 Å); (E) 500 nm (5000 Å); (F) 550 nm (5500 Å); (G) 650 nm (6500 Å); (H) 800 nm (8000 Å). The (A), (B), and (D) passbands are comparable to those of the filters used in this experiment. The strong wavelength dependence of the surface contrast should be noted.

[a]State University of New York.

†Principal Investigator.

basis of the theories of molecular and particle scattering that surface contrast would also be reduced in the UV because of the increase in scattered light from the atmosphere. It was not clear how contrast on the land masses themselves would change before being blocked out by atmospheric effects or at what wavelengths this atmospheric screening would begin.

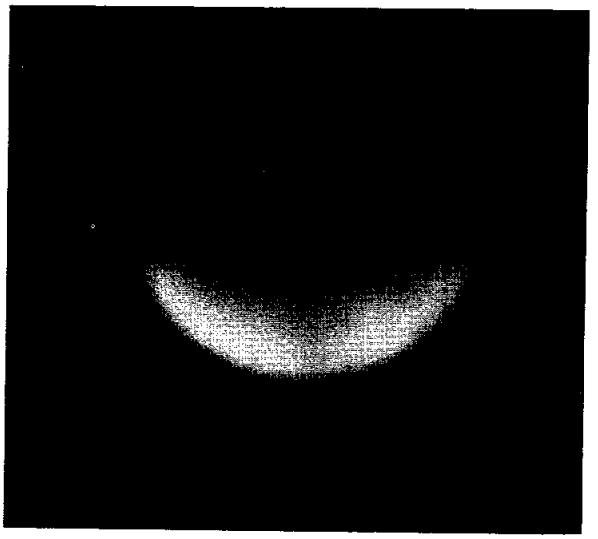


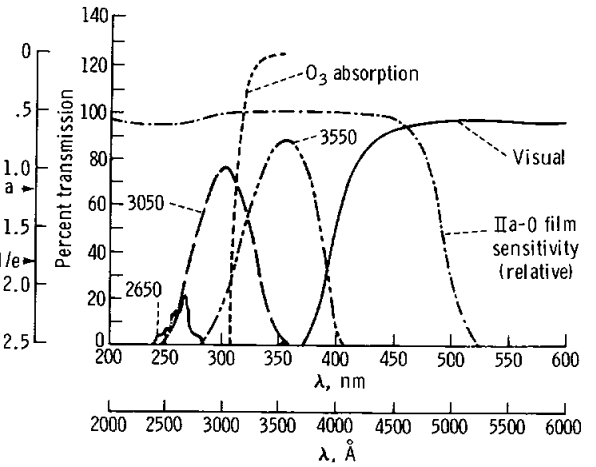
FIGURE 17-2.–Venus photographed at New Mexico State University April 6, 1966, at an effective wavelength of 360 nm (3600 Å).

THE EXPERIMENT

A Hasselblad 70-mm camera equipped with a UV-transmitting (quartz) lens was used with Eastman IIa-0 film to obtain the pictures. Color photography was carried out with the same system by substituting a color film magazine and using a UV cut-off filter in front of the camera lens. The camera was mounted on a bracket behind window 5 in the command module, the customary window elements having been replaced with panes that did not block UV radiation. Plexiglass and cardboard shields were provided to protect the crew. A filter wheel containing the following four filters permitted the isolation of specific passbands for the photography.

Filter designation	*Passband, nm*	*Passband, Å*
UV cut-off	λ> 400	λ> 4000
3750	315 to 390	3150 to 3900
3050	270 to 330	2700 to 3300
2650	255 to 270	2550 to 2700

Figure 17-3 is a diagram showing the transmission characteristics and film sensitivity. The filters were selected to provide overlap with ground-based images of the planets and to extend the wavelength range farther into the UV (at 265 nm (2650 Å)) than can be achieved from the ground. As is evident from figure 17-3, the terrestrial ozone cut-off is overlapped by the passband of the 305-nm (3050 Å) filter. Hence, when this filter is used to photograph celestial objects from the ground, its effective passband is shifted to approximately 320 nm (3200 Å) (fig. 17-1). From space, when the Earth is viewed, the same shift occurs. When the Moon is viewed, however, the effective wavelength will be 305 nm (3050 Å).



Note: The outer ordinate scale is applicable for the curve of the ozone absorption coefficient.

FIGURE 17-3.–The filter and film characteristics for this experiment. The curve of the ozone absorption coefficient is included for reference.

Of the filters listed previously, the first two had been successfully used during the Apollo 15 mission; the 305-nm (3050 Å) filter did not pass flight qualifications, and the 265-nm (2650 Å) filter proved defective on the earlier mission. Both of these filters were rebuilt for the Apollo 16 mission, but the new 265-nm (2650 Å) filter still failed to perform satisfactorily. The multiple-reflection problem that plagued the Apollo 15 version of this filter was solved, but pinholes in the dielectric coating apparently produced distorted, unfiltered images which will require further testing for proper interpretation.

Problems with the flight plan and with centering of the lunar image resulted in the loss of some data. However, 66 images of the Earth and the Moon at varying resolution (distance) were obtained, and the quality of these data is uniformly high, a testament to the excellent performance of the Apollo 16 crew. Each set of UV pictures of the Earth is also accompanied by a color photograph except for the last set during transearth coast (TEC), owing to premature stowage of the color film magazine.

PRELIMINARY RESULTS

A comparison of the appearance of the Earth at effective wavelengths of 320 nm (3200 Å) and 460 nm (4600 Å) is given in figures 17-4 and 17-5, respectively. At first glance, very little difference is noted at these two wavelengths. The area shown in the figures is the Pacific Ocean, with Baja California just disappearing at the terminator. Thus, the detail seen is primarily cloud patterns against the ocean background. Close inspection of second generation positives reveals that low-altitude clouds and air-sea boundaries have almost entirely disappeared from the image obtained at the shorter wavelength (fig. 17-4). The diffusely reflected image of the Sun present on the 460-nm (4600 Å) picture (fig. 17-5) is also missing from figure 17-4. These results are entirely consistent with predictions from the elementary scattering theory, which suggests that a marked increase in the brightness of a planet's atmosphere will occur with decreasing wavelength.

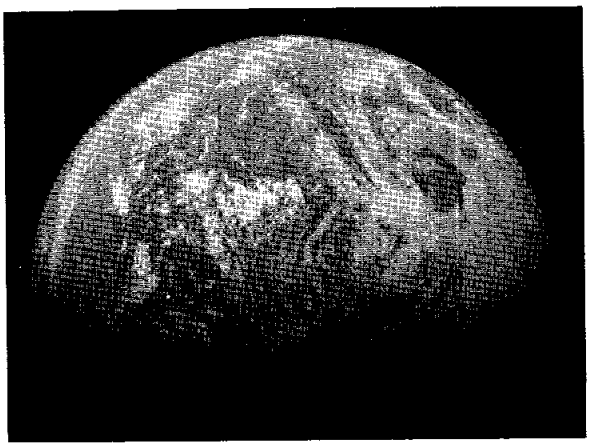


FIGURE 17-4.–The Earth at 320 nm (3200 Å): f/4.3, 1/125; translunar coast (TLC). Distance: ~33 000 n. mi., GET: ~08:00 (AS16-131-20106).



FIGURE 17-5.–The Earth at 460 nm (4600 Å): f/8, 1/500; TLC. Distance: ~33 000 n. mi., GET: ~08:00 (AS16-131-20100).

If simple Rayleigh scattering is used, the extinction coefficient β at 460 nm (4600 Å) and 320 nm (3200 Å) can be compared. Coefficient β is defined from the relation for the decrease of intensity Io of a beam of light over a path L: $I = Io\, e^{-\beta L}$; thus, $\beta_{3200}/\beta_{4600} = 11.21/2.47 = 4.53$ (ref. 17-4). This value is the difference between an optical depth of 0.2 at 460 nm (4600 Å) and 0.9 at 320 nm (3200 Å). Because an optical depth of unity is commonly regarded as opaque, Rayleigh scattering alone essentially can explain the observed effects, although there is undoubtedly a contribution from aerosols.

Unfortunately, these results reveal nothing about Mars and Venus. In the case of Mars, the wavelength dependence of the surface contrast observed at various regions on a land mass would need to be examined. The constraints of the flight plan and the vagaries of terrestrial weather prevented obtaining a clear view of a terrestrial land mass during the Apollo 16 mission. For Venus, a much higher look into the atmosphere of the Earth for possible analogies to the Cytherean ultraviolet clouds is needed. The 265-nm (2650 Å) filter was designed for this purpose but was unsuccessful, as mentioned.

However, by chance, some imagery was obtained that may have a bearing on the Venus atmosphere. The final TEC sequence caught a localized brightening at the limb of the crescent Earth (fig. 17-6). Inspection of second generation copies indicates that this surge of brightness is caused by a reflection from an irregularly shaped area, presumably a bank of clouds. Alternatively, an open

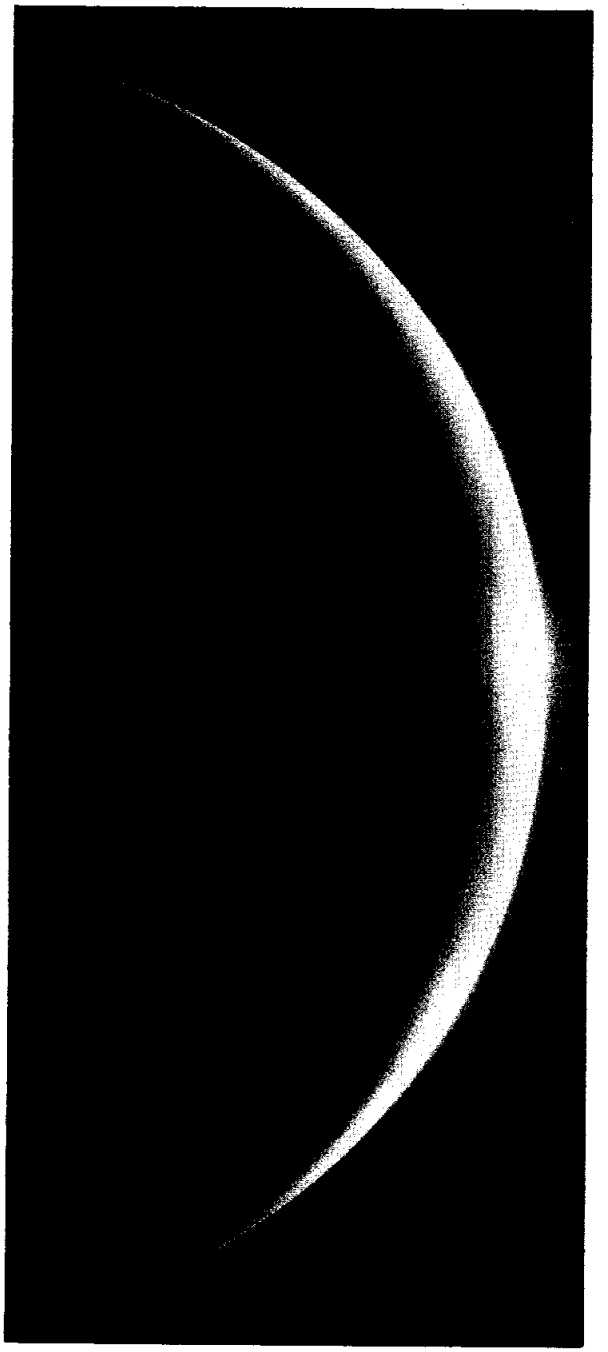


FIGURE 17-6.–The Earth at 460 nm (4600 Å): f/8 1/500; TEC. Distance: <30 000 n. mi. (to be determined), GET: ~263:00.

body of water framed by clouds may be responsible. A preliminary analysis of the geometry of the observation suggests that the brightening occurred in a region over the South Atlantic. The identification of the reflecting surface will be accomplished with the help of photography of the Earth from the applied technology satellite (ATS) stationed at 70° W (ATS 3). At the time this report was being prepared, the ATS negatives that were obtained during the interval centered on the time of the Apollo 16 UV photography were not available for inspection, but, when available, should provide the necessary evidence for distinguishing between the two hypotheses.

If clouds are responsible, the natural explanation is that the reflection occurs from freely falling, flat hexagonal ice crystals in a suitably located cirrus deck (e.g., ref. 17-5). The brightening is invisible on the frames shot at 320 nm (3200 Å), partially apparent at 355 nm (3550 Å), and strongest at 460 nm (4600 Å). At the extreme limb, very large optical depths caused by the large angles of incidence and observation are visible. Thus, the reflecting surface responsible for the observed effect simply may not be brightly illuminated or visible at the shortest wavelength because of its relative proximity to the planet's surface. A possibility also exists that the elapsed time between frames was sufficient to allow enough of a change in the viewing geometry to prevent the brightening from being visible during the (earlier) short wavelength photograph. The resolution of this question, as well as the unequivocal identification of the reflecting surface itself, must await further study.

This observation is interesting for the present program because such an effect never has been observed on images or by direct observations of Venus, although this planet passes through similar phase angles (fig. 17-2). Several investigators have looked very carefully into the possibility of detecting ice crystals in the Venus clouds by using the 22° halo they would produce (ref. 17-6). In this case, the hexagonal crystals would be elongated prisms rather than flat plates. The observations always have been rather marginal, with no clear evidence for ice detection. If the surge of brightness at the limb of the Earth observed from the Apollo 16 spacecraft is caused by clouds, an attempt to look for a similar effect in the atmosphere of Venus might be a much more sensitive test for the presence of ice than the 22° halo. Thus, the absence of such phenomena would place rather severe constraints on the possibility that hexagonal ice crystals are an important component of the visible cloud deck of that planet.

The appearance of the Moon at effective wavelengths of 305 nm (3050 Å) and 460 nm (4600 Å) is illustrated in figures 17-7 and 17-8, respectively. Once again, there is little apparent difference between images obtained at these two wavelengths, certainly nothing as dramatic as the loss of contrast that occurs on Mars (fig. 17-1). The hypothesis that contrast will disappear at short wavelengths rests on the idea that the difference in appearance of dark and light areas is caused by different translucencies in the particles making up the maria and the terrae. At sufficiently short wavelengths, absorption becomes complete, and only externally scattered light is visible (ref. 17-3). Possibly, short enough wavelengths for the effect to become apparent simply have not been reached, or perhaps some modifications in this interpretation of the observations are required.

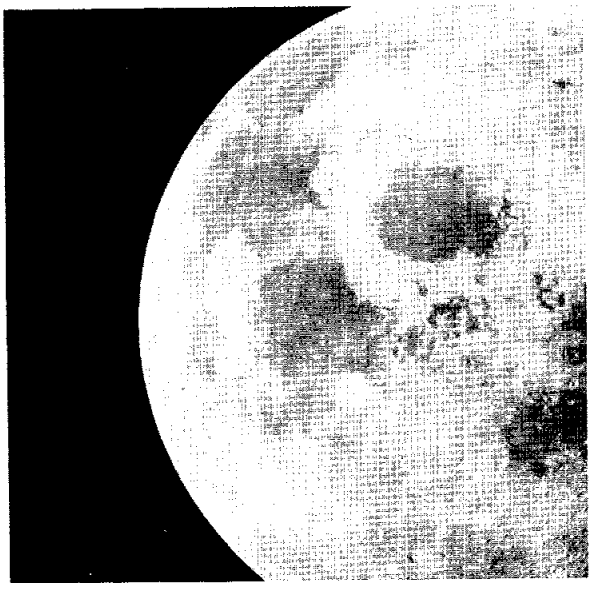


FIGURE 17-7.–The Moon at 305 nm (3050 Å): f/4.3, 1/60; TEC (AS16-131-20165).

There is an indication that the rays and ray craters are more prominent on the photographs obtained with the 305-nm (3050 Å) filter. The tendency for such an enhancement is apparent on both the full-disk photographs and on the imagery obtained with higher spatial resolution from lunar orbit. However, this possible increase in contrast requires verification by accurate densitometry of the original negative before it can be considered a real effect.

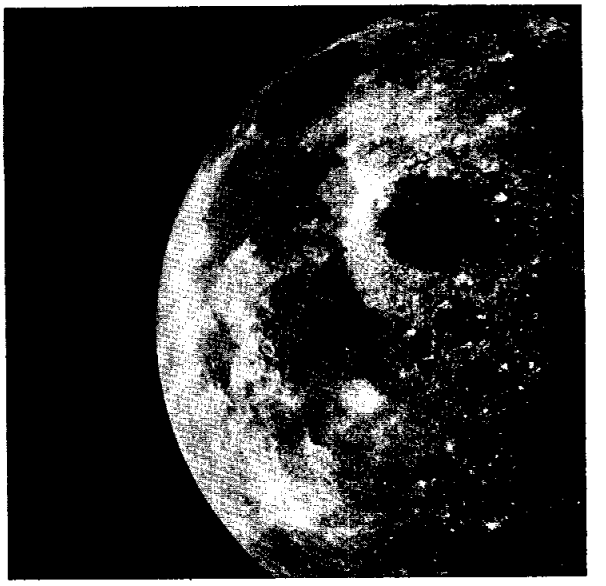


FIGURE 17-8.–The Moon at 460 nm (4600 Å): f/4.3, 1/500; TEC (AS16-131-20158).

Detection and analysis of a large-scale contrast change on the Moon, if it does occur, would be especially interesting, because the properties of the lunar soil are being determined from direct analysis. As a result, it may be possible to provide a better model for Martian soil from a detailed comparison of the optical properties of Mars and the Moon in the near UV.

REFERENCES

17-1. Pollack, James B.; and Sagan, Carl: An Analysis of Martian Photometry and Polarimetry. Space Sci. Rev., vol. 9, C. de Jager, ed., D. Reidel Publishing Co. (Dordrecht, Holland), 1969, pp. 243-299.

17-2. Smith, Bradford A.: Rotation of Venus: Continuing Contradictions. Science, vol. 158, no. 3797, Oct. 6, 1967, pp. 114-116.

17-3. Pellicori, S. F.: Polarizing Properties of Pulverized Materials with Special Reference to the Lunar Surface. Appl. Optics, vol. 10, no. 2, Feb. 1971, pp. 270-285.

17-4. van de Hulst, H. C.: Scattering in the Atmospheres of the Earth and Planets. The Atmospheres of the Earth and Planets, Gerard P. Kuiper, ed., The University of Chicago Press (Chicago), 1952, pp. 49-111.

17-5. Minnaert, Marcel Gilles Jozef (H. M. Kremer-Preist, trans. and revised by K. E. Brian Jay): Iridescent Clouds. The Nature of Light & Color in the Open Air, Dover (New York), 1954, pp. 226-230.

17-6. O'Leary, Brian: Venus Halo: Photometric Evidence for Ice in the Venus Clouds. Icarus, vol. 13, no. 2, Sept. 1970, pp. 292-298.

18. Gamma Ray Spectrometer Experiment

James R. Arnold,[a†] Albert E. Metzger,[b] Laurence E. Peterson,[a] Robert C. Reedy,[a] and J. I. Trombka[c]

The Apollo 16 gamma ray spectrometer experiment is one of a group of three orbital geochemistry experiments flown for the second and last time on this mission. All three experiments have in common the broad objective of geochemical mapping of the lunar surface. Because the landing sites for which chemical information is available are limited in number and not necessarily representative, it is important for understanding the origin and evolution of the Moon to have a data source concerning chemical composition over as wide an area of the Moon as possible. The detailed studies of returned lunar samples have permitted some progress in identifying major components of the soil, some components indigenous to the sites explored, and some external to the sites. One task of the orbital geochemical experiments is to verify the occurrence of the suggested components. More importantly, the regions of the Moon in which each distinct material is the dominant constituent will be mapped. A knowledge of the distribution of these materials is essential to understanding the nature and origin of the materials. The transearth coast period of this mission provided an opportunity for a detailed study of the astronomical sources of gamma radiation, using the spacecraft to occult possible source regions.

BASIC THEORY

Gamma rays are absorbed or scattered by passing through lunar soil or rock tens of centimeters thick. Therefore, the gamma ray experiment can sample the composition of the Moon to that depth. This layer of soil and rock is generally well within the regolith and can be assumed to be well mixed.

The chemical information in a gamma ray spectrum is carried by discrete lines with energies that are characteristic of individual elements. Two broad classes of such lines exist. The first class, which traditionally is called natural radioactivity, results from the decay of potassium-40 and the radioactive daughters of thorium and uranium. Important examples are the 1.46-MeV line emitted in the decay of potassium-40 to argon-40 and the 2.62-MeV line of thallium-208, a daughter of thorium-232. The second class is composed of the lines that result from the bombardment of the lunar surface by high-energy-charged particles, the cosmic rays. These particles interact with the lunar surface to produce secondary particles and excited nuclei.

The galactic cosmic rays are responsible for nearly all the emitted gamma rays of this type. A typical galactic-cosmic-ray (GCR) particle is a proton with a kinetic energy comparable to the rest mass, approximately 10^9 eV. The GCR particle interacts near the lunar surface to produce a cascade of lower energy particles, of which the most important are neutrons. These neutrons in turn give rise to excited nuclei that are capable of emitting line radiation in three ways. First, the neutrons may scatter inelastically, leaving the target nucleus in an excited state. This process is important for neutron energies of a few million electron volts. Each major element produces such lines. An example is the 0.84-MeV line of iron. The second major process is neutron capture. Neutrons lose energy by successive collisions until they either escape from the surface or are captured. The binding energy of the added neutron, typically approximately 8 MeV, is emitted from the product nucleus in a complex decay scheme, which sometimes contains a few dominant lines. The line emitted by iron at 7.64 MeV is an important case. Finally, gamma rays are emitted by radioactive nuclides produced by nuclear reactions, such as aluminum-26 from aluminum and silicon. These reactions are generally less important but not negligible.

[a]University of California, San Diego.

[b]Jet Propulsion Laboratory.

[c]NASA Goddard Space Flight Center.

†Principal Investigator.

During major solar flares, the Sun emits high-energy particles, the solar cosmic rays. The important energy region for these particles is in the range of 10 to 100 MeV. The particles lose energy mainly by ionization, but sometimes nuclear reactions occur. Except during the occurrence of a solar flare, the rapid processes of capture and scattering discussed previously cannot be observed. The solar-cosmic-ray-induced radioactivity is found to be a small component in the Apollo 16 data.

The expected intensities of the spectral lines as functions of chemical composition can be calculated from a knowledge of the physical processes involved. In the case of the natural radioactivities, this calculation is simple and unambiguous. For the lines induced by high-energy bombardment, the required particle fluxes and cross sections are known only approximately. The availability of "ground truth" for areas such as Mare Fecunditatis and the Descartes landing site, overflown by the Apollo 16 command and service module, is of great value.

The instrument is omnidirectional and, therefore, has some response to all areas within the field of view. However, counts come mainly from the areas relatively close to the detector, which subtend the largest solid angle. Resolution on a scale of approximately 2° to 3° on the Moon, or approximately 70 km, has been inferred from theory and verified in the Apollo data.

INSTRUMENT DESCRIPTION

The gamma ray spectrometer is shown in figure 18-1, and a generalized block diagram is shown in figure 18-2. Within the cylindrical thermal shield are the detection, amplification, encoding, and data-processing systems that identify and characterize the incident gamma rays as functions of time and energy. The sensing element of the detector is a 6.99- by 6.99-cm cylindrical scintillation crystal of sodium iodide (thallium (Tl) activated) (NaI(Tl)). The energy lost by gamma rays in traversing the crystals is converted, by means of ionization processes, into light that is sensed and transformed into a proportionate charge output by a 7.62-cm-diameter photomultiplier tube (PMT), which is optically coupled to the NaI(Tl) crystal. After amplification and shaping, the output signal passes to an analog-to-digital converter (ADC), which is controlled by a crystal-clock pulse generator that transforms the detector signal

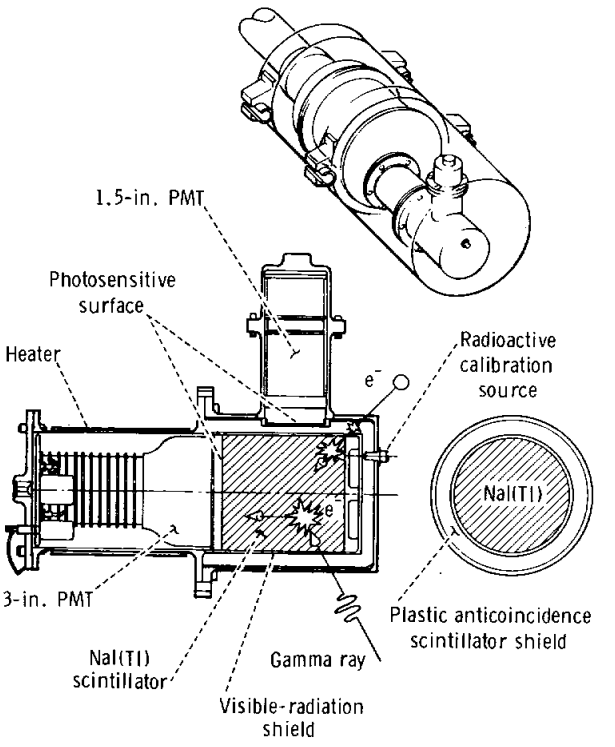


FIGURE 18-1.–Gamma ray spectrometer.

into an accurately measured pulse train. This pulse train is counted in an accumulator and results in a number proportional to the charge output of the detector for that particular event. The data are sent on an event-by-event basis either to the spacecraft telemetry system for direct transmission or to a tape recorder for intermediate storage when the spacecraft is behind the Moon.

The NaI(Tl) scintillator responds to charged particles as well as to gamma rays. To eliminate charged-particle events, a plastic-scintillator shield surrounds the NaI(Tl). The plastic scintillator detects all charged particles above a minimum energy but has a low probability of interacting with gamma rays. Events in the plastic scintillator produce a signal in the 3.81-cm PMT that is transmitted to a gate ahead of the ADC to inhibit (veto) the acceptance of a coincident pulse from the NaI(Tl) PMT.

In addition to the accumulators that process the primary-data pulse train, separate accumulators are provided for counting the number of events in the plastic-scintillator shield, the number of events coincident in both the NaI(Tl) and plastic

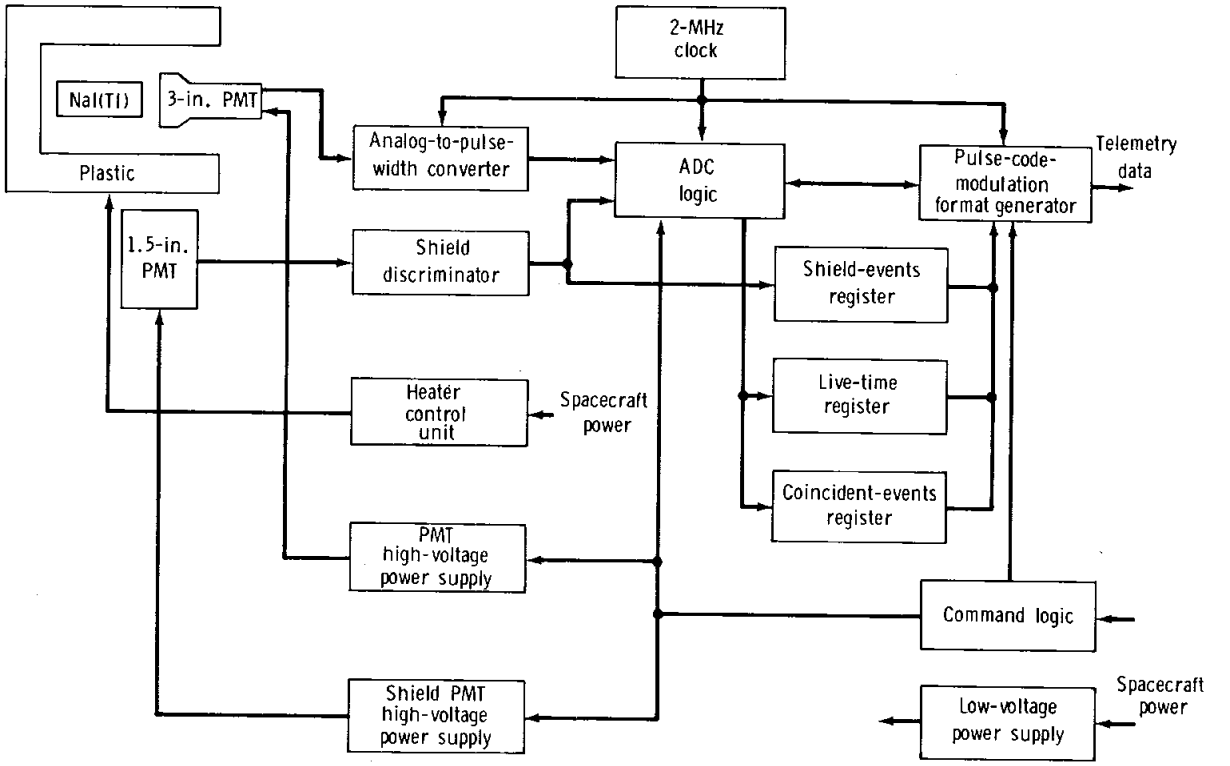


FIGURE 18-2.—Block diagram of the gamma ray spectrometer.

scintillators, and a live-time pulse train. The live-time pulse train provides the factor to derive the rate at which gamma rays are entering the NaI(Tl) crystal from the number that are analyzed. The command capability of the instrument allows the veto function to be enabled and disabled, the high-voltage bias on the 7.62-cm PMT to be varied in steps amounting to a total range in gain of a factor of approximately 3, and the power to be turned on and off.

Besides the passive thermal control provided by the striped paint pattern on the thermal shield, a thermal-control circuit supplies power to a heating blanket around the central detector when a control sensor indicates that the temperature in the immediate vicinity of the central detector has dropped to less than 288° K. The purpose of this capability is to minimize thermally induced variations in gain that, if rapid and continuous, would degrade the energy resolution of the instrument.

In normal operation, the instrument is deployed on a 7.6-m boom that extends normal to the surface of the scientific instrument module bay. The purpose of the boom is to decrease the response of the instrument to cosmic ray interactions and radioactive sources in the spacecraft. The importance of these effects can be seen from the observation that the count rates observed when the boom was retracted during transearth coast were close to those in lunar orbit with the boom extended; that is, the instrument response to the spacecraft was approximately the same as that to the Moon. In the extended position, the instrument response to the spacecraft is reduced to a few percent of the total count rate.

APOLLO 16 EXPERIMENT

The Apollo 16 experiment was an advance over that performed on Apollo 15 in the following manner (ref. 18-1).

(1) The energy resolution of the spectrometer has been improved from approximately 8.5 to 7.5 percent. This improvement has resulted in a clearer resolution of lines and a greater precision of analysis (fig. 18-3).

(2) The data made available during the mission included preliminary data-stream tapes. These tapes allowed a more rapid and complete analysis of the data during the mission itself.

(3) The mission plan included a substantial increase in the amount of prime data obtained in lunar orbit. The decision to return 1 day early reduced the amount of data, but the gain was still significant.

(4) The results of the Apollo 15 experiment in the transearth coast phase indicated that the correction of the lunar data for sky background was largely understood and also gave indications of further possibilities in gamma ray astronomy. The Apollo 16 spacecraft was maneuvered in an extended series of special rotations and was pointed to exploit these possibilities.

(5) The Apollo 15 experiment experienced two instrument problems: a drift in gain stabilizing throughout the mission and a discontinuous zero offset that occurred during a large part of the transearth coast phase. On Apollo 16, as predicted, the gain drift was much smaller and the other difficulty did not occur. A noisy auxiliary channel seen before and during the mission caused no serious problems, and overall performance was excellent.

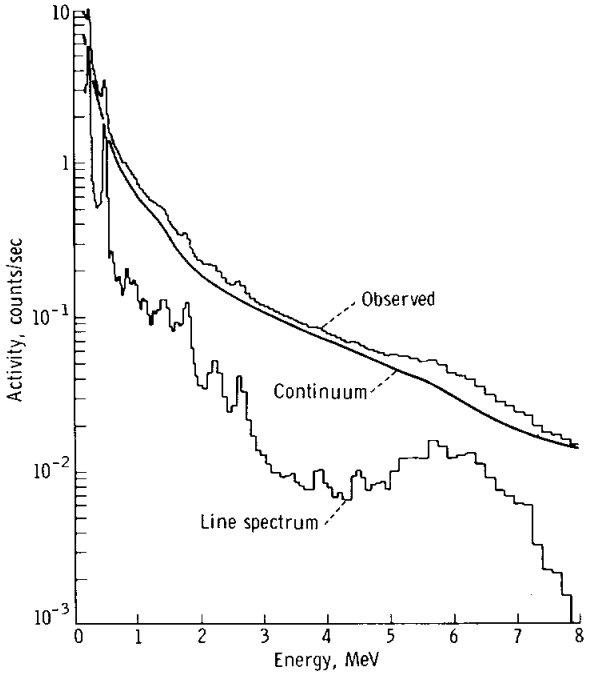


FIGURE 18-3.–Typical Apollo 16 spectrum.

RESULTS

A typical Apollo 16 spectrum is shown in figure 18-3. The improved resolution of the instrument shows plainly in the spectrum after continuum subtraction. (See ref. 18-1 for comparison.)

The first analysis for this mission emphasized the energy region from 0.55 to 2.75 MeV, which contains the main radioactive lines of thorium, uranium, and potassium. In this energy band, the regional differences in count rate are the result of the varying intensities of the lines of the radioactive elements thorium, uranium, and potassium. This is fortunate because the statistical precision of the total count rate in the region (fixed in practice at 0.55 to 2.75 MeV) is excellent and the best possible areal resolution can be obtained. At a nominal altitude of 100 km above the lunar surface, the theoretical distance resolution of the system is approximately 70 km, or 2.5°.

The flux of particle radiation as observed during veto disable periods was 5 percent greater on Apollo 16 than on Apollo 15. When the gamma ray results are normalized to the Apollo 15 results using this factor (the procedure used here), the results in the trajectory crossover regions are in excellent agreement. The source of this increase is being investigated. The data from both missions have been corrected to an altitude of 100 km; the solid angle subtended by the Moon at the detector is a reasonably accurate normalization over the narrow range of altitudes at which data were taken. The data were also corrected for instrument live time; no other corrections have been applied.

The range of the corrected counting rates is from 73 to 93 counts/sec, or approximately 25 percent. The corrected count rate as a function of longitude for one period early in the mission is shown in figure 18-4. Figure 18-4 also shows the most striking observation of the mission (the high count rates in the western mare regions, with the highest count rate observed south of the crater Fra Mauro). This region is at the southern end of the Fra Mauro formation; the Apollo 14 landing site was near the northern edge of this north-south trending feature.

A more complete representation of the data is in the form of a map of the count rate summed in 5° by 5° areas of the overflown surface. Such a map has

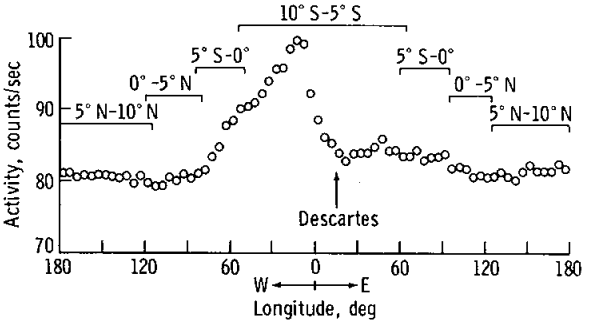


FIGURE 18-4.—Corrected count rate for a period early in the mission.

previously been prepared from the Apollo 15 prime data. The standard deviation for a typical counting time of 300 sec/5° square is approximately 0.5 count/sec based on counting statistics alone; it is approximately 1 count/sec for the shortest counting times used. The reproducibility of successive passes, and in regions overflown on both missions, is good.

The combined results for Apollo 15 and 16 are plotted in figures 18-5(a) and (b) for the front and back sides, respectively. The data are plotted on a simplified map of the Moon for ease of interpretation.

The conclusions concerning the lunar portion of the experiment are as follows.

(1) The Apollo 16 results extend and confirm the Apollo 15 finding that all 5° regions within the boundaries of the western maria are higher in radioactivity than any 5° region outside this area. These results strongly suggest that the western mare regions not flown over are also highly radioactive and that other regions of the Moon are generally less so.

(2) Detailed structure exists within the high-radioactivity region. The high observed in the Fra Mauro area is at about the same level as those seen around Aristarchus and south of Archimedes on Apollo 15. These levels are comparable to that observed in the soil at the Apollo 14 landing site.

(3) The eastern maria show evidence of lower (and variable) radioactivity. Structure is visible in Mare Fecunditatis (more apparent on a 2° scale) and elsewhere.

(4) The highland regions show low radioactivity, except near the western maria where some lateral mixing has occurred. The maximum seen near Van de Graaff on Apollo 15 has no counterpart on this track. A visible low near 120° E may reflect slightly higher values in the large basins on either side.

The Descartes landing site is one of the places where some admixture of radioactive material has occurred. Two members of the investigating team made predictions of the thorium content of the soil at Descartes; 1 to 2 ppm (J.R.A.) and 2 to 3 ppm (A.M.). The values observed in representative samples range from 2.0 to 2.8 ppm (private communication, Lunar Surface Preliminary Examination Team).

GAMMA RAY ASTRONOMY

The transearth coast period of Apollo 16 presented an opportunity to continue measurements of the cosmic gamma ray spectrum started on Apollo 15. This period on Apollo 15 was devoted primarily to operating the instrument and spacecraft in a mode designed to provide measurements of the total spectrum in space and various background effects that may confuse this spectrum. Based on the results, it was concluded that some knowledge of the directionality or anisotropy of the cosmic-gamma-ray fluxes was obtainable and would provide badly needed astrophysical information. Positioning the detector boom at approximately 2 m during transearth coast causes an appreciable region of the sky to be occulted by the spacecraft. As the spacecraft rotates at approximately 3 revolutions/hr for thermal control, various regions of the sky become occulted. Changing the spacecraft spin axis causes various planes to become occulted. Preflight analysis indicated that a "map" could be obtained of the sky in 1-MeV gamma rays containing 40 resolution elements at approximately the 2-percent difference level.

The uncorrected counting-rate spectrum obtained on Apollo 15 and 16 is compared in figure 18-6 with previous results on the energy-loss spectrum measured in cislunar space on the Ranger III and ERS-18 satellites (refs. 18-2 and 18-3). The near agreement of Apollo 15 and 16 data, which also agree with other data to approximately 2 MeV, give considerable confidence in the new results. Above 2 MeV, these results are below a previous measurement. The Apollo data shown in figure 18-6 still contain a small contribution caused by gamma ray lines from spacecraft natural and induced radioactivity and caused by continuum processes as a result of high-energy cosmic

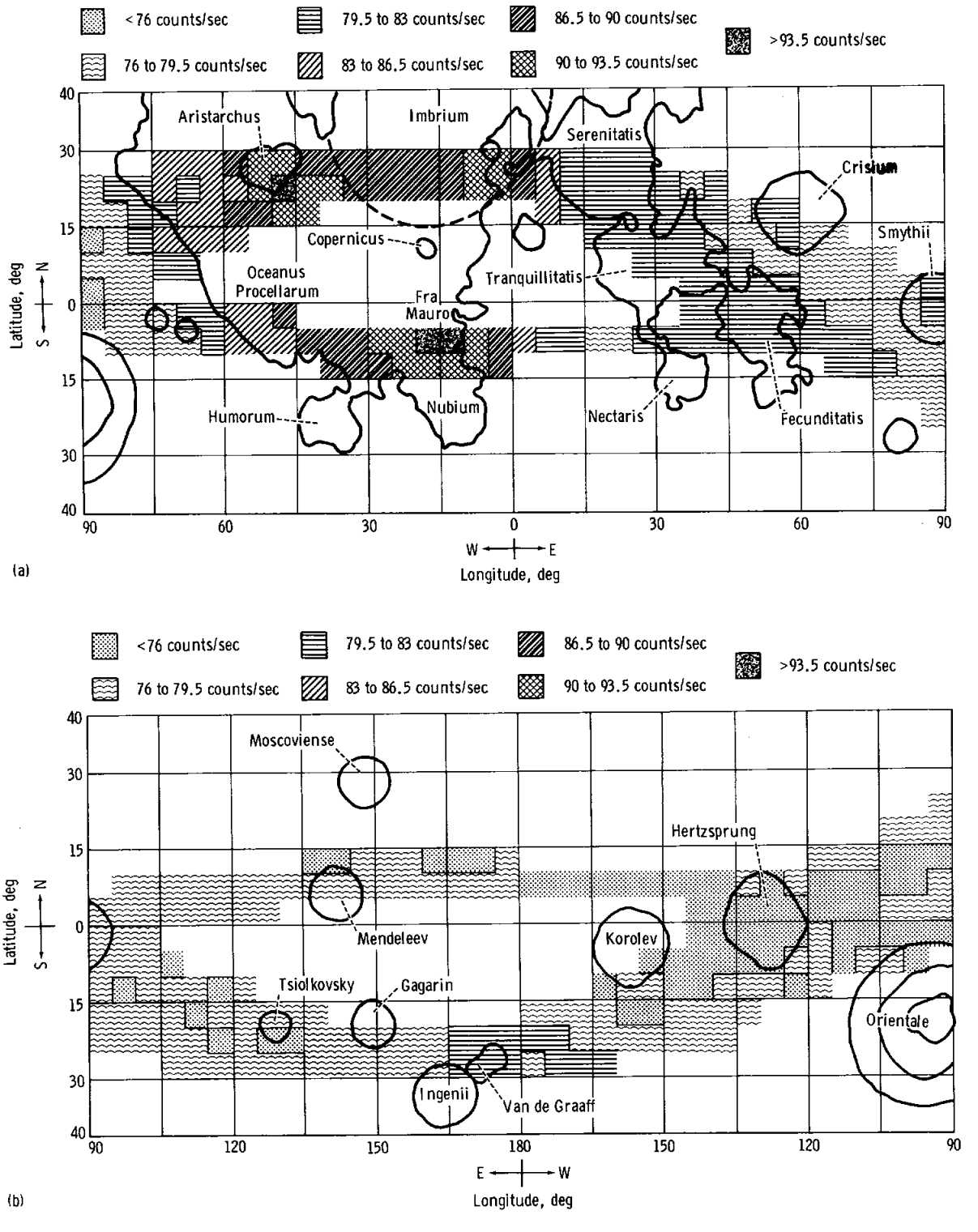


FIGURE 18-5.–Combined count rate results for Apollo 15 and 16. (a) Front side. (b) Back side.

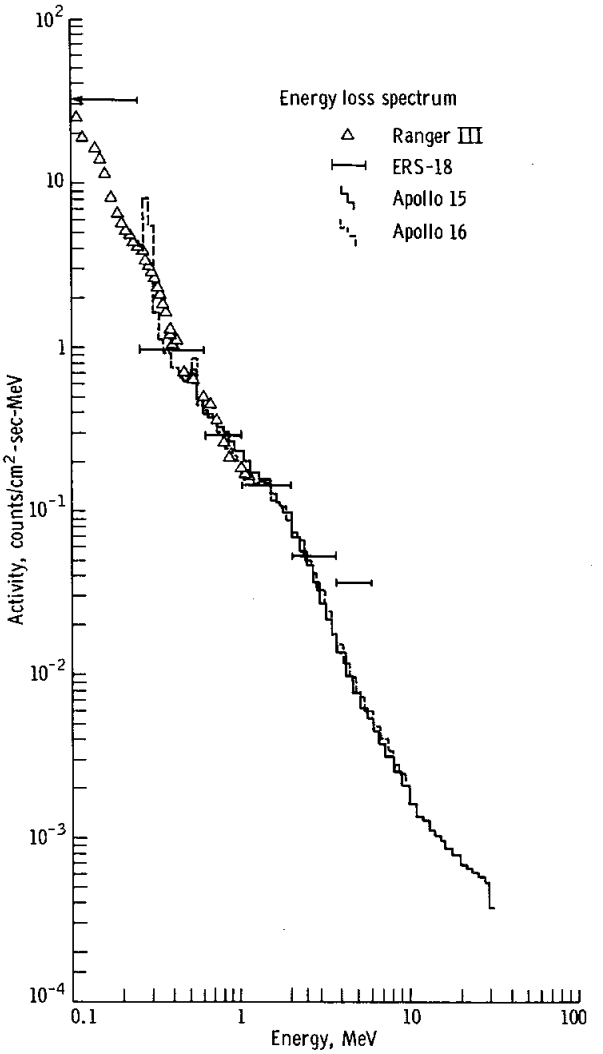


FIGURE 18-6.–Comparison of uncorrected counting rate spectrum from Apollo 15 and 16 with the energy loss spectrum measured in cislunar space by satellites.

rays. Furthermore, there is an appreciable but uncertain contribution caused by cosmic-ray-produced spallation (ref. 18-4) in the scintillation crystal. The total cosmic gamma ray flux above approximately 2 MeV is considerably less than that implied by the ERS-18 satellite and rejects some cosmological models that had been proposed to explain the high flux in the 2- to 6-MeV range (ref. 18-5).

The spin-axis positions, scan planes, and resultant occulted regions selected for the Apollo 16 operation are shown in figure 18-7. These four scans permit occultation of possible strong, compact gamma ray sources such as the Crab Nebula, Sagittarius, and perhaps others that may be in the galactic plane. In addition, scan planes were selected that would provide information on anisotropies associated with the

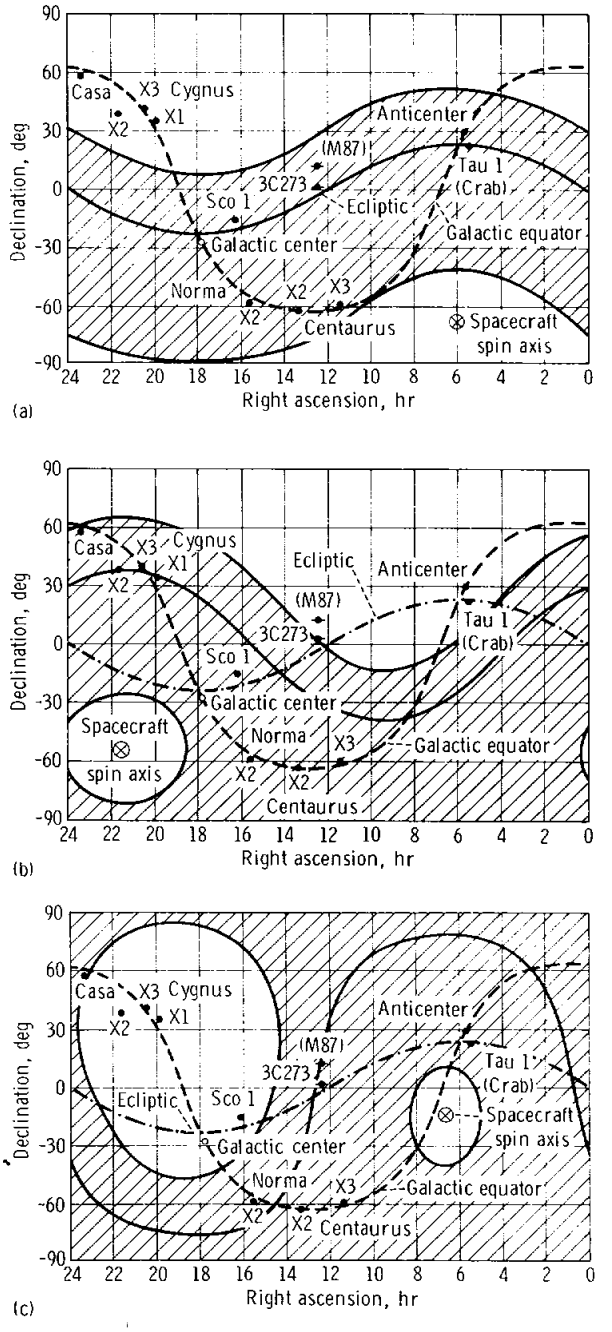


FIGURE 18-7.–Spin-axis positions, scan planes, and occulted regions selected for Apollo 16. (a) Ecliptic scan. (b) Ecliptic auxiliary scan. (c) Supergalactic scan.

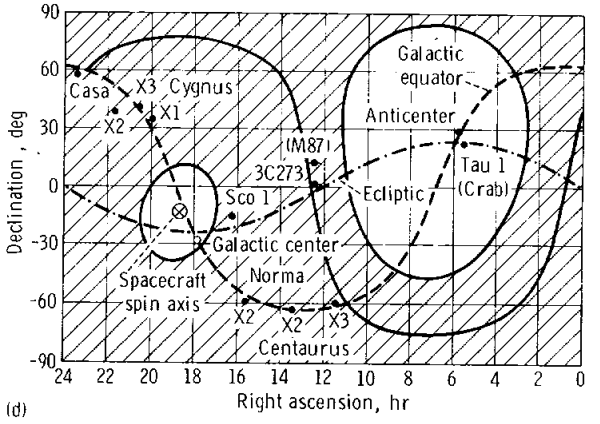


FIGURE 18-7.–Concluded. (d) Supergalactic auxiliary scan.

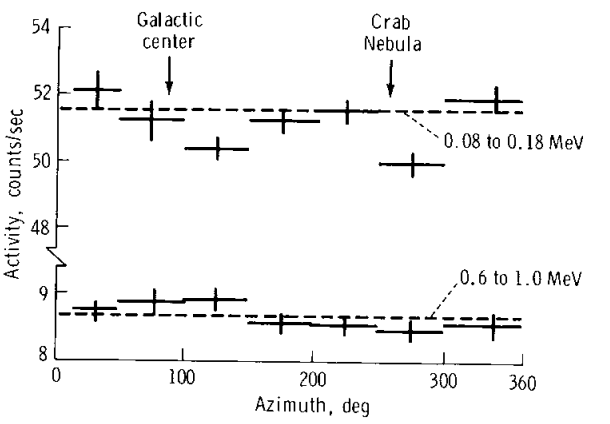


FIGURE 18-8.–Apollo 16 ecliptic scans.

local cluster of galaxies and the supercluster, which contains the Virgo cluster. It may also be possible to detect global anisotropies associated with the initial formation of the universe, to which these gamma rays are thought to be coupled, at least on a "big-bang" model of the universe.

Although the final data base has not yet been obtained to perform the extensive analysis required to search for and interpret anisotropies, some preliminary results are available, based on preliminary data tapes received during the mission. The counting rates in two energy ranges as a function of azimuth during several ecliptic plane scans are shown in figure 18-8. As can be seen from figure 18-7, this scan also includes the galactic center and the Crab Nebula, sources which emit in the 0.3- to 1-MeV range, based on previous data. The data clearly confirm the presence of appreciable gamma ray emission from these regions, because the counting rate of the isotropic counter decreases when these regions become occulted. Further analysis probably will indicate other sources and allow determination of the spectrum of the stronger emitters. Measurements of celestial gamma rays obtained on Apollo 15 and 16 clearly promise new and hitherto unobtainable information on this important astronomical component.

REFERENCES

18-1. Arnold, J. R.; Peterson, L. E.; Metzger, A. E.; and Trombka, J. I.: Gamma Ray Spectrometer Experiment. Sec. 16 of Apollo 15 Preliminary Science Report. NASA SP-289, 1972.

18-2. Metzger, A. E.; Anderson, E. C.; Van Dilla, M. A.; and Arnold, J. R.: Detection of an Interstellar Flux of Gamma Rays. Nature, vol. 204, no. 4960, 1964, pp. 766-767.

18-3. Vette, J. I.; Gruber, D.; Matteson, J. L.; and Peterson, L. E.: A New Component of Cosmic Gamma Rays Near 1 MeV Observed by the ERS-18 Satellite. NASA TM X-63912, 1970.

18-4. Fishman, G. J.: Cosmic-Ray Effects on Diffuse Gamma-Ray Measurements. Astrophys. J., vol. 171, Jan. 1972, pp. 163-167.

18-5. Stecker, F. W.: Primordial Cosmic-Ray Sources. Nature, vol. 224, no. 5222, 1969, p. 870.

ACKNOWLEDGMENT

The map used in figure 18-5 is adapted from one supplied through the courtesy of Farouk El-Baz.

19. X-Ray Fluorescence Experiment

I. Adler,[a†] J. Trombka,[a] J. Gerard,[ab] P. Lowman,[a] R. Schmadebeck,[a]
H. Blodget,[a] E. Eller,[a] L. Yin,[a] R. Lamothe,[a] G. Osswald,[a] P. Gorenstein,[c]
P. Bjorkholm,[c] H. Gursky,[c] B. Harris,[c] L. Golub,[c] and F. R. Harnden, Jr.[c]

The X-ray fluorescence spectrometer, carried in the scientific instrument module bay of the command and service module, was used for orbital mapping of the lunar surface composition and X-ray galactic observations during transearth coast. The lunar surface measurements involved observations of the intensity and characteristic energy distribution of the secondary or fluorescent X-rays produced by the interaction of solar X-rays with the lunar surface. The astronomical observations consisted of relatively long periods of X-ray measurement of preselected galactic sources such as Cygnus (Cyg X-1) and Scorpius (Sco X-1).

COMPOSITIONAL MAPPING OF THE LUNAR SURFACE

The lunar surface was mapped with respect to magnesium (Mg), aluminum (Al), and silicon (Si) as Al/Si and Mg/Si ratios along the projected ground tracks by the orbiting Apollo 16 spacecraft. The results confirm the Apollo 15 observations and provide new data for several features not previously covered. The data are consistent with the theory that the Moon has a widespread differentiated crust (the highlands). The Al/Si and Mg/Si chemical ratios of the highlands correspond to those of anorthositic gabbro and gabbroic anorthosite. The X-ray results suggest that this premare crust or material similar to it occurs at the Descartes landing site.

Unlike the high inclination orbit of the Apollo 15 spacecraft, the Apollo 16 flightpath was nearly equatorial (9° inclination) so that the areas covered were somewhat smaller than those of the Apollo 15 flight. Although the original flight plan called for a plane change, the circumstances of the mission did not permit this. Consequently, some of the ground coverage was lost.

Theoretical Basis

The theoretical basis for the X-ray fluorescence experiment and a description of the instrument have been given in some detail previously (refs. 19-1 to 19-3). Briefly, the experiment involves orbital measurements of the characteristic secondary X-rays produced by the interaction of the solar X-rays with the lunar surface. Because of the spectral nature of the solar flux, the measurements are limited to the K-shell spectra of the elements Mg, Al, and Si. The heavier elements are not appreciably excited, and the elements lighter than Mg are inefficiently detected. Furthermore, the measurements are limited to that part of the lunar surface that is illuminated by the Sun.

Description of the Instrument

The Apollo 16 instrument is essentially identical to that flown on the Apollo 15 mission and consists of three main subsystems (fig. 19-1).

(1) Three large-area proportional counters that have state-of-the-art energy resolution and 0.0025-cm-thick beryllium windows

(2) A set of large-area filters for energy discrimination among the characteristic X-rays of Al, Si, and Mg

(3) A data handling system for count accumulation, for sorting into eight pulse-height channels, and for relaying the data to the spacecraft telemetry

The X-ray detector assembly consists of three proportional-counter detectors, two X-ray filters, mechanical collimators, an inflight calibration device, temperature monitors, and associated electronics. The detector assembly senses X-rays that are emitted from

---

[a]NASA Goddard Space Flight Center.
[b]National Academy of Sciences.
[c]American Science and Engineering.
†Principal Investigator.

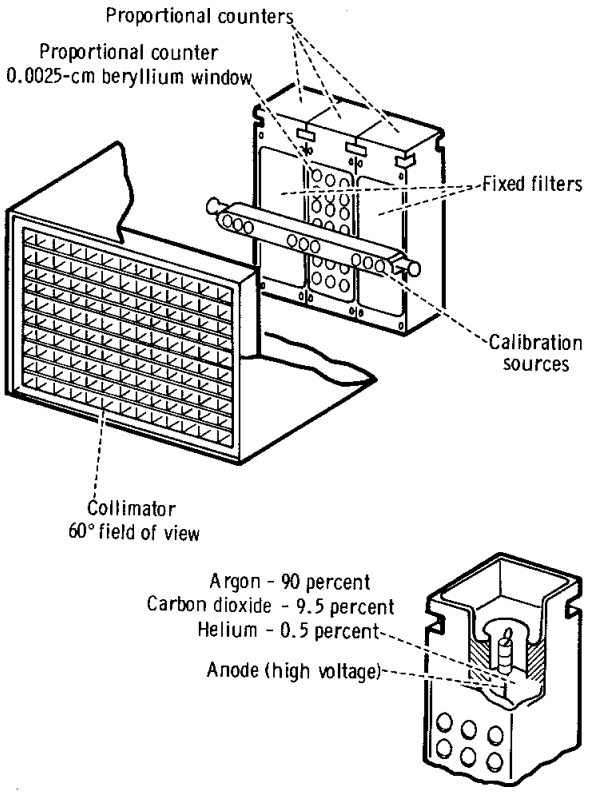


FIGURE 19-1.–Functional configuration of the X-ray spectrometer.

the lunar surface and converts the X-rays to voltage pulses which are processed in the X-ray processor assembly. Provisions for inflight calibration are made by means of programed calibration sources, which, upon internal command, assume a position in front of the three detectors for calibration of gain, resolution, and efficiency. Thermistors, which are located at strategic points, sense the temperature of the detector assembly for telemetry monitoring and temperature control of the detectors by means of heaters located near the proportional-counter windows.

The behavior of the X-ray output of the Sun was simultaneously monitored with the lunar surface measurements by means of the solar monitor, a small proportional detector mounted on the opposite side of the spacecraft from the surface detectors. On the Apollo 16 spacecraft, a thin beryllium foil filter was added in front of the detector window to enable the spectrometer to view high-Sun X-ray fluxes without experiencing the detector gainshifts that were observed during the Apollo 15 flight.

Operation of the Experiment

The X-ray experiment began to function on April 20, 1972, at approximately 02:00 Greenwich mean time (G.m.t.) and was operated for approximately 12 hr in an elliptical orbit (approximately 10 by 60 n. mi.). At approximately 04:00 G.m.t. on April 21, the experiment was again activated; the spacecraft was in a circular lunar orbit of approximately 60 n. mi. As in the Apollo 15 flight, the estimated field of view for each data point used in this report is approximately 60 by 80 n. mi. The data were reduced during the mission. Thus, conclusions about the Descartes landing site could be made and reported to the crewmen while they were on the surface.

The overlap of orbital coverage between the Apollo 15 and 16 ground tracks (mainly from 50° to 100° E) makes it possible to compare the reproducibility of the measurements for both missions. The total coverage for the two missions is greater than 20 percent of the surface of the Moon. The Apollo 16 spectrometer provided data for a number of features not previously covered; for example, Mare Cognitum, Mare Nubium, Ptolemaeus, Descartes, and Mendeleev as well as several other areas (fig. 19-2). It is encouraging that, for these areas, the Al/Si and Mg/Si chemical ratios for both flights agreed to better than 10 percent (table 19-I). This agreement makes it possible to draw comparisons between the two flights. It also demonstrates that the X-ray spectral distribution of the Sun, which produces lunar fluorescent X-rays, was about the same on both missions. In fact, this conclusion has been confirmed by examination of the SOLRAD data[1] available for those periods. Another point of considerable interest is that the spectrometer obtained a large number of data points over the Descartes landing site (fig. 19-2 and tables 19-II and 19-III). Hopefully, the results will show how representative the data are of the Descartes area.

Results and Observations

The following preliminary results and observations are based on the reduction of the data tapes supplied

[1]The SOLRAD data are obtained by satellite monitoring solar radiation and are reported by the National Oceanic and Atmospheric Administration, Rockville, Maryland, in Solar-Geophysical Data (Prompt Reports).

TABLE 19-I.–Overlap Between the Apollo 15 and 16 Ground Tracks

Feature (a)	Apollo 16 concentration ratio		Apollo 15 concentration ratio	
	Al/Si ± 1σ	Mg/Si ± 1σ	Al/Si ± 1σ	Mg/Si ± 1σ
Mare Fecunditatis	0.41 ± 0.05	0.26 ± 0.05	0.36 ± 0.06	0.25 ± 0.03
Mare Smythii	.45 ± .08	.25 ± .05	.45 ± .06	.27 ± .06
Langrenus area	.48 ± .07	.27 ± .06	.48 ± .11	.24 ± .06
Highlands west of Smythii	.57 ± .07	.21 ± .03	.55 ± .06	.22 ± .03
Western border of Smythii	.58 ± .08	.22 ± .04	.52 ± .06	.22 ± .06
Eastern border of Smythii	.61 ± .09	.20 ± .06	.60 ± .10	.21 ± .03

[a]The overlap between corresponding areas of the Apollo 16 and 15 ground tracks is not exact, so that differences for the same area may be real (fig. 19-2).

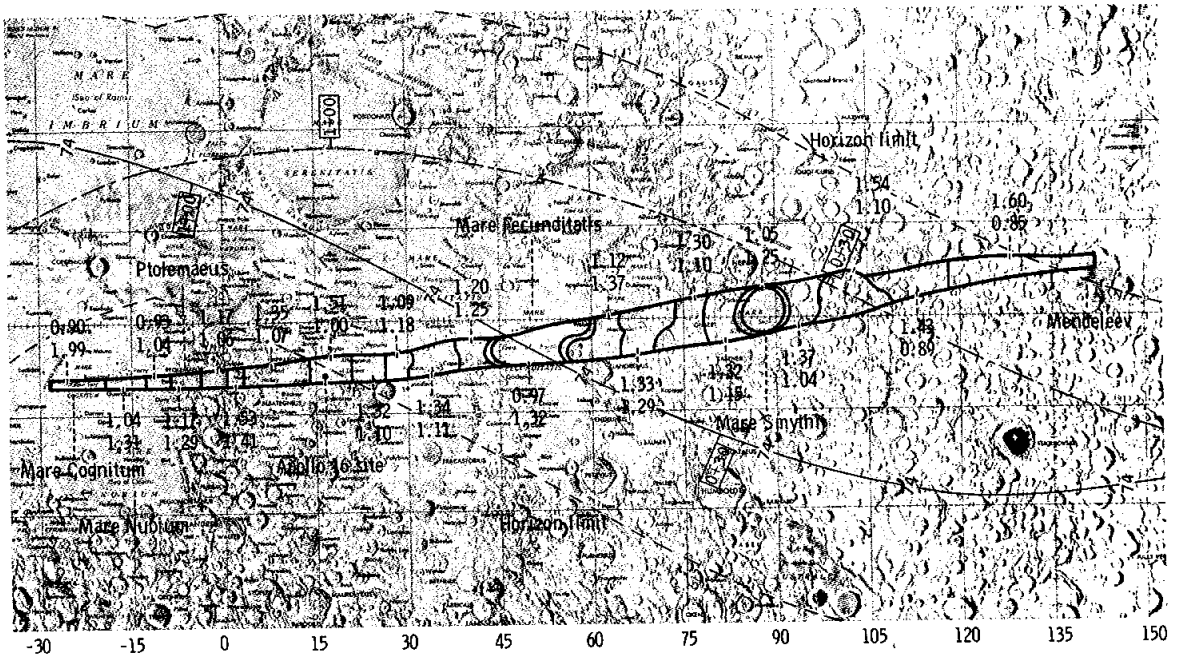


FIGURE 19-2.–Al/Si and Mg/Si intensity ratios for specific areas along the Apollo 16 ground tracks. The first values are Al/Si and the second values are Mg/Si. The double lines represent the transition zones between the mare basins and the highlands. The intensity ratios in these zones reflect an overlap between the lower mare values and the higher highland values.

during the Apollo 16 mission. For the most part, the data points represent 64-sec accumulations, so that the surface spatial resolution is not optimal. The reduced data have been treated in several ways. The Al/Si and Mg/Si intensity ratios have been plotted along the ground tracks and related to gross features as well as other phenomena such as optical albedo. (The refined data will be treated at shorter intervals and published subsequently.)

Figure 19-2 shows the variation of Al/Si and Mg/Si intensity ratios plotted along the projected Apollo 16 ground tracks. These ground tracks have been divided into areas based in part on obvious geologic features and in part on intensity contours. Because of the relatively low inclination of the orbit and the repetitive ground tracks, there is a high

TABLE 19-II.–Concentration Ratios of Al/Si and Mg/Si for Various Features

Feature	N (a)	Concentration ratio	
		Al/Si ± 1σ	Mg/Si ± 1σ
Mare Cognitum	8	0.38 ± 0.11	0.40 ± 0.29
Upper part of Sea of Clouds (9° to 13° W)	8	.39 ± .12	.20 ± .05
Mare Fecunditatis (42° to 57° E)	80	.41 ± .05	.26 ± .05
South of Fra Mauro (13° to 19° W)	9	.45 ± .07	.26 ± .04
Mare Smythii (82° to 92.5° E)	24	.45 ± .08	.25 ± .05
Southern edge of Mare Tranquillitatis, Torricelli area (26° to 30° E)	21	.47 ± .09	.23 ± .05
Eastern edge of Fecunditatis, Langrenus area (57° to 64° E)	44	.48 ± .07	.27 ± .06
Ptolemaeus (4° W to 0.5° E)	17	.51 ± .07	.21 ± .04
Highlands west of Ptolemaeus to Mare Nubium (4° to 9° W)	16	.51 ± .11	.25 ± .12
Highlands west of Mare Fecunditatis (37.5° to 42° E)	29	.52 ± .07	.24 ± .05
Highlands west of Smythii (72° to 77° E)	35	.57 ± .07	.21 ± .03
Western border of Smythii (77° to 82° E)	33	.58 ± .08	.22 ± .04
Highlands east of Descartes (20.5° to 26° E)	23	.58 ± .07	.21 ± .04
South of Mare Spumans (64° to 72° E)	45	.58 ± .07	.25 ± .04
Isidorus and Capella (30° to 37.5° E)	38	.59 ± .11	.21 ± .05
Highlands west of Descartes (3° to 14° E)	44	.59 ± .11	.21 ± .05
Eastern border of Mare Smythii (92.5° to 97.5° E)	17	.61 ± .09	.20 ± .06
Far-side highlands (106° to 118° E)	29	.63 ± .08	.16 ± .05
Descartes area, highlands, Apollo 16 landing site (14° to 20.5° E)	30	.67 ± .11	.19 ± .05
East of Ptolemaeus (0.5° to 3° E)	12	.68 ± .14	.28 ± .09
Highlands (97.5° to 106° E)	31	.68 ± .11	.21 ± .05
Far-side highlands west of Mendeleev (118° to 141° E)	30	.71 ± .11	.16 ± .04

[a]N is the number of individual data points used to determine the average Al/Si and Mg/Si values ±1 standard deviation and was obtained from the various passes over each feature.

density of plotted data points. Thus, each value shown represents the average of a substantial number of points.

Detailed results expressed as concentration ratios are given in tables 19-II and 19-III. A brief summary of the main observations follows.

(1) The early reports of very high Al/Si ratios in the Descartes area, given while the mission was in progress, have been confirmed by the analysis of some of the returned lunar samples. The value of 25 to 29 percent aluminum oxide, reported in reference 19-5, agrees very well with the preliminary estimate of 26 to 27 percent. From figure 19-2, it appears reasonable that some of the material sampled at Descartes may be similar to the eastern limb and far-side highlands. This conclusion is further justified by the fact that the Mg/Si concentration ratio for some of the returned material is approximately 0.18, close to the anticipated value of 0.19 ± 0.05. The Mg/Si concentration ratios for the eastern limb and far-side highlands are approximately 0.16 to 0.21 (tables 19-II and 19-III).

(2) The Apollo 15 observations of high Al and low Mg values in the highlands and the reverse in the mare areas are confirmed by the Apollo 16 data. However, there are exceptions. For example, the area east of Ptolemaeus has both high Al/Si and Mg/Si ratios.

(3) In both missions, the Al and Mg values show an inverse relationship, although this is not true

TABLE 19-III.–Concentration Ratios of Al/Si and Mg/Si for Selected Lunar Samples

Selected lunar samples	Concentration ratio		Reference
	Al/Si	Mg/Si	
Apollo 12, Oceanus Procellarum type AB rocks, average	0.22	0.22	19-4
Apollo 15, Hadley-Apennine rocks, average	.22	.27	19-5
Apollo 12, Oceanus Procellarum type B rocks, average	.22	.37	19-4
Apollo 11, Mare Tranquillitatis high potassium rocks, average	.23	.24	19-6
Apollo 12, Oceanus Procellarum type A rocks, average	.24	.31	19-4
Apollo 12, rock 12013	.24 to .30	.20	19-4
Apollo 11, Mare Tranquillitatis low potassium rocks, average	.29	.23	19-6
Apollo 12, dark portion of rock 12013	.33	.22	19-7, 19-8
Apollo 12, Oceanus Procellarum soil, average	.33	.29	19-4
Surveyor VI, Sinus Medii regolith	.34	.20	19-9, 19-10
Apollo 15, Hadley-Apennine soil	.34	.30	19-5
Surveyor V, Mare Tranquillitatis regolith	.35	–	19-10, 19-11
Luna 16, Mare Fecunditatis rocks	.35	.21	19-12
Apollo 11, Mare Tranquillitatis bulk soil, average	.37	.24	19-6
Apollo 14, Fra Mauro rocks, average	.38	.26	19-13
Apollo 11 and 12, potassium, rare-Earth elements, and phosphorus (KREEP), average	.39	.21	19-7, 19-8
Apollo 14, Fra Mauro soil	.41	.26	19-13
Apollo 12, norite material, average	.42	.20	19-14, 19-15
Luna 16, Mare Fecunditatis bulk soil	.42	.27	19-12
Surveyor VII, rim of Tycho, regolith	.55	.20	19-10, 19-16
Luna 20, Apollonius Highlands	.58	.26	19-12
Apollo 11 and 12, anorthositic gabbro	.64	.21	19-14, 19-15
Apollo 15, rock 15418, gabbroic anorthosite	.67	.15	19-5
Apollo 11 and 12, gabbroic anorthosite	.82	.074	19-14, 19-15
Apollo 11 and 12, anorthosite	.89	.038	19-14, 19-15
Apollo 15, rock 15415, anorthosite, Genesis Rock	.91	.003	19-5

everywhere.

Figures 19-3 and 19-4 show detailed plots of Al/Si and Mg/Si values (intensities and concentration ratios) as compared to longitude for the projected Apollo 16 ground track. Various mare and highland features are identified. Analyzed material is shown for reference on the left-hand concentration scale. Marked differences exist between the highland and mare areas. For example, the extreme variation in Al/Si concentration is almost a factor of 2 between the low values in Mare Cognitum and the high values in the highlands west of Mendeleev. The Mg/Si ratios vary inversely, with the Al/Si ratios being highest in the mare and lowest in the highlands.

One of the results to emerge from the Apollo 15 mission was the excellent correspondence between the Al/Si values and the optical albedo values. This observation was particularly significant in view of the long-standing discussion as to whether these albedo differences were solely representative of topographic differences or were also a reflection of compositional differences among surface materials. Early investigators, such as Whitaker (ref. 19-17), recognized convincing evidence for compositional changes where sharp albedo changes occur. However, it remained for the later Surveyor, Luna, Lunokhod, and Apollo

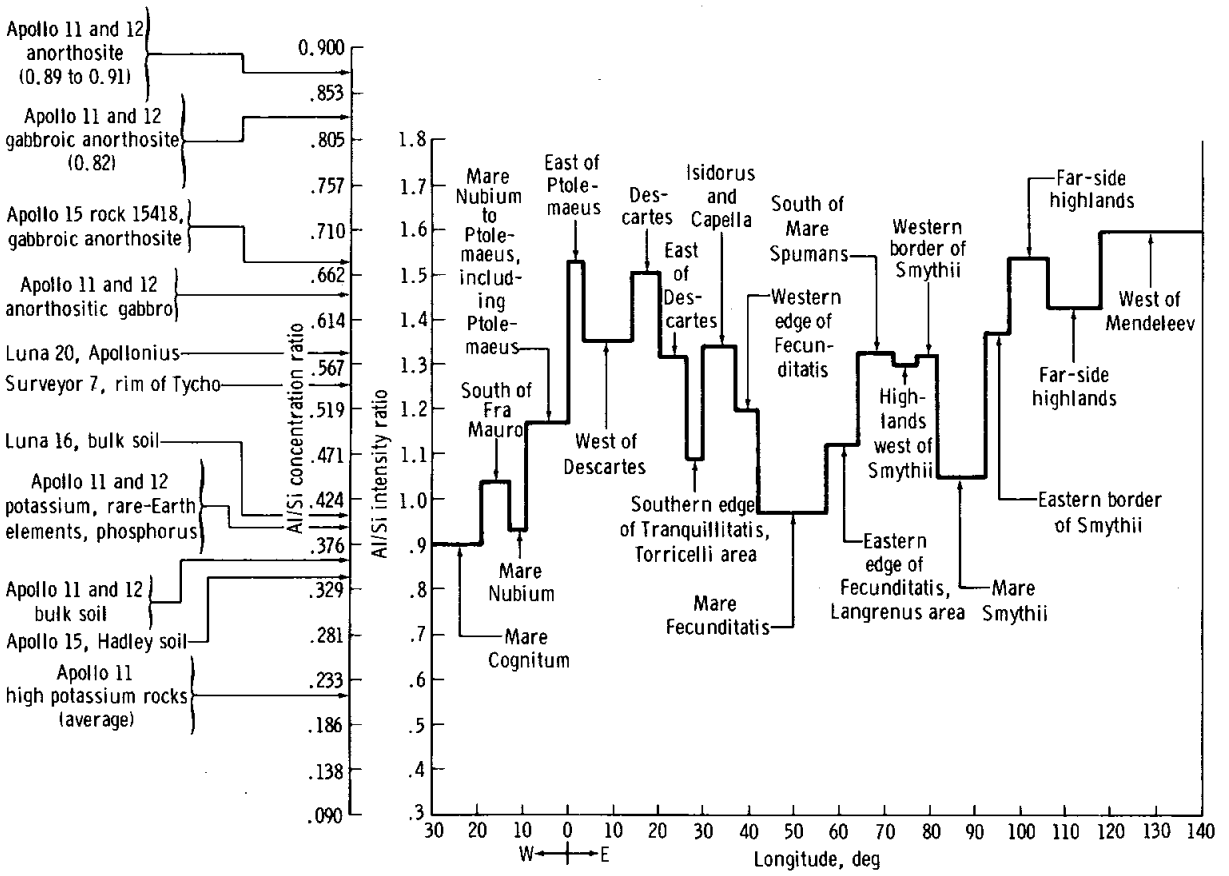


FIGURE 19-3.–Al/Si intensity and concentration ratios as compared to longitude.

missions to provide quantitative compositional data. Chemical differences related to the albedo were first confirmed by the alpha scattering experiments of Surveyor V, VI, and VII. The Surveyor V soft lander tested widely separated mare sites and reported chemically similar surfaces for each. Surveyor VII, on the other hand, returned samples from a highland site; significant chemical differences between the highlands and the two mare locations were reported (ref. 19-18). The Surveyor results and analyses of returned lunar samples confirmed that albedo is indeed affected by compositional as well as topographic differences. The X-ray fluorescence experiment on the Apollo 15 and 16 missions has now provided the means to correlate regional albedo with surface composition (for selected elements).

Data locations for selected Apollo 15 and 16 orbits covered by the X-ray fluorescence experiment were plotted on the map of the normal albedo of the Moon by Pohn, Wildey, and Sutton (ref. 19-19). Average albedo was then computed for each 3° area for which the X-ray data were available and plotted against the Al/Si intensity ratios. The positive correlation between the albedo and Al/Si values is strong, although the rate of change is not always similar. In the Apollo 15 plots, the main anomalies were observed where an occasional small Copernican crater occurred, which produced an abnormally high albedo value. The brightness of these craters is generally considered to be due to the highly reflective, finely divided ejecta rather than compositional changes. A similar anomaly is noted in the Apollo 16 data at approximately 27° E in a Tranquillitatis embayment north of Theophilus. Four Apollo 16 revolutions were plotted (fig. 19-5), and revolutions 58 and 60 show the expected decrease in Al/Si values with decreasing albedo. Revolutions 55 and 59, on the other hand, show an occasional increase in Al/Si values although the albedo decreases. This may record the existence of old "weathered" rays consisting of

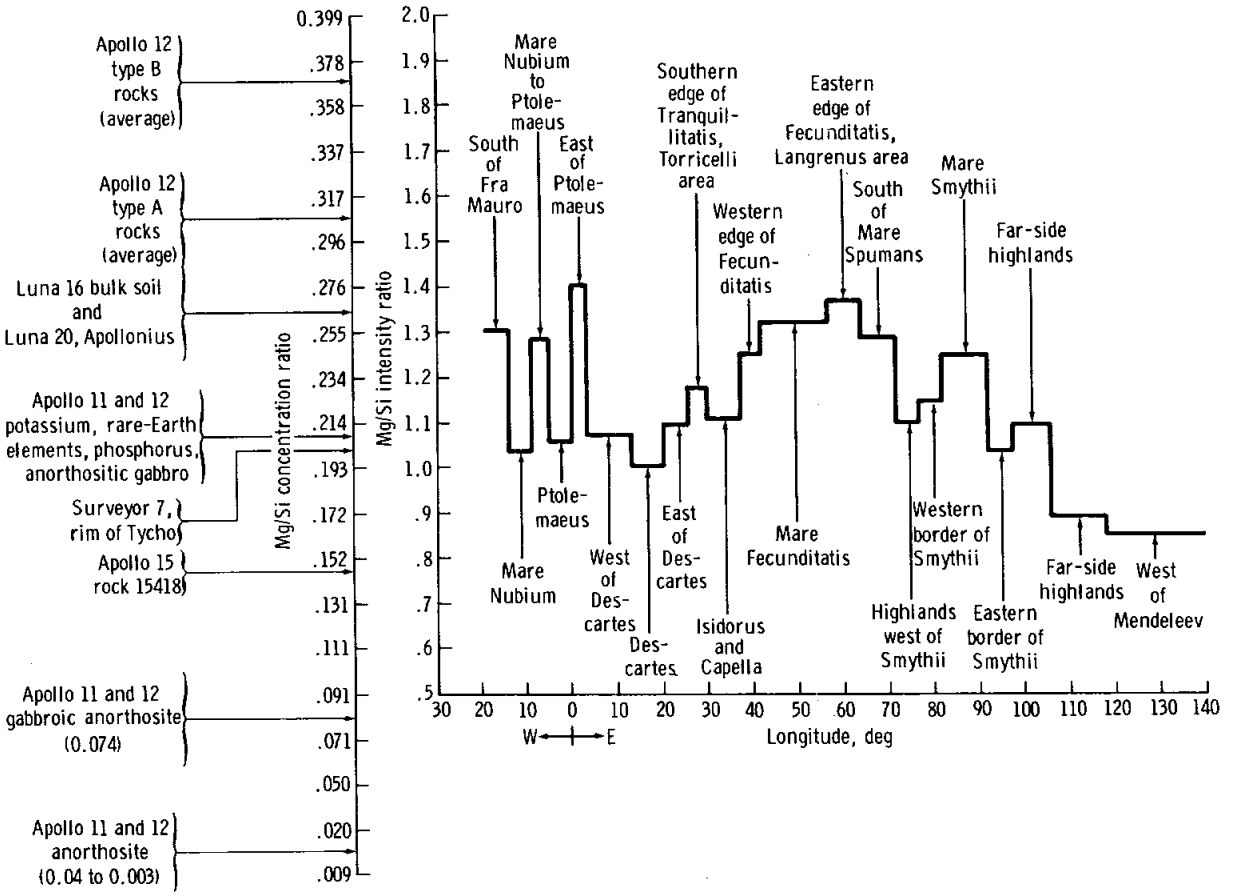


FIGURE 19-4.–Mg/Si intensity and concentration ratios as compared to longitude.

aluminum-rich highland-derived ray material that has now lost its high reflectivity.

Geologic Interpretation

The results of the Apollo 16 X-ray fluorescence experiment generally support the main conclusions reached after the Apollo 15 mission (ref. 19-2). However, further conclusions are now possible.

First, and most important, the good correlation between the aluminum oxide content inferred from the X-ray data and the returned samples implies that the X-ray measurements are a reliable guide, at least to this aspect of the surface composition of the Moon. Second, the strong correlation between albedo and Al/Si ratios suggests that, if allowance is made for features the brightness of which is primarily caused by physiographic youth (such as Copernican craters), the albedo is a reasonable guide to highland composition, specifically to its plagioclase content. Together, these conclusions imply that the plagioclase-rich highland crust, the existence of which was first inferred from the Apollo 11 samples, is global in extent, although albedo measurements are not yet available from the far side of the Moon.

The data from the highland area covered by the Apollo 16 spectrometer have maximum Al/Si ratios that lie between those of anorthositic gabbro and gabbroic anorthosite returned from previous Apollo missions (fig. 19-3). Despite the frequent occurrence of anorthositic fragments in regolith samples, nowhere are the Al/Si ratios as high as those of anorthosite. This high ratio implies that anorthosite is a subordinate though widespread constituent of the highland crust, the bulk of which is anorthositic gabbro (using the term in a chemical sense). Local concentrations of anorthosite could form by crystal flotation from a gabbroic magma; how the magma itself formed is not clear.

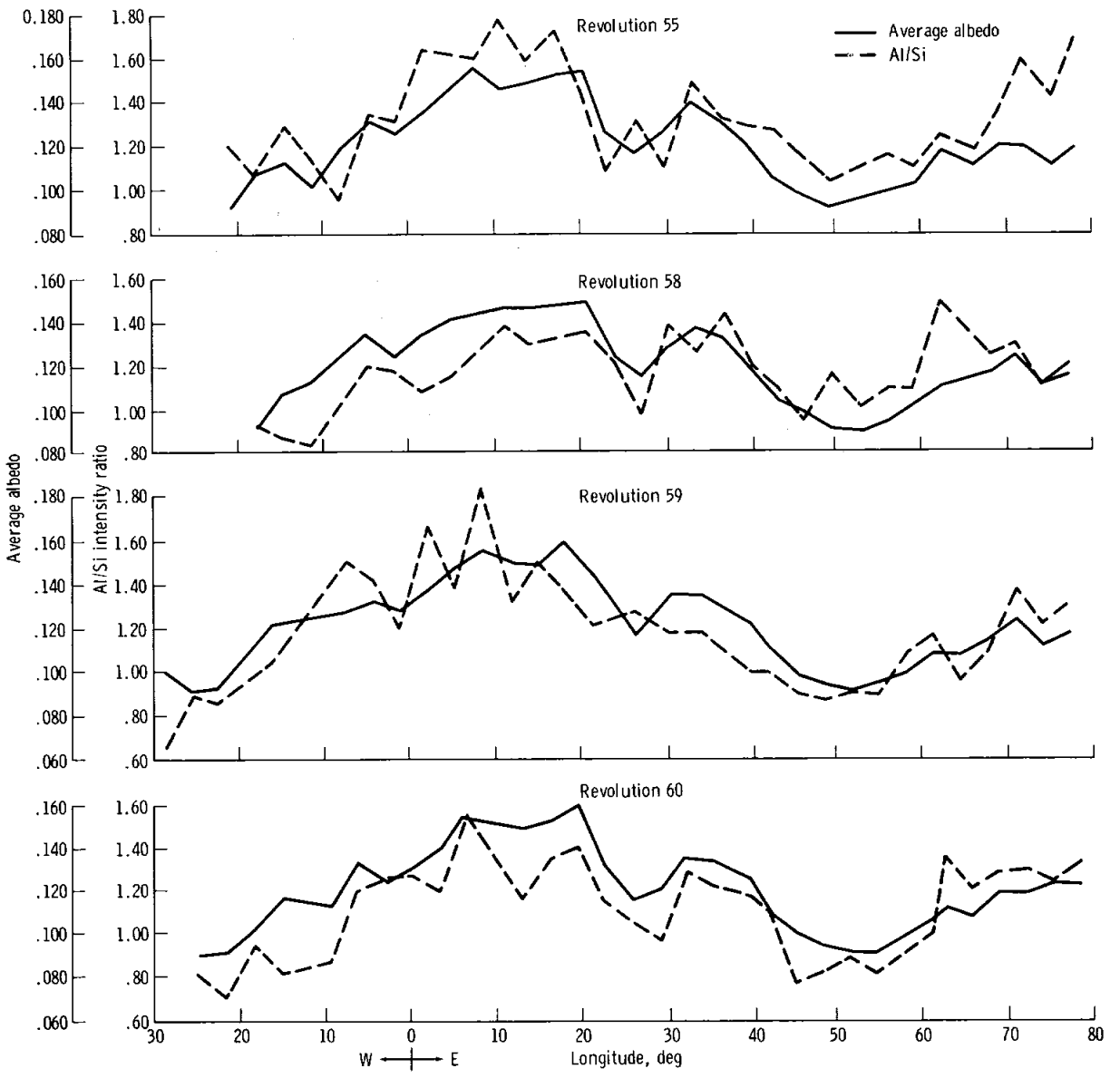


FIGURE 19-5.–Al/Si intensity ratios as compared to optical albedo for revolutions 55, 58, 59, and 60.

The good correlation between optical albedo and aluminum (or plagioclase) content suggests an explanation for the unexpected abundance of breccias in the Apollo 16 samples of the Descartes Formation. This formation had been interpreted as volcanic flows and pyroclastics (refs. 19-20 and 19-21); Head and Goetz had considered the Descartes Formation to be partially of Copernican age because of its high albedo content and other characteristics. Such a young unit would not be expected to be extensively brecciated by small impacts, as are older lunar rocks. However, the X-ray fluorescence/albedo correlation suggests that the high albedo content may be the expression of a high plagioclase content, as might be found in a local anorthositic occurrence, rather than a Copernican age. The Descartes Formation might then be much older than had been expected, and the abundance of breccias would therefore be understandable.

Summary

The Apollo 16 X-ray fluorescence experiment has been successful, confirming earlier results from the Apollo 15 mission and providing compositional data over new areas of the Moon. The data are still being analyzed and integrated with information from other remote sensing experiments and returned sample analyses. However, the data have so far provided further confirmation of the existence of an extensive lunar crust consisting largely of what may be anorthositic gabbro. This crust, which was probably global in extent before formation of the mare basins, is of broad scientific interest in that it represents an early period of planetary differentiation of which virtually no direct evidence remains on the Earth. Additional study of both X-ray data and their implications is therefore highly desirable.

GALACTIC X-RAY OBSERVATIONS

Objectives and Theory

During transearth coast, the X-ray fluorescence spectrometer was used to observe the temporal behavior of two pulsating X-ray sources within our galaxy. The Apollo 16 studies of time variations in the output of galactic X-ray sources were a continuation of an observational program that began with the Apollo 15 mission. (There is an introductory discussion on the scientific objectives and theoretical basis of the observations in ref. 19-2.)

As a result of advances in the understanding of the nature of pulsating X-ray sources, it was decided that the Apollo 16 experiment should concentrate on the two most intense sources, Sco X-1 and Cyg X-1. Sco X-1 has been identified with a visible and radio star; since the Apollo 15 mission, a good case has been made for identifying Cyg X-1 with a ninth-magnitude BO supergiant, which is also a spectroscopic binary star (refs. 19-22 and 19-23). Therefore, it was planned to make coordinated observations from the Apollo 16 spacecraft and ground-based observatories on both Sco X-1 and Cyg X-1 in X-rays, visible light, and radio wavelengths, simultaneously or nearly simultaneously.

The primary objective of the Apollo 16 transearth coast studies was to measure the temporal variation of the X-ray luminosity of Sco X-1 and Cyg X-1 in the time regime from 8 sec (the minimum time resolution of the instrument) to 2 hr (the maximum time of a celestial pointing position), and to correlate it with radio and optical activity. A secondary objective was to study the cislunar space environment as a site for pointed X-ray astronomy observations. Specifically, the objective was to determine how the soft particle background in the X-ray detectors from trapped electrons or protons in cislunar space compared to the near-Earth and lunar environments. During data reduction, it became necessary to study the pointing stability of the command and service module during long periods. Data analysis from the standpoint of these secondary objectives may be useful in planning future observations from other spacecraft.

Operation of the Experiment

Operation of the experiment consists of steadily pointing the X-ray fluorescence spectrometer at a fixed celestial location for the entire interval of 1 to 2 hr. The instrument was intentionally pointed approximately 7° away from both Sco X-1 and Cyg X-1 to avoid a significant contribution from other known X-ray sources. It is important to minimize spacecraft motion, because it results in spurious temporal variations in count rate. The instrument has an angular-dependent intensity response as a result of the effect of the collimator, its field of view being 30° full width, half maximum (FWHM) in two directions. (The FWHM is the total angular width at which the collimator drops to one-half of its peak response.) The spacecraft was commanded to maintain the finest pointing control possible to avoid spurious variations in count rate. A 10.5-hr period of pointed X-ray data was obtained. The total observation time obtained was about equal to the amount planned prior to the mission.

Arrangements were made with a network of ground-based observatories to cover Sco X-1 and Cyg X-1 at various times during the Apollo 16 mission. At any particular time, only a limited number of observatories are in a favorable position. In principle, a broad geographic distribution would cover all observations. The cooperating optical observatories included the Crimean Astrophysical Observatory (U.S.S.R.), the Leyden Observatory (South Africa), the Wise Observatory (Israel), the McDonald Observatory (U.S.A.), and the Yerkes Observatory (U.S.A.). The radio facilities were the Westerbork Observatory

(the Netherlands), the Algonquin Observatory (Canada), and the National Radio Astronomy Observatory (U.S.A.).

The fact that the beginning of transearth coast occurred approximately 1 day earlier than was planned did create difficulties for the coordinated observation program with ground-based observatories. As changes in the flight plan occurred, participating ground observatories were asked to adjust their schedules to maintain near simultaneity with Apollo 16 observations. However, in many cases, the observatories were not able to do so; thus, not as much near-simultaneous optical and radio coverage was obtained as was anticipated. In addition, bad weather conditions at the Crimean Astrophysical Observatory prevented their observations.

The spectrometer performed very well throughout transearth coast. Deep space pointing attitudes for periods of 2 hr did result in low temperatures in the vicinity of the instrument. However, judging from the calibration sources, the experiment heaters did maintain the instrument in a proper operating condition.

Recent Developments in Pulsating X-Ray Sources

During the time between the Apollo 15 and 16 missions, much was learned from Explorer 42 (UHURU) observations about the nature of pulsating X-ray sources. It is clear that there are several classes. One class is characterized by a highly regular period of several seconds plus additional periods of several days (ref. 19-24). Centaurus (Cen X-3) is an example of this class. The parameters of the class definitely require a binary system, possibly involving a low mass star. In terms of observations, if not in theory, such regular pulsating systems are comparatively well understood. However, their characteristic periods are not in a time regime suitable for study by the X-ray fluorescence spectrometer.

The attention of astronomers has been focusing upon Cyg X-1. Cyg X-1 has been identified with a massive BO star (ref. 19-22), the spectrum of which indicates a binary star system. The identification has strengthened the case of those who argue that a "black hole" is involved in the X-ray production. According to their models, X-rays originate from the accretion of matter upon a dark binary companion of the massive star. From the period of the binary system as determined by periodic Doppler shifts in the visible line spectrum, the mass of the dark companion of the BO star can be inferred to be significantly greater than one solar mass. The fast time variability in the X-ray luminosity of Cyg X-1 (significant changes in less than 1 sec (ref. 19-25)) requires that the dark companion be compact; that is, have a radius no larger than that of a white dwarf. According to present theories of stellar structure, a star as massive as the binary companion of the BO star cannot exist in a stable form as a white dwarf or even as a neutron star. A black hole appears to be the only acceptable alternative. For this reason, Cyg X-1 is perhaps the most provocative of all galactic X-ray sources; consequently, about half the available Apollo 16 pointing time was devoted to it.

The remainder of the pointing time was devoted to observing Sco X-1, the most intense of all observed galactic X-ray sources. A single Apollo 15 observation of Sco X-1 of 26-min duration indicated the presence of a variability on a time scale of several minutes that suggested further investigation. More favorable thermal conditions for Sco X-1 at the time of the Apollo 16 mission plus a better understanding from the Apollo 15 experience of the thermal behavior of the spacecraft during extended periods of pointing permitted longer observations of approximately 2 hr.

By observing Sco X-1 and Cyg X-1 for the first time continuously for 2 hr in coordination with ground-based optical and radio astronomers, it was hoped that more could be learned about the X-ray emission processes. Specifically, it was hoped to determine that Cyg X-1 and Sco X-1 are similar-appearing objects on time scales of more than several seconds and that they are examples of related objects under somewhat different physical conditions. For example, in the case of Sco X-1, a thin atmosphere could disperse the subsecond time variability seen in Cyg X-1 but not affect slower time changes.

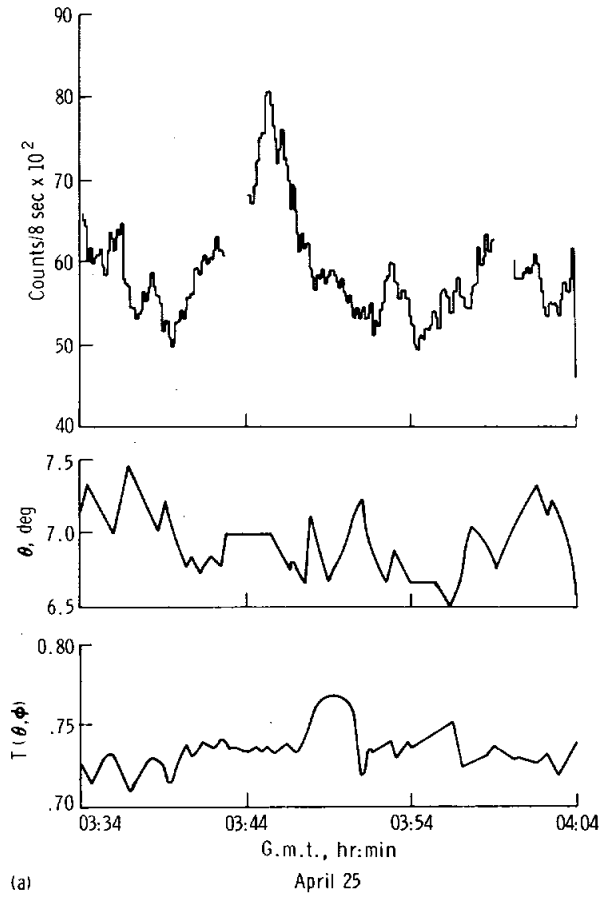
Results

Sco X-1.—Some results are available from preliminary analysis of the Apollo 16 data. Figures 19-6(a) and 19-6(b) show the temporal behavior of Sco X-1 during the first two observation periods, respectively. Significant changes in count rate originate partly from Sco X-1 and partly from motion of the spacecraft. The motion of the spacecraft, as indicated by the angle of the detector axis with respect to the

celestial location, is shown for comparison in figure 19-6. Although spacecraft steadiness was well within the nominal Apollo capability, spacecraft motion does appear to be reflected in the variation of count rate. However, there are important changes in the count rate of Sco X-1 that cannot be explained by spacecraft motion.

The first sighting of Sco X-1 was made from 03:34 to 04:04 G.m.t. on April 25. During this time, the spacecraft motion showed little uniformity. Variations in the polar angle occurred with amplitudes of $\pm 0.1^\circ$ to $\pm 0.5^\circ$ and periods of 1 to 5 min. The mean polar angle during the sighting was approximately 7° as was planned. The large increase in the counting rate from 03:39 to 03:49 G.m.t. occurred during a time of minimum spacecraft motion.

The second sighting of Sco X-1 was made from 02:14 to 04:52 G.m.t. on April 26. During the course of this sighting, four distinct and separate types of spacecraft motion were discernible. From 02:14 to 02:52 G.m.t., the motion was characterized by regular variations of large amplitudes of $\pm 0.5^\circ$ and periods of 2 min, with a mean polar angle of approximately 6.6° between Sco X-1 and the normal to the detector face. From 02:52 to 03:39 G.m.t., the variations were irregular with amplitudes of 0.1° to 0.8° and separations of 1 to 7 min between peaks. The mean polar angle remained at approximately 6.6°. At 03:39 G.m.t., the mean angle shifted to 6.9° and the amplitude of the variations decreased to 0.1° to 0.3° with a peak separation of 1 to 5 min. The motion again became regular and periodic at 04:06 G.m.t., with an amplitude of $\pm 0.2^\circ$, a period of approximately 1 min, and a mean polar angle of 6.9°. This motion continued until the end of the second sighting.



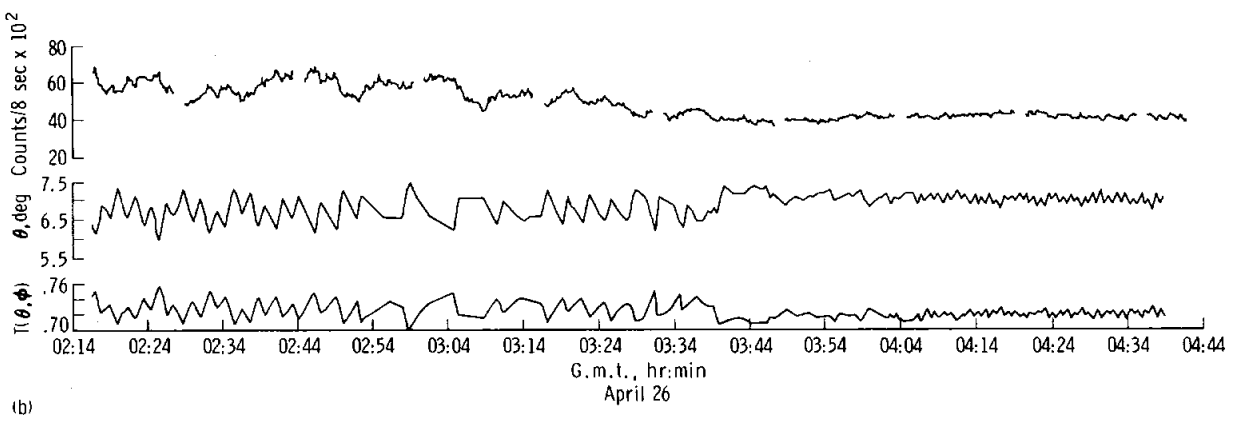


FIGURE 19-6.–Variations of count rate from Sco X-1. The spacecraft motion as reflected by changes in the polar angle θ is shown as well as its expected effect upon the counting efficiency $T(\theta, \phi)$. (a) First observation. (b) Second observation.

In general, Sco X-1 was active during the first sighting. After allowing for spacecraft motion, significant changes (10 to 30 percent) in its intensity could be identified in a few minutes. Because of a late change in the scheduled time for the first sighting of Sco X-1, there was no simultaneous optical or radio data. However, reports received from the McDonald and Algonquin Observatories indicate that Sco X-1 was active optically and in radio for at least several hours following the Apollo 16 observation. Flare activity was detected at the ground observatories. There was continued activity at the beginning of the second observation of Sco X-1; during the final hour, the count rate settled down and was relatively constant.

Cyg X-1.–Two observations of Cyg X-1 were made during the Apollo 16 mission. Figure 19-7 shows the variation of count rate during the second observation. There are two large increases in count rate. However, neither of these appears to be intrinsic to Cyg X-1. The pulse shape discriminator (PSD) channel shown in the lower portion of figure 19-7 is conditioned primarily by the strength of the particle background. It is also affected by X-rays with $E > 7$ keV. The fact that the PSD channel exhibits a stronger counting rate change than the two energy ranges is probably an indication of a sudden increase in the particle background. The spacecraft encountered two pulses of electrons or protons (or both) of durations of approximately 2 to 5 min in cislunar space. It may be possible that hard X-ray flares have occurred in Cyg X-1, but the particle interpretation is more likely.

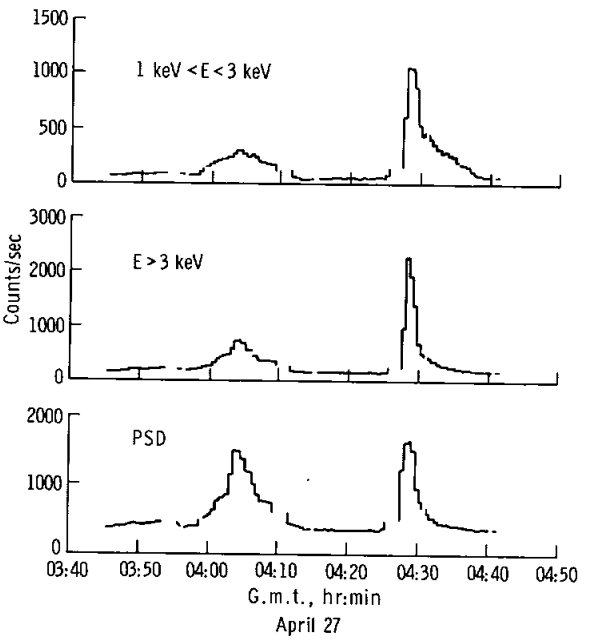


FIGURE 19-7.–Count rate during the second Apollo 16 observation of Cyg X-1. The two large increases in rate at 04:05 and 04:28 G.m.t. are probably particle effects in cislunar space because the PSD rates also increase.

In addition to the effect described previously, there is a significant change in the mean intensity of Cyg X-1 between two Apollo 16 observations. Table 19-IV summarizes this difference. The near equality between the PSD count rates of the two observations (prior to the particle events) indicates that the particle background is the same. Cyg X-1 is twice as

TABLE 19-IV.–Count Rates During Cygnus X-1 Observations

Energy channel	*Apollo 15 (a)*	*Apollo 16*	
		First observation	*Second observation (b)*
3 keV $> E >$ 1 keV	260	360	750 → 2 500 ↘ 8 600
$E >$ 3 keV	900	860	1500 → 5 800 ↘ 18 000
PSD	3000	2900	3100 → 12 000 ↘ 13 000

[a]Units are counts/8 sec.

[b]The first set of values is the average count rate; the second and third numbers refer to each of two particle event intensities.

intense in the second observation. The slight excess of PSD events, 3100 as compared to 2900, can be explained as a doubling of the number of events in the range above 7 keV.

Conclusions

The following conclusions can be made from the pointed observations of Sco X-1 and Cyg X-1.

(1) Sco X-1 is characterized by quiet periods and by periods in which there are intensity changes of approximately 10 to 30 percent in a few minutes. The active periods can last for at least a day.

(2) When Sco X-1 shows changes in X-ray intensity, there are concurrent but not necessarily simultaneous changes in its optical and radio intensity.

(3) Cyg X-1 can double in intensity within a day or so, an increase which is larger than the observed changes in Sco X-1. The increase occurs in all three energy ranges: 1 to 3 keV, >3 keV, and >7 keV. The average intensity of Cyg X-1 over a several-minute interval can remain relatively stable for at least an hour.

(4) The time variability of Sco X-1 and Cyg X-1 does not appear to be similar in the time regime of several seconds to 2 hr. Although Cyg X-1 exhibits subsecond pulsations during its active periods, Sco X-1 has greater variability on a time scale of a few minutes than Cyg X-1 as it appears during the Apollo 16 mission.

(5) Transient particle effects that last several minutes exist in cislunar space. The strength of the two events observed during the Apollo 16 mission is approximately 100 particles/cm^2-sec. These events can lead to background problems in instruments with broad fields of view and can simulate flares in X-ray stars.

REFERENCES

19-1. Adler, I.; Trombka, J.; Gerard, J.; Lowman, P.; et al.: Apollo 15 Geochemical X-Ray Fluorescence Experiment: Preliminary Report. Science, vol. 175, no. 4020, Jan. 28, 1972, pp. 436-440.

19-2. Adler, I.; Trombka, J.; Gerard, J.; Schmadebeck, R.; et al.: X-Ray Fluorescence Experiment. Sec. 17 of Apollo 15 Preliminary Science Report. NASA SP-289, 1972.

19-3. Adler, I.; Gerard, J.; Trombka, J.; Schmadebeck, R.; et al.: The Apollo 15 X-Ray Fluorescence Experiment. Proceedings of the Third Lunar Science Conference, vol. 3, David R. Criswell, ed., MIT Press (Cambridge, Mass.), 1972.

19-4. Levinson, A. A., ed.: Proceedings of the Second Lunar Science Conference. MIT Press (Cambridge, Mass.), 1971.

19-5. Apollo 15 Preliminary Examination Team: The Apollo 15 Lunar Samples: A Preliminary Description. Science, vol. 175, no. 4020, Jan. 28, 1972, pp. 363-375.

19-6. Levinson, A. A., ed.: Proceedings of the Apollo 11 Lunar Science Conference. Pergamon Press (New York), 1970.

19-7. McKay, D. S.; Morrison, D. A.; Clanton, U. S.; Ladle, G. H.; and Lindsay, J. F.: Apollo 12 Soil and Breccia. Proceedings of the Second Lunar Science Conference, vol. 1, A. A. Levinson, ed., MIT Press (Cambridge, Mass.), 1971, pp. 755-774.

19-8. Meyer, C.; Brett, R.; Hubbard, N. J.; Morrison, D. A.; et al.: Mineralogy, Chemistry, and Origin of the KREEP Component in Soil Samples From the Ocean of Storms. Proceedings of the Second Lunar Science Conference, vol. 1, A. A. Levinson, ed., MIT Press (Cambridge, Mass.), 1971, pp. 393-412.

19-9. Turkevich, Anthony L.; Patterson, James H.; and Franzgrote, Ernest J.: Chemical Analysis of the Moon at the Surveyor VI Landing Site: Preliminary Results. Science, vol. 160, no. 3832, Jan. 7, 1968, pp. 1108-1110.

19-10. Mason, Brian; and Melson, William G.: The Lunar Rocks. John Wiley & Sons, Inc., 1970, p. 11.

19-11. Turkevich, Anthony L.; Franzgrote, Ernest J.; and Patterson, James H.: Chemical Analysis of the Moon at the Surveyor V Landing Site: Preliminary Results. Science, vol. 158, no. 3801, Nov. 3, 1967, pp. 635-637.

19-12. Vinogradov, A. P.: Preliminary Data on Lunar Ground Brought to Earth by Automatic Probe Luna-16. Proceedings of the Second Lunar Science Conference, A. A. Levinson, ed., MIT Press (Cambridge, Mass.), 1971, pp. 1-16.

19-13. Lunar Sample Preliminary Examination Team: Preliminary Examination of Lunar Samples From Apollo 14. Science, vol. 173, no. 3998, Aug. 20, 1971, pp. 681-693.

19-14. Wood, J. A.; Marvin, U. B.; Powell, B. N.; and Dickey, J. S., Jr.: Mineralogy and Petrology of Apollo 11 Samples. Smithsonian Astrophysical Observatory Special Rept. 307, Jan. 1970. (Also available as NASA CR-107932, Jan. 1970.)

19-15. Marvin, U. B.; Wood, J. A.; Taylor, G. J.; Reid, J. B.; et al.: Relative Proportions and Probable Sources of Rock Fragments in the Apollo 12 Soil Samples. Proceedings of the Second Lunar Science Conference, vol. 1, A. A. Levinson, ed., MIT Press (Cambridge, Mass.), 1971, pp. 679-700.

19-16. Turkevich, Anthony L.; Franzgrote, Ernest J.; and Patterson, James H.: Chemical Analysis of the Moon at the Surveyor VII Landing Site: Preliminary Results. Science, vol. 162, no. 3849, Oct. 4, 1968, pp. 117-118.

19-17. Whitaker, E. A.: The Surface of the Moon. Sec. 3 of The Nature of the Lunar Surface; Proceedings of the 1965 IAU-NASA Symposium, Wilmot N. Hess, Donald H. Menzel, and John A. O'Keefe, eds., Johns Hopkins Press (Baltimore), 1966, pp. 79-98.

19-18. Gault, D. E.; Adams, J. B.; Collins, R. J.; Kuiper, G. P.; et al.: Lunar Theory and Processes. Sec. 9 of Surveyor

VII, A Preliminary Report. NASA SP-173, May 1968.

19-19. Pohn, H. A.; and Wildey, R. L.: A Photoelectric-Photographic Study of the Normal Albedo of the Moon, Accompanied by an Albedo Map of the Moon by H. A. Pohn, R. L. Wildey, and G. E. Sutton.(Contributions to Astrogeology). U.S. Geological Survey Professional Paper 599-E, 1970.

19-20. Milton, Daniel J.; and Hodges, Carroll Ann: Geologic Map of the Descartes Region of the Moon. Geol. Atlas of the Moon, Apollo 16 Pre-Mission Map, Sheet 1. U.S. Geol. Survey Misc. Geol. Inv. Map I-748, 1972.

19-21. Head, James W., III; and Goetz, Alexander F. H.: Descartes Region: Evidence for Copernican-Age Volcanism. J. Geophys. Res., vol. 77, no. 8, Mar. 10, 1972, pp. 1368-1374.

19-22. Webster, B. Louise; and Murdin, Paul: Cygnus X-1 – A Spectroscopic Binary With a Heavy Companion? Nature, vol. 235, no. 5332, Jan. 7, 1972, pp. 37-38.

19-23. Bolton, C. T.: Identification of Cygnus X-1 with HDE 226868. Nature, vol. 235, no. 5336, Feb. 4, 1972, pp. 271-273.

19-24. Schreier, E.; Levinson, R.; Gursky, H.; Kellogg, E.; et al.: Evidence for the Binary Nature of Centaurus X-3 From UHURU X-Ray Observations. Astrophys. J. (Letters), vol. 172, no. 3, pt. 2, Mar. 15, 1972, pp. L79-L89.

19-25. Oda, M.; Gorenstein, P.; Gursky, H.; Kellogg, E.; et al.: X-Ray Pulsations From Cygnus X-1 Observed From UHURU. Astrophys. J. (Letters), vol. 166, no. 1, pt. 2, May 15, 1971, pp. L1-L7.

20. Alpha-Particle Spectrometer Experiment

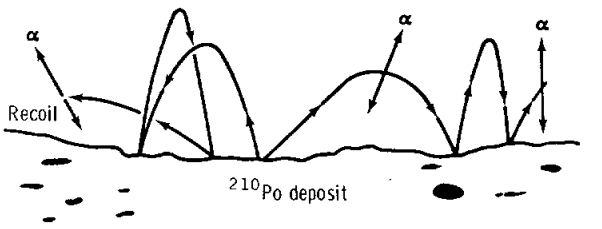
Paul Gorenstein[a†] *and Paul Bjorkholm*[a]

INTRODUCTION

The scientific objectives of the alpha-particle spectrometer experiment are to measure the rate of emanation of radioactive radon gas from the Moon and to locate and identify lunar regions with unusual activity. Any lunar region that is characterized by a locally higher rate of radon emanation is a good candidate for being a site of internal activity. Orbital investigations from the Apollo 15 and 16 command and service module have shown that areas on the Moon with detectable rates of radon emanation do exist and that certain lunar regions are characterized by transient or nonequilibrium radon emanation. Identification of radon isotopes and their daughter products is based on the detection of their characteristic alpha particles in an array of detectors with good energy resolution.

Natural concentrations of uranium and thorium are the source of radon gas. A qualitative description of the processes that lead from natural uranium and thorium concentrations to the existence of a thin radon atmosphere above the lunar surface is given in reference 20-1. There are two decaying radon isotopes of interest: radon-222 (^{222}Rn) with a 3.7-day half life (an intermediate product of the uranium series) and ^{220}Rn with a 56-sec half life (a member of the thorium series). Decay of these isotopes results in the production of monoenergetic alpha particles that escape from the Moon. Their heavy decay products are deposited directly upon the uppermost layer of the lunar surface and are themselves unstable against radioactive decay. This process is illustrated in figure 20-1.

A third decaying species is very significant, lead-210 (^{210}Pb), a descendant of ^{222}Rn with a half life of 21 yr. The lifetime of ^{210}Pb is long, compared to all other intermediate members of the series. The ^{210}Pb atom, which does not produce alpha particles,



Note: Average distance traveled per trajectory is approximately 5 km. Average number (zero accommodation time) is approximately 2×10^4. Mean displacement from origin is 700 km.

FIGURE 20-1.–Representation of radon diffusion through the lunar material to a gravitationally trapped condition above the surface. Radon, which is traveling in a ballistic trajectory, decays and ejects an alpha particle. The nucleus is recoiled to the lunar surface, where it will eventually emit three additional alpha particles.

is detected indirectly through its alpha-emitting granddaughter, polonium-210 (^{210}Po). The significance of ^{210}Po is that the existence of a transient or non-steady-state radon emanation within a 21-yr period will cause its activity to be higher than predicted from observations of ^{222}Rn. Thus, at locations where the ^{210}Po/^{222}Rn ratio departs from radioactive equilibrium, there is evidence for transient emanation.

The alpha-particle spectrometer, mounted in the Apollo scientific instrument module, detects individual alpha particles and measures their energy. The presence of radon and its daughter products appears as a distinct set of peaks in an energy spectrum. The background is caused primarily by cosmic-ray effects. Spatial resolution is achieved by restricting the field of view of the spectrometer to 45° by 45° (full width at half maximum).

EQUIPMENT

The alpha-particle spectrometer has been described elsewhere in detail (ref. 20-1). The sensing elements are 10 totally depleted silicon surface-barrier detectors, each approximately 100 μm thick,

[a]American Science and Engineering, Inc.

†Principal Investigator.

having 3 cm^2 of active area. The combination of detector thickness and processing electronics causes the instrument to be sensitive only to alpha particles between 4.7 and 9.2 MeV and to any cosmic-ray interactions that yield a similar signal. The detectors each had a weak source of alpha particles (E = 5.14 MeV) in their field of view, allowing an inflight calibration of the instrument. The spectrometer functioned very well during the Apollo 16 mission.

RESULTS

Results from a still incomplete analysis of Apollo 15 data indicate the existence of lunar regions with local increases in radon emanation. Excess ^{222}Rn was observed in an area that included Aristarchus Crater. Schröter's Valley and Cobra Head were also in the field of view, and it is not possible to make a further definition of the region. In addition, ^{210}Po (a daughter product of ^{222}Rn) has been detected in a broad region from west of Mare Crisium to the Van de Graaff-Orlov region. The observed count rate is $(4.6 \pm 1.4) \times 10^{-3}$ disintegration/cm^2-sec. The observed level of ^{210}Po activity is in excess of the amount that would be in equilibrium with ^{222}Rn by about an order of magnitude, indicating transient radon emanation from this region in the recent past.

A real-time analysis of the Apollo 16 data provides an even stronger indication of a local ^{210}Po concentration in the region located at approximately 40° E, centered around Mare Fecunditatis.

APOLLO 15 OBSERVATIONS

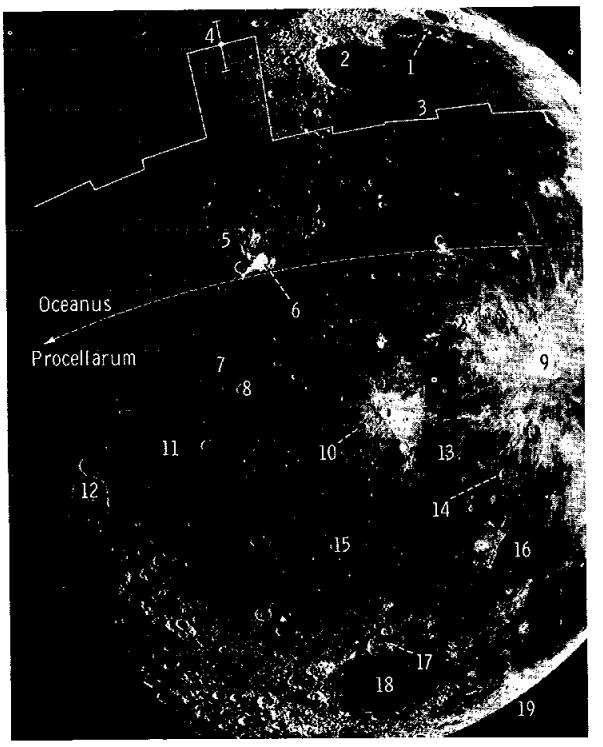
Radon-222

In order to determine whether any alpha particles were observed from the decay of ^{222}Rn, the Apollo 15 data were treated in a gross manner with little or no spatial resolution. Long periods of data were taken over the surface and examined in two ways.

The first method is comparing the total number of counts obtained with the detector in a lunar orientation with the total number of counts obtained with the detector in an orientation with the Moon out of the field of view and restricting the comparison to the appropriate energy channels. The second method consists of examining the total energy spectrum in a lunar orientation and looking for an increase in those energy channels in which alpha particles from ^{222}Rn are expected, as compared to a background level that is given by neighboring channels. In the absence of radon emanation, essentially all counts are due to cosmic-ray interactions, and the spectrum is expected to be uniform and featureless. By using the first method for the region from 40° to 180° E, an excess of $(2.9 \pm 1.1) \times 10^{-3}$ count/sec is found in the detector, which corresponds to a lunar rate of $(1.3 \pm 0.50) \times 10^{-3}$ disintegration/cm^2-sec. For the same region, the second method yields a rate of $(0.92 \pm 0.25) \times 10^{-3}$ disintegration/cm^2-sec. Thus, on the basis of the statistical significance, there is evidence for the existence of ^{222}Rn over a large part of the Moon.

The next step in the analysis is to see if any of this signal can be localized to a particular region on the lunar surface. The data were overlaid in bins of longitude, each 5° wide. The data were also divided into three time groups, each consisting of 25 to 30 hr. Energy spectra were computed for each of these bins; count rates were calculated for ^{222}Rn and its daughter products. In essence, a crude map of alpha-particle activity over the ground track can be formulated, each bin 5° in longitude and of variable sizes in latitude (less than approximately 12°).

Two features are obvious from an examination of the data. First, there is a general increase in the count rate over Oceanus Procellarum and Mare Imbrium. However, because the increase is small and subject to further study, this count rate will not be discussed further in this report. The second feature occurs between 45° and 50° W and only in those sections of data where Aristarchus Crater is within the field of view of the instrument. Figure 20-2 shows the count rate from the decays of ^{222}Rn and its daughter products (excluding ^{210}Po) as a function of longitude. The dashed line is the approximate average ground track during the period used in obtaining the data (revolutions 33 to 46). The ground track is also used as the baseline for the data histogram. The count rate seen over the region of Aristarchus Crater exceeds the mean count rate for the entire Moon, which may crudely be taken as the background level, by 4.3 standard deviations. To improve confidence in the validity of this increase, the distribution of deviations of count rates from the entire Moon coverage was determined for all data points (fig. 20-3).



1 Plato
2 Sinus Iridum
3 Mare Imbrium
4 Sinus Roris
5 Schröter's Valley
6 Aristarchus
7 Marius Hills
8 Marius
9 Copernicus
10 Kepler
11 Reiner Gamma
12 Hevelius
13 Kunowsky
14 Lansberg
15 Flamsteed
16 Mare Cognitum
17 Gassendi
18 Mare Humorum
19 Tycho

FIGURE 20-2.–Count rate of alpha particles from the decays of ^{222}Rn and its daughter products (excluding ^{210}Po) as a function of longitude. The dashed line corresponds approximately to the average ground track during Apollo 15 revolutions 33 to 46 and also represents the baseline for the data histogram.

The observed distribution is in good agreement with a normal distribution (solid line), except for the point at Aristarchus Crater, which is well off the distribution. The probability of observing at least one 4.3-standard-deviation positive statistical fluctuation among all the data points is approximately 1 percent. The probability that a statistical fluctuation would coincide with the Aristarchus region is only 1×10^{-4}. Furthermore, the excess is correctly distributed among all the detectors and among all the orbits over this region. Thus, the excess from the Aristarchus

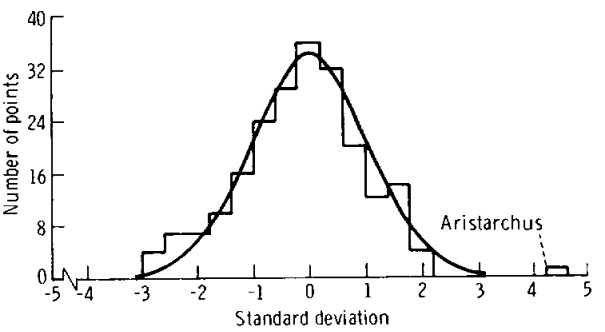


FIGURE 20-3.–Distribution of deviations of the ^{222}Rn count rate from the entire Moon average. All data points from revolution 18 to transearth injection during the Apollo 15 mission (111:00:00 to 222:00:00 ground-elapsed time) are included. The solid curve is the expected distribution.

region at the alpha energies associated with ^{222}Rn appears to be a true effect. There is no significant excess (greater than 3 standard deviations) from this region at other alpha energies; for example, ^{220}Rn, ^{210}Po, or at higher energies that are presumably dominated by cosmic-ray interactions. The failure to see an excess at other alpha-particle energies indicates that the ^{222}Rn excess is not easily explained as a result of systematic errors. Analysis of the data in smaller bins of longitude data does not improve the degree of localization.

Figure 20-3 also illustrates that there are no other sources of ^{222}Rn on the Moon as well localized as the Aristarchus region. The distribution of all other data points is consistent with counting statistics. However, this does not preclude the possibility of finding other ^{222}Rn anomalies for larger regions.

Radon-220

The second method of data analysis, as described previously, is more powerful in the case of looking for an indication of ^{220}Rn from the Moon as a whole. No excess counts are observed in the energy region of ^{220}Rn disintegration in an energy spectrum consisting of 20 hr of data from the entire lunar surface. The 3-standard-deviation upper limit to the average decay rate of ^{220}Rn is 3.8×10^{-4} decay/cm^2-sec. This limit does not preclude the possibility of finding local concentrations of ^{220}Rn that exceed this limit.

Polonium-210

The result of the analysis does provide some evidence for a nonuniform distribution of ^{210}Po on the surface of the Moon. One example is the region of the Moon overflown by the Apollo 15 command and service module during revolutions 18 to 33. The sensitivity for detecting lunar surface concentrations of ^{210}Po was reduced because the detectors were slightly contaminated by an external source of ^{210}Po during a calibration procedure. However, it is still possible to look for variations of the total count rate of ^{210}Po with longitude. The contamination level will be constant with the position on the Moon, so true changes in the count rate in the appropriate energy range can be interpreted as a lunar component.

A lunar region is within the field of view of the spectrometer for many orbits, the exact number of orbits depending on lunar latitude. Thus, to look for local concentrations, data are combined from numerous orbits by folding over the orbital period of the Apollo spacecraft. The folded data from revolutions 18 to 33 were grouped in bins of 20° of longitude. The count rates in various energy bands of the spectrum were then examined as a function of longitude. Because the amount of contamination varied, those five detectors with the least amount of contamination were examined separately and provided most of the sensitivity.

For those five detectors, the count rate from 5.1 to 5.5 MeV tended to be systematically higher in the region from 40° to 180° E. To increase the statistics, all data from 32 consecutive hours were added. Figure 20-4 shows the count rate in the region from 5.1 to 5.5 MeV as a function of longitude for revolutions 18 to 33 of the Apollo 15 mission. The data between 40° and 180° E, which extends from the western edge of Mare Crisium to the Van de Graaff-Orlov region, are systematically higher than those in other longitude bins. The average count rate between 40° and 180° E is 0.072 ± 0.002 count/sec, and between 0° to 40° E plus 180° W to 0°, it is 0.062 ± 0.001 count/sec. These average count rates are shown as dashed lines. The excess between 40° and 180° E corresponds to $(4.6 \pm 1.4) \times 10^{-3}$ disintegration/cm^2-sec.

To verify that this is a true lunar signal and not a systematic live time variation, all the data outside this energy bin were treated in a similar fashion. The

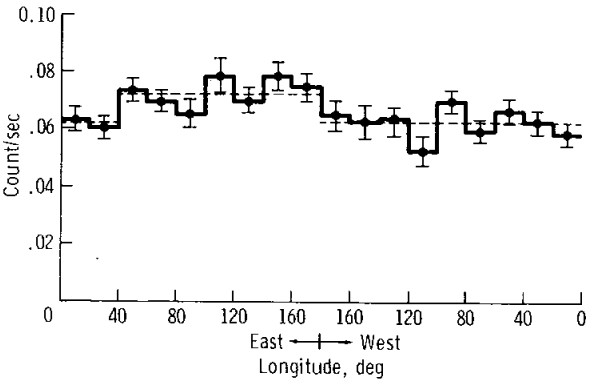


FIGURE 20-4.–Count rate of alpha particles with energies from 5.1 to 5.5 MeV for the five least contaminated detectors as a function of longitude. This energy range includes ^{210}Po, a descendant of ^{222}Rn. This figure includes all available data from revolutions 18 to 33 of the Apollo 15 mission. The dashed lines indicate the average value of the count rate over the two sections of longitude.

results are shown in figure 20-5. These data do not show this variation. The count rate between 40° and 180° E is 0.070 ± 0.002 count/sec, and between 0° to 40° E plus 180° W to 0°, it is 0.073 ± 0.001 count/sec. If the variation seen in figure 20-4 were due to a live time variation, both these energy bins should be affected identically. Because they are not, the excess in figure 20-4 is due to a true lunar signal. The energy spectra of the counts indicate that the excess is due to ^{210}Po only.

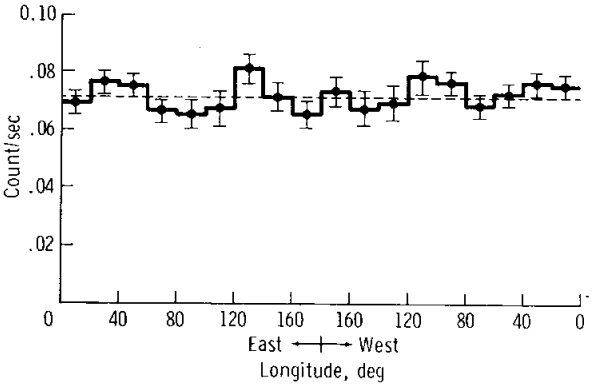


FIGURE 20-5.–Count rate of alpha particles with energies from 4.7 to 5.1 MeV or 5.5 to 9.0 MeV for the five least contaminated detectors as a function of longitude. This figure includes all available data from revolutions 18 to 33 of the Apollo 15 mission. The dashed line indicates the average count rate.

APOLLO 16 OBSERVATIONS

The results discussed in this section are from quick-look data only. Therefore, all results must be considered preliminary until such systematic effects as temperature-dependent gain shifts and attitude corrections can be studied further.

No strong indications of ^{220}Rn or ^{222}Rn hot spots are evident in the Apollo 16 quick-look data. However, the Apollo 15 data, at the same stage of analysis, would not have provided evidence for these effects either. Any discussion of the evidence for ^{220}Rn or ^{222}Rn in the Apollo 16 ground track must therefore be delayed for further analysis.

There is, however, some strong evidence for the existence of decays from ^{210}Po. This evidence is demonstrated by the count rate as a function of longitude in the energy region of approximately 5.3 MeV (fig. 20-6). Each data bin contains data collected within 18° of longitude. The dashed line indicates the

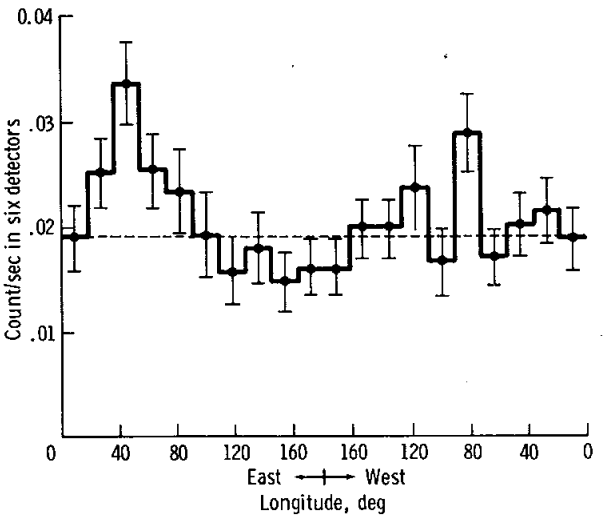


FIGURE 20-6.–Count rate of alpha particles from the decay of ^{210}Po as a function of longitude. The dashed line is the average count rate for the lunar surface, excluding the region from 18° to 90° E (Apollo 16 mission). Only six detectors were used in the preliminary study. All 10 detectors will be used in the final study.

average count rate for the lunar surface, excluding the region from 18° to 90° E. It is clear that this region, approximately centered over the Sea of Fertility, has a statistically significant higher count rate.

DISCUSSION

The data from the Apollo 15 and 16 alpha-particle spectrometers have shown that the excess alpha-particle activity on the lunar surface caused by the emanation and diffusion of radon isotopes through the lunar regolith is small but detectable.

The absence of a detectable signal from ^{220}Rn is not surprising. The ^{220}Rn atom has a half life of 55 sec and therefore cannot migrate as far as ^{222}Rn from its point of origin. Therefore, the $^{222}Rn/^{220}Rn$ ratio above the lunar surface would be expected to be very large. Any ^{220}Rn signal need be only a factor of approximately 3 weaker than the ^{220}Rn to be below the experiment sensitivity.

Another feature of the data which deserves some comment is the fact that the excess ^{222}Rn and ^{210}Po signals were not observed over the same lunar region. This is possible because ^{210}Po production is delayed by the 21-yr half life of ^{210}Pb. If the higher ^{210}Po count rate over the approximately eastern half of the Moon were the result of a transient event that had occurred more than approximately 10 to 20 days prior to the Apollo 15 lunar orbit, the associated ^{222}Rn would no longer be observable. The higher than equilibrium values of ^{210}Po indicate that the emanation of radon gas from the regolith is variable with time.

The observation of excess ^{222}Rn over the Aristarchus region is suggestive of internal activity. Aristarchus Crater has long been studied as a site of anomalous, transient optical events (ref. 20-2). There is no clearly defined relationship between these optical events and physical processes occurring at the lunar surface or as a result of an interaction of the lunar surface with its environment. However, some of the proposed mechanisms – gas release, tectonic activity, tidal friction (refs. 20-2 and 20-3) – are likely to affect the amount of local radon diffusion.

Clearly, at this stage of analysis, no direct (or indirect) relationship between the data available and physical processes on the lunar surface can be deduced. The previous discussion should indicate some of the more obvious correlations that will have to be considered. Further studies correlating the data to the uranium and thorium content of the regolith and broad classes of lunar features will be made.

CONCLUSIONS

Observation of lunar radon emanation during the Apollo 15 and 16 missions shows the existence of areas with locally high emanation rates. The most conspicuous ^{222}Rn feature found thus far in the data analysis is a region that includes Aristarchus Crater. The excess emanating power of the Aristarchus region may be an indication of internal activity at that site. In addition, there are regions with anomalously high rates of ^{210}Po activity, which indicates transient phenomena involving the release of ^{222}Rn gas from certain areas of the Moon.

REFERENCES

20-1. Gorenstein, P.; and Bjorkholm, P.: Alpha-Particle Spectrometer Experiment. Sec. 18 of Apollo 15 Preliminary Science Report. NASA SP-289, 1972.

20-2. Middlehurst, Barbara M.: An Analysis of Lunar Events. Reviews of Geophysics, vol. 5, no. 2, May 1967, pp. 173-189.

20-3. Kozyrev, N. A.: Spectroscopic Proofs for Existence of Volcanic Processes on the Moon. The Moon, ch. 21, Zdenek Kopal and Zdenka Kadla Mikhailov, eds., Academic Press (London), 1962, pp. 263-271.

21. Lunar Orbital Mass Spectrometer Experiment

R. R. Hodges,[a] J. H. Hoffman,[a†] and D. E. Evans[b]

A lunar orbital mass spectrometer carried by the Apollo 16 command and service module (CSM) and a similar experiment carried on the Apollo 15 CSM were dedicated to the detection of lunar atmosphere and to a search for active lunar volcanism. Study of the lunar atmosphere obviously is important to understanding the evolution of the Moon. In addition, the tenuous atmosphere of the Moon is unique among accessible planets. Gas molecules do not collide with each other but, instead, travel in ballistic trajectories between encounters with the lunar surface to form a nearly classical exosphere, in which lateral transport can be observed in an idealized form. This study will aid in understanding transport mechanisms in other, more complex planetary exospheres.

The Apollo 14 and 15 cold cathode gages have provided an upper bound on the concentration of gases at the lunar surface of approximately 1×10^7 particles/cm^3 (ref. 21-1). This value has been shown by Hodges et al. (ref. 21-2) to imply that the upper bound on the average lunar volcanic release of gas is 1.5×10^{-16} g/cm^2/sec. Interestingly, this rate is only three or four orders of magnitude less than the degassing rate for the Earth, although the surface concentrations for the Earth and the Moon differ by more than 12 orders of magnitude. The difference in these ratios is attributable mainly to a shorter lifetime for lunar gases. It is important to note that the tenuous lunar atmosphere does not a priori imply a totally dead planet.

A persistent pattern of the Apollo 14 cold cathode gage data for 10 lunar days of operation can be seen in Johnson et al. (ref. 21-1) to be a daytime maximum more than an order of magnitude in excess of the nighttime concentration. This pattern suggests dominant gases that are adsorbed readily on the cold nighttime surface. Hodges and Johnson (ref. 21-3) have shown that gases that are not adsorbed on the nighttime surface, such as neon (Ne), argon, and probably nitrogen, should be distributed roughly as the inverse 5/2 power of surface temperature and thus have nighttime maximums. The daytime maximum in the cold cathode gage data may be influenced by contaminant gases released from remnant spaceflight hardware, but the persistent level of this maximum suggests otherwise. If the daytime maximum is a natural feature of lunar atmosphere, then it results entirely from condensable volcanic gases, whereas the nighttime level represents the noncondensable gases, of which neon of solar wind origin is expected to dominate.

In lunar orbit (altitude ~100 km), the distribution of gases is influenced by the barometric law. Over the daytime side of the Moon, the scale height of neon (20 atomic mass units (amu)) is roughly 100 km, whereas that of argon (40 amu) is 50 km. Thus, in a 100-km orbit, the concentration differs from that at the surface by less than an order of magnitude for most gases; and, if the daytime maximum detected by the cold cathode gages is not artifact, it should be detected in orbit. A noncondensable gas, such as neon, should be approximately 30 times more abundant at the nighttime surface than in daytime (ref. 21-3). However, the night-to-day variation of scale height by a factor of nearly 4 compensates for this difference and results in very little variation along the orbit path (ref. 21-4).

Detection of active volcanism from lunar orbit requires the fortuitous passage of the spacecraft through a perturbation of lunar atmosphere over an active gas release. It is most likely that these events would be detected over the night side, where surface adsorption precludes multiple surface collisions and hence limits the lateral spreading of the perturbation to form a distinct disturbance that can be reçognized in the mass spectrometer data. This problem has been analyzed by Hodges et al. (ref. 21-2). Evidence for one event has been found in the Apollo 15 data, but the certainty that it is not artifact has not yet been

[a]The University of Texas at Dallas.
[b]NASA Manned Spacecraft Center.
†Principal Investigator.

established. Further study of all orbit data is needed before any definitive statement on active lunar volcanism can be made.

Details of the lunar orbital mass spectrometers have been presented by Hoffman et al. (refs. 21-5 and 21-6), and the calibration of the instruments is described by Yeager et al.[1] In this report, these facets are discussed in summary form, with emphasis on differences between the two flight instruments. Much of the Apollo 16 data analysis has been delayed, awaiting the availability of trajectory data. However, some significant results regarding the abundance of neon on the Moon have emerged from a preliminary study of fragmentary data.

EXPERIMENTAL PROCEDURE

The lunar orbital mass spectrometer (fig. 21-1) carried on the Apollo 16 CSM was similar to that carried on the Apollo 15 CSM. In flight, the instrument was mounted on a boom, which extended approximately 7.3 m from the CSM, with the opening of the inlet plenum facing the -X direction (that is, parallel to the roll axis and toward the service module (SM) end of the spacecraft). When the flight path was oriented so that the velocity vector was in the -X direction (SM forward), the gas inlet was in a ram condition with respect to native gases of lunar atmosphere, whereas the reverse direction of flight (command module end forward) produced a wake condition at the inlet. This scheme was conceived to permit separation of data contributions from native gases and from spacecraft contaminants.

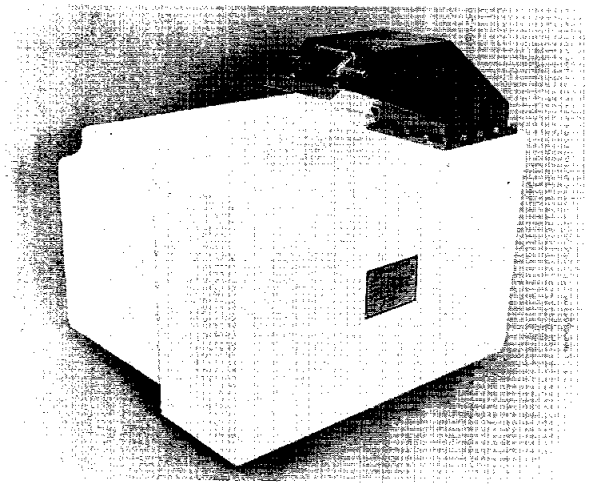


FIGURE 21-1.–Photograph of the lunar orbital mass spectrometer. The structure on the top of the instrument is the gas inlet plenum.

Data from the Apollo 15 experiment indicated that a large background of contaminant gases was present in lunar orbit but that these gases did not emanate directly from the spacecraft (refs. 21-5 and 21-6). The main source of the background was thought to be the vaporization of ice and other particles coorbiting with the CSM. Another suspected source was the release of adsorbed gases from the walls of the inlet plenum. To minimize the latter effect in the Apollo 16 experiment, the inlet structure was fitted with a thermally controlled inner plenum, which was heated to approximately 520° K to outgas for approximately 1 hr before operation of the experiment and then was held at 343° K during data collection.

The rest of the instrument has been described in detail previously by Hoffman et al. (refs. 21-5 and 21-6). The instrument consists of a magnetic sector-field analyzer with two ion collectors. One collector covers the mass range of 12 to 28 amu, whereas the other collector simultaneously sweeps through masses 28 to 67 amu. Ions of a given mass, when focused on one of the collectors, are counted for a period of 0.1 sec, after which the accumulated count is telemetered. Formation of ions at the junction of the gas inlet plenum and the analyzer is accomplished by an electron beam with energy of 70 eV. Sensitivity of this type of instrument is a function of ionization cross section of each gas species. To establish the absolute sensitivity factors for this instrument, the flight model was calibrated at the NASA Langley Research Center Molecular Beam Facility (MBF) as described by Yeager et al.[2] For most gases, one telemetered ion count corresponded to approximately 260 molecules/cm^3; but an important exception is neon, which is not easily ionized and for which one count corresponded to 1100 atoms/cm^3 in the lunar atmosphere. These numbers imply the capability to detect partial pressures in the range of

[1] P. Yeager, A. Smith, J. Jackson, and J. H. Hoffman: Absolute Calibration of Apollo Lunar Orbital Mass Spectrometer. To be published in J. Vac. Soc., 1972.

[2] Ibid.

1×10^{-14} torr (1×10^{-13} torr for neon), but unexpectedly high levels of contamination make the realization of this capability in data analysis quite difficult, as will be noted in subsequent discussion.

RESULTS

Analysis of the Apollo 16 data currently is in a preliminary stage, awaiting the availability of trajectory data. However, the examination of one segment of the data gives some interesting results on the pressure of ^{20}Ne on the Moon.

Shortly after the plane change and rendezvous of the Apollo 16 CSM and lunar module, the mass spectrometer detected the lowest levels of contamination yet found in lunar orbit. This state resulted in data in which very close scrutiny of the neon content of the lunar atmosphere can be made. A typical spectrum obtained on the lunar dark side at approximately 180:32 ground elapsed time (GET) is shown in figure 21-2. At that time, the spacecraft presumably was oriented with the -X-axis in the direction of the velocity vector so that the gas inlet of the mass spectrometer should have been collecting lunar gases. The dominant peak at mass 18 amu, which results from water, had an amplitude of approximately 1.75×10^4 ion counts per sample period (0.1 sec), which is well below the level at which the counting system became nonlinear (at approximately 4×10^4 counts). Because of the high level of this peak on the dark side of the Moon, it is certain that the water vapor is mainly of spacecraft origin.

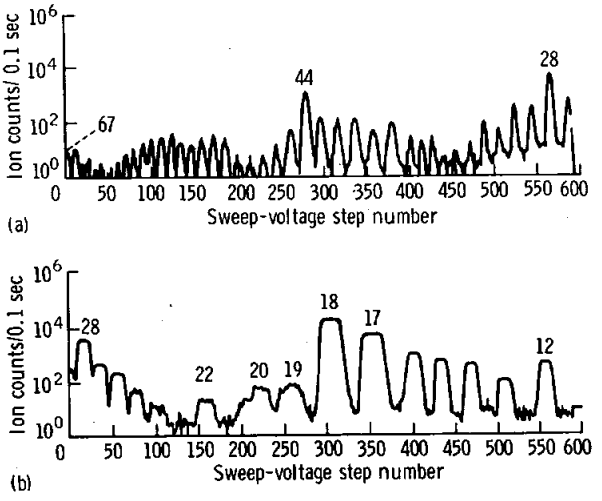


FIGURE 21-2.–Mass spectrum from Apollo 16 obtained at 180:32 GET over the dark side of the Moon. The horizontal scale gives the number of the data step corresponding to the sweep voltage that accelerates ions through the analyzer. (a) High mass range from 67 to 28 amu. (b) Low mass range from 28 to 12 amu.

The dominance of water vapor in the mass spectrum has important effects on nearby peaks. For example, the 17-amu peak is attributable essentially to hydroxyl (OH) ions formed by fractionation of water molecules in the ion source. Because the water is terrestrial in origin, the abundance of $H_2{}^{18}O$ is 0.2 percent of that of $H_2{}^{16}O$, giving rise to 35 ± 1 counts at 20 amu at the time in question. A corresponding contribution of approximately 10 counts at 19 amu is attributable to ^{18}OH.

An expanded portion of the measured spectrum at 19 and 20 amu is shown in figure 21-3. Each data point is the average of three measurements at the indicated sweep-voltage step from three successive spectra. Dispersion of the data points about the fitted curve is in good agreement with the expected variance of an average of samples in a Poisson distribution of the ion count rate.

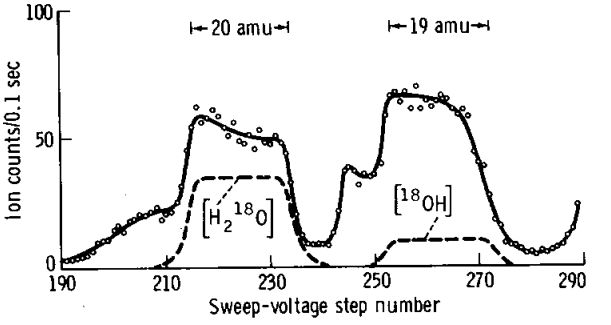


FIGURE 21-3.–Expanded portion of the low mass spectrum at 180:32 GET. Each data point represents the average of three measurements at the same sweep-voltage step number from three successive spectra. Contributions from $H_2{}^{18}O$ at 20 amu and ^{18}OH at 19 amu are indicated by dashed lines.

It can be noted in figure 21-3 that the 19- and 20-amu peaks do not have the nearly trapezoidal form that is typical of the low mass spectrum. Hence, rote subtraction of the 35-count contribution from $H_2{}^{18}O$ would not lead to a direct determination of the amount of the remaining gas at 20 amu, presumably ^{20}Ne. The only other 20-amu candidate is hydrogen fluoride, but its presence in lunar orbit is completely unexpected. Doubly ionized argon can be

ruled out because of the improbability of its presence as a contaminant or as a significant part of the nighttime lunar atmosphere at orbit altitude. (One count in the spectral data at 40 amu would imply approximately 1×10^6 atoms/cm^3 of argon at the surface.) The contribution of doubly ionized molecules of mass 40 amu probably is similar to that of other molecules, forming a fairly smooth background of multiply ionized gases with a level on the order of 1 count in the vicinity of the 20-amu peak.

The atypical shapes of the 19- and 20-amu peaks are the result of scatter of the intense $H_2{}^{16}O$ ion beam as it impinges on various protuberances, such as slit mounts, within the mass analyzer. Ion-molecule collisions contribute a nearly constant background of approximately 3 counts. In addition, at 19 amu, many hydrated protons (H_3O^+) are formed in collisions of water ions with water molecules. Because these hydrated ions are not formed in the electron beam of the ion source, they are not monoenergetic and thus contribute greatly to the distortion of the 19-amu peak.

To evaluate the actual amplitude of the 20-amu peak, it is necessary to understand the quantity of scattered water ions present. Inexact knowledge of the scattering process necessitates postulation of its behavior. It is assumed that scatter of ions from an obstacle would result in some thermal accommodation of the ions, giving rise to a nearly Gaussian spatial dispersion of the beam and, hence, of the resulting ion counts. This assumption has been applied to the rise in counts to the left of the 20-amu peak (sweep-voltage steps 190 to 211) and to the fall in counts at the top of the peak (sweep-voltage steps 216 to 232). A least-squares fit of these data to a uniform background, to a Gaussian distribution of scattered ions, and to an idealized, trapezoidal peak at 20 amu resulted in an amplitude of 46 counts for the trapezoidal-peak case. This result is illustrated in figure 21-4, in which the Gaussian distribution in question is labeled A and the background is 3 counts. The hump labeled B also results from scatter. The hump labeled C is the residual after subtraction of the 10 counts attributable to ^{18}OH known to be present. Hump C is caused by a combination of scatter of the water-ion beam and the H_3O^+ ions. Because the shapes of these scattered-ion curves are not easily predictable, it is not possible to accurately infer the effect of the scattered ions on the valley between the 19- and 20-amu peaks.

The value of 46 counts of mass 20-amu ions synthesized in figure 21-4 is most likely as large as could be obtained with any set of assumptions. If it were assumed that the ion-molecule scattering

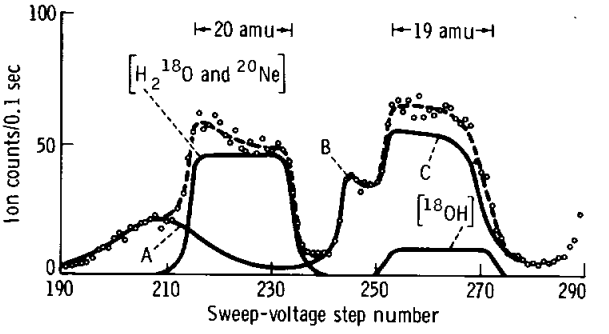


FIGURE 21-4.–Synthesis of the data of figure 21-3. The amplitude of the 20-amu peak, attributable to $H_2{}^{18}O$ and ^{20}Ne, is found from a least-squares error fit of this peak, a 3-count background, and the Gaussian scatter perturbation labeled A. Scatter is also the origin of hump B, whereas the form denoted C results from a combination of the scatter of water ions and H_3O^+ ions formed by ion-molecule collisions.

background increases gradually from 3 to 5 counts between sweep-voltage steps 190 and 240, then the use of the least-squares curve-fitting process for a Gaussian contribution resulting from scatter would lead to a 20-amu peak of 44 counts. However, the supposition of a Gaussian characteristic for the obstacle-scatter process leads to the largest plausible values of ^{20}Ne. If a non-Gaussian scatter pattern were assumed, then the total peak amplitude resulting from 20-amu ions could be as small as 39 counts. Thus, the probable range of mass 20-amu ions is between 39 and 46 counts. Subtraction of the 35 ± 1 counts known to result from $H_2{}^{18}O$ leads to an uncertainty in the amount of ^{20}Ne in the range of 3 to 12 counts. Absolute calibration of the Apollo 16 instrument in the MBF at the NASA Langley Research Center (Yeager et al.[3]) showed that 1 count in the data would correspond to 1100 atoms of neon with ram velocity equal to the CSM orbit speed. Thus, at the orbit altitude of approximately 100 km, the concentration of ^{20}Ne is estimated to be approximately $(8.3 \pm 5) \times 10^3$ atoms/cm^3. Because this

[3]Ibid.

concentration is approximately 4 scale heights above the lunar surface at night, the surface concentration must be e^4 times that at orbit altitude, or $(4.5 \pm 3) \times 10^5$ atoms/cm^3. This value is roughly a factor of 3 less than the nighttime estimate of 1.5×10^6 atoms/cm^3 made by Johnson (ref. 21-7) for neon of solar wind origin.

Attempts to determine the amount of lunar ^{22}Ne have been inconclusive because of the large amount of doubly ionized carbon dioxide (CO_2) produced in the ion source. Presumably, most of the CO_2 was of spacecraft origin and reached the instrument after vaporization of particles that had been ejected earlier from the CSM. Peaks at masses 44 and 22 have a nearly constant ratio throughout the flights of both the Apollo 15 and 16 spacecraft, although the levels vary from orbit to orbit and from day to night in each orbit. Preliminary analysis indicates that all of the 22-amu peak is attributable to CO_2^{++}, but the current error estimate is equivalent to several counts. Subsequent data processing should reduce this error and allow a more definitive search for the existence of ^{22}Ne to be made.

The temperature-controlled inlet plenum of the Apollo 16 instrument helped to confirm the conjecture that much of the contamination present in the spectra arises from vaporization of coorbiting particulate matter. The plenum temperature varied less than 2° K throughout an orbit, whereas levels of various contaminants varied as much as a factor of 5 from day to night, with all having daytime maximums. If the walls of the plenum had been an important source, their contribution would have shown significantly less diurnal variation. This observation vindicates the plenum as the major contamination source and supports the coorbiting-particulate-matter theory. Because of a boom malfunction and the subsequent jettisoning of the mass spectrometer just before the Apollo 16 transearth injection burn, it was not possible to confirm the Apollo 15 observation of significantly less contamination in transearth coast than in lunar orbit.

DISCUSSION

The current estimate of the nighttime surface concentration of ^{20}Ne at $(4.5 \pm 3) \times 10^5$ atoms/cm^3 and Johnson's theoretical value of 1.5×10^6 atoms/cm^3 (ref. 21-7) differ by approximately a factor of 3. This is reasonable agreement, considering the uncertainties in the values of solar wind abundance of neon and the photoionization rate assumed by Johnson. A ramification of the near agreement of the experimental and theoretical results is the verification of the assumption made by Johnson that most of the solar wind neon ions that impinge on the Moon (with approximately 1-keV energy) are neutralized and subsequently emitted into the lunar atmosphere. This assumption implies that the surface soil is saturated with neon.

It is important to recognize the implication of the possibility that a real discrepancy exists between the present analysis and the theoretical value of the amount of lunar neon. If the actual amount were much less than the theoretical value, then the surface currently would be absorbing most of the solar wind ions. To maintain the low level of neon in returned fines at less than 1 ppm (ref. 21-8), it would be necessary to continually overturn the soil to a depth of approximately 1 km, if the solar wind flux has remained relatively constant over geologic time. The lack of evidence of recent large-scale overturning of the soil leads to the conclusion that the current neon content in surface materials represents the saturation level, and that any difference between actual and theoretical levels of neon cannot be credited to absorption of solar wind ions.

The current estimate of $(4.5 \pm 3) \times 10^5$ neon atoms/cm^3 is in fair agreement with the data from the Apollo 14 and 15 cold cathode ionization gages operating on the lunar surface. Johnson et al. (ref. 21-1) report that the total concentration in these gages at night is approximately 2×10^5 atoms/cm^3. To aid in correlating the results of these experiments, a laboratory model of the cold cathode gage is to be calibrated in the NASA Langley Research Center MBF under conditions similar to those used in calibration of the lunar orbital mass spectrometers.

REFERENCES

21-1. Johnson, Francis S.; Evans, Dallas E.; and Carroll, James M.: Lunar Atmosphere Measurements. Proceedings of the Third Lunar Science Conference, vol. 3, David R. Criswell, ed., MIT Press (Cambridge, Mass.), 1972.

21-2. Hodges, R. R.; Hoffman, J. H.; Yeh, T. T. J.; and Chang, G. K.: Orbital Search for Lunar Volcanism. J. Geophys. Res., vol. 77, no. 22, Aug. 1, 1972, pp. 4079-4085.

21-3. Hodges, R. R., Jr.; and Johnson, F. S.: Lateral Transport in Planetary Exospheres. J. Geophys. Res., vol. 73, no. 23, Dec. 1, 1968, pp. 7307-7317.

21-4. Yeh, T. T. J.; and Chang, G. K.: Density and Flux Distributions of Neutral Gases in the Lunar Atmosphere. J. Geophys. Res., vol. 77, no. 10, Apr. 1, 1972, pp. 1720-1728.

21-5. Hoffman, J. H.; Hodges, R. R.; and Evans, D. E.: Lunar Orbital Mass Spectrometer Experiment. Sec. 19 of Apollo 15 Preliminary Science Report. NASA SP-289, 1972.

21-6. Hoffman, J. H.; Hodges, R. R.; and Evans, D. E.: Lunar Orbital Mass Spectrometer Experiment. Proceedings of the Third Lunar Science Conference, vol. 3, David R. Criswell, ed., MIT Press (Cambridge, Mass.), 1972.

21-7. Johnson, F. S.: Lunar Atmosphere. Rev. Geophys. Space Phys., vol. 9, no. 3, Aug. 1971, pp. 813-823.

21-8. Bogard, D. D.; and Nyquist, L. E.: Noble Gas Studies on Regolith Materials From Apollo 14 and 15. Proceedings of the Third Lunar Science Conference, vol. 2, Dieter Heymann, ed., MIT Press (Cambridge, Mass.), 1972.

ACKNOWLEDGMENTS

Valuable discussions with Dr. F. S. Johnson and Dr. R. O. Pepin are gratefully acknowledged. Thanks are also extended to the many persons at The University of Texas at Dallas and with NASA whose efforts made this experiment possible.

22. Subsatellite Measurements of Plasma and Energetic Particles

K. A. Anderson,[a†] L. M. Chase,[a] R. P. Lin,[a]
J. E. McCoy,[b] and R. E. McGuire[a]

The Apollo 16 particles and fields subsatellite is instrumented to measure (1) plasma and energetic-particle fluxes, (2) vector magnetic fields, and (3) velocity of the subsatellite to a high precision for the purpose of determining lunar gravitational anomalies.

Results from the magnetic-field and gravitational-field experiments are discussed in other sections of this report. In this section, the results obtained from the plasma and energetic-particle detectors are discussed briefly. The objectives of the plasma and energetic-particles experiment are to describe the various plasma regimes in which the Moon moves, to determine how the Moon interacts with the plasma and magnetic fields in the environment, and to determine certain features of the structure and dynamics of the magnetosphere of the Earth.

INSTRUMENTATION

The plasma and energetic-particle detectors consist of two solid-state telescopes and four hemispherical-plate electrostatic analyzers that use channel electron multipliers. The electrostatic analyzers are designed to measure electrons with energies from 0.5 to 15 keV in four energy ranges. One analyzer has two outputs that have different geometric factors to provide a wider dynamic range. The solid-state telescopes measure electrons from 20 to 300 keV and protons from 40 keV to 2 MeV. The characteristics of the various detectors are summarized in table 22-I. For a more detailed description of the instrumentation, see reference 22-1. Although the detectors on the Apollo 16 subsatellite are the same as those on the Apollo 15 subsatellite, there were two important operational differences: (1) the solid-state telescopes on the Apollo 16 subsatellite operated at a lower temperature, resulting in a lower background-counting rate, a lower energy threshold, and higher sensitivity, and (2) one analyzer output on the Apollo 16 subsatellite had a lower background-counting rate and, thereby, provided higher sensitivity to 6-keV electrons.

[a]University of California at Berkeley.
[b]NASA Manned Spacecraft Center.
[†]Principal Investigator.

RESULTS

Much of the Apollo 16 subsatellite data is in substantial agreement with the results of the Apollo 15 subsatellite reported elsewhere (refs. 22-1 and 22-2). In this report, new results made available by the Apollo 16 subsatellite will be emphasized.

Solar-Particle Increases at an Interplanetary Shock

On May 15, 1972, the Apollo 16 subsatellite detected a solar-particle event starting between 08:00 and 10:00 G.m.t. At this time, the Moon was in the solar wind 35° from the Earth-Sun line. The event reached its peak at approximately 18:00 G.m.t. and lasted several days. Fluxes of electrons at energies above approximately 2 keV increased by more than an order of magnitude above background levels. Energetic-proton fluxes throughout the event were typically a factor of approximately 10 higher than electron fluxes at the same energy.

An interesting feature during this event was the passage of an interplanetary shock. Energy spectra of the electrons and protons both before the solar event and at the time of the shock passage are shown in figure 22-1. The profile of the shock in the 300- to 528-keV protons and in the 13.5- to 15-keV electrons is shown in figure 22-2. The shock wave produced a rapid increase in the particle fluxes. The increase was characterized in the protons by an order-of-magnitude increase in flux beginning at 18:29 G.m.t. and cutting off sharply at 18:42 G.m.t. The increase

TABLE 22-I.–Summary of Detector Characteristics

Detector designation	*Detector type*	*Energy range*		*Geometric factor, cm^2-sr*	*Angular aperture*	*Angle to spin axis, deg*	*Approximate value of minimum detectable flux, particles/cm^2-sec-sr*
		Protons, MeV	*Electrons, keV*				
SA_{1-6}	Open solid-state detector, with anticoincidence detector in back (six-channel pulse-height analyzer)	0.04 to 2	20 to 300	0.045	40°, cone	0	0.01
SB_{1-6}	Same as SA_{1-6}, except with a 375-$\mu g/cm^2$ foil over the detector	.3 to 2	20 to 300	.045	40°, cone	0	.01
C_1	Channel electron multiplier in a hemispherical-plate electrostatic analyzer	No response	.52 to .58	5.3×10^{-5}	20° by 60°; full width, half maximum (FWHM)	90	10^4
C_2	Channel electron multiplier in a hemispherical-plate electrostatic analyzer	No response	1.9 to 2.1	2.13×10^{-4}	20° by 60°, FWHM	90	10^4
C_3	Channel electron multiplier in a hemispherical-plate electrostatic analyzer	No response	5.9 to 6.4	2.4×10^{-4}	15° by 60°, FWHM	90	10^4
C_4	Funnel-mouthed channel electron multiplier in a hemispherical-plate electrostatic analyzer	No response	5.8 to 6.5	.08	18° by 60°, FWHM	90	.1
C_5	Funnel-mouthed channel electron multiplier in a hemispherical-plate electrostatic analyzer	No response	13.5 to 15.0	.17	13° by 60°, FWHM	90	.1

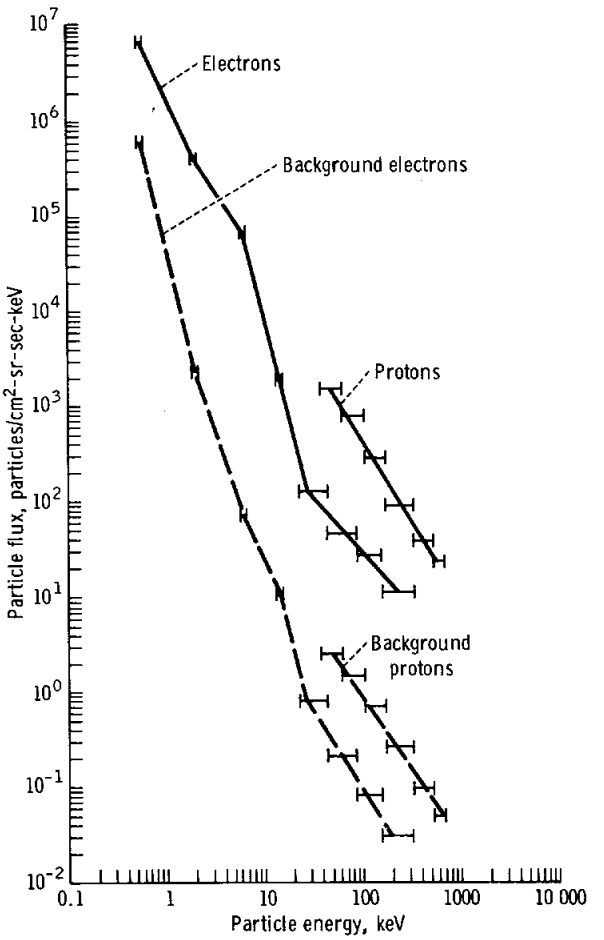


FIGURE 22-1.–Energy spectra of electrons and protons obtained from 2-hr background averages on May 15, beginning with a quiet time (02:28 G.m.t.) before the solar-particle event, extending through the time of the interplanetary shock wave (18:42 G.m.t.), and ending with a sharp electron cut-off (18:50 G.m.t.).

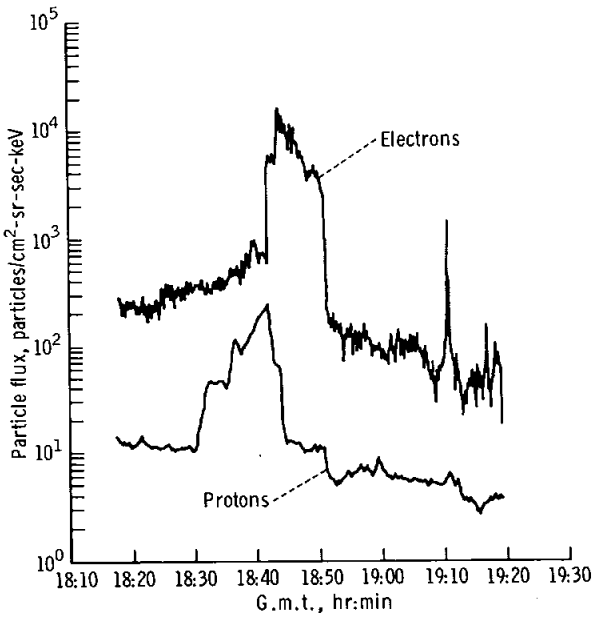


FIGURE 22-2.–Particle flux profiles of 300- to 528-keV protons and 13.5- to 15-keV electrons covering an interplanetary shock wave at 18:42 G.m.t. on May 15.

was not seen in the electrons until approximately the time of the proton cut-off. The electrons from 0.5- to 15-keV energies then showed a sharp order-of-magnitude increase, which lasted until 18:50 G.m.t. when the electrons were cut off sharply. The increase of the 0.5-keV electron flux indicates that the shock heated the solar wind to abnormally high temperatures.

The conclusion that the observed increase in particle fluxes is a manifestation of a hydromagnetic shock wave in the solar wind (refs. 22-3 and 22-4) is supported by the fact that the interplanetary magnetic field showed a sharp discontinuity at the time of the electron onset and by a storm sudden commencement observed 10 min later on ground-based magnetometers (refs. 22-3 and 22-4). From the time delay between the time of the discontinuity at the subsatellite and the time of the storm sudden commencement at the Earth, the propagation velocity of the shock wave was found to be greater than approximately 400 km/sec. The shock wave apparently was preceded by energetic protons extending approximately 300 000 km in front of the shock. For comparison, the gyroradius of a 0.5-MeV proton is 10 000 km. The rise time of the electron increase probably is a more accurate indication of the discontinuity thickness because the electrons have a gyroradius of approximately 100 km. The inferred thickness of the electron-discontinuity region is approximately 4000 km.

Because sunset on the spacecraft occurred at approximately the same time as the proton cut-off and electron increase, the possibility that magnetic-field line-shadowing effects influenced the measurement of the shock increase was considered. Because protons of energy >300 keV have gyroradii greater than 4 times the radius of the Moon, deep shadows can be seen only in energetic protons with pitch angles near 0°. Because the proton detectors were

looking at only 90° ± 20° pitch angles, shadowing could not have caused the sharp cut-off observed in the protons. Under certain conditions, the electron increase could be explained by particle shadowing. The magnetic-field data show that the angle of the field to the Sun was 157° at the time of the electron increase. For this direction of the field, an increase attributable to the spacecraft leaving the shadow should have occurred approximately 4 min earlier than observed. It is concluded that the proton and electron burst was of solar origin and that the separation of protons and electrons was not a particle-shadowing effect. It is likely, however, that the sharp cut-off of electron flux at 18:50 G.m.t. was enhanced by particle shadowing.

The 520- to 580-eV electron flux remained high for more than 12 hr after the shock, whereas the higher energy electrons decayed within 3 hr.

Particle Fluxes in the Magnetotail

At the time of the Apollo 16 subsatellite launch, the Moon was just entering the geomagnetic tail. During the time the Moon was in the magnetotail, there were 39 orbits of the subsatellite around the Moon. Complete data coverage was obtained on 33 of these orbits. Of the orbits for which data were obtained, 22 were in the high-latitude magnetotail and, on nine orbits, the plasma sheet was encountered.

Particles in the high-latitude magnetotail are characterized by steady fluxes and distinct shadow patterns. Typical fluxes of 520- to 580-eV electrons are between 4×10^5 to 8×10^5 electrons/cm^2-sr-sec-keV. Energy spectra of electrons and protons in the high-latitude magnetotail are shown in figure 22-3.

Shadow patterns of electrons at three different energies are shown in figure 22-4. The patterns can be divided into three distinct regions.

(1) The shadow region of low fluxes on the near side of the Moon

(2) The limb region of high fluxes beginning approximately 10 min before sunset

(3) The region on the far side of the Moon in which the flux is approximately one-half the limb flux

An interesting result is that the depth of the shadows is a function of energy. At 520 to 580 eV,

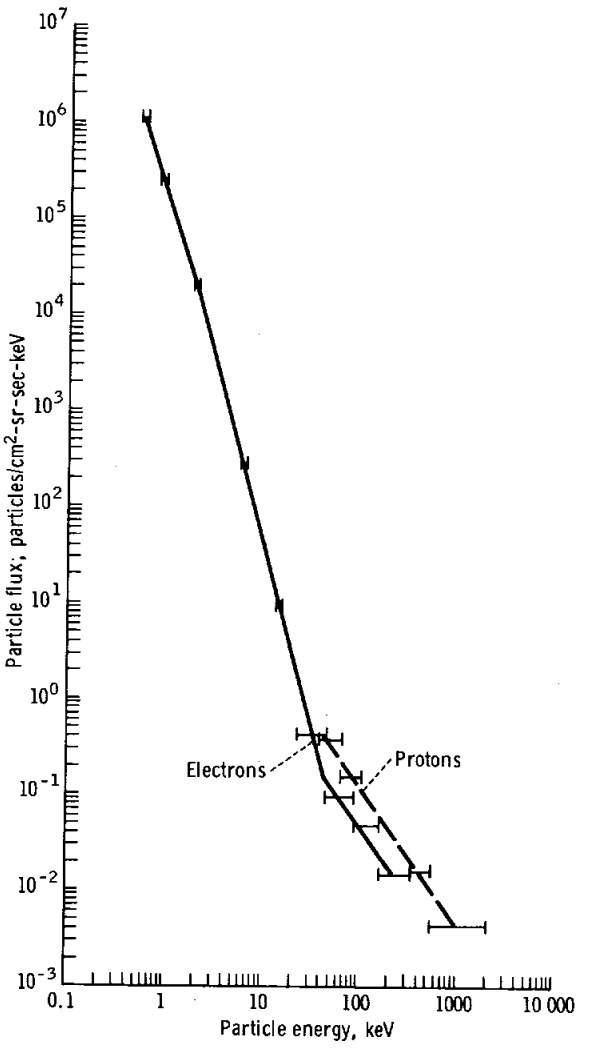


FIGURE 22-3.–Energy spectra of electrons and protons in the high-latitude magnetotail (08:49 G.m.t., April 27).

the shadow flux is well above the detector background level and is approximately one-half the flux on the far side. At 5.8 to 6.5 keV, the shadow flux is approximately an order of magnitude less than the far-side flux. An energy dependence of shadow depth is observed on all 22 orbits of the subsatellite in the high-latitude magnetotail.

Shadow patterns of the type seen in the 5.8- to 6.5-keV electrons can be explained by a relatively simple model. Consider particles streaming toward the Earth along magnetic-field lines from a continuous source deep in the magnetotail. As the particles approach the Earth, the greater magnetic-field

strength will mirror the particles, causing them to return back down the tail. A large absorber such as the Moon causes the particles in the shadow region between the Moon and the Earth to be quickly depleted because the source is cut off and the mirrored particles will collide with the Moon and be absorbed. Beyond limbs of the Moon, the particles are unaffected by its presence. On the far side of the Moon, only particles from the source can be seen. The omnidirectional intensity of these particles will be approximately one-half the limb flux because the limb flux includes both source and mirrored particles. A source mechanism for the upstreaming particles is the interconnection of the tail magnetic field to the interplanetary field, an action which allows particles of solar origin to enter the magnetotail (ref. 22-5).

One possible explanation for the observed filling in of low-energy electrons into the shadow region is that particle drifts are produced by an electric field across the magnetotail (ref. 22-6). If the field direction were dawn to dusk, then particles in the northern high-latitude magnetotail would undergo a southward drift and particles in the southern magnetotail would drift northward. Because the subsatellite orbital plane is essentially parallel to the ecliptic plane, particles clearing the north limb of the Moon will drift toward the subsatellite orbital plane, where they can be detected. The distance that a particle moves toward the orbital plane depends on the time required for the particle to reach its mirror point and return to the Moon.

Low-energy particles and small-pitch-angle particles will drift farther than high-energy particles and large-pitch-angle particles. For the example shown in figure 22-4, it has been calculated that a field of approximately 3×10^{-4} V/m would be required to move approximately 50 percent of an initially isotropic distribution of 0.5-keV electrons across the orbital plane and fill the shadow. This field would have little effect on the 2- and 6-keV electron shadows. For other orbits, it has been calculated that the required electric field ranged from $< 1 \times 10^{-4}$ V/m to approximately 9×10^{-4} V/m.

Particles in the Plasma Sheet

Particles in the plasma sheet can be characterized by variable particle fluxes that run from 5 to 100 times more than the fluxes observed in the high-latitude magnetotail. A continuing feature of the plasma sheet is a large flux of energetic protons. Plasma-sheet protons >40 keV often have flux an order of magnitude greater than electrons of the same energy. This difference is in contrast to the high-latitude magnetotail, in which the electron and proton fluxes are approximately the same. Energy spectra of electrons and protons in the plasma sheet are shown in figure 22-5.

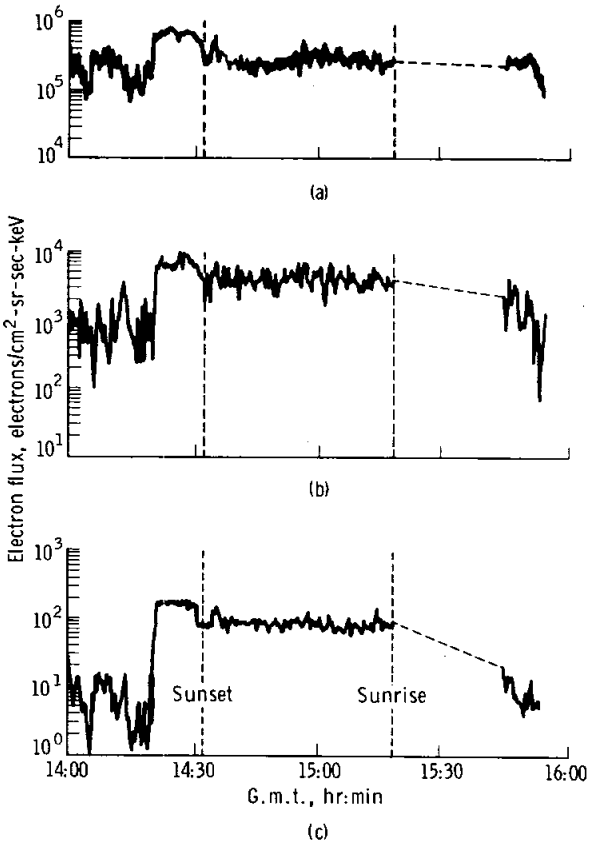


FIGURE 22-4.–Shadow patterns of electrons in the high-latitude magnetotail (April 29). (a) Shadowing of 520- to 580-eV electrons. (b) Shadowing of 1.9- to 2.1-keV electrons. (c) Shadowing of 5.8- to 6.5-keV electrons.

SUMMARY

(1) The Apollo 16 subsatellite encountered a hydromagnetic shock wave at 18:42 G.m.t. on May 15, 1972.

(2) The shock wave was traveling at >400 km/sec.

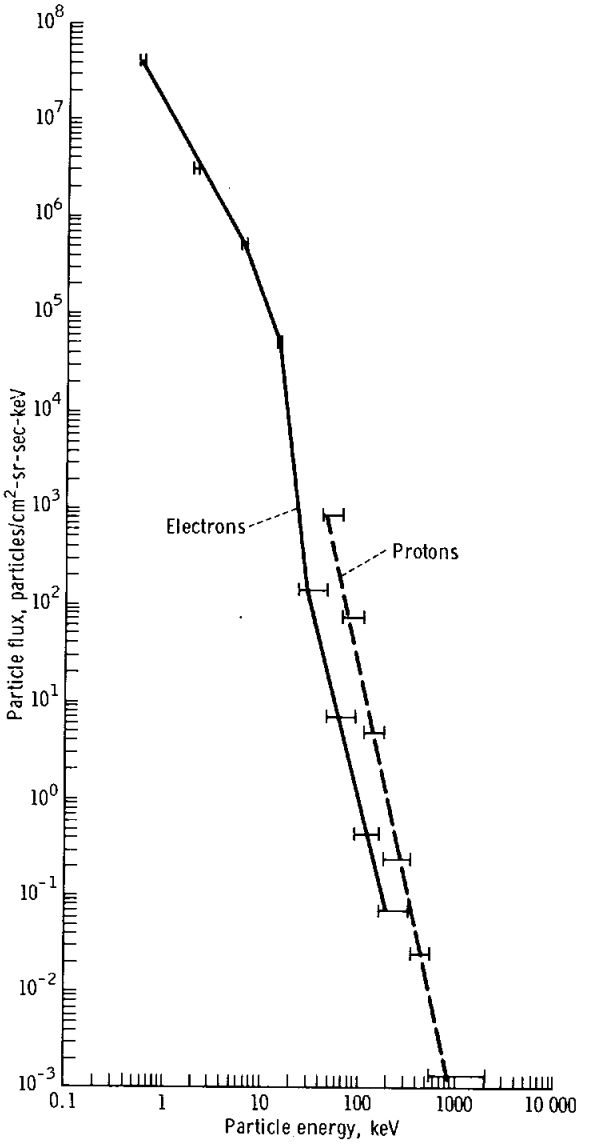


FIGURE 22-5.–Energy spectra of electrons and protons in the plasma sheet at 08:23 G.m.t. on April 29.

(3) The shock wave was preceded by energetic protons extending to approximately 300 000 km in front of the shock.

(4) The energetic-electron discontinuity was 4000 km thick behind the magnetic-field discontinuity.

(5) The solar wind electrons were at abnormally high temperatures for approximately 12 hr after the shock.

(6) In the magnetotail, 6-keV electrons were observed traveling toward the Earth from deep in the magnetotail.

(7) A dawn-to-dusk electric field across the magnetotail could explain the observed filling in of low-energy electron shadows. The required field strengths range from $<1 \times 10^{-4}$ V/m to 9×10^{-4} V/m.

REFERENCES

22-1. Anderson, K. A.; Chase, L. M.; Lin, R. P.; McCoy, J. E.; and McGuire, R. E.: Subsatellite Measurements of Plasmas and Solar Particles. Sec. 21 of the Apollo 15 Preliminary Science Report. NASA SP-289, 1972.

22-2. Anderson, K. A.; Chase, L. M.; Lin, R. P.; McCoy, J. E.; and McGuire, R. E.: Solar Wind Interactions with the Moon, Results from the Apollo 15 Subsatellite. J. Geophys. Res., vol. 77, no. 25, Sept. 1972, pp. 4611-4626.

22-3. Burlaga, L. F.; and Ogilvie, K. W.: Causes of Sudden Commencements and Sudden Impulses. J. Geophys. Res., vol. 74, no. 11, June 1, 1969, pp. 2815-2825.

22-4. Ogilvie, K. W.; and Burlaga, L. F.: Hydromagnetic Shocks in the Solar Wind. Solar Phys., vol. 8, no. 2, 1969, pp. 422-434.

22-5. Anderson, K. A.; and Lin, R. P.: Observation of Interplanetary Field Lines in the Magnetotail. J. Geophys. Res., vol. 74, no. 16, Aug. 1, 1969, pp. 3953-3968.

22-6. Anderson, K. A.: Method To Determine Sense and Magnitude of Electric Field From Lunar Particle Shadows. J. Geophys. Res., vol. 75, no. 13, May 1, 1970, pp. 2591-2594.

23. The Particles and Fields Subsatellite Magnetometer Experiment

P. J. Coleman, Jr.,[a†] *B. R. Lichtenstein,*[a] *C. T. Russell,*[a]
G. Schubert,[a] *and L. R. Sharp*[a]

INTRODUCTION

The objectives of the particles and fields subsatellite (PFS) magnetometer experiment are to calculate the interior electrical conductivity of the Moon, to survey the remanent magnetization of the lunar surface, and to study the interaction of the Moon with its plasma environment. The calculation of the interior electrical conductivity by measuring the transfer function of the Moon to hydromagnetic oscillations constrains the thermal profile of the lunar interior and thus complements the heat-flow measurements. The mapping of the remanent field provides knowledge of the magnetization over a wide area of the Moon, thus supplementing the site surveys made at the landing sites and complementing the studies of the natural remanent magnetization of the returned lunar samples. The observation of the magnetic features associated with the interaction of the supersonic flow of the solar wind with the Moon complements those made previously on the Explorer 35 satellite at higher altitudes and the measurements on the lunar surface. The magnetometers also support the PFS particle experiment by providing onboard magnetic sectoring and a posteriori pitch angle data and plasma diagnostics.

Dual magnetometer correlations are involved in many of the objectives of this experiment. Both the spectrum of magnetic fluctuations at the subsatellite (the input) and the spectrum of fluctuations at the surface (the output) are necessary to derive the lunar transfer function. Dual orbital measurements are also desirable to separate temporal from spatial features. The surface magnetometer can aid in this regard, but temporal variations are modified at the lunar surface.

Dual PFS magnetometer studies were planned until a failure of the Apollo 15 PFS telemetry system in February 1972 prevented the transmission of magnetometer data. Fortunately, the Ames Research Center Explorer 35 magnetometer was still operating at the time of the Apollo 16 launch so that some dual satellite measurements could still be made.

The Apollo 16 subsatellite was launched on April 24, 1972, into an approximately circular orbit at an altitude of 100 km with an orbital period of nearly 2 hr. Because of the decision not to perform a shaping burn before jettisoning the subsatellite, the Apollo 16 PFS crashed into the Moon after 34 days in lunar orbit. Although this had a serious impact on the mapping studies, the final few orbits provided some spectacular data at extremely low altitudes.

EARLY MEASUREMENTS

The magnetic field of the Moon has been subject to experimental investigation for more than a decade. Magnetometers were carried on the Luna 1 and 2 probe missions in 1959 and the Luna 10 and Explorer 35 orbiters in 1966 and 1967, respectively. These experiments revealed that any intrinsic lunar magnetic field was much smaller than that of the Earth. The Explorer 35 measurements, for example, show that the lunar field is less than 2 nT (2 γ; 1 $\gamma = 10^{-5}$ gauss) at an altitude of 840 km (ref. 23-1). However, investigations of the first returned lunar samples revealed natural remanent magnetization in the lunar material (refs. 23-2 to 23-8). These results were soon complemented by in situ measurements of the lunar-surface magnetic field obtained on the Apollo 12 mission.

The lunar-surface magnetometer (LSM) in the Apollo lunar-surface experiments package (ALSEP) deployed during the Apollo 12 mission measured a surface field of 38 ± 3 nT (38 ± 3 γ) with no detectable gradient (i.e., <400 nT/km) (ref. 23-9). The lunar portable magnetometer (LPM) carried on the Apollo 14 mission measured fields of 43 ± 6 nT (43 ± 6 γ) and 103 ± 5 nT (103 ± 5 γ) at sites separated by 1.1 km (ref. 23-10). The linear gradient

[a]University of California at Los Angeles.
†Principal Investigator.

between the two sites was thus 54 ± 10 nT/km (54 ± 10 γ). The size of the natural remanent magnetization in the returned lunar samples and the strength of the surface field and its apparent scale size suggested that, despite the lack of a detectable global lunar field, it would be possible to map the small-scale lunar field from a low-altitude (~100 km) orbit.

During the lunar month, the Moon passes through three distinct plasma environments. First, for approximately 5 days around full Moon, it is immersed in the relatively strong (10 to 20 nT) field of the geomagnetic tail. In this region of low plasma density and steady background field, the measurement of the lunar field is relatively straightforward. Surrounding the geomagnetic tail is the turbulent magnetosheath, a region in which flows the shocked solar-wind plasma. This region contains large-amplitude hydromagnetic waves that, although providing temporal variations for sounding studies, prevent the unambiguous identification of spatial features. For approximately 10 days on either side of the new Moon, the Moon is in the relatively undisturbed supersonic flow of the solar wind, where spatial features can again be readily detected. However, these spatial features are, in general, related to the interaction of the flowing solar wind with the Moon rather than to the direct detection of the lunar field.

The general properties of the interaction of the solar wind with the Moon were first investigated with the Explorer 35 satellite (refs. 23-11 to 23-13). No bow shock was observed, implying that the solar wind impacts the lunar surface and is absorbed, leaving a plasma void behind the Moon. The absorption by the lunar surface has been confirmed by studies of the aluminum foils returned by the astronauts (refs. 23-14 and 23-15) and by the solar-wind spectrometer in the ALSEP.[1] The magnetic field in the plasma void is enhanced over that in the solar wind. This enhancement may be due either to diamagnetism of the solar-wind plasma or to the requirement of pressure balance in a steady-state flow. The solar wind expands into the void as it flows past the Moon. Associated with this rarefaction wave are dips in the magnetic field strength on either side of the diamagnetic enhancement (ref. 23-16). This situation is shown schematically in figure 23-1.

[1]Neugebauer, M.; Snyder, C. W.; Clay, D. R.; and Goldstein, B. F.: Solar Wind Observations on the Lunar Surface with the Apollo 12 ALSEP. Planet. Space Sci., in press.

Occasionally, increases in the magnetic field strength are observed on the solar-wind side of the rarefaction dips. These field increases have been correlated with increases in the plasma density using simultaneous particle and field data from Explorer 35 (ref. 23-17). Sonett and Mihalov (ref. 23-18), using data from the Ames magnetometer aboard Explorer 35, have called these regions "limb shocks" and have shown a correlation between the occurrence of "limb shocks" and the appearance of specific selenographic features at the limbs. They concluded that the "limb shocks" are caused by the deflection of part of the flow near the limb by regions of strong magnetization. Whang and Ness (ref. 23-19) have named this same phenomenon "penumbral increases." Using data from the Goddard Space Flight Center magnetometer also on board Explorer 35, they have shown that the occurrence of "penumbral increases" has a strong positive correlation with the upstream solar-wind β (ratio of plasma to magnetic pressure) and no clear correlation with the selenographic coordinates of the lunar limb.

THE MAGNETOMETER

The Apollo 16 subsatellite magnetometer consists of two fluxgate sensors mounted orthogonally at the end of a 1.83-m boom and an electronics unit housed in the spacecraft. The design of the Apollo 16 subsatellite magnetometer is identical to that of the Apollo 15 magnetometer, which is described in detail in reference 23-20. The only significant difference between the two magnetometers is an increase by a factor of 2 in the gain of the Apollo 16 magnetometer, increasing the resolution to 0.2 and 0.8 nT (0.2 and 0.8 γ) and decreasing the range to ±25 and ±100 nT (±25 and ±100 γ) for high and low sensitivity ranges, respectively.

The vector magnetic field is constructed from the measurement of the amplitude and sign of the component of the field along the spin axis and the amplitude and phase of the field in the spin plane. The amplitude in the spin plane is determined on the ground by Fourier analysis for high-telemetry-rate data (one sample per second) and by analog techniques on the spacecraft for the low-rate stored data. The phase is determined by measuring the time delay between the crossing of solar direction and the positive-going zero crossing of the magnetic field. During eclipse, the time of the positive-going zero

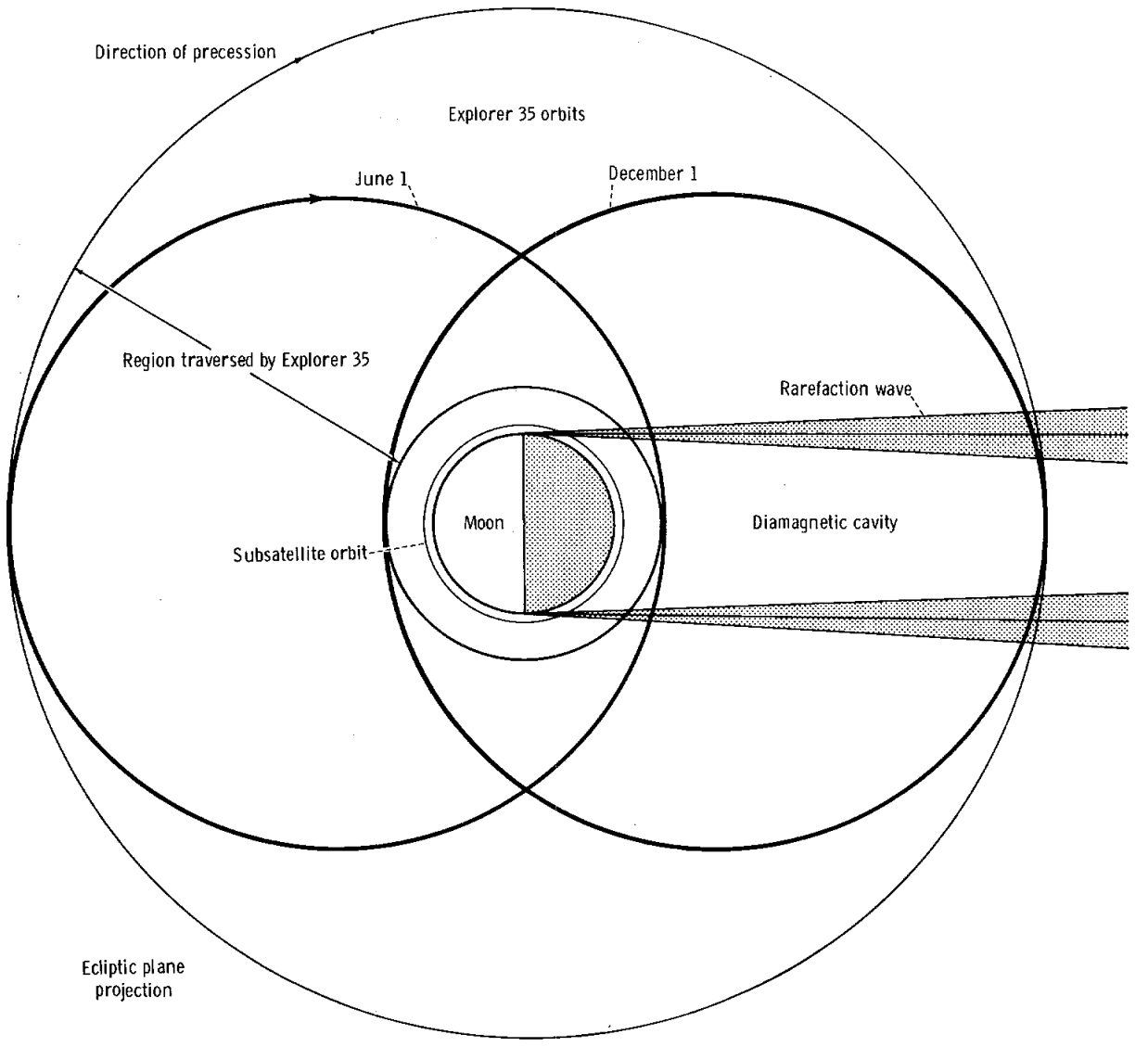


FIGURE 23-1.–The solar-wind/Moon interaction region and the orbits of Explorer 35 and the Apollo subsatellites. The Apollo 15 subsatellite is inclined approximately 30° to the ecliptic plane; the Apollo 16 subsatellite, approximately 10°; and the Explorer 35 satellite, approximately 15°. Each 6 months, the perilune of Explorer 35 moves from the solar meridian of the Moon to behind the Moon because of the motion of the Earth/Moon system about the Sun.

crossing is telemetered to Earth, and the times of crossings of the solar direction are computed from an empirical model of the change in spin rate as the subsatellite cools during eclipse together with the phase of the Sun both before and after eclipse.

The sensitivity range of the magnetometer is sampled every eighth reading for both the parallel and transverse ranges. The low sampling rate of the range bit provides a source of latent ambiguity in decoding the data in rapidly varying fields. However, the range of the magnetometer remained in the high-sensitivity mode throughout the useful lifetime of Apollo 15 and only changed on Apollo 16 at perilune during the last few passes. An attempt has been made to resolve ambiguities for these latter times by following the evolution of the magnetic field on successive orbits as the satellite drifted over magnetized regions and as perilune decreased.

REMANENT MAGNETIZATION

The geomagnetic tail in which the Moon spends 5 days each lunation provides a relatively noise-free environment for mapping the lunar-surface magnetic field. Even here, there are occasional temporal variations. Hence, passes over the same ground track have been averaged together to increase the ability to identify the lunar field. Only during low-altitude passes over relatively strong features have individual passes been used to construct field maps.

The result of averaging 17 orbits of Apollo 15 tail data (ref. 23-21) is shown in figure 23-2. The top trace is the component parallel to the spin axis and the bottom trace is the magnitude of the field in the spin plane. The field is quite irregular, especially on the far side of the Moon. The largest feature occurs near 180° longitude, near the crater Van de Graaff. Craters have been associated with many of these features in the magnetic field. The degree of correspondence of the magnetic field with lunar topography is shown in figure 23-3, which gives the orbital track of the subsatellite across the far side of the Moon at the time when the data shown in figure 23-2 were obtained. The bars show where the maxima occurred, the dots where the minima occurred. The minima occur roughly in conjunction with craters, but the correlation with lunar topography is only approximate.

The approximate nature of this correlation is illustrated by the high-resolution contour map of the Van de Graaff region shown in figure 23-4.[2] This map was constructed from a series of individual passes, during an interval in which the subsatellite perilune was at low altitudes over the Van de Graaff region. The map shows a well-defined feature with a 4.5-nT (4.5-γ) peak-to-valley variation. This feature is clearly not centered over either Aitken or Van de Graaff, which suggests that these magnetic features are not necessarily associated with crater formation.

The inclination of the Apollo 16 subsatellite orbit to the lunar equator was 10° as opposed to the 28° inclination of the Apollo 15 subsatellite. Thus, the Apollo 16 mapping is restricted to the band from 10° N to 10° S. This region and a typical orbital track are shown in figures 23-5 and 23-6. Eleven orbits of data obtained in the tail along this orbital track have been averaged and are shown in figure 23-7. These data contrast sharply with the Apollo 15 data at higher latitudes shown in figure 23-2. Although statistically significant features exist in this plot, the features lack the clear definition of figure 23-2.

The Apollo 16 subsatellite crashed shortly after the Moon had exited from the magnetotail into the magnetosheath in the second lunation. The second tail pass, therefore, contains intervals of data at very low altitudes as perilune approached the surface, and many strong features have been identified in the data. However, because orbital data for this interval have not been received, these features cannot yet be associated with particular selenographic regions.

The component of the field parallel to the spin axis for three successive orbits of the Apollo 16 PFS during the second tail pass is shown in figure 23-8. The magnitude of the field in the spin plane at the corresponding times is shown in figure 23-9. The data on the latter part of each orbit are highly fluctuating and appear almost random. However, this structure is repeated on successive orbits, with only a slow evolution of features. This indicates that this highly fluctuating field is caused by the near approach to the lunar surface and that the sample rate of the magnetometer is sufficiently fast to define the features. The increased variability of the data here as opposed to that observed at higher altitudes over a large anomaly such as Van de Graaff is the result of the smaller scale size that is being probed as the satellite approaches the surface.

The magnitude of the magnetic field in the spin plane for the last eight orbits before the subsatellite crashed is shown in figure 23-10. The time scale has been expanded here, and only 20 min around perilune are shown. The amplitude scale, however, has been drastically compressed so that the extremely large fields (some are greater than 50 nT) can be plotted. The gradual evolution of the field pattern and the growth and decay of specific features can be seen as perilune drifts across the region. These data were obtained while the Moon was in the magnetosheath and the satellite in the plasma void behind the Moon.

---

[2]Coleman, P. J., Jr.; Russell, C. T.; Sharp, L. R.; Schubert, G.: Preliminary Mapping of the Lunar Magnetic Field. Phys. Earth Planet. Interiors, in press.

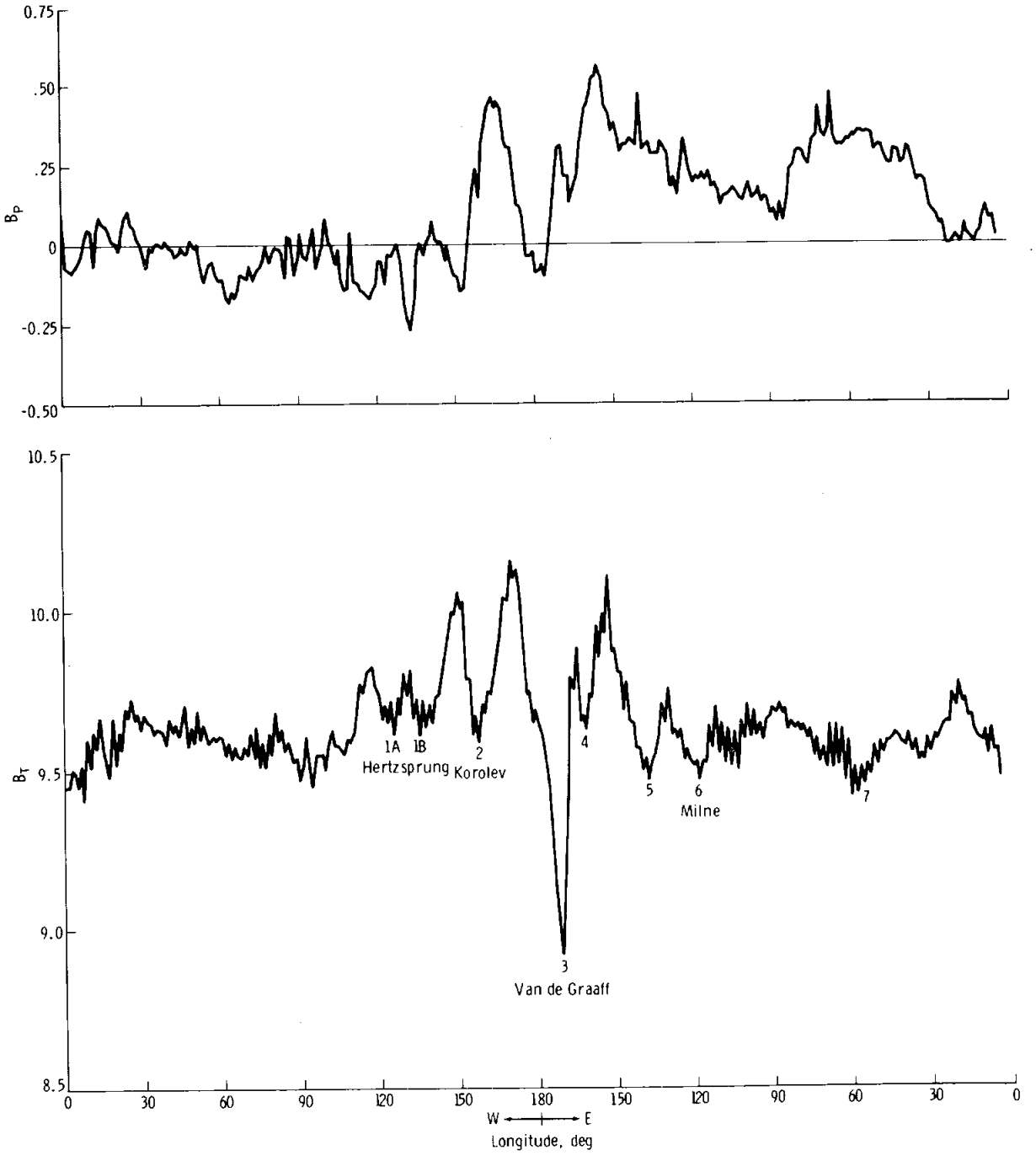


FIGURE 23-2.–The magnetic field parallel to the spin axis of the Apollo 15 subsatellite B_P and the field transverse to the spin axis B_T averaged over 17 successive orbits while the Moon was in the geomagnetic tail. Major dips in the transverse magnitude have been numbered to facilitate comparison with the ground track shown in figure 23-3.

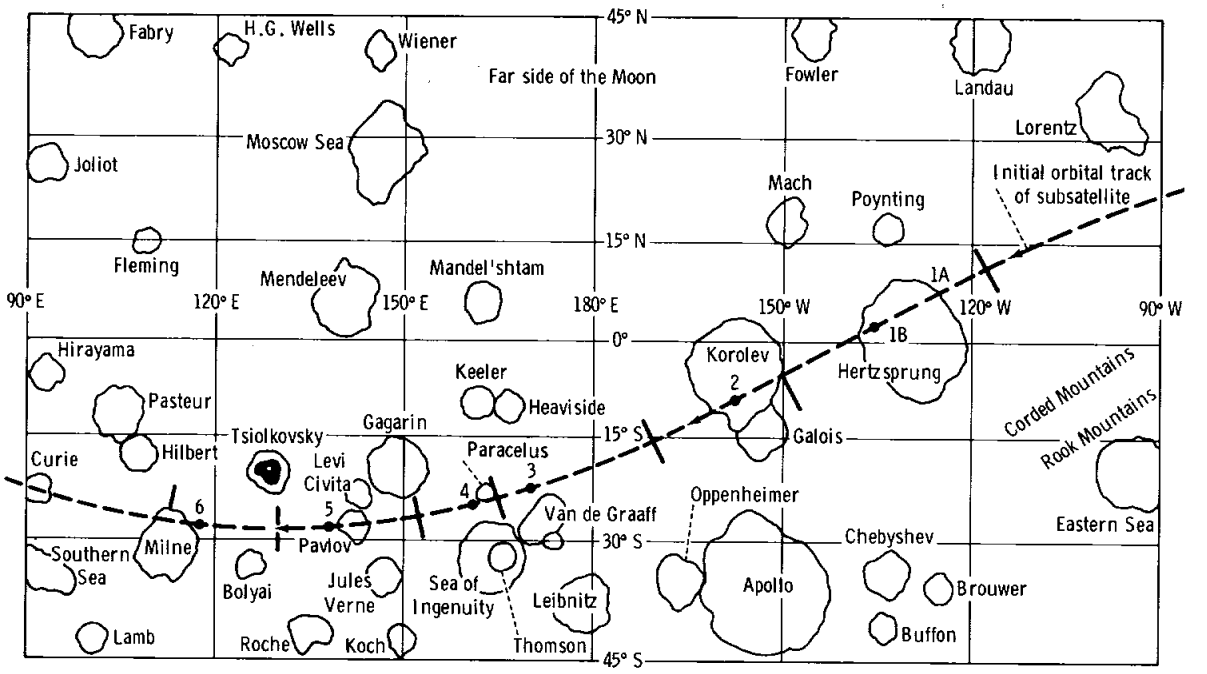


FIGURE 23-3.–The ground track of the subsatellite on the far side of the Moon for the fifth orbit of the 17-orbit sequence for which the data are plotted in figure 23-2. The bars mark the location of the maxima in B_T; the dots, the minima. The numbers reference the dips noted in B_T in figure 23-2.

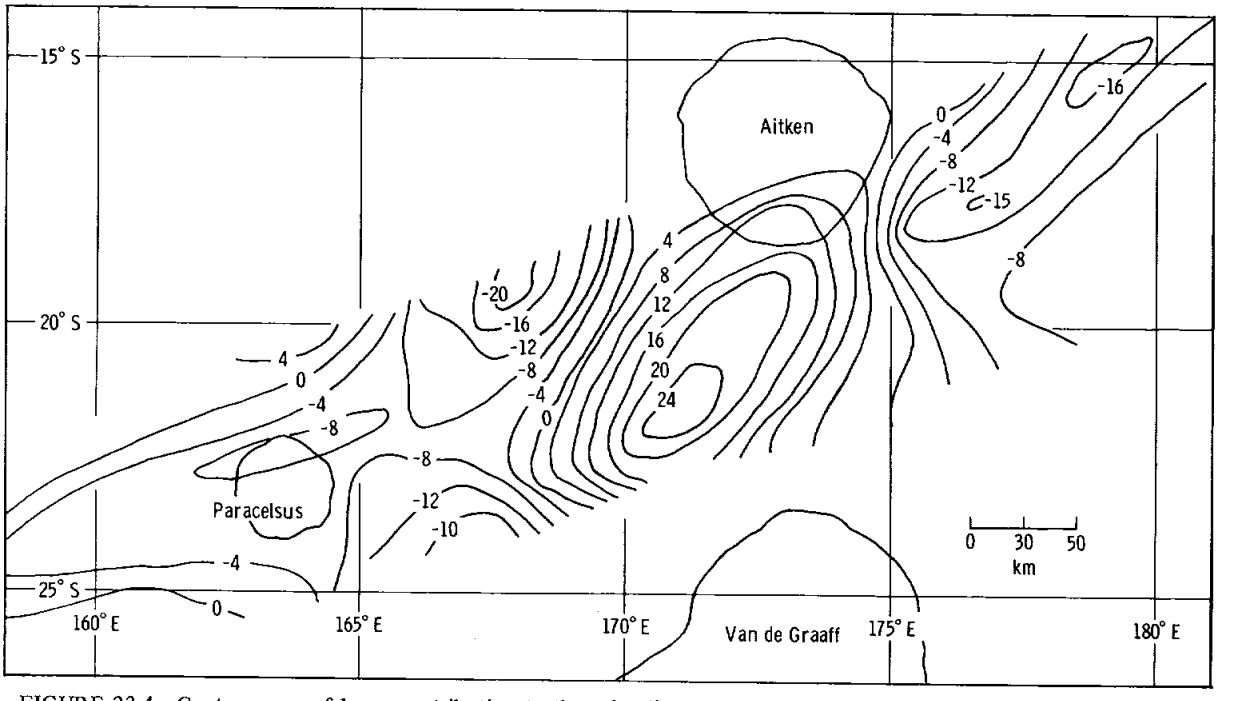


FIGURE 23-4.–Contour map of lunar contribution to the solar-directed component of the magnetic field as measured on the Apollo 15 subsatellite at an altitude of 67 km in the Van de Graaff region. This map was constructed from 10 successive orbits of data in quiet magnetotail conditions. The average field for each orbit was subtracted from individual readings for that orbit. The resulting data were then used to create this map. Contours are labelled in units of tenths of nanoteslas (gammas). Contour lines are drawn every 0.4 nT (0.4 γ).

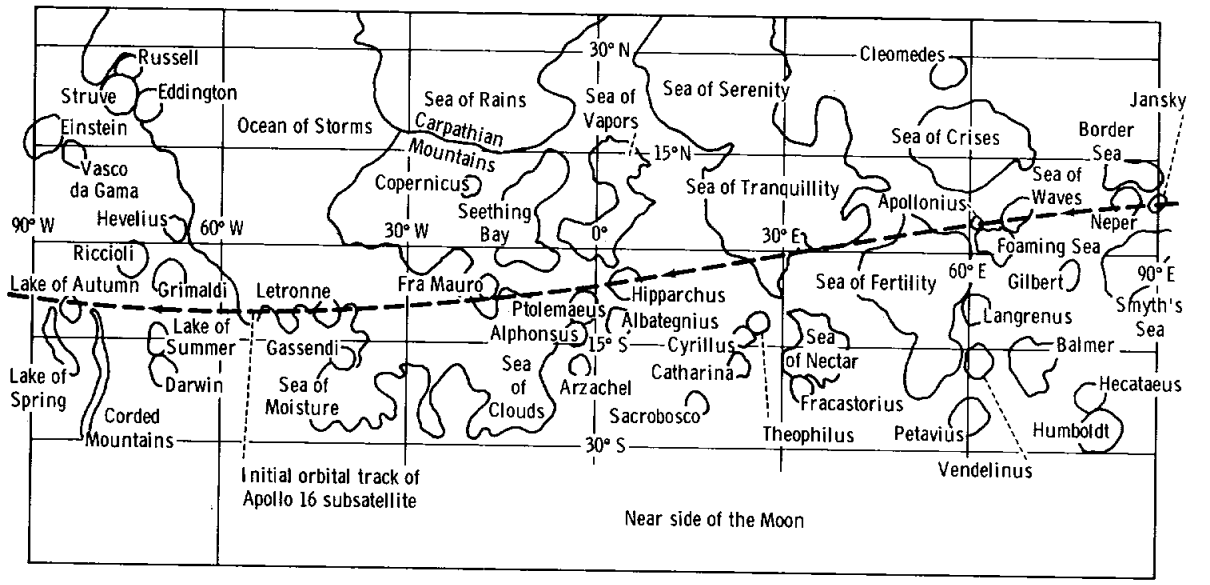


FIGURE 23-5.–Initial ground track of the Apollo 16 subsatellite over the near side of the Moon.

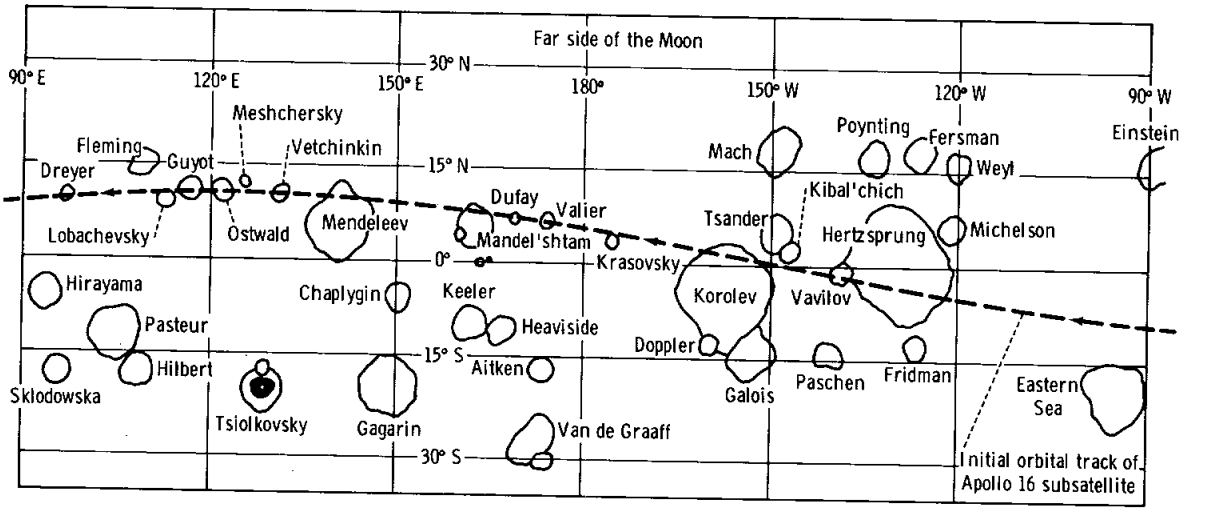


FIGURE 23-6.–Initial ground track of the Apollo 16 subsatellite over the far side of the Moon.

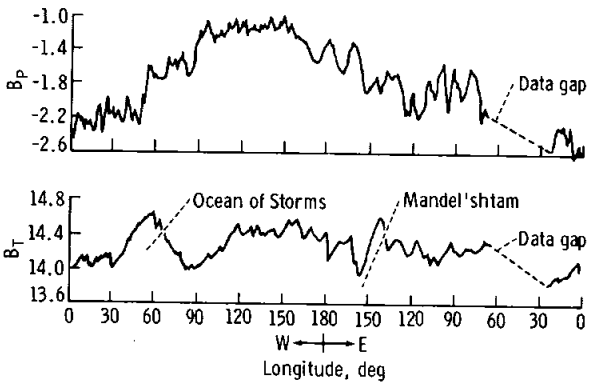


FIGURE 23-7.–The magnetic field parallel to the Apollo 16 spin axis B_P and the field transverse to the spin axis B_T averaged over 11 successive orbits while the Moon was in the geomagnetic tail.

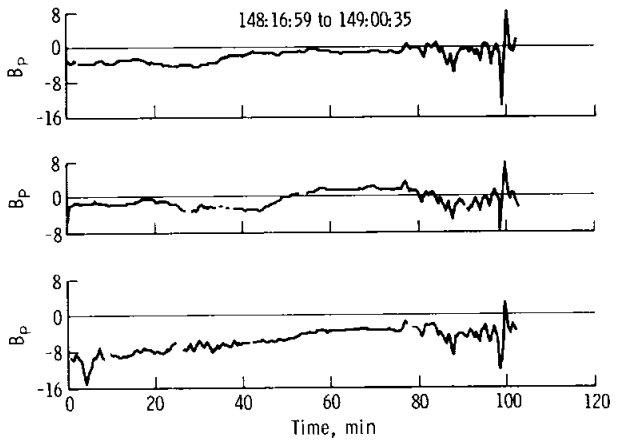


FIGURE 23-8.–The magnetic field parallel to the Apollo 16 spin axis B_P for three orbits in the geomagnetic tail during the second lunation when perilune was at extremely low altitudes.

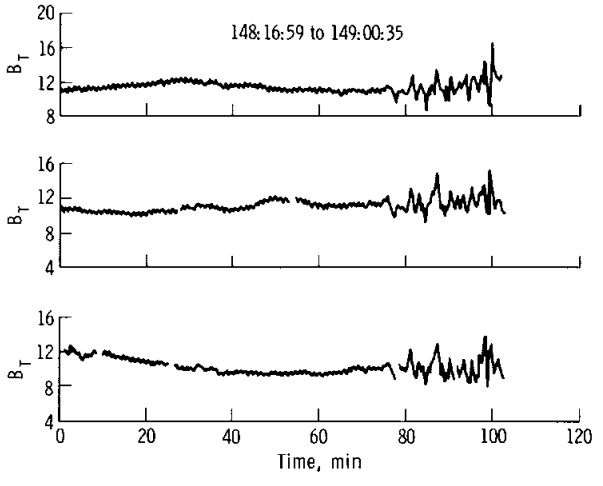


FIGURE 23-9.–The magnetic field in the spin plane B_T for the same three orbits as shown in figure 23-8.

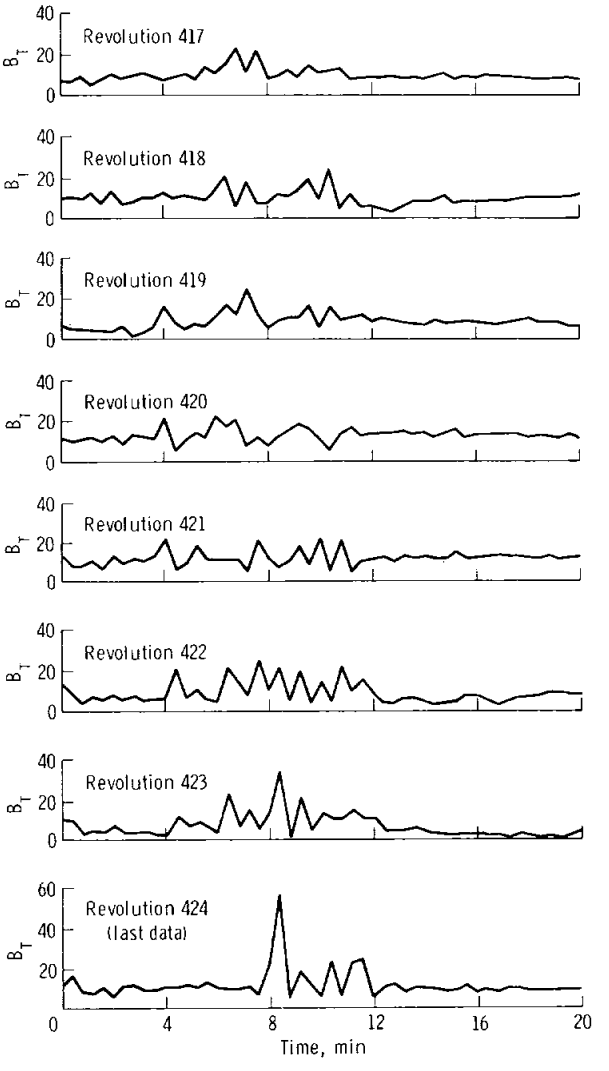


FIGURE 23-10.–The magnetic field in the spin plane B_T for the last eight orbits of the Apollo 16 subsatellite. Only data near perilune are shown. Note the change of the vertical scale from previous figures.

SOLAR-WIND/MOON INTERACTION

The characteristic magnetic signature of the solar-wind/Moon interaction is best demonstrated by making a long-term average over many orbits so that the effects of temporal variations are minimized. Figure 23-11 shows the results of averaging 121 orbits of Apollo 15 subsatellite magnetometer data. Only the magnitude of the field in the spin plane B_T is shown. In constructing this average, the data were ordered by the time of optical sunrise and sunset.

The data used in this average were taken from the first lunation of Apollo 15, in the region defined by the trace of the Moon's orbit in figure 23-12. Entire orbits of data were deleted from the average if temporal fluctuations were judged to be unusually strong. During this period, the subsatellite orbit was nearly circular at an altitude of approximately 100 km.

The magnetic enhancement in the diamagnetic cavity between sunset and sunrise and the presence of the dips in field magnitude caused by the rarefaction

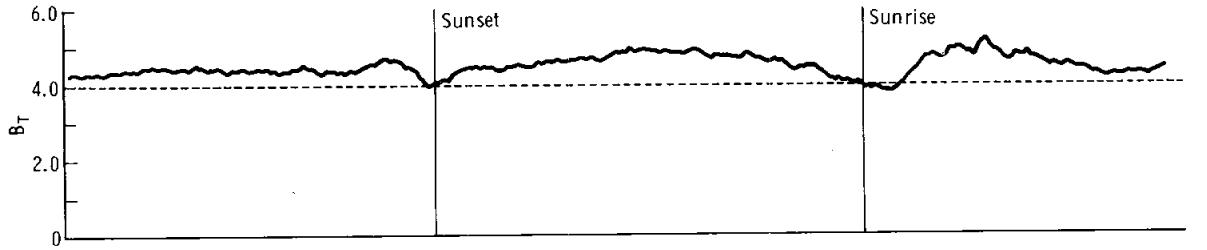


FIGURE 23-11.–A 121-orbit average of the magnetic field transverse to the Apollo 15 subsatellite spin axis while the Moon was in the solar wind. The dips in the field strength caused by the rarefaction wave at sunrise and sunset and the diamagnetic increase in the plasma void behind the Moon can be seen. The increases in the field strength preceding sunset and following sunrise are due to the occasional presence of limb compressions.

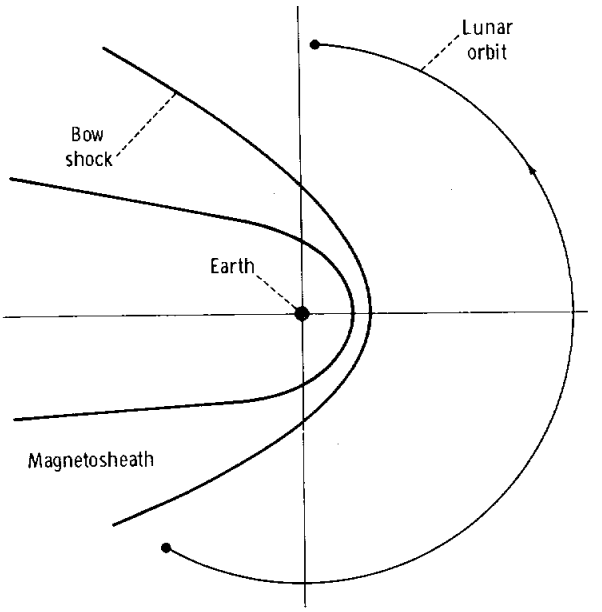


FIGURE 23-12.–The ecliptic plane projection of the orbit of the Moon in the geocentric solar ecliptic coordinate system for the interval from which the data averaged in figure 23-11 were taken. The average position of the bow shock of the Earth and the geomagnetic cavity in this plane are also shown.

wave are clearly illustrated in figure 23-11. There is an average enhancement of approximately 1/2 nT (1/2 γ) in the plasma void, over the average solar-wind value of B_T (~4.3 nT), and an average decrease of approximately 1/2 nT (1/2 γ) in the rarefaction dips. Thus, the average diamagnetic enhancement and rarefaction dip are both approximately 10 percent of the average solar-wind value. It should be noted that the asymmetry of the position of the sunset and sunrise dips with respect to the Moon-Sun line is at least partly due to the aberration of the solar-wind velocity in the satellite frame caused by the motion of the Moon and may have a contribution due to the average solar-wind magnetic field not being alined with the flow. This remains to be investigated. The structure evident in figure 23-11 is completely masked by time-dependent fluctuations when the Moon is in the magnetosheath.

A strong average increase in the field external to the rarefaction dips is also revealed in figure 23-11. This effect in the average is due to the occasional presence of very large increases in B_T, always external to the rarefaction dips near sunrise or sunset. Under the assumption that these large increases originate at the lunar limb grazed by the incident solar wind, the same data that were averaged in figure 23-11 have been used to calculate the selenographic position of the hypothetical source of these large disturbances (ref. 23-21). A lunar limb region was associated with a large disturbance if there was a well-defined increase of at least 2 nT (2 γ) on the solar-wind side of a rarefaction decrease.

The calculated sources are shown in two ways in figure 23-13. The upper panel shows each determined source location but does not indicate the selenographic positions associated with an absence of disturbances. The lower panel shows the normalized occurrence rate of limb disturbances. During its first month, the Apollo 15 subsatellite always encountered sunset near latitude 20° N and sunrise near latitude 28° S. Each box in the lower Mercator projection represents at least four observations. The 20° latitude extent of the boxes is only an approximate estimate of the possible latitude variation of the source of an observed disturbance.

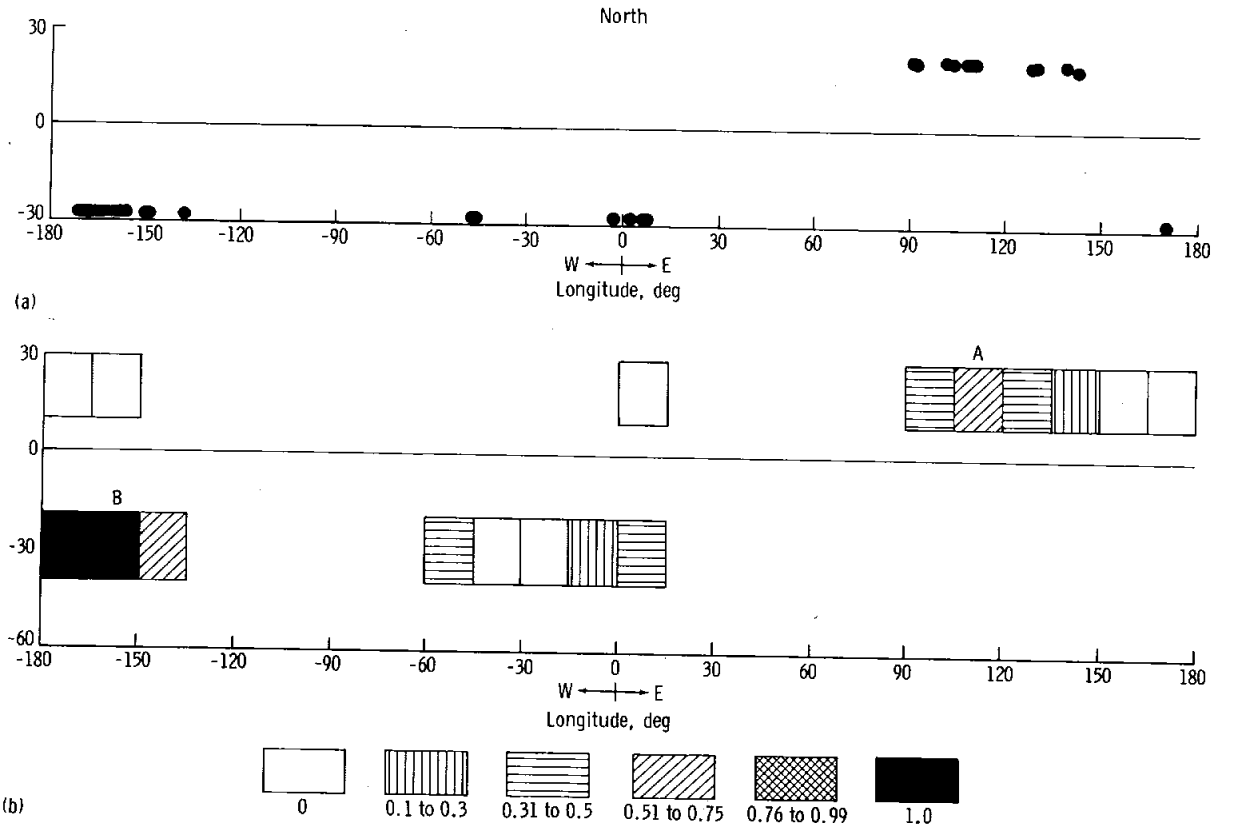


FIGURE 23-13.–The projected selenographic location associated with limb compression features exterior to the plasma void that were greater than 2 nT (2 γ) as measured by the Apollo 15 subsatellite. The upper panel gives the projected positions when increases occurred. The lower panel gives the normalized occurrence rate. (a) Lunar limbs associated with large increases in B_T. (b) Fraction of lunar limbs associated with large increases in B_T.

Some examples of large disturbances in B_T associated with regions A and B are shown in figure 23-14. When region B is at the lunar limb, the largest and most consistent perturbations are observed. Some of these increases are as much as 100 percent more than the solar-wind value. Figure 23-14 indicates that there may be a positive correlation between the size of a limb increase and the magnitude of the solar-wind field. However, this study has not been pursued using these data nor has the correlation with the plasma β been investigated.

The Apollo 16 subsatellite has observed basically the same phenomena during its one pass through the solar wind. However, no source regions have yet been calculated for the Apollo 16 data because the final orbital data have not been received. The extremely low perilune altitudes of the Apollo 16 subsatellite may enable the structure of these limb interactions to be probed very near the lunar surface.

SUMMARY AND CONCLUSIONS

The Apollo 15 and 16 subsatellite magnetometer data obtained in the geomagnetic tail have shown that it is feasible to map the lunar remanent magnetism from a single orbiting vehicle. High-resolution maps of magnetic features, however, can be achieved only with dual magnetometer surveys to separate temporal and spatial changes in the fields or with low-altitude data below approximately 70 km. The latter data are available from the Apollo 15 and 16 missions only for limited areas. The character of the magnetic features

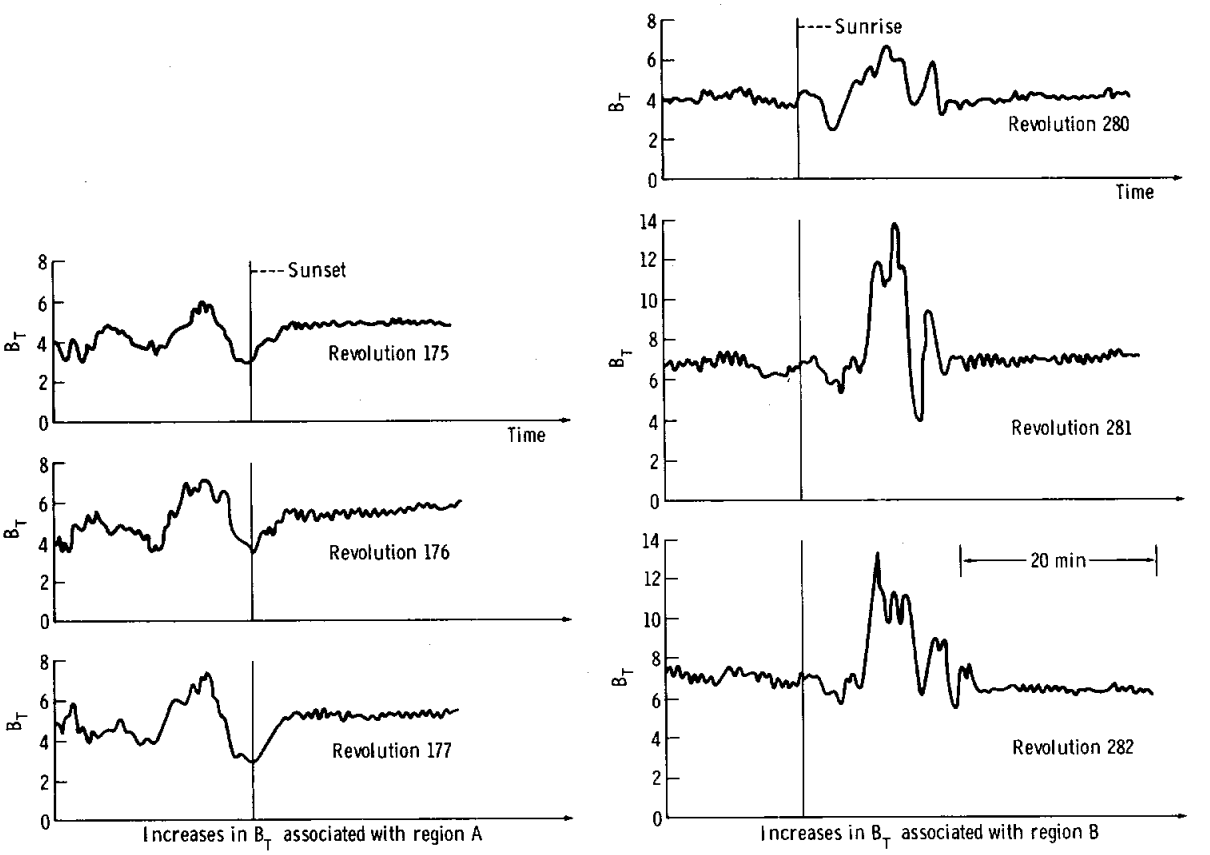


FIGURE 23-14.–Examples of limb compression features found in the high-occurrence-rate regions A and B shown in figure 23-13.

observed tends to follow the character of the lunar topography beneath the subsatellite but there is no one-to-one correlation of magnetic signature with surface features.

One goal of this study is to determine whether there is some overall order to the magnetization of the lunar surface and, perhaps, thereby to identify whether the original magnetizing field was of external or internal origin. To do this requires a distribution of accurately mapped features over a wide area of the lunar surface. It is not known yet whether the Apollo 15 and 16 data at low altitudes in the tail will be sufficient to achieve this objective. If it is not, the results, at the very minimum, show that such maps can be achieved with a relatively small satellite and simple instrumentation. If such a lunar magnetic survey were to be repeated, the ideal satellite would have a polar orbit and be maneuverable to the extent that perilune altitude could be adjusted. This would maximize the lifetime of the satellite while still maintaining the low-altitude coverage desired.

The subsatellite magnetometer data taken in the solar wind indicate that the diamagnetic enhancement and rarefaction dips discovered by Explorer 35 magnetometers are also distinctly present at the much lower altitude of approximately 100 km. The phenomenon of large increases in the field external to the rarefaction dips is also clearly observed and appears to be stronger at the subsatellite altitude. This supports the conclusion of Whang and Ness (ref. 23-19) that penumbral increases diminish in magnitude as distance from the Moon increases. However, a correlation is found between the occurrence of limb compressions and the selenographic position of the lunar limb exposed to the grazing solar wind. The results seem to indicate

that there are regions of the Moon, of at least 30° longitude, that cause limb compressions to stand in the solar wind for periods of approximately 1 day and that there are other regions of equal size that have no such effect. The results shown in figure 23-13 agree very well with the Explorer 35 results of Sonett and Mihalov (ref. 23-18) if one takes into account the uncertainty in the latitudes that is inherent in this preliminary analysis. Although this study does not yet have the statistical weight of the Explorer 35 studies, it is believed that the general agreement between the maps of the lunar regions associated with limb compressions strongly supports the hypothesis that this phenomenon is caused by deflection of the solar wind by regions of high magnetization.

Finally, the detailed analysis of these data has only just begun. High-resolution maps like those constructed for the Van de Graaff region will be created for other regions. The study of the diamagnetic cavity and rarefaction wave will be extended. More data will be added to the map of the selenographic regions associated with limb compressions in the solar wind using six more Apollo 15 lunations and one more Apollo 16 lunation. Dual satellite correlations between the Apollo 15 subsatellite and Explorer 35 satellite and correlations between the subsatellite and lunar-surface magnetometer data are also underway.

REFERENCES

23-1. Sonett, C. P.; Colburn, D. S.; and Currie, R. G.: The Intrinsic Magnetic Field of the Moon. J. Geophys. Res., vol. 72, no. 21, 1967, pp. 5503-5507.

23-2. Strangway, D. W.; Larson, E. E.; and Pearce, G. W.: Magnetic Properties of Lunar Samples. Science, vol. 167, no. 3918, Jan. 30, 1970, pp. 691-693.

23-3. Helsley, C. E.: Magnetic Properties of Lunar Dust and Rock Samples. Science, vol. 167, no. 3918, Jan. 30, 1970, pp. 693-695.

23-4. Doell, R. R.; Grommé, C. S.; Thorpe, A. N.; and Senftle, F. E.: Magnetic Studies of Lunar Samples. Science, vol. 167, no. 3918, Jan. 30, 1970, pp. 695-697.

23-5. Runcorn, S. K.; Collinson, D. W.; O'Reilly, W.; Stephenson, A.; et al.: Magnetic Properties of Lunar Samples. Science, vol. 167, no. 3918, Jan. 30, 1970, pp. 697-699.

23-6. Larochelle, A.; and Schwarz, E. J.: Magnetic Properties of Lunar Sample 10048-22. Science, vol. 167, no. 3918, Jan. 30, 1970, pp. 700-701.

23-7. Nagata, T.; Ishikawa, Y.; Kinoshita, H.; Kono, M.; et al.: Magnetic Properties of the Lunar Crystalline Rock and Fines. Science, vol. 167, no. 3918, Jan. 30, 1970, pp. 703-704.

23-8. Doell, R. R.; and Grommé, C. S.: Survey of Magnetic Properties of Apollo 11 Samples at the Lunar Receiving Laboratory. Proceedings of the Apollo 11 Lunar Science Conference, Vol. 3, A. A. Levinson, ed., Pergamon Press (New York), 1970, pp. 2093-2096.

23-9. Dyal, P.; Parkin, C. W.; and Sonett, C. P.: Apollo 12 Magnetometer: Measurements of a Steady Magnetic Field on the Surface of the Moon. Science, vol. 169, Aug. 21, 1970, pp. 762-764.

23-10. Dyal, P.; Parkin, C. W.; Sonett, C. P.; DuBois, R. L.; and Simmons, G.: Lunar Portable Magnetometer Experiment. Sec. 13 of Apollo 14 Preliminary Science Report. NASA SP-272, 1971.

23-11. Colburn, D. S.; Currie, R. G.; Mihalov, J. D.; and Sonett, C. P.: Diamagnetic Solar-Wind Cavity Discovered Behind Moon. Science, vol. 158, no. 3804, Nov. 24, 1967, pp. 1040-1042.

23-12. Ness, N. F.; Behannon, K. W.; Scearce, C. S.; and Cantarano, S. C.: Early Results from the Magnetic Field Experiment on Lunar Explorer 35. J. Geophys. Res., vol. 72, no. 23, 1967, pp. 5769-5778.

23-13. Lyon, E. F.; Bridge, H. S.; and Binsack, J. H.: Explorer 35 Plasma Measurements in the Vicinity of the Moon. J. Geophys. Res., vol. 72, no. 23, 1967, pp. 6113-6117.

23-14. Bühler, F.; Eberhardt, P.; Geiss, J.; Meister, J.; and Signer, P.: Apollo 11 Solar Wind Composition Experiment: First Results. Science, vol. 166, no. 3912, Dec. 19, 1969, pp. 1502-1503.

23-15. Geiss, J.; Eberhardt, P.; Bühler, F.; Meister, J.; and Signer, P.: Apollo 11 and 12 Solar Wind Composition Experiments: Fluxes of He and Ne Isotopes. J. Geophys. Res., vol. 75, no. 31, 1970, pp. 5972-5979.

23-16. Colburn, D. S.; Mihalov, J. D.; and Sonett, C. P.: Magnetic Observations of the Lunar Cavity. J. Geophys. Res., vol. 76, no. 13, 1971, pp. 2940-2957.

23-17. Siscoe, G. L.; Lyon, E. F.; Binsack, J. H.; and Bridge, H. S.: Experimental Evidence for a Detached Lunar Compression Wave. J. Geophys. Res., vol. 74, no. 1, 1969, pp. 59-69.

23-18. Sonett, C. P.; and Mihalov, J. D.: Lunar Fossil Magnetism and Perturbations of the Solar Wind. J. Geophys. Res., vol. 77, no. 4, 1972, pp. 588-603.

23-19. Whang, Y. C.; and Ness, N. F.: Magnetic-Field Anomalies in the Lunar Wake. J. Geophys. Res., vol. 77, no. 7, 1972, pp. 1109-1115.

23-20. Coleman, P. J., Jr.; Schubert, G.; Russell, C. T.; and Sharp, L. R.: The Particles and Fields Subsatellite Magnetometer Experiment. Sec. 22 of Apollo 15 Preliminary Science Report. NASA SP-289, 1972.

23-21. Coleman, P. J., Jr.; Lichtenstein, B. R.; Russell, C. T.; Sharp, L. R.; and Schubert, G.: Magnetic Fields Near the Moon. The Proceedings of the Third Lunar Science Conference, MIT Press, Oct. 1972.

ACKNOWLEDGMENTS

The authors express appreciation to G. Takahashi and his staff at Time Zero Corporation for their efforts in the design and fabrication of the subsatellite magnetometer; to T. Pederson and R. Brown and their staff at TRW Systems Group for their work in the design, fabrication, and testing of the subsatellite and the integration of the magnetometer; and to C. Thorpe who controlled the magnetic fields of the subsatellite.

The University of California at Los Angeles engineering team was led by R. C. Snare. Preliminary circuit designs were done by the late R. F. Klein. The testing and calibration of the magnetometer was supervised by F. R. George.

24. S-Band Transponder Experiment

W. L. Sjogren,[a†] *P. M. Muller,*[a] *and W. R. Wollenhaupt*[b]

The purpose of this experiment is to measure the lunar gravitational field, which in turn provides information on the distribution of lunar mass and its correlation with surface features such as craters, mountains, and maria. Lack of correlation would imply subsurface structures. The lunar gravitational field is measured by observing the dynamical motion of spacecraft in free-fall orbits. Effective detection of mass variations is greatly enhanced by low-altitude trajectories, such as the eccentric orbits during revolutions 3 to 16 of the Apollo 16 spacecraft and the 11-km periapsis of the Apollo 16 subsatellite during May 1972. The observational data are the precise Earth-based radio tracking measurements initially used for real-time navigation. However, these line-of-sight velocity measurements can be obtained only while the spacecraft is in view of the Earth. As a result, no direct far-side measurements are available. The only information about the far-side gravity field is indirectly inferred from the spacecraft conditions immediately after occultation over many revolutions (refs. 24-1 and 24-2).

In this section, the initial results of the Apollo 16 spacecraft eccentric-orbit data reduction and the status of the Apollo 16 subsatellite data are described. Results from the Apollo 15 subsatellite data taken during December 1971, when periapsis altitudes were 40 to 50 km, also are discussed briefly. The coverage for each of these is shown in figure 24-1.

TECHNIQUE

Figure 24-2 is a schematic diagram of the basic measuring system. A very stable frequency of 2115 MHz obtained from a cesium reference is transmitted to the orbiting spacecraft. The transponder in the spacecraft multiplies the received frequency by the constant 240/221 (to avoid self-lockup) and transmits the signal to the Earth. (The transmitted and received frequencies are within the S-band region.) At the Earth receiver, the initial transmitted frequency (multiplied by the same constant) is subtracted, and the resulting cycle-count differences are accumulated in a counter along with the precise time at which differencing occurred. These cycle-count differences are the Doppler shift in frequency f_d caused by the line-of-sight (radial) component V_r of the spacecraft velocity, or $2V_r/c$ X 2300 MHz, where c is the speed of light. At times of high resolution, the counter is read every second; at low resolution, it is read once a minute. Not only is the cycle-count difference recorded, the fractional part of the cycle is measured. This capability allows a resolution of approximately 0.01 Hz or 0.65 mm/sec in the measurements.

The approach for reducing these data is the same as that applied to the Lunar Orbiter data for the mascon analysis (ref. 24-3) (i.e., not spherical harmonics or brute-force dynamic estimation). The raw data contain many components of motion that must be removed before gravity analysis can proceed. Factors to be accounted for include the tracking station rotation about the Earth spin axis; the spacecraft motion perturbed by point-mass accelerations from the Sun, Earth, Moon, and planets; and atmospherics and signal transit times. All these quantities are known a priori and are determined to accuracies well beyond those required to evaluate local gravitational effects.

The data reduction was performed by using elaborate computer programs that contain the theoretical model with all the dynamic constraints and parameters mentioned previously. Each arc of data (approximately 65 min) was evaluated independently. Only the six state parameters of initial position and velocity were adjusted in a least-squares fit to the observations. The resulting systematic residuals (i.e., real observations minus theoretically calculated observations) are then attributed to lunar gravitational

[a]Jet Propulsion Laboratory.

[b]NASA Manned Spacecraft Center.

†Principal Investigator.

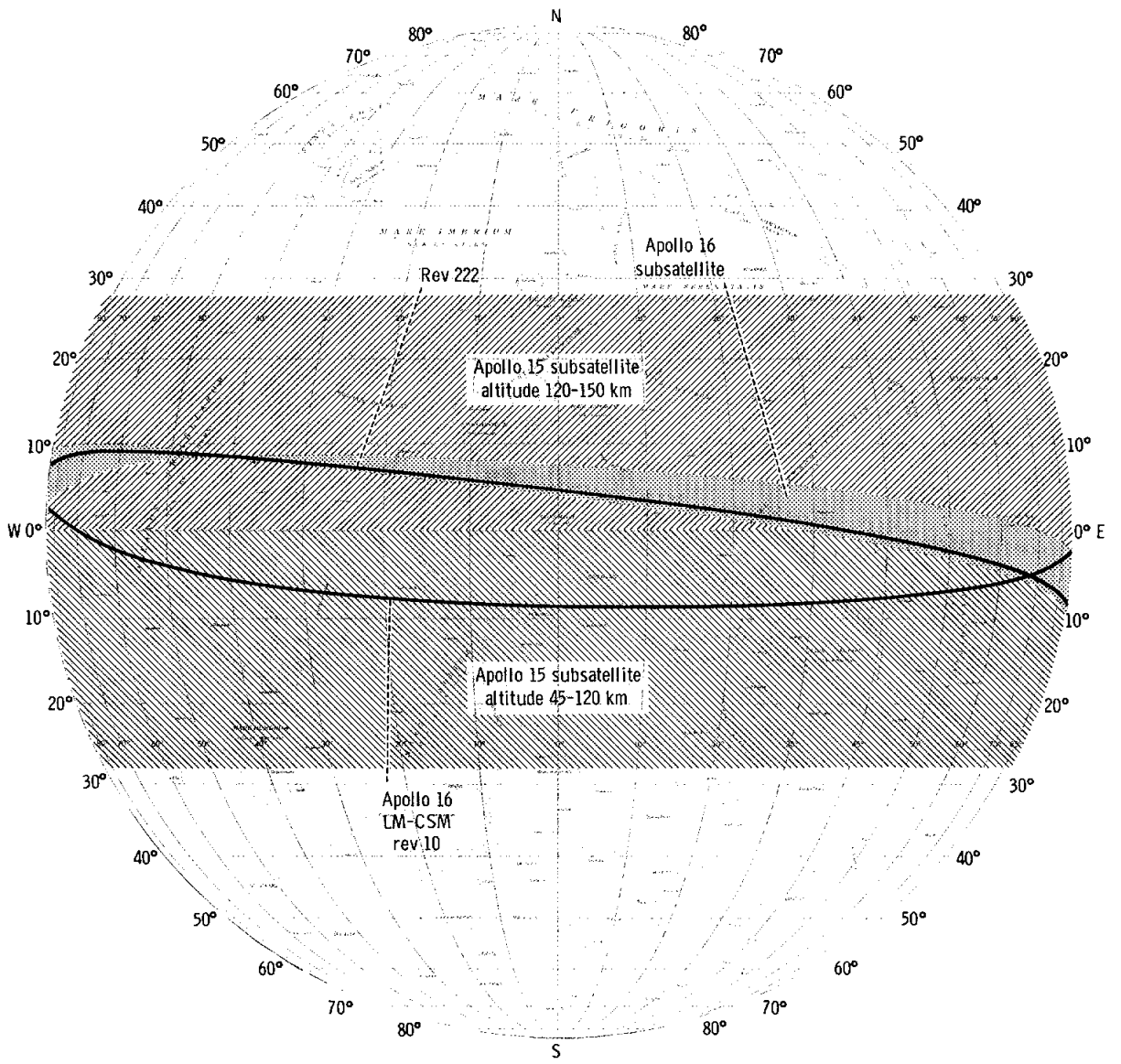


FIGURE 24-1.—Data coverage for the Apollo 16 spacecraft, the Apollo 16 subsatellite from May 9 to 14, 1972, and the Apollo 15 subsatellite from December 1 to 19, 1971.

effect. The velocity residuals from revolution 10 are shown in figure 24-3. The signature is very definite and is far above the noise level of 0.01 Hz.

Once the residuals are checked for consistency between adjacent revolutions and all obviously erroneous points are removed, analytic patched cubic splines with continuous second derivative are least-squares fitted to the residuals. These functions are then differentiated, and the line-of-sight accelerations ("gravity") are analyzed and correlated with the subspacecraft lunar track and existing topography. The accelerations derived from revolution 10 velocity residuals are shown in figure 24-4. Spacecraft thrusting has corrupted the data in two regions. These are indicated in figure 24-3 and are easily detected at this point in the reduction. A gravity profile generated in the same manner as that in figure 24-4 is shown for the Apollo 16 subsatellite in figure 24-5.

An additional step has been taken for the Apollo 15 subsatellite data; 77 independent profiles similar to figures 24-4 and 24-5 have been contoured to overlay a lunar Mercator map (figs. 24-6 to 24-9). All suitable nonredundant data will eventually be presented in this form (ref. 24-4).

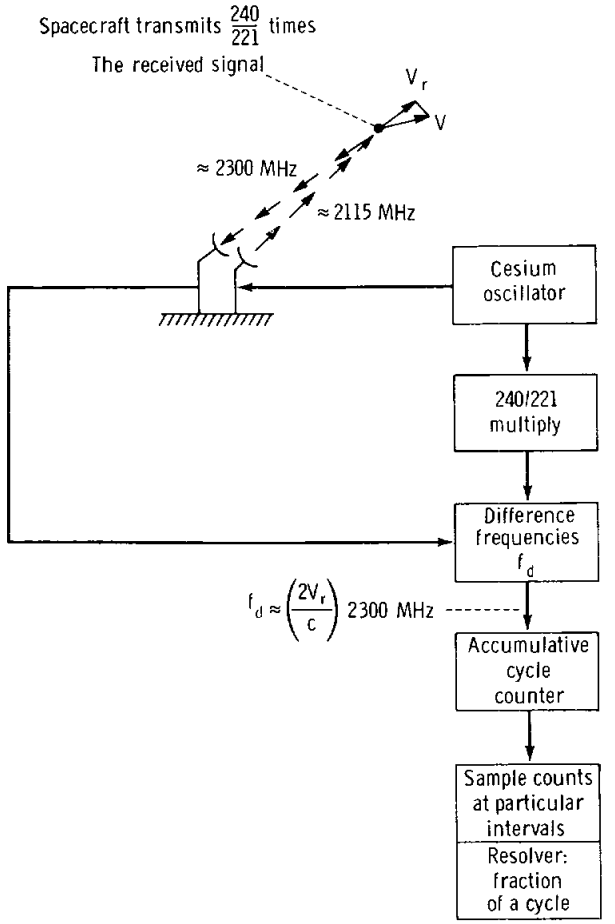


FIGURE 24-2.–Simplified schematic diagram of Doppler transponder system.

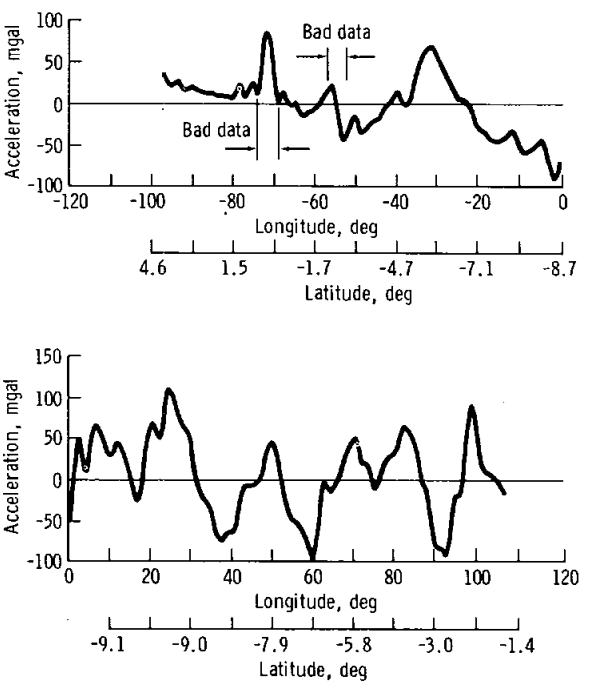


FIGURE 24-4.–Line-of-sight gravity profile derived from Apollo 16 spacecraft revolution 10.

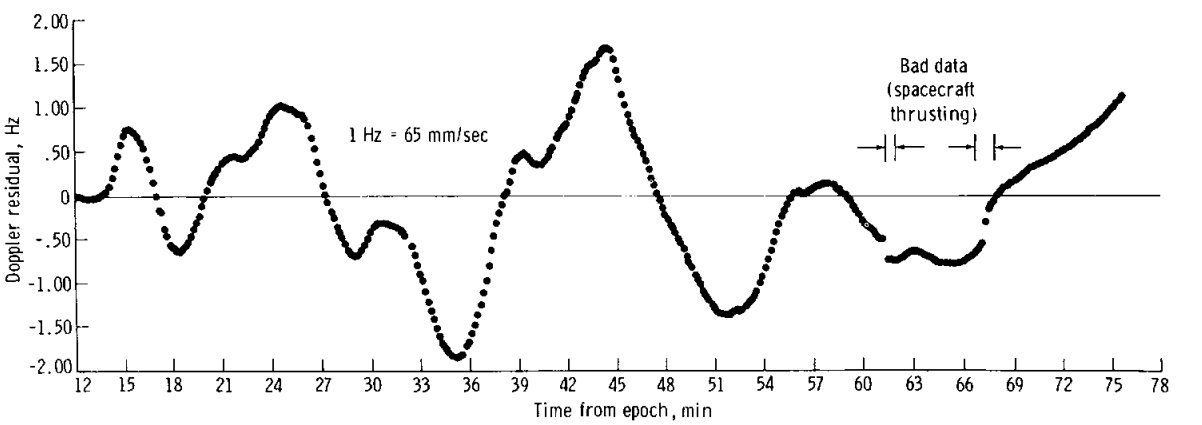


FIGURE 24-3.–Doppler residuals from Apollo 16 spacecraft revolution 10 on April 20, 1972, 14:22:40 Greenwich mean time (G.m.t.).

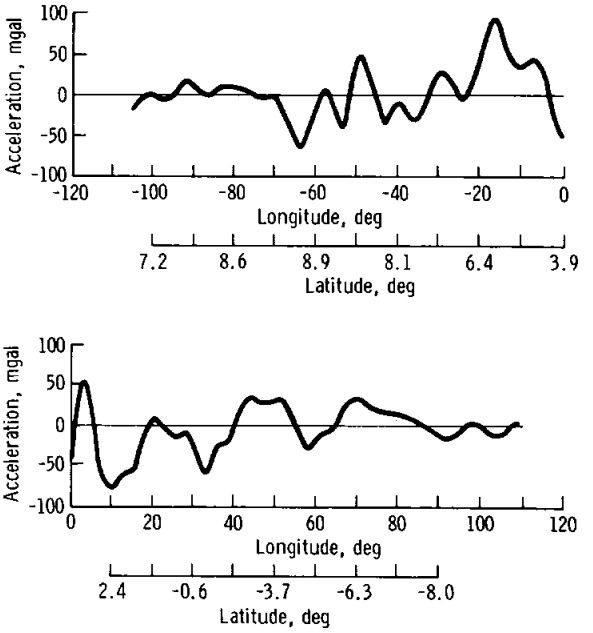


FIGURE 24-5.–Line-of-sight gravity profile derived from Apollo 16 subsatellite on revolution 222, May 13, 1972, 03:00:00 G.m.t.

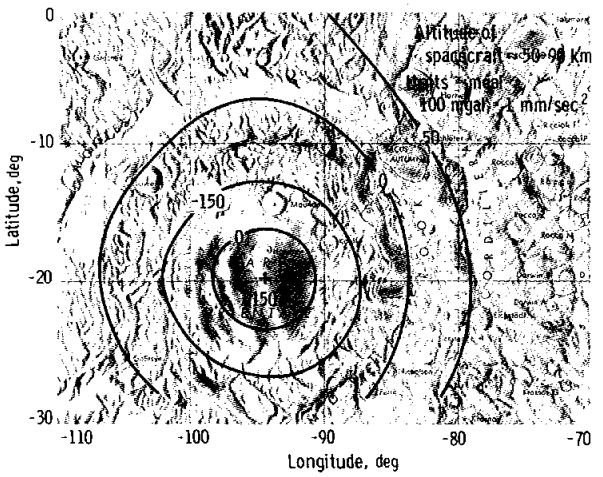


FIGURE 24-6.–Contour map of Mare Orientale gravity from the Apollo 15 subsatellite data taken during December 1971.

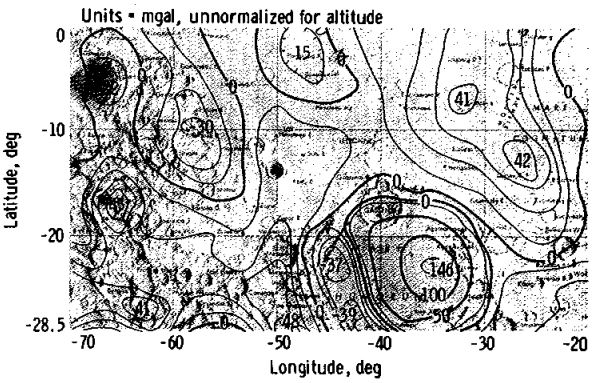


FIGURE 24-7.–Contour map of gravity from -70° to -20° longitude: Apollo 15 subsatellite data taken during December 1971.

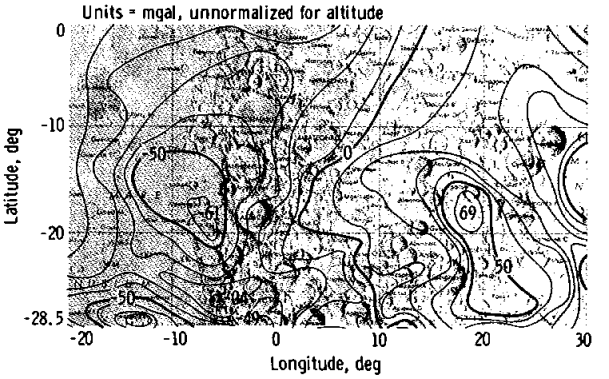


FIGURE 24-8.–Contour map of gravity from -20° to 30° longitude: Apollo 15 subsatellite data taken during December 1971.

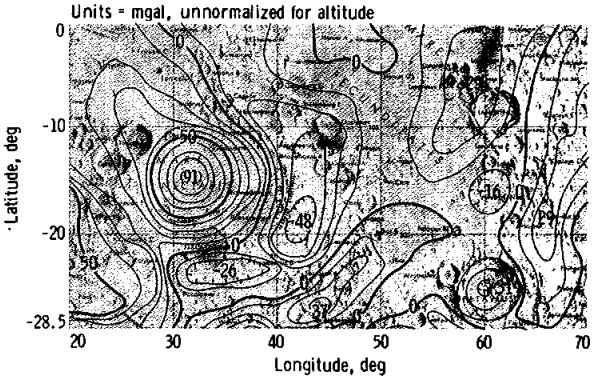


FIGURE 24-9.–Contour map of gravity from 20° to 70° longitude: Apollo 15 subsatellite data taken during December 1971.

PRELIMINARY RESULTS

The Apollo 16 spacecraft did not traverse any known completely visible mascons[1] as did the Apollo 12, 14, and 15 spacecraft (i.e., Nectaris, Serenitatis, and Crisium; refs. 24-4 and 24-5). However, several strong signatures appear in the figure 24-4 profile. In the regions of -36° to -25° longitude, an extensive gravity high is present and does not appear to correlate well with any surface feature. The Montes Riphaeus are in this region, and an additional larger subsurface structure is possibly associated with them. The Nubium-Fra Mauro region is a negative anomaly area, with the large crater Ptolemaeus providing the sharpest departure of almost -100 mgal. This observation is in excellent agreement with the results of the Apollo 12 and 14 spacecraft, the trajectories of which crossed this area (refs. 24-4 and 24-6).

The next pronounced region is the central highlands region from 0° to 20° longitude. Although this is essentially a positive anomaly, there is a definite negative region near 17° longitude, just east of the Apollo 16 landing site. The U.S. Geological Survey map (LAC-78) of the Theophilus Quadrangle shows this region as a different geologic unit. It can be inferred that the region is somewhat lower than the surrounding terrain or that the material is less dense (or both). Possibly, it is part of a negative ring structure associated with Mare Nectaris. The large positive anomaly at 25° longitude correlates well with the maria region between Mare Tranquillitatis and Mare Nectaris that also was detected in the original mascon mapping (ref. 24-3). The Apollo 15 subsatellite results (fig. 24-9) also indicate this gravity high,[2] and reveal it as a tongue from Nectaris rather than from Tranquillitatis.

The negative anomaly region between 31° and 40° longitude might be associated with the partial negative ring around Nectaris, which is more evident in figure 24-9. For the first time, a small positive anomaly of 45 mgal has been detected in the center of Mare Fecunditatis at 50° longitude, with the eastern portion mostly negative. The increased negative dip at 61° longitude may be attributable to the crater Langrenus; reductions of data from revolutions 3 and 4, the ground tracks of which cross this crater, will definitely provide much better evidence.

The Apollo 16 subsatellite had an unfortunately short lifetime because of unknown gravitational perturbations not represented in the theoretical model used for the trajectory analysis studies. The subsatellite crashed to the lunar surface on May 29, 1972, or 35 days after release from the spacecraft. A plot of its periapsis altitude during this interval is shown in figure 24-10. The secular trend in the prediction beyond the low point at 43 days is upward; had the subsatellite made it beyond this point, it would have been orbiting today.[3] The lack of any direct far-side gravity measurements is the primary cause for the incomplete gravity model. Another factor contributing to the crash was the omission, because of fuel constraints, of a planned shaping burn to put the subsatellite into a different orbit. Although predictions of periapsis altitudes were much lower in the unshaped orbit, a crash was not predicted. For a 5-day period after May 9, 1972, Apollo 16 subsatellite periapsis altitudes of near 12 km provided new detailed gravity measurements over many near-side features such as Copernicus, Sinus Medii, and Mare Fecunditatis. A typical acceleration profile is shown in figure 24-5. An areal reduction of these data is just beginning.

The Apollo 15 subsatellite was tracked for a 21-day period during December 1971. Periapsis altitudes were between 40 and 50 km and were located near latitude 28° S. This is the first time that this region has been sampled at such low altitudes; the Lunar Orbiter missions were flown at approximately 200-km altitudes over this southern area. Seventy-seven independent data profiles were contoured to produce the results shown in figures 24-6 to 24-9. Detailed coverage of Mare Orientale definitely shows the ringed gravity structure corresponding with the surface topography. This ring structure is not as clear about the Humorum and Nectaris (figs. 24-7 and

[1]Mare Smythii was observed. However, limb observations are not directly interpretable in the same way as observations between ±70° longitude. Its detection is confirmed with the +65, 0, -85 mgal profile between 82° and 90° longitude.

[2]Not at 110 mgal, because the subsatellite was at a 90-km altitude; the spacecraft at this point was at an altitude of 20 km.

[3]Fortunately for the Apollo 15 subsatellite, where deviations were as large as those of Apollo 16, the deviations were above the predicted values. Apparently, the Apollo 15 subsatellite will have years of lifetime.

25. Bistatic-Radar Investigation

H. T. Howard[a†] *and G. L. Tyler*[a]

The Apollo Program has provided an excellent opportunity to test the rapidly developing experimental and theoretical techniques of bistatic radar. The experiment seeks to determine the principal electromagnetic and structural properties of the lunar surface from the observation of command and service module (CSM) radio transmissions that have been reflected from the lunar surface and received on Earth. These transmissions emanate from the CSM communication systems at wavelengths of 13 cm (S-band) and 116 cm (very high frequency (VHF)).

During the bistatic-radar data pass, the vehicle is oriented so that the energy is radiated toward that portion of the lunar surface that produces the strongest echo on the Earth. Because of the changing geometry, the CSM must be continuously maneuvered to maintain this condition. For each near-side pass, echoes are received from a roughly 10-km-diameter spot that moves across the lunar disk with the CSM. The bistatic investigation is, thus, a scanning experiment. The size of this spot and its precise location are determined by the scattering laws for the lunar surface. In particular, the quasi-specular mechanism dominates the scattering process. The signals received on the Earth are processed by methods that preserve the frequency, phase, polarization, and amplitude information contained in them. These properties are presented as a function of location on the lunar surface. The characteristics of the echoes are compared with the known characteristics of the transmitted signals; the differences between the characteristics are used in conjunction with a well-developed and generally accepted scattering theory (ref. 25-1) to derive quantitative inferences about the Moon.

Lunar crustal properties such as dielectric constant, average slope and slope probability, density, small-scale surface roughness, and embedded rocks to a depth of 20 m may be determined. The results are proving to be most useful in understanding the processes that have produced and modified the crust and in distinguishing between adjacent and subjacent geological units. The experimental observations are also of intrinsic interest to those involved in the study of electromagnetic scattering.

Radar techniques and the associated interpretive theories have developed rapidly in recent years. The Apollo bistatic-radar experiment provided a basis of comparison between the radar results and those of other techniques. Comparisons have been made with both interpretive geologic maps and quantitative topographic work primarily by using photogrammetric techniques. To date, the agreement between these diverse methods has been excellent.

Several such comparisons are shown in figures 25-1, 25-2, and 25-3. Values of root-mean-square (rms) lunar surface tilts derived from simultaneous 13- and 116-cm observations have been plotted as a function of lunar longitude. Corresponding portions of the geologic maps (ref. 25-2) made from Earth-based observations are included for comparison. The 13-cm tilts are generally about 4° through the mare areas of Serenitatis and Imbrium but range between 5° and 7° in the central highlands just south of the landing site. The 116-cm tilts agree very well with the 13-cm tilts in both general behavior and magnitude through the highlands region, although the tilts are generally smaller by a factor of 2 in the mare regions. This correlation has been a common factor in Apollo 14, 15, and 16, and the implications will be discussed in the subsequent parts of this section. The large slopes associated with the crater Euler at 29° W mean little quantitatively because the region containing the crater is clearly inhomogeneous and thus violates the assumptions of the scattering theory at that point.

The Apollo 16 bistatic-radar experiment discussed in this report used continuous-wave transmissions from both the S-band telemetry system (the spacecraft-to-Earth communications link) and the VHF communications system (normally used for voice transmissions and ranging between the CSM and lunar module in lunar orbit). The overall techniques are similar to those that had been used previously with the Lunar Orbiter 1 and 3 and Explorer 35

[a]Stanford University.
†Principal Investigator.

instrument module (SIM) bay attitude (i.e., with the antenna pointed directly at the surface below the CSM). Echoes of the S-band transmissions were received with the NASA 64-m-diameter antenna located at Goldstone, California; VHF echoes were received with the 46-m-diameter antenna of the Stanford Center for Radar Astronomy located on the Stanford University campus.

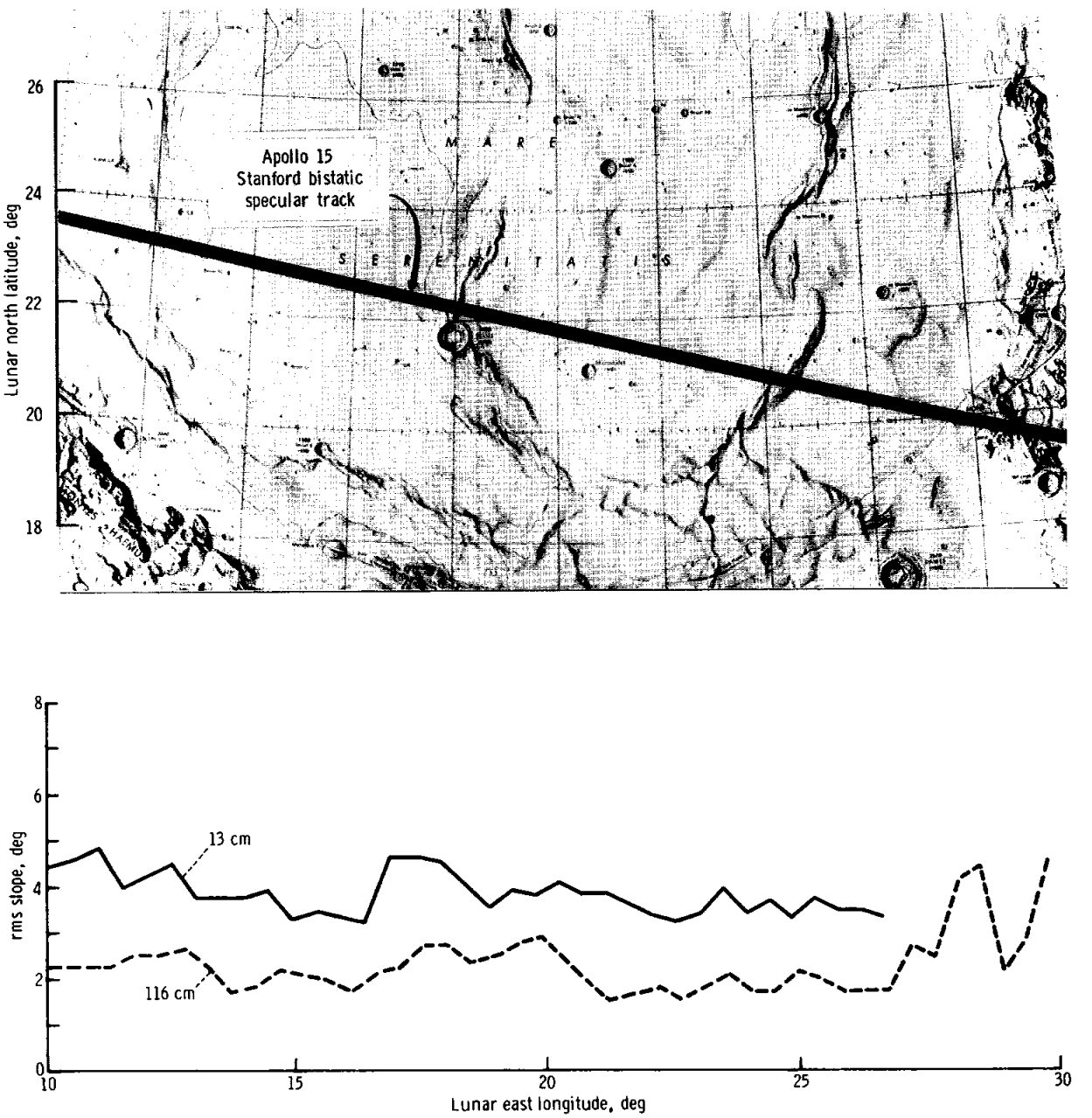


FIGURE 25-3.—Bistatic-radar, geological map comparison for the Serenitatis region of the Moon (ref. 25-2).

Excellent 13-cm data were received throughout the simultaneous pass; several difficulties were experienced with the 116-cm data. The prime pass had weak echoes, and it has not been determined whether this was a CSM attitude problem or an inflight equipment malfunction. Future analysis of the reflected signals and the trajectory data should isolate the problem completely. Interference was experienced from an NASA satellite, TETR-D, originally launched for Apollo communication system test and training exercises. The satellite had a circuit malfunction that prevented turnoff of the 116-cm transmitter. In general, however, the SIM bay pass data are of very high quality.

BASIC THEORY

The bistatic-radar echo is composed of the sum of the reflections from the area of the Moon that is mutually visible from the spacecraft and the Earth. Because continuous-wave transmissions are used, echoes from this entire area are received simultaneously. Observation of the echo-signal properties, as well as its separation from the often stronger, directly propagating wave, is based on the frequency spectrum.

For the purposes of analysis, the echo signal may be considered as a composite of the reflections from a large number of elemental surfaces, each with an area ds. Then, from the radar equation, the power received from a particular area ds is

$$dP_R = \frac{P_T G_T}{4\pi r_1^2} \sigma_0 \, ds \, \frac{1}{4\pi r_2^2} A \qquad (25\text{-}1)$$

where dP_R = power received from the elemental area ds
P_T = transmitted power
G_T = gain of the transmitting antenna
r_1 = distance from the transmitter to ds
σ_0 = incremental radar cross section at ds
ds = elemental area on the lunar surface
r_2 = distance from ds to the receiving antenna
A = effective aperture of the receiving antenna

The geometry of the experiment is illustrated in figure 25-4. The total received power is obtained by integration over the surface S (the surface that is mutually visible from the spacecraft and the Earth), or

$$P_R = \frac{P_T G_T A}{(4\pi)^2 r_2^2} \int_S \frac{\sigma_0}{r_1^2} \, ds \qquad (25\text{-}2)$$

where it is assumed that the variations in r_2 and G_T over the area S are negligible. The quantity σ_0 is retained within the integral because it varies considerably with the scattering geometry and with the location of ds.

The total radar cross section σ is related to the incremental cross section by

$$\sigma = R_p^2 \int_S \frac{\sigma_0}{r_1^2} \, ds \qquad (25\text{-}3)$$

where R_p is the distance of the spacecraft from the center of the Moon.

In general, the principal contributions to σ arise from a small region about the center of the first Fresnel zone, which is the specular point, on the mean lunar surface. In ray-optics terminology, this is the point at which the angles of incidence and reflection are equal. If the Moon were a perfectly smooth sphere, all the echo would originate from a Fresnel-zone-size spot surrounding this point. By roughening the surface through the introduction of large-scale (with respect to a wavelength) topographic undulations, this spot is caused to break into a number of glints. The location of these glints will correspond to specular reflection from local surface undulations. Echoes that result from this type of surface are designated quasi-specular.

Quasi-specular reflection constitutes the principal scattering mechanism in this experiment. To the first order, the effects of surface material composition and shape are separable; that is, if $\hat{\sigma}$ is the radar cross section of a perfectly conducting surface of a particular shape, then the radar cross section of a dielectric surface of precisely the same shape and with reflectivity ρ is

$$\sigma = \rho \hat{\sigma} \qquad (25\text{-}4)$$

Substituting equations (25-3) and (25-4) into

equation (25-2) and solving for ρ yields

$$\rho = \frac{(4\pi)^2 r_2^2 R_p^2 P_R}{P_T G_T A \hat{\sigma}} \qquad (25\text{-}5)$$

Thus, if σ can be found, then ρ may be determined.

The quantity σ may be computed on the basis of statistical surface models. The results of one such computation for a gently undulating surface with a Gaussian height distribution and an autocorrelation function are given for bistatic geometry in figure 25-5. The radar cross section is plotted as a function of the angle formed by the spacecraft, the center of the Moon, and the Earth. The radius is measured from the center of the Moon (ref. 25-4). The dashed curve corresponds to a perfectly smooth sphere, and the solid curve corresponds to a surface with rms slopes of 10°. The effect of the surface slopes on the cross section is second order. The reflectivity of the Moon is inferred from the data by measuring the total echo powers received and by normalizing the results by the use of the theoretical reflectivity values (plotted in fig. 25-5 from the data given in ref. 25-7) for a perfectly conducting sphere. The inferred reflectivity is then compared with the reflectivity of a dielectric surface under oblique geometry. The effective dielectric constant of the surface may be determined directly from the observation of the Brewster angle and indirectly by a quantitative comparison of the reflectivity values.

The bandwidth of the echo depends directly on the surface slope. For the surface model considered previously, the bandwidth is given by

$$\Delta f = 4.9 \left(\frac{v_s}{\lambda}\right) \cos \gamma_s \tan \beta_0 \qquad (25\text{-}6)$$

where Δf = one-half the power bandwidth of the echo spectrum

v_s = velocity of the specular point with respect to the lunar surface

λ = wavelength

γ_s = angle of incidence on the mean surface at the specular point

β_0 = rms surface slope

On the basis of this model, surface slopes may be obtained directly from the orbital parameters and the width of the echo spectrum.

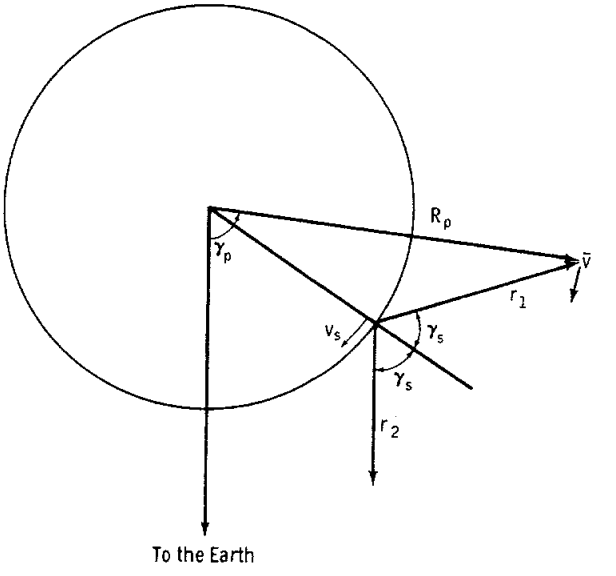


FIGURE 25-4.–Bistatic radar geometry. Source is located at tip of the R_p vector.

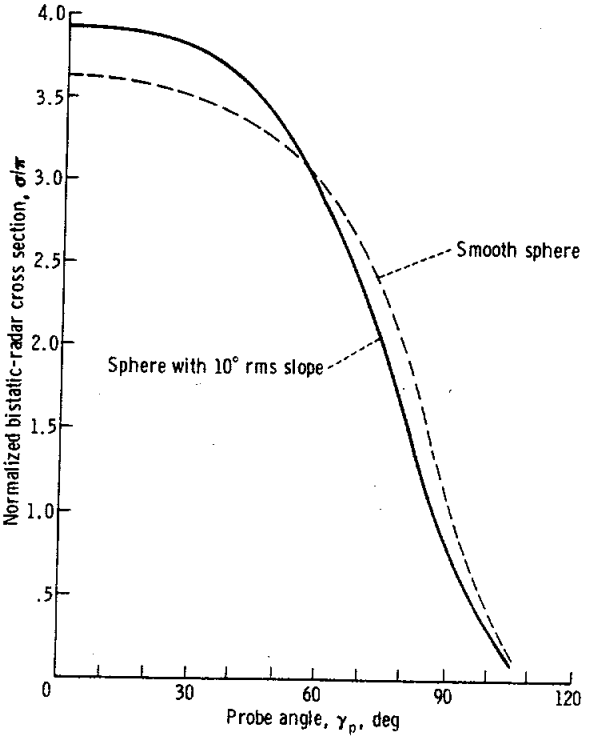


FIGURE 25-5.–Normalized bistatic-radar cross section σ/π as a function of spacecraft-Moon-Earth angle γ_p for a perfectly reflecting sphere with a gently undulating surface (calculated for a spacecraft altitude of 100 km).

Physically, the spectrum is broadened according to the probability-density function of the surface slopes and the Doppler shift. In figure 25-4, the reflection from a point ahead of the mean reflecting point will have a greater Doppler shift (determined by the angle between $\bar{r}_1$ and $\bar{v}$) than those points behind the mean reflecting point. At every point (on the basis of the quasi-specular model), the probability of obtaining a reflection depends on the probability of finding a local surface undulation with the proper slope. Slopes, then, also determine the surface resolution of the experiment. Reflections are obtained from an area with a radius of 5 to 10 km (which is approximately equal to the rms slope multiplied by the spacecraft altitude).

Inferences based on this model are valid on a set of scales related to the wavelength of the probing wave. Quantitative comparisons of slope distributions inferred from Explorer 35 data and from photogrammetry have been conducted with good results for a limited number of locations on the lunar surface (ref. 25-8). Under fairly broad assumptions, the quasi-specular scattering may be considered to occur at a fictitious surface that is a low-pass-filtered version of the actual surface. Although the bounds on this filter cut-off have been only approximated, it is known that they scale with the length of the probing wave. Typically, slopes on the order of 10 wavelengths (or longer) are expected to be important in the scattering process. Thus, for quasi-specular scattering, bistatic S-band data are sensitive to surface structure on the order of 1.3 m (and larger) while for VHF, 12 m is the lower bound. A more complete discussion of these theoretical concepts and results is available in reference 25-8.

Surface-reflectivity measurements are also sensitive to wavelength. Dry geological materials with approximately the density of the lunar regolith exhibit loss tangents that are independent of the radio frequency for frequencies greater than approximately 10 MHz (ref. 25-9). Penetration depths between 10 and 20 wavelengths are typical. Thus, the reflection coefficient inferred from S-band data will be sensitive to vertical structure within the lunar crust to a depth of 1 to 2 m and, from VHF data, to a depth of approximately 10 to 20 m. Such penetration effects have been observed with Explorer 35 data obtained at a wavelength of 2.2 m (ref. 25-10).

Diffuse scattering arises from wavelength-size (and smaller) surface structures and from second-order effects of the gently undulating surface. In the lunar case, the diffuse component of the reflected radiation is normally associated with the presence of large numbers of wavelength-size (or smaller) rocks or rock fragments. Very small rocks will be in the Rayleigh regime and will not contribute individually to the echo. Some attempts to provide quantitative descriptions of diffuse scattering in terms of rock distributions from the Moon have been made (ref. 25-11). However, in terms of surface structure, the diffuse scattering is not understood nearly so well as the quasi-specular scattering.

Experimentally, quasi-specular and diffuse scattering can be distinguished by polarization and coherence properties and by the scattering law (ref. 25-12). Quasi-specular scattering, which by definition originates from those portions of the surface that produce mirrorlike reflections, is deterministically polarized and is the predominant scattering mechanism. Although the echo polarization will change with variations in the polarization of the illuminating wave and the geometry, the polarization is the same as would be produced by a smooth surface of the same material. Diffusely scattered waves are not expected to exhibit this behavior. To the extent that the diffuse component arises from randomly oriented structures on or within the surface, it will be unpolarized. A decomposition of the echo spectrum into the polarized and unpolarized components provides a mechanism for separating the scattering from large-scale (wavelength) surface and small-scale randomly oriented features or roughness.

EQUIPMENT DESCRIPTION

Schematic block diagrams of the receiving and data-processing systems are shown in figure 25-6. The NASA Deep Space Network 64-m-diameter parabolic antenna at Goldstone, California, was used to receive the S-band signals. Both the open- and closed-loop receivers, which were installed for the Mariner spacecraft that orbited Mars in 1971, were used for the bistatic-radar experiment. Normal Apollo mission operations are conducted with the regular ground-station receivers. A signal-conditioning unit processes the Mariner receiver 10-MHz intermediate-frequency output. This unit determines the overall system

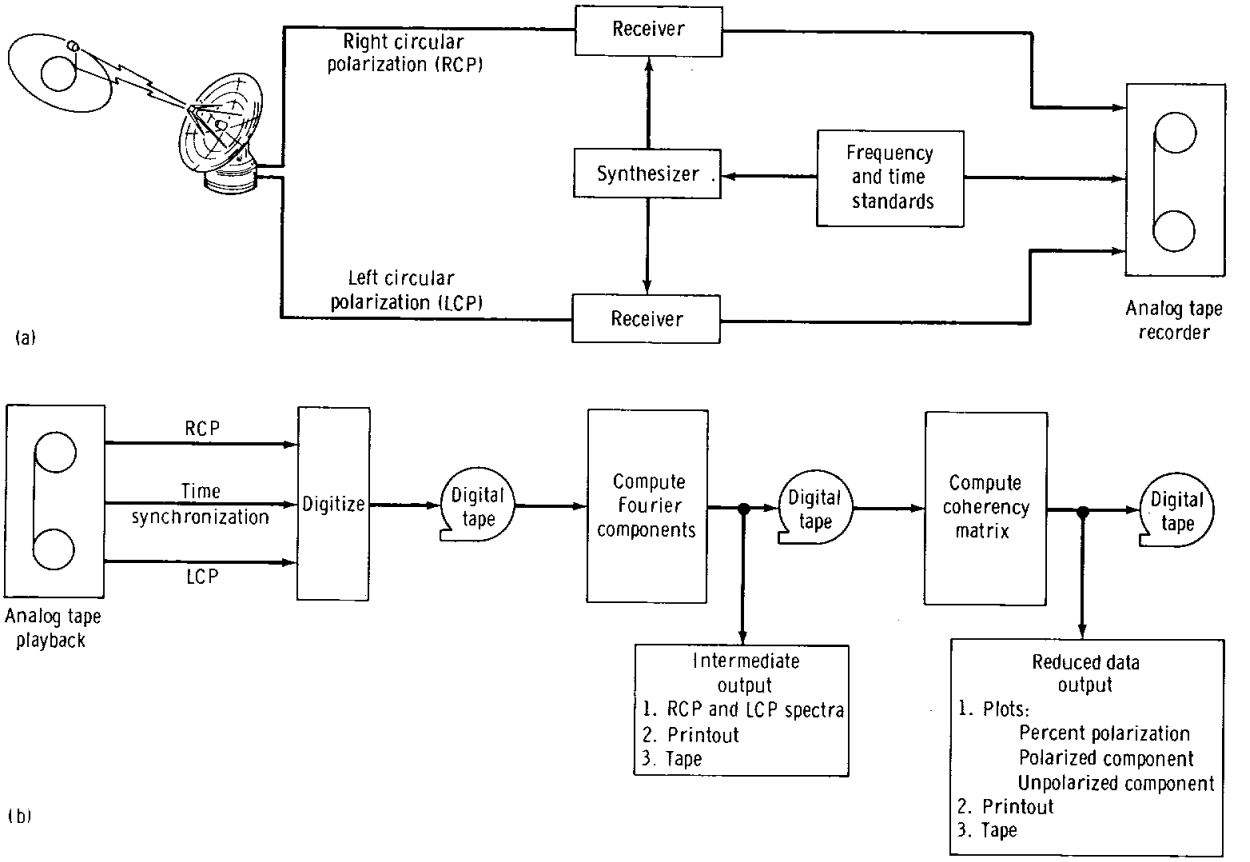


FIGURE 25-6.–System block diagram. (a) Signal receiving system. (b) Data-processing system.

bandwidth for bistatic echoes, provides signal-level control, and produces an audio frequency for magnetic-tape recording.

The use of the open- and closed-loop systems provides redundancy and additional operational flexibility. Because the cost of the digital data reduction is directly proportional to the signal bandwidth, it is desirable to keep this bandwidth as small as possible. However, the possibility existed that the CSM-transmitted frequency would change by several times the echo bandwidth during the experiment.

Filters (80 kHz) are used in conjunction with the open-loop receivers. This bandwidth was selected to ensure that the echo would be within the passband at all times during observation with only a single, predetermined frequency setting. The closed-loop bandwidth is 20 kHz. This bandwidth is sufficiently wide to ensure that the echo is within the passband as long as the receiver is locked on the direct signal from the CSM. The disadvantage of using the closed-loop system alone is that brief periods exist when the direct signal fades below the threshold required for receiver lock. Wideband data can be processed for those periods when lock is lost. On the Apollo 15 mission, only one period of several minutes was experienced during which the direct signal was below the closed-loop threshold.

Both left and right circular polarizations are received. All receivers are driven from a single frequency source, which enables the relative phase between polarizations to be preserved. The system noise temperature in this configuration is near 30° K when the antenna is aimed at the sky alone and 192° K when the Moon fills the beam of the antenna.

The VHF receiving facility was the 46-m-diameter parabolic antenna at the Stanford Center for Radar Astronomy. A complete, open-loop receiver was

constructed, which consists of solid-state preamplifiers for 259.7 MHz with frequency conversions to 50 MHz, 10 MHz, and audio. The data bandwidth is determined at 10 MHz by 3.5-kHz-wide multipole crystal filters. This bandwidth is narrower than the bandwidth used at S-band by the ratio of the transmitted frequencies. Only open-loop channels were used. As was the case for the S-band receiving system, left and right circularly polarized signals were received, and the system is coherent. The system noise temperature is approximately 700° K.

Open-loop operation is similar at 13 cm and 116 cm. Based on a Doppler ephemeris calculated from elements supplied by NASA Manned Spacecraft Center personnel, the receivers are tuned so that the direct signal will be centered in the passband at the time the CSM crosses the Earth-Moon line. The closed-loop receiver is initially tuned according to the operational-frequency predictions for the CSM. Once lock is achieved, the receiver automatically compensates for Doppler effects.

Two magnetic-tape recorders are used simultaneously for data recording. Tapes are started at different times so that overlapping records (with no gaps for tape changes) are available.

DATA REDUCTION

Data reduction consists of a three-step process that is independent of the data source, S-band (open or closed loop) or VHF. This process is outlined in the signal channel shown in figure 25-6(b). First, the analog tapes are replayed and digitally sampled. The sampled data are converted to weighted Fourier coefficients and spectral estimates. Finally, the weighted Fourier coefficients from the two polarization channels are combined to determine the polarization spectra of the echo.

As the analog data are played back, the signals are low-pass filtered to avoid aliasing of the high-frequency tape-recorder noise in the sampling process. Sampling is synchronized with the original recording time through the use of an NASA 36-bit time code and a synchronizing waveform, both of which are multiplexed onto the data tracks of the tape recorder. The two receiver channels, for right and left circular polarization, are sampled simultaneously so that the coherence between channels is preserved. Calibration signals are recorded, sampled, and processed in the same manner as the data.

Weighted Fourier coefficients are computed by using fast Fourier transform techniques. Groups of data samples from each channel are multiplicatively weighted with a sine-squared data window, and the Fourier coefficients are computed. Because the three-analog-data sources are each sampled at different rates, the corresponding frequency and time resolutions of the spectral estimates are not uniform. When the effects of the data window are considered, a spectral resolution of approximately 40 Hz is achieved with the closed-loop S-band data. A spectral resolution of approximately 5 Hz is obtained with the VHF data.

The Fourier coefficients are easily manipulated to provide a variety of data presentations. For example, sums of the squares of successive Fourier coefficient magnitudes yield spectral estimates of the received signals. The time resolution and stability of these estimates may be varied simply by changing the number of terms included in the time average. Spectral estimates for signals in two orthogonal polarizations may be combined with the cross spectra to obtain the polarization properties of the echo (ref. 25-5).

RESULTS

The Apollo 16 data have been sampled, the Fourier coefficients computed, and the preliminary spectra examined. Final computing steps and analysis must await CSM trajectory data both for a decision on whether to process certain data, which may be invalid because of peculiar antenna pointing, and for final ground track, specular point location.

Figures 25-7 and 25-8 summarize several minutes of data for three very different regions along the Apollo 16 ground track. The frequency increases to the right, and the ordinate is linear in the polarized part of the echo power spectrum. Time increases by 2.5-sec intervals in the vertical direction. The frequency resolution is approximately 40 Hz. Numerous features, which move from right to left with time, are apparent. These features correspond to reflections from relatively discrete areas. The variation in Doppler shift as the spacecraft approaches and then

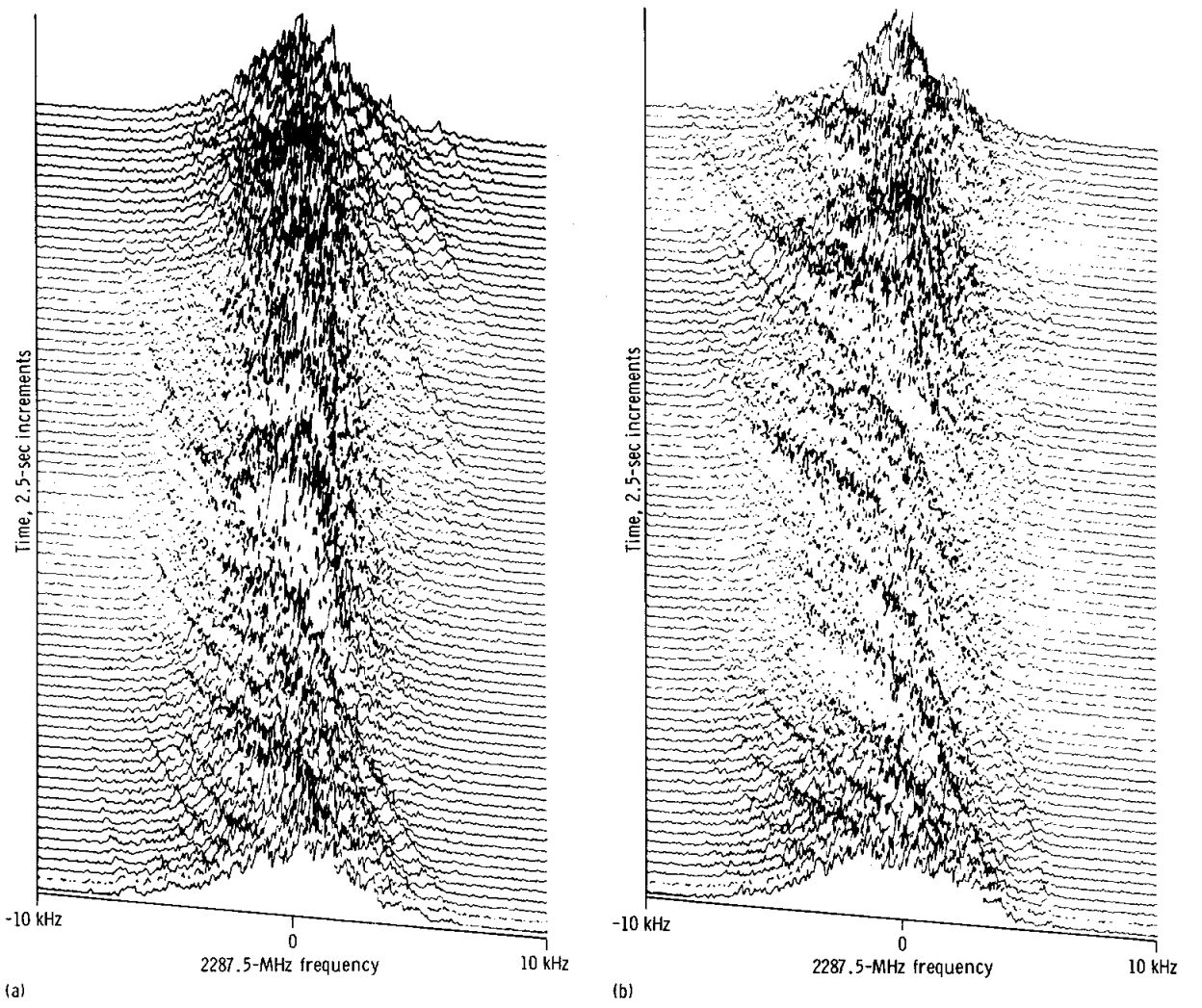


FIGURE 25-7.–Apollo 16 typical 13-cm polarized power spectral plots. (a) Ptolemaeus region. (b) Descartes highland region (4° north of landing site).

passes one of these areas produces the characteristic S-shaped signature. Spectra such as these are typical of the Apollo 14, 15, and 16 data. In general, the wider the individual spectra, the rougher the reflecting region; the greater the quantity of S-shaped Doppler signatures, the larger the number of individual small craters or surfaces with tilts great enough to exhibit quasi-specular reflection far ahead and behind the geometric specular point.

It can be seen from the figures that there are several regions where such scatterers completely dominate the reflection process, mask the normal homogeneous surface characteristics, and make quantitative slope determination with first order theory impossible. Homogeneous and inhomogeneous areas are easily distinguished on the basis of echo spectra. Theoretical results regarding the inference of surface reflectivity and slopes apply only to homogeneous regions. In the area of a crater such as Euler, the localized, increased roughness of the crater results in a decrease in the forward scattering radar cross section, caused by scattering out of the beam. A homogeneous region with constant surface reflectivity would exhibit a slight increase in cross section with increasing roughness caused by the increase in effective scattering area.

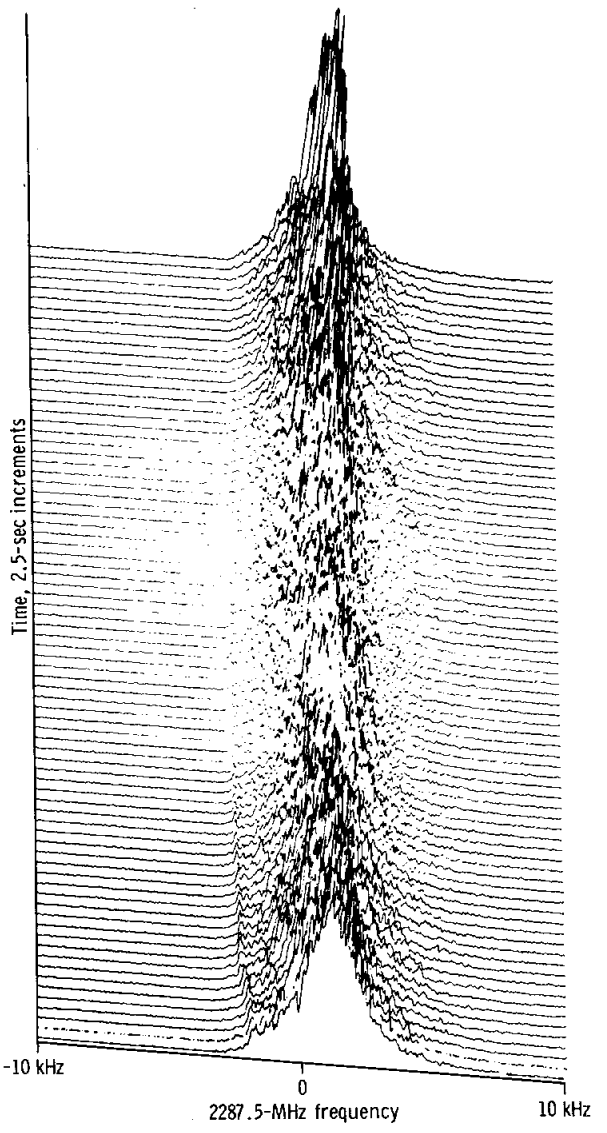


FIGURE 25-8.–Apollo 16 typical 13-cm polarized power spectral plots for the smooth region in Oceanus Procellarum (northeast of Letronne).

A decomposition of an echo spectrum into its polarized and unpolarized components is shown in figure 25-9. The arrows indicate the minimum frequency possible as calculated for the geometrical horizon. The flat portion to the left of the spectrum is therefore unambiguously determined as the system noise level. The difference in noise level for the two components is a consequence of the method used to separate them. Because system noise is equal in magnitude and uncorrelated in the two receivers, it is interpreted as an unpolarized signal. Noise in the polarized spectra is caused by noise and gain differences between the two receivers and by finite statistics in the evaluation of the coherency matrix. Isolation between the two channels has been measured by using the direct signal as a polarized source and found to be on the order of 40 dB.

The increase in level to the right of the arrow is the unpolarized power from the lunar surface. It is apparent that there is unpolarized energy at frequencies beyond the receiver passband. This sharp rise in power and broad spectrum is characteristic of an extremely broad scattering function. Comparison with two well-known cosine scattering laws, Lambert and Lommel-Seeliger, indicates that the unpolarized return is generally consistent with laws of this type. Limitations of the spacecraft antenna and ground receivers have thus far prevented a quantitative comparison.

The polarized spectrum of figure 25-9 is clearly governed by a different scattering law. For much of the lunar surface, the maria in particular, the polarized scattering within a few degrees of specular may be well approximated by a Gaussian law. There are, however, numerical solutions to the integral equation for the scattering law in terms of the bistatic-radar spectra that yield non-Gaussian solutions for the scattering from certain lunar features. This scattering has been observed once in the Apollo Program, in the region just west of Lalande, and only at the longer wavelength. The 116-cm spectra in this case are bimodal, and the conclusion drawn from them is that on the scale of several hundred meters, there are no 0° slopes. The spectra at 13 cm for this region are of the normal, quasi-specular type.

Figure 25-10 is a plot of reflectivity inferred from the received power at both wavelengths during Apollo 14. The power has been normalized by using the geometry of the bistatic case to yield ρ within a constant of proportionality. The scales have been adjusted to give nearly equal values of ρ near a 10° angle of incidence. The data, viewed as a whole, are typical of reflection from a dielectric surface. The smooth curves are the best fit to the data that use the theoretical reflection coefficient for a plane, smooth, semi-infinite dielectric with dielectric constant $\epsilon = 3.1$. The data are not plotted for angles of incidence greater than approximately 80° because shadowing by lunar features causes the quasi-specular theory to break down and the inferred reflectivity to

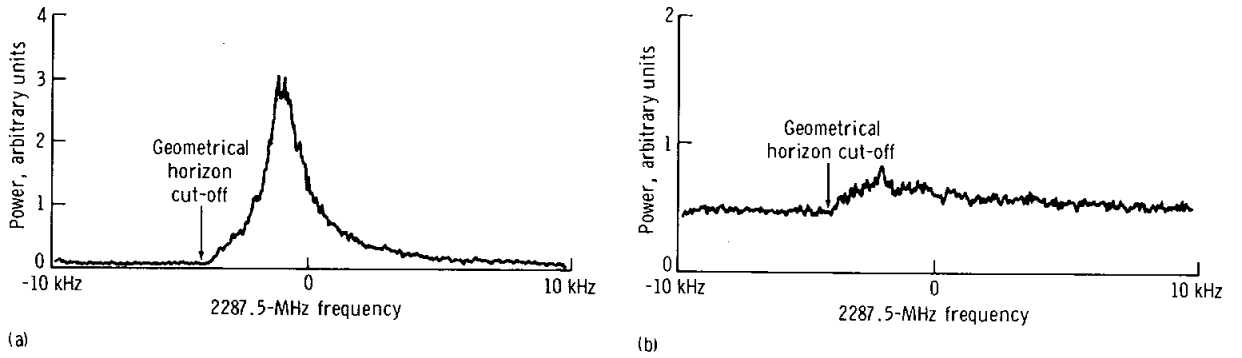


FIGURE 25-9.–Apollo 16 13-cm spectra showing the different scattering law responses for the two cases. Note the geometrical horizon cut-off. (a) Polarized. (b) Unpolarized.

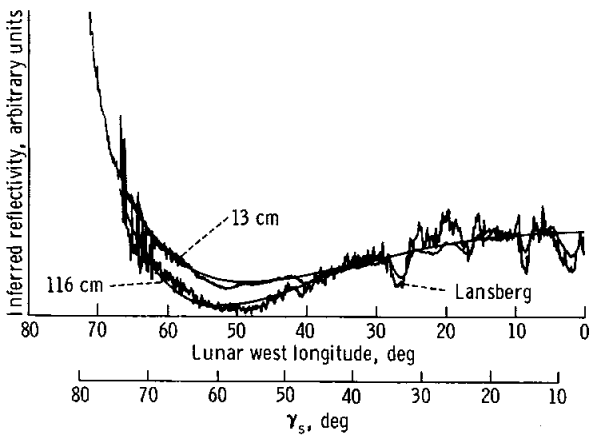


FIGURE 25-10.–Inferred reflectivity as a function of lunar longitude and angle of incidence from the Apollo 14 data. The smooth curve is calculated for a dielectric constant of 3.1.

approach zero as the spacecraft nears the horizon. As discussed previously, there are marked, localized decreases in reflectivity for certain features. The crater Lansberg (fig. 25-10) also shows clearly at both wavelengths in the frequency-time plots.

CONCLUSIONS

It is now clear that the oblique geometry scattering properties of the surface of the Moon are wavelength dependent in the decimeter-to-meter range. At a given wavelength, the scattering law is highly dependent on local topography. Further, there are systematic differences in the average scattering properties of mare and highland units.

At 13 cm, the reflectivity of the mare surfaces is remarkably uniform except for local deviations associated with specific features. As shown in figure 25-10, the reflectivity is well matched by the classical reflection coefficients for scattering from a plane, semi-infinite dielectric interface with a dielectric constant of 3.1 ± 0.1. The 116-cm results frequently contrast sharply with the ones at the shorter wavelength. Although it is possible to fit a classic curve to portions of the data in figure 25-10, the fit is poor over several extended areas. This is generally true over both the Apollo 14 and 15 ground tracks. No simple model consisting of a uniform dielectric interface or a contiguous set of such interfaces will match the data. A frequency-dispersive mechanism involving layering in a lossy dielectric is required to explain some of these observations. The highlands ejecta region south of Mare Crisium exhibits a dielectric constant of approximately 2.8 at the 116-cm wavelength, and the 13-cm reflectivity result suggests an even lower value. This is an unusual area in terms of 13-cm data, for the departure from uniform dielectric sphere response is very sharp. Modeling of this region has not been completed. In the Apennines and the central highlands, both wavelengths show a reduction in reflectivity consistent with a change in relative dielectric constant from 3.1 to 2.8.

The 116-cm variations that are not correlated with the 13-cm data cannot be caused by surface effects because such effects would also be observed at the shorter wavelength. Explanation of the differential behavior in some cases requires layering or an inversion of density with depth such as might be produced by a flow over older regolith. The

Apollo 14 observations suggest that the upper 5 to 50 cm of the crust must be extremely uniform over the surface of the Moon or that the change with depth must be gradual. Surface-modifying processes have apparently acted to these depths along the major portion of the radar ground tracks. Further, the 116-cm data suggest that there must be large variations (on the order of 2:1) in impedance contrast within 1 to 10 m of the surface. Variation in depth of a thin regolith or covering blanket is one obvious candidate to model this effect.

The rms slopes deduced from the Apollo 14 and 15 spectra exhibit very systematic behavior with respect to maria, highlands, and discrete features such as craters. Typical highland slopes are in the range of 5° to 7° at both wavelengths, suggesting that on the scale lengths of 30 and 300 m, the surface has equal roughness. Within the maria, the 13-cm slopes are typically within 2° to 4°, but those obtained at 116 cm are only half as large. Thus far, no exceptions to this rule have been observed. Detailed correlations have been made between slope changes and terrain changes, with excellent results.

REFERENCES

25-1. Evans, J. V.; Radar Studies of Planetary Surfaces. Annual Review of Astronomy and Astrophysics, vol. 7, L. Goldberg, David Layzer, and J. G. Phillips, eds., Annual Reviews, Inc. (Palo Alto, Calif.), 1969, pp. 39-66.

25-2. USGS Geologic Maps of the Moon, scale 1:1,000,000. LAC 40 by M. H. Carr, 1965; LAC 41 by R. J. Hackman, 1966; and LAC 42 by M. H. Carr, 1966.

25-3. Tyler, G. L.; Eshleman, V. R.; Fjeldbo, G.; Howard, H. T.; and Peterson, A. M.: Bistatic-Radar Detection of Lunar Scattering Centers with Lunar Orbiter I. Science, vol. 157, no. 3785, July 14, 1967, pp. 193-195.

25-4. Tyler, G. L.; Ingalls, D. H. H.; and Simpson, R. A.: Stanford Telemetry Monitoring Experiment on Lunar Explorer 35. Final Rept. SU-SEL-69-006, Stanford Electronics Lab., Oct. 1969.

25-5. Howard, H. T.; and Tyler, G. L.: Bistatic-Radar Investigation. Sec. 17 of Apollo 14 Preliminary Science Report. NASA SP-272, 1971.

25-6. Howard, H. T.; and Tyler, G. L.: Bistatic-Radar Investigation. Sec. 23 of Apollo 15 Preliminary Science Report. NASA SP-289, 1972.

25-7. Tyler, G. L.; and Ingalls, D. H. H.: Functional Dependences of Bistatic Radar Frequency Spectra on Lunar Scattering Laws. J. Geophys. Res., vol. 76, no. 20, July 1971, pp. 4775-4785.

25-8. Tyler, G. L.; Simpson, R. A.; and Moore, H. J.: Lunar Slope Distributions: A Comparison of Bistatic Radar and Photographic Results. J. Geophys. Res., vol. 76, no. 11, Apr. 1971, p. 2790.

25-9. Campbell, Malcolm J.; and Ulrichs, Juris: Electrical Properties of Rocks and Their Significance for Lunar Radar Observations. J. Geophys. Res., vol. 74, no. 25, Nov. 1969, pp. 5867-5881.

25-10. Tyler, G. L.: Oblique-Scattering Reflectivity of the Lunar Surface: Preliminary Results from Explorer 35. J. Geophys. Res., vol. 73, no. 24, Dec. 1968, pp. 7609-7620.

25-11. Thompson, T. W.; Pollack, J. B.; Campbell, M. J.; and O'Leary, B. T.: Radar Maps of the Moon at 70-cm Wavelength and Their Interpretation. Radio Science, vol. 5, no. 2, Feb. 1970, pp. 253-262.

25-12. Beckman, Petr; and Spizzichino, André: The Scattering of Electronic Waves From Rough Surfaces. International Series of Monographs on Electromagnetic Waves. Pergamon Press, 1963.

26. Apollo Window Meteoroid Experiment

Burton G. Cour-Palais,[a†] Milton L. Brown,[b] and David S. McKay[a]

The purposes of the Apollo window meteoroid experiment are to use the Apollo command module (CM) heat shield window surfaces to obtain additional information about the flux of meteoroids with masses of 10^{-7} g and less, to examine the residue and the morphology of the craters produced by these meteoroids to obtain information regarding the dynamic and physical properties of the meteoroids, and to discover possible correlations with the lunar-rock-crater studies.

In addition to information regarding meteoroid flux, this experiment could yield information on the mass density and, possibly, on the composition of meteoroids. To determine the mass density would require the assumption that the velocity distribution, as determined from optical and radar observations of much larger meteoroids, is applicable to the smaller meteoroids.

Laboratory calibration data have been generated and are currently being analyzed. Glass targets identical to the CM heat shield windows were impacted by particles of different sizes, mass densities, and velocities using electrostatic accelerators for correlation with the observed crater characteristics.

When the effects of entry heating, subsequent immersion in salt water, and all the other contaminating sources are accounted for, the composition of the meteoroid residue in the crater or in the shock-fused glass will be determined by use of a scanning-electron-microscope (SEM) nondispersive X-ray detector. The significance of the use of this detector is that compositions and mass densities obtained in space can be compared with those obtained from the lunar rock samples without the long-term exposure to the environmental effects of space. Knowledge of the mass density is also important for designing meteoroid shielding. So far, mass density can only be inferred from observations of meteoroid breakup in the atmosphere. Controversy exists as to whether the typical meteoroid is a low-density (1.0 g/cm^3 or less) dust or ice ball or a stony object that froths during atmospheric entry and breaks off in chunks. If it is the latter, the mass density could be 2.5 to 3.0 g/cm^3.

With the exception of the Apollo 11 mission, all the CM heat shield windows have been examined for meteoroid impacts 40 μm and larger in diameter. So far, 10 impacts have been observed. The flux represented by the number of impacts observed and the area-time of exposure by the Apollo windows is compatible with the flux estimates obtained from the results of penetration sensors mounted on the Pegasus 1, 2, and 3 satellites, by the Explorer 16 and 23 satellites, and by the Surveyor III shroud. The Apollo 16 windows had not been received for study at the time of publication of this report.

BASIC THEORY

Meteoroids are solid particles moving in interplanetary space that originate from both cometary and asteroidal sources. They are classified as sporadics when the orbits are random and as streams when many have nearly identical orbits. A meteor is the light phenomenon associated with the interaction of a meteoroid with the atmosphere of the Earth. The portion that survives interaction with the atmosphere and is found on the surface of the Earth is a meteorite. It is generally accepted that most meteorites are of asteroidal origin (ref. 26-1) and that the typical meteoroid originates from a cometary nucleus, is frangible, and does not reach the surface of the Earth. Thus, very little is known about the composition and mass density of meteoroids, whereas meteorites have been collected and examined very thoroughly (ref. 26-2). The typical meteoroid has been described

[a]NASA Manned Spacecraft Center.

[b]Lockheed Electronics Corporation.

†Principal Investigator.

(ref. 26-3) as a conglomerate of dust particles bound together by frozen gases or "ices"; another author (ref. 26-4) postulates that meteoroids are "dust balls." The mass density of these conglomerates is assumed to be no greater than 1 g/cm^3 because of the evidence of breakup high in the atmosphere. Recent experiments with carbonaceous chondrites in arc jets (ref. 26-5) have shown that a sufficient amount of water is present to cause frothing during the entry heating and that this frothy material breaks off along the path because of aerodynamic pressure. Thus, laboratory evidence has shown that the breakup of meteoroids in the atmosphere of the Earth is not necessarily indicative of a low-density conglomerate.

The near-Earth flux of meteoroids entering the atmosphere has been determined from photographic observation of meteors, radar echoes from the ionized column produced by meteoroids, and direct measurements by satellite detectors. The results of these observations have been combined in the plot of cumulative number/m^2-sec for each size (fig. 26-1). Details of the observation techniques, direct measurements, and conversion of the observed data to mass may be found in references 26-6 to 26-8. Detectors flown on spacecraft have furnished information on the meteoroid flux in the mass range of 10^{-13} to 10^{-6} g (refs. 26-8 to 26-11). Fluxes for masses 10^{-7} g and less have been detected primarily by acoustic impact (microphone) sensors, whereas fluxes of 10^{-9} to 10^{-6} g have been determined by the detection of perforations in thin metallic sheet sensors. The acoustic impact sensor measurements (ref. 26-8) indicate a much higher particle flux than do the penetration sensors for the same mass range (refs. 26-9 to 26-11). The examination of the Gemini spacecraft windows for meteoroid impacts confirmed the lower flux estimates obtained by the penetration sensors (ref. 26-12) for masses of 10^{-7} g and less. The cumulative flux plot of figure 26-1 reflects the low flux estimate of the penetration sensors and the Gemini window examination. The proponents of the higher flux measurements obtained from the acoustic sensors do not completely accept the penetration sensor results. Because the Apollo windows have had a much greater total area-time exposure to the environment than the Gemini windows, it is believed that the Apollo window meteoroid experiment could settle the controversy.

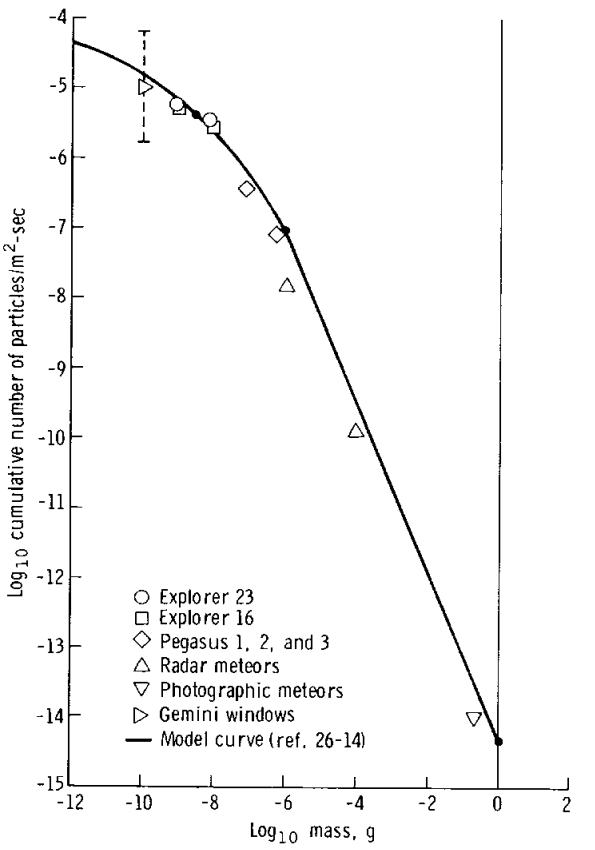


FIGURE 26-1.–Comparison of cumulative meteoroid flux-mass data with the adopted model.

DESCRIPTION OF THE INSTRUMENT

The Apollo window meteoroid experiment is passive in that it uses approximately 0.4 m^2 of the external surfaces of the Apollo CM windows as meteoroid-impact detectors. The windows are made of 99-percent-pure silica glass and are mounted almost flush with the external surface of the heat shield contour. The rendezvous windows were originally included in the total area of glass to be scanned but have not been used since the Apollo 10 mission for the following reasons.

(1) The rendezvous windows are inset into the heat shield and are fairly well shielded from the environment.

(2) In all missions involving lunar module (LM) rendezvous, the surfaces of the rendezvous windows are subject to impacts by particles emanating from

the thrusters of the LM reaction control system (RCS). During the postflight examination of the Apollo 9 spacecraft, the rendezvous windows showed a significant increase in pitting over that of previous missions with no LM rendezvous.

The window is an ideal detector because the surface is smooth and the spallation diameter can be many times the diameter of the impacting meteoroid. This ratio allows a 20X optical scan to detect the 40-μm-diameter crater that could be caused by a 2-μm-diameter meteoroid. Hence, the time necessary to scan the large areas involved is considerably reduced, and the detection threshold is small enough to include cosmic dust particles.

During entry, the heat shield windows are subjected to a surface temperature of almost 1175° K for the side windows; the hatch window is subjected to a somewhat lower temperature. These temperatures are well below the annealing and softening temperatures of the glass; therefore, the crater morphology should not be affected. It is hoped that both the temperature effect and the contamination caused by ablative products from the heat shield and the subsequent immersion in sea water can be accounted for in the chemical analyses.

EXAMINATION PROCEDURE

The heat shield and hatch windows from the Apollo 7 to 14 command modules were scanned at 20X magnification before flight to determine the general condition of the external surfaces. All chips, scratches, and other features that could be confused with meteoroid-impact craters were noted on a surface map. As a result of the stringent quality control and optical requirements, the windows have been generally free of such defects, and this mapping practice has been discontinued. The windows are received with a fairly thick coating of surface contamination, which is removed before the optical scan by washing with water and isopropyl alcohol and by careful scraping with a razor blade if necessary. Tests have shown that any pit or scratch caused by the scraping cannot be confused with an impact crater.

The windows are next scanned at 20X magnification with a stereozoom microscope by two different observers, and suspected impact craters are marked on a map. From experience with hypervelocity impacts in fused silica, it is possible to separate the meteoroid impacts from other surface effects (ref. 26-13). When viewed with bottom lighting, laboratory hypervelocity impact craters (detectable by a 20X scan) have less than 10 percent of the total damaged area blacked out because of total reflection; the central area consists of pulverized glass that is generally 4 to 6 times the diameter of the impacting particle. This central zone, often raised above the surrounding chipped area, is dome shaped and has a shallow depression at the point of impact for speeds of 5 to 7 km/sec. For very high velocities (10 km/sec and faster), the center of this dome shows signs of fusion, and a lip often extends above the original surface of the glass. The central pulverized zone is surrounded by an inner ring of a generally rough, chipped-out appearance and an outer ring of a generally smoothed, conchoidal, terraced look. The periphery of the spalled surface is very rarely symmetrical because of the inhomogeneous fracture strength of the glass.

Every suspected meteoroid crater is subjected to the following procedure.

(1) The crater is photographed in detail with top and bottom lighting.

(2) The crater depth and diameter are measured.

(3) The section of the window containing the crater is removed by coring or sectioning as close as possible to the crater.

(4) The window section is prepared for residue analysis with the SEM nondispersive X-ray detector by applying a thin carbon coating.

(5) Residue analysis is performed, and all constituents are recorded.

(6) The same window section is cleaned, and a thin gold coating is applied for normal, tilt, and stereoscopic crater photography at high magnifications.

The data from these examinations will be compared with the laboratory test data mentioned previously, and the following meteoroid characteristics will be determined.

(1) The probable meteoroid mass, using assumed velocity and impact angle

(2) The flux of particles of this probable mass and larger, using exposure time and area

(3) Probable meteoroid composition, determined from elemental constituents and by comparison with lunar-crater, meteorite, and comet studies

(4) Impact shock pressure, estimated by correlating actual crater characteristics with test data

(5) Probable mass density, estimated by using Hugoniot equations for the Apollo window glass and from the results of the impact shock pressure determination

RESULTS

The Apollo 15 windows were received with the outer surfaces contaminated with the hard deposit that has been present on all Apollo windows examined to date. The results of a chemical analysis of samples taken from the Apollo 9 windows and the possible sources of the contaminants are listed in table 26-I. The sources chosen were the Mylar protective coating on the heat shield surface, scrapings from an RCS thruster nozzle, and a piece of charred heat shield material. High to very high concentrations of sodium were found in the thruster-nozzle crust and in the heat shield "char," but only a trace of sodium was found in the Mylar. Because the Mylar ablates before CM splashdown, the origin of the sodium is clear. The concentration of magnesium found in the thruster material was greater than 10 percent, whereas it was less than 1 percent in the heat shield char and the Mylar, indicating another possible source. Also, the Mylar, rich in titanium and silicon, is identified as the source of these two elements on the window surfaces. Because the CM entry and landing conditions are similar for all missions, it is assumed that the Apollo 9 results are typical of all other spacecraft.

After scanning approximately 3 m^2 of Apollo heat shield windows at a general level of 20X magnification, 10 meteoroid impacts have been identified. Of these, the five craters shown in figure 26-2 were found on the Apollo 7 window. One crater was found on the Apollo 8 windows, one on the Apollo 9 windows, one on the Apollo 13 windows, two on the Apollo 14 windows, and none on the Apollo 15 windows. The surface spallation diameters of these craters range from 25 to 500 μm.

The Apollo 13 crater, shown as viewed through an optical microscope in figure 26-3, is characteristic of all the Apollo meteoroid craters found up to this event. The tilted SEM view shown in figure 26-4 reveals the relationship of the central pit to the surface spallation zone. The spall zone is roughly circular, measuring 430 to 460 μm in diameter, and the pit has

TABLE 26-I.–Apollo 9 Window Surface Contaminants and Possible Sources

Sample area	Element, percent[a]																				
	Al	*B*	*Ca*	*Cr*	*Cu*	*Fe*	*Pb*	*Mg*	*Mn*	*Mo*	*Ni*	*P*	*K*	*Si*	*Ag*	*Na*	*Sn*	*Ti*	*W*	*Zn*
Hatch window	Tr	–	Tr	Tr	Tr	<1	–	>10	Tr	–	–	–	–	1 to 10	–	>10	Tr	<1	–	Tr
Side windows	<1	Tr	<1	Tr	<1	<1	Tr	>10	Tr	Tr	–	–	–	1 to 10	Tr	⩾10	Tr	1 to 10	–	Tr
Rendezvous windows	<1	Tr	<1	<0.1	<1	<1	Tr	>10	Tr	Tr	Tr	–	–	>10	Tr	⩾10	Tr	1 to 10	–	Tr
CM Mylar layer	<1	Tr	Tr	Tr	Tr	Tr	Tr	<1	Tr	–	–	–	–	>10	–	Tr	Tr	⩾10	–	<0.1
Thruster nozzle residue	Tr	–	Tr	–	Tr	<1	–	>10	Tr	Tr	–	–	–	1 to 10	–	⩾10	–	<1	–	–
CM heat shield char	<1	<0.1	Tr	–	Tr	<1	–	<1	–	–	–	–	–	1 to 10	–	>10	–	1 to 10	–	–

[a]Tr = trace (in range of ppm).

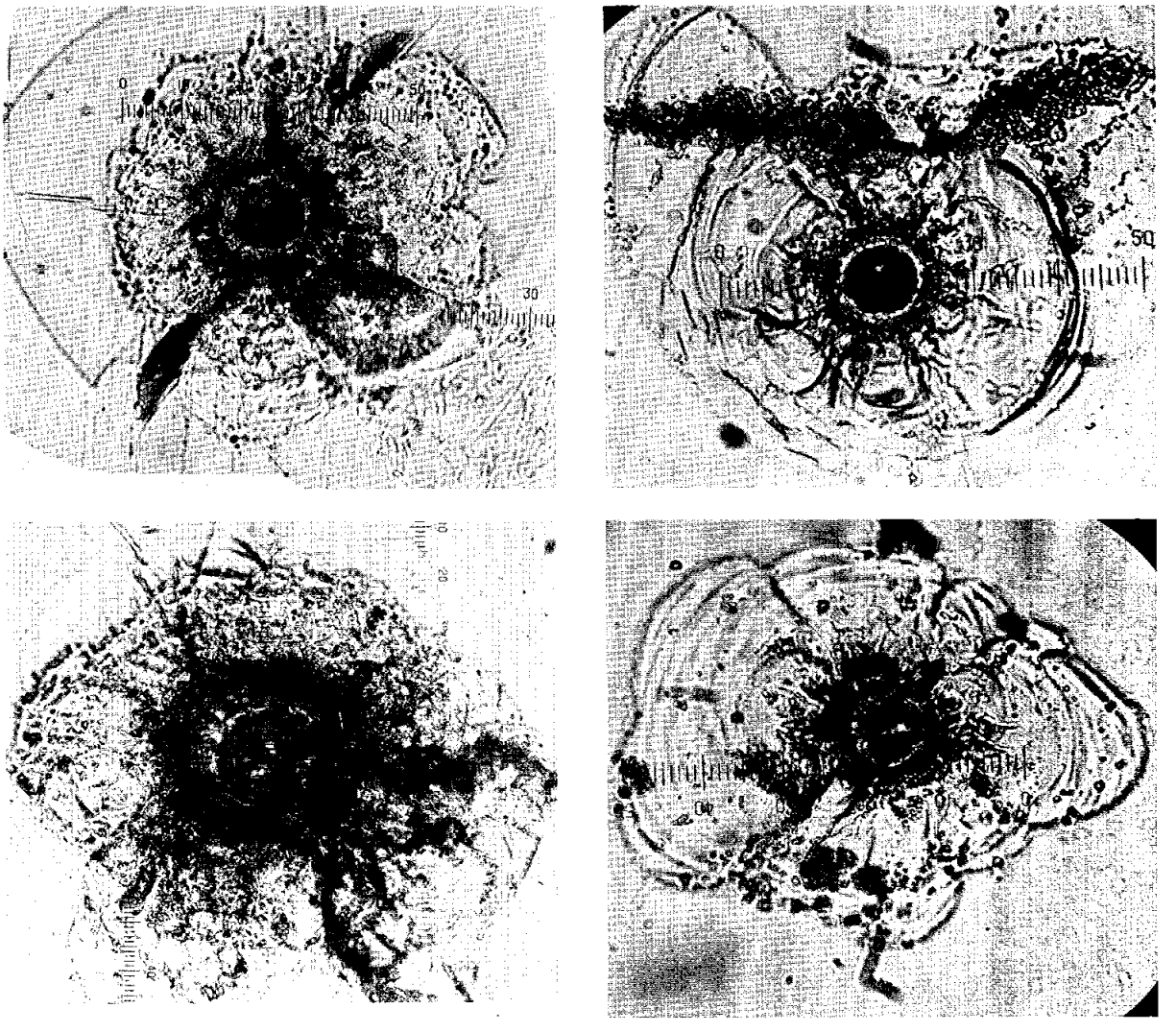


FIGURE 26-2.–Meteoroid-impact craters found on the Apollo 7 window surfaces.

evidently been molten, is elliptical, and measures 130 by 110 μm. The 520X SEM photograph of the pit region (fig. 26-5) clearly shows that the lip of the pit was ejected, leaving only the bottom portion of the original melt.

An SEM examination of the two Apollo 14 impact craters, one approximately 25 μm in diameter and the other 85 by 130 μm, reveals low-angle spallation and radial fractures, a shattered central zone, and lack of a central pit.

No trace of any meteoritic material could be identified in or around either the Apollo 13 or 14 craters. However, the pits and spallation zones contain the

same particulate contamination from the spacecraft thrusters, CM Mylar heat shield coating, and sea water as found on the window surfaces.

A number of surface effects from low-velocity particles have been found after many of the flights. Typical examples (fig. 26-6) have a very different appearance from meteoroid craters. Their origins are most probably the CM launch escape system jettison rocket and RCS thrusters; hence, they are excluded from consideration.



FIGURE 26-3.–Optical microscope photograph of meteoroid-impact crater found on the Apollo 13 right-hand side-window surface.



FIGURE 26-4.–An SEM photograph of the Apollo 13 meteoroid-impact crater.

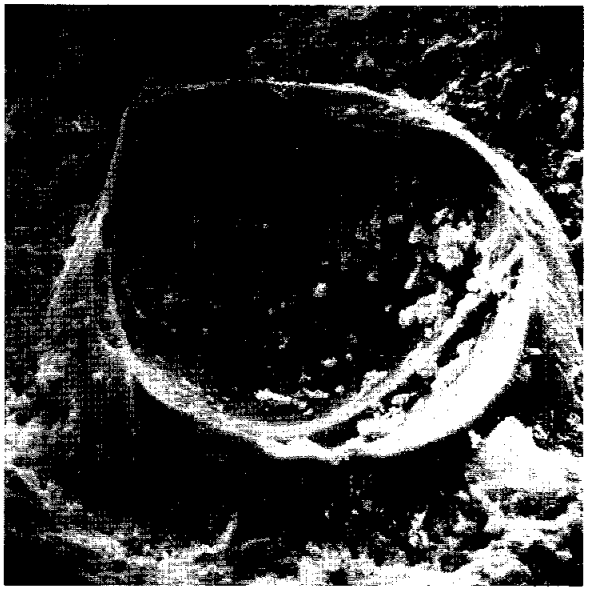


FIGURE 26-5.–A 520X SEM photograph of the pit in the Apollo 13 meteoroid impact crater.



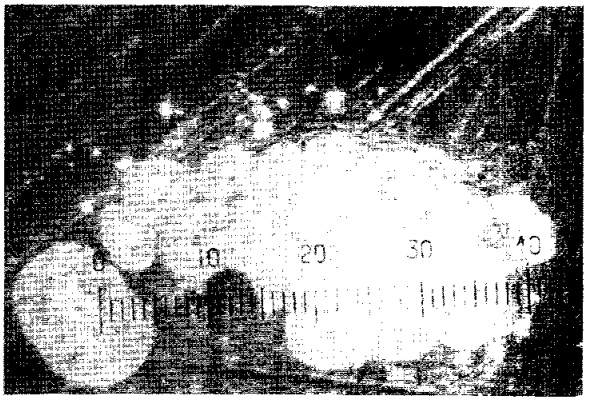
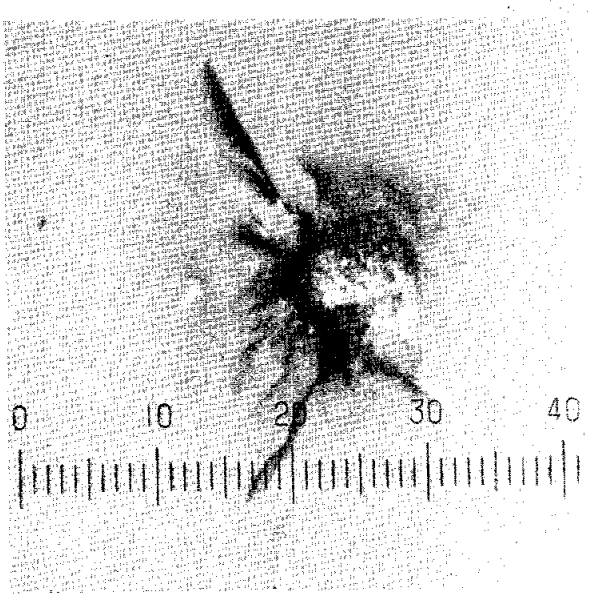
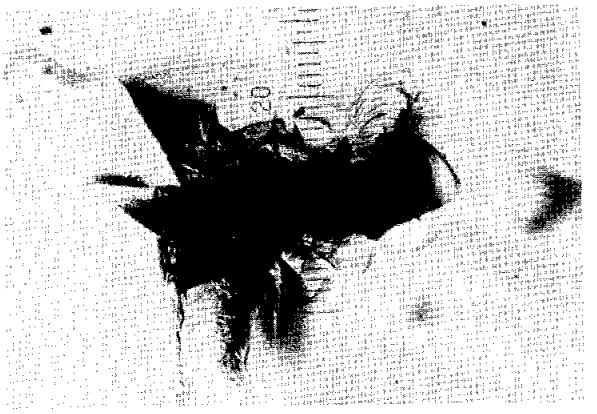
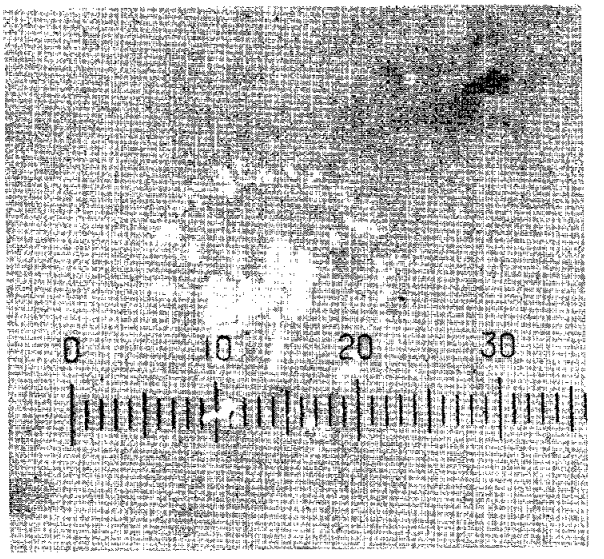
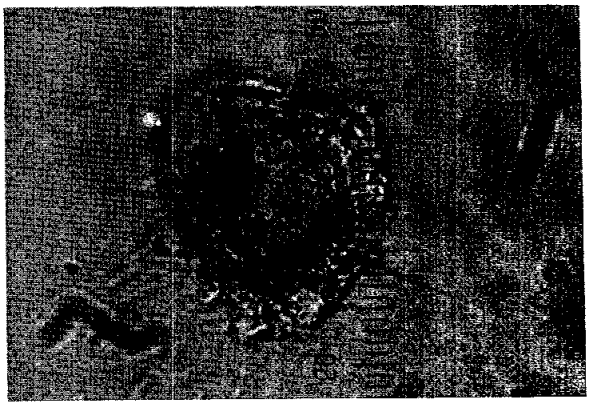


FIGURE 26-6.–Typical low-velocity surface effects.









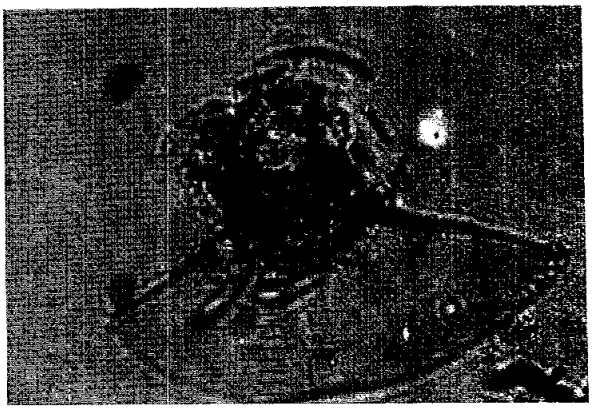


FIGURE 26-6.–Concluded.

A list of the craters is given in table 26-II, which includes an estimate of the exposure (product of window area and time) to the meteoroid environment for each mission, the resultant flux, the upper and lower 95-percent confidence limits, and an estimate of the impacting meteoroid mass. The mass determination is preliminary and is based on spall-diameter-to-meteoroid-diameter ratios and a mass density of 2 g/cm^3. The diameter ratio used is obtained from the calibration tests previously mentioned and a prior series of hypervelocity tests in silica glass. The flux estimate includes the window area, mission time, planetary shielding during the Earth- and lunar-orbital periods, an allowance for the additional shielding provided by the LM during Earth-Moon transit, and a factor to account for the focusing effect of the gravitational field of the Earth (ref. 26-14) on the meteoroid population. The resulting data points are shown in figure 26-7 compared with the near-Earth meteoroid-flux model of reference 26-14 and the Surveyor III shroud data (ref. 26-15).

TABLE 26-II.–Meteoroid Craters and Related Information

Mission	*Window exposure, m^2-sec*	*Number of impacts*	*Meteoroid flux, number/m^2-sec*	*95-percent confidence limits, number/m^2-sec*	*Minimum meteoroid mass, g*
Apollo 7 (Earth orbital without LM)	2.21×10^5	5	2.26×10^{-5}	5.29×10^{-5} 7.23×10^{-6}	1.31×10^{-10}
Apollo 8 (lunar orbital without LM)	1.8×10^5	1	1.07×10^{-5}	5.96×10^{-5} 1.07×10^{-6}	7.86×10^{-11}
Apollo 9 (Earth orbital with LM)	1.87×10^5	1	5.36×10^{-6}	3.0×10^{-5} 5.36×10^{-7}	5.37×10^{-10}
Apollo 10 (lunar orbital with LM)	1.99×10^5	0	–	1.86×10^{-5} –	7.86×10^{-11}
Apollo 12 (lunar landing)	2.43×10^5	0	–	1.52×10^{-5} –	7.86×10^{-11}
Apollo 13 (circumlunar abort with LM)	1.42×10^5	1	1.36×10^{-5}	7.6×10^{-5} 1.37×10^{-6}	5.91×10^{-9}
Apollo 14 (lunar landing)	2.35×10^5	2	1.64×10^{-5}	5.9×10^{-5} 1.64×10^{-6}	1.64×10^{-11}
Apollo 15 (lunar landing)	2.88×10^5	0	–	1.28×10^{-5}	5.37×10^{-10}

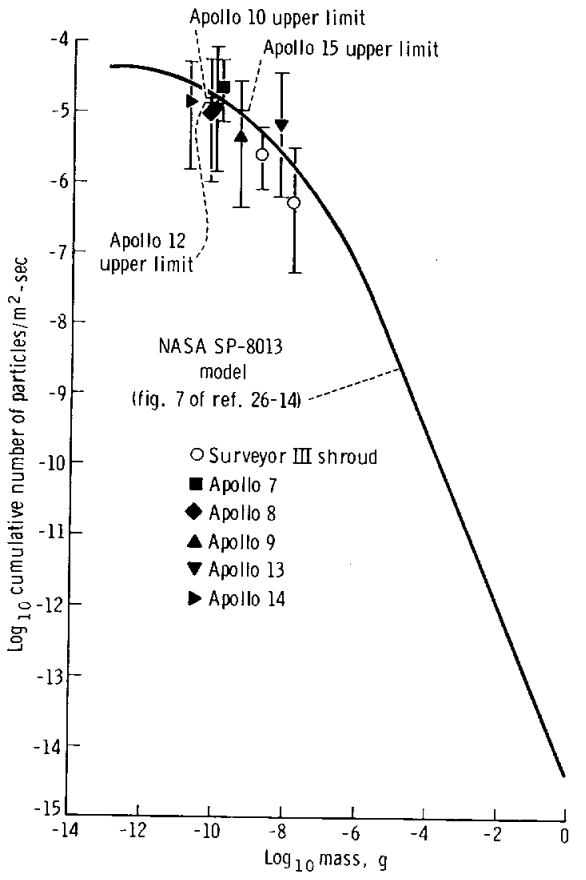


FIGURE 26-7.–Comparison of Apollo window experiment data with the reference model environment curve.

DISCUSSION

Since the publication of the preliminary flux results for the Apollo window meteoroid experiment (ref. 26-16), the mass calibration from laboratory tests on glass and LM shielding studies have been completed. In addition, the attitude of the windows relative to the surface of the Moon during lunar orbit has been clarified and a corrected planetary shielding factor obtained. As a result, the effective area-time product of the window surfaces is now accurately known. However, the mass calibration, though different from that given in reference 26-16, must still be considered preliminary because the test results became available just before publication of this report. Nevertheless, a quick look at the data for craters ranging from 1 to 40 μm indicates that the meteoroid mass limit at the detection threshold for the 20X scan is approximately 10^{-11} g. In addition, it is evident from the combination of these test data with previous hypervelocity data in glass targets, for craters ranging from 250 μm to 4 cm, that several crater regimes exist. Initially, there is a crater typical of those in soft metal, hemispherical in shape, with a lip extending above the target surface. Next, at a higher energy, a spall zone forms around the crater, removing the lip. At higher impact energy levels, outer spall zones appear and, eventually, the original hemispherical crater is ejected and the residual crater is conical with conchoidal ridges described previously.

The effect of the new mass calibration and increased area-time product can be seen in figure 26-7. The data are shown with 95-percent confidence error bars in flux compared with the current NASA meteoroid environment model for near-Earth (ref. 26-14) and the results of the Surveyor III television camera examination (ref. 26-15). As mentioned previously, a gravitational focusing factor has been applied to increase the flux for the lunar missions for comparison with the Earth-orbital missions and the near-Earth model. The factor used was 1.92 (ref. 26-14).

The effects of the recalibration are to improve the consistency of the Apollo data and to obtain better correlation with the meteoroid environment model and the Surveyor III results. The zero impacts for the Apollo 10, 12, and 15 spacecraft are represented by 95-percent upper-limit error bars.

The trend of the data as a whole is to a slightly lower level than the line representing the referenced environment model. Because the area-time product is now accurately known and the mass calibration is consistent with that of other workers in this field (ref. 26-17), it is believed that this may be a real effect. It can be explained by the differences in the detectors themselves. The reference environment model has resulted from the perforation of thin metallic surfaces, whereas the window (and Surveyor III) data are due to the cratering of glass and metallic surfaces. The flux measured in each case depends upon the velocity exponent: 0.875 for perforation and 0.67 for cratering. At the average meteoroid velocity of 20 km/sec, the perforation flux is higher than the cratering flux by a factor of 1.85.

The mass limit of 10^{-11} g for the 20X scan of the Apollo window surfaces represents a meteoroid of approximately 4 μm diameter at the average meteoroid velocity of 20 km/sec and mass density of 2 g/cm^3. As cosmic dust can exist down to the radiation pressure limit (0.16 μm diameter for a metallic particle) and the laboratory test data permit calibration to submicron-sized particles, a scan at higher magnification is obviously indicated. Accordingly, cores from the Apollo 14 and 15 window surfaces are currently being scanned with the SEM.

The extent of the window contamination described in the previous subsection could cause some doubt that the meteoroid composition can be positively identified from the residue associated with each crater. Certainly, the uncombined surface meteoroid debris within and around an impact site is contaminated, as the nondispersive X-ray analysis of the Apollo 13 and 14 craters has shown. However, the shock pressure generated is sufficient to melt (see fig. 26-4) and vaporize the glass and the meteoroid. It is possible that some meteoroid material could be contained within the molten glass, although the Apollo 13 and 14 analyses have not thus far identified any. Also, laboratory impact tests with glass targets have produced "mounds" in the bottoms of craters that indicate the presence of the projectile material in association with the host material (ref. 26-18). Hence, it is possible that meteoroid elements may yet be identified within similar mounds or within the molten layer in the pits associated with impact events in the 99-percent-pure silica glass window material.

CONCLUSIONS

The estimate of the mass flux resulting from examination of the Apollo 15 and seven prior spacecraft window surfaces, a calibration based on experimental hypervelocity tests, and an accurate determination of the area-time product are in good agreement with the Surveyor III data and the near-Earth model environment of reference 26-14. A trend toward a lower but parallel curve, remaining after an allowance has been made for the effect of gravitational focusing by the Earth, may be explained by differences in detectability between perforation and cratering surfaces. Although a nondispersive X-ray analysis of residue in and around meteoroid-impact sites on the Apollo 13 and 14 window surfaces revealed only spacecraft contaminants, it is not concluded that meteoritic residue cannot be detected by this experiment.

REFERENCES

26-1. Whipple, Fred L.: On Maintaining the Meteoritic Complex. Studies in Interplanetary Particles, Fred L. Whipple, Richard B. Southworth, and Carl S. Nilsson, eds., Special Rep. 239, Smithsonian Astrophysical Observatory (Cambridge, Mass.), 1967, pp. 1-46.

26-2. Wood, J. A.: Physics and Chemistry of Meteorites. The Moon, Meteorites and Comets. Vol. IV of The Solar System, Barbara M. Middlehurst and Gerard P. Kuiper, eds., University of Chicago Press, 1963, pp. 337-401.

26-3. Whipple, Fred L.: The Meteoritic Risk to Space Vehicles. Vistas in Astronautics, Morton Alperin, ed., Pergamon Press (Los Angeles), 1958.

26-4. Opik, Ernst Julius: Physics of Meteor Flight in the Atmosphere. Interscience Pub., Inc. (New York), 1958.

26-5. Allen, H. Julian; and Baldwin, S., Jr.: Frothing as an Explanation of the Acceleration Anomalies of Cometary Meteors. J. Geophys. Res., vol. 72, no. 13, July 1, 1967, pp. 3483-3496.

26-6. Lovell, Alfred Charles Bernard: Meteor Astronomy. Clarendon Press (Oxford), 1954.

26-7. McKinley, Donald William Robert: Meteor Science and Engineering. McGraw-Hill Book Co., Inc., 1961.

26-8. Alexander, W. M.; McCracken, C. W.; Secretan, L.; and Berg, O.: Review of Direct Measurements of Interplanetary Dust from Satellites and Probes. Proceedings of the Third International Space Science Symposium. Wolfgang Priester, ed., Interscience Pub., Inc. (New York), 1963, pp. 891-917.

26-9. Hastings, Earl C., Jr.: The Explorer 16 Micrometeoroid Satellite. Supplement III, Preliminary Results for the Period May 27, 1963, Through July 22, 1963. NASA TM X-949, 1964.

26-10. O'Neal, R. L.: The Explorer 23 Micrometeoroid Satellite. Description and Results for the Period Nov. 6, 1964, Through Nov. 5, 1965. NASA TN D-4284, 1968.

26-11. Clifton, Stuart; and Naumann, Robert: Pegasus Satellite Measurements of Meteoroid Penetration (Feb. 16, 1965, Through Dec. 31, 1965). NASA TM X-1316, 1966.

26-12. Zook, Herbert A.; Flaherty, Robert E.; and Kessler, Donald J.: Meteoroid Impacts on the Gemini Windows. Planet. Space Sci., vol. 18, no. 7, July 1970, pp. 953-964.

26-13. Flaherty, Robert E.: Impact Characteristics in Fused Silica for Various Projectile Velocities. J. Spacecraft and Rockets, vol. 7, no. 3, Mar. 1970, pp. 319-324.

26-14. Cour-Palais, B. G.; Whipple, Fred L.; D'Aiutolo, C. T.; Dalton, C. C.; et al.: Meteoroid Environment Model - 1969 (Near Earth to Lunar Surface). NASA SP-8013, 1969.

26-15. Cour-Palais, B. G.; Flaherty, R. E.; High, R. W.; Kessler, D. J.; et al.: Results of the Surveyor III Sample Impact Examination Conducted at the Manned Spacecraft Center. Proceedings of the Second Lunar Science Conference, vol. 3, A. A. Levinson, ed., MIT Press (Cambridge, Mass.), 1971, pp. 2767-2780.

26-16. Cour-Palais, Burton G.; Flaherty, Robert E.; and Brown, Milton L.: Apollo Window Meteoroid Experiment. Sec. 24 of Apollo 15 Preliminary Science Report, NASA SP-289, 1972.

26-17. Hartung, Jack B.; Horz, Friedrich; and Gault, Donald E.: Lunar Microcraters and Interplanetary Dust. Proceedings of the Third Lunar Science Conference, vol. 3, David R. Criswell, ed., MIT Press (Cambridge, Mass.), 1972.

26-18. Carter, J. L.; and McKay, D. S.: Influence of Target Temperature on Crater Morphology and Implications on the Origin of Craters on Lunar Glass Spheres. Proceedings of the Second Lunar Science Conference, vol. 3, A. A. Levinson, ed., MIT Press (Cambridge, Mass.), 1971, pp. 2653-2670.

27. Biomedical Experiments

PART A

BIOSTACK EXPERIMENT

Horst Bücker,[a†] G. Horneck,[a] E. Reinholz,[b] W. Scheuermann,[c] W. Rüther,[d] E. H. Graul,[d] H. Planel,[e] J. P. Soleilhavoup,[e] P. Cüer,[f] R. Kaiser,[f] J. P. Massué,[f] R. Pfohl,[f] R. Schmitt,[f] W. Enge,[f] K. P. Bartholomä,[g] R. Beaujean,[g] K. Fukui,[g] O. C. Allkofer,[g] W. Heinrich,[g] H. François,[h] G. Portal,[h] H. Kühn,[i] H. Wollenhaupt,[a] and G. H. Bowman[j]

The biostack experiment was designed to study the biologic effects of individual heavy nuclei of galactic cosmic radiation during space flight outside the magnetosphere of the Earth. Specifically, the biostack experiment was designed to promote research on the effects of high energy/high Z (HZE) particles of galactic cosmic radiation on a broad spectrum of biologic systems, from the molecular to the highly organized and developed forms of life. The experiment was considered unique and scientifically meritorious because of its potential yield of information – currently unavailable on Earth – on the interaction of biologic systems with the heavy particles of galactic cosmic radiation.

Objectives

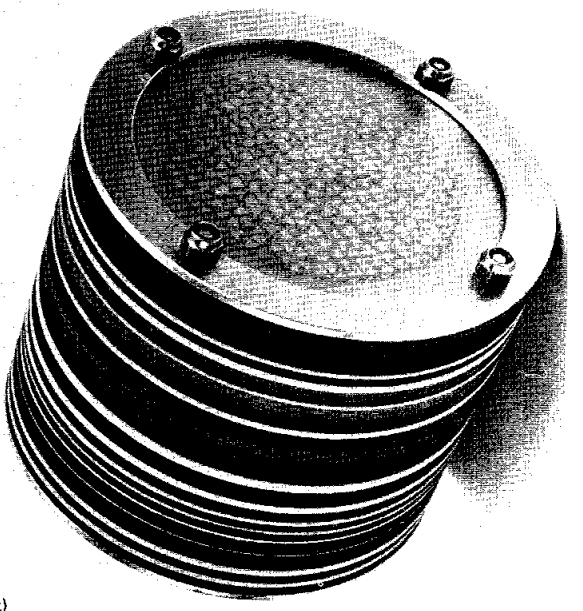
The flight objectives of the biostack experiment were achieved by using a hermetically sealed aluminum container (fig. 27-1), which contained a series of monolayers of select biologic material, each of which was sandwiched between several different types of detectors of galactic cosmic radiation particles. The biologic systems included spores or inactive forms of the bacterium *Bacillus subtilis*; dry seeds of *Arabidopsis thaliana*, commonly known as the European water cress; radiculae or embryos of the bean *Vicia faba*; and encysted eggs of the tiny brine shrimp *Artemia salina*, one of the most primitive crustaceans. The biologic effects of HZE particles under consideration in this Apollo 16 experiment are (1) physicochemical inactivation of molecular and cellular function, (2) radiation-induced damage to nuclei and other subcellular systems, (3) radiation-induced mutations leading to genetic changes of biologic significance, and (4) modification of growth and development of tissues.

The biologically passive or dormant systems were stacked alternately between physical detectors of HZE particle tracks, which included nuclear emulsions (Ilford K2 and K5) and plastics (cellulose nitrate (CN) and polycarbonate (PC)) as well as lithium fluoride (LiF) thermoluminescent (radiation) dosimeters (TLD's) located at the top and bottom of the biostack. A typical configuration of biologic layers and detectors is illustrated in figure 27-2. This arrangement was used because it permits correlation of the incident HZE particle with its interaction with ("hit" of) a biologic structure and the physicochemical characteristics and properties of the particle. This combination of track detectors with overlapping sensitivities to ionizing radiation was chosen to differentiate between the types and relative quantity (fluence) of HZE particles traversing or stopping in the biostack. Nuclear emulsions can detect, essentially, all ionizing events and, therefore, can provide information on (1) the total fluence of particles from galactic cosmic radiation and (2) the protons and electrons deriving from the trapped radiation belts. The emulsions will record particles with a low energy

[a]University of Frankfurt.
[b]Max Planck Institut fur Biophysik, Frankfurt.
[c]Technical University of Hanover.
[d]University of Marburg.
[e]University of Toulouse.
[f]University of Strasbourg.
[g]University of Kiel.
[h]Atomic Energy Commission, Republic of France.
[i]Abteilung für Biophysikalische Strahlenforschung, Frankfurt, Gesellshaft für Strahlen und Umweltforschung.
[j]U.S. Representative for University of Frankfurt for biostack.
†Principal Investigator.

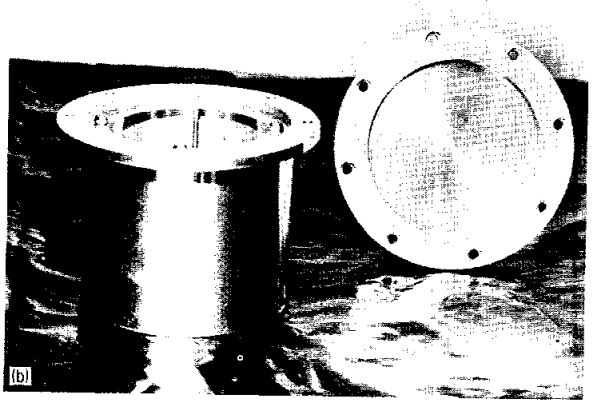


(a)



(c)

FIGURE 27-1.–The biostack. (a) Hermetically sealed. (b) Partially disassembled after flight. (c) Monolayers of biologic materials and detectors of galactic cosmic radiation particles.



(b)

loss rate (a low linear energy transfer), whereas the plastic detectors respond to particles with an energy loss rate above a critical value. Cellulose nitrate, for instance, does not respond to protons and electrons but records particles of charge Z of $Z \geqslant 4$ and of a restricted energy loss REL of $REL \geqslant 0.8 \times 10^3$ MeV cm^2/g. The least sensitive to all particles is polycarbonate, which responds to particles of $Z \geqslant 10$ with an $REL \geqslant 3.3 \times 10^3$ MeV cm^2/g. Thus, particles can be discriminated by energy loss, charge, and radius of interaction with the polymeric materials of the detector.

Apollo 16 Flight Unit

The 2-kg, 4.0- by 5.0-in. biostack experiment was stowed in the Apollo 16 command module as shown in figure 27-3. The structural shielding against ambient radiation in the command module stowage area for the biostack experiment is represented schematically. Thus, the experiment was located in an area of the command module where the shielding to ambient cosmic radiation appears to have been minimal.

Immediately following their return to Frankfurt, the flight unit (serial number (S/N) 5) and the backup unit (S/N 6) were taken to the University of Strasbourg for disassembly. The backup unit, which served as an Earth control during the mission, was disassembled first. The disassembly was performed without complications, and no changes or damage to the software were noticed. Thereafter, the flight unit was dismantled. The temperature recorded on the two minimum-maximum thermometers in the ground-support equipment indicated a range of 293° to 298° K, which was within the limits of 248° to 298° K specified for the experiment. The temperature in the command module ranged from 289° to

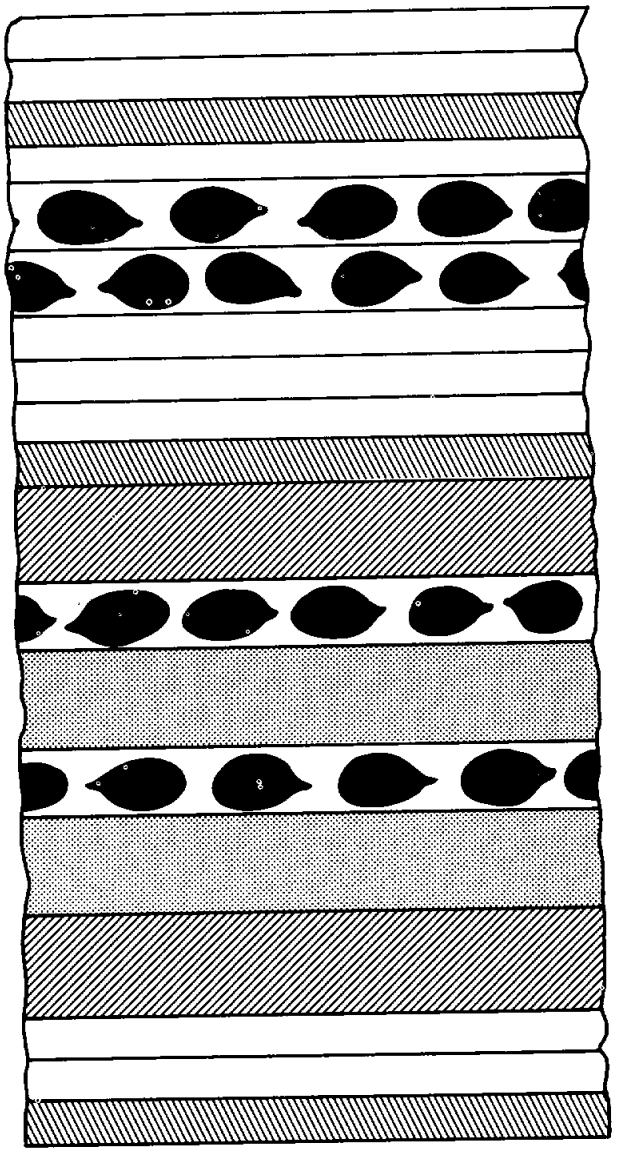
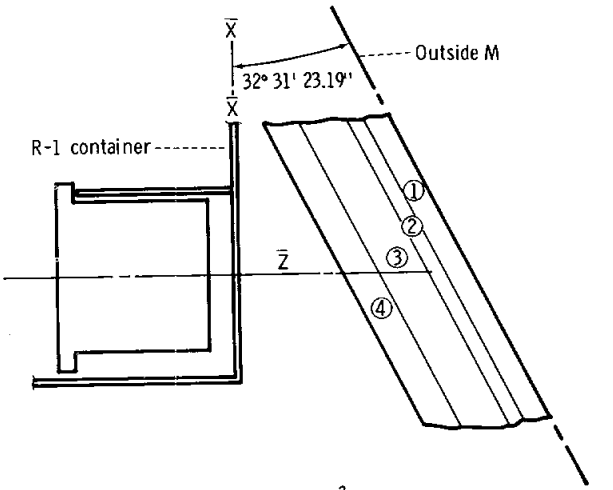


FIGURE 27-2.–Typical configuration of biologic layers and detectors in the biostack.

300° K, within an accuracy of ±3° K, indicating the possibility of a slight, but experimentally insignificant, temperature excursion beyond the specified upper limit.



① Ablator - 0.7 in. thick, 32 lb/ft^3

② Honeycomb consisting of face sheet, core, and face sheet:
Face sheet - 15-7 stainless steel, 0.008 in. thick
Core - 15-7 stainless steel, 0.484 in. thick;
cell diameter, 3/16 in.; cell wall, 0.001 in.

③ Insulation - TG 15 000, 1.25 in. thick, 0.6 lb/ft^3

④ Honeycomb consisting of face sheet, core, and face sheet:
Face sheet - T6 aluminum, 0.01 in. thick
Core - 5052 H39 aluminum, 0.9 in. thick;
cell diameter, 3/16 in.; cell wall, 0.001 in.

FIGURE 27-3.–Stowage location of the biostack and structural shielding of the Apollo 16 command module.

During disassembly, the pattern of the biologic objects positioned directly over a K2 nuclear emulsion was transferred to the upper side of the adjacent emulsion by optical illumination. This illumination took place when the biologic layer under consideration was still stacked on the biostack support bolts and pressed onto its supporting emulsion sheet. On each sheet of nuclear emulsion, a coordinate grid was placed on the bottom side by optical illumination. After disassembly, each biologic layer that was stacked over a K2 nuclear emulsion was photographed to identify the exact position of the biologic objects, with respect to the emulsion, following removal of the biologic specimen for individual evaluation.

Preliminary Observations

Dosimetry and particle detection.–The LiF TLD's were used to measure the ambient (background) radiation, which consists of the protons and electrons of the trapped radiation belts and the electromagnetic

component. The doses recorded are shown in table 27-I. The total dose for the mission as measured by the LiF TLD was determined to range between 505 and 622 mrad. The LiF TLD on the bottom of the flight biostack (A 1-0, table 27-I), which was directed to the command module outer wall, indicated a higher dose than the one on the top of the stack (A 9-15, table 27-I). The measured doses have been corrected for the presence of thermal neutrons, considering the results of earlier Apollo missions (refs. 27-1 and 27-2). The LiF TLD preparation used in the biostack did not contain lithium fluoride enriched with the isotope ^{7}Li, which is insensitive to thermal neutrons.

TABLE 27-I.–Dose of Cosmic Radiation During the Apollo 16 Mission Measured by LiF TLD

Layer no.	Dose, mrad		
	Read (a)	Ground control dose subtracted	Correction for thermal neutrons
Flight sample			
A 1-0	680	645	575 to 622
A 9-15	610	575	505 to 552
Ground control sample			
B 1-0	35	0	–
B 9-15	35	0	–

[a]Mean value, calculated from 10 measurements, precision ±2 percent.

Nuclear emulsion analyses.–Precise evaluations are possible from the processed K2 nuclear emulsions. The coordinate grid and the tracks of heavy ions are seen clearly in figure 27-4. The procedure for processing nuclear emulsions has been described in detail in the Biostack Quick-Look Report (submitted to NASA June 5, 1972). Approximately 1 particle track/mm^2, resulting from the penetration of HZE particles of $Z \geqslant 4$, and approximately 1 ender/cm^2 have been detected by rough scanning. Figures 27-5 and 27-6 record a track of a heavy ion ending in a K2 emulsion layer of the biostack flight unit.

The K5 emulsions, which are more sensitive to protons and electrons than are the K2 emulsions, are very dark because of the high background of protons and electrons. The fluence measured by the K5



FIGURE 27-4.–A K2 nuclear emulsion layer of the biostack flight unit.

emulsions is approximately 100 000 particles/cm^2 (fig. 27-7). This fluence was greater than anticipated. Thus, a quantitative evaluation of the HZE tracks and of the particles that created the tracks is rather difficult because of the dense background.

Cellulose nitrate analyses.–The recording of charged particles in plastic detectors is based on a preferential etching along the path of the particle as it penetrates the plastic sheets. The energy lost by the particle along the path changes the molecular structure of the plastic and thereby results in the preferential etching. The CN sheets not in contact with biologic layers were etched in a mechanically stirred 6N sodium hydroxide (NaOH) bath at 313° K and were agitated ultrasonically at the same time. Figure 27-8 shows the etch cone of the trajectory of a particle with high energy loss and estimated to be an iron particle of Z = 26. For the entire Apollo 16 mission, a fluence of 33 particles/cm^2 of $REL \geqslant 0.8 \times 10^3$ MeV cm^2/g was determined at the bottom of the biostack, which was close to the outer wall of the

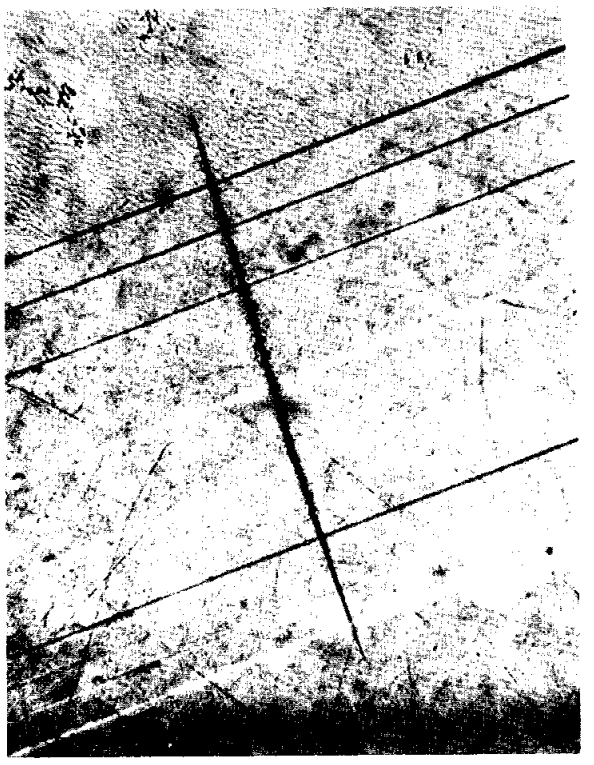


FIGURE 27-5.–An ender in a K2 nuclear emulsion layer of the biostack flight unit.

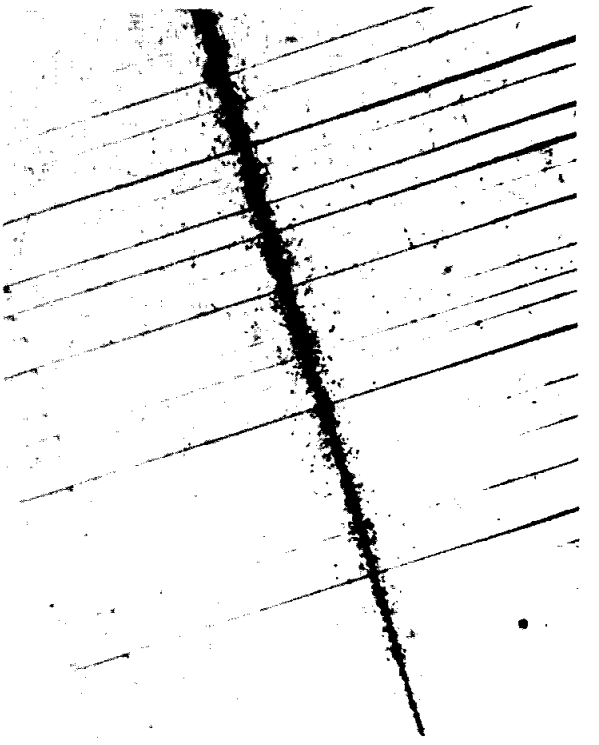


FIGURE 27-6.–An ender in a K2 nuclear emulsion layer of the biostack flight unit (same view as fig. 27-5).

command module. At the top of the biostack (farther away from the outer wall), a fluence of 18 particles/cm^2 was measured. This change of particle fluence results from absorption because of the 10- to 15-g/cm^2 effective shielding deeper in the stack. The particles have been grouped in the following categories according to the etch cone characteristics observed.

(1) Connected etch cones resulting in an etch hole through the plastic

(2) Two separated etch cones

(3) One etch cone with a rounded point indicative of a particle from outside the spacecraft stopping in the plastic

(4) One etch cone with a rounded point indicative of a particle from inside the spacecraft stopping in the plastic.

The track etching rate is a function of the energy loss of the particle. Therefore, particles of each category (1 to 4) are of the same range of energy loss. The results are presented in table 27-II. As in nuclear emulsions, approximately 100 heavy particle tracks/cm^2 were observed, and the total fluence was composed of (1) 33 particles/cm^2 of $REL \geqslant 0.8 \times 10^3$ MeV cm^2/g and (2) 67 particles/cm^2 of $REL < 0.8 \times 10^3$ MeV cm^2/g.

During the etching in NaOH of those CN sheets that were in fixed contact with a biologic layer, precautions were taken to protect the biologic objects from the noxious and caustic solution. A specially designed etching frame is used (fig. 27-9) so that the side of the sheet containing the biologic specimen in polyvinyl alcohol (PVA) is sealed and no etching liquid can attack the biologic materials. The other side of the sheet (CN) is etched to develop the cones. Etching is performed at 303° K in a well-stirred 6N NaOH solution for 4.5 hr.

Hit biologic objects.–Biologic layers in contact with K2 nuclear emulsions, biologic layers in contact with CN sheets, and comparative viability of biologic



FIGURE 27-7.–A K5 nuclear emulsion layer from the biostack flight unit.

objects are considered in the following discussion of hit biologic objects.

Biologic layers in contact with K2 nuclear emulsions: The K2 nuclear emulsions, which were positioned below a biologic layer, carry (on their upper side) a faint, negative photograph of these biologic objects in the exact geometry of exposure. The pattern of the objects in natural size was reproduced in the emulsion by weak illumination during disassembly of the biostack. The bottom side of the emulsion carries a faint photograph of the coordinate grid. Thus, the same emulsion shows the tracks of the penetrated particles, the pattern of the biologic objects, and the coordinate grid (fig. 27-10). Microscopic analysis of this emulsion establishes the exact region of the biologic object that has been hit by a galactic cosmic particle.

Biologic layers in contact with CN sheets: The CN sheets are in fixed contact with the PVA foils containing biologic materials. This contact is main-



FIGURE 27-8.–Etch cone of a trajectory of an HZE particle with high energy loss (total projected length, 2.300 mm) in a CN layer of the biostack flight unit.

tained during flight, during etching and microscopic analysis of the detector, and, in the case of *Bacillus subtilis* spores, during the biologic analyses. The path of the particle inside the biologic layer can be located by measuring all coordinates of the etch cone in the CN and extending the path of the particle into the biologic layer (fig. 27-11). This procedure has been detailed previously (ref. 27-3).

Viability of the biologic objects: The viability of the flown but unhit *Bacillus subtilis* spores (weightless and non-HZE-irradiated controls) was compared

TABLE 27-II.–Particles in 20 cm^2 During Apollo 16 Mission From CN Analysis

Location and layer no.	Particles in 20 cm^2 (a)				Fluence	
	Etch holes (1)	Two cones (2)	Stopping tracks from –			
			Outside (3)	Inside (4)	In 20 cm^2	In 1 cm^2
Bottom sheet,[b] A 1-1	263	292	62	34	651	32.6
Top sheet, A 9-9	151	182	13	12	358	17.9

[a]Number in parentheses represents particle category.
[b]The bottom sheet (A 1-1) is close to the outside of the vehicle.

with the viability of those of both Earth-based controls. One control was maintained in Frankfurt at 277° K during the mission, and the other (S/N 6) accompanied the flight unit to the NASA John F. Kennedy Space Center (KSC) and later was transferred to the NASA Manned Spacecraft Center (MSC) during the mission. From table 27-III, it can be seen that germination and outgrowth of the flight-unit, nonirradiated control spores did not differ remarkably from those of the Earth control spores. Therefore, the unusual environmental parameters and factors of space flight exerted no significant influence on the development of *B. subtilis* spores. The process of germination (full phase microscopy darkening) and outgrowth is shown in figures 27-12(a) to 27-12(g).

The germination of Apollo 16 *Arabidopsis thaliana* seeds that were not hit by an HZE particle (the flight-unit, nonirradiated control) was 84 percent. This degree of germination agrees with the Earth control values of 84 percent for seeds from one layer of S/N 6 and 83 percent for seeds from the Earth control that was maintained in Frankfurt during the Apollo 16 mission. These results indicate that the flown but unhit seeds of *A. thaliana* possess the biologic capacity for full viability.

The rather thick and moist PVA layers enclosing the radiculae of *Vicia faba* were partially dried during the mission. Therefore, the water content of the radiculae is assumed to be reduced from the 15-percent preflight value. This additional drying favors the viability of the radiculae.

The hatchability of 100 flown but unhit eggs of *Artemia salina* tested as a flight control was shown by the hatching of 70 percent of the eggs into normal adults. This value agrees with the Earth control data.

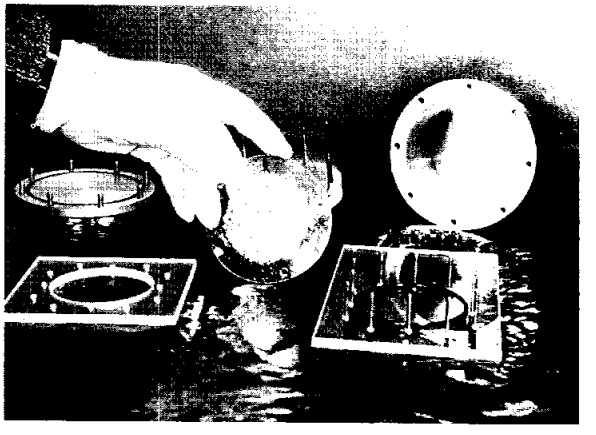


FIGURE 27-9.–Etching frame for CN sheets carrying biologic layers designed to protect the biologic material from the NaOH etching liquid.

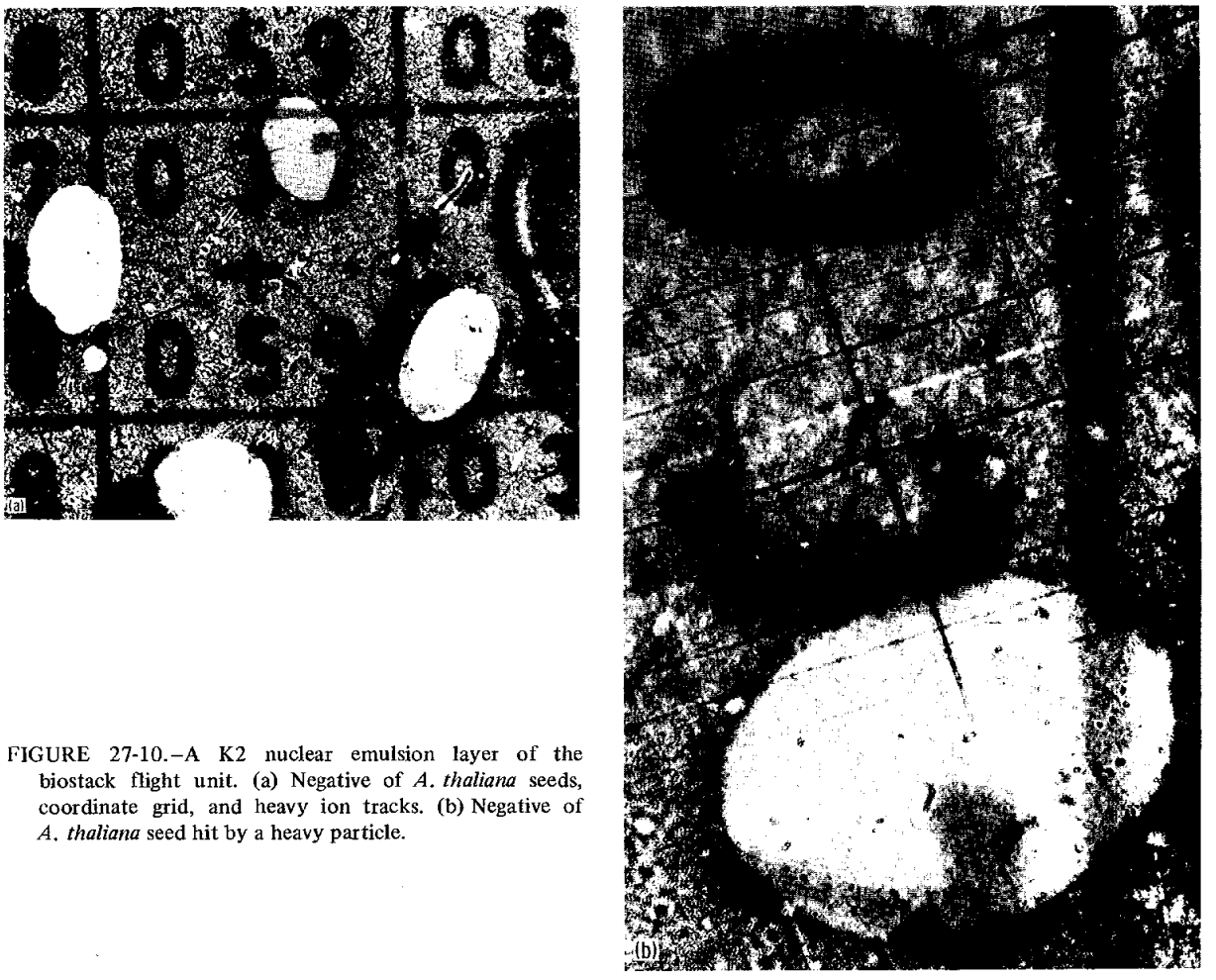


FIGURE 27-10.–A K2 nuclear emulsion layer of the biostack flight unit. (a) Negative of *A. thaliana* seeds, coordinate grid, and heavy ion tracks. (b) Negative of *A. thaliana* seed hit by a heavy particle.

TABLE 27-III.–Germination and Outgrowth of B. Subtilis Spores During Incubation on Nutrient Agar

Incubation time at 310° K, min	*Flight control unit, etched 4.5 hr at 303° K*		*Ground control unit at KSC/MSC, etched 4.5 hr at 303° K*		*Ground control unit at Frankfurt, stored at 277° K*	
	Germination, percent	*Outgrowth, percent*	*Germination, percent*	*Outgrowth, percent*	*Germination, percent*	*Outgrowth, percent*
70	94.7	67.4	98.3	95.0	97.8	81.6
100	96.5	86.7	98.3	95.0	97.8	82.8
130	97.3	86.6	98.3	95.0	97.8	84.7
160	97.5	86.7	98.3	95.0	97.9	85.0

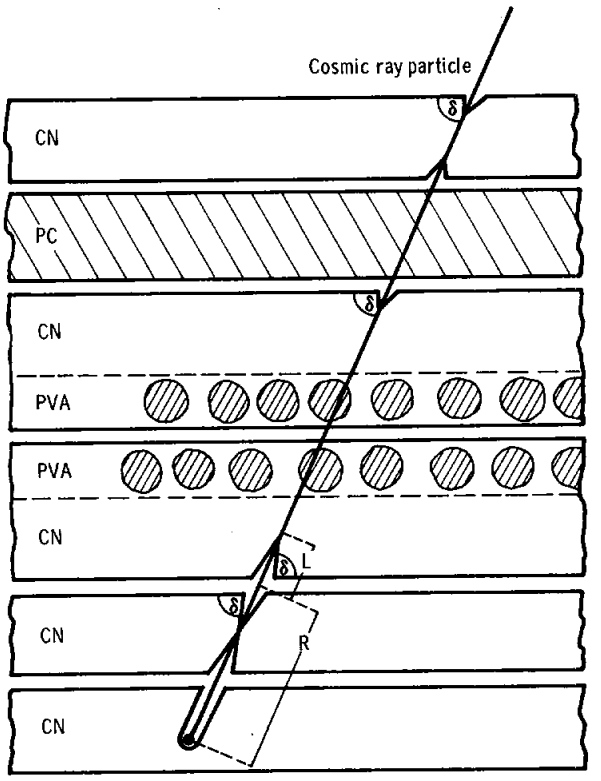


FIGURE 27-11.–Schematic of part of a biologic unit in fixed contact with the CN sheets. Measurement of the dip angle δ is made to determine (1) the hit biologic object, (2) the cone length L (to determine energy loss), and (3) the residual range R (to establish the particle charge).



FIGURE 27-12.–Germination and outgrowth of *B. subtilis* spores, flight control unit. (a) A CN sheet with *B subtilis* spores.

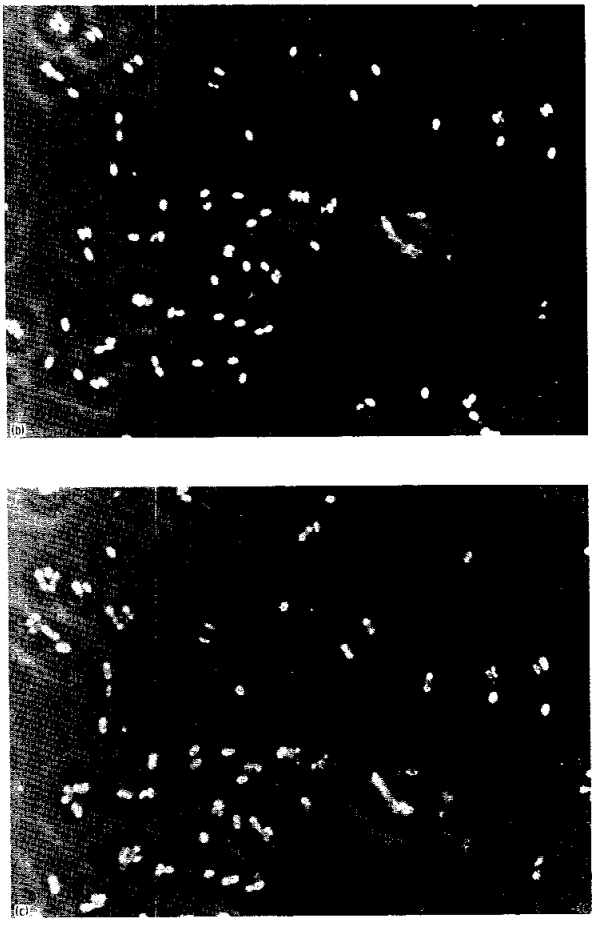
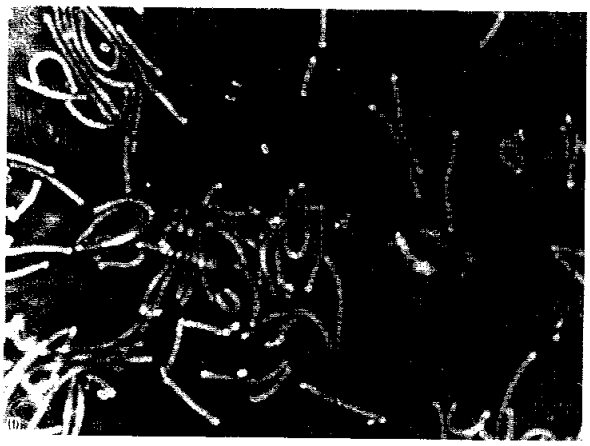


FIGURE 27-12.–Continued. (b) After addition of nutrient agar. (c) After incubation for 100 min at 310° K. (d) After incubation for 130 min at 310° K.





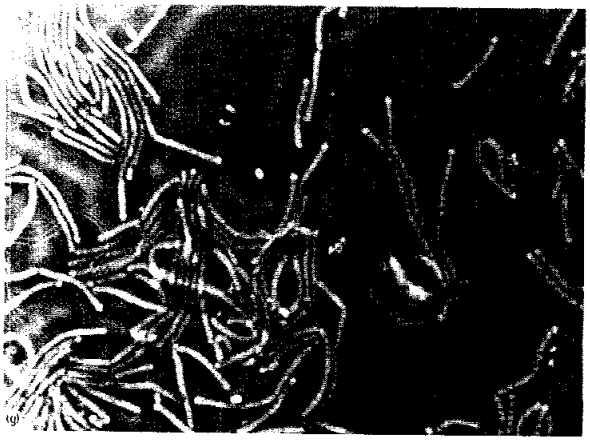


FIGURE 27-12.–Concluded. (e) After incubation for 160 min at 310° K. (f) After incubation for 200 min at 310° K. (g) After incubation for 260 min at 310° K.

Conclusions

The first postflight treatment of the biostack experiment material was scientifically satisfactory. The transport of the flight, backup, and Earth control units from MSC to Frankfurt, their disassembly, the HZE particle detector development, and the preliminary analyses were performed without untoward difficulties.

The preliminary results indicate (1) that the fluence and the physicochemical characteristics of the HZE particles can be determined by visual (microscopic) analyses of the detectors in the experimental configuration, (2) that the hit region of the biologic object can be identified and correlated with the track of the HZE particle, and (3) that the biologic material unhit by an HZE particle is not injured biologically by the other factors of the space-flight environment.

The unhit biologic objects of the flight unit served as flight controls not exposed to or encountering HZE particles. The backup unit, S/N 6, was used as an Earth control for this phase of the analyses. Two additional Earth control units, S/N 3 and S/N 4, remained fully assembled and hermetically sealed. These units were retained for additional tests that might be required, such as simulation of the actual flight profile, especially temperature, of the Apollo 16 command module and/or participation in a balloon flight. However, the temperature profile of of the Apollo 16 command module ranged approximately within the limits specified for the experiment. Because this information and data on the viability of the biologic objects were experimentally satisfactory, it was unnecessary to use S/N 3 and S/N 4 for a simulation of flight temperature. Instead, biostack S/N 3 was flown on a balloon flight in July 1972 launched from Fort Churchill during the 1972 Skyhook Program of the Office of Naval Research. Biostack S/N 4 was maintained as an Earth control.

Systematic postflight analyses are continuing. These analyses include (1) the identification of biologic objects hit by HZE particles, (2) studies on the biologic effects caused by radiation from the interaction of HZE particles, and (3) determination of charge and energy loss of the biologically effective heavy particles from further analyses of the nuclear emulsions and of the CN and PC detectors.

PART B

MICROBIAL RESPONSE TO SPACE ENVIRONMENT

G. R. Taylor,[a†] C. E. Chassay,[a] W. L. Ellis,[b] B. G. Foster,[c‡]
P. A. Volz,[d‡] J. Spizizen,[e‡] H. Bücker,[f] R. T. Wrenn,[b] R. C. Simmonds,[a]
R. A. Long,[b] M. B. Parson,[b] E. V. Benton,[g] J. V. Bailey,[a]
B. C. Wooley,[a] and A. M. Heimpel[h]

Introduction

Microorganisms have been subjected to a large variety of space-flight conditions on the following U.S. and Soviet missions: Sputnik 4 to 6, Vostok 1 to 6, Voskhod 1 and 2, Cosmos 110, Nerv I, Discoverer XVIII, Gemini IX, X, and XII, Agena VIII, and Biosatellite II. These flights carried a large array of viruses, bacteria, and fungi that were exposed to many different space-flight conditions.

Most of these microbiology studies were concerned with establishing the now-accepted principle that microbes can survive in the harsh space environment. However, during the conduct of these viability studies, certain anomalies were noticed. These anomalies suggested that the survival of some microbes were affected synergistically, whereas others were adversely affected by the space environment. For example, aqueous suspensions of spores from members of the genus *Streptomyces (Actinomyces* in U.S.S.R.) demonstrated quite different results after exposure to space-flight conditions aboard the third, fourth, and fifth Russian satellites (ref. 27-4). The space-flight conditions reportedly increased the incidence of spore germinations of strain 2577 of *S. erythreus* by approximately six times that of the ground controls; however, the viability of strain 8594 decreased sharply. These examples are typical of past survival studies in which results were evenly divided among those that report synergism, antagonism, or no relationship between space flight and microbial viability (refs. 27-4 to 27-9). Unfortunately, most of these studies were hindered by technical constraints, mission anomalies, or the inability to provide meaningful controls; despite the best efforts of the investigators, equivocal results were often produced. Some of the objectives of the microbial response to space environment experiment system were to take advantage of the considerable array of past experimentation, to overcome as many equivocating obstacles as possible, and to help establish a relationship between space flight and the viability of several different microbial systems.

A few of the more recent U.S. and U.S.S.R. microbiology studies have investigated the effect of space flight on other parameters. Generally, these studies have involved genetic changes; as with the survival studies, variable results have been obtained (refs. 27-5, 27-7, 27-8, and 27-10 to 27-15). However, the combined results of these studies overwhelmingly suggest synergistic or antagonistic relationships between microbial genetic alterations and space-flight conditions. Recognizing this situation, the National Academy of Sciences (ref. 27-16) observed that "The possibility that the special conditions of long-duration space missions may give rise to microbial mutants must be carefully considered" and recommended that future experimentation should "investigate the effect of spacecraft conditions on the rate of mutations in different microorganisms. . . ." The microbial response to space environment experiment was conducted in an effort to help satisfy this requirement.

Experiment Design

From the many microbial species and challenge systems available, the experiment system outlined in

[a]NASA Manned Spacecraft Center.
[b]Northrop Services, Inc.
[c]Texas A. & M. University.
[d]Eastern Michigan University.
[e]Scripps Clinic and Research Foundation.
[f]University of Frankfurt.
[g]University of San Francisco.
[h]U.S. Department of Agriculture.
†Principal Investigator.
‡Coinvestigator.

TABLE 27-IV.–Biological Components

Phenomenon studied	*Assay system*	*Microorganism*	*Investigator*
Lipolytic α toxin production Deforming β toxin production Fatal δ toxin production	Lytic zone on agar *Sarcina flava* and house fly Silk worm and crystal assay	*Bacillus thuringiensis*	R. T. Wrenn, W. L. Ellis Northrop Services, Inc. Houston, Texas G. R. Taylor, R. C. Simmonds NASA Manned Spacecraft Center Houston, Texas A. M. Heimpel U.S. Dept. of Agriculture Beltsville, Maryland
Infectivity	Mouse	*Nematospiroides dubius*	R. A. Long, W. L. Ellis Northrop Services, Inc. Houston, Texas G. R. Taylor NASA Manned Spacecraft Center Houston, Texas
Hemorrhagic factor production Hemolytic enzyme production	Guinea pig and hemoglobin Human erythrocytes	*Aeromonas proteolytica*	B. G. Foster, D. O. Lovett Texas A. & M. University College Station, Texas
Genome alteration	Spore production	*Bacillus subtilis* spores, strains HA 101 (59) and HA 101 (59) F	J. Spizizen, J. E. Isherwood Scripps Clinic and Research Foundation La Jolla, California
UV and vacuum sensitivity	Colony formation	*Bacillus subtilis* spores, strain 168	H. Bücker, G. Horneck, H. Wollenhaupt University of Frankfurt, Germany
Bacteria phage infectivity	Host lysis	*Escherichia coli* (T-7 phage)	J. Spizizen, J. E. Isherwood Scripps Clinic and Research Foundation La Jolla, California
Cellulolytic activity	Cloth fibers	*Chaetomium globosum*	P. A. Volz, Y. C. Hsu, D. E. Jerger, J. L. Hiser, J. M. Veselenak Eastern Michigan University Ypsilanti, Michigan
Animal tissue invasion	Human hair	*Trichophyton terrestre*	
Drug sensitivity	Antibiotic sensitivity in agar	*Rhodotorula rubra* *Saccharomyces cerivisiae*	

table 27-IV was established. In most cases, the studied phenomena represent well-known model systems that can be directly correlated with disease or other medically important conditions that could affect the health of future astronauts. Scientific investigators were invited to study those phenomena within their area of expertise and to conduct critical investigations in their laboratories. This method allowed many individual studies to be conducted in a coordinated manner and permitted a variety of

microorganism species to be housed within a single piece of flight hardware. Each investigator selected a species of microorganism that was nonpathogenic to man (to avoid possible contamination of the crew), was well characterized relative to the phenomenon to be studied, was well suited to simple and rapid screening tests, and was compatible with the unique environment of the flight hardware.

To allow for dose-response studies and comparative investigations, certain variables were provided within the flight hardware. Microbes could be suspended in 50 μl of fluid or could be dried on a suitable carrier. Some microbes were exposed to the vacuum of space, whereas others were retained at 1 atmosphere. Because detailed genetic studies require the exposure of test systems to a mutagenic source, provisions were made to expose the systems to the full light of space or to components of the solar UV spectrum at peak wavelengths of 254, 280, and 300 nm. An optical filtering system was provided to control the total radiant energy reaching exposed test systems from a minimum of 4×10^1 ergs/cm^2 to a maximum of 8×10^8 ergs/cm^2. The use of ambient solar radiant energy as the mutagen necessitated close monitoring of this factor. Photographic emulsion and a modification of the potassium ferrioxalate system of Wrighton and Witz (ref. 27-17) were used to record the amount of radiant energy that actually reached selected tests systems (table 27-V). The possible mutagenic activity of galactic radiation necessitated the inclusion of lithium fluoride (LiF) thermoluminescent dosimeters (TLD's) and a package of passive nuclear track detectors capable of recording high-energy multicharged particles (table 27-V).

Description of the Flight Hardware

Each microbial sample, containing 100 to 1 million live cells (as appropriate), was housed in a 4-mm quartz-glass-windowed cube (fig. 27-13). The use of nearly 1400 of these chambers (called cuvettes) in the flight and ground control units permitted adequate experimental replication. All loaded cuvettes that were to be exposed to UV irradiation were placed beneath neutral density filters situated under bandpass filters. These combined optical filters controlled, respectively, the amount and the wavelength of light reaching the microbial system (fig. 27-14). Cuvettes and optical filters were placed in trays (fig. 27-15) mounted in an 11.43- by 11.43- by 25.4-cm hardware case. The flight hardware (fig. 27-16), called the microbial ecology evaluation device (MEED), contained 798 cuvettes with microorganisms, 140 neutral density filters, 28 bandpass filters, eight recording thermometers, one high-energy

TABLE 27-V.–Dosimetry Components

Measurement	*Monitor used*	*Assay systems*	*Investigator*
High-energy multicharged particles	Passive nuclear track detectors	Lexan Cellulose nitrate Photographic emulsion Silver chloride	E. V. Benton University of San Francisco San Francisco, California
Ultraviolet light	Passive dosimeters	Potassium ferrioxalate actinometry Photographic emulsion	M. B. Parson, R. A. Long, W. Ellis Northrop Services, Inc. Houston, Texas G. R. Taylor NASA Manned Spacecraft Center Houston, Texas
Penetration of galactic irradiation	Thermoluminescent dosimeters	Lithium fluoride	J. V. Bailey NASA Manned Spacecraft Center Houston, Texas R. A. English, R. D. Brown Kelsey-Seybold Clinic Houston, Texas

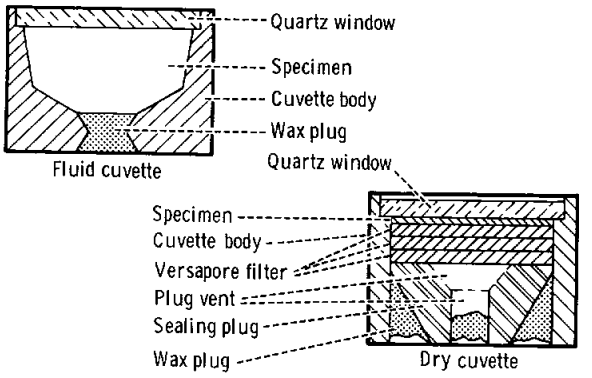


FIGURE 27-13.–The MEED cuvette design.

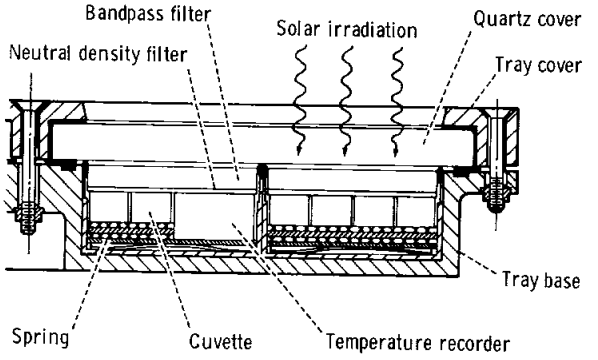


FIGURE 27-14.–Optical filter configuration.

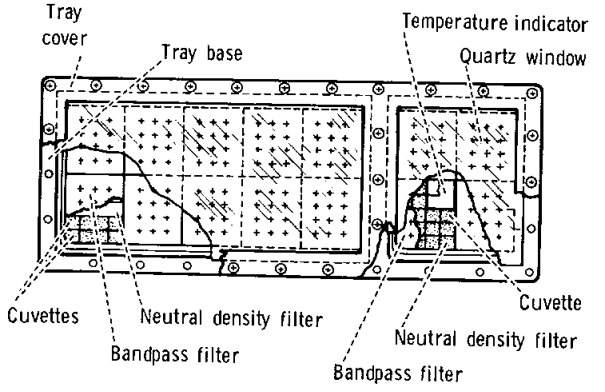


FIGURE 27-15.–Tray interior details of the MEED.

multicharged particle dosimeter, 64 potassium ferrioxalate actinometry cuvettes, 44 photographic film cuvettes, and 18 TLD cuvettes. A similar number of components were used in the various ground control units.

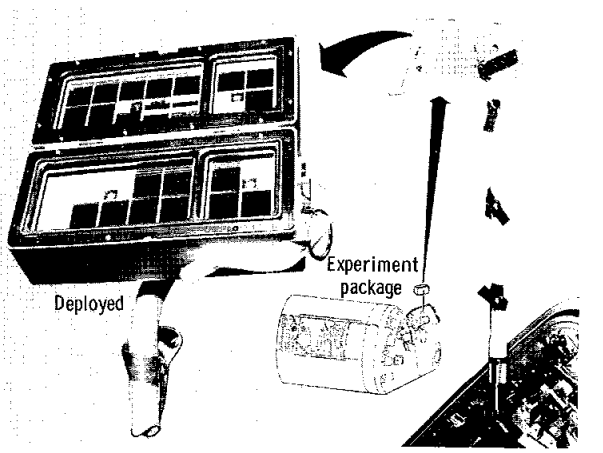


FIGURE 27-16.–Hardware for the microbial response in space environment experiment.

Deployment of the MEED

During the Apollo 16 transearth coast extravehicular activity, the MEED hardware was removed from its protective stowage bag in the crew compartment and affixed to the distal end of the television boom, which was then attached to the handle of the opened hatch door (fig. 27-16). A small attitude adjustment of the spacecraft was required to place the appropriate surface of the MEED directly perpendicular to rays of the Sun. This adjustment was indicated by a solar-positioning device incorporated into the exterior surface of the MEED. After the spacecraft attained the proper attitude, the MEED was opened by the command module pilot so that the microbial test systems and actinometers were exposed to the direct rays of the Sun (fig. 27-16). After exactly 10 min of such exposure, the device was closed, removed from the television boom, and replaced in the protective bag for transport back to the NASA Manned Spacecraft Center.

Analysis of Preliminary Data

The results of survival studies are presently available for most systems. However, full evaluation of many of the more detailed genetic studies must await more lengthy investigation and cannot be incorporated into this report. Information provided by the cognizant investigator for each test system is presented in the following paragraphs.

Aeromonas proteolytica.—The microorganism *A. proteolytica* produced an endopeptidase that can cause intracutaneous hemorrhage and necrosis in laboratory animals (ref. 27-18). A second factor, elaborated into the culture fluid, has the ability to hemolyze human erythrocytes (ref. 27-18). This microbe was retained in fluid suspension and was exposed to all wavelengths of UV irradiation. Early comparisons of survivors recovered from the experimental and control units indicate no significant differences in viability. Although the space flight appears to have effected no difference in the survival of this species, the more sensitive characteristics of endopeptidase and hemolysin production are still under investigation, and results are not yet available.

Fungi.—Four species of fungi were studied. *Trichophyton terrestre* was selected because it has the ability to attack human hair under laboratory conditions. *Chaetomium globosum,* the other filamentous fungus, was of special interest because of the cellulolytic activity it demonstrates on cloth fibers, such as those composing parts of the flight garments of the astronauts. The two yeasts, *Rhodotorula rubra* and *Saccharomyces cerevisiae*, were included because they are well suited to drug sensitivity studies. These and other studies are being investigated concurrently with viability evaluations. Results are not available for this preliminary report.

Bacillus subtilis.—The manner in which spores of *B. subtilis* survive when exposed to one or several factors of space has been critically studied in simulation experiments (ref. 27-19) and in the biostack experiment flown in the Apollo 16 command module. Different strains were evaluated by two different groups (table 27-IV). Spores of strain 168 were exposed in monolayers to space vacuum and/or to UV irradiation at a peak wavelength of 254 nm. Detailed analysis of recoverable colony-forming units demonstrated that the survival of this strain was not affected by space vacuum or by UV irradiation in space or by a combination of these factors in a manner discernible from the ground control and ground test subjects.

Spores of strains HA 101 (59) and HA 101 (59) F were exposed to the space-flight environment in aqueous suspensions and in dry layers. Spores of these strains were selected because of their known stability in extreme environments. These strains require three specific amino acids for growth, which are used as identification and mutation detection markers. In addition, strain HA 101 (59) F is defective in the capability to repair radiation damage (ref. 27-20) and is therefore highly susceptible to the damaging effects of UV irradiation. Preliminary evaluations of mutation rates are based on the percent of colony-forming units demonstrating loss of spore-producing capability or demonstrating other obvious morphological differences. Comparisons of nonirradiated flight cells with ground controls as yet have failed to demonstrate any space-flight-mediated effect. Complete and detailed genetic studies are in progress but are not available for this preliminary report.

Bacillus thuringiensis var. thuringiensis.—The species *B. thuringiensis var. thuringiensis* was chosen for the experiment because it produces a lipolytic α toxin, a deforming β toxin, and a crystalline δ toxin and because it has widely been used as a biological insecticide (ref. 27-21). Toxins from this species are highly quantitative and are well suited to rapid screening and critical in vivo analyses. As with the other bacilli, the space-flight conditions appear to have had no effect on cell viability as measured by surviving colony-forming units. Detailed analyses of enzyme production demonstrated by surviving clones are in progress, and data are not yet available.

Phage T-7 of Escherichia coli.—Survival studies of the T-7 bacteriophage of *E. coli* were performed in an attempt to relate the present experiment to the space-flight-mediated effects reported by Russian scientists for *E. coli* phage specimens that were flown on numerous manned flights (refs. 27-9, 27-15, 27-22, and 27-23). Rather than the T-1 or K-12 (λ) phage, commonly used on the Russian flights, the simpler and more stable T-7 phage was chosen for this study because this phage was expected to be more resistant to the rigors of space flight and thus would be a better UV test subject. Early calculations support this hypothesis because large losses in the flight subjects (as compared to the ground controls) are not indicated. Critical comparisons of flight and control test samples demonstrate no discernible space-flight-mediated antagonism or synergism.

Nematospiroides dubius.—The nematode *N. dubius* was chosen for study because it is a complex multicellular organism that has been successfully cultured in vitro from the egg to the third-stage infective larvae (ref. 27-24), is pathogenic to laboratory mice but not to humans, and is quite insensitive

to the special holding conditions of the flight hardware. Comparison of nonirradiated flight and ground control subjects revealed no differences in survival, infectivity in mice, formation of adults, or subsequent egg productions. However, early calculations do indicate that the space-flight environment (excluding UV irradiation and vacuum) had a profound effect on the ability of the eggs to develop further.

Ultraviolet dosimetry.—Two methods were employed to monitor the actual radiant energy penetrating selected optical components of the flight hardware. One of these methods involved Kodak high-resolution film SO-343 that had been purged of oxygen and sensitized with dry nitrogen gas. This system was reliable over a range of 4×10^1 to 4×10^2 ergs/cm^2 total energy with a peak wavelength of 254 nm. Postflight analysis indicates that the dosimeters received at least as much energy as had been calculated from the NASA-established solar spectral irradiance standard (ref. 27-25). Exact values are a function of postflight calibrations that are not complete at this time.

Solar irradiation within the range of 4×10^4 to 4×10^5 ergs/cm^2 was monitored by an adaptation of the potassium ferrioxalate actinometry system described by Wrighton and Witz (ref. 27-17). Comparisons of calculated and expected values verify the validity of the calculated values.

High-energy multicharged particle dosimetry.—In the design of the flight hardware, it was impossible to protect test systems from galactic irradiation. Therefore, this factor had to be measured to better understand any observed mutagenic or killing effects. Data were obtained with two systems.

One set of measurements was obtained by strategically distributing 76 extruded TLD's composed of LiF wafers throughout the flight hardware. This distribution was used to allow dose determinations for each tier, for each of the six sides, and for the central volume of the closed assembly. Statistical analysis of the resulting data indicates that the various areas within the MEED received extremely uniform irradiation from the ionizing irradiation components of the space environment. Therefore, omitting this factor as a variable is valid when inflight test systems are compared. The mean dose of all the MEED TLD's was 0.48 ± 0.02 rad with a range of 0.44 to 0.51 rad. Doses to crewmen (from crew passive TLD measurements) are reported to range from 0.48 to 0.54 rad, with a mean of 0.51 ± 0.02 rad. The dose of 0.48 ± 0.02 rad represents a total absorption of 48 ± 2 ergs of ionizing energy per gram of biological material within the MEED. This value is applicable to all samples within the flight hardware, including flight controls and UV-irradiated samples.

The other set of galactic irradiation measurements was conducted in response to current concern for the effect of high-energy multicharged particles on biological systems. A 2.54- by 3.175-cm container was provided within the flight hardware and ground control units to house four types of dosimeters capable of recording these entities. Lexan dosimeters, identical to those contained in the crew passive dosimeters, were used so that direct correlation could be made. Cellulose nitrate (CN) dosimeters were included in the MEED as well as in the Apollo light flash moving emulsion detector (ALFMED), which again allowed for direct comparisons. The other two detectors, Ilford G5 and silver chloride crystals, were flown only in the MEED, but they were of considerable value in the establishment of the high-energy multicharged-particle environment to which the flight hardware was subjected.

The Lexan and the CN detectors revealed track fluences (tracks/cm^2) of high-energy multicharged particles. Because the CN detector is more sensitive, it showed track fluences substantially higher than those found in Lexan. The sensitivity of the two detectors is such that the CN records particles with an atomic number Z greater than 6, whereas Lexan records particles with a Z greater than 10. A comparison of Lexan and CN tracks found in the MEED flight hardware showed the track fluence to be somewhat lower than that found in the ALFMED or the crew passive dosimeters. These observations and the depressed TLD values discussed previously imply that the MEED flight hardware had a somewhat greater average shielding as compared with either the ALFMED or the crew passive detectors. Likewise, these data are slightly lower than those obtained from the TLD and CN detectors used in the biostack hardware, which was stowed in the command module in an area of minimal shielding to ambient cosmic radiation.

Conclusions

The performance of the microbial response to space environment experiment is considered excellent by all investigators. For most microbial systems, only preliminary survival data are available at this time. None of the available data indicate space-flight-mediated changes in cell viability or recovery. One quite important observation has been made at this early date, however. The eggs produced after mice had been infected with *N. dubius* larvae demonstrated a significant decrease in hatchability when compared to identical ground controls. Except for the fact that the Apollo 16 flight larvae had been on board the command module, treatment of the flown larvae and ground control larvae was the same; neither had been exposed to UV irradiation. The significance and implications of this finding are currently being studied.

Acknowledgments

The authors gratefully acknowledge the support of those who contributed to the success of this experiment system. Particular thanks are given to the following persons: Jim Isherwood and Linda McEneany of Scripps Clinic and Research Foundation; Carolyn Carmichael and Jim Lindsay of Northrop Services, Inc.; Don Lovett of Texas A. & M. University; and Doug Jerger, Jim Hiser, and Jim Veselenak of Eastern Michigan University. The employees of Aerojet Medical and Biological Systems are recognized for fabrication of the flight hardware.

PART C

VISUAL LIGHT FLASH PHENOMENON

Richard E. Benson[a] and Lawrence S. Pinsky[a]

Beginning with the Apollo 11 lunar mission, crewmen have reported seeing flashes of light while they were relaxing in the darkened command module or wearing light-tight eyeshades. These events have been described as colorless starlike flashes, narrow streaks of light, or diffuse light flashes and have been observed during translunar coast, in lunar orbit, on the lunar surface, and during transearth coast. At the times of the observations, the crewmen were relaxed and had their eyes closed or covered with eyeshades, or had their eyes open in the darkened spacecraft cabin. The frequency of the light flashes has been one flash every 1 to 2 min.

Information concerning the light flashes observed on the Apollo 11, 12, and 13 missions was obtained during crew debriefings. During the Apollo 14 and 15 missions, light-flash observations were reported to the Mission Control Center (MCC) as they occurred, as well as during postflight crew debriefings. Light-tight eyeshades were first worn during the Apollo 15 mission to provide a uniform and reproducible degree of darkness. The Apollo 16 mission provided the opportunity to obtain additional data on the characteristics and frequency of the light flashes and also provided the first opportunity to obtain a direct physical record of incident cosmic ray particles with the Apollo light flash moving emulsion detector (ALFMED).

Evaluation of reports obtained from the Apollo crewmen has established the existence of the phenomena and their origin within the crewmembers' eyes. The generally accepted hypothesis explaining the origin of the light flashes involves exposure to high-energy cosmic ray particles (refs. 27-26 to 27-28). One or both of the following mechanisms are suggested: (1) relativistic cosmic ray particles passing through the eye emit Cerenkov radiation that produces light-flash sensations, and (2) direct interactions of high-energy cosmic ray particles or their secondaries with the retinal cells or associated optic nervous tissues produce light-flash sensations. Results of laboratory experiments during which human subjects were exposed to X-rays and several types of particulate radiations have shown that such radiation does produce similar light-flash sensations and further suggests that most of the light flashes observed by the

[a]NASA Manned Spacecraft Center.

Apollo crewmen are caused by direct interactions of ionizing radiation with cells of the visual nervous system (ref. 27-28). Analyses of the results of the Apollo 16 and 17 light-flash observations and ALFMED data should define the mechanisms involved in this phenomenon.

Apollo 16 Protocol

Two light-flash observation sessions were conducted as scheduled during the mission. The first session was conducted during translunar coast and the second during transearth coast. Each session was approximately 1 hr in duration. The lunar module pilot (LMP) wore the ALFMED, and the commander (CDR) wore eyeshades during the translunar coast observation session. During the transearth coast observation session, the crewmen wore eyeshades only; the ALFMED was not worn. The observation period began when the crewmembers reported by voice to the MCC that they had donned the ALFMED and/or eyeshades. Thereafter, each crewman verbally reported the occurrence and characteristics of each light flash. Personnel at the MCC recorded times of occurrence and crew comments for each light flash event as reported. At the conclusion of the sessions, the crewmen reported when the ALFMED and/or eyeshades were removed. Information reported by voice to the MCC during the mission and obtained at postmission crew debriefings has been tabulated and will be correlated with results obtained from the ALFMED to determine the relationships between the occurrence of light flashes and the cosmic ray particles that passed through the ALFMED and the eyes of the crewmen.

ALFMED Description

The ALFMED is an electromechanical device that is worn on the head somewhat like a helmet and supports cosmic-radiation-sensitive emulsions around the head of the test subject (figs. 27-17 to 27-19). A direct physical record is provided of cosmic ray particles that pass through the emulsion plates and, in turn, through the head of the subject. The ALFMED contains two sets of glass plates coated on both sides with special nuclear emulsion and supported in a protective framework. One set of nuclear emulsion plates is fixed in position within the headset and surrounds the front and sides of the head. A second similar set of plates is located exterior and parallel to the inner fixed plates and may be translated at a constant rate (10 μm/sec) with respect to the fixed plates. This configuration provides a time resolution for events to within 1 sec. Postflight analysis of the emulsion plates will provide an accurate measure of the time of occurrence of events, as well as information concerning the energy, charge, and trajectory of the incident cosmic ray particles.

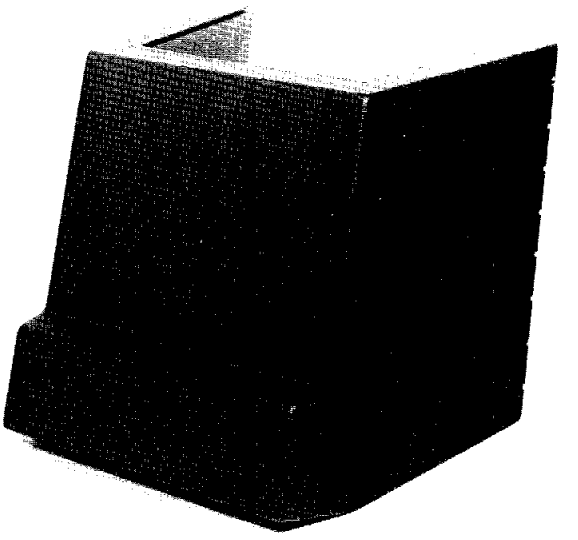


FIGURE 27-17.–Exterior view of ALFMED device.

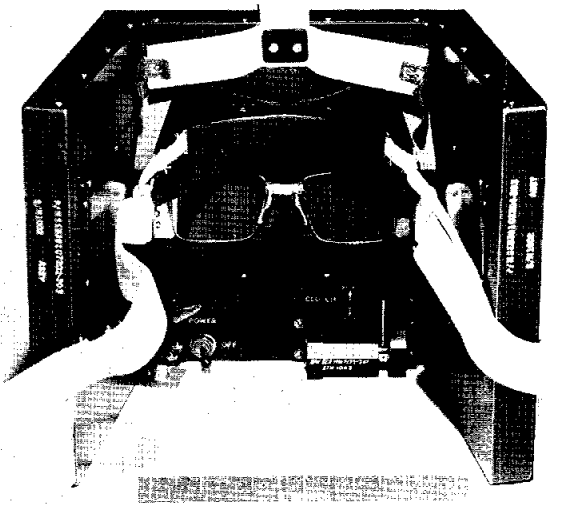


FIGURE 27-18.–Interior view of ALFMED device.

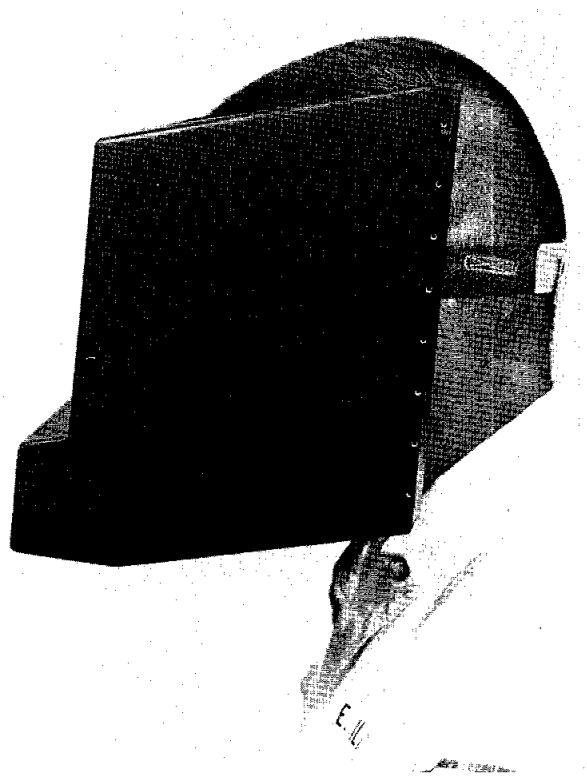


FIGURE 27-19.–The ALFMED device as worn by crewman.

Preliminary Observations

Characteristics of the light flashes observed and reported by the Apollo 16 crewmembers were generally similar to those reported on previous missions. The flashes were described as small dotlike or starlike events, narrow streaks of light exhibiting a sensation of directional movement, and diffuse light flashes. All events appeared colorless. The events usually appeared in one eye only, and the crewmembers expressed no difficulty in distinguishing the eye in which the flash occurred. There were three reports of a double light flash occurring in the same eye; two were reported during the first observation session and one during the second. There were two reports of a light flash occurring simultaneously in both eyes, once during each of the observation sessions. The flashes occurred at random locations in the field of vision, and the streaks exhibited horizontal, vertical, or diagonal orientation. The ratio of dot or star flashes to streaks was approximately 3 to 1 for both observation sessions.

Analysis of the times of occurrence of the light-flash events yielded an apparent random distribution. During the translunar coast observation session, the mean rate of occurrence of the flashes was one event every 1.2 min for the LMP and one event every 3.6 min for the CDR. During the transearth coast session, the mean rate of occurrence was one event every 2.1 min for the LMP and one event every 4.5 min for the CDR.

The command module pilot reported that he had not observed any light flashes during the mission. This was the first negative report since the light flashes were first reported on the Apollo 11 mission. The frequency of light flashes reported during transearth coast was significantly less than that reported during translunar coast. A similar relationship was reported during the Apollo 15 mission. The explanation for this finding has not been determined.

Analyses of the ALFMED emulsion plates are proceeding as scheduled, although results are not yet available. The ALFMED results should provide conclusive evidence establishing the correlation, if any, between the incident cosmic ray particles and the perception of light flashes as reported by Apollo crewmembers.

A valid assessment of any potential hazards associated with the visual light-flash phenomenon cannot be completed until the biophysical mechanisms involved can be determined and evaluated. No changes in visual acuity have been detected. Retinal photography performed before and after the mission has revealed no evidence of changes attributable to radiation.

REFERENCES

27-1. Schaefer, H. J.; and Sullivan, J. J.: Nuclear Emulsion Recordings of the Astronauts' Radiation Exposure on the First Lunar Landing Mission, Apollo 11. NASA CR-115804, 1970.

27-2. English, R. A.; and Liles, E. D.: Iridium and Tantalum Foils for Spaceflight Neutron Dosimetry. Health Phys., vol. 22, no. 5, May 1972, pp. 503-507.

27-3. Bücker, H.; et al.: The Biostack Experiment on Apollo 16. Paper L.6.6, COSPAR Meeting (Madrid, Spain), 1972.

27-4. Glembotskiy, Ya. L.; Prokof'yeva-Belgovskaya, A. A.; Shamina, Z. B.; Khvostova, V. V.; et al.: Influence of Space-Flight Factors on Heredity and Development in Actinomycetes and Higher-Order Plants. Problems of Space Biology, vol. 1, N. M. Sisakyan, ed., U.S.S.R. Academy of Sciences Publishing House (Moscow), 1962, pp. 259-271. (Also available as NASA TT F-174, 1963.)

27-5. De Serres, F. J.: Effects of Radiation During Space Flight on Micro-organisms and Plants on the Biosatellite and Gemini XI Missions. Life Sciences and Space Research VII, W. Vishniac and F. G. Favorite, eds., North-Holland Publishing Co. (Amsterdam), 1969, pp. 62-66.

27-6. Kovyazin, N. V.; Lukin, A. A.; and Parfenov, G. P.: The Effect of Space Flight Factors of the Satellite "Vostok-2" on Haploid and Diploid Yeasts. Problems of Space Biology, vol. 2, N. M. Sisakyan and V. I. Yazdovskiy, eds., Nauku Press (Moscow), 1962, pp. 156-160. (Also available as OTS 63-21437, 1963.)

27-7. Mattoni, R. H. T.: Space Flight Effects and Gamma Radiation Interaction on Growth and Induction of Lysogenic Bacteria: A Preliminary Report. Biosci., vol. 18, no. 6, June 1968, pp. 602-608.

27-8. Parfenov, G. P.: Genetic Investigations in Outer Space. Cosmic Research, vol. 5, no. 1, Jan.-Feb. 1967, pp. 121-133.

27-9. Lorenz, P. R.; Hotchin, J.; Markusen, A. S.; Orlob, G. B.; et al.: Survival of Micro-organisms in Space. Space Life Sci., vol. 1, no. 1, 1968, pp. 118-130.

27-10. De Serres, F. J.; Miller, I. R.; Smith, D. B.; Kondo, S.; and Bender, M. A.: The Gemini XI S-4 Spaceflight Radiation Interaction Experiment. II. Analysis of Survival Levels and Forward-Mutation Frequencies in *Neurospora crassa*. Radiation Res., vol. 39, no. 2, Aug. 1969, pp. 436-444.

27-11. De Serres, F. J.; and Webber, B. B.: The Combined Effect of Weightlessness and Radiation on Inactivation and Mutation – Induction in *Neurospora crassa* during the Biosatellite II Mission. Biosci., vol. 18, no. 6, June 1968, pp. 590-595.

27-12. Jenkins, D. W.: U.S.S.R. and U.S. Biosciences. Biosci., vol. 18, no. 6, June 1968, pp. 543-549.

27-13. Antipov, V. V.; Delone, N. L.; Nikitin, M. D.; Parfyonov, G. P.; and Saxonov, P. P.: Some Results of Radiobiological Studies Performed on Cosmos-110 Biosatellite. Life Sciences and Space Research VII, W. Vishniac and F. G. Favorite, eds., North-Holland Publishing Co. (Amsterdam), 1969, pp. 207-209.

27-14. Zhukov-Verezhnikov, N. N.; Mayskiy, I. N.; Yazdovskiy, V. I.; Pekhov, A. P.; et al.: Evaluating the Biological Effectiveness of Space Flight Factors by Means of the Lysogenic Bacteria *E. coli* K-12 (λ). Aviation and Space Medicine, V. V. Parin, ed., Akademiya Meditsinskikh Nauk (Moscow), 1963, pp. 158-160. (Also available as NASA TT F-228, 1964.)

27-15. Antipov, V. V.: Biological Studies Aboard the Spacecraft "Vostok" and "Voskhod." Problems of Space Biology, vol. 6, N. M. Sisakyan, ed., Nauka Press (Moscow), 1967, pp. 67-83. (Also available as NASA TT F-528, 1969.)

27-16. Townes, C. H.: Infectious Diseases in Manned Spaceflight: Probabilities and Countermeasures. Space Sci. Board, Natl. Acad. Sci. (Washington, D.C.), 1970, p. 86.

27-17. Wrighton, M.; and Witz, S.: Stability of Fe (II) in Ferrioxalate Solutions. Mol. Photochem., vol. 3, 1972, pp. 387-394.

27-18. Foster, B. G.: Toxic Properties of *Aeromonas proteolytica*. Abstracts of the Annual Meeting of the American Society for Microbiology, 1972, p. 110.

27-19. Horneck, G.; Bücker, H.; and Wollenhaupt, H.: Survival of Bacterial Spores Under Some Simulated Lunar Surface Conditions. Life Sciences and Space Research IX, Wolf Vishniac, ed., Akademie-Verlag (Berlin), 1971, pp. 119-124.

27-20. Gass, K. B.; Hill, T. C.; Goulian, M.; Strauss, B. S.; and Cozzarelli, N. R.: Altered Deoxyribonucleic Acid Polymerase Activity in a Methyl Methanesulfonate-Sensitive Mutant of *Bacillus subtilis*. J. Bacteriology, vol. 108, no. 1, Oct. 19, 1971, pp. 364-374.

27-21. Heimpel, A. M.: A Critical Review of *Bacillus thuringiensis* var. *thuringiensis* Berliner and Other Crystalliferous Bacteria (Biological Control of Insects). Ann. Rev. Entomology, vol. 12, 1967, pp. 287-322.

27-22. Zhukov-Verezhnikov, N. N.; Rybakov, N. I.; Kozlov, V. A.; Saksonov, P. P.; et al.: Results of Microbiological and Cytological Investigations Conducted During the Flights of "Vostok" Type Vehicles. Problems of Space Biology, vol. 4, N. M. Sisakyan, ed., U.S.S.R. Academy of Science Publishing House (Moscow), 1965, pp. 252-259. (Also available as NASA TT F-368, 1966.)

27-23. Hotchin, J.: The Microbiology of Space. J. Brit. Interplanetary Soc., vol. 21, 1968, pp. 122-130.

27-24. Weinstein, P. P.; Newton, W. L.; Sawyer, T. K.; and Sommerville, R. I.: *Nematospiroides dubius*: Development and Passage in the Germfree Mouse, and a Comparative Study of the Free-Living Stages in Germfree Feces and Conventional Cultures. Trans. Am. Microscopic Soc., vol. 88, 1969, pp. 95-117.

27-25. Thekaekara, M. P.: Solar Electromagnetic Radiation: NASA Space Vehicle Design Criteria (Environment). NASA SP-8005-Rev, 1971.

27-26. Fazio, G. G.; Jelley, J. V.; and Charman, W. N.: Generation of Cherenkov Light Flashes by Cosmic Radiation Within the Eyes of the Apollo Astronauts. Nature, vol. 228, Oct. 17, 1970, pp. 260-264.

27-27. Chapman, P. K.; Pinsky, L. S.; Benson, R. E.; and Budinger, T. F.: Observations of Cosmic Ray Induced Phosphenes. Proceedings of the National Symposium on Natural and Manmade Radiation in Space. NASA TM X-2440, 1972, pp. 1002-1006.

27-28. Tobias, Cornelius A.; Budinger, Thomas F.; and Lyman, John T.: Radiation–Induced Light Flashes Observed by Human Subjects in Fast Neutron, X-ray and Positive Pion Beams. Nature, vol. 230, Apr. 30, 1971, pp. 596-597.

28. Observations and Impressions from Lunar Orbit

T. K. Mattingly,[a] Farouk El-Baz,[b] and Richard A. Laidley[a]

The objective of visual observations from lunar orbit was fulfilled for the first time, and with extraordinary success, on the Apollo 15 mission. The concept and means of achieving the objective have previously been detailed, and summaries of the significant results have been published (ref. 28-1).

On Apollo 16, the command module pilot (CMP) made observations of particular surface features and processes to complement photographic and other remotely sensed data. Emphasis was placed on geological problems that required the extreme dynamic range and color sensitivities of the human eye; repetitive observations at varying Sun angles and viewing directions; and, in some cases, on-the-scene interpretations. A byproduct of this emphasis was the identification of specific areas of the remotely sensed data for early review in the data reduction process.

The task of intelligently observing from orbit is complicated by several constraints. The first constraint is that, because of orbital velocity and spacecraft window geometry, only 1 min of each 118-min revolution is normally available for viewing a given point. The second constraint is also tied to the orbital ephemeris in that the observations must be performed at a prescribed time. Relative Sun angle and other mission time line activities further bound the choice of acceptable viewing periods. Because of the limited observational opportunities and the fact that the observed scene changes with Sun elevation, it was deemed important both to investigate particular features repetitively and to compare similar features under different conditions.

The human observer adds a unique dimension to the exploration of the Moon. He assigns priority to the data collected by the cameras and other experiments and acts as a detector of subtle phenomena and an integrator of vast amounts of simultaneous data input. Even the observations that cannot be documented are of value because they serve as a provocative note to the theorist and as a guide to the types of observations and equipment that should be planned for the future. Within this concept, the accuracy of the interpretation is less important than the fact that something was observed.

[a]NASA Manned Spacecraft Center.
[b]Bell Telephone Laboratories.

DATA ACQUISITION

Several years of planning and training went into the development of a plan that would allow the orbiting observer to complement the data collected by the spacecraft remote sensors and the surface exploration team. The tools available in the command module (CM) were limited to the maps, photographs, and other graphic materials prepared in support of the task; a pair of 10-power binoculars (carried for the first time on the Apollo 16 mission); a reference color wheel; two handheld cameras; and a voice-recording capability.

In the course of training, the CMP simulated the observation tasks by studying aerial photographs of geologically complex regions in the United States and by flying over those areas and adding information to the photographs by making and recording visual observations.

From the many lunar regions scheduled to be overflown by the Apollo 16 crew, 11 areas were selected for detailed study (fig. 28-1). Adequate segments of time in the flight plan were allocated to the task, and the astronauts were supplied with photographs of the features and a list of the questions to be answered. Observations were made from the command module windows without disturbing the operations of the scientific instrument module. Data were acquired on 10 visual observations targets, including two (in the western maria) not scheduled in the flight plan.

On far-side passes, observations were recorded on the onboard tape recorder; and, on near-side passes, observations were recorded by real-time voice com-

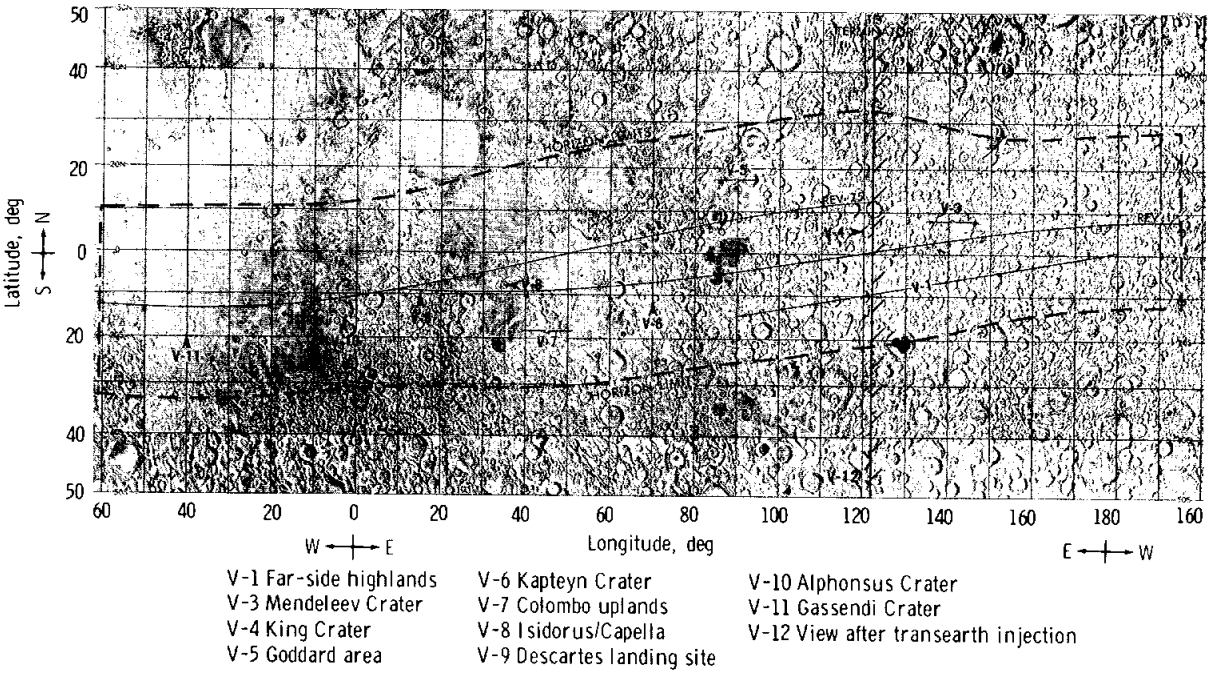


FIGURE 28-1.–Index map of Apollo 16 visual observation targets relative to the mission ground tracks. The envelope indicated by dashed lines represents the planned maximum lunar surface area visible from the CM windows during the mission. North is to the top in this and all subsequent figures.

munications with the Mission Control Center. Where appropriate, observations were documented by marking onboard graphic materials and charts. After the mission, a debriefing was held during which the authors discussed the studied features and the geologic significance of the observations. Excerpts from both the real-time comments and the debriefing statements (edited for clarity) are included in the following discussion.

RESULTS

An attempt will be made in the following discussion to detail some of the significant results of the visual observations on Apollo 16 and to point out the geological importance. Because of the limitations of space, only a selection of the visual observation targets will be discussed.

General Impressions

The first impression of the Moon was that it was a brilliant, heavily battered, and uniformly colored body. As the spacecraft continued its initial orbit, the view of the near-side maria surrounded by rugged mountains and black skies introduced the first hint of the variety that would follow. During the 5 days the Apollo 16 CM spent in lunar orbit, the Moon became an old friend. Just as with a human personality, there were many easily recognized dominant features that formed a basic character modified by evolutionary changes and apparent contradictions. The more closely one observed, the more complex the subject became.

By the time the Apollo 16 spacecraft left lunar orbit, the crew had formed the general impression that the detailed characteristics of units commonly mapped on both the near side and the far side of the Moon (e.g., the rugged terra and the plains-forming units) were surprisingly similar (figs. 28-2 and 28-3). Therefore, any hypotheses that attempt to explain these units should be reviewed for compatibility with both the near side and the far side of the Moon.

Highland Characteristics

The Apollo 16 mission was basically an expedition to explore the lunar highlands. Surface exploration of the Descartes region was accompanied by a survey of the overflown highland units. Emphasis was placed largely on a study of the similarities or differences (or

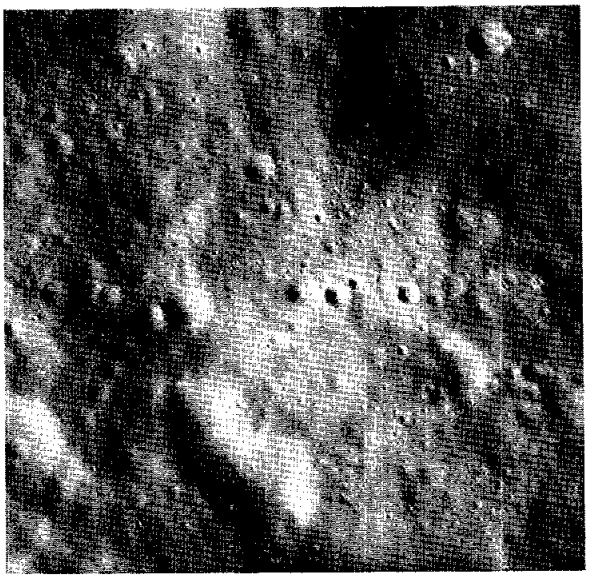


FIGURE 28-2.–Typical example of rugged terra on the lunar far side (7.8° N 148.9° E). The photograph covers an approximate 30- by 30-km area (AS16-120-19209).(See fig. 28-3 for comparison).

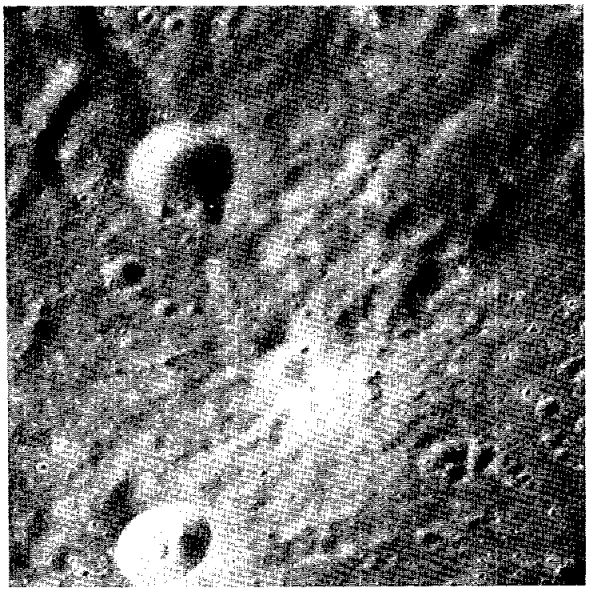


FIGURE 28-3.–Typical segment of the near-side rugged terra (10.3° S 17.3° E). The crater at the lower left is 4.2 km in diameter (AS16-120-19239).

both) between the detailed characteristics of the far-side and near-side highlands.

The first and dominant impression of the highlands is that they represent a remarkably uniform mass of heavily cratered white material. On a gross scale, the highlands on the near side and far side of the Moon appeared distinctly different. This difference may be due to the absence of maria on the far side. However, in a search for definitive characteristics, these highlands units appeared to be quite similar at small scales.

Photogeologic interpretations suggest the presence of a thicker regolith (fine-grained and fragmental, uppermost lunar surface layer) on the highlands than on the maria. This appears to affect the general appearance of the lunar highlands.

A general impression was that the Moon, with the exception of the mare-filled areas, had been covered with a "fairly heavy snow." Despite this apparent cover, there were sharp scarps and crater rims as well as blocks around many of the large and relatively fresh-appearing highland craters.

One subtle difference between the overflown far-side highlands and the central near-side highlands was that the latter displayed Imbrium sculpture (an extensive system of large fractures, tens of kilometers long, that are subradial to Mare Imbrium) and, at very low Sun angles, presented a large-scale hummocky appearance, whereas the far side was devoid of these and had a rolling topography [figs. 28-4, 28-5, and 28-6].

Although the surface textures of the near-side and far-side highlands are varied, surface striations cover both. In some cases, the striations are indicative of the local topography; and, in other cases, the striations crosscut the local topography. Photographic evidence also confirms that, in small areas, crater distribution is extremely complex.

There are patches of smooth, almost uncratered, units interspersed on all lunar highlands.

The smooth units seemed to become most obvious around some large craters. For example, there are patches of texturally smooth material in the vicinity of Isidorus Crater (fig. 28-7). Adjacent to many of these smooth patches are areas of unusually high concentrations of small craters.

Numerous patches of light-colored, plains-forming units appear to have filled valleys between far-side highland ridges. Colors, although generally similar, appear as relatively dark areas adjacent to lighter ones. All of these texturally distinct patches have boundaries, although close scrutiny fails to reveal a sharp contact such as would be characteristic of terrestrial analogs [fig. 28-5].

Fine scarps that are generally irregular and somewhat subdued occur on the far side. No similar features were observed on the near-side highlands. The fine scarps have the appearance of "flow fronts," yet they lack evidence of source or of surface flow

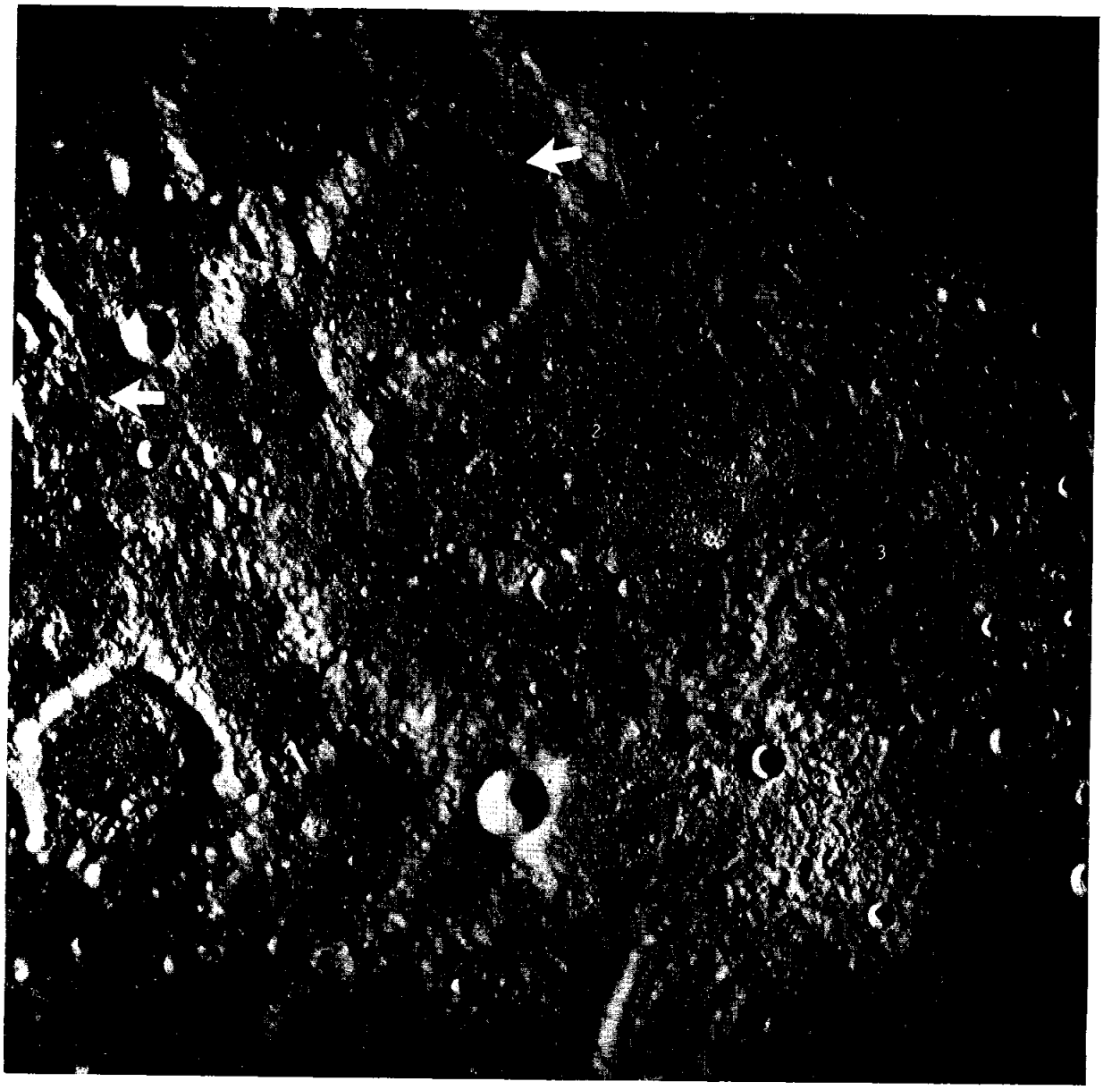


FIGURE 28-4.–Apollo 16 metric camera frame 162 showing part of the central lunar highlands centered near the landing site. Numerals indicate (1) an area of contrast between (2) the flat plains-forming unit (Cayley Formation) and (3) the rugged terra units. The unusually high albedo of the area indicated by the numeral 4 is presently not understood. Arrows point to two examples of the long fractures subradial to the Imbrium Basin that are referred to as Imbrium sculpture. The photograph is approximately 165 km on the side.

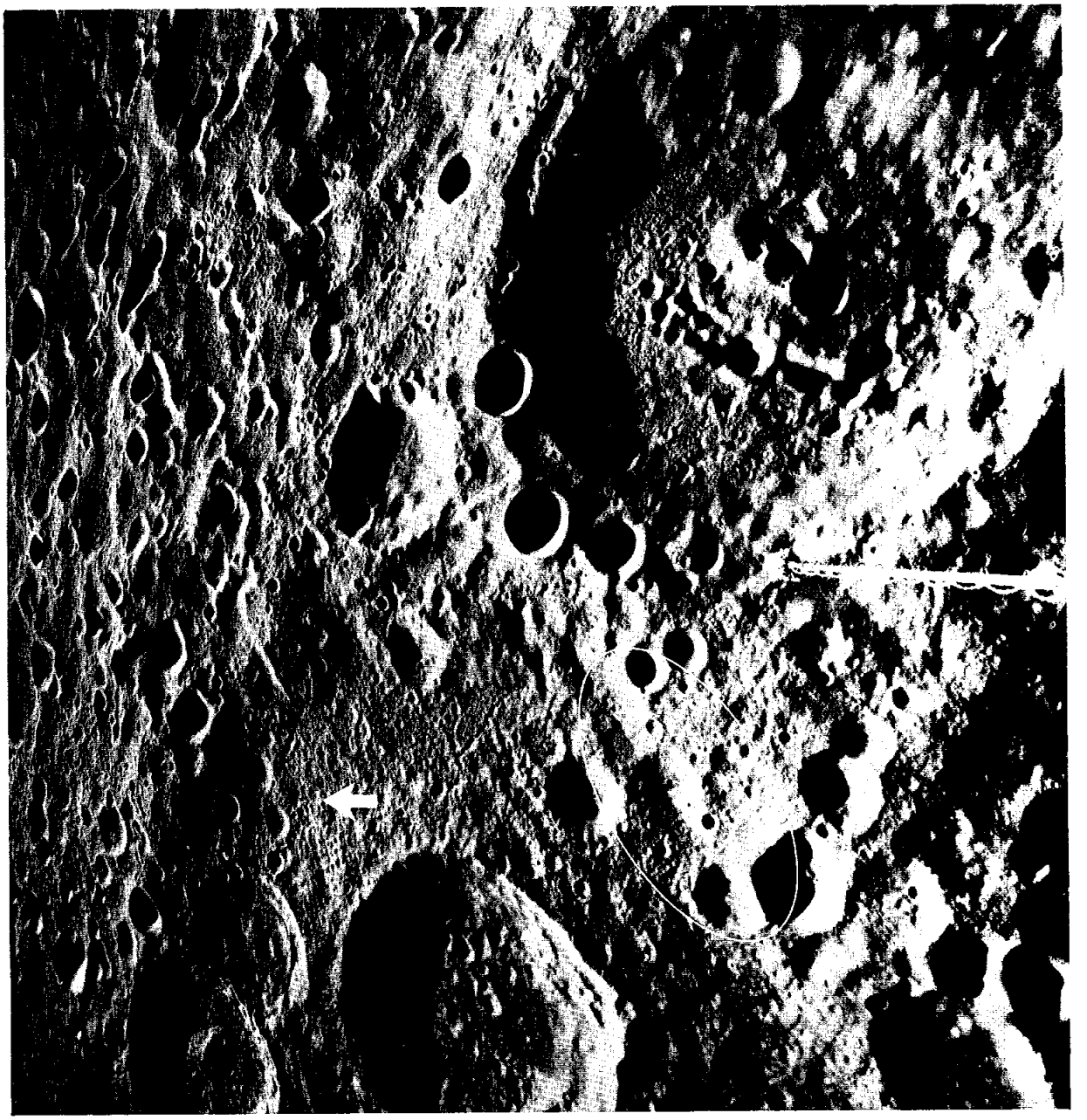


FIGURE 28-5.–Apollo 16 metric camera frame 458 forward oblique view of Mandel'shtam Crater (lower left) and the 70-km-diameter Papaleski Crater (upper right). The left side of the photograph portrays typical far-side rolling topography. Note the difference in brightness between the left and right parts of the area marked by an ellipse. (Visually, there was also a color difference.) The arrow points to a scarp shown in detail in figure 28-6. The extended boom of the gamma ray spectrometer is in right center.

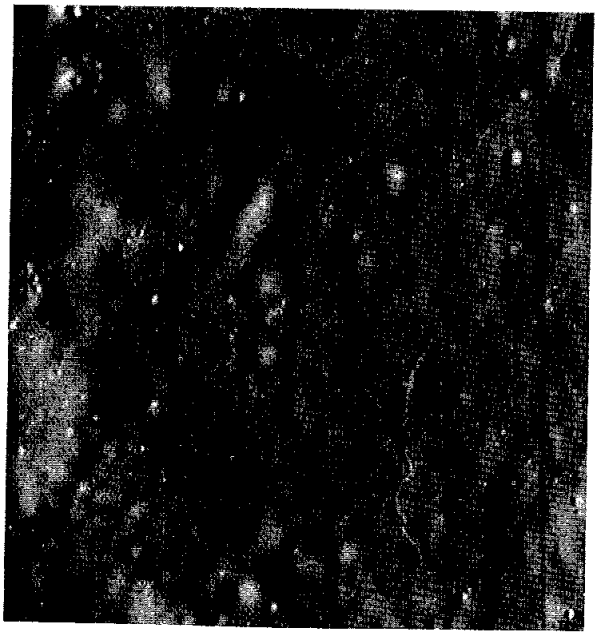


FIGURE 28-6.–Part of Apollo 16 pan camera frame 4150 showing details of a typical far-side highlands scarp in the floor of Mandel'shtam Crater (fig. 28-5). The picture width is approximately 10 km.



FIGURE 28-7.–View of the smooth area (1) west of Isidorus Crater. The 25-km-diameter crater in the lower left is Mädler (Apollo 16 pan camera frame 149).

patterns. Visual study of these fine scarps on the Apollo 16 mission pointed out additional complexity (fig. 28-6).

A perplexing phenomenon was that when tracing an apparent west-facing scarp it would suddenly become an east-facing scarp. These unusual patterns overlay all types of topography; the patterns climb hills and drop into subdued craters, leaving an impression that these features were laid on a rolling surface. It was noted that craters and scarps seemed to be sharper in the darker units.

One of the planned visual-observation targets was the area of the swirl patterns around Ibn Yunus and Goddard Craters. As the photographs taken after transearth injection show, the swirl belt extends to the highlands west of King Crater (sec. 29, part M, of this report). It was observed that,

at the higher Sun angles available for viewing at the beginning of the mission, these curved dark and light patterns seemed to be associated with topographic contours [figs. 28-8 and 28-9]. As the Sun angle decreased, the apparent topographic variations became less obvious.

Highland masses in the western maria appear to be similar to the more extensive far-side and central highlands.

The color tones of these units show more distinctive differences at low Sun angles than they do at higher Sun elevations.

Particular attention was paid to a unit near Lassell C Crater and a feature informally called on the Apollo 16 mission "the helmet" (figs. 28-10 and 28-11). The unit around Lassell C shows two distinct zones (sec. 29, part V, of this report), the real colors of which were obvious from lunar orbit.

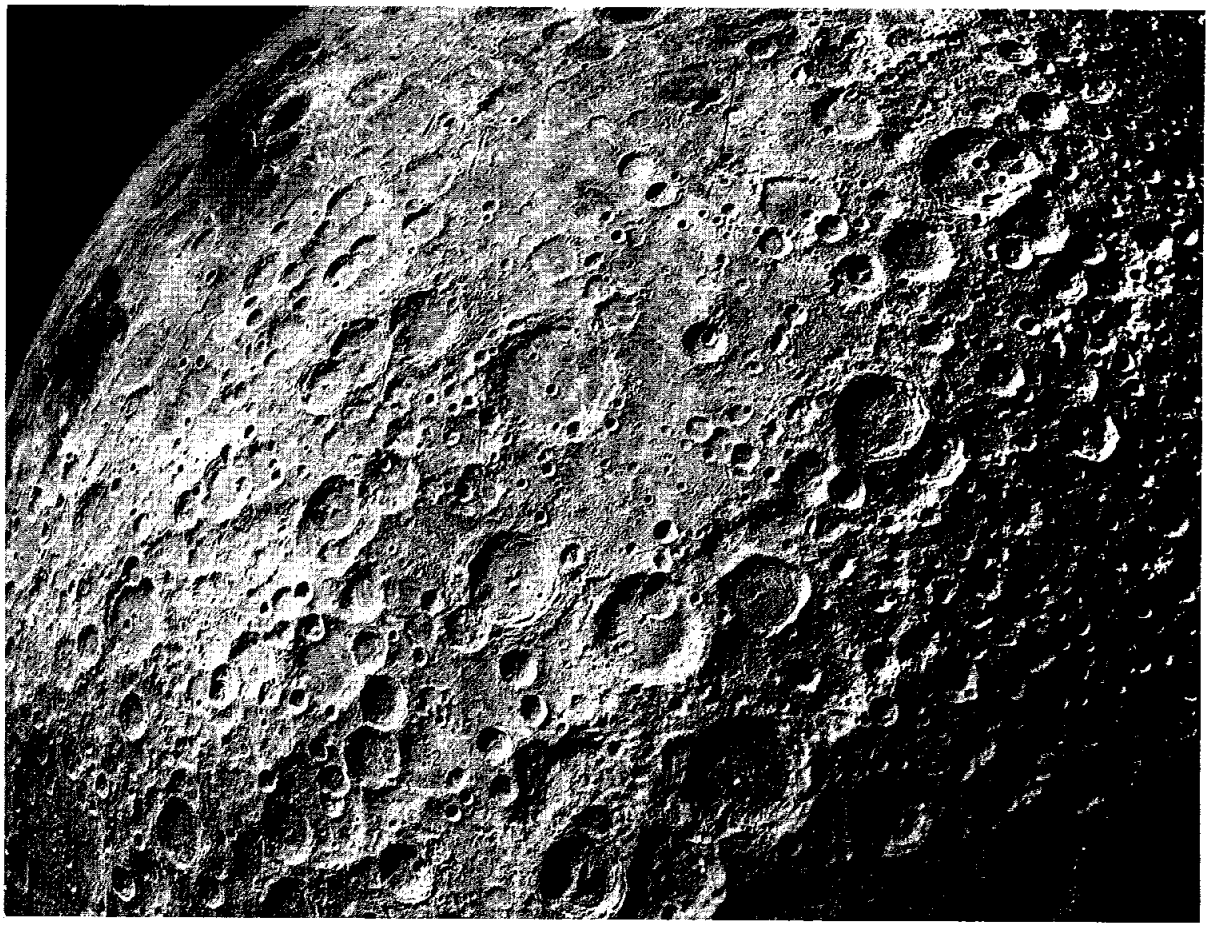


FIGURE 28-8.–View of part of the far-side highlands after transearth injection. The zone of bright swirls extends from area (1) to area (2) (detail in fig. 28-9) (Apollo 16 metric camera frame 3005).

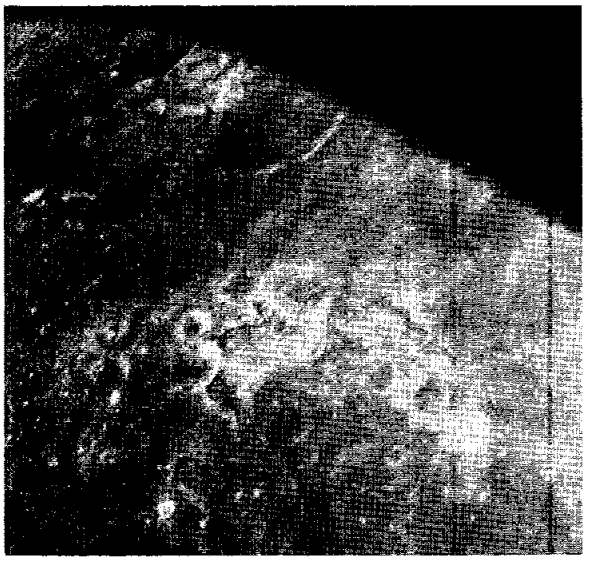


FIGURE 28-9.–Bright swirls located at 5.5° N 115.2° E (AS16-118-18898).

The southern portion appeared to be more tan while the northern section had a more grayish cast . . . "The helmet" was tannish in hue and had a somewhat ropy texture with fewer small craters than seen on the adjacent mare.

Based on premission photogeologic interpretations and geologic maps (ref. 28-2), elongate craters and furrowed features were anticipated in sections of the far side, as well as around Descartes, but were never detected.

An attempt was also made to look for some evidence of the "Soviet Mountains" (sec. 29, part H, of this report). No sharp topographic rise was detected; however, the CMP

had the impression that this feature could easily represent the western margin of a plateau similar to the Kant Plateau. Although this cannot be demonstrated, it remains a distinct possibility since the Kant Plateau did not stand out very dramatically from the nominal 110-km orbital altitudes.

Two areas of the far-side highlands should be studied for possible evidence of actual surface flow features. The first is in the Mandel'shtam Crater where a lobate pattern extends to the north and west (figs. 28-5 and 28-6). The second is an area northwest of Green Crater.

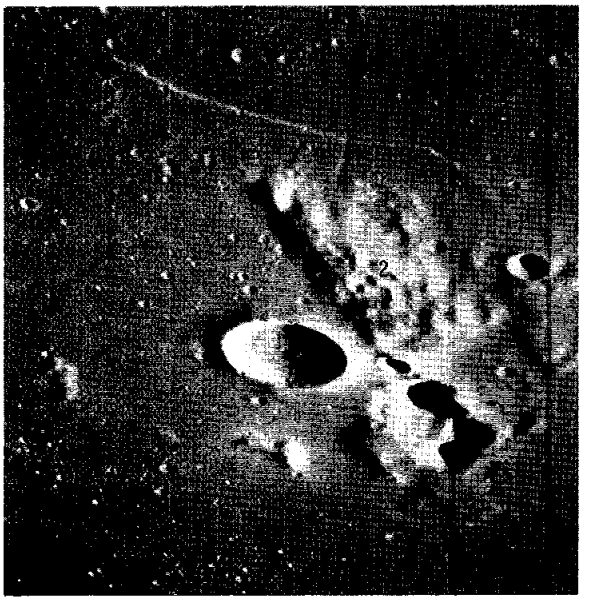


FIGURE 28-10.–Highland mass in Mare Nubium shows a distinct color boundary; area (1) is more tan than area (2) (AS16-120-19234).



FIGURE 28-11.–Distinct color boundaries of highland mass in Oceanus Procellarum, termed "the helmet" by Apollo 16 crew (AS16-119-19132).

Surface Striations

The Apollo 15 observations of small-scale linear features on "Silver Spur" and Mount Hadley (refs. 28-3 and 28-4) prompted the crew of Apollo 16 to look for similar features and to pay particular attention to the possible effects of the Sun, the target, and the observer geometry on visibility.

The first observation of these lineaments occurred shortly after establishment of the 110- by 15-km parking orbit. It was determined that these features became visible to the unaided eye once the observer was within approximately 50 km. They were clearly visible through the binoculars from the 110-km orbit. The impression was that these features were superposed on all highlands material [fig. 28-12]. In general, these striations occurred in thatched patterns with one orientation appearing to be more pronounced. The central peak of Theophilus displays patterns that were strikingly similar to those on Mount Hadley. Interior crater walls also displayed these striation patterns that were detectable, with equal frequency, on horizontal as well as inclined surfaces.



FIGURE 28-12.–Part of photograph showing striation patterns that are most obvious in the middle of the photograph (AS16-120-19303).

No attempt was made to check for any global orientation of the striation patterns. This can best be accomplished by analysis of panoramic camera data. One unanticipated observation was that, in crater walls, the striations frequently followed the contours of the surface topography. This was first noted in the eastern wall of Theophilus Crater and later in Lobachevsky Crater (fig. 28-13).

Another interesting observation was that several prominent linear patterns were found to run parallel to the Imbrium sculpture system, cross the central peak of Alpetragius Crater, and continue as far south as Arzachel Crater. Also, it was the impression of the CMP that

these patterns are not a function of the viewing geometry since they did not noticeably change as the orbiting spacecraft passed overhead.

These striations are probably the surface expressions of small-scale fracture patterns as well as downslope movement of fine-grained surface materials.

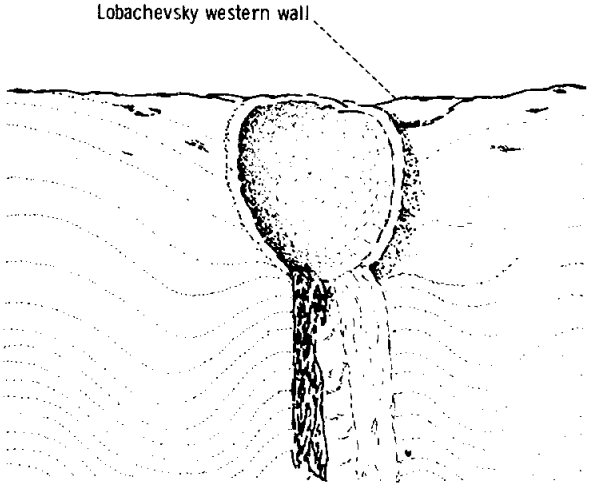


FIGURE 28-13.–Schematic drawing of the striation patterns on the western wall of Lobachevsky Crater.

Cayley Formation

For the purpose of this discussion, the term "Cayley Formation" applies to any surface unit that is apparently level, displays no "flow" structure, is extensively covered with subdued craters, and has an intermediate albedo between the brighter highlands and the darker maria (fig. 28-14). From orbital distances, the primary discriminator between mare material and Cayley Formation appeared to be color and albedo.

Cayley surfaces appeared to have distribution over the entire Moon. For example, the floors of Albategnius and Mendeleev Craters were similar in texture

and appearance. The Cayley Formation generally appeared in three different settings: as large basin fill, as small patches in the bottom of steep-sided craters, and as valley filling in the hummocky far-side highlands. The Cayley Formation borders were fairly indistinct, and it was the CMP's impression that regolith mixing has created a uniform surface layer that hides the demarcation between the various units.

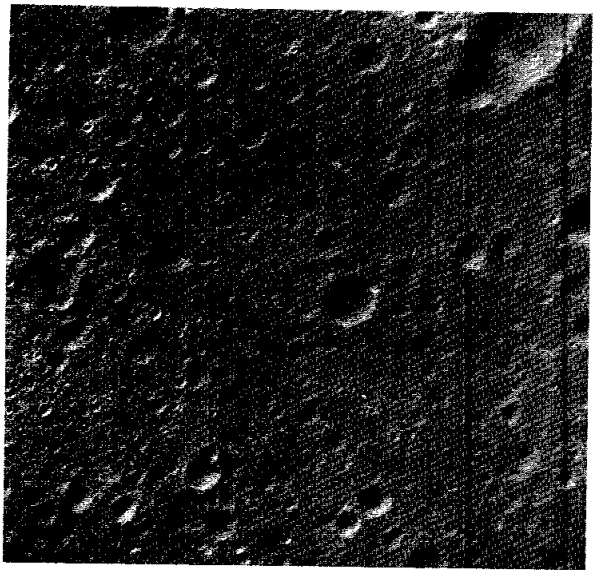


FIGURE 28-14.–Typical Cayley Formation photographed in the floor of Mendeleev Crater on the lunar far side (AS16-118-18972).

Most craters in the Cayley Formation generally have concave interiors, low depth-to-diameter ratios, and rims that were indistinct from orbital altitudes, even at low Sun angles. The general appearance that resulted was that these craters looked like what might be expected if "gas bubbles" rose to the surface through a relatively viscous material, rather than mechanical collapse or meteorite impact.

One additional and related observation of common occurrence was that many craters had floor characteristics that were most easily described as "mud pies" (fig. 28-15). The surfaces of these features appeared distinctly different from talus units. In fact, these surfaces, except for their limited extent, fit the Cayley definition given previously. It was an impression that the crater density in these floors was occasionally greater than that found in the areas surrounding the corresponding craters.

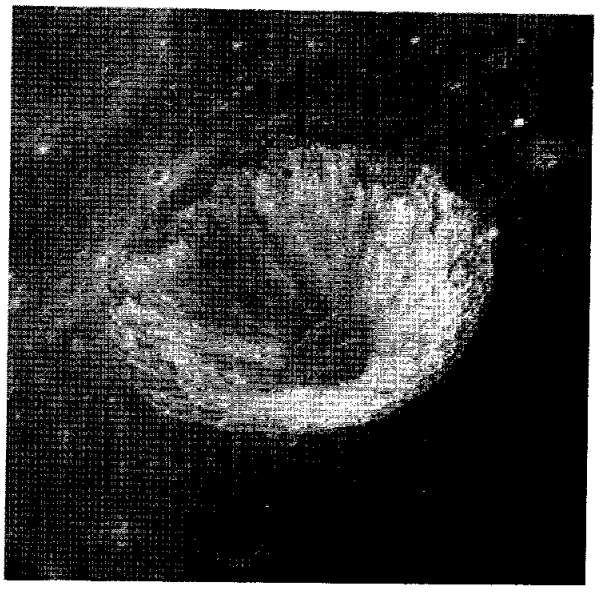


FIGURE 28-15.–The flat and apparently raised floor of this 10-km-diameter crater gives an impression of a "mud pie." Note the convex upper margins of the light wall material (AS16-120-19217).

KANT PLATEAU MATERIALS

Visual observations of the central near-side highlands were made to complement data from remote-sensing instruments in the ultimate task of establishing a proper perspective of the landing site in a global context and to provide the surface geology team with a real-time assessment of the accuracy of the preflight photointerpretation.

REGIONAL OBSERVATIONS

While approaching perilune in the 110- by 15-km prelanding orbits, the Kant Plateau appeared as a very spectacular rise to the west of Theophilus. From the nominal 110-km circular orbits, however, it appeared as a very gentle rise.

The general impression of the Descartes highlands at low Sun illumination angles can be seen from figure 28-16, which was taken on lunar revolution 2. Although the far-side highlands did not display this same jumbled appearance at low Sun, both did look very much alike at moderate-to-high Sun angles. Specifically, when the texture and small-scale topographic features (<1 km) were compared, the Kant Plateau materials, including the Descartes Mountains and the rest of the lunar highlands, look

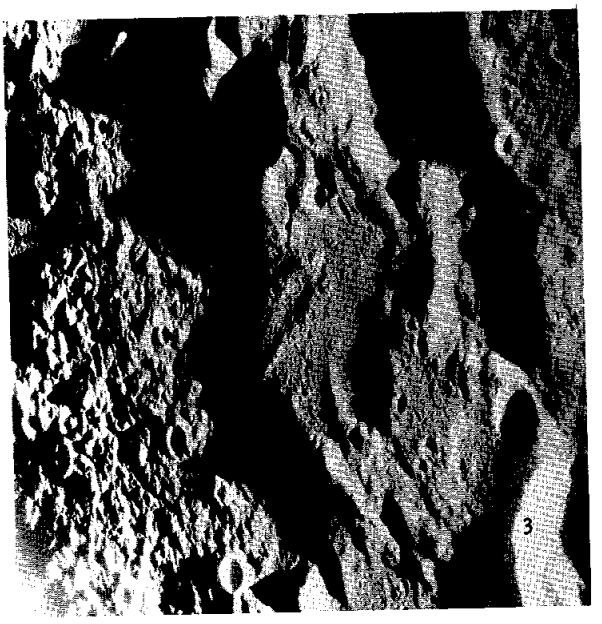


FIGURE 28-16.–Low Sun elevation angle (approximately 2°) emphasizes textural differences between the Cayley Formation (1) and the rugged terra (2) in the Descartes landing site area. The arrow points to the approximate location of the landing point. Kant Crater (3) is in the lower right corner, and the Descartes Crater is just below the left corner (AS16-124-19830).

strikingly similar. For example, the area between Ptolemaeus, Alphonsus, and Albategnius looked similar to the Descartes highlands when viewed at the same Sun angle. Based on gross surface texture, the material that appeared to flood the crater Descartes in fact seems to extend from south of Descartes to north of Taylor Crater. The general impression was that this unit (the Descartes Mountains) was continuous and that Stone Mountain and Smoky Mountain were two points on the margin between the Descartes Mountains and the Cayley Plains.

The very high albedo ellipse-shaped area that is centered around Descartes C and Dollond E did not appear to have any significantly different characteristics when viewed at low Sun elevations. In fact, it was not obvious on revolution 2 but became more obvious with increasing Sun angles exactly as do the light crater rays [fig. 28-4].

Elongate vents and cones were specifically looked for, but none were observed.

Landing Area Observations

Tracking of the landed lunar module (LM) with the command module optics was deleted because of the altered mission time line. Several attempts to locate the LM (fig. 28-17) with the aid of 10-power

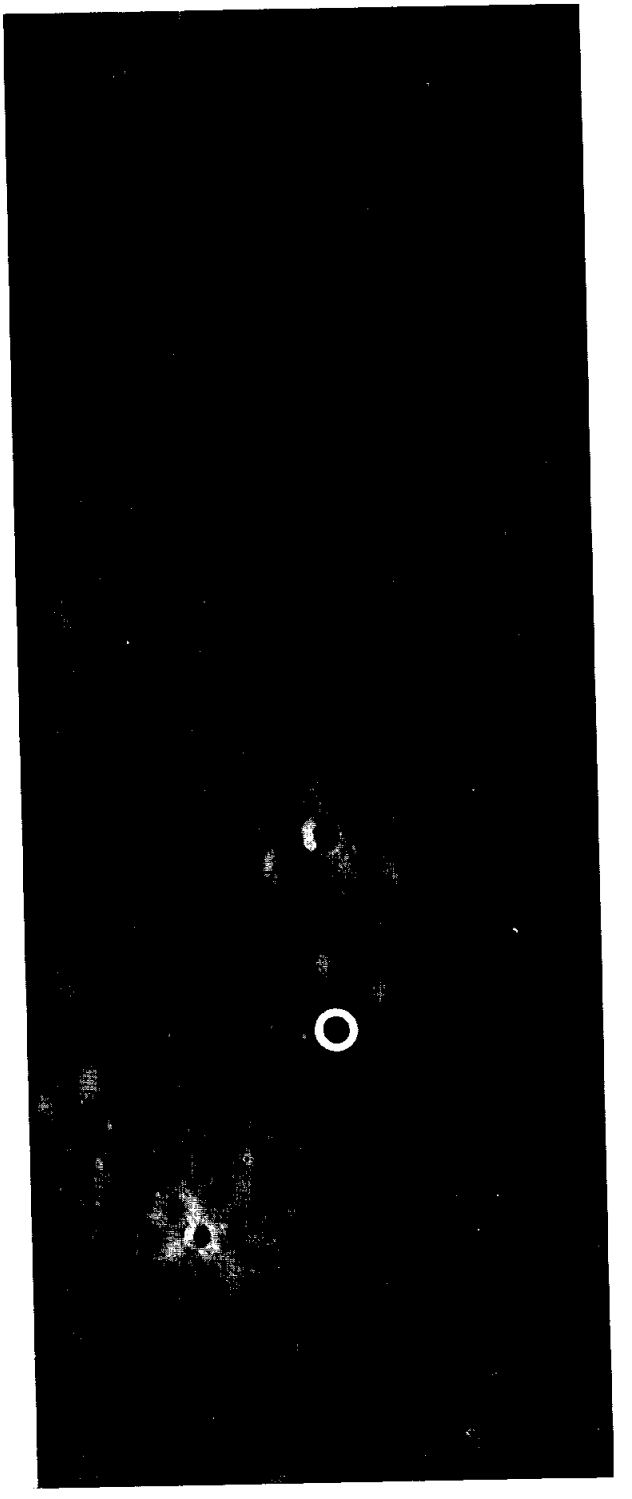


FIGURE 28-17.–View of the Apollo 16 landing site. The landing point is in the center of the circle (Apollo 16 pan camera frame 4558).

One feature noticed around the central peak in Langrenus Crater was a series of pock marks or small craters that formed two horizontal contour lines, one around the base and the other near the apex of this peak.

Dark halos were observed around craters in Alphonsus Crater and south of Mädler. Those in Alphonsus were immediately apparent to the naked eye. However, when the binoculars were used, no difference other than color could be determined. Both sets of dark halo craters showed evidence of lighter material in the crater interior.

Ray-excluded zones are interesting features. The ray pattern around Mädler is particularly unusual because the margin of the excluded zone changes direction as shown in figure 28-7.

There is a line of ridges and craters that extended along the ray-excluded zone from Mädler to the small crater at the break in the ray pattern. The texture of the light-ray material is distinctly different from the darker surfaces; it is more like the highlands than mare materials. Although the bright material is rather extensive, this prominent textural change seems to be concentrated in an area around the contact with the mare units. There is an extension of this light material that protrudes through the crater, across its floor, and up the northwest wall. This feature could not be definitely traced to the northwest, although there is, however faint, some expression in that direction.

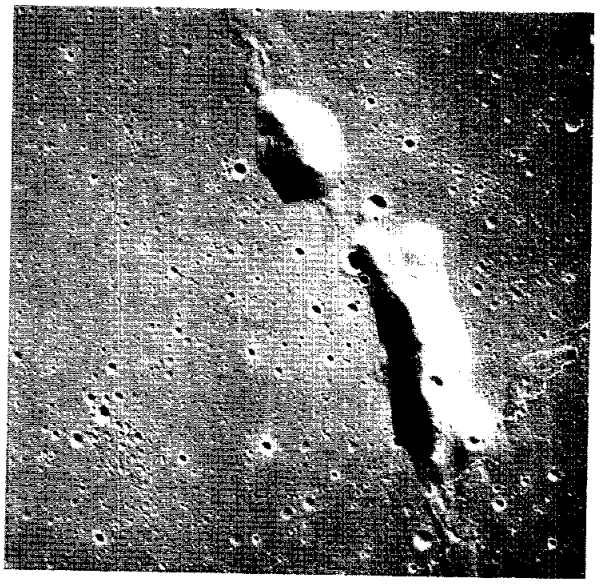


FIGURE 28-21.–The dark band ringing these two protuberances in Mare Cognitum was characteristic of highland features throughout the western maria (AS16-120-19244).

Mare Characteristics

Mare surfaces provided the setting for the most obvious color contrasts on the Moon. Perhaps the most fascinating result of the visual study of the mare surfaces, on Apollo 16, is the delineation of the small step that appeared to ring all observed highland masses and crater walls in the western maria. This type of feature had been previously noted on the Flamsteed ring (ref. 28-6). This step of material had an apparently uniform width, curvature, texture, and color. This uniformity appears to be independent of the type of feature and its height (fig. 28-21).

Once the idea of a "high water" mark occurred, the crew looked for other evidence of this characteristic. It was observed throughout the western maria and possibly as far east as the interior of Albategnius Crater. It was not seen in the maria of Nectaris, Fecunditatis, or Smythii.

These steps or marks are interpreted as an expression of the remains of a higher mare level than exists today. The lava that filled the basins and lowlands may have occupied a larger volume than the maria now do and, on solidification by cooling, may have receded to the present level, leaving a mark on highland slopes. This interpretation is consistent with the finding that the lunar lavas decreased approximately 10 percent in volume on solidification (ref. 28-7).

Another interesting expression is the sharp, nearly straight demarcation that separates areas of slightly different tonal characteristics in the western maria. These units appear just as previously mapped (sec. 29, part V, of this report).

One aspect was that these color differences were most pronounced in low Sun elevations.

Mare domes are another interesting feature on the western lunar maria. One exceptionally dark feature (fig. 28-22) with a crater on its apex was chosen for observation. The outer flanks appeared convex and of the same color as the surrounding mare. The CMP reported that apparently a portion of the crater rim was missing. Several of these small domes were observed in Mare Nubium and Mare Cognitum. Most did not have craters on top. Further examination of the panoramic camera photographs indicates that there may be some evidence of structure inside the crater walls, even though none was noticed during the mission.

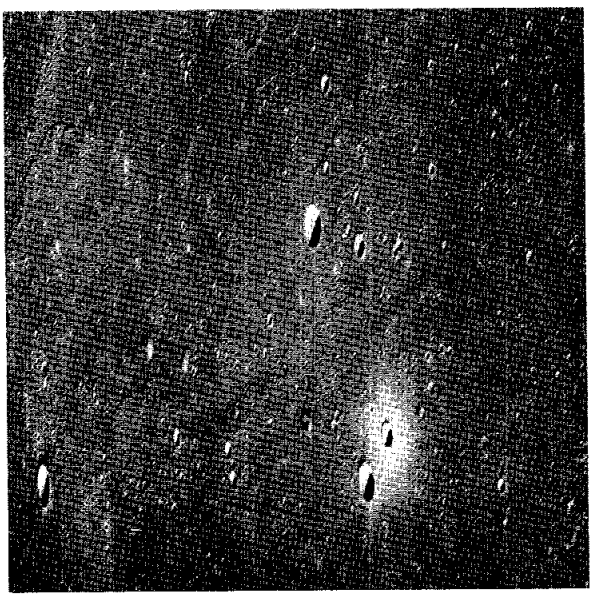


FIGURE 28-22.–The shallow dome structure with a crater at its apex (1) appeared, through the binoculars, to have a portion of its eastern rim missing (AS16-120-19237).

Rilles were observed only in the Fra Mauro vicinity, and the CMP had two distinct impressions. The first impression was that the floors appeared quite smooth and exhibited a dramatically lower density of small craters than the surroundings. The second impression is that at very low Sun the rille to the west of Fra Mauro Crater seemed to have a slightly raised rim.

Future photographic analysis, particularly with the help of topographic data to be gathered from the metric camera photographs, will help clarify these characteristics and establish their importance in the genesis of this and similar rilles.

Miscellaneous Observations and Comments

Davy Crater chain.–An attempt was made to determine if any relationships exist between the Davy Crater chain and the dark halo craters on the floor of Alphonsus Crater.

No relationship to Alphonsus could be found, nor were any rims detectable around the craters at the lowest Sun angle. A few north-south trending, topographically high features cross the chain but are completely obliterated at the crossing points.

Lobachevsky Crater.–The CMP observed that the small crater on the western wall [fig. 28-23] with apparently two dark "flow" lobes was the most exciting observation of the mission. The striation pattern [sketched in fig. 28-13] was also surprising. Qualitatively, the darkest unit was the same color as the darkest units in King Crater. The second flow unit was a lighter tone (more tan than gray).

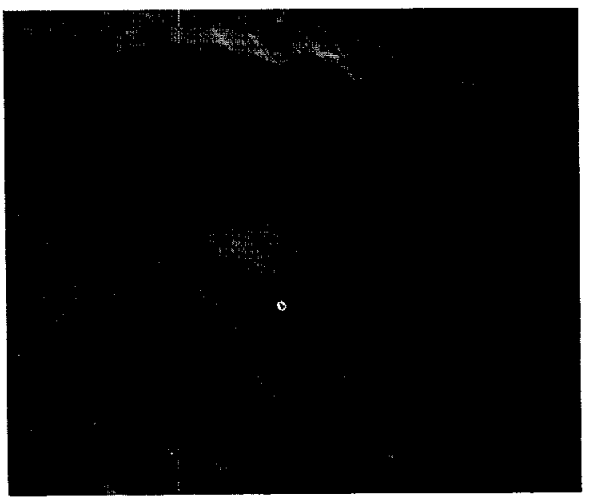


FIGURE 28-23.–Two dark ribbons of material apparently emanate from the base of the small crater in the western wall of Lobachevsky Crater (Apollo 16 pan camera frame 5022). (See also fig. 28-13.)

Messier and Messier A Craters.–The CMP made the following comments about the craters.

These two big craters left the impression that they were indeed connected. The ropy floor in Messier looked like what would be expected if a fairly viscous fluid receded over and around some large blocks. There was also some indication of a light color around the northeast part of the floor that suggested, by its similarity in color to the central material, that perhaps this represented an older surface.

King Crater.–Observations made of King Crater revealed the following.

This crater had all of the characteristics associated with Copernicus and was indeed unique to the observed portions of the far side. The area that reflects the presence of King is at least two crater diameters in size. There is a rather extensive ejecta pattern that followed the contours to the northwest and ended against the northwest walls of some relatively subdued craters [figs. 28-24 and 28-25]. The "ejecta" patterns to the southeast do not extend nearly as far, only one-half crater diameter, and have the appearance of a rather solid flow. The characteristics of the unit to the east lie somewhere between. The most distinctive characteristic of King Crater is its Y-shaped central peak. The dark spots on the central peak first appeared to be shadows from large blocks because there seemed to be a higher concentration of these on the eastern flanks. However, when viewed from the west looking east, these dark spots appeared to be unchanged in color or frequency, implying that they may well be dark materials.

(For more details, see section 29, parts M and N, of this report.)



FIGURE 28-24.–Dark and smooth deposits (1), an unusual Y-shaped central feature (2), and numerous subradial surface patterns around King Crater make this an intriguing area of the lunar far side (AS16-122-19601).

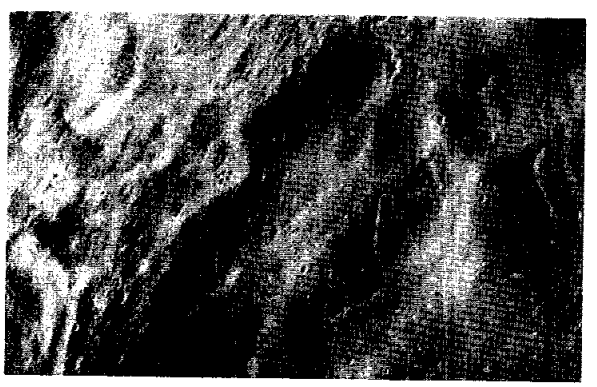


FIGURE 28-25.–Lobate patterns, in the lower right portion of the picture, are suggestive of material ejected from King Crater, which is 75 km to the southeast. This pattern was not noticed on the walls nearest to King Crater (AS16-120-19231).

CONCLUDING REMARKS

Visual observations and impressions recorded during the Apollo 16 mission verified the effectiveness of the hardware and techniques used. The orbiting observer functioned both as a sensor, in otherwise inaccessible areas such as earthshine and shadows, and as a designator of potentially significant data that were acquired on the photographic record.

REFERENCES

28-1. El-Baz, Farouk; and Worden, A. M.: Visual Observations from Lunar Orbit. Sec. 25 of Apollo 15 Preliminary Science Report, Part A. NASA SP-289, 1972.

28-2. El-Baz, Farouk; and S. A. Roosa: Significant Results from Apollo 14 Lunar Orbital Photography. Proceedings of the Third Lunar Science Conference, MIT Press (Cambridge, Mass.), Oct. 1972.

28-3. Scott, D. R.; Worden, A. M.; and Irwin, J. B.: Crew Observations. Sec. 4 of Apollo 15 Preliminary Science Report. NASA SP-289, 1972.

28-4. Howard, K. A.; and Larsen, B. R.: Lineaments That are Artifacts of Lighting. Sec. 25 of Apollo 15 Preliminary Science Report, Part G. NASA SP-289, 1972.

28-5. Elston, D. P.; Boudette, E. L.; Schafer, J. P.; Muehlberger, W.; and Sevier, J. F.: Apollo 16 Field Trip. Geotimes, vol. 17, no. 3, Mar. 1972, pp. 27-30.

28-6. Kosofsky, L. J.; and El-Baz, Farouk: The Moon as Viewed by Lunar Orbiter. NASA SP-200, 1970.

28-7. Wood, J. A.; Dickey, J. S.; Marvin, V. B.; and Powell, B. N.: Lunar Anorthosites. Apollo 11 Lunar Science Conference. Science, vol. 167, no. 3918, Jan. 30, 1970, pp. 602-604.

29. Photogeology

Reports of preliminary geologic analyses of the Apollo 16 orbital photography are presented in this section. These reports are examples of uses of the photography for geologic study. Photogrammetric work in support of geologic studies has barely begun (sec. 30 of this report), and many important geologic data will ultimately come from this source.

The central lunar highlands (the target of the Apollo 16 landing mission) were also the focus of much of the orbital photogeology. Other areas that have been studied include parts of Mare Nubium, southeastern Oceanus Procellarum, and far-side highlands around King Crater. As geologic and topographic analyses continue, new results can be expected along the lighted part of the orbital track.

Stratigraphy and structure are discussed in parts A to H, craters in parts I to N, volcanic and other landforms in parts O to U, and physical properties in parts V to Y. Discussions that pertain directly to the Apollo 16 landing site are found in parts A to D, F, U, W, and X. The principal results are summarized as follows.

Lunar problems brought into focus by results from the landing mission have guided preliminary orbital photogeology to an unprecedented degree. The discovery of abundant impact breccias at the landing site has prompted reevaluations of possible impact origins for the Cayley Formation, materials of the Descartes mountains, and similar landforms (sec. 6 of this report).

Light plains-forming materials, including the Cayley Formation upon which Apollo 16 landed, were dated at many places by crater shapes using Soderblom's crater degradation model (refs. 29-1 and 29-2 and part A of this section). The results suggest that plains materials on both the near side and far side are restricted in age within a span of 100 million yr or less, being approximately 3.7 to 3.8 billion yr old. They are significantly younger than the Fra Mauro Formation (3.9 billion yr) (part A). The origin of these plains is uncertain, and they may have a variety of origins. In part B, the hypothesis is revived that the plains materials represent fluidized ejecta (more fluidized than the Fra Mauro Formation) from multi-ring basins. Supporting evidence includes annular concentrations of plains materials around the basins, level ponds at varied elevations, mantled uplands, ghost craters in Cayley possibly caused by differential compaction, and flow lobes of Cayley-like materials. This origin could be reconciled with the young age reported in part A if ejecta from the Orientale Basin is quantitatively sufficient to have formed the upper part of the plains over most of the Moon. A miniature analog of Cayley-like plains superposed on the ejecta blanket of Aristarchus Crater is described in part C.

The materials of the Descartes highlands are also reevaluated in parts D and F. New photographs show the distinctive hilly and furrowed nature of the Descartes highlands (part U) and suggest division into a northern and a southern unit (part D). A volcanic origin is still attractive for the southern unit, but if evidence becomes available from the landing mission to exclude this explanation, other possibilities are texturally modified ejecta from either the Imbrium or Nectaris Basins (parts D and F). Possible analogs exist around the Orientale Basin (parts D, E, and F), and a miniature analog is suggested at Mösting C Crater (part C). The northern Descartes highlands appear to be cut by Imbrium sculpture and so were influenced (or possibly deposited) by the Imbrium event (parts D and F). The origin of Imbrium sculpture remains controversial. Pits and grooves support an origin by gouging from secondary cratering (part F). Conversely, an origin by fracturing and volcanism is supported by a wide variation in apparent age, furrows without rims, asymmetry of sculpture, association with faults, and an absence of ballistic shielding and randomly oriented crater clusters (part G). Imbrium sculpturing of the Descartes region may have obliterated landforms related to the Nectaris Basin; farther east, however, hummocky and other landforms can be recognized in the Nectaris Basin that mimic younger analogs at the Orientale Basin (part F). An ancient basin, the mountain rings of which are nearly obliterated, has been discovered on the lunar far side (part H).

The Apollo 16 photographs allow many types of craters to be studied in detail. The artificial craters made by the impact of two Ranger and two Apollo

spacecraft were identified and are the expected sizes (parts I and J). Elsewhere, a natural crater with asymmetric ejecta is similar to experimental missile-impact craters (part J). The characteristic V-shaped patterns of secondary impact craters can be reproduced experimentally by multiple impacts at low angles to the ground (part K). Changes in shape as a function of size are documented for fresh natural craters ranging from 0.4 km to more than 15 km (part J). Photogrammetric profiles on five craters allow them to be classified morphometrically; although two of these had previously been suspected to be calderas, their shapes place them in the impact-crater class (part L). The morphometry of 75-km King Crater also indicates an impact origin (part L). King Crater is very fresh and has a number of unusual features, including a large Y-shaped central peak and distinct dark and bright areas on the crater wall and rim (part M). The ejecta blanket of King Crater has several types of features that indicate the ejecta flowed radially outward along the ground (part N). These include avalanchelike lobes where the ejecta banked against preexisting hills – a type of feature not recognized previously (parts M, N, and O). Superposed on the ejecta blanket are flows and a large pool of lavalike material with extraordinarily clear channel levees, wrinkles, and cracks (parts M, N, and O). These materials are similar to those that occupy the floors of King, Tycho, Copernicus, and other craters, and may be either younger lava (part O) or impact melt (part N). The smallest crater recognized with possibly analogous flows on the rim is 15 km across (part J).

The Davy Crater chain appears to be old and degraded (part U). Other possible volcanic features recognized in the highlands are dark-halo craters (part O) and cracked floors (part R). Cracked crater floors such as in Goclenius Crater are typically near mare borders and may result from intrusion or extrusion of mare magma from below (part R). The cracklike rilles in Goclenius are straighter than rilles generally classified as sinuous, as demonstrated by a Fourier analysis of one of them. This kind of quantitative analysis of the planimetric shapes of rilles will lead to refined classifications and a way of comparing rilles with proposed terrestrial analogs (part Q).

In the mare, sinuous rilles near Herigonius Crater appear to be closely associated with mare ridges. Evidence for a genetic association includes the observation that rilles either begin at or cross the sites of ridges (parts P, Q, and S) and Fourier analysis, which shows that one rille is measurably straighter where it crosses a ridge (part Q). Some sinuous rilles can be interpreted as lava conduits (parts P and Q). Leveelike rims are present on a rille of intermediate sinuosity near Fra Mauro (part Q).

Mare ridges in the Herigonius area are of two main types. Very low broad arches visible at low Sun angles tend to be fractured on top, suggestive of an origin by arching; more typical ropy-appearing ridges do not show this (part S). One sharp-crested ridge appears to offset a premare crater in a manner indicative of faulting (part S). Subtle ring structures and a feature resembling a terrestrial cinder cone are also present in the mare (part U).

Photography can be compared with various other remote sensing techniques to yield additional data on geologic properties. Verification of color contrasts in Mare Nubium that were determined earlier from telescopic photography suggests that the color contacts may be flow boundaries; in addition, the toe or bench surrounding many old hills in Mare Nubium shows the mare rather than the hill color (part V). Bright swirl-shaped markings near Mare Marginus were found to be extensively developed over a region 1000 km long (part T). Regoliths on the Cayley and Descartes materials at the landing site are equally blocky at fine scales as suggested by 3.8-cm radar and infrared; however, the Descartes materials may have a thinner regolith as suggested by 70-cm radar (part W). The brightness of Descartes highlands, which has been postulated to represent young volcanic material, is still of uncertain origin but may be related to the ejecta of a nearby crater (part W). Photographs confirm that, at the landing site, South Ray Crater is blockier than North Ray Crater, as determined by 3.8-cm radar; the ground truth will allow radar data to be extrapolated elsewhere more confidently (part X). The surge of reflected light (heiligenschein) within 1.5° of zero phase shows a considerable variation over the Moon, but there is a puzzling lack of correlation with known geology (part Y).

PART A

RELATIVE AGES OF SOME NEAR-SIDE AND FAR-SIDE TERRA PLAINS BASED ON APOLLO 16 METRIC PHOTOGRAPHY

Laurence A. Soderblom[a] *and Joseph M. Boyce*[a]

Introduction

The materials of most light or terra plains predate the lunar maria and postdate the Imbrian event. In the vicinity of the Imbrium Basin, these materials have been called the Cayley Formation (ref. 29-3) but because of the subtle diversity of the terra plains over the near side, Wilhelms and McCauley (ref. 29-4) simply called these materials Imbrian plains (Ip). The age relationships between the light plains and the Fra Mauro Formation are of principal importance in placing the Apollo 14, 15, and 16 samples in a regional context and in understanding the transitional period between the enhanced cratering rate of pre-Imbrian time and the comparatively quiescent period of impact cratering since the generation of mare surfaces.

The techniques used here for the determination of relative ages have been previously presented (ref. 29-2). Basically, the method involves visually scanning an orbital photograph to determine the maximum diameter D_s of a crater the interior slope of which has been eroded below the Sun elevation angle S_s. All craters larger than D_s are still shadowed, being too large to be eroded below S_s. By using a model of small-impact erosion (ref. 29-1), the measurements are converted to D_L, the diameter of a crater that could be eroded to some arbitrary small slope (1°) under the impact flux that has accumulated on a surface of unknown age. This conversion allows the effect of varying illumination angles among various photographs to be removed.

This technique was applied where possible to Lunar Orbiter photography (ref. 29-2). Most of these photographic data pertained to mare units; very little data existed for Cayley Formation or terra plains. The Apollo 16 metric camera photography provides a good data base to evaluate the relative ages of these light plains in two parts of the equatorial regions of the Moon – one on the far side and one on the near side.

Results

Relative age measurements were made for 14 light plains areas, using 30X enlargements of Apollo 16 metric camera photography. The results of those measurements are tabulated in table 29-I. A crude estimate for an area rejuvenated by Imbrium sculpture is included. This estimate was made from Apollo 16 camera frame 1676, which shows that several post-sculpture craters 2 to 3 km in diameter were degraded and eroded to slopes well below the solar elevation angle (15°). Like the Fra Mauro Formation, Imbrium sculpture was formed at the time of the Imbrian event. As previously noted (ref. 29-2), the technique is not strictly applicable to hummocky terrain or associated sculpture because the morphologic evolution of craters on irregular terrain is not understood. Futhermore, physical processes unrelated to impact erosion, such as thermal creep or mass wasting, could be involved in modifying craters in complex terrain.

The erosion model on which the technique is based predicts that D_L is a linear function of integrated impact flux (ref. 29-2). The age estimate for Fra Mauro and Imbrium sculpture can be improved by using crater counts. Cumulative crater frequency curves obtained from Lunar Orbiter IV and Apollo 16 photography of the Cayley and Fra Mauro Formations are shown in figure 29-1. Crater counts on both surfaces were made for craters larger than the steady-state limit. The steady-state function found by Trask (ref. 29-5) is also shown. The craters included in the figure fall on the production curve, which has a characteristic form approximately $N = KD^{-3}$ where N is the number of craters per 10^6 km^2 of diameter greater than D (meters) (ref. 29-6). The parameter K

[a]U.S. Geological Survey.

TABLE 29-I.–Relative Ages of Various Light Plains Areas[a]

Frame no.	*Lunar areas*	D_s, *m*	S_s, *deg*	D_L, *m*
0013	Plains east of Valier	700 to 1050	10	510 ± 100
0020	Valier floor	1060 to 1460	18	515 ± 75
0161	Cayley north of Descartes A	960 to 1300	16	505 ± 75
0165	Cayley north of Apollo 16 site	770 to 1180	10	540 ± 90
0165	Cayley near Anděl A	864 to 1285	11	600 ± 120
0169	Albategnius floor	650 to 950	5	550 ± 80
1562	Plains east of Mendeleev	870 to 1210	13	530 ± 90
1563	Mendeleev floor	980 to 1360	19	575 ± 95
1673	Ptolemaeus floor	1280 to 1780	19	585 ± 100
1676	Plains west of Ptolemaeus	920 to 1420	16	520 ± 110
1676	Imbrium sculpture near Ptolemaeus	>2260	19	>1000
2203	Guericke floor	920 to 1240	15	505 ± 75
2205	Parry floor	875 to 1240	13	545 ± 95
2205	Bonpland floor	1030 to 1290	13	595 ± 65
2205	Fra Mauro floor	875 to 1180	13	525 ± 75

[a]From Apollo 16 metric photography expressed in terms of D_L.

is a measure of the integrated impact flux. The values of K found in this study are $10^{13.4}$ and $10^{13.8}$ for the Cayley and Fra Mauro Formations, respectively, which indicates that the Fra Mauro Formation is considerably older than the Cayley Formation. The Fra Mauro Formation counts are in agreement with those obtained by Swann et al. (ref. 29-7).

By using these values of K and D_L for the Cayley and Fra Mauro Formations and Imbrium sculpture, and by using similar data (refs. 29-2, 29-8, and 29-9) for maria and younger craters, the relationship between D_L and K can be tested. Figure 29-2 shows this comparison. The predicted linear relationship is supported, and D_L, like K, is a linear index of the integrated accumulation of impacts. Figure 29-2 futher substantiates the indication that the Fra Mauro Formation and Imbrium sculpture are older than the Cayley Formation.

Figure 29-3 displays the relative age data from table 29-I for the light plains or the Cayley Formation along with the results of crater counts for the Fra Mauro Formation and of an earlier study of younger maria and craters (ref. 29-2). The areal distribution of the light plains dated in this study is shown in figure 29-4. Three things are readily apparent from these figures.

(1) The Cayley Formation appears to have a fairly small range in age; in fact, these surfaces may conceivably be synchronous, because the spread in the data is approximately equal to the uncertainty in the measurements.

(2) Light plains of Cayley age are found on both the lunar near side and far side.

(3) The Cayley Formation appears to be transitional with the early maria, and a considerable hiatus appears between the Cayley Formation and the Fra Mauro Formation, all of which indicates that the Cayley Formation is not part of basin ejecta blankets.

The relative ages determined in this study for the light plains or the Cayley Formation can be compared with isotopic ages determined from Apollo samples to estimate absolute ages. Figure 29-5 shows relative age data from Soderblom and Lebofsky (ref. 29-2) plotted against isotope ages for Copernicus (ref. 29-10), for Apollo 11 and 12 maria (ref. 29-11), for minimum ages of Fra Mauro breccias (refs. 29-12 and 29-13), and for Apollo 15 maria (ref. 29-14). Even if the uncertainty in the relative age of the Cayley Formation, 550 ± 50 m, represents a real spread in age, the Cayley material sampled here must have been emplaced throughout the Moon during a period of less than 100 million years.

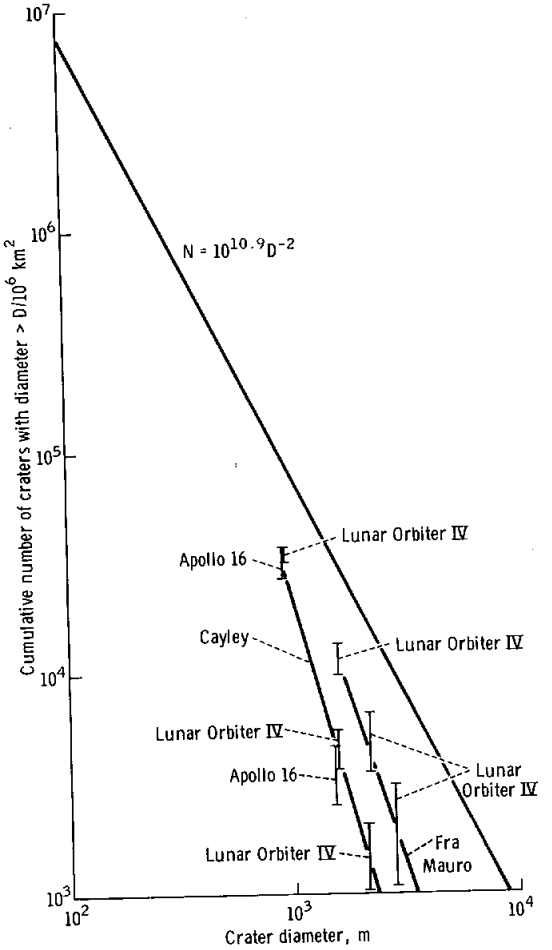


FIGURE 29-1.–Cumulative diameter frequency of lunar craters formed on the Fra Mauro and Cayley Formations. The steady-state curve of Trask (ref. 29-5) is drawn to indicate that the data obtained relate to the steeper production functions in both areas.

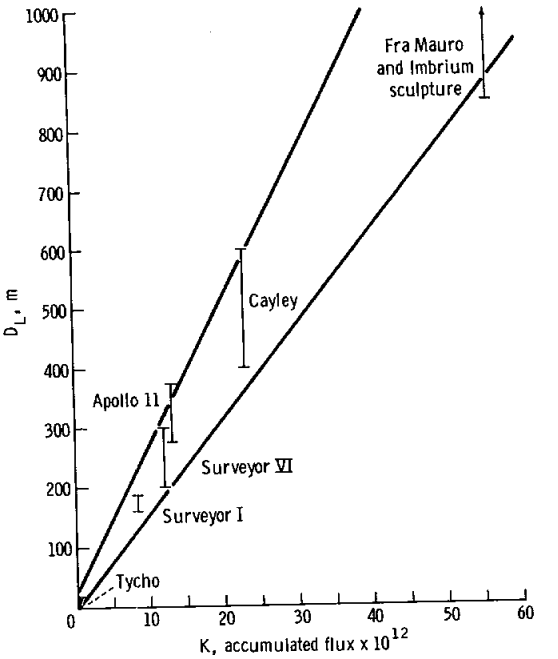


FIGURE 29-2.–Relationship between D_L (maximum diameter of a crater the interior wall of which has been eroded below 1°) and K (the integrated impact flux determined from crater counts). Crater counts are taken from references 29-6, 29-7, and 29-9.

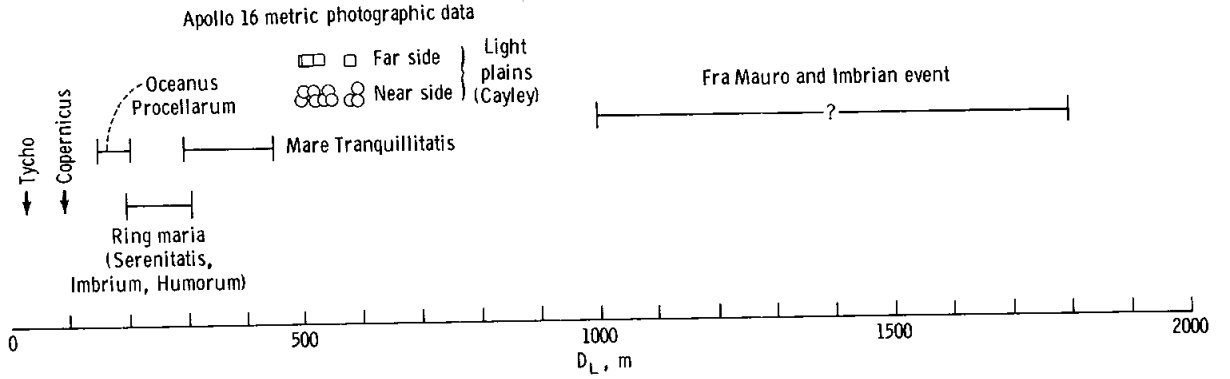


FIGURE 29-3.–Ranges of relative age for young craters, maria, light plains, and the Fra Mauro Formation. The distribution of relative ages for light plains or Cayley Formation measured in this study is compared with the data of Soderblom and Lebofsky (ref. 29-2). Note that the light plains were dated at a similar age on both the near side and the far side.

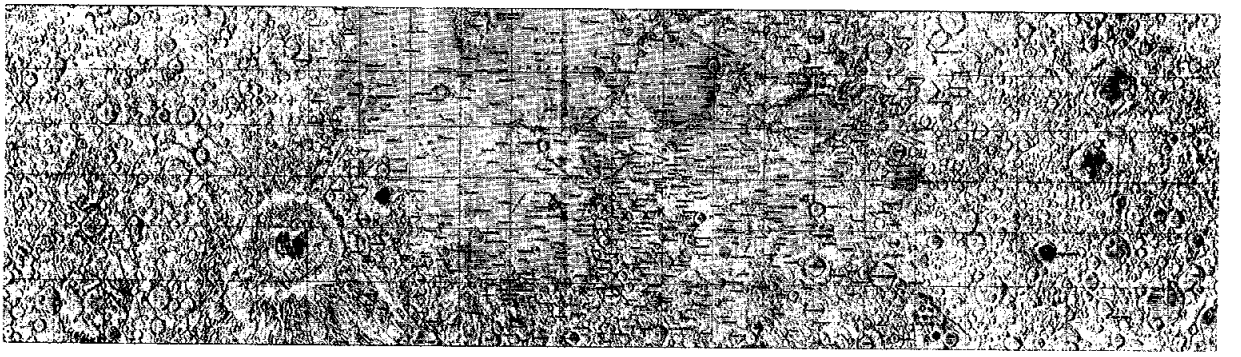


FIGURE 29-4.–Distribution of light plains areas listed in table 29-I.

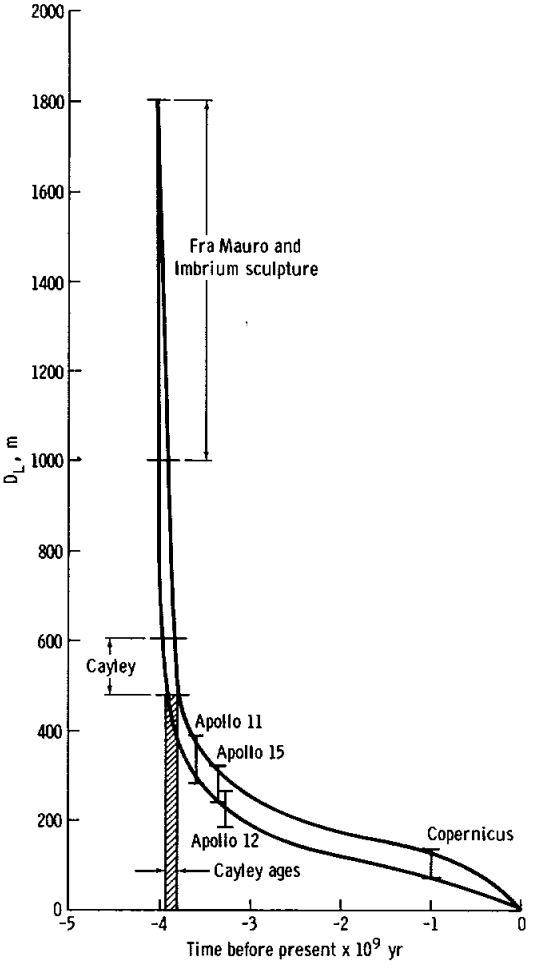


FIGURE 29-5.–Comparison of relative age determinations made from orbital photography and isotope ages determined from Apollo samples. The small range of D_L for the Cayley Plains indicates a short period for their formation.

Conclusions

The results of this study indicate the following conclusions.

(1) Crater morphology and frequency studies consistently indicate that the Fra Mauro Formation has received 2.5 to 3 times as much impact flux as the Cayley Formation.

(2) Crater counts and the relative age dating technique used in this study indicate that the Cayley Formation is only slightly older than the oldest mare units.

(3) If it is assumed that the rubidium-strontium ages of Apollo 14 basalt breccias give a minimum age for the Fra Mauro Formation, the Cayley Formation must have been generated throughout a period of less than 100 million years, approximately 3.8 to 3.9 billion years ago.

(4) The Cayley Formation ages obtained in this study on the near side and far side are the same, indicating a synchrony throughout the Moon in these units.

(5) The linear relationship as predicted by the small-impact erosion model between net accumulated flux and the maximum diameter of a crater that could be eroded below recognition is confirmed.

PART B

CAYLEY FORMATION INTERPRETED AS BASIN EJECTA

R. E. Eggleton[a] *and G. G. Schaber*[a]

The discovery that samples returned from the Cayley Formation at the Apollo 16 landing site consist mainly of nonvolcanic breccias (secs. 6 and 7 of this report) suggests that the hypothesis in which light plains-forming materials may be ejecta from multi-ring basins should be reevaluated (refs. 29-15 to 29-17). Improved information on the morphology and distribution of the Cayley Formation, provided by Apollo 16 orbital photography, leads to a concept in which the Cayley Formation was deposited as fluidized debris that traveled beyond the presently recognizable extent of the Imbrium Basin ejecta. An elaboration of this genetic model is in preparation; the description, a summary of the model, and its implications are presented in this subsection.

Cayley Formation (refs. 29-18 and 29-19) is a formal lunar stratigraphic name applied to material that forms numerous light-colored or terra plains of Imbrian age in the central near side of the Moon (refs. 29-3 and 29-19 to 29-22). In the Cayley Formation near Cayley Crater (400 km north of the Apollo 16 site), the formation overlies Imbrium sculpture but is embayed by mare material and has a higher crater density than nearby maria (ref. 29-19). Thus, the Cayley Formation predates the mare but postdates sculpturing by the Imbrian event. Similar light-colored plains-forming materials inside the main bounding scarp of the Imbrium Basin near Archimedes Crater have been named the Apennine Bench Formation (ref. 29-23). In areas distant from the Imbrium Basin, similar materials are generally mapped as simply Imbrium plains-forming material (ref. 29-4).

The idea that the materials now called Cayley Formation are Imbrium ejecta was suggested in the past on the basis of (1) gradations between the Fra Mauro Formation (ridgy ejecta of the Imbrium Basin (refs. 29-3 and 29-24)) and the Cayley Formation as seen at the 1- to 2-km resolution of Earth-based telescopic observation and (2) a concentration of patches of Cayley Plains peripheral to the Fra Mauro Formation on the south and southeast (ref. 29-15). (The evolution of the nomenclature and interpretation is discussed in ref. 29-3.) Lunar Orbiter and Apollo photographs now suggest that the gradation was only apparent and that contacts are distinct in most locations. However, the pattern of concentration of terra plains-forming materials of Imbrian age peripheral to the Fra Mauro Formation on the south and southeast (ref. 29-4) still suggests that those plains materials are associated with the Imbrian event.

Continued lunar mapping, aided by Lunar Orbiter photographs, led to a general favoring of a volcanic origin for the Cayley and similar terra-plains deposits, although several investigators (refs. 29-4, 29-20, 29-25, and 29-26) have maintained that rocks of diverse origin and age may be included within these units. The Cayley Formation clearly has depositional characteristics very different from those of the Fra Mauro Formation. The Cayley Formation generally forms flat-surfaced "pools" filling local depressions. In contrast, the Fra Mauro Formation is ridged and draped over the pre-Imbrian surface. Furthermore, the Fra Mauro Formation forms a continuous wreath around the Imbrium Basin, whereas light plains are scattered widely over the lunar surface (ref. 29-4). These major differences may be explained if ejecta from multi-ring basins is segregated into two drastically different transport regimes, one which produces a continuous topographically textured blanket and one which is highly mobile and flows into depressions to form pools.

Morphology of Terra Plains

Several aspects of the morphology of terra-plains materials bear on the problem of the nature and origin of the deposits: (1) the materials form flat-surfaced pools within depressions; (2) the pools have

[a]U.S. Geological Survey.

a distinctive population of subdued or ghost craters; (3) relatively steep-sided, kilometer-sized hills are common within the pools; and (4) some Cayley-like deposits appear to be lobate sheets.

Level pools.—The flat surfaces of the Cayley Formation pools have been demonstrated, using photogrammetric techniques and Apollo 16 metric camera stereoscopic photography. By using an AP/C analytical stereographic plotter, spot elevations, determined for 170 points that were selected to measure the flatness of the pools of the Cayley Formation and elevation differences between pools (fig. 29-6), indicate that the pools are flat and level. The average standard error of measurement of elevations was approximately ±8 m. Most surfaces slope less than 1°. The estimates of levelness of the surfaces of the pools may be affected a small amount because the area studied is eight times larger than the map that was used for vertical control (ref. 29-27). Small distortions are expected near the edge of the stereoscopic model; postflight data on absolute camera orientation are not available at this time. Thus, the stereoscopic model may have been tilted 1/3° to 1/2° toward the east or east-southeast as suggested by the trend of elevations across many of the larger pools.

Such a small tilt has little effect on the results. If the tilt is removed, the Cayley patches are generally level to within 1/4° to 1/2° for slope lengths of 5 to 10 km. A few local patches (or parts of patches) measuring several kilometers across have slopes of 1° to 2.5°.

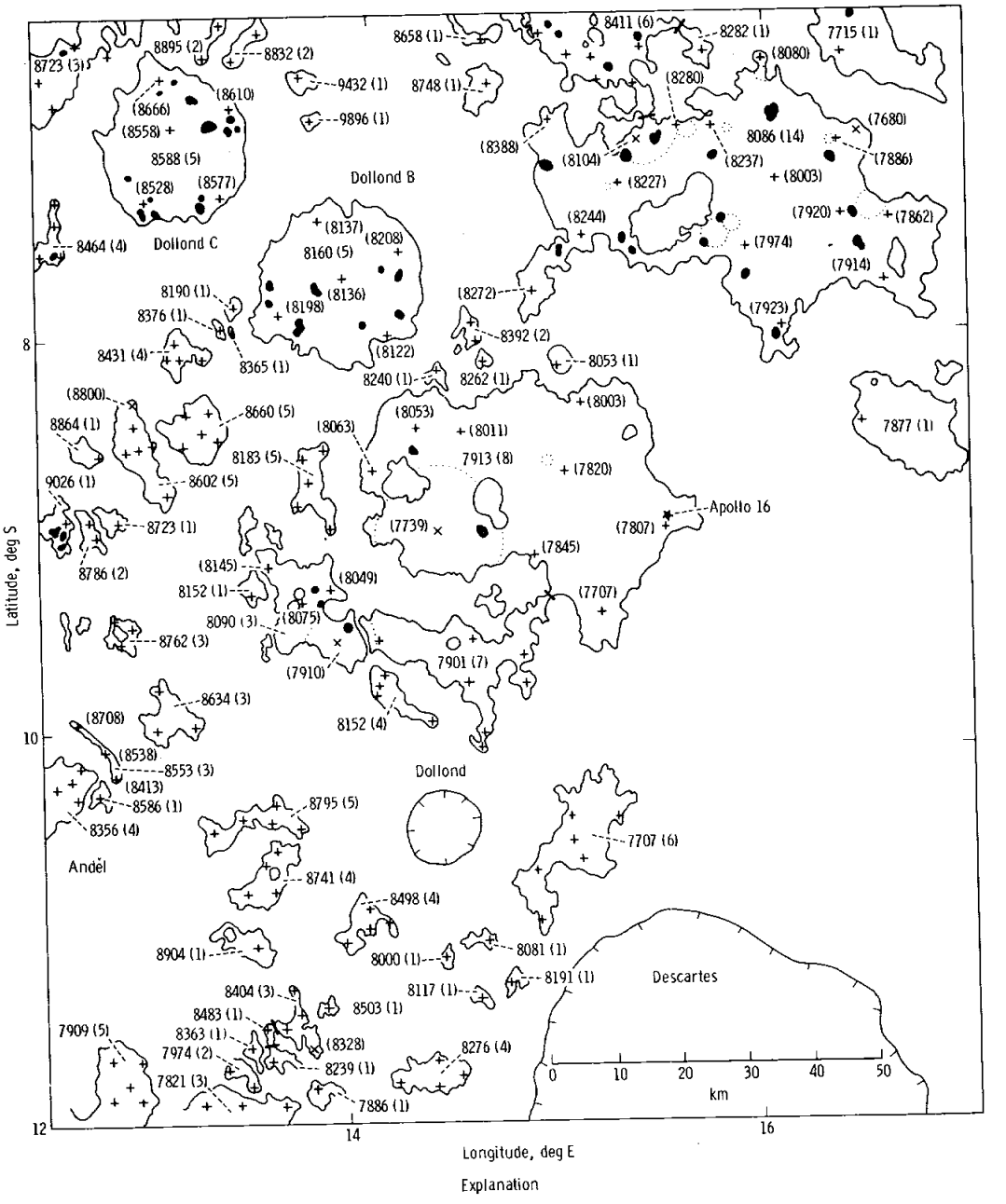
Most investigators have attributed the flat, level topography of Cayley Plains to fluid emplacement.

Subdued craters.—Strongly subdued crater forms in the terra plains are widely distributed. They were previously noted in Ptolemaeus Crater, the Fra Mauro Crater, and around Mare Humorum by use of telescopic observations (ref. 29-15). Similar ghost craters are seen under low Sun in Lunar Orbiter IV photographs of extensive terra plains north of the Imbrium Basin, beyond Mare Frigoris. A widespread population of 23 such craters, with diameters of 4 to 20 km, was mapped in the Ptolemaeus quadrangle in the craters Ptolemaeus, Hipparchus, Lade, and Albategnius and southeast of Albategnius Crater around Burnham Crater (ref. 29-20). Some in Albategnius are quite evident in low-Sun Apollo 16 photographs (fig. 29-7). With the aid of stereoscopic viewing of the Apollo 16 metric camera frames, 12 such craters have been noted so far in patches of the Cayley Formation near the Apollo 16 landing site in the Theophilus quadrangle (fig. 29-6). Spot elevations measured photogrammetrically indicate depth-to-diameter ratios of approximately 1:100 and 1:20 for two craters near the landing site with diameters of 20 and 12 km, respectively. These craters typically appear to have relatively much more subdued interiors than rim flanks. It has been suggested that the ghost craters resulted from differential compaction over buried craters (ref. 29-20).

The circular patch of Cayley Formation within Parry Crater (fig. 29-8) forms a very subdued depression about 50 km across (at the edge of the present floor of Parry Crater). The central part of the depression is circular, flat, and 35 km in diameter. This shallow depression may mimic the unfilled form of Parry Crater, again suggesting differential compaction.

Domical hills.—Several domical to conical hills, kilometer-sized and smaller, on a patch of the Cayley Formation occupying the floor of Alphonsus Crater were noted in Ranger 9 pictures by Strom (ref. 29-28). A number of similar features present in the Cayley terrain on the floor of Fra Mauro Crater and in surrounding areas have been noted. Other such hills in the area around the Apollo 16 landing site are shown in figure 29-6. Similar hills, such as in Hipparchus Crater, are conspicuous in the Apollo 16 metric camera photographs across the full width of the central highlands. The lack of a clear relationship between the hills and preexisting topography suggests that the domical hills possibly may be constructional landforms intrinsic to the Cayley Formation.

Sinuous scarps.—Although most of the Cayley Formation is found as pools within depressions, some similar material is in lobate sheets partly bounded by outward-facing sinuous scarps. Such Cayley-like lobes occur northwest, northeast, and south of the Orientale Basin (figs. 29-9 to 29-11). The sheets, estimated to be 200 to 500 m thick, are lobate outward from Orientale, suggesting that they are part of the Orientale ejecta. They overlap relatively rough-surfaced deposits of the rim material (ejecta) of Orientale and rough-surfaced deposits associated with Orientale satellitic (secondary impact) craters (figs. 29-9 to 29-11). Apollo 16 photography indicates that similar but more eroded lobate flow sheets are also present around the Imbrium Basin (figs. 29-12 and 29-13).



Explanation

- Cayley Formation
- Rim crest of ghost crater
- Small hill
- 8152 (4) Average or representative elevation of patch of Cayley Formation; number of points averaged given in parentheses
- +(8059) Elevation of point of Cayley Formation
- × (8104) Elevation of point of Cayley Formation not included in average
- \+ Point where elevation was determined
- Boundary between areas where elevations were averaged
- ★ Apollo 16 landing site

FIGURE 29-6.–Map of photogrammetrically derived elevations of the Cayley Formation around the Apollo 16 landing site. The elevations are in meters above a 1730-km-radius reference sphere. (The base for this map is Apollo 16 metric camera frame 0440.)

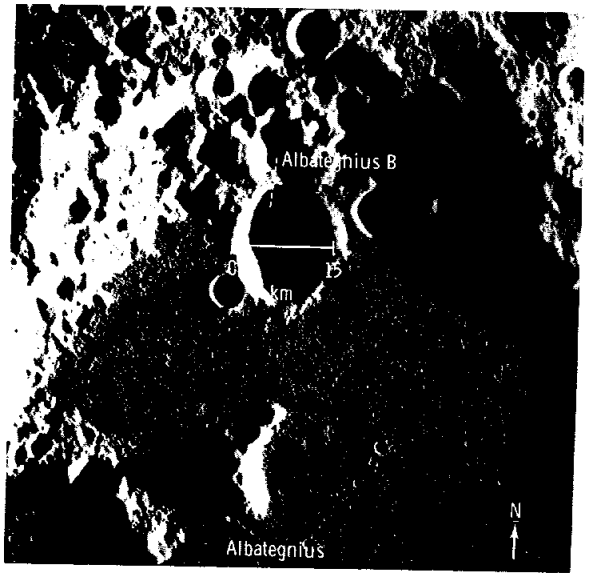


FIGURE 29-7.–Ghost craters on the surface of the Cayley Formation in the bottom of Albategnius Crater. Albategnius B crater is approximately 15 km across. Subdued troughs trending north-northwest may be buried Imbrium sculpture (part G of this section) (Apollo 16 metric camera frame 0449). The Cayley Formation may be mantling fresh craters to produce a subdued flat-bottomed bowl shape.

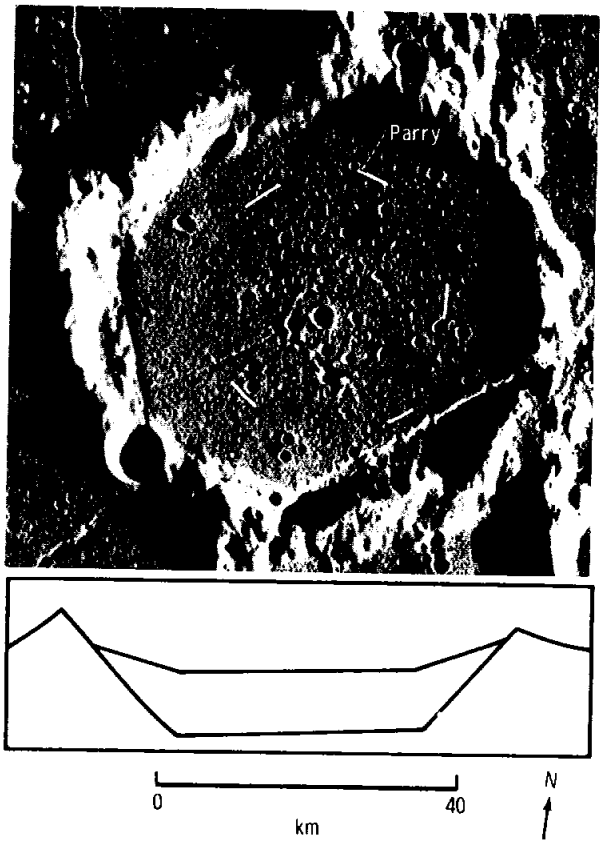


FIGURE 29-8.–A patch of the Cayley Formation with its surface in the form of a subdued depression occupying the bottom of Parry Crater near Fra Mauro (Apollo 16 metric camera frame 1685). Dashes in the photograph indicate the edges of a flat floor. The cross-section sketch (below the photograph) suggests the relationship to the unfilled shape of Parry Crater.

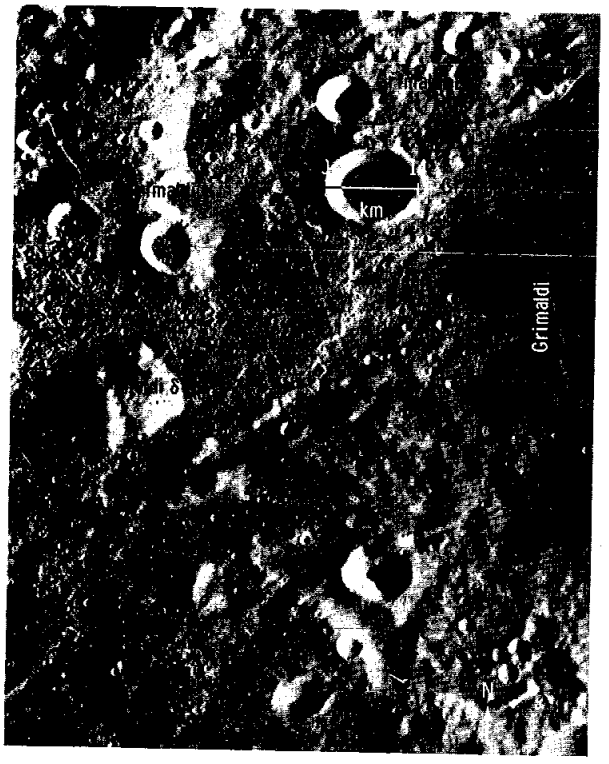


FIGURE 29-9.–Flow lobes of Cayley-like material in the western part of Grimaldi Basin, northeast of the Orientale multi-ringed basin (fig. 29-16). Small tongues of Cayley-like material have flowed around smooth, preexisting hills 7 to 17 km west of Grimaldi T Crater. Parallel ridges in the southwestern corner of the figure are radial to the Orientale Basin and are characteristic of the Hevelius Formation (continuous ejecta of the Orientale Basin) (refs. 29-29 to 29-31). The Cayley-like material overlaps similar but more subdued ridges south of Grimaldi A Crater and, southwestward, appears to grade into or thinly overlap the Hevelius Formation (Lunar Orbiter IV photograph H168).

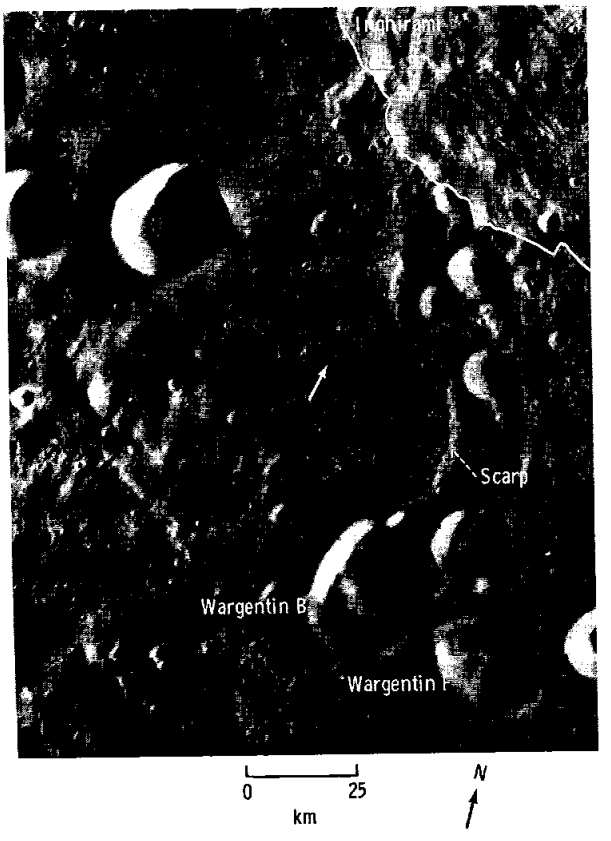


FIGURE 29-10.–Flow lobe near Inghirami Crater south-southeast of the Orientale Basin (fig. 29-16). The western margin flowed around smooth, preexisting hills as did the small lobes west of Grimaldi T Crater in figure 29-9. Rudimentary longitudinal ridges trending south-southeast, radial to the Orientale Basin, are present over the entire lobe in the photograph. These might reflect ridges on the Hevelius Formation if it underlies the lobe. Alternatively, the lobe may be genetically transitional in character between the ridged Hevelius and the smooth Cayley-like materials. A 3-km-diameter ghost crater is indicated by the arrow (Lunar Orbiter IV photograph H180).

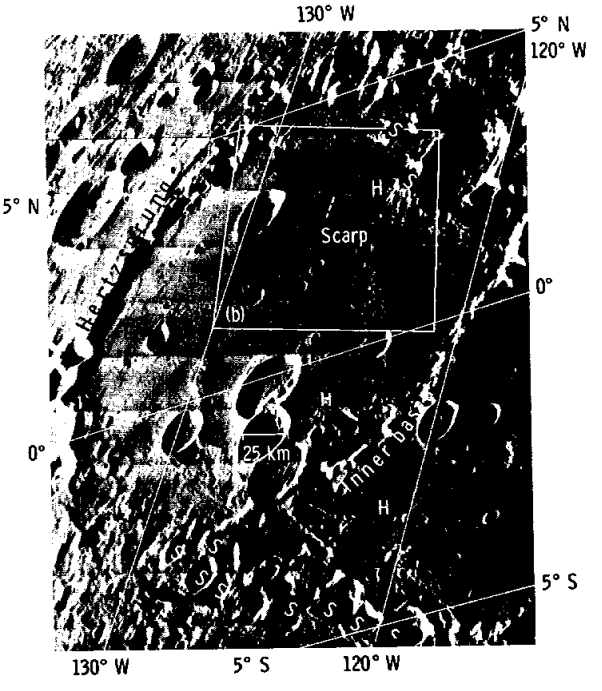


FIGURE 29-11.–Terra-plains material in the inner basin of the Hertzsprung multi-ringed basin, 750 to 900 km west-northwest of the Orientale Basin. (a) Chains of Orientale secondary craters 15 to 25 km across (indicated by "S") and textured Hevelius Formation (indicated by "H"). Terra-plains material conspicuously overlaps the Hevelius Formation and rough topography associated with the Orientale secondary craters along the indicated scarp contact.



FIGURE 29-11.–Concluded. (b) An enlargement to show terra-plains material flow front. Irregular topography in much of the southern half of the inner basin of Hertzsprung suggests mantling and only partial obscuration of underlying relief by the terra-plains material (Lunar Orbiter V photograph H26).

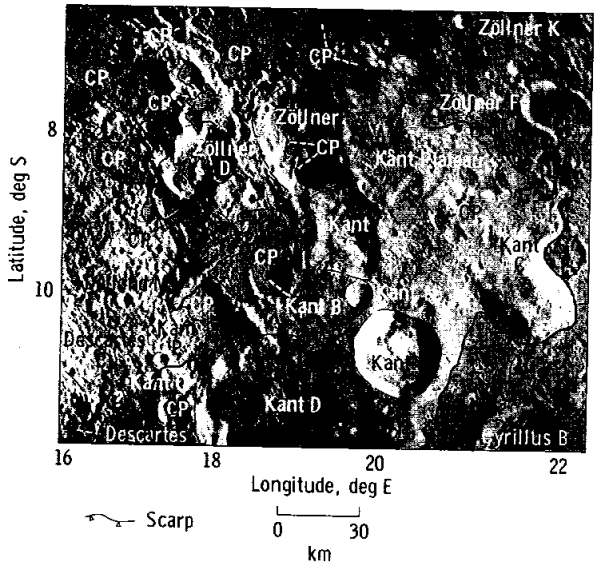


FIGURE 29-12.–Annotated mosaic of Apollo 16 metric camera frames 0435 and 0439 showing the highest portion of the Kant Plateau (heavy line), distribution of smooth plains of the Cayley Formation (cp), and the sinuous scarps associated with them. The sinuous scarp on western wall of Kant D (fig. 29-13) is noteworthy.

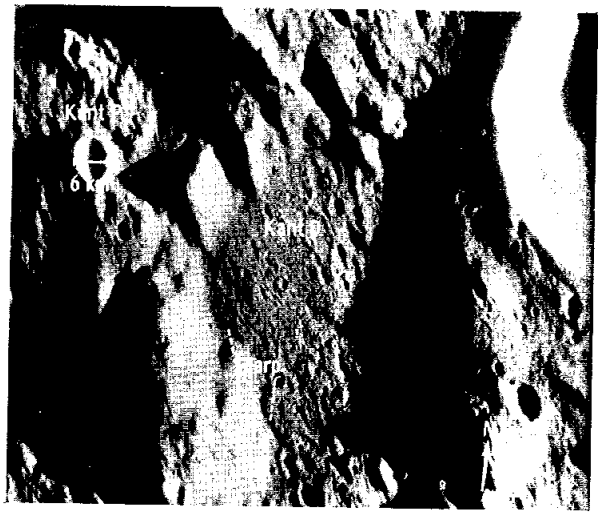


FIGURE 29-13.–Enlargement of 500-mm photograph AS16-124-19831 showing the sinuous scarp bounding Cayley-like material and lapping the western wall of Kant D Crater (fig. 29-12).

Distribution of Terra Plains

The following patterns of distribution also bear on the origin of terra-plains deposits: (1) pools are at widely different elevations, (2) plains tend to be concentrated in belts peripheral to the conspicuous ejecta blankets of multi-ring basins, and (3) certain uplands deposits have some characteristics in common with the plains deposits.

Elevation of pools.—A wide variation of pool elevations in Cayley Plains exists. A spread of more than 2 km in Cayley elevations was observed in the area studied (170 by 140 km shown in fig. 29-14). This variation is in marked contrast to the nearly uniform elevations of mare surfaces in similarly restricted areas.

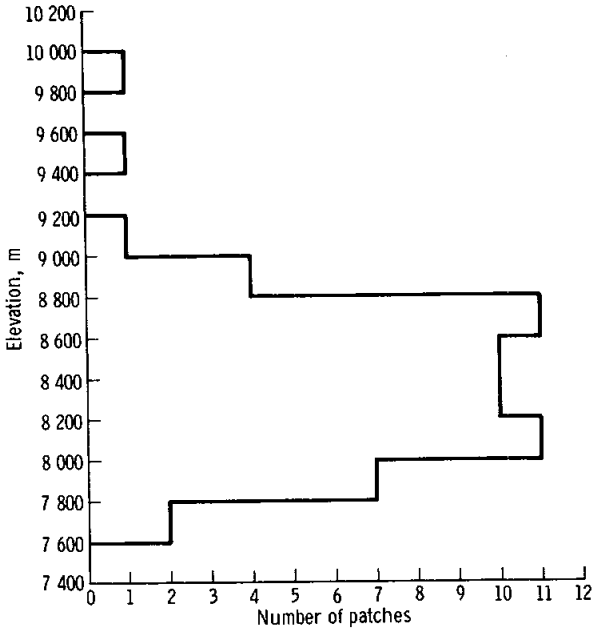


FIGURE 29-14.—Histogram of elevations of pools of Cayley Formation Plains shown in figure 29-6.

Areal distribution.—Numerous large patches of the Cayley Formation are concentrated in a belt peripheral to the Fra Mauro Formation between Fra Mauro Crater on the west and Cayley Crater on the east (refs. 29-4 and 29-15). A similar belt of large patches of Imbrian terra-plains materials occupies an analogous position north of the Imbrium Basin, from Arnold Crater to Volta Crater (fig. 29-15).

The Orientale Basin is fresher and better preserved than the Imbrium Basin. The basin is surrounded to a

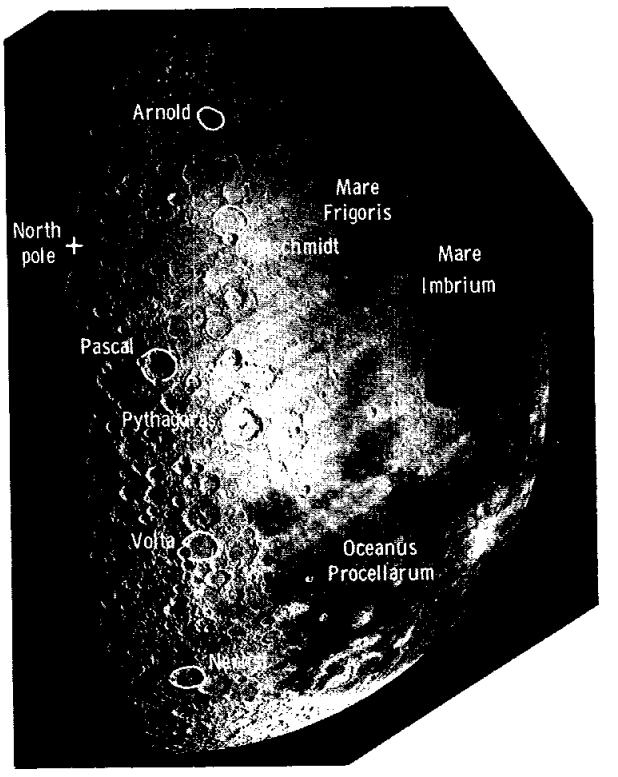


FIGURE 29-15.—Imbrian terra-plains materials north of Mare Frigoris are concentrated in an annulus on the northern side of the Imbrium Basin (Lunar Orbiter IV photograph M190).

distance of 300 to 500 km by a blanket of textured ejecta (refs. 29-29 to 29-31), and beyond that are numerous patches of plains-forming material. In figure 29-16, large patches occur near Riccioli Crater; in and near the Grimaldi Basin; in Darwin Crater and to the east for 300 km; from Vieta Crater to Schickard Crater; and beyond to the south and southeast. Some of these plains near the Orientale Basin locally show surface textures (e.g., faint ridges and furrows). These textures are of such low relief that similar textures in deposits as old as the Imbrium Basin would probably be degraded beyond recognition. West of the Orientale Basin on the far side, large patches of youthful plains-forming material are not conspicuous except in Hertzsprung Basin (fig. 29-11). Elsewhere, the area west of the Orientale Basin is rugged, heavily cratered terrain. As shown in figure 29-17, instead of large pools, there are numerous closely spaced small pools at different elevations commonly filled to the brim with plains material. The appearance is similar to the apparently heavily

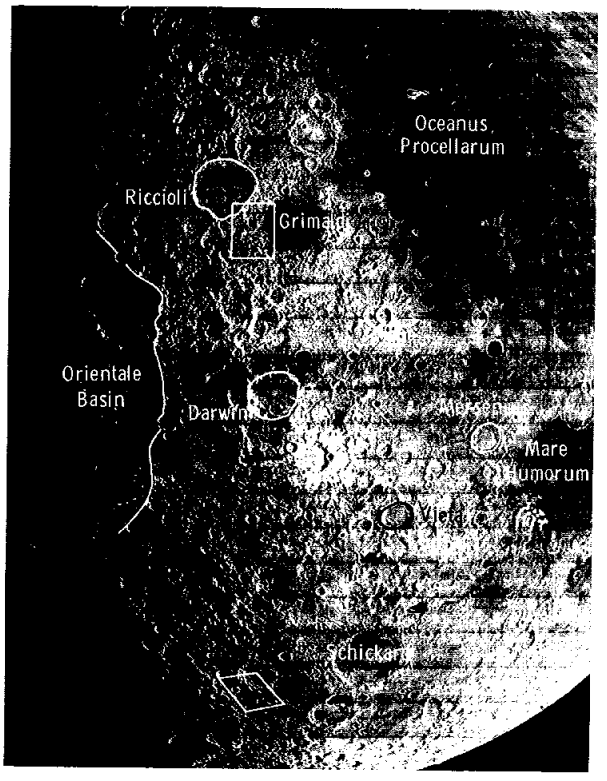


FIGURE 29-16.–Imbrian terra-plains materials east of the Orientale Basin. The outlined area near Grimaldi Crater is shown in figure 29-9. The outlined area southwest of Schickard Crater is shown in figure 29-10 (Lunar Orbiter IV photograph M190).

mantled terrain northeast and northwest of Ptolemaeus Crater in the near side central highlands.

The pre-Imbrian Nectaris Basin also appears to have remnants of a surrounding belt of plains-forming materials, at least on the south (fig. 29-18). These pre-Imbrian plains are far to the south of the basin beyond a belt with topographic grain radial to the basin. The grain is caused by the intrinsic ridges of the mid-pre-Imbrian Janssen Formation (ejecta of the Nectaris Basin, ref. 29-32) and by the "sculpture" of the Nectaris event. The plains appear to be superposed on the sculpture. Beyond the plains is a heavily cratered terrain with few patches of plains.

Possibly related uplands deposits.–Areas of subdued topography adjacent to the Cayley Plains, in some cases, are gradational in albedo and topography with plains-forming materials. This has led to the inference that such subdued areas are mantled by the plains-forming material or related materials (refs. 29-20 to 29-22). One large upland that may be

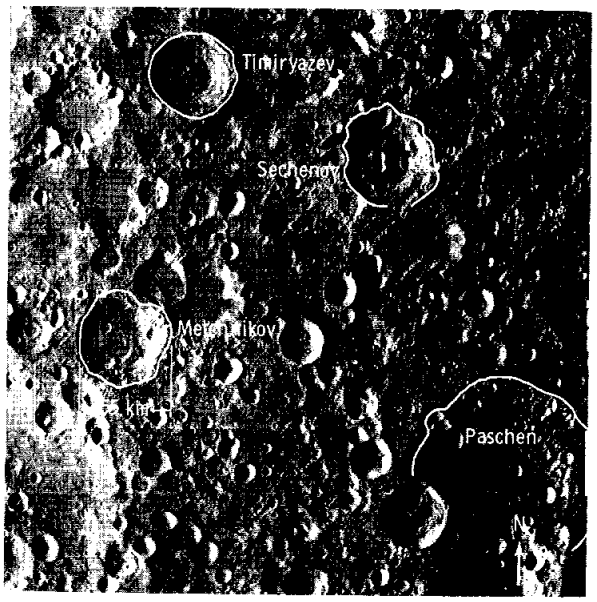


FIGURE 29-17.–Area 750 to 1200 km west of the western rim crest of the Orientale Basin showing locally heavy mantling by terra-plains material; for example, just north of the center of the figure (Lunar Orbiter I photograph M28).

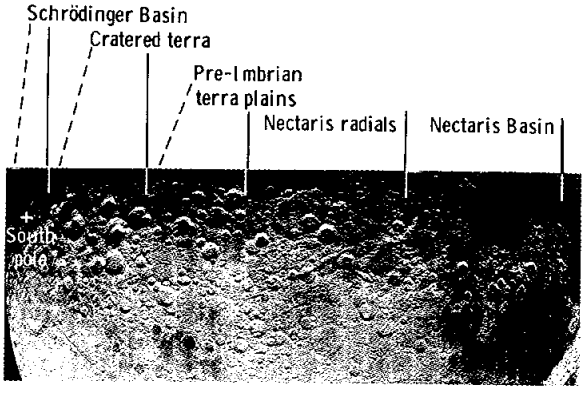


FIGURE 29-18.–Nectaris Basin and the area to the south. Pre-Imbrian terra-plains material is peripheral to the area with radial topographic grain. The plains appear to be superposed on Nectaris sculpture (Lunar Orbiter IV photograph M52).

heavily mantled by draped, rather than pool-like, Cayley materials is the Kant Plateau (ref. 29-21).

The Kant Plateau is one of the highest points on the near side (ref. 29-33). The plateau rises above adjacent terrain along scarps as high as 2.0 km, especially on its eastern side, and is part of the main mountainous ring, including the Altai Scarp (Rupes Altai) to the south, that bounds the Nectaris Basin. The surface of the Kant Plateau is partly smooth and partly undulating at distances of 1 to 10 km but generally is distinctly smoother than surrounding lunar terrain. Locally level surfaces suggest the plateau is heavily mantled by materials of the Cayley Formation. At the south end of the plateau, prominent scarp-bounded lobes of Cayley-like material occur (figs. 29-12 and 29-13).

Another possible lobate form at approximately the same distance from the Imbrium Basin occurs near Ritchey J and Abulfeda D Craters, 300 km to the west-southwest. Both there and at the plateau, the lobes are roughly south of large clustered craters elongated radial to the Imbrium Basin. The craters referred to on the Kant Plateau are Zöllner and Kant G (fig. 29-12).

Interpretation

The foregoing characteristics can be explained by the hypothesis that terra plains-forming deposits are a facies of ejecta from the impacts that formed multi-ring basins. This facies must have been transported and deposited in a distinctly different regime than the radially ridged, continuous ejecta blankets such as the Fra Mauro Formation. In the model, the basin ejecta segregates into two principal transport regimes, one mainly ballistic and the other highly fluid. The terra plains result from deposition of the fluid portion, mainly beyond and after deposition of the continuous, topographically textured blanket.

This interpretation of the Cayley Formation accounts for its circumbasin distribution and occurrence in level pools. Each patch of terra-plains material pooled in a local preexisting depression, so that the resulting pools have a variety of elevations, depths, and drainage areas.

The subdued or ghost craters might be produced by differential compaction of an initially level cover as suggested by Howard and Masursky (ref. 29-20), or by an initially draped mantle of fragmental material. The patch of the Cayley Formation that occupies the entire floor of Parry Crater shows a profile that can best be explained by differential compaction (fig. 29-8). The heightened rim flank relative to the interior of many of the subdued craters could be explained by the partial draining away of a blanketing flow sheet in intercrater areas while portions of the sheet are trapped inside the mantled craters. In Ptolemaeus Crater, for instance, the subdued craters are located in the northern two-thirds of the crater (ref. 29-20), and it seems possible that Cayley materials could have flowed toward the southern third, totally obscuring any preexisting craters there with the resulting thicker cover.

The domical hills in the Cayley Formation possibly may be built of lithic fragmental debris, silicate melt spatter, or viscous silicate flows erupted by degassing or other fluid loss from the Cayley itself, more or less analogous to the formation of fumarolic mounds on the Bishop ash-flow tuff in California described by Sheridan (ref. 29-34).

The lobate flow sheets of Cayley-like material around the Orientale multi-ring basin (figs. 29-9 to 29-11) appear to flow from the textured Orientale ejecta blanket and Orientale secondary craters. At least some such sheets and lobes may represent parts of the Cayley-type flows that became more viscous by addition of extra material from the ballistic system into the still-flowing, fluid transport system.

The presence of an unusually heavy mantle of Cayley-like material on the Kant Plateau possibly is associated with the formation of the Zöllner and Kant G Craters (fig. 29-12). The age, clustering, size, elongation, degree of irregularity in shape, and distance from the Imbrium Basin of these craters, and their similarity with others alined roughly radial to the Imbrium Basin (Hypatia Crater, 150 km northeast; the elongate cluster from Andel M Crater to Andel P Crater approximately 240 km to the west-southwest; and Ritchey Crater and the cluster from Ritchey J Crater to Abulfeda D Crater approximately 60 km beyond), suggest that they all may be Imbrium secondary-impact craters. If Zöllner and Kant G Craters impacted on the Kant Plateau at the same time that the postulated fluid Cayley debris was passing the area, the sheet of flowing Cayley material may have become overloaded with the secondary ejecta. The resulting more viscous flow then might have partly moved southeast and southwest off the

plateau in thick, lobate tongues (figs. 29-12 and 29-13), while much of the material was deposited before it flowed off the plateau.

If the Cayley Formation originated from the Imbrium Basin, the material must have segregated from the continuous ejecta now represented by the Fra Mauro Formation. The continuous ejecta may have traveled primarily on ballistic trajectories to near its site of deposition and then flowed along the ground as a mobilized debris sheet during deposition to produce the radially ridged Fra Mauro deposit. It is possible that the segregated Cayley material was transported as a fluid system generally later than and to greater distances than the Fra Mauro material. This fluid or fluidized material pooled in low places, rarely leaving a conspicuous subduing mantle over adjacent terrain. As a partial explanation for the lack of a conspicuous continuous blanket, the fluid material may have been partly channeled into separate tongues or at least may have been partly channeled into thick streams and thin intervening webs.

Although other mechanisms may be possible, the high fluidity of the transport system that formed the Cayley Formation seems to imply that it was gas fluidized. The particulate component may have included both solids and drops or shreds of rock melt. The gas may have been vaporized target, projectile, or both.

Conclusions

By the hypothesis discussed earlier, each basin-forming event produced thick plains deposits in a belt peripheral to the continuous ejecta blanket and may have deposited a thinner layer in pools over the entire Moon. Thus, each patch of terra plains is likely to be underlain by a sequence of fluidized ejecta deposits, which were derived from most or all multi-ring basins younger than the occupied depression. If the light color of the plains results from a high feldspar content of the excavated crustal rocks, an explanation of the absence of exposed pre-Cayley mare rocks may be that they are buried or dusted over.

The last basin-forming event was Orientale. If the dusting of plains materials from the Orientale Basin has a significant thickness on plains throughout the Moon, this could account for the post-Fra Mauro coeval ages for near-side and far-side plains patches along the Apollo 16 orbital track determined from crater shapes (part A of this section).

PART C

SMALL-SCALE ANALOGS OF THE CAYLEY FORMATION AND DESCARTES MOUNTAINS IN IMPACT-ASSOCIATED DEPOSITS

James W. Head[a]

Introduction

The exploration of the Cayley Formation and material of the Descartes Mountains and an understanding of the origin and evolution of these units were primary objectives of the Apollo 16 lunar mission. The purpose of this subsection is to examine several areas associated with impact crater deposits that show small-scale features similar in morphology to the regional characteristics of the Cayley and Descartes units shown in the Apollo 16 photography.

[a]Bell Telephone Laboratories.

Cayley Formation

In the central highlands of the Moon, the Cayley Formation forms locally hummocky but regionally flat plains that fill in older highland craters and intercrater areas. Figure 29-19(a) shows the filled craters Dollond B and C, less than 100 km northwest of the Apollo 16 landing site. These plains show an albedo that is intermediate between the maria and the highlands, and the surface generally shows a higher crater frequency than the maria. The contact between the plains and surrounding deposits is generally sharp on a regional scale and gradational on a local scale. The different isolated areas of the plains occur at a wide variety of elevations. The highland materials

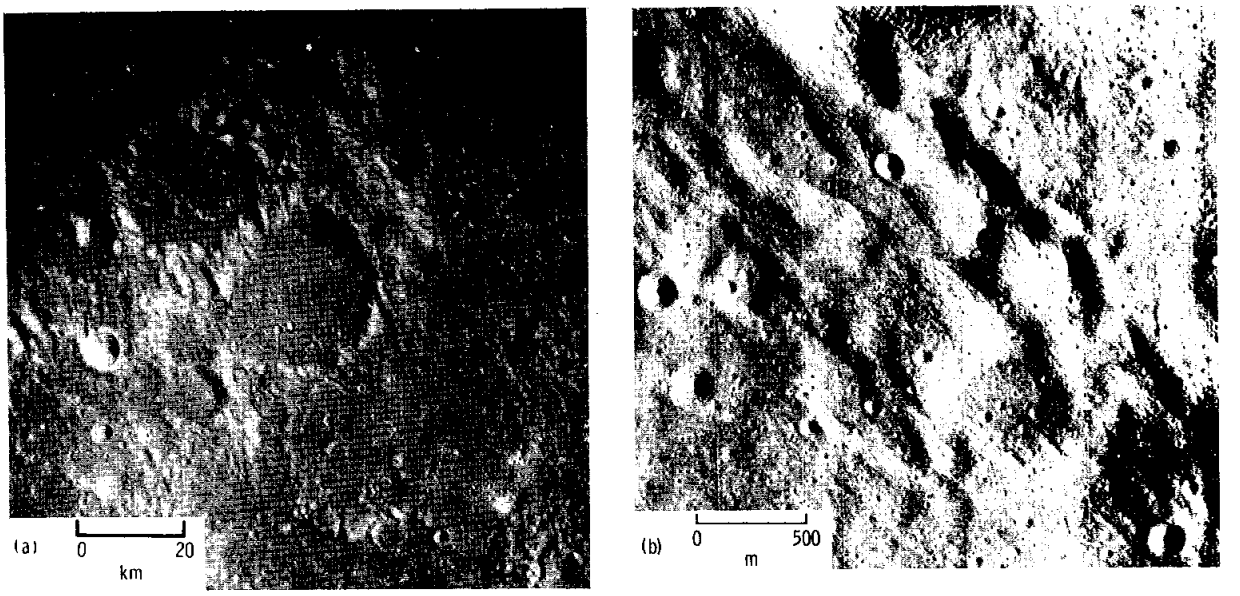


FIGURE 29-19.—Analogous regions of the Cayley Plains and Aristarchus Crater. (a) Central highland region. Cayley Plains fill Dollond B Crater (center), Dollond C Crater (upper left, adjacent to Dollond B), and low intercrater areas. The Apollo 16 landing site is in the lower right corner (portion of Apollo 16 metric camera frame 1955). (b) Analogous region near Aristarchus Crater, showing lineated highlands and plains in low areas. The location of Aristarchus Crater is shown in figure 29-20 (portion of Lunar Orbiter V photograph 205 H3).

surrounding the Cayley Plains usually are in the form of old cratered terrain, forming either heavily cratered plateaus or rims of large old craters (fig. 29-19(a)). This terrain is often striated or grooved and furrowed by parallel to subparallel lineations that are generally radial to a nearby major multi-ringed basin (Imbrium Basin in fig. 29-19(a)) but that do not transect the plains. The crater frequency of the highland regions is generally lower than the flat plains, but this difference is probably caused by more rapid erosion of craters on the topographically more irregular highland surfaces.

Certain deposits associated with Aristarchus Crater show particular similarity to the Cayley Plains and surrounding highlands, both in morphology and in position relative to adjacent impact craters. The deposits and structures differ markedly in scale, however. Figure 29-19(b) illustrates this area and shows two distinct deposits of plains material: one fills in the crater at the lower right center, and the other is elongated in a furrow trending northwestward (parallel to the regional structural trend) at the upper left. These plains deposits are characterized by a smooth surface with regionally sharp boundaries with the surrounding units and an apparently higher crater frequency. The surrounding terrain in figure 29-19(b) is plateaulike and contains several large craters, some of which have been greatly modified. This terrain is regionally grooved and furrowed by parallel lineations radial to a surrounding nearby large crater (Aristarchus), but the grooves and furrows do not cut the plains. The deposits and associated structures from Aristarchus (fig. 29-19(b)) are therefore very similar to those seen in the central highlands. However, the circular plains deposit in figure 29-19(b) is only 410 m in diameter. The diameter of the plains that fill Dollond B (fig. 29-19(a)) is approximately 32 km, more than 75 times larger. The Aristarchus structure occurs between one and two crater diameters away from the rim of Aristarchus (fig. 29-20) in an area apparently dominated by secondary crater strings, which have been modified either by subsequent outward sweep of Aristarchus continuous ejecta or by material deposited in the same event that produced the secondary craters. Little evidence exists for any subsequent event that might have filled the lows and formed the plains. The similarity between these

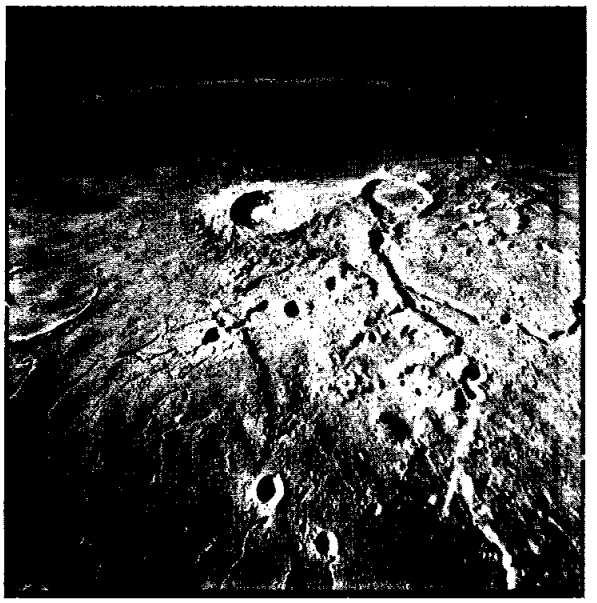


FIGURE 29-20.–Aristarchus Crater and Aristarchus Plateau regions. The young crater Aristarchus in the upper left center is 40 km in diameter. The location of the area shown in figure 29-19(b) is indicated by the arrow (Apollo 15 metric camera frame 2609).

deposits and the Cayley Plains and associated units in the central highlands suggests that an impact-related origin should be thoroughly investigated for the formation and modification of this terrain. The gross scale differences suggest that cratering on a much larger scale than Aristarchus (e.g., the Imbrium impact) may be the event to which the Cayley deposits are related.

Materials of the Descartes Mountains

The units comprising the hills and uplands from Descartes Crater north to the region of the Apollo 16 landing site include a wide variety of rugged topography with local relief of several hundred meters (refs. 29-21 and 29-35). Hilly, domed, furrowed, and subdued subunits have been mapped (ref. 29-35). Particular attention is focused here on the furrowed subunit of the Descartes Mountains, which is characterized by twisting elongate depressions that range from 1 to 2 km in width. These elongate furrows or depressions tend to be more continuous than the other subunits; their trend, while locally variable, tends to be parallel or normal to regional lineations (fig. 29-21(a)) such as those radial to the Imbrium



FIGURE 29-21.–Descartes region and Mösting C Crater. (a) Apollo 16 landing area, Descartes region, showing the grooved and furrowed structures of the rough Descartes upland terrain (portion of Apollo 16 pan camera frame 4563).

Basin. Individual furrows are often surrounded by raised rims, and occasionally two parallel furrows are connected by a short perpendicular furrow in a zigzag manner (upper part of fig. 29-21(a)). Similar furrowed deposits occur in the Zupus Crater region, northwest of the Humorum Basin.

An area adjacent to the fresh, young impact crater Mösting C (1°50′ S 8°10′ W) shows features that are remarkably similar to the Descartes furrowed units in almost every aspect except scale. The elongate furrows in this area (fig. 29-21(b)) show linear and twisting depressions median to ridges that trend dominantly concentric to the rim of Mösting C Crater. Occasionally, two furrows are connected by a short, radially trending furrow to produce a zigzag structure. These furrowed structures appear to differ from other dunelike structures surrounding Mösting C Crater only in the presence of the furrow. Although at present it is not clear why the furrowed structures are locally developed, their similarity to other structures surrounding Mösting C Crater suggests an impact-associated, rather than volcanic, origin. The dunelike structures may be clots or mounds of ejecta that have been modified by additional ejecta flows immediately following their deposition. They may also be dunes of material deposited around the crater during the sweep of ejecta associated with the formation of Mösting C Crater (fig. 29-22). Where furrows occur in the dunelike structures (fig. 29-21(b)), they appear not to have been modified by the general outward sweep, thus suggesting that they may have been formed in the latest stages of or subsequent to the Mösting C event. In addition, the down-range side of several of these structures appears to lie just inside an older crater or depression (lower center of fig. 29-21(b)). These relationships suggest

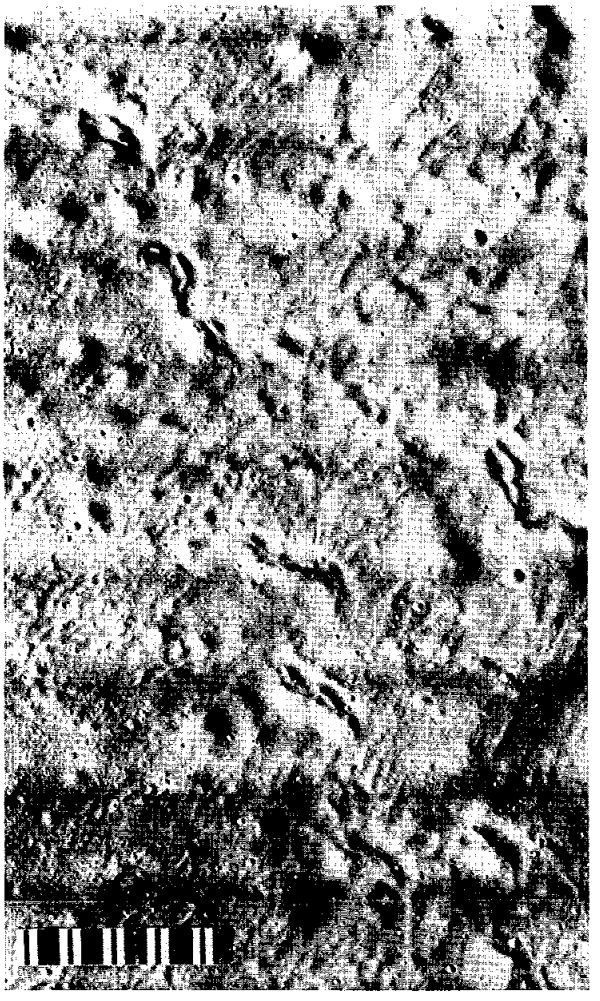


FIGURE 29-21.–Concluded. (b) Furrowed dunelike structures near Mösting C Crater (portion of Lunar Orbiter III frame 112 H2).

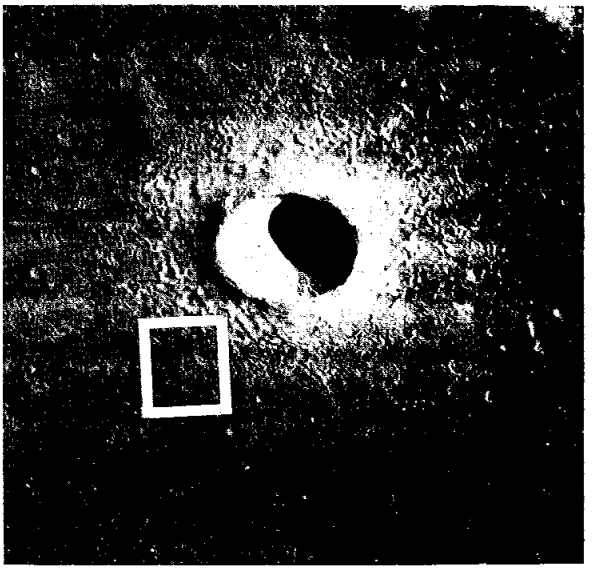


FIGURE 29-22.–Mösting C Crater, approximately 3.5 km in diameter. The inset shows the location of the area shown in figure 29-21(b) (portion of Lunar Orbiter III frame 113 M).

that at least some of the dunelike structures formed at the edge of a depression during the Mösting C event and then partially collapsed or slid down into the depression, which caused the formation of the furrow. Under this hypothesis, the furrows would originate through the mass wasting or faulting of impact-generated deposits.

Although the deposits associated with Mösting C are similar in morphology to the furrowed units of the Descartes region (figs. 29-21(a) and 29-21(b)), they differ radically in scale. The ridges and furrows of Mösting C Crater average approximately 70 m in width and approximately 200 m in length (fig. 29-21(b)), and those in the Descartes region average approximately 2 by 8 km, approximately 30 to 40 times larger. The similarity between these deposits suggests that an impact-related origin, or an origin related to the structural modification of impact-related deposits, should be thoroughly investigated for the formation and modification of this terrain.

PART D

DESCARTES HIGHLANDS: POSSIBLE ANALOGS AROUND THE ORIENTALE BASIN

Carroll Ann Hodges[a]

The Descartes highlands are adjacent to the terra plain on which the Apollo 16 lunar module landed (fig. 29-23). A variety of volcanic origins was proposed for the highlands before the mission (refs. 29-4, 29-21, and 29-35 to 29-37), but the returned samples of the area consist almost exclusively of nonvolcanic breccias. The breccias obtained from Stone Mountain have not been identified conclusively as sample materials of the Descartes Mountains (ref. 29-35). A volcanic origin is thus not yet precluded (sec. 6 of this report), but a review of possible impact-related origins seems to be appropriate. The orbital photography acquired during the Apollo 16 mission provides excellent imagery on which geomorphic interpretations may be based. No obvious local crater is a plausible source of the material, but there may be a relation to either the Nectaris or Imbrium Basin. The less degraded Orientale Basin (fig. 29-24) provides a model by which these comparisons can be made (part F of this section).

The Descartes highlands can be subdivided into two major geomorphic units. These units are designated in this discussion as the Smoky Mountain (north) unit and Stone Mountain (south) unit (fig. 29-23(b)). Both are characterized by furrows or grooves of various dimensions. Some furrows have straight walls and V-shaped cross sections, but many are chains of small coalescent craters. The Stone Mountain unit has a rounded, knobby surface, produced by a network of closely spaced, branching, curved furrows. A steep escarpment marks the contact of the mountain with the plains along the northwestern edge. The unit apparently fills and partly buries the rim of Descartes Crater, thus suggesting a depositional or constructional origin. In contrast, the generally south-sloping Smoky Mountain unit exhibits a smoother, more subdued surface with broader spacing between furrows; the predominant trend of these furrows is northwest. Because of these northwest trends, the surface appears gradational with pre-Imbrian crater rims to the northwest, which are furrowed or "sculptured" radially to the Imbrium Basin (fig. 29-23(b)).

Stone Mountain Analogs

Two small patches of dunelike ejecta east of the Orientale Basin (fig. 29-24) are similar morphologically to the Stone Mountain unit (fig. 29-25). These features apparently were formed by ejecta that flowed outward from the Orientale Basin and crowded against preexisting crater walls. The resulting crenulate ridges have been termed "deceleration dunes" (ref. 29-31), and their textural similarity to the materials of the Descartes Mountains has been discussed by Trask and McCauley (ref. 29-37). The

[a]U.S. Geological Survey.

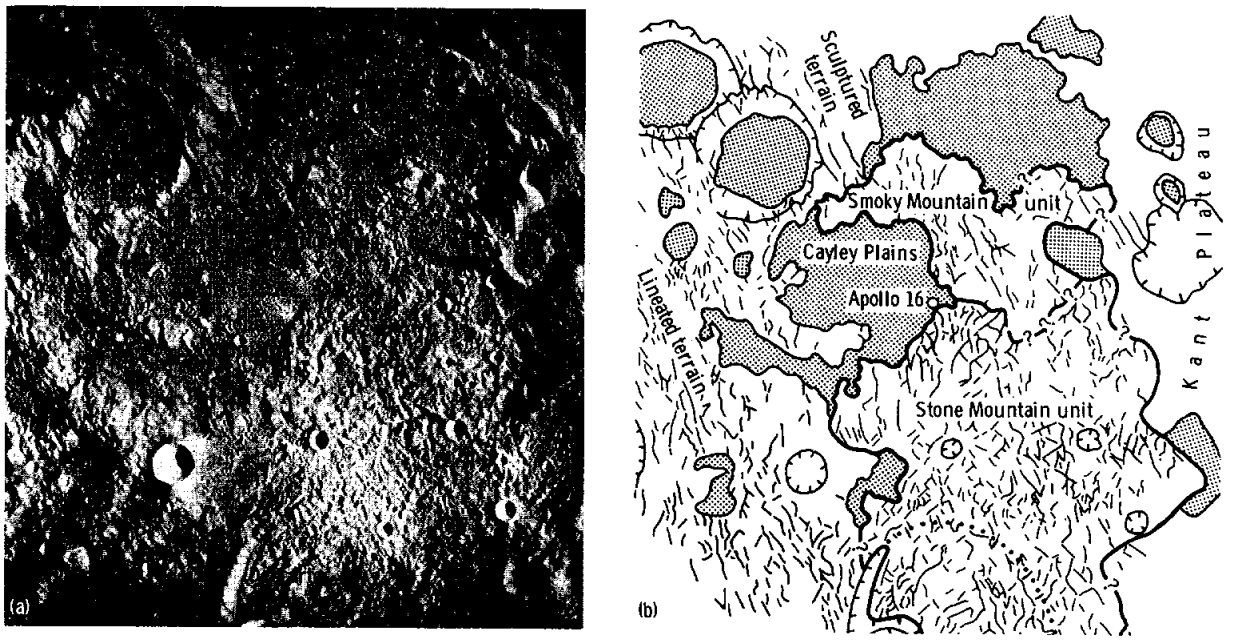


FIGURE 29-23.–The Descartes highlands region. (a) Photographic base for the accompanying map of the Descartes region (Apollo 16 mapping camera frames 0439 and 0440). (b) Sketch map of the same area; furrows and approximate outline of the two units of the Descartes highlands are indicated. Plains of the Cayley Formation are shaded; craters are shown by hachures. Northwest-southeast trend of the furrows on the western side of the map area is radial to the Imbrium Basin.

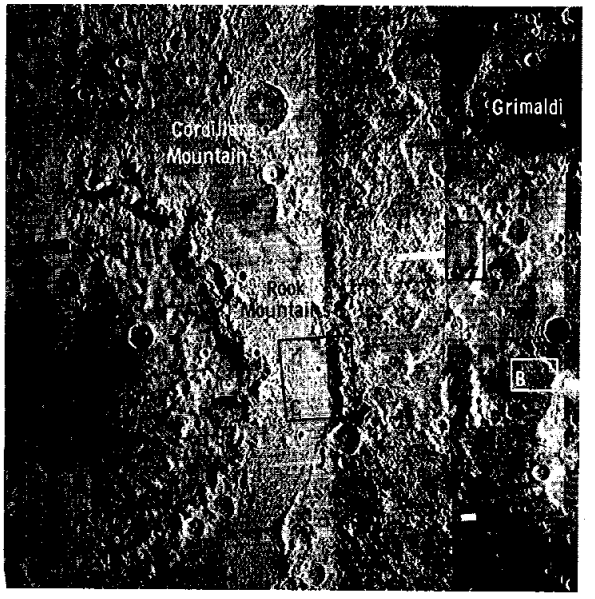


FIGURE 29-24.–The Orientale Basin. Areas outlined are shown separately: area A is shown in figure 29-25(a); area B is shown in figure 29-25(b); and area C is shown in figure 29-28 (Lunar Orbiter IV mosaic).

Stone Mountain unit is adjacent to a west-facing escarpment of the Kant Plateau (part of the Nectaris ring structure, fig. 29-26), suggesting that this unit may have been similarly derived from the Imbrium Basin to the northwest. Deceleration dunes from the Nectaris Basin are unlikely, because ejecta from the basin would have crowded against east-facing escarpments. The apparent gradation of the materials in Descartes Crater with lineated terrain immediately to the west (fig. 29-23) supports an Imbrium-ejecta hypothesis. This terrain has a ridged and braided texture radial to the Imbrium Basin and resembles the Fra Mauro Formation (Imbrium ejecta) (fig. 29-27). However, several problems remain unexplained by this hypothesis.

(1) Whereas similar dunelike deposits occur at several places around the Orientale Basin, the Stone Mountain unit appears unique around the Imbrium Basin, despite the prevalence of scarps against which ejecta could have accumulated, such as the southern walls of Ptolemaeus, Albategnius, Alphonsus, and other craters (fig. 29-26).



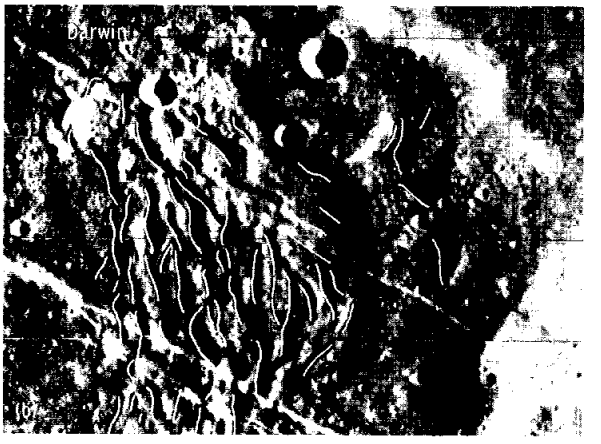


FIGURE 29-25.–Ejecta dunes in preexisting craters east of the Orientale Basin. Furrows between dunes are indicated. These locations are shown in figure 29-24. (a) Ejecta dunes in Rocca Crater. (b) Ejecta dunes in Darwin Crater. (The enlargements are from Lunar Orbiter IV photograph H168).

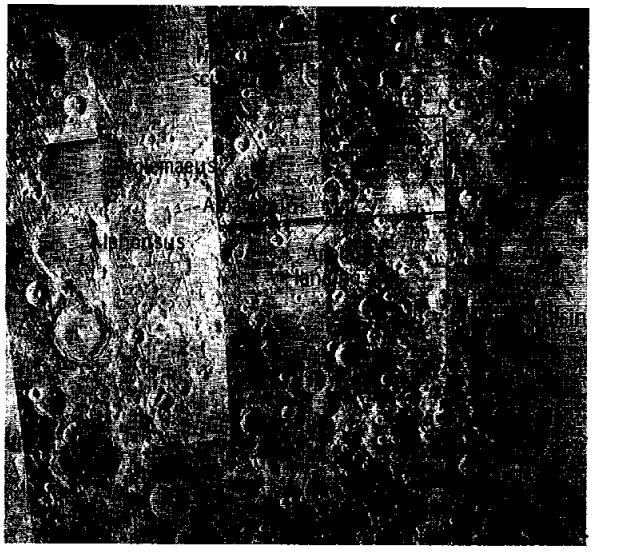


FIGURE 29-26.–Central highlands, showing Nectaris Basin ring structures, selected craters, and area of Imbrium sculpture. The location of figure 29-23 (Descartes region) is outlined (Lunar Orbiter IV mosaic).

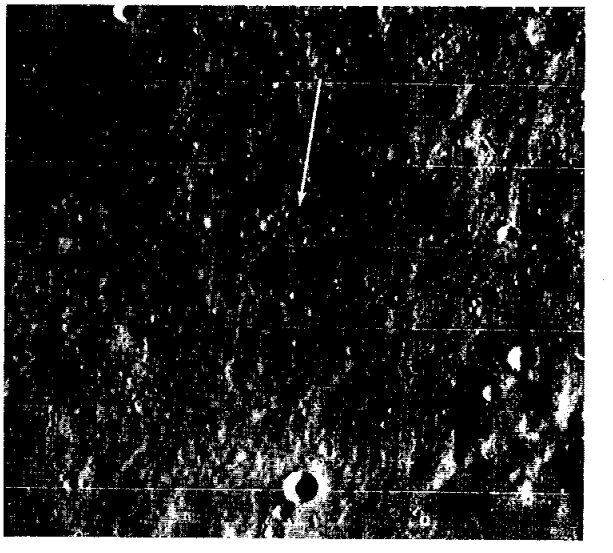


FIGURE 29-27.–Type locality of the Fra Mauro Formation. Arrow indicates the direction from Imbrium Basin. The area shown is approximately 70 km across (Lunar Orbiter IV photograph H120).

(2) The Descartes area is considerably farther from the Imbrium Basin (1000 km from the Apennine ring) than are the deceleration dunes from the Orientale Basin (300 km from the Cordillera ring).

(3) Within Descartes Crater are prominent concentric furrows (fig. 29-23), which conflict with the deposition hypothesis.

(4) If the Stone Mountain unit is Imbrium ejecta, it predates the Cayley material, which is superposed on Imbrium sculpture. However, crater frequencies on Stone Mountain appear lower than those of the Cayley Formation, suggesting relative ages that are the reverse of those obtained by superposition relationships. A possible explanation is the observation that crater populations on Stone Mountain have been reduced by mass wasting on the steep slopes.

A second analog at the Orientale Basin suggests as an alternative that there is a possible relation of the Stone Mountain unit to the nearby pre-Imbrian Nectaris Basin. The hummocky, furrowed terrain between the Rook and Cordillera Mountain rings of the Orientale Basin (fig. 29-28) resembles the Stone

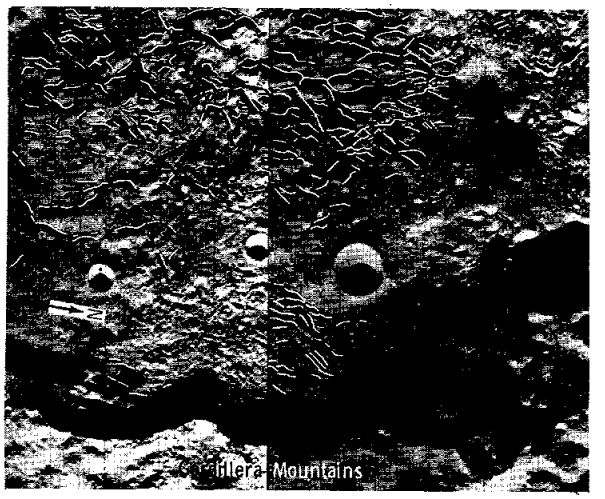


FIGURE 29-28.—Hummocky terrain between the second and third rings of the Orientale Basin. Furrows are indicated. Mare materials flood the hummocky terrain on the north (Lunar Orbiter IV photograph H181).

Mountain unit; the materials appear to be localized mainly in the inter-ring depression. Preexisting landforms are not recognizable and thus must have been obliterated during basin formation. Where later mare materials have filled low areas within this terrain, the morphologic relations are slightly similar to those of the Cayley Plains and the Descartes highlands at the landing site. Despite the similarities, however, some observations seem inconsistent with an analogous origin for the Descartes materials.

(1) The Stone Mountain unit appears to be a unique occurrence and is outside the third ring of Nectaris. At the Orientale Basin, however, the Descartes-like materials are virtually ubiquitous between the second and third rings.

(2) Superposition of the unit on Descartes Crater indicates that, unlike the Orientale analog, preexisting landforms were not obliterated.

(3) The low density of superposed craters on Stone Mountain suggests a post-Nectaris age.

Smoky Mountain Unit

Possible nonvolcanic interpretations of the Smoky Mountain unit include (1) pre-Imbrian crustal rock or Nectaris ejecta, sculptured by secondary cratering or faulting radial to the Imbrium basin, or (2) Imbrium ejecta. The trend of the furrows is predominantly northwest, radial to the Imbrium Basin, suggesting Imbrium sculpture. Smooth, broad surfaces are more prominent than in the Stone Mountain unit, and crater densities appear slightly higher (similar to those on the plains). The close spatial association with the Nectaris Basin implies that the sculptured materials might include Nectaris ejecta.

Alternatively, the Smoky Mountain unit may be radially textured Imbrium ejecta. This possibility is suggested by a gradational, although highly discontinuous, relationship with lineated deposits in the north that resemble the Fra Mauro Formation. Ridged deposits which are also similar in appearance to the Fra Mauro Formation occur farther south, west of Descartes Crater (fig. 29-23). The Smoky Mountain unit, however, does not itself appear ridged and braided as does the Fra Mauro Formation (fig. 29-27) and similar deposits.

Conclusion

These analogs, although not entirely satisfactory, offer reasonable alternatives to the volcanic interpretation of the Descartes highlands. Reconsideration of this complex terrain, prompted by the preliminary results of the Apollo 16 mission, will lead to the revision of some theories on lunar volcanism and also to a better understanding of the landforms caused by the formation of multi-ring basins.

PART E

ORIENTALE BASIN DEPOSITS (RICCIOLI AREA) IN APOLLO 16 EARTHSHINE PHOTOGRAPHY

D. D. Lloyd[a] *and J. W. Head*[a]

Photography of Orientale Basin deposits was obtained under earthshine illumination conditions on the Apollo 16 mission. Although the quality of these photographs is less than that obtainable in sunshine, these regions are in the dark during Apollo missions because of the locations of Apollo landing sites. Photography of these regions under different lighting geometry and from different viewpoints is therefore a useful addition to previous photographic data. Oblique photography was obtained of Riccioli Crater and adjacent areas, which lie northeast of the Orientale Basin.

A Nikon 35-mm camera with an f/1.2 lens was used. The photographs were obtained at 122:39 ground elapsed time with an exposure time of 1/8 sec under lighting conditions of approximately 15° from the earthshine terminator. The location of these photographs is shown in figure 29-29. The two

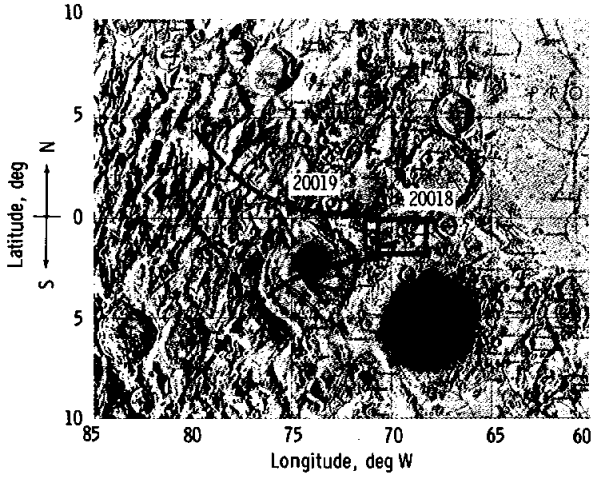


FIGURE 29-29.–Location of two earthshine photographs (AS16-127-20018 and 20019) obtained on the Apollo 16 mission.

[a]Bell Telephone Laboratories.

earthshine photographs obtained on the Apollo 16 mission as well as Lunar Orbiter IV coverage of the same area are shown in figure 29-30.

The region between Riccioli Crater and the Orientale Basin is characterized by grooved, furrowed, and braided terrain that generally has a linear aspect radial or subradial to the Orientale Basin (fig. 29-31). These units are related to the gigantic ejecta blanket deposited at the time the Orientale Basin originated. Riccioli Crater existed before this origin, and the presence of Riccioli Crater appears to have modified the regional characteristics of the ejecta blanket in this local area. In particular, the outer edge of the radially patterned ejecta blanket (fig. 29-31) is indented toward the Orientale Basin as if the presence of Riccioli Crater may have obstructed the outward flow of material.

The photograph of the northern half of Riccioli Crater (fig. 29-30(b)) shows the northeastern rim of the crater enhanced in brightness by the viewing direction. Several small craters on the inner wall show high brightness characteristics of zero-phase viewing (here in earthshine). In the oblique earthshine and in the Lunar Orbiter photograph, there is a distinct impression of material preferentially piled up or deposited along the northeast crater wall. A distinctive aspect of this material is that the structures are oriented in a direction generally parallel to the crater wall in this area, but normal to the general radial structure of the Orientale blanket. This observation has led to the suggestion that these linear structures might be "deceleration dunes" (ref. 29-31); that is, dunes deposited when the outward flow of material was locally slowed by the interference of the Riccioli Crater wall to such an extent that it largely ceased flowing radially at this point and was deposited in transverse dunes. This theory also would explain the regional embayment in the outer edge of the distinct radial structures (fig. 29-31), because much of the material would have been trapped within Riccioli Crater. It seems clear, however, that at least some

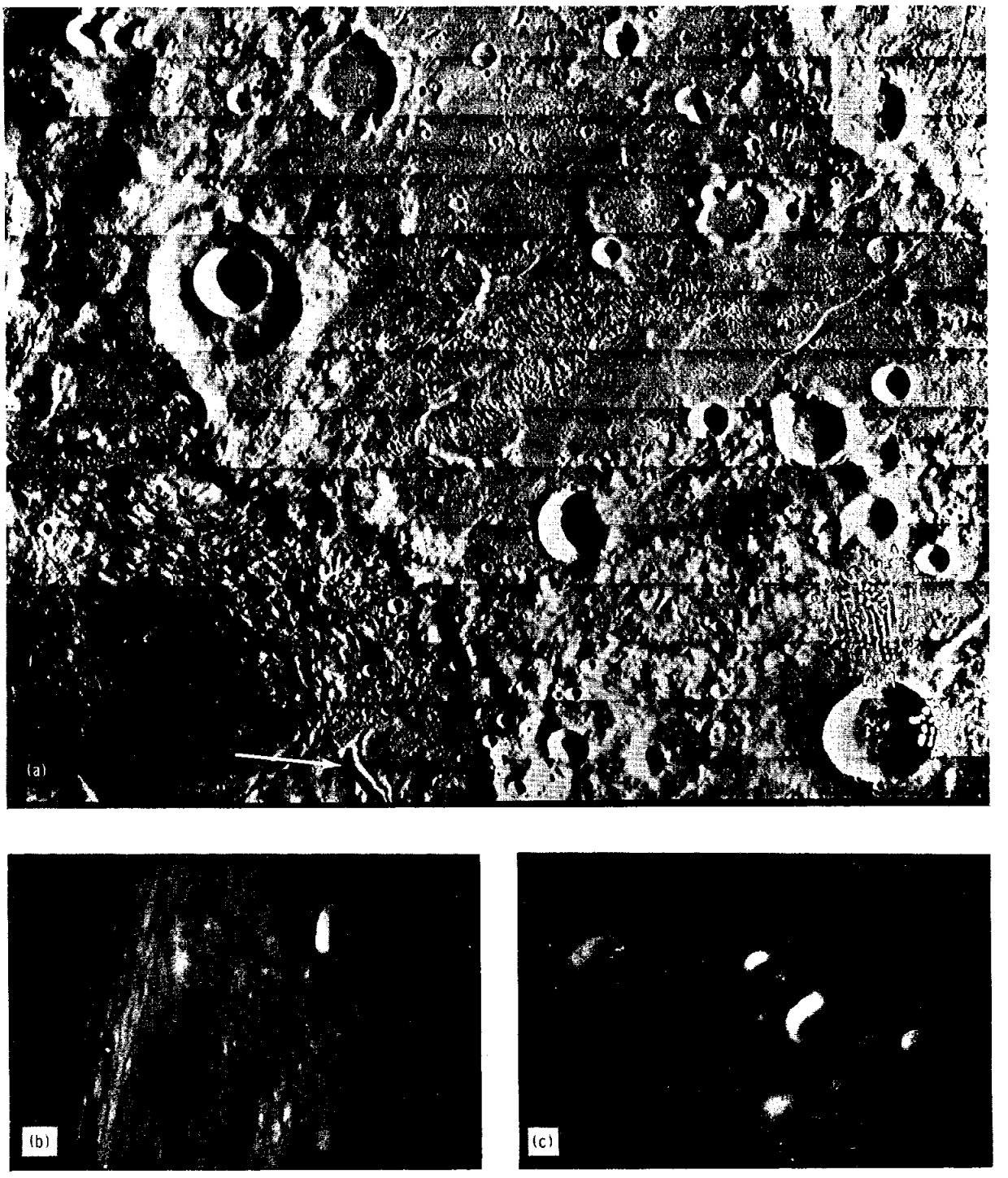


FIGURE 29-30.–Apollo 16 earthshine photography compared to Lunar Orbiter IV coverage. (a) Lunar Orbiter IV photograph H169. (b) Earthshine photograph looking west at Riccioli Crater showing north half of Riccioli and area east of Riccioli, including Riccioli G Crater (AS16-127-20019). (c) Earthshine photograph showing craters east of Riccioli Crater, including Riccioli G and Lohrmann B Craters (AS16-127-20018).

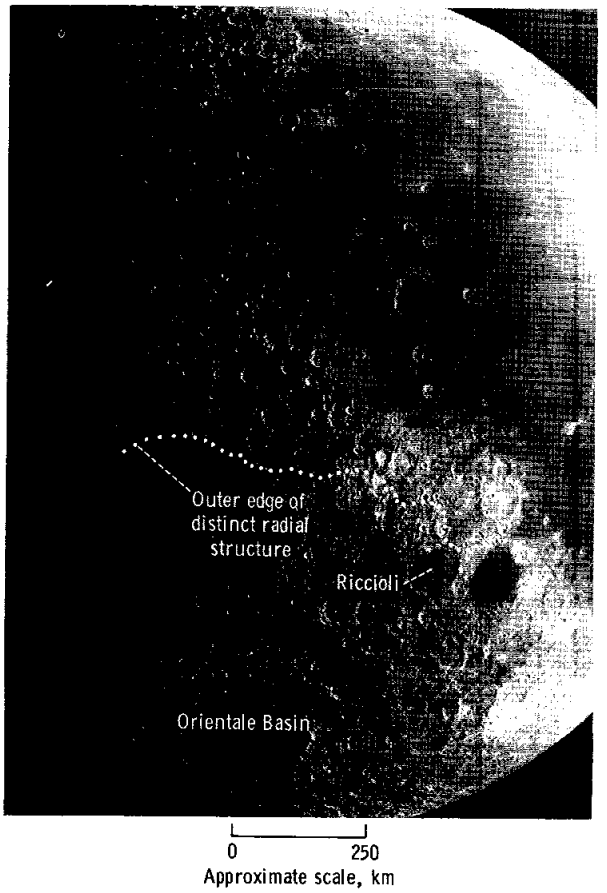


FIGURE 29-31.–Regional embayment in the outer edge of the distinct radial structures in the Orientale Basin near Riccioli Crater.

material surmounted the wall and was deposited to the northeast (fig. 29-30(a)).

An alternative possibility for these transverse ridges is that they may represent slumping of material back down the crater wall after being piled up against the wall of Riccioli Crater during the ejection of Orientale material. This hypothesis would differ from the deceleration dune explanation in the formation mechanism of the deposit structure, not in the material of the deposit. R. Eggleton (personal communication) has pointed out parts of the materials of the Descartes Mountains and associated deposits that may have originated as a result of major slumping and faulting, rather than from constructional volcanism. Some of the structures associated with and forming these transverse ridges in Riccioli Crater show marked morphologic and scale similarities to structures seen in the Descartes material. (In particular, see the area indicated by the arrow in fig. 29-30(a).) The possibility that morphologies such as those seen in Riccioli Crater and similar deposits could have originated through slumping and down-faulting of deposits associated with major basins should be seriously considered.

PART F

REINTERPRETATIONS OF THE NORTHERN NECTARIS BASIN

Don E. Wilhelms[a]

Geologic units of the Nectaris Basin rim have been interpreted as partly impact and partly volcanic in origin (refs. 29-4, 29-21, 29-35, 29-38, and 29-39). An exclusively volcanic origin was proposed for the material in the vicinity of the Apollo 16 landing site, slightly northwest of the Nectaris Basin (ref. 29-36). In view of the dominance of breccia and the paucity of volcanic material in the returned Apollo 16 samples, it now seems appropriate to reevaluate this part of the Moon to test whether the geology of the units mapped to date can be reconciled with an impact origin. Therefore, photogeologic analysis was attempted on a strip of Apollo 16 metric photographs; the superior quality and stereographic properties of the photography permit this reevaluation (fig. 29-32). Geologic contacts, as redrawn, closely resemble those of the earlier maps cited, but some differences result because of improved photographic quality and a conscious attempt to test fully the impact hypothesis.

For the purpose of this study, an area including the Nectaris Basin rim is compared with an analogous area of a younger basin of similar size, Orientale (fig. 29-33), which is doubtless of impact origin. A sketch map and a description of the major impact-produced units in and around the Orientale Basin provide a useful comparison (ref. 29-26). Materials of the two basins appear to be similar in surface properties and distribution patterns; the differences observed can be ascribed to the greater age, state of degradation, and lava fill of the Nectaris Basin. However, some landforms, including the hilly (southern) unit of the Descartes Mountains (ref. 29-35), are difficult to fit into a pure impact model.

The comparison with the Orientale Basin suggests that three major units are part of the impact stratigraphic sequence of the Nectaris Basin. As suggested by most workers, the first unit, material of mountains (fig. 29-34), probably represents uplifted multiple ring segments produced during basin formation. At both the Nectaris and Orientale Basins (fig. 29-33), the rings are composed of massifs of various heights and degrees of ruggedness. Dashed lines on figure 29-32 show the approximate position of the Nectaris rings. The inner ring bounds Mare Nectaris itself, as the inner Rook Mountains ring would bound Mare Orientale if post-Orientale lavas had filled the basin to a higher level. The second Nectaris ring corresponds to, though is less conspicuous than, the ring of massifs formed by the outer part of the Rook Mountains at Orientale. The third ring at Nectaris (Altai-Kant-Censorinus) corresponds to the Cordillera ring around the Orientale Basin.

The second major unit related to the Nectaris Basin, material of small peaks, was not recognized previously as a separate photogeologic unit (fig. 29-34). Parts of it were assigned to various terra units interpreted as basin-related material and other parts to hilly and pitted units interpreted as probable volcanic material. The Apollo 16 metric photographs show that the pattern of the small peaks resembles the less rugged parts of the Orientale rings. At each basin, the small peaks appear basically the same as the more conspicuous massifs, but are broken into smaller pieces.

The third unit, hummocky material (fig. 29-35), has been variously interpreted; Elston (ref. 29-39) suggested two possibilities, volcanic or basin-related material. The Apollo 16 photographs convincingly favor the second interpretation. The unit resembles the sharply hummocky material that occurs mainly between the Rook and Cordillera rings of Orientale Basin and in radial troughs on and beyond Montes Cordillera. Hummocky material at Nectaris occurs also mainly between the second and third basin rings, in a radial trough west of Lubbock D Crater, and in patches beyond the third ring. The origin of this material remains uncertain; it may be basin ejecta, bedrock fractured during basin formation, or slump material, but it almost certainly is related to the formation of the Nectaris Basin.

[a]U.S. Geological Survey.

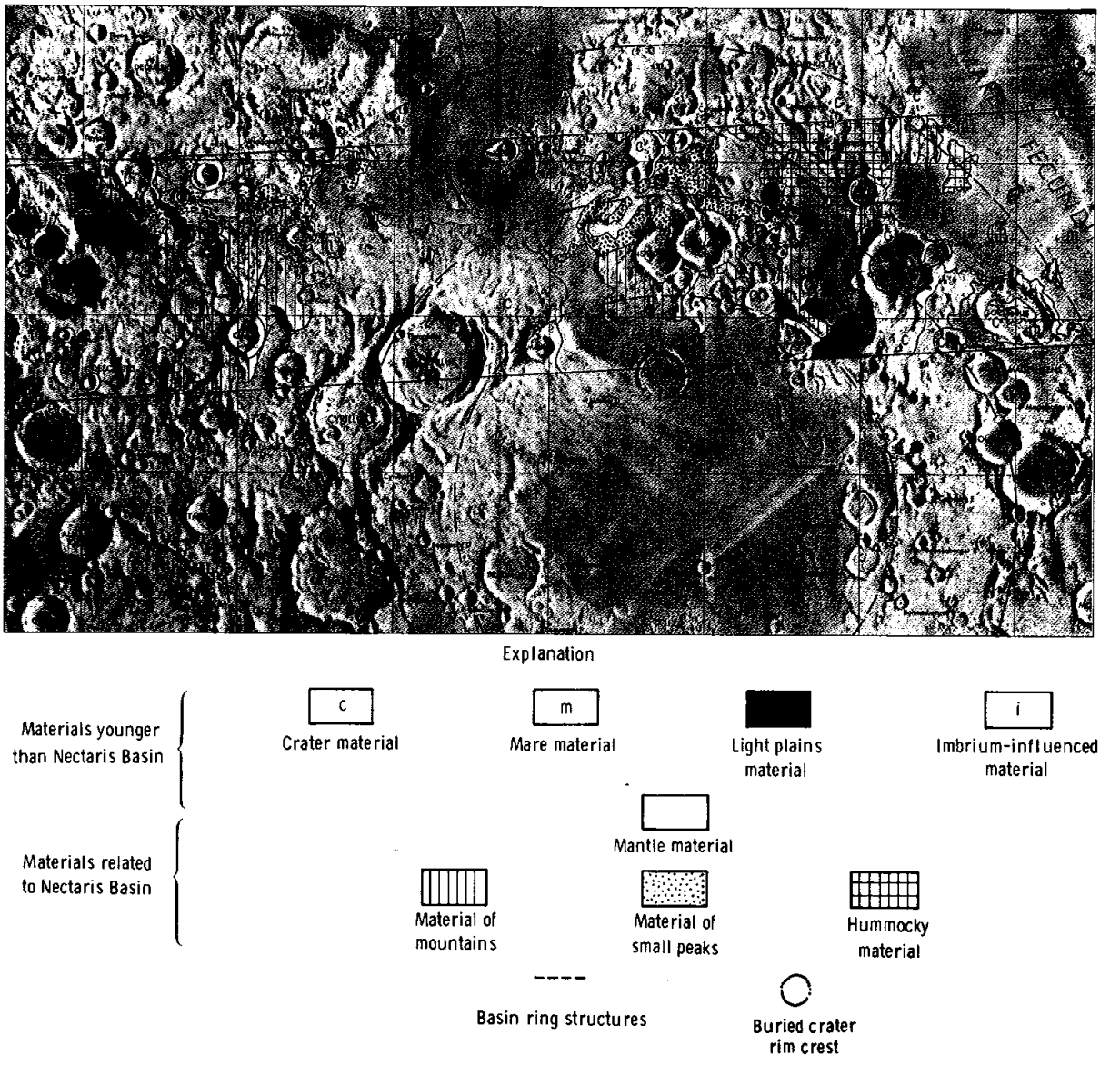


FIGURE 29-32.–Geologic map of the northern part of the Nectaris Basin.

Around the Nectaris Basin, as nearly everywhere within the terra, there are large areas of undulatory material of rather characterless appearance and uncertain age. Many of the Orientale landforms, if sufficiently degraded by meteorite bombardment and mass wasting, might resemble this circum-Nectaris unit.

West of the Nectaris Basin, small pits and grooves dominate the landscape, including the Descartes Highlands (fig. 29-36). Previously, a volcanic origin seemed best to explain the mix of hills and depressions and the fact that this type of terrain seems to blanket some areas such as that south of the Apollo 16 landing site where material of the Descartes Mountains drapes over Descartes Crater (refs. 29-4, 29-21, 29-35, and 29-37). As concluded earlier from telescopic observation (ref. 29-38), basin-related genesis is a reasonable alternative for much of the terrain because it is near the Nectaris Basin and because many of its landforms appear to be allied to Imbrium sculpture (part D of this section). In a broad belt west of the Apollo 16 landing site, the Imbrium sculpture,

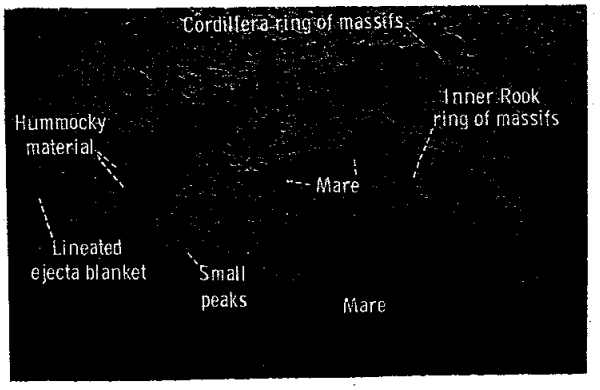


FIGURE 29-33.–Orientale Basin (Lunar Orbiter IV mosaic).

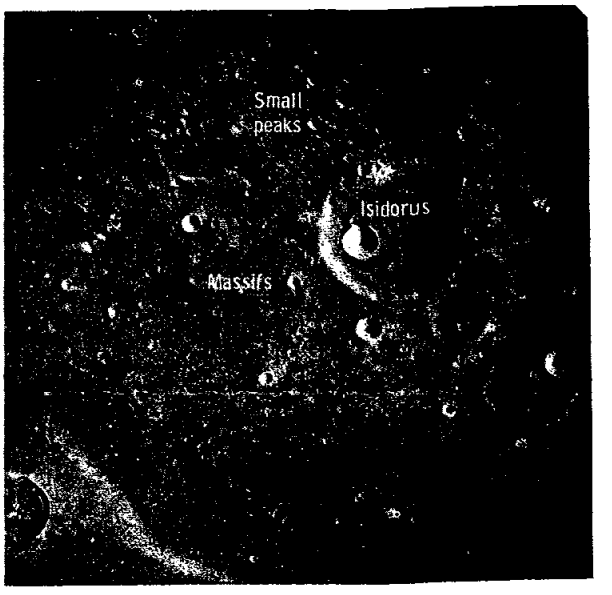


FIGURE 29-34.–Material of mountains and small peaks in the Nectaris Basin. Isidorus Crater is 40 km across. Typical broad massifs of the Nectaris inner ring adjoin Isidorus Crater on the west and south; typical small peaks are to the north and northwest (Apollo 16 metric camera frame 0148).

trending radially to the Imbrium Basin, is seen in Apollo 16 photographs to consist of pits or grooves. The Imbrium sculpture is commonly interpreted as fractures (ref. 29-40 and part G of this section), but these pits and grooves lend support to the early interpretation (ref. 29-41) that sculpture results from gouging by secondary impacts of ejecta from the Imbrium Basin. Hence, sculptured areas, including the Descartes material, are interpreted as Imbrium-influenced terrain (fig. 29-32). It should be stressed that, at this great distance from Mare Imbrium, the secondary craters and gouges
to the amount of impacting
them; hence, only a small am
material should be mixed with
In addition to the northwest
Descartes material south of th
does have some northeast-tren
are not radial to Mare Iml
Descartes Crater, and appea
young population of superpo
this section). A possible nonv
these observations is that tl
Basin ejecta which was modif
gouging and faulting that des
craters. A sequence of impact
explain the Descartes materia
cartes Crater, formation of t
swamping of Descartes Crater
the Imbrium Basin and pittin
faulting along a northeast-sou
Imbrian cratering. The bulk o
would then be Nectaris Basin r

The Imbrium-influenced u
taris Basin (fig. 29-32) refer to clustered craters of

pits that are sharper than those west of the basin. A
considered for these units
gular craters that do not
sin secondaries (refs. 29-4

s the one certain lunar
s material in this region
be basin ejecta (part B of
reworked erosional debris
rigins that have been long
the volcanic origin of the
ne of the light plains are
d Nectaris ring as is the
tale Basin, as if light plains
valent lavas.
t of the nonmare material
ern Nectaris Basin rim can
tion of impact basins. This
ed only for some irregular
1 of Mare Nectaris and for
Descartes material. If the
have been sampled and to
extensive hill and crater-
of Imbrian or younger age
probably does not exist on the lunar terra.

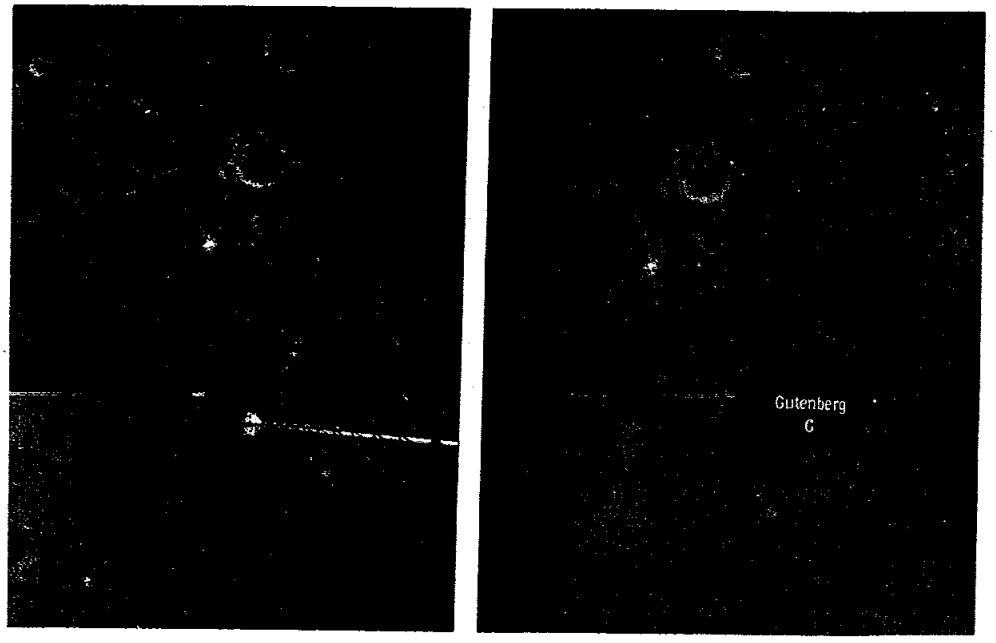


FIGURE 29-35.–Hummocky material in the Nectaris Basin. Gutenberg G Crater is 30 km across. Typical hummocky material is shown in most of the figure and is best developed in the trough extending north of Gutenberg G Crater (stereopair, Apollo 16 metric camera frames 1641 and 1639).

PART G

STRUCTURAL ASPECTS OF IMBRIUM SCULPTURE

David H. Scott[a]

Apollo 16 metric photographs taken at low to high Sun angles (from approximately 7° to 40°) provide the first stereographic coverage of the distinctive landforms collectively referred to as "Imbrium[1] sculpture" (refs. 29-40 and 29-41). The sculpture consists of a series of nearly linear ridges and troughs extending radially outward for more than 1000 km from the rim of the Imbrium Basin. The sculpture is particularly well developed in the highlands southwest of the basin, where individual segments have lengths measured in tens of kilometers. The origin of the ridges and troughs, whether by deposition and impact scoring by fluidized clouds of ejecta from the Imbrium Basin or by faulting and volcanism during and subsequent to basin formation, is controversial. Similar appearing features occur around other large basins on both the near and far sides of the Moon; thus, information leading to a better interpretation of Imbrium sculpture has significance throughout the Moon.

Studies of Apollo 16 stereographic photographs in the vicinity of the large craters Albategnius and Hipparchus (fig. 29-37) show that some troughs have relatively sharp rims or edges, whereas others are moderately to highly subdued. In this respect, variations in morphology of the troughs are probably analogous to some of the criteria used for the age classification of impact craters (ref. 29-42). On this basis, the sharpest appearing troughs may be as young as late Imbrian in age. Some may have volcano-tectonic origins and thus may be younger than similar appearing features formed by impact, if endogenetic processes produce forms with an inherently old appearance. However, most of the troughs seem to be older than plains material, and their buried outlines on the floor of Albategnius Crater are shown well on Apollo 16 metric camera frames 0448 and 0449 adjacent to figure 29-37. In the area of figure 29-37 (best seen at higher Sun angles as in Apollo 16 metric camera frames 2803 and 2804), grabenlike, rimless, linear furrows grade into arcuate rimmed depressions resembling highly coalescent crater chains. These latter characteristics are not definitive and may reflect either a volcano-tectonic or secondary-impact crater origin.

Several topographic characteristics supporting an endogenetic origin for the larger elements of Imbrium sculpture are shown in figure 29-38. The wide, prominent depression in the upper right corner of the photograph extends across the entire rim and wall of Ptolemaeus Crater on the side nearest the Imbrium

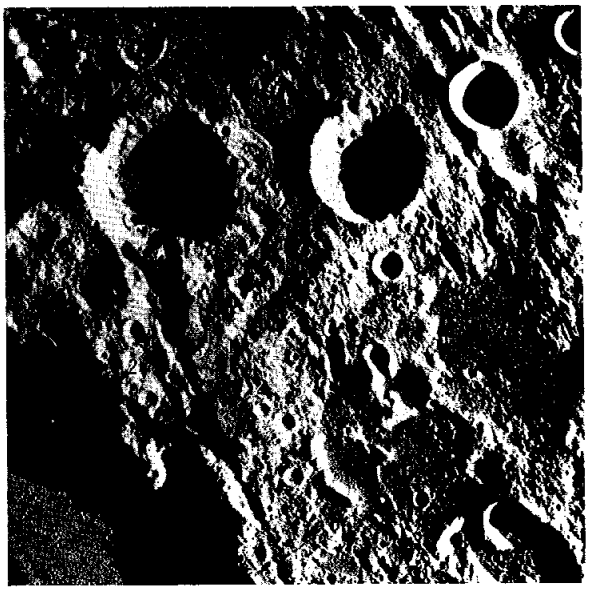


FIGURE 29-37.–Imbrium sculpture between Albategnius Crater (lower left) and Hipparchus Crater (top). Progression in degradation of furrows is shown by: 1, sharp rimmed; 2, moderately subdued; 3, highly subdued (north toward top, Apollo 16 metric camera frame 0168).

[a]U.S. Geological Survey.

[1]Both "Imbrium" and "Imbrian" have been applied by various authors to describe the sculpture. Imbrium is preferred because it shows association with the Imbrium Basin rather than the Imbrian Period.

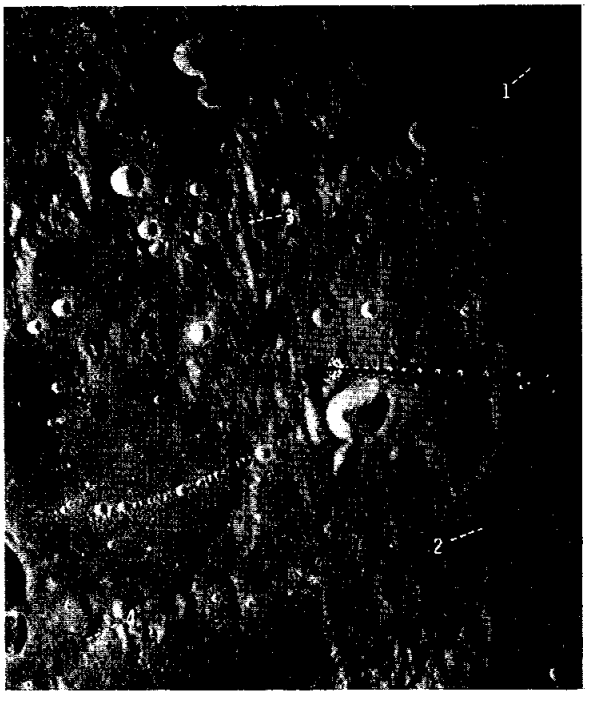


FIGURE 29-38.–Sculptured terrain around west side of Ptolemaeus Crater (right center). 1, large depression extending across rim and wall of Ptolemaeus; 2, trough with prominent eastern wall; 3, furrow with high rims; 4, smooth, lineated texture (north toward top, Apollo 16 metric camera frame 2814).

Basin. From the figure, no evidence of the rim shielding the wall against missile gouging is detectable, such as is noted in the disposition of secondary crater clusters around large, young, primary-impact craters such as Tycho Crater (ref. 29-43). In the lower right corner of the figure, one side of a large trough appears to be much higher and better defined than the other. This type of asymmetry is more suggestive of a structural origin than gouging and scoring by impact ejecta. In this photograph, as well as in several others, some of the furrows have conspicuous rims, more readily explained by high-velocity, surface-grazing impacts than by tectonism. However, similar rimmed furrows farther to the south in the vicinity of Airy and Delaunay Craters are associated with lobate, flowlike materials and may be of volcanic origin.

Toward the lower left corner of figure 29-38, a continuous gradation is noted between coarse sculpture patterns and finely lineated materials, which elsewhere have been mapped as the Fra Mauro Formation. In figures 29-37 and 29-38, the absence of randomly oriented, overlapping crater clusters is in contrast to the patterns of secondary craters usually observed around large craters.

In figure 29-39, a series of elongate hills forms a linear ridge extending approximately 100 km along the east side of Fra Mauro Crater. The ridge is radial to the Imbrium Basin (approximately 500 km to the north) and parallels Rima Parry, a large linear rille presumably of structural origin. Toward the south, the ridge of hills grades into typically sculptured topography. Smaller, isolated, oval-shaped hills project above the mare material to the east. All these hills resemble constructional landforms, probably formed by a combination of faulting and volcanism. A similar origin is suggested for Imbrium sculpture in this region.

Evidence indicative of the mode of origin of Imbrium sculpture is summarized as follows. Evidence of a volcano-tectonic mode of origin is favored by (1) wide variation in relative age of parts of the sculpture, (2) furrows without rims, (3) absence of ballistic shielding, (4) asymmetry of sculpture, (5) absence of randomly oriented clusters, and (6) association with other features of structural

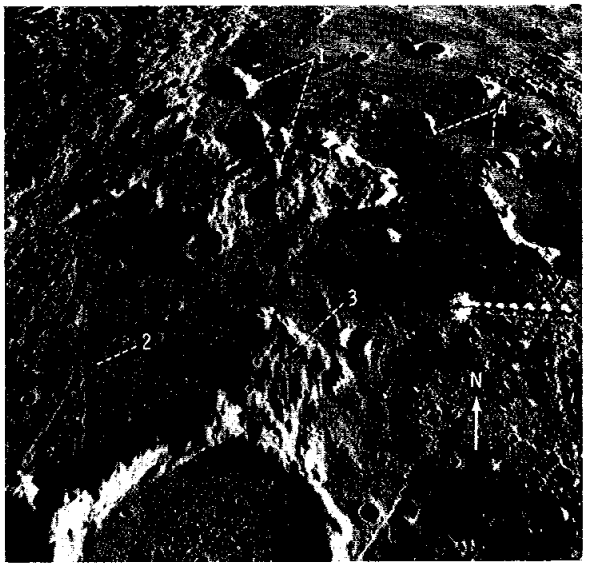


FIGURE 29-39.–Area around Fra Mauro Crater (left center). 1, ridge-forming hills; 2, Rima Parry; 3, typical sculpture; 4, elongate hills surrounded by mare material (north toward top, Apollo 16 metric camera frame 1418).

origin. An origin by ejecta scoring and deposition is favored by the gradational ejecta with a Fra Mauro-type texture. Features that are ambiguous as to mode of origin are furrows made up of coalesced crater chains and prominent rims on furrows.

Empirical data show that the distance fractures extend from underground nuclear explosions is a power function of explosive energy (ref. 29-44). The application of this relationship to energy estimates required to produce the Imbrium Basin indicates that radial fractures produced by the Imbrium impact might well have been propagated around the Moon. Many of these fractures may have provided conduits for later volcanism.

PART H

DISCOVERY OF TWO LUNAR FEATURES

Farouk El-Baz[a]

Study of the Apollo 16 photographs resulted in the discovery of two large features in the far-side highlands near the eastern limb of the Moon not indicated on existing lunar maps and charts. The larger unnamed feature is a three-ringed, 1000-km-diameter basin that is centered at 1° N 112° E. The smaller feature is a 200-km-diameter crater that is located between the eastern middle and outer rings of the aforementioned basin. This crater is centered at 2° S 125° E, surrounding Bečvar Crater.

Reexamination of Lunar Orbiter and earlier Apollo photography reveals that portions of the newly discovered features are portrayed. However, their discovery was made possible by the more complete coverage of Apollo 16 photography. The features were revealed in the course of geological mapping of the eastern limb region of the Moon. Their revelation was also a result of further investigation as to whether a mountain range existed (the so-called "Soviet Mountains") or was only bright albedo materials. Because the eastern part of the middle ring of the new-found basin corresponds generally to the area previously labeled the Soviet Mountains, a short summary of the debate concerning the Soviet Mountains will be given before describing the new-found features.

[a]Bell Telephone Laboratories.

History

In October 1959, the unmanned Russian spacecraft Luna 3 obtained the first photographs of the far side of the Moon. The photographs were published in 1960 by the U.S.S.R. Academy of Sciences along with a map and a table of identifiable features (ref. 29-45). In that report, the name Soviet Mountains was assigned to an elongate, bright area extending from approximately 20° N 110° E to 10° S 120° E (fig. 29-40(a)). This area lies along a line connecting Giordano Bruno Crater to the north and Tsiolkovsky Crater to the south. The bright area was named and described as a range of mountains because of its high reflectivity. This interpretation was later disputed, and the brightness was assigned to extensive nimbi surrounding two craters, together with some of the rays (ref. 29-46).

Following the flight of Zond 3 in 1965, a revised version of the Russian atlas of far-side features was published (ref. 29-47). In this version, the Soviet Mountains assume a position between 10° N 115° E and 5° S 120° E (fig. 29-40(b)). This position is also held in the official U.S.S.R. Topogeodetic Service (GAISH) "Complete Chart of the Moon," first edition, 1:5,000,000 scale (1967) (fig. 29-41(a)). The Soviet Mountains were, however, moved to between 5° S 115° E and 22° S 120° E in the second edition of the same chart published in 1969 (fig. 29-41(b)).

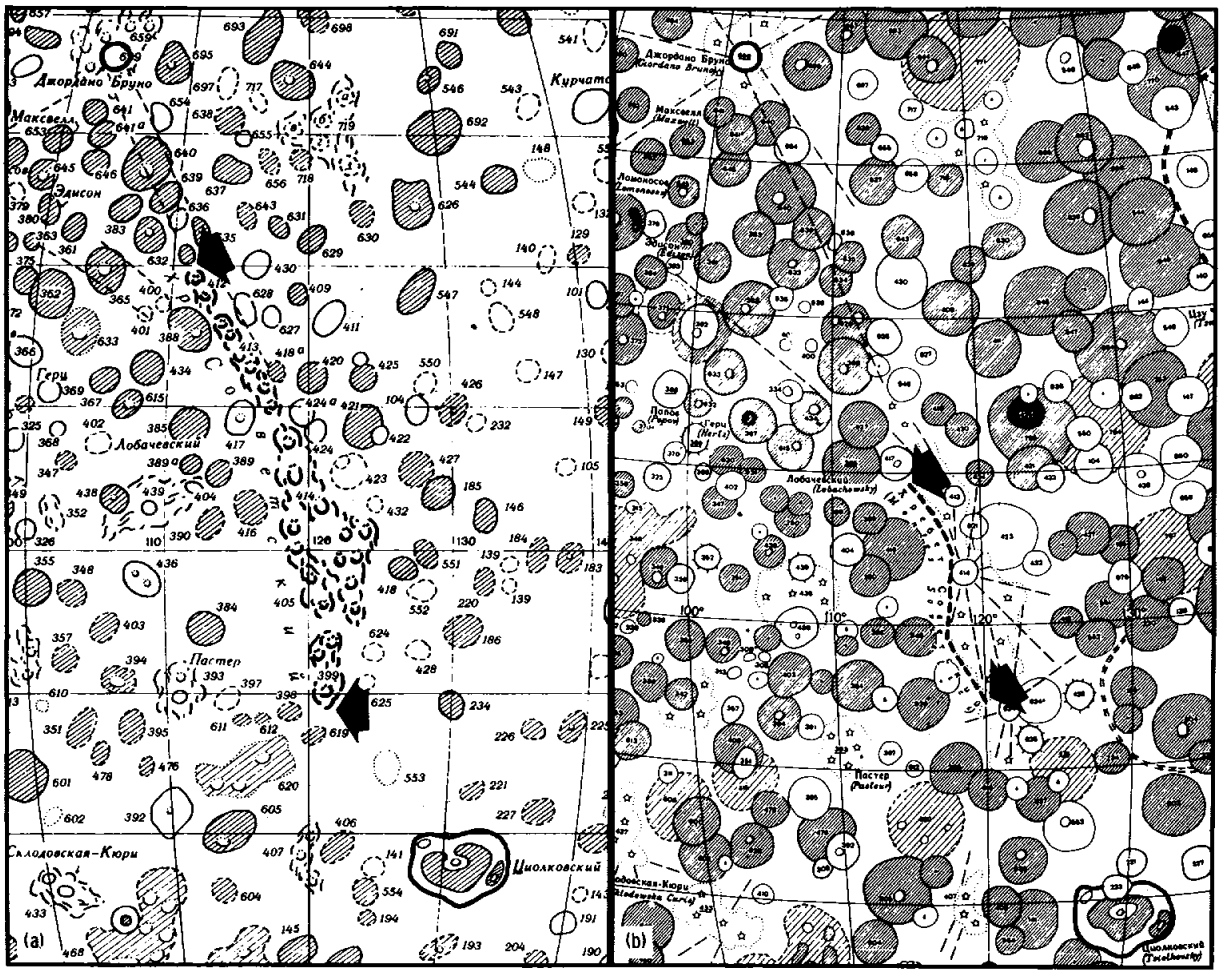


FIGURE 29-40.–Portions of two editions of the "Schematic Chart of the Farside of the Moon" based on data from the Soviet automatic interplanetary station Luna 3. Both editions were compiled by the U.S.S.R. State Astronomical Institute at Shternberg jointly with the Central Scientific Research Institute of Geodesy, Aerial Photography, and Cartography. The Soviet Mountains occur along a line connecting Giordano Bruno Crater to the northwest and Tsiolkovsky Crater to the southeast. Arrows indicate the points of termination in both cases. (a) 1960 edition. (b) 1967 edition.

The existence of the mountain range was again disputed on the basis of Lunar Orbiter (1966 to 1967) and Apollo 8 (December 1968) photography; Apollo 8 frame 2056 was used to illustrate that the bright area was the result of two distinct overlapping ray systems from two craters charted at 4° N 120° E and 5.7° S 121.5° E (ref. 29-48). Much discussion followed until the 1970 meeting of the International Astronomical Union (IAU), where the name Soviet Mountains was finally rejected.

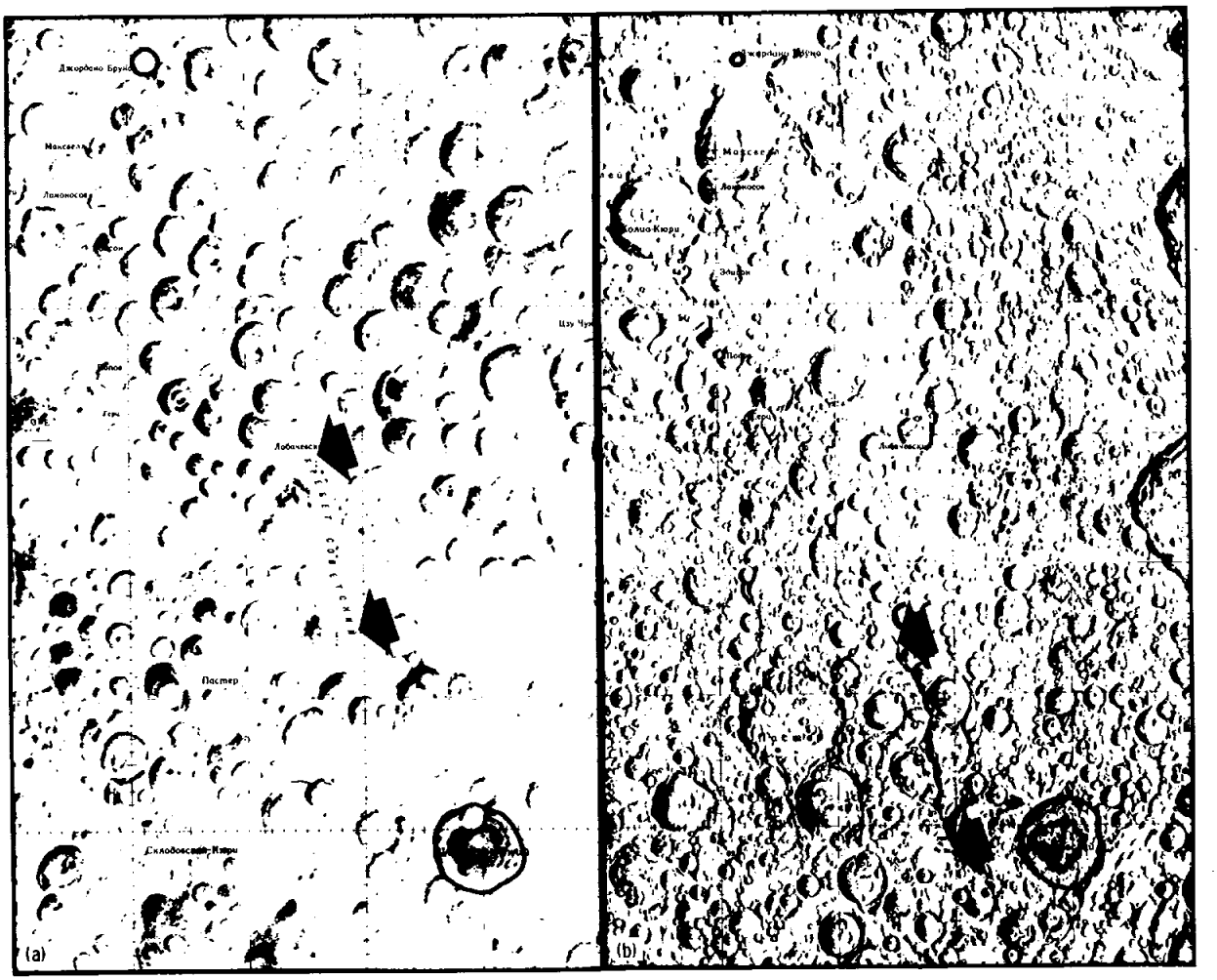


FIGURE 29-41.–Portions of the official Russian maps of the far side of the Moon produced by the U.S.S.R. Topogeodetic Service (GAISH) at 1:5,000,000 scale. Note that the so-called Soviet Mountains are between 10° N 115° E and 5° S 120° E in the first edition, and between 5° S 115° E and 22° S 120° E in the second edition. (a) 1967 edition. (b) 1969 edition.

Discovery

Orbital science photography and visual observations for the Apollo 16 mission were planned jointly with the Apollo 16 crewmen. During the planning sessions, the interesting King Crater (5.5° N 120.5° E) and its environs (refs. 29-49 and 29-50) were studied. During the mission, photographs were taken and visual observations were made of the features in this area of the far-side highlands. The Apollo 16 command module pilot described the area that was previously labeled the Soviet Mountains as a plateau, a gentle rise, and he compared it to the Kant Plateau on the near-side highlands.

Detailed analysis of the photographic records of the Apollo 16 mission revealed a large basin extending from 95° E to 131° E along the lunar equator (fig. 29-42). The basin is centered at 1° N 112° E, and it displays three rings that are old and somewhat subdued. It is comparable to Orientale Basin in gross morphology as well as size, but it is much older. Visible remains of its features are more subdued than those of Nectaris Basin; that is, it appears to be pre-Nectarian in age. Since Nectaris Basin is believed to be older than Imbrium Basin (ref. 29-51), the new-found basin appears to have formed very early in lunar surface history.

Sharpness of the three rings of the basin decreases outward (fig. 29-42); the innermost ring (270 km across) is sharpest, and the last (1000 km across) is the most degraded. The eastern and western portions of the middle ring (500 km across) are represented by broad (but subdued) mountain chains characteristic of intermediate rings of large impact basins, although they are discontinuous and more degraded than in other cases. The eastern mountain chain of the middle ring is approximately 300 km in length and 120 km in width; the western mountain range is 600 km in length with a maximum width of 90 km. The relationships of the three-ringed basin to named formations near the eastern limb of the Moon are shown in figure 29-43.

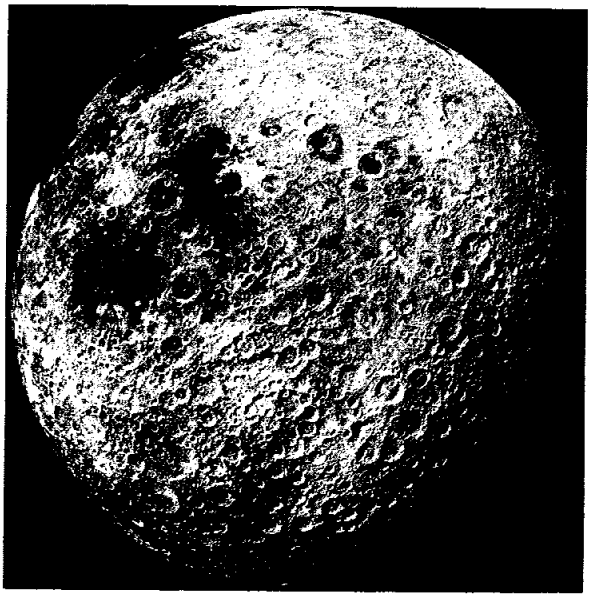


FIGURE 29-42.–Full-disk view of the Moon obtained by the Apollo 16 mapping camera during the transearth coast. Mare Crisium is near the horizon to the upper left. Tsiolkovsky Crater is on the horizon at the bottom, and the new-found, three-ringed basin is in the middle of the lower part of the disk (Apollo 16 metric camera frame 3023).

Preliminary laser altimeter data from the Apollo 15 and 16 missions were analyzed by the author to study the new-found basin further; Apollo 16 ground tracks crossed the middle of the basin, and the Apollo 15 spacecraft flew over the southwestern part (figs. 29-44 and 29-45). On both missions, range measurements from the orbiting spacecraft to the lunar surface were made. The altitude was computed from altimeter slant range, assuming that the Moon is a sphere having a radius of 1738 km (ref. 29-52 and part A of sec. 30 of this report). The laser altimeter profiles provide height measurements of the basin rings (fig. 29-45).

Starting at 140° E, the Apollo 16 laser altimeter profile shows the floor of the large crater Mendeleev to be approximately 5.5 km deep. Next is a depression representing Green Crater, and then the third and outermost ring of the new-found basin is encountered at 130° E. After a drop of 3.5 km, a gentle rise indicates the beginning of the intermediate

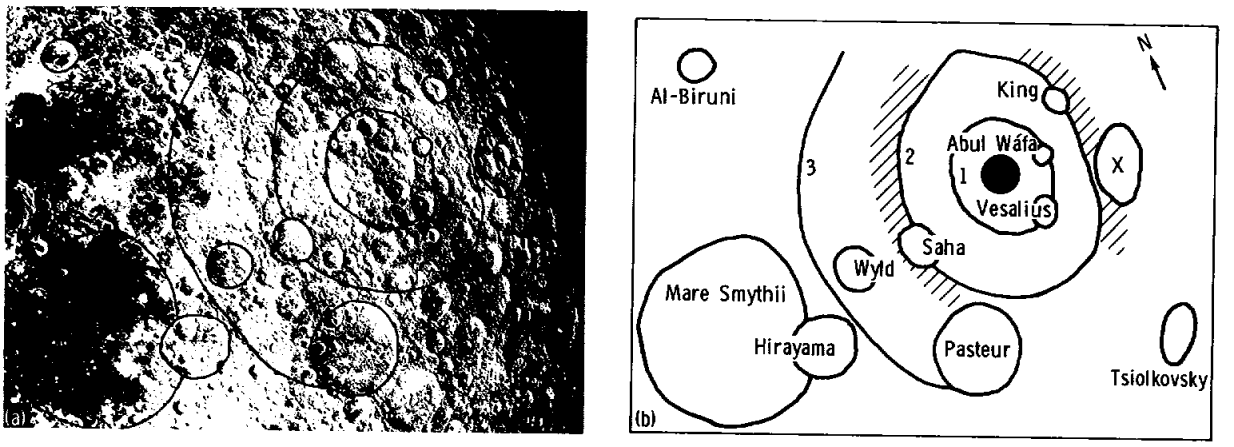


FIGURE 29-43.–New-found basin on the far side of the Moon. (a) Portion of Apollo 14 camera frame 10313 showing the three-ringed basin. (b) Schematic display of the relationship of the new-found basin to named lunar formations near the eastern limb of the Moon.

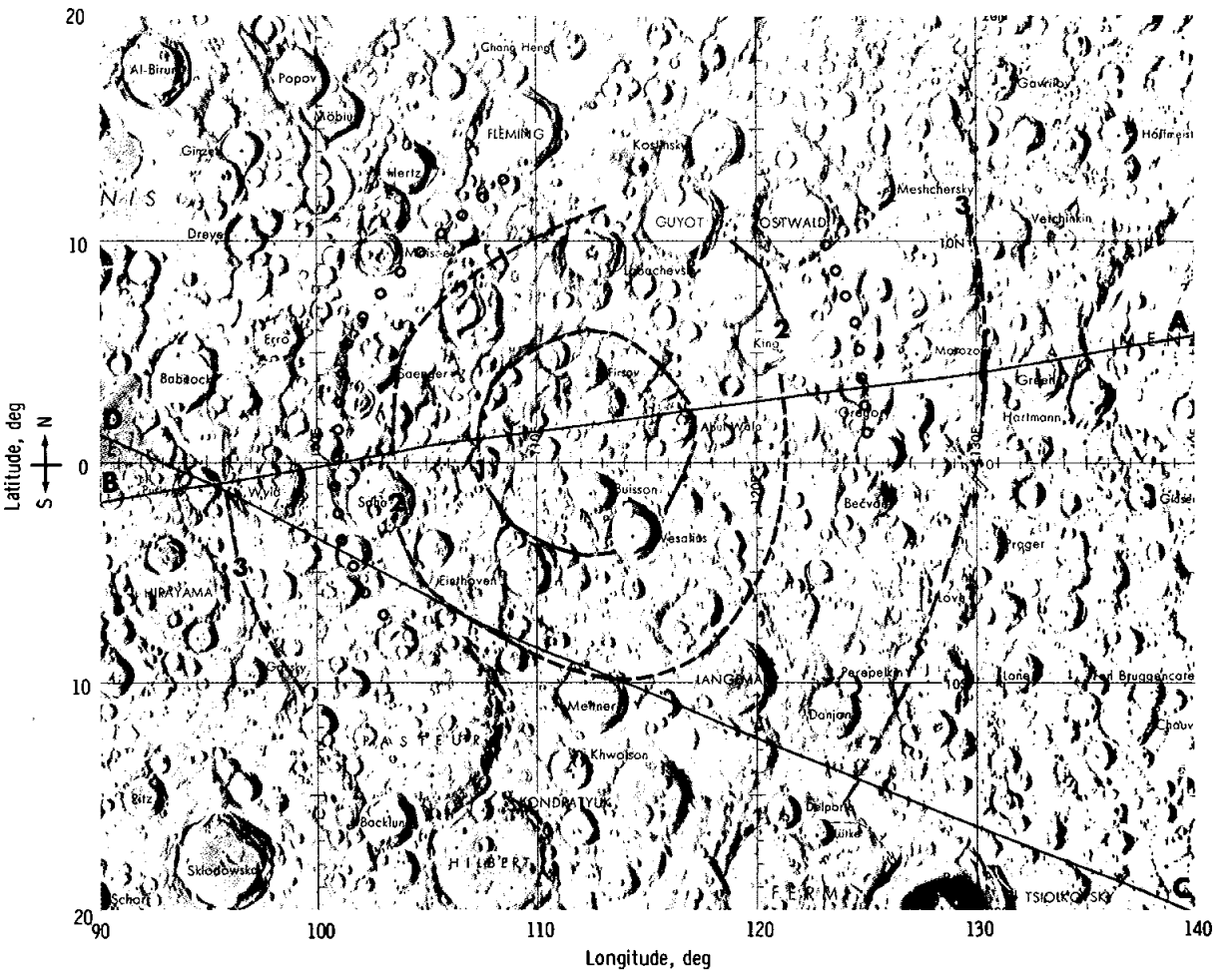


FIGURE 29-44.–Portion of the Air Force Aeronautical Chart and Information Center Lunar Farside Chart (LMP-2), 1:5,000,000 scale, second edition, 1970, from 20° N to 20° S and 90° E to 140° E with the boundaries of the three-ringed basin and the traces of the laser altimeter profiles of Apollo 16 (A to B) and Apollo 15 (C to D) (fig. 29-45).

ring the peak of which occurs at 120.5° E with a scarp height of approximately 1 km above the mean lunar radius. The eastern border of the innermost ring is at Abul Wafa Crater, and its western border under the orbital track apparently is destroyed by a relatively younger crater. (Within the innermost ring and centrally located is a considerable rise that is 75 km across. This rise may represent a surface expression of an uplift in the center of the excavation caused by the impact that created the basin.) The scarp of the western part of the middle ring rises 2 km above the mean lunar radius; following a depression that is magnified by Wyld Crater, the outermost ring is detected at 95° E. At this point, however, the peak is lower than the mean lunar radius. This condition is probably caused by the fact that a part of the lunar surface has been considerably depressed, perhaps before the formation of both Mare Smythii and the new-found basin.

The applicable portion of the Apollo 15 laser altimeter profile starts at 125° E with the scarp of the outermost ring (figs. 29-44 and 29-45). The scarp is approximately 2 km high, and it separates the basin from the rougher and relatively higher terrain to the east. The altitude traverse encounters the second ring at two locations on both sides of 110° E; it is clear

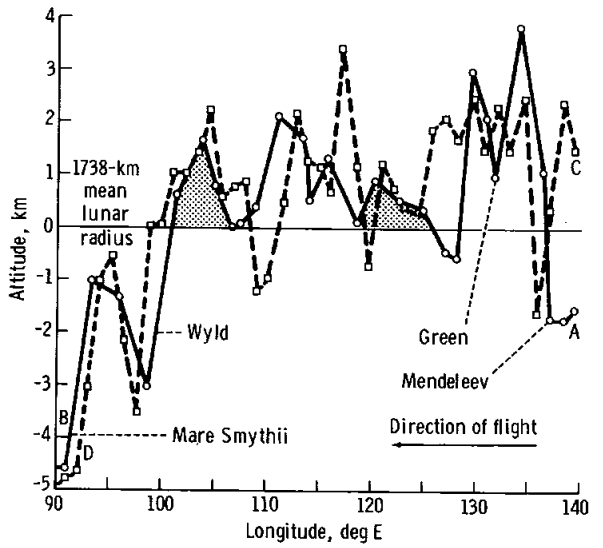


FIGURE 29-45.–Altitude profiles and radius deviations from the spherical Moon (1738-km radius) based on preliminary laser altimeter data (ref. 29-52 and part A of sec. 30 of this report). Lines connecting circles from A to B represent data obtained on the Apollo 16 mission; dashed lines connecting squares from C to D are from Apollo 15 laser altimeter data; shaded areas signify the eastern and western scarps at the middle ring. The three rings of the new-found basin are between Mare Smythii to the west and Green Crater to the east.

from the laser altimeter traces that the rim is crossed in these cases diagonally or tangentially or both. From the peak of the westernmost scarp of the middle ring at 105° E (2.3 km higher than the mean lunar radius) westward, the profile closely follows the Apollo 16 laser altimeter profile. It is obvious from both profiles that, in general terms, the basin represents a transition between the relatively lower near-side surfaces and the relatively higher far-side highlands.

As shown in figs. 29-42 and 29-43, the area between the eastern middle and outer rings of the basin is occupied by a large, old and subdued crater (designated "X" in fig. 29-43(b)). The crater is approximately 200 km in diameter and is pitted by numerous smaller craters; only the crater in its central part is named, Bečvar Crater (fig. 29-44). Both the new-found large crater and Bečvar Crater are centered at approximately 2° S 125° E, with the center of Bečvar being slightly shifted toward the east. The southwestern rim of the large crater is interrupted by a bright-rayed, 35-km-diameter crater, the rays of which are part of what was previously misinterpreted as a mountain range (the Soviet Mountains).

The crater appears to be a few kilometers deep, based on comparison with nearby features and shadow measurements. (No laser altimetry or photogrammetric data are as yet available.) The crater rim and its deposits portray numerous superposition relationships that indicate its young age relative to the larger, three-ringed basin. Because of its size, it is suggested that future issues of lunar charts and maps must include this crater and additional details of its surroundings.

Recommended Nomenclature

According to the rules of the International Astronomical Union, the newly discovered features are large enough and significant enough to warrant assignment of names. The following names have been recommended to the Committee on Nomenclature of the IAU for consideration.

"Arabia" is the name suggested for the new-found basin that is centered at 1° N 112° E. The name is after the geographical division to honor Arab contributions to astronomy, particularly the study of the Moon.

"Rupes Sibericus" (Siberian Scarp) is the name suggested for the 1-km-high scarp that borders the eastern part of the middle ring of the basin, in the vicinity of King Crater (particularly an arc from 10° N 119° E to 1° N 121° E). The name is after Siberia in the U.S.S.R.

"Rupes Apalaches" (Appalachian Scarp) is the name suggested for the 2-km-high scarp that borders the western part of the middle ring of the basin, in the vicinity of Saha Crater (particularly an arc from 10° N 111° E to 0° 104° E). The name is after the mountain range in the eastern U.S.A.

"Necho" is the name suggested for the new-found, 200-km-diameter crater between the eastern middle and outer rings of the basin. The name is that of the ancient Egyptian pharaoh (ruled 609 to 593 B.C.) and pioneer geographer who commissioned a successful 3-yr expedition to prove that Africa was a continent.

PART I

ARTIFICIAL LUNAR IMPACT CRATERS: FOUR NEW IDENTIFICATIONS

Ewen A. Whitaker[a]

The Apollo 16 panoramic camera photographed the impact locations of the Ranger 7 and 9 spacecraft and of the SIVB stage of the Apollo 14 Saturn launch vehicle. Identification of the craters produced by the two Ranger spacecraft was very simple because each photographed its target point before impact. Identification of the SIVB impact crater also proved to be a simple matter because the impact location, as derived from Earth-based tracking, displayed a prominent and unique system of mixed light and dark rays. This system is distinctly visible on many Apollo 16 metric camera frames; indeed, it was noted as an oddity before the plotting of the impact location revealed its actual origin.

North-facing oblique sequences of the metric camera photography covered the impact locations of several other pieces of Apollo hardware, but most photographs were taken at considerable slant distances from the ground tracks. Nevertheless, examination of these frames revealed one other dark halo feature that was found to correspond closely with the tracked impact point of the Apollo 14 lunar module (LM) ascent stage.

By using the criterion of a dark ray pattern, a reexamination of the Apollo 14 500-mm Hasselblad sequence taken of the Apollo 13 SIVB impact area was made. This examination quickly led to the discovery of the ray system and the impact crater.

Crater Dimensions

Before these four new identifications were made, the only artificial lunar impact crater to have been photographed was that produced by Ranger 8, which appears on Lunar Orbiter II photograph H70. This crater was correctly identified for the first time by Baldwin (ref. 29-53), following misidentifications by other investigators. The measured dimensions of the crater, given in reference 29-53 as 13 m and remeasured in this discussion as 13 by 14 m, are given exactly by equation number 8-5A of reference 29-54.[1]

Measurements of the four newly found craters are shown in table 29-II, together with the diameters (computed after the measurements were taken, to prevent biasing the measurements) obtained separately from the equation and factor from references 29-53 and 29-54. A comparison of the measurements shows the accuracy of the computed diameters. The computed crater diameters for the LM ascent stage impacts are also shown in table 29-II.

Impact Locations

Because the calculated velocities of seismic waves depend upon an accurate knowledge of the distances between the impact sites and the Apollo lunar surface experiments package (ALSEP) sites, determination of the impact site coordinates by means other than tracking can be a valuable check. Preliminary estimates of the impact crater coordinates, as obtained from the Orthographic Atlas (ref. 29-55), are given in table 29-III. The persistent bias between the longitude determinations was first noticed with Ranger 7 and 9 and Surveyor I and III when the possibly more reliable inflight data for the latter (ref. 29-56) were used. The differences between longitude coordinates, as determined from tracking data and from the selenographic system for a number of spacecraft, are shown in table 29-IV. The difference clearly increases with increasing westerly longitude, apart from the Apollo 14 ascent stage, and undoubtedly exists because the center of mass of the Moon is displaced from the center of the optical figure of the near side. In fact, the differences are reduced to a small random scatter if the center of

[a]Lunar and Planetary Laboratory, University of Arizona.

[1]This equation uses a scale depth of burst ($H/W^{1/3}$) of 0.25 (where H is burial in feet and W is equivalent weight of trinitrotoluene in pounds) multiplied by the theoretical gravity scaling factor of 1.569.

TABLE 29-II.–Calculated and Measured Diameters of Artificial Impact Craters

Spacecraft	*Impact velocity, km/sec*	*Mass, kg*	*Input angle, horizontal, deg*	*Input angle, azimuth, deg*	*Energy, ergs*	*Calculated crater diameter, m*	*Measured crater diameter, m*
Ranger 7	2.616	365.6	64	117	1.25×10^{16}	13.3	14.5
Ranger 8	2.653	369.7	–	–	1.30×10^{16}	13.5	13 by 14
Ranger 9	2.671	369.7	–	–	1.32×10^{16}	13.6	15.5
Apollo 13 SIVB	2.58	13 925	76	78	[a]4.63×10^{17}	41.1	41
Apollo 14 SIVB	2.54	14 016	69	103	[a]4.52×10^{17}	40.8	39.5
Apollo 15 SIVB	2.58	13 852	–	–	4.61×10^{17}	41.1	–
Apollo 12 LM ascent stage	1.68	2 383	–	–	3.36×10^{16}	18.2	–
Apollo 14 LM ascent stage	1.68	2 303	36	282	3.25×10^{16}	18.0	–
Apollo 15 LM ascent stage	1.70	2 385	–	–	3.44×10^{16}	18.3	–

[a]Values given in reference 29-57 are incorrect.

TABLE 29-III.–Coordinates of Impact Craters

Impacting object	*Tracking (selenocentric) coordinates*	*Map (selenographic) coordinates*
Surveyor I	2.50° S 43.32° W	2.45° S 43.22° W
Apollo 13 SIVB	2.75° S 27.86° W	2.54° S 27.79° W
Apollo 14 SIVB	8.02° S 26.02° W	8.17° S 25.95° W
Surveyor III	3.06° S 23.32° W	2.97° S 23.34° W
Ranger 7	10.70° S 20.67° W	10.65° S 20.61° W
Apollo 14 LM ascent stage	3.42° S 19.67° W	3.37° S 19.40° W
Surveyor VII	40.97° S 11.44° W	40.86° S 11.47° W
Ranger 9	12.91° S 2.38° W	12.81° S 2.36° W
Surveyor VI	.46° N 1.37° W	.53° N 1.40° W
Ranger 8	2.71° N 24.81° E	2.69° N 24.80° E

mass is assumed to be displaced approximately 3.5 km in the near-side direction from the center of the optical figure. This value agrees closely with the value obtained from the Apollo 15 laser altimetry (ref. 29-52). The longitudes obtained by tracking should be corrected if they are to be used in conjunction with map coordinates.

TABLE 29-IV.–Longitude Dependence of Differences Between Map and Tracking Coordinates

Spacecraft	*Approximate longitude, deg*	*Selenographic minus selenocentric longitude, deg*
Surveyor I	-43	+0.10
Apollo 13 SIVB	-28	+.07
Apollo 14 SIVB	-26	+.07
Surveyor III	-23	+.07
Ranger 7	-21	+.06
Apollo 14 LM ascent stage	-19	+.27
Surveyor VII	-11	[a]-.02
Ranger 9	-2	+.02
Surveyor VI	-1	-.03
Ranger 8	+25	-.01

[a]Adjusted for latitude.

Crater and Ejecta Blanket Descriptions

Although the Apollo panoramic camera has slightly better angular resolution than the Lunar Orbiter telephotographic system, the higher orbit of Apollo spacecraft and the slant ranges involved for objects situated off the ground track result in photographs with lower spatial resolution. Thus, the Lunar Orbiter II photograph of the Ranger 8 crater has a resolution of approximately 1 m; the Apollo 16 panoramic camera photographs of the Ranger 7 and Apollo SIVB craters have approximately a 3-m resolution, and the resolution of the Ranger 9 crater photographs is approximately 4 m. The Ranger 8 crater (center of fig. 29-46) is slightly elliptical and sharp-rimmed and has a small central mound. The asymmetrical shape is probably caused by the comparatively oblique impacting direction (42°) (ref. 29-58). The interior has approximately the same albedo as the general mare surface, a fact which led some investigators (who confidently expected a very bright crater) into an incorrect identification. The ejecta pattern (fig. 29-47) is asymmetrical and unexpectedly darker than the average surface.



FIGURE 29-46.–The Ranger 8 impact crater, dimensions 13 by 14 m (from Lunar Orbiter II photograph H70, frame-lets 601 and 602).

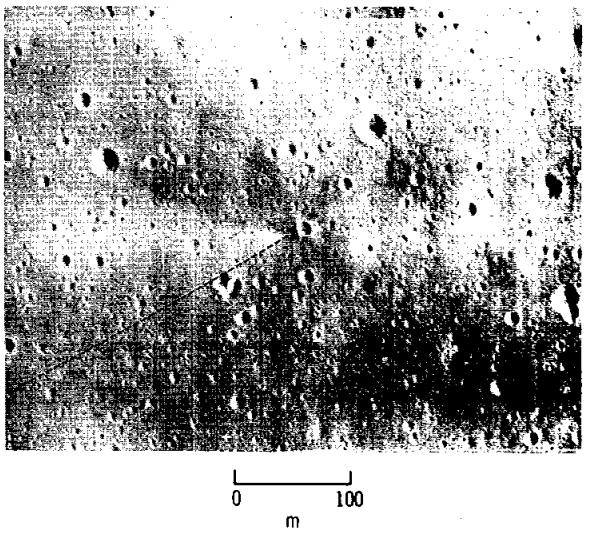


FIGURE 29-47.–Dark ejecta blanket surrounding the Ranger 8 crater. The incoming trajectory trace is indicated.

The Ranger 7 and 9 craters are illustrated in figures 29-48 and 29-49, respectively. The impacts were essentially vertical in these cases, and the craters are circular, as well as can be judged. The resolution is too low for the detection of possible central mounds. The Ranger 7 crater interior is brighter than the surrounding mare, and a small, bright nimbus extends approximately the length of a crater diameter beyond the rim. Beyond this nimbus, an asymmetrical, dark ejecta blanket may be seen, with three or four distinct narrow rays, one of which extends

approximately 250 m. The Ranger 9 crater appears to be generally similar and displays a small, bright, asymmetrical nimbus. On Apollo 16 panoramic camera frame 5387, there is some evidence of a weak, dark ejecta blanket surrounding the nimbus.

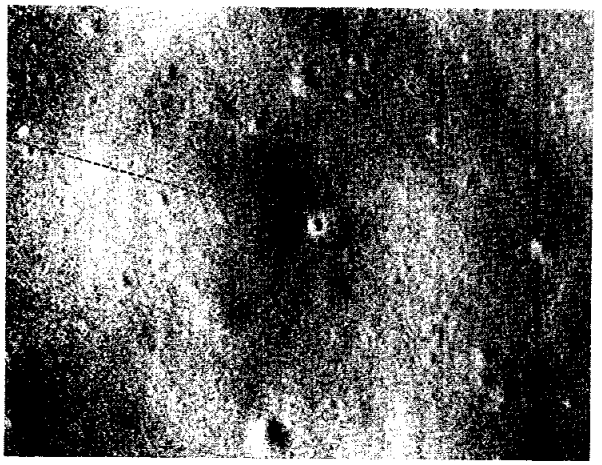


FIGURE 29-48.–The Ranger 7 impact crater with small, bright nimbus; dark ejecta blanket; and narrow, dark rays. The incoming trajectory trace is indicated (portion of Apollo 16 pan camera frame 5435).

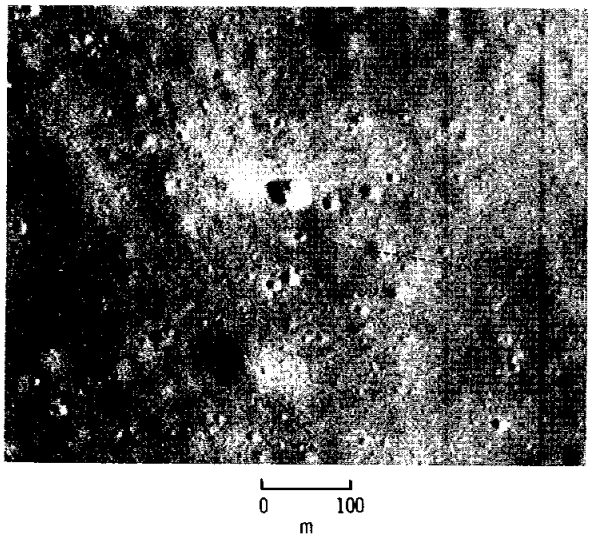


FIGURE 29-49.–The Ranger 9 impact crater with small, bright, asymmetrical nimbus. The incoming trajectory trace is indicated (portion of Apollo 16 pan camera frame 4658).

The Apollo 14 SIVB impact crater, the surrounding ray system, and the ejecta blanket are very interesting. The crater (fig. 29-50) is sharp and slightly elliptical (long axis north to south), with a distinct and comparatively large central mound that is connected to the south wall by a low ridge. The ray system, unlike any naturally occurring system thus far seen on the Moon, consists of light and dark rays, with an asymmetrical ejecta blanket of even darker material (fig. 29-51). The longest rays (toward east-northeast) extend approximately 5 km from the crater (fig. 29-52). For any given angle of solar illumination, the dark ejecta pattern and rays are seen only with difficulty for small phase angles but are prominent for large phase angles (fig. 29-53). This characteristic may be partially caused by the fact that the SIVB is a highly unnatural impacting body, especially with regard to its shape, velocity, and composition. The residual fuel may also be a factor.

The Apollo 13 SIVB impacted the eastern outer slope of the Lansberg B Crater. It produced a star-shaped pattern of dark rays by which the impact

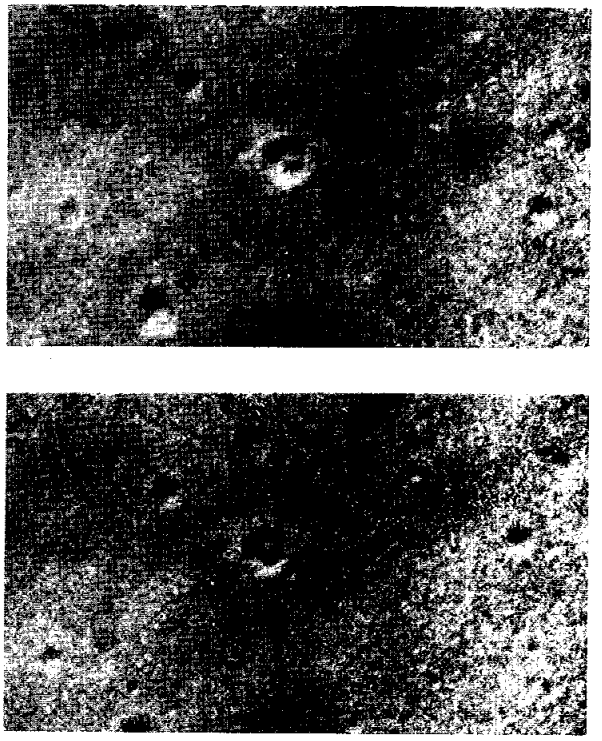


FIGURE 29-50.–Stereoscopic view of the Apollo 14 SIVB crater, dimensions approximately 38 by 41 m (portion of Apollo 16 pan camera frames 5449, left, and 5444, right).

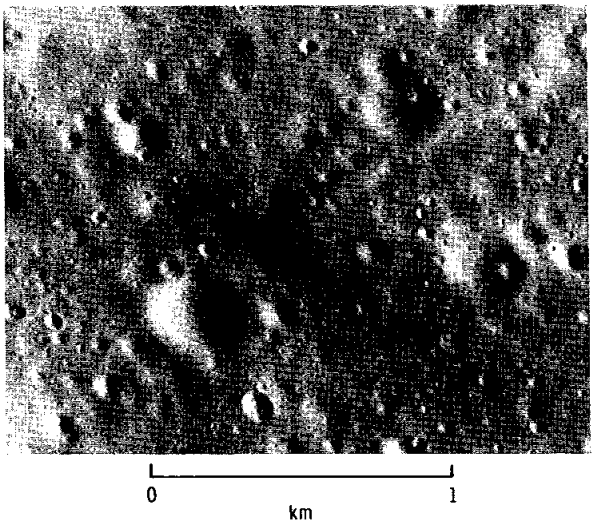


FIGURE 29-51.–The Apollo 14 SIVB dark ejecta blanket and system of dark and light rays (portion of Apollo 16 pan camera frame 5444).

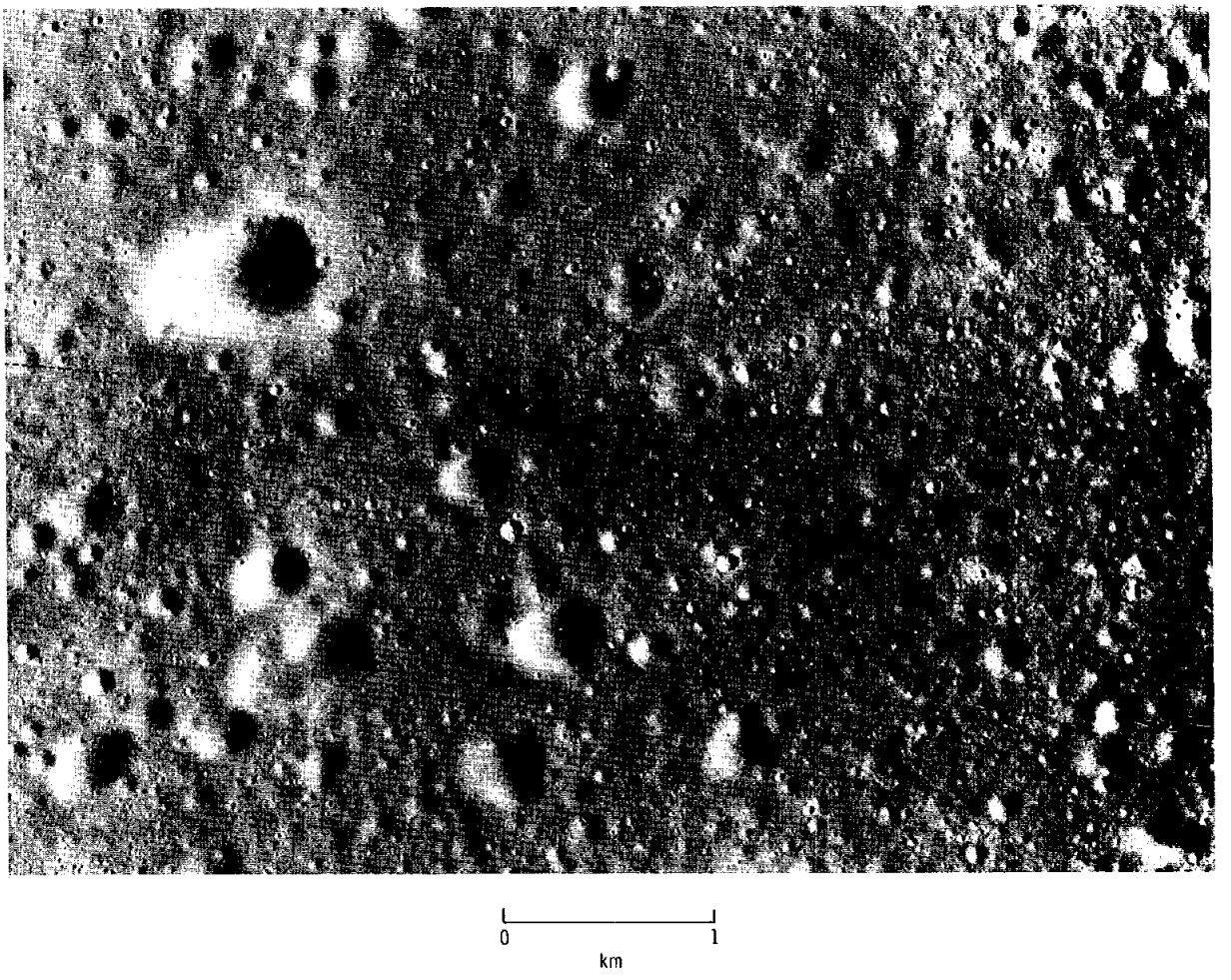


FIGURE 29-52.–The Apollo 14 SIVB inner ejecta blanket and ray system. The incoming trajectory trace is indicated (portion of Apollo 16 pan camera frame 5451).

location was first recognized (fig. 29-54). The crater appears to be generally similar to the previous one and again has a well-defined central mound (fig. 29-55).

Table 29-V contains a list of Apollo 16 panoramic camera frames and Apollo 14 500-mm Hasselblad camera frames that illustrate the artificial impact craters identified by this study. General statements about each series of photographs to aid in classification and selection also are given in the table.

The Apollo 14 LM ascent stage impact location was scrutinized on the appropriate metric camera frames; the search criterion was a dark nimbus that is seen more clearly at larger phase angles. Figure 29-56 is an enlargement of one of these frames, and shows just such an area. Because this dark nimbus is within 0.25° of the tracking position, it is assumed to have been caused by the LM impact, although this assumption cannot be proved currently.

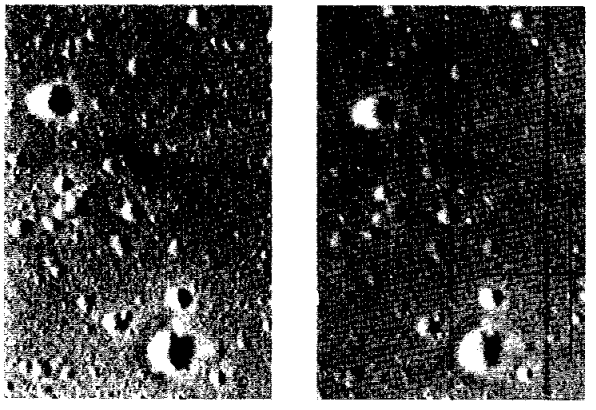


FIGURE 29-53.–The Apollo 14 SIVB ejecta pattern, showing decreasing contrast with decreasing phase angle (portion of Apollo 16 metric camera frames 2831, left, and 2827, right).

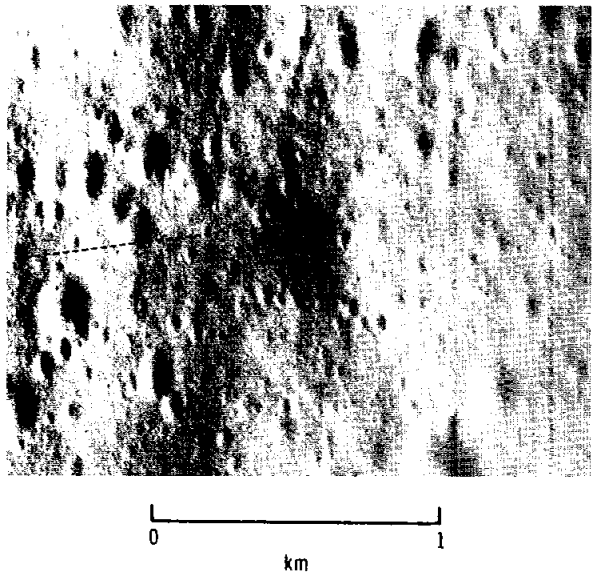


FIGURE 29-54.–The Apollo 13 SIVB impact site, showing a system of narrow, dark rays. The incoming trajectory trace is indicated (AS14-69-9656).

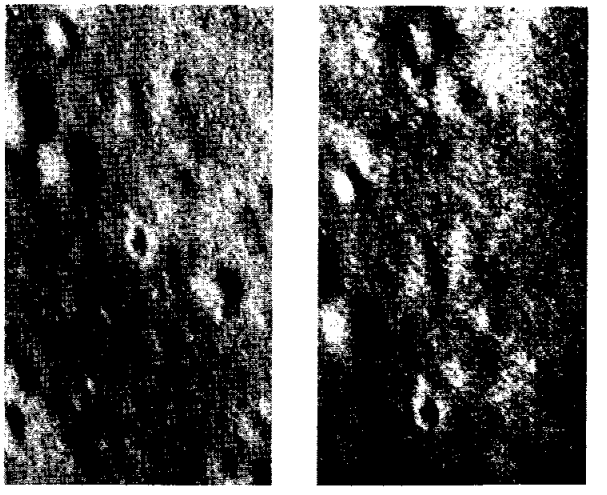


FIGURE 29-55.–The Apollo 13 SIVB impact crater, diameter 41 m, centered in left photograph (portion of AS14-69-9636, left; AS14-69-9638, right).



FIGURE 29-56.–The Apollo 14 LM ascent stage impact location, showing dark ejecta blanket at large phase angle (portion of Apollo 16 metric camera frame 2512).

TABLE 29-V.–Apollo Photographs That Illustrate Artificial Impact Craters

Object	*Photograph numbers*	*Remarks*
Ranger 7	Apollo 16 pan camera frames 4710 and 4712	Very low Sun angle (underexposed)
	Apollo 16 pan camera frames 5430 and 5435	Good stereoscopic pair
Ranger 9	Apollo 16 pan camera frames 4656, 4658, and 4663	Good stereoscopic series
	Apollo 16 pan camera frames 5380, 5385, and 5387	High Sun angle
Apollo 14 SIVB	Apollo 16 pan camera frames 5444, 5449, and 5451	Good stereoscopic series
Apollo 13 SIVB	[a]AS14-69-9631 to 9638	Best series for crater
	[a]AS14-69-9650 to 9656	Best series for ray system

[a]Apollo 14 500-mm Hasselblad camera.

Conclusion

The study of artificial lunar impact craters, ejecta blankets, and ray systems provides the long-needed link between the various experimental terrestrial impact and explosion craters, and the naturally occurring impact craters on the Moon. The elementary study in this discussion shows that lunar impact crater diameters are closely predictable from a knowledge of the energies involved, at least in the size range considered, and suggests that parameters, such as velocity, may have a profound effect on crater morphology and ejecta blanket albedo.

Acknowledgment

The author wishes to thank R. G. Strom of the Lunar and Planetary Laboratory, University of Arizona, for the computations given in table 29-II.

PART J

RANGER AND OTHER IMPACT CRATERS PHOTOGRAPHED BY APOLLO 16

H. J. Moore[a]

Introduction

The Apollo 16 crew photographed an unusual variety of impact craters, including the two craters produced by the impacts of Ranger 7 and 9 spacecraft, small craters produced by boulders as they bounced downslope, craters with marked bilateral symmetry, and primary craters with a wide range of morphologies and sizes. Ranger impact craters and examples of other craters are discussed briefly in this subsection.

Ranger Impact Craters

The Ranger 7 and 9 spacecraft impacted the lunar surface July 31, 1964, and March 24, 1965, respectively, after transmitting to the Earth the first closeup views of the lunar surface. Ranger 7 impacted in Mare Cognitum at a velocity of 2.65 km/sec along an oblique trajectory inclined 64.2° and along an azimuth 114.9° east of north (ref. 29-59). The last image obtained with the A-camera of Ranger 7 covered the impact point with a resolution smaller than the expected crater (fig. 29-57). Comparison of Apollo 16 panoramic (pan) camera photographs of the Ranger 7 impact site with the last A-camera image reveals that there is, indeed, a new bright-rimmed crater (compare figs. 29-57 and 29-58) and at the proper location (ref. 29-60). Plots of the locations of Ranger 7 A-, B-, and P-camera reticles on enlargements of the Apollo 16 panoramic camera photographs confirm that this bright-rimmed crater is at the proper location. The rim-to-rim diameter of the crater is approximately 13.8 m.

[a]U.S. Geological Survey.

Ranger 9 impacted the floor of Alphonsus Crater near a 51-m-diameter crater (ref. 29-61) at a velocity of 2.67 km/sec along an oblique trajectory inclined 64.9° from horizontal and along an azimuth 99° east of north (ref. 29-62). Like Ranger 7, Ranger 9 obtained images of the impact area before crashing onto the lunar surface (fig. 29-59). Comparison of Apollo 16 panoramic camera photographs with Ranger 9 photographs of comparable resolution reveals a new crater near the predicted impact point (compare figs. 29-59 and 29-60). Although the Ranger 9 crater was formed near or on the rim of a preexisting 8-m-diameter crater (as seen in high-resolution Ranger imagery), craters of 8 m across cannot be resolved clearly in the Apollo photograph. The new crater, which measures approximately 13.5 m across, is resolved clearly in the Apollo 16 photograph.

Preliminary examination of the Apollo 16 photographs does not permit a clear assessment of the ejecta asymmetry that should arise from the oblique impacts. The ejecta at the Ranger 7 and 9 craters are expected to prove more symmetrical than the markedly asymmetric ejecta produced by Ranger 8 (ref. 29-58), which impacted at an inclination of only 41°.

The sizes of the three Ranger craters are comparable. Figure 29-61 shows their sizes relative to numerous craters produced by missile impacts on Earth. Because of gravitational effects (ref. 29-58),



FIGURE 29-58.–Enlargement of Apollo 16 photograph showing Ranger 7 impact crater. Arrow indicates crater, which is approximately 13.8 m across (Apollo 16 pan camera frame 5430).

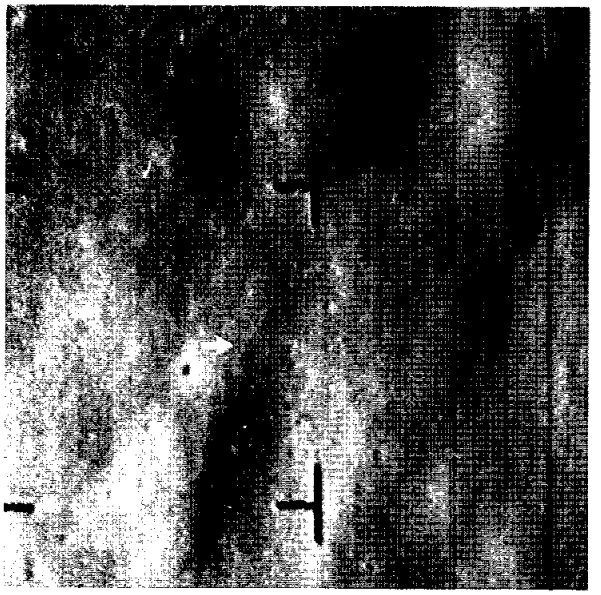


FIGURE 29-57.–Last A-camera image taken by Ranger 7 before impact on lunar surface; arrow indicates area of predicted impact.

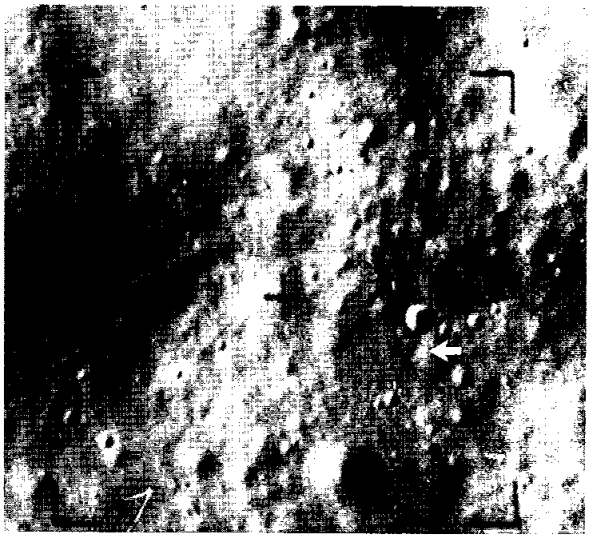


FIGURE 29-59.–Ranger 9 P-3 camera image of predicted impact area, arrow showing predicted impact point. Resolution in figures 29-59 and 29-60 is approximately the same.

the Ranger craters are predictably larger than would be expected by a simple cube-root scaling of the missile craters (fig. 29-61). Alternatively, cube-root scaling may be invalid for craters in this size range (e.g., ref. 29-63).

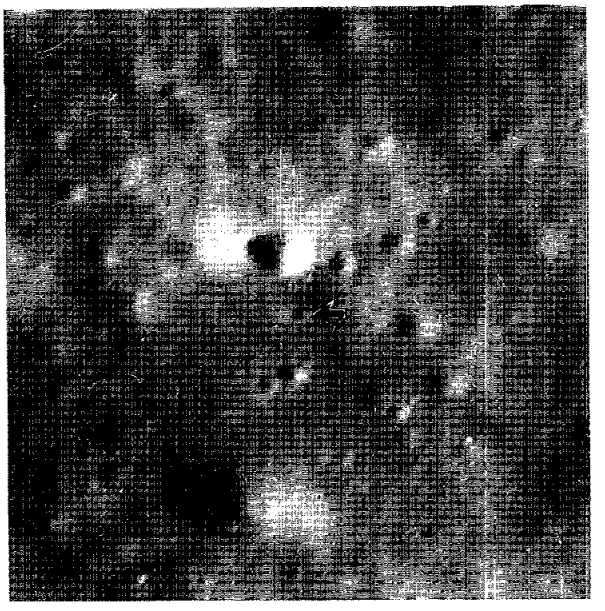


FIGURE 29-60.–Apollo 16 photograph showing Ranger 9 impact crater. Arrow indicates crater, which is approximately 13.5 m across (Apollo 16 pan camera frame 4658).

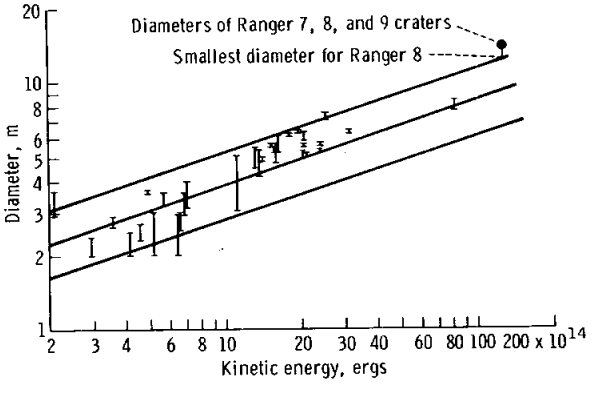


FIGURE 29-61.–Comparison between diameters of craters produced by missile impacts with their kinetic energies at impact and those for Ranger 7, 8, and 9. Straight lines represent the predictions of cube-root scaling for which the crater diameter is proportioned to the kinetic energy of the projectile when angles of impact are the same.

Boulder Craters

Small craters produced by boulders bouncing downslope were observed in the panoramic camera photographs. One large example was found in a crater 24 km across on the lunar far side near 108° E 4°30′ N (fig. 29-62), where a linear array of small craters is found on a slope 4 to 5 km in length. Near the upper part of the slope, large, elongate craters 40 to 50 m long and 20 to 35 m wide are spaced 50 to 100 m apart. Near the base of the slope, the craters decrease in size to 20 to 30 m across and, commonly, their spacing is near 20 to 30 m, so that they form a closely spaced linear array of craters. Near the end of the linear array at the base of the slope, two boulders are found that measure approximately 23 and 37 m across. One of these probably produced the track. Judging from their appearance, they are subrounded or ellipsoidal.

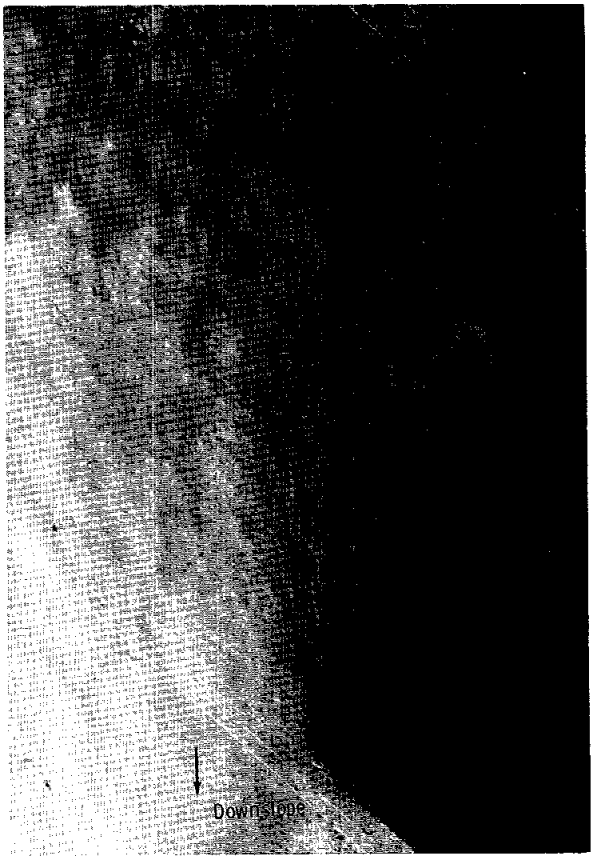


FIGURE 29-62.–Enlarged photograph showing craters (indicated by arrow) that were produced by boulder bouncing downslope (Apollo 16 pan camera frame 4863).

Linear arrays of craters caused by bouncing boulders have been found in photographs of the Moon taken earlier by Lunar Orbiter spacecraft, and they also have been observed on the Earth (ref. 29-64). Mechanical properties of lunar surface materials have been assessed by using dynamic analyses of these tracks (ref. 29-65). Such analyses require that the slopes on which the tracks occur be known accurately. The metrical capabilities of Apollo 16 metric and panoramic camera photographs ultimately can yield these necessary data on slope angles and lead to more accurate determination of soil properties.

Crater With Bilateral Symmetry

The distribution of ejecta and debris of a lunar crater photographed in Daguerre Crater (33°10′ E 11°45′ S) is strikingly similar to that of craters produced by oblique missile impacts at White Sands Missile Range, New Mexico. Although the lunar crater is approximately 2 km across and 250 times larger than the missile-impact craters (ref. 29-63), it shares with them a decidedly bilateral symmetry with respect to ejecta, debris within the crater, and morphology. The light-gray ejecta from the lunar crater (fig. 29-63) is bilaterally symmetrical about a north-northeast plane and extends to beyond two crater diameters from the rim through 270° of arc. This ejecta forms a continuous deposit from the rim to the near flanks, where blocks as large as 33 m in diameter are found. Beyond, the ejecta becomes discontinuous, forming light rays and filaments across the dark mare surfaces. The southerly 90° sector of the rim (toward the top of fig. 29-63) appears to be an unmodified dark mare surface, having little or no ejecta. For impact craters produced by missiles with trajectories at angles near 45°, the plane of the trajectory is the plane of bilateral symmetry, ejecta is absent on the "up-range" side of the crater, the up-range wall is shattered, and fractured "target" materials show little or no displacement. For the lunar crater (fig. 29-63), this relatively unmodified material appears to be represented by the dark exposures on the south part of the upper crater wall. Below these exposures, dark debris forms talus. Thus, the lunar crater was produced by a bolide impacting along an oblique trajectory from the south-southwest toward the north-northeast.



FIGURE 29-63.–Enlargement of Apollo 16 photograph showing 2-km-diameter crater. The asymmetrical ejecta, exposures, and talus of dark mare material on up-range crater wall and the large blocks on flanks are noteworthy (Apollo 16 pan camera frame 4511).

Morphology and Size of Craters

The Apollo 16 crew collected important photographic data on the variation in morphology of primary impact craters with size of the crater. Typically, young lunar craters in the 400 to 600 m sizes, such as South Ray Crater and the crater shown in figure 29-64, have central mounds or concentric structures within the crater, depending on the target material (ref. 29-66). For these craters, abundant blocks between 1 and 20 m in size occur in the ejecta. Large blocks also are found in the ejecta of larger craters (2 to 10 km across), such as Mosting C, Censorinus, and the 3.1-km-diameter crater shown in figure 29-65. Such blocks may be as large as 35 to 60 m, depending on the crater diameter. In contrast to the smaller craters, dunelike structures with long axes concentric to the crater are found around the flanks. Commonly, such dunelike structures completely surround the crater, but they may be confined



FIGURE 29-64.–Photograph of crater 430 m across with blocky ejecta and central mound; largest block is approximately 11 m across (Apollo 16 pan camera frame 5400).

to sectors of the ejecta as in figure 29-65. These craters are typically bowl shaped and devoid of concentric structures and central mounds within the crater.

Large craters 40 to 90 km across, such as Aristarchus and Tycho Craters, differ markedly from the smaller craters. The large craters are characterized (ref. 29-67) by (1) bright, blocky central peaks; (2) bright, generally level crater floors with irregular fissures, blocks, and local domical hills; (3) bright, steeply terraced crater walls strewn with blocks and streaked by radial channels; (4) flat, fissured hills on the wall terraces; (5) a bright crater rim with concentric ridges and valleys, radial shallow valleys, and radial rimmed channels; (6) generally bright crater flanks with radial, braided, and chevron ridges; (7) smooth, flowlike surfaces extending over part of the rim and flanks and short, ribbonlike to stubby ridges; and (8) alined, isolated to clustered, rimmed depressions beyond the flanks (ref. 29-67).

An excellent photograph of a crater (fig. 29-66) that is transitional between the smaller craters (2 to 10 km across) and the larger craters (40 to 90 km across) was obtained on the Apollo 16 mission. This crater is approximately 15 km across and lacks the terraced walls of the larger craters (40 to 90 km across). Although the crater floor cannot be seen, the form of the crater is more akin to the smaller craters (2 to 10 km across). Like the larger craters, the near-rim areas have radial rimmed channels but only a limited number of weakly developed concentric ridges and valleys. Beyond the near rim, the flanks are chiefly characterized by radial ridges, some braided and chevronlike. At greater distances from the crater, alined, isolated, and clustered rimmed depressions are found. More importantly, smooth, flowlike surfaces extend from the crater rim over the near-rim surfaces and outward onto the flanks (fig. 29-67).

This is the smallest crater with these distinct smooth, flowlike units known to date. The example of a flowlike body shown in figure 29-67 originates near the rim of the crater, is approximately 0.5 km wide, and extends from the rim along an arcuate path some 3.0 km in length. Close inspection shows that there are three or four individual flows. The longest flow fills a small depression on the rim, whereas the others appear superposed on the larger one. The edges of the large flow are convex outward, although the center is somewhat depressed. Smaller flows form lobate, fingerlike extensions and are clearly convex

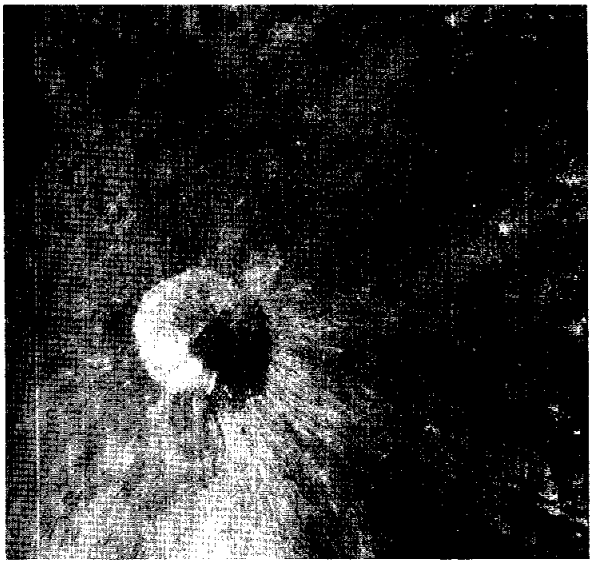


FIGURE 29-65.–Dunelike structures (indicated by arrow) in ejecta of 3.1-km-diameter crater. Blocks as large as approximately 35 m are found around the crater (Apollo 16 pan camera frame 5063).



FIGURE 29-66.–Photograph showing crater that is transitional in morphology between small (2 to 10 km), bowl-shaped craters and large (40 to 90 km) craters (Apollo 16 pan camera frame 4136).

upward and outward near their distal parts. One flow is particularly interesting because it is complex and composed of a broad ridge with a linear depression parallel to the ridge axis. On the downslope and more distal end of the depression, a smaller flow issues from the linear depression.

The origin of these flowlike units is controversial and needs further study. It has been postulated that these units represent volcanic flows (ref. 29-68), flows of molten material generated by an impact producing the crater (refs. 29-58 and 29-69), flows of

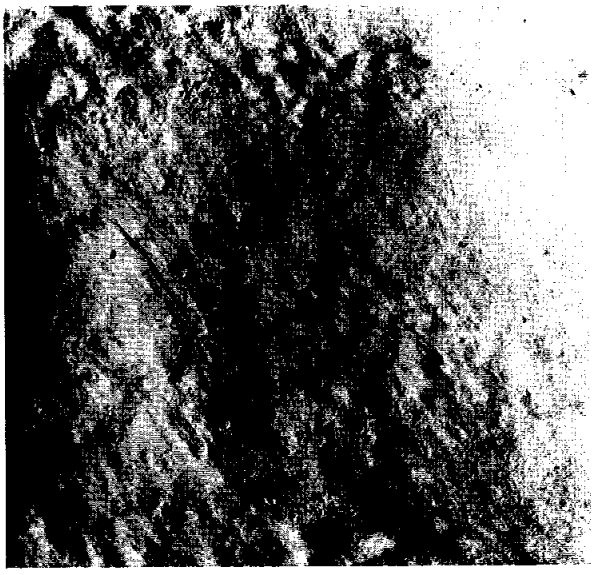


FIGURE 29-67.–Enlarged photograph showing smooth, flowlike surfaces on western rim of crater from figure 29-66. Arrow indicates end of flowlike surface (Apollo 16 pan camera frame 4131).

fluid-solid mixtures,[1] and simply flows of solid debris.

Finally, the Apollo 16 mission has supplied additional data on the maximum size of blocks found around large impact craters (fig. 29-68). Significant amounts of data have been obtained from Lunar Orbiter photographs, but data for craters larger than 5 km are being supplied by Apollo photographs (ref. 29-70).

In summary, Apollo 16 orbital photography has supplied important new data on craters in the lunar surface. Continued study of these craters and use of the metrical capabilities of the metric and panoramic camera photography will yield additional scientific results on lunar craters.

[1]Crittenden, M. D.: Lunar "Mudflows" in Orbiter V Imagery. A Preliminary Geologic Evaluation of Areas Photographed by Lunar Orbiter V, Including an Apollo Landing Analysis of One of the Areas. NASA LWP-506, 1968, pp. 158-164.

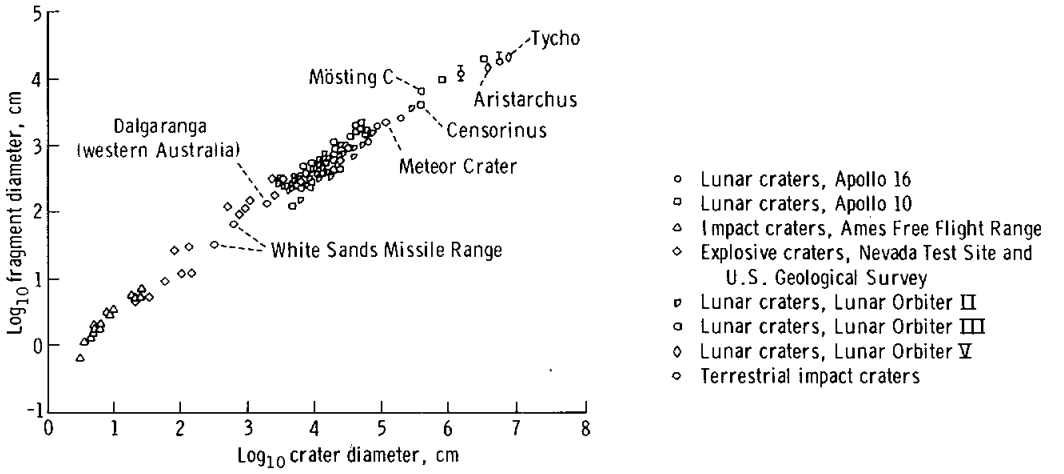


FIGURE 29-68.–Comparison of largest block or fragment diameter found on crater rim and crater diameter.

PART K

LUNAR SECONDARY CRATERS

Verne R. Oberbeck,[a] Robert H. Morrison,[a] and John Wedekind[a]

Recently, considerable interest has been shown in the peculiar clusters of V-shaped ridges that form a herringbone pattern on parts of the secondary crater fields of certain large lunar craters. These features were described in a study of the Apollo 8 photographs (ref. 29-71), and it was hypothesized that they were produced by high-speed gas flow associated with the base surge that is thought to have occurred during the formation of large lunar craters. Later, in a study of Copernicus Crater (ref. 29-72), V structures associated with Copernicus ejecta and its secondary craters were described and measured. A mechanism involving deposition of ejecta from the primary crater was favored in this study, but it was noted that the V-shaped ridges typically were associated with groups of secondary craters. Laboratory studies[1] later demonstrated that V-shaped ridges are produced between craters formed simultaneously by projectiles impacting near one another at high angles to the surface normal. These conditions are characteristic of secondary-impact crater formation. For the laboratory craters, V-shaped ridges that project from the point of overlap of the craters resemble those associated with lunar secondary craters surrounding Copernicus Crater.

The purpose of this discussion is to suggest that these features have been observed in a poor state of preservation in the Apollo 16 photographs of the Theophilus secondary crater field. Additional results of experimental impact cratering are described and used to examine the possible conditions of secondary crater formation.

V-Shaped Ridges in the Secondary Crater Field of Copernicus

A review of V-shaped structures surrounding the fresh Copernicus Crater will be useful before the limited, preliminary observations of the more extensively eroded secondary crater field of Theophilus are presented. This review will be especially useful because most of the preliminary observations of features surrounding Theophilus Crater were made

[a]NASA Ames Research Center.

[1]Oberbeck, V. R.: Simultaneous Impact and Lunar Craters. The Moon (in press).

from Apollo 16 metric camera photographs. Only a few of these V-shaped ridges have been located on the metric camera photographs because of limited resolution and the eroded nature of the features. However, consideration of the ridges is important because, if they can be found around a number of lunar craters, variation in conditions under which material is ejected from impact craters can be determined. This could produce knowledge of variation in initial conditions of formation of the parent craters.

Copernicus Crater and part of its ejecta field are shown in figure 29-69. Three groups of Copernicus secondary craters are indicated; magnifications of these craters are shown in insets at the top of the figure. The V-shaped ridge from the crater string on the left is slightly displaced from a radial line extending from Copernicus Crater, but a ridge projects from each side of the crater doublet. For the second crater doublet (from the left), the ridge is better developed, especially where the craters overlap. The point of the V is directed toward Copernicus Crater. The secondary crater string (third inset from the left) is nearly concentric with the rim of Copernicus Crater. Ridges between these craters are very well developed and are almost perpendicular to a line connecting crater centers; the ridges are best developed at the point of crater intersection.

A theoretical analysis of the formation of Copernicus Crater (ref. 29-73) yields ejection angles of 68° to 76° (measured from the normal to the surface) for fragments forming secondary craters. To demonstrate formation of overlapping Copernicus secondary craters,[2] two projectiles were launched simultaneously in an evacuated ballistic range and were allowed to impact against a quartz sand target at a velocity of approximately 2 km/sec and at an angle of 69° from the surface normal. Impact velocity of 2 km/sec is higher than necessary for correct simulation of these secondary craters, but no effect of velocity on geometry of the V-shaped structure has been noted. The result of this experiment is shown in the inset on the right in figure 29-69. A V-shaped ridge emanates from the point of overlap of the two craters. The V opens in a direction down range from the impact direction and is best developed where the craters

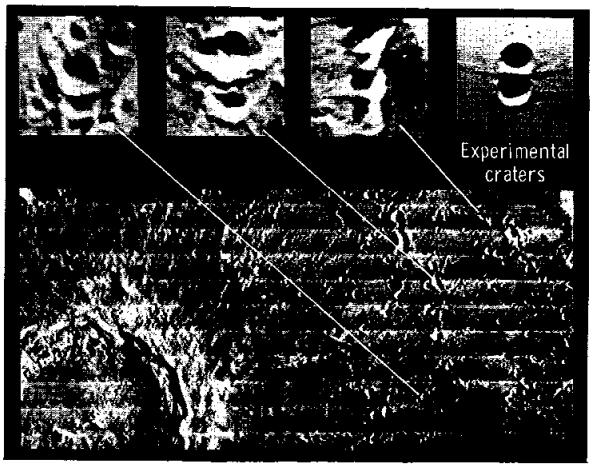


FIGURE 29-69.–Northeast quadrant of Copernicus Crater with magnifications of three groups of secondary craters. Inset at the right shows two experimental craters produced simultaneously at an impact angle of 69°, measured from the surface normal.

overlap. The modeled secondary crater is similar to the Copernicus secondary craters shown in figure 29-69.

Impact velocity of 2 km/sec is representative of only a very small percentage of the material that is ejected from lunar primary craters and that falls back to the lunar surface. The relationship between ejection velocity and ejection angle for constant ranges in distance from the point of ejection to the point of impact is shown in figure 29-70. The ejection angle θ is measured from the surface normal. These values were derived from ballistic equations given in reference 29-74, and adequately describe the ballistic conditions for most of the ejected material that forms secondary craters around large lunar craters. The area between the upper and lower curves (fig. 29-70) represents all the possible conditions of impact angles and impact velocities that could produce secondary craters at ranges from 100- to 400-km distance from any large lunar crater, ranges at which many secondary craters are found. The 2-km/sec impact velocity[3] is a valid condition for simulation of Copernicus secondary craters only for impact angles less than 4.5° or greater than 1.5°. However, it has been determined that velocity does not have a strong control on the shape of the V-shaped ridges from

[2]Ibid.

[3]Ibid.

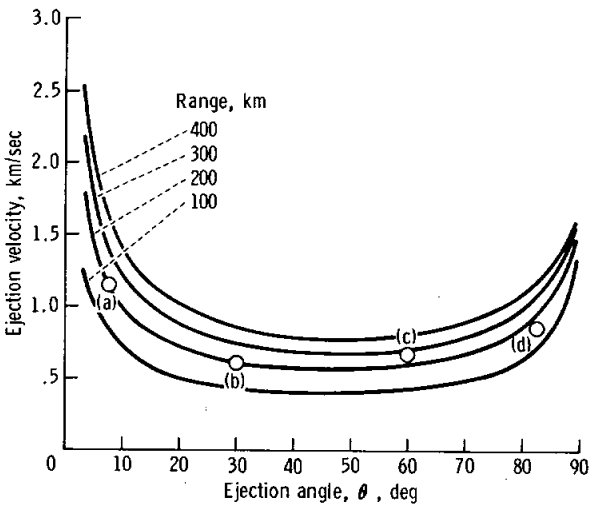


FIGURE 29-70.–Conditions of ejection velocity and ejection angle for material ejected from the lunar surface and impacting at the indicated range. Letters (a) to (d) refer to conditions of formation of craters shown in figure 29-71.

secondary craters. Results of additional experiments under more realistic ranges of impact angle and velocity will next be presented to compare these results to secondary craters observed around Copernicus Crater and to two groups of secondary craters observed near Theophilus Crater.

Laboratory Simulation of Lunar Secondary Craters

Certain experimental conditions were incorporated into the simulation of secondary lunar craters to examine their effects on V-shaped ridges. These conditions are: variations in the spacing of impact points relative to crater diameter for determining the effect on the included angle of the V-shaped ridge; azimuth angle changes; changes in the size of one crater in a secondary crater string; and changes in time of impact of one projectile relative to another.[4] Preliminary results suggest that the main control on the magnitude of the angle included by the V-shaped ridge is the variation of the impact angle.

A series of doublet laboratory impact craters (fig. 29-71) was produced under conditions indicated in figure 29-70. The photographs of these craters are keyed by letters to impact velocities and impact angles given in figure 29-70. Craters shown in figure 29-71(a) were formed simultaneously by projectiles that impacted at a nearly vertical angle (7.5° measured from the surface normal). The ridges projecting from the crater overlap are nearly perpendicular to a line connecting the center of one crater to the other. These craters do not resemble the secondary craters surrounding Copernicus. Craters (fig. 29-71(b)) formed at impact angles of 30° measured from the surface normal also do not resemble the lunar secondary craters. The included angle of the V-shaped ridge is 171°. However, craters shown in figure 29-71(c) begin to show a resemblance to some of the V-shaped structures associated with lunar secondary craters. The included angle of the V-shaped ridge is 150° when the impact angle is 60°. Finally, for impact angles of 82.5° (fig. 29-71(d)), the V-shaped ridges show strong similarities to those associated with lunar secondary craters. These preliminary results suggest that the secondary projectiles that produced many of the craters surrounding Copernicus Crater were probably ejected at high angles from the normal to the lunar surface. With further experimentation and study of photographs of V-shaped ridges, it may be possible to approximate the impact velocity and angle of the ejected material that produced any given secondary crater. A number of such measurements might then be used to reconstruct the conditions of angles and velocities of material ejected from lunar craters. These techniques might also be applied to the study of other large lunar craters.

V-Shaped Ridges in the Secondary Crater Field of Theophilus

Preliminary examination of Apollo 16 metric camera frame 1259 has shown that V-shaped ridges also are associated with the secondary craters of Theophilus Crater. This crater is older than Copernicus Crater, and its ejecta blanket and secondary craters are more degraded. However, two examples of secondary craters with V-shaped ridges have been observed. Part of Theophilus Crater and the surrounding field of secondary craters are shown in figure 29-72. The two areas outlined in this figure

[4]Although these experiments have involved simultaneous impact of only two projectiles, the results can probably be applied also to the interpretation of longer secondary crater strings.

show two secondary crater clusters with associated V-shaped ridges. An enlargement of the upper outlined area is shown in figure 29-73. The secondary crater string, located in the center of the photograph, is the largest crater cluster shown. The V-shaped ridge projects from near the bottom of this crater group. The right arm of the V is approximately twice the length of the secondary crater cluster; the other part of the V is approximately three times the length of the cluster. The secondary craters in figure 29-73 are shown again in figure 29-74, in which the V-shaped ridge can be seen more clearly. For this secondary cluster, the included angle of the ridge is only approximately 70°. Therefore, the experimental results presented earlier suggest that these craters were formed under conditions similar to those for the

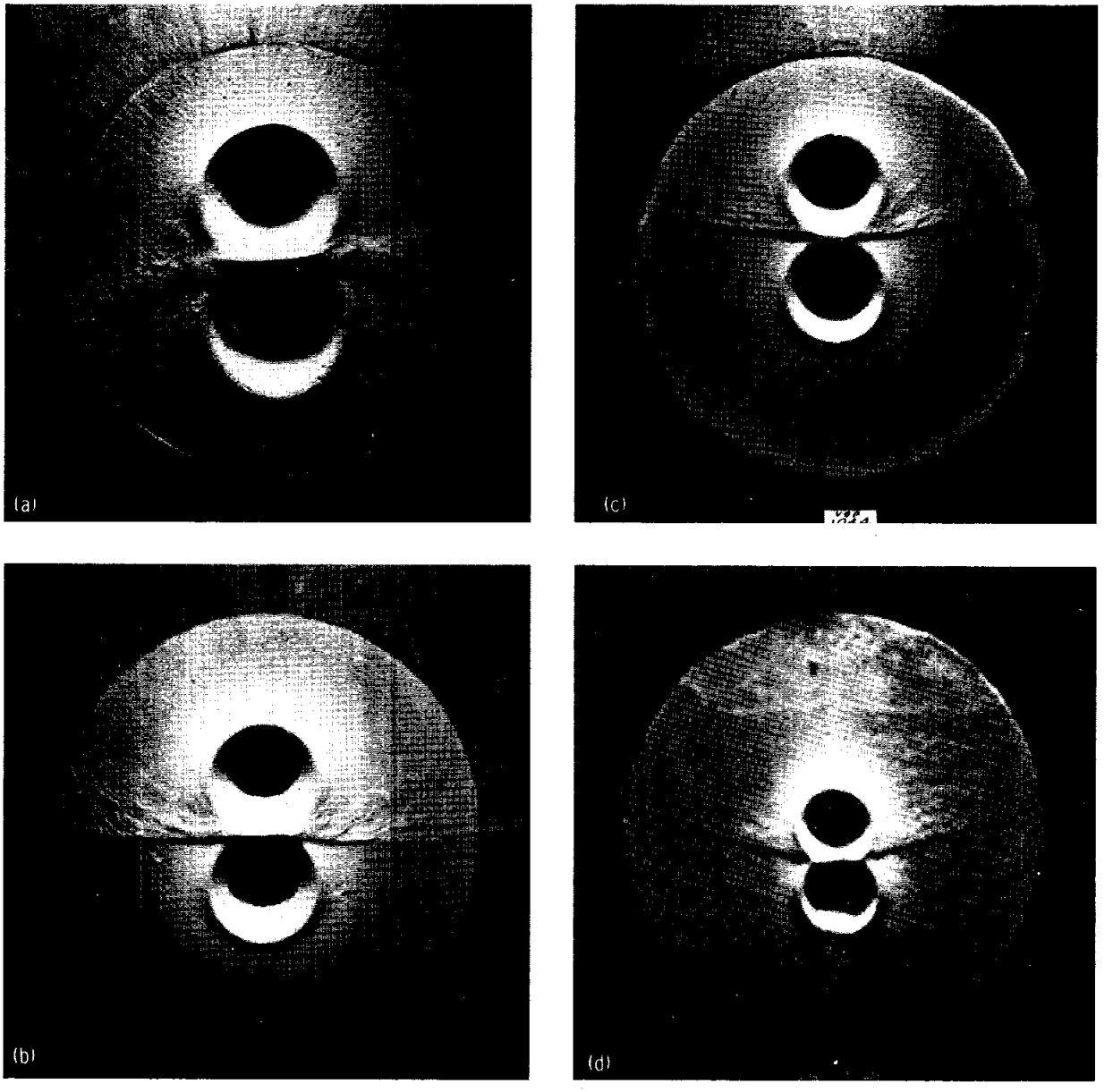


FIGURE 29-71.–Impact crater pairs produced simultaneously under conditions shown by letter designation in figure 29-70. (a) $\theta = 7.5°$. (b) $\theta = 30°$. (c) $\theta = 60°$. (d) $\theta = 82.5°$.

Copernicus secondary craters. Material was probably ejected from Theophilus Crater at high angles from the surface normal.

Ridges associated with secondary craters are sometimes irregular, being well developed only on one side of the secondary crater string. Part of an Apollo 16 panoramic camera photograph (fig. 29-75) shows an area of the secondary crater field north of Theophilus Crater and northwest of Torricelli Crater. There are several examples in this photograph of ridges projecting from clusters of secondary craters.

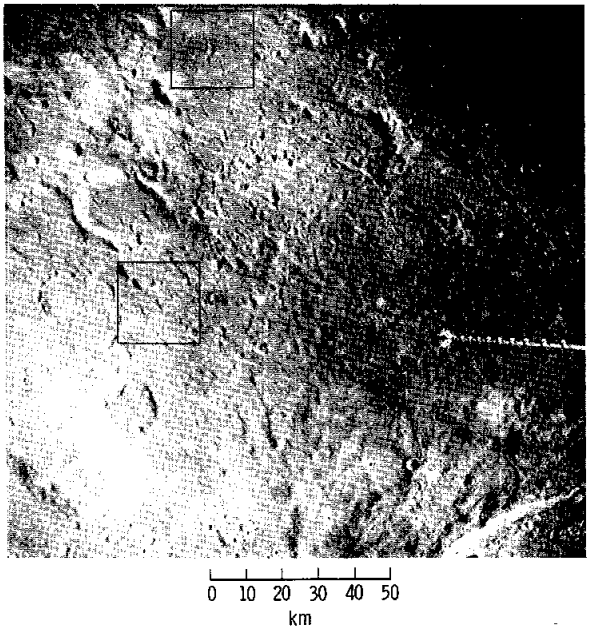


FIGURE 29-72.–Part of Theophilus Crater and part of Theophilus secondary crater field (Apollo 16 metric camera frame 1259). Outlined area at top of figure is enlarged in figure 29-73.



FIGURE 29-73.–Secondary craters of Theophilus Crater and associated V-shaped ridge (enlargement of outlined area at the top of figure 29-72).

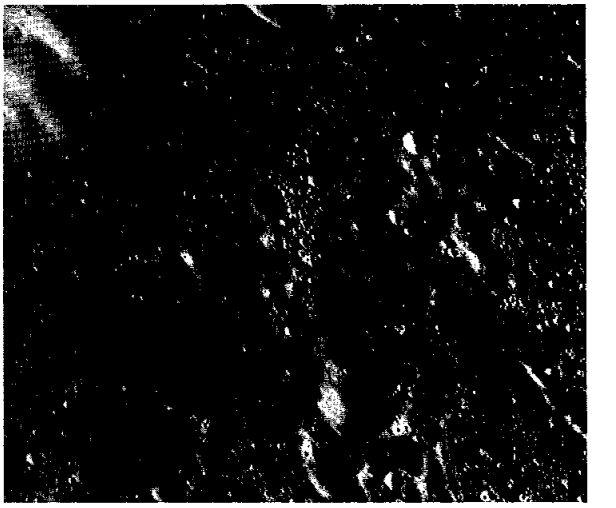


FIGURE 29-74.–Part of Apollo 16 pan camera frame 4543, showing secondary craters of Theophilus Crater and associated V-shaped ridge shown in figure 29-73.



FIGURE 29-75.–Part of Apollo 16 pan camera frame 4531, showing secondary craters of Theophilus Crater.

Similar results have been obtained under certain conditions of simultaneous impact in laboratory experiments. For example, when the azimuth of the trajectory is varied, ridge development increases on one side of a crater cluster and decreases on the other. Although the ridges associated with the secondary craters in figure 29-75 are not similar to the typical symmetrical V-shaped ridges that are formed under ideal conditions in the laboratory, they are believed to have originated similarly from interaction of material ejected from simultaneous formation of adjacent craters.

PART L

CRATER MORPHOMETRY

Richard J. Pike[a]

Morphometric analysis of lunar craters (ref. 29-75) complements the more traditional photointerpretive study of crater morphology. These two indirect approaches to the scientific investigation of lunar craters continue to be productive because the preferred alternative method, direct field examination of specific large craters, is not being undertaken in the current series of manned lunar landings and will not be implemented for some time. Metric camera photography returned from the Apollo flights is essential to the continued study of lunar crater geometry. The material provides raw data of a quality far superior to and more uniform than comparable data available from Lunar Orbiter or Earth-based sources.

This subsection presents a sampling of morphometric results for five selected medium-sized craters photographed on the Apollo 16 mission: Mädler, Langrenus B, Isidorus, Capella, and King (fig. 29-76). Mädler and King Craters are fresh-appearing, rayed craters; the remaining three craters are older and more subdued. All are upland craters; comparable postmare craters were not photographed on the Apollo 16 flight. Four topographic profiles were generated for each crater by the photogrammetric unit at the Center of Astrogeology in Flagstaff, Arizona. The profiles are oriented north-south, east-west, northeast-southwest, and northwest-southeast; most of them intersect the crater centers. Selected profiles are shown in figure 29-77. In the following discussion, these profiles are assumed to represent the lunar surface accurately.

Apollo metric camera data present the first real opportunity to evaluate previous topographic measurements in terms of accuracy rather than in terms of precision. Previous investigations have established at least six descriptive variables that specify the overall surface geometry of a crater: rim-crest diameter; width of exterior rim slope; diameter of flat inner floor, if present; average depth; average height of rim crest above surrounding terrain datum; and degree of circularity of the rim crest. These measurements from Apollo 16 metric camera data for the five sample craters are given in table 29-VI. Similar data from previous measurements are available for four of the craters. Differences between the two sets of values are expressed in table 29-VI as percentages of the Apollo 16 results. If the Apollo 16 data are 100 percent accurate, then the older measurements deviate by 3 to 74 percent, with an average error of 20 percent. Data at this level of accuracy probably are adequate for analyses that rely on generalized, statistical procedures, such as scatter-diagram comparison. For more critical types of analysis, especially detailed studies of individual craters, the error should be no more than 5 to 10 percent. Errors in three of the variables appear to be systematic: rim diameter and floor diameter are overestimated by the older data; rim width is underestimated by the older data. Differences in depth, rim height, and circularity are not systematic. Expectedly, errors in rim diameter and circularity are small; errors in rim width and rim height are quite substantial. The four-crater sample of older measurements examined here is far too small to provide a definitive evaluation of the quality of pre-Apollo morphometric data. However, older crater measurements should be used conservatively until

[a]U.S. Geological Survey.

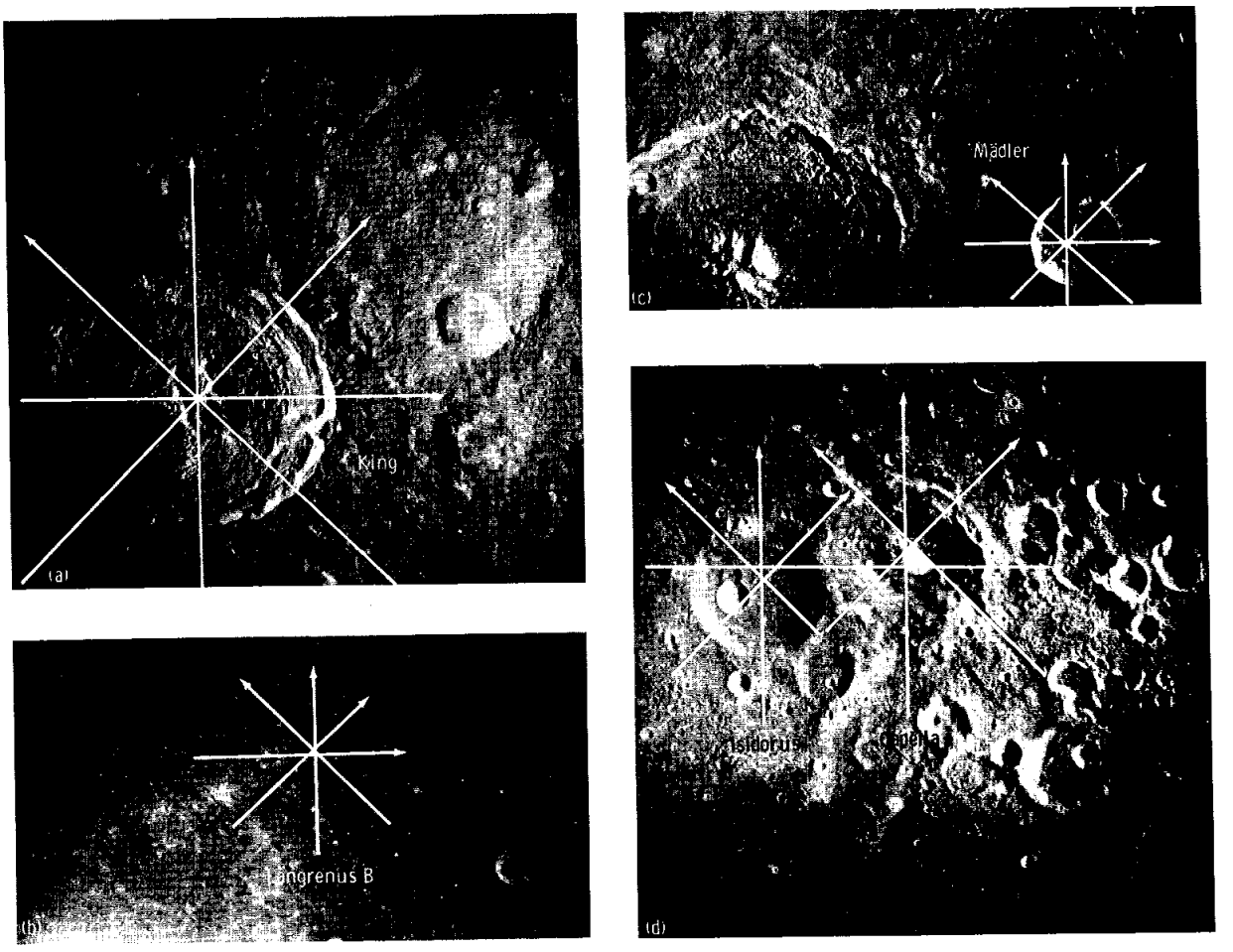


FIGURE 29-76.–Apollo 16 photographs of five selected lunar craters. (a) King, 5° N 120° E (Apollo 16 metric camera frame 1870). (b) Langrenus B, 4.5° S 58° E (Apollo 16 metric camera frame 0128). (c) Mädler, 11° S 30° E (Apollo 16 metric camera frame 0430). (d) Isidorus and Capella, 8° S 34° E (Apollo 16 metric camera frame 0146).

more of them can be checked against data from Apollo metric cameras.

The photogrammetric method of generating crater measurements also furnishes far more complete data than does the shadow-length method that yielded most of the previous morphometric information on lunar craters. The advantage is strikingly exemplified in profiles of the fresh far-side King Crater. Profiles in figure 29-77 show that King Crater is nearly twice as deep along the east-west diameter as it is along the north-south diameter. Shadow-length measurement procedures would register only the east-west data and, thus, would misrepresent the average depth of the crater. Additional problems inherent in data obtained by the shadow-length technique have been discussed elsewhere.[1] Depth figures used for morphometric work must be averages rather than extreme values, because depths are used in estimating crater rim and bowl volumes and in constructing models of the relative-age ranking of craters. Accurate morphometric data are especially required from craters located in the lunar highlands, where the exterior terrain datum is very irregular. Although the best morphometric data require good topographic maps,

[1]Pike, R. J.: Meteoritic Origin and Consequent Endogenic Modification of Large Lunar Craters – A Study in Analytical Geomorphology. Unpublished Thesis, Univ. of Mich., 1968.

TABLE 29-VI.–Crater Variables From Apollo 16 Metric Camera Data

Crater	*Rim diameter, m (a)*	*Rim width, m (b)*	*Floor diameter, m (a)*	*Depth, m (b)*	*Rim height, m (b)*	*Circularity (c)*	*Height/ depth*	*Width/ diameter*
Mädler	27 000 [d](+3)	8 300 (-33)	12 000 (+25)	2830 (-15)	885 (-32)	0.79 (+3)	0.31	0.31
Langrenus B	32 000 (+9)	5 400 (-44)	18 000 (+17)	1865 (+34)	470 (+74)	.88 (-5)	.25	.17
Isidorus	36 800 (+6)	7 000 (-14)	22 000 (+27)	2110 (-18)	830 (+5)	.82 (-5)	.39	.19
Capella	38 800 (+15)	8 000 (-30)	16 000 (+25)	2800 (-4)	895 (+34)	.73 (+5)	.32	.21
King	71 000 –	17 000 –	40 000 –	3830 –	1690 –	.80 –	.44	.24

[a]From four measurements.
[b]From eight measurements.
[c]Defined as ratio of squared radius of inscribed circle to squared radius of circumscribed circle fitted to outline of crater rim crest. Parentheses contain approximate values from Apollo 16 pictures.
[d]Percentages by which best previous measurements exceed (+) or fall short of (-) the Apollo 16 values.

data of adequate reliability can be extracted from at least four topographic profiles and an accurate planimetric map of the rim crest.

The rim crests of large lunar craters may vary systematically in evenness with azimuth. The photogrammetric profiles of King Crater show that the east and west wall segments are much higher than the north and south wall segments. The low north and south walls may be partially explained by the unevenness of the highlands on which King Crater is superposed, but similarly low north and south walls are evident[2] in several large (>40 km), fresh craters on the lunar near side. If further reduction of Apollo metric camera photographs establishes the prevalence of this azimuthal variation for many craters, the explanation may be that a relationship exists between the linear structural trends of the lunar grid system and their angle of intersection with various segments of the rim of a crater. Grid fracture systems also may account for the deltoids (triangular topographic projections) occurring on north and south rims of many large lunar craters (ref. 29-76). Uneven rim crests and deltoids probably develop during the formational impact because they occur in very fresh craters, such as King Crater (fig. 29-76(a)).

The depth-diameter relations of freshly formed lunar impact craters follow one of three very general exponential models (fig. 29-78): simple craters less than 20 km in diameter; complex upland craters more than 20 km in diameter; and complex craters formed on mare surfaces. Aging lunar craters become progressively shallower and acquire broader flat interior floors. A different set of lines, drawn parallel to and below each of the three models in figure 29-78, defines a relative-age sequence for those lunar craters not affected by catastrophic aging processes (ref. 29-77). Depth-diameter data for the five sample craters exemplify such a trend with respect to the complex upland crater model (curve 2 in fig. 29-78). The reasonable spatial relation of the five craters to curve 2 suggests that Apollo 16 metric camera depth-diameter data are in accord with older data. Also, the relative order of the five craters agrees with a morphologic and stratigraphic assessment of crater relative ages. A quantitative scheme for ranking lunar craters by relative age has been developed, based on these principles and pre-Apollo measurements of crater depth and floor diameter.[3] Metric camera measurements of additional craters will permit a critical appraisal of the workability and utility of this system.

Crater rim-crest circularity and certain combinations of the five other dimensions have genetic significance. These parameters tend to divide most craters into two distinct major groups: rimmed lunar craters of all sizes, terrestrial meteorite impact craters, and experimental explosion craters; and all types of rimmed volcanic craters and summit craters atop lunar domes (maars fall into both categories). The much-used depth-diameter proportion is not a

[2]Ibid., p. 70.

[3]See footnote 1.

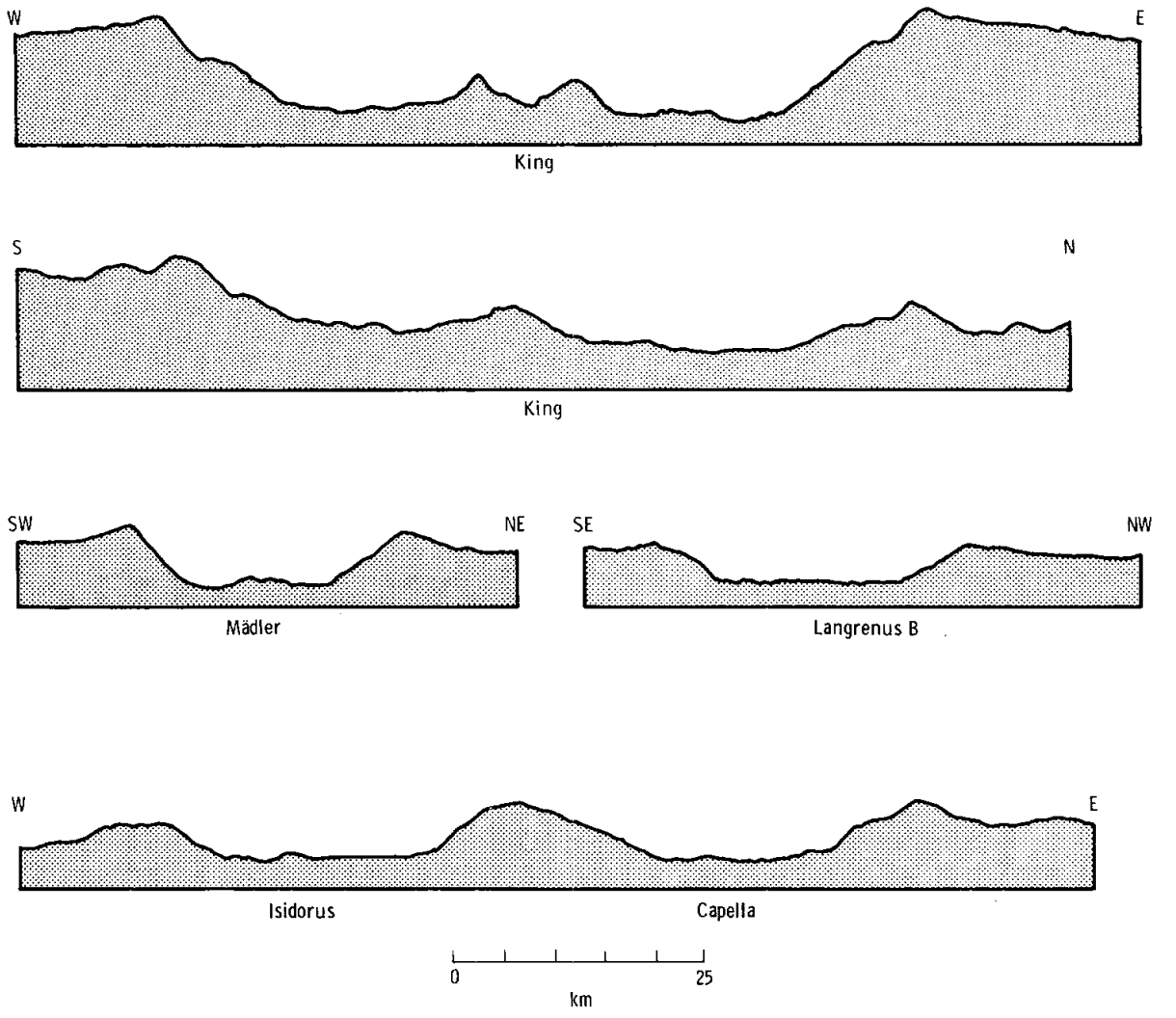


FIGURE 29-77.–Selected topographic profiles of five lunar craters from photogrammetric reduction of Apollo 16 metric camera data. Vertical exaggeration is 2X. All profiles are on the same scale. Control is preliminary and subject to change.

diagnostic genetic criterion; but circularity, the rim height/depth ratio, and the rim width/diameter ratio do effectively discriminate between the two principal types of craters (ref. 29-78). The last three parameters have been applied to two sample craters, Capella and Langrenus B, in an effort to clarify some questions concerning their genesis.

Langrenus B Crater is classified in reference 29-4 as a crater (type Ics) that "... may differ sufficiently from main-sequence (impact) craters to suggest a different origin." Ics craters lack well-developed impact rim textures and structures such as hummocks and radial ridges. In addition, "... floors are commonly about level with the surrounding terrain." Wilhelms and McCauley (ref. 29-4) suggest a caldera genesis for these craters. Capella is one anomaly in a morphologic scheme ranking lunar craters by relative age (ref. 29-79). According to this scheme, Capella should be older than adjacent Isidorus; however, Capella appears superposed on Isidorus. Again, a volcanic genesis has been suggested to explain the anomaly.

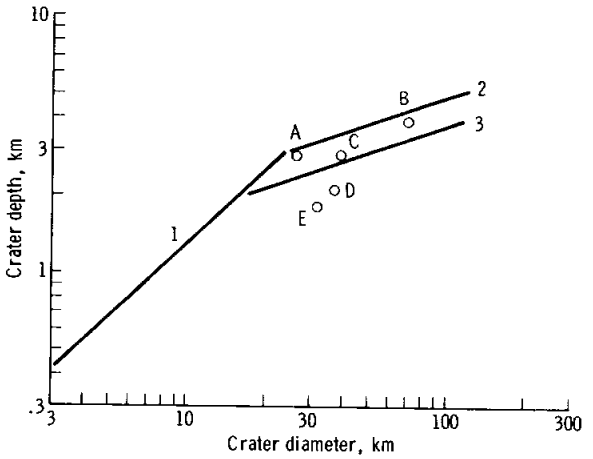


FIGURE 29-78.–Depth-diameter models for three types of fresh lunar impact craters. Curve 1 (n = 900) extends down to a diameter of only 1 m. The portion shown here comprises fresh simple craters on uplands and maria. Curve 2 (n = 270) comprises fresh complex craters on lunar uplands. Curve 3 (n = 150) comprises fresh complex craters on lunar mare surfaces. All curves are mean fits to shadow-length data from near-side craters. Data points are five sample craters (Apollo 16 metric camera data): A, Mädler; B, King; C, Capella; D, Isidorus; and E, Langrenus B.

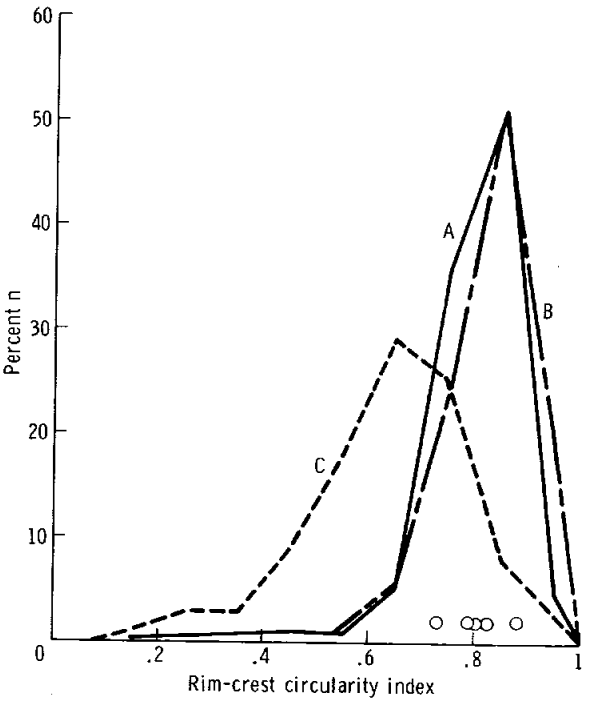


FIGURE 29-79.–Percentage-frequency distributions of index of rim-crest circularity for 167 lunar craters of all ages (curve A), 41 terrestrial meteorite impact craters and explosive test craters (curve B), and 117 terrestrial calderas, tuff cones, maars, and cinder cones (curve C). Data from Apollo 16 photographs for five sample craters are shown by single data points. The circularity index is the ratio of the squared radius of the inscribed circle to the squared radius of the circumscribed circle fitted to the outline of the crater rim crest. The volcanic-crater curve differs significantly in shape and location from the other two curves in this figure and figures 29-80 and 29-81.

Apollo 16 metric camera data (table 29-VI) show that neither of these problem craters differs morphometrically from normal, main-sequence lunar craters. Profiles (fig. 29-77) show that the floors of both craters are depressed well below exterior datum. Data in figures 29-79 to 29-81 further suggest that Capella Crater and Langrenus B Crater are impact craters. Percentage-frequency distributions for the variables circularity index, rim height/depth ratio, and rim width/diameter ratio are presented in figures 29-79 to 29-81, respectively. The distributions in each graph contain representative samples (where n is the number of craters) of terrestrial volcanic craters (n = 117), terrestrial meteorite craters (n = 41), and rimmed lunar craters (n = 167). The Apollo 16 data (table 29-VI) for the five sample craters are shown by heavy dots in figures 29-79 to 29-81. According to the three criteria, all five sample craters exhibit an impact-crater morphometry rather than a volcanic-crater shape. In all three diagrams, the overlap between volcanic and lunar craters mainly reflects the inclusion of 43 maar craters, many of which have lunarlike geometric proportions. However, the possibility that Langrenus B and Capella Craters are colossal maar-type craters is remote; these two craters are over 30 times larger than typical terrestrial maars. Explanations other than primary volcanic genesis will have to be found to account for the unusual morphologies of Capella, Langrenus B, and other anomalous lunar craters.

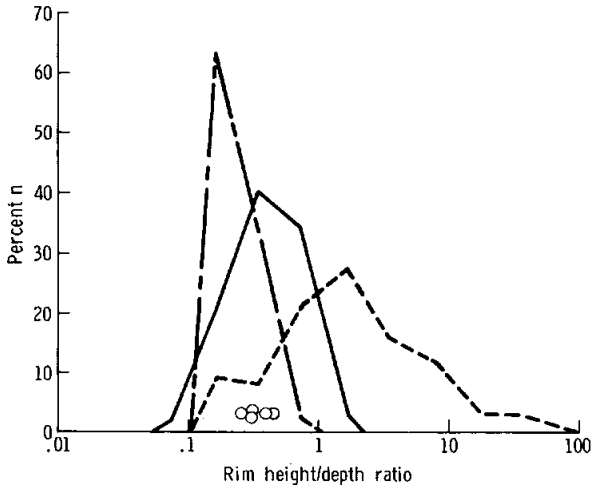


FIGURE 29-80.–Percentage-frequency distributions of rim height/depth ratio for the same craters as in figure 29-79. Displacement of lunar distribution (solid curve) toward higher ratio values reflects many older, shallower craters included in the sample (ref. 29-80).

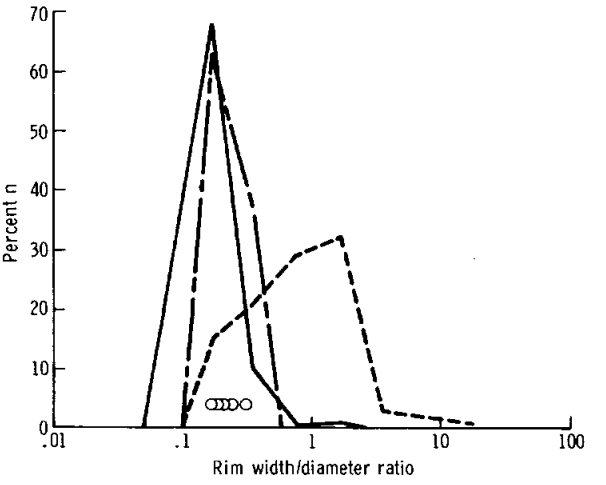


FIGURE 29-81.–Percentage-frequency distributions of rim width/diameter ratio for the same craters as in figures 29-78 and 29-80. Displacement of lunar distribution toward lower ratio values reflects a diminution of rim widths of older lunar craters or possibly an underestimation of the rim widths.

PART M

KING CRATER AND ITS ENVIRONS

Farouk El-Baz[a]

Introduction

King Crater, approximately 75 km in diameter and, on the average, 3.8 km deep (part L of this section), is among the most significant features that were photographed and visually studied from lunar orbit on the Apollo 16 mission. It is the freshest crater on the far side in its size range and has several unique characteristics.

(1) Although its ejecta blanket displays very sharp features, the crater does not appear to have extensive ray systems (fig. 29-82) and secondary crater chains.

(2) As depicted for the first time by Apollo 16 photographs, the ejecta blanket is strewn with numerous flow fronts and scarps.

(3) A flat and smooth, dark, lavalike deposit 15 km across is on the northern rim of the crater.

(4) The central peak of the crater is a Y-shaped structure that begins at the southern rim.

(5) Bright units that are alined with the central peak on the northern wall and rim suggest that a preexisting tabular body was excavated by the cratering process.

The crater is charted at 120° E 5.5° N (ref. 29-81) and, as described by the Apollo 16 command module pilot, is located on a gentle, broad rise or plateau (fig. 29-83). The Apollo 16 photographs indicate that this plateau probably represents the middle ring of an old and subdued three-ringed basin (part H of this section).

Superb photographs of King Crater were returned by the Apollo 16 crew. Some of the unique characteristics of the crater and its environs were described previously (refs. 29-49, 29-50, and 29-82 to 29-84) but were not viewed in such detail as on the Apollo 16 mission. Apollo 16 metric camera frames 1868 to 1873, panoramic camera frames 4990 to 5006 (fig. 29-84), and Hasselblad camera frames AS16-120-19229 to 19266 are particularly good. More importantly, the metric and panoramic cameras provided stereoscopic coverage of King Crater with which high quality topographic maps may be made.

This discussion provides a brief description of the general setting of King Crater and its features. A detailed treatment of the ejecta blanket is presented in part N of this section. Part O of this section provides a detailed analysis of the pool on the northern rim of King Crater.

Crater Exterior

One of the sharpest features of King Crater, the rim, rises an average of 1.7 km above its surroundings, but locally its height varies significantly (part L of this section). The rim crest is generally round but partly crenulated. Deposits on the rim are finely sculptured with numerous small-scale lineaments that are arranged radially around the crater (fig. 29-84). The rim deposits are bright at high Sun illumination, but the boundaries of the bright halo are difficult to establish because of the proximity of smaller bright, haloed, and rayed craters. Rays from Giordano Bruno Crater to the north and from an unnamed 35-km-diameter crater to the south overlap in the area of King Crater (fig. 29-82).

Continuous deposits extend from the crater rim crest outward to approximately 100 km. The deposits are thickest near the rim, and they become thinner as they extend progressively outward. Fine radial to subradial lineations are followed outward by numerous dunelike features and flow scarps that are partially controlled by local topography (figs. 29-85 and 29-86). The flow scarps lap against old slopes (fig. 29-85) and suggest high-velocity flowage at or near the surface where the velocity is increased by crossing a depression.

A sharp and rather steep flow scarp surrounds the southeastern corner of the crater (ref. 29-84). Panoramic camera photographs reveal some arcuate lineaments on the lobe behind this scarp that are subradial

[a]Bell Telephone Laboratories.

to the crater (fig. 29-87). This unit may represent a rockslide similar to that described on the northwest rim of Tsiolkovsky Crater (ref. 29-85).

Due north of King Crater and approximately 10 km from the rim crest lies the boundary of a relatively flat, dark, pool-shaped deposit (fig. 29-88). The deposit is localized in the bottom of an old crater approximately 15 km across and appears to have been fed by the flow of material from higher levels (refs. 29-49, 29-50, and 29-82 to 29-84). Flow channels abound on the surface, and many have arcuate textures that delineate the downhill direction of flow (figs. 29-89 and 29-90). The sharpness of detail within this unit, as well as superposition relationships, indicates that the deposit was formed after the crater ejecta were deposited (fig. 29-89). The contrast between the albedo of this material and that of the rest of the rim material is lost in the panoramic camera photographs because of a malfunction during the mission. The dark material may be interpreted as an impact melt (part N of this section) or a volcanic lava flow (part O of this section). Characteristics that support a volcanic interpretation include the large size of the deposit and localization of the deposit in one segment, rather than radially around the crater. The characteristics that support an impact origin are the lack of an apparent source and the wide distribution of small feeder pools and channels. Topographic data will ultimately contribute to determining the origin of the deposit.

Crater Interior

The depth of King Crater, measuring from the rim crest, varies with the amount of fill. The northern segment of the floor is partially filled with material similar to that in the dark pool to the north (figs. 29-89 and 29-90).

On the basis of Apollo 10 photography, four different types of materials were distinguished by color, texture, and morphology in the terraced northern wall of the crater (refs. 29-49, 29-50, and 29-84). Dark bands on the lower terraces (fig. 29-91) were interpreted as probable intrusive bodies (refs. 29-49 and 29-50). An unusually bright segment in the north wall and rim of the crater was also interpreted as exposure of an intrusive body (refs. 29-49 and 29-50). Two light-colored units also extend northward approximately 30 km beyond the crater. These

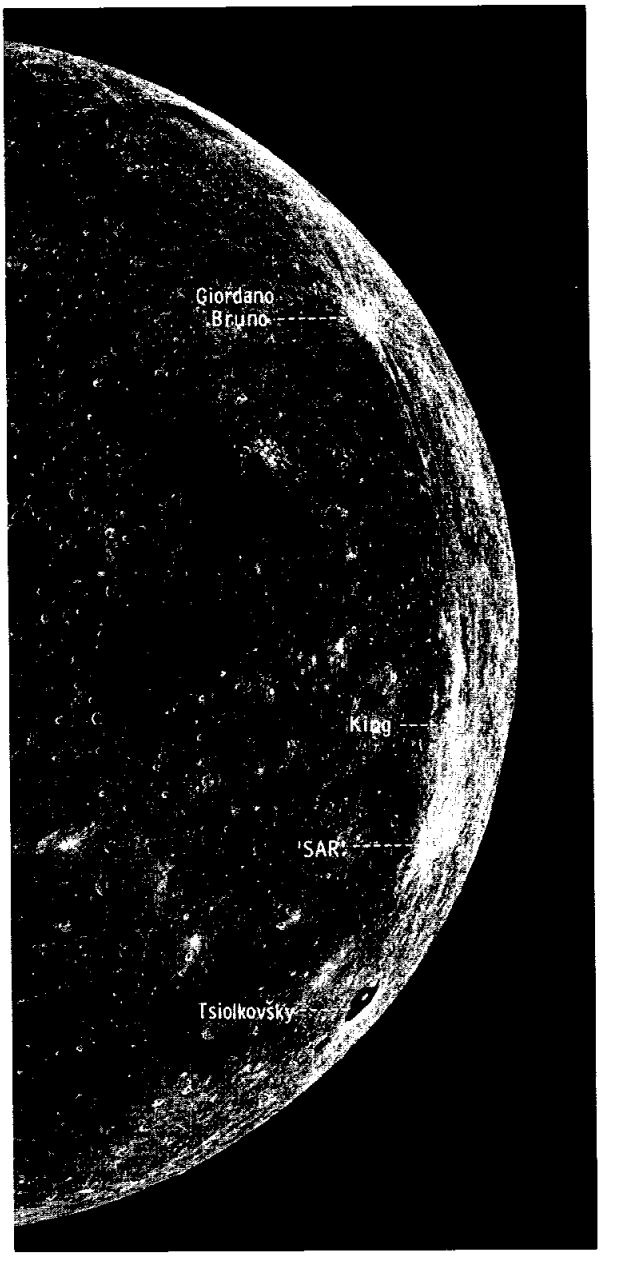


FIGURE 29-82.–The eastern limb region of the Moon at high Sun illumination angle. Rays from two bright craters (Giordano Bruno Crater and an unnamed crater termed "SAR" for identification on the Apollo 16 mission) overlap in the area of King Crater. It is evident that, although King Crater displays a bright rim, a few rays are probably related to it (Apollo 8 frame AS8-14-2506).

may represent ejecta of material similar to that on the northern rim. Furthermore, alinement of the light-colored units with the central peak (figs. 29-84 and

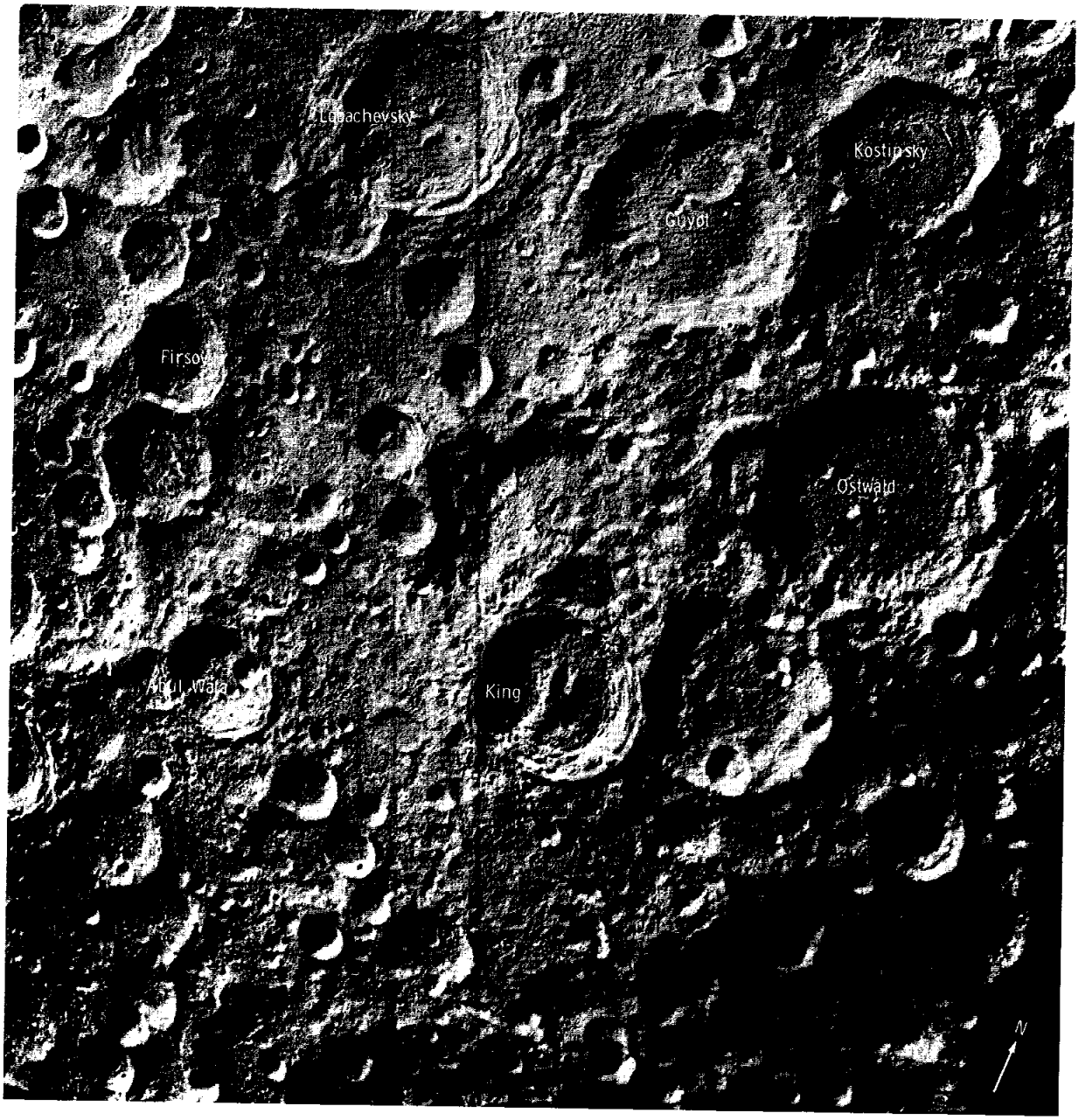


FIGURE 29-83.—Enlargement of Apollo 16 metric camera frame 3004, showing the relationship of King Crater to named features. The plateau on which the crater is situated trends in a north to northwesterly direction toward the southern edge of Guyot Crater and in a southerly direction east of Abul Wáfa Crater.

29-91) suggests a common origin. Both units may be remains of a tabular body that was excavated by the cratering process.

Panoramic camera photography of flow structures within the crater floor (figs. 29-92 and 29-93) supports the observation that there are several flow generations and probably several sources for the flow materials (refs. 29-49, 29-50, and 29-82). This observation indicates that filling of the crater was not a single event.



FIGURE 29-84.–King Crater and its surroundings. This photomosaic of the unrectified Apollo 16 pan camera frames 5002, 5000, 4998, 4996, 4994, and 4992 (from left to right) serves as an index for the location of photographs used in this report.

Domical hills strewn with blocks are numerous in the northern half of the floor. Many of the hills are furrowed or show elongated, irregular depressions on the top (area A of fig. 29-92), suggesting that they may be volcanoes.

Fractures indicating flow directions within the floor material are similar to those in Copernicus, Aristarchus, and Tycho Craters, but in King Crater, they are particularly fresh appearing. Detailed study of the floor of King Crater will shed light on the process of crater floor filling in general and on the mobility and contraction of lunar surface melts in particular.



FIGURE 29-85.–Flow fronts and scarps, indicated by arrows, in the northeastern ejecta blanket of King Crater. These features are similar to deceleration dunes (ref. 29-31) produced by high-velocity movement of material at or near the surface. The arrows show the direction of movement as the flow fronts lap against the walls of older crater and depressions (Apollo 16 pan camera frame 4992). (See also fig. 29-86.)



FIGURE 29-86.–Numerous flow fronts and scarps on the northwestern segment of the King Crater ejecta blanket. At least four fronts of superposed deceleration dunes lap against the walls of preexisting depressions. Arrows indicate the direction of flow, away from the crater (AS16-120-19231).

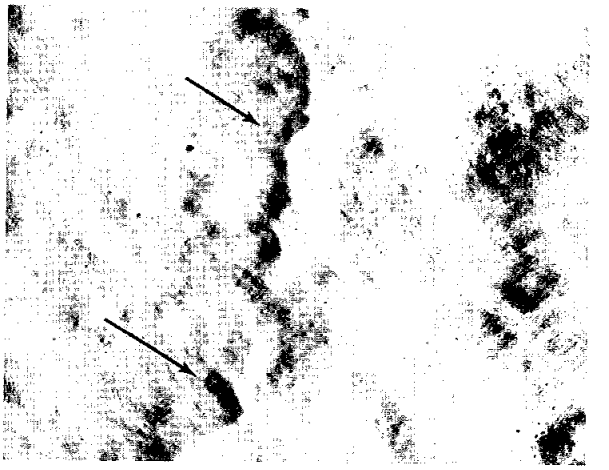


FIGURE 29-87.–Flow scarp of a massive unit (approximately 40 km long and 20 km wide) on the southeastern sector of King Crater ejecta (left side of photograph). The unit is interpreted as a landslide that may have originated near the rim of the crater and proceeded downward and away from the crater. (Arrows indicate direction of flow.) Lineations that are subradial to the crater occur both on the flow unit and on the relatively thinner surrounding ejecta blanket (right side of photograph) (portion of Apollo 16 pan camera frame 4992).

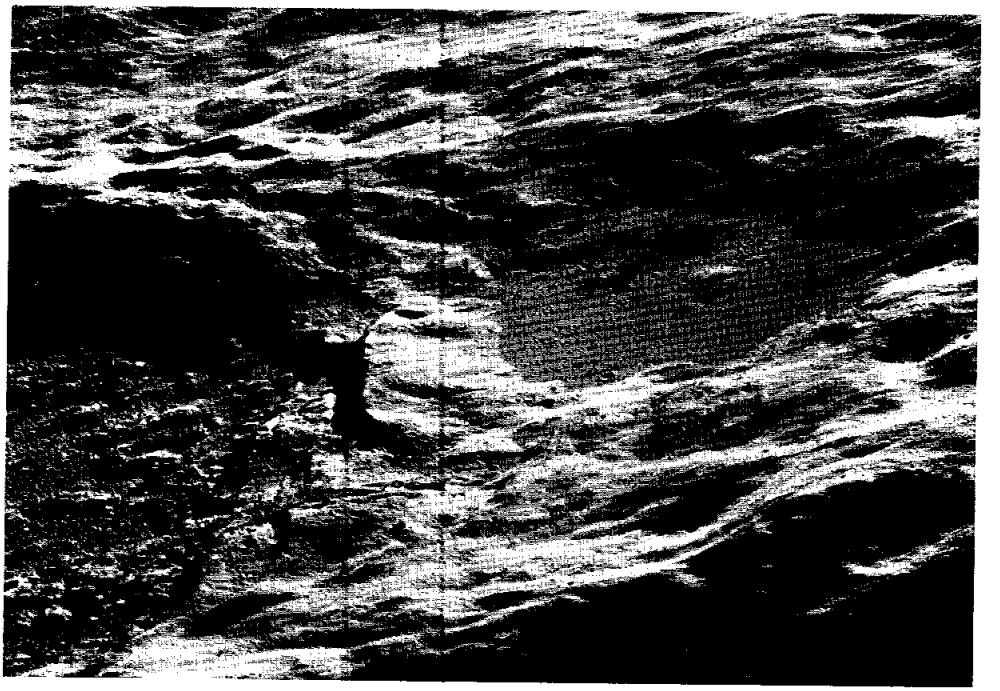


FIGURE 29-88.–Oblique view, looking westward, of the northern segment of King Crater and the dark, pool-shaped deposit on its rim. The obliquity of the view clearly shows the various levels from which the dark material flowed to fill the floor of an old depression (AS16-120-19266).

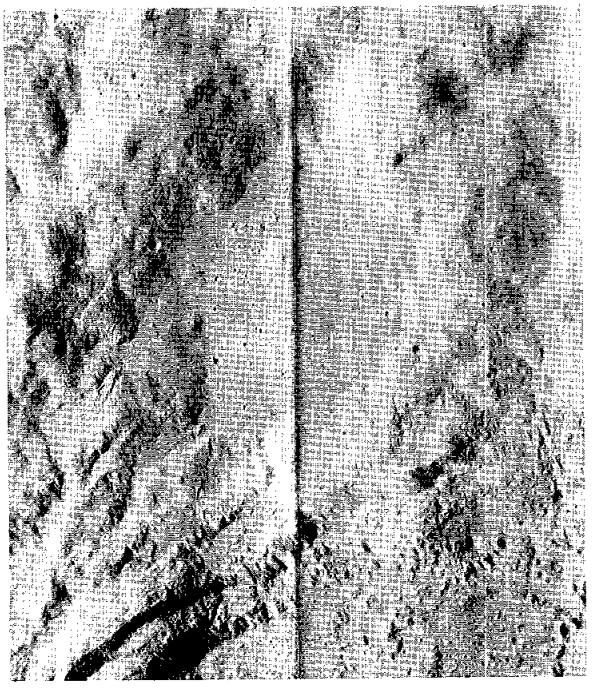


FIGURE 29-89.–Mosaic of portions of Apollo 16 panoramic camera frames 4998 (right) and 5000 (left), showing the smooth, relatively flat deposit of low albedo on the north rim of King Crater. Flow channels can be seen in the middle part of the frame on the left. Fractures and flow fronts indicate directions of flow (fig. 29-90).

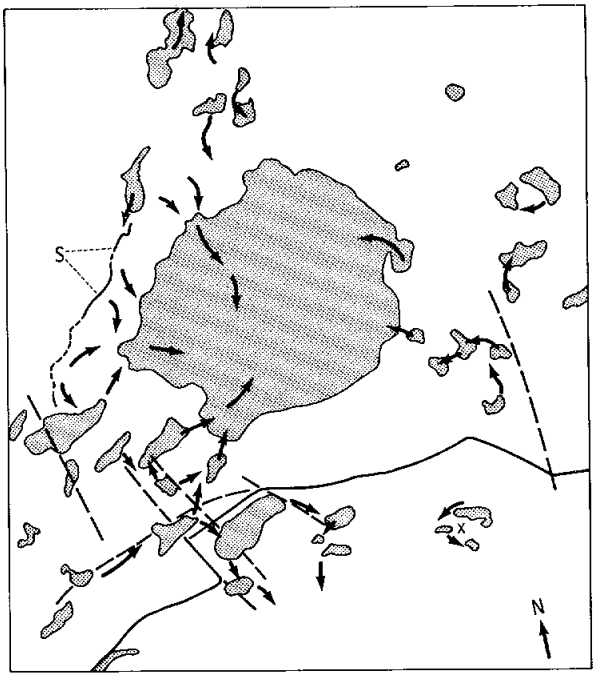


FIGURE 29-90.–Schematic illustration of the same area of figure 29-89, showing the northern rim of King Crater (solid line) and the superposed dark deposits (shaded). Dashed lines represent lineaments that may be the surface expression of faults. The faults may have served as channelways for the extrusion of melts that accumulated in low areas. Arrows indicate directions of flow; "S" represents a scarp presently unexplained (possibly a flow scarp); and "X" indicates an area in the northern wall that is strewn with very dark, almost black rocks (fig. 29-91).



FIGURE 29-91.–Oblique view (40° N) of northern rim of King Crater and its surroundings (Apollo 16 metric camera frame 1318). Note black deposit on northern wall (area X in fig. 29-90). The deposit is surrounded by light-colored material texturally similar to that extending to the center of the photograph. The brightness appears to be due to textural differences and is different from that of ray material farther north (near Guyot Crater) and on both sides north of the dark pool on the rim.

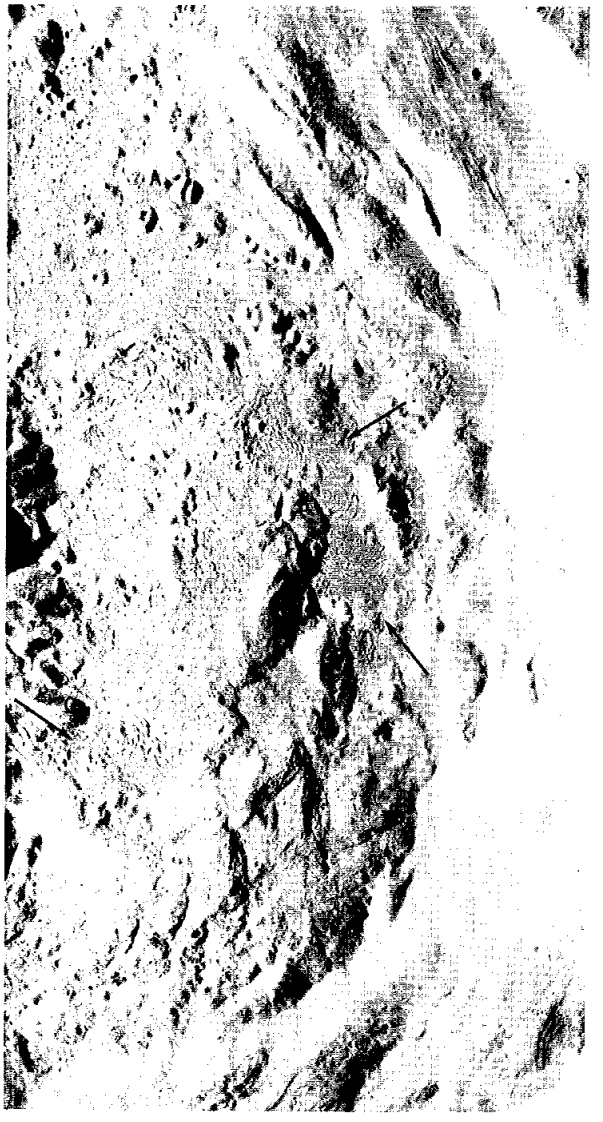


FIGURE 29-92.–Portion of Apollo 16 pan camera frame 4996, showing the eastern segment of King Crater floor. Domical hills with furrows and grooves are numerous on the floor (area A). Fresh fractures indicate the young age of the floor material (area B). Arrows indicate direction of the flow of material from the wall terraces and central mountain onto the floor. Flow channels (area C) suggest that the material was molten during its downslope movement.



FIGURE 29-93.–Portion of Apollo 16 pan camera frame 5000, showing the western segment of the King Crater floor, on which domical hills, flow channels, and fractures are numerous. On the first terrace from the bottom, a partly sinuous channel ends at a circular depression shown by the arrow. This feature is reminiscent of lava channels and tubes.

The most distinctive feature of King Crater is its massive Y-shaped central peak (figs. 29-94 and 29-95). This unit starts at the southern wall of the crater and extends northward, where it forks into two segments near the center of the crater. The right arm of the Y trends nearly due north.

The structural setting of the peaks is more vividly portrayed at low Sun elevation angles. As shown in figure 29-94, the base of the Y portrays a ropy appearance caused by a system of fractures that trend northeast to southwest. These structures grade into the concentric fractures of the southern wall, and the

material of the central mountain at this point is texturally similar to the southern segment of the wall (fig. 29-95).

The rest of the central peak is cut by northeast to southwest and northwest to southeast fractures, which create small, rhomboidal segments (fig. 29-96). The central peak materials are characterized by a large number of blocks, many of which are concentrated atop hills. Some leave tracks of their downslope movement (fig. 29-96).

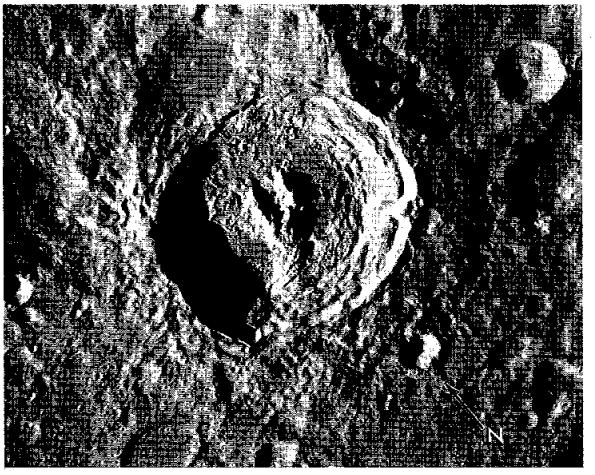


FIGURE 29-94.—View of King Crater that shows the structural setting of the central peak at low Sun elevation angle. The ropy appearance of the lower part of the Y-shaped feature is probably caused by fractures that trend northeast to southwest (AS16-122-19580).

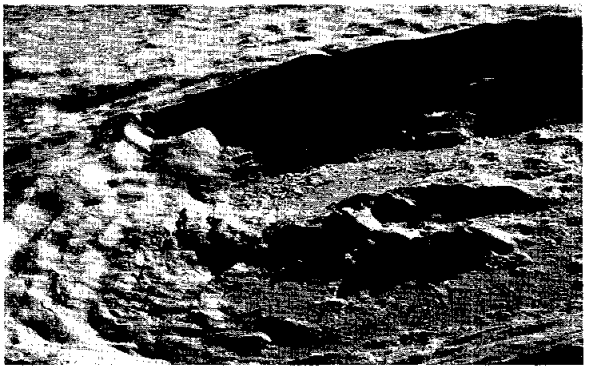


FIGURE 29-95.—Oblique view of the interior of King Crater, emphasizing the similarity between the southern part of the central peak and the material slumped on the southern wall of the crater. This alinement and other factors suggest that the unique shape of the central peak of King Crater is caused by a preexisting tabular body that was excavated by formation of the crater (AS16-120-19268).



FIGURE 29-96.—High-resolution photograph of the central peak of King Crater. Note the segmentation of the central peak material by fractures that trend northeast and northwest. Many blocks appear on the central peak material and the southern crater wall (bottom edge of photograph) (Apollo 16 pan camera frame 4998).

Conclusions

The sharpness of the crater morphology and the extensive bright rim deposits suggest that King Crater is probably Copernican in age. Although many of the features of the crater suggest an impact origin (e.g., a few rays and secondary crater clusters, extensive rim deposits and deceleration dunes, and many wall terraces), other features are baffling (the lack of extensive ray systems and secondary crater chains, the Y-shaped central peak, and the many volcanic-appearing features in and around the crater).

Photogeologic interpretations of the many interesting features and units associated with King Crater will be guided by precise topographic data, as a result of reduction of metric camera data, and by the high-resolution photography obtained with the panoramic camera on board the Apollo 16 spacecraft. Additional photographic coverage and visual observations of the crater and its surroundings are planned on the Apollo 17 mission.

PART N

EJECTA BLANKETS OF LARGE CRATERS EXEMPLIFIED BY KING CRATER

Keith A. Howard[a]

Details of the ejecta blankets of large, fresh craters provide insight into the mechanics of deposition and the sequence of emplacement of impact debris. King Crater is the freshest of the three large, rayed craters photographed from Apollo 16; the others are Theophilus and Langrenus Craters. King Crater is comparable in youth to Tycho Crater, and the details of its ejecta blanket help to interpret degraded equivalents at older craters. The clarity of detail and the occurrence of new types of lunar landforms rank King Crater among the most significant targets photographed from orbit in the Apollo Program (part M of this section).

King Crater is 75 km across (fig. 29-97), and the rugged landscape on which it formed clearly affected the transport and disposition of its ejecta blanket. The ejecta appears to have flowed radially outward. It was deflected by local highs, accelerated on slopes facing away from the crater, and decelerated on slopes facing the crater. Later, lavalike material drained downhill to form ponds in depressions; as an alternative to volcanic lava (parts M and O of this section), this mobile material is interpreted as impact melt.

Evidence of Radial Flow

Continuous ejecta extends outward 50 to 150 km from King Crater. Textures on the ejecta blanket are indicated in figure 29-98. The following textural facies (from the crater outward) are interpreted to

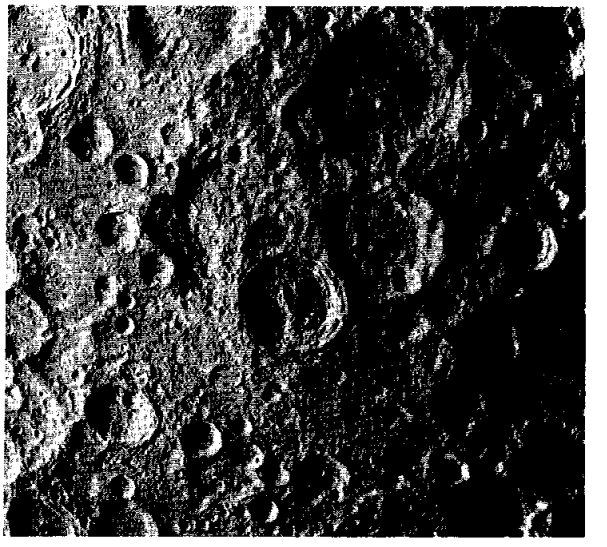


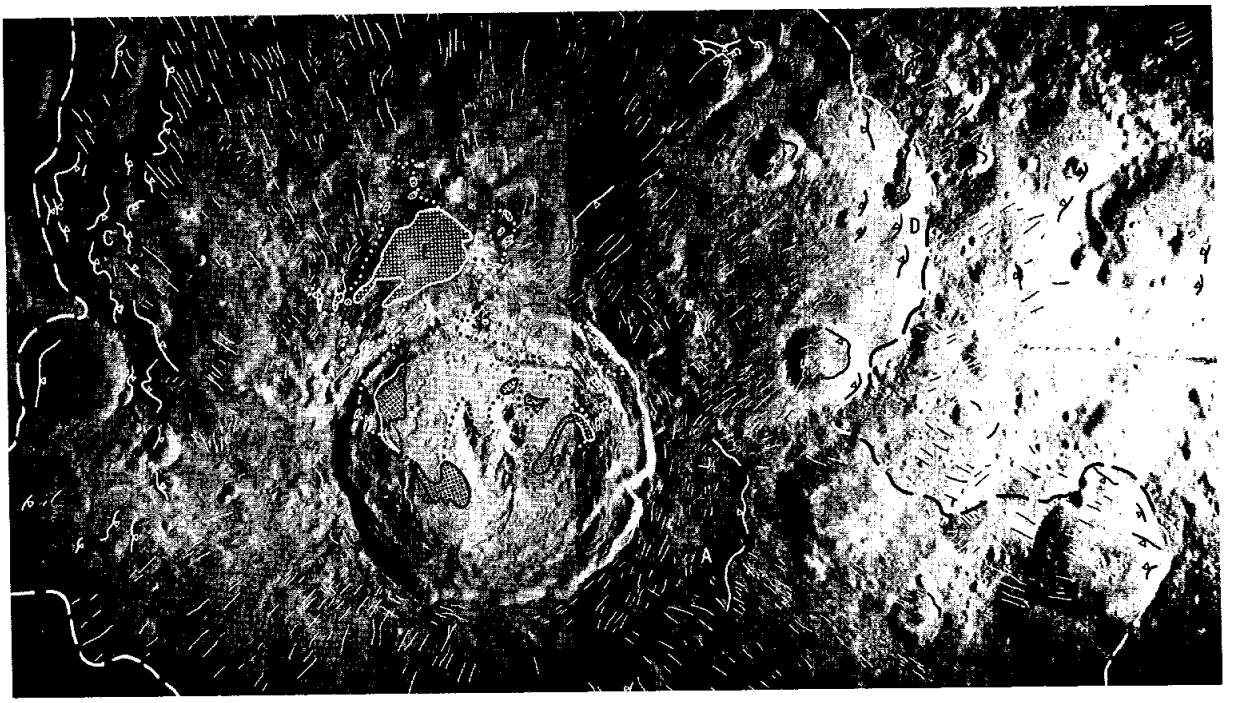
FIGURE 29-97.–King Crater in the far-side highlands as viewed from the Apollo 16 spacecraft after transearth injection (Apollo 16 metric camera frame 3002).

[a]U.S. Geological Survey.

indicate various types of radial transport: parallel concentric texture, longitudinal dunes, irregular transverse dunes, deceleration lobes, and secondary craters.

Parallel concentric texture.–The rim of King Crater is dominated by parallel concentric texture out to a distance of 5 to 20 km. This texture consists of sharply defined, parallel ridges and furrows spaced approximately 100 m apart (fig. 29-99). Similar features at Tycho Crater and Copernicus Crater locally show fault offset; therefore, at least some of the concentric furrows probably represent fractures. Depositional dunes also appear to be represented by the concentric texture, as evidenced in figure 29-99 by concentric ridges that swerve outward to become longitudinal ridges radial to King Crater. In places, the concentric texture appears superposed on radial ridges.

Longitudinal dunes.–Longitudinal dunes and striations radial to King Crater occupy most of the ejecta blanket (figs. 29-98 to 29-100). These ridges or lineations vary in spacing from 100 m to 1 to 2 km;



Explanation

Lobelike flow fronts (deceleration lobes)

Limit of continuous ejecta (Secondary craters can be identified beyond these lines.)

Dunelike ridges and striations

A (fig. 29-99)
B (fig. 29-101)
C (fig. 29-102)
D (fig. 29-104)
E (fig. 29-105)

Pond material on floor and north rim of crater

Areas draped by pond material

FIGURE 29-98.–Textures in King Crater ejecta. The scarcity of identified textures oriented east-west is attributed to illumination bias (Apollo 16 metric camera frames 1578 and 1581).



FIGURE 29-99.–Ejecta on southeast rim near lip of King Crater (locality A in fig. 29-98). Arrow indicates radial direction from King Crater, which is just outside the field of view. Parallel concentric texture (dunes and fractures?) appears nearest the rim, and longitudinal dunes appear farther out from the rim. Pointers show where transverse dunes curve around to become longitudinal dunes (Apollo 16 pan camera frame 9994).

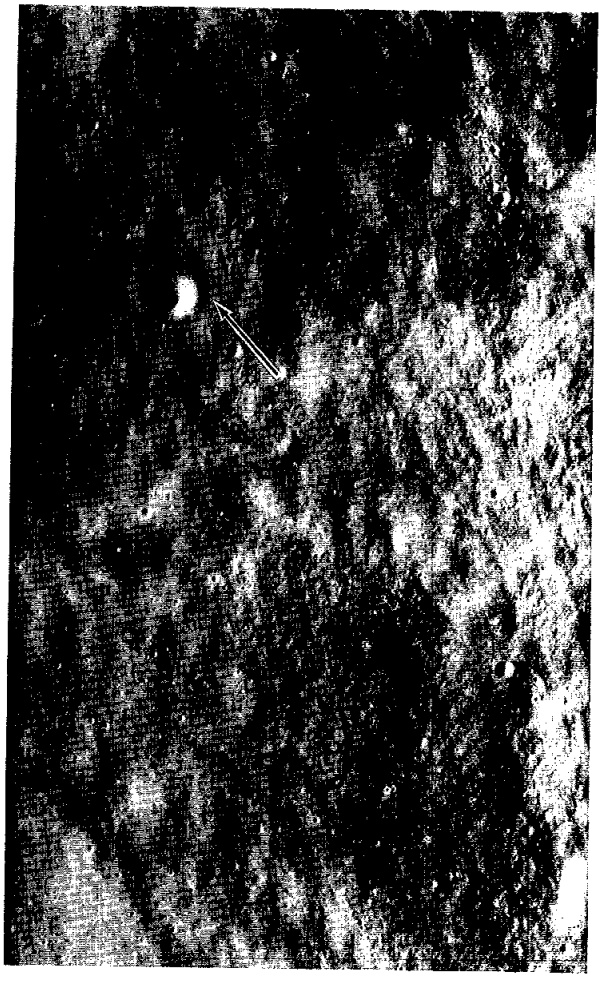


FIGURE 29-100.–King Crater ejecta. Arrow indicates ejecta movement direction from King Crater, which is 70 km to southwest. Linear longitudinal dunes are at top, and irregular transverse dunes are at bottom of photograph. Width of area shown in photograph is approximately 25 km (Apollo 16 pan camera frame 5004).

their subdued, streamlined forms indicate that they are depositional features. Many of them are probably dunes. Subparallel, streamlined ridges or dunes that coalesce so as to appear braided are present locally; examples are found 50 to 75 km north and northeast of the crater. The dunes and striations are commonly best developed on slopes inclined away from the crater, as if material accelerated down these slopes and produced better defined lineations. Radially outward transport along the ground is also indicated on oblique slopes, where the lineations almost invariably veer downslope away from the radial direction (fig. 29-98). The degree to which slopes deflect lineations from a radial direction appears to increase outward from the crater, showing that the radial transport velocity decreased outward. When accurate topographic maps are made, it should be possible to determine the components of velocity caused by gravity and radial flow (Grant H. Heiken, personal communication). A further indication of flow along the ground is shown in figure 29-101, where ejecta appears to wrap around an old crater peak.

Irregular transverse dunes.–The irregular transverse dunes shown in figure 29-100 are not well developed and occur only locally, midway out on the ejecta blanket of King Crater. Unlike the concentric



FIGURE 29-101.–King Crater ejecta wraps around the central peak of an older, 35-km-diameter crater (locality B in fig. 29-98; symbols same as in fig. 29-98). Deceleration lobes are located on the distal (east) crater wall. Arrow indicates direction from King Crater, 120 km to the west (a distance of 1.5 diameters of King Crater) (Apollo 16 pan camera frame 4811).

texture near the crater, these low ridges are only roughly subparallel.

Deceleration lobes.–The deceleration lobes shown in figures 29-101 and 29-102 are a type of lunar feature not recognized previously. The prevalence of deceleration lobes in the King Crater ejecta (fig. 29-98) suggests that such lobes will be found in the ejecta of other highlands craters. These lobes resemble flow fronts having rounded scarps facing away from King Crater. Longitudinal striations tend to be conspicuous behind them, toward King Crater. Most lobes are near the outer limits of the blanket of continuous ejecta, and some occur even farther away, beyond the east and west limits of the area shown in figure 29-98. Virtually all the lobes are on preexisting slopes facing toward King Crater. This condition indicates that the lobes border thick flows or slide masses of ejecta that decelerated and came to rest where steep hills were encountered (fig. 29-103). The

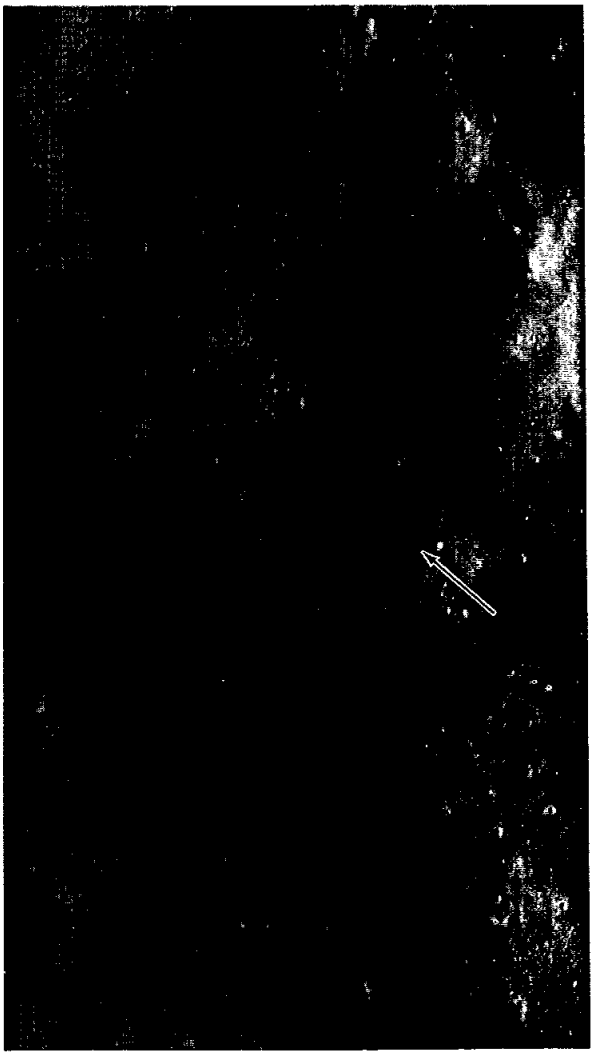


FIGURE 29-102.–Deceleration lobes in King Crater ejecta (locality C in fig. 29-98). Arrow indicates direction from King, 80 km to the southeast (Apollo 16 pan camera frame 5008).



FIGURE 29-103.–Diagrammatic cross section of overlapping deceleration lobes. Arrow indicates direction of movement over old landscape.

potential energy represented by the height attained by the material must have been transferred from the kinetic energy of motion; therefore, accurate topographic profiles of these lobes will lead to an estimate of the minimum transport velocity. The heights climbed tend to decrease outward, but there are exceptions. The lobes resemble terrestrial rock avalanche deposits that came to rest after climbing a small slope. Several lobes or fronts of material may overlap each other outward in a shingling fashion (fig. 29-101), from which the presence of imbricate flows is inferred (fig. 29-103). These flows may be analogous to the Blackhawk avalanche, where successive frontal ridges are interpreted as imbricate thrusts (ref. 29-86).

Secondary craters.—Secondary craters (secondaries) are recognizable at a distance beyond one to one and a half crater diameters from King Crater. Many secondaries are breached on the side away from King Crater. As at other lunar craters, the secondaries are overlapped by the more continuous ejecta and, for this reason, are not visible near the primary crater. Both northwest and northeast of King Crater, the inner limit of recognizable secondaries (and outer limit of continuous ejecta (fig. 29-98) coincides with the far rims of some old, large craters (fig. 29-104). In each case, numerous deceleration lobes are banked against the old crater wall, and apparently the main bulk of the ejecta did not quite reach the rim. This condition illustrates again that the continuous ejecta traveled along the ground and was greatly influenced by topography. Longitudinal dunes and, locally, V-shaped herringbone patterns (part K of this section) extend beyond the continuous ejecta, and some of these are down range from secondary craters. Some of these dunes and the deceleration lobes that lie far from King Crater may represent ejecta that was transported ballistically from King Crater, impacted obliquely, and threw out secondary ejecta that then behaved as a flow.

To summarize, material was transported radially outward at high velocities from King Crater at or near the ground. Dune forms and deceleration lobes suggest that the material acted as a fluid propelled away from the crater. When detailed topographic maps become available so that flow velocities can be calculated, it may be possible to correlate depositional texture with flow regime. The flow arrived later than secondary impacts of ballistic ejecta. The



FIGURE 29-104.—Ejecta and secondary craters 80 km northeast of King Crater (locality D in fig. 29-98). Bright area is the west-facing wall of an old crater, upon which several deceleration lobes of King ejecta are banked (area 2). Numerous unburied secondary craters (area 1) occupy the old crater rim; apparently, they were shielded from the flow of continuous ejecta by the old crater wall. Arrow shows radial direction from King Crater. Area shown is 15 to 20 km wide (Apollo 16 metric camera frame 1578).

secondary impacts themselves may have produced radial flows.

Evidence of Impact Melt

A second type of lunar feature for which new evidence of origin is available at King Crater is fluidlike material that flowed downhill after the main deposition of ejecta. Flows on the rims of Tycho, Aristarchus, and Copernicus Craters have been studied previously by Moore,[1] Crittenden,[2] Howard,[3] and others (refs. 29-67 to 29-69 and 29-87 to 29-89). The unusually large flow features on the north rim of King Crater (figs. 29-98 and 29-105) were recognized on Apollo 10 and 14 photographs to represent downhill flowage and ponding of dark material in a large depression (refs. 29-49 and 29-82 to 29-84). Similar-appearing material occupies part of the floor of the crater. A volcanic source for this lavalike material is possible (parts M and O of this section), but no vent is apparent. The material appears to mantle a large area and to have drained off the hills (ref. 29-83).

The area apparently mantled by this material is indicated in figure 29-98. As shown in figure 29-105, locally, this mantle terminates abruptly high on slopes facing King Crater, as if it had surged there. Elsewhere, the mantle appears to merge gradationally with underlying radially textured ejecta. Similar material is draped over part of the crater floor and walls as indicated by cracks on both the ponds and the hills. These cracks are evidently due to stretching of crusted or semifluid material. Where material drained northwestward toward the main pond on the crater rim (fig. 29-106), flow into channels caused cracks in tensional zones and festoonlike folds in compressional zones. Levees border one channel or lobe and indicate that the outer part of the viscous flow solidified, presumably by cooling, before the center drained away. These features have perfect analogs in lava flows.

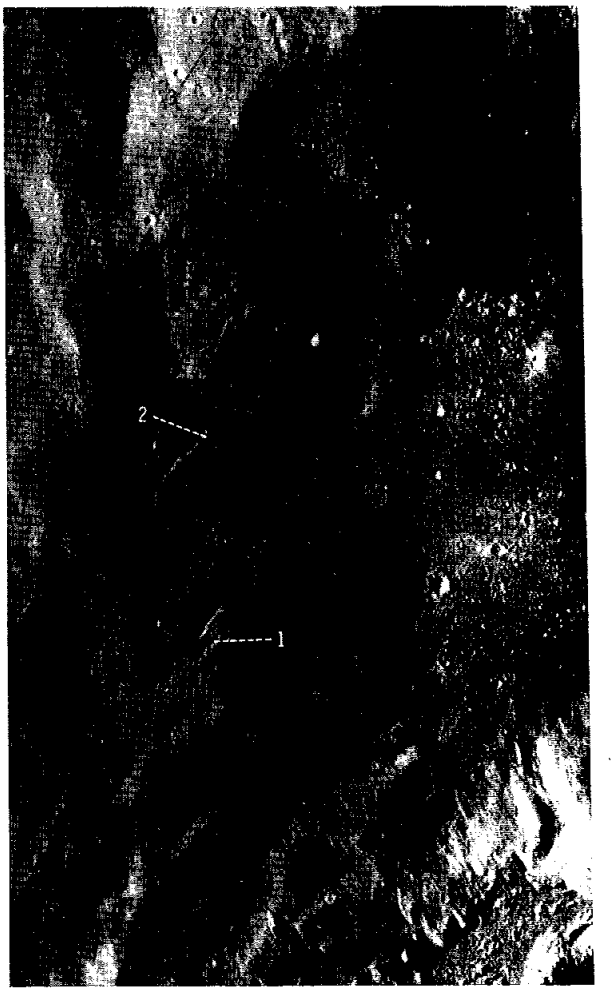


FIGURE 29-105.–Downhill flow features and pools of lavalike material on north rim of King Crater (locality E in fig. 29-98). Shown are (1) flow channel, (2) sharp margin of veneer of flow material, (3) thin flow lobes, (4) partly buried texture radial to King Crater, and (5) hummocks or knobs in large pool. The crater wall is visible at bottom of the figure; field of view is approximately 25 km wide (Apollo 16 pan camera frame 5000).

The floor of the large pond (fig. 29-105) contains numerous, more or less random cracks and resembles exactly the pooled material in the floors of King Crater, Copernicus Crater, and others. A further close resemblance is in the presence of numerous sharp knobs or hummocks (fig. 29-105). Whether the knobs on fresh crater floors were related to wall slumping,

[1]Moore, H. J.: Site V-48, Aristarchus. A Preliminary Geologic Evaluation of Areas Photographed by Lunar Orbiter V, Including an Apollo Landing Analysis of One of the Areas. NASA LWP-506, 1968, pp. 129-132.

[2]Crittenden, M. D.: Lunar "Mudflows" in Orbiter V Imagery. A Preliminary Geologic Evaluation of Areas Photographed by Lunar Orbiter V, Including an Apollo Landing Analysis of One of the Areas. NASA LWP-506, 1968, pp. 158-164.

[3]Howard, K. A.: Geologic Map of the Crater Copernicus. U.S. Geol. Survey Misc. Geol. Inv. Map, in preparation.



FIGURE 29-106.–Detail from figure 29-105, showing (1) levees on drained channel, (2) festoon folds convex downstream, and (3) tension cracks. Arrows indicate flow direction.



FIGURE 29-108.–Numerous ponds (degraded because of age) on the north rim of Theophilus Crater (110 km in diameter). These materials (shown by the arrow), part of the Theophilus Formation, are restricted to the north rim (ref. 29-21) (Apollo 16 metric camera frame 0154).

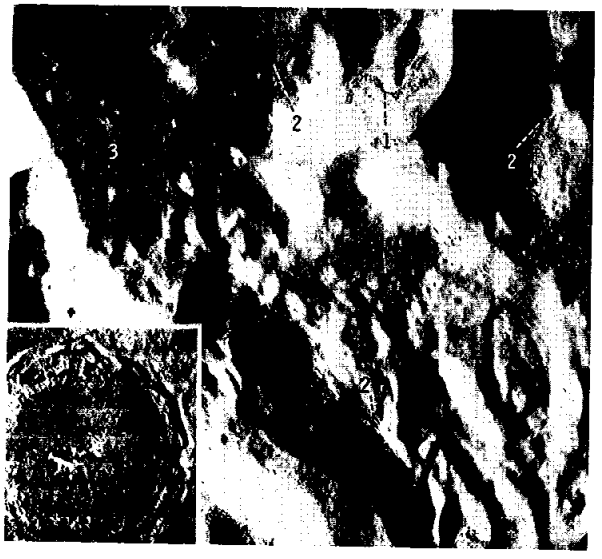


FIGURE 29-107.–Veneer of hard rock on walls of Copernicus Crater. Inset shows location of enlargement, which shows (1) edge of veneer, (2) cracks in veneer, and (3) ponded material (Lunar Orbiter photographs).

to fallback, or to the lavalike floor filling has been obscure. The knobs in figure 29-105 are clearly much sharper than the general terrain mantled by the pond materials and, thus, must be genetically tied to the pond material. Inasmuch as the pond material seems to have drained mostly from the surrounding hills, the knobs are not likely to be rooted volcanoes.

Smaller ponds and the cracked veneer (fig. 29-105) duplicate similar features on the walls and rims of Tycho and Copernicus Craters. Because of this condition, it seems clear that, despite its much larger volume, the large pond at King Crater is also analogous to the small ponds on the rims of these craters. In Copernicus Crater, much of the walls and near rim are coated by a thin veneer of hard rock.[4] This veneer (fig. 29-107) is very blocky where exposed and is cracked where it drapes over hills; it

[4]Ibid.

appears to merge both with flow channels and lobes and with ponded material. The wide distribution and lack of apparent source can be explained if the veneer is impact melt that remained fluid and drained downhill after radial flow from the cratering event had ceased. These materials may have been only partly molten and may have contained abundant unmelted clasts.

An objection to the impact-melt hypothesis is offered by crater counts at Tycho and Aristarchus Craters, which imply several ages of the flow and pond materials (refs. 29-68 and 29-90). This condition can be reconciled if some of the cratering was caused by high-trajectory ballistic ejecta that fell after gravity flow of the melt had begun (ref. 29-69). Another objection to the hypothesis is the large bulk of the material on the north rim of King Crater and its absence in other sectors. At Copernicus Crater, the small ponds are nearly evenly distributed, but asymmetric pond distributions are seen at Tycho Crater and at Theophilus Crater (fig. 29-108). The north rim of King Crater is lower than other sectors (part L of this section), which would allow easier egress of ejecta. Further, an old crater that the large pond occupies would serve to collect drainage from a large area, possibly analogous to the situation seen in figure 29-109.

A less attractive possibility than impact melt is that the lavalike materials were wet debris flows. The anhydrous nature of returned lunar samples, however, suggests that water is less likely as a liquefying agent than is rock melt.

Flow features suggestive of impact melt have been recognized on craters as small as 15 km (fig. 29-109 and part J of this section) and increase in relative bulk with the size of the crater. For craters the size of King, Copernicus, and Theophilus (75 to 110 km), the interpretation implies that rock melt is present as fallback on the crater floor and walls and in ejecta on the rim out to a distance of one-half to one crater radius. Suevite (impact-melted rock) localities are similarly distributed on the rim of the Ries Crater in Germany (ref. 29-91).

By comparison, larger craters and multi-ring basins should have even more widely distributed hot ejecta. This is consistent with the evidence of high temperatures in the Fra Mauro breccias (ref. 29-92). Ponded lavalike materials are nearly absent on the textured ejecta blanket of the relatively young Orientale Basin, which suggests that if impact melts were ejected at Orientale Basin and other large basins, they remained within the basin or possibly were dispersed beyond the main ejecta blanket.



FIGURE 29-109.–Far-side crater nested in a larger crater. Arrow shows a large pool of lavalike material in the moat, which suggests that impact melt may have been confined by the older crater and drained to the bottom of the moat from a broad area (Lunar Orbiter V photograph H103).

PART O

SELECTED VOLCANIC AND SURFICIAL FEATURES

R. A. Young,[a] W. J. Brennan,[a] and R. W. Wolfe[a]

Preliminary examination of metric camera photographs from the Apollo 16 mission has revealed a number of interesting volcanic and surficial features in the area between Mare Smythii and King Crater (6° N 121° E). Immediately northwest of King Crater is a depression filled with a relatively smooth-surfaced, low-albedo material that may be composed of debris or, more likely, lava flows. This feature was briefly described by El-Baz (ref. 29-50). The surface of the material displays what appear to be flow levees (area A, fig. 29-110) and wrinkles (area B, fig. 29-110), and the material mantles lineated topography that appears to radiate outward from King Crater (area C, fig. 29-110). The existence of smaller depressions filled with the same material to the southwest and at higher elevations than the large depression, the absence of strand lines within the large depression, and the flow features on the surface of the large depression all suggest that the main source of lava was in the high area to the southwest rather than in the large depression.

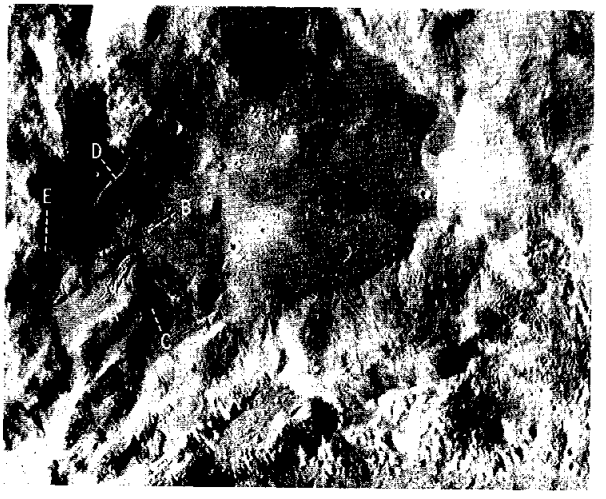


FIGURE 29-110.–Enlargement of Apollo 16 metric camera frame 1581.

A lobate escarpment that trends northeast can be observed along the western margin of the depression (area D, fig. 29-110). This escarpment appears to have formed on a part of the ejecta blanket from the impact that formed King Crater. The escarpment extends into the source area of the flows where the escarpment is mantled by the flows (area E, fig. 29-110). The apparent absence of lava domes, dark halo craters, and other common volcanic features suggests that the flows emanated from one or more fissures.

A long, sinuous, lobate escarpment is well exposed approximately one crater diameter west of the west rim of King Crater. This escarpment appears to be the edge of the base surge portion of the ejecta blanket, which formed as a result of the impact that produced King Crater. Along the escarpment, the flow direction is generally away from King Crater and, locally, is upslope (shown by arrows in fig. 29-111). The presence of wrinkles on the ejecta blanket (area A, fig. 29-111) and the lobate nature of its terminus suggest that the flow may have occurred while the ejected material was in a somewhat viscous state. The absence of any "backwash" features downslope from the escarpment suggests that the flow was continuously away from King Crater.

The possibility exists that this ejecta, like some terrestrial landslides, may have contained gaseous material that contributed to its fluid state. Progressive leakage of the gaseous component with increasing distance would have resulted in increasing viscosity and would help explain the absence of backflow on steep slopes near the escarpment.

In the flat floor of an old crater located east of Babcock Crater (4° N 94° E) are several sharply defined, yet nearly rimless craters (areas A and B, fig. 29-112). These craters have somewhat irregular halos of dark material and resemble other craters in the dark, smooth material that occurs in the Taurus

[a]State University of New York at Genesco.



FIGURE 29-111.–Enlargement of Apollo 16 metric camera frame 1582. The area may be viewed stereoscopically in Apollo 16 metric camera frames 1582 and 1583.



FIGURE 29-112.–Enlargement of Apollo 16 metric camera frame 1596.

Mountains near Mare Serenitatis (fig. 25-64 in ref. 29-93). The dark, smooth material in the Taurus Mountains has been described by El-Baz as probably pyroclastic. The morphology and the presence of halos of possibly pyroclastic material suggest that these rimless craters may be maars.

PART P

LUNAR VOLCANISM: MARE RIDGES AND SINUOUS RILLES

Richard A. Young[a]

Additional evidence of the volcanic origin of mare ridges and sinuous rilles is provided by near-terminator photography of the Herigonius Rille area (12° S 37° W) northeast of Gassendi Crater. A possible genetic relationship between ridges and rilles is illustrated in figure 29-113. From the figure, the following relationships are evident.

(1) The most prominent rille crosses several ridges without distortion, which indicates that the

[a]State University of New York at Geneseo.



FIGURE 29-113.–Herigonius Rille (lower right) crosses four mare ridge segments before joining a second rille and continuing far south of this photograph. Note the close connection between rille and ridge elements (Apollo 16 metric camera frame 2991).

mare ridges did not form after the sinuous rilles.

(2) The rilles could not have formed by flow up and over the ridges.

(3) The rilles extend from their widest ends toward distinctly lower elevations, and the largest one branches both north and south from the vent area. Elevations are evident in stereographic views that clearly indicate the local slopes.

(4) The wider end of each rille is marked by an elongate vent (?) near the summit of the mare ridge from which the rille appears to issue.

(5) The two most prominent rilles join south of the vent area and continue southward for more than 130 km.

A plausible explanation of such relationships involves the formation of the sinuous rilles as lava channels or tunnels during upwelling and outpouring of lava beneath a thin or viscous crust to form the mare ridges. The vent areas may have been enlarged or deepened by the melting action of the outflowing lava. The fluid dynamics of the molten, flowing lava could cause development of the sinuous channel form with erosion occurring by partial remelting of the adjacent crust.

When considered in light of the high density of impact craters documented by Soderblom (ref. 29-94), it may be difficult to demonstrate conclusively anywhere on the lunar surface that all or most sinuous rilles on the Moon were once roofed over. It now appears to have been clearly demonstrated that saturation cratering by objects producing craters in the range of 100 to 300 m in diameter is common on the mare surfaces. If such is the case, the roofs of lava tunnels would have been destroyed and any jagged edges gradually smoothed out by the numerous smaller impacts that have degraded the 100- to 300-m-diameter craters down to interior slopes of a few degrees.

Some portions of certain mare ridges resemble flow fronts. If this is the case, the basic genetic relationship between rilles and ridges previously enumerated could still hold. Not all sinuous rilles need to have this specific origin, but the complex interrelationships shown near Herigonius Rille are strong evidence in the present case.

PART Q

PLANIMETRIC SHAPES OF LUNAR RILLES

Verne R. Oberbeck,[a] Michio Aoyagi,[a] Ronald Greeley,[a] and Michael Lovas[a]

A quantitative classification for the planimetric shape of rilles can be based on the high-resolution lunar photography from the Apollo 15, 16, and 17 missions and on topographic data to be derived from this photography. The purpose of this preliminary report is (1) to provide a description of a quantitative method for describing rille shape, (2) to apply the method to the description of three grossly different

[a]NASA Ames Research Center.

rilles photographed by the Apollo 16 metric mapping cameras, (3) to describe quantitatively the shape of a terrestrial analog that has been proposed for lunar sinuous rilles, and (4) to use the method to illustrate the control of topography on rille shape. The need for a planimetric classification is briefly reviewed in the following paragraphs.

In the past, lunar rilles have been described in terms of presence or absence of associated craters, width, depth, floor shape, planimetric shape, and other characteristics. Terms in common usage for description of rilles refer to planimetric shape because it is probably the most important descriptive characteristic. This can be documented from examination of results of early telescopic studies of the Moon as well as recent photographic studies of these features. In the first complete photographic atlas of the Moon, examples of rille types known at that time were described and discovery of a new type of lunar rille was noted (ref. 29-95). This type of rille, always terminating in a pear-shaped craterlet, was described as a riverbed. The new type of lunar rille was described as being composed almost entirely of very short radius curves, giving the feature a meandering appearance that resembles a terrestrial riverbed.

In more recent investigations, rilles also have been described in terms of their planimetric shape. For example, the rilles referred to as riverbeds are now known as sinuous rilles. Terms now in common usage for description of lunar rilles are straight, arcuate, and sinuous (ref. 29-76). Another classification (ref. 29-96) uses these three terms and an additional class for branching rilles. In a more recent study (ref. 29-97), linear rilles were described as those with radii of curvature on the order of the radius of the Moon and arcuate rilles were described as those that ring circular features and have smaller radii of curvature. Sinuous rilles were described as those with radii of curvature on the order of 1.6 km. Thus, planimetric shape has been of primary importance for the classification of lunar rilles. Moreover, these investigators have related rille origin to rille planimetric shape. It is clear that planimetric shape should reflect rille origin. However, the terms that have been used thus far to describe rilles (straight, arcuate, and sinuous) are poorly defined, qualitative terms. With the present subjective classification, there is no knowledge of the actual number of rille classes or of whether there may be, in fact, a complete gradation in form between all rilles. Thus, an accurate quantitative method of describing rille shape is required as a preliminary step in the study of rille origin. If such a method can be used to define the types of lunar rilles, it can then be used to describe the shapes of terrestrial analogs for lunar rilles. Comparison of the shapes of analogs and rilles then will be helpful in the determination of rille origin. The technique also should be of use in demonstrating control of rille shape by geologic structures.

Method of Analysis of Lunar Rilles

To mathematically define the planimetric shape of lunar rilles, it is first necessary to establish some reference coordinate system, which is accomplished by connecting one end of a rille to the other with a line to define a rille baseline. This baseline is further used to establish the X-axis of a Cartesian coordinate system where the origin is defined at one end of the rille. Points along the rille bank then can be assigned (x,y) values where y represents the rille amplitude at a distance x from the origin. If for each x value only one y value exists, then the amplitude can be approximated directly by the finite Fourier approximation, denoted here by $F(x)$. This type of analysis is useful because it permits a mathematical definition of the rille and also enables a quantitative study of rille characteristics within the frequency domain. However, a direct analysis of rille shape can, in fact, be used only to characterize rilles that do not recurve upon themselves, because recurvature would result in $F(x)$ being multivalued.

The problem of rille recurvature has led to the development of an extension of the standard finite Fourier analysis. Instead of approximating the actual rille bank with the Fourier analysis, the angles of small vectors that are 1/250th of the rille baseline length constructed along the rille bank in a head-to-tail fashion are approximated and plotted as a function of cumulative vector length along the rille bank. By necessity, this function must always be single valued and can be easily characterized by the finite Fourier analysis. To permit comparison of one rille with another according to a standard index of rille shapes, all rilles are first mathematically reduced or enlarged to a unit baseline length. When this is done and a constant vector length (1/250th of unit length) is used, differences in shapes of lunar rilles are

easily expressed through study of the normalized power spectrum. The normalized power spectrum gives the relative contribution of each harmonic to the total variation of the magnitude of a vector angle about its average magnitude. However, without some knowledge of the absolute magnitude of the rille itself, spectral characteristics do not completely describe the rille. Absolute average magnitude of the rille bank relative to the baseline that connects one end to the other is obtained by numerically integrating the area between the rille bank and the baseline and dividing this area by rille length. When the result (average amplitude) is divided by rille length and multiplied by 100, a percentage index of rille amplitude relative to rille length is obtained. This index is referred to as APBL and, in conjunction with the normalized power spectrum, provides a complete description of rille shape.

A rille just west of Herigonius Crater is shown in figure 29-114; it will be referred to here as the "Herigonius" rille. The rille is suitable for illustrating the method of analysis because it recurves at several places and is a typical sinuous rille. As mentioned earlier, the rille bank is approximated numerically by a digitizing process at N points. The resulting $[(x_i, y_i)]_{i=1,N}$ sequence of points is then transformed into the sequence $(S,\theta_1)_{i=0,M}$ where S is the magnitude of a vector of angular direction θ_i relative to the baseline that connects one end of the rille to the other. For analysis, each vector is 1/250th the length of the rille, and each rille is adjusted to a common length mathematically before the vector angles are obtained. A plot of θ as a function of cumulative vector length for the Herigonius rille is shown in figure 29-115(a). This plot was obtained by placing the tail of one vector at the head of the preceding vector along the rille bank. A standard finite Fourier analysis of this plot is performed to yield a quantitative description of a rille. The frequency information is quantified by means of a periodic regression analysis where the directional change θ_i is approximated by the Fourier series

$$\theta_i = a_0 + \sum_{k=1}^{M/2} a_i \cos \frac{2\pi ki}{M} + \sum_{k=1}^{M/2} b_i \sin \frac{2\pi ki}{M} \quad (29\text{-}1)$$

where a_i and b_i are the Fourier coefficients, and harmonic order k ranges from 1 to $M/2$ where $M+1$ is the number of vectors along the rilles and M is even.

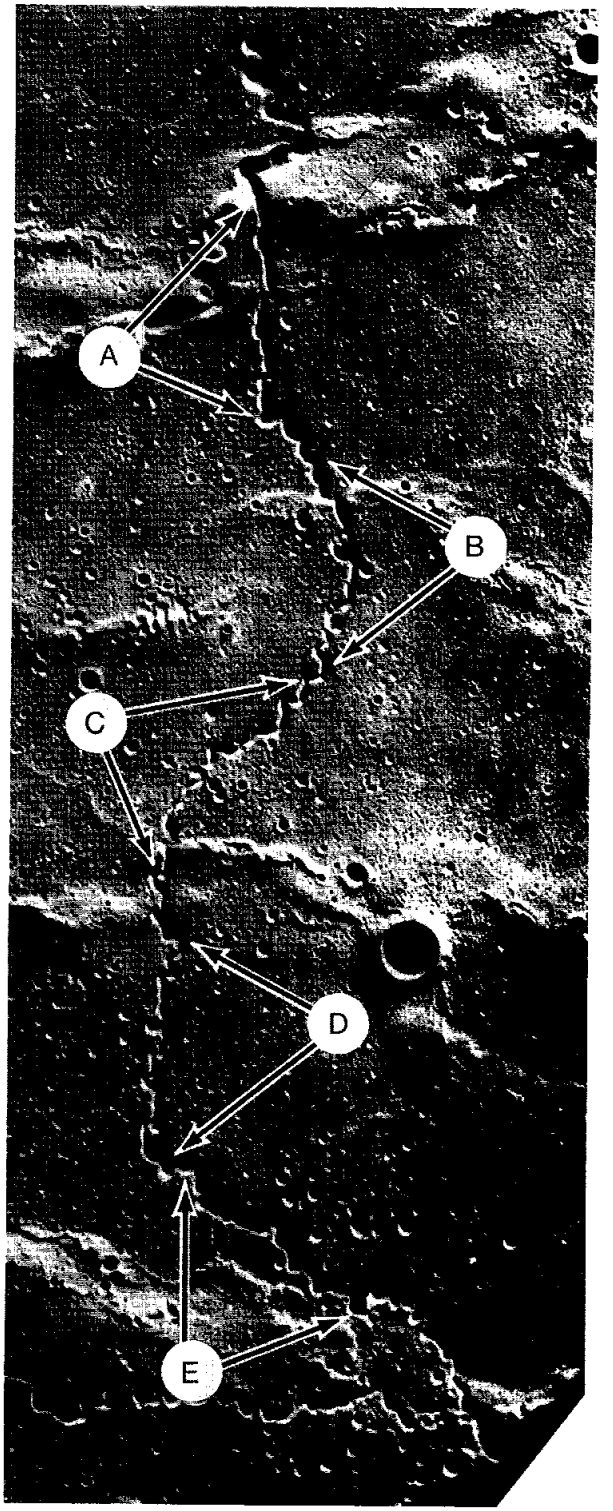


FIGURE 29-114.—Rille west of Herigonius Crater (portion of Apollo 16 metric camera frame 2838).

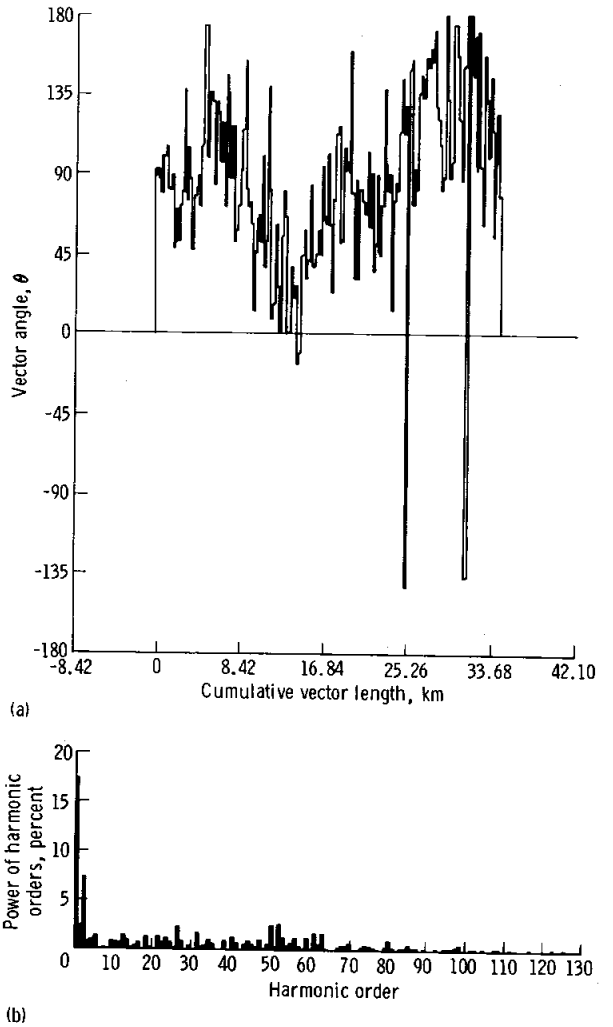


FIGURE 29-115.–The Herigonius rille bank plot and power spectrum. (a) Angle θ of small vectors placed along the Herigonius rille bank plotted as a function of cumulative vector length. (b) Power spectrum for the Herigonius rille.

The frequency characteristics are quantified in terms of the relative contributions of each harmonic to the total squared variation exhibited by the θ sequence about its mean. That is, letting θ denote the average θ value, the total squared variation is then given by

$$SS = \sum_{k=0}^{M} (\theta_k - \bar{\theta})^2 \qquad (29\text{-}2)$$

and the relative contribution of the ith harmonic is then given by

$$P_i = \frac{M+1}{2}\left(a_i^2 + b_i^2\right) \Big/ SS \quad i = 1, 2 \ldots \frac{M}{2} \qquad (29\text{-}3)$$

The power of the ith harmonic (P_i) is then used as a means of expressing the frequency content of the rille and as a means of comparing it to the frequency content of any other rille.

Examination of the power spectrum of the Herigonius rille (fig. 29-115(b)) reveals that 91 harmonics contribute to the total variation of θ as a function of cumulative rille length. Only approximately 30 percent of the total power is accounted for by harmonics of order less than 20. Higher frequency harmonics account for most of the variation of θ as a function of total cumulative rille length. In other words, changes in direction of the rille bank occur more often on a scale approximately equal to or less than 1/20th the length of the rille than on a scale larger than 1/20th the length of the rille. The power of harmonics larger than 20 in characterizing this variation in θ is large compared to the importance of lower order harmonics. The rille amplitude expressed in terms of percentage of rille length (APBL) is 8.88 percent, which means that the changes in θ with cumulative rille length represent relatively large changes in amplitude of the original rille bank with respect to the baseline. As a check that the normalized power spectrum provides an adequate description of the rille bank, part of the analysis presented in this discussion includes computer plots of the rille bank with progressively higher order harmonics included in the calculation. These plots yield progressively more accurate approximations to the original x,y data points of the rille bank. Comparison of the Herigonius rille and the computer plot of the Herigonius rille (fig. 29-116) indicates that the level

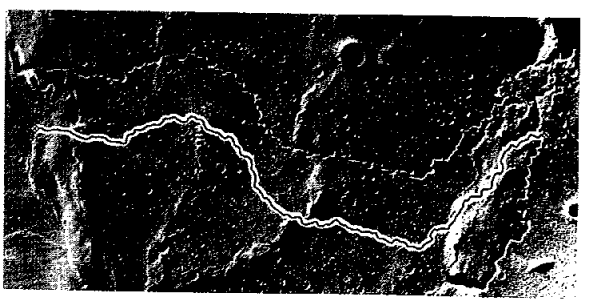


FIGURE 29-116.–The Herigonius rille and computer plot, accurate to within 1 percent of the original x,y rille bank data points of the Herigonius rille bank. The computer plot is calculated from the normalized power spectrum of figure 29-115(b).

of accuracy with respect to the original x,y data points is 99 percent. This plot is based on the normalized power spectrum in figure 29-115(b). Most investigators would classify the Herigonius rille as a sinuous rille. Thus, our preliminary analysis indicates that sinuous rilles might be characterized by a large number of contributing harmonics with orders as high as 120. Moreover, the higher order harmonics should be more important than low-order harmonics in characterizing the rille.

West of Bonpland F Crater (7° S 18° W) is an unnamed lunar rille (fig. 29-117) .that extends in a northerly direction into the Fra Mauro Formation and in the southerly direction for approximately 50 km, where it becomes a ridge. The total length of the feature is approximately 135 km. Leveelike features are present at several places along the rille, and they are especially well developed at points marked A and B in this figure. The power spectrum for only the part of the rille shown on this photograph (fig. 29-117) is given in figure 29-118(a). It, too, is characterized by a large number of contributing harmonics (67), but not as many (91) as characterize the sinuous Herigonius rille. Most of the variation of θ with cumulative rille length is accounted for by low-frequency harmonics for the unnamed rille of figure 29-117. Approximately 65 percent of the total power is contributed by harmonics of order less than 10, and 75 percent of the total power is accounted for by harmonics of order less than 20. Thus, high-frequency contributions (25 percent from harmonics greater than 20) are not as important for this rille as for the Herigonius rille, where 58 percent of the total power is given by harmonics greater than 20. For the rille of figure 29-117, rille amplitude expressed in terms of percentage of baseline is 5.48 percent.

A possible example of a linear rille, Goclenius III Rille, is shown in figure 29-119. The normalized power spectrum for this rille is shown in figure 29-118(b). This power spectrum is unlike the power spectrum for either of the previously discussed rilles. There appears to be a more nearly uniform distribution of power of all harmonics to the variation in θ for this rille than for the others. Aside from this exception, it is expected that rille amplitude expressed in terms of percentage of baseline length will prove to be of greatest quantitative use in separating linear rilles from others. The APBL for Goclenius III Rille is only 0.94, which is much smaller than the APBL for either of the other rilles.



FIGURE 29-117.–Unnamed rille west of Bonpland F Crater. Levees are present at locations A and B (portion of Apollo 16 metric camera frame 1983).

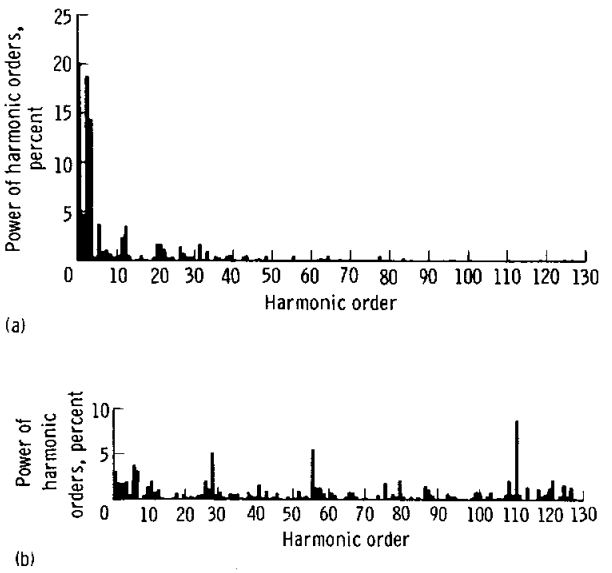


FIGURE 29-118.–Power spectra. (a) The "Bonpland" rille of figure 29-117; APBL = 5.48. (b) Goclenius III Rille; APBL = 0.94.



FIGURE 29-119.–Goclenius III Rille (portion of Apollo 16 metric camera frame 0419).

The normalized power spectrum data presented for the rilles just described are of a preliminary nature because they have not been refined through consideration of operator errors in digitizing. Nevertheless, these three Fourier analyses of rilles with markedly different appearances yield different types of normalized power spectra and different average amplitudes. Preliminary results suggest that it will probably be possible to use the Fourier analysis in conjunction with the ratio of average rille amplitude and rille length to classify lunar rilles and to determine the number of discrete classes of rilles. When this classification has been accomplished, the origins of each rille class may be studied by a variety of methods.

Comparison With Terrestrial Analogs

One fruitful approach in the study of rilles has been analyses of terrestrial analogs to lunar rilles. This approach has been especially important in the study of lunar sinuous rilles (refs. 29-97 to 29-99). One method used in these studies has been a comparison of the similarities or differences in planimetric shape of terrestrial volcanic features and lunar sinuous rilles. The brief discussion that follows is given to illustrate the plausibility of using this method in the comparison of terrestrial analogs and lunar rilles. The comparisons are made for only one lunar rille and one terrestrial lava tube. No conclusions of origin can be drawn from such a restricted comparison. The comparison is made only to demonstrate the method of analysis that can be employed with any analog. A complete study will require classification of a large sample of lunar rilles and analysis of all possible terrestrial analogs.

Lava tubes are hollow conduits that develop in active basalt flows; they are known to form only in lava of low viscosity. Figure 29-120 is a photograph of the Modoc lava tube in Lava Beds National Monument, California. The Modoc lava tube originates in a 260-m-diameter crater in basalts of recent age. It can be traced across the plain downslope for more than 14 km, where it appears to end within a few kilometers of the flow front. It is collapsed intermittently along the tube course line, and the tube and collapsed sections of the tube have been compared previously (ref. 29-98) to features thought



FIGURE 29-120.–Modoc lava tube, Lava Beds National Monument, California.

to represent transitional forms of sinuous rilles. The angular change of course line with cumulative course line of the Modoc lava tube has been analyzed with the finite Fourier analysis. The power spectrum for the Herigonius rille and the normalized power spectrum for the Modoc lava tube are shown in figures 29-121(a) and 29-121(b), respectively.

Although the power spectra for both features are similar in that there is a nonuniform distribution of power with the various harmonics, the power spectra differ in an important way. Higher order harmonics contribute to the variation of θ with rille length for the Herigonius rille than for the Modoc lava tube. However, further studies of a variety of terrestrial analogs and comparisons of the frequency content of these features with the frequency content of lunar rilles may yield important clues to the study of the origin of lunar rilles.

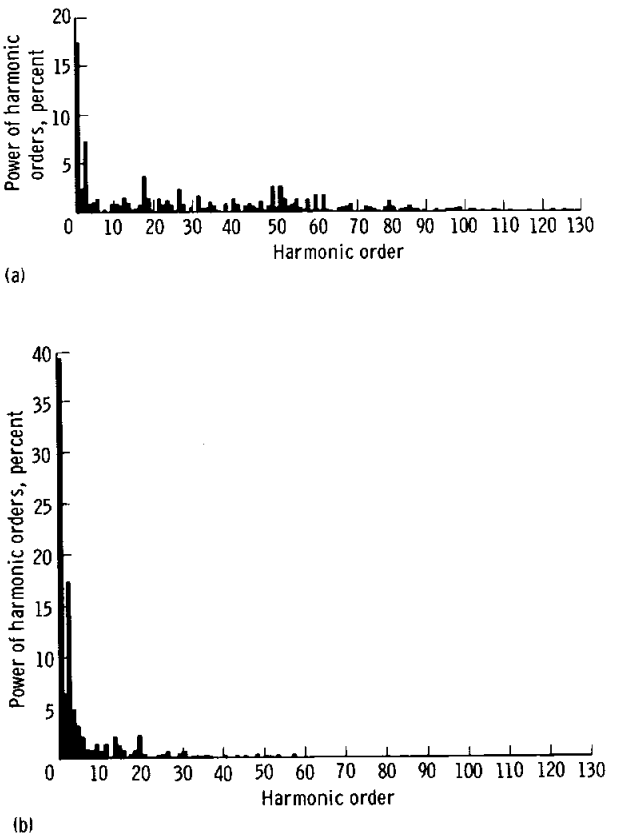


FIGURE 29-121.–Power spectra. (a) The Herigonius rille; APBL = 8.88. (b) Modoc lava tube; APBL = 8.37.

Analysis of Structural Control

In addition to rille classification and comparison of terrestrial analogs with rilles, the Fourier analysis technique should be useful for demonstrating structural control of rille shape. For example, when a rille approaches a mare/highland boundary, its shape may change markedly. While this change is visually obvious, it can be documented quantitatively with this method and control of the rille by a landform can thus be demonstrated. An example where control is less obvious can be seen in the photograph of the Herigonius rille (fig. 29-114). In this case, the rille appears to originate in an irregular depression near the edge of the wrinkle ridge. It then passes through a gap in the ridge system and enters the smooth terrain of the open mare. It appears that the course of rille segment A may have been controlled by the wrinkle ridge where it passed through the break in the ridge. To test this hypothesis, the short segment of the rille that passes through the break in the ridge has been analyzed separately for comparison with other parts of the rille. The normalized power spectrum of rille segment A is shown in figure 29-122(a). None of the

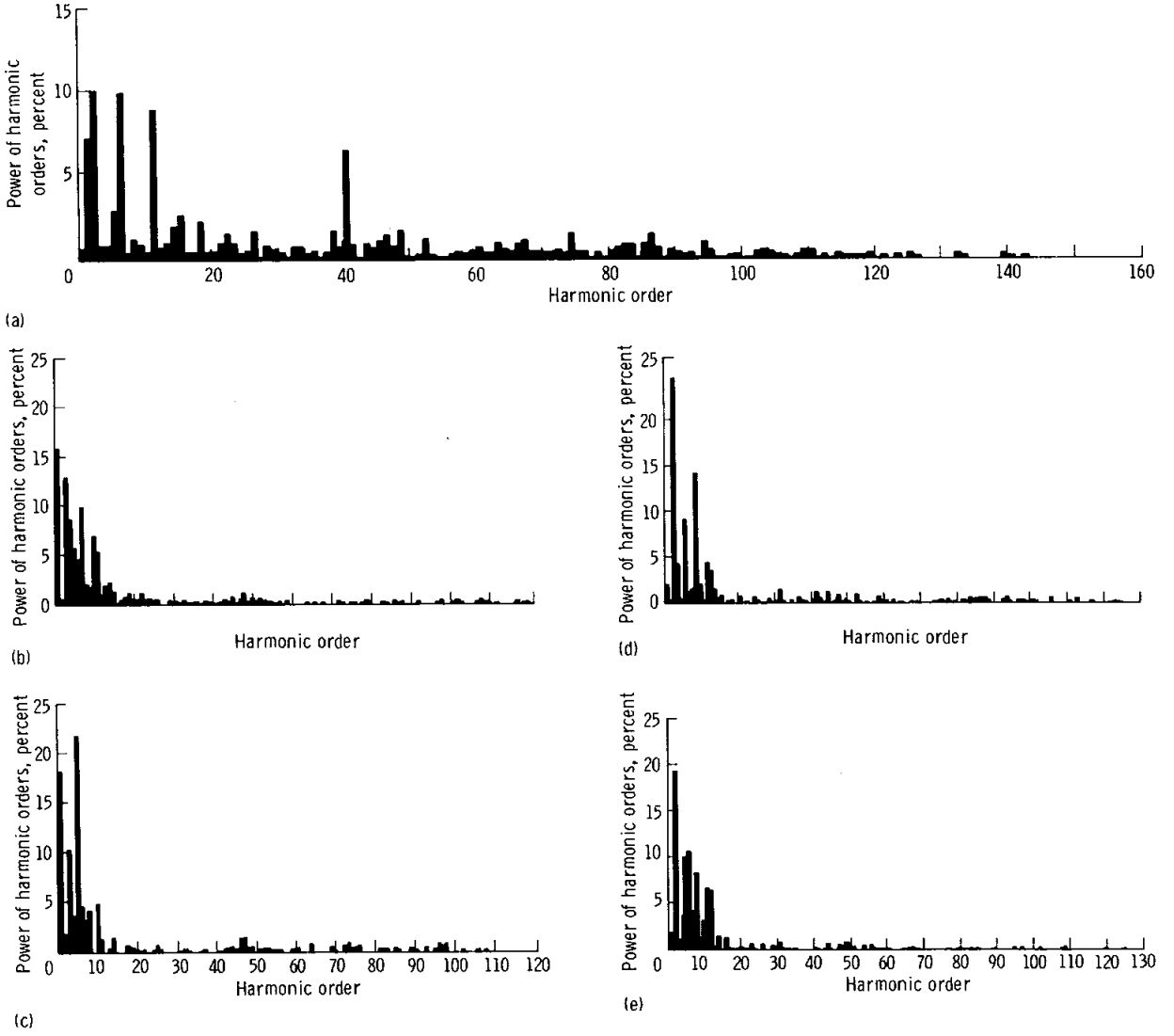


FIGURE 29-122.–Power spectra of segments of rille in figure 29-114. (a) Segment A; APBL = 2.93. (b) Segment B; APBL = 11.73. (c) Segment C; APBL = 7.19. (d) Segment D; APBL = 6.40. (e) Segment E; APBL = 4.29.

harmonics contribute more than 10 percent of the total power of variation of θ with cumulative rille length. The rille amplitude in terms of percentage of rille segment baseline is 2.93 percent. With respect to both the power spectra and the numerical value of rille amplitude percentage of baseline, this segment of the rille resembles the linear Goclenius III Rille more than it resembles the entire course line of the Herigonius rille or other segments of the Herigonius rille located in the smooth, open mare terrain. Normalized power spectra for these segments are shown in figures 29-122(b) to 29-122(e). Comparisons of these power spectra show that higher frequency components of the original rille are now expressed as lower order harmonics of the rille segments. These low-order harmonics are of much greater importance for rille segments B, C, D, and E in figure 29-114 than for segment A, and the amplitudes of all the segments are greater than the amplitude of segment A. Thus, there are significant quantitative differences in shape between segment A and segments B, C, D, and E. Therefore, the wrinkle ridge may have controlled the planimetric shape of the rille. Further studies of this nature will be performed to relate other less obvious changes in rille shape with controls such as change in rille gradient.

Conclusion

In summary, selected Apollo 16 photographs of lunar rilles have been analyzed with a new technique that includes a finite Fourier analysis. Preliminary results suggest that it will be possible to classify rilles quantitatively by their planimetric shape. Shapes of possible terrestrial analogs for lunar rilles also can be compared to the shapes of lunar rilles by using this new technique. Preliminary results also suggest that the new technique may be useful for demonstrating structural control of shape of lunar rilles.

PART R

LUNAR VOLCANISM: FRACTURE PATTERNS AND RILLES IN MARGINAL PREMARE CRATERS

Richard A. Young[a]

Large premare craters around the margins of the major maria can be loosely divided into three types. Type 1 craters, with rims breached by mare flows, are those that have undergone late-stage filling coincident with the adjacent mare. Most of these old craters are filled to the same level as the adjacent mare. The crater floors show little structure; for example, Sirsalis E. Type 2 craters are unbreached but evenly filled craters at or near the same level as the adjacent mare; for example, Plato. Type 3 craters are partially flooded, but the rims are unbreached by the adjacent mare materials. Most of these craters have, or appear to have, crater floors below the level of the adjacent mare surfaces. Many type 3 craters contain a network of arcuate rilles and radial, grabenlike fractures; occasionally, they contain sinuous rilles. The fracture patterns often suggest general expansion of the crater floor. Figures 29-123 and 29-124 are examples of type 3 craters photographed on the Apollo 16 mission. Many of the type 3 craters, such as Alphonsus, contain dark vent areas associated with certain fractures.

These features of the type 3 craters must have an obvious relationship to the maria because of their distribution along mare margins. Because type 3 craters are old and degraded, the absence of distinct impact rim facies does not justify classifying some of them as calderas. Nor do these craters seem to be related to the various normal conditions of crater aging hypothesized by many geologists. Such type 3 crater floor features almost entirely lack upland areas. Because the floor fractures are markedly concentrated within the area of the crater floor, it is unlikely that the floor fractures can be readily explained as being caused by large-scale isostatic adjustments along the mare boundaries.

The following hypothetical sequence of events might explain the distribution and nature of these type 3 craters. Perhaps these craters are the sites where mare lava has welled up through older regional fracture systems produced during mare basin formation (similar to those around Mare Orientale) and modified by the impact of the particular crater. Lavas may have moved laterally and vertically from the adjacent, flooding mare through fractures under the crater floors. The lava would accumulate to great depths in these local basins, possibly influenced by the hydrostatic gradient from the higher, adjacent mare surface. A surface crust would form in the crater during several possible periods of intermittent filling as the lava lake slowly rose toward the level of the adjacent mare. Continued filling by lava beneath the thickening crust would cause foundering of the crust, expansion of its surface area, and tensional fracture patterns.

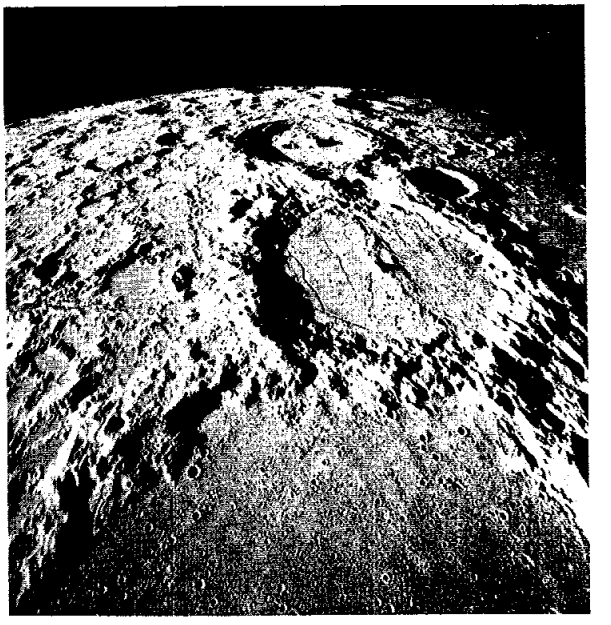


FIGURE 29-123.–Alphonsus Crater (center) exhibits many of the characteristics of type 3 craters. The most conspicuous characteristics are the fracture pattern and dark vent areas (Apollo 16 metric camera frame 0712, south oblique view).

[a]State University of New York at Geneseo.

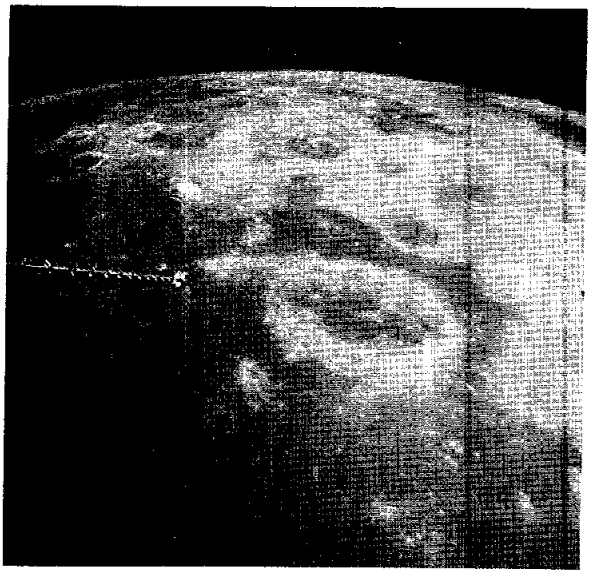


FIGURE 29-124.–This south oblique view of Goclenius Crater exhibits the characteristic fracture and vent features of type 3 craters and a crater floor elevation that is conspicuously below that of the surrounding mare (Apollo 16 metric camera frame 0678).

Some of the type 3 crater floors do not resemble typical mare material but resemble more normal crater floor materials that appear to mantle partially buried fracture systems. Perhaps, in some cases, the crater is subjected to the injection of a sill-like body of lava during the initial stages of lava intrusion beneath the original floor material. A similar history of injection and expansion could then follow, as described in the first instance. Similar-appearing fracture patterns are produced if a fluid is pumped from below into a vessel with sloping sides containing finely pulverized solids. The weaker gravity field of the Moon might accentuate this flotation process. If the filling of a crater is complete or if large volumes of lava well up through the crater floor fractures, a type 2 crater could result.

Two well-known craters (Gassendi and Doppelmayer) show evidence of a type 3 origin followed by partial breaching from the adjacent mare. Both craters show distinctive fractured floors with darker (younger) mare lavas filling the floor near the breach in the rim. The formation of sinuous rilles (lava channels or tunnels) at this stage is plausible because the crater completely fills and excess lava drains through a low breach in the rim, as exemplified by the rille in Posidonius. Other type 3 craters are Repsold, Lavoisier, Atlas, Briggs, Hevelius, Taruntius, Damoiseau, Hansteen, Mersenius, Vitello, and Bohnenberger.

PART S

MARE RIDGES AND ARCHES IN SOUTHERN OCEANUS PROCELLARUM

George W. Colton,[a] Keith A. Howard,[a] and Henry J. Moore[a]

Low-relief mare features such as ridges and arches are best studied by using stereoscopic photographs taken at low Sun angles. Apollo 16 metric camera photography of the southern Oceanus Procellarum east of Letronne Crater reveals a diversity of subtle features (fig. 29-125) and adds significantly to an understanding of the forms of mare ridges and arches, their relative ages, and their association with fractures and sinuous rilles.

Arches and mare ridges[1] are common features on mare surfaces. When viewed stereoscopically in low Sun angle photographs (fig. 29-125), many mare ridges have proven to be composites of both arches and ridges. This combination has been discussed by Strom (ref. 29-100). In this area, however, approximately 12 arches do not culminate in ridges; rather,

[a]U.S. Geological Survey.

[1]The term "arch" has been applied to low, broad structures generally visible only at Sun angles less than 15°, and "mare ridge" (or "wrinkle ridge") applies to long ridges (or complexes of shorter ridges) with somewhat sharper relief (ref. 29-100).

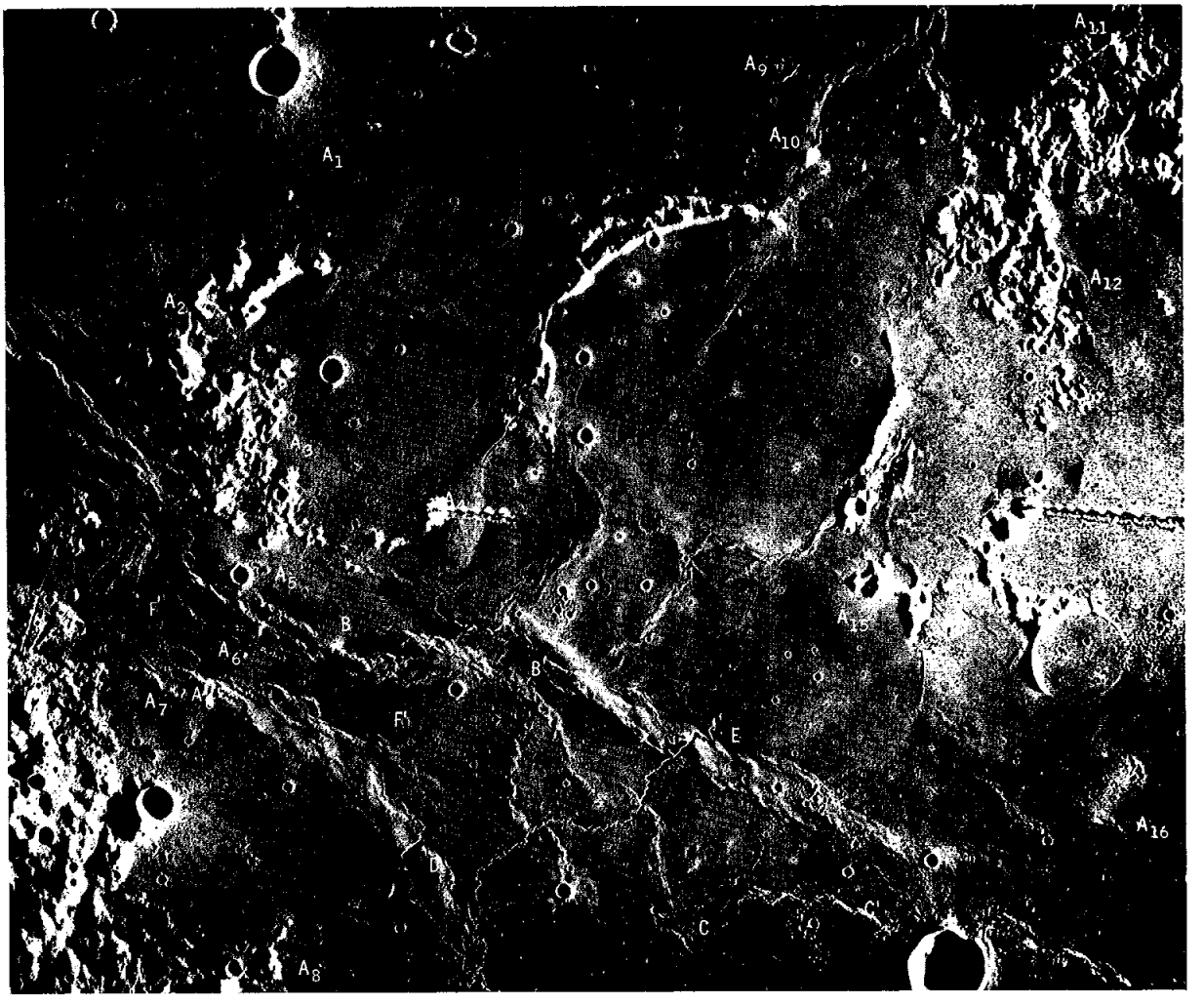


FIGURE 29-125.–Part of the southern Oceanus Procellarum. The area covered is approximately 230 km wide and 190 km high. Numerous low-relief mare structures are shown with clarity in these low Sun pictures (Apollo 16 metric camera frames 2836 and 2839).

they are very gentle, symmetric, smoothly surfaced uplifts. Straight or curved rilles along the crests of several arches (A_4, A_8, A_9, A_{11}, and A_{13} in fig. 29-125) indicate that the arches are fractured. These crestal fractures have analogs on terrestrial tumuli and other anticlinal folds in lava flows where the lava crust has been stretched. Locally, as in arches A_4 and A_{14}, vertical displacement along the crestal rilles is suggested by a difference in elevation on opposite sides of the rilles. The fact that the rille on arch A_4 transects a hill of premare material on its northeast end further indicates that the crestal rilles are fractures.

Some arches may be related to shallowly buried topography. Rugged islands of bright premare highlands protrude from several arches (A_1, A_2, A_4, A_9, A_{10}, and A_{13} in fig. 29-125). This relationship can be explained if these arches are remnants of an originally planar lava surface that has subsided elsewhere, where the mare fill is deeper. Intrusions appear to have produced some arches, and subsidence above preexisting topography has produced others.

Mare ridges, more rugged and more narrow than arches, are commonly asymmetric in profile and have relatively steep flanks; their crestlines are sharper and more irregular in plan view. Crestal elevations, widths,

and cross-sectional shapes vary along the strike. In contrast with the arches, the ridges in figure 29-125 do not have rilles at or near their crests.

Ridge systems tend to be straight or gently curved in plan view; some trace submare topography such as buried craters (for example, the southwestern margin of the large crater slightly above and to the right of the center of fig. 29-125). The trends of crestlines of individual elements superposed on the broad trends vary considerably. Commonly, the combined trends of individual elements form braided, sinuous patterns; locally, they form zigzag patterns. The zigzag patterns (between B and B′ and between C and C′ in fig. 29-125) can be resolved into short, straight segments trending mainly northeast and northwest. Northeast-trending segments are en echelon and are offset dextrally. Those segments that trend northwestward are en echelon and are offset sinistrally. The sense of en echelon offset in each case agrees with patterns observed by Tjia (ref. 29-101) in the northern Oceanus Procellarum. This observation adds support to his concept that these patterns are global.

The en echelon ridge segments are part of a major system of ridges that trend northwestward across the map area. This trend is not obviously related to local topography or to structures in adjacent highlands. Such ridge complexes may reflect regional structural control in the lunar crust (refs. 29-100, 29-102, and 29-103). As seen stereoscopically, a deep, northwest-trending trough (F to F′ in fig. 29-125) lies between two major ridge complexes. Part of an arch (A_6) has been dropped down within the trough, suggesting that the ridges are younger than this arch and that mare ridge development is related to faulting. A further suggestion that some mare ridges are associated with faulting is shown in figure 29-126. Here a premare crater in Mare Cognitum appears to be offset along the trend of a small mare ridge, and the impression is that the fault dips at a low angle to the west. Additional study may indicate that low-angle faulting could account for the irregular traces of many ridges.

Strom (ref. 29-100) found evidence that some mare ridges override adjacent terrain and suggested that they represent lava extruded along fissures. Such fissures could be shallow because the braided ridges with steep flanks (fig. 29-125) recall laval squeezeups on Earth in which still-molten lava emerged from cracks in a solidified lava crust. An extrusive origin of

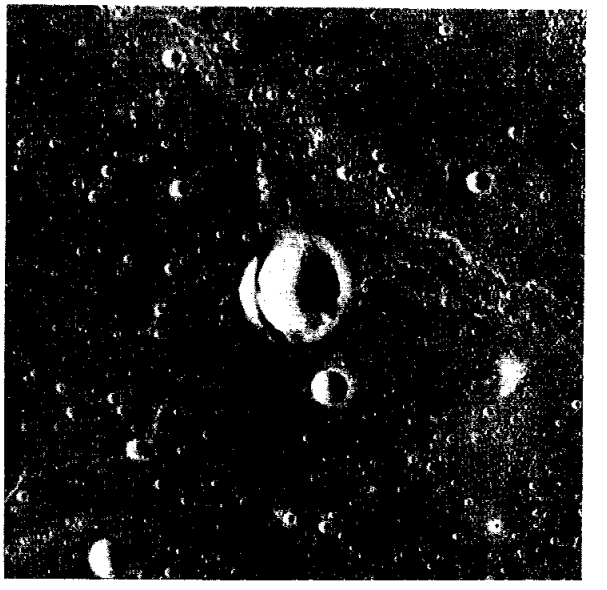


FIGURE 29-126.–An example of a faulted mare ridge. The partially buried premare crater, approximately 5.1 km in diameter, appears to be transected by a fault along the west edge of a branch of a mare ridge in Mare Cognitum. Apparent displacement along the ridge and across the crater is downward on the west (Apollo 16 metric camera frame 2823).

ridges is consistent with the ridge locations of ventlike craters from which two sinuous rilles appear to originate (D and E in fig. 29-125). These rilles may be lava channels (part P of this section), or they may partially coincide with deep-seated fractures because southward they merge and cross highlands (Lunar Orbiter IV photograph H137). This fact could imply that the ridges also overlie deep-seated fractures. Age relations between ridges and rilles are complex. A shallow, possibly partly buried, sinuous rille that meanders northwest from point E is interrupted twice along its course by ridges that apparently formed later.

Mare ridge complexes and arches have probably formed by a combination of intrusion, extrusion, lava subsidence, and faulting. Furthermore, the sequence of formation was complex; thus, the time of formation of any given type of feature (rilles, ridges, arches, and faults) was not the same. If the lavas were emplaced as very thick flows or were ponded in lava lakes of considerable size, late intrusion of still-liquid parts of the body beneath a solidified surface might have formed the arches, and late extrusion through

vent fissures and through near-surface fissures in the lava crust might have formed the ridges. Better distinctions between the various possible origins of ridges and arches may be possible with topographic data to be derived from the photographs and with data about other mare areas from the lunar sounder experiment to be placed aboard the Apollo 17 spacecraft.

PART T

THE ALHAZEN TO ABUL WÁFA SWIRL BELT: AN EXTENSIVE FIELD OF LIGHT-COLORED, SINUOUS MARKINGS

Farouk El-Baz[a]

At high Sun illumination angles, crater rays and ejecta blankets compose the majority of very bright and light-colored units on the Moon. Although not fully understood, the brightness is easily correlated with blocky and more recently exposed deposits (ref. 29-104). However, in three regions of the Moon, surface brightness exists that is not related to observable features (ref. 29-105). Swarms of light-colored markings that display sinuous patterns occur in Mare Ingenii on the lunar far side, in Oceanus Procellarum (Reiner γ and associated markings), and in what was thought to be two areas of limited extent in and around Mare Marginis on the eastern limb of the Moon and near Firsov Crater, which is 700 km to the southeast (ref. 29-82).

Apollo 16 photographs indicate that the swirls of Mare Marginis and those near Firsov Crater are at opposite ends of an extensive belt (fig. 29-127). This belt occupies a large segment of the eastern limb of the Moon from Alhazen A Crater (16° N 75° E) to Abul Wáfa Crater (2° N 116° E). As shown in figure 29-128, the belt is triangular, although the main concentrations of swirls form an irregular pattern within the triangle.

Swirls of light-colored markings in this region occur in all types of geomorphologic units; they abound in the relatively dark and flat mare material of Mare Marginis due west and south of Goddard Crater (15° N 89° E). The north rim of Goddard Crater is brighter than the rest of the area because of the ejecta and rays of a small, bright-rayed crater on that rim (fig. 29-129). Also, the swirls are highly concentrated in highland units, especially those east and southeast of Al-Biruni Crater (17.5° N 92.5° E).

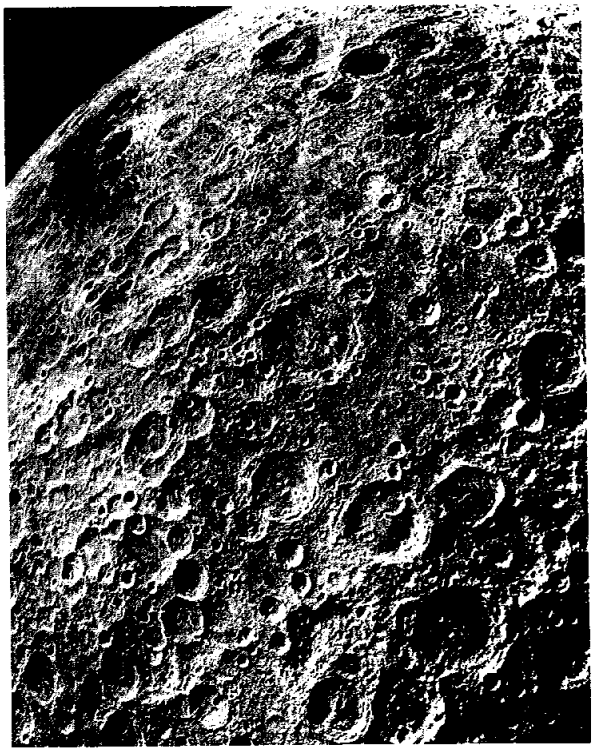


FIGURE 29-127.–Enlargement of Apollo 16 metric camera frame 3005 taken after transearth injection (north is in the upper right direction). Light-colored, sinuous markings extend from near the horizon through northern Mare Marginis (upper left) and through Fleming Crater (center) to the area of Abul Wáfa Crater (lower left center). The crater with a Y-shaped central peak is King (lower right center).

[a]Bell Telephone Laboratories.

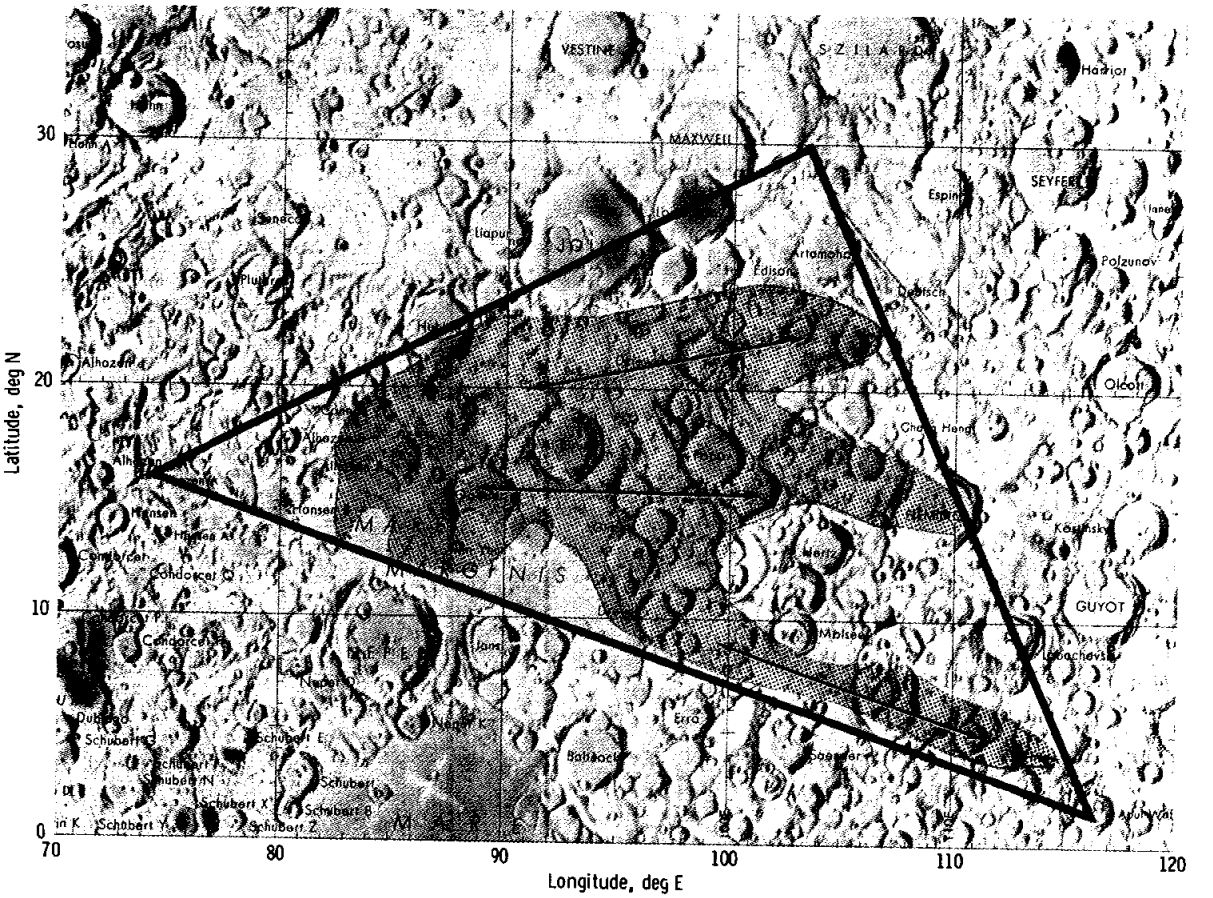


FIGURE 29-128.–Location map of the Alhazen A (16° N 75° E) to Abul Wáfa (2° N 116° E) swirl belt on the eastern limb of the Moon. Large concentrations of sinuous markings form irregular shapes (shaded area) that are enclosed in a triangle. Arrows indicate three major trends of swirl distribution.

In these highlands, swarms of light-colored markings are observable in crater rims, rim deposits, floor units, and plains between the craters.

Recognition of the extensive nature of this belt (approximately 1000 km in length) provides a new dimension to the problematic nature of these markings. Their unusual characteristics may be compatible with exogenetic or endogenetic origins.[1] A discussion of the alternate interpretations, which are graphically illustrated in figures 29-130 and 29-131, follows.

[1]Exogenetic processes are those originating from without the Moon that change or otherwise alter the morphology or nature (or both) of the lunar surface material; endogenetic processes are those originating from within the Moon that change or otherwise alter the morphology or nature (or both) of the lunar surface material.

Exogenetic Processes

Deposition of impact ejecta.–An exogenetic process of common occurrence on the Moon that produces lunar surface brightening is the exposure of blocky material by impact. Generally, the resulting deposits are a continuous ejecta blanket up to two crater diameters from the rim crest of the crater and a system of rays that extends beyond that. Most probable impact craters show secondary craters and crater chains that may be arranged in arcuate patterns. Also, some of the impact ejecta deposits form dune-shaped markings, which are interpreted as termini of deceleration flows at or near the surface (figs. 29-130 and 29-131). However, the bright markings of the Alhazen to Abul Wáfa belt are not likely to be the product of this process for the following reasons.

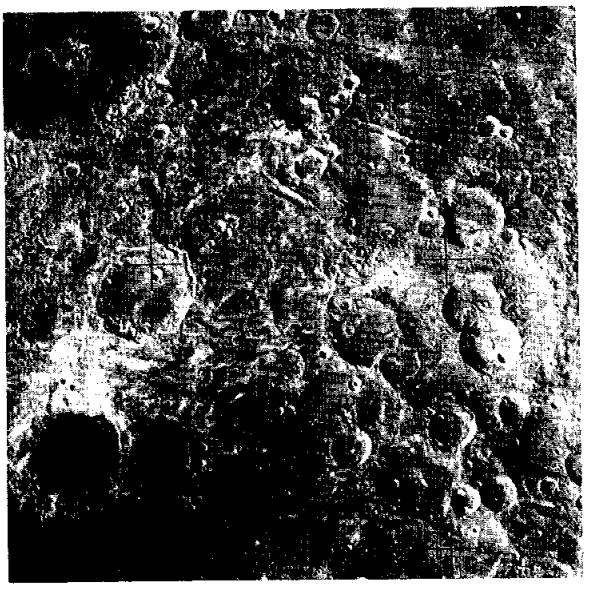


FIGURE 29-129.–Portion of AS14-75-10302 that shows the sinuous markings of northern Mare Marginis. Note that the swirls southeast of Al-Biruni (near the middle of the photograph) trend in an east-west direction. The brightness in the lower left portion of the north rim of Goddard Crater is caused by ejecta and rays of a small bright-rayed crater.

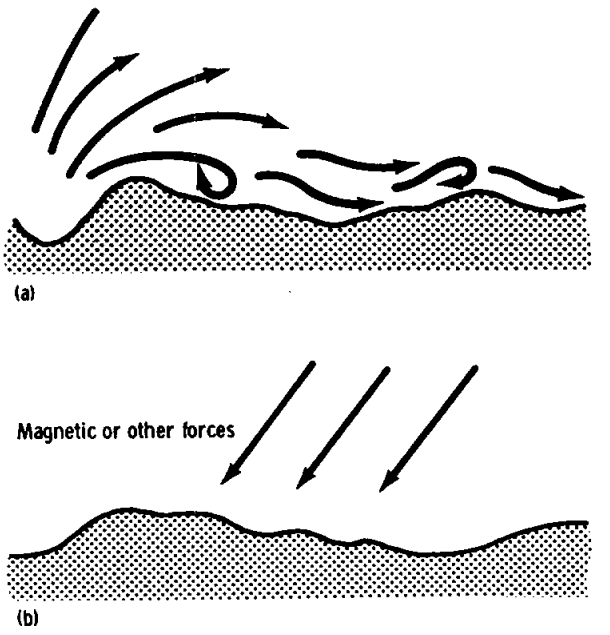


FIGURE 29-130.–Schematic illustration of the two possible exogenetic-origin theories for the sinuous, light-colored markings on the eastern limb of the Moon. (a) Deposition of impact ejecta. (b) Surface disturbances.

(1) There is a lack of evidence of direct association with probable impact structures; that is, these bright markings are not distributed around any particular feature. The general directions in which these markings trend (arrows in fig. 29-128) do not lead to any discernible feature.

(2) The shape of individual swirls and the patterns portrayed by their swarms differ from those of known impact-produced features. This fact is best illustrated in the region of the easternmost boundary of the Alhazen to Abul Wáfa belt (fig. 29-132). In this belt (in one metric camera view) are three different patterns of bright materials: swirls of light-colored markings (area A); bright rim deposits northwest of King Crater (area B); and rays and ray material from Giordano Bruno Crater to the north (area C). The swirls of light-colored markings in area A are somewhat brighter and more sinuous than the other two types of bright deposits.

(3) There is a lack of directional association with secondary craters and crater chains. The described markings in area A trend roughly to the north-northwest. As depicted by the panoramic camera (fig. 29-133), a chain of possible secondary craters within

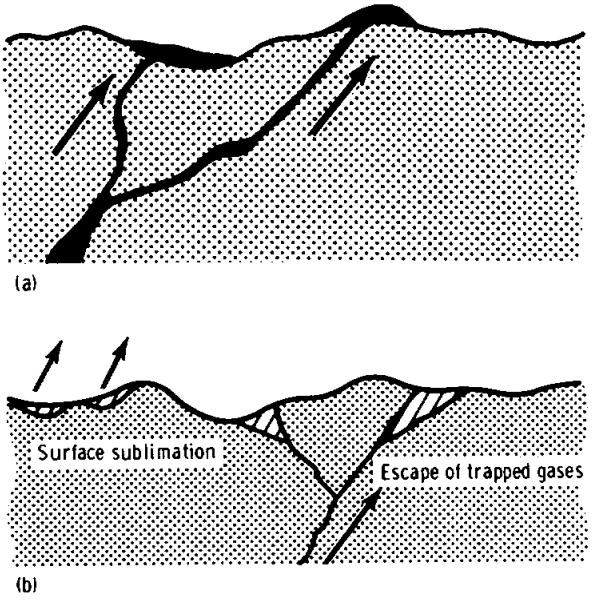


FIGURE 29-131.–Schematic illustration of the two possible endogenetic-origin theories for the sinuous, light-colored markings on the eastern limb of the Moon. (a) Extrusive volcanism. (b) Sublimation, alteration, or both.

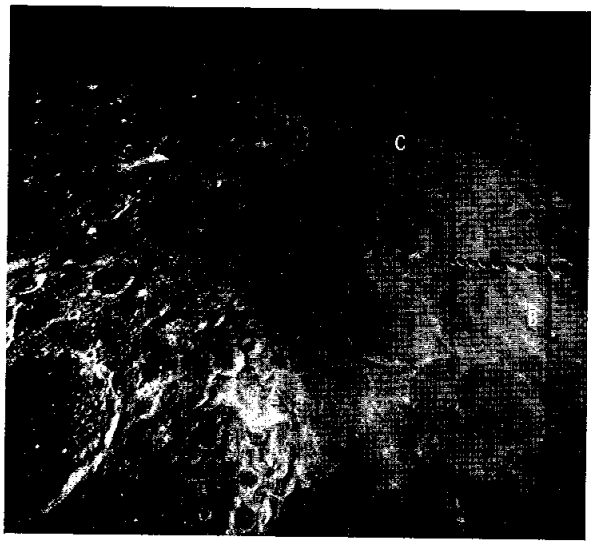


FIGURE 29-132.–Apollo 16 metric camera frame 0758 taken at the oblique angle of 40° looking north of the ground track. The photograph contrasts the sinuous nature of the light-colored markings of area A (see detail in fig. 29-133) with the more regular ejecta deposits northwest of King Crater (area B) and with the more straight bright rays of Giordano Bruno Crater (area C). The object that protrudes into the right-hand side of the picture is the gamma ray spectrometer boom.

this area trends to the northwest. This chain forms the southern border of a bright raylike area, but the brightest and most sinuous markings are removed from the chain. Another example of the lack of association of crater chains and sinuous markings is that found in Mare Ingenii on the lunar far side. In this case, secondary crater chains, originating at O'Day Crater on the western rim of the Mare Ingenii Basin, cut across the swirls and expose light-colored material (ref. 29-104).

Surface disturbances.–Possibly, some poorly understood extralunar disturbance of the surface caused the brightness. Such disturbances might include solar magnetic storms or collisions with cometary material that result in brightening of the surface. Brightening (probably by compaction) of a 150-m-diameter halo around the lunar module in the Apollo 15 landing site was interpreted to be caused by the descent-engine exhaust plume (ref. 29-106). It is difficult to envision an analogous process that could cause disturbances of the surface layer over a 1000-km belt.

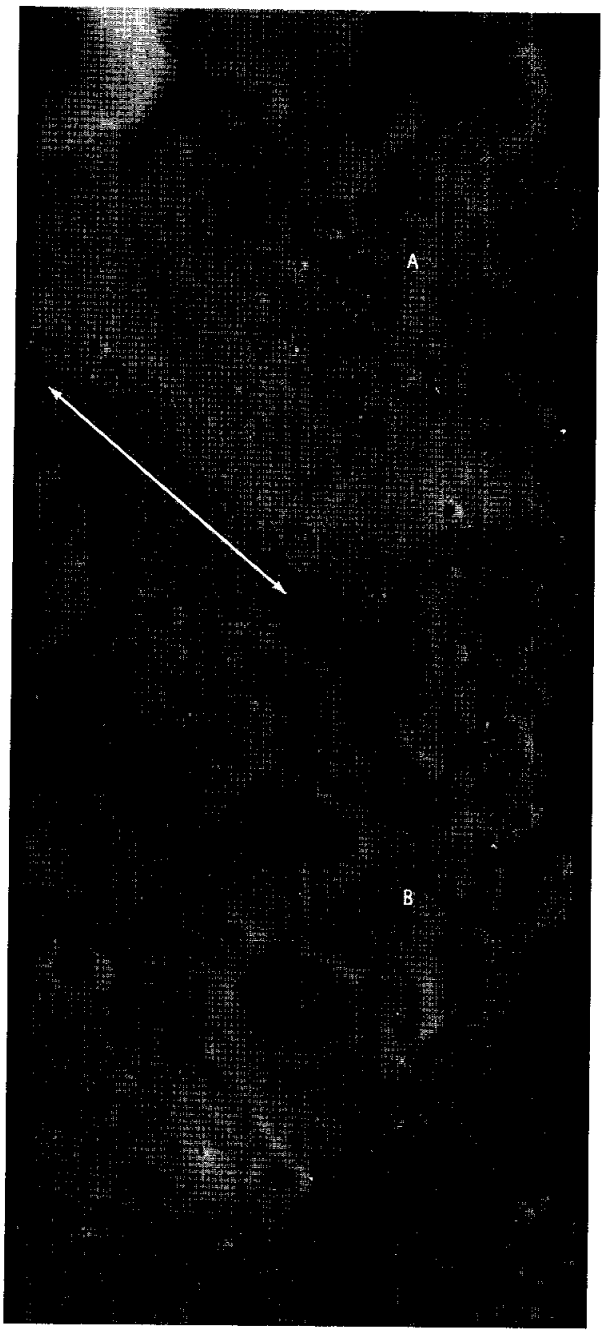


FIGURE 29-133.–Portion of Apollo 16 camera frame 5016 that illustrates details of a portion of figure 29-132. The arrow indicates the trend of a large crater chain (approximately 40 km in length). In area A, most light-colored markings are found atop hills and positive features. Most swirls in area B occur within depressions, especially along their borders. These relationships are particularly clear upon stereoscopic viewing of Apollo 16 pan camera frames 5016 and 5021.

Endogenetic Processes

Extrusive volcanism.—Several probable volcanic units on the lunar surface are characterized by high albedo (e.g., the Hansteen α structure and the Jura domes on the near side of the Moon). Although much larger in extent than these units, the light-colored swirls possibly represent a type of material brought to the surface by volcanism.

Analysis of the available photography failed to indicate specific sources or vents. A visual search on the Apollo 15 mission found no topographic expressions of the swirls at Mare Ingenii (at approximately a 15° Sun angle) or at Mare Marginis (at approximately an 85° Sun angle) (ref. 29-107). Apollo 16 photographs show that the local markings are located preferentially, though not consistently, on preexisting topographic highs (fig. 29-133). The lack of association with probable volcanic features and the absence of positive topographic expressions appear to preclude extrusive volcanism as a source for the light-colored markings.

Sublimation and/or alteration.—The bright markings of Mare Marginis were previously interpreted as sublimates (ref. 29-108). A similar alternative is chemical alteration of the material at or near the surface. These possibilities might account for the observation that many of the swirls on the Alhazen to Abul Wáfa belt are found atop hills and on topographically high rims of craters (fig. 29-133). Gases from the interior may have penetrated the materials through fractures and may have deposited sublimates or chemically altered the surface materials. The escape of gases may have been seismically triggered by large impacts (ref. 29-105). The irregular and sinuous patterns remain enigmatic, but alteration might explain the other unusual characteristics of these features such as the wide distribution, the lack of association with specific landforms, the lack of topographic expressions, and the occurrence in topographically high and low places.

PART U

LOW-RELIEF FEATURES IN TERRAIN OF THE DESCARTES REGION AND OTHER AREAS: NEAR-TERMINATOR PHOTOGRAPHY

J. W. Head[a] *and D. D. Lloyd*[a]

Introduction

The primary purpose of this subsection is to outline areas where low-relief features in the Apollo 16 landing site and associated plains and mare units were intensified in near-terminator photography. A description and, in some cases, a preliminary interpretation of several of these areas is included in an attempt to provide additional data relevant to the interpretation of the hills, plains, and associated units investigated on the Apollo 16 mission.

Near-terminator photography for areas discussed in this paper and for similar areas is listed in table 29-VII. For Apollo 16 near-terminator photography, the Hasselblad EL camera was used with very-high-speed black-and-white film (Kodak 2485, magazine SS) on 70-mm film format. A 250-mm lens was used with a 1/125-sec shutter speed; the f number was set by the lens at 5.6. Most of the photographs were obtained from a spacecraft altitude of approximately 110 km; thus, each vertical photograph covers an area of approximately 20 to 30 km by 20 to 30 km. The photography of the Descartes region was made from a high, elliptic orbit and covered an area approximately 100 by 100 km. The location of the general areas from which near-terminator photography was obtained on the Apollo 16 mission is shown in figure 29-134.

Descartes Mountains, Cayley Plains, and Kant Plateau

A series of five pictures was obtained in a strip stretching from Delambre Crater southward to

[a]Bell Telephone Laboratories.

TABLE 29-VII.–Selected Apollo 16 Near-Terminator Photography[a]

Frame number	*Lunar Orbiter Atlas plate number*[b]	*Location*	*Significant features*
AS16-124-19827 to 19831	312; D/5 to 15 313; H/1 to 5	Near side: from Delambre south to Descartes	Descartes Mountains, surrounding highlands, Cayley Formation, and Apollo 16 landing site
AS16-124-19833 to 19837	304; E/12 to H/12	Near side: from Halley west to Müller area	Cayley Formation and surrounding highlands and a portion of a crater chain near Müller
AS16-124-19838	304; G/9	Between Gyldén and Hipparchus	Highlands near Cayley Formation
AS16-124-19839 to 19844	301; J/5	Near side: southern edge of Ptolemaeus	Highlands-Cayley Formation contact, series of domes, and crater degradation/morphology in Cayley Formation
AS16-124-19845 to 19853	297; J/3	Near side: northeast of and including Davy and floor of Davy Y	Davy Crater, mare and Cayley Formation, featherlike markings (Davy ejecta?), and end of Davy Crater chain
AS16-124-19854 and 19855	297; L/3	Near side: northeast of Davy in Davy Y	End of Davy Crater chain, mare and Cayley Formation, and Davy ejecta(?)
AS16-124-19856	301; E/9	Near side: southwest wall of Alphonsus and Alpetragius (oblique)	Alphonsus: floor, dark halo area, and pools on wall
AS16-124-19857 to 19866	297; H/8	Near side: Mare Nubium northwest of Lassell, and southeast of Guericke C	Mare structures, craters, mare ridges, flow fronts, fault scarps, collapse structures, rilles, buried craters, and secondary craters

[a]Very-high-speed black-and-white film (magazine SS).

[b]Reference 29-109.

Descartes Crater (fig. 29-135). The flat areas are patches of the Cayley Formation, and the extremely rough looking terrain stretching from Descartes northward to the area of the landing site is the Descartes Mountains. An isolated patch of the domical structures typical of the material of the Descartes Mountains is seen just southwest of Taylor Crater at the top of figure 29-135. Surrounding the Cayley and Descartes units are broad plateaus and large hills and mountains of highland materials. The near-terminator photography enhances the domical and furrowed nature of the Descartes material, which is elongated in a northerly direction, and demonstrates how the material is morphologically distinct from the surrounding highland units. The Cayley Formation is seen as crater-saturated plains in low areas. The area of the Apollo 16 landing site (fig. 29-136) is seen at a Sun-elevation angle of approximately 1°, where Flag, Spook, and Palmetto Craters are just visible.

Cayley Plains and Their Relationship to Surrounding Highland Crater Rims

A series of six photographs was obtained at the southern edge of Ptolemaeus Crater (fig. 29-137). Of particular interest are the characteristics of the light plains or Cayley material filling the floor of the old highland crater (a unit similar to the Cayley Formation at the Apollo 16 landing site); the series of domes near the wall of the crater (similar to the

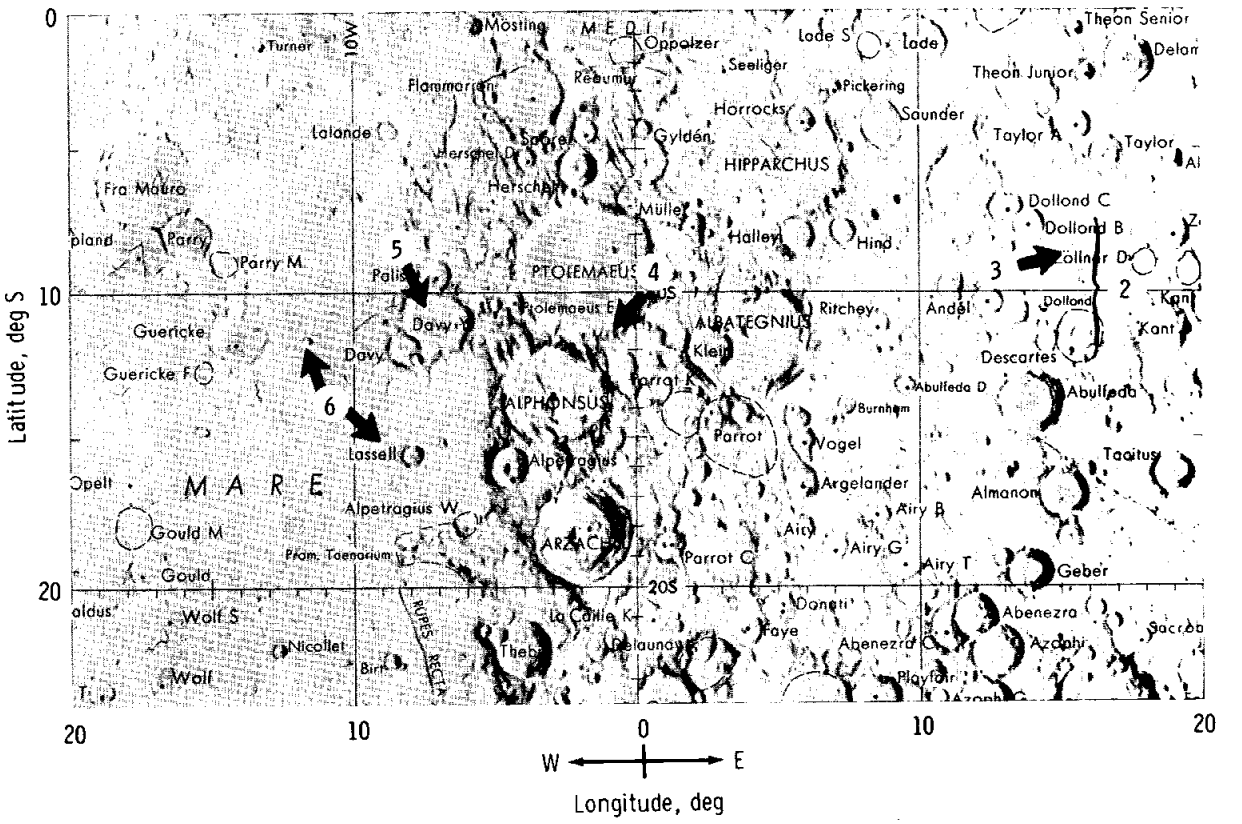


FIGURE 29-134.—Lunar near-side areas of near-terminator photography. Numbers refer to general areas of subsequent figures.

Descartes material); and the relationship between the crater fill and crater walls. The form of a possible buried crater in the plains, the outline of which is seen only because of the low Sun conditions, is shown in figure 29-137(a).

Cayley Plains and Mare

A series of 11 photographs was obtained in two passes over the Davy Y area; these photographs provide a unique opportunity to compare the same area under very similar low Sun conditions. Photographs from both passes are shown in figure 29-138(a) (Sun-elevation angle = 1°) and figure 29-138(b) (Sun-elevation angle = 4°). Compare the length of the shadow cast by the isolated domical structure in figure 29-138(a) and 29-138(b). This small, isolated domical structure is located precisely in the center of the ancient Davy Y Crater and may be a remnant of a central peaks structure. A small patch of mare occupies the northwest portion of Davy Y Crater. This area is shown (fig. 29-138(a)) at a Sun-elevation angle of 1°, and the surface appears saturated; however, at a 3° higher Sun angle (fig. 29-138(b)), the surface does not show the same saturated condition. In Apollo 14 near-terminator photography (ref. 29-94), a similar relationship has been noted in the analysis of areas adjacent to each other, but this is the first time the relationship has been documented in the same area. This observation strengthens the conclusion that the erosion of lunar craters (0.01- to 1-km-diameter range) is primarily caused by small impacts that produce such minute changes in crater form that the interior of the crater is worn to a slope of approximately 1° (ref. 29-94). The heavily cratered plains dominating the floor of Davy Y Crater have been mapped and interpreted as volcanic plains (ref. 29-20). The grooves and ridges seen in figure 29-138(a) (just north of the isolated peak) trend in a direction radial to the premare Davy

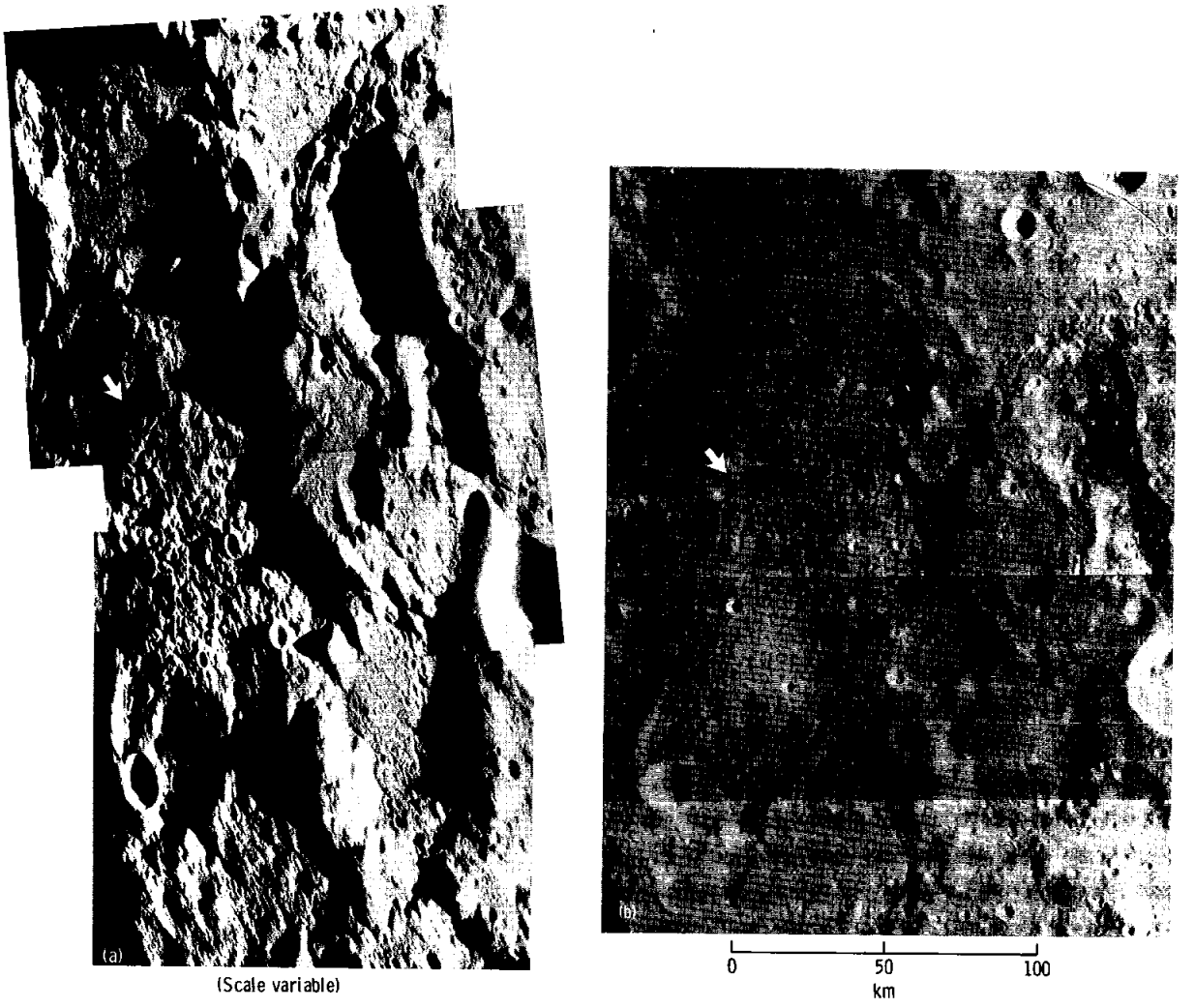


FIGURE 29-135.–Area from Delambre Crater south to Descartes Crater. (a) Near-terminator photography of the Descartes region, showing materials of the Descartes Mountains, Cayley Formation, and surrounding highlands (AS16-124-19829 to 19831). (b) Lunar Orbiter IV photograph 89 of the same area at a 22° Sun-elevation angle. In both cases, the arrow indicates the Apollo 16 landing point.

Crater (located just at the edge of the photograph). These structures, which rapidly disappear at higher Sun angles (fig. 29-138(b)), may be related to the formation of Davy Crater and may indicate that the plains are formed or mantled by Davy Crater ejecta rather than by volcanic deposits. The Davy crater chain, a series of alined craters of probable endogenetic origin, stretches from the highlands across the floor of Davy Y Crater (lower right of fig. 29-138(b)). The near-terminator photography suggests an old age for these craters based on their subdued rims and a lack of structures indicative of recent rim deposits.

Mare Regions

A series of 10 near-terminator photographs was obtained in Mare Nubium showing a variety of detailed mare features. Figure 29-139(a) shows an

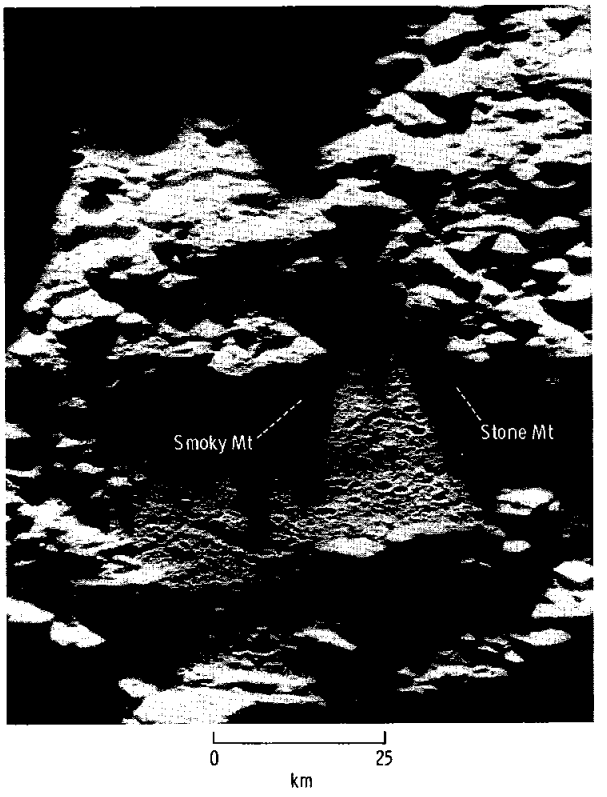


FIGURE 29-136.–Blowup of the Apollo 16 landing site at a Sun-elevation angle of approximately 1° (portion of AS16-124-19829).

elongated scarp a little farther north, outlining a structural trend that is not obvious on higher Sun photographs (fig. 29-139(b)). An entire series of low mare ridges with a left-lateral offset trends in a direction almost normal to these scarps. A second series of scarps is seen in the upper portion of figure 29-139(a); these scarps differ from those of the lower set because of their obliquity and because of the fact that they define, in part, two linear rilles, one of which is parallel to a very low mare ridge to the north. In addition, just to the north, three circular structures are defined by very low mare ridges undetected in photographs taken at higher Sun elevations. To determine if these craters are volcanic and are sources for some of the mare material or if they are premare craters indicating the morphology of the old unflooded surface will require further study. These photographs provide significant information relating to the origin and evolution of the mare regions that is not available on higher Sun photography. Other points of interest include a series of

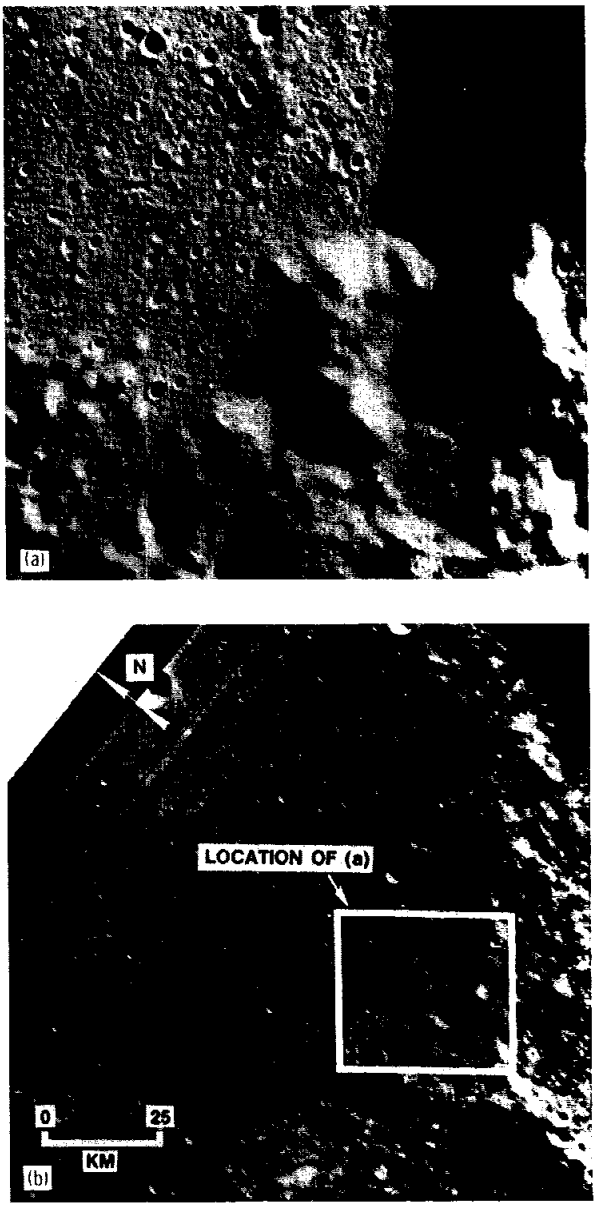


FIGURE 29-137.–Southern edge of Ptolemaeus. (a) Domes and plains at a Sun-elevation angle of approximately 2°. The circular outline of a possible buried crater is seen in the upper left-hand corner (AS16-124-19839). (b) Lunar Orbiter IV photograph 108(H2) of the same area at 21° Sun-elevation angle.

three craters in the left central portion of figure 29-139(a). As seen in figure 29-139(b), the northern crater is a bright halo crater, the central crater is an older crater with no visible bright ejecta, and the southern crater is perched on top of a low albedo

cone reminiscent of a terrestrial cinder cone. Preliminary analysis of the smallest detectable crater populations in this area shows little areal variation from the smooth mare up to the base of the crater rim slopes of the three craters. For the bright-halo crater, this analysis seems to indicate that the bright ejecta seen in figure 29-139(b) are not thick enough to destroy the population of craters with extremely low interior slopes that show up so significantly in near-terminator illustration in unmantled mare deposits. If further analysis shows this supposition to be true, it may also indicate that the same small impacts, which gradually reduce slopes of larger craters to very low angles (ref. 29-94), are also responsible for the obliteration of the thin, bright ejecta blankets. Thus, the bright-halo crater should ultimately lose its halo and appear more like the crater just below it, with little overall change occurring in the general crater population. The relationships at the low-albedo cone are not easily interpretable from preliminary analysis.

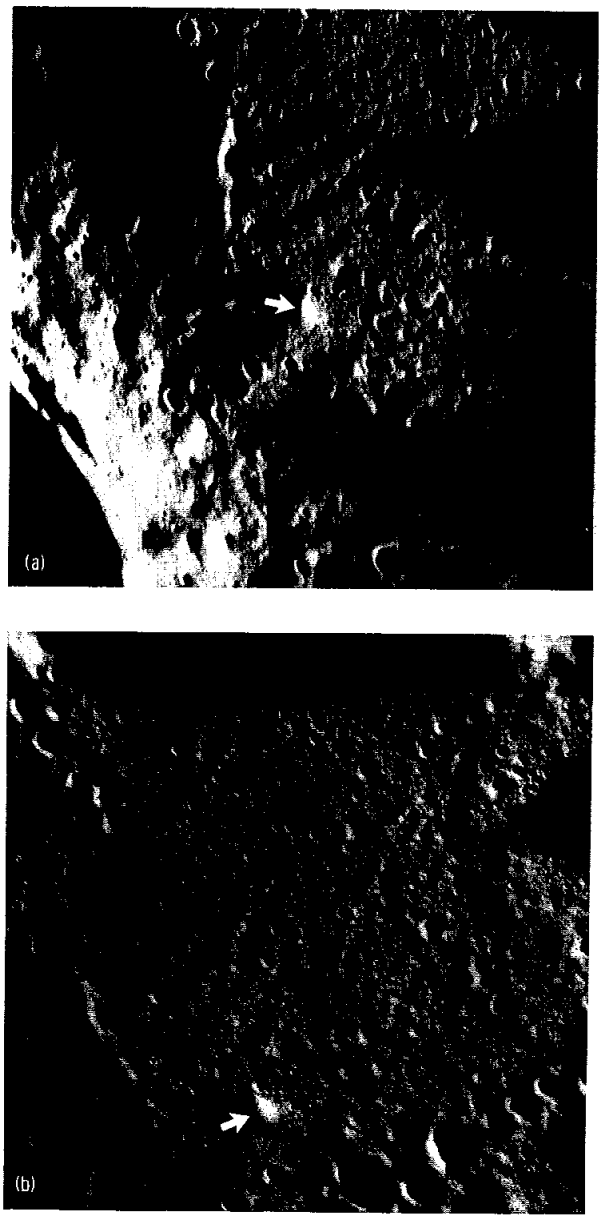
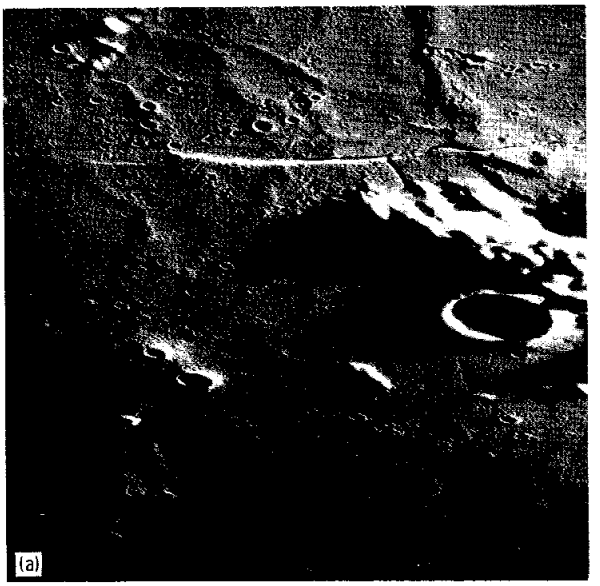
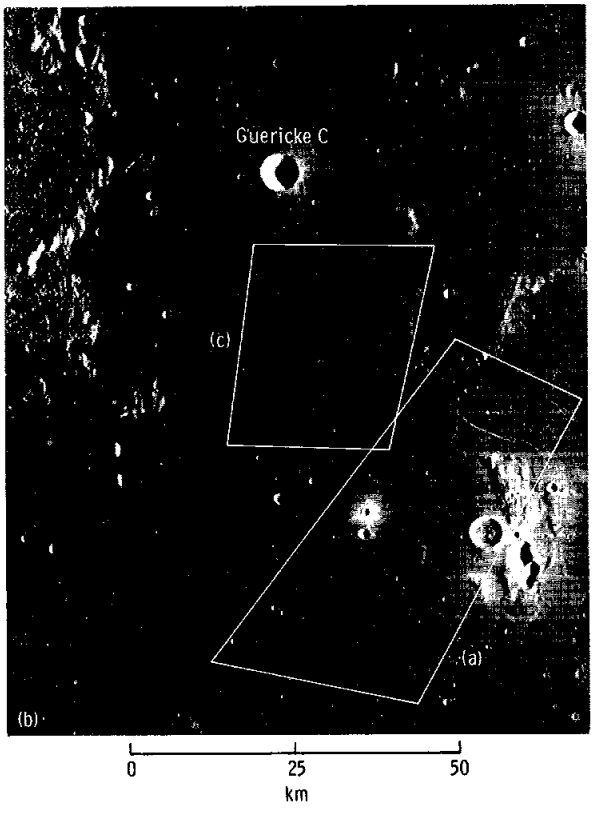


FIGURE 29-138.–Floor of Davy Y Crater. (a) Very-near-terminator photograph, showing mare in upper left and heavily cratered plains with ridged and grooved structure possibly related to ejecta from Davy Crater in lower left. End of Davy Crater chain is partly obscured by shadow in lower right (AS16-124-19846). (b) Sun elevation is now 4° (3° higher than in (a)). Note the subduing of the grooved structure and the disappearance of many of the mare craters. Davy Crater chain is now in illumination (AS16-124-19855). (c) Lunar Orbiter IV photograph 113(H2) of same area at a Sun-elevation angle of 20°. The arrow points to the domical hill in (a), (b), and (c).





If a cinder cone exists, pyroclastic activity associated with this structure should tend to decrease the crater population surrounding the cone. However, the normal distribution of craters around its base suggests that the structure originated before the final flooding of the mare. Detailed analysis of these structures is continuing.

A portion of Mare Nubium is shown in figure 29-139(c), illustrating crater saturation of the mare surface at the base of the mare ridge to the left. Crater density appears to decrease from the terminator toward the chain of hills to the right, suggesting that saturation is caused by the presence of craters with very low (~1°) interior slopes, as seen near Kunowsky (ref. 29-94) and at Davy Y.

The previous discussions have outlined areas where near-terminator photography is valuable in studying lunar history and processes, and they have also noted preliminary results from studies that are underway in the analysis of near-terminator photography related to the types of units investigated at the Apollo 16 landing site.

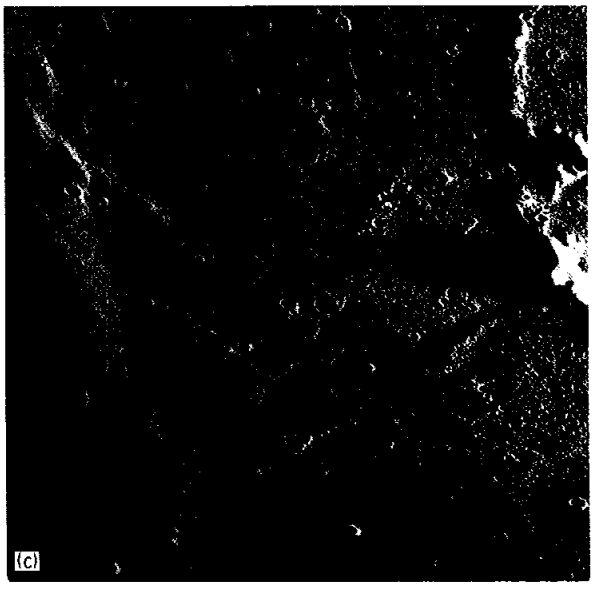


FIGURE 29-139.–Mare structures in the northern part of Mare Nubium. (a) Island of highlands material surrounded by distinctly structured mare material (note faults, rilles, scarps, buried craters, and mare ridges) just west of Lassell (AS16-124-19859). (b) Lunar Orbiter IV photograph 113(H2) of the same region at a 20° Sun-elevation angle. (c) Mare ridge (left) and remnants of the wall of an old flooded crater (right) just south of Guericke C (AS16-124-19864).

PART V

COLOR CONTRASTS IN MARE NUBIUM AND THE SOUTHERN OCEANUS PROCELLARUM

Ewen A. Whitaker[a]

The existence of subtle but definite variations in the color of the lunar surface has long been recognized, but reliable Earth-based composite photographs showing the distribution of many of these areas have become available only recently (ref. 29-110). The strongest color variations and most distinct boundaries are concentrated in the northwest quadrant of the Moon (Mare Imbrium), where the major boundaries correspond with the distal fronts of a complex and prominent series of lava flows (refs. 29-110 and 29-111).

The areas scheduled to be overflown by the command module pilot (CMP) displayed only two moderately well-marked boundaries in the mare region and five small, isolated areas that are notably redder than their surroundings. These areas are illustrated in figure 29-140 (an infrared minus ultraviolet composite of the region), in which the redder lunar areas appear lighter. Area A, having rather indefinite boundaries, covers the region shown diagrammatically in figure 29-141. Areas B and C (fig. 29-140) are the color boundaries in the mare. Areas D to G are patches of highland-type material but are notably redder than the average highlands. Having been briefed on the locations of these areas of slightly abnormal color, the CMP was asked to note if the contrasts were visible and to photograph the areas with color film as time permitted.

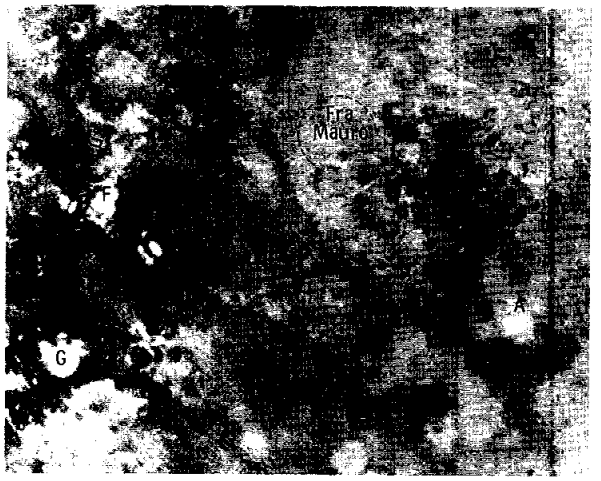


FIGURE 29-140.–Subtractive color-composite photograph (infrared minus ultraviolet) of part of Mare Nubium and adjacent regions. The area shown extends from approximately 0° to 17° S and 4° to 28° W.

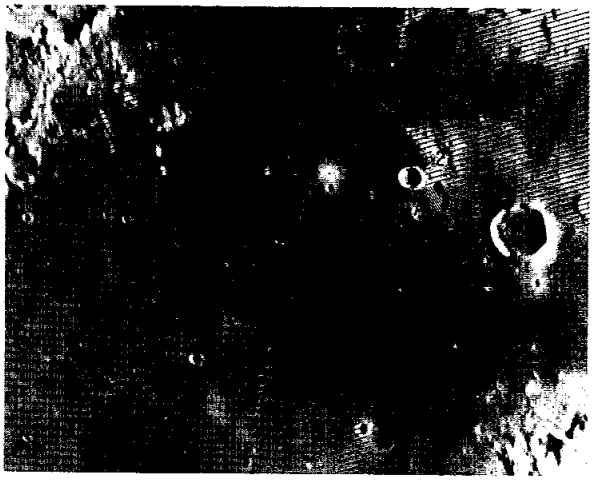


FIGURE 29-141.–Earth-based photograph of the Lassell-Guericke region in the northern Mare Nubium. The area shown is approximately 240 by 200 km. Area A is reddest, areas 3 and 5 are intermediate, and area 4 is the least red.

All the areas mentioned were successfully photographed, and the color contrasts were detected visually in all cases. The real-time description of these areas, as given by the CMP and recorded in the technical transcription, agrees remarkably well with the data of figure 29-140. Figure 29-141 is an Earth-based photograph (Lunar and Planetary Laboratory Catalina Observatory) of part of Mare Nubium on which some of the more prominent color areas are given diagrammatically. The letters A to C in figure 29-141 correspond with those letters of figure

[a]Lunar and Planetary Laboratory, University of Arizona.

29-140. With slight editing and the addition of identifying numbers, the CMP's description of this area reads as follows.

LR38/06:03:59:22 GET: I'm looking at Lassell C (1) and the little highlands clump by it (2). . . . right now the southern piece with a crater in it is a sort of a tan color, and the northern piece is a gray. When I look at the mare, I see a big swatch of the tan-colored mare down to the south that goes over towards Guericke (3). And I see a tongue of darker gray material (4). The area around Lassell C (5) has the tan tone to it. Then it goes out about as far as our little cone (6).

The CMP also remarked that the color differences were more noticeable at low solar illumination. He also commented on the low hills of Darney χ et cetera (D in fig. 29-140), noting their "different color" from the surrounding mare. Furthermore, he remarked that the "toe" or bench surrounding these and all other hills in the region (E, F, G, et cetera) showed the mare rather than the hill color.

All these color contrasts are noticeable in the relevant color photographs taken by the CMP; thus, area A may be seen in several frames, including AS16-119-19068 and AS16-120-19234. The contrast between the gray area 4 and the tan areas 3 and 5 is particularly well shown in frame AS16-120-19237. By analogy with Mare Imbrium, one may surmise that this particular feature may represent flows of different age and composition. The indefinite boundaries of area A and the fact that the area surrounds three peculiar craters of possible volcanic origin suggest that this area may be an ash deposit. These observations give one considerable confidence in the reality of the color boundaries revealed by the subtractive color-composite photographic method.

PART W

APOLLO 16 LANDING SITE: SUMMARY OF EARTH-BASED REMOTE SENSING DATA

S. H. Zisk,[a] Harold Masursky,[b] D. J. Milton,[b] G. G. Schaber,[b] R. W. Shorthill,[c] and T. W. Thompson[d]

Introduction

The purpose of the infrared (IR) and radar study of the Apollo data is to establish lunar surface conditions in the vicinity of the orbital tracks of the Apollo command modules during the J-series missions. Correlations and comparisons between the Earth-based radar observations, IR observations, and other data will be plotted on photomaps produced from the mapping and panoramic cameras. In addition, the Apollo photography will be used to improve the classifications of the anomalous IR and radar features. The three sets of Earth-based data have already been obtained. The IR (11 μm) data (ref. 29-112) were obtained during a total lunar eclipse. More than a thousand thermally anomalous regions with an unusually high population of exposed boulders have been identified (ref. 29-113). The 70-cm radar backscatter observations[1] made at the same resolution as the IR measurements show regions of anomalous backscatter. These regions have been explained as roughness caused by boulders on the surface and below the surface. The high-resolution 3.8-cm radar backscatter measurements (ref. 29-114) reveal in great detail regions of anomalous radar backscatter. At this short radar wavelength, small-scale surface and subsurface roughness and boulders less than the order of 10 cm are responsible for the anomalous returns. Previous studies have revealed strong correlation between these three data sets (refs. 29-115 to 29-117). The strongest anomalies (anomalous at all three wavelengths) correspond to features interpreted geologically as young Copernican craters.

[a]MIT Haystack Observatory.

[b]U.S. Geological Survey.

[c]The Boeing Company and the Lunar Science Institute.

[d]Jet Propulsion Laboratory.

[1]Thompson, T. W.: Atlas of Lunar Radar Maps at 70-cm Wavelength. To be published in The Moon.

There are, however, many combinations of enhancements from IR only, 70-cm radar only, 3.8-cm radar only, or combinations of two of these types but not a third. The variation of intensity in all combinations indicates a very complex set of features. These data provide information about the surface on a centimeter- and meter-sized scale although the basic instrumental resolution was 2 to 15 km. The Apollo orbital photography and observations at the landing sites, used in conjunction with the remote sensing data, can significantly improve geologic and geophysical interpretations of lunar surface conditions.

In this discussion of the Apollo 16 landing site and its environs, the application of remote sensing data has been concentrated on two problems.

(1) Is there a physical difference between the Cayley and Descartes geologic units in the vicinity of the landing site?

(2) What is the nature of the bright unit of the material of the Descartes Mountains?

Remote Sensing Data of the Descartes Area

An Apollo 16 metric camera photograph of the Descartes area is shown in figure 29-142, and the remote sensing data are shown in figures 29-143 to 29-146. The largest anomalies in the infrared (fig. 29-143) and radar (figs. 29-144 and 29-145) maps are associated with the Copernican craters Alfraganus A (6.1° S 18.1° E) and Dollond E (10.2° S 15.8° E). In addition, the 3.8-cm radar map resolves many of the smaller caters, including North Ray and South Ray at the Apollo 16 landing site (part X of this section).

Comparison of Cayley and Descartes Materials

The two major geologic units at the Apollo 16 landing site are the Cayley Formation and the material of the Descartes Mountains (refs. 29-21 and 29-35 and fig. 29-142). Examples are located on either side of the landing site, centered at 8.6° S 14.8° E for the Cayley Formation and at 9.2° S 16.6° E for the Descartes material. Both examples are at least 40 km in diameter and are clearly evident on both the metric camera frame of figure 29-142 and the 3.8-cm radar frame of figure 29-144. In spite of the differences in the structure of the surface that defines these two units (clearly apparent in the optical photograph), the 3.8-cm radar data show very little distinction. The Descartes material may be slightly brighter (≤10 percent) at 3.8 cm, but such a difference would certainly result, in any event, from the greater slopes in the mountainous region. It can be concluded that the upper meter of the regolith developed on the Cayley Formation and the regolith layer that developed on the Descartes material contain approximately the same low proportion of boulders.

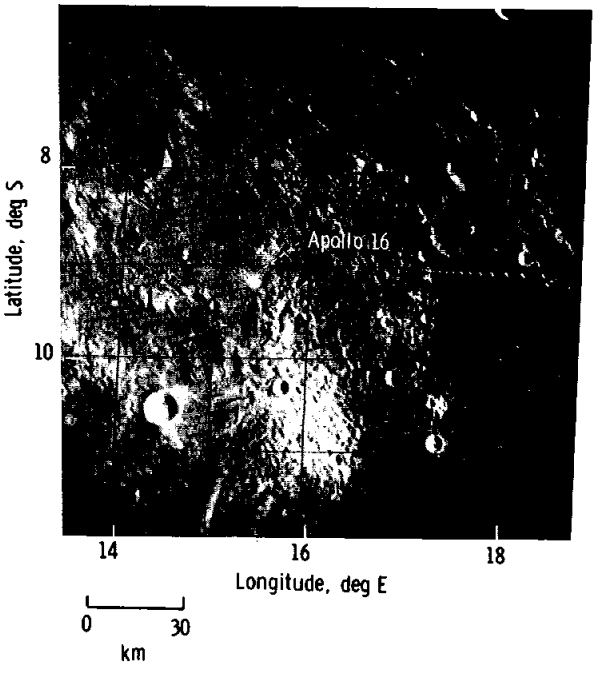


FIGURE 29-142.–Apollo 16 metric camera frame 1265 of the Descartes area. The major terrain units near the landing site include the approximately level Cayley Plains to the west of the Apollo 16 landing site and the hummocky Descartes Mountains to the east. The bright Descartes unit occupies the approximately elliptical hummocky area with high optical albedo that contains Dollond E and Descartes C Craters. Figures 29-142 to 29-146 are at the same scale for ease of comparison.

Unlike the Apennine region (ref. 29-116), where steep-sided peaks rise from the mare level, the gentler slopes of the Descartes Mountains apparently permit the buildup of a thick, eroded regolith layer that possesses a general level of block density similar to the Cayley Plains. This condition agrees with the preliminary findings (discussed in sec. 6 of this report) of the crew and the surface geology team,

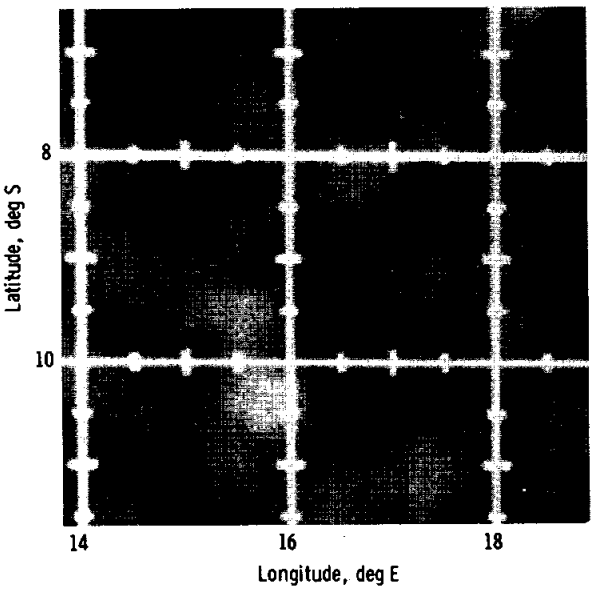


FIGURE 29-143.–Infrared (11 μm) image of the Descartes area observed during an eclipse. The contour interval is 4° K, and the nominal resolution is 15 km. The infrared data have been normalized to the typical mare background eclipse temperature at each point.

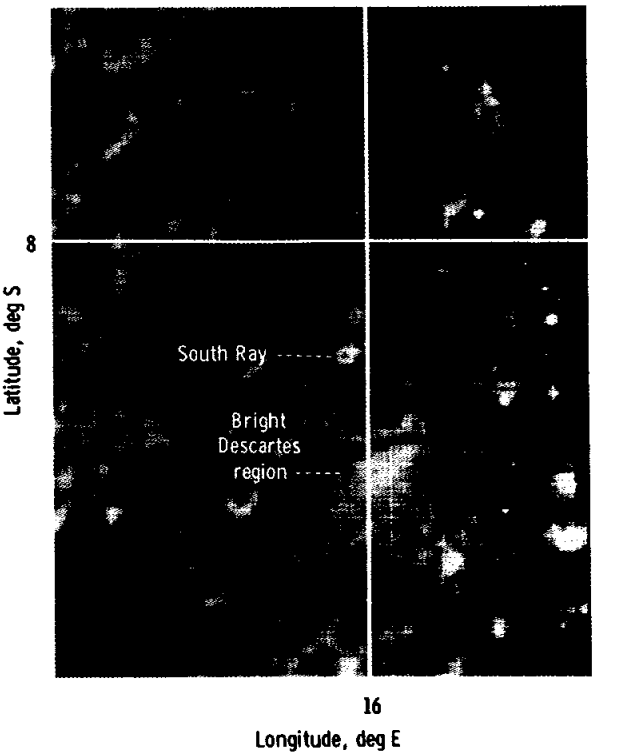


FIGURE 29-144.–Radar (3.8 cm) image of the Descartes area, showing normalized polarized backscatter. The smallest brightness increment is 20 percent of the mean backscatter. The typical resolution in this depolarized image is 2 km.

who found little change in surface materials on crossing the contact between the Cayley and Descartes terrain.

Examination of the 70-cm radar maps gives information about the deeper structure of the regolith. From figure 29-145, it is evident that the 70-cm radar backscatter from the Descartes Mountains is approximately twice that from the Cayley material. For these depolarized maps, the effects of rms slope should be essentially the same for both 3.8-cm and 70-cm wavelengths. The conclusion, therefore, is that 5 to 10 m deep in the regolith covering the Descartes Mountains, there is an increase in the number of meter-sized boulders – either as a constituent of the regolith or because the regolith layer is as thin as 5 to 10 m and the underlying rock structure is visible to the 70-cm radar telescope. Some independent support suggests that the regolith layer on the mountains is thin or contains large boulders, because one of four penetrometer measurements on Stone Mountain met with progressively increasing resistance, whereas the others showed relatively unconsolidated regolith down to 0.75 m (sec. 8 of this report). The 70-cm radar shows that the Cayley regolith is freer of meter-sized boulders to depths as great as the total thickness (10 to 15 m at the landing site, according to geologic and seismic findings) than is the Descartes regolith.

Bright Descartes Material

The bright Descartes material is a high-albedo unit occupying the area between Dollond E and Descartes C Craters, approximately 50 km south of the landing site. It shares the same furrowed or hilly surface texture as other units of the Descartes Mountains, differing only in its unusually high albedo. On the 3.8-cm depolarized radar map of figure 29-144, the area also appears bright, with a radar reflectivity of approximately twice the nearby more ordinary units of the Descartes Mountains. The edges of the 3.8-cm bright area are relatively sharply bounded, with a uniform brightness over much of the area. Dollond E and Descartes C Craters are both clearly depicted as

bright, well-resolved radar enhancements of approximately four to eight times the average reflectivity, with weaker halos of ejecta. Dollond E Crater shows the radar characteristic of fresh Copernican craters, with the crater brightness almost merging with the surrounding halo at the rim. Descartes C Crater seems to have a smaller concentration of decimeter-sized blocks in its ejecta blanket than within the crater itself, judging by the well-marked boundary between the crater and its somewhat weaker radar halo. Therefore, it is probably somewhat older than Dollond E Crater with more of the ejecta blanket eroded away or covered by soil (ref. 29-115).

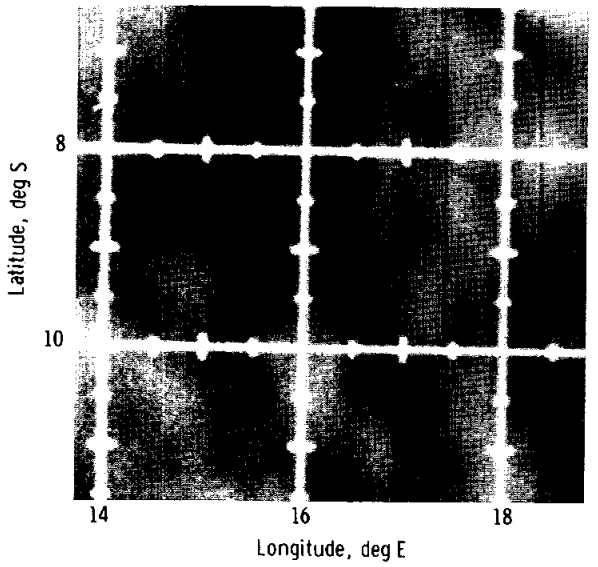


FIGURE 29-145.—Radar (70 cm) image of the Descartes area, showing normalized polarized backscatter. The smallest brightness increment is 30 percent of the mean backscatter. The typical resolution in this depolarized image is 15 km.

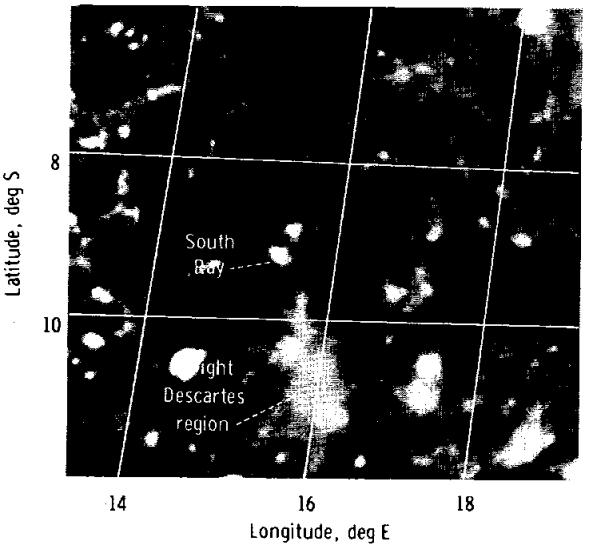


FIGURE 29-146.—U.S. Naval Observatory (Flagstaff) photograph N5818 in full Moon showing Descartes area. The bright Descartes material is shown between Dollond E and Descartes C Craters.

If the bright Descartes material were part of the ejecta blanket from one or both these craters, it would be expected to be symmetrically placed around the crater (or craters) and to exhibit a general decrease in radar brightness with distance from the crater rim. Also, a detectable anomaly in the IR-eclipse map would be expected because the rocks that are responsible for the 3.8-cm brightness should, if exposed at the surface, also produce a higher-than-average IR-eclipse brightness. Neither of these criteria is met, however. On the IR map of figure 29-143, there is no detectable anomaly over the bright Descartes material, although the size of the area is approximately three times the resolution of the map and several IR scans must have crossed it during the measurement. Conversely, a strong IR anomaly appears at Dollond E Crater, as well as a possible response at Descartes C Crater.

The lack of symmetry of the bright unit poses another question. On the panoramic (pan) camera photography (fig. 29-147), there is a band of mantling ejecta surrounding Dollond E Crater out to approximately 5 km from the rim, and Descartes C Crater has a similar but more subdued appearance. Within the Dollond E ejecta, features appear strongly subdued or buried and the mantle itself shows radial flow lines or striations. Beyond the mantle, there are no obvious signs of ejecta, except possibly the higher surface albedo. Discontinuous radial ejecta striations and secondary craters can be traced 20 km to the northwest and 17 km to the northeast of Dollond E Crater and a comparable distance extending to the southeast throughout most of the bright Descartes region toward Descartes C Crater to the southeast. Three separate bright rays extend 20 km toward the west where they cross Cayley Plains material. The continuous mantle of ejecta surrounding Descartes C Crater is similar to that of Dollond E Crater, but

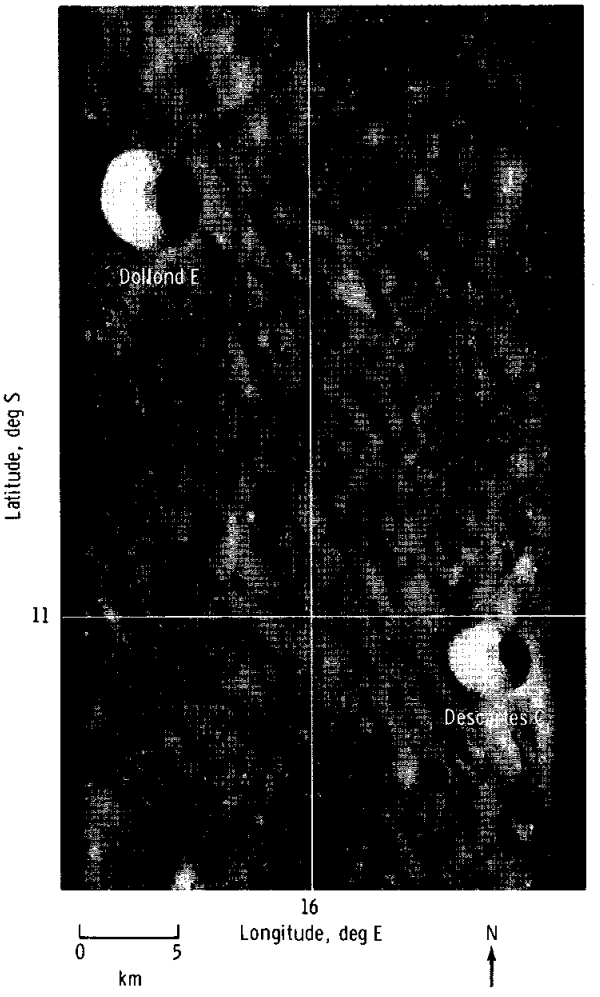


FIGURE 29-147.–Apollo 16 pan camera frame 4616 of the Dollond E and Descartes C Craters with the bright Descartes material between.

there are few well-preserved radial striations beyond 7 km, presumably because of the greater age of Descartes C. The apparent lack of radial striations to the west and east of either crater is probably the result of the eastern solar illumination that does not shadow these trends.

The Apollo 16 orbital photography appears to substantiate the existence of discontinuous, symmetrical radial ejecta surrounding Dollond E Crater out to 20 km. However, the asymmetrical nature of the bright Descartes region as an ejecta blanket is not explained.

Additional evidence in favor of the ejecta-blanket hypothesis is the multispectral visual and near-visual photography. Two sets of data are available: Earth-based detailed spectral measurements of spots on the lunar surface, including the bright Descartes material (ref. 29-118), and Apollo orbital photographs with a multifilter camera (ref. 29-119). Both sets of data agree, and the conclusions from the more detailed spectral measurements (ref. 29-118) are that the surface layer of the bright Descartes material consists of crystalline rock with a composition similar to other terra materials and of fairly young age because of the absence of extensive vitrification. One acceptable explanation of the surface layer composition would be a recently formed ejecta blanket of material from a nearby upland crater. The absence of an IR response suggests a thin mantling layer of fine-grained material, which might result if the rocks at the parent crater are unusually friable. Large blocks are less abundant than expected on the rim of Descartes C Crater, as indicated by the panoramic camera photographs (fig. 29-147). In addition, compared with mare rocks, the reduced amount of iron and titanium in the feldspathic terra material would appear as a decrease in the dielectric loss in the surface (ref. 29-120). The resulting penetration of the 3.8-cm radar signal would be somewhat deeper, and it might observe a higher reflection from the correspondingly longer path within the rocky surface layer. The 70-cm radar shows little enhancement over the bright Descartes material, although appearance of the two bright boundary craters on the map indicates that there are few meter-sized rocks in the bright Descartes layer, which might be the result of the friable nature of the rocks.

One alternative explanation for the bright Descartes material has been proposed by Goetz and Head (ref. 29-119), who suggest that the bright Descartes material is a pyroclastic deposit resulting from recent volcanism. The thin layer of high-albedo material may, in fact, have resulted from volcanism instead of impact, and the problem of asymmetry would then not be of concern. However, no sign of the volcanic vents appears in the orbital photography. Even more important, none of the returned samples appear to be of recent igneous origin; rather, complex impact breccias are the rule. In spite of the ambiguities remaining in the data, the ejecta-blanket hypothesis as the simpler origin for the bright region is preferred.

Another possible explanation might be an exposure of very old feldspathic crust, the mantling regolith of which is highly transparent to 3.8-cm radar because of a low iron and titanium content. However, the multispectral optical data show the surface to be highly crystalline with little sign of the vitrification that results from a long period of erosion.

Acknowledgments

The authors express appreciation to H. J. Moore and R. E. Eggleton for helpful discussions and other encouragements; to M. Charette for discussions and clarification of the multispectral optical data; to Robin Madden; and to personnel at the Lunar Science Institute, Houston, Texas, for their help and the use of their facilities.

PART X

CALIBRATION OF RADAR DATA FROM APOLLO 16 RESULTS

S. H. Zisk[a] *and H. J. Moore*[b]

Introduction

Orbital and surface photography collected during the Apollo 16 mission can be used to calibrate existing Earth-based, high-resolution radar maps of the lunar surface. The absence of any theoretical treatment of the radar backscatter from irregular rocks has prevented the assignment of radar-echo cross sections to specific size distributions of rocks. This gap will now be filled with the use of ground truth provided by metric and panoramic camera photographs and by surface photographic data collected by the astronauts.

Estimates were made before the Apollo 16 mission of the frequency distributions of fragments to be expected at North Ray Crater.[1] These estimates, which predicted a large number of blocks and fragments on the flanks of North Ray Crater, proved to be too pessimistic by a factor of more than 2 or 3, largely because of the background calibration method adopted for the radar backscattering.

In the premission analysis, the background was assumed to be represented by low values of the returned depolarized echo in the Descartes Mountains to the north. This procedure was used because the echoes in the Descartes area were unusual. As a result of Apollo 16 data, the method of estimating the background was revised. In the revised method, an average of many resolution cells around the craters is obtained to acquire a background value. Values of resolution cells for the feature of interest are then averaged and divided by the background value. This ratio is the enhancement for the feature.

Although there are still unresolved problems, the combined use of data collected by the Apollo 16 astronauts on the surface and from orbit to calibrate the radar data will allow the estimation of surface blockiness with more confidence; it may also be the first step in sorting out the complex theoretical problems of radar backscattering from planetary surfaces.

Radar Observations

The radar observations were made with the MIT Haystack Observatory telescope at a wavelength of 3.8 cm. Circularly polarized signals were transmitted from Earth and reflected from the lunar surface (ref. 29-114). Two polarizations of the radar echo were measured – polarized and depolarized. An approximately 2.0-km resolution, which varies with location on the Moon, was achieved for the areas discussed here.

Particular attention was given to the depolarized radar echoes because these echoes are a clearer indication of the roughness of lunar surfaces. North Ray and South Ray Craters (part W of this section, fig. 29-144) and a 512-m-diameter lunar crater in the Flamsteed ring were studied. The crater near Flamsteed was studied because it had a radar response similar to those of North Ray and South Ray Craters and was photographed at high resolution (1 m) by

[a]MIT Haystack Observatory.

[b]U.S. Geological Survey.

[1]S. H. Zisk and H. J. Moore, unpublished report, 1972.

Lunar Orbiter III. No such premission photography was available for North Ray and South Ray Craters. A local enhancement of the depolarized radar echo can be caused by the following factors.

(1) An increase in the number of blocks in the upper one-half meter of the lunar regolith

(2) An increase in the dielectric constant of a normally rough or blocky surface

(3) A decrease in the electromagnetic absorption in the upper meter of the regolith

(4) To a variable extent, a slope that tilts the surface toward the Earth-based radar

Lunar experience shows that item 1 does produce an enhancement where the surfaces are blocky, such as the flanks of fresh craters or possibly where the regolith is thin. If large regions contain anomalous numbers of blocks in the upper one-half meter, the enhancement ratios will be affected when the ratio is computed as the reflectivity divided by the reflectivity of its surroundings. On the average, this effect is small. Judging from previous lunar experiences, items 2 and 3 are unlikely to affect enhancement. The slope effect (item 4) would be strong on the polarized echo but relatively weak on the depolarized component for areas within 50° of the mean sub-Earth point (as are the areas discussed in this report). Thus, enhancement of the depolarized echo is interpreted to be the result of blocks that, from theoretical considerations, range from 0.02 to 0.5 m.

Improved Enhancement Estimates

Two improved procedures are currently being considered. In both cases, background echo strengths were obtained by averaging resolution cells around the craters: 204 resolution cells of 2 km each were averaged around North Ray and South Ray Craters, and 151 resolution cells of the same size were averaged around the crater in the Flamsteed ring. The averaged background was 46.7 for the Descartes area and 37.7 for the Flamsteed area. In the first improved method, the backgrounds at Flamsteed and Descartes are assumed to be equal to include the possibility that the blockiness of large areas of the Moon is fairly uniform and that the aforementioned average numbers are not absolute. Averaged values of resolution cells representing the craters were then divided by the background to yield the enhancement caused by the craters. Enhancements computed in this way are 4.4 for South Ray Crater, 2.6 for North Ray Crater, and 6.1 for the crater in the Flamsteed ring. These enhancements are in agreement with photographic data, which indicate that North Ray is the least blocky of the three craters and that the crater in the Flamsteed ring is the most blocky (fig. 29-148).

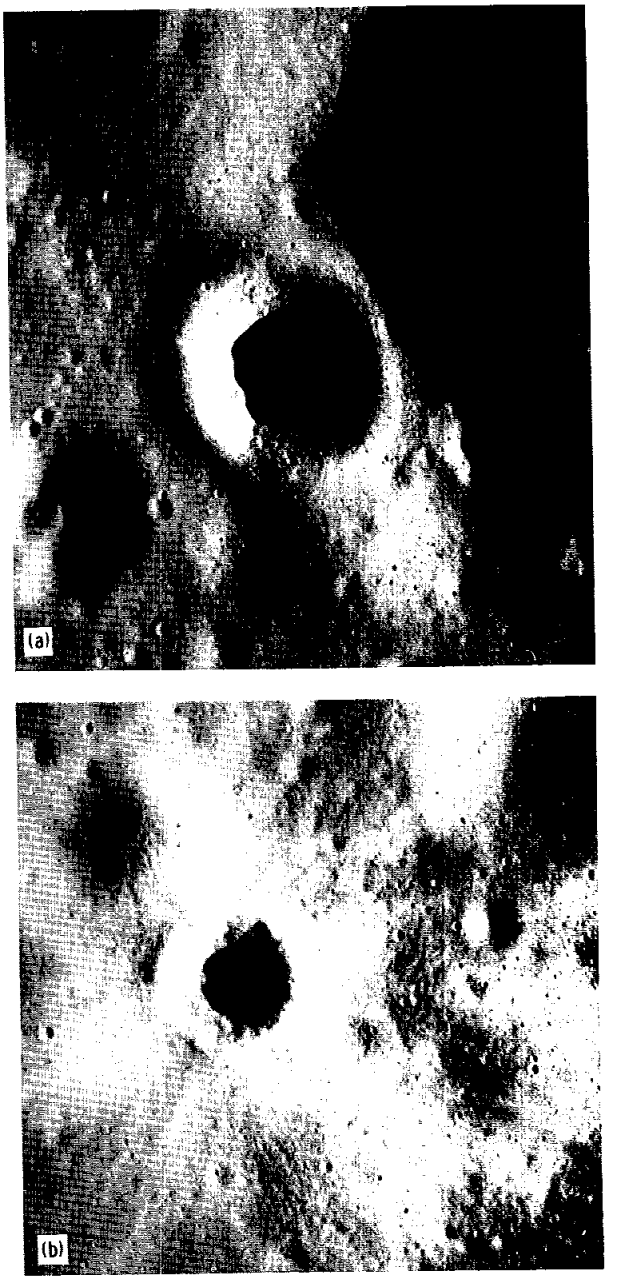


FIGURE 29-148.–Craters with large backscatter. (a) North Ray Crater, 900 to 950 m across (Apollo 16 pan camera frame 4558). (b) South Ray Crater, 650 m across (Apollo 16 pan camera frame 4558).

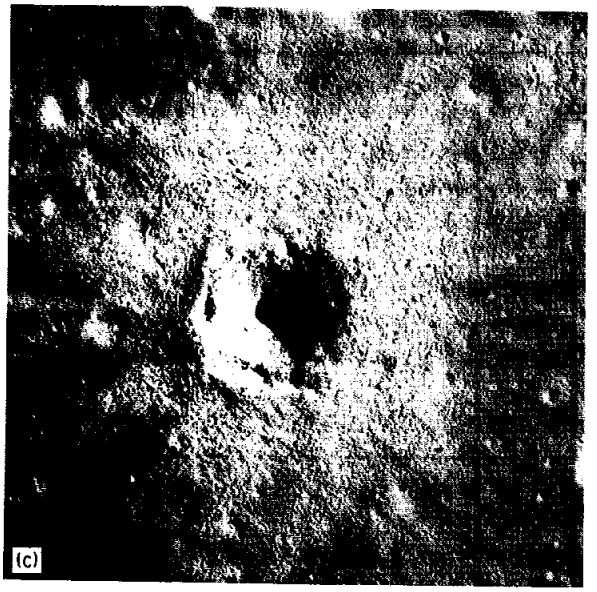


FIGURE 29-148.–Concluded. (c) Lunar Orbiter III high-resolution photograph H189 of crater in Flamsteed ring. The crater is 512 m across.

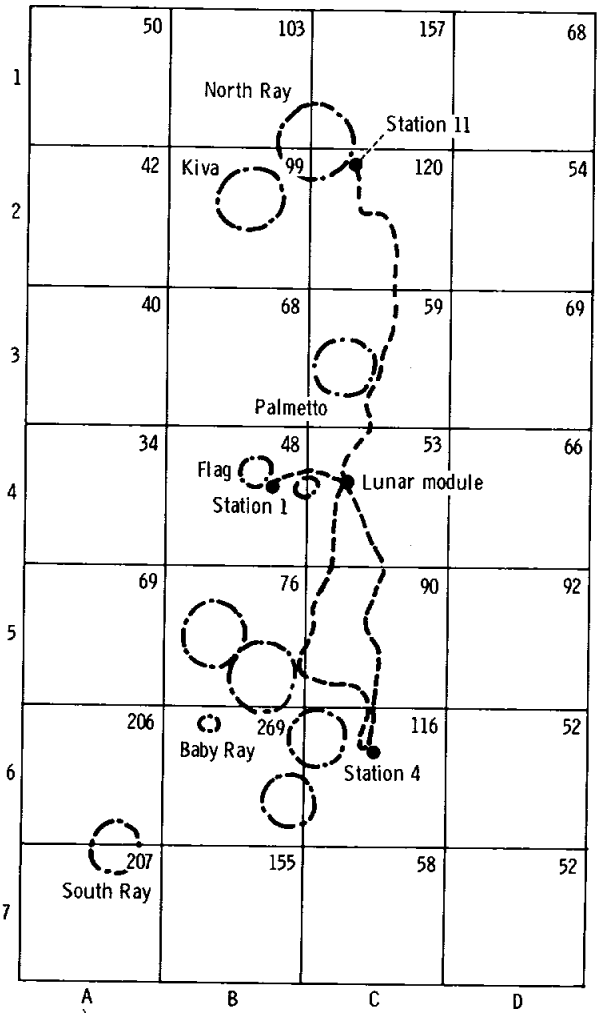


FIGURE 29-149.–Grid showing approximate depolarized radar-echo resolution cells with the Apollo 16 traverses at Descartes. Values in cells indicate echo strength. For the Descartes area, the average of 204 cells is 46.7.

However, the averaged value for the background at Descartes was 24 percent larger than the background at Flamsteed. This fact is consistent with the more general conclusion that terra is more reflective than mare and therefore may be more blocky. Thus, in the second procedure, the normalized echo strengths are taken as absolute (as they should be according to theory). Relative to the background at Descartes, the crater in the Flamsteed ring is enhanced 4.9 to 5.5 times; the enhancement was close to that of South Ray Crater and approximately twice as large as that of North Ray Crater. Thus, the conclusions remain that North Ray Crater is the least blocky and the Flamsteed crater is marginally the most blocky.

Comparison With Lunar Surface Results

Detailed comparison of the radar-echo data with preliminary data collected on the lunar surface showed mixed results. Ground-traverse data indicated that more fragments are found south of the landing site than north of it; this fact generally agrees with the radar results. This agreement may be seen by comparing traverse data (sec. 6 of this report, fig. 6-6) and resolution cells (fig. 29-149), where the largest values are found in cells C-5 and C-6 and the smaller values are found in C-3. However, the preliminary ground-traverse data showed fewer blocks than average adjacent to North Ray Crater, and radar indicates the reverse to be true. This lack of correlation could arise for several reasons. Firstly, the radar detects fragments from the surface to depths of 0.5 m; such fragments could have been completely to partially buried. The astronauts found that the regolith was thin in many places on the rim of North Ray Crater and that large, buried rocks lay under the surface. Secondly, much of the radar echo could have come from the walls of North Ray Crater, which are clearly blocky, producing an unrealistically large value in a

resolution cell (approximately 2 km across) that actually covers surfaces with a varied fragment distribution. Thirdly, selection effects may have occurred in the surface photographs that were used for the preliminary fragment counts because the photographs were obtained from the lunar roving vehicle (Rover), and the path navigated by the Rover may not have included the most blocky areas in the vicinity. Finally, illumination conditions that vary with slope and time could have affected the results of the surface data.

Conclusions

Substantial improvement in the prediction of surface and near-surface blockiness can be achieved by using Earth-based radar measurements. The Apollo 16 mission was the first opportunity to test a hypothesized correlation between block frequencies and radar backscattering. When additional and more refined surface data become available, comparisons will improve the understanding of radar data. This knowledge will allow the estimation of surface blockiness with more confidence.

PART Y

PHYSICAL AND GEOLOGICAL ASPECTS OF HEILIGENSCHEIN MEASUREMENTS

Robert L. Wildey[a]

Heiligenschein is the upsurge in reflected brightness as zero-phase angle is approached. For the first time, an effort has been made to investigate the diagnostic value of the heiligenschein photometric magnitude on a statistically significant scale. This investigation was performed by using the vertical photography of the Apollo 16 metric camera. The brightness surge of reflected light near zero-phase angle was studied with the expectation that it might be related to lunar geologic setting. Although previous work suggests that a real effect is present (refs. 29-121 and 29-122), the data set was small, and no correlations with other lunar surface properties were attempted. The problem is complex enough to warrant massive effort. This subsection is merely a status report.

A total of 111 frames containing heiligenschein photography was selected for this study. These frames were photometrically readable, and the areas within the heiligenschein did not have major gradients in terrain type. The track of the zero-phase-angle point does not cover a large fraction of the lunar surface on a single Apollo mission; nevertheless, heiligenschein tracks were recorded on the Apollo 16 mission within all of the four major time-stratigraphic systems of the Moon. The zero-phase point traversed Mare Fecunditatis and terrae to the east and west. Within the terrae are many small and variegated terrain types. As the line of nodes of the Apollo command module orbit precessed, a considerable surface variety was viewed under zero phase.

This subsection is the sixth paper in a series using this type of measurement (ref. 29-122). In this case, it was necessary to devise an appropriate numerical figure of merit to characterize the heiligenschein intensity. The chosen heiligenschein index was the logarithm of the ratio of the brightness at zero-phase angle to the brightness at a phase angle of 1.5°. The photometric accuracy of an index defined on a wider base in phase angle would be greater. However, the figure chosen has several advantages.

(1) It is precisely the region of the lunar photometric function that cannot be observed from Earth (refs. 29-123 and 29-124).

(2) It entails a small spot (6 km) on the lunar surface over which there is a better chance of finding a suitably homogeneous terrain.

(3) The narrow range in phase angle near 0° ensures that the only geometric parameter of significance to the photometric function is the phase angle; therefore, any dispersion in the heiligenschein index can be considered exclusive property of the surface rather than a result of subtle differences in lighting-viewing configuration. Calibration uncertainties caused by film characteristics are estimated to be no more than 0.01 in the heiligenschein index.

[a]U.S. Geological Survey.

To assess the effect of lighting-viewing configuration (fig. 29-150), the standard deviation of each heiligenschein measurement pair was plotted against the local angle of incidence (which is also the angle of emergence at zero phase). Each such measurement pair consisted of the brightness relative to zero phase of the two points at 1.5° from zero phase on a photometric scan profile. The brightnesses at identical phase angles on two different sides of the zero-phase point have different angles of emergence (for an Apollo camera station) and the same angles of

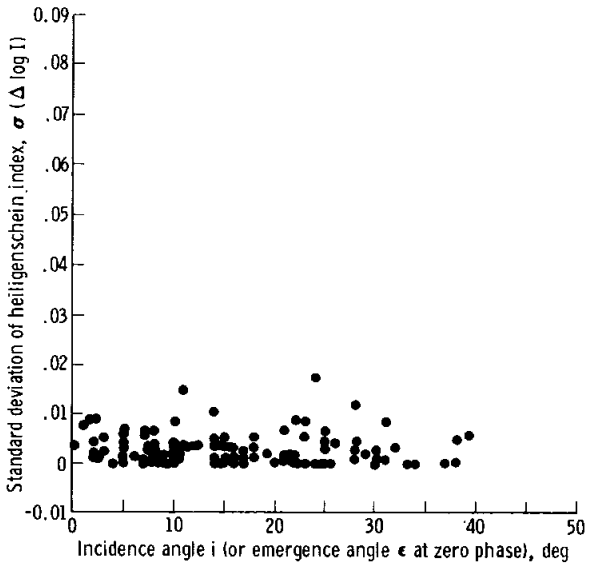


FIGURE 29-150.–Plot of the standard deviation of each heiligenschein index (log ($I_{0°}/I_{1.5°}$)) against the angle of incidence (also emergence) characterizing the heiligenschein spot.

incidence at all but absolute vertical orientations; therefore, such a plot should show any significant departure from zero in the partial derivative of the photometric function with respect to the angle of incidence ($\partial\phi/\partial\epsilon$), which is so close to zero phase. In fact, the diagrams showed only scatter along a line of zero correlation. This result suggests that an upper bound on the average value of $\partial\phi/\partial\epsilon$ on the region ($0 <$ phase angle $g < 1.5°$; $0 <$ emergence angle $\epsilon < 35°$) can be set at 0.01. The average value of the standard deviation for each heiligenschein index was approximately 0.002. The heiligenschein index also was plotted against the local angle of incidence (fig. 29-151). The point plot was too globular to enable

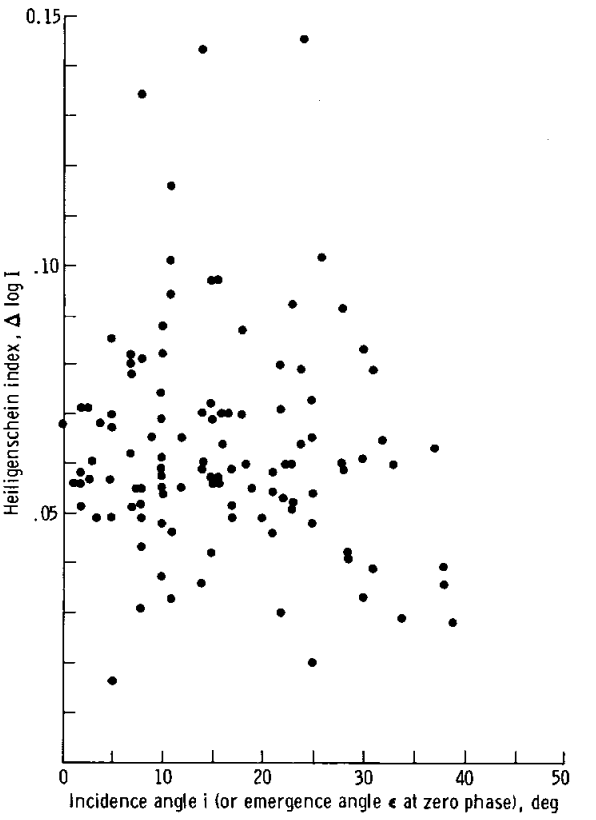


FIGURE 29-151.–Plot of the heiligenschein index against the angle of incidence (also emergence).

bounds to be placed on the appropriate property of the function; however, it demonstrated the widespread existence of dispersion in the heiligenschein index. The point plot also demonstrated that the dispersion is not the result of a subtle geometric effect but is a real property of the particular terrain. The heiligenschein index should be related to microscopic surface roughness (ref. 29-125).

A preliminary attempt was made to evaluate the geological significance of the dispersion in the heiligenschein index. Heiligenschein coordinates were plotted rapidly and somewhat imprecisely on the 1:5,000,000 geologic map of the near side of the Moon (ref. 29-4). The purpose was to evaluate the specific geologic unit involved in the case of each heiligenschein display. Tentative results that list the mean heiligenschein index and the rms deviation for each geologic map unit are given in table 29-VIII.

Considerable spread exists in the heiligenschein index within each unit. Considering the roughness of

TABLE 29-VIII.–Geologic Map Units

Crater systems		*Mean heiligenschein index*	*Deviation, rms*
Copernican System			
Cp	plains material	0.0600	(a)
Cc_1	crater material	.0591	0.0122
Eratosthenian System			
Ec	crater material	.0460	.0130
Imbrian System			
Im	mare material	.0565	.0148
Ip	plains material	.0677	.0139
Ih	hilly material	.0430	–
Ihf	hilly and furrowed material	.0520	.0137
Ihp	hilly and pitted material	.1140	.0200
It	terra material, undivided	.0420	–
Ic_1	crater material	.0390	–
Ici	irregular crater material	.0550	–
Ics	smooth-rimmed crater material	.0552	–
Ic	crater material	.0570	–
Pre-Imbrian or Imbrian System			
pIpIt	terra material, undivided	.0712	.0127
pIl	lineated material	.0470	.0131
pIr	rugged material	.0890	.0056
pIc_2	crater material	.0630	.0056
pIc	crater material	.0652	.0443

[a]The absence of rms deviation implies a single case.

the geologic classification employed, a cautious view of these results is urged. Tentatively, the heiligenschein index seems to have a complex relationship to geologic units. This relationship has not yet been established. Clearly, the heiligenschein index is not related simply to age or to differences in chemical composition between mare and terra rocks. Nor does a breakdown into major structural types (maria, terrae, ejecta blankets, et cetera) show any clear relationship. The most geologically homogeneous unit is mare material (Im), but many measurements (47) on mare surfaces show a broad range in the heiligenschein index and are not distinctly different from all other units grouped together. Because of the large albedo differences between mare and most other units, no simple relationship seems to exist between the heiligenschein index and normal albedo.

Hopefully, future work will clarify whether and how the heiligenschein index is related to geologic materials.

REFERENCES

29-1. Soderblom, Lawrence A.: A Model for Small-Impact Erosion Applied to the Lunar Surface. J. Geophys. Res., vol. 75, no. 14, May 10, 1970, pp. 2655-2661.

29-2. Soderblom, Lawrence A.; and Lebofsky, Larry A.: Technique for Rapid Determination of Relative Ages of Lunar Areas From Orbital Photography. J. Geophys. Res., vol. 77, no. 2, Jan. 10, 1972, pp. 279-296.

29-3. Wilhelms, D. E.: Summary of Lunar Stratigraphy–Telescopic Observations. U.S. Geol. Survey Prof. Paper 599-F, 1970.

29-4. Wilhelms, D. E.; and McCauley, J. F.: Geologic Map of the Near Side of the Moon. U.S. Geol. Survey Misc. Geol. Inv. Map I-703, 1971.

29-5. Trask, Newell J.: Size and Spatial Distribution of Craters Estimated From Ranger Photographs. In Part II of Ranger VIII and IX, JPL-TR-32-800, Mar. 15, 1966, pp. 252-262.

29-6. Morris, E. C.; and Shoemaker, E. M.: Craters. In Part II of Surveyor Project Final Report, JPL-TR-32-1265, June 15, 1968, pp. 65-68.

29-7. Swann, G. A.; Bailey, N. G.; Batson, R. M.; Eggleton, R. E.; et al.: Preliminary Geologic Investigations of the Apollo 14 Landing Site. Sec. 3 of Apollo 14 Preliminary Science Report. NASA SP-272, 1971.

29-8. Shoemaker, E. M.; Batson, R. M.; Holt, H. E.; Morris, E. C.; et al.: Observations of the Lunar Regolith and the Earth From the Television Camera on Surveyor 7. J. Geophys. Res., vol. 74, no. 25, Nov. 15, 1969, pp. 6081-6119.

29-9. Shoemaker, E. M.; Hait, M. H.; Swann, G. A.; Schleicher, D. L.; et al.: Lunar Regolith at Tranquillity Base. Science, vol. 167, no. 3918, Jan. 30, 1970, pp. 452-455.

29-10. Silver, Leon T.: V-Th-Pb Isotopic Systems in Apollo 11 and Apollo 12 Regolithic Materials and a Possible Age for the Copernicus Event (abs.). Trans. Am. Geophys. Union, vol. 52, no. 7, July 1971, p. 534.

29-11. Papanastassiou, D. A.; and Wasserburg, G. J.: Lunar Chronology and Evolution From Rb-Sr Studies of Apollo 11 and 12 Samples. Earth Planet. Sci. Letters, vol. 11, Aug. 1971, pp. 37-62.

29-12. Wasserburg, G. J.; Huneke, J. C.; Papanastassiou, D. A.; Podsek, F. A.; et al.: Age Determinations on Samples From the Apollo 14 Landing Site. Space Res., 12, 1972.

29-13. Papanastassiou, D. A.; and Wasserburg; G. J.: Rb-Sr Ages of Igneous Rocks From the Apollo 14 Mission and the Age of the Fra Mauro Formation. Earth Planet. Sci. Letters, vol. 12, no. 1, Sept. 1971, pp. 36-48.

29-14. Wasserburg, G. J.; and Papanastassiou, D. A.: Age of an Apollo 15 Mare Basalt; Lunar Crust and Mantle Evolution. Earth Planet. Sci. Letters, vol. 13, no. 1, Dec. II, 1971, pp. 97-104.

29-15. Eggleton, R. E.; and Marshall, C. H.: Notes on the Apenninian Series and Pre-Imbrian Stratigraphy in the Vicinity of Mare Humorum and Mare Nubium. In Astrogeological Studies Semiannual Progress Report, February 1961-August 1961, U.S. Geol. Survey, Mar. 1962, pp. 132-137.

29-16. Hackman, R. J.: Stratigraphy and Structure of the Montes Apenninus Quadrangle of the Moon. In Part A of Astrogeological Studies Annual Progress Report, August 1962-July 1963, U.S. Geol. Survey, May 1964, pp. 1-8.

29-17. Eggleton, R. E.: Geologic Map of the Riphaeus Mountains Region of the Moon. U.S. Geol. Survey Misc. Geol. Inv. Map I-458, 1965.

29-18. Wilhelms, D. E.: Fra Mauro and Cayley Formations in the Mare Vaporum and Julius Caesar Quadrangles. In Part A of Astrogeological Studies Annual Progress Report, July 1964-July 1965, U.S. Geol. Survey, Nov. 1965, pp. 13-28.

29-19. Morris, E. C.; and Wilhelms, D. E.: Geologic Map of the Julius Caesar Quadrangle of the Moon. U.S. Geol. Survey Misc. Geol. Inv. Map I-510, 1967.

29-20. Howard, K. A.; and Masursky, Harold: Geologic Map of the Ptolemaeus Quadrangle of the Moon. U.S. Geol. Survey Misc. Geol. Inv. Map I-566, 1968.

29-21. Milton, D. J.: Geologic Map of the Theophilus Quadrangle of the Moon. U.S. Geol. Survey Misc. Geol. Inv. Map I-546, 1968.

29-22. Wilhelms, D. E.: Geologic Map of the Mare Vaporum Quadrangle of the Moon. U.S. Geol. Survey Misc. Geol. Inv. Map I-548, 1968.

29-23. Hackman, R. J.: Geologic Map of the Montes Apenninus Region of the Moon. U.S. Geol. Survey Misc. Geol. Inv. Map I-463, 1966.

29-24. Eggleton, R. E.: Preliminary Geology of the Riphaeus Quadrangle of the Moon and Definition of the Fra Mauro Formation. In Part A of Astrogeological Studies Annual Progress Report, August 1962-July 1963, U.S. Geol. Survey, May 1964, pp. 46-63.

29-25. Schaber, G. G.: Geologic Map of the Sinus Iridum Quadrangle of the Moon. U.S. Geol. Survey Misc. Geol. Inv. Map I-602, 1969 [1970].

29-26. Mutch, Thomas A.: Geology of the Moon: A Stratigraphic View. Princeton Univ. Press, 1970.

29-27. Anon.: Descartes (1:100,000) (lunar topographic map). U.S. Army Topographic Command, 1972.

29-28. Strom, Robert G.: Small Domical Structures in the Ranger Photographs. In Part II of Ranger VIII and IX, JPL-TR-32-800, Mar. 15, 1966, pp. 188-198.

29-29. McCauley, J. F.: Geologic Map of the Hevelius Region of the Moon. U.S. Geol. Survey Misc. Geol. Inv. Map I-491, 1967.

29-30. McCauley, J. F.: The Nature of the Lunar Surface as Determined by Systematic Geologic Mapping. Mantles of the Earth and Terrestrial Planets, S. K. Runcorn, ed., Interscience (London), 1967, pp. 431-460.

29-31. McCauley, J. F.: Geologic Results From the Lunar Precursor Probes. AIAA J., vol. 6, no. 10, Oct. 1968, pp. 1991-1996.

29-32. Stuart-Alexander, D. E.: Geologic Map of the Rheita Quadrangle of the Moon. U.S. Geol. Survey Misc. Geol. Inv. Map I-694, 1971.

29-33. Westfall, John E.: A New Contour Map of the Moon. The Strolling Astronomer, vol. 20, no. 5-6, June 1967, pp. 80-87.

29-34. Sheridan, Michael F.: Fumarolic Mounds and Ridges of the Bishop Tuff, California. Bull. Geol. Soc. Am., vol. 81, no. 3, Mar. 1970, pp. 851-867.

29-35. Milton, D. J.; and Hodges, C. A.: Geologic Maps of the Descartes Region of the Moon, Apollo 16 Pre-Mission Map. U.S. Geol. Survey Misc. Geol. Inv. Map I-748, sheets 1 and 2, 1972.

29-36. Elston, D. P.; Boudette, E. L.; Schafer, J. P.; Muehlberger, W. R.; and Sevier, J. R.: Apollo 16 Field Trips. Geotimes, vol. 17, no. 3, Mar. 1972, pp. 27-30.

29-37. Trask, N. J.; and McCauley, J. F.: Differentiation and Volcanism in the Lunar Highlands–Photogeologic Evidence and Apollo 16 Implications. Earth Planet. Sci. Letters, vol. 14, Mar. 1972, pp. 201-206.

29-38. Wilhelms, D. E.; and Trask, N. J.: Compilation of Geology in the Lunar Equatorial Belt. In Part A of Astrogeological Studies Annual Progress Report, July 1964-July 1965, U.S. Geol. Survey, Nov. 1965, pp. 29-34.

29-39. Elston, D. P.: Geologic Map of the Colombo Quadrangle of the Moon. U.S. Geol. Survey Misc. Geol. Inv. Map I-714, 1972.

29-40. Hartmann, William K.: Radial Structures Surrounding Lunar Basins, I: The Imbrium System. Commun. Lunar Planet. Lab., Univ. of Ariz., vol. 2, no. 24, 1963, pp. 1-15.

29-41. Gilbert, G. K.: The Moon's Face, A Study of the Origin of Its Features. Phil. Soc. Washington Bull., vol. 12, 1893, pp. 241-292.

29-42. Pohn, H. A.; and Offield, T. W.: Lunar Crater Morphology and Relative-Age Determination of Lunar Geologic Units–Part 1, Classification. Geological Survey Research 1970, U.S. Geol. Survey Prof. Paper 700-C, 1970, pp. C153-C162.

29-43. Pohn, H. A.: The Geology of the Tycho Quadrangle of the Moon. U.S. Geol. Survey Misc. Geol. Inv. Map I-713, 1972.

29-44. Wilmarth, V. R.; and McKeown, F. H.: Structural Effects of Ranier, Logan and Blanca Underground Nu-

clear Explosions, Nevada Test Site, Nye County, Nevada. Geological Survey Research 1960, U.S. Geol. Survey Prof. Paper 400-B, 1960, pp. B418-B423.

29-45. Anon.: An Atlas of the Far Side of the Moon, The Lunik III Reconnaissance. N. P. Barbashov, A. A. Mikhailov, and Yu. N. Lipskiy, eds., Nauka Press (Moscow), 1960. (English translation available from Interscience Publishers (New York), 1961.)

29-46. Whitaker, E. A.: Evaluation of the Russian Photographs of the Moon's Far Side. Commun. Lunar Planet. Lab., Univ. of Ariz., vol. I, no. 13, May 18, 1962, pp. 67-71.

29-47. Anon.: Atlas of the Farside of the Moon, Part II. Yu. N. Lipskiy et al., eds., Nauka Press (Moscow), 1967. (Also available as NASA TT F-514, 1969.)

29-48. Whitaker, E. A.: Comparison with Luna III Photographs. In Analysis of Apollo 8 Photography and Visual Observations, ch. 2. NASA SP-201, 1969.

29-49. El-Baz, Farouk: Lunar Igneous Intrusions. Science, vol. 167, no. 3914, Jan. 2, 1970, pp. 49-50.

29-50. El-Baz, Farouk: Lunar Igneous Intrusions. In Analysis of Apollo 10 Photography and Visual Observations, ch. 2. NASA SP-232, 1971.

29-51. Stuart-Alexander, Desiree E.; and Howard, Keith A.: Lunar Maria and Circular Basins—A Review. Icarus, vol. 12, no. 3, May 1970, pp. 440-456.

29-52. Wollenhaupt, W. R.; and Sjogren, W. L.: Comments on the Figure of the Moon Basin on Preliminary Results from Laser Altimetry. The Moon, vol. 4, nos. 3/4, June/July 1972, pp. 337-347.

29-53. Baldwin, Ralph B.: Ranger VIII and Gravity Scaling of Lunar Craters. Science, vol. 157, no. 3788, Aug. 4, 1967, pp. 546-547.

29-54. Baldwin, Ralph B.: The Measure of the Moon. Univ. of Chicago Press, 1963, p. 162.

29-55. Latham, Gary V.; Ewing, Maurice; Press, Frank; Sutton, George; et al.: Passive Seismic Experiment. Sec. 6 of Apollo 14 Preliminary Science Report. NASA SP-272, 1971.

29-56. Arthur, D. W.; and Whitaker, E. A.: Orthographic Atlas of the Moon. G. P. Kuiper, ed., Univ. of Ariz. Press, 1960.

29-57. Winn, F. B.: Surveyor III. In Part II of Surveyor Final Report, JPL-TR-32-1265, June 15, 1968, p. 420.

29-58. Moore, Henry J.: Ranger VIII and Gravity Scaling of Lunar Craters. Science, vol. 159, no. 3812, Jan. 19, 1968, pp. 333-334.

29-59. Anon.: Ranger VII Photographs of the Moon, Part I: Camera "A" Series. NASA SP-61, 1964.

29-60. Anon.: Ranger VII Lunar Chart, RLC 4, Bonpland PQC, Mare Cognitum (1:10,000). Air Force Aeronautical Chart and Information Center, 1964.

29-61. Anon.: Ranger IX Photographs of the Moon, Cameras "A," "B" and "P." NASA SP-112, 1966.

29-62. Anon.: Ranger IX Lunar Chart, RLC 17, Alphonsus GLH (1:2,000 and 1:400). Air Force Aeronautical Chart and Information Center, 1966.

29-63. Moore, H. J.: Craters Produced by Missile Impacts. J. Geophys. Res., vol. 76, no. 23, Aug. 10, 1971, pp. 5750-5755.

29-64. Moore, H. J.; Vischer, W. A.; and Martin, G. L.: Boulder Tracks on the Moon and Earth. U.S. Geol. Survey Prof. Paper 800-B, 1972, pp. B165-B174.

29-65. Hovland, H. J.: Mechanics of Rolling Sphere-Soil Slope Interactions. Ph. D. Thesis, Univ. of Calif. at Berkeley, 1971. (Available from University Microfilms, Ann Arbor, Mich.)

29-66. Oberbeck, Verne R.; and Quaide, William L.: Estimated Thickness of a Fragmental Surface Layer of Oceanus Procellarum. J. Geophys. Res., vol. 72, no. 18, Sept. 15, 1967, pp. 4697-4704.

29-67. Moore, H. J.: Geologic Interpretation of Lunar Data. Earth-Sci. Rev., vol. 7, no. 1, Feb. 1971, pp. 5-33.

29-68. Strom, Robert G.; and Fielder, Gilbert: Multiphase Eruptions Associated with the Lunar Craters Tycho and Aristarchus. Commun. Lunar Planet. Lab., Univ. of Ariz., vol. 8, no. 150, pp. 235-288.

29-69. Shoemaker, E. M.; Batson, R. M.; Holt, H. E.; Morris, E. C.; et al.: Television Observations From Surveyor VII. In Part II of Surveyor VII Mission Report, JPL-TR-32-1264, Mar. 15, 1968, pp. 9-76.

29-70. Moore, H. J.: Large Blocks Around Lunar Craters. In Analysis of Apollo 10 Photography and Visual Observations, ch. 2. NASA SP-232, 1971.

29-71. O'Keefe, J. A.; Cameron, W. S.; and Masursky, Harold: Hypersonic Gas Flow. In Analysis of Apollo 8 Photographs and Visual Observations, ch. 2. NASA SP-201, 1969.

29-72. Guest, J. E.; and Murray, J. B.: A Large Scale Surface Pattern Associated with the Ejecta Blanket and Rays of Copernicus. The Moon, vol. 3, no. 3, Dec. 1971, pp. 326-336.

29-73. Shoemaker, E. M.: Interpretation of Lunar Craters. Physics and Astronomy of the Moon, Zdeněk Kopal, ed., Academic Press (New York), 1962.

29-74. Wright, Fredrick E.; Wright, F. H.; and Wright, Helen: The Lunar Surface: Introduction. Vol. IV of the Solar System, Barbara Middlehurst and Gerard P. Kuiper, eds., Univ. of Chicago Press, 1963, pp. 1-56.

29-75. Baldwin, Ralph B.: The Face of the Moon. Univ. of Chicago Press, 1949.

29-76. Fielder, Gilbert: Lunar Geology. Lutterworth Press (London), 1965.

29-77. Pike, R. J.: Genetic Implications of the Shapes of Martian and Lunar Craters. Icarus, vol. 15, no. 3, Dec. 1971, pp. 384-395.

29-78. Pike, R. J.: Geometric Similitude of Lunar and Terrestrial Craters. Sec. 15 of Proceedings of the 24th International Geological Congress (Montreal), Aug. 21-30, 1972, pp. 41-47.

29-79. Offield, T. W.; and Pohn, H. A.: Lunar Crater Morphology and Relative-Age Determination of Lunar Geologic Units—Part 2, Applications. U.S. Geol. Survey Prof. Paper 700-C, 1970, pp. C163-C169.

29-80. Pike, R. J.: Height-Depth Ratios of Lunar and Terrestrial Craters. Nature Phys. Sci., vol. 234, Nov. 15, 1971, pp. 56-57.

29-81. Anon.: Descartes Lunar Far Side Chart, LMP-2, second ed. (1:5,000,000). Air Force Aeronautical Chart and Information Center, 1970.

29-82. Strom, R. G.; and Whitaker, E. A.: An Unusual Far-Side Crater. In Analysis of Apollo 10 Photography and Visual Observations, ch. 2. NASA SP-232, 1971.

29-83. Howard, Keith: The Apollo 10 Lunar Highlands. In Analysis of Apollo 10 Photography and Visual Observations, ch. 2. NASA SP-232, 1971.

29-84. El-Baz, Farouk; and Roosa, S. A.: Significant Results From Apollo 14 Lunar Orbital Photography. Proceedings of the Third Lunar Science Conference, vol. 1, E. A. King, ed., MIT Press (Cambridge, Mass.), 1972.

29-85. El-Baz, Farouk; Worden, A. M.; and Brand, V. D.: Astronaut Observations From Lunar Orbit and Their Geologic Significance. Proceedings of the Third Lunar Science Conference, vol. 1, E. A. King, ed., MIT Press (Cambridge, Mass.), 1972.

29-86. Shreve, Ronald L.: The Blackhawk Landslide. Geol. Soc. Am. Spec. Paper, no. 108, 1968.

29-87. Gault, D. E.; Adams, J. B.; Collins, R. J.; Kuiper, G. P.; et al.: Lunar Theory and Process. In Part II of Surveyor VIII Mission Report, JPL-TR-32-1264, Mar. 15, 1968, pp. 267-313.

29-88. Lowman, Paul D., Jr.: Lunar Panorama. Weltflugbild Reinhold A. Müller (Feldmeilen/Zurich, Switzerland), 1969.

29-89. Cruikshank, D. P.; and Wood, C. A.: Lunar Rilles and Hawaiian Volcanic Features: Possible Analogues: The Moon, vol. 3, no. 4, Mar. 1972, pp. 412-447.

29-90. Hartmann, William K.: Lunar Crater Counts. VI: The Young Craters Tycho, Aristarchus, and Copernicus. Commun. Lunar Planet. Lab., Univ. of Ariz., vol. 7, no. 119, Mar. 15, 1968, pp. 145-156.

29-91. Hörz, F.: Untersuchungen an Riesgläsern. Beitr. Mineral. Petrogr., vol. 11, no. 7, 1965, pp. 621-661.

29-92. Warner, Jeffery L.: Apollo 14 Breccias: Metamorphic Origin and Classification. Lunar Science–III, Revised Abstracts of Papers Presented at the Third Lunar Science Conference (Houston, Tex., Jan. 10-13, 1972), Carolyn Watkins, ed., Lunar Science Institute Contribution 88, Feb. 18, 1972, pp. 782-784.

29-93. El-Baz, Farouk: The Cinder Field of the Taurus Mountains. Sec. 25 of Apollo 15 Preliminary Science Report, Part I. NASA SP-289, 1972.

29-94. Soderblom, L. A.: The Process of Crater Removal in the Lunar Maria. Sec. 25 of Apollo 15 Preliminary Science Report, Part P. NASA SP-289, 1972.

29-95. Pickering, W. H.: The Moon. Doubleday Page and Company (New York), 1903.

29-96. Quaide, William: Rilles, Ridges and Domes–Clues to Maria History. Icarus, vol. 4, no. 4, Sept. 1965, pp. 374-389.

29-97. Cameron, W. S.: Lunar Sinuous Rilles. Proceedings of the AAS/AIP Symposium on Geological Problems in Lunar and Planetary Research (Las Vegas), Nov. 1968, Jack Green, ed., vol. 25, Am. Astronautical Soc., Tarzana, Calif., 1971.

29-98. Oberbeck, Verne R.; Quaide, William L.; and Greeley, Ronald: On the Origin of Lunar Sinuous Rilles. Mod. Geol., vol. 1, 1969, pp. 75-80.

29-99. Greeley, Ronald: Lava Tubes and Channels in the Lunar Marius Hills. The Moon, vol. 3, no. 3, Dec. 1971, pp. 289-314.

29-100. Strom, R. G.: Lunar Mare Ridges, Rings and Volcanic Ring Complexes. Mod. Geol., vol. 2, 1971, pp. 133-157.

29-101. Tjia, H. D.: Lunar Wrinkle Ridges Indicative of Strike-Slip Faulting. Bull. Geol. Soc. Am., vol. 81, Oct. 1970, pp. 3095-3100.

29-102. Fielder, Gilbert; and Kiang, T.: The Segmental Structure of Wrinkle Ridges and the Lunar Grid System. Observatory, vol. 82, no. 926, Feb. 1962, pp. 8-9.

29-103. Strom, R. G.: Analyses of Lunar Lineaments: I–Tectonic Maps of the Moon. Commun. Lunar Planet. Lab., Univ. of Ariz., vol. 2, nos. 36-39, 1964, pp. 205-216.

29-104. El-Baz, Farouk: New Geological Findings in Apollo 15 Orbital Photography. Proceedings of the Third Lunar Science Conference, vol. 1, F. A. King, ed., MIT Press (Cambridge, Mass.), 1972.

29-105. El-Baz, Farouk: Light-Colored Swirls in the Lunar Maria. Trans. Am. Geophys. Union, vol. 52, no. 11, Nov. 1971, p. 856.

29-106. Hinners, N. W.; and El-Baz, Farouk: Surface Disturbances at the Apollo 15 Landing Site. Sec. 25 of the Apollo 15 Preliminary Science Report, Part E. NASA SP-289, 1972.

29-107. El-Baz, Farouk; and Worden, A. M.: Visual Observations from Lunar Orbit. Sec. 25 of the Apollo 15 Preliminary Science Report, Part A. NASA SP-289, 1972.

29-108. Whitaker, E. A.: Sublimates. Analysis of Apollo 8 Photography and Visual Observations, ch. 2. NASA SP-201, 1969.

29-109. Bowder, David E.; and Hughes, Kenrick J.: Lunar Orbiter Photographic Atlas of the Moon. NASA SP-206, 1971.

29-110. Whitaker, Ewen A.: Lunar Color Boundaries and Their Relationship to Topographic Features: A Preliminary Survey. The Moon, vol. 4, nos. 3/4, June/July 1972, pp. 348-355.

29-111. Whitaker, Ewen A.: Mare Imbrium Lava Flows and Their Relationship to Color Boundaries. Sec. 25 of Apollo 15 Preliminary Science Report, Part M. NASA SP-289, 1972.

29-112. Shorthill, R. W.; and Saari, J. M.: Nonuniform Cooling of the Eclipsed Moon: A Listing of Thirty Prominent Anomalies. Science, vol. 150, no. 3693, Oct. 8, 1965, pp. 210-212.

29-113. Shorthill, Richard W.: Infrared Moon–A Review. J. Spacecraft Rockets, vol. 7, Apr. 1970, pp. 385-397.

29-114. Zisk, S. H.; and Hagfors, T.: Radar Atlas of the Moon, Final Report. Vols. 2 and 3 (NAS 9-7830), MIT (Lincoln Lab.), 1970.

29-115. Thompson, T. W.; Masursky, H.; Shorthill, R. W.; Zisk, S. H.; and Tyler, G. L.: A Comparison of Infrared, Radar and Geologic Mapping of Lunar Craters. Contribution 16, Lunar Sci. Inst., Symposium on the Geophysical Interpretation of the Moon (Houston, Tex.), June 1970.

29-116. Zisk, S. H.; Carr, M. H.; Masursky, H.; Shorthill, R. W.; and Thompson, T. W.: Lunar Apennine-Hadley Region: Geological Implications of Earth-Based Radar and

Infrared Measurements. Science, vol. 173, no. 3999, Aug. 21, 1971, pp. 808-811.

29-117. Shorthill, R. W.; Thompson, T. W.; and Zisk, S. H.: Infrared and Radar Maps of the Lunar Equatorial Region. The Moon, vol. 4, nos. 3/4, June/July 1972, pp. 442-446.

29-118. McCord, Thomas B.; Charette, Michael P.; Johnson, Torrence V.; Lebofsky, Larry A.; et al.: Lunar Spectral Types. J. Geophys. Res., vol. 77, no. 8, Mar. 10, 1972, pp. 1349-1359.

29-119. Head, James W.; and Goetz, Alexander F. H.: Descartes Region: Evidence for Copernican-Age Volcanism. J. Geophys. Res., vol. 77, no. 8, Mar. 10, 1972, pp. 1368-1374.

29-120. Campbell, Malcom J.; and Ulrichs, Juris: Electrical Properties of Rocks and Their Significance for Lunar Radar Observations. J. Geophys. Res., vol. 74, no. 25, Nov. 15, 1969, pp. 5867-5881.

29-121. Wildey, R. L.; and Pohn, H. A.: The Normal Albedo of the Apollo 11 Landing Site and Intrinsic Dispersion in the Lunar Heiligenschein. Astrophys. J., vol. 158, no. 2, Nov. 1969, pp. L129-L130.

29-122. Wildey, R. L.; Pohn, H. A.; Tompkins, D. N.; Calvert, D. R.; et al.: Remote Sensing of the Lunar Photometric Function From the Orbiting Apollo Command Service Module. Proceedings of the Sixth International Symposium on Remote Sensing of Environment, Willow Run Laboratories, Univ. of Mich. (Ann Arbor), 1969, pp. 1291-1303.

29-123. Gehrels, T.; Coffeen, T.; and Owings, D.: Wavelength Dependence of Polarization. III. The Lunar Surface. Astronom. J., vol. 69, no. 10, Dec. 1964, pp. 826-885.

29-124. Wildey, Robert L.; and Pohn, Howard A.: Detailed Photoelectric Photometry of the Moon. Astronom. J., vol. 69, no. 8, Oct. 1964, pp. 619-634.

29-125. Pohn, Howard A.; Wildey, R. L.; and Offield, T. W.: Correlation of the Zero-Phase Brightness Surge (Heiligenschein) with Lunar-Surface Roughness. Sec. 18 of Apollo 14 Preliminary Science Report, Part F. NASA SP-272, 1971.

30. Photogrammetry and Altimetry

The cameras and the laser altimeter carried in the scientific instrument module bay of the Apollo 16 spacecraft represent an integrated system that is capable of yielding high-quality quantitative data on the Moon. Laser altimetry, when combined with a knowledge of spacecraft positions, yields data on the shape and size of the Moon, the topography on a grand scale, and the displacement of the center of mass with respect to the center of figure of the Moon. Photogrammetric analyses of the stereophotographs obtained with the metric and panoramic cameras provide data on the topography of the Moon at the finer scales. Such quantitative data on the physical shape of the Moon and the topography of lunar features at a variety of scales provide fundamental information required to establish and test geophysical and geologic theories of lunar origin and processes.

This section contains preliminary results obtained from the laser altimeter data and the orbital photographs. The results of the laser altimeter are reported in part A, and photogrammetric mapping is described in part B. In part C, photogrammetric results on frequencies of lunar slopes are compared with radar data. The initial photogrammetric results reported here will be refined when more precise data on camera orientations become available.

PART A

APOLLO 16 LASER ALTIMETER

W. R. Wollenhaupt[a] *and W. L. Sjogren*[b]

The laser altimeter measures precise altitudes of the command and service module (CSM) above the lunar surface and can function either with the metric (mapping) camera or independently. In the camera mode, the laser altimeter ranges at each exposure time, which varies between 20 and 28 sec (i.e., 30 to 43 km on the lunar surface). In the independent mode, the laser altimeter ranges every 20 sec.

These altitude data and the spacecraft attitudes that are derived from simultaneous stellar photography are used to constrain the photogrammetric reduction of the lunar surface photographs when cartographic products are generated. In addition, the altimeter measurements alone provide broad-scale topographic relief around the entire circumference of the Moon. These data are useful in investigating the selenodetic figure of the Moon and may provide information regarding gravitational anomalies on the lunar far side.

[a]NASA Manned Spacecraft Center.
[b]NASA Jet Propulsion Laboratory.

The Instrument

The laser altimeter weighs approximately 22.5 kg (50 lb) and consists of a ruby laser, transmitting and receiving optics and telescopes, and a range counter. When a signal is received from the control circuit (ref. 30-1), the pulse-forming network discharges through flashlamps, producing a light pulse which primes the ruby rod such that light amplification occurs. A Q-switch is used to transfer the light pulse to the output resonant reflector. The output of the laser at this point has a diameter of 0.635 cm (0.25 in.) and a beam width of 4.8 mrad. A 16-power telescope then expands the beam to a 10.16-cm (4-in.) diameter with a beam width of 0.3 mrad. This range corresponds to 30 m on the lunar surface for a spacecraft altitude of 100 km. A portion of the output is applied to a photodiode to generate a start pulse, which is sent to the range counter through a delay line. The delay line is calibrated to compensate for the delay through the receiver photomultiplier and the video amplifier. The range counter counts increments of 6.67 nsec (providing a 1-m resolution) supplied by a 149.8962-MHz

crystal oscillator. The return pulse, which is reflected from the lunar surface, is applied to the photomultiplier tube through the receiver telescope. The electrical output of the photomultiplier, amplified by the video amplifier, stops the range counter.

Mission Operation

During the Apollo 16 mission, laser altimeter measurements were obtained during lunar revolutions 3 and 4, 17 and 18, 28 and 29, 37 to 39, 47 and 48, 60, and 63. Most of the time, the altimeter was operating under mapping camera control. At least four of the data periods contained measurements made during the entire revolution plus some overlap. A fifth period, revolutions 37 to 39, contained measurements made during almost two consecutive revolutions. Although a system modification had been incorporated to avoid the short lifetime of the instrument experienced during the Apollo 15 mission, performance was somewhat degraded during the second operating period. The laser altimeter continued to degrade during subsequent operating periods and stopped recording valid data during revolution 63. A total of 2372 laser firings was made during the mission; however, only 69 percent of the total was either received or indicated as valid range measurements. This figure may be too pessimistic because some of the data that were indicated as invalid appeared to contain valid or at least reasonable range measurements. Hopefully, much more of the data can be recovered after minor computer program modifications have been completed.

Analytical Techniques

An accurate estimate of spacecraft position with respect to the Moon is required to interpret the altimeter measurements for the purpose of selenodetic figure investigation. This estimate was made by reducing the Earth-based Doppler radio tracking data of the orbiting CSM. These are essentially line-of-sight velocity measurements taken every 10 sec by at least two tracking stations of the space-flight tracking and data network. The Doppler data are processed using a weighted least-squares technique to determine a unique orbit for the CSM. A theoretical model of the Earth-Moon system is included in the computations. The accuracy of the determined orbit limits the accuracy of the laser altimeter results. The dominant error source in the orbit determination and trajectory prediction process is the mathematical model used to describe the lunar gravitational effects. No known mathematical model accurately describes the observed gravitational effects, at least in a global sense. (The far side has never been measured.) The radial position uncertainty is approximately 400 m.

After the spacecraft orbit has been determined, the laser altimeter measurements are subtracted from the corresponding selenocentric radius vectors of the CSM orbit to obtain complete lunar topographic profiles. Because the CSM orbit is a dynamic solution about the center of gravity (c.g.) of the Moon, the profile is referenced to the c.g. rather than the center of the optical figure. There are corrections that should be applied to the laser measurements to correct for timing and laser pointing to adjust the slant range measurements to altitudes above the local vertical. The data required to make these corrections are usually not available until several months after the mission. However, these corrections should not significantly change the following results.

Preliminary Results

The general lunar surface coverage for both the Apollo 15 and 16 missions is shown in figure 30-1. The topographic profile resulting from processing the altimeter measurements as outlined previously is presented in figure 30-2. There is very good agreement between the Apollo 15 and 16 altitude measurements where the two trajectories crossed, particularly in the flat region of Mare Smythii. The profiles of the near-side basins appear relatively flat. The central highlands near the Apollo 16 landing site are a definite high region, with the landing site having a radius very close to the presently accepted mean radius of 1738 km. Hertzsprung on the lunar far side is a depressed basin with respect to surrounding terrae. The large far-side depression observed during the Apollo 15 mission (refs. 30-2 and 30-3) does not appear in the Apollo 16 data. Instead, a rather extensive mountainous region is noted on the Apollo 16 far-side profile.

A preliminary estimate of shape parameters was obtained by performing an additional least-squares regression using an offset ellipse and a circle. The results from these solutions are shown in table 30-I with the corresponding Apollo 15 results (refs. 30-2 and 30-3). The differences between the data from the

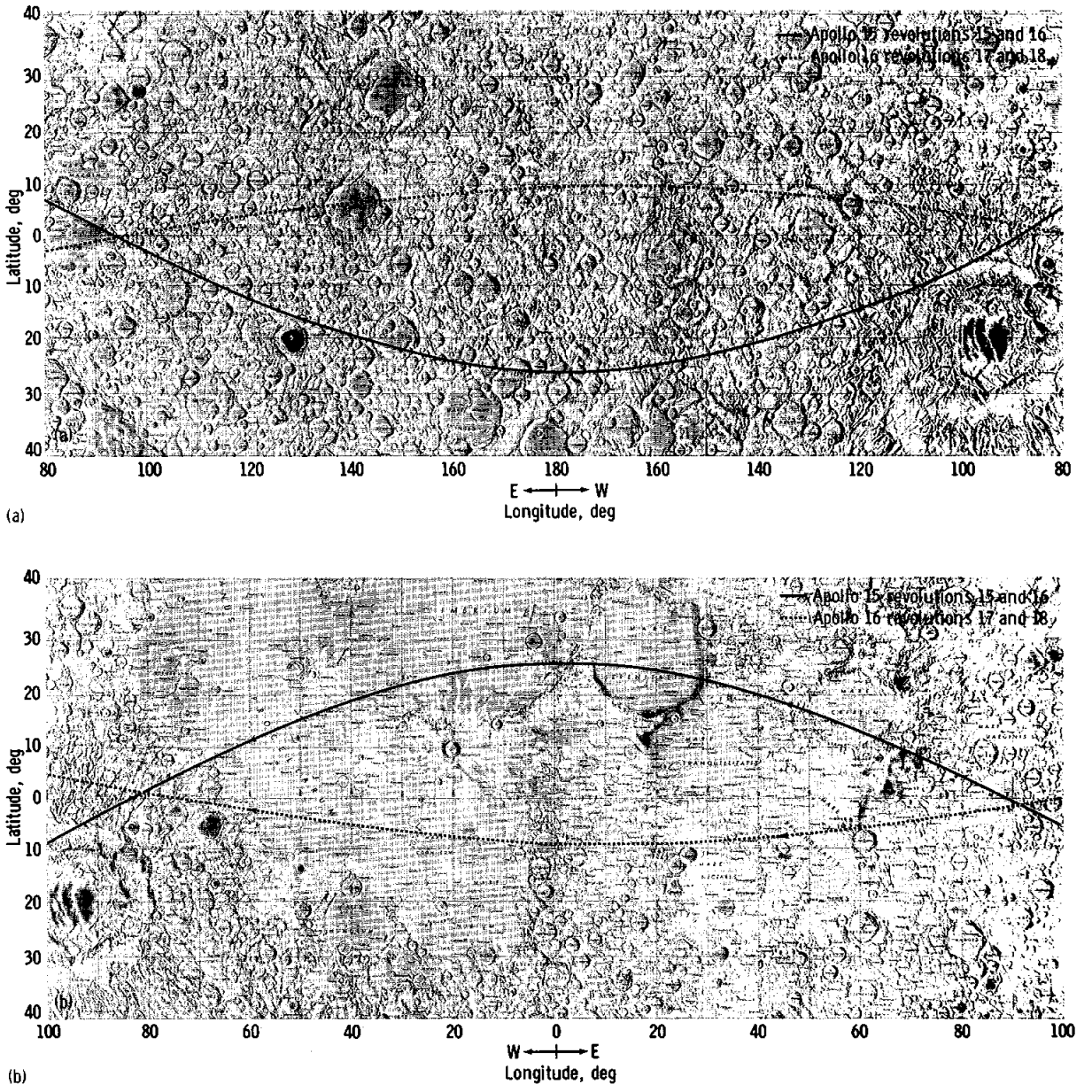


FIGURE 30-1.–Altimeter measurement trace. (a) Lunar far side. (b) Lunar near side.

two missions are expected because of the differences in the major topographic features that were measured. (The Apollo 15 CSM passed over the large ringed basins of Imbrium, Serenitatis, Crisium, Smythii, and a large far-side depression.) The X-axis is greater than the Y-axis on the Apollo 16 ellipse solution, which is in general agreement with presently accepted values. The best radius circle for the Apollo 16 data is 1737.8 km, which is only 0.2 km different from the presently accepted value of 1738.0 km. The offsets from all four solutions are in reasonable agreement. They indicate that the c.g. is approximately 2 km closer to the Earth than the center of the optical figure and is displaced approximately

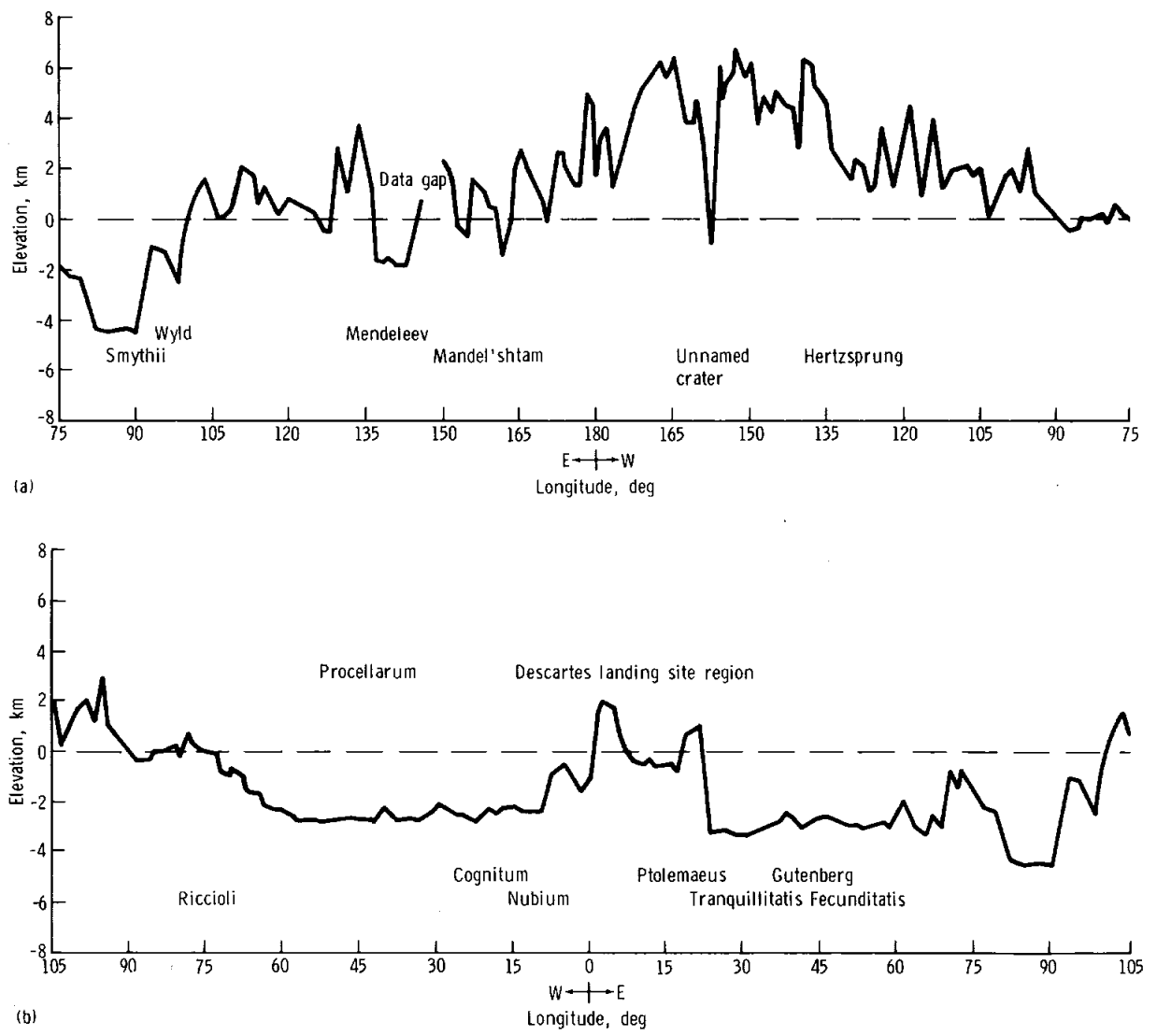


FIGURE 30-2.–Apollo 16 altitude profile and radius deviations from spherical Moon. (a) Lunar far side. (b) Lunar near side.

TABLE 30-I.–Selenodetic Figure Estimates

Shape	*Data*	*x, km (a)*	*y, km (b)*	*Δx, km (c)*	*Δy, km (c)*
Ellipse	Apollo 15 laser	1736.4	1737.7	-1.79	-1.15
Ellipse	Apollo 16 laser	1738.7	1736.7	-2.52	-1.03
Circle	Apollo 15 laser	1737.1	–	-1.76	-1.19
Circle	Apollo 16 laser	1737.8	–	-2.78	-1.00

[a]Toward the Earth.
[b]East in the equatorial plane.
[c]Offset in x and y coordinates from c.g. to optical center.

1 km eastward. The two complete laser profiles, measured along two distinctly different ground tracks, appear to remove all doubt that a center-of-figure to center-of-gravity offset exists. There is not enough information in the data to obtain solutions in a polar (z) direction.

Acknowledgments

The authors wish to thank O. R. Bergman, H. H. Cunningham, and R. Thomas of TRW Systems, Houston, Texas, for their support in developing the data retrieval and analysis programs used for the laser altimeter data.

PART B

PHOTOGRAMMETRY USING APOLLO 16 ORBITAL PHOTOGRAPHY

Sherman S. C. Wu,[a] Francis J. Schafer,[a] Raymond Jordan,[a] and Gary M. Nakata[a]

The Apollo 15 and 16 metric and panoramic cameras have provided photographs for accurate topographic portrayal of the lunar surface using photogrammetric methods. In turn, quantitative morphologic analyses of topographic results are invaluable aids in the interpretation of the geologic processes.

Nine stereoscopic models of Apollo 16 metric photographs and three models of panoramic photographs were evaluated photogrammetrically in support of the Apollo 16 geologic investigations. Four of the models were used to collect profile data for crater morphology studies (part K of sec. 29); three models were used to collect elevation data for the frequency distributions of lunar slopes (part C of this section); one model was used to prepare a map of the Apollo 16 traverse area (sec. 6 of this report); and one model was used to determine elevations of the Cayley Formation (part B of sec. 29). The remaining three models were used to test photogrammetric techniques using oblique metric and panoramic camera photographs.

In the course of this work, two preliminary contour maps were compiled and a high-oblique metric photograph was rectified. A discussion of these follows.

Methods and Results

Photogrammetric data were extracted from the metric camera photographs using the AP/C analytical plotter of the U.S. Geological Survey in Flagstaff, Arizona. The AS-11-A1 plotter at the NASA Manned Spacecraft Center was used for extracting photogrammetric data from the panoramic photographs. Because photographic support data for the Apollo 16 photographs were not available, scales for the stereoscopic models were determined from Lunar Orbiter postmission support data, and the models were leveled by assuming that extensive plains were, in fact, level. Coordinates obtained from the metric camera models were transferred to the panoramic camera models and used for control.

The quality of the photographs was determined using repeatability of elevation measurements for selected points as a criterion (table 30-II). These measurements indicate that the quality of the photographs is excellent and that good topographic data can be derived from the photographs when the Apollo 16 photographic support data become available and analytical aerotriangulation networks are completed.

A test was conducted to illustrate that valuable topographic data can be obtained from the high-oblique photographs. For the test, second-generation master transparencies of metric camera photographs of Alphonsus Crater (Apollo 16 metric camera frames 2477 and 2478) were placed in the AP/C plotter, scaled using Lunar Orbiter support data, and oriented assuming that the floor of Alphonsus is level. The tilt angle (approximately 43°) of the high-oblique photographs is so large that the horizon is shown (fig. 30-3). Despite the large tilt angle, the average standard error of repeatability of elevation measurements within the area outlined in figure 30-3 was near 10.5 m. Thus, it may be possible to attain a contour

[a]U.S. Geological Survey.

TABLE 30-II.–Average Standard Errors

Model	*Plotter*	*No. of operators*	*Average standard errors, m*	
			Horizontal	*Vertical*
Metric frames 2167 and 2168	AP/C	2	--	8.40
Metric frames 2931 and 2932	AP/C	2	--	6.40
Panoramic frames 4558 and 4563	AP/C	2	--	.67
Metric frames 2811 and 2812	AP/C	2	12.11	15.49
Metric frames 2931 and 2932	AP/C	2	5.28	16.45
Metric frames 2167 and 2168	AP/C	2	4.38	11.51
Metric frames 1870 and 1871	AP/C	3	6.52	6.22

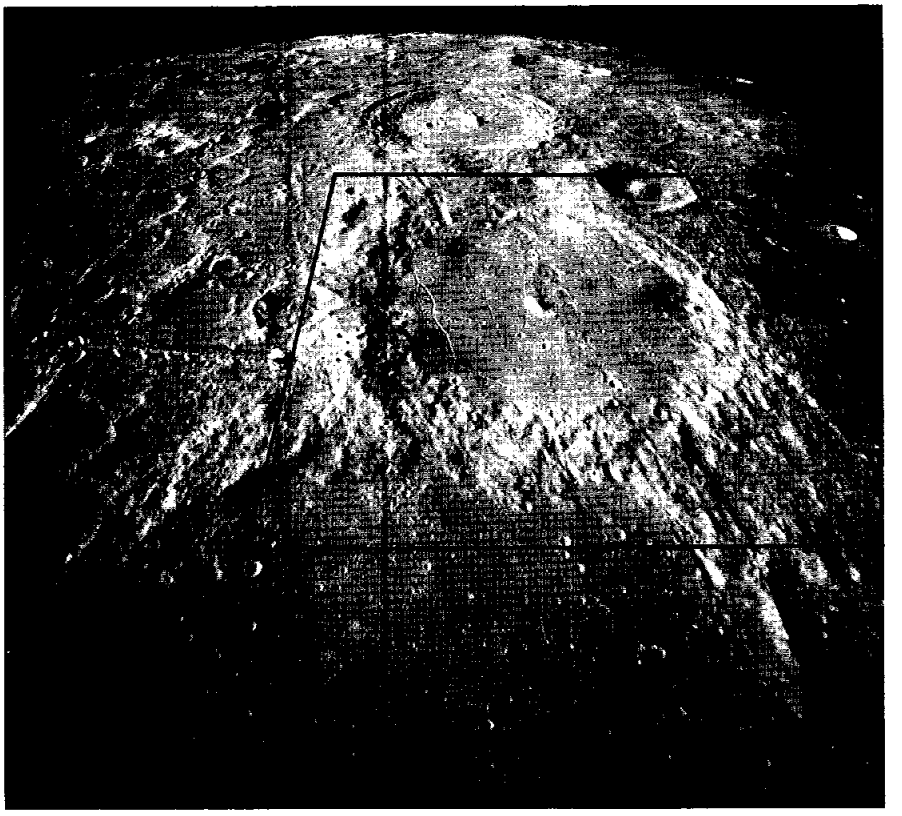


FIGURE 30-3.–Apollo 16 metric camera photograph 2477 used in compiling the topographic map of the floor of Alphonsus Crater shown in figure 30-4.

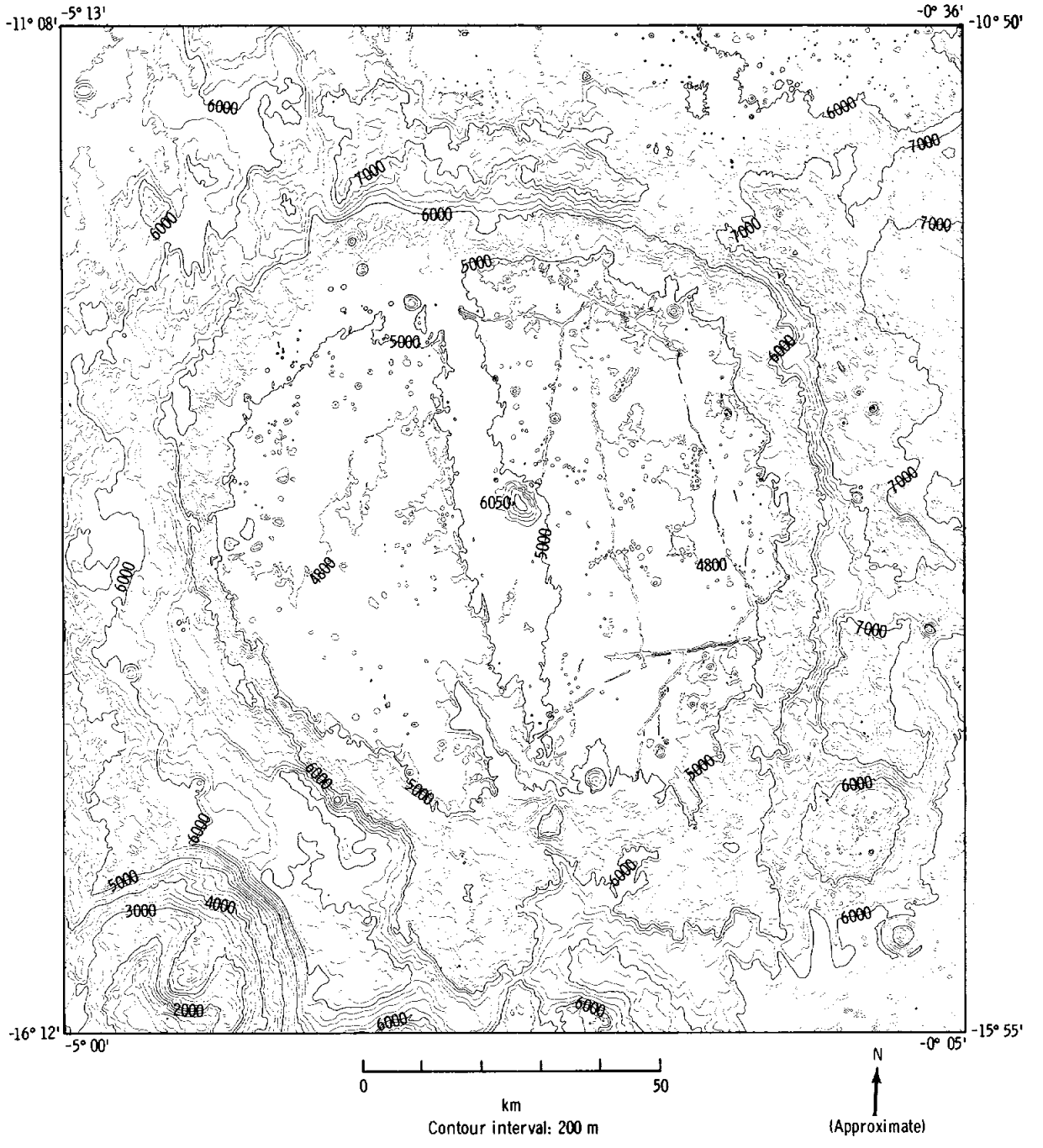


FIGURE 30-4.—Contour map of Alphonsus Crater (compiled from Apollo 16 metric camera frames 2477 (fig. 30-3) and 2478 (fig. 30-7)).

interval of 100 m when more precise data become available. To illustrate the topographic data that can be obtained from such high-oblique photographs, a contour map of Alphonsus Crater was compiled at a scale of 1:250,000 with a contour interval of 200 m (fig. 30-4).

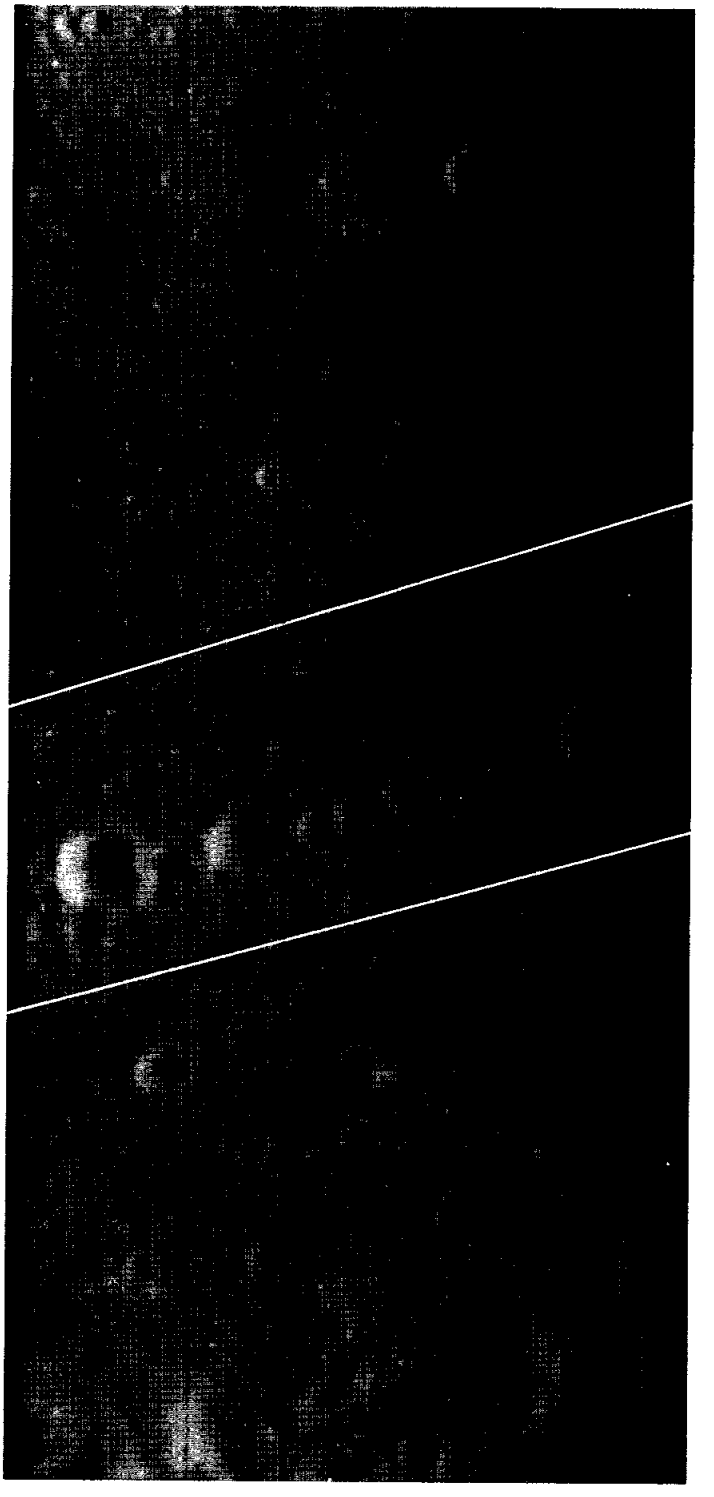


FIGURE 30-5.–Panoramic photograph used in compiling the map of the Davy Crater chain shown in figure 30-6 (Apollo 16 pan camera frame 5397).

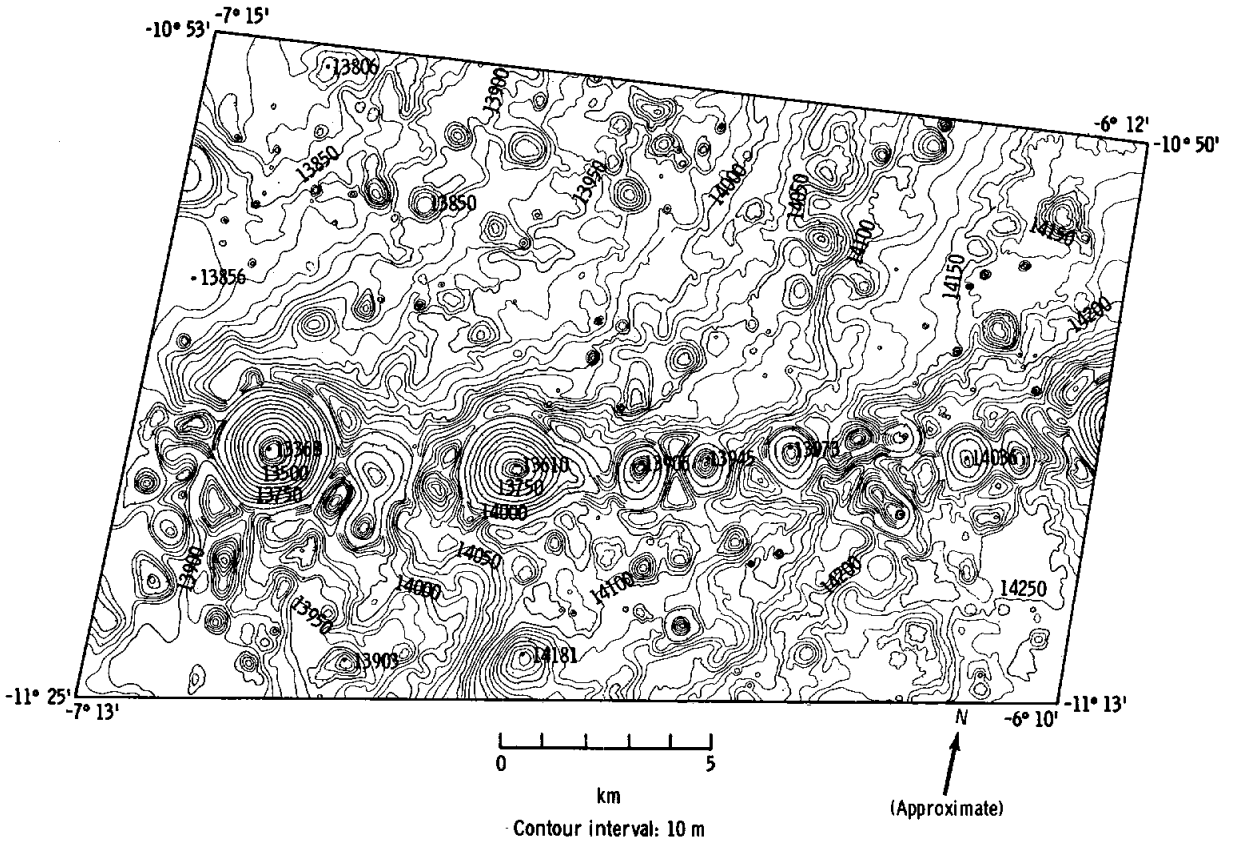


FIGURE 30-6.–Contour map of the Davy Crater chain (compiled from Apollo 16 pan camera frames 5392 and 5397).

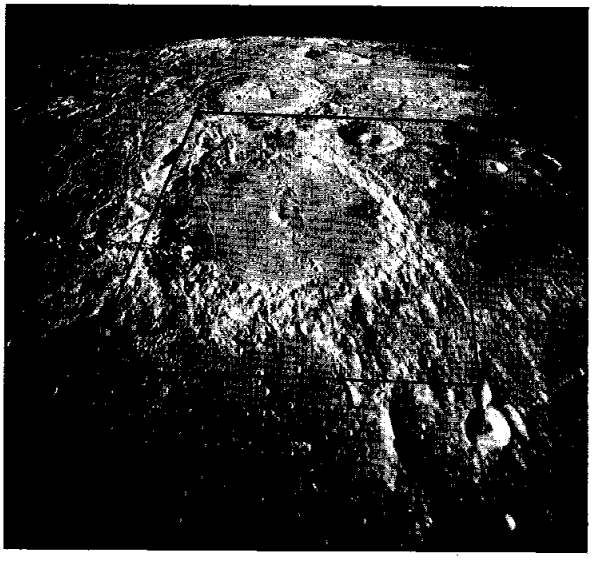


FIGURE 30-7.–Unrectified, oblique photograph of Alphonsus Crater (Apollo 16 metric camera frame 2478).

Panoramic camera photographic quality was demonstrated using Apollo 16 pan camera frames 5392 and 5397 (fig. 30-5) and the AS-11-A1 plotter. The standard error of repeatability of elevation measurements for this model was 1.86 m, which indicates that small contour intervals can be achieved. A contour map of the Davy Crater chain was then compiled at a scale of 1:50,000 and a small contour interval of 10 m. The contour map is shown in figure 30-6, where it can be seen that data on the slopes and shapes of the craters and their flanks can be extracted from the map, together with planimetric data.

A high-oblique metric photograph of Alphonsus Crater, Apollo 16 metric camera frame 2478 (fig. 30-7), was successfully rectified on a Bausch and Lomb rectifier using a 1:250,000-scale topographic map of Alphonsus Crater for control. Two stages of rectification were required. The resulting rectified photograph is shown in figure 30-8, where it can be

seen that displacements caused by surface relief cannot be rectified using single photograph techniques.

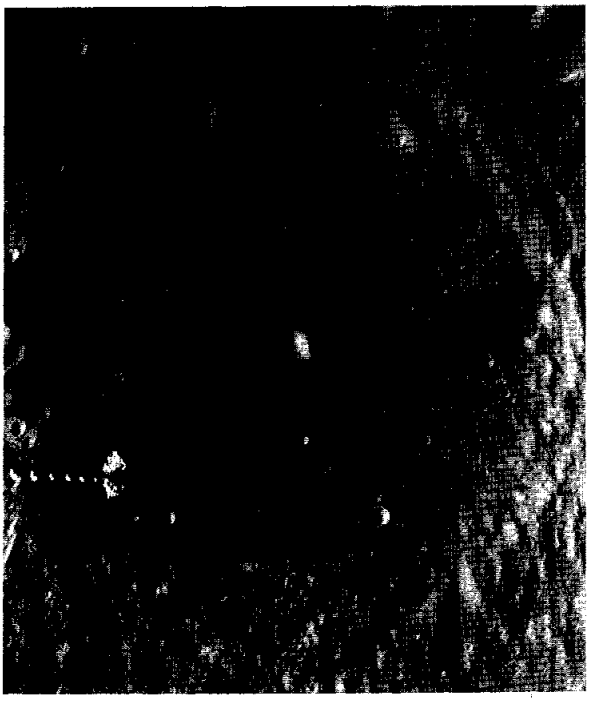


FIGURE 30-8.–Rectified portion of the oblique photograph shown in figure 30-7.

Conclusions

From this photogrammetric work in support of geologic investigations of the lunar surface, the following conclusions were reached.

(1) Oblique metric camera photographs can be used satisfactorily for topographic compilation.

(2) High-oblique photographs can be rectified to obtain planimetric data.

(3) With a precision analytical plotter, the use of second-generation master transparencies will result in average standard errors of repeatability of almost 7 m for horizontal measurement and 10 to 11 m for vertical measurements on oblique metric photography.

(4) Because the average standard error of elevation measurements ranges from 0.6 to 1.9 m, detailed topographic data may be extracted from panoramic photographs.

Acknowledgments

The authors wish to thank Harold Masursky for his valuable suggestions and Victoria Lobato and the Illustrations Unit at the Center of Astrogeology for the preparation of data and maps.

PART C

FREQUENCY DISTRIBUTIONS OF LUNAR SLOPES

Sherman S. C. Wu[a] *and H. J. Moore*[a]

The metric and panoramic cameras aboard the Apollo 16 spacecraft provided photographs on which photogrammetric techniques may be used to obtain precise measurements of horizontal distances and elevations. These measurements may in turn be used to obtain slope-frequency distributions of lunar surfaces at various slope lengths and for various types of terrain and geologic map units (ref. 30-4). Bistatic radar and photoclinometric methods have also been used to obtain slope-frequency distributions of lunar surfaces. The problem arises as to how well these varied methods correlate with one another (ref. 30-5).

Tyler et al. (ref. 30-6) found that estimates of rms slopes obtained with the radar of 2.2-m wavelength aboard Explorer 35 generally correlated with photoclinometric estimates of algebraic standard deviations of slope-frequency distributions for slope lengths of

[a]U.S. Geological Survey.

approximately 500 m. They also found fair agreement between the photogrammetrically determined algebraic standard deviation (1.33°) of a mare surface in Flamsteed and the bistatic radar rms slope (1.07°). Also, it was noted that the rms slopes of the Censorinus highlands were very large and those in mare areas such as the Sea of Fertility were low.

Photogrammetric data have been obtained from Apollo 16 metric photographs for both the Censorinus highlands and the Sea of Fertility at a slope length of approximately 500 m. Data for the Descartes landing site were also collected at a slope length of 25 m to test the capability of the panoramic camera.

Method

Three stereoscopic models using second-generation positive-master transparencies were processed in an AP/C precision analytical plotter that is capable of measurements of 1 μm. Two of the models used Apollo 16 metric camera frames 2167 and 2168 (Censorinus, fig. 30-9(a)) and frames 2931 and 2932 (Sea of Fertility, fig. 30-9(b)). The third model used Apollo 16 pan camera frames 4558 and 4563 (Descartes landing site, fig. 30-9(c)). Because photographic support data for Apollo 16 photography are not yet available, the metric camera stereoscopic models were scaled from Lunar Orbiter postmission support data, and, for the Descartes area, from premission topographic maps prepared by the U.S. Army Topographic Command. The level at the Descartes landing site was established using the premission topography. The mare surface was arbitrarily assumed to be level in the Sea of Fertility, and the Censorinus model was leveled arbitrarily.

In each of these models, more than 1000 elevations were measured at equally spaced intervals along the traverse lines shown in figure 30-9. An average of three readings was used to obtain each elevation. For the metric camera photographs, the intervals were approximately 500 m, and for the panoramic camera photographs, the interval was approximately 25 m. Intervals and scales are shown in table 30-III. Averaged standard errors for elevation readings were ±8.4 m for the Censorinus highlands; ±6.40 m for the Sea of Fertility; and ±0.67 m for the Descartes landing site. Slopes and other statistical data were then computed by a program on the PDP-11 computer.

Results

The resulting mean slopes, estimated standard deviations, and slope-frequency distributions are shown in figure 30-10 and tables 30-III and 30-IV. In qualitative agreement with the results from bistatic radar (ref. 30-6), the Censorinus highlands are substantially rougher than the Sea of Fertility. This is not surprising because visual inspection of the imagery yields the same result. However, quantitatively, the estimates differ significantly. For the Censorinus highlands, the average absolute slope is approximately 7.8°, and the estimated algebraic standard deviation is approximately 9.1°. For the Sea of Fertility, the average absolute slope is approximately 3.2°, and the

TABLE 30-III.–Parameters and Results for Slope-Frequency Distribution Obtained From Three Stereoscopic Models Using Apollo 16 Photographs

Parameters	Model		
	Censorinus highlands	Sea of Fertility	Descartes landing site
Model scale	1:1,511,824	1:1,440,630	1:192,539
Number of slopes	1001	1031	1005
Mean slope, deg	7.82	3.21	5.54
Standard error of mean slope, deg	.04	.03	.07
Slope base length, m	505.36	499.69	25.08
Averaged standard error of one elevation reading, m	8.40	6.40	.67

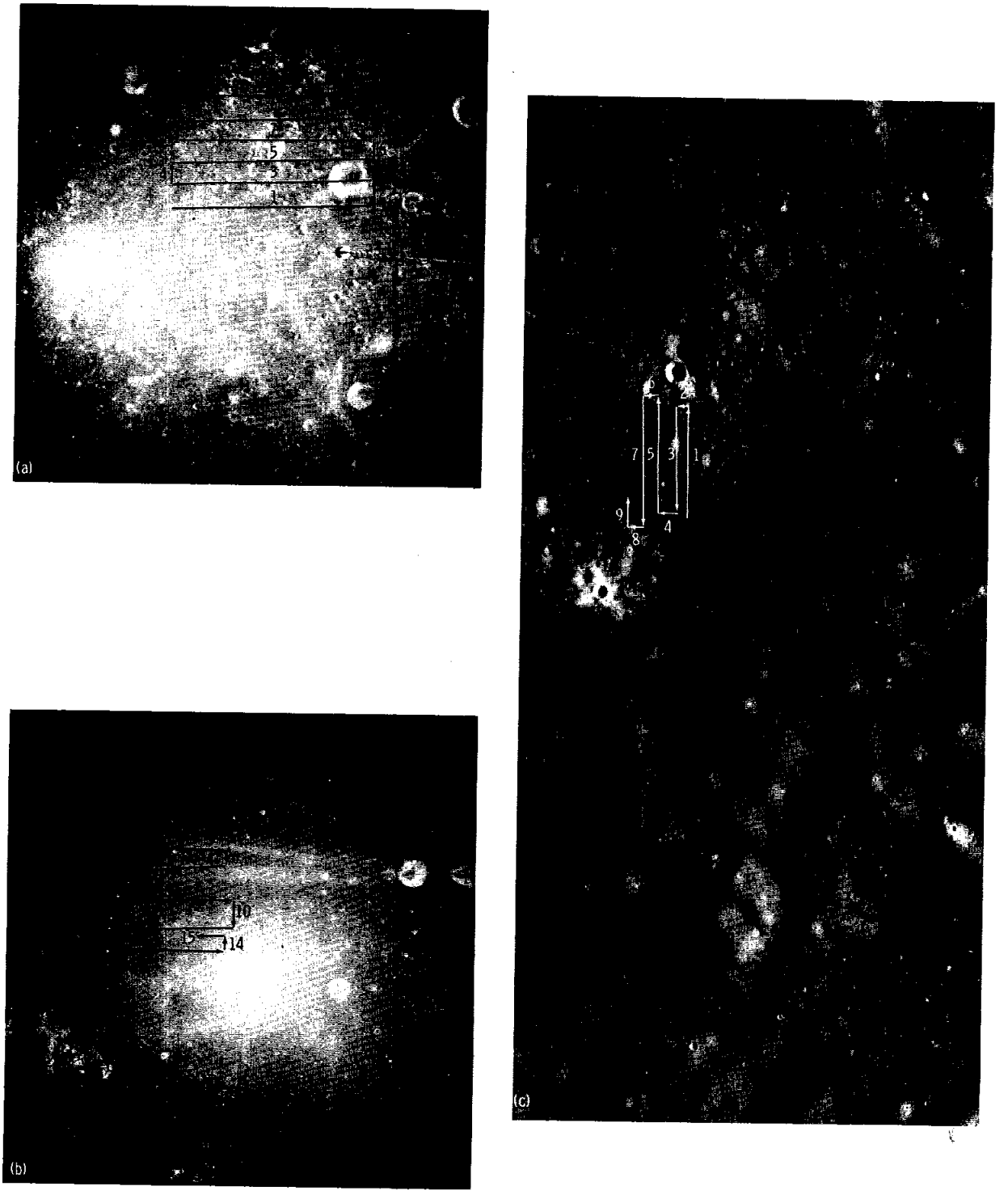


FIGURE 30-9.–Apollo 16 photographs showing traverses along which elevation data were obtained. (a) Censorinus highlands (Apollo 16 metric camera frame 2167). (b) Sea of Fertility (Apollo 16 metric camera frame 2931). (c) Descartes landing site (Apollo 16 pan camera frame 4558).

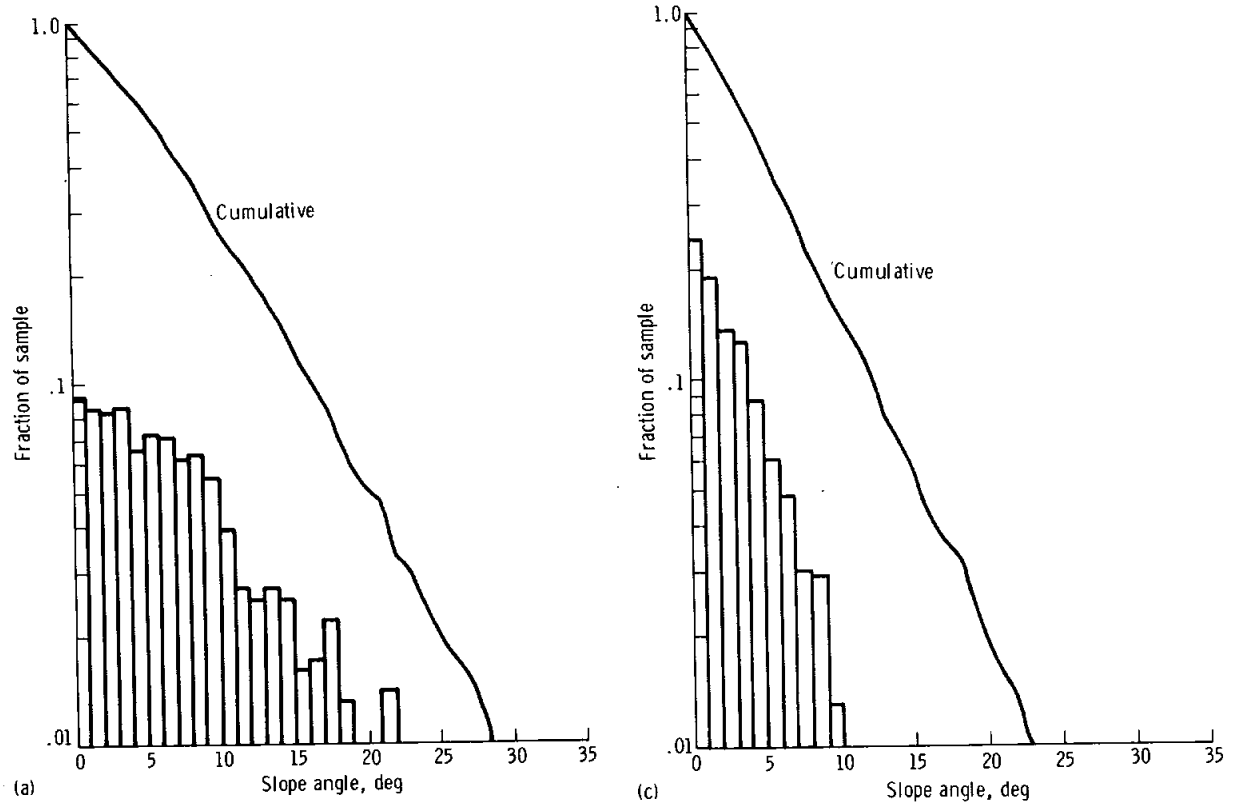


FIGURE 30-10.–Apollo 16 slope-frequency distribution. (a) Censorinus highlands at a slope length of approximately 500 m. (b) Sea of Fertility at a slope length of approximately 500 m. (c) Descartes landing site at a slope length of approximately 25 m.

estimated algebraic standard deviation is approximately 3.8°. The rms slopes of the bistatic radar should compare with the estimated algebraic standard deviation from the photogrammetry for a 500-m slope length. As shown in table 30-V, the photogrammetrically determined values are significantly larger by a factor of 1.5 to 1.6. Photogrammetry also indicates rougher terrain than does photoclinometry, as was found previously (ref. 30-5).

The slope-frequency distribution for the Descartes landing site (slope length, 25 m) yields a mean slope of approximately 5.5° and an estimated algebraic standard deviation of approximately 6.3°. The rms slopes from the S-band radar aboard the Apollo 14 spacecraft should be comparable for this slope length.

TABLE 30-IV.–Slope-Frequency Distributions Computed From Photogrammetric Measurements of Three Areas Photographed During the Apollo 16 Mission

Slope class, deg	Model								
	Censorinus highlands			Sea of Fertility			Descartes landing site		
	Frequency	Relative frequency, percent	Accumulative frequency, percent	Frequency	Relative frequency, percent	Accumulative frequency, percent	Frequency	Relative frequency, percent	Accumulative frequency, percent
>0 to ≤1	92	9.2	9.2	255	24.7	24.7	147	14.6	14.6
>1 to ≤2	84	8.4	17.6	204	19.8	44.5	128	12.7	27.4
>2 to ≤3	83	8.3	25.9	139	13.5	58.0	116	11.5	38.9
>3 to ≤4	85	8.5	34.4	129	12.5	70.5	96	9.6	48.5
>4 to ≤5	65	6.5	40.9	90	8.7	79.2	96	9.6	58.0
>5 to ≤6	72	7.2	48.1	62	6.0	85.3	78	7.8	65.8
>6 to ≤7	71	7.1	55.2	49	4.8	90.1	59	5.9	71.6
>7 to ≤8	61	6.1	61.2	31	3.0	93.0	56	5.6	77.2
>8 to ≤9	63	6.3	67.5	30	2.9	95.9	44	4.4	81.6
>9 to ≤10	54	5.4	72.9	13	1.3	97.2	35	3.5	85.1
>10 to ≤11	39	3.9	76.8	9	.9	98.1	20	2.0	87.1
>11 to ≤12	27	2.7	79.5	3	.3	98.4	19	1.9	89.0
>12 to ≤13	25	2.5	82.0	6	.6	98.9	23	2.2	91.2
>13 to ≤14	27	2.7	84.7	3	.3	99.2	19	1.9	93.1
>14 to ≤15	25	2.5	87.2	1	.1	99.3	13	1.3	94.4
>15 to ≤16	16	1.6	88.8	2	.2	99.5	14	1.4	95.8
>16 to ≤17	17	1.7	90.5	–	–	–	6	.6	96.4
>17 to ≤18	22	2.2	92.7	1	.1	99.6	3	.3	96.7
>18 to ≤19	13	1.3	94.0	1	.1	99.7	8	.8	97.5
>19 to ≤20	9	.9	94.9	1	.1	99.8	6	.6	98.1
>20 to ≤21	4	.4	95.3	1	.1	99.9	3	.3	98.4
>21 to ≤22	14	1.4	96.7	1	.1	100.0	3	.3	98.7
>22 to ≤23	3	.3	97.0	–	–	–	4	.4	99.1
>23 to ≤24	6	.6	97.6	–	–	–	3	.3	99.4
>24 to ≤25	4	.4	98.0	–	–	–	–	–	–
>25 to ≤26	3	.3	98.3	–	–	–	2	.2	99.6
>26 to ≤27	2	.2	98.5	–	–	–	1	.1	99.7
>27 to ≤28	3	.3	98.8	–	–	–	–	–	–
>28 to ≤29	4	.4	99.2	–	–	–	1	.1	99.8
>29	8	.8	100.0	–	5.0	–	2	.2	100.0

TABLE 30-V.–Slope Parameters From Apollo 16 Photogrammetry Compared to Bistatic Radar

Site	*Bistatic radar slope, deg (a)*	*Apollo 16 photogrammetric slope, deg (b)*
Censorinus highlands	[c]6	[d]≈9.1
Sea of Fertility	[c]2.4	[d]≈3.8
Descartes landing site	[e]5.6 to 6.0	[f]≈6.3

[a]Radar results are given as rms slopes.

[b]Apollo 16 results are given as estimated algebraic standard deviation of slopes.

[c]Explorer 35 bistatic radar (ref. 30-6).

[d]Slope length, 500 m.

[e]Apollo 14 S-band bistatic radar in Cayley Plains northwest of landing site at 8.38° S 15.08° E and 8.33° S 14.74° E (preliminary estimates by G. L. Tyler, 1971).

[f]Slope length, 25 m.

Table 30-V lists preliminary radar results for plains near the landing site that Milton (ref. 30-7) mapped geologically the same (Cayley Formation). The radar rms slopes are lower but are reasonably close to the photogrammetric results.

Discussion

Differences between the radar rms slopes and photogrammetrically derived algebraic standard deviations may result for several reasons. The radar may penetrate the actual surface and yield data on some surface or combinations of surfaces beneath the actual surface. However, photogrammetric results do not necessarily represent the actual surface. For example, the average standard error of elevation for the Sea of Fertility was ±6.40 m and the slope length was near 500 m. Thus, if the surface had been perfectly flat, photogrammetrically derived elevations would yield a frequency distribution of slopes although the hypothetical surface was perfectly flat. The fictitious roughness obtained for the hypothetical flat surface using photogrammetry would be small, and the algebraic standard deviation would be between 0.75° and 1.5°. The fictitious roughness introduced would be strongly dependent on the ratio of the standard error and the slope length.

Analyses of the problem of correlation between bistatic radar rms slopes and photogrammetrically derived algebraic standard deviations are in progress, and the effect of the standard error on the resulting slope-frequency distributions is not presently understood. However, one would expect reasonable agreement between the bistatic radar results and photogrammetrically derived results.

Acknowledgments

The authors wish to thank Francis J. Schafer, Ray Jordan, Gary Nakata, Bobby C. Philpott, and Alfred G. Dahl for their valuable assistance. Without their help, this paper could not have been written.

References

30-1. Anon.: Operating and Instruction Manual for Laser Altimeter. RCA (Burlington, Mass.), CR70-588-14J1, 1970.

30-2. Roberson, F. I.; and Kaula, W. M.: Apollo 15 Laser Altimeter. Sec. 25 of the Apollo 15 Preliminary Science Report, Part D. NASA SP-289, 1972.

30-3. Wollenhaupt, W. R.; and Sjogren, W. L.: Comments on the Figure of the Moon Based on Preliminary Results From Laser Altimetry. The Moon, vol. 4, nos. 3/4, June/July 1972, pp. 337-347.

30-4. Pike, Richard J.: Preliminary Quantitative Terrain-Analysis Results from Three Apollo 10 Photographs. Analysis of Apollo 10 Photography and Visual Observations. NASA SP-232, 1971, pp. 5-14.

30-5. Lucchitta, B. K.: Evaluation of Photometric Slope Deviation. Analysis of Apollo 10 Photography and Visual Observations. NASA SP-232, 1971, pp. 31-35.

30-6. Tyler, G. Leonard; Simpson, Richard A.; and Moore, Henry J.: Lunar Slope Distributions: Comparison of Bistatic-Radar and Photographic Results. J. Geophys. Res., vol. 76, no. 11, Apr. 10, 1971, pp. 2790-2795.

30-7. Milton, D. J.: Geologic Map of the Theophilus Quadrangle of the Moon. U.S. Geol. Survey Misc. Geol. Inv. Map I-546, 1968.

31. Astronomical Photography

PART A

GUM NEBULA, GALACTIC CLUSTER, AND ZODIACAL LIGHT PHOTOGRAPHY

R. D. Mercer,[a] L. Dunkelman,[b] and Thomas K. Mattingly[c]

Purpose

Astronomical photography was performed again from the command module during the night portions of Apollo 16 lunar orbits. This photography was the continuation of work begun two missions earlier (ref. 31-1) and dealt with three phenomena: the diffuse structure of the Gum Nebula, galactic clusters, and zodiacal light. These phenomena all give off light of very low brightness. The phenomena are difficult to study from the surface of the Earth because the atmospheric nightglow creates an intervening veil of light, which obscures them. However, during approximately 20 min of each orbit, when the Moon occults sunlight and earthshine from the spacecraft, surface brightnesses as low as one-tenth of the lowest brightness measurable from the surface of the Earth have been recorded. This doubly shadowed region, the double umbra, also prevents effluent particles, which usually are present to some degree around the spacecraft, from scattering external light into the observing optics.

Command module astronomical photography was performed under the sponsorship of the Apollo Lunar Orbital Photographic Science Team, with the specific objective of capitalizing on the uniqueness of the double umbra as a vantage point to collect astronomical data that are obtainable only near our Moon. For this reason, these data will be compared directly to analogous photography performed from Earth orbit during Project Mercury and the Gemini Program as well as to the Apollo-duplicated photography taken from sites on the Earth surface. Comparison with Earth-based photography should yield direct information on the Earth airglow layer and on atmospheric scattering and extinction.

Theory

The Gum Nebula region was in an accessible position for photography from the double umbra during the Apollo 16 mission. This celestial object was named after the astronomer who performed early studies on the several clouds of radiating gases that seemed completely unrelated to each other. Later, Gum and other scientists realized that it might be a large region of expanding size with these clouds defining its outer boundary. The large apparent size of the Gum Nebula would be caused by its proximity to our solar system, and estimates of its extent currently range from 35° to 90°, with its center in the southern Milky Way. Some (ref. 31-2) describe the Gum Nebula as a supernova remnant of expanding gases, which may be excited to glowing by strong radiations from pulsars recently discovered in its interior.

Because of the bright Milky Way background, clear observation of detailed features of the Gum Nebula is very difficult. Because of its large size, all of its parts can be related only through synoptic photographs. It was hoped that, on the Apollo 16 mission, both of these problems could be reduced. Instead of narrow-band optical filters normally used to avoid the Earth airglow, wide-band filters were used to collect more light. A red filter was used to pass light from glowing hydrogen, and a blue filter was used to pass light from singly and doubly ionized oxygen; both filters excluded most of the excessive Milky Way light.

[a]Dudley Observatory.

[b]NASA Goddard Space Flight Center.

[c]NASA Manned Spacecraft Center.

Exposures of 5-min durations were made of the two different clusters of galaxies specified by Dr. Halton C. Arp of the Hale Observatories in California. One cluster is in the constellation Virgo, and the other is in Centaurus. This work attempted to show the existence of filaments of low-brightness material connecting individual galaxies within these clusters. Radial velocities, as indicated by red-shift measurements, are quite different between some of the apparently adjacent galaxies; therefore, it would seem that the galaxies are not actually in proximity. However, optical proof of connecting gaseous regions between such different neighbors would require an abrupt revision in current thinking on their locations and origins (ref. 31-3).

The zodiacal light photography continued work accomplished successfully on the Apollo 15 mission, but with polarization measurements of the white light. Zodiacal light is sunlight scattered toward the observer by interplanetary dust particles, and this scattering causes a wedge-shaped band of light to be superimposed on the constellations of the zodiac; hence, its name. The maximum change in polarized brightness occurs between two perpendicular planes: the first plane contains the Sun, the spacecraft, and whatever point in the zodiacal light is being observed, and the second plane is perpendicular to the first and also contains the spacecraft and the same point in zodiacal light. A series of photographs with shorter and shorter durations of exposure was taken as the orbiting command module approached sunrise. Two exposures were taken for each celestial position eastward from the Sun along the ecliptic. A plane polaroid filter over the objective lens was set first to one orientation and then to a second orientation 90° in rotation away from the first. Variations in brightness with plane of polarization can provide details on the optical properties and size distributions of these interplanetary particles (ref. 31-4).

Equipment

The photography of these low-brightness sources used the 35-mm Nikon camera with a 55-mm lens, set at f/1.2 and infinity. Eastman Kodak type 2485, black-and-white, high-speed recording emulsion was used. The camera was mounted on a special bracket to use the right-hand rendezvous window. To prevent stray, internal illumination produced by cabin and instrument lights from entering the camera optics, a special window shade was used. This shade, designed for the study of the gegenschein/Moulton region, isolates the window so that reflections and scattering of unwanted cabin light cannot occur.

Filters used for Gum Nebula photography had the following characteristics. The blue filter in combination with transmission properties of the command module window passed wavelengths from approximately 420 to 510 nm. The red filter along with the emulsion cut-off accepted wavelengths from 610 to 700 nm. For the zodiacal light, a standard polaroid filter was modified to make its end-stops of rotation exactly 90° apart. The white light bandpass of the polarized and unfiltered light is 420 to 700 nm, with the coated windowpanes cutting off in the blue and emulsion characteristics cutting off in the red.

Preflight and postflight calibration exposures were added to the flight film. These calibrations were performed by using an illuminated step-wedge from the High Altitude Observatory (ref. 31-5) to provide brightness values in terms of Sun surface brightness. The preflight calibration exposures underwent the same radiation, temperature, pressure, and humidity history as the data frames, and every shutter speed that was planned for use in the data frames was used in the calibrations so that emulsion-reciprocity characteristics could be taken completely into account.

Results

For the Gum Nebula, 1- and 4-min exposures in each color were planned in each of three overlapping regions. Nine frames were acquired for the two most important regions. The photography of the third region had to be omitted as a result of service module engine problems and the 24-hr shortening of lunar orbit time. Preliminary analysis of these data frames shows that vehicle pointing was accurate, and suppression of the Milky Way appears to be quite good. A detailed analysis has not yet begun to locate the oxygen regions with respect to the hydrogen regions. The signal level is very faint, as expected, and positive results are not readily evident at this time. Nevertheless, even small success in photography of the Gum Nebula would add greatly to the data currently being gathered from the ground.

Single 5-min exposures for each of the two galactic cluster regions were obtained successfully. Acquisition of a like exposure of the north ecliptic pole to measure the interstellar brightness in the Milky Way galaxy also was planned. This low-priority target had to be omitted because of the shortened lunar stay.

For the long exposures on the Gum Nebula and the galactic clusters, the spacecraft was pointed at the appropriate celestial target, and vehicle rates were damped for several minutes. Just prior to shutter opening, all thrusters were turned off so that the plumes would not light up any cloud of particles extant around the spacecraft. In a few of the resulting exposures, residual rates caused image smear that will make the data reduction difficult. On the other hand, it is quite remarkable that the demonstrated stability of the vehicle for this astronomical work has already undergone more than a tenfold increase for long exposures over the maximum times considered feasible on the Apollo 14 mission, before image-smear limitations were reached.

The polarized zodiacal light photography was not successful because the preflight-computed pointing information was in error. A series of photographs 20° north of the ecliptic plane resulted. Because the exposure times were specified for in-plane brightnesses, the exposures were of durations too short to provide useful results. However, this series of 28 exposures of zodiacal light presented the command module pilot with a very complex set of manual camera manipulations that had to be performed on a precise schedule before sunrise. Although the polaroid filter came loose in the middle of the exposure series, the command module pilot was able to quickly correct the problem and get back on schedule within the prescribed sequence of photographs while missing proper exposures on only three frames.

PART B

SOLAR CORONA PHOTOGRAPHY

R. M. MacQueen,[a] C. L. Ross,[a] and Thomas K. Mattingly[b]

Introduction

Photographic observations of the solar corona by the Apollo 16 command module pilot while in lunar orbit were designed to provide data on outer coronal forms and intensities to elongation angles[1] of 25°. The results of Apollo 15 solar corona photography verified the procedures and provided the first photographs of identifiable coronal streamers curving at elongation angles of some 10°. By using the Apollo 15 data, exposure settings were optimized for Apollo 16, and the results show a significant improvement in photometric quality over the large range (approximately 10^4) of brightness to be photographed. Ground observations of the inner solar corona (to approximately 2 solar radii from Sun center) indicate a general lack of coronal structure, and results of data reduction thus far show no streamer structure at large elongation angles.

The detailed objective of the observations included two lunar sunrise sequences and two lunar sunset sequences, but revisions to the flight plan, caused by the early return from lunar orbit, would not permit the sunset sequences. Two sequences of the eastern half of the solar corona were therefore obtained in accordance with a procedure that specified seven exposures starting 75 sec before sunrise and ending 10 sec before sunrise. Exposures of 10, 4, 1, 1/2, 1/8, 1/30, and 1/60 sec were made on Kodak 2485 high-speed recording film, using the electric Hasselblad with 80-mm lens at f/2.8. The spectral region photographed with the spacecraft window/2485 film combination is about 425 to 700 nm.

Results

The exposures provide detailed photometric information on the difficult-to-observe region between what is commonly referred to as the zodiacal light and the solar F-coronal light. This region extends from a solar elongation angle of approximately 13.5°, the limit of measurements made by Blackwell (ref. 31-6) from an aircraft during the eclipse of 1954, to

---

[a]High Altitude Observatory.

[b]NASA Manned Spacecraft Center.

[1]The distance from the center of the Sun as measured on the celestial sphere.

solar elongation angles of 20° to 30°, the practical limit of ground-based zodiacal light measurements (refs. 31-7 and 31-8). The Apollo 16 measurements are particularly suited for photometric studies of the F-coronal light, as a result of the lack of solar-electron-scattered coronal features present on the east limb. This was not the case for the Apollo 15 photographs, where the individual streamer structure is evident to large elongation angles.

Photometric reduction of the Apollo 16 measurements are under way, with preliminary scans of the solar equatorial region accomplished on the McBeth model TD-102 quanta log densitometer and detailed scans completed with a 45- by 100-μm slit on the High Altitude Observatory Boller and Chivens model 14213 microphotometer. Extraction of the absolute brightness of the corona from approximately 4 solar radii from Sun center to approximately 80 solar radii from Sun center is under way.

The flight film was calibrated photometrically with a sensitometer developed by the High Altitude Observatory, and all but four frames of coronal data are being reduced. The 1- and 1/2-sec exposures on both sequences are not usable because the Hasselblad shutter remained open for the entire time between the programed start of the 1-sec exposure and the completion of the 1/2-sec exposure. The film transported between programed exposures, creating one exposure of less than 1-sec duration and the other exposure of greater than 10-sec duration.

Figure 31-1 is frame AS16-124-19904, which was taken on April 23, 1972, at 16:40 Greenwich mean time, 75 sec before lunar sunrise. The Sun is approximately 3° below the lunar limb, and the corona is visible clearly at π-Aries, some 13.5° from Sun center.

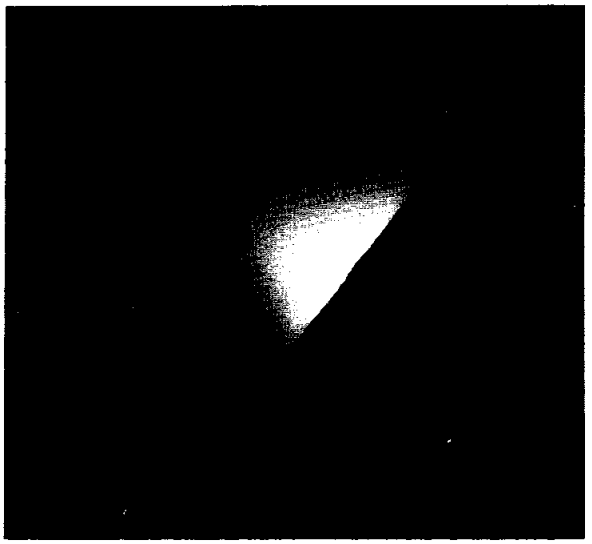


FIGURE 31-1.–The solar corona photographed approximately 75 sec before sunrise on April 23, 1972 (AS16-124-19904).

Acknowledgments

The authors gratefully acknowledge the assistance of R. D. Mercer, Dudley Observatory, and L. Dunkelman, NASA Goddard Space Flight Center, in obtaining these observations.

REFERENCES

31-1. Dunkelman, L.; Mercer, R. D.; Ross, C. L.; and Worden, A.: Astronomical Photography. Sec. 25 of the Apollo 15 Preliminary Science Report, Part T. NASA SP-289, 1972.

31-2. Maran, Stephen P.; Brandt, John C.; and Stecher, Theodore P.: The Gum Nebula–A New Kind of Astronomical Object. Phys. Today, vol. 24, no. 9, Sept. 1971, pp. 42-47.

31-3. Arp, Halton; and Bertola, Francesco: Faint Outer Regions of Elliptical Galaxies. Astrophys. J., vol. 163, no. 1, Jan. 1, 1971, pp. 195-201.

31-4. Hanner, Martha S.: Physical Properties of the Interplanetary Dust. In Part II of Physical Studies of Minor Planets, T. Gehrels, ed. NASA SP-267, 1971, pp. 377-388.

31-5. Pizzo, V.; and Gosling, J. T.: AAS Phot. Bull., vol. 1, 1972, p. 19.

31-6. Blackwell, D. E.: A Study of the Outer Corona From a High Altitude Aircraft at the Eclipse of 1954 June 30. Part I, Observational Data. Monthly Notices Roy. Astron. Soc., vol. 115, no. 6, 1955, pp. 629-649.

31-7. Blackwell, D. E.; and Ingham, M. F.: Observations of the Zodiacal Light From a Very High Altitude Station. Part I, The Average Zodiacal Light. Monthly Notices Roy. Astron. Soc., vol. 122, no. 2, Feb. 1961, pp. 113-127.

31-8. Smith, L. L.; Roach, F. E.; and Owen, R. W.: The Absolute Photometry of the Zodiacal Light. Planet. Space Sci., vol. 13, Mar. 1965, pp. 207-217.

APPENDIX A

Glossary

achondrite–a stony meteorite devoid of rounded granules

agglutinate–a deposit of originally molten ejecta

albedo–the percentage of the incoming radiation that is reflected by a natural surface

anhedral–pertaining to mineral grains that lack external crystals

anorthite–a calcium-rich variety of plagioclase feldspar

anorthosite–a granular, plutonic, igneous rock composed almost exclusively of a soda-lime feldspar

apatite–any of a group of calcium-phosphate minerals that occur variously as hexagonal crystals, as granular masses, or in fine-grained mass as the chief constituent of phosphate rock

aphanite–a dark rock of such close texture that the individual grains are invisible to the unaided eye

aphyric–not having distinct crystals

augite–one of a variety of pyroxene minerals that contain calcium, magnesium, and aluminum; usually black or dark green in color

bleb–a small particle of distinctive material

bow shock–a shock wave in front of a body, such as an airfoil

breccia–a rock consisting of sharp fragments embedded in a fine-grained matrix

Brewster angle–the angle of incidence for which a wave polarized parallel to the plane of incidence is wholly transmitted

bytownite–a calcium-rich variety of plagioclase feldspar

chondrite–a meteoritic stone characterized by the presence of rounded granules

chromosphere–a thin layer of relatively transparent gases above the photosphere of the Sun

cislunar–pertaining to the space between the Earth and the orbit of the Moon

clast–a discrete particle or fragment of rock or mineral; commonly included in a larger rock

clinopyroxene–a mineral that occurs in monoclinic, short, thick, prismatic crystals and that varies in color from white to dark green or black (rarely blue)

coherent–a term used to describe two or more parts of the same series that are in contact more or less adhesively but are not fused

collimator–an optical device that renders rays of light parallel

comminution–the reduction of a substance to a fine powder

conchoidal–a term used to describe a shell-like surface shape that has been produced by the fracturing of a brittle material

cristobalite–an isometric variety of quartz (SiO_2) that forms at high temperatures

Curie temperature–the temperature in a ferromagnetic material above which the material becomes substantially nonmagnetic

dendrite–a crystallized arborescent form

devitrification–the change of a glassy rock from the glassy state to a crystalline state after solidification

diamagnetic–pertaining to substances having a permeability less than that of a vacuum

dielectric constant–a measure of the amount of electrical charge a given substance can withstand at a given electric field strength

dunite–a peridotite that consists almost entirely of olivine and that contains accessory chromite and pyroxene

ephemeris–a tabulation of the predicted positions of celestial bodies at regular intervals

epicenter–the point on a planetary surface directly above the focus of an earthquake

eucrite–a meteorite composed essentially of feldspar and augite

euhedral–pertaining to minerals the crystals of which have had no interference in growth

exsolution–unmixing; the separation of some mineral-pair solutions during slow cooling

fayalite–an iron-rich variety of olivine (Fe_2SiO_4)

fiducial–taken as a symbol of reference

fractional process–separation of a substance from a mixture (e.g., one isotope from another of the same element)

Fresnel zone–any one of the array of concentric surfaces in space between transmitter and receiver over which the increase in distance over the straight line path is equal to some multiple of one-half wavelength

gabbro–a granular igneous rock of basaltic composition with a coarse-grained texture

gardening–the overturning, reworking, and changing of the lunar surface due to such processes as meteoroid impact, volcanic action, aging, and such

gegenschein–a round or elongated spot of light in the sky at a point 180° from the Sun

holocrystalline–consisting wholly of crystals

hypabyssal–pertaining to minor intrusions, such as sills and dikes, and to the rocks that compose them

ilmenite–a mineral rich in titanium and iron; usually black with a submetallic luster

indurated–a term used to describe masses that have been hardened by heat; baked

intersertal–a term used to describe the texture of igneous rocks in which a base or mesostasis of glass and small crystals fills the interstices between unoriented feldspar laths

isostatic–subject to equal pressure from all sides

isotopic–relating to, or having the relationship of any of two or more species of atoms of a chemical element that possess the same atomic number and position in the periodic table and nearly identical chemical behavior but with differing atomic mass or mass number and different behavior in the mass spectrograph, in radioactive transformations, and in physical properties; formed in the same sedimentary basin or geologic province

isotropic–exhibiting properties (as velocity of light transmission) with the same values when measured along axes in all directions

lath–a long, thin mineral crystal

lenticular–having the shape of a double-convex lens

leucocratic–a term used to describe light-colored rock, especially igneous rocks that contain between 0 and 30 percent dark minerals

limb–the edge of the apparent disk of a celestial body

lithic–refers to sediments and rocks in which rock fragments are more important proportionally than feldspar grains

lithification–consolidation and hardening of fines into rock

magcon–a magnetized concentration

magma–molten rock material that is liquid or pasty

magnetopause–the outer boundary of the magnetosphere

magnetosheath–the transition region between the magnetopause and the solar-wind shock wave

magnetosphere–the region of the atmosphere where the geomagnetic field plays an important role; the magnetosphere extends to the boundary between the atmosphere and the interplanetary plasma

magnetotail–a portion of the magnetic field of the Earth that is pulled back to form a tail by solar plasma

mascon–a large mass concentration beneath the surface of the Moon

maskelynite–a feldspar found in meteorites

massif–a mountainous mass

melanocratic–a term used to describe dark-colored rocks, especially igneous rocks that contain between 60 and 100 percent dark minerals

metamorphic–a term used to describe rocks that have formed in a solid state as a result of drastic changes in temperature, pressure, and chemical environment

mica–any of various colored or transparent minerals crystallizing in monoclinic forms that readily separate into very thin leaves

microlite–small lath-shaped minerals, commonly plagioclase feldspar, occurring as minute phenocrysts in basalt

mosaic–a term used to describe the texture sometimes seen in dynamo-metamorphosed rocks that have angular and granular crystal fragments and that appear like a mosaic in polarized light

multiplex–to transmit two or more signals simultaneously within a single channel

muscovite–a mineral that is a colorless to pale brown potassium mica

norite–a type of gabbro in which orthopyroxene is dominant over clinopyroxene

olivine–an igneous mineral that consists of a silicate of magnesium and iron

ophitic–a rock texture characterized by lath-shaped plagioclase crystals enclosed in augite

peridotite–an essentially nonfeldspathic plutonic rock consisting of olivine, with or without other dark minerals

perilune–the orbital point nearest the Moon, when the Moon is the center of attraction

permeability–the ratio of the magnetic induction to the magnetic-field intensity in the same region

phenocryst–a large crystal of the earliest generation in a porphyritic igneous rock

photocathode–a photoelectric cell that emits electrons when exposed to light or other radiation

photogrammetry–the science of obtaining reliable measurements by means of photography

photosphere–the intensely bright portion of the Sun visible to the unaided eye

pigeonite–a variety of pyroxene

plagioclase–a feldspar mineral composed of varying amounts of sodium and calcium with aluminum silicate

plasma–an electrically conductive gas; specifically a mass of ionized gas flowing out of the Sun

plutonic–pertaining to igneous rock that crystallizes at depth

poikilitic–a term used to describe the condition in which small granular crystals are irregularly scattered without common orientation in a larger crystal of another mineral

polarimetry–the measurement of the angle of rotation of linearly polarized light

poloidal–geometric shape of a dipole magnetic field

porphyritic–having larger crystals set in a finer groundmass

pyroxene–a mineral occurring in short, thick, prismatic crystals or in square cross section; often laminated; and varying in color from white to dark green or black (rarely blue)

rarefaction wave–a wave in a compressible fluid such that when a fluid particle crosses the wave in the direction of its motion, the density and pressure of the particle decrease

regolith–the layer of fragmental debris that overlies consolidated bedrock

remanent–pertaining to the residual induction when the magnetizing field is reduced to zero from a value sufficient to saturate the material

schlieren–tabular bodies that occur in pluton, generally several centimeters to several meters long

slickenside–a polished and striated surface that results from friction along a fault plane

solar wind–streams of plasma flowing outward from the Sun

spall–a relatively thin, sharp-edged piece of rock that has been produced by exfoliation

specular reflection–reflection in which the reflected radiation is not diffused

spinel–a mineral that is noted for great hardness ($MgAl_2O_4$)

sporadic meteor–a meteor which is not associated with one of the regularly recurring meteor showers or streams

subhedral–pertaining to minerals that are intermediate between anhedral and euhedral

talus–a collection of fallen disintegrated material that has formed a slope at the foot of a steeper declivity

tectonism–crustal instability; the structural behavior of an element of the crust of the Earth during or between major cycles of sedimentation

tektite–a glassy body of probably meteoritic origin and of rounded but indefinite shape

tephra–a collective term for all clastic volcanic materials that are ejected from the volcano and transported through the air

terminator–the line separating illuminated and dark portions of a celestial body

terra–that portion of the lunar surface other than the maria; the lighter area of the Moon that is visible to the unaided eye

terrane–the area or surface over which a particular rock or group of rocks is prevalent

transponder–a combined receiver and transmitter which transmits signals automatically when triggered by an interrogator

troilite–a mineral that is native ferrous sulfide

vermicular–a term used to describe a group of platy minerals that are closely related to the chlorites and montmorillonites

vesicle–a small cavity in a mineral or rock, ordinarily produced by expansion of vapor in a molten mass

vug–a small cavity in a rock

zircon–a mineral, $ZrSiO_4$; the main ore of zirconium

zodiacal light–a faint cone of light extending upward from the horizon in the direction of the ecliptic

APPENDIX B

Abbreviations and Acronyms

ADC	analog-to-digital converter
AEI	aerial exposure index
AFD	alternating field demagnetization
ALFMED	Apollo light flash moving emulsion detector
ALSEP	Apollo lunar surface experiments package
ALSRC	Apollo lunar sample return container
ASE	active seismic experiment
ATS	Applied Technology Satellite
AZ	azimuth
CDR	commander
CM	command module
CMP	command module pilot
CN	cellulose nitrate
CSM	command and service module
CSSD	contact soil sampling device
CSVC	core sample vacuum container
CTA	cellulose triacetate
DAC	data acquisition camera
DC	data camera
dec	declination
DT	drive tube
DU	digital unit
EVA	extravehicular activity
GCR	galactic cosmic ray
GET	ground elapsed time
GLEP	group for lunar exploration planning
G.m.t.	Greenwich mean time
HFE	heat flow experiment
HZE	high-charge energy
IAU	International Astronomical Union
IMP	Interplanetary Monitoring Platform
IRM	isothermal remanent magnetization
ISA	interim stowage assembly
KG	makrofol
KREEP	potassium, rare-Earth elements, and phosphorus
KSC	John F. Kennedy Space Center
LM	lunar module
LMC	Large Magellanic Cloud
LMP	lunar module pilot
LOI	lunar orbit insertion
LP	long period
LPM	lunar portable magnetometer
LRL	Lunar Receiving Laboratory, NASA Manned Spacecraft Center
LRV	lunar roving vehicle (Rover)
LSM	lunar surface magnetometer
LSPET	Lunar Sample Preliminary Examination Team
LTC	lunar terrain camera
MBA	mortar box assembly
MBF	Molecular Beam Facility, NASA Langley Research Center
MCC	midcourse correction
MEED	microbial ecology evaluation device
MPA	mortar package assembly
MSC	Manned Spacecraft Center
NRM	natural remanent magnetization
PC	polycarbonate
PFS	particles and fields subsatellite
PMT	photomultiplier tube
PSD	pulse-shape discriminator
PSE	passive seismic experiment
PVA	polyvinyl alcohol
RA	right ascension
RCS	reaction control system
REL	restricted energy loss
RTG	radioisotope thermoelectric generator
SCB	sample collection bag
SEM	scanning electron microscope
SIM	scientific instrument module
SIVB	third stage (IVB) of Saturn launch vehicle
SP	short period
SRP	self-recording penetrometer
SWC	solar wind composition
TEC	transearth coast
TEI	transearth injection
TLC	translunar coast
TLD	thermoluminescent dosimeter
TLI	translunar injection
TN	triafol
TOPOCOM	U.S. Army Topographic Command
TV	television
UV	ultraviolet
VHF	very high frequency
VRM	viscous remanent magnetization

APPENDIX C

Units and Unit-Conversion Factors

In this appendix are the names, abbreviations, and definitions of International System (SI) units used in this report and the numerical factors for converting from SI units to more familiar units.

Names of International Units Used in This Report

Physical quantity	*Name of unit*	*Abbreviation*	*Definition of abbreviation*
	Basic Units		
Length	meter	m	
Mass	kilogram	kg	
Time	second	sec	
Electric current	ampere	A	
Temperature	kelvin	K	
Luminous intensity	candela	cd	
	Derived Units		
Area	square meter	m^2	
Volume	cubic meter	m^3	
Frequency	hertz	Hz	sec^{-1}
Density	kilogram per cubic meter	kg/m^3	
Velocity	meter per second	m/sec	
Angular velocity	radian per second	rad/sec	
Acceleration	meter per second squared	m/sec^2	
Angular acceleration	radian per second squared	rad/sec^2	
Force	newton	N	$kg \cdot m/sec^2$
Pressure	newton per square meter	N/m^2	
Work, energy, quantity of heat	joule	J	$N \cdot m$
Power	watt	W	J/sec
Voltage, potential difference, electromotive force	volt	V	W/A
Electric field strength	volt per meter	V/m	
Electric resistance	ohm	Ω	V/A
Electric capacitance	farad	F	$A \cdot sec/V$
Magnetic flux	weber	Wb	$V \cdot sec$
Inductance	henry	H	$V \cdot sec/A$
Magnetic flux density	tesla	T	Wb/m^2
Magnetic field strength	ampere per meter	A/m	
Luminous flux	lumen	lm	$cd \cdot sr$
Luminance	candela per square meter	cd/m^2	
Illumination	lux	lx	lm/m^2
Specific heat	joule per kilogram kelvin	$J/kg \cdot K$	
Thermal conductivity	watt per meter kelvin	$W/m \cdot K$	
	Supplementary Units		
Plane angle	radian	rad	
Solid angle	steradian	sr	

Unit Prefixes

Prefix	Abbreviation	Factor by which unit is multiplied
giga	G	10^9
mega	M	10^6
kilo	k	10^3
centi	c	10^{-2}
milli	m	10^{-3}
micro	μ	10^{-6}
nano	n	10^{-9}

Unit-Conversion Factors

To convert from–	To–	Multiply by–
ampere/meter	oersted	1.257×10^{-2}
candela/meter^2	foot-lambert	2.919×10^{-1}
candela/meter^2	lambert	3.142×10^{-4}
joule	British thermal unit (International Steam Table)	9.479×10^{-4}
joule	Calorie (International Steam Table)	2.388×10^{-1}
joule	electron volt	6.242×10^{18}
joule	erg	1.000×10^{7} a
joule	foot-pound force	7.376×10^{-1}
joule	kilowatt-hour	2.778×10^{-7}
joule	watt-hour	2.778×10^{-4}
kelvin	degrees Celsius (temperature)	$t_C = t_K - 273.15$
kelvin	degrees Fahrenheit (temperature)	$t_F = 9/5\ t_K - 459.67$
kilogram	gram	1.000×10^{3} a
kilogram	kilogram mass	1.000×10^{3} a
kilogram	pound mass (pound mass avoirdupois)	2.205×10^{0}
kilogram	slug	6.852×10^{-2}
kilogram	ton (short, 2000 pound)	1.102×10^{-3}
lumen/meter^2	foot-candle	9.290×10^{-2}
lumen/meter^2	lux	1.000×10^{0} a
meter	angstrom	1.000×10^{10} a
meter	foot	3.281×10^{0}
meter	inch	3.937×10^{1}
meter	micron	1.000×10^{6} a
meter	mile (U.S. statute)	6.214×10^{-4}
meter	nautical mile (international)	5.400×10^{-4}
meter	nautical mile (U.S.)	5.400×10^{-4}
meter	yard	1.094×10^{0}
meter/second^2	foot/second^2	3.281×10^{0}
meter/second^2	inch/second^2	3.937×10^{1}
newton	dyne	1.000×10^{5} a
newton	kilogram force (kgf)	1.020×10^{-1}
newton	pound force (avoirdupois)	2.248×10^{-1}
newton/meter^2	atmosphere	9.870×10^{-6}
newton/meter^2	centimeter of mercury (0° C)	7.501×10^{-4}
newton/meter^2	inch of mercury (32° F)	2.953×10^{-4}
newton/meter^2	inch of mercury (60° F)	2.961×10^{-4}
newton/meter^2	millimeter of mercury (0° C)	7.501×10^{-3}
newton/meter^2	torr (0° C)	7.501×10^{-3}
radian	degree (angle)	5.730×10^{1}
radian	minute (angle)	3.438×10^{3}
radian	second (angle)	2.063×10^{5}

Unit-Conversion Factors--Concluded

To convert from–	*To–*	*Multiply by–*
tesla	gamma	1.000×10^{9} [a]
tesla	gauss	1.000×10^{4} [a]
watt	British thermal unit (thermochemical)/second	9.484×10^{-4}
watt	calorie (thermochemical)/second	2.390×10^{-1}
watt	foot-pound force/second	7.376×10^{-1}
watt	horsepower (550 foot-pound force/second)	1.341×10^{-3}
weber	maxwell	1.000×10^{8} [a]

[a]An exact definition.

NATIONAL AERONAUTICS AND SPACE ADMINISTRATION
WASHINGTON, D.C. 20546

OFFICIAL BUSINESS

FIRST CLASS MAIL

POSTAGE AND FEES PAID
NATIONAL AERONAUTICS AND
SPACE ADMINISTRATION

POSTMASTER: If Undeliverable (Section 1
Postal Manual) Do Not Re

"The aeronautical and space activities of the United States shall be conducted so as to contribute . . . to the expansion of human knowledge of phenomena in the atmosphere and space. The Administration shall provide for the widest practicable and appropriate dissemination of information concerning its activities and the results thereof."

—NATIONAL AERONAUTICS AND SPACE ACT OF 1958

NASA SCIENTIFIC AND TECHNICAL PUBLICATIONS

TECHNICAL REPORTS: Scientific and technical information considered important, complete, and a lasting contribution to existing knowledge.

TECHNICAL NOTES: Information less broad in scope but nevertheless of importance as a contribution to existing knowledge.

TECHNICAL MEMORANDUMS: Information receiving limited distribution because of preliminary data, security classification, or other reasons.

CONTRACTOR REPORTS: Scientific and technical information generated under a NASA contract or grant and considered an important contribution to existing knowledge.

TECHNICAL TRANSLATIONS: Information published in a foreign language considered to merit NASA distribution in English.

SPECIAL PUBLICATIONS: Information derived from or of value to NASA activities. Publications include conference proceedings, monographs, data compilations, handbooks, sourcebooks, and special bibliographies.

TECHNOLOGY UTILIZATION PUBLICATIONS: Information on technology used by NASA that may be of particular interest in commercial and other non-aerospace applications. Publications include Tech Briefs, Technology Utilization Reports and Notes, and Technology Surveys.

Details on the availability of these publications may be obtained from:

SCIENTIFIC AND TECHNICAL INFORMATION OFFICE

NATIONAL AERONAUTICS AND SPACE ADMINISTRATION

Washington, D.C. 20546